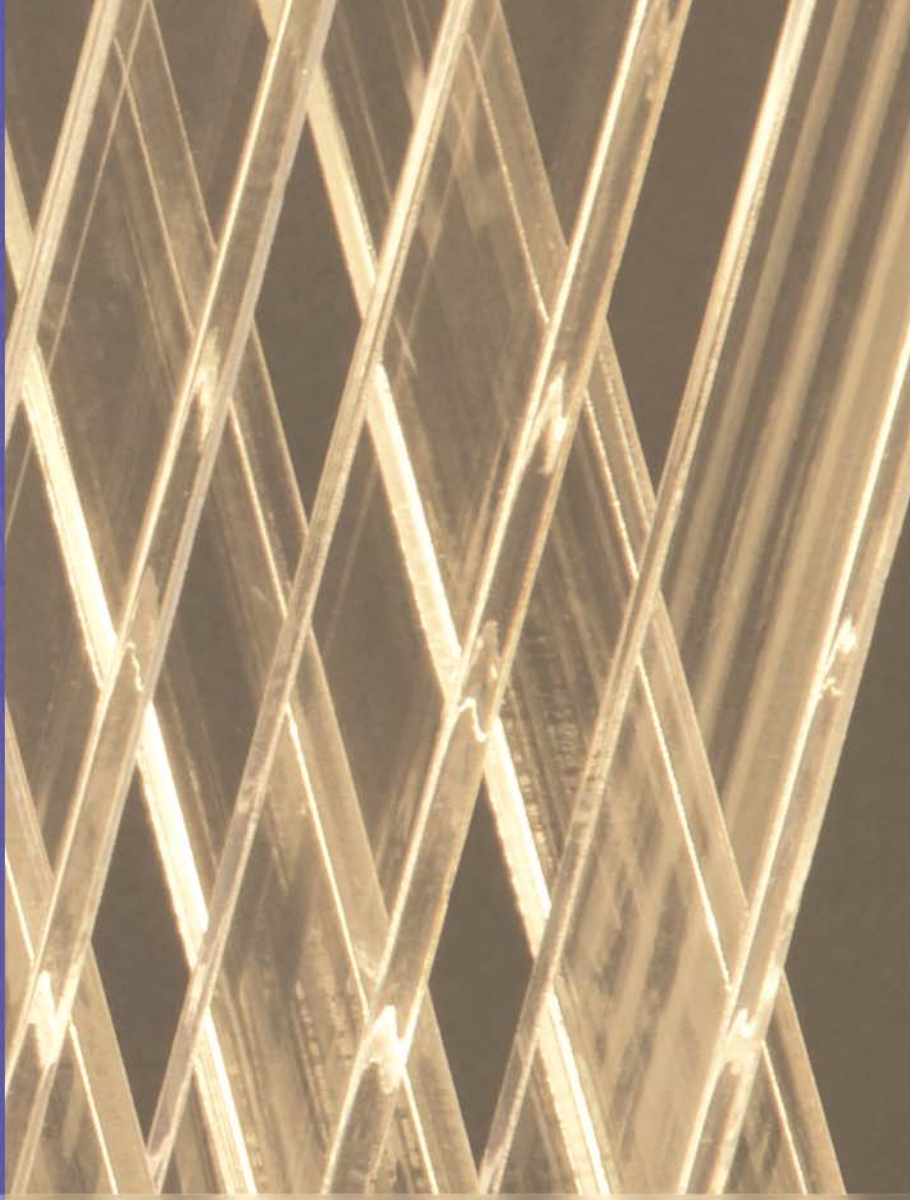

MAX-lab

Activity Report 2009

National Laboratory
Lund Sweden

Activity Report 2009

Edited by

U. Johansson, A. Nyberg, R. Nyholm

Preface

It is time to report another year of fruitful and interesting research and of continued development of the laboratory. The number of annual users is now well over 800. The geographic breakdown remains similar as preceding years with a little less than 50% Swedish users and a continued large number of Nordic and Baltic users.

The user operation develops and there is a continued upgrade of some of the MAX II and MAX III beamlines. During the year there has also been further progress with the test Free Electron Laser (FEL). The original targets have been reached and exceeded. Coherent Harmonic Generation was obtained at the 5th and 6th harmonic of the seed laser, 55 nm and 43 nm, respectively. I want to congratulate the FEL research team for their excellent achievements.

There has been a rapid increase of the MAX-lab staff. This is motivated by the increased number of users and the expanding research activities at MAX-lab as well as by the demands set by the start-up of the MAX IV project.

There have been two evaluations during the year. MAX-lab was evaluated by the Swedish Research Council (VR) as a follow-up of the previous evaluation of the National Laboratories in 2003. The conclusions were very positive. The report states: "MAX-lab is a very successful enterprise in science and technology. Such a conclusion can be reached using international standards, in comparison with the top synchrotron facilities in Europe and in the world" and "MAX-lab has specifically become a recognized leader in experimental methods based on soft X-rays". The report further notes: "MAX-lab has a factual, unmatched record of cost effectiveness both for the construction and operation of facilities. This is a striking point considering the very high quality of its sources and beamline instrumentation as well as the continuing attention to the user needs". The second evaluation concerns the revised design of the MAX IV facility. The previous evaluations have been based on the design with two rings placed on top of each other. The Swedish Research Council therefore decided to conduct a review of the revised design, which is based on a large 530 m 3 GeV ring and a smaller 96 m 1.5 GeV ring. The evaluation panel supports the redesign and concludes that it is technically feasible. They also conclude that the redesign can be made without significant cost increases.

The establishment of the MAX IV project is continuing. The funders of the base version of MAX IV (VR, the Swedish Governmental Agency for Innovation Systems (VINNOVA), Region Skåne and Lund University) are finalizing an agreement that will regulate the initial funding and the organization of the laboratory. The City of Lund has furthermore made significant commitments in connection with the MAX IV site. The site is decided and is now included in the city plan. The task to build and own the MAX IV building has been given to the companies PEAB and Wihlborgs.

I would like to take this opportunity to acknowledge the support by VR, the Knut and Alice Wallenberg foundation (KAW), VINNOVA, the Swedish Foundation for International Cooperation in Research and Higher Education (STINT), the European Commission, Lund University, Region Skåne, Uppsala University as well as all other agencies and organizations that contribute to the funding of the laboratory. Finally, I want to thank the MAX-lab staff and all the users for their excellent work on which the MAX-lab depends so heavily.

Lund June 24, 2010

Nils Mårtensson

Director MAX-lab

Contents

On April 27th at the Old Bishops House in Lund a Memorandum of Understanding was signed between the Swedish Research Council (VR), the Swedish Governmental Agency for Innovation Systems (VINNOVA), Lund University and Region Skåne, defining the start of the MAX IV project. These stakeholders represent a large fraction of the first phase investment costs.
Photo: Annika Nyberg, Bengt-Erik Wingren

MAX-lab Organization December 2009

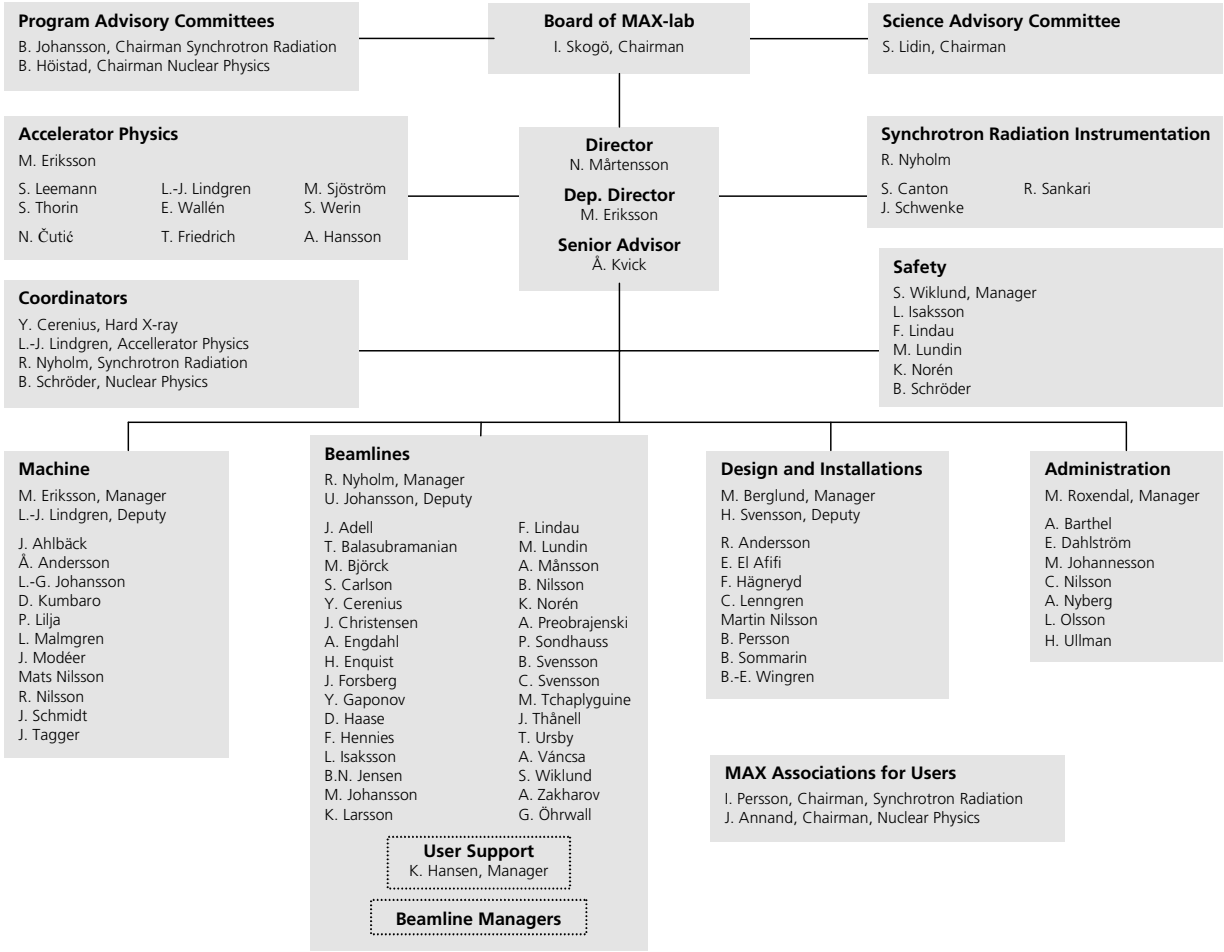

MAX-lab Personnel From January 2009 – December 2009

Department of Accelerator Physics

Position	Name	Area of responsibilities
Professor	Mikael Eriksson	Head of the accelerator physics department and deputy director for MAX-lab
Lecturer (Universitetslektor)	Lars-Johan Lindgren	Research and development in accelerator physics and coordinator for accelerator physics research
Lecturer (Universitetslektor)	Sverker Werin	Research and development in accelerator physics
Research Associate (Forskarassistent)	Erik Wallén	Research and development in accelerator physics
Researcher Forskare	Simon Leemann	MAX IV project
Ph.D. student (Doktorand)	Roderik Bruce	MAX-lab and CERN, theses defence 2009-09-18
Ph.D. student (Doktorand)	Nino Čutić	
Ph.D. student (Doktorand)	Thilo Friedrich	MAX-lab and KTH
Ph.D. student (Doktorand)	Anders Hansson	
Ph.D. student (Doktorand)	Magnus Sjöström	Theses defence 2009-06-03, now on the MAX IV project
Ph.D. student (Doktorand)	Sara Thorin	Theses defence 2009-05-19, now on the MAX IV project

Department of Synchrotron Radiation Instrumentation

Position	Name	Area of responsibilities
Professor	Ralf Nyholm	Head of the synchrotron radiation instrumentation department
Lecturer (Universitetslektor)	Rami Sankari	Research and development of beamlines and instrumentation
Research Associate (Forskarassistent)	Sophie Canton	Research and development of time-resolved X-ray methods
Ph.D. student (Doktorand)	Jörg Schwenke	

Operating staff

Design and Installations

Position	Name	Area of responsibilities
Research engineer (Forskningsingenjör)	Magnus Berglund	Manager
Research engineer (Forskningsingenjör)	Håkan Svensson	Deputy manager

Operating staff, cont.

Design and Installations, cont.

Position	Name	Area of responsibilities
Technician (Instrumentmakare)	Robert Andersson	Workshop, mechanics
Constructor (Konstruktör)	El Sayed El Afifi	Design and construction
Electrical technician (Eltekniker)	Fredrik Hägneryd	Electrical installations
Electrical engineer (Elingenjör)	Claes Lenngren	Responsible for electrical installations
Technician (1:e instrumentmakare)	Martin Nilsson	Workshop, mechanics
Technician (1:e instrumentmakare)	Bo Persson	Workshop, mechanics
Research engineer (Forskningsingenjör)	Bengt Sommarin	Installations
Technician (Tekniker)	Bengt-Erik Wingren	Maintenance, service

Beamlines

Professor	Ralf Nyholm	Manager and coordinator for synchrotron radiation research
Research engineer (Forskningsingenjör)	Ulf Johansson	Deputy manager
Research engineer (Forskningsingenjör)	Kurt Hansen	Head of the user support group
Researcher (Forskare)	Johan Adell	Maintenance of beamlines and experimental stations, especially beamline I4
Research engineer (Forskningsingenjör)	Thiagaraian Balasubramanian	Design, installation and maintenance of beamlines, especially I3 and I4
Researcher (Forskare)	Matts Björck	Design, installation and maintenance of beamlines, especially beamline I1011
Research engineer (Forskningsingenjör)	Stefan Carlsson	Design, installation and maintenance of beamlines, especially beamline I811
Research coordinator (Forskningskoordinator)	Yngve Cerenius	Research coordinator for hard X-ray activities
Researcher (Forskare)	Jeppe Christensen	Design, installation and maintenance of beamlines, especially beamline I711
Research engineer (Forskningsingenjör)	Anders Engdahl	Maintenance of beamlines and experimental stations, especially beamline 73
Researcher (Forskare)	Henrik Enquist	Design of the short-pulse facility for MAX IV
Researcher (Forskare)	Johan Forsberg	Design of the new beamline I511
Researcher (Forskare)	Yury Gaponov	Software development for hard X-ray beamlines
Research engineer (Forskningsingenjör)	Dörthe Haase	Maintenance of hard X-ray beamlines and experimental stations
Researcher (Forskare)	Franz Hennies	Design, installation and maintenance of beamlines, especially beamline I511

Operating staff, cont.

Beamlines, cont.

Position	Name	Area of responsibilities
Research engineer (Forskningsingenjör)	Lennart Isaksson	Nuclear physics and radiation safety
Research engineer (Forskningsingenjör)	Brian N. Jensen	Design, installation and maintenance of beamlines
Research engineer (Forskningsingenjör)	Mikael Johansson	Electronics for the experiments
Research engineer (Forskningsingenjör)	Krister Larsson	Head of computing services and control systems
Research engineer (Forskningsingenjör)	Filip Lindau	FEL test experiments and laser safety
Research engineer (Forskningsingenjör)	Magnus Lundin	Computers for the experiments and radiation safety
Research engineer (Forskningsingenjör)	Anders Månsson	Maintenance of vacuum and cryo systems
Research engineer (Forskningsingenjör)	Björn Nilsson	Nuclear physics
Researcher (Forskare)	Katarina Norén	Design, installation and maintenance of beamlines and experimental stations, especially beamline I811 and chemical safety
Researcher (Forskare)	Alexei Preobrajenski	Maintenance of beamlines and experimental stations, especially beamline D1011
Researcher (Forskare)	Peter Sondhauss	Design and simulation of X-ray optics
Engineer (Ingenjör)	Bertil Svensson	Maintenance of hard X-ray beamlines and experimental stations
Research engineer (Forskningsingenjör)	Christer Svensson	Software development for hard X-ray beamlines
Researcher (Forskare)	Maxim Tchaplyguine	Design, installation and maintenance of beamlines, especially beamline I411
Research engineer (Forskningsingenjör)	Johan Thånell	Maintenance of beamlines and experimental stations
Research engineer (Forskningsingenjör)	Thomas Ursby	Design, installation and maintenance of beamlines, especially beamline I911
Computer engineer (Datortekniker)	András Váncsa	Installation and maintenance of computer systems
Research engineer (Forskningsingenjör)	Stefan Wiklund	Maintenance of beamlines, experimental stations and safety manager
Researcher (Forskare)	Alexei Zakharov	Maintenance of beamlines and experimental stations especially the SPELEEM at beamline I311
Researcher (Forskare)	Gunnar Öhrwall	Design, installation and maintenance of beamlines, especially beamline I1011

Machine

Professor	Mikael Eriksson	Manager
Lecturer (Universitetslektor)	Lars-Johan Lindgren	Deputy manager and coordinator for accelerator physics research
Research engineer (Forskningsingenjör)	Jonny Ahlbäck	Vacuum system design, MAX IV

Operating staff, cont.

Beamlines, cont.

Position	Name	Area of responsibilities
Researcher (Forskare)	Åke Andersson	Maintenance and development of accelerators
Research engineer (Forskningsingenjör)	Lars-Gösta Johansson	High-tension current systems for the accelerators and coordinator for electronics and electrical installations
Research engineer (Forskningsingenjör)	Dionis Kumbaro	Maintenance and operation of accelerators
Research engineer (Forskningsingenjör)	Per Lilja	Maintenance and operation of accelerators
Research engineer (Forskningsingenjör)	Lars Malmgren	Micro-wave electronics for the accelerator system
Project coordinator (Projektsamordnare)	Jonas Modéer	Build-up of accelerators, MAX IV
Research engineer (Forskningsingenjör)	Mats Nilsson	Computers for the accelerator system
Research engineer (Forskningsingenjör)	Robert Nilsson	RF and diagnostics
Research engineer (Forskningsingenjör)	Jerry Schmidt	Development and maintenance of the accelerator system, especially insertion devices
Research engineer (Forskningsingenjör)	Jüri Tagger	Electronics for the accelerator system

Administration

Financial manager (Ekonomichef)	Mats Roxendal	Manager
Administrative officer (Ekonomisekreterare)	Ann Barthel	Office work, invoicing
Administrative officer (Enhetssekreterare)	Elisabeth Dahlström	Office work, reception
Project assistant (Projektassistent)	Markus Johannesson	IRUVX-PP project
Custodian (Lokalvårdare)	Catarina Nilsson	Cleaning
Information officer (Informatör)	Annika Nyberg	Web editor and graphical design
Custodian (Lokalvårdare)	Lisbeth Olsson	Cleaning
Administrative officer (Personaladministratör)	Helena Ullman	Personnel and executive support

Personnel with administrative assignments at MAX-lab

Professor	Nils Mårtensson	Director
Guest Professor	Åke Kvick	Senior advisor
Professor	Bent Schröder	Coordinator for nuclear physics research

Postdoctors and visiting scientists

Position	Name	Beamline	Affiliation
Ph.D. student (Doktorand)	Tomas Andersson	I411	Uppsala University
Postdoctor	Jason Brudvik	Nuclear physics	MAX-lab
Visiting scientist (Gästforskare)	Piotr Goryl	Accelerators	MAX-lab
Postdoctor	Carsten Gundlach	I811	MAX-lab
Research engineer (Forskningsingenjör)	Maria Håkansson	Protein crystallization facility	SARomics Biostructures AB
Postdoctor	Iwona Kowalik	I1011	MAX-lab
Research engineer (Forskningsingenjör)	Mats Leandersson	I3	Chalmers University of Technology
Researcher (Forskare)	Bengt Nelander	73	MAX-lab
Ph.D. student (Doktorand)	May Ling Ng	D1011	Uppsala University
Ph.D. student (Doktorand)	Jesper Nygaard	I711 and I911	University of Copenhagen and MAX-lab
Postdoctor	Prabir Pal	I3	Uppsala University
Ph.D. student (Doktorand)	Andreas Persson	I1011	Uppsala University
Postdoctor	Annette Pietsch	I511	MAX-lab
Postdoctor	Tomás Plivelic	I711 and I911	MAX-lab
Researcher (Forskare)	Janusz Sadowski	MBE at 41 and I3	MAX-lab
Postdoctor	Karina Schulte	I311	MAX-lab
Research engineer (Forskningsingenjör)	Keld Theodor	I911	University of Copenhagen and MAX-lab
Postdoctor	Wimal Ubhayasekera	I911	University of Copenhagen
Ph.D. student (Doktorand)	Intikhab Ulfat	MBE at 41 and I3	Chalmers University of Technology
Postdoctor	Johan Unge	I911	MAX-lab
Researcher (Forskare)	Per Uvdal	73	Lund University and MAX-lab
Visiting scientist (Gästforskare)	Adriana Wawrzyniak	Accelerators	MAX-lab
Ph.D. student (Doktorand)	Nikolay Vinogradov	D1011	Uppsala University
Ph.D. student (Doktorand)	Chaofan Zhang	I411	Uppsala University

General Information

Introduction

MAX-lab is a Swedish National Laboratory for research using synchrotron radiation and high-energy electrons and for research in accelerator physics. The laboratory is based upon a linac injector, a storage/pulse-stretcher ring, MAX I, and two third generation storage rings, MAX II and MAX III.

During 2009 MAX-lab has accommodated about 850 scientists representing scientific groups from more than 150 industry, academic and government laboratories from more than 30 countries.

Synchrotron radiation based research at both MAX I and MAX II is done in a large variety of disciplines including surface science, semiconductor physics, materials science, atomic and molecular physics, chemistry, biology, medicine and environmental science.

At the 550 MeV MAX I storage ring there are four beamlines for synchrotron radiation research in the infra-red through VUV photon energy range using various spectroscopic techniques. At the 1.5 GeV MAX II storage ring thirteen beamlines are now in operation. Three planar undulators and one EPU for the VUV and soft X-ray regions are used for various spectroscopic techniques. Three multi-pole wigglers, two of which have superconducting magnets, are used for absorption and diffraction experiments in the X-ray region. In addition to these insertion device beamlines also two bending magnet ports are utilized. For the MAX III ring one planar undulator and one EPU are used for spectroscopy in the UV and VUV regions.

In the pulse-stretcher mode the MAX I ring is used for experiments in nuclear and hadron physics. The electron energy range available is at present 145 to 200 MeV, resulting in monochromatic photons from 15 to 185 MeV. The program used 18 weeks of beam time in 2009.

Prof. Nils Mårtensson **Director**	**Prof. Mikael Eriksson** **Deputy Director**	**Reception**
Phone: +46-(0)46-222 96 95	Phone: +46-(0)46-222 76 96	Phone: +46-(0)46-222 98 72 Fax: +46-(0)46-222 47 10
nils.martensson@maxlab.lu.se	mikael.eriksson@maxlab.lu.se	maxlab@maxlab.lu.se

Mailing address: MAX-lab, Lund University, P.O. Box 118, SE-221 00 Lund, SWEDEN
Visiting address: Ole Römers väg 1, Lund, SWEDEN
Web-site: www.maxlab.lu.se

Organization

MAX-lab is operated by Lund University (LU) under a contractual agreement with the Swedish Research Council (Vetenskapsrådet, VR). VR is responsible for the main operating budget, the scientific programs and periodic reviews of the activities. As host university LU is responsible for employee relations and the conventional facilities.

Since March 1, 2004, until February 28, 2009, MAX-lab has been part in the Integrated Infrastructure Initiative (I3) "Integrating Activity on Synchrotron and Free Electron Laser Science" (IA-SFS). Since March 1, 2009, this program has been followed by the I3 program "European Light Sources Activity" (ELISA). This means that a number of European projects within synchrotron radiation research are sponsored, including support for travel and subsidiary costs for users from EU and other associated countries.

An outline of the internal organization of MAX-lab is found on page 1 in this report.

MAX-lab is governed by a Board, consisting of six members and a chairperson. The Board is appointed by LU. Two members of the Board are chosen upon recommendation by VR and two by the User's Organization (FASM). The Board appoints the Director of MAX-lab.

The current members of the Board are listed in table I.

The Board of MAX-lab is charged with the responsibility of working towards national and international use of the laboratory, to prepare and monitor the operating budget, to prioritize the research programs and facility developments, to appoint personnel, and to promote the overall growth and development of the laboratory. The MAX-lab Board also decides how to divide the operating time between research with synchrotron radiation, energetic electrons, accelerator physics research and system maintenance and development. To facilitate these decisions the Board has appointed program advisory committees (PACs) and a scientific advisory committee (SAC) to guide it on matters connected with the scientific programs and facility developments at the laboratory. The committees consist of national and international scientists whose backgrounds encompass the various areas of research which are possible at MAX-lab.

The members of the program advisory committees are listed in table II and the members of the scientific advisory committee in table III.

Table I

Board of MAX-lab
July 2007 - June 2010

Member	Representing
I. Skogö	Chairman
A. Borg	VR
L. Kloo	VR
M. Fahlman	Users
S. Svensson	Users
B. Söderström	Lund University
S. Sörensen	Lund University

Table II

MAX-lab Program Advisory Committees (in 2009)

Synchrotron Radiation

B. Johansson, Chairman	Uppsala, Sweden
H. Aksela	Oulu, Finland
M.C. Asensio	Paris, France
D. Chandesris	Paris, France
R. Feidenhans'l	Copenhagen, Denmark
R. Fourme	Paris, France
M. Gajhede	Copenhagen, Denmark
Å. Kvick	Lund, Sweden
L.H. Tjeng	Köln, Germany
K. Wilson	York, UK
D.P. Woodruff	Warwick, UK

Energetic Electrons

B. Höistad, Chairman	Uppsala, Sweden
J. Ahrens	Mainz, Germany
D. Phillips	Ohio, USA
D. Watts	Edinburg, UK

Table III

MAX-lab Scientific Advisory Committee

S. Lidin, Chairman	Stockholm, Sweden
L. Braicovich	Milano, Italy
C. Nave	Daresbury, UK
B. Schoch	Bonn, Germany
A. Wrulich	Villigen, Switzerland

Research

MAX-lab supports three distinct areas of research: Accelerator physics, research based on the use of synchrotron radiation and nuclear physics research using energetic electrons. The use of the facility is shared by the groups working in these three research areas as is the responsibility for different aspects of the facility.

The laboratory is operated primarily in a user oriented fashion. Those interested in making experiments using synchrotron radiation or the electron-beam facility should obtain more information from the coordinators (see table IV) about requirements for experiments and available equipment. Technical information on beamlines and experimental stations can also be found on the MAX-lab web-site, www.maxlab.lu.se.

Table IV

MAX-lab Research Coordinators

Synchrotron Radiation	**Energetic Electrons**	**Accelerator Physics**
Prof. Ralf Nyholm	Prof. Bent Schröder	Ass. Prof. Lars-Johan Lindgren
Phone: +46-(0)46-222 44 52	Phone: +46-(0)46-222 76 36	Phone: +46-(0)46-222 94 66
ralf.nyholm@maxlab.lu.se	bent.schroder@maxlab.lu.se	lars-johan.lindgren@maxlab.lu.se

Mailing address: MAX-lab, Lund University, P.O. Box 118, SE-221 00 Lund, SWEDEN
Visiting address: Ole Römers väg 1, Lund, SWEDEN

Those who wish to make experiments using synchrotron radiation or energetic electrons should apply in the form of a research proposal to the appropriate coordinator. Proposals are periodically reviewed by the MAX-lab Program Advisory Committees (see Table III), and scheduling of time on beamlines is made by the research coordinators based upon user requests.

Most of the beamlines are equipped with experimental chambers, analyzers and detectors available to all users. In addition some user groups provide their own experimental set-ups. More information about the storage ring parameters and the beamlines may be found in the introductions to the sections on accelerator physics research, synchrotron radiation research and research with energetic electrons in this report.

The machines are usually operated 24 hours per day, six days per week. Each week one day is devoted to machine maintenance and development of storage ring instrumentation.

The users should take full responsibility for carrying out their research projects and thus should become familiar with the experimental equipment and data-taking systems which are available at the laboratory before they begin the experiments in order to optimize the use of beam time. User equipment which is used in the ultra-high vacuum environment required for connection to the storage ring and monochromators must be checked and approved by the laboratory.

Safety guidelines pertaining to samples and experimental procedures must also be followed by users. Prior to experiments all participating researchers must register their beamtime through our web-server. Also a declaration of substances and hazardous equipment has to be submitted to MAX-lab for approval.

Much of the design of monochromators and experimental equipment is the result of collaborations with research groups outside MAX-lab. If a user group is seeking funding for equipment which is intended for use at MAX-lab, the proposal should be discussed with MAX-lab so that planning can be made together with the laboratory personnel. Funding organizations in Sweden may appeal to the laboratory staff for information on the feasibility of projects connected to the laboratory. This ensures that new equipment will be compatible with the standards of the laboratory and with the existing beamline structure.

User Associations

MAX Association for Synchrotron Radiation Users at MAX-lab – FASM

The 22nd annual meeting of the "Föreningen för Användare av Synkrotronljuset vid MAX-laboratoriet"/"The association for Synchrotron Radiation Users at MAX-lab", FASM, took place November 2-4, 2009, at hotel Scandic Star in Lund, with more than 300 registered attendants. The meeting was coordinated with a number of small workshops devoted to beamlines at the planned MAX IV facility, entitled "New Highly Brilliant Coherent X-Ray Sources: Imaging and Dynamics", "Macromolecules Crystallography at MAX IV", "Micro- and Nano Focusing Beamlines: Prerequisites", "High-Energy Beamline on MAX IV", "Laser Back-scattering at MAX IV", "XAFS Spectroscopy at MAX IV", "Medical Imaging/Therapy Using Synchrotron Radiation", "Opportunities in Soft X-Ray Spectroscopy at New Synchrotron Radiation Sources" and "Tomography and Imaging".

The detailed program of the meeting can be found at:
http://www.maxlab.lu.se/usermeeting/2009/index.html

All users of the MAX-lab facility are encouraged to become members of the FASM organization, which aims to have a broad participation involving all parts of the user community and efficient communication with the MAX-lab broad and management. It is thereby possible to communicate current and future needs within the user community and the MAX-lab Board. At the same time the association disseminates information to the users about MAX-lab plans and prospects. FASM's mission is increasingly important as the user community is growing rapidly and more scientific disciplines are actively using the MAX-lab facility. In view of this, FASM will introduce a number of proposals aimed to strengthen the activities at MAX-lab and be of further aid to new users. Scientists interested in becoming members of the association for Synchrotron Radiation Users at MAX-lab should contact:

Ingmar Persson
Department of Chemistry, Swedish University of Agricultural Sciences
P.O. Box 7015, SE-750 07 Uppsala, Sweden
E-mail: Ingmar.Persson@kemi.slu.se

Table V

Board of Association for Synchrotron Radiation Users (FASM)	
I. Persson, Chairman	Uppsala, Sweden
L. Arleth	Copenhagen, Denmark
K. Børve	Bergen, Norway
E. Kukk	Turku, Finland
R. Neutze	Göteborg, Sweden

MAX Association for Nuclear Physics Users

The Association of Nuclear Physics Users at MAX-lab met on November 3 at the MAX-lab Annual User Meeting at Hotel Scandic Star in Lund. The program consisted of status reports from ongoing experiments and a more general session where the research activities at the tagged photon facility were discussed. The PAC did not meet this time. The detailed program of the meeting is found on:

http://www.maxlab.lu.se/usermeeting/2009/sessions/nuclear_meeting.html

Election of the board of the Association resulted in the following composition: John Annand, University of Glasgow (chairperson), William Briscoe, George Washington University and Lennart Isaksson, Lund University. Peter Grabmayr, University of Tübingen, remains as election coordinator.

The possibilities for a laser backscattering facility at MAX IV were discussed at a workshop on November 4. For the electron energy of the MAX IV ring, a 500 MeV polarized photon beam would be obtained, of large interest for hadronic and nuclear research. Similar existing facilities (although at different energies) were presented by four invited speakers and the opportunities at MAX IV were discussed. The detailed program of the workshop is found on:

http://www.maxlab.lu.se/usermeeting/2009/sessions/backscattering.html

The Association for nuclear physics users at MAX-lab has the following composition:

Table VI

Board of MAX Association for Nuclear Physics Users	
J.R.M. Annand, Chairman	Glasgow, Scotland UK
W. Briscoe	Washington, USA
P. Grabmayr, Election coordinator	Tübingen, Germany
L. Isaksson	Lund, Sweden

Commercial utilization of MAX-lab

MAX-lab is selling synchrotron radiation beamtime as well as consulting services in connection to this. Several companies are regular customers at the laboratory. MAX-lab can furthermore provide consulting services in accelerator technology and synchrotron radiation instrumentation. Further information can be obtained from our director Nils Mårtensson.

A macromolecular crystallization facility is available at MAX-lab. The facility is operated under a contractual agreement with SARomics Biostructures AB and is at present used approximately equally for commercial and academic projects.

Workshops and schools

High Resolution Electron Spectroscopy – Future and Perspectives, SOLEIL, France, February 3-4, 2009.

The workshop High Resolution Electron Spectroscopy – Future and Perspectives was held at the SOLEIL synchrotron site February 3-4, 2009. The workshop attracted 25 registered attending participants, from European countries and from the USA. The workshop was organised jointly by the two clusters of Large Scale Infrastructures; the I3 on Synchrotron and Free Electron Laser Science (IA-SFS) and the RTRA – Triangle de la Physique in Paris, France. Three commercial firms active in building high performance electron spectrometers were present and gave their view of the future.

The scope of the workshop was to collect the leading experts and commercial firms and identify roadmaps for the future development of electron spectroscopy at the upcoming 4th generation ultra brilliant storage rings, short pulse facilities and FEL's. Applications were presented from experiments with ultra high resolution and with experience from the FLASH facility. Also plans for other future sources were presented.

The organizing committee consisted of Prof. Svante Svensson (Uppsala University and SOLEIL) (Chair and organizer), Prof. Nils Mårtensson (MAX-lab), Prof. Wolfgang Eberhardt (Helmholtz Zentrum Berlin (BESSY II)), Dr. Catalin Miron (SOLEIL) and Dr. Paul Morin (SOLEIL).

The speakers were:
Svante Svensson, Uppsala University, Sweden and SOLEIL, France
Mitsuse Masuki, MB Scientific AB, Sweden
Nils Mårtensson, MAX-lab, Sweden
Thorsten Kampen, Specs GmbH, Germany
Herrmann Dürr, BESSY, Germany
Amina Taleb, SOLEIL, France
Paul Morin, SOLEIL, France
Luc Patthey, SLS, Switzerland
Fulvio Parmigiani, ELETTRA, Italy
Catalin Miron, SOLEIL, France
Peter Johnson, BNL, USA
Gerd Ganteför, Uni-Konstanz, Germany
Oscar Tjernberg, KTH, Sweden
Alexander Föhlisch, Uni-Hamburg, Germany
Måns Lundqvist, VG-Scienta AB, Sweden
John Bozek, LCLS, USA

Material from the workshop is available on:
http://www.maxlab.lu.se/euproject/i3_n2/index.html

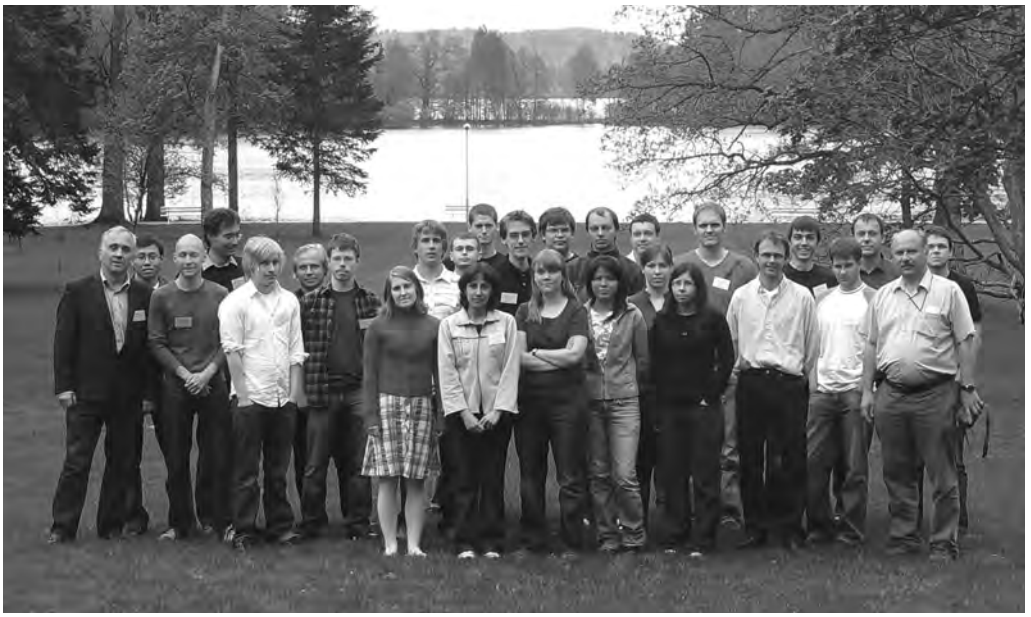

New methods using ultra-high brilliant sources for surface and cluster physics, Summer course for Nordic and Baltic Research Students, Pühajärve Estonia, May 18-23, and June 7-8, 2009, MAX-lab.

The school has been meant to broaden the PhD students' outlook in the field of advanced spectroscopic methods and tools based on synchrotron and X-ray radiation. Thus the scope of the 2009 school has been somewhat narrower than of those from the previous years. The first part of the school with lectures given by international experts took place in Estonia at a conference centre on the bank of a picturesque lake at Pühajärve, the lake deeply connected with the local history and legends. There were more than 20 participating PhD students from Nordic and Baltic countries, and from St.Peterburg, Russian Federation. The lectures dwelt on various theoretical and experimental issues of synchrotron-based spectroscopies utilizing already existing facilities. Also some aspects of the arising X-ray sources, namely free electron lasers were illuminated. The second part of the school was arranged as usual at MAX-lab, and included practical measurements at four different spectroscopy beamlines: I311, I411, I511 and D1011. Also two lectures were given at MAX-lab, with connection to the experimental techniques and equipments used at synchrotron radiation facilities for producing and utilizing X-ray radiation. At the end of this second part the students presented posters on their own research.

Lecturers and Organizers:

Arvo Kikas, Tartu University, Estonia
Edwin Kukk, Turku University, Finland
Svante Svensson, Uppsla University, Sweden
Stacey Ristinmaa Sörensen, Lund University, Sweden
Gordon Robb, University of Strathclyde, Scotland
Alexander Föhlisch, Institute Methods and Instruments for Synchrotron Radiation Research, Germany
Knut Børve, University of Bergen, Norway
Gunnar Öhrwall, MAX-lab, Lund University
Anne Borg, Trondheim University, Norway
Anders Mikkelsen, Lund University, Sweden
Stephan Fritzsche, Oulu University
Rami Sankari, MAX-lab, Sweden
Denis Céolin, Lund University, Sweden
Maxim Tchaplyguine, MAX-lab, Sweden

More information is found on:
http://www.maxlab.lu.se/nordforsk/summerschool/index.html

Course in Small Angle X-ray Scattering, MAX-lab, Lund, August 20 and August 27, 2009.

A practical course for small angle X-ray scattering (SAXS) experiments at beamline I711 was held at two occasions in August 2009. The objective was that the predominantly local (Lund / Copenhagen) students should be able to independently collect SAXS data on the I711 beamline after the course. In total more than 20 students participated in the course. The focus was on practical beamline related advices and measurements on real samples although the initial steps of data treatment using different software packages were also covered. The experience was that the course gave the staff an opportunity to explain both the set-up in details and also issues like data collection strategies which is often difficult to cover during a hectic beamtime shift.

XAFS for beginners, Workshop, MAX-lab, Lund, October 5-4, 2009.

The workshop, XAFS for beginners, is a comprehensive introduction to the field of X-ray absorption fine structure (XAFS) data collection and analysis. It was organized by MAX-lab and lectured by Prof. I. Persson (SLU, Uppsala), K. Norén, S. Carlson, S. Werin and S. Wiklund (MAX-lab). The aim of the workshop was to introduce basic concepts of XAFS experiment design, theory and data analysis. It was divided into a first three-day part with a more practical orientation, and a second six-day part for theory and analysis. The first three days were dedicated to synchrotron radiation facilities, insertion devises, beamlines, safety training and, in particular, the operation of beamline I811. The following six days were spent mainly on XAFS theory and data analysis using the software EXAFSPAK. Two evenings (and nights) were used for data collection on samples provided by the workshop participants. The workshop was truly international with 21 participants from Sweden, Denmark, Germany, Hungary, Spain and Brazil.

More information is found on:
http://www.maxlab.lu.se/maxlab/workshops/xafs/index.html

Outreach Activities

On August 14, 2009, a study day was organized, at MAX-lab, for teachers from local high-schools. The idea was to promote the teacher's awareness of MAX-lab activities in general, and the planned activities for teachers and their students in particular. Over 40 teachers from five high-schools visited experimental stations and learned about synchrotron radiation and its applications. The study day was highly appreciated by the participants, and encouraged by the feedback a three-day workshop will be organized for physics teachers in collaboration with the National Centre for Education in Physics (http://www.fysik.org/) on June 14-16, 2010. During this workshop 30 teachers nation-wide have a possibility to test the experiments planned for high-school students at MAX-lab. Plans to continue with both of these outreach activities (teacher workshop and student experiments) have also been made. During the fall 2009 preparations were done for the first pilot project with high school students. The students visited MAX-lab in February 2010 and the activities are described on page 94-95.

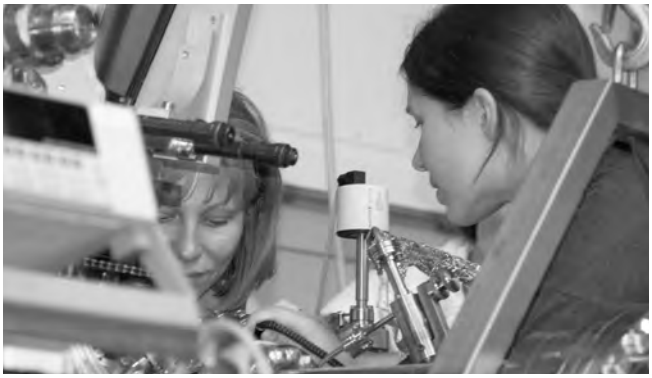

Annette Pietzsch is demonstrating the experimental station at beamline I511 during the study day for teachers.
Photo: Annika Nyberg

Åke Andersson, accelerator physicist, is celebrated on his birthday, January 2009.
Photo: Annika Nyberg

Floor maintenance in the experimental hall, January 2009.
Photo: Annika Nyberg

List of Users at MAX-lab January 2009 – December 2009

University of **Aarhus**, Denmark

Center for Structural Biology

M. Blaise, M. Bublitz, O. Jensen Hamming, R. Kidmose

Department of Chemistry

M. Andersen, J. Becker, H. Birkedal, B. Brummerstedt
T. Cao, M. Christensen, P.R. Christensen, J. Rostgaard Eltzholtz
B. Iversen, K.M. Ørnsbjerg Jensen, T.R. Jensen, N. Lock
J. Mi, C. Holm Olesen, D. Ravnsbäk, B. Richter
L. Houkjær Sørensen, C. Tyrsted, H. Yin

Department of Inorganic Chemistry

O. Gaarn Larsen, B. Jensen, U. Jensen, M. Krüger Thomsen
J. Skovgaard

Department of Molecular Biology

C.B.F. Andersen, G.R. Andersen, J.L. Andersen, B. Arnou
T. Boesen, J.D. Clausen, P. Gourdon, M. Grøftehauge
Y. He, A.K. Kantcheva, M. Laursen, X. Liu
S. Midtgaard, M. Nyblom, S.R. Midtgaard, T. Steffensen
S. Thirup, D. Vaicaityte, I. Vandecaetsbeek, A.-M. Lund Winther

Department of Physics

R. Balog, L. Merte

Interdisciplinary Nanoscience Center (iNANO)

T. Kollin, W. Kudernatsch, M. Brix Ley, S. Porsgaard
L. Holdt Rude, H. Zeuthen

Aberystwyth University, United Kingdom

Institute of Mathematical and Physical Sciences

G.O. Jones, N. Poolton

Swedish University of Agricultural Sciences, **Alnarp**, Sweden

Agricultural Systems, Technology and Product Quality

R. Kuktaite

National Hellenic Research Foundation, **Athens**, Greece

Institute of Organic and Pharmaceutical Chemistry

S. Zographos

Structural Biology and Chemistry Group

C. Drakou

Novo Nordisk A/S, **Bagsværd**, Denmark

J.K. Jacobsen E. Johansson G. Schluckebier

Indian Institute of Science, **Bangalore**, India

Department of Physics

D. Choudhury

University of **Bergen**, Norway

Department of Chemistry

M. Abu-samha K. Børve J. Harnes R. Hatteland
A. Holme V. Myrseth L.J. Sæthre A. Wagner
M. Winkler M. Gundersen Zahl

Fritz-Haber-Institut der Max-Planck-Gesellschaft, **Berlin**, Germany

Department of Molecular Physics

Y. Dedkov Y. Rehder M. Weser

Helmholtz-Zentrum, **Berlin**, Germany

BESSY

J. Bahrdt K. Holldack

Technische Universität **Berlin**, Germany

P. Vogt

Bielefeld University, Germany

Department of Physics

A. Helmstedt M. Sacher

Eka Chemicals AB, **Bohus**, Sweden

M.C. Camerani Pinzani

University of **Bologna**, Italy

Department of Physics

E. Callini L. Pasquini R. Persiani

MTA – MFA, **Budapest**, Hungary

Thin Fim and Nanosystems Laboratory

C. Sandor Daroczi G. Peto

University of **Cambridge**, United Kingdom

Department of Physics

L. De Los Santos Valladares D. Lee J. Seo

Chiba University, Japan

Graduate School of Advanced Integration Science

T. Kuzumaki K. Sakamoto

University of **Coimbra**, Portugal

Department of Chemistry

J. Balogh, H. Burrows, T. Costa, R. Evans, D. Lundberg

University of **Copenhagen**, Denmark

Department of Basic Sciences and Environment

L. Arleth, R. Hoeiberg-Nielsen, L. Malik, H. Munch, J. Nygaard

Department of Biology

J. Gotthardt Olsen

Department of Chemistry

M. Andersson, N. Bovet, U. Christensen, S. Christoffersen, J.A. Cuesta-Seijo, C. Ebbesen Jessen, C. Hem, M. Javadi, J. Langholm Jensen, M. Johnson, V. Karlsson, L. Lo Leggio, S. Nedel, J. Nielsen, H. Otten, C. Schack Pedersen, J.-C. Poulsen, K. Krighaar Rasmussen, I. Sánchez, K. Krarup Sand, E. Shkondin, E. Svensson, H. Osholm Sörensen, M. Thymark, S. Torpenholt, R.W. Andersen, D. Welner, S. Wendel, C. Wilkens

Department of Medicinal Chemistry

A. Ceravalls, O. de Barrios, M. Fiorentini, V. Foderà, K. Frydenvang, M. Gajhede, H. Hald, J. Sandholm Kastrup, C. Krintel, J. Kristensen, O. Kristensen, O. Mirza, M. Møller, P. Naur, P. Sørensen, L. Thomsen, R. Venskutonyte, B. Vestergaard

Department of Neuroscience and Pharmacology

K. Madsen, T. Thorsen

Department of Physics

M. Glyvradal

Niels Bohr Institute

R. Feidenhans'l, D. Khakhulin, H. Till Lemke, L. Nuccio, K. Theodor

Delft University of Technology, The Netherlands

Applied Sciences (TNW-R3-RD&M)

A.J.J. Bos

Leibnitz Institute for Solid State and Materials Research, IFW, **Dresden**, Germany

Electronic and Optical Properties

V. Aristov

IFF

O. Molodtsova

Dublin City University, Ireland

School of Physical Sciences

A. Cafolla C. Doyle S. Krasnikov

Trinity College **Dublin**, Ireland

School of Physics

D. Cockburn J. Cunniffe B. Kennedy C. McGuinness
D. McNally

Duke/TUNL, **Durham, NC**, USA

Department of Physics

S. Stave

Eindhoven University of Technology, The Netherlands

Chemical Engineering and Chemistry

T. Verhoeven

Department of Applied Physics

A. Dzwilewski

Scheikundige Technologie

H. Gericke K.-J. Weststrate

University of Twente, **Enschede**, The Netherlands

MESA+ Institute for Nanotechnology

M. de Jong Y. Lee

SKB, **Figeholm**, Sweden

D. Svensson

Technische Universität München, **Garching**, Germany

Department of Physics

P. Feulner

GKSS Research Centre, **Geesthacht,** Germany

Institute of Materials Research

C. Bonatto Minella U. Bösenberg M. Dornheim R. Gosalawit
C. Pistidda I. Saldan

Hagedorn Institute, **Gentofte**, Denmark

Receptor Systems Biology Laboratory

N. Kulahin

SOLEIL Synchrotron, **Gif sur Yvette**, France

M.C. Asensio J. Avila

University of **Glasgow**, United Kingdom

Physics and Astronomy

R. Al Jebali J.R.M. Annand D. Hamilton K. Livingston
D. MacGregor

Karl-Franzens University, **Graz**, Austria

Department of Experimental Physics

F. Allegretti F. li F.P. Netzer S. Surnev

ESRF, **Grenoble**, France

A. Labrador M. Orlova

Göteborg University and Chalmers University of Technology, Sweden

Chemical and Biological Engineering

C. Ekberg K. Larsson K. Rödström W. Wahlgren
S. Westenhoff

Department of Applied Physics

L. Ilver J. Kanski L. Simonsson I. Ulfat

Department of Chemistry

D. Arnlund G. Fischer E. Nazarenko R. Neutze

Department of Energy and Environment

J. Groot

Department of Physics

H. Starnberg

Environmental Inorganic Chemistry

B.-M. Steenari

Nuclear Chemistry

E. Aneheim A. Fermvik A. Knutsson T. Retegan
G. Skarnemark

Universität **Göttingen**, Germany

Institut für Physikalische Chemie

M. Nedic R. Wugt Larsen

DESY, **Hamburg**, Germany

CFEL

J. Schulz

Universität **Hamburg**, Germany

Institut für Experimentalphysik

M. Berglund A. Föhlisch

Universität **Heidelberg**, Germany

Angewandte Physikalische Chemie

F. Chesneau S. Rausch M. Zharnikov

University of **Helsinki**, Finland

Department of Chemistry

L. Khriachtchev T. Rajala

Hiroshima University, **Higashi-Hiroshima**, Japan

Graduate School of Science

K. Kanomaru

Hiroshima Synchrotron Radiation Center

K. Miyamoto

Japan Atomic Energy Research Institute, **Hyogo**, Japan

Synchrotron Radiation Research Center

A. Agui

University of **Ioannina,** Greece

Department of Physics

S. Foulias M. Kamaratos D. Vlachos

Yeditepe University, **Istanbul**, Turkey

Department of Chemical Engineering

S. Bucak

Karlstad University, Sweden

Department of Physics

A.S. Anselmo L. Ericsson J. Hirvonen Grytzelius L. Johansson
E. Moons K. Svensson H. Zhang

Keuka College, **Keuka Park, NY**, USA

Department of Chemistry

T. Carroll

University of **Kiel**, Germany

Institute of Experimental and Applied Physics

S. Hellmann E.B. Ludwig D. Rahn K. Rossnagel

Kiev National T. Shevchenko University, Ukraine

Department of Physics

I. Doroshenko

National Kyiv Taras Shevchenko University, **Kiev**, Ukraine

Experimental Physics Department

V. Pogolerov

Institute for Energy Technology, **Kjeller**, Norway

Department of Physics

M. Knaapila

Indian Association for the Cultivation of Science, **Kolkata**, India

Department of Materials Science

S. Jana S. Ray

Universität **Konstanz**, Germany

Fachbereich Physik

M. Fonin P. Leicht

Jagiellonian University, **Kraków**, Poland

B. Penc P. Starowicz

University of Kentucky, **Lexington, KY**, USA

Department of Physics

M. Kovash K. Shoniyozov

Linköping University, Sweden

Department of Physics, Chemistry and Biology (IFM)

M. Ahrén L. Axelsson S. Braun E. Carlegrim
J. Eriksson M. Fahlman L. Johansson F. Li
L. Lindell X. Liu M. Magnuson J. Osiecki
H. Muhammad Sohail R. Uhrberg K. Uvdal C. Vahlberg
C. Virojanadara Y. Zhan

Technical University of **Lodz**, Poland

Biotechnology and Food Sciences

I. Redzynia

Institute of Technical Biochemistry

A. Bujacz G. Bujacz

University College **London**, United Kingdom

School of Chemistry

G. Thornton

Polish Academy of Sciences, **Lotników**, Poland

I. Kowalik

Lund University, Sweden

Department of Accelerator Physics

N. Čutić, M. Eriksson, A. Hansson, S. Leemann, L.-J. Lindgren, M. Sjöström, S. Thorin, E. Wallén, S. Werin

Department of Atomic Physics

C. Erny, M. Harb, A. Jurgilaitis, J. Larsson, E. Mansten, H. Navirian, R. Nüske, C. von Korff-Schmising

Department of Biochemistry and Structural Biology

E.-C. Ahlgren, S. Al-Karadaghi, K. Fornvik, M. Hasan, C. Helgstrand, R. Johansson, S. Kadhirvel, W. Lambert, S. Rajan, C. Söderberg, C. Söderberg, M. Thunnissen, R. Yengo

Department of Cell and Organism Biology

T. Saravanamuthu

Department of Chemical Engineering

A. Andersson, R. Häggblad, M. Massa

Department of Chemical Physics

P. Uvdal

Department of Combustion Physics

F. Ossler, L. Vallenhag

Department of Experimental Medical Science

G. Svensson

Department of Food Technology, Engeneering and Nutrition

O. Börjesson

Department of Geology

J. Lindgren

Department of Nuclear Physics

V. Avdeichikov, K. Fissum, P. Golubev, B. Jacobsson, B. Schröder, S. Shende

Department of Organic Chemistry

C.J. Wallentin, O. Wendt, K. Wärnmark

Department of Physical Chemistry 1

A. Abbas, V. Alfredsson, J. Algotsson, M. Asad Ayoubi, A. Bilalov, M. Björklund, J. Carlstedt, C. Cenker, T. Garting, A. Gonzalez-Perez, S. Gustavsson, J. Janiak, M. Knitter, P. Knöös, G. Lazzara, P. Nilsson, A. Nowacka, T. Nylander, U. Olsson, N.V. Reichhardt, A.R. Salah, S. Santos, S. Schetzberg, K. Schillén, B. Silva, E. Sunneskär, T. Suutari, M. Yanez, M. Zackrisson

Department of Polymer & Materials Chemistry

S. Hansen

Department of Synchrotron Radiation Instrumentation

S. Canton, R. Nyholm, R. Sankari, J. Schwenke

Department of Synchrotron Radiation Research

J. Andersen, E. Ataman, S. Blomberg, B. Calvet, D. Céolin, M. Gisselbrecht, J. Gustafson, E. Hilner, M. Hjort, C. Isvoranu, A. Ahmad Kirmani, J. Knudsen, J. Laksman, E. Lundgren, A. Mikkelsen, E. Månsson, H. Qin, A. Sankari, J. Schnadt, S. Sörensen, R. Timm, R. Westerström

Department of Theoretical Chemistry

M. Segad

Division of Solid Mechanics

H. Levin, P. Ståhle

ESS Scandinavia

S. Botegård

Lund Observatory

R. Blackwell-Whitehead, H. Hartman, S. Huldt, T. Lennartsson, H. Nilsson

MAX-lab

J. Adell, Å. Andersson, T. Balasubramanian, J. Brudvik, S. Carlson, Y. Cerenius, A. Engdahl, H. Enquist, K. Hansen, F. Hennies, L. Isaksson, B. Jensen, U. Johansson, I. Kowalik, K. Larsson, P. Lilja, F. Lindau, M. Lundin, L. Malmgren, B. Nelander, B. Nilsson, R. Nilsson, K. Norén, A. Pietsch, T. Plivelic, A. Preobrajenski, J. Sadowski, K. Schulte, P. Sondhauss, C. Svensson, M. Tchaplyguine, J. Unge, T. Ursby, P. Warnicke, S. Wiklund, A. Zakharov, G. Öhrwall

Numerical Analysis and Scientific Computing

E. Hansen

SARomics Biostructures AB, **Lund**, Sweden

M. Håkansson, D. Logan

Tetra Pak, **Lund**, Sweden

J. Wahlberg

University of **Lübeck**, Germany

Institute of Biochemistry

S. Chen, G. Hansen, R. Hilgenfeld, J.R. Mesters, R. Ponnusamy, R. Saleem Batcha, H. Schmidt, R. Wrase

Haldor Topsoe A/S, **Lyngby,** Denmark

R. Christensen, P. Beato, A. Boubnov, M. Höj, F. Morales Cano, A. Puig-Molina, A. Stahl, T.V.W. Janssens

Technical University of Denmark, **Lyngby,** Denmark

Department of Chemical and Biochemical Engineering

J.-D. Grunwaldt M. Beier B. Voss

Department of Chemistry

J. Boesen H.E.M. Christensen L. Haahr P. Harris
C.G. Hartmann M.N. Løvgreen K. Ståhl T. Vognsen

Department of Micro- and Nanotechnology

A. Berthold D. Snakenborg S.S. Nielsen

Department of Systems Biology

F. Fredslund

Instituto de Ciencia de Materiales de **Madrid**, CSIC, Spain

Intercaras y Crecimiento

M.E. Davila

Universidad Autónoma de **Madrid**, Spain

Departemento de Fisica de la Materia Condensada

J.J. de Miguel A.F. Estrada Parra F.J.L. Gutierrez E. Michel
P. Prieto M.A. Valbuena L. Walczak

Universidad Politécnica de **Madrid**, Spain

ISOM

M.P. Dominguez

Malmö University, Sweden

BML/BMT; Faculty of Health and Society

J. Engblom V. Kocherbitov Y. Znamenskaya

University of **Manchester**, United Kingdom

Faculty of Life Sciences

K. Pogson

School of Electrical & Electronic Engineering

B. Towlson

School of Physics and Astronomy

W. Flavell D. Graham S. Hardman

Campus de Luminy, **Marseille**, France

CINaM-CNRS

B. Aufray G. Le Lay

Mersin University, Turkey

Electrical Technologies

O.M. Ozkendir

Montgomery College, **Montgomery County, MD**, USA

M. Litwack

Moscow Engineering Physics Institute, Russia

Physics of Solid State and Nanosystems

A. Ivanov

Russian Research Centre, **Moscow**, Russia

ISSSPH

M. Tsetlin

Ludwig-Maximilians-Universität, **München**, Germany

Department of Earth and Environmental Sciences

A. Laumann

Novo Nordisk A/S, **Måløv**, Denmark

M. Norrman A. Svensson

Hvitfeldtska Gymnasiet, **Mölnlycke**, Sweden

Fysikinstutitionen

V. Lindén

University of **Newcasle upon Tyne**, United Kingdom

School of Chemical Engineering and Advanced Materials

R. Little L. Siller

University of Massachusetts Dartmouth, **North Dartmouth, MA**, USA

Department of Physics

C. Allen J. Lemrise G. O'Rielly

University of East Anglia, **Norwich**, United Kingdom

School of Chemical Sciences and Pharmacy

Y. Chao K. Wang Q. Wang

University of **Nottingham**, United Kingdom

School of Physics and Astronomy

A. Britton J.N. O'Shea A. Rienzo A. Saywell
M. Weston

Université d'Orléans, **Orléans**, France

Centre de Recherche sur la Matière Divisée

S. Guillot S. Serieye

Université Paris Sud, **Orsay**, France

Laboratoire de Physique des Solides

A. Mougin

LIXAM

M. Gisselbrecht

The Andrzej Soltan Institut for Nuclear Studies, **Otwock**, Poland

Plasma Physics and Technology

R. Nietubyc K. Nowakowska Langier

University of **Oulu**, Finland

Department of Biochemistry

P. Kursula V. Majava B. Saligram Prabhakar A. Haapalainen
K. Koski M. Myllykoski O.G. Uzodinma R. Wierenga

Department of Physical Sciences

H. Aksela S. Aksela A. Calo' S. Fritzsche
S. Heinäsmäki M. Huttula S.-M. Huttula D. Iablonskyi
K. Jänkälä T. Kantia A. Kettunen M.-H. Mikkelä
A. Mäkinen J. Niskanen S. Osmekhin L. Partanen
M. Patanen P. Turunen S. Urpelainen

Consejo Superior de Investigaciones Cientificas, **Oviedo**, Spain

Instituto Nacional del Carbon

L. Fernandez J.L. Menendez M. Suarez

University of **Oviedo**, Spain

Department of Physics

C.Q. Fernández

University of **Oxford**, United Kingdom

Inorganic Chemistry Laboratory

D. Payne H. Zhang

Laboratoire de Chimie Physique Matiere et Rayonnement, LCPMR, **Paris**, France

J. Palaudoux M. Simon

Université Paris Sud 11, **Paris**, France

Laboratoire de Chimie Physique Matière Rayonnement

S. Lacombe

Université Pierre et Marie Curie – **Paris** VI, France

Institut des Nanosciences de Paris

I. Bidermane S. Boudet N. Witkowski

Laboratoire de Chimie Physique Matière Rayonnement

C. Bomme F. Bournel J.-J. Gallet R. Guillemin
D. Pierucci

University of Bordeaux 2, **Pessac-Cedex**, France

C. Petibois

University of **Potsdam**, Germany

Department of Physics and Astronomy

M. Herzog

Adam Mickiewicz University, **Poznan**, Poland

Department of Macromolecular Physics

M. Kozak | Z. Pietralik | M. Taube | K. Maciej

Faculty of Chemistry

J. Darul | W. Nowicki

Institute of Physics, **Prague**, Czech Republic

Physics of Surfaces

I. Bartos | M. Cukr | P. Jiricek

Institute of Protein Research RAS, **Pushchino**, Russia

The X-ray group

O. Kravchenko | A. Nikuln | S. Tishchenko

University of **Reading**, United Kingdom

Department of Chemistry

T. Eralp | I. Hamley | G. Held | C. Moulton
R. Nicklin | A. Shavorskiy

Weizmann Institute of Science, **Rehovot**, Israel

Computing Center

M. Taragin

University of Iceland, **Reykjavik**, Iceland

Department of Physics

S. Olafsson | B. Qi

Latvian Biomedical Research and Study Center, **Riga**, Latvia

K. Tars

University of Latvia, **Riga**, Latvia

Institute of Solid State Physics

A.Kuzmin

CNR, **Rome**, Italy

ISM

P. De Padova

Risø National Laboratory – DTU, **Roskilde**, Denmark

DTU Nanotech
S. Ndoni

Materials Research
J. Oddershede

Radiation Research
K. Jensen

University of **Roskilde**, Denmark

Department of Physics
J. Eriksen

Faculty of Medicine, University of **Sherbrooke**, Canada

Nuclear Medicine and Radiobiology
M. Huels

Empa, **St Gallen**, Switzerland

Protection and Physiology
S. Chatterjee P. Brühwiler

University of **St. Petersburg**, Russia

Insitute of Physics
A. Vinogradov

Karolinska Institute, **Stockholm**, Sweden

Department of Biosciences and Nutrition
X. Lou

Department of Cell- and Molecular Biology
M. Hallberg E. Seif

Department of Medical Biochemistry and Biophysics
S. Eshaghi M. Moche M. Rapp T. Sandalova
G. Schneider R. Schnell M. Siponen

Structural Genomics Consortium
P. Schuetz M. Welin M. Wisniewska

Royal Institute of Technology (KTH), **Stockholm**, Sweden

AlbaNova, Section of Atomic and Molecular Physics
E. Rachlew

Department of Applied Electrochemistry
M. Klett P. Svens R. Wreland Lindström

Department of Biotechnology
C. Divne T.C. Tan

Department of Material Physics

B. Agnarsson, S. Ahmadi, M. Berntsen, B. Bruhn, R. Dumas, O. Götberg, M. Göthelid, K. Olsson, D. Stoltz, J. Weissenrieder, S. Yu, M. Zuleta

Fiber and Polymer Technology

N. Sanandaji

Land and Water Resources Engineering

J.P. Gustafsson, C. Sjöstedt

Wood Biotechnology

O. Spadiut

Stockholm University, Sweden

Department of Biochemistry and Biophysics

M. Högbom, A. Magnusdottir, M. Tarry

Department of Materials and Environmental Chemistry

L. Eriksson, D. Gebauer, D. Grüner, L. Han, N. Hedin, A. Inge, J. Sun, P.-E. Werner, E. Wetterskog, H. Yue, X. Zou

Department of Physics

L. Gerén, K.M. von Würtemberg, P. Salen, P.-E. Tegnér, P. Van der Meulen

YKI, Institute for Surface Chemistry, **Stockholm**, Sweden

R. Corkery, D. Kalnin

Max-Planck Institute for Metals research, **Stuttgart**, Germany

Dosch Department

C. Ellinger, A. Vlad

Max Planck Institute for Solid State Research, **Stuttgart**, Germany

Interface Analysis Group

A. Al-Temimy, C. Coletti, S. Forti, T. Iwasaki, U. Starke, K. Emtsev, C. Riedl

University of **Szeged,** Hungary

Department of Inorganic and Analytical Chemistry

E. Bajnoczi, A. Pallagi, P. Sipos, D.F. Sranko

Tampere University of Technology, Finland

Institute of Physics / Surface Science Laboratory

H. Ali-Löytty, M. Hirsimäki, P. Jussila, M. Valden

University of **Tartu**, Estonia

Biomedical Technology

V. Hauryliuk

Institute of Physics

U. Joost, A. Kikas, V. Kisand, K. Kooser
I. Kuusik, T. Käämbre, E. Nõmmiste, R. Pärna

University of **Tokyo**, Japan

Department of Chemistry, School of Science

M. Ohtomo

Trento University, Italy

Department of Physics

M. Boselli

INFM, **Trieste**, Italy

TASC Laboratory

A. Kivimäki

Sincrotrone **Trieste**,Basovizza, Italy

L. Badano, P. Craievich, M. Nino, G. Penco
L. Rumiz, M. Trovo`

University of **Tromsø**, Norway

Institute of Pharmacy

L. Cavalcanti

HIST, Sør-Trøndelag University College, **Trondheim**, Norway

Department of Technology

T. Højberg Andersen

Norwegian University of Science and Technology, **Trondheim**, Norway

Department of Physics

A. Borg, J.B. Flöystad, J.O. Fossum, T. Höjberg Andersen
Z. Rozynek, I.-H. Svenum, L.E. Walle

University of **Turku**, Finland

Department of Chemistry

J. Hölsä, T. Laamanen, M. Lastusaari, L. Rodrigues
L.C.V. Rodrigues

Department of Physics

M. Ahola-Tuomi, J. Dahl, S.S. Granroth, K.D.T. Ha
M. Heinonen, E. Itälä, L. Järvinen, H. Karhu
E. Kukk, M. Kuzmin, P. Laukkanen, J. Leiro
J. Lång, S. Mattila, R. Perälä, V. Tuominen

Universität **Tübingen**, Germany

Physikalisches Institut

P. Grabmayr D. Middleton C. Schmitt

Swedish Defense Research Agency, FOI, **Umeå**, Sweden

Department of Threat Assessment

F. Ekström

Division of NBC Defense

A. Hörnberg

Swedish University of Agricultural Sciences, **Umeå**, Sweden

Department of Forest Ecology

R.-M. Kronberg U. Skyllberg

Umeå University, Sweden

Department of Chemistry

M.Bergknut A. Edwin M. Hall T. Karlsson
E. Lundberg M. Murphy P. Persson U.H. Sauer
E. Sauer-Eriksson A. Sundman

Department of Odontology

N. Forsgren Å. Nylander K. Persson

Swedish University of Agricultural Sciences, **Uppsala**, Sweden

Department of Chemistry

G. Almkvist A. Hernell C. Johansson V. Kessler
D. Lundberg O. Nikonova I. Persson G. Seisenbaeva
N. Torapava

Department of Molecular Bioscience

G. Askarieh H. Hansson T. Ishida S. Karkehabadi
N. Mikkelsen S. Sooriyaarachchi K.Valegård J. Zhang
M. Wu

Uppsala University, Sweden

Department of Biochemistry and Organic Chemistry

P. Vasudev

Department of Cell and Molecular Biology

C. Björkelid A. Jansson T.A. Jones M.C. Juergens
C.S. Koh M. Selmer T. Unge

Department of Materials Chemistry

Y. Brandt Andersson K. Ciosek K. Edstrom R. Eriksson
R. Eriksson T. Gustafsson E. Lewin

Department of Nuclear and Particle Physics

S. Ohlsson T. Johansson E. Thomé

Department of Pharmacy

J. Gråsjö

Department of Physics and Materials Science

D. Arvanitis
E. Göthelid
E. Henke
O. Karis
R. Marinho
P. Pal
S. Plogmaker
H. Rensmo
M.N. Shariati
M. Wikberg
O. Björneholm
A. Hagfeldt
H. Hollmark
R. Knut
M.L.Ng
P. Palmgren
W. Pokapanich
J.-E. Rubensson
H. Siegbahn
N. Vinogradov
R. Cherifi
M. Hahlin
E. Johansson
V. Lebec
J. Nordgren
A. Persson
C. Puglia
A. Sandell
S. Svensson
K. Fransson
M. Hedlund
I. Josefsson
A. Lindblad
N. Ottosson
M.N. Piancastelli
D. Ragazzon
R. Schölin
J. Vegelius

Department of Photochemistry & Molecular Science

J. Davidsson
A. Nasedkin

Engineering Sciences / Solid State Electronics

J. Andersson

Nanotechnology and Functional Materials

E. Jämstorp

Physical and Analytical Chemistry

S. Kaufmann

Brookhaven National Labs, **Upton**, USA

NSLS/ 725 D

D. Arena

University of Illinois, **Urbana, IL**, USA

Department of Physics

L. Myers
A. Nathan

Carlsberg Laboratory, **Valby**, Denmark

A. Henriksen
R. Jorgensen
M. Palcic
V. Pye

Universidad de **Valencia** Burjassot, Spain

Fisica Aplicada y Electromagnetismo

J.F.S. Royo

Nencki Institute of Experimental Biology, **Warsaw**, Poland

Biochemistry

P. Wilk

Polish Academy of Science, **Warsaw**, Poland

Institute of Bioorganic Chemistry

W. Rypniewski

Institute of Catalysis and Surface Chemistry
R. Socha

Institute of Physics
B. Kowalski R. Minikayev W. Paszkowicz M. Pietrzyk
E. Werner-Malento A. Wolska

George Washington University, **Washington, DC**, USA

Department of Physics
W. Briscoe J. Feldman

Purdue University, **West Lafayette**, USA

Department of Physics
Y. Pushkar

University of Natural Resources and Applied Life Sciences, **Vienna,** Austria

Food Science
M. Klausberger

University of **Vienna**, Austria

Department of Structural and Computational Chemistry
M. Beich-Frandsen K. Djinovic

Institute of Biochemistry, **Vilnius**, Lithuania

Department of Bioanalysis
J. Barauskas M. Jankunec

Vilnius University, Lithuania

General Physics and Spectroscopy
J. Ceponkus V. Sablinskas S. Strazdaite

Ural Division of the Russian Academy of Sciences, **Yekaterinburg**, Russia

Institute of Metal Physics
V. Galakhov

Institute of Solid State Chemistry
A. Semenova

ETH **Zürich**, Switzerland

Department of Materials
D. Koziej

Örebro University, Sweden

School of Science and Technology
E. Grahn N. Nathalie

Lars Malmgren and Robert Nilsson next to the old modulator, August, 2009.
Photo: Annika Nyberg

Dionis Kumbaro next to the new modulator, August, 2009.
Photo: Annika Nyberg

Accelerator Physics and Machine Development

Jacek Osiecki preparing experiments at beamline I3, November, 2009.
Photo: Annika Nyberg

Mikael Eriksson, Per Lilja, and Dionis Kumbaro are taking turns supervising the machine in the control room, August, 2009.
Photo: Annika Nyberg

Machine and Accelerator Physics

There are three storage rings at MAX-lab: MAX I, MAX II and MAX III. All three rings are used for synchrotron radiation production and the MAX I ring is also used for experiments in nuclear physics, working as a pulse-stretcher.

The continuous upgrade of the accelerators is paying off. So is the MAX injector now operating more smoothly with faster transitions between the different operating modes and the beam current and beam lifetime in MAX II has been increased to their theoretical limits.

The studies on **the MAX IV facility** has been deepened and the work on a Detailed Design Report has started. Prototypes for critical items like girders, magnets and RF equipment are being built and characterized.

The FEL experiments at the MAX injector are progressing well. The electron beam has been characterized at the FEL, the gun laser system is upgraded as well as the timing system.

The MAX injector is primarily used for injection into the three storage rings and for free electron laser (FEL) experiments. One of the klystrons and the FEL gun laser has also been used for conditioning and characterization of the FERMI gun (ELETTRA).

The MAX I ring is injected at 190 MeV and the MAX II and MAX III rings at 380 MeV.

This injector consists of an RF gun and two S-band linac sections 5.2 m long equipped with SLED cavities. A recirculation magnet system is used to double the electron energy. These linacs are now conditioned to a little more than 100 MeV energy gain each and the maximum energy gain for both linacs is 210 MeV. By recirculating the electron beam once through the linacs, a maximum electron energy of 420 MeV can be reached.

The RF electron gun used for injection is equipped with a thermal cathode. This gun is quite reliable, but the beam quality is rather poor, due to space-charge effects during the early acceleration in the gun. The performance of this thermionic gun is however quite sufficient for injection into the rings.

For the FEL runs, a photo-cathode has been installed to deliver an electron beam suitable for these experiments.

A 400 kV DC gun is being developed for injection purposes. The beam from this gun will be chopped and bunched prior to injection into the linacs.

The MAX injector is now quite reliable and negligible time is lost due to malfunctioning of this accelerator.

The MAX I ring has been brought up to a higher performance regarding beam lifetime by improvement of the vacuum system.

In the pulse-stretching mode for nuclear physics, the properties of the electron beam are now rather close to the design values and the ring and injector are working under stable conditions.

The MAX II ring is now working as well as a low-energy injected storage ring can do. The electron beam stability is in the micrometer range. Close to 300 mA is injected twice a day and with a beam lifetime of 5-6 Ah some 160 mA remains at the next injection. The mean current is now exceeding 200 mA. 7% of the total time is spent on injection and ramping of the lattice magnets, undulators and the superconducting wigglers. The 100 MHz RF system is now equipped with circulators.

The MAX III ring is now conditioned and delivers beam to the first two beamlines. The beam lifetime has improved to some 1-1,5 Ah, which is what can be expected from a low energy storage ring with small emittance.

Machine Parameters

Injector Linac	
Max. energy	420 MeV
Pulse current	50 mA
Pulse length	50 ns
Energy spread	Not verified
Emittance	Not verified
MAX I RING	
Storage mode	
Max. energy	550 MeV
Max. circ. current	300 mA
Hor. emittance	40 nm rad
RF	500 MHz
Bunch length (FWHM)	80 ps
Beam lifetime	4 h
Pulse-stretcher mode	
Electron energy	144, 188 MeV
Duty factor	75 %
Stretched pulse current	20 nA
MAX II RING	
Max. energy	1.5 GeV
Max. circ. current	290 mA
Hor. emittance	8.8 nm rad
RF	100 MHz
Beam lifetime	5-6 Ah (25-30 h at 200 mA)
MAX III RING	
Max. energy	700 MeV
Max. circ. current	300 mA
Hor. emittance	14 nm rad
RF	100 MHz
Beam lifetime	1-1.5 Ah

Reports from Accelerator Physics

COHERENT HARMONIC GENERATION RESULTS AT THE TEST FEL AT MAX-LAB

N. Čutić, F. Lindau, S. Thorin, S. Werin, MAX-lab, Lund, Sweden, J. Bahrdt, K. Holldack, BESSY GmbH, Berlin, Germany, C. Erny, E. Mansten, Dep. for Atomic Physics, Lund University, Sweden

With the aim of testing the design and performance relevant for the proposed seeded FEL light sources a test facility for a seeded Harmonic Generation (HG)-FEL [1] has been completed at MAX-lab[2, 5]*. The aim is to study the processes around seeded harmonic generation at 130/88/54 nm, the 2/3/5 harmonic of a Ti:Sapphire laser. During 2009 the first results have been recorded of coherent radiation at 133 nm, the second harmonic.*

The test FEL is built around the existing linac injector at MAX-lab. This source can provide 400 MeV electrons from an RF-gun. A combined laser system both driving the photo cathode in the gun and, synchronised via an optical fibre, the seed laser pulse has been installed. An optical klystron, consisting of two 30 period undulators and a 4-magnet chicane, has been built by the Helmhotz Zentrum Berlin (HZB) and installed at MAX-lab. Beam loss monitors along the optical klystron are in use and a THz system for additional synchronisation studies installed. A system to measure the overlap between seed laser pulses and electron pulses with 1 ps precision, utilising an Electron optical (EO) crystal has been built.

In December 2009 the first Coherent Harmonic Genration was achieved at the second harmonic, 133 nm, of the seed laser.

LAYOUT OF THE FACILITY

A schematic view of the facility can be seen in figure 1.

Accelerator and transport

The MAX-lab injector [3] consists of a thermionic gun, a linac and a beam transport system. Using the gun together with a 10 ps, 263 nm laser pulse has turned out very well as a photo cathode gun for injection into the FEL.
The acceleration is done in the two linac structures each providing 100 MeV and passed twice to give a total beam energy of around 400 MeV. The magnetic optics in the recirculator and following chicane and dogleg provide enough first and second order momentum compaction for compressing the beam and producing a short spike of high current electrons needed for the FEL interaction.

FEL and OK

The main component of the test facility is the optical klystron [4] which was provided by HZB and consists of a modulator undulator (λ_w=48 mm, N=30, K=2.34, planar type), a radiator undulator (λ_w=56 mm, N=30, K=1.05) which is an APPLE II type undulator plus an intermediate magnetic chicane.

Laser system

The laser system is a combined system which provides both the RF gun pulse and the seed laser pulse for the Harmonic generation. The two parts are placed almost 100 m apart and synchronised via a fibre link.
A laser oscillator (Femtolasers Synergy, 93.71 MHz, 790 nm central wavelength, bandwidth 13 nm FWHM) is locked to the 3 GHz system with a time jitter less than 400 fs. The oscillator is common for both the seed and the gun laser.
The gun laser system was also used for the initial tests of the FERMI@Elettra RF gun, in a temporary set up at MAX-lab in an Elettra – MAX-lab collaboration.

RESULTS

The commissioning process has been performed alternating with the routine operation for users of the MAX-lab facility.
By focusing the seed laser onto the electron beam in the modulator undulator we create the necessary energy modulation. This is then transformed into a density modulation with the same period as the seed laser wavelength (263 nm) in the chicane. The thus micro bunched beam enters the radiator undulator, where it can radiate coherent photons at 263 nm and harmonics of this wavelength, depending on the gap of the radiator undulator.

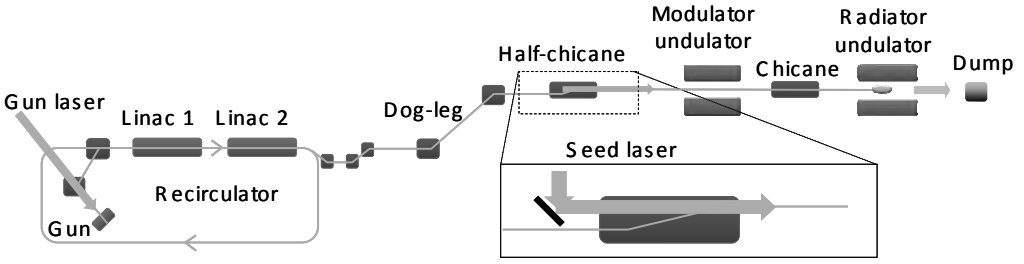

Figure 1. Layout of the MAX-lab test-FEL.

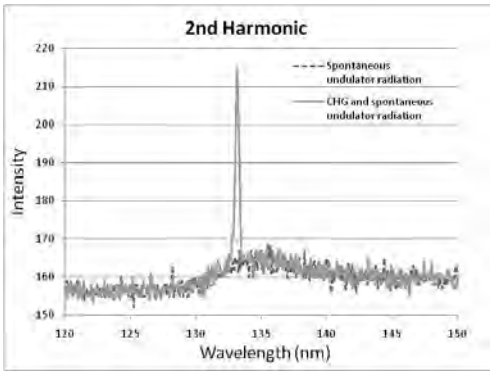

Figure 2. Spectrum of the radiation around 133 nm. blue-dashed: only spontaneous radiation, greed-solid: spontaneous+coherent signal.

Figure 2 shows the signal at the second harmonic, 133 nm, of the seed laser. Here the modulator undulator is tuned to 263 nm to allow resonance with the seed laser and thus the imprint of energy spread. The radiator undulator is tuned to 133 nm, which is then the first harmonic of the radiator. In Figure 2 the characteristic linewidth narrowing of the coherent signal relative the spontaneous is clearly seen. The coherent enhancement is also seen. The linewidth of the coherent signal is limited by the spectrometer resolution, and thus the spectral enhancement in the coherent signal is larger than recorded.

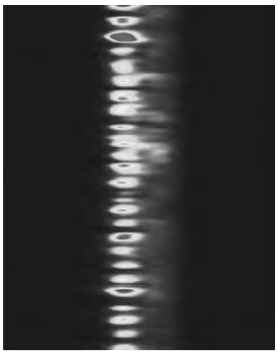

Figure 3. A series of 50 spectra (from top to bottom) in the range 260-270 nm (the fundamental). The coherent signal can be seen as intense peaks, the medium blue is the seed laser “leaking through” and the spontaneous radiation is too weak to be visible.

Stability of the system has been studied by recording the coherent signal at the fundamental (263 nm) see figure 3. It can be seen that a rather regular jitter is present, which can probably be referred to energy oscillations in the electron beam from the linac system.

Temporal overlap between the seed laser and the electron bunch is crucial for the operation. As both pulses are < 1ps special diagnostics have been installed. An electro optical crystal system can resolve overlap to 1 ps (figure 4 and 5).

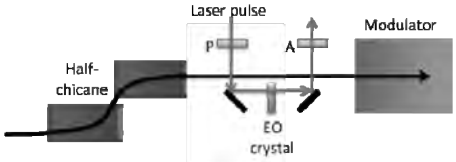

Figure 4. Schematics of the electro-optical technique to measure the overlap between the seed laser pulse and electron bunch.

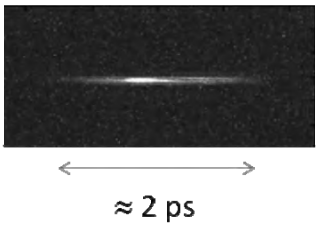

Figure 5. Spectrum of the probe laser pulse with the enhancement at the time the electron pulse passes.

Conclusion and future work

The work is currently proceeding into the higher harmonics and also operation in circular polarisation mode. The stability is also being approached.

Seeding at shorter wavelength by installing a HHG gas jet chamber is funded [6] and will be initiated in due time within the Lund Laser Center (LLC) collaboration.

REFERENCES

[1] L.H. Yu, Phys. Rev A 44 (1991) 5178.
[2] S. Werin et al, The Test FEL Facility at MAX-lab, 31st International Free Electron Laser Conference, Proceedings, Liverpool 2009
[3] S.Werin et al., ``Commissioning of the 500 MeV Injector for MAX-lab", EPAC 2004.
[4] J. Bahrdt et al., ``Undulators for a Seeded HGHG-FEL at MAX-lab", EPAC 2006.
and
J. Bahrdt et al., DIAGNOSTIC TOOLS FOR THE UNDULATOR SYSTEM OF THE SEEDED HGHG-FEL AT MAX-LAB, Proceedings of FEL08, Gyeongju, Korea.
[5] S. Thorin et al., ``Start-to-end simulations for a seeded harmonic generation free electron laser", Phys. Rev. ST Accel. Beams 10, 110701 (2007).
[6] A. L'Huillier, F. Krausz, ``High-Order Harmonic Generation, Handbook of Lasers and Optics" (ed. F. Träger), Springer, New York (2007) p.219.

An electro-optical system for MAX-lab test-FEL facility

Nino Čutić, Filip Lindau, Sara Thorin, Sverker Werin, MAX-lab, Lund
Christian Erny, Lund Laser Centre, Lund, Sweden

To get information about arrival of the electron bunch relative to the laser pulse; electro-optic detection scheme in near-crossed polarizer configuration was set up and tested. Electron bunch induced birefringence in ZnTe crystal leaves a polarization footprint in a chirped infrared pulse. The IR pulse is sampled before third harmonic generation from the amplifier, stretched and synchronized to the ultraviolet beam that is used for seeding. We report details of this setup and preliminary jitter measurements.

To seed a free electron laser good information about the electron bunch arrival time relative to the seed laser pulse is needed. Electro-optic effect (in which birefringence is induced by the electric field of electron bunch which is passing by a crystal) is often used for either timing measurements or for longitudinal bunch profile measurements. [1] The crystals that are used are those of zincblende structure, most often ZnTe and GaP (ZnTe usually gives better signal, but GaP has resonances on higher frequencies than ZnTe which makes it useful for bunch profile measurements). Those crystals are not birefringent in the absence of electric field. Technique (called spectral decoding) that is used at MAX-lab is using chirped infrared pulse to pass through the crystal. When electron bunch is passing by the crystal, the crystal becomes birefringent and the polarization of corresponding part of the infrared pulse is changed. The infrared pulse is then sent through polarizer which gives intensity modulation from change of polarization. After the polarizer, IR pulse is then spectrally decomposed to determine which part of spectrum experienced change in polarization. The wavelength corresponds to time (ideally, with certain limitations [2]), and information about timing of electron pulse, relative to the electron bunch, is determined.

The test-FEL at MAX-lab uses two Ti:Sapphire lasers (Thales Alpha 10) with a common oscillator (Femtolasers Synergy, 93.7 MHz, locked to 3 GHz RF clock). One of them (263 nm, 10 ps, 10 Hz, 500 μJ) is used for photocathode operation and the other one (263 nm, 10 Hz, 300 fs, 150 μJ) is used for seeding the FEL. A part of the beam (about 10%) from the second laser is sampled before tripling to 263 and used for this electro-optical scheme. [3] The IR beam is sent to a stretcher (two 1200 l/mm gratings with changeable separation currently giving 10 ps/nm stretch), focusing lenses (effective focal length 6.5 m) and a delay stage. After the delay stage, it is combined with the UV beam (which passed its own focusing lenses) and they both go through a motorized delay stage (Thorlabs 150 mm) which controls the effective delay between electrons and the laser beams. Beams are then guided to the vacuum system and the seed laser insertion mirror.

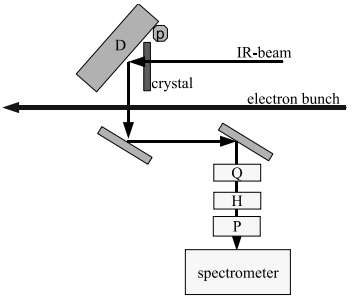

Figure 1: Position of the crystal relative to the electron bunch path. Infrared beam passes through crystal, is reflected of the D-mirror (D) and leaves the vacuum chamber. It is directed with two mirrors onto the quarter-wave plate (Q), half-wave plate (H), Glan-Thompson polarizer (P) and finally spectrometer. The reverse biased photo diode is on the same mount as the crystal (p).

The goal for a seeded FEL is to overlap the UV laser pulse with the electron pulse. Here we use the stretched IR as a common reference and separately center both the UV and electrons on the IR profile. In the setup for UV-IR overlap both pulses are focused on a glass plate. The high intensity UV pulse generates a change in refractive index in the glass, affecting part of IR. Using a spectrometer it is then possible to position the UV pulse with an accuracy of 2 ps.

The chamber in which the crystals are placed is positioned 30 cm in front of the modulator-undulator and after the first screen. Figure 1 shows the important part of timing setup. The crystals are mounted next to each other on a translatable stage (the distance to electron beam can be controlled). The stage carries both crystals (ZnTe and GaP), a D-mirror and a reverse biased photo-diode (which is used with an oscilloscope for rough time synchronization). The crystals are mounted next to each other in front of the D-mirror. D-mirror is rotated for 45° so that it sends the IR-laser beam out of the chamber under right angle. The translation stage is inserted by the amount so that the crystal is just about to start scraping off the alignment beam, and thus the electron beam and the UV-beam since they are all made to coincide (by use of two YAG-screens, before and after the modulator). The distance from the electron bunch to the point at the crystal through which the IR-laser is passing is approximately 4 mm. The IR-

beam is coming from the EO-chamber and after passing one of the crystals it hits the D-mirror positioned behind the crystals, so that electrons pass next to it and the laser beam is reflected by it. The IR-beam then continues onto two silver mirrors, a quarter-wave plate, a half-wave plate, a Glan-Thompson polarizer, and finally a slit which is the entrance point to the spectrometer (consisting of a lens, a grating (1200 mm/l), and a CCD camera). The polarizer is set so that its trans-polarization plane is s-polarization for the grating of spectrometer. The quarter-wave-plate is then rotated so that the signal passing through to the camera (without the electron beam) is minimal. It is possible to stop anything noticeable to go through (due to high polarization ratio, and low residual polarization rotation when there are no electrons). This is done in order to minimize any polarization that builds up in the crystals and the whole system when there are no electrons. Then, the half-wave plate is inserted. If it is left in minimum-signal position that would be similar to crossed polarizer setup; instead, it is a bit rotated off so that it is possible to measure change in sign of THz polarization flip. The half-wave plate is rotated so that the signal of electrons will still not saturate the camera and that opposite polarization will not change sign. This rotation is about two degrees. The background on the camera when there are no electrons needs to be recorded and subtracted later in analysis of the data.

IR laser beam that is used for EO was stretched to 50 ps (FWHM) and focused on the crystal. The wave plates were positioned and rotated as previously described. The electron bunch with energy of 400 MeV and estimated charge of 50 pC that is planned for running of the FEL was used to induce birefringence in the 1 mm thick ZnTe crystal. A thick crystal and highly chirped pulse were selected in order to get higher signal and be sure that something will be observed in initial measurements. The CCD camera in the spectrometer was triggered on the repetition of the injector (in this case 2 Hz).

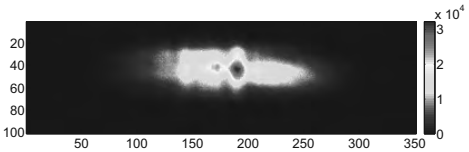

Figure 2: Colored signal on the spectrometer (x and y axis both in pixels). Although horizontally the wavelength span of 5 nm is changing linearly, the corresponding time is due to non-linear chirp of the IR laser pulse.

Figure 2 shows the signal on the spectrometer. The horizontal scale is actually frequency (5 nm of bandwidth mapped). From this image the background still needs to be subtracted. The image is summed vertically into bins (corresponding to one pixel).

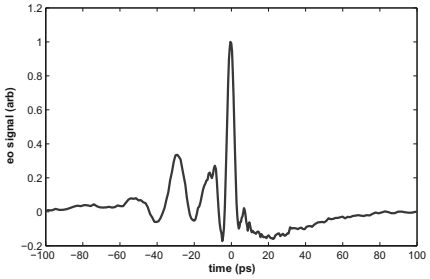

Figure 3: Measured signal obtained from one shot, after background subtraction. The horizontal axis is chirp-adjusted and translated to the maximum. The origin of the oscillations with 20ps period is to be investigated. The dip in signal between 10 and 40 ps is because of spectral instabilities of the oscillator.

The actual timing on the horizontal axis was measured by shifting the laser in time with delay stage and observing the electron signal characteristics. Using changes in time resolution (number of ps per pixel) the non-linearity of the laser chirp was modeled by a polynome of second order. The horizontal axis was adjusted to proper time scale. Figure 3 shows the signal obtained in such a way with adjusted horizontal scale.

Measurement of the relative jitter between the laser pulse and the electron bunch was done by acquiring data from the EO system without changing anything else. The preliminary results show a root mean square jitter of 2 ps which would be too high for normal operation of the FEL. Further measurements are needed to confirm this initial one, get more statistics and to test what might be the dominant underlying cause of this significant jitter.

[1] I. Wilke, A. M. MacLeod, W. A. Gillespie, G. Berden, G. M. H. Knippels and A. F. G. van der Meer, "Single-Shot Electron-Beam Bunch Length Measurements", Phys. Rev. Lett. **88**, 124801 (2002).

[2] S. P. Jamison et al. "Limitations of electro-optic measurements of electron bunch longitudinal profile", Proceedings of EPAC08, Genoa, (2008) TUPC042

[3] S. Werin, et al. "Commissioning of the Test FEL at MAX-lab", FEL2008, South Korea

[4] B. Steffen, PhD thesis "Electro-Optic Methods for Longitudinal Bunch Length Diagnostics at FLASH", (2007).

Experiences from NEG-coated vacuum chambers at MAX II

Anders Hansson, Magnus Berglund, Erik Wallén, MAX-lab, Lund, Sweden
Roberto Kersevan, M.Hahn, ESRF, Grenoble Cedex, France

Introduction

Throughout the past 10 years, the use of vacuum chambers coated with thin films of non-evaporable getter (NEG) materials in particle accelerators and storage rings has steadily increased. To a large extent the NEG material used for these ultrahigh vacuum applications has been a ternary alloy of titanium, zirconium, and vanadium. An overview of the properties of thin films of the Ti–Zr–V NEG alloy is given in [1]. In short, NEG improves the vacuum in the chambers both by direct pumping of the residual gas and by reducing the electron and photon-induced desorption.

The first storage ring to install a NEG-coated vacuum chamber was ESRF, where a narrow-gap aluminium insertion device (ID) vacuum chamber was installed in 1999 [2]. Today, a majority of the ID vacuum chambers in ESRF are NEG coated [3] and NEG-coated vacuum chambers are used at several light sources, e.g., at ELETTRA [4], Diamond [5], SOLEIL [6], and MAX III [7]. At SOLEIL 56% of the ring circumference is NEG coated, including the quadrupole and sextupole straight sections. However, MAX II is the first light source to also use NEG-coated dipole vacuum chambers. This report outlines the experiences from NEG-coated vacuum chambers at MAX II. More detailed information is given in an article published in Journal of Vacuum Science and Technology A [8].

NEG at MAX II

The original vacuum system in MAX II was made of stainless steel. To allow smaller gaps for the insertion devices, NEG-coated aluminium ID vacuum chambers were installed in the straight section between cells 4 and 5 and in the straight section between cells 9 and 10. Figure 1 depicts the vacuum system of cells 2 and 3 in MAX II, where all further installations of NEG-coated vacuum chambers have been done. Since 2007, two ID chambers have been replaced with NEG-coated aluminium ID chambers and three dipole chambers have been replaced with NEG-coated copper dipole chambers. The dipole chambers were installed to test the feasibility of a vacuum system containing NEG-coated

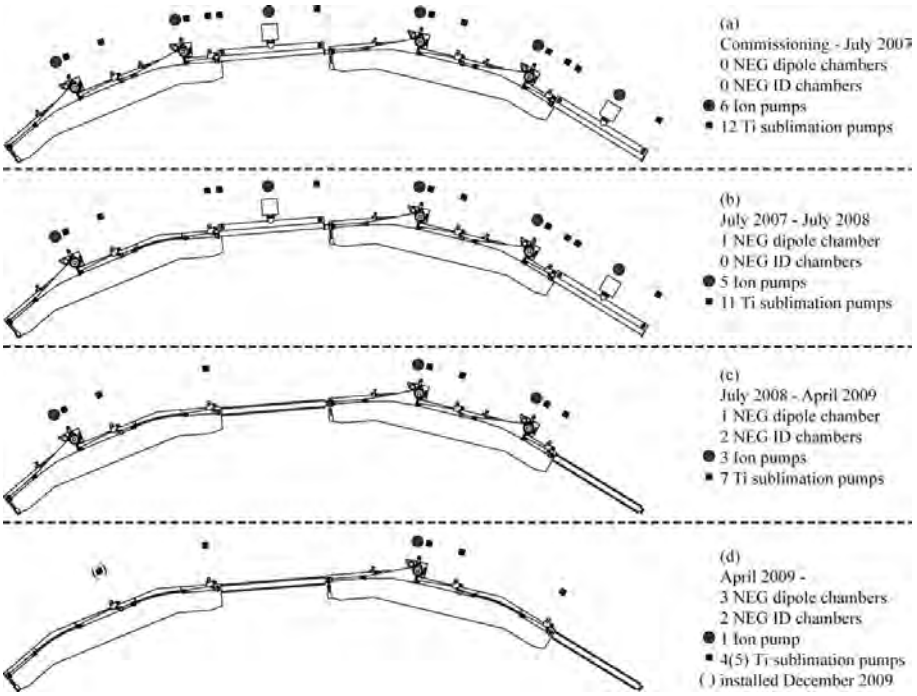

Figure 1: Vacuum system of cells 2 and 3 in the MAX II storage ring from (a) commissioning to July 2007, (b) July 2007 to July 2008, (c) July 2008 to April 2009, and (d) from April 2009 onward.

dipole chambers. The chambers are 1 mm thick OFHC copper tubes with an inner diameter of 31 mm. An additional 1 mm thick copper tube, with an inner diameter of 10 mm, is spot welded and soldered outside the larger tube and it is used for the cooling water supplying the necessary cooling of the vacuum chamber. The NEG coating of the copper chambers was performed at ESRF.

As Figure 1 shows, the total amount of pumps in cells 2 and 3 (including the ID vacuum chambers) decreased from six ion pumps and twelve titanium sublimation pumps to only one ion pump and five titanium sublimation pumps. The NEG-coated vacuum chambers also have a significantly smaller cross-section. To test how this impacts the storage ring bremsstrahlung and scraper measurements were performed. The bremsstrahlung measurement intended to measure the bremsstrahlung levels from the dipole vacuum chambers, but due to difficulties in determining if the detected photons emanated from brehmsstrahlung losses or other losses it gave rise to large uncertainties. Instead, scraper measurements were performed to determine the lifetimes and average rest gas pressure in MAX II. The results were compared to a similar measurement performed in 2003, before any NEG-coated vacuum chambers were installed [9]. Figure 2 shows the pressure in MAX II from February 2009 to July 2009. The installation of two NEG-coated dipole chambers in April 2009 can clearly be seen in the figure. By July 2009, less than three months after the installation of the vacuum chambers, the pressure was already below the level it was in 2003. Further measurements done in spring 2010 showed that the pressure was down again to the same levels as in February and March 2009.

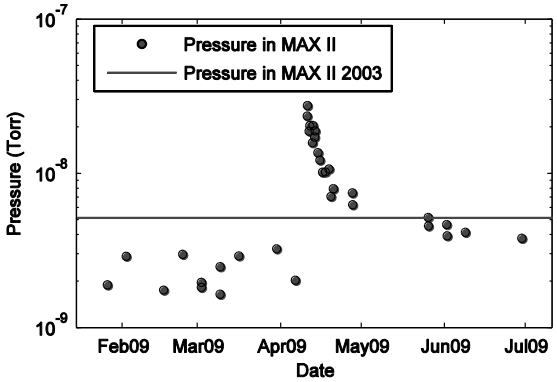

Figure 2: Pressure in the MAX II storage ring from February 2009 to July 2009. The solid line corresponds to the pressure in MAX II in 2003 [9].

Conclusions

Since 2003 four NEG-coated aluminium ID vacuum chambers and three NEG-coated copper dipole vacuum chambers have been installed in MAX II. Even though the cross sections of the new vacuum chambers are significantly smaller than for the old chambers and even though there are no extra pumps connected to the new chambers, the pressure and lifetime in MAX II are still similar to the values from 2003. During a month in early 2009 and again in spring 2010, the average stored current in MAX II was over 200 mA, the highest average current recorded in MAX II for a 30-day period. Judging by the experiences from MAX II, NEG-coated vacuum chambers, including dipole vacuum chambers, do not appear to have any negative impact on the performance and operation of a synchrotron light source.

References

[1] P. Chiggiato and P. Costa Pinto, Thin Solid Films **515**, 382 (2006).
[2] R. Kersevan, Proceedings of EPAC, Vienna, Austria, p. 2291 (2000).
[3] M. Hahn and the ESRF Vacuum Group, Vacuum **81**, 759 (2007).
[4] F. Mazzolini, J. Miertusova, F. Pradal, et al., Proceedings of EPAC, Paris, France, p. 2577 (2002).
[5] J. D. Herbert, O. B. Malyshev, K. J. Middleman, and R. J. Reid, Vacuum **73**, 219 (2004).
[6] C. Herbeaux, N. Béchu, and J.-M. Filhol, Proceedings of EPAC, Genoa, Italy, p. 3696 (2008).
[7] M. Sjöström, E. Wallén, M. Eriksson, and L.-J. Lindgren, Nucl. Instrum. Methods Phys. Res. A **601**, 229 (2009).
[8] A. Hansson, E. Wallén, M. Berglund, R. Kersevan, and M. Hahn, J. Vac. Sci. Technol. A **28(2)**. 220 (2010).
[9] E. Wallén, Nucl. Instrum. Methods Phys. Res. A **508**, 487 (2003).

The MAX III diagnostic beam line

Anders Hansson, Erik Wallén, Åke Andersson, MAX-lab, Lund, Sweden

Introduction

The MAX III synchrotron light source was commissioned in late 2006 and characterized in 2008. Ref. [1] describes the storage ring and the characterization. A useful tool when characterizing a storage ring is a synchrotron radiation (SR) monitor. With it is possible to determine the transversal electron beam size and relative position changes of the beam. This information can be used to determine important machine properties like the emittance and dispersion. A preliminary set-up was available for the measurements in Ref. [1], but a better version was needed for precision measurements. This report describes the new improved diagnostic beam line at MAX III.

There are several different ways to determine the transverse electron beam size in a storage ring. Among them are imaging methods using visible or X-ray SR and interference methods using visible or X-ray SR. The MAX III diagnostic beam line utilizes the SR in the visual to ultra-violet (vis-UV) range to form images of the electron beam. This method has previously been used to determine the beam sizes at e.g. MAX I [2], MAX II [3] and SLS [4].

The MAX III diagnostic beam line

Figure 1 shows a drawing of the MAX III diagnostic beam line and cell 6 dipole magnet as seen from the side. The source point of the beam line is the central part of the dipole magnet in cell 6 of MAX III. Downstream in the beam line, the SR in the vis-UV range is redirected 90 degrees by a SiC mirror. The SR is focused in a fused silica (FS) symmetric spherical lens, after which the horizontal acceptance of the beam line is determined by movable aperture restrictions. The SR propagates out of

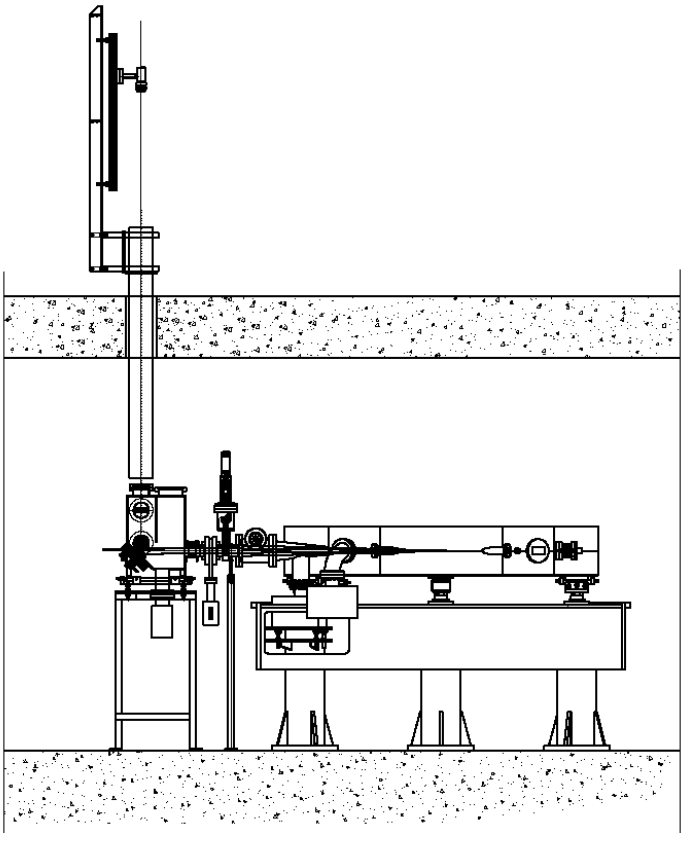

Figure 1: Drawing of the MAX III diagnostic beam line and cell 6 dipole magnet as seen from the side

the vacuum system through a FS vacuum window. The mirror, lens and window have been manufactured with very high surface accuracy to minimize the distortion of the wavefront. An optical rail is situated on top of the MAX III roof, on which optical filters and a CCD camera are placed. The CCD of the camera is positioned at the image plane. Narrow bandpass filters and a Glan-Taylor polarizer are used to select the wavelength and polarization of the measurement.

In the ideal case, the beam size measured by the diagnostic beam line camera would correspond to the beam size at the source point scaled by the magnification factor of the system. However, effects such as e.g. diffraction effects and SR generation along the longitudinal electron trajectory complicate the matter. To correct for these and other effects, the Filament-Beam-Spread Function (FBSF) of the system is calculated theoretically for horizontally and vertically polarized SR using the software SRW together with IGOR. The FBSF corresponds to the image a single electron passing through the bending magnet would give rise to at the image plane (where the camera CCD is situated) after the SR has propagated through the optical components of the beam line. By de-convoluting the image taken with the CCD camera with the FBSF an estimation of the ideal image is obtained. This de-convoluted image can now be scaled with the magnification factor to obtain an image of the transverse electron beam profile. From the electron beam profile the horizontal and vertical beam sizes at the source point can be determined.

The MAX III diagnostic beam line was installed into MAX III in early 2010. Measurements can be done at three different SR wavelengths: 364 nm, 488 nm and 633 nm. Examples of measured beam sizes can be found in Table 1 and Table 2. All measurements were done with the same horizontal acceptance and the same settings in MAX III, so the measured beam sizes in each table should all be, within the uncertainty of the measurement, identical. Work is still underway to set up the beam line and calculate the FBSF, so the results in Table 1 and Table 2 are only preliminary. The vertical beam size depends to a large extent on the coupling in MAX III. For the measurement presented in Table 1 and Table 2 MAX III was tuned to achieve a small vertical beam size.

Table 1: Preliminary results for the horizontal electron beam size in MAX III (sigma, μm) as determined from de-convoluted images for horizontally and vertically polarized light at three different wavelengths of the SR.

	Horizontal beam size (sigma, μm)		
	364 nm	488 nm	633 nm
Horizontally polarized light	98.8	99.4	98.4
Vertically polarized light	99.1	101.2	99.5

Table 2: Preliminary results for the vertical electron beam size in MAX III (sigma, μm) as determined from de-convoluted images for horizontally and vertically polarized light at three different wavelengths of the SR.

	Vertical beam size (sigma, μm)		
	364 nm	488 nm	633 nm
Horizontally polarized light	19.3	18.4	19.1
Vertically polarized light	18.3	18.4	18.6

Conclusions

A diagnostic beam line has been built at MAX III. Using the vis-UV range of the synchrotron radiation emanating from the MAX III cell 6 dipole magnet, the transverse electron beam size can be determined. The diagnostic beam line will be an important tool to further understand the properties of MAX III. Work is underway to finish the set up, and the MAX III diagnostic beam line will soon be ready for operation.

References

[1] M. Sjöström, E. Wallén, M. Eriksson, and L.-J. Lindgren, Nucl. Instrum. Methods Phys. Res. A **601**, 229 (2009).
[2] Å. Andersson and J. Tagger, Nucl. Instrum. Methods Phys. Res. A **364**, 4 (1995).
[3] M. Sjöström, H. Tarawneh, E. Wallén, and M. Eriksson, Nucl. Instrum. Methods Phys. Res. A **577**, 425 (2007).
[4] Å. Andersson, M. Böge, A. Lüdeke, V. Schlott, and A. Streun, Nucl. Instrum. Methods Phys. Res. A **591**, 437 (2008).

Correction coils feed-forward tables for the undulators I1011, I3, and I4

E. Wallén

SUMMARY

The undulators I1011, I3, and I4 are equipped with correction coils surrounding the magnetic structures of the undulators [1]. The correction coils are excited with DC currents in order to compensate for the varying first and second field integral with varying gap and phase of the undulators.

The DC currents depending on gap and phase are interpolated from feed-forward tables which are established by measurements with stored beam in the storage ring. The response from the beam position monitors from the individual coils are measured and then the influence from a changing gap or phase is minimised by a root mean square minimisation routine for obtaining the correct corrector coils setting for the points in the feed-forward table.

CORRECTION COIL SETTINGS OF THE I1011 UNDULATOR

The correction coils feed-forward table for the I1011 undulator was established on June 15, 2009. The correction coil values are illustrated in Table 1 and the numerical values can be found in an XML-table at the MAX-lab web pages [1].

Table 1: Correction coil values for the I1011 undulator

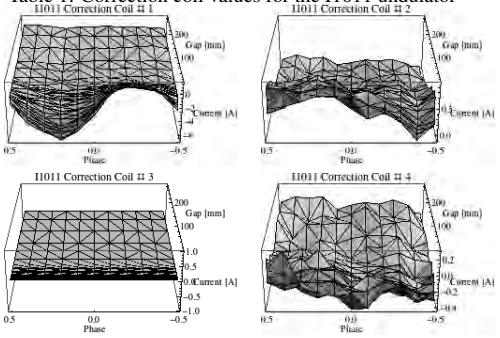

CORRECTION COIL SETTINGS OF THE I3 UNDULATOR

The correction coils feed-forward table for the I3 undulator was established on November 30, 2009. The correction coil values are illustrated in Table 2 and the numerical values can be found in an XML-table at the MAX-lab web pages [1].

Table 2: Correction coil values for the I3 undulator

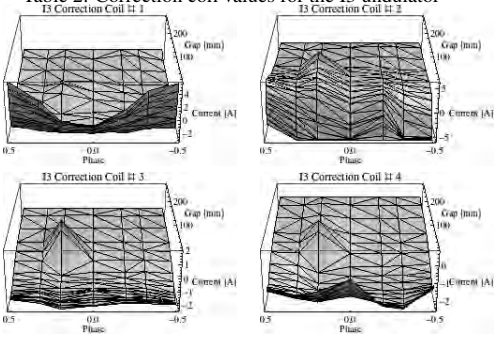

CORRECTION COIL SETTINGS OF THE I4 UNDULATOR

The correction coils feed-forward table for the I4 undulator was established on May 18, 2009. The correction coil values are illustrated in Table 3 and the numerical values can be found in an XML-table at the MAX-lab web pages [1].

Table 3: Correction coil values for the I4 undulator

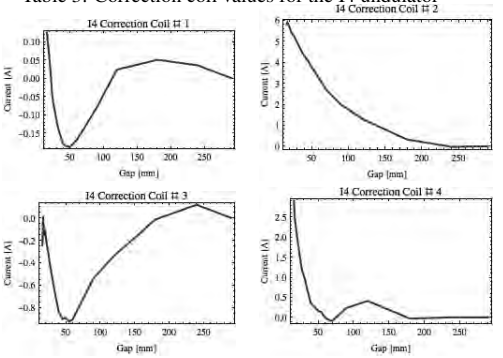

REFERENCES

[1] http://www.maxlab.lu.se/local/UndWeb/UndWeb.html.

Synchrotron Radiation

Synchrotron Radiation Research

General

During 2009 the MAX I, MAX II and MAX III storage rings have been operated for synchrotron radiation research for 22, 40 and 40 weeks, respectively. About 800 scientists have been performing experiments during this time period. Of these about 50 % came from abroad. The scientific projects include experiments in atomic and molecular physics, solid state physics, surface physics, material science, chemistry, biochemistry and environmental science. Reports from the users on recent experimental results are given on the following pages.

Most beamlines on MAX I utilize radiation from bending magnets which provide radiation with a critical energy of 300 eV. In addition a hybrid undulator (period length 75 mm) covering the photon energy range 15 to 150 eV is used for a spectromicroscopy beamline. In total there are four beamlines in operation. The characteristics of the beamlines are summarized in the table on page 59 and a short description of each beamline is given below.

The MAX II storage ring is now equipped with three planar undulators and one EPU for the VUV and soft X-ray regions and three multi-pole wigglers for the X-ray region. One conventional multi-pole wiggler beamline is used for small angle X-ray scattering, small molecule crystallography and powder diffraction. Of the two superconducting multi-pole wigglers, one is used for a materials science beamline and one for a system of three independent protein crystallography beamlines. The undulators serve beamlines with a variety of spectroscopic techniques such as X-ray absorption (including circular dichroism), X-ray emission, X-ray photoemission spectroscopy and photoemission electron microscopy in the VUV and soft X-ray regions. A fourth spectroscopy beamline is installed on a bending magnet port where circularly polarized radiation can be used. A bending magnet beamline is also used for time resolved X-ray diffraction.

Two beamlines are now operational at the 700 MeV MAX III storage ring: A high-resolution beamline for the low energy region (5 – 50 eV) utilizing undulator radiation with variable polarization and the relocated beamline 33 from MAX I to an undulator port at MAX III. A third beamline for infra-red microspectroscopy, utilizing bending magnet radiation, is under construction.

More detailed descriptions of these beamlines are found at the end of this chapter and in the tables on pages 59 – 62.

The synchrotron radiation research program is financially supported by Lund University, the Swedish Research Council (VR). Also many private foundations contribute with substantial grants for investments in experimental equipment, among these are the Knut & Alice Wallenberg Foundation, the Crafoord Foundation, the Carl Tryggers Foundation, and Kungl. Fysiografiska Sällskapet i Lund.

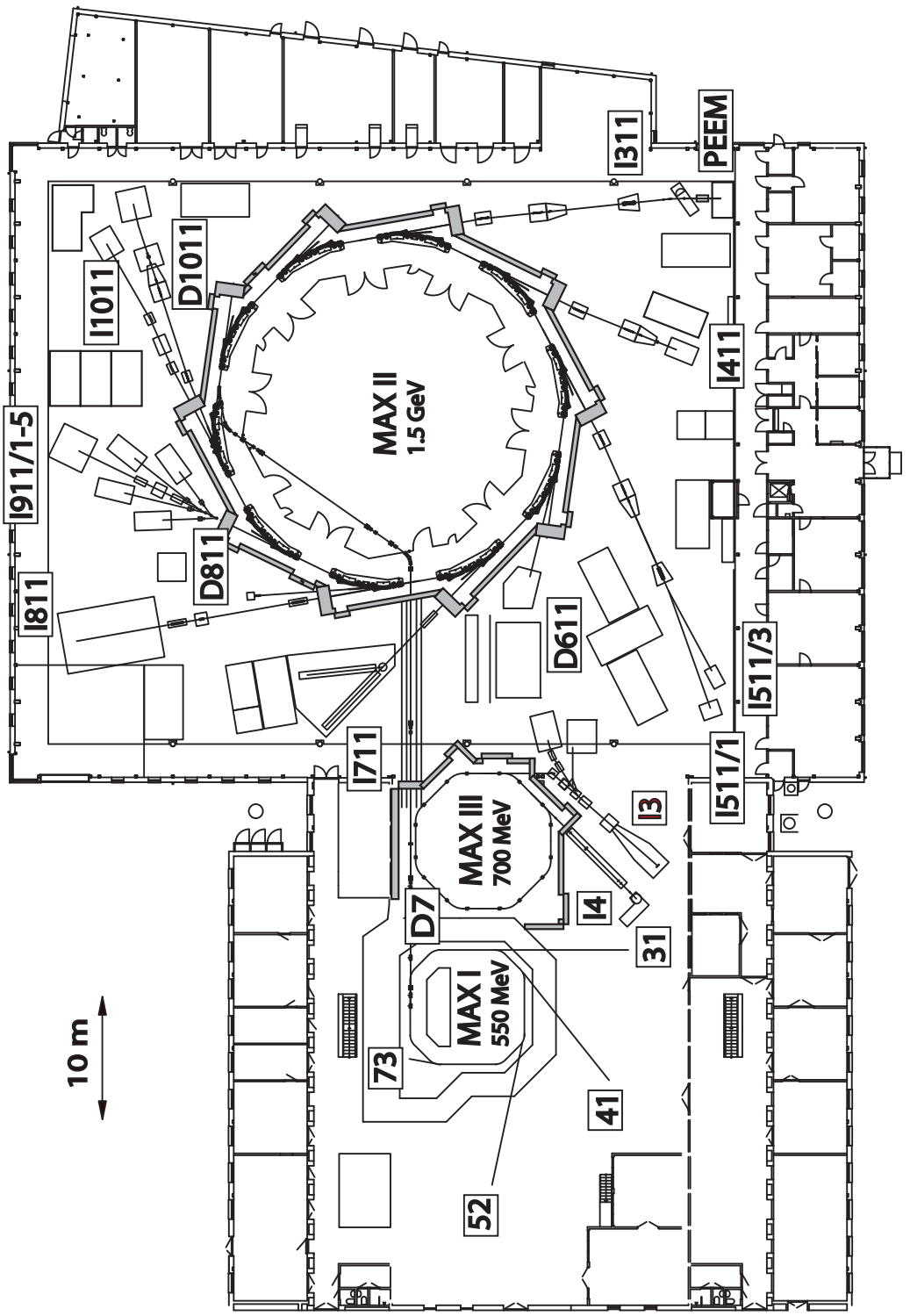
MAX II
1.5 GeV
MAX III
700 MeV
MAX I
550 MeV
I311
PEEM
D1011
I1011
I911/1-5
I811
D811
I411
D611
I511/3
I511/1
I711
I3
I4
31
D7
73
41
52
10 m

MAX I Beamlines
(see www.maxlab.lu.se/beamline/index.html for more details).

Beamline 31 utilizes undulator radiation in the energy range 15 to 150 eV for scanning photoelectron microscopy with a lateral resolution in the one micrometer range. The instrument can be used to obtain chemical information from a surface either by recording photoelectron spectra from selected areas on the sample surface or by tuning the electron energy analyzer to a specific spectral feature and then scanning the sample to obtain an image showing the lateral distribution of this atomic species. The photon energy range and resolution are well suited for measurements of valence bands and shallow core levels.

The experimental system consists of separate analyzer and preparation chambers accessible via a transfer arm. The analyzer chamber, which also holds an ellipsoidal focusing mirror, is equipped with a hemispherical sector electron energy analyzer (VG CLAM2) and a piezo-driven sample scanning stage. The scanning range is 100 * 100 μm^2 with an accuracy of < 0.5 μm. Coarse sample movements, ±3 mm, are made manually with micrometer screws. The preparation chamber is equipped with LEED, ion sputtering gun, sample storage magazine and a number of optional ports for user owned sample preparation accessories.

Beamline 41 Beamline 41 is used for angle resolved photoelectron spectroscopy on solids in the photon energy range from 15 to 200 eV using a toroidal grating monochromator (TGM). The beamline is suited for measurements of both valence bands and shallow core levels.

The experimental station consists of an analyzer chamber with a goniometer mounted electron energy analyzer (VSW HA50), a sample storage chamber and a sample introduction chamber. The analyzer chamber is equipped with LEED, ion sputtering gun, gas-inlet system and a number of optional ports for user owned sample preparation accessories.

In addition to this basic set-up a molecular-beam epitaxy (MBE) system with six Knudsen cells and a RHEED optics is available for the growth and in situ studies of III-V compound semiconductors.

Beamline 52 consists of a normal incidence monochromator working in the photon energy range 5 to 30 eV. The beamline is equipped with a differential pumping stage that makes it useful for measurements on gases as well as on solids. There is no permanent end-station installed at this beamline; instead several user owned experimental stations are being used. These cover a variety of experimental techniques: Mass spectrometry and fluorescence of ions and molecular fragments, angle-resolved photoemission on solids, low temperature luminescence and gas-phase photoemission.

Beamline 73 Beamline 73 is used for spectroscopy and microscopy in the far, mid and near infrared region (10-12 000 cm^{-1}). It is equipped with two different Fourier transform spectrometers.

A Bruker HR 120 is used for high resolution, 0.001 cm^{-1}, spectroscopy. The set up has several options for introducing gases, liquids and solid samples. A gas cell, usable between 90 and 300 K, with a variable optical path length (maximum 120 m) is connected to the spectrometer.

A Bruker 66v/S spectrometer along with a Hyperion 3000 microscope is used for chemical imaging and mapping with a spatial resolution down to the diffraction limit. The microscope can operate both in transmission and reflection mode. Additional objectives for gracing angle and ATR measurements are available as well.

MAX II Beamlines
(see http://www.maxlab.lu.se/beamline/index.html for more details).

Beamline I311 is an undulator based VUV, soft X-ray beamline for high resolution X-ray Photoemission Spectroscopy (XPS) and X-ray Absorption Spectroscopy (XAS) including a future option for scanning photoelectron and photoabsorption microscopy. The monochromator is a modified SX-700 type PGM with spherical optics and a movable exit slit, which allows a high flexibility concerning the interplay between photon flux, resolving power and higher order suppression. Together with the 38-period, 66 mm period length, undulator the photon energy range 30 eV to about 1500 eV is covered.

The experimental station consists of separate analyzer and preparation chambers accessible via a long-travel manipulator. The preparation chamber includes the usual equipment for preparation and characterization of surfaces (ion sputtering gun, LEED optics etc.). A hemispherical electron energy analyzer (SCIENTA SES200) is used for photoelectron spectroscopy and Auger XAS.

A SPELEEM instrument for photoemission electron microscopy is installed downstream from the existing experimental station. This microscope has a spatial resolution better than 10 nm in the LEEM mode and 30 nm in the PEEM mode. It can also perform energy filtered XPEEM with a bandwidth of 300 meV in imaging mode, routinely achieving a lateral resolution of 30 nm.

Beamline I411 is based on an SX-700 type PGM and an undulator source (43-period, 59 mm period length) that covers the photon energy range 40 eV to about 1500 eV. The end-station has the unique versatility of being able to handle solid, liquid and gaseous samples. Thus the beamline is well suited for high-resolution electron spectroscopy on free atoms and molecules as well as for studies of liquid and solid surfaces.

The experimental system consists of separate analyzer and preparation chambers accessible via a long-travel manipulator. The analyzer chamber is equipped with a hemispherical electron energy analyzer (SCIENTA R4000) which can be rotated around the incoming beam for polarization dependent measurements. In front of the experimental station a one-meter long section of the beamline can host other types of equipment for atomic and molecular spectroscopy, e.g. ion-electron coincidence detectors.

A laser system for two-colour experiments is also available.

Beamlines I511/1 and I511/3 are used for XAS, XPS, and X-ray Emission Spectroscopy (XES) in the VUV and soft x-ray range. The two beamlines utilize a common undulator and monochromator with a flip-mirror placed immediately after the exit slit to direct the radiation alternately into two experimental stations. The undulator has 49 periods and a 52 mm period length originally giving a photon energy range of 50 to about 1500 eV. The monochromator is the same type of modified SX-700 monochromator as used on beamline I311.

Beamline I511/1 is built for surface studies under UHV and is equipped with a hemispherical electron energy analyzer (SCIENTA R4000) for XPS. For XAS measurements an electron yield large area detector based on multichannel plates is used.

Beamline I511/3 is equipped with a grazing incidence grating spectrometer for XES and can handle non-UHV compatible solids.

The end stations at both beamlines are built so that the analysis chamber can be rotated around the incoming beam which makes it possible to utilize the linear polarization of the radiation.

Beamline D611 is a bending magnet beamline dedicated to time-resolved studies. We are exploiting the fact that MAX II is a pulsed source operating at 100 MHz. The duration of the pulses has been measured to be approximately 350 ps using a streak camera. The beamline has a toroidal focusing mirror and a double crystal mononchromator. A laser providing pulses with durations of 20 – 30 fs has been synchronised to the ring, and a streakcamera yielding a temporal resolution of about 500 fs is available. The temporal resolution in the experiments does not depend on the relative jitter between the laser and the synchrotron (10 ps) but mainly on the jitter between the streak camera and the laser. The laser operates at a maximum repetition rate of 10 kHz which sets the data accumulation rate. Experiments can be performed in air or in vacuum (10^{-6} mbar). More information about our activities can be found at: http://www-atom.fysik.lth.se/txrd

Beamline I711 is an X-ray beamline used for small angle X-ray scattering (SAXS), small molecule crystallography and powder diffraction. It utilizes a 13-period, 1.8 T, multipole-wiggler and is designed to operate in the 0.8 Å (15.5 keV) to 1.6 Å (7.8 keV) region. The beamline has a vertical focusing mirror and a focusing single crystal monochromator working in the horizontal plane. This design sacrifices easy tunability and high energy resolution for high flux at the sample.

The detectors that are available today include a Marresearch 165 mm CCD detector and a Huber imaging foil Guinier camera for powder diffraction. Depending on the application several different types of sample environment equipment, i.e. a pressure cell, a furnace, a thermostat and a Cryojet can be offered.

Beamline I811 is intended for materials science research using X-ray absorption spectroscopy (XAS) and X-ray diffraction (XRD). It is based on a super-conducting multi-pole wiggler insertion device that produces high-flux photons in the energy range 2.4 – 20 keV (0.6 – 5 Å). The design is based on adaptive optics where the beam is collimated and focused vertically by cylindrical bendable first and second mirrors, respectively. Horizontal focusing is obtained by sagittal bending of the second monochromator crystal. The typical flux in a 1 x 1 mm^2 beam spot on the sample is 5 x 10^{11} photons/sec. One experimental station is used for XAS research with detectors for transmission and fluorescence yield techniques. A second station is equipped with a diffractometer for surface, interface and thin-film crystallography.

Beamlines I911/1-5 are used mainly for macromolecular crystallography. The beamlines use a super-conducting multi-pole wiggler. The central beamline I911-3 is tunable in the range 0.7 – 2.0 Å and is optimized for MAD experiments. The beam is vertically collimated by a Rh-coated mirror, monochromatized by a Si(111) double-crystal monochromator and focused by a Rh-coated toroidal mirror. The optics for the four side stations consists of horizontally focusing monochromator crystals and vertically focusing curved multilayer mirrors providing fixed wavelength beams. I911-3 is equipped with a kappa axis diffractometer and 225 mm CCD detector. Two side stations, I911-2 (wavelength 1.04 Å) and I911-5 (wavelength 0.91 Å) are equipped with single axis diffractometers and 165 mm CCD detectors.

Beamline D1011 is a bending magnet beamline covering the energy range 30 to 1500 eV. An adjustable local bump of the electron beam provides out of plane radiation. This makes magnetic circular dichroism (MCD) possible in addition to photoemission and photoabsorption using linearly polarized light.

The monochromator is a modified SX-700 PGM of the same design as the monochromator on beamline I411. The experimental system consists of separate analyzer and preparation chambers accessible via a long-travel manipulator. The analyzer chamber is equipped with a SCIENTA SES200 electron energy analyzer (with a lens of SES2002 type) and an MCP detector for electron yield measurements. The preparation chamber is equipped with LEED, ion sputtering guns, gas-inlet system and a number of optional ports for user owned sample preparation accessories.

A second experimental station receives radiation that is let through the first station and re-focused by a KB mirror system. This station is specifically designed for NEXAFS, XMCD and soft X-ray reflectivity experiments. Measurements can be performed under static magnetic fields of up to 500 G. One of the unique features of the station is to offer element specific reflection-based hysteresis measurements.

Beamline I1011 is used for studies of magnetic materials using magnetic circular dichroism and related techniques. An elliptically polarizing undulator (EPU), with variable polarization (linear and circular), in the energy range 200 to 2000 eV is the source of the soft X-rays.

The undulator radiation is monochromatized by an SX-700-type of PGM with vertical collimation and focused into an experimental chamber for magnetic circular dichroism measurements.

There are currently two different chambers available to users. One being a chamber equipped with an octupole magnet allowing for work under applied magnetic fields in an arbitrary direction in space with a design goal of producing a field of 1T. The chamber is also designed to conduct soft X-ray magnetic reflectivity measurements. The second experimental system consists of separate preparation and analysis chambers. The analysis chamber is equipped with an UHV electromagnet providing a peak field of 0.1 T in pulsed mode and 35 mT with a continuous field. The preparation chamber is equipped with a LEED and an ion sputter gun as well as a number of extra ports for user supplied auxiliary equipment.

MAX III Beamlines
(see http://www.maxlab.lu.se/beamline/index.html for more details).

Beamline I3 is an undulator beamline for the low energy region (5 – 50 eV). It is equipped with a normal incidence monochromator with a very high energy resolution (resolving power greater than 10^5). The undulator is of the "apple-type" providing variable polarization (the undulator is not yet characterized for circular polarization). There are two branch-lines, one with a fixed end-station for high resolution angle- and spin-resolved photoemission on solids, equipped with a rotatable Scienta R4000 analyzer and a Scienta 2D spin detector. Angle resolved photoemission can be made in ±15, ±7 and ±3.5 degree mode. An on-line MBE system provides the possibility for studying in-situ grown samples. The second branch-line, with a differential pumping stage, is designed for an easy exchange of end-stations for atomic and molecular spectroscopy and luminescence measurements.

Beamline I4 is an SGM beamline previously used at MAX I (beamline 33) now connected to an undulator source on MAX III. The beamline covers the energy range 13 – 200 eV and is used for angle resolved photoemission.

The end station from beamline 33 is used also at I4 except that the main analyzer chamber is exchanged for a new one. This new chamber hosts the old VG ARUPS 10 analyzer and in addition a new PHOIBOS 100 mm CCD analyzer from SPECS. This analyzer is fixed on the chamber unlike the VG ARUPS 10. However, by rotating (and in future tilting) the sample one can do a full Fermi surface mapping.

The SPECS analyzer has an ultimate resolution of less than 3 meV. There are three angular dispersion modes namely MAD (medium angular dispersion), LAD (low angular dispersion) and WAM (wide angular dispersion).

The MAD mode has angular acceptance of ±3 deg with angular resolution of less than 0.1 deg. The LAD mode has angular acceptance of ±6 deg with angular resolution of about 0.15 deg. The WAM mode has angular acceptance of ±10.5 deg with angular resolution of about 0.4 deg.

Beamline D7. This is an infrared microspectroscopy beamline presently under construction. It will be attached to a bending magnet port. During the design and construction work for the beamline the microscope is used at the existing infrared beamline, 73, at MAX I.

Beamlines at MAX I

Beam port	Source type	Beamline/Monochromator	Energy or wavelength range	Experimental techniques
31	Undulator	PGM with Kirkpatrick-Baez objective and ellipsoidal focusing mirror.	15 – 150 eV	Scanning photoelectron microscopy.
41	Bending magnet 18 mrad	4.7m-TGM, 162°.	15 – 200 eV	Angular resolved photoemission. On-line MBE system.
52	Bending magnet 20 mrad	1m NIM.	5 – 30 eV	Atomic and molecular spectroscopy. Angle-resolved photoemission. Luminescence.
73	Bending magnet 60 * 100 $mrad^2$	Two ellipsoidal mirrors, 1:1.	12000 – 10 cm^{-1}	Infrared spectroscopy using a high resolution FTIR spectrometer. Infrared microspectroscopy.
NP	Tagged photon beam	Tagging spectrometer	15 – 185 MeV	Nuclear physics.

Beamlines at MAX II

Beam port	Source type	Operational status	Beamline/Monochromator	Energy or wavelength range	Experimental techniques
I311	Undulator	Operative	PGM (modified SX-700, with spherical focusing mirror).	30 – ~1 500 eV	High resolution XPS. X-ray absorption spectroscopy. Photoemission microscopy, PEEM.
I411	Undulator	Operative	PGM (modified SX-700 with plane-elliptical focusing mirror).	40 – ~1 500 eV	High resolution XPS. X-ray absorption spectroscopy. Coincidence spectroscopy.
I511/1	Undulator	Operative	PGM (modified SX-700, with spherical focusing mirror).	50 – ~1 500 eV	High resolution XPS. X-ray absorption spectroscopy. UHV compatible.
I511/3	Undulator	Operative	PGM (modified SX-700, with spherical focusing mirror).	50 – ~1 500 eV	X-ray absorption spectroscopy. X-ray emission spectroscopy. Non-UHV compatible.
D611	Bending magnet	Operative	Be-windows, Double-crystal monochromator.	2 – 10 keV	Time resolved X-ray diffraction.
I711	Multi-pole wiggler	Operative	Be-window, Bent Si(111) crystal.	0.8 – 1.6 Å	Small angle X-ray scattering. Small molecule crystallography. Powder diffraction.
I811	Superconducting multi-pole wiggler	Operative	Double-crystal monochromator.	2.4 – 20 keV	EXAFS. Surface, interface and thin film crystallography.

Beamlines at MAX II, cont.

Beam port	Source type	Operational status	Beamline/Monochromator	Energy or wavelength range	Experimental techniques
I911/1	Superconducting multi-pole wiggler	Presently test station	Diamond crystal, multi-layer mirror.	Quasi-fixed wavelength, 1.2 Å	Presently used for education/ test station.
I911/2	Superconducting multi-pole wiggler	Operative	Bent Si crystal, multi-layer mirror.	Fixed wavelength, 1.04 Å	Protein crystallography.
I911/3	Superconducting multi-pole wiggler	Operative	Collimating mirror Double-crystal monochromator. Focusing toroidal mirror.	0.7 – 2.0 Å	Protein crystallography. MAD technique.
I911/4	Superconducting multi-pole wiggler	Under construction	Bent Si crystal, multi-layer mirror.	Fixed wavelength, 0.91 Å	Small Angle X-ray Scattering.
I911/5	Superconducting multi-pole wiggler	Operative	Bent Si crystal, multi-layer mirror.	Fixed wavelength, 0.91 Å	Protein crystallography and other scattering experiments.
I1011	Undulator with variable polarization	Operative	Collimated PGM.	200 – 2000 eV	MCD and related techniques for studies of magnetic materials.
D1011	Bending magnet	Operative	PGM (modified SX-700 with plane-elliptical focusing mirror). Off-plane radiation for circular polarized radiation.	40 – ~1500 eV	Circular dichroism. High resolution XPS. X-ray absorption spectroscopy.

Beamlines at MAX III

Beam port	Source type	Operational status	Beamline/Monochromator	Energy or wavelength range	Experimental techniques
I3	Undulator with variable polarization.	Operative	6.65 m Off-axis Eagle Type NIM.	5 – 50 eV	High resolution (meV) angle- and spin-resolved photoemission on solids, atomic and molecular spectroscopy, and luminescence. On-line MBE system.
I4	Undulator	Operative	5.5 – 5.8m-SGM, 162°.	13 – 200 eV	Angle-resolved photoemission.
D7	Bending magnet	Under construction	Transfer optics, FTIR spectrometer and IR microscope.	12 000 – 10 cm^{-1}	Infrared microspectroscopy.

The new SAXS station under construction at beamline I911-4, February 2009.
Photo: Annika Nyberg

Reports from Synchrotron Radiation Research

MAX I

Beamline 31

Beamline 33

Beamline 41

Beamline 52

Beamline 73

MAX II

Beamline I311

Beamline I411

Beamline I511

Beamline D611

Beamline I711

Beamline I811

Beamline I911

Beamline D1011

Beamline I1011

MAX III

Beamline I3

Beamline I4

Intercalation dynamics of well-defined Cs domains on the layered correlated electron material 1*T*-TaS_2

D. Rahn[1], *S. Hellmann*[1], *E. Ludwig*[1], *K. Rossnagel*[1], *A. Zakarov*[2] *and L. Kipp*[1]

[1] *Institute for Experimental and Applied Physics, University Kiel, Germany*
[2] *MAX-lab, Lund, Schweden*

The layered transition-metal dichalcogenides have been in the focus of numerous scientific studies in the last decades [1]. Beside their unique variety of electrical properties (supercondutor, metal, semi metal, insulator) and low dimensional phenomena (charge-ordering) a lot of work focused on the possibility to intercalate foreign metal ions inbetween the layers [2]. On the one hand the storage of ions could contribute to the development of new long lasting batteries but on the other hand the intercalation provides a tool for a controlled tuning of the dimension, geometry, band filling and electronic structure of these compounds [3]. However up to now the question how the metal atoms adsorb or intercalate in an in vacuo deposition experiment is still under debate. Recent calculations [4] and STM measurements [5] support the idea that the atoms preferentially intercalate through existing step edges. By contrast, also the adsorption induced formation of nanowires [6] and nanofolds [7] which could serve as self created intercalation channels is reported.
To get new insight in the correlation between all these processes we tried to achieve spatially well confined alkali depositions on a liquid nitrogen (LN2) cooled sample surface in order to study the spatial distribution and dynamic behavior of adsorbed and intercalated alkali atoms during warm up of the sample.
The two images in Fig. 1(b) show the sample surface (1*T*-TaS_2) after a spatially confined Cs deposition

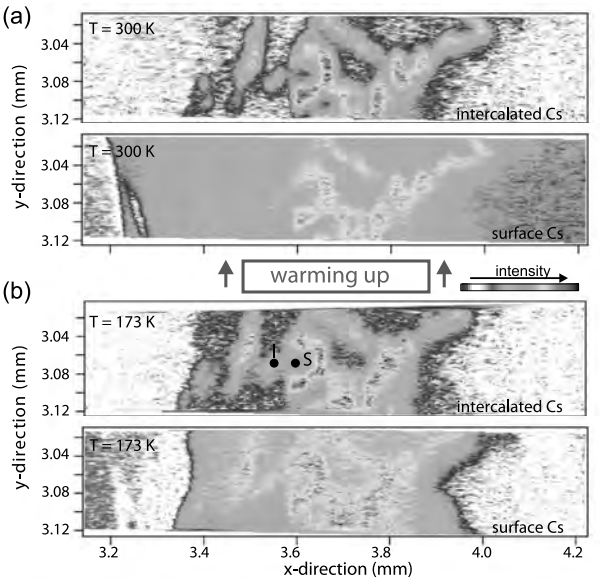

Figure 1: Spatial distribution of adsorbed and intercalated Cs after a spatially confined deposition of 20 min at 60 A on a LN2 cooled sample surface before (a) and after the warm up (b) of the crystal. The Cs 4*d* core levels were used for imaging the different Cs species see Fig. 2.

of 20 min at 6 A. The upper one shows the spatial distribution of the intercalated Cs atoms and the lower

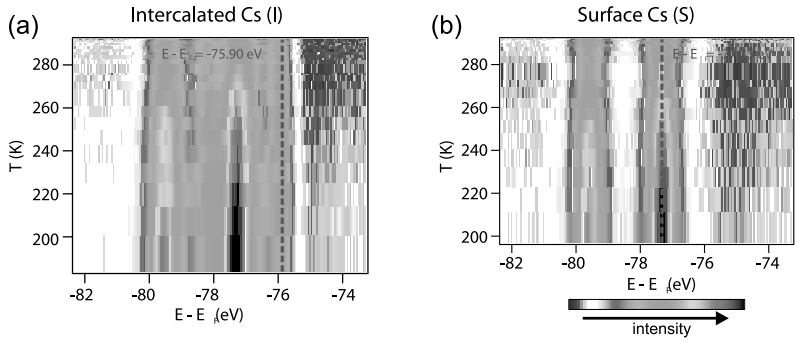

Figure 2: Temperature dependence of the Cs 4*d* core level on two different sample sites. a) Sample site where intercalation has occurred. b) Sample site without intercalated Cs. See Fig. 1(b) for the positions where the spectra were taken from.

one the distribution of surface adsorbed Cs. The upper image reveals that intercalation only takes place in a narrow stripe with an lateral extension in the x-direction of round about 350 µm. Because this width fits very well to the size of the aperture which was used to confine the deposition one can conclude that intercalation only takes place in the directly hit sample region. The lower image (distribution of surface Cs) show that the stripe shaped sample region of intercalated atoms is surrounded by a corona of surface Cs atoms which shows a sharply confined boundary to the rest of the sample surface and a width between 60 µm and 100 µm. The two images in Fig. 1(a) show the same sample region after warm up to room temperature. Again the upper and the lower image show the distribution of intercalated respectively of surface adsorbed atoms. Obviously, there is no further intercalation in previously non intercalated sample areas albeit the surface Cs distribution smears out.

Fig. 2 shows the temperature dependence of the Cs 4*d* core level at the marked positions in Fig. 1(b). The reduction of Cs signal during the warm up allows the conclusion that the smear out of the surface distribution is mainly due to desorbtion. In addition Fig. 2(a) reveals that the intercalation doesn't proceed through existing channels.

Finally one can draw the following picture for the mechanism. The intercalation starts in the directly hit sample region through existing or self created channels. Surface Cs diffuses away from the boundaries of the directly hit sample region without creating new intercalation channels. During the warm up intercalation doesn't proceed through existing channels nor create new channels in Cs covered regions. This provides the picture, that a threshold of surface Cs atoms is needed for intercalation to occur.

References

[1] J. A. Wilson and A. D. Yoffe, Adv. Phys. **18**, 193 (1969)
[2] R. H. Friend and A. D. Yoffe, Adv. Phys. **36**, 1 (1986)
[3] K. Rossnagel, E. Rotenberg, H. Koh, N. V. Smith, and L. Kipp, Phys. Rev. Lett. **95**, 126403 (2005).
[4] C. Ramirez, R. Adelung, R. Kunz, L. Kipp, and W. Schattke, Phys. Rev. B **71**, 035426 (2005)
[5] P. Schmidt, B. Murphy, J. Kröger, H. Jensen, and R. Berndt, Phys. Rev. B **74**, 193407 (2006)
[6] R. Adelung, L. Kipp, J. Brandt, L. Tarcak, M. Traving, C. Kreis, and M. Skibowski, Appl. Phys. Lett. **74**, 3053 (1999).
[7] E. Spiecker, A. K. Schmid, A. M. Minor, U. Dahmen, S. Hollensteiner, and W. Jäger, Phys. Rev. Lett. **96**, 086401 (2006).

Observation of a curious spin-split surface band on Tl/Si(111)-(1x1)

K. Sakamoto[1], T. Oda[2], P.E.J. Eriksson[3], and R.I.G. Uhrberg[3]

[1] *Graduate School of Advanced Integration Science, Chiba University, Chiba 263-8522, Japan*
[2] *Graduate School of Natural Science and Technology, Kanazawa University, Kanazawa 920-1192, Japan*
[3] *Department of Physics, Chemistry and Biology,, Linköping University, S-581 83 Linköping, Sweden*

Due to the presence of both time-reversal and space-inversion symmetry, the electronic states of opposite spin orientation are generally considered to be degenerate in nonmagnetic materials. However, this degeneracy will be lifted by the spin-orbit interaction when one of these symmetries is broken. At crystal surfaces, the latter symmetry is broken and the spin-orbit interaction leads to a pair of split bands in the momentum space. This is called the Rashba-Bychkov (RB) (or simply Rashba) effect [1], and has been observed on clean surfaces of noble metals [2] and heavy group V elements [3]. Recently the RB effect has been reported to be enhanced in systems in which heavy element atoms are adsorbed on light element substrates, such as Bi or Pb on a Ag(111) surface [4]. Since the same phenomenon on semiconductor surfaces has a technological importance in spintronic devices such as spin-transistors [5], we have chosen Si as a light element substrate and Tl as the heavy element adsorbate to study a semiconducting system with enhanced RB splitting.

Figure 1 shows the LEED pattern and the schematic illustration of the Tl/Si(111)-(1x1) surface, and Fig. 2 displays the electronic band dispersion measured using ARPES along the $\bar{\Gamma}-\bar{\mathrm{K}}-\bar{\mathrm{M}}$ direction. Two bands are observed at binding energies (E_{B}) of approximately 0.25 eV and 1.6 eV at the $\bar{\Gamma}$ point. Of these two bands, the lower E_{B} one is located in the gap of the projected bulk band indicating that this is the surface state band of Tl/Si(111)-(1x1). This surface state band shows a "curious splitting" around the $\bar{\mathrm{K}}$ point (the splitting can be observed clearly in the inset of Fig. 2 taken at a higher energy resolution). The $6s^2$ electrons of the Tl atoms are inactive in the Tl-Si bonding [6], and thus the observed surface-state band originates from the hybridization between the single Tl 6*p* electron and one electron from the surface Si atom. This means that there is no orbital degeneracy in the observed surface-state band, and the only possible explanation for the phenomenon at the $\bar{\mathrm{K}}$ point is spin-splitting. Note that the splitting appears along the energy axis at around $\bar{\mathrm{K}}$ only, while if the split is due to a simple RB effect it would be observed in the whole surface Brillouin zone except at high symmetry points such as $\bar{\Gamma}$ and $\bar{\mathrm{M}}$. By performing a first-principles electronic structure calculation, we concluded that this curious splitting, which has not been observed on any other 2D or 3D system so far, is a peculiar RB splitting originating from the "C_3 symmetry" of the $\bar{\mathrm{K}}$ point [7].

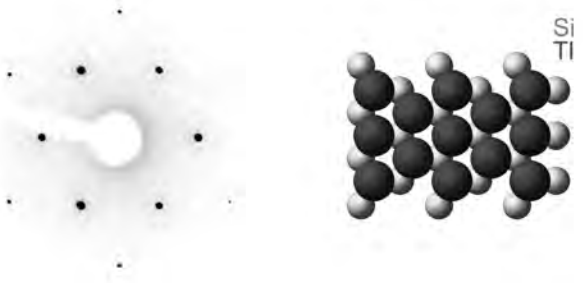

Fig. 1: LEED pattern and the schematic illustration of the Si(111)-(1x1) surface formed by the adsorption of 1 ML of Tl.

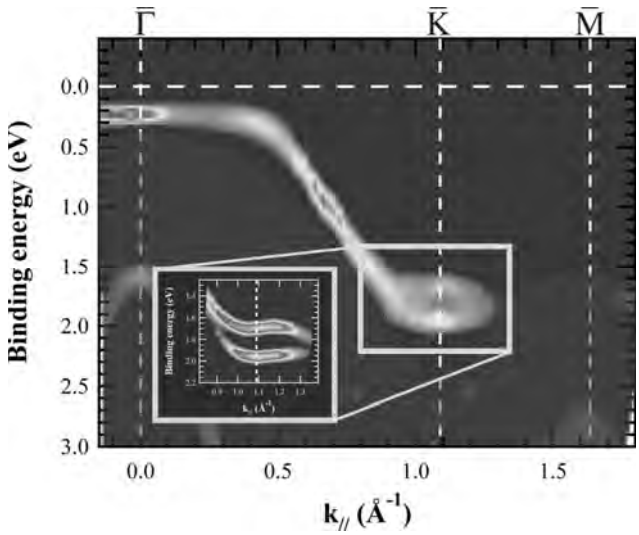

Fig. 2: Band structures measured along the $\bar{\Gamma}-\bar{K}-\bar{M}$ direction.

[1] Y.A. Bychkov and E.I. Rashba, JETP Lett. **39**, 78 (1984).

[2] *see for example*, F. Reinert, G. Nicolay, S. Schmidt, D. Ehm, and S. Hüfner, Phys. Rev. B **63**, 115415 (2001).

[3] *see for example*, Yu. M. Koroteev, G. Bihlmayer, J. E. Gayone, E. V. Chulkov, S. Blügel, P. M. Echenique, and Ph. Hofmann, Phys. Rev. Lett. **93**, 046403 (2004).

[4] *see for example*, C. R. Ast, J. Henk, A. Ernst, L. Moreschini, M. C. Falub, D. Pacilé, P. Bruno, K. Kern, and M. Grioni, Phys. Rev. Lett. **98**, 186807 (2007).

[5] *see for example*, S. Datta and B. Das, Appl. Phys. Lett. **56**, 665 (1990).

[6] K. Sakamoto, P. E. J. Eriksson, S. Mizuno, N. Ueno, H. Tochihara, and R. I. G. Uhrberg, Phys. Rev. B **74**, 075335 (2006).

[7] K. Sakamoto, T. Oda, A. Kimura, K. Miyamoto, M. Tsujikawa, A. Imai, N. Ueno, H. Namatame, M. Taniguchi, P.E.J. Eriksson, and R.I.G. Uhrberg, Phys. Rev. Lett. **102**, 096805 (2009).

Photoelectron diffraction from AlAs layers

P. Jiříček[1], M. Cukr[1], I. Bartoš[1], and J. Sadowski[2]

[1]*Institute of Physics, Academy of Sciences of the Czech Republic, Cukrovarnicka 10, 162 53 Prague 6, Czech Republic*

[2] *Max-lab, Lund University, SE-221 00 Lund, Sweden and Institute of Physics, Polish Academy of Sciences, al. Lotnikow 32/46, 02-668,Warsaw, Poland*

The photoelectron diffraction (PhD) is one of important methods used for determining the surface atomic structure of solids [1]. The atomic structure of studied sample is obtained by comparison of the measured polar or azimuthal plots with that modeled by theoretical simulations [2]. These simulations show that the single electron-atom scattering events can be used to properly explain behavior of polar plots for higher kinetic electron energy [3-5].

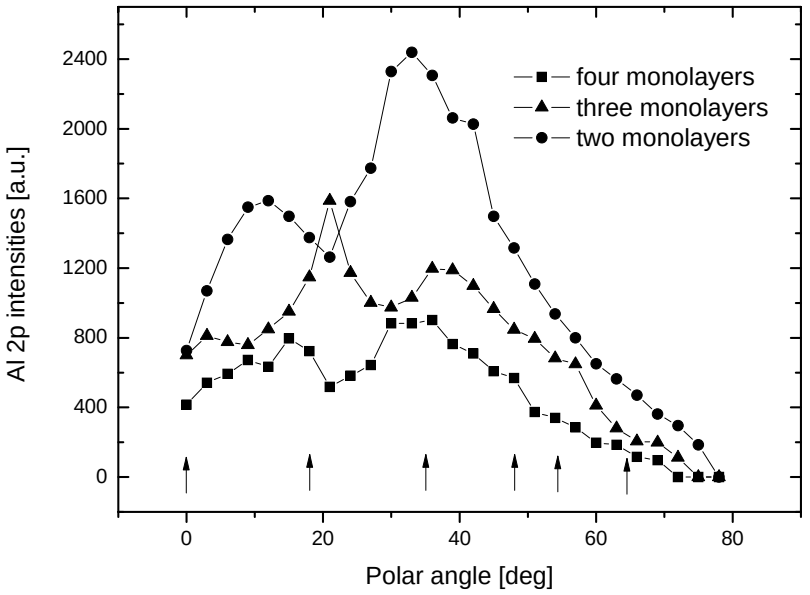

Fig. 1. Polar plots of Al 2p photoelectron line. Photoelectrons were emitted from the AlAs monolayer, burried under different number of the top GaAs monolayers of the GaAs(001)-c(4x4) surface. The excitation energy of the synchrotron radiation was 105 eV. The arrows show directions of the highly packed rows of atoms .

From this reason, in the PhD experiments the photoelectrons with kinetic energy higher than 500 eV are applied in most cases for determination of atomic structure of studied samples. The aim of this contribution is to measure the PhD curves using low energy photoelectrons excited by synchrotron radiation.

Three samples with AlAs monolayer burried bellow two, three and four GaAs momolayers were grown by MBE at the Physical Institute at Prague. The surface of the samples was protected by As cap. Removing the As cap and preparation c(4x4) reconstruction on the samples surface was done in the MBE chamber attached to the BL 41. The quality of the reconstructed surfaces was checked by LEED after sample transport to the photoemission chamber. LEED diffraction images showed sharp spots in all cases.

The PhD measurements were carried out in the angle scanned mode. The polar plots of Al 2p photoelectron line are shown in Fig. 1. The plots were recorded in [110] direction by irradiation the sample surface by synchrotron radiation (hν=105 eV). The arrows in the graph show directions of the highly packed rows of atoms in the samples.

It is clearly seen that the intensities of the Al 2p core level decrease with increasing thickness of the top GaAs layer as can be observed at polar plots in Fig.1. Positions of the peaks on the graph do not coincide with the arrows, which indicate directions with the highly packed atomic rows. However, for photoelectrons with higher kinetic energy the positions of the peaks in polar plots correspond to these directions (angles) better [6]. In this experiment the kinetic energy of Al 2p photoelectrons was 26 eV. At this energy the multiple-scattering processes dominate (electronic structure has to be taken into account for low energy electrons) and forward scattering enhancement can be modified. The behavior of polar plots for photoelectrons emitted from Al layer below two and four GaAs monolayers is very similar in contrast to angular dependence of Al 2p photoelectrons, which originate from Al layer located below three GaAs monolayers. The behavior of polar plots in PhD measurement is sensitive to the geometrical neighbourhood around the emitting atom. The Al atoms in the prepared layer structures are in position of the Ga atoms in the lattice of the GaAs samples. The geometrical position of Al atoms in the AlAs layer located below two or four GaAs monolayers is to be the same but different from the position of the Al atoms below three GaAs monolayers. To support these qualitative conclusions, the theoretical simulation should be done.

[1] D. P. Woodruf, J. Electron Spectrosc. Relat. Phenom., 126 55, (2002).
[2] F.J. García de Abajo, M.A. Van Hove and C.S. Fadley, Phys. Rev. B 63 (2001) 075404
[3] J. Osterwalder, T. Greber, J. Schlapbach, S. Hufner, Phys. Rev. B 41 (1990) 12495.
[4] S. Hufner, J. Osterwalder, T. Greber, J. Schlapbach, Phys. Rev. B 42 (1990) 7350.
[5] T. Greber, J. Osterwalder, D. Naumovic, A. Stuck, S. Hufner, J. Schlapbach, Phys. Rev. Lett. 69 (1992) 1947.
[6] I. Bartoš Surf. Sci. 603 (2009) 369.

Electronic structure of $Ge_{1-x}Mn_xTe$

B.J. Kowalski[1], M. Pietrzyk[1], R. Nietubyć[2], J. Sadowski[1,3], W. Knoff[1], T. Story[1]

[1]*Institute of Physics, Polish Academy of Sciences, Al. Lotników 32/46, 02-668 Warsaw, Poland*

[2]*The Andrzej Soltan Institute for Nuclear Studies*, 05-400 Swierk/Otwock, Poland

[3] *MAX-lab, Lund University, Box 118, SE-22100 Lund, Sweden*

The ferromagnetic interaction was observed in several IV-VI–based diluted magnetic semiconductors. It was governed by the RKKY mechanism and mediated by free holes occurring due to the presence of native defects. It could be modified by relatively easy technological measures (like annealing under suitable atmosphere) reducing the density of defects. The GeTe-based diluted magnetic semiconductors acquired recently particular interest due to discovered features, advantageous in view of spintronic applications. Observations of relatively high Curie temperature of $Ge_{1-x}Mn_xTe$ (up to $T_C \approx 190$ K for $x=0.08$[1]) inspire extensive investigations of magnetic properties of this material as well as a quest for the most suitable preparation methods. However, the set of experimental data concerning the electronic band structure of $Ge_{1-x}Mn_xTe$ and other GeTe-based diluted magnetic semiconductors still has to be markedly increased. In particular, detailed experimental data about the band structure of $Ge_{1-x}Mn_xTe$ are not available in the literature.

Therefore, we undertook a study, by means of angle-resolved photoelectron spectroscopy, of the valence band structure of $Ge_{0.85}Mn_{0.15}Te$. The experiments were carried out with use of the photoelectron spectrometer of the beamline BL 41. The epilayers of $Ge_{1-x}Mn_xTe$ were grown on BaF_2 (111) substrates by means of an MBE method in the Institute of Physics, Polish Academy of Sciences. The X-ray diffraction measurements at room temperature showed that the layers had monocrystalline (111)-oriented rhombohedral (a distorted NaCl-type) structure. The chemical composition of the layers was assessed by the electron probe microanalysis. The clean and ordered sample surface, suitable for angle-resolved photoemission experiments, was prepared *in situ* by cycles of Ar^+ ion sputtering and annealing under UHV conditions. Such a procedure was previously applied for preparation of GeTe samples for angle-resolved photoemission experiments[2].

We investigated the valence band of $Ge_{0.85}Mn_{0.15}Te$ along the Γ-T, T-W-L, and T-K directions in the Brillouin zone. The band dispersion along Γ-T was probed by collecting the spectra in the normal-emission regime for the photon energy range of 17-50 eV. The spectra were normalized for the fluctuations of the photon beam intensity. It was proved by the analysis of the dispersion of the revealed bands that emission from the maximum of the valence band (at the T point) was observed for $h\nu=20$ eV.

The bands along T-W-L and T-K, two non equivalent directions parallel to the sample surface, were investigated in the off-normal regime. For normal emission ($\theta=0$), the photon energy was kept at 20 eV. For higher emission angles, the photon energy was increased in order to compensate for the decrease of the normal component of the **k** vector. Fig. 1 shows the sets of spectra acquired for T-W-L and T-K. The main features can be ascribed to the bands of GeTe with rhombohedrally distorted NaCl structure. The dispersion of these bands also corresponds well to the electronic structure of GeTe.

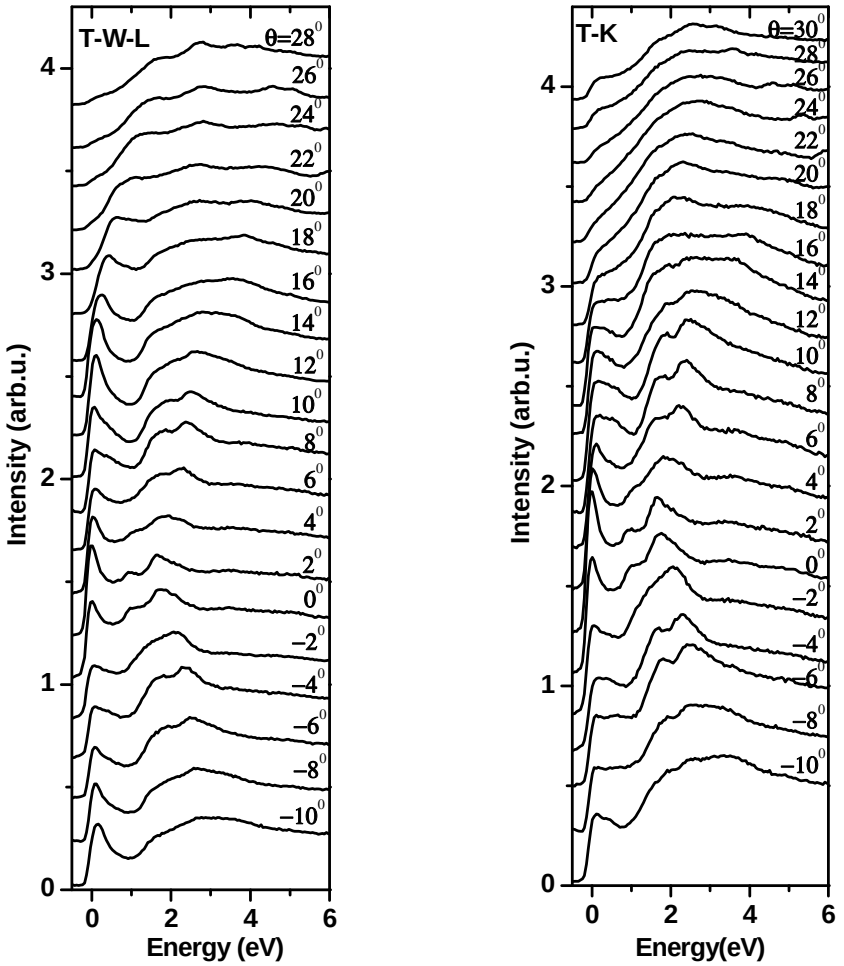

Fig. 1. The sets of photoemission spectra collected in the off-normal mode, corresponding to the scans of the valence band along the T-W-L and T-K directions in the Brillouin zone. The origin of the energy scale was set at the maximum of the valence band. Spectra taken for normal emission correspond to the T point.

A comparison of the acquired results with previously collected for GeTe and $Ge_{1-x}Mn_xTe$ surface alloy[2] enabled us to show that the contribution of Mn 3d states did not modify the top part of the valence band. Some changes could rather be found in the deeper part of the band – about 3.5 eV below the valence band edge.

The research leading to these results has received funding from the European Community's Seventh Framework Programme (FP7/2007-2013) under grant agreement nº 226716.

[1] Y. Fukuma, H.Asada, S. Miyawaki, T. Koyanagi, S. Senba, K. Goto, H. Sato, Appl. Phys. Lett. **93** 252502 (2008)

[2] B.J. Kowalski, M.A. Pietrzyk, W. Knoff, A. Łusakowski, J. Sadowski, J. Adell, T. Story, Physics Procedia, **3**, 1357 (2010)

Core-level shifts of the *c*(8x2)-reconstructed InAs(100) and InSb(100) surfaces

P. Laukkanen[1,2], M. P. J. Punkkinen[1,3], M. Ahola-Tuomi[1], J. Lång[1], K. Schulte[4], A. Pietzsch[4], M. Kuzmin[1], J. Sadowski[4], J. Adell[4], R. E. Perälä[1], M. Ropo[1], K. Kokko[1], L. Vitos[3,5], B. Johansson[3,5], M. Pessa[2], and I. J. Väyrynen[1]

[1] *Department of Physics and Astronomy, University of Turku, FI-20014 Turku, Finland*
[2] *Optoelectronics Research Centre, Tampere University of Technology, FI-33101 Tampere, Finland*
[3] *Department of Materials Science and Engineering, Royal Institute of Technology, SE-10044 Stockholm, Sweden*
[4] *MAX-lab, Lund University, SE-221 00 Lund, Sweden*
[5] *Department of Physics and Materials Science, Uppsala University, SE-75121 Uppsala, Sweden*

Producing In-stabilized *c*(8x2)-reconstructed (100) substrate on the heteroepitaxial III-V growth front (e.g., InP/InGaAs and InAs/GaSb) has been found to improve the properties of these interfaces for electronics devices [1-4]. This III-V(100)*c*(8x2) surface is also a potential starting substrate for producing insulator/III-V interfaces for future metal-insulator-semiconductor (MIS) transistors [5]. To understand reasons for the beneficial effects of the *c*(8x2) reconstructions and to controllably utilize these reconstructions, it is essential to know the properties of the III-V(100)*c*(8x2) surfaces.

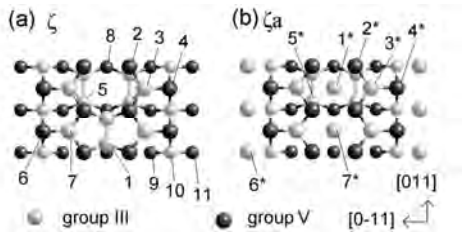

The III-V(100)*c*(8x2) surface has been found to be composed of unique ζ building blocks [6,7], which include dimers in the subsurface rather than top layer, monomer rows, and partially occupied atomic sites. Their "borderline" atomic configurations, labeled here ζ and ζa, with the 0% (for ζ) and 100% (for ζa) occupations [7] of the both atomic sites 1* and 6* are shown in the adjacent figure. The ζ and ζa (4x2) cells, of which relative shift along the [011] direction causes the *c*(8x2) periodicity, provide an established basis to model the III-V(100)*c*(8x2) properties since depending on the surface preparation, both ζ and ζa areas have been found without significant disorder related to the partial occupancy. Mainly due to the lack of theoretical ab initio analysis of surface core level shifts (SCLSs), the number of SCLSs and their physical origins for the III-V(100)*c*(8x2) surface have previously remained unclear. To elucidate these issues, we have studied the InAs- and InSb(100)*c*(8x2) surfaces by core level photoelectron spectroscopy at *the beamlines 41 and I511* and by first-principles calculations [8].

Theoretical SCLS results in Table 1 for InSb(100)*c*(8x2) provide a clearly different interpretation (i.e., number, energies, and origins of SCLSs) for the spectra of III-V(100)*c*(8x2) surfaces in general, as compared to the previous SCLS experiments, which typically showed one or two SCLS(s) around -0.4 and +0.4 eV. The calculated SCLSs for GaAs- and InAs(100)c(8x2) are similar to those in Table 1 [8].

Table 1. Calculated SCLSs (eV) for the InSb(100)*c*(8x2)-ζ and -ζa structures within the initial-state model. Also complete screening ζ SCLSs are shown. Negative values mean smaller BE as compared to the bulk. Numbers in parentheses show atomic origins of SCLSs in the above atomic models, and numbers in brackets show number of atoms in unit cell contributing to the SCLSs. The In layer below unit cell drawn in the above figure causes both -0.10 and +0.26 eV shifts of ζ. The Sb sites 9 and 11 and Sb layer below the cell cause ζ shift of -0.11 eV. This deeper Sb layer also contributes to +0.11 eV shift of ζ. Sb 8* (not shown) is below the In 6*. Sb layer below the cell contributes to +0.06 eV shift of ζa. The In layer below cell causes both -0.11 and +0.09 eV shifts of ζa.

InSb	**ζ (initial-state)**	**ζ (compl. screen.)**	**ζa**
In 4d	-0.29 (10) [4], -0.10 [4], +0.07 (5) [4], +0.17 (7) [2], +0.26 [2], +0.30 (3) [2], +0.36 (1) [2]	-0.32 [4], -0.17 [4], -0.13 [4], -0.05 [2], +0.06 [3]	-0.18 (5*) [4], -0.11 [3] +0.09 [2], +0.21 (1*,3*,6*,7*) [8]
Sb 4d	-0.38 (6) [2], -0.26 (4) [2], -0.11 (9 and 11) [8], +0.11 (2) [8], +0.38 (8) [2]	-0.48 [4], -0.22 [6], -0.12 [6], -0.06 [2], +0.10 [2]	-0.11 (2* and 4*) [8], +0.06 (8*) [6]

To analyze the measured spectra of the InSb- and InAs(100)*c*(8x2), we fitted the As 3d, In 4d, and Sb 4d spectra with the different SCLS sets calculated for the ζ and ζa structures [8]. The prerequisite for utilizing calculated SCLSs in the spectral analysis is the knowledge of the atomic structure of a surface studied. Thanks to the previous structural studies of the III-V(100)*c*(8x2) surfaces [6,7], it is now widely accepted that the ζ and ζa or their combination describes the III-V(100)*c*(8x2) surface. Fittings (e.g., the figure below) were done using the standard methods with the Voigt-profile peaks and Shirley background subtraction. Lorentzian width (LW), spin orbit splitting (SOS), branching ratio (BR), and calculated SCLS values were fixed input parameters which we have previously found to be reasonable.

The presented ab initio surface core-level shifts (SCLSs) for the ζ and ζa structures yield hitherto not reported interpretation for the core-level spectra of the technologically important III-V(100)*c*(8x2) surfaces, concerning the number and origins of SCLSs. The fitting analysis of the measured spectra with the calculated ζ and ζa SCLS sets shows that (i) the InSb spectra are reproduced by the ζ SCLSs better than by the ζa SCLSs, proposing the formation of ζ areas on the InSb(100)*c*(8x2) surface, (ii) the ζa SCLSs agree with the InAs spectra better than ζ SCLSs do, proposing that the ζa structure describes better the InAs- than InSb(100)*c*(8x2) surface, and (iii) the complete screening ζ SCLSs do not improve the InSb fittings as compared to the initial state one, proposing the suitability of the initial state model for describing SCLSs of the III-V(100)*c*(8x2) surfaces.

In general, SCLSs have been discussed with one or more of three common factors: changes in on-site atomic charges (ionic character), in Madelung potential, and in final state screening, as compared to the bulk. For example, origins for SCLSs of III-V(110)(1x1) surfaces have been under an intensive research. The discussion of these SCLSs has mainly focused on the two initial state factors: differences in the atomic charge state and in the Madelung potential, which have been two competing explanations in the literature. Our results: the ab initio on-site charges and test calculations for the Madelung potential effects clearly support the conclusion according to which changes in the Madelung potential are the dominant factors behind the SCLSs of the III-V(100)*c*(8x2) surfaces [8].

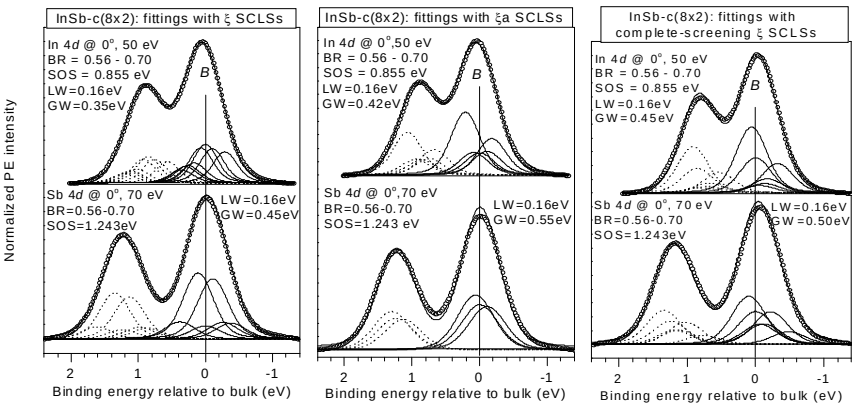

[1] T. Anan, S. Sugou, K. Nishi, Appl. Phys. Lett. 63 (1993) 1047.
[2] Q. Xue, T. Ogino, H. Kiyama, Y. Hasegawa, T. Sakurai, J. Cryst. Growth 175/176 (1997) 174.
[3] B. Z. Nosho, W. H. Weinberg, W. Barvosa-Carter, B. R. Bennett, B. V. Shanabrook, L. J. Whitman, Appl. Phys. Lett. 74 (1999) 1704.
[4] F. Maeda, M. Sugiyama, Y. Watanabe, Phys. Rev. B 62 (2000) 1615.
[5] B. Shin, D. Choi, J. S. Harris, P. C. McIntyre, Appl. Phys. Lett. 93 (2008) 062111.
[6] S.-H. Lee, W. Moritz, M. Scheffler. Phys. Rev. Lett. 85 (2000) 3890.
[7] C. Kumpf, L. D. Marks, D. Ellis, D. Smilgies, E. Landemark, M. Nielsen, R. Feidenhans'l, J. Zegenhagen, O. Bunk, J. H. Zeysing, Y. Su, R. L. Johnson, Phys. Rev. Lett. 86 (2001) 3586.
[8] P. Laukkanen, M. P. J. Punkkinen, M. Ahola-Tuomi, J. Lång, K. Schulte, A. Pietzsch, M. Kuzmin, J. Sadowski, J.Adell, R.E. Perälä, M. Ropo, K. Kokko, L. Vitos, B. Johansson, M. Pessa, I. J. Väyrynen, Journal of Electron Spectroscopy and Related Phenomena 177 (2010) 52.

Bismuth-stabilized *c*(2x6) reconstruction on InSb(100) substrate

P. Laukkanen[1,2], M. P. J. Punkkinen[1,3], N. Räsänen[1], M. Ahola-Tuomi[1], M. Kuzmin[1], J. Lång[1], J. Sadowski[4], J. Adell[4], R. E. Perälä[1], M. Ropo[1], K. Kokko[1], L. Vitos[3,5], B. Johansson[3,5], M. Pessa[2], and I. J. Väyrynen[1]

[1] *Department of Physics and Astronomy, University of Turku, FI-20014 Turku, Finland*
[2] *Optoelectronics Research Centre, Tampere University of Technology, FI-33101 Tampere, Finland*
[3] *Department of Materials Science and Engineering, Royal Institute of Technology,SE-10044 Stockholm, Sweden*
[4] *MAX-lab, Lund University, SE-221 00 Lund, Sweden*
[5] *Department of Physics and Materials Science, Uppsala University, SE-75121 Uppsala, Sweden*

The *c*(2x6) reconstruction commonly appears on the III-Sb(100) substrate surfaces in the Sb-rich conditions. The knowledge of the properties of this particular surface structure is important to understand and control [e.g., with reflection high energy electron diffraction, RHEED] the epitaxial growth of III-Sb materials for electronics devices since the growth usually proceeds via the *c*(2x6)-reconstructed substrate [1,2]. We have recently found that the group-V element bismuth (Bi) also induces a *c*(2x6) reconstruction on the InSb(100) substrate [3]. By combining photoemission measurements at *the beamline 41*, STM measurements, and ab initio calculations, we have elucidated the atomic structure of this InSb(100)*c*(2x6)-Bi surface [3]. The knowledge of the InSb(100)*c*(2x6)-Bi surface properties is essential not only for understanding the detailed formation mechanisms of the technologically important *c*(2x6) reconstructions but also for understanding the Bi surfactant-mediated growth of III-V's. The Bi/InSb(100)*c*(2x6) substrate also represents a starting surface to study the growth phenomena of the epitaxial Bi and MnBi films, which both are almost lattice-matched to the InSb substrates.

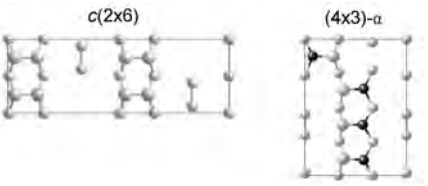

FIG. 1: Total energy calculations [3] reveal that depending on the chemical potentials, two basic geometries: metallic *c*(2x6) and semiconducting (4x3)α structures, are energetically stable on InSb(100)*c*(2x6)-Bi. Indium atoms are shown by black spheres and the Bi atoms by grey spheres. The first layer atoms are shown by larger spheres than the second layer atoms. Atoms in deeper layers are not shown.

Scanning tunneling spectroscopy (STS) results in Fig. 2 show the presence of both metallic and semiconducting InSb(100)*c*(2x6)-Bi areas The occurrence of both the metallic and semiconducting areas can be understood with the formation of areas with the metallic *c*(2x6) structure and areas with the semiconducting (4x3)α structure (Fig. 1). The valence band spectra near the Fermi level in Fig. 2 support the existence of metallic areas on the InSb(100)*c*(2x6)-Bi surface because its photoemission includes a small signal around the Fermi level, as compared to the semiconducting InSb(100)*c*(8x2) substrate. In passing, Bi might be a useful surfactant for the epitaxial growth of III-Sb materials since the metallic Bi-stabilized *c*(2x6) growth front of III-Sb substrates can be expected to lead to an increase in the III-atom diffusion on the growing surface and, therefore, to improved III-Sb layers [4].

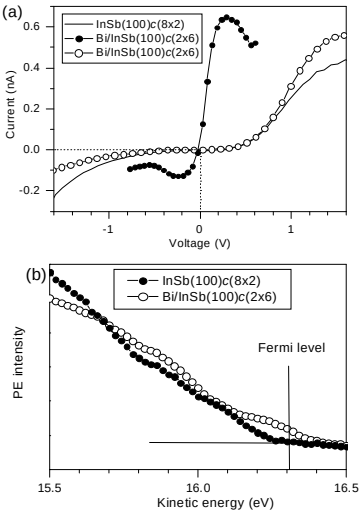

FIG. 2: (a) Current voltage curves measured by STS mode from the InSb(100)*c*(8x2) area and two different areas on the InSb(100)*c*(2x6)-Bi surface. (b) Valence band photoemissions near the Fermi level (vertical line) measured from the InSb(100)*c*(8x2) and InSb(100)*c*(2x6)-Bi surfaces. Fermi energy was determined from a Ta plate connected to the sample holder. The horizontal line is a zero-emission level.

Also the comparison of the calculated and measured surface core level shifts (SCLSs) in Table I supports the coexistence of two or more phases on InSb(100)*c*(2x6)-Bi. The measured Bi 5d, Sb 4d, and In 4d spectra of the InSb(100)*c*(2x6)-Bi surface were fitted by means of the minimum number of the components. Thus, in the comparison of measured and calculated SCLSs, an important criterion is that the calculated maximum and minimum SCLSs agree reasonably with the measured SCLSs since the smaller shifts

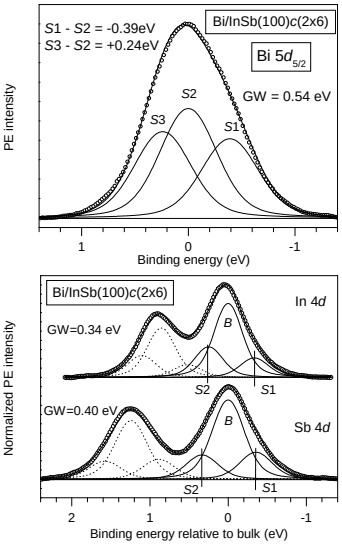

are most likely unresolved in the experiments. In the case of the Bi 5d shifts, the separation between different components is a reasonable criterion since the 0-eV references for the measured and calculated Bi shifts are not aligned. Table I shows that none of the models alone describes all the measured SCLSs well. The two-phase combinations of *c*(2x6) and *c*(2x6)-2 as well as of (4x3)α and (4x3)α-2 do not improve much the agreement between the calculated and measured SCLSs. The end number -2 in Table I means that Bi atoms occupy the group-V sites in the two topmost layers. In contrast, the SCLSs of the *c*(2x6) and (4x3)α phases complete each other better and together they improve the agreement with the measurements and calculations. This agrees well with our STM and total energy results [3]. Furthermore, the atomic origins of the Bi shifts *S*1, *S*2, and *S*3 are studied by means of the calculations. In the *c*(2x6)-2 structure, the calculated Bi shifts -0.29, -0.06, and +0.11 eV arise, respectively, from the dimers in the second layer, from the second layer Bi atoms below the topmost dimers, and from the topmost dimer. In the (4x3)α structure, the shifts 0, +0.17, and +0.34 eV are caused by the topmost dimers in the 4x kink site, in the site next to the kink, and in the middle of the three-dimer stack, respectively. For the (4x3)α-2 structure, the origins of three highest BE shifts are similar to those of the (4x3)α, and the lower BE shifts -0.31, -0.37, -0.53, and -0.65 eV all arise from the second layer atoms, respectively, in the sites below the middle dimers, in the dimer sites, in the corner sites of the dimer stack, and in the sites below the kink dimer. Combining these origins, we propose that the highest BE shift *S*3 arises from the topmost Bi dimers (excluding the 4x kink dimers), the middle shift *S*2 is caused by the kink dimers and a part of the second layer Bi atoms below the topmost dimers, and that the lowest BE shift *S*1 is caused by the second layer dimers and the other second layer Bi atoms below the dimers.

The results show that the atomic structure of the measured InSb(100)*c*(2x6)-Bi sample is not uniform and that the surface also includes semiconducting areas, which can be understood with the coexistence of areas with the stable metallic *c*(2x6) structure and areas with the stable semiconducting (4x3) structure. Our calculations reveal that the existence of the metallic *c*(2x6) phase, which does not obey the famous electron counting model, is attributed to the partial prohibition of the relaxation in the direction perpendicular to dimer rows in the competing reconstructions and the peculiar stability of the Bi-stabilized dimer rows [3].

Table I. Measured surface core-level shifts (eV) and calculated ones (by VASP *ab initio* code) for the energetically stable structures of the InSb(100)-Bi surface within the initial state model. Negative value indicates smaller binding energy (BE) as compared to the bulk BE. For the calculated Bi 5d shifts, the topmost dimer in the 4x kink site of the (4x3)α phase is taken as the 0-eV reference. Calculated shifts smaller than 0.05 eV are not listed.

	Calculated c(2x6)	Calculated c(2x6)-2	Calculated (4x3)α	Calculated (4x3)α-2	Measured
In 4d	+0.10	-0.09	-0.21, +0.23, +0.48	-0.26, -0.10, +0.14, +0.35	-0.33, +0.25
Sb 4d	+0.18, +0.35	+0.19	-0.37, -0.22, -0.12, +0.10, +0.38, +0.51	-0.12	-0.35, +0.33
Bi 5d	+0.23	-0.29, -0.06, +0.11	0, +0.17, +0.34	-0.65, -0.53, -0.37, -0.31, -0.18, -0.11, +0.10	-0.39, 0, +0.24

[1] M. T. Sieger, T. Miller, and T.-C. Chiang, Physical Review B, Vol. 52, 8256 (1995).
[2] W. Barvosa-Carter, A. S. Bracker, J. C. Culbertson, B. Z. Nosho, B. V. Shanabrook, L. J. Whitman, Hanchul Kim, N. A. Modine, and E. Kaxiras, Physical Review Letters, Vol. 84, 4649 (2000).
[3] P. Laukkanen, M. P. J. Punkkinen, N. Räsänen, M. Ahola-Tuomi, J. Sadowski, J. Adell, M. Kuzmin, J. Lång, R. E. Perälä, M. Ropo, K. Kokko, L. Vitos, B. Johansson, M. Pessa, and I. J. Väyrynen, Physical Review B, Vol. 81 (2010) 035310.
[4] J. Neugebauer, T. K. Zywietz, M. Scheffler, J. E. Northrup, H.Chen, and R. M. Feenstra, Physical Review Letters, Vol. 90, 056101 (2003).

Photoelectric Properties of Ge-Mn Layer Induced by Mn ion Implantation onto Ge(100)

G. Pető, and Cs. S. Daróczi
Research Institute for Technical Physics and Materials Science (MTA MFA),
H-1525 Budapest, P.O. Box 49, Hungary

Introduction: Magnetic **s**emiconductors represent one of the most promising materials in the field of spintronics. The magnetic behaviour in semiconductors can be achieved by incorporating transition metal (TM) impurities in a diluted phase. These new class of materials are referred to as diluted magnetic semiconductors (DMS). The solubility of TM impurities are usually very limited in the generally used MBE grown III-V semiconductors. The limitation can be overcome by using IV-based semiconductors (Ge or SiGe). The Mn doping of Ge at high concentration (1-10 at%) would be far the most promising material for DMS application, via TM substitution of Ge atoms by Mn in the lattice. An alternative non-equilibrium technique for the DMS fabrication is the ion implantation of TM elements into III-V or IV-IV semiconductors. In this case the surface reconstruction after the ion implantation induced radiation damage is the main challenge to realise a DMS device. The regrowing of the damaged layer with the required high doping TM concentration needs a very careful process. Another challenge is to avoid the intermetallic formation caused by the large TM concentration.

Experimental: We use low temperature regrowth to ensure the substitution of TM atoms into the host semiconductor. The regrowth was carried out in UHV to avoid the effect of the usual contamination. Special attention is needed to the damaged-undamaged interface and the surface.
Undoped Ge(100) wafer was implanted with Mn ions at 100 keV and $8x10^{16}$ at/cm^2 dose at room temperature (Institute of Ion Beam Physics and Material Research, Dresden-Rossendorf, Germany). The regrowth process was in situ investigated at the surface by photoemission and LEED techniques at BL41 in MAX-lab (Lund University, Sweden). The magnetic properties and structural data were obtained after the regrowth in MTA MFA.

Photoemission Results: In **t**he spectrum of the as received sample it was seen the oxidized state of Ge 3d together with some oxygen and carbon 2s contamination were present. After a short Ar^+ bombardment (15 min, 0.5 keV), the Ge 3d and the valance band levels were clear, while strong reduction of the oxidized Ge 3d was obtained. After a much longer sputtering (60 min, 0.5 keV) the Ge 3d emission was unchanged, and the sample could be regarded as clean. The valence band of this clean sample is given in Fig. 1 (3.048 and 3.049), where the photon energy was 51 eV and 49 eV, respectively. It is well known that there is a resonance photoemission at 51 eV photon energy of the Mn 3d valence state. However, the valence bands obtained at 51 eV and 49 eV are practically equivalent (there was no Mn intermetallic present). The valence band of the Ge-Mn layer after annealing at 400 ^{o}C with simultaneous sputtering (15 min, 0.5 keV) is given in Fig. 2 (3.075 and 3.074) at 51eV and 49 eV photon energies, respectively. Now the effect of the resonance photoemission of the Mn in the valence band is clearly visible. The photoemission spectra at the Fermi level of the sputtered-only (cleaned) Ge-Mn sample is given in Fig. 3 (3.018) together with the calibration of the Fermi edge of the sample holder (3.019). We can see a not very well pronounced Fermi cut off in the case of Ge-Mn sample. The photoemission spectra of the sputter-cleaned then annealed Ge-Mn sample at the Fermi level is shown in Fig. 4 (3.133) together with the reference Fermi level of the metal sample holder (3.134), respectively. In this case the existence of the Fermi cut off and the metallic Fermi level is even much less pronounced than in the case of the sputter-cleaned sample, and even the existence of the metallic is questionable. However, it is clear that the valence band edge coincides with the metallic Fermi level, only the metallic characteristics of this Ge-Mn can not be clearly detected.

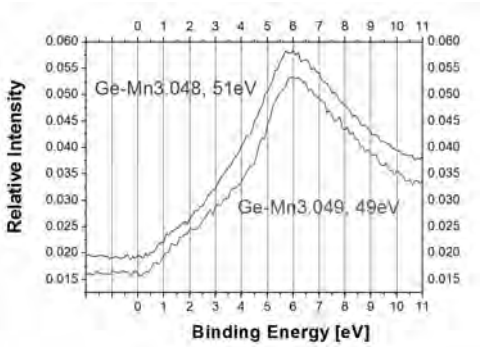

Figure 1. *The valence band of the* ***cleaned*** *sample measured at 51 and 49 eV photon energies.*

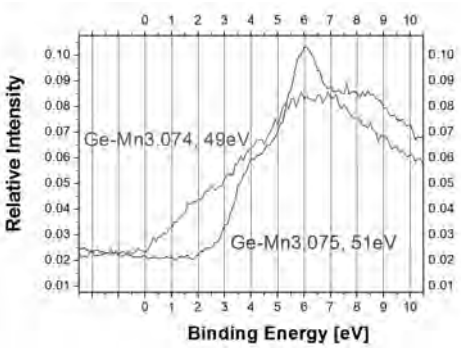

Figure 2. *The valence band of the* ***annealed*** *(15 min, 400 ^{o}C) sample measured at 51 and 49 eV photon energies.*

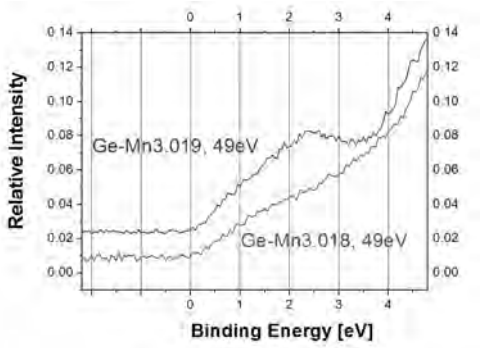

Figure 3. *Fermi level spectrum of the* ***cleaned*** *Ge-Mn sample (3.018) with the sample holder's Fermi edge (3.019).*

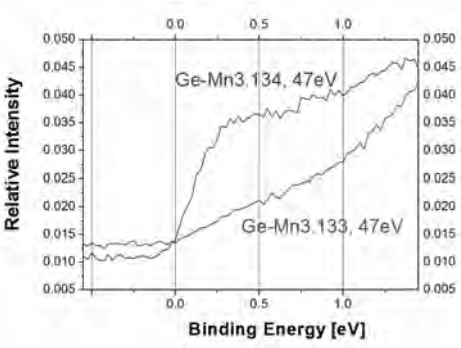

Figure 4. *Fermi level spectrum of the* ***annealed*** *Ge-Mn sample (3.133) with the sample holder's Fermi edge (3.134).*

According to transition electron microscopy measurements the structure of the Mn implanted Ge was amorphous after the implantation and the surface cleaning. The annealing of this structure modified some grains in the amorphous background. The magnetic properties could be characterised by super-paramagnetic clusters in the as-implanted case. After the annealing some ferromagnetic „material" and clusters were observable. The LEED pattern was not observable, similarly to the ARUPS spectrum. Probably the annealing temperature of the thermal budget was too low, and the crystallization has started only. The pre-crystallization process was not localized to the damaged-undamaged interface, instead the whole damaged layer was involved. This indicates an unusual regrowing process. The effect of some possible contaminations was not observed as the source of the experimental data.

Acknowledgements: We would like to acknowledge the help from MAX-lab staff and wish to thank the financial support from ARI.

Investigations of post-growth annealing of (GaMn)As under Sb capping

I. Ulfat [1,2], J. Adell [1,2], J. Sadowski [2,3], L. Ilver [1], J. Kanski [1]

[1] *Department of Applied Physics, Chalmers University of Technology, SE-41296 Göteborg, Sweden*
[2] *MAX-lab, Lund University, SE-22100 Lund, Sweden*
[3] *Institue of Physics, Polish Academy of Sciences, al Lotnikow 32/46, 02-668 Warszawa, Poland*

It has been demonstrated previously that *in-situ* post-growth annealing of (GaMn)As under As capping is a successful approach to raise the Curie temperature [1]. We have recently shown that the epitaxial layer formed via solid phase reaction of out-diffusing Mn with As capping results in formation of a uniform epitaxial continued layer of MnAs with a 1x2 surface reconstruction [2]. The ability to prepare such a surface opens the possibility to incorporate MnAs layers in a controlled way into an epitaxial composite MnAs/(GaMn)As structure. There is, however, one problem with this treatment: it is very difficult to control the deposition of the As and consequently there is always excess As on the surface after the annealing process is completed. Additional heating at an elevated temperature must, therefore, be employed to desorb this As. Though the initial annealing is advantageous for the magnetic properties, it is well known that extended annealing has the opposite effect and should thus be avoided.

In order to get around this limitation we replaced As with isoelectronic element Sb, expecting a similar surface reaction with out-diffusing Mn. The advantage with Sb over As in this context is that dosing can be controlled, so with adequate amount of Sb on the surface one should get a reacted MnSb monolayer with no need of supplementary desorption. The interest in introducing epitaxial layers of MnSb in the annealed (GaMn)As is also motivated by the predicted half-metallic ferromagnetic properties of ZB MnSb.

The experiments were performed at beamline 41. The samples were grown on epi-ready n-type GaAs (100) substrates, In-glued on Mo holders. After the usual oxide desorption and deposition of a GaAs buffer at 560 °C, the substrate temperature was lowered to 230 °C for the growth of (Ga,Mn)As with 6% Mn. As_2 was supplied from a cracker source maintaining the As_2 / Ga pressure ratio to just about 2. The (Ga,Mn)As surface was then capped with 2 ML Sb and annealed at 200°C in the MBE chamber. Following the same scheme a reference sample was made without any Mn (i.e. LT-GaAs), capped with same amount of Sb and annealed at 200 °C in the MBE chamber.

The photoemission spectra from the two samples were then recorded under the same conditions, i. e. in normal emission and with 81 eV photons. We focus here on the Sb 4d spectra, where we expect to find one component reflecting the reacted MnSb layer. For the as-deposited samples the Sb 4d spectra were quite narrow, and were considered to contain one spectral component characteristic of the disordered Sb_4 molecules. The fitting parameters for this spectrum are given in Table 1.

ΔE_{SO} (eV)	1.250
Br. ratio	1.450
ΔE_{LOR}(eV)	0.495
ΔE_{Gauss}(eV)	0.280

Table 1. Fitting parameters for Sb 4d

With annealing the spectra were gradually broadened and shifted towards low kinetic energy until saturation, which was reached after about 10 min at around 150 °C. In Fig. 1a

we show the spectrum of the Sb/(GaMn)As sample as it appears after 10 min annealing at 200 °C. Using the same fitting parameters as those found adequate for the sample, we find that three major components are needed to account for the shape of this broadened spectrum.

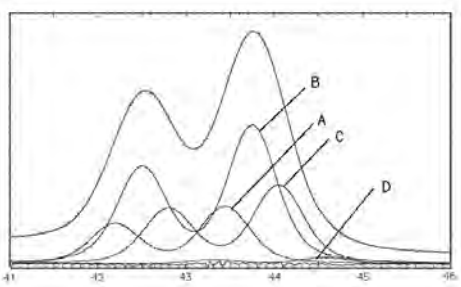

Fig 1a. Sb4d spectrum from annealed Sb/(GaMn)As

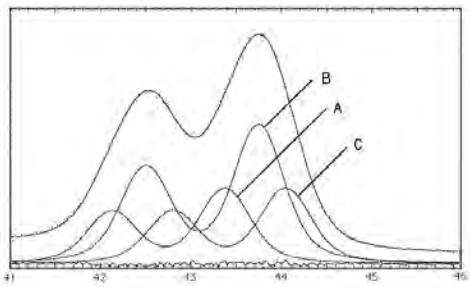

Fig 1b. Sb4d spectrum from annealed Sb/GaAs

In order to identify the expected component of the expected MnSb layer, we compare with the spectrum from the reference GaAs sample, Fig 1b. Unexpectedly we find that the two spectra are very similar except for a very small component ”D” found for the (GaMn)As sample. Considering that the total amount of deposited Sb is only 2 ML, it is clear that component D corresponds to a very small number of Sb sites, far less than expected for a reacted ML. We must conclude that the expected reaction did not take place. The different components developed during annealing must be ascribed to other modifications that are the same on the two surfaces. The identification of the different components is not yet completed, but we believe that the main component (B) reflects crystallized Sb, while components A and C represent different interface/surface sites.

It is of course important to clarify why Sb behaves co differently from As in this context. One possible explanation is that the As that was evaporated from a cracker source, i.e. in the form of As_2, while a conventional Knudsen cell source was used for Sb. It is possible then that the Sb_4 clusters are more stable and therefore less likely to react with the out-diffused Mn. This issue will be investigated in near future by using an Sb cracker source.

References

[1]. M. Adell et al., Appl. Phys. Lett. **86**, 112501 (2005)
[2]. I. Ulfat et al., Surf. Sci. **604(2)**, (2010)

Lead growth on the indium reconstructed Si(111)4x1-In surface at low temperature

D. Vlachos, M. Kamaratos and S.D. Foulias

Department of Physics, University of Ioannina, P.O. Box 1186, GR-451 10 Ioannina, Greece

Nanostructures on surfaces are of great importance in nanotechnology. This is because the shape, the size and the symmetry of the developed nanostructures affect and finally determine the physicochemical and electronic properties of the adsorbate/substrate system. These properties are strongly related with the quantum size effects, QSE, i.e. the dependence of the energy of the confined electrons on the structure size) [1]. The QSE leads to the formation of symmetrical self-assembled nanostructures, especially when deposition takes place at low temperatures. Unfortunately this prevents the applications of these adsorption systems at room or higher temperatures. However, it has been recently shown that growth of Pb on the reconstructed In(4x1)/Si(111) surface at low temperature can preserve the uniform size and geometry up to the room temperature (RT) [2]. More specifically, it has been shown that Pb forms mostly uniform 4-layer high islands on the In(4x1)/Si(111) at 180 K which are stable up to RT [2]. The reason for this is not known. Therefore, in this contribution as a first step we study the electronic and structural properties of the developed islands of lead on the silicon reconstructed by indium silicon surface, In(4x1)/Si(111) at low (~160 K) temperature. The investigation is based on the Si 2p, Pb 5d, In 4d and valence band photoemission measurements on 41 beamline in MAX I. The measurements were taken with geometry of 45^{o} incidence angle and normal emission. The Pb dosing (1D) was roughly estimated ~0.7ML/D.

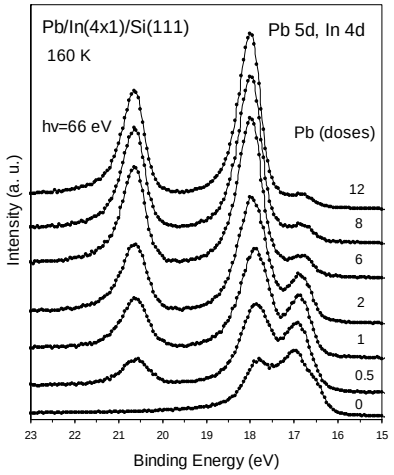

Figure 1. Pb 5d and In 4d doublets for Pb growth on the In(4x1)/Si(111) surface at 160 K.

In Fig.1 the Pb 5d and In 4d atomic levels are shown as the Pb coverage increases at 160 K. We note that the In 4d doublet is being gradually covered by the Pb 5d one. Although the two doublets overlap each other, the Pb $5d_{3/2}$ component is not convoluted and can be analyzed fruitfully. Thus, the Pb $5d_{3/2}$ and Si 2p peak height intensity variation versus the coverage indicates the formation of islands on the surface. In addition, LEED observations show that the 4x1 pattern is lost for dosing at least equal to 2D. It is also found that the FWHM of the Pb 5d3/2 peak decreases with the coverage by at least ~0.2 eV. This might be due to the different local atomic configuration in Pb islands between the low and higher coverage. Actually, scanning tunnelling microscopy (STM) measurements have shown that Pb up to ~2 ML forms a wetting layer which progressively turns into self assembled four layer islands [2]. So it seems that Pb adsorption starts with relatively isolated two dimensional islands, which progressively forms an amorphous wetting layer and finally end up with the formation of mostly four layer uniform islands.

We tried to follow this morphological transformation of Pb by recording the valence band (VB) measurements are shown in Fig. 2. At first, we observe the characteristic spectrum of the

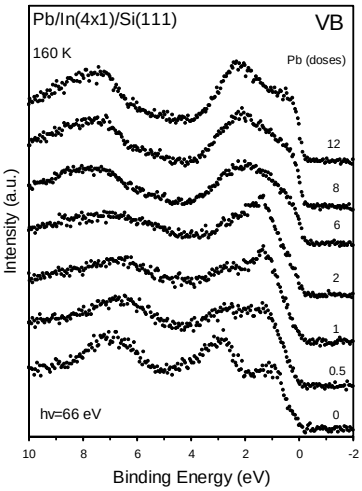

Figure 2. Valence band for Pb adsorption on the In(4x1)/Si(111) surface at 160 K.

4x1 phase which has a metallic character [3]. Gradual Pb dosing on the In(4x1) surface induces the population of the Fermi level. This means that the metallicity of the surface increases with the coverage of lead. In addition, the overall VB range also changes drastically. For dosing up to 2D, the evolution of the sharp emission feature at ~1.3 eV and the ~6.35 eV can be attributed to the wetting layer formation. The first feature can be considered as interfacial Pb-In states while the second one is probably related with the Pb 6p atomic orbitals. For dosing >2D, the VB spectra changes drastically, with the previously mentioned features to be vanished and two new ones to be developing at ~2.2 eV and 7.3 eV respectively. Also a shoulder at ~0.45 eV appears progressively stronger as the metallicity increases. This drastic VB spectral change is attributed to the morphological transformation of the wetting layer into uniform island height formation. The 2.2 eV and 7.3 eV can be considered bulk Pb states as the islands are growing in three dimensions.

In conclusion, the morphology of the Pb overlayer seems to affect significantly both the valence band as well as the low core levels of the adsorbate. Next task will be to investigate how the electronic properties of the Pb overlayer change, as the temperature increases up to the RT. It will be interesting to correlate these properties with the morphology of the adsorbate on the In(4x1) reconstructed surface, already known by STM measurements [2].

References

[1] Z. Zhang, Q. Niu, C.K. Shih, *Phys. Rev. Lett.* **80**, 5381 (1998).
[2] M. Yakes, J. Chen, M. Hupalo, M.C. Tringides, *Appl. Phys. Lett.* **90**, 163117 (2007).
[3] T. Abukawa, M. Sasaki, F. Hisamatsu, T. Goto, T. Kinoshita, A. Kakizaki, S. Kono, Surf. Sci. 325 (1995) 33.

High-school students doing physics studies at MAX-lab

Gunilla Johansson[a], Brian N Jensen[b], Kurt Hansen[b], Sverker Werin[b] and Stacey L. Sörensen[c]

[a] *Polhemskolan, Box 4047, S-227 21 Lund*
[b] *MAX-lab, Lunds Universitet, Box 118, S-221 00 Lund*
[c] *Synkrotronljusfysik, Lunds Universitet, Box 118, S-221 00 Lund*

INTRODUCTION

In order to give high-school students the possibility to see how experimental research at MAX-Lab is really done the ageing BL52 and its surroundings have been developed as an experimental platform for pedagogical activities at MAX-Lab. The laboratory invested in an upgrade of the monochromator control system and some new experimental equipment has been acquired for the project. During 2009 preparations and tests were made and in February 2010 the first high-school students visited the laboratory. We report on the first experience with this type of activity at MAX-lab.

EXPERIMENTAL AREAS

The class was divided into two groups of 15 students; each group would spend one day doing labs at MAX-lab. These student groups were further split into 3 lab groups (of approximately 5 students), which would each carry out two different laboratory exercises. The first phase of experiments contained the following areas

a) The electromagnetic spectrum from IR to UV and its polarization,
b) Auto-ionization in Ar using BL52 and a gas cell ,
c) Magnetic studies on a quadrupole magnet.

Lab instructions and the experimental hardware were prepared during the fall 2009/early 2010.

The Electromagnetic Spectrum, IR to UV

The old BL53 tube was equipped with a sapphire window in order to allow dipole radiation from MAX I to be viewed by the students. A lens and a grating capable of focusing and diffracting both visible and UV light was used to investigate the spectrum. The grating equation was deduced and the light from the ring was used to estimate the line density of the grating.

The UV part of the light was investigated using a glass plate with some florescent material and also the use of "Optical Brightener" in ordinary paper and washing detergents was discussed.

Some of the infrared part of the spectrum could be seen with a digital camera. IR was also demonstrated with another setup with a TV camera and an IR lamp reading secret messages hidden behind black screens.

The content of polarized light of the dipole radiation was investigated. Both linear and circular light polarizations were discussed and these were identified in the beam.

FIGURE 1. Bright students deducing the grating equation. Note the glowing foreheads.

The recent developments in 3D cinemas and the technique of using right- and left-hand circular polarized light was discussed and demonstrated with the synchrotron radiation and some "3D-glasses". The buildup of a circularly polarizing filter (linear filter + ¼ wave plate) was discussed. Furthermore the mainly linear polarized content in reflected light was investigated.

The photon energy of visible light and also of IR at room-temperature-radiators was calculated using Wien's displacement law. Planck's law and the Stefan-Boltzmann law were mentioned and their importance for the history of quantum physics was pointed out.

An IR camera, showing temperatures, was used to illustrate Wien's displacement law. The students were looking for hot things in the surroundings (at the beamline) and were also investigating reflection of black body radiation looking at their own image reflected from a surface.

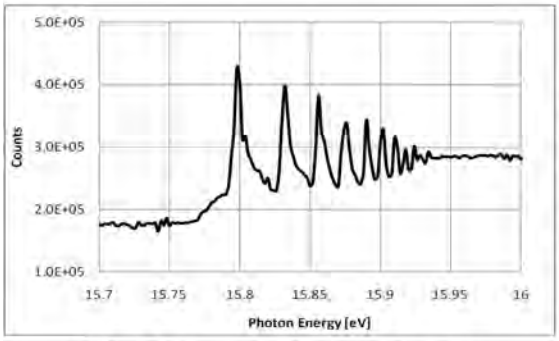

FIGURE 2. An example of data taken by the students.

Auto-Ionization of Argon

The students were introduced briefly to atomic physics. Rydberg's formula and Bohr's model for the atom were presented. Energy levels of the electrons in the hydrogen and argon atoms were discussed and the auto-ionization was explained.

Experiments were done at BL52 with an attached gas cell. The students experienced how complex a beamline and experimental setup needs to be in order to obtain data. The experimental setup consists of the gas cell, electrometers for the ion current and a normalization signal, voltage to frequency converters and counters for collecting the data.

Energy scans were done around the Ar 3p1/2 edge. The importance of monochromator resolution and the effect of using second-order diffraction was investigated. Also the effect of the counting time was discussed.

Magnetic Studies on a Quadrupole Magnet

A Hall probe was used to investigate the magnetic field in a quadrupole used in the MAX-lab injection system in the years 1980-2000.

The quadrupole strength was measured and the number of windings was estimated using the quadrupole strength equation.

The focal length for 100MeV electrons was calculated using the measured quadrupole strength and the focus equation.

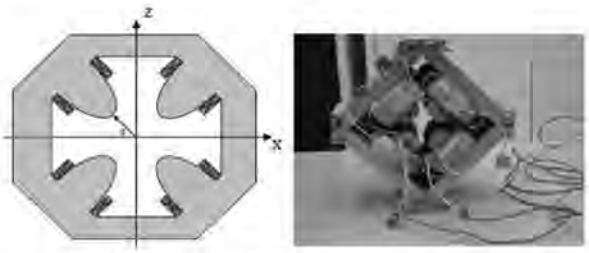

FIGURE 3. Quadrupole under investigation.

LESSONS LEARNED AND PLANS FOR FURTHER WORK

The days at MAX-lab were successful, although rather tough for the students. A lot of information had to be digested in a short time. We probably have to improve the handouts and more clearly emphasize the importance of being well prepared beforehand.

The students were interested, positive and engaged in the work and they were not afraid of asking about things. The presentations made for the experiments were improved on the run between each time they were done. The polarization of light proved to be a difficult concept. More work on the pedagogical approach could help.

We are considering the possibility of placing the handouts and also external links on our web page. More work on increasing the palette of experiments should be done.

We consider the possibility to offer this type of service to other high-schools and even physics students at the university. The amount of work for this should be visible and allocated by the lab/university.

All participants in the project think it has been very worthwhile the effort.

http://www.lund.se/Gymnasieskolor/Polhem/Nyheter/Elever-laborerar-pa-MAX-lab/

Geochemical Relationships between Organic Compounds and Sandstone Particles

M.P. Andersson, C. Hem, C.S. Pedersen, S.L.S Stipp

Nano-Science Center, Department of ChemistryUniversity of Copenhagen, Universitetsparken 5, DK- 2100 Copenhagen, Denmark

The demand for energy in the world is ever increasing and renewable sources have not yet become mature enough to decrease the demand for oil significantly. Most of the world's easy-to-produce oil has been extracted, so innovative methods will be required to reach the more than 60% that is left in depleted reservoirs. The oil industry has made huge efforts to enhance oil recovery, but trial and error and macroscopic investigations have failed to provide the insight needed to develop more effective extraction strategies. Fundamental information about the molecular level processes controlling the composition of fluids and particle structure is required.

We present here our first results from an infrared microspectroscopic study of a sandstone sample from an oil reservoir performed at Beamline 73 at MAX-lab. Key questions we seek to answer are:

Where does oil prefer to adhere? To sand grains? To nanoparticles of clay attached to the sand? Or in the capillary fringes in the pores between the grains?

In Figure 1 is a reflection image of a cut and polished sample of sandstone, with the aperture set to about 30x30 μm^2. This image illustrates that the characteristic sizes of the various components in sandstone have a suitable length scale for infrared microscopy. It allows for study of either the sand grains (bright in Fig. 1), or the intergrain material (dark in Fig. 1).

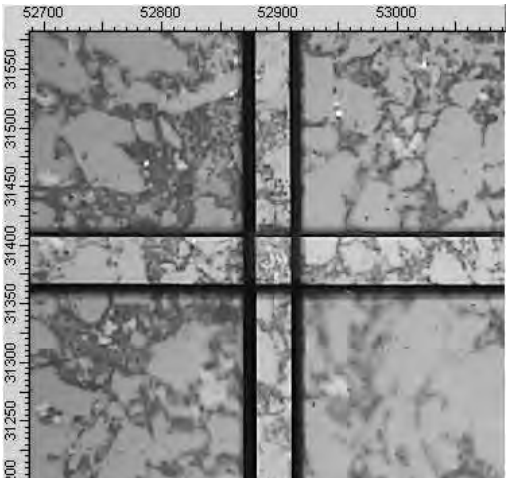

Figure 1. Microscope image of a cut and polished sample of sandstone. The center square is the aperture for the infrared microscopy analysis. All scales are in µm.

In Figure 2, infrared transmission spectra of two different parts of a single sand grain clearly demonstrate the chemical heterogeneity of the grain. The red (top) spectrum shows strong infrared absorption around 900-1200 cm^{-1}, which is consistent with Si-O or Al-O stretch vibrations from quartz or feldspar, the two dominant types of minerals in this sandstone sample, determined from X-ray diffraction (data not included). The peaks in the range 1400-1900 are most likely overtones and combination bands of the same features, but we have not yet performed a detailed analysis of these peaks. At ~2900 cm^{-1}, weak C-H stretch vibrations indicate that hydrocarbons are present and at 3400-3600 cm^{-1}, weak O-H

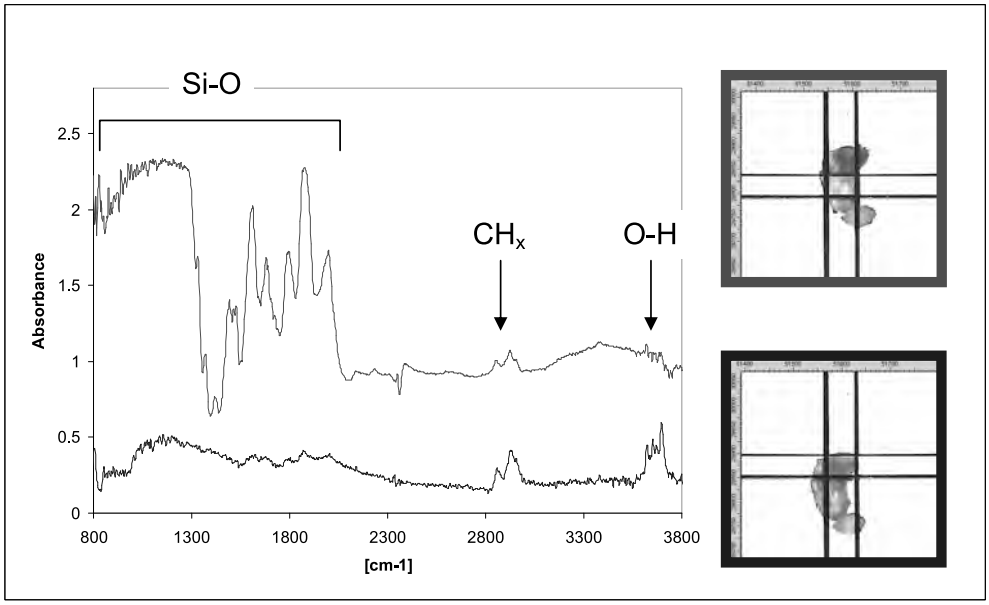

Figure 2. Infrared spectra from two different sites on a single sand grain. The red (top) image and spectrum are from the center part of the grain, transparent in visible light. The blue (bottom) image and spectrum is from the dark edge of the grain.

stretch vibrations are found, which are probably from water or clays.

In the blue (bottom) spectrum absorption from Si-O and Al-O stretches are much weaker. At the same time, much stronger infrared absorption for C-H and O-H stretches are observed. By comparing the spectral appearance in the O-H stretch region to reference mineral spectra (not shown) we can conclude that the majority of the O-H stretch vibrations come from the clay type kaolinite. Small amounts of water and the clay illite are present as well. The spectrum in the C-H stretch region is consistent with aliphatic hydrocarbons. No aromatic rings are present. These would produce absorption at ~3050 cm^{-1}. Functional groups in the oil are difficult to identify without more detailed analysis and better statistics. Most functional groups have characteristic spectral features in regions of the spectrum that are obscured by other spectral details such as Si-O stretches or O-H stretches.

We have used infrared microspectroscopy to identify various minerals present in the sandstone as a test for its capability for future studies. Future work will aim at improving sample statistics so we can quantify and confirm the relationships that these preliminary studies hint at.

Temperature controlled kinetics of growing and relaxation of alcohol clusters in Ar matrix

I.Doroshenko[1], V.Pogorelov [1], P.Uvdal[2], V.Balevicius[3], V.Sablinskas[3]

[1]Department of Physics, Kyiv National Taras Shevchenko University, Kiev, UKRAINE
[2]MAX-lab, Lund University, Lund, SWEDEN
[3]Department of Physics, Vilnius University, Vilnius, LITHUANIA

The clustering phenomena and structural peculiarities of partially ordered liquids are of great interest in the scientific community. This interest is even growing in context of recent trends and developments in studies on modern multifunctional materials, heterogeneous systems and nanotechnologies. Monohydric alcohols, that usually build broad variety of H-bond aggregates, are quite simple and convenient models to investigate properties of molecular systems sized over the mezoscopic scale (1 – 100 nm). The importance of the problems connected with the alcohol clustering, structure and, in particular, with the mechanisms of the diffuse absorption band formation reflects in the great number of experimental [1, 2], theoretical [3 -5] and combined works [6, 7] published in the recent years.

The cause of cluster formation in alcohols is the intermolecular hydrogen bond. The vibrational spectra of liquid alcohols differ from their spectra in gas phase or in matrix by the absence of the vibrational band of free hydroxyl group vibrations. Instead of this the red-shifted diffuse band, which is usually associated with the presence of molecular aggregations (clustering), is observed. There are also the investigations of the dependence of the O–H stretching vibrations on the concentration of the alcohols in different solvents, for example in CCl_4 [8, 9] and hexane [10]. In these experiments one can observe the existence of monomeric molecules at low concentrations and their aggregation with the increasing of the concentration.

It is necessary to note that in all accessible works on alcohols in matrices, droplets and jets the spectra were investigated at fixed temperatures. The redistribution in intensities of the bands of H-bonded and non-bonded alcohols was achieved by changing the concentration of investigated molecules, or by changing the matrix composition, annealing, irradiation *etc*. It is obvious that more respectable challenge it would be to find the tools to trace and to control the processes of molecular clustering continuously. The softening the matrices by heating, and thus producing more ways (channels) to get alcohols molecules together, seems to be one of such possibilities.

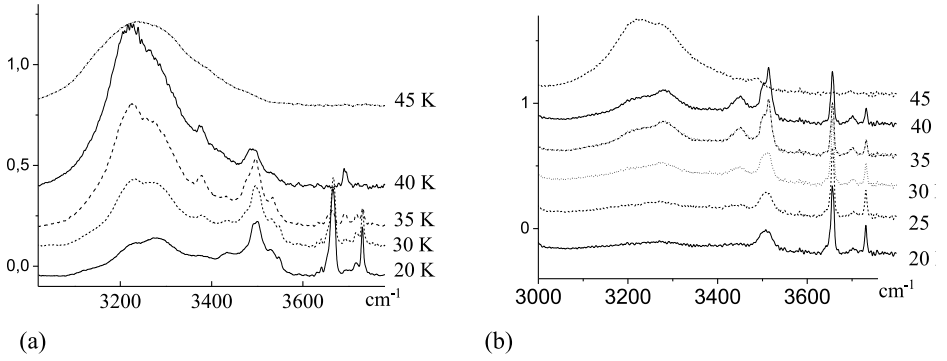

Fig.1 Temperature evolution of FTIR spectra of methanol (a) and ethanol (b) trapped in Ar matrix.

We have registered the FTIR spectra of the homologous series of monohydric alcohols (methanol through hexanol) trapped in Ar matrices and analyzed the changes in spectra at increasing temperature. The transformation of FTIR bands of free hydroxyl groups (3600 – 3800 cm^{-1}) into diffuse bands (3000 – 3600 cm^{-1}), which were assigned to the stretching vibrations of the H-bonded O–H groups in various clusters, was monitored in its initial stage softening the matrices by heating from 20 K to 50 K. The results of these experiments are presented at Fig.1, 2.

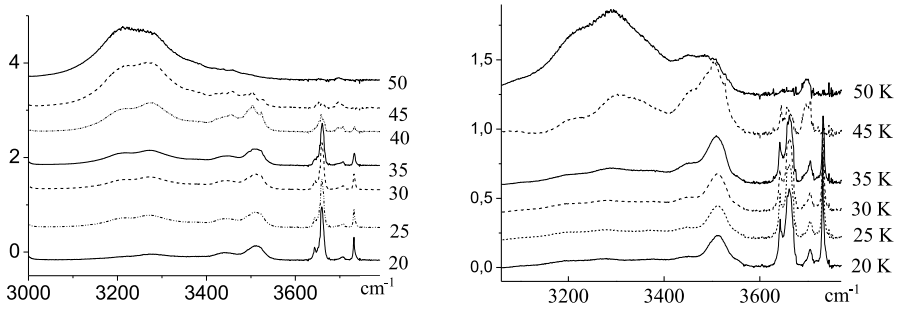

Fig.2 Temperature evolution of FTIR spectra of propanol (a) and hexanol (b) trapped in Ar matrix.

This work provides valuable additional information on the process of cluster formation in alcohols and on the mechanisms of the diffuse absorption band formation during the phase transition from gas to condensed matter.

Acknowledgment

This work was supported by Swedish Institute through Visby program.

References

[1] X. Wu, Y. Chen, T. Yamaguchi, J. Mol. Spectr. 246, 187 (2007)
[2] R. Wugt Larsen, P. Zielke, M.A. Suhm, J. Chem. Phys. 126, 194307 (2007)
[3] E.F. Fileti, M. Castro, S. Canuto, Chem. Phys. Lett. 452, 54 (2008)
[4] S. Boyd, R. Boyd, J. Chem. Theory Comput. 3, 54 (2007)
[5] K.Bloch, C.P.Lawrence. J.Phys.Chem.B, 114, 293 (2010)
[6] F.H. Tukhvatullin, V.E. Pogorelov, A. Jumabaev, H.A. Hushvaktov, A.A. Absanov, A. Shaymanov, J. Mol. Struct. 881, 52 (2008)
[7] Y. Tamenori, K. Okada, O. Takahashi, S. Arakawa, K. Tabayashi, A. Hiraya, T. Gejo, K. Honma, J. Chem. Phys. 128, 124321 (2008)
[8] K. Gaffney, P. Davis, I. Piletic N.E. Levinger, M.D. Fayer, J. Phys. Chem. A, 106, 12012 (2002)
[9] K. Gaffney, I.R. Piletic, and M.D. Fayer, J. Phys. Chem. A, 106, 9428 (2002)
[10] A. Yokozeki, D.J. Kasprzak, M.B. Shiflett, Appl. Energy 84, 863 (2007)

High-resolution FTIR spectra of methanol in the region of O–H stretch vibration in gas phase

I.Doroshenko[1], V.Pogorelov [1], P.Uvdal[2], J.Ceponkus[3], V.Sablinskas[3]

[1]Department of Physics, Kyiv National Taras Shevchenko University, Kiev, UKRAINE
[2]MAX-lab, Lund University, Lund, SWEDEN
[3]Department of Physics, Vilnius University, Vilnius, LITHUANIA

It is known (see, e.g. [1 - 7]) that in liquid phase the individual molecules aggregate in larger formations – so called clusters. The special attention in literature is devoted to the researches of the structure of liquid methanol. In early 60-th L. Pauling [8] supposed that cyclic hexamer is the most probable form of molecules aggregation in liquid methanol. The structure of liquid methanol has been investigated by different methods: neutron [9] and X-ray [10] scattering, vibrational spectroscopy [11], and femtosecond experiments where the lifetimes of molecular clusters were calculated [12]. The IR spectra of methanol clusters with the different (fixed) numbers of molecules in a cluster in helium droplets were registered in [13].

In the present contribution we report the high-resolution infrared absorption spectrum of gaseous methanol in the region of O–H stretch vibration recorded with the Bruker 120 FTIR HR Fourier transform infrared spectrometer and the infrared synchrotron radiation component offered by the MAX-I storage ring. Spectra were registerd at five different pressures from 0,1 torr to 2 torr with resolution 0,1 cm^{-1}. In Fig. 1 the recorded spectrum of methanol in frequency region from 3500 to 3800 cm^{-1}, the region of free OH group stretch vibrations (lower curve) at the pressure 0, 1 torr is presented. For comparison in this figure we also show the spectrum, recorded for the same region with low resolution – 1 cm^{-1} (upper curve). In both spectra one can see the rotational structure of the studied vibrational band with P-, Q- and R-branches.

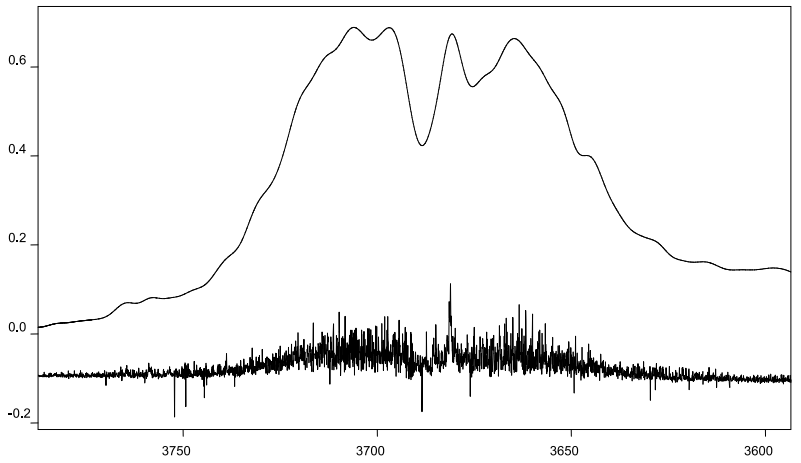

Fig. 1 The registered infrared absorption spectra of methanol in gas phase

Methanol is the smallest organic molecule with large amplitude, low frequency, torsional motion, which couples to rotation and to the vibrational modes. The analysis of these couplings requires special treatment of the rotational [14] and rovibrational spectra [15] based on the existence of torsion-vibration levels. It is evident from the high-resolved infrared absorption spectrum in the frequency range of the non-bonded hydroxyls groups which are present in gaseous methanol. In the condensed phase, where the individual molecules aggregate in clusters, this band is shifted towards lower frequencies and became very broad (with the half-width of about 200 cm^{-1}). The IR spectrum of liquid methanol is presented in Fig.2.

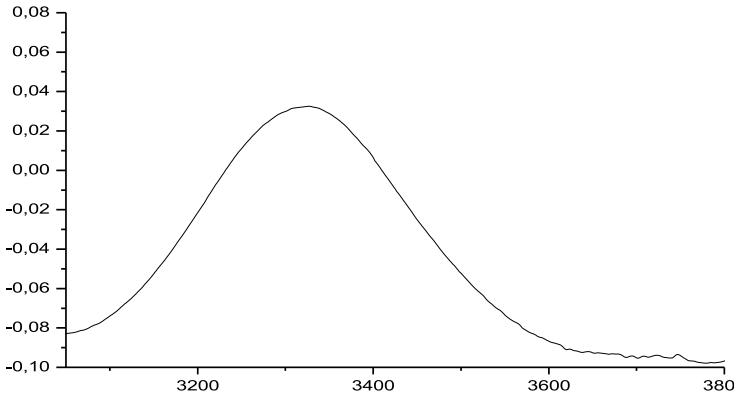

Fig. 2 Infrared absorption spectrum of liquid methanol registered using ATR technique

The pressure increasing from the value of 0,1 torr to 2 torr has not shown any changes in the registered infrared absorption spectra of methanol in this frequency region. It is seen that such low pressures are not sufficient for the beginning of clusterization at room temperature.

[1] E.F. Fileti, M. Castro, S. Canuto. Chem. Phys. Lett. 452, 54 (2008)
[2] S. Boyd, R. Boyd. J. Chem. Theory Comput. 3, 54 (2007)
[3] K.Bloch, C.P.Lawrence. J.Phys.Chem.B, 114, 293 (2010)
[4] K.Takahashi, M.Sugawara, S.Yabushita. J.Phys.Chem.A. 107, 11092 (2003)
[5] X. Wu, Y. Chen, T. Yamaguchi. J. Mol. Spectr. 246, 187 (2007)
[6] J.P. Perchard, Z. Mielke. Chem. Phys. 264, 221 (2001)
[7] F.H. Tukhvatullin, V.E. Pogorelov et al. J. Mol. Struct. 881, 52 (2008)
[8] Pauling L., The Nature of the Chemical Bond. Cornell Univ. Press, Ithaca, NY, 1960
[9] Sarkar S., Joarder R.N., J. Chem. Phys., 99, 2032 (1993)
[10] Wilson K.R., Cavalleri M., et al. J. Phys. Chem., B 109, 10194 (2005)
[11] V. Pogorelov, L. Bulavin, I. Doroshenko et al. J. Mol. Struct. 708, 61 (2004)
[12] Buck U., Huisken F., Chem. Rev. 100, 3863 (2002)
[13] Laenen R, Gale G.M., Lascoux N., J. Phys. Chem. A, 103, 10708 (1999)
[14] O.V.Boyarkin, T.R.Rizzo, D.S.Perry, J.Chem.Phys. 110, 11359 (1999)
[15] D.Rueda, O.V.Boyarkin, T.R.Rizzo, I.Mukhopadhyay, D.S.Perry. J.Chem.Phys. 116, 91 (2002)

Microspectroscopic characterization of Cretaceous bone proteins

J. Lindgren[1], P. Uvdal[2], A. Engdahl[2], and A. H. Lee[3]

[1] *Dept. of Earth and Ecosystem Sciences, GeoBiosphere Science Centre, Lund University, Sölvegatan 12, SE-223 62 Lund, Sweden*

[2] *MAXLAB, Lund University, P. O. Box 118, SE-221 00 Lund, Sweden*

[3] *College of Osteopathic Medicine, Ohio University, Athens, Ohio 45701, USA.*

Claims of endogenous biomolecules[1] and *still*-soft tissues[2] in fossils millions of years old have been met with scepticism[3] and some findings have been reinterpreted subsequently as artefacts, e.g., modern bacterial biofilms[4]. In order to test current hypotheses on high fidelity preservation of labile tissues over deep time, fibrous cortical bone from a 70-million-year-old mosasaur (a giant, secondarily aquatic reptile allied to extant monitor lizards or snakes[5]) were, for the first time, analysed under infrared microspectroscopy (the event took place at beamline 73, MAX-lab I, Lund University). The infrared absorbance spectra of demineralized fibre bundles exhibited peaks corresponding to proteinaceous materials (Fig. 1A). Typical amide bands of collagen were found at the frequencies of 3210 (Amide A), 1634 (Amide I, random coil form), 1556 (Amide II, α-helix), 1292 (Amide III, α-helix), and 1251 (Amide III, ß-sheet) cm^{-1}, respectively. These bands are associated with stretching and bending vibrations of the peptide (CO–NH) bonds, and their positions and heights are sensitive to structural changes of the triple-helical conformation of the collagen molecule. Vibrational bands corresponding to nonproteinaceous materials were also indentified (Fig. 1A), and ascribed to, among other things, phosphate groups (1040 and 1097 cm^{-1}) and A-B carbonate (901, 1338, 1373, 1416, and 1456 cm^{-1}) of hydroxyapatite.

The mosasaur fibre signature was compared with vibrational spectra obtained from demineralized cortical bone from an extant monitor lizard (*Varanus exanthematicus*) and type I collagen. Significant similarities between the three spectra included the characteristic 1630, 1660 and 1690 cm^{-1} peaks, and amide bands located in the same wavenumber regions. Moreover, the distinctive bands of methyl and methylene groups in the 2800–3000 cm^{-1} interval, which is typical of lipids, were also virtually identical.

In order to substantiate our findings comparisons were made also with bacterial biofilms (i.e., 3-dimensional aggregations of bacteria within a cohesive exopolysaccharide matrix) and a bacterial collagen-like protein to assess the possibility of protein contamination from microbial sources. The biofilms and collagen-like protein had compound signatures that were markedly different from those of the animal collagens, reflecting disparity in molecular conformation and discrepancies in the vibrational modes of the component bonds.

This observation was further corroborated by cluster analysis of the spectral regions 1200–1800 and 2785–3730 cm^{-1}, corresponding to the Amide I–III and lipid intervals, respectively, with Ward's algorithm. All spectra were pre-processed using first derivative and vector normalization, and the spectral distances were calculated using the factorization method (Bruker OPUS 6.5 software). In Figure 1B, two clusters are clearly distinguished and the mosasaur sample groups robustly with modern animal collagens.

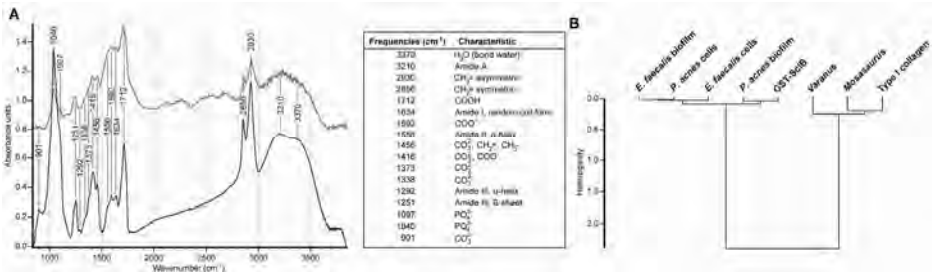

Figure. 1. A, Synchrotron infrared spectrum (red) from a mosasaur fibre bundle together with another spectrum (blue) recorded with a 140 × 140 μm aperture (conventional light source) showing the typical frequencies of collagen components and peaks attributed to phosphate and carbonate bands. B, Cluster analysis of various bacterial biofilms, a collagen-like bacterial protein, mosasaur and varanid cortical tissues, and type I collagen based on the spectral regions 1200–1800 and 2785–3730 cm^{-1} (peptide bond and lipid interval, respectively).

1. M. H. Schweitzer *et al*., Science **324**, 626 (2009).
2. M. H. Schweitzer, J. L. Wittmeyer, J. R. Horner, and J. K. Toporski, Science **307**, 1952 (2005).
3. M. Buckley *et al.* Science **319**, 33c (2008).
4. T. G. Kaye, G. Gaugler, and Z. Sawlowicz, PLoS ONE **3**, 1 (2008).
5. D. A. Russell, Peabody Mus. Nat. Hist., Bull. **23**, 1 (1967).

Investigation of the spectroscopic properties of combustion generated particles from the near to far infrared regions using synchrotron radiation at MAX-lab, beamline 73.

Frederik Ossler[1], Linda Vallenhag[1], Sophie E. Canton[2], Anders Engdahl[2], Per Uvdal[3]

[1]Division of Combustion Physics, Department of Physics, Lund University, LUND, Sweden; [2]MAXlab, Lund University, LUND, Sweden; [3]Department of Chemical Physics ,Lund University, LUND, Sweden

The project concerns studies of carbon-based particles formed under different conditions of combustion and how they interact with the environment, radiation and biological systems. Structural and chemical information is obtained from the identification and composition of spectral signatures, which are related to different types of bonds, e.g., C-C and C-H, and C-O. These studies also show a clear connection with problems related the origin of our universe: Much of the so called unidentified interstellar bands in the infrared region is believed to originate from polycyclic aromatic hydrocarbons (PAHs) [1-3], which also play a key role in the formation of soot particles in combustion [4]. Very little is known about the spectral properties below 500 cm^{-1} [5,6], although one PAH publication, which is not related combustion shows interesting features [7]. In combustion it is also believed that particle formation may be induced by more polymeric heterogeneous structures including elements of aliphatic and aromatic units and experiments have shown interesting results [4,6]. Thus the C/H ratio can be a significant indicator of the history of the soot particles. The oxidation of soot particles in the atmosphere is also important to understand. The level and the types of bonds oxygen is bound to the carbon can tell us about the aging history of the soot particles. The first implications on the level of toxicity can also be obtained from a chemical analysis based on the IR-spectral properties.

The first sets of experiments have been performed on diffusion-like propane Bunsen and ethylene flames. The species produced were condensed on CaF_2 and Si plates inserted at different heights of the flames. The plates were exposed to the flame gases for different periods of time ranging from 30 seconds to 2 minutes. They were then extracted and cooled before being inserted into the spectrograph (FTIR) and then analyzed. The images showed clearly different pattern-like structures that indicated domains of different solubility or degree of polarity of the species composition distributed over the plate. In order to increase the spatial resolution in some of the measurements only a small section the synchrotron beam was used (~10 μm x 10 μm). Measurements were also performed on some species standards like aromatic substances and carbynoid samples containing Cu-terminated polyynes. Data from these measurements is currently being analyzed and will be presented during 2010.

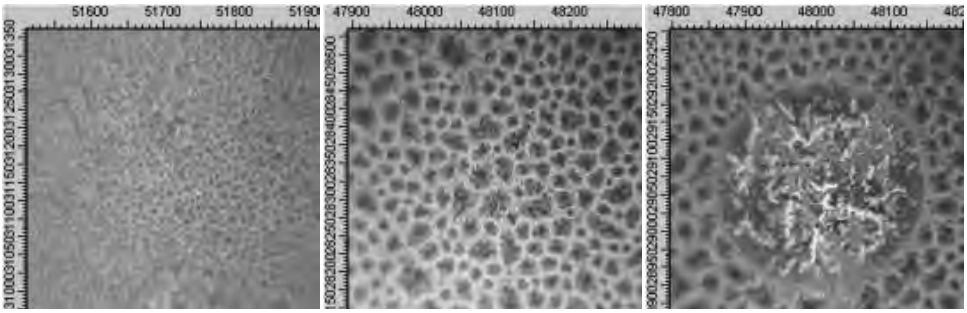

Fig. 1: Visible wavelength transmission images of CaF_2 plates exposed to flames.

References

1. L. J Allamandola,., A. G. G. M Tielens, J. R. Barker, “Polycyclic aromatic hydrocarbons and the unidentified infrared emission bands: Auto exhaust along the Milky Way”. Ap. J., 290, L25. 1985.
2. L. J Allamandola,., A. G. G. M.Tielens, J. R. Barker, “Interstellar Polycyclic Aromatic Hydrocarbons: the Infrared Emission Bands, the Excitation-Emission Mechanism and the Astrophysical Implications”. *Ap. J. Suppl. Ser.*, **71**, 733, 1989.
3. L. J Allamandola, D. M Hudgins,. S. A. Sandford, “Modeling the Unidentified Infrared Emission with Combinations of Polycyclic Aromatic Hydrocarbons”. Ap. J., 511, L115, 1999.
4. H. Bockhorn (Editor), “Soot formation in Combustion Mechanisms and models”, Springer, Berlin 1994.
5. J. T. McKinnon, E. Meyer, J. B. Howard, “Infrared analysis of flame-generated PAH samples”, Combust Flame, 105, 161, 1996.
6. G. Rusciano, G. Cerrone, A. Sasso, A. Bruno, P. minutolo, “Infrared analysis of nano organic particles produced in laminar flames”, Appl. Phys. B, 82, 155, 2006.
7. J. R. Goicoechea, J. Cernicharo, H. Masso, M. L. Senent, “A new unidentified far-infrared band in NGC 7027[1]”, Astroph. J, 609, 225, 2004.

Studies of diffusion of signal substances in bone tissue using infrared microspectroscopy

P. Stahle[1,2], I. Svensson[1], W. Rehman[2], L. Banks-Sills[1,3], and G. Lindberg[1]

[1] *Solid Mechanics, Lund Institute of Technology, Lund University, SE221 00 Lund Sweden,*
[2] *Materials Science, Malmo University, SE205 06 Malmo, Sweden,*
[3] *Mechanical Engieering, Tel Aviv University, Tel Aviv, Israel.*

The purpose of this project is to increase the understanding of the interaction between mechanical load and bone growth in mammals. It is commonly known that physical exercise lead to increase of the bone mass and that the morphology of the bone changes. Further, a capability of healing when fractured, as well as altering its shape and structure as a result of imposed strain has been observed Lanyon and Rubin [1], and Isaksson et al.[2].

A wide range of various experiments show that mechanical load directly or indirectly promote bone growth. Models of the phenomena based on an assumed direct influence of load sometimes lead to confusing results and unexpected load rate dependences. The conclusion has been that the interplay between mechanical load and transport of nutrients and signal substances play an important role which is not covered in the existing models. In the proposed project an indirect mechanical influence is suggested (cf. Banks-Sills et al. [3]). The model is based on the hypothesis that the primary condition leading to bone growth is a change of the chemical environment caused by stress driven diffusion.

The most important substances that are believed to be transported through stress driven diffusion are the prostaglandins, e.g. prostaglandin E2 (PGE2), which according to results from in vivo studies stimulate osteoblast activity. An alternative could be nitric oxide (NOS) is a strong inhibitor of bone resorption through processes which decrease the recruitment of osteoclasts.

The role of stress gradients as driving forces of diffusion or other mechanisms of mass transport is studied. The long term goal is to improve medical treatment of skeletal bone fractures and disorders like e.g. osteoporosis. Nutrients and signal substances are known to move through the bone, via so called Haversian canals and narrow channels, canaliculi, and also through segments of compact bone. The motion is supposed to be a combined convective flow and diffusion, where both are believed to be affected by mechanical straining. Thus, experimentally determined diffusivity and its stress sensitivity is required. Further it is necessary to understand the paths through the bone that are used for the communication of substances.

A previous study has been undertaken using the escape of ions from saturated bone and measurement of conductivity of the surrounding fluid. Additional investigations show that infrared microspectroscopy operating in ATR mode is an efficient tool to measure e.g. water diffusion in bone. In a pilot study performed in the autumn of 2009 raise and fall of deutrium and normal water was followed

[1] Lanyon, L.E., Rubin, C.T., 1984. Static vs dynamic loads as an influence on bone remodelling. Journal of Biomechanics 17, 897–905.

[2] Isaksson, H., van Donkelaar, C.C., Huiskes, R., Ito, K., 2006. Corroboration of Mechanoregulatory Algorithms for Tissue Differentiation during Fracture Healing: Comparison with in Vivo Results. Journal of Orthopaedic Research 24, 898–907.

[3] Banks-Sills, L., Stahle, P., I. Svensson, and Noam, E., Strain Driven Transport for Bone Modelling at the Periosteal Surface, Report from Solid Mechanics Div., LTH, Lund Sweden.

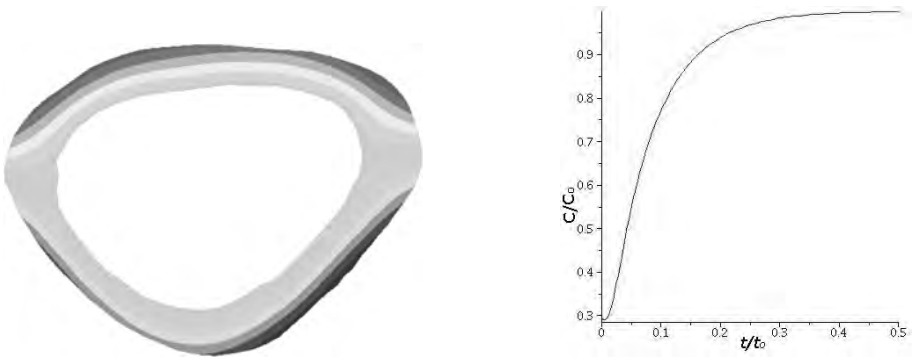

Figure 1: (a) Computed distribution of deutrium after almost 3 hours. The deutrium is injected at the upper edge of the bone cross section. (b) Computed evaporated deutrium. Here t_o is a free time scale parameter that remains to be determined. The concentration referense C_o is irrelevant in the present analysis and remains undetermined.

in time. Deutrium was selected for its visibility in the infrared spectrum. The samples were around 2.5 to 3 mm thick cross-sections of the ulna long-bone of a sheep. Three different experiments were performed. First, the evaporation rates from the sample surfaces were studied for water and deutrium. The water and deutrium content at the surface was followed for fully saturated samples, that were placed in the observation chamber. Three different points were monitored. This gave a background to the measurements following thereafter. Second, transport of water and deutrium in dry bone was measured in two different tests. The mechanism of transport, presumably different from diffusion was measured to provide background data for rewetting of partially dried bone. Third, duetrium was injected along a part of the bone surface and the diffusive transport of deutrium in the fully saturated wet bone was monitored.

The result is compared with an analytical result for diffusion in bone. A body with a rectangular cross section is considered. It occupies a rectangular and is assumed to be very large in one direction. The flux of C is therefore confined to a plane. The governing equation for diffusion is as follows:

$$\frac{\partial C}{\partial t} + \nabla D \nabla C = 0 \tag{1}$$

The analytical solution is obtained as a Fourier series expansion in two dimensions. The result is compared with an approximate solution for a more realistic geometry computed using a finite element method. Fig. 1a shows the calculated distribution of deutrium after around two hours. A characteristic accumulated flux is displayed in Fig. 1b. The curve has the features of an exponential approach of an upper limit with increasing time. The diffusivity coefficient D, here assumed to be constant in the entire body, is found after the least square adoption of the computed result to the experimental result. A preliminary result gives a diffusivity constant of $D = 2 \times 10^{-5}$ m^2/s.

User report
2010-03-23

Colloidal Resource

Colloidal Resource

User report at MAX lab 2009

Colloidal resource AB is a consultant company in the field of chemistry, especially physical chemistry and surface chemistry. In our work we assist industry and start up companies with their chemistry related questions and problems. We use the facilities at Lund University including MAX lab. During 2009 we used the IR facility together with Anders Engdahl and the X-ray facility with Yngve Cerenius.

IR is used both in transmission mode and with the ATR crystal. IR is used in projects to determine absorption on filters and the permeability of membranes. It is often the medically associated products that are studied but during 2009 we also looked at laminated packaging materials.
X-ray was used only once during 2009 and this was to study a n iron complex for an medical purpose.

Contact person at Colloidal Resource is Dr. Anna Stenstam
+46 (0)702 599 755
anna@colloidalresource.se
www.colloidalresource.se

Colloidal Resource AB, Kemicentrum, Box 124, 221 00 Lund, +46(0)707 522 031, www.colloidalresource.se

Anders Engdahl is giving a guided tour around beamline 73 during the *Study day for teachers about research at MAX-lab,* August 2009.
Photo: Annika Nyberg

Structures of 1-butene secondary ozonide- conformers or isomers?

S. Strazdaite, R. Bariseviciute, J. Ceponkus, K. Vaskevicius and V. Sablinskas

Department of General Physics and Spectroscopy, Vilnius University, Universiteto str. 3, Vilnius-01513, Lithuania

The investigations of chemical reactions between alkenes and ozone have considerable practical importance in modeling of photochemical smog formation. This reaction starts from breaking down C=C bond of alkene and goes through a few steps forming intermediate unstable species- primary ozonide (POZ), *Criege* intermediates (CI) and secondary ozonide (SOZ). The SOZ is much more stable than primary ozonide and CI. Under atmospheric conditions it can stay undissociated up to a couple of days. During this time it can react with other atmospheric species. Reactivity of the secondary ozonide depends on various parameters including spatial structure of the compound. 1-butene SOZ can form different structures due to two reasons - (I) different orientation of the aliphatic radical in respect to the five membered ring of the ozonide, (II) different attachment of radical to the ring. The first reason gives so called *gauche* and *trans* structures, while the second one – equatorial and axial structures. Analyzing reactivity of the secondary ozonides in the atmosphere it is crucial to know if transitions between different structures are taking place at atmospheric temperatures. It depends on the height of energy barriers separating various staggered structures of the secondary ozonide.

We have proceeded the ozonization reaction in the infrared gas cell of BL73 and obtained FTIR absorption spectra of gaseous 1-butene SOZ in the temperature range from 200 K to 300 K. The spectra in the fingerprint region of the five membered ring are presented in Fig. 1. Combining the experimental spectra with the spectra of theoretically calculated staggered structures it can be concluded that (I) the gaseous 1-butene SOZ consists from at least four stable structures; (II) according to the intensities of infrared absorption bands all the structures are abundant at the same level (III) change of the sample temperature from 200 to 300 K has no influence to relative concentration of the staggered structures in the gaseous sample of 1-butene ozonide. In order to explain this experimental fact we have calculated energy differences and transition barriers between various staggered structures of 1-butene SOZ. The results are presented in Table 1. The energy differences suggest that amount of the different species should vary with temperature significantly if transitions between structures are possible. The lowest calculated barrier (7.8 kJ/mol) is the barrier between two O-O half chair equatorial conformers *gauche* I and *anti*. Even this smallest barrier is much higher than the thermal energy at 300 K. It means that conformational transitions are not possible at room temperature gas phase sample, which is in agreement to the experimentally observed fact that the intensities of the spectral bands attributed to different structures do not change in the very broad temperature interval.

Our theoretical and experimental studies allows to conclude that 1-butene reaction with ozone in condensed phase results in 1-butene SOZ formed as two isomers axial and equatorial, more over equatorial isomer consists from three different conformers *gauche* I, *anti* and *gauche* II. The fact that four structures with significantly different energies are observed in the very similar amounts suggests that izomerization (and conformation) is possible only in the electronically exited state – the state of SOZ molecule in the first moments after formation. In order to have detailed picture about formation of various isomers some theoretical calculations of the potential surface of excited electronic state should be performed. Such studies are underway in our group.

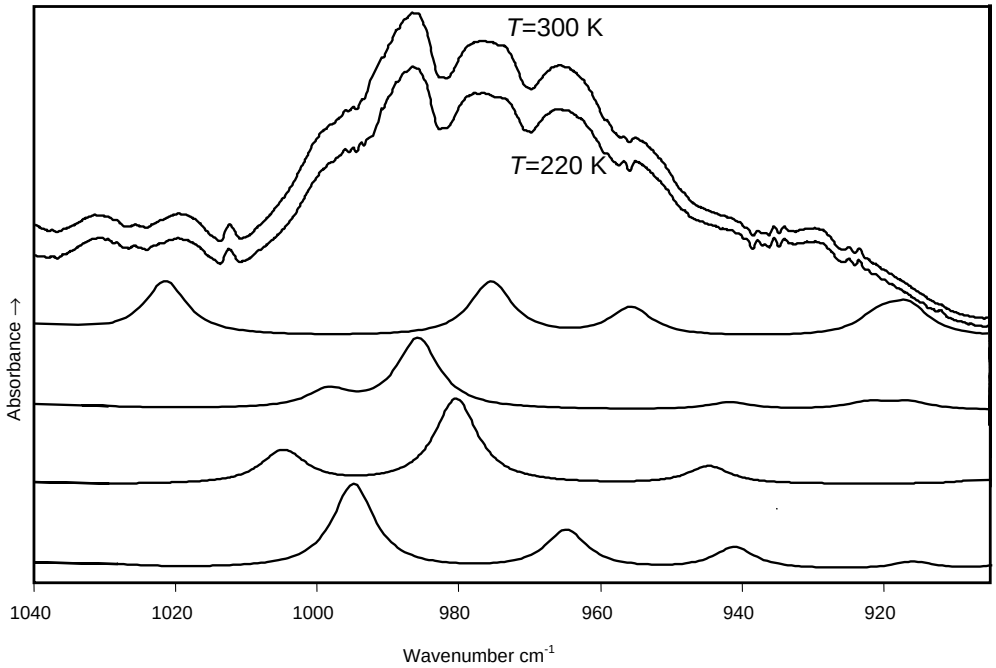

Fig. 1. From top to bottom: experimental FTIR absorption spectrum of gaseous 1-butene ozonide at 300 K and 220 K; *ab initio* at B3LYP 6-311++G (3df, 3pd) level calculated spectra of *gauche* I equatorial, *anti* equatorial, *gauche* II equatorial and *gauche* axial structures of secondary ozonide of 1-butene.

Table 1. B3LYP calculated (6-311++G(3df, 3pd)) relative potential energies (ΔH) and potential barriers for four most stable staggered structures of 1-butene secondary ozonide

Staggered structure	τ_{OCCC}	ΔH, kJ/mol	Transition barrier from less stable to more stable structure, kJ/mol
O-O half chair equatorial *gauche* I	-66.1°	0	-
O-O half chair equatorial *anti*	-177.5°	0.3	7.8
O-O half chair equatorial *gauche* II	56.2°	1.6	8.5
O-O half chair axial	175.5°	2.1	33.0

[1]R. Bariseviciute, J. Ceponkus, A .Gruodis, V. Sablinskas, *Central European Journal of Chemistry*, **4**, 578-591 (2006).
[2]R. Bariseviciute, J. Ceponkus, V. Sablinskas, L. Kimtys, *J. Mol. Struct.*, 844-845, (2007) 186-192.

Infrared spectroscopy of single micrometer sized droplets

E. A. Svensson[1], M. S. Johnson[2], J. B. C. Pettersson[1] and P. Uvdal[3]

[1]*Deparment of Chemistry, Atmospheric Science, Göteborg University*
[2]*Copenhagen Center for Atmospheric Research, Department of Chemistry, Copenhagen University*
[3]*Department of Chemical Physics, Kemicentrum, Lund University*

Aerosol particles and their interaction with clouds are of great importance for the understanding of atmospheric processes. The uptake of water vapor on aerosol particles play crucial role in cloud formation. Most studies of such processes are performed on ensembles of particles, but in this experiment we study the hygroscopic behavior and chemical properties of single droplets.

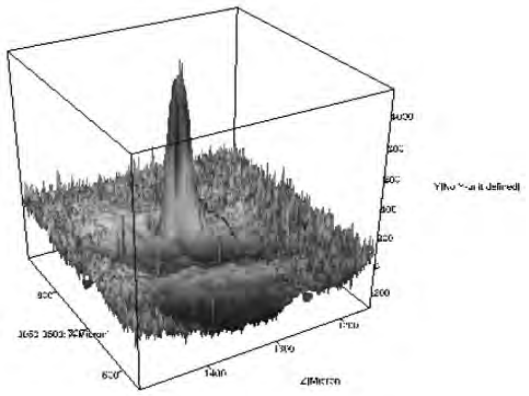

Figure 1. Polyethylene glycol/water mixture droplet (diameter ~30 µm) FPA spectrum integrated between 3050 cm^{-1} and 3500 cm^{-1}.

We have continued the development and testing of the University of Copenhagen electrodynamic balance (EDB) in the infrared microscope at beamline 73 at Maxlab. The EDB uses a combination of AC and DC electrical fields to trap single, charged particles or droplets for any desired time period. Hence, the chemical development can be followed in detail. Using the infrared microscope we are also able to get a two-dimensional chemical map of the particle.

The test system which has been used is a mixture of polyethylene glycol (PEG) and water. In figure 1, the results from the Focal Plane Array (FPA) detector is shown. Each point on the surface corresponds to the integrated absorption between 3050 cm^{-1} and 3050 cm$^{-1,}$ which is the range of the C-H stretch band. Essentially, this view highlights the distribution of the PEG in the droplet without showing the water. We thus have the possibility of determining the distribution of various substances within a droplet.

In addition to the studies of single trapped particles we have also initialized experiments on pollen, which cause allergy to people. Generally, allergens on the surfaces of pollen particles become more aggressive when they are exposed to air pollution.

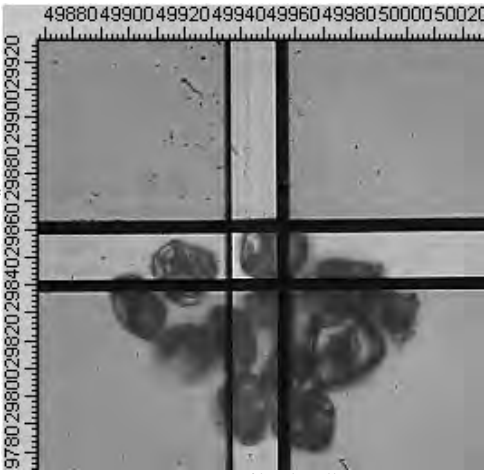

Figure 2. Microscope image of birch pollen.

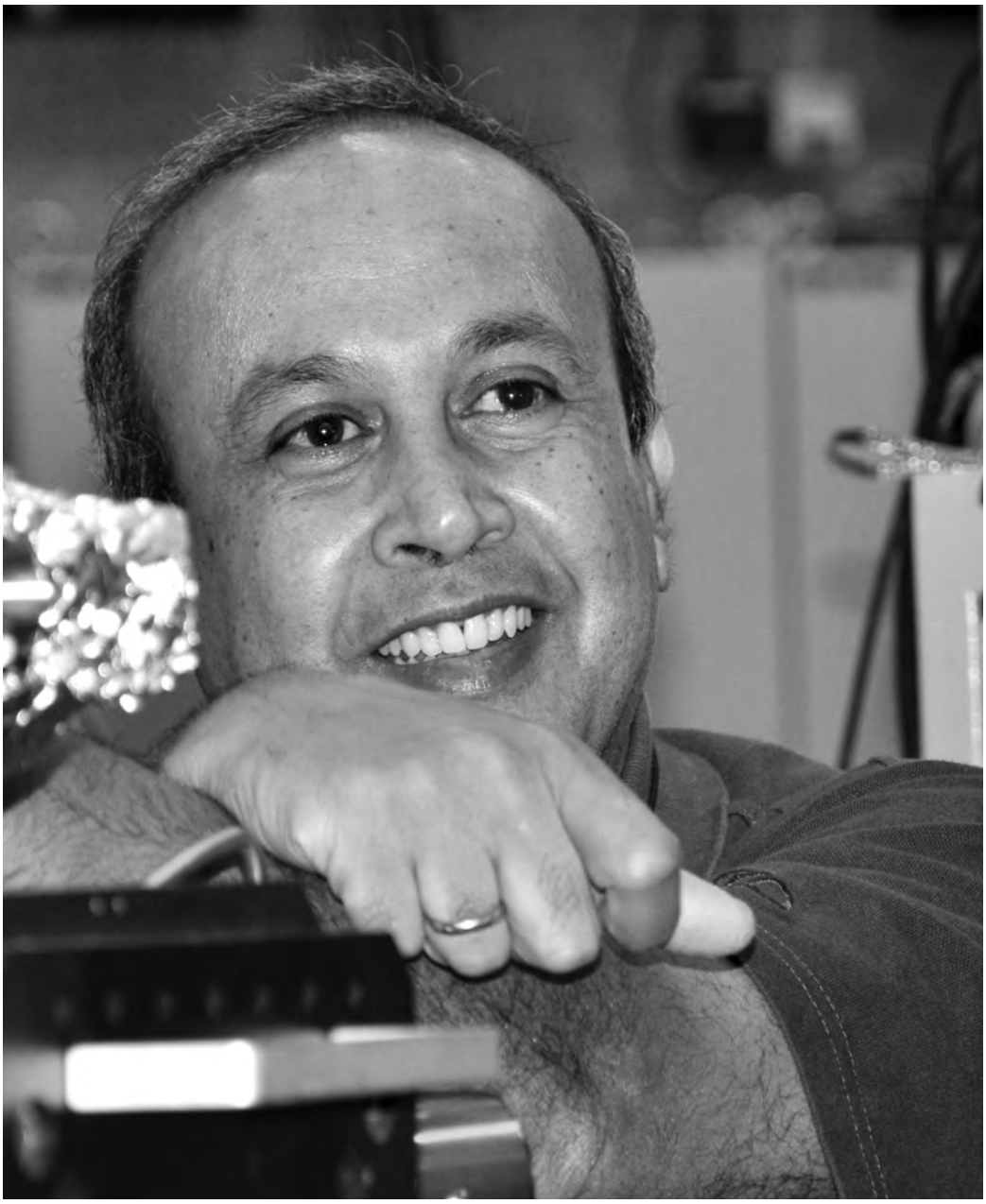

Balasubramanian Thiagarajan, beamline manager at beamline I3 and I4, November, 2009.
Photo: Annika Nyberg

High-Resolution Infrared Absorption Spectrum of $CH_2D^{79}Br$

René Wugt Larsen[1], A. Baldacci[2], P. Stoppa[2] and S. Giorgianni[2]

[1]*Department of Chemistry, University of Copenhagen, Denmark*
[2]*Dipartimento di Chimica Fisica, Università Ca' Foscari di Venezia, Italy*

Methyl bromide, CH_3Br, is classified as a Class I ozone-depleting substance since it is readily photolyzed to form elemental bromine in the atmosphere which is destructive to Earth's stratospheric ozone layer. Highly accurate infrared spectroscopic data of regular methyl bromide and its most abundant isotopomers for the atmospheric spectral windows are therefore crucial to model the opacity of this compound in the stratosphere.

It has been shown that broadband infrared synchrotron radiation from an electron storage ring source has several advantages for high resolution infrared gas phase spectroscopy close to the Doppler limit regime owing to the extremely high brilliance and intrinsic polarization compared with conventional black body radiation sources. An electron storage ring acts as a source with an effective temperature of the order of 10 000 K. The radiating electrons are confined to a very small volume, so that the storage ring acts as a point source and a limiting entrance aperture is not required to collect high-resolution spectra.

The infrared absorption spectrum of an isotopically enriched $CH_2D^{79}Br$ sample has been recorded with a resolution of 0.0015 cm^{-1} in the spectral region between 650 and 1100 cm^{-1} employing the Bruker IFS 120 HR Fourier transform infrared spectrometer and the MAX-I storage ring as an external radiation source [1]. The studied spectral region is characterized by the ν_5 (A', 768.8 cm^{-1}) and ν_9 (A'', 930.3 cm^{-1}) fundamental bands describing D-C-Br deformation and CH_2 rocking modes, respectively. The ν_5 fundamental appears as an a/b-hybrid band with predominant a-type character and the ν_9 band shows the typical c-type appearance. The spectral analysis including both these bands has allowed rovibrational line assignments up to high quantum numbers (J = 72 and K_a = 16) in the *P*- and *R*-branches of the congested but still well resolved ${}^qQ$-branch of the ν_5 band. Figure 1 displays the rotational structure of the ${}^qQ_K(J)$ sub-branches of this band. Ground-state combination differences of unblended *P*, *Q* and *R* lines from the two bands have been employed to extract the ground-state rotational constants, the five quartic and four sextic centrifugal distortion constants for the first time adapting Watson's A-reduced Hamiltonian in the I^r-representation. The upper state parameters have been determined by fixing the fitted ground-state constants in a dyad model including the higher order a-Coriolis coupling parameter $\eta_{5,9}^{bc}$ as listed in Table 1.

REFERENCES

[1] A. Baldacci, P. Stoppa, S. Giorgianni and R. Wugt Larsen, *Mol. Phys.* **108**, DOI: 10.1080/00268970903567270 (2010)

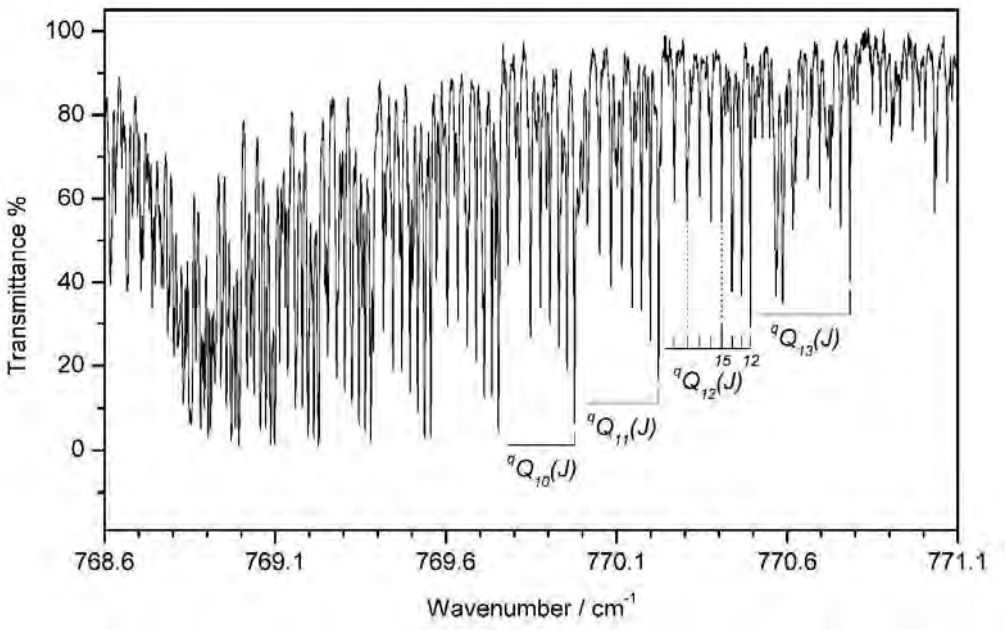

Fig. 1. The high-resolution infrared absorption spectrum of the ν_5 fundamental band of $CH_2D^{79}Br$ showing the resolved rotational structure of the a-type Q-branch.

Table 1. Spectroscopic parameters (cm^{-1}) for the ground, $v_5 = 1$ and $v_9 = 1$ states of $CH_2D^{79}Br$ [a].

Parameters	Ground state	$v_5 = 1$	$v_9 = 1$
ν_0		768.808516(82)	930.353789(82)
A	3.97445755(114)	3.9862648(39)	4.0006428(31)
B	0.29756678(20)	0.29658963(29)	0.29668616(32)
C	0.29232654(20)	0.29128939(29)	0.29137974(35)
$\Delta_J \times 10^6$	0.272868(92)	0.272223(99)	0.273700(104)
$\Delta_{JK} \times 10^5$	0.330164(113)	0.31944(31)	0.35180(25)
$\Delta_K \times 10^4$	0.562090(102)	0.56476(44)	0.59830(27)
$\delta_J \times 10^8$	0.47691(84)	0.4290(27)	0.5160(33)
$\delta_K \times 10^6$	0.5525(154)	0.445(65)	0.617(77)
$\Phi_J \times 10^{13}$	–0.764(128)	–0.914(147)	–0.827(160)
$\Phi_{JK} \times 10^{11}$	0.347(28)	0.258(67)	0.478(52)
$\Phi_{KJ} \times 10^{10}$	0.517(38)	–0.460(127)	0.902(84)
$\Phi_K \times 10^8$	0.2727(28)	0.2288(137)	0.3465(65)
$\eta_{5,9}^{bc}$		0.8182(100)	
N[b]	12462	6765	7070

[a]The quoted errors are one standard deviation in units of the last significant digits. [b]The number of observations.

Adsorption of L-cystine and S-methyl-L-cysteine on rutile TiO_2(110)

Evren Ataman, Cristina Isvoranu, Jan Knudsen, Jesper N. Andersen, Joachim Schnadt
Division of Synchrotron Radiation Research, Department of Physic, Lund University, Box 118, 221 00 Lund, Sweden.

As a continuation of our previous study, in which the adsorption of L-cysteine (Figure 1(a)) on TiO_2(110) was investigated [1], we have studied the adsorption of two similar molecules on TiO_2(110), namely, L-cystine and S-methyl-L-cysteine (Figures 1(b)-(c)). The goal was to investigate the effects of different functional groups on the adsorption geometry and intra- and intermolecular interactions for different molecules.

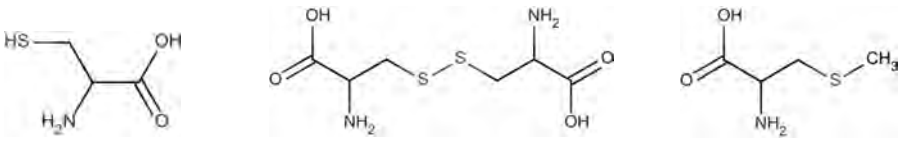

(a) **(b)** **(c)**

Figure 1. The structures of **(a)** L-cysteine **(b)** L-cystine and **(c)** S-methyl-L-cysteine. L-cysteine has three functional groups, namely, the carboxylic ($-COOH$), amino ($-NH_2$), and thiol ($-SH$) groups. The thiol group is replaced by the disulfide bond in L-cystine, and in S-methyl-L-cysteine hydrogen atom is replaced by a methyl group.

In Figure 2, the S 2p photoemission spectra are shown for the three molecules adsorbed on TiO_2(110) at similar (sub-monolayer) coverages. For L-cysteine the doublets at ~164.3 (specified by the binding energy of the $2p_{3/2}$ component) and ~162.3 eV are attributed to the intact thiol group of the molecules and to either a thiolate or atomic sulfur species on the surface bridging oxygen defects, respectively [1]. In the case of L-cystine the binding energy value of the most pronounced peak at ~163.8 eV is in line with the value reported in literature for disulfide species. The two peaks at ~166.9 and ~162.8 eV are possible indicators of different adsorption geometries or a dissociation process. This has not been fully clarified yet. For S-methyl-L-cysteine the position of the peak at ~164 eV is in line with literature values for the $-S-CH_3$ species. The observation of essentially a single doublet indicates that the largest fraction of all S–CH_3 bonds are not dissociated. The two weak doublets at high and low binding energies are indicative of the presence of small fractions of dissociated adsorbates.

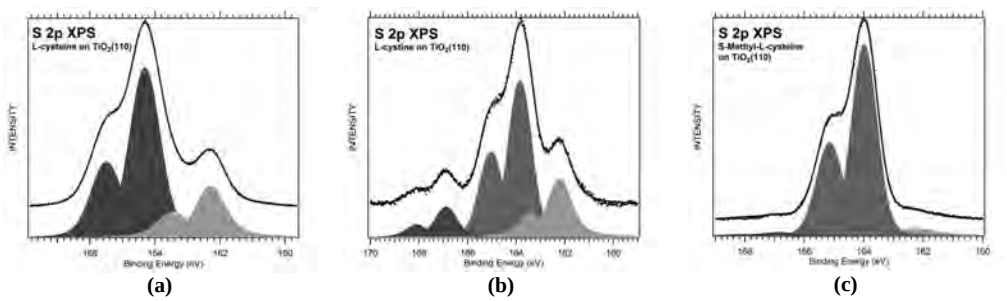

(a) **(b)** **(c)**

Figure 2. S 2p photoemission spectra for **(a)** L-cysteine, **(b)** L-cystine, and **(c)** S-Methyl-L-Cysteine molecules adsorbed on TiO_2(110) surface at similar sub-monolayer coverages.

In Figure 3, the C 1s and O 1s spectra are shown for the same coverages as in Figure 2. The contributions to the wide low binding energy peaks of the C 1s spectra are not resolved; however, a peak at around 288 eV binding energy is seen in the L-cystine spectrum. The peak at 289 eV found in all C 1s spectra is attributed to the carbon atom of the carboxylate group. The energy agrees with that found for deprotonated carboxylic groups, which bind to the substrate in a bidentate mode. This has, e.g., been observed for L-cysteine on TiO_2(110) [1]. The peak at around 288 eV found in the L-cystine spectrum is attributed to a non-surface-bonded carboxylate group., i.e., L-cystine bind to the surface through a fraction of their carboxylate groups, while the remaining carboxylates are not involved in the surface bond. In the N 1s spectra (not shown) we observed that the peak characteristic of NH_3^+ dominated, which can be a sign of that proton of the carboxylic group is transferred to the amino group for at least early stages of adsorption. In the O 1s spectra only one peak additional to that of the substrate is observed. It is attributed to the two equivalent oxygen atoms of the carboxylates.

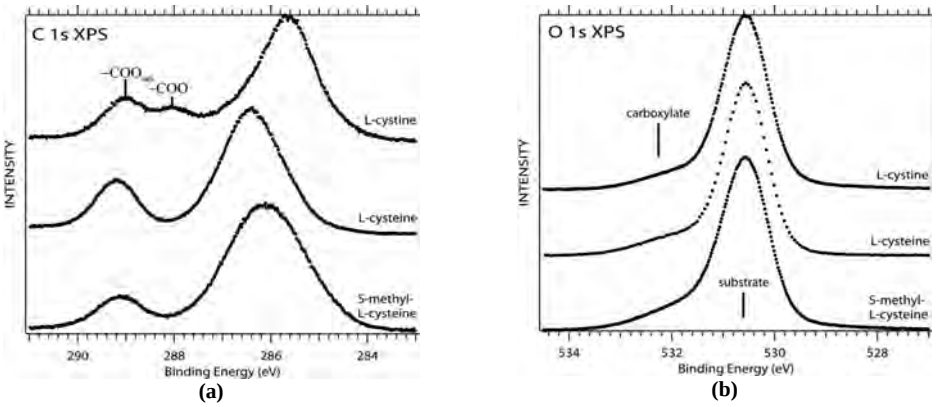

Figure 3. (a) C 1s and **(b)** O 1s spectra for L-cystine (top), L-cysteine (middle), and S-methyl-L-cysteine (bottom) adsorbed on TiO_2(110) surface. The spectra were recorded at similar adsorbate coverages. The contributions to the wide peaks in the C 1s spectra at lower binding energies than 288 eV are not fully clarified. In the O 1s spectra one molecular peak is observed at 532 eV, and it is attributed to the two equivalent oxygen atoms of the carboxylates.

In conclusion, our preliminary analysis of the experimental data show that all three molecules most likely adsorb on TiO_2(110) through their carboxylate group in a bidentate mode. For L-cystine molecules all carboxylic groups are deprotonated, but not all of them are involved in the substrate bond. We suggest that the proton is transferred to the amino group. While both the L-cysteine and L-cystine molecules suffer from dissociation at their sulfur sites, dissociation is negligible for S-methyl-L-cysteine if present at all.

[1] L-cysteine adsorption on a rutile TiO2(110) surface studied by X-ray photoelectron spectroscopy, E. Ataman, C. Isvoranu, J. Knudsen, K. Schulte, J. N. Andersen, and J. Schnadt, in manuscript.

Europium-alloyed Gd_2O_3 nanoparticles studied by PEEM

Linnéa Axelsson[1], Linnéa Selegård[1], Alexei Zakharov[2] and Kajsa Uvdal[1]
[1]*Division of Molecular Surface Physics and Nanoscience, Department of Physics, Chemistry and Biology (IFM), Linköping University, SE-581 83 Linköping, Sweden*
[2]*MAX-lab, Lund University, S-221 00 Lund, Sweden*

The interest in Gd_2O_3 nanoparticles have arisen in recent years as a nanomaterial for contrast enhancement in Magnetic Resonance Imaging (MRI).[1-2] Gd_2O_3 nanoparticles are also highly interesting as host materials for other lanthanide ions in luminescent nanomaterials.[3-4] The aim of this project is to acquire lanthanide-alloyed Gd_2O_3 nanoparticles as multifunctional luminescent and contrast enhancing nanoprobes for biomedical imaging.

Europium-alloyed Gd_2O_3 nanoparticles were investigated by means of photoelectron emission microscopy (PEEM) at the MAX II synchrotron storage ring, beamline I311, at MAX-lab, Lund. The nanocrystals were synthesized by the polyol route,[3-4] yielding a nanocrystal suspension in diethylene glycol (DEG). The nanoparticles sample was then dialyzed against water to exchange solvents. Dialyzed Eu:Gd_2O_3 nanocrystals were spincoated onto a TL1-cleaned Si-surface with a thin natural silicon oxide layer.

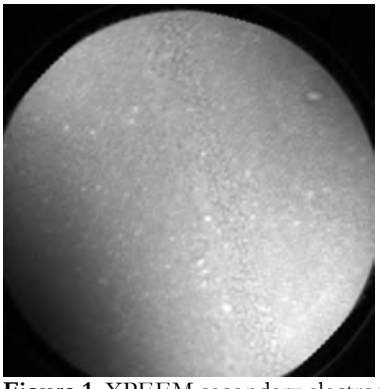

Figure 1. XPEEM secondary electron images of 20%Eu-alloyed Gd_2O_3 nanoparticles on Si-surface with hν = 150 eV, SV= 3 V, FoV 50 μm.

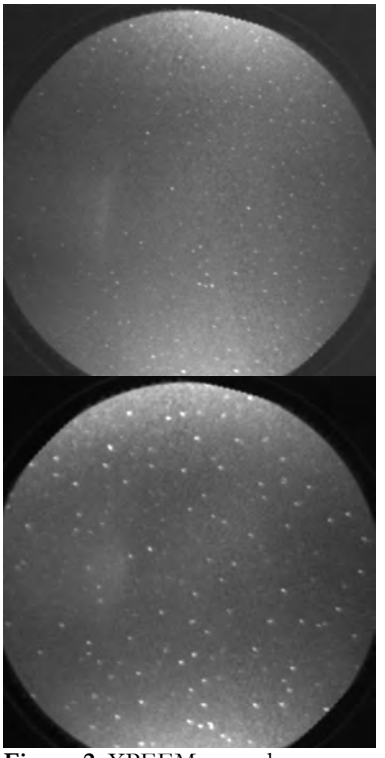

Figure 2. XPEEM secondary electron images of 1%Eu-alloyed Gd_2O_3 nanoparticles on Si-surface. a) 1%Eu:Gd_2O_3 with SV = -0.1 V, FoV 50 μm and b) 1%Eu:Gd_2O_3 nanoparticles, hν = 150 eV, FoV 25 μm.

With XPEEM (X-ray photoelectron emission microscopy), elemental specific images are obtained, utilizing the contrast in the XPEEM images due to the lower work function of Gd nanoparticles as compared to the Si substrate. In this study, the distribution of gadolinium in 20% and 1% Eu-alloyed Gd_2O_3 nanoparticles on the Si-surface is studied by XPEEM secondary

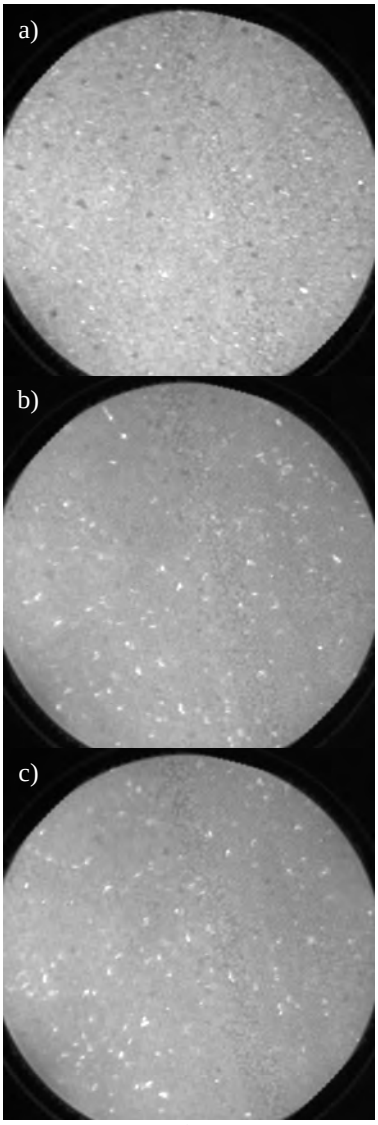

Figure 3. LEEM images (FoV 20 μm) of 20%Eu:Gd_2O_3 at a) 185 °C, SV = 5.15 V, b) 230 °C, SV = 7.4 V and c) 760 °C, SV = 7.4 V.

electron images (hν = 150 eV), see Figures 1 and 2.

The surface was annealed by current heating on the back side to remove hydrocarbon from the air and remaining DEG. The oxidized layer on Si-wafers is normally evaporated at 850 °C. When the oxide layer is removed, the Si is exposed and the surface becomes very reactive, forming SiC.

The surface was annealed to remove carbon in order to image the nano-crystals, while keeping the annealing temperature below 850 °C. The sample was slowly heated and simultaneously imaged by LEEM images (Figure 3) of 20%Eu:Gd_2O_3 nanocrystals on Si-surface at ~ 185, 230 and 760 °C. As the temperature increases, crystal growth starts and larger crystals are formed.

This project is supported by grants from the Swedish Research Council (VR), The Swedish Governmental Agency for Innovation Systems (VINNOVA) and Carl Tryggers Foundation. The authors are also grateful for all help from the Max-lab staff during the measurements.

References:

(1) Park, J. Y.; Baek, M. J.; Choi, E. S.; Woo, S.; Kim, J. H.; Kim, T. J.; Jung, J. C.; Chae, K. S.; Chang, Y.; Lee, G. H. *ACS Nano* **2009**, *3*, 3663.

(2) Engstrom, M.; Klasson, A.; Pedersen, H.; Vahlberg, C.; Kall, P. O.; Uvdal, K. *Magn Reson Mater Phy* **2006**, *19*, 180.

(3) Bazzi, R.; Flores, M. A.; Louis, C.; Lebbou, K.; Zhang, W.; Dujardin, C.; Roux, S.; Mercier, B.; Ledoux, G.; Bernstein, E.; Perriat, P.; Tillement, O. *J Colloid Interf Sci* **2004**, *273*, 191.

(4) Petoral, R. M.; Soderlind, F.; Klasson, A.; Suska, A.; Fortin, M. A.; Abrikossova, N.; Selegard, L.; Kall, P. O.; Engstrom, M.; Uvdal, K. *J Phys Chem C* **2009**, *113*, 6913.

Charge transfer from a gold surface to adsorbed C_{60} molecules: resonant photoemission and new core-hole decay channels

Andrew J. Britton,[1] Anna Rienzo,[1] Karina Schulte,[2] and James N. O'Shea[1]
[1]*School of Physics and Astronomy, University of Nottingham, Nottingham, NG7 2RD, UK*
[2]*MAX-lab, Lund University, Box 118, 221 00 Lund, Sweden*

C_{60} is an ideal building block for molecular devices because electrons can easily be donated to the fullerene cage from other molecules, atoms and surfaces. The core-hole clock[1] implementation of resonant photoemission (RPES) has led to the quantification of charge-transfer dynamics from adsorbed molecules to both semiconductor[2] and metal surfaces[3,4]. Nevertheless, in the case of metallic surfaces, where there is the possibility for the core-excited LUMO to lie below the Fermi edge of the substrate such as gold (111), our RPES data have shown possible evidence for ultra-fast back donation into a small chemisorbed aromatic molecule (bi-isonicotinic acid) on the timescale of the core-hole lifetime[3,4].

Experiments were carried out on the I311 beamline at MAX II using the Scienta SES200 hemispherical analyzer. The gold (111) substrate was a single crystal of dimensions 10mm diameter × 2.5mm. The substrate was cleaned using cycles of sputtering using 1kV Ar ions and then annealing at 900K by passing a current through the tungsten wire mount. The cleanliness of the sample was checked by monitoring the disappearance of the C 1s core level.

C_{60} was evaporated using a Knudsen cell type evaporator onto the sample at a distance of ∼ 20cm. The evaporation took place at a temperature of ∼ 425 °C and the substrate was kept at room temperature during the deposition. A multilayer of C_{60} was produced by depositing it for sufficient time so as to suppress the substrate Au 4f photoemission signal and to produce the characteristic symmetric lineshape and shake-up features in the C 1s spectrum[5]. To obtain a monolayer coverage, the sample was then heated to 300°C to desorb the physisorbed multilayer so as to leave the chemisorbed monolayer. Again, the monolayer coverage was checked by monitoring the C 1s and Au 4f core-level peaks and the emergence of the characteristic monolayer C 1s lineshape[5].

Two-dimensional resonant photoemission datasets were measured for the clean Au(111) surface, a multilayer of C_{60} and a C_{60} monolayer. The monolayer and multilayer datasets are shown in figure 1 and are obtained by measuring the valence band photoemission from around 16 eV binding energy at a range of photon energies covering the C 1s absorption edge in 0.1 eV steps. The clean surface spectrum (not shown) exhibits simply an intense band due simply to the direct valence band photoemission of the clean Au(111). The faint vertical lines in the background of the multilayer and monolayer spectra are the direct photoemission peaks of C_{60} valence band. At the resonance for the LUMO (Lowest Unoccupied Molecular Orbitals) there is a strong resonant enhancement of the HOMO (Highest Occupied Molecular Orbitals). This is known as participator decay, arising from the originally excited electron being involved in the non-radiative core-hole decay, leading to a final state identical to that of direct photoemission[1]. In addition to these participator electrons, there are features that track with constant kinetic energy which arises from spectator decay of the core-hole. In this case, the originally excited electron is not involved in the decay process, but merely spectates as an otherwise normal Auger process occurs. The spectator decay features occur in the upper triangle of the graph where there is a high intensity so they can not be observed easily.

In the RPES spectrum for the C_{60} monolayer shown in figure 1b, three low binding energy (high kinetic energy) features are clearly observed. These are absent from either the clean surface or multilayer spectra. These three features track with constant kinetic energy and must, therefore, arise from a new Auger-like decay channel available only to those molecules directly coupled to the metal surface. The spacings and profile of the constant KE features are reminiscent of the spacings and the profile of peaks in valence band spectra for the C_{60} multilayer, suggesting a connection between them.

As a consequence, it is reasonable to assume that the origin of the three constant kinetic energy features lies in an Auger-like core-hole decay process involving the HOMO, HOMO-1 and HOMO-2 of the fullerene molecule. Furthermore, it is clear that the resulting decay process must involve an interaction with the gold substrate since these features are absent from the multilayer or the clean Au(111) spectra. Calibrated NEXAFS and valence band spectra of the monolayer show that the LUMO lies partially below the Fermi level of the gold, allowing charge transfer between the substrate and the LUMO energetically possible.

The highest kinetic energy feature of the three tracks back to the binding energy of the HOMO at the LUMO position, and hence results in a final state indistinguishable from both direct photoemission of the charge-transferred molecule HOMO and participator decay in resonant photoemission. The kinetic energy of these features is higher than can be achieved by the molecule with its ground state complement of electrons, requiring an additional electron to be transferred from states near the Fermi level of the Au(111) substrate into the LUMO, which can then take part in the autoionization core-hole decay process. The electron which has come from the substrate acts as a spectator electron in a core-hole auger decay.

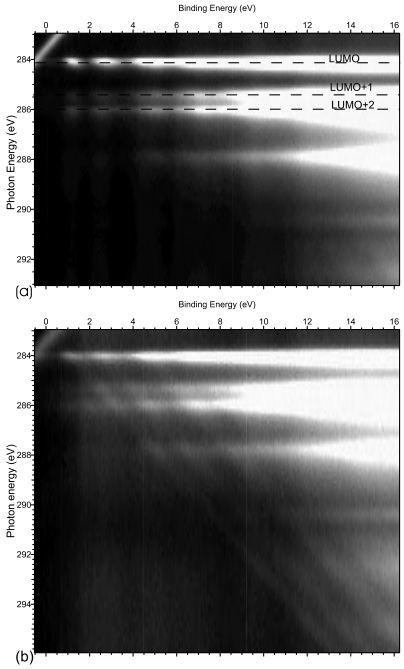

FIG. 1: Resonant Photoemission spectra for a multilayer of C_{60} (a) and monolayer of C_{60} (b). The horizontal axis represents the binding energy and the vertical axis is the photon energy. The multilayer spectrum has been calibrated using the diagonal 2nd order C 1s line in the top right hand corner to take account of steady state charging. Note the three diagonal lines on the monolayer spectra that represent phenomena with constant kinetic energy.

The observed kinetic energy features do not depend on the timing of the charge transfer, whether it occurs in the ground state or the core-excited state. However, the additional electron is most likely transferred from the substrate in the ground state rather than within the core-hole lifetime in the core-excited state. This assertion is based on the observation of very slow charge transfer in the forward direction from the molecule into the conduction band of the substrate, certainly outside the core-hole lifetime. "Corehole clock" analysis calculates the upper limit of the charge transfer to the surface using the ratios of the normalized intensity of the LUMO peaks in the NEXAFS and RPES for both the monolayer and multilayer along the lines along the lines of Brühwiler *et al.*[1,4].

Charge transfer in the ground state agrees with evidence from angle resolved photoemission in which LUMO-derived intensity was found where we measure the core-excited LUMO to be located[6]. In the context of x-ray absorption, this would suggest that core-excitonic effects do not play a significant role where the molecule is chemisorbed to a metallic surface in a bonding mechanism largely characterized by charge transfer.

[1] P. A. Brühwiler, O. Karis, and N. Mårtensson, Reviews of Modern Physics **74**, 703 (2002).
[2] J. Schnadt, P. A. Brühwiler, L. Patthey, J. N. O'Shea, S. Södergren, M. Odelius, R. Ahuja, O. Karis, M. Bässler, P. Persson, H. Siegbahn, S. Lunell, and N. Mårtensson, Nature **418**, 620 (2002).
[3] J. B. Taylor, L. C. Mayor, J. C. Swarbrick, and J. O'Shea, Journal of Chemical Physics **127**, 134707 (2007).
[4] J. B. Taylor, L. C. Mayor, J. C. Swarbrick, J. N. OShea, and J. Schnadt, Journal of Physical Chemistry **111**, 16646 (2007).
[5] C. J. Satterley, L. M. A. Perdigäo, A. Saywell, G. Magnamo, A. Rienzo, L. C. Mayor, V. R. Dhanak, P. H. Beton, and J. N. OShea, Nanotechnology **18**, 455304 (2007).
[6] C.-T. Tzeng, W.-S. Lo, J.-Y. Yuh, R.-Y. Chu, and K.-D. Tsuei, Physical Review B **61**, 2263 (2000).

Corel level photoemission spectroscopy studies of hydrogen intercalated zerolayer graphene on SiC(0001)

C. Coletti, K.V. Emtsev, T. Iwasaki, A. Al-Temimy, S. Forti, and U. Starke

Max-Planck-Institut für Festkörperforschung, Heisenbergstr. 1, D-70569 Stuttgart, Germany

During the beamtime of April 2009 our group obtained insightful results concerning hydrogen intercalated epitaxial graphene on SiC(0001) (see the respective report) which was published in [1]. In the work performed in December 2009 at beamline I311 we carried on further investigations on the nature and evolution upon annealing of the chemical bonds for H-intercalated zerolayer graphene on SiC(0001). To that end, epitaxial zerolayer graphene samples were annealed in a chemical vapor deposition (CVD) reactor in hydrogen atmosphere in the home-lab in Stuttgart as in [1] and transported to MAX-Lab for high resolution core level photoemission studies (CLPES).

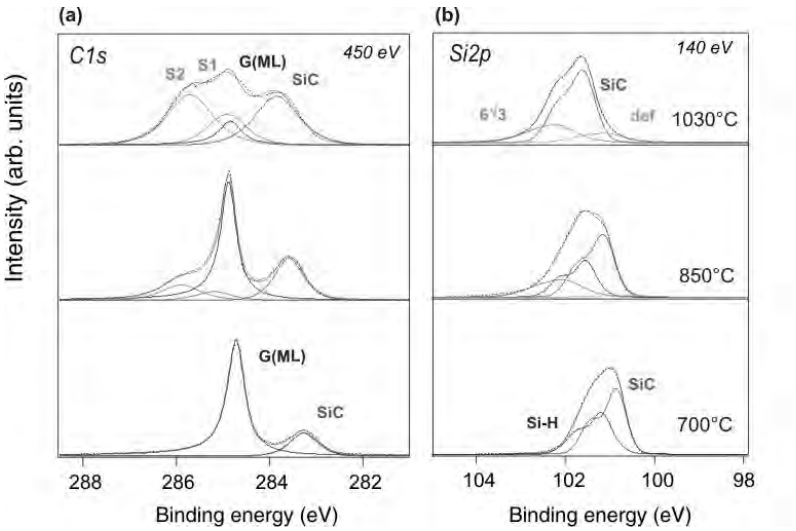

Figure 1. C 1s (a) and Si 2p (b) core level spectra for a H-treated zerolayer graphene sample (bottom spectra) and the same sample annealed at increasing temperatures.

Fig. 1 shows the C1s and Si2p core level spectra measured for a H-intercalated zerolayer sample after annealing at stepwise increasing temperatures. Different photon energies were used to investigate these core level regions so that the vertical position of the different species could be identified. The energies shown in Fig. 1 are 140 eV and 450 eV for the Si 2p and C1s spectra, respectively. The components contributing to the spectra were decomposed by a curve fitting procedure. With the exception of the graphene component, which was realized through a Doniach-Sunjic profile to account of the metallic behavior [2], all other curves were Gaussian-Lorentzian line shapes. The energy calibration for each spectrum was performed by using a reference Ta4f peak measured every time the photon energy was varied. The experimental data points are displayed in black dots. The gray solid line is the envelope of the

fitted components. The bottom curve in Fig. 1 shows the C1s spectrum measured after outgassing the H-treated sample at a temperature of 700 °C. At this temperature according to [1] and to angle resolved photoemission spectroscopy (ARPES) analysis we obtain neutrally charged quasi-free standing monolayer graphene thanks to the passivation of the substrate Si dangling bonds operated by the hydrogen and the consequent lifting of the zerolayer. Hence, the dominant peak at 284.5 eV (black line) is attributed to the neutrally charged monolayer graphene while the SiC bulk component is observed at 283.2 eV (red line). The absence of the S1 and S2 interface components is indicative of a fully successful H-intercalation and hence zerolayer lifting. Similar to the case of H-intercalated monolayer samples [1], annealing at temperature higher than 800 °C causes a progressive hydrogen desorption with consequent appearance of the S1 and S2 interface components (light blue lines) [4]. Their contribution increases in the C1s spectrum for increasing annealing temperatures and concurrently the monolayer graphene related component decreases in relative intensity, symptom of a progressive retrieve of the original zerolayer structure. Moreover, the SiC related component gradually shifts towards higher binding energies (BE). After annealing at 1030 °C, the hydrogen is completely desorbed. The SiC bulk component is observed at 283.9 eV (total shift from the bottom spectrum ~ 0.7 eV). A minor contribution from patches of the sample where monolayer was originally present can be observed (as indicated by the persistence of the black monolayer line shape in the top C1s spectrum).

After outgassing at 700 °C, the Si2p line shape can only be fitted by using two spin-orbit split doublets. The one at lower BE originates from the SiC bulk while the one located at higher BE arises from Si-H bonds. Annealing at a temperature higher than 800 °C leads to a decrease in the intensity of the Si-H related component, to a progressive shift to higher BE of the SiC component and to the appearance of two additional doublets. The one at lower BE (light blue line) is attributed to the Si atoms bonded to the $(6\sqrt{3}\mathbf{x}6\sqrt{3})R30°$ reconstructed zerolayer while the very small one at lower BE (green line) to surface defects. The Si-H component completely disappears after annealing at 1030 °C. The total shift observed for the Si 2p bulk component amounts to 0.7 eV consistent with the C 1s level and similar with what reported for H-treated monolayer [1].

In conclusion, the data shows that zerolayer graphene can be completely decoupled from the SiC substrate via H-intercalation thus becoming a quasi-free standing monolayer graphene. This is well demonstrated by the absence, after H-treatment and for annealing temperature below 700 °C, of the S1 and S2 interface components and by the presence of Si-H chemical bonds. Moreover at those low annealing temperatures the peak location for the decoupled quasi-free standing monolayer graphene indicates a charge neutrality condition which confirms a successful electronic passivation of the Si dangling bonds of the SiC(0001) surface so that negative charge is not transferred to the graphene overlayer. The SiC related peaks shift of 0.7 eV from H-treated to clean samples confirming that the SiC surface presents chemical bonding with hydrogen and therefore experiences a band bending. Moreover, the FWHM of the SiC and graphene peaks present lower values for H-treated than for clean samples. This might suggest that the H-intercalation relieves the mechanical strain caused in graphene and SiC by the lattice mismatch.

[1] C. Riedl, C. Coletti, T. Iwasaki, A. A. Zakharov, and U. Starke, *Phys. Rev. Lett.*, **103** (24), 24684 (2009).
[2] K.V. Emtsev , A. Bostwick, K. Horn, et al., *Nature Materials* **8**, 203-207 (2009).
[3] T. Seyller, *J. Phys.: Condens. Matter* **16**, S1755 (2004).
[4] K.V. Emtsev, F. Speck, Th. Seyller, L. Ley, and J.D. Riley, *Phys. Rev. B* **77**, 155303 (2008).

LEEM studies of quasi-free standing epitaxial graphene on SiC(0001) obtained by hydrogen intercalation

C. Coletti[1], C. Riedl[1], K.V. Emtsev[1], T. Iwasaki[1], A. Al-Temimy[1], S. Forti[1], A.A. Zakharov[2], and U. Starke[1]

[1]*Max-Planck-Institut für Festkörperforschung, Heisenbergstr. 1, D-70569 Stuttgart, Germany*

[2]*MAX-Lab, Lund University, Lund, S-22100, Sweden*

The preparation of epitaxial graphene on SiC(0001) by high temperature annealing [1,2] is one of the most promising approaches to exploit the recently discovered spectacular properties of graphene [3] for applications in carbon based nanoelectronics. However, the influence of the interface layer between graphene and the SiC(0001) substrate has so far imposed strong limitations. Recently, we offered a promising solution by the method of hydrogen intercalation below epitaxial graphene on SiC(0001) [4,5,6]. The hydrogen passivates the SiC substrate and decouples the epitaxial graphene generating quasi-free standing graphene on SiC(0001). At beamline I311 we investigated the morphology of the ex-situ prepared hydrogen intercalated graphene samples with low energy electron microscopy (LEEMIII instrument) at different sample temperatures.

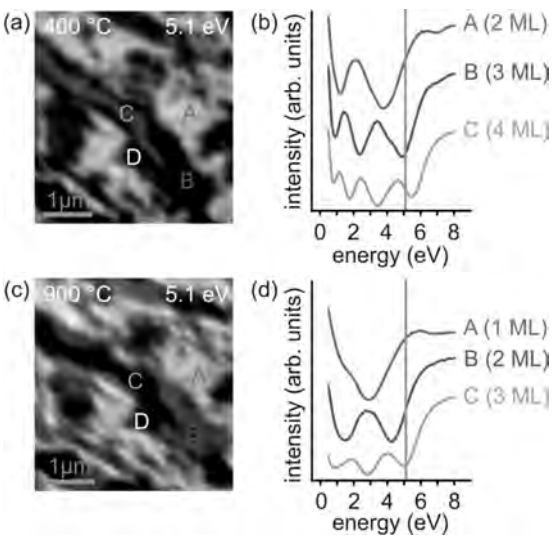

Fig. 1. (4 4) µm^2 LEEM micrographs recorded with an electron energy of 5.1 eV for the same area of (a) a hydrogen-treated graphene sample after outgassing at 400°C and (c) annealed at 900°C. The electron reflectivity spectra obtained for the regions A, B, and C are plotted in panels (b) and (d), respectively, labeled with the number of graphene monolayers (ML).

LEEM allows to identify the number of graphene layers on SiC from the number of dips in the electron reflectivity spectra between 0 and 8 eV [7,8]. In Fig. 1, LEEM micrographs are shown for an electron energy of 5.1 eV measured in the same area of the sample with (panel (a)) and without (panel (c)) intercalated hydrogen. The electron reflectivity spectra for the different surface domains A, B and C as labeled in panel (a) are plotted in panel (b). The number of dips in the spectra identifies region A, B and C as bi-, tri-, and four layer graphene. The advantage of the low homogeneity of the sample is that the effect of hydrogen on patches with different thickness can be observed. After desorbing the hydrogen through an annealing step at 900°C, the spatial distribution of these domains does not change as shown in panel (c). However, their LEEM intensity changes and the reflectivity spectra as plotted in panel (d) identify a complete transformation of (n+1)-layer thick areas into (n)-layer thick areas (n=1,2,3). Note that the region labeled D in Fig. 1 displays the same intensity before and after desorption of the hydrogen (and a flat reflectivity spectrum) and is attributed to surface defects, e.g. from residual polishing damage.

The powerful combination of hydrogen intercalation and the recently developed atmospheric pressure graphitization technique (Ref. [9]) leads to the growth of a defined number of quasi-free-standing epitaxial graphene layers with a homogeneity in the (10 μm)² range and could be groundbreaking for the future implementation of graphene-based nanoelectronics. Figure 2 (a) displays a bright field LEEM image from quasi-free-standing monolayer graphene on an originally chemically mechanically polished 4H-SiC(0001) sample. The surface shows a state of the art homogeneity with terrace sizes in the (10 μm)² range. An inspection of different surface areas, which are marked in the LEEM image, clearly identify all regions to be monolayer graphene (panel (b)) since the intensity curves exhibit one minimum only. The slight contrast difference between the domains A,B and C, D at around 5.0 eV (panel (a-b)), is not due to a different number of graphene layers. At a different sample position we investigated the gray and white area in more detail by micro-LEED. The corresponding diffraction patterns measured at 111 eV are shown in the insets of panel (a). They exhibit the threefold symmetry of the SiC-substrate whereas the gray and the white region differ by a rotation of the substrate of 60°C with respect to each other. This observation just reflects the two different possible stacking terminations of the 4H-SiC(0001) surface. After hydrogen desorption monolayer graphene has completely transformed back to zerolayer graphene without changes in the morphology. Fig. 2 (c) displays the corresponding LEEM image at 2.0 eV of the same surface area as before. The intensity spectra shown in panel (d) for different surface regions indeed have no pronounced minimum and are of zerolayer character [4].

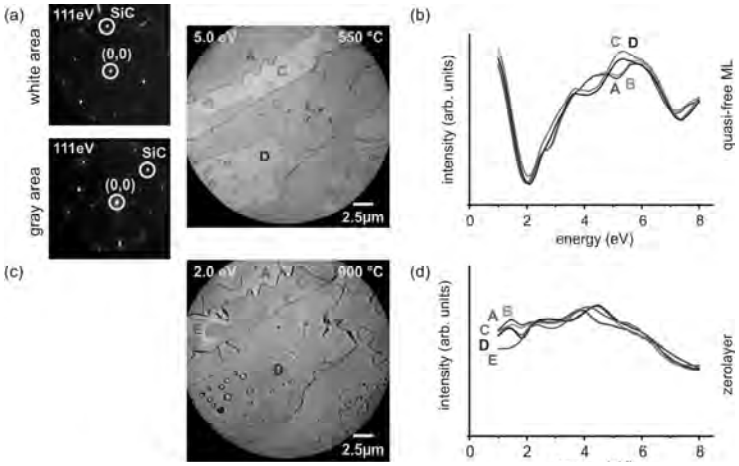

Fig. 2. LEEM images together with electron reflectivity spectra of the indicated surface areas showing quasi-free-standing monolayer graphene on a large scale before (panel (a-b)) and after (panel (c-d)) hydrogen desorption. The slight contrast change between different surface domains in panel (a) is due to SiC substrate domains with a mutual rotation of 60°C as shown in the micro-LEED patterns in the insets of panel (a).

References:

[1] T. Ohta, A. Bostwick, T. Seyller, K. Horn, and E. Rotenberg, Science **313**, 951 (2006).
[2] C. Riedl, U. Starke, J. Bernhardt, M. Franke, and K. Heinz, Phys. Rev. B **76**, 245406 (2007).
[3] A.K. Geim and K.S. Novoselov, Nat. Mater. **6**, 183 (2007).
[4] C. Riedl, C. Coletti, T. Iwasaki, A.A. Zakharov, and U. Starke, Phys. Rev. Lett. **103**, 246804 (2009).
[5] C. Riedl, C. Coletti, T. Iwasaki, and U. Starke, Mat. Sci. Forum **645-648**, 623 (2010).
[6] C. Riedl, C. Coletti, T. Iwasaki, and U. Starke, Max-lab activity report 2010.
[7] H. Hibino, H. Kageshima, F. Maeda, M. Nagase, Y. Kobayashi, and H. Yamaguchi, Phys. Rev. B **77**, 075413 (2008).
[8] C. Riedl, A.A. Zakharov, and U. Starke, Appl. Phys. Lett. **93**, 033106 (2008).
[9] K.V. Emtsev et al., Nature Materials **8**, 203 (2009).
[10] U. Starke, in: Silicon Carbide, Recent Major Advances (eds: W.J. Choyke, H. Matsunami, G. Pensl), p. 281-316, (Springer, 2004).

Electronic and structural decoupling of epitaxial graphene from SiC(0001) surface by a germanium buffer layer

Konstantin Emtsev, Alexei Zakharov*, and Ulrich Starke

Max-Planck-Institut für Festkörperforschung, Heisenbergstr. 1, D-70569 Stuttgart, Germany

**MAX-Lab, Lund University, Lund, S-22100, Sweden*

Due to its unique properties graphene has attracted enormous interest of physicists and material scientists in the last five years. Epitaxial growth of graphene on single crystal SiC wafers is considered among the most promising methods for large scale graphene fabrication [1]. From previous photoemission measurements [2] we know that as-grown epitaxial graphene on SiC(0001) resides on top of the so-called buffer layer (also referred to as $6\sqrt{3}$ reconstruction according to its LEED pattern, see Fig. 1(a)). The latter consists of a carbon layer with graphene-like topology and bond lengths but with strong covalent bonds to the SiC substrate. The $6\sqrt{3}$ buffer layer plays an important role passivating dangling bonds of the substrate, so that overlying graphene layers exhibit truly delocalized π-orbitals [2]. The interface, however, contains a high density of surface states that pin the position of the Fermi level in graphene at a very high electron doping level of about $1 \cdot 10^{13}$ cm^{-2}. Interface states were also suggested to act as scattering centers responsible for the lowered mobility of charge carriers in epitaxial graphene. An elegant way to circumvent this problem by passivating interface states with hydrogen was recently demonstrated [3]. In this contribution we show that the electrically inactive $6\sqrt{3}$ buffer layer can be structurally and electronically decoupled from the SiC substrate by intercalating an atomic layer of germanium at the interface with the substrate. This results in the formation of a quasi-free standing graphene film that is separated from the substrate by a Ge buffer layer.

The buffer layer samples were prepared by annealing the SiC(0001) samples in argon at T=1550°C in our home CVD reactor in Stuttgart. In contrast to conventional UHV annealing utilized earlier this novel preparation method preserves the very smooth morphology of the substrate and significantly improves the homogeneity of the buffer layer domains [4].

Fig. 1 presents the LEED patterns, high resolution C1s core level spectra, as well as ARPES valence band maps of the samples before and after deposition of several monolayers of Ge followed by subsequent annealing at T=720°C. As evident from the LEED patterns in Fig.1(a, b) such a treatment result in a complete disappearance of the initial $6\sqrt{3}$ reconstruction. Only graphene related spots remain visible. Further strong changes can be seen in the C1s core level spectra in Fig. 1(c, d). Two broad components (s_1 and s_2) of the buffer layer which reflect different chemical bonding of carbon atoms within the buffer layer (see Ref. [2]) are now converged into a single sharp graphene-like peak. Note also that the signal of the SiC substrate is significantly damped in comparison to the initial surface. The above observations can be reconciled in a model where Ge atoms diffuse underneath the buffer layer, break its covalent bonds to the substrate and hence structurally decouple the graphene from the SiC substrate. Furthermore, ARPES valence band maps in the vicinity of the K-point of graphene's Brillouin zone in Fig. 1(e, f) demonstrate a complete recovery of the electronic structure expected for quasi-free standing graphene after the Ge intercalation process.

The microsctucture of the surface before and after decoupling of the buffer layer from the SiC surface was investigated by means of low energy electron microscopy (LEEM). Corresponding LEEM micrographs are presented in Fig.2. As can be seen the domains of the decoupled graphene film are of the same size as on the initial samples, that is, of the order of several μm in width.

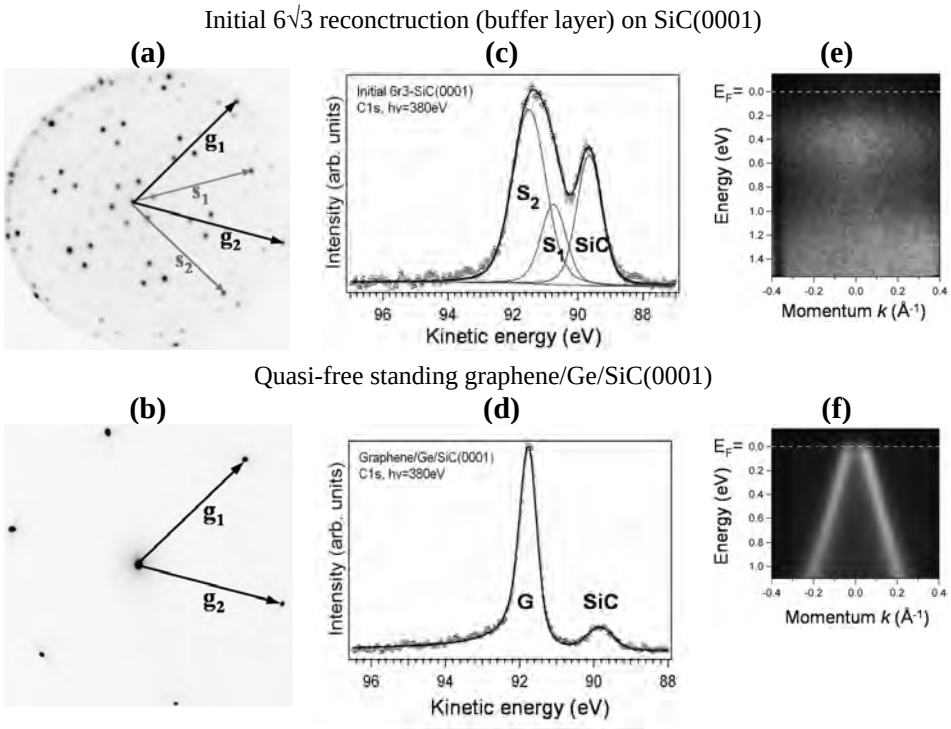

Fig. 1. MicroLEED patterns (*a, b*), C1s core level spectra (*c, d*), and ARPES valence band maps in the vicinity of the K-point of graphene's Brillouin zone (*e, f*) taken from the intial 6√3 reconstructed surface (*upper panel*) and after germanium deposition followed by vacuum annealing at T=700°C (*lower panel*). In (a, b) the electron energy was 40 eV. Vectors ($\mathbf{s_1}$, $\mathbf{s_2}$) and ($\mathbf{g_1}$, $\mathbf{g_2}$) correspond to reciprocal lattice vectors of graphene and the SiC lattice, respectively.

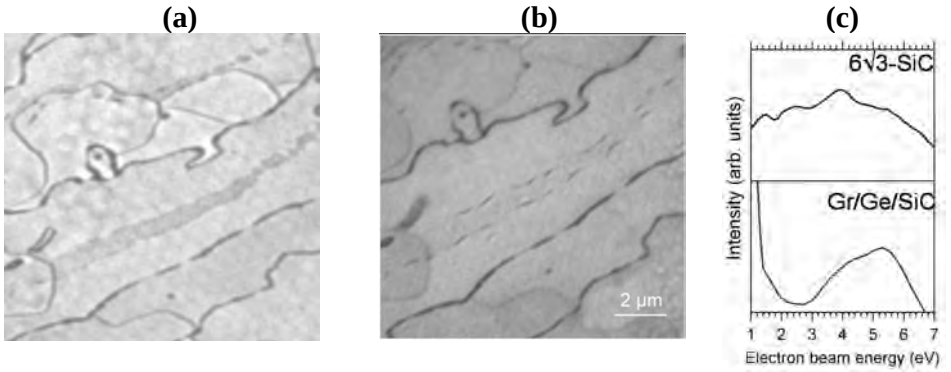

Fig. 2. LEEM micrographs of the initial 6√3 reconctruction (a) and of quasi-free standing graphene obtained by intercalation of Ge atoms at the interface with SiC (b) as well as their corresponding reflectivity LEEM I-V spectra (c).

[1] P.N. First, W.A. de Heer, Th. Seyller, C. Berger, J.A. Stroscio, J.-S. Moon, to appear in the April 2010 issue of the MRS Bulletin, http://arxiv.org/abs/1002.0873
[2] K.V. Emtsev, F. Speck, Th. Seyller, L. Ley, J.D. Riley, Phys.Rev.B **77**,155303(2008).
[3] C. Riedl, C. Coletti, T. Iwasaki, A.A. Zakharov, U. Starke, Phys. Rev. Lett. **103**, 246804 (2009).
[4] K.V. Emtsev, A. Bostwick, K. Horn, et al. Nature Materials 8, 203-207 (2009).

Surface core-level shifts on clean Si(001) studied with photoelectron spectroscopy and DFT calculations

P.E.J. Eriksson and R.I.G. Uhrberg
Department of Physics, Chemistry and Biology,
Linköping University, S-581 83 Linköping, Sweden

The clean Si(001) surface has a well-established structure consisting of tilted Si-dimers that form a c(4x2) periodicity, see Fig. 1. This reconstruction affects the binding energy of the Si 2p core-level of the atoms in the near surface layers. By applying high-resolution core-level spectroscopy in combination with calculations of core-level shifts, we are able to make a one-to-one identification of surface core-level shifts with the unique atoms down to the fourth atomic layer [1].

The Si 2p data were acquired at BL I311 using the Scienta SES200 electron analyzer. The experimental energy resolution was about 30 meV and the acceptance angle was about ± 5.5°. The clean Si(001) sample (n-type P, 2 Ωcm) was prepared by direct resistive heating up to 1520 K until no photoemission intensity from the C 1s or O 1s core-levels could be observed. The quality of the surface reconstruction was assessed by inspection of the low-energy electron diffraction pattern. Liquid nitrogen was used to cool the sample resulting in a temperature of 100 K. A Si 2p spectrum is shown by the dots in Fig. 2. The spectrum has been decomposed into various components that originate from the different unique atoms of the c(4x2) reconstruction, see Fig. 1. The fitting parameters and the information about the various components are found in table I. To make a one-to-one identification of the components with a specific type of atom we have here compared with our calculated surface core-level shifts.

All calculated results were obtained by density functional theory calculations in the generalized gradient approximation using the full-potential (linearized) augmented plane-wave+local orbitals method within the WIEN2k code [2]. The repeated slabs consisted of eleven (001)-layers. The slabs had the dimer structure of the c(4x2) reconstruction on one side, and were H terminated on the other side. Calculated surface core-level shifts were obtained both with and without final state effects included. Significant core-level shifts were found within the four outermost atomic layers. In agreement with an earlier study [3] we conclude that final state effects are important in order to reproduce the experimental core-level shifts. The final state effect on the core-level Si 2p energy is particularly strong for the down-atom due very efficient screening, which originates from the fact that the empty dangling bond band is located on this type atom. Our combined experimental and theoretical study has resulted in a very detailed assignment of the surface shifted components of the Si 2p spectrum from Si(001)c(4x2) down to the fourth atomic layer.

[1] P.E.J. Eriksson and R.I.G. Uhrberg, Phys. Rev. B 81, 125443 (2010).
[2] P. Blaha, K. Schwarz, G. K. H. Madsen, D. Kvasnicka and J. Luitz, *WIEN2k*, An Augmented Plane Wave + Local Orbitals Program for Calculating Crystal Properties (Karlheinz Schwarz, Tech. Universität Wien, Austria), 2001. ISBN 3-9501031-1-2.
[3] E. Pehlke and M. Scheffler, Phys. Rev. Lett. 71, 2338 (1993).

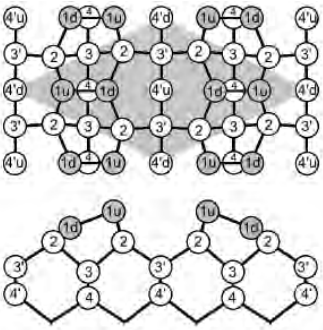

FIG. 1: Top and side views of the c(4x2) reconstruction.

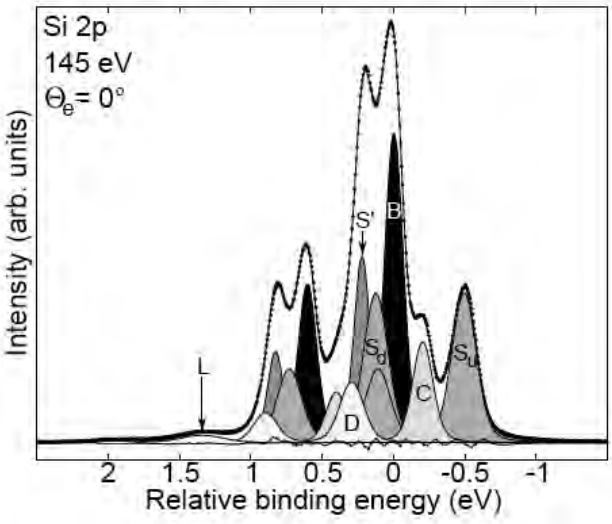

FIG. 2: Normal emission Si 2p core-level spectrum (dots) obtained at 100 K. A bulk (black) and six shifted surface components (gray), constructed of spin-orbit split Voigt functions, are used to generate the fit (solid curve). The residual intensity is shown relative to the base line.

TABLE I: Fitting parameters of the Si 2p components in Fig. 2. The parameters are binding energy relative to the bulk (E), Gaussian width (GW) and percentage (%) of the total intensity. The Lorentzian width was 0.046 eV. The spin-orbit split was 0.605 eV and the branching ratios were in the range 0.488-0.511. The last two rows, labeled "Origins", summarize the identification of the atomic origins of the various components.
The number that appears as a subscript on the atom label is the calculated core-level shift.

	L	D	S'	S_d	B	C	S_u
E (eV)	1.34	0.30	0.22	0.13	0	-0.22	-0.49
GW (eV)	0.33	0.17	0.11	0.18	0.13	0.14	0.18
%	1.5	7.2	15.4	18	29.4	10.4	18.1
Origins			$3'_{0.24}$	$1d_{0.10}$	$bulk_{0.00}$	$4_{-0.26}$	$1u_{-0.49}$
			$4'u_{0.19}$	$4'd_{0.10}$	$2_{0.00}$	$(3_{-0.11})$	

Influence of Au Nano Particles on the Self-Propelled Motion of Mesoscopic Droplets

E. Hilner, J. N. Andersen, E. Lundgren and A. Mikkelsen
Synchrotron Radiation Research, Lund University

A. A. Zakharov
MAX-lab, Lund University

Ga droplets form on the GaP(111)B surface when it is annealed above the maximum temperature for congruent evaporation. After the droplets have formed they start to move across the surface. On the clean surface the droplets move perpendicular to and uphill the steps introduced by the wafer miscut. We have now found that nanometer sized Au particles deposited on the surface can drastically change the dynamics of the micrometer sized Ga droplets. Instead of the unidirectional movement seen on the clean surface the droplets on the Au particle covered surface will move in random directions. We have also found that the Au particles themselves move during annealing on the GaP(111)B surface and that they act as starting points for oxide desorption.

Thermal decomposition of III-V surfaces is well known and has been studied for a long time [1]. Above the maximum temperature for congruent evaporation the group V component preferentially desorbs and droplets of the group III component form on the surface. Traditionally the droplet formation has been considered a nuisance complicating the growth of perfect epitaxial interfaces but the droplets also have many useful and interesting properties. One very interesting property of droplets on surfaces is self-propelled motion. It is found in many different types of materials systems [2, 3]. Recently self-propelled motion was observed for Ga droplets on the GaAs(001)[4] and GaP(111)B [5] surfaces. On GaP(111)B annealing at 700°C leads to the formation of Ga droplets. All droplets move in the same direction across the surface perpendicular to and uphill the surface steps. A simple mechanism has been proposed recently[5], based on extensive Spectroscopic PhotoEmission and Low energy Electron Microscopy (SPELEEM) and Scanning Tunneling Microscopy (STM) measurements.
We have now found using SPELEEM and STM that the presence of nanometer sized Au particles alter the dynamics of Ga droplets on the GaP(111)B surface. When Au nano particles are present the droplets do not move unidirectionally, but in random directions.

SPELEEM measurements were performed with the Elmitec LEEM III connected to the soft x-ray beamline 311 at MAX-lab. The STM measurements were carried out with a commercial Omicron VT STM Xa at a base pressure of 1×10^{-10} mbar.The GaP(111)B samples were cut from epi-ready substrates. Au nano particles (50-80 nm, 0.5-1/μm²) were deposited by an aerosol deposition method [6] on the whole or on one half of the sample. The surface oxide was desorbed by annealing at a temperature around 650°C. The oxide desorption was followed live in with the SPELEEM. It was also observed that at this temperature the Au particles move around on the surface. When only half the sample was covered by Au particles it could be noted that the oxide desorption begin at the Au particle covered side since the Au particles act as starting points for oxide desorption. After further annealing above 700°C the Au particles can no longer be

observed. An explanation for this could be that the particles dissolve the GaP to form an Au-Ga compound and thus sink into the surface. At this temperature the Ga droplets also start to form and move in random directions. It is interesting to note that when Au particles are present on half the sample the Ga droplets move in random directions only on the Au particle covered side. If they cross the boundary to the clean side of the sample their movement will become unidirectional. This suggests that the Au particles have a very local effect. No differences in the atomic scale structure between the clean and the Au particle covered surface could however be observed with STM or μ-LEED. It is intriguing how the extremely low amount of Au in the particles can completely change the dynamics of the micrometer sized Ga droplets. It is also useful since the Au particles could be used as a means to steer the droplet movement.

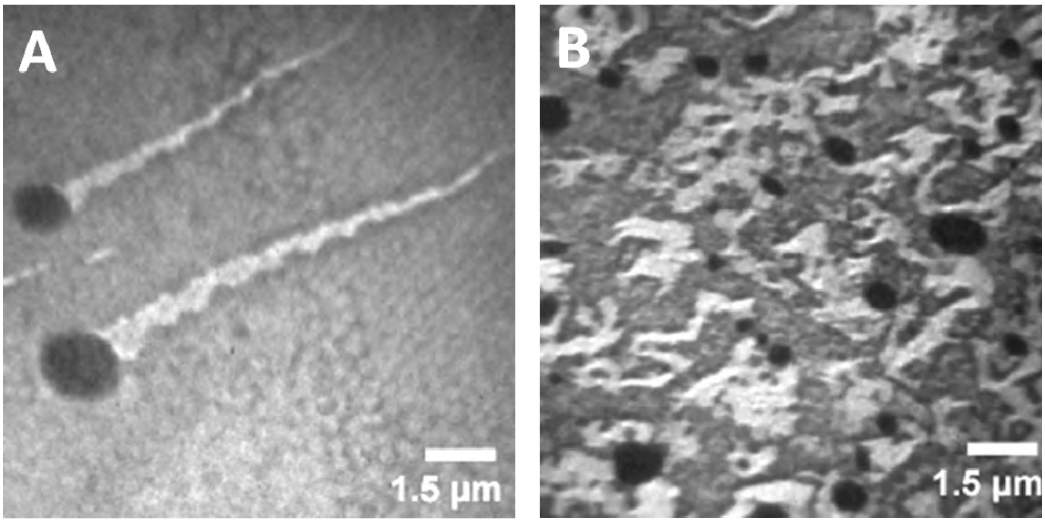

A) LEEM image of Ga droplets on GaP(111)B. The droplets move in the same direction and have left trails on the surface.
B) LEEM image of Ga droplets on GaP(111)B with deposited Au nano particles (not visible in the image). The Ga droplets have moved in random directions on the surface.

[1] D. Haneman, J. Appl. Phys. **11**(3-4), 217 (1959)
[2] A. K. Schmid, N. C. Bartelt and R. Q. Hwang, R. Q. , Science **290**, 1561 (2000)
[3] H. Linke, B. J. Alemán, L. D. Melling, M. J. Francis, C.C. Dow-Hygelund, V. Narayanan, R. P. Taylor, A. Stout, Phys. Rev. Lett. **96**, 154502 (2006)
[4] J. Tersoff, D. E. Jesson and W. X. Tang, Science **324**, 236 (2009)
[5] E. Hilner, A. A. Zakharov, K. Schulte, P. Kratzer,
J. N. Andersen, E. Lundgren and A. Mikkelsen, Nano Lett. **9**(7), 2710 (2009)
[6] M. H. Magnusson, K. Deppert, J. –O Malm, J. –O. Bovin, L. Samuelson, J. Nanopart. Res. **1**, 243 (2004).

Doped InP Nanowires Studied by SPELEEM

M. Hjort[1], A.A. Zakharov[2], R. Timm[1], M.T. Borgström[1], K. Deppert[1], L. Samuelson[1], J.N. Andersen[1], E. Lundgren[1], A. Mikkelsen[1]

[1]Department of Physics, Lund University
[2]MAX-lab, Lund University

III-V semiconductor nanowires (NWs) have long been proposed as future key components within a wide range of areas, e.g. sensing, (opto)electronics and photovoltaics. Because the nanowires allow integration of III-V materials directly with the existing Si platform used in industry, they enable high performance at low cost. Much of the research performed so far has been focused on growing perfect single crystal nanowires, but a prerequisite for most devices is the ability to in a controlled manner, both spatially and magnitude wise, dope the structures.

We have performed combined Spectroscopic PhotoEmission and Low Energy Electron Microscopy (SPELEEM) and X-ray Photoemission Spectroscopy (XPS) on doped InP nanowires at beamline i311 at MAX-lab. The nanowires were grown using Metal Organic Vapor Phase Epitaxy (MOVPE) and an Au-seed particle was used to define the size of the wires. The precursors for the growth were trimethylindium (TMI) and phosphine (PH_3) while dimethylzinc (DMZn) and tetraethyltin (TESn) were used as precursors for p- and n-type dopants respectively. In addition to homogenously doped wires, we have also investigated double pn-junction nanowires where the dopants have been switched during growth resulting in an n-p-n-p type structure. A detailed description of the growth of pn-junction NWs have been published previously[1]. After growth the nanowires were transferred to a HF-etched Si-wafer and put into vacuum. The nanowires were cleaned in an atomic hydrogen atmosphere at 400°C, removing most of the native oxide.

In Fig 1 a. a scanning electron micrograph showing a free-standing double pn-junction nanowire can be seen. No apparent change of the contrast occurs along the nanowire. In the SPELEEM, however, it is immediately evident that the NWs are comprised of segments, as seen in Fig 1 b. and c. When low energy electrons are used to image the nanowires, Fig 1 b., both the n- and p-parts are possible to distinguish as well as the catalytic gold particle in the top. The different segments are even more apparent if X-rays are incident on the sample and the secondary electrons are analyzed, as is seen in Fig 1 c. The contrast arises due to a small change in the secondary emission peak between the n and p part which demands a narrow energy window (0.2eV) when imaging. The magnitude of the secondary electron emission can be correlated with a specific dope level similar to what has previously been seen on patterned Si surfaces [2]. With the SPELEEM we also imaged using electrons from specific core levels and thus became very surface sensitive; in contrast to when secondary electrons were used which were emitted from many nanometers down in the sample. In Fig 1 d. only electrons from the In4d core make up the image and no contrast can be seen along the NW indicating that we still have some In-oxide on the nanowire and therefore we cannot probe the bulk properties.

[1]M.T. Borgström et al., Nanotechnology 19, 445602 (2008)

[2] M. Hovorka et al., Journal of Microscopy 230, 42 (2008)

Figure:

a) SEM image of a double pn-junction NW. The sample is tilted 30°.
b) Mirror Electron Microscope (MEM) image of a double pn-junction InP NW. The n and p segments are indicated as well as the Au-particle. Start voltage 0.1 eV.
c) XPEEM image using secondary electrons. The n and p segments are indicated as well as the Au-particle. Start voltage 0.1 eV, hv 70 eV
d) XPEEM image using In4d electrons. No contrast difference can be seen at the different segments. Start voltage 47.6 eV, hv 70 eV

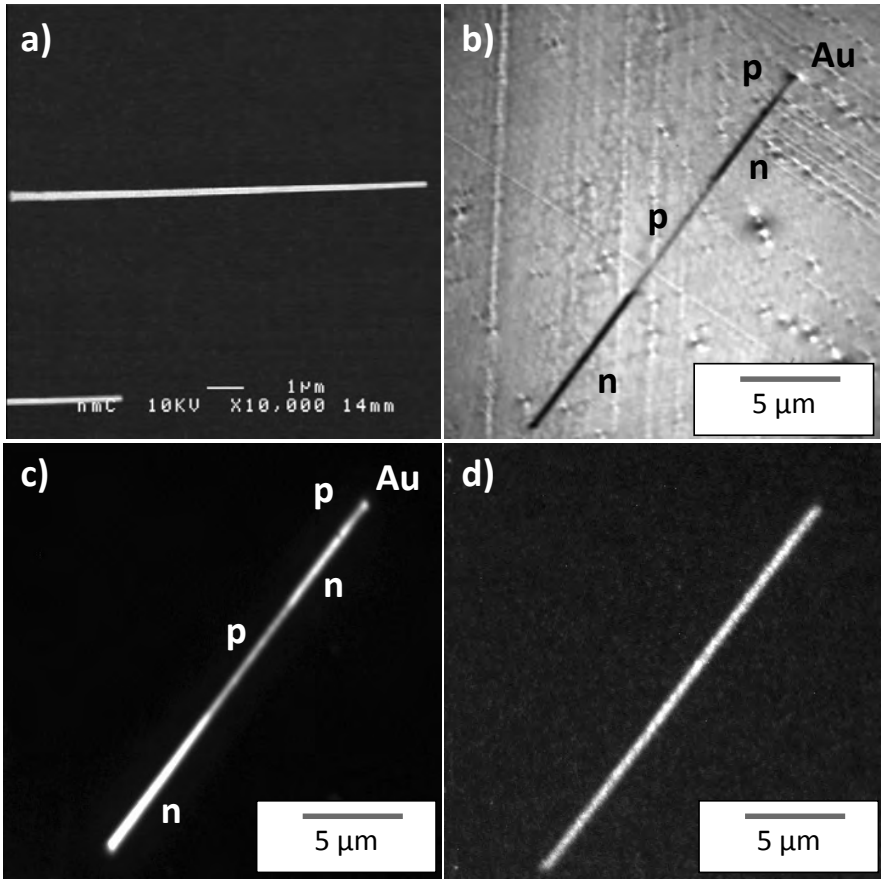

Spin Quench on the Iron 3*d* States of Iron Phthalocyanine Caused by Metal-Ligand Bond Formation

Cristina Isvoranu[1], Evren Ataman[1], Jan Knudsen[1], Karina Schulte[2], Jesper N. Andersen[1], and Joachim Schnadt[1]

[1]*Division of Synchrotron Radiation Research, Department of Physics, Lund University, Box 118, 221 00 Lund, Sweden*

[3]*MAX-lab, Lund University, Box 118, 221 00 Lund, Sweden*

In the present study the interaction between the electron acceptor carbon monoxide (CO) and nitric oxide (NO) molecules and iron phthalocyanine (FePc) monolayers on a Au(111) support was studied by means of x-ray photoemission spectroscopy. Nitric oxide and carbon monoxide are diatomic molecules with unique and rich chemistry. Nitric oxide molecule has one unpaired electron on the nitrogen atom, being thus a free radical species, expected to be very reactive. It is a signalling molecule in many physiological processes in the human body [1] and also an air pollutant. Carbon monoxide is a highly toxic gas, produced from the partial oxidation of hydrocarbons. What makes CO chemistry unique is that the negative part of the dipole is at the carbon end of the molecule, making the carbon atom the reactive part of the molecule [2].

The results show the formation of FePc(CO) and FePc(NO) complexes. It is important to notice that the ligand adsorption changes the open shell structure on the iron atom into a close shell structure, the new FePc(CO) and FePc(NO) complexes being low spin compounds, as can be seen from the changes involved in the Fe 2*p* core levels (Figure 1). Figure 1 shows the Fe 2*p* core-levels of FePc monolayers before and after adsorption of an amount of gas which corresponds to 4 Langmuir. The changes involved are quite similar in both cases. A significant narrowing of the spectra occurs upon adsorption and also a shift towards higher binding energies is observed. The broad, multiplet structure characteristic for the Fe 2*p* spectrum of the monolayer with a FWHM of 3.7 eV becomes 1.1 eV in the case of CO adsorption, while NO gives a FWHM of the Fe $2p_{3/2}$ line of 1.3 eV. It is the narrowing of the Fe 2*p* photoemission line that we attribute to the formation of the low spin complexes.

Also, a 1.15 eV shift of the low binding energy feature in the spectra occurs in the case of CO adsorption, while NO causes a shift with the magnitude of 1.35 eV, consistent with the knowledge that NO is a stronger electron acceptor than CO [3]. In conclusion, apart from a spin quench, the CO and NO ligands also decrease the electronic density around the iron atom. Our findings indicate the possibility of controlling and tailoring the spin state on organic complexes by adsorption of molecular ligands.

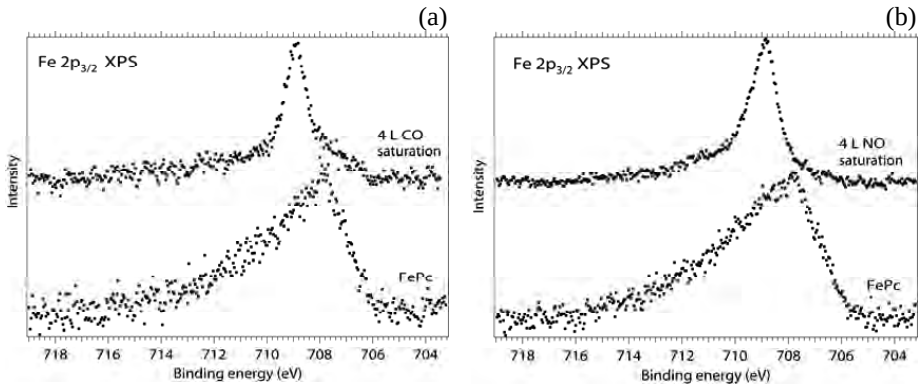

Figure 1 (a) Fe $2p_{3/2}$ photoemission spectra for an FePc monolayer on Au(111) before and after adsorbing 4 Langmuirs of CO (a) and NO(b). A significant narrowing of the spectra occurs upon gas adsorption, together with a shift towards higher binding energy of the low binding energy feature at around 707.8 eV.

[1] L. J. Ignarro, Nitric Oxide – Biology and Pathology, Academic Press, San Diego 2000.
[2] D. F. Shriver, P. W: Atkins, and C. H. Langford, Inorganic Chemistry 2nd edition, Oxford University Press, Oxford Melbourne Tokyo 1994.
[3] D. F. Shriver, P. W: Atkins, and C. H. Langford, Inorganic Chemistry 2nd edition, Oxford University Press, Oxford Melbourne Tokyo 1994.

Pyridine Adsorption on Iron Phthalocyanine on Au(111)

Cristina Isvoranu[1], Evren Ataman[1], Karina Schulte[2], Jan Knudsen[1], Jesper N. Andersen[1], and Joachim Schnadt[1]

[1]*Division of Synchrotron Radiation Research, Department of Physics, Lund University, Box 118, 221 00 Lund, Sweden*

[2]*MAX-lab, Lund University, Box 118, 221 00 Lund, Sweden*

Because of their unique properties pththalocyanines are among the most important class of macrocycle compounds. The macrocycles exhibit aromatic character, due to the planar structure consisting in a conjugated array of π electrons. As a consequence of their aromaticity, the molecules have high thermal and chemical stability [1] and they are stable under electromagnetic radiation. In particular, phthalocyanines on solid supports are are promising candidates for novel catalytic [2,3,4] and gas sensing applications [5,6,7,8,9].

The adsorption of pyridine on well ordered, flat lying iron phthalocyanine (FePc) monolayers on Au(111) was investigated by means of x-ray photoemission spectroscopy and x-ray absorption spectroscopy. The adsorption experiments were carried out at liquid nitrogen temperature. The results show that pyridine coordinates to the iron site of iron phthalocyanine and that the coordination causes significant changes in the electronic structure of the iron phthalocyanine molecular network. The N 1*s* and Fe $2p_{3/2}$ photoemission spectra before and after adsorbing increasing amount of pyridine on iron phthalocyanine monolayers on Au(111) are shown in Figure 1. As proved by the narrowing of the Fe 2p spectra, the ligand field produced by the pyridine ligand results in a spin quench of the FePc molecule. The saturation coverage indicated in Figure 1 corresponds to the point where the Fe 2*p* spectrum shape stops changing, indicating the coverage where all the iron centres in the monolayer are coordinated to pyridine molecules. Also, in the N 1*s* spectra additional peak features show up on the high binding energy side of the N 1*s* FePc peak, indicating different adsorption sites for pyridine. The highest binding energy peak at around 400.2 eV is due to pyridine molecules coordinated to iron, while the feature at around 399.3 eV is due to pyridine molecules physisorbed on the FePc macrocycle on other sites than the

iron. These results fit in well with previous studies, which have shown the possibility of tailoring the electronic structure of phthalocyanine derivatives by ligand attachment [10,11] or by atom-by-atom manipulation [12].

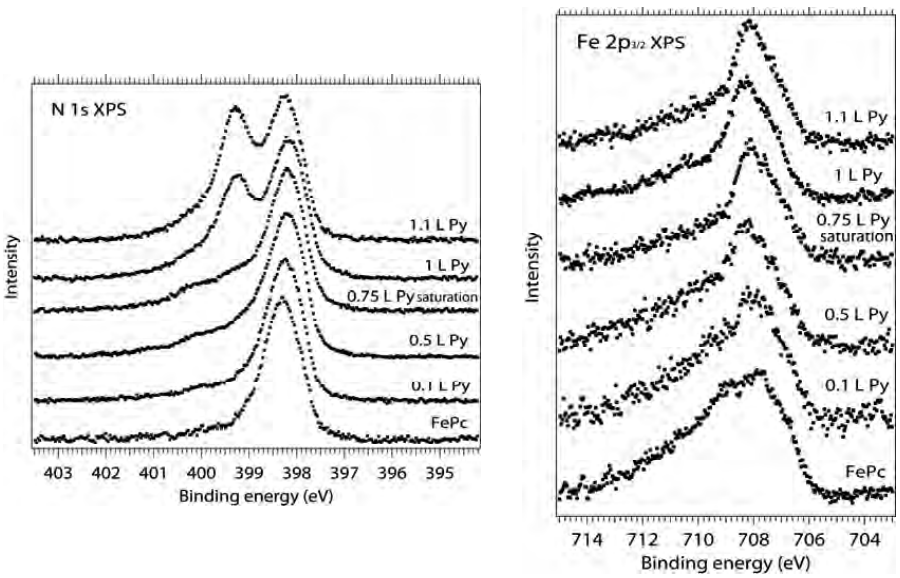

Figure 1 (a) N 1*s* and (b) Fe $2p_{3/2}$ photoemission spectra before and after adsorption of increasing amounts of pyridine on FePc monolayers on Au(111). Additional peak features show up on the high binding energy side of the N 1*s* FePc peak, indicating different adsorption sites for pyridine. Also, the Fe $2p_{3/2}$ spectra get significantly narrower after pyridine adsorption.

[1] L. R. Milgrom, The Colours of Life – An Introduction to the Chemistry of Porphyrins and Related Compounds, Oxford University Press, New York (1997).
2 Y. Lu and R.G. Reddy, Int. J. Hydrogen Energy, 33 (2008) 3930–3937.
3 M. Toledo, A. M. S. Lucho, and Y. Gushikem, J. Mater. Sci., 39 (2004) 6851 – 6854.
4 S. Baranton, C. Coutanceau, C. Roux, F. Hahn, and J.-M. Léger, J. Electroanal. Chem., 577 (2005) 223–234.
5 M. Newton, T. Starke, M. Willis, and G. McHale, Sens. Actuators B, 67 (2000) 307-311.
6 K. Ho and Y. Tsou, Sens. Actuators B, 77 (2001) 253–259.
7 C. Liu, J. Shih, and Y. Ju, Sens. Actuators B, 99 (2004) 344–349.
[8] S. Singh, S. Tripathi, and G. Saini, Mater. Chem. Phys., 112 (2008) 793-797.
[9] J. Spadavecchia, G. Ciccarella, and R. Rella, Sens. Actuators, 106 (2005) 121-220.
[10] P. Wahl, L. Diekhöner, G. Wittich, L. Vitali, M. A. Schneider, and K. Kern, Phys. Rev. Lett., 95 (2005) 166601.
[11] K. Flechtner, A. Kretschmann, H.P. Steinrück, and J. M. Gottfried, J. Am. Chem. Soc., 129 (2007) 12110-12111
[12] N. Néel, J. Kröger, R. Berndt, T.O. Wehling, A. I. Lichtenstein, and M. I. Katsnelson, Phys. Rev. Lett., 101 (2008) 266803(1)-(3).

CO adsorption on Au-particles grown on ultrathin and partly reduced iron-oxide films

Jan Knudsen[a*], Karina Schulte[b], Evren Ataman[a], Cristina Isvoranu[a], Joachim Schnadt[a], and Jesper N. Andersen[a]

[a]Division of Synchrotron Radiation Research, Department of Physics, Lund University, Box 118, 221 00 Lund, Sweden
[b]MAX-lab, Lund University, Box 118, 221 00 Lund, Sweden

The development of and research into new and better catalysts for the preferential oxidation of CO (CO-PROX) immersed in a mixture of H_2, CO and O_2 gases has gained renewed interest due to the increasing importance of low-temperature fuel cells [1] with operating temperatures between 80 - 100°C. CO poisons the anodes of such fuel cells and thus it has to be removed from the fuel cell feed. Conventional CO-PROX catalysts (Pt, Ru, Rh supported on alumina) operate at temperatures between 150 - 200°C, too high for low temperature fuel cells, while Au particles on α-Fe_2O_3 have been suggested as a new and effective low-temperature catalyst [2].

Here we used X-ray photoelectron spectroscopy (XPS) to study the CO adsorption properties of Au-particles vapor deposited onto an ultrathin FeO(111) film supported on Pt(111). The iron-oxide film is very inert and it is thus an excellent support material for UHV studies of gas-adsorption and reactions on metallic nano-particles.

We found that it is possible to tune the CO adsorption properties considerably by changing the temperature, at which the Au particles are grown at the FeO(111) film. This is illustrated on fig. 1 (a) and (b), showing the $Au4f_{7/2}$ peak of Au particles deposited at room temperature and 100 K, respectively. The CO induced shift towards higher binding energies [3, 4] is clearly increased when Au adsorption is done at 100 K.

Interestingly, we observe an increased CO adsorption on Au-particles deposited at room temperature on partly reduced FeO(111) film [5, 6] (see fig. 1(c)) as compared to Au particles supported on a pristine FeO(111) film. Using Scanning tunneling microscopy (STM) we explain the increased CO adsorption with a decreased Au particle size induced by the defects.

Fig. 2 (a) shows a STM-image of an ultrathin FeO film grown by sublimating Fe in-situ followed by oxidation. Individual atoms and the characteristic moiré superstructure are clearly observed. Previously, we have shown how one can make and control the density of dislocations by reduction the oxide film with atomic hydrogen [5,6]. The dislocations disappear completely after Au-deposition suggesting that the Au-particles bind close to the dislocations (see fig. 2(b-c)). A tentative model explaining how the defects are removed by Au adsorption is shown in fig. 2(d).

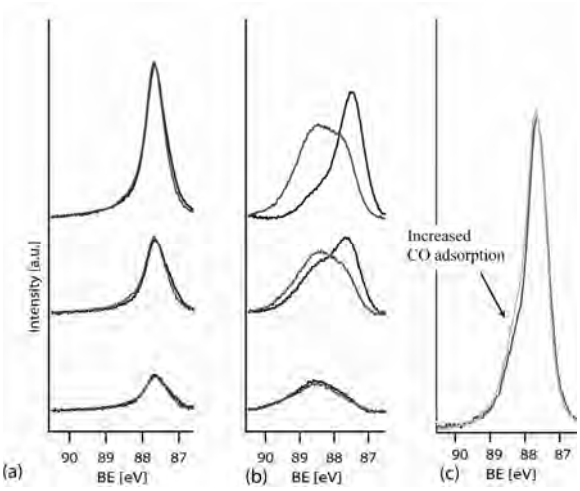

Fig. 1: (a) XPS spectra of Au $4f_{7/2}$ region of Au particles deposited onto a FeO(111) film at RT before (black) and after (red) CO adsorption(10 L) at 100 K. (b) XPS spectra of Au $4f_{7/2}$ region of Au particles deposited onto a FeO(111) film at 100 K before (black) and after (red) CO adsorption (10 L) at 100 K. (c) XPS spectra of Au $4f_{7/2}$ region of Au particles deposited onto a pristine (red) and partly reduced (blue) FeO(111) film at RT after CO adsorption at 100 K.

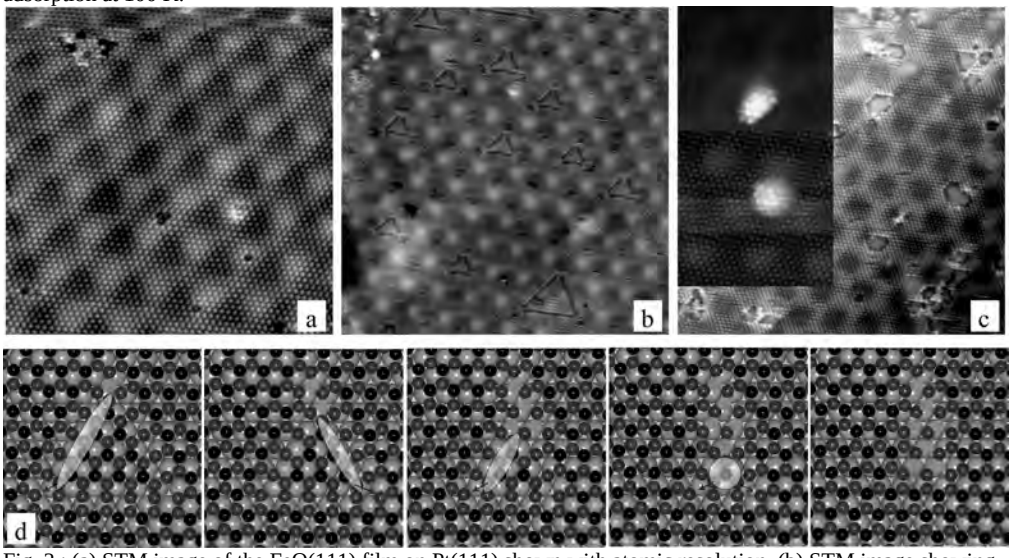

Fig. 2.: (a) STM image of the FeO(111) film on Pt(111) shown with atomic resolution. (b) STM image showing dislocations formed after partly reduction with atomic hydrogen. These dislocations act as anchoring sites for the Au-particles and they can thus be used to control the size-distribution of the Au-particles. (c) STM images of Au-particles grown in-situ on the partly reduced FeO(111) film. Clearly, the Au-particles remove the dislocations. (d) Tentative model explaining how the Au-particles remove the dislocations. O (red), twofold coordinated Fe (dark-grey), threefold coordinated Fe (black), Pt (light-grey), and Au (orange).

References

[1] Oetjen *et al.* Jour. Elec. Soc. **143**, 3838 (1996)
[2] Kahlich *et al.*, Jour. Cat. **182**, 430 (1999)
[3] Weststrate *et al.*, JPC **112**, 6900 (2008)
[4] Westrate *et al.*, JPC **113**, 729 (2009)
[5] Merte *et al.*, Surf. Sci. **603**, L15 (2009)
[6] Knudsen *et al.*, Surf. Sci. **604**, 11 (2009)

Oxygen adsorption on stepped Pd(100) surfaces

F. Li, F. Allegretti, S. Surnev, F.P. Netzer
Institute of Physics, Surface and Interface Physics,
Karl-Franzens University Graz, A-8010 Graz, Austria

Y. Zhang, W.-B. Zhang, K. Reuter
Fritz-Haber-Institut der Max-Planck-Gesellschaft,
Faradayweg 4–6, D-14195 Berlin, Germany
and
Technische Universität München, Lichtenbergstr. 4, D-85747 Garching, Germany

The interaction of oxygen with transition metal surfaces has long gained significant attention in both fundamental and applied research, due to its importance in heterogeneous catalysis and corrosion. For well-defined low-index single crystal surfaces this has established a rather profound understanding, which ranges from the early stages of on-surface oxygen adsorption to the formation of surface- and bulk-oxide phases [1]. Recently and as a step towards higher material's complexity, the interaction of oxygen with vicinal metal surfaces, consisting of periodic arrays of atomic steps, has become an intriguing subject of investigation. Here, we employ a scanning tunneling microscopy (STM) and high-resolution core-level spectroscopy (HR-XPS) measurements using synchrotron radiation to study the initial oxidation of vicinal Pd(100) surfaces exhibiting close-packed (111) steps. The XPS data analysis is supported by detailed surface-core level shift calculations based on density-functional theory (DFT).

Two stepped Pd(100) surfaces have been employed in our experimental investigation, Pd(119) and Pd(1 1 17) which consist of (100) terraces that are 5 and 9 atom rows wide, respectively, and separated by {111} faceted steps, 12.6 Å and 23.4 Å apart. The STM image (Fig. 1) demonstrate that exposing both surfaces to oxygen at a pressure of $5x10^{-9}$ mbar and at 520 K results in the decoration of the Pd steps by a (2x1) zigzag chains, while a p(2x2) superstructure can be discerned on the larger (100) terraces. Recent cluster-expansion based density functional theoretical study [2] has predicted that over a wide range of an oxygen chemical potential oxygen adatoms decorate the alternating sites at the (111) steps of a stepped Pd(100) surface in a characteristic Pd-O zigzag structure, while the (100) terraces are covered by a chemisorbed p(2x2) layer (see the model sketched in the right panel of Fig. 2). To test the validity of this structure model we have performed peak decomposition analysis of the corresponding experimental Pd 3d core-level shapes according to the calculated surface core-level shifts (SCLS): the results are displayed in Fig. 2. The computed SCLS for the various Pd atoms labeled on the structure model in the right panel of Fig.2 are displayed as bars below the spectrum. They reveal an intriguing complexity beyond what one would expect from simply accounting for the number of directly coordinated O atoms. In such a view, the similarly coordinated upper step atoms Pd1 and Pd2 should exhibit roughly similar SCLSs, while the actually computed values differ by about 150 meV. The same holds for the difference of atoms Pd3 and Pd4, and in turn their largely different SCLSs compared to those of the other terrace atoms Pd5 – Pd8. The reason for this symmetry breaking is that the position of the upper step edge O atom, denoted Thu in Fig. 2, does not really correspond to the ideal fourfold hollow site. Instead it is better described as a quasi-threefold coordination, with the Thu O atom much stronger bound to the Pd4 atom with a bond length of 2.01 Å than to the Pd3 atom with a bond length of 2.83 Å. As a result, the computed SCLSs divide roughly into four groups that comprise in parts seemingly inequivalent Pd surface atoms, cf. Fig. 2: One component at -400±20 meV due to the essentially zerofold O-coordinated atoms Pd3 and Pd10, one centered around the bulk peak from the terrace atoms Pd5 – Pd8, one

component at 330±40 meV due to Pd4 and Pd9, and finally an even further shifted component due to the most strongly O-coordinated Pd1 and Pd2 atoms at the upper step edge. As shown in Fig. 2 a corresponding deconvolution of the experimental spectrum into four components yields indeed an excellent fit after only minor optimization of the binding energies to A (-370 meV), B (0 meV), C (+330 meV) and D (+580 meV).

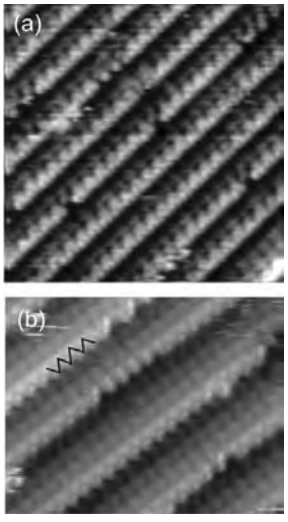

Fig.1: STM images of oxygen dosed (a) Pd(119),100Åx100Å, +0.4V, 0.1nA and (b) Pd(1 1 17) surfaces, 100Åx75Å, +4 mV, 0.1 nA).

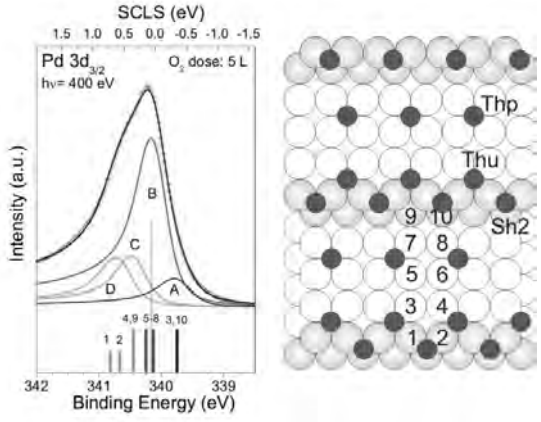

Fig.2: (left panel) Peak decomposition analysis of the Pd $3d_{3/2}$ line shape of the Pd(119) surface exposed to 5L O_2 at $5x10^{-9}$ mbar. The calculated SCLSs for the p(2x2)-O + zigzag step model are displayed as bars at the bottom, following the notation for the different Pd surface atoms given in the schematic top view in the right panel.

In conclusion we have presented STM and high-resolution XPS data to address the initial oxidation of vicinal Pd surfaces exhibiting (100) terraces and close-packed (111) steps. Supported by a detailed SCLS analysis through DFT calculations our measurements indicate a rapid oxygen decoration of the (111) steps in a characteristic (2x1) zigzag pattern, followed by the formation of a p(2x2)-O overlayer on the terraces.

Financial support was provided by the Austrian Science Funds (FWF) within project S90 "Nanoscience on Surfaces", and the ERC Advanced Grant SEPON. Support during experiments by MAX-Lab is gratefully acknowledged.

References:

[1] "*Nanometer and Sub-Nanometer Thin Oxide Films at Surfaces of Late Transition Metals*", K. Reuter, in "Nanocatalysis", p. 343-376, U. Heiz, U. Landman (Eds.), Springer, Berlin (2006). ISBN 978-3-540-32645-8
[2] Y. Zhang and K. Reuter, Chem. Phys. Lett. 465 (2008) 303

Quasi-free standing epitaxial graphene on SiC(0001) obtained by hydrogen intercalation

C. Riedl, C. Coletti, T. Iwasaki, and U. Starke

Max-Planck-Institut für Festkörperforschung, Heisenbergstr. 1, D-70569 Stuttgart, Germany

Graphene is one promising candidate for the next generation of electronic devices [1] with high temperature annealing of SiC(0001) wafers being the preparation method of choice [2,3]. However, the influence of the (6√3x6√3)R30° reconstructed interface layer between epitaxial graphene and the SiC(0001) substrate has so far imposed strong limitations. Recently, we offered a promising solution by the method of hydrogen intercalation below epitaxial graphene on SiC(0001) [4,5,6]. The hydrogen treatment of the samples was conducted ex-situ in a chemical vapor deposition (CVD) reactor at temperatures between 600 °C and 1000 °C in ultra-pure molecular hydrogen at atmospheric pressures. At beamline I311 we investigated the C 1s and Si 2p core level spectra of the hydrogen intercalated graphene samples at different sample temperatures.

The interface layer between graphene and SiC(0001) is a covalently bound initial carbon layer. Since it does not yet exhibit the typical electronic properties of graphene (i.e. π-bands) it is often called "zerolayer (ZL) graphene". As shown in the side view models in Fig. 1 (a) for zerolayer graphene and in Fig. 1 (f) for monolayer graphene the hydrogen breaks and saturates the respective bonds of the interface layer and decouples the epitaxial graphene generating quasi-free-standing monolayer and bilayer graphene, respectively. In angular resolved photoemission spectroscopy (ARPES) using He II excitation in the "home laboratory" the transformation between zerolayer graphene (panel (b)) and quasi-free-standing monolayer graphene (panel (c)) as well as between monolayer graphene (panel (g)) and quasi-free-standing bilayer graphene (panel (h)) is straight away evident. Note that after outgassing to 700 °C the samples show conditions very close to charge neutrality. From low energy electron diffraction (LEED) measured at beamline I311 a geometrical decoupling is obvious from the strong suppression of the (6√3x6√3)R30° related diffraction spots (panel (d) and (i)). At temperatures around 1000 °C the hydrogen has completely desorbed so that zerolayer graphene and monolayer graphene, respectively, are re-established as can be seen from the LEED patterns in panel (e) and (j).

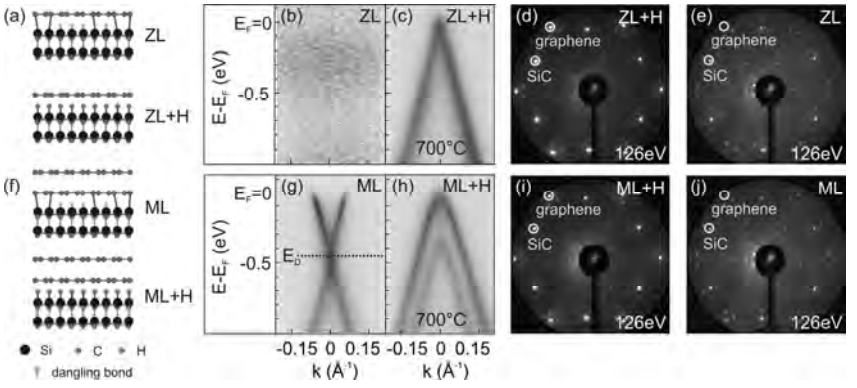

Fig. 1. Hydrogen intercalation below (a-e) zerolayer (ZL) and (f-j) monolayer (ML) epitaxial graphene on SiC(0001). (a) and (f) Side view models of the hydrogen intercalation process. (b-c) and (g-h) Dispersion of the graphene π-bands measured before and after hydrogen intercalation plus subsequent outgassing to 700°C, (d-e) and (i-j) LEED patterns of zerolayer and monolayer graphene before and after hydrogen desorption.

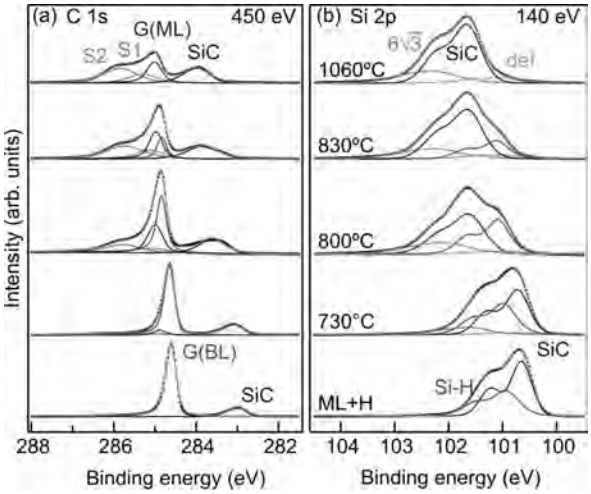

Fig. 2 C 1s (a) and Si 2p (b) core level spectra for a hydrogen treated monolayer graphene sample (bottom spectra) and the same sample annealed at increasing temperatures. The experimental data are displayed in black dots. Different components, accordingly labeled in the spectra, are fitted into the C 1s and Si 2p regions by a line shape analysis. The gray solid line is the envelope of the fitted components.

For detailed information about the chemical bonds in the near surface region C 1s and Si 2p core level spectra for an ex-situ hydrogen-treated monolayer sample annealed at different temperatures are plotted in Fig. 2. Bulk and surface related species are identified by varying the incident photon energy; the energy shown in Fig. 3 is 450 eV for the C 1s and 140 eV for the Si 2p spectra. The bottom curve in Fig. 2 (a) shows the C 1s spectrum measured after outgassing the ex-situ hydro-gen-treated sample at a temperature of around 400 °C. The dominant peak at 284.6 eV is the graphene related (bilayer) component G(BL) while the broader, less intense peak at 283.0 eV is the SiC (bulk) related component. We emphasize the complete absence of the $(6\sqrt{3}x6\sqrt{3})R30°$ reconstruction related components [7]. At annealing temperatures higher than 700 °C the hydrogen starts to desorb, as indicated by the appearance of the interface components S1 and S2, which result from the carbon atoms in the re-establishing interface layer [7]. The hydrogen desorption is accompanied by the appearance of a second (monolayer) graphene related peak G(ML) (black line), representing those patches where the hydrogen has left. Eventually, after annealing at 1060 °C, the C 1s spectrum assumes the shape of normal epitaxial monolayer graphene. The total shift of the SiC bulk component amounts to 1 eV confirming the presence of hydrogen bonds. which cause a corresponding band bending.

Further evidence of the existence of Si-H bonds is brought by the Si 2p data. The Si 2p spectrum obtained after initial outgassing (bottom curve in Fig. 2 (b)) consists of two spin-orbit split doublets. The binding energies are given with respect to the Si $2p_{3/2}$ component. The dominant peak at 100.6 eV (dark blue line) can be assigned to the bulk component and the one at 100.9 eV (red line) to Si-H bonds. After annealing at 730 °C the Si 2p spectrum can be accurately fitted only by introducing two additional components: the one at higher binding energy (light blue line) is attributed to the Si atoms bonded to the $(6\sqrt{3}x6\sqrt{3})R30°$ structure, the small one at lower binding energy (green line) to surface defects. These components increase in intensity for increasing annealing temperatures while the Si-H component gradually vanishes and completely disappears at 1060 °C. The total shift observed for the Si 2p bulk component amounts to 1 eV in agreement with the C 1s bulk peak.

References:

[1] A.K. Geim and K.S. Novoselov, Nat. Mater. **6**, 183 (2007).
[2] T. Ohta, A. Bostwick, T. Seyller, K. Horn, and E. Rotenberg, Science **313**, 951 (2006).
[3] C. Riedl, U. Starke, J. Bernhardt, M. Franke, and K. Heinz, Phys. Rev. B **76**, 245406 (2007).
[4] C. Riedl, C. Coletti, T. Iwasaki, A.A. Zakharov, and U. Starke, Phys. Rev. Lett. **103**, 246804 (2009).
[5] C. Riedl, C. Coletti, T. Iwasaki, and U. Starke, Mat. Sci. Forum **645-648**, 623 (2010).
[6] C. Coletti, C. Riedl, K.V. Emtsev, T. Iwasaki, A. Al-Temimy, S. Forti, A.A. Zakharov, and U. Starke, Max-lab activity report 2010.
[7] K.V. Emtsev, F. Speck, T. Seyller, L. Ley, and J.D. Riley, Phys. Rev. B **77**, 1553037 (2008).

Chemistry of glycine at the water – Pt{111} interface

A. Shavorskiy[1], T. Eralp[1], K. Schulte[2], J.N. Andersen[2] and G. Held[1]

[1] *Department of Chemistry, The University of Reading, Whiteknights, Reading, RG6 6AD, UK*

[2] *Dept. of Synchrotron Radiation Research, Institute of Physics, Lund University P.O. Box 118, S-221 00 Lund, Sweden*

Adsorption of the amino acid glycine on clean and water-covered Pt{111} was studied in ultra-high vacuum by means of X-ray Photoelectron Spectroscopy. On the clean platinum surface glycine adsorbs molecularly in the first layer giving rise a single peak in N1s at the binding energy of 399.6 eV (Figure 1 (a)) and two peaks with similar intensities in O1s region (not shown here), which is associated with the intact molecules in its neutral state. In the second and consecutive layers glycine adsorbs in its zwitterionic form, which has a characteristic N 1s peak at 401.1 eV (or higher for multilayers) and a single O1s peak (not shown). The observation of neutral glycine on clean Pt{111} disagrees with earlier XPS results, where the authors report the zwittrionic form already at mono- and submonolayer coverages [1], however this appears to be due to a disagreement in the coverage calibration. The photoelectron spectra shown in [1] are clearly those that we assign to glycine multilayers (see Figure 1) by comparing the peak intensities with those of known coverages of oxygen and CO.

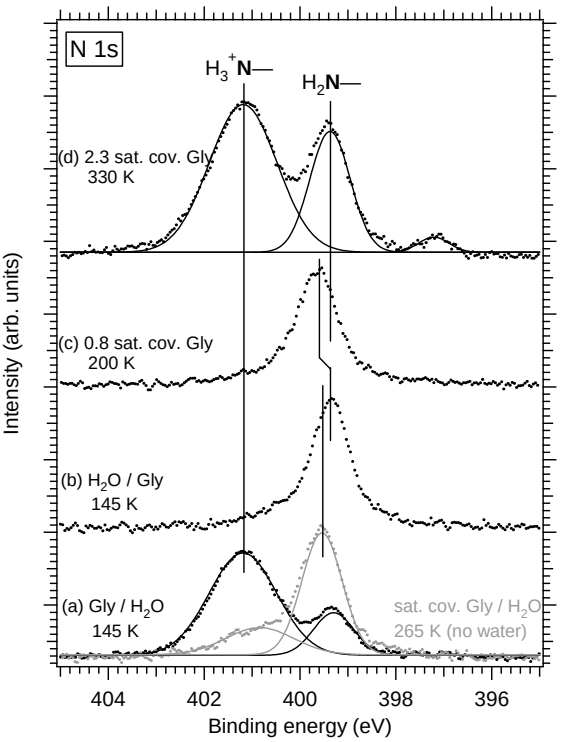

Figure 1. N 1s photoelectron spectra of (a) glycine adsorbed on water bilayer at 145 K (black) and 265 K (after complete water desorption, grey); (b) water adsorbed on glycine overlayer at 145 K; (c) glycine overlayer on clean Pt{111} in vacuum at 200K; (d) glycine multilayers annealed to 330 K. Photon energy 525 eV

Annealing multilayers to 330 K leads to the desorption of the third and consecutive layers and a bilayer of glycine molecules is obtained (Figure 1 (d)). At this temperature glycine molecules in the first layer appear to re-order on the surface, which leads to the shift in binding energy on N 1s peak (Figure 1 (a and b)). The second layer is more stable than the multilayers and desorbs at higher temperature competing with decomposition. The glycine overlayer decomposes completely above

370K. The increased stability of the second layer is in agreement with earlier TPD experiments on glycine adsorption on Pt{111} and Pd{111} surfaces [1,2].

Adsorption of *water on top of glycine overlayers* on Pt{111} does not lead to significant changes in the chemical state of the molecules. Only a small shift of binding energy in the N1s region is observed implying the formation of hydrogen bonds with water molecules (Figure 1 (b)).

The N1s spectrum of *glycine adsorbtion ontop of a water layer* on Pt{111} at 145 K is shown in Figure 1(a) (black data points). Clearly, the majority of glycine adsorbs in its zwitterionic form. This is in a good agreement with the observation of zwitterionic glycine in the second and following layers on clean Pt{111}. Figure 2 shows N1s temperature-programmed XPS as a plot of intensity against binding energy and sample temperature. The spectrum clearly shows continuous transition of zwitterionic form of glycine to the molecular. The glycine layer left on the surface after annealing to 265 K (Figure 1 (a) grey data points) is spectroscopically indistinguishable from the layer prepared by adsorption in vacuum (Figure 1 (c).

The experiments show that the presence of water (ice) in UHV at temperatures below 200K, does not change the chemical state of glycine on Pt{111}. On the other hand, our recent studies of glycine on Cu{110} [3] showed a dramatic change of the surface chemistry when water is present at room temperature at near-ambient pressure, which indicates that the higher temperature is required to overcome the activation barrier for reaction.

References:

[1] Lofgren, P.; Krozer, A.; Lausmaa, J.; Kasemo, B. *Surf. Sci*. 1997, 370, 277
[2] Gao, F.; Li, Z.; Wang, Y.; Burkholder, L.; Tysoe, W. T. *J. Phys. Chem. C* 2007, *111*, 9981.
[3] A. Shavorskiy, F. Aksoy , Z. Liu, H. Bluhm and G. Held, *in preparation*

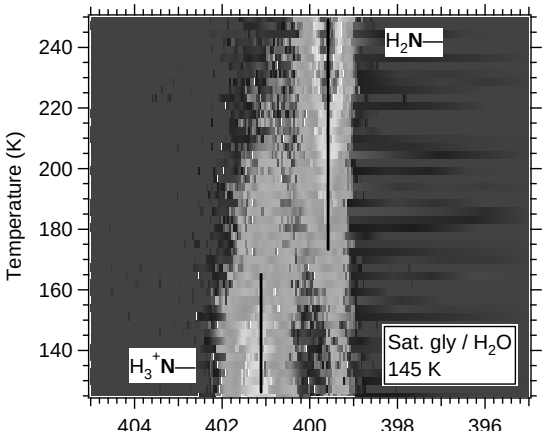

Figure 2. N 1s TP-XP spectrum as a plot of intensity against binding energy and sample temperature during annealing Gly / H_2O / Pt{111}. Temperature ramp 0.1 K/s. Photon energy 525 eV.

Adsoption of Ca on the $TiSe_2$ surface

Hans Starnberg

Department of Physics, University of Gothenburg, SE-412 96 Göteborg, Sweden

The layered transition metal dichalcogenides are of great interest due to their strongly anisotropic properties. Their properties can be altered by intercalation with e.g. alkali metals, which has been extensively studied by photoelectron spectroscopy. Intercalation is possible also with other metals, but few such systems have been significantly explored. Intercalation with polyvalent metals may result in new interesting phenomena. If some valence electrons remain on the metal atoms, they may form localized or delocalized states, depending on the density and ordering of intercalated atom. The aim of this study is to determine the behaviour of Ca atoms when deposited on the $TiSe_2$ surface, and whether intercalation is achieved at room temperature in this system.

Core level and valence band photoelectron spectra from the Ca/$TiSe_2$ system were measured on the I311 beamline. A clean and flat surface was obtained by cleaving a $TiSe_2$ single crystal. Ca was deposited onto the surface from a resistively heated evaporator. A quartz crystal resonator was used to monitor the deposition rate. A series of depositions were done and photoelectron spectra were recorded before, between and after the depositions. The sample was kept at room temperature.

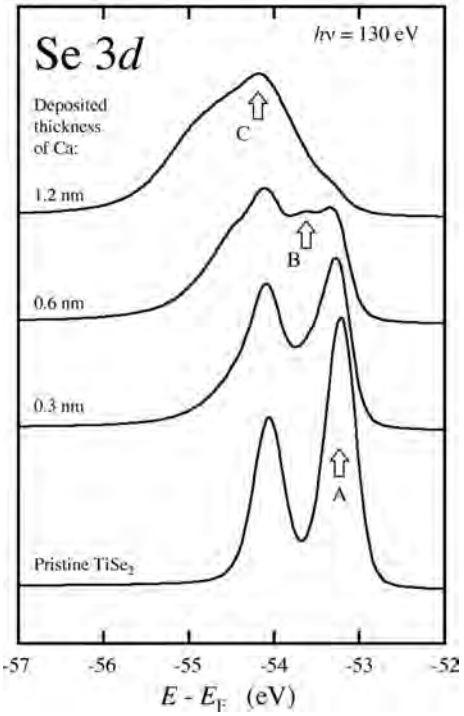

Fig 1: Normal emission Se 3d spectra from the Ca dosed $TiSe_2$ surface.

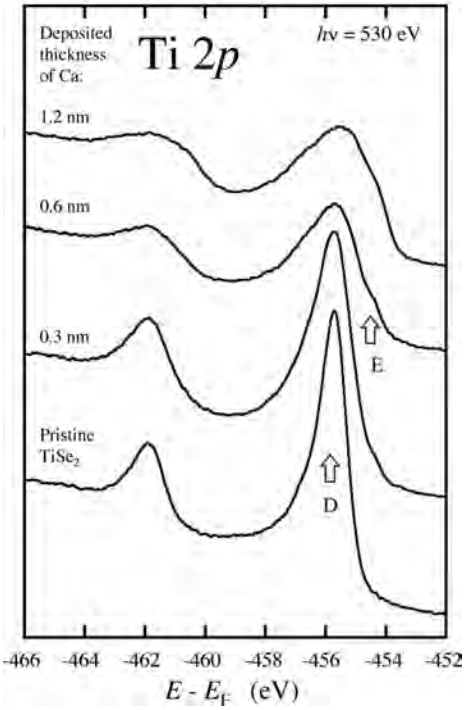

Fig 2: Normal emission Ti 2p spectra from the Ca dosed $TiSe_2$ surface.

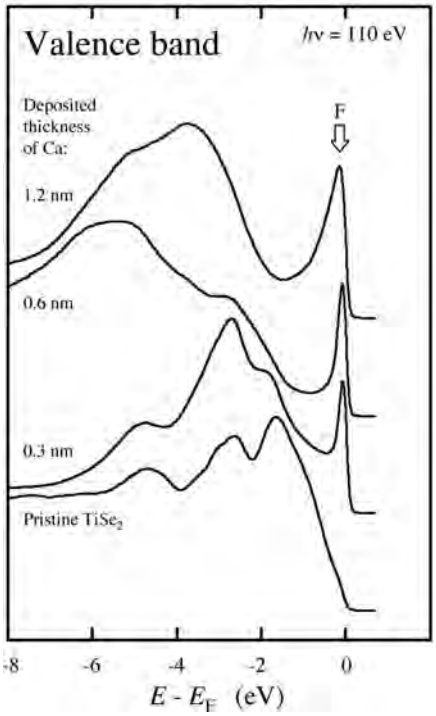

Fig 3: Normal emission valence band spectra from the Ca dosed $TiSe_2$ surface.

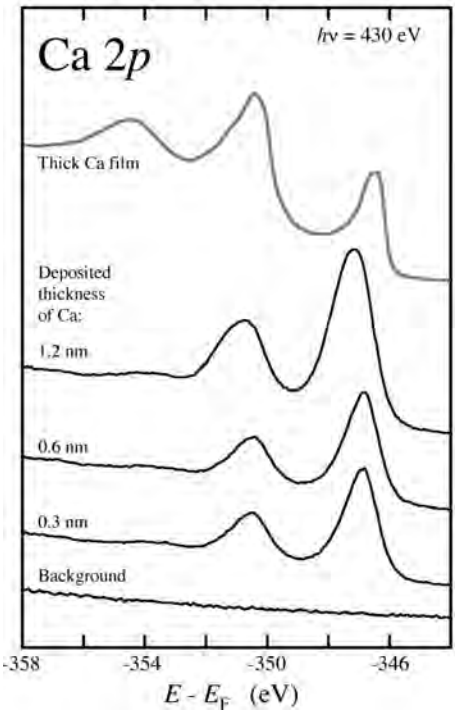

Fig 4: Normal emission Ca 2p spectra from the Ca dosed $TiSe_2$ surface. The uppermost spectrum was obtained from a thick Ca film deposited with the sample at liquid nitrogen temperature.

Figure 1 shows that the Ca deposition has a strong effect on the Se 3*d* emission. Three distinct components are clearly visible: Peak A is due to pristine $TiSe_2$ is , peak B appears during the early stage of the deposition, and peak C becomes dominant as the deposition continues. The two latter peaks are possibly due to formation of CaSe and Ca_xTiSe_2.

The effect of Ca deposition on the Ti 2*p* emission, as seen in figure 2, is less dramatic. The pristine peak D is broadened, but not markedly shifted. The shoulder E could possibly be due to formation of Ti metal.

The valence band spectra in figure 3 indicate that electrons are transferred from Ca to the Ti 3*d* band of the host layers (peak F), in analogy with alkali intercalation systems.

Figure 4 shows the Ca 2*p* spectra, and here the almost constant emission going from 0.3 to 0.6 nm coverage suggests that the Ca deposited at this stage is intercalated rather than building up at the surface.

In conclusion, this preliminary study suggests that Ca intercalation occurs in in the studied system, but there are also indications of a competing reaction that break up the host layers.

One-dimensional oxide-metal hybrid structures: site-specific enhanced reactivity for CO oxidation

[1]S. Surnev, [1]F. Allegretti, [1]G. Parteder, [2]T. Franz, [2]F. Mittendorfer, [3]J.N. Andersen, [1]F.P. Netzer
[1] Institute of Physics, Surface and Interface Physics, Karl-Franzens University Graz, A-8010 Graz, Austria
[2]Faculty of Physics, University of Vienna, A-1090 Vienna, Austria
[3] Department of Synchrotron Radiation, Institute of Physics, Lund University, S-22362 Lund, Sweden

We have employed quasi-one-dimensional (1-D) oxide-metal hybrid structures, which consist of nickel oxide nanowires attached to the step atoms of a vicinal Rh(553) surface. The decoration of the Rh steps with monoatomic rows of Ni adatoms followed by selective oxidation generates pseudomorphically strained 1-D stripes of NiO_2 stoichiometry [1,2]. Here we report that these NiO_2/Rh nanowires exhibit superior reactivity for the oxidation of CO, as compared to the bare stepped Rh(553) surface. This reaction has been probed by adsorbing CO onto the O covered surfaces at 90K followed by stepwise annealing to elevated temperatures to initiate the oxidation reaction. The reactant species at the surface have been followed experimentally by high-resolution core level X-ray photoelectron spectroscopy (HR-XPS) with the use of synchrotron radiation, and theoretically by *ab initio* density functional theory (DFT) calculations.

The oxidation of CO on the NiO_2–Rh(553) surface is illustrated in Fig. 1: the NiO_2–Rh(553) surface has been saturated with CO at 90 K and subsequently flashed to elevated temperatures. The C 1s spectrum of the CO saturated NiO_2–Rh(553) surface is similar to the one from the CO saturated O-Rh(553) surface, with two main components due to CO molecules adsorbed in on-top terrace (T-t) and high-coordinated hollow and/or bridge terrace (HC-t) sites. On heating, the C 1s spectra show that the HC-t component decreases first and vanishes at ~300K, whereas the T-t starts to decrease at T > 250 K and has disappeared at T 420 K (Fig. 1a,c). The O 1s spectra reveal a more complex behavior: there is a transfer of spectral weight from the NiO_2 component to a new O component, at somewhat higher BE, with increasing temperature (Fig. 1b). The latter is associated with reduced NiO_{2-x} nanostructures. This reduction of NiO_2 to NiO_{2-x} is unambiguously confirmed by the Ni $2p_{3/2}$ core level shift to lower BE of the corresponding XPS spectra. The BE shift of the Ni $2p_{3/2}$ core level line is included in Fig. 1(d): the shift of the Ni core level to lower BE indicating the reduction of the NiO_2 nanowires follows closely the trend of the decrease of the intensity of the NiO_2 component. The Ni $2p_{3/2}$ BE after completion of the oxidation cycle is close to the calculated DFT value for the NiO zig-zag structures. The O 1s spectra indicate that the NiO_2 reduction, and thus the CO oxidation reaction, sets in at T > 150 K, i.e. at much lower temperature than on the O-Rh(553) surface. Three stages can be distinguished in the evolution of the O 1s spectra with temperature. Stage I between 150 - 250 K, where the decrease of the intensity of the NiO_2 component correlates well with the intensity reduction of the CO HC-t peak, indicating that CO molecules in higher-coordinated (HC) sites react first with the oxygen atoms of the NiO_2 nanowires. The NiO_{2-x} component appears in the spectra as a result of this reduction/oxidation reaction. Competitively with the reaction, some desorption of CO_{HC-t} takes also place. In stage II, between 250-320 K, most of the CO_{HC-t} molecules have disappeared from the surface, the NiO_2 and NiO_{2-x} intensities remain approximately constant, but the CO_{T-t} component loses half of its initial intensity mainly due to thermal desorption. Above 320 K (stage III), the NiO_2 NiO_{2-x} reaction is accelerated and is completed after heating to 440 K.

The calculation of the reaction barriers confirms several reaction steps. The lowest energy path of the initial step is sketched in Fig. 2. Starting from CO in HC-t sites, the CO molecule reacts with O at the lower NiO_2 step edge. The highest energy barrier along this path (TS2) is 1.05 eV, which is significantly lower than the energy barrier of ~1.30 eV on the Rh terraces or on a flat Rh(111) surface. The second reaction step is the further reduction of NiO_{2-x} by the reaction of CO with O at the upper NiO_{2-x} step edge to yield the NiO zig-zag structures. This step is predicted to happen significantly

slower, as the TS of this reaction sequence involves O-$Rh_{upper\text{-}step}$ bond breaking with a barrier of 1.30 eV. Therefore the second reaction step is similar to the corresponding reaction at the Rh terraces. The experimentally observed low temperature onset of the CO oxidation reaction (stage I in Fig. 1) on the NiO_2-Rh(553) surface is in full accord with this reaction scenario. In addition, the oxidation occurring during stage III in Fig. 1 is then most naturally attributed to the reaction of CO with $O_{upper\text{-}step}$ of $NiO_{2\text{-}x}$ to yield the NiO zig-zag structures. Although the simulations predict again a low barrier of 1.1 eV for a further reduction of the NiO stripes, this was not observed in the present experiments, because the CO adsorbed at low temperature had already been removed from the surface by reaction steps 1 + 2 and by desorption.

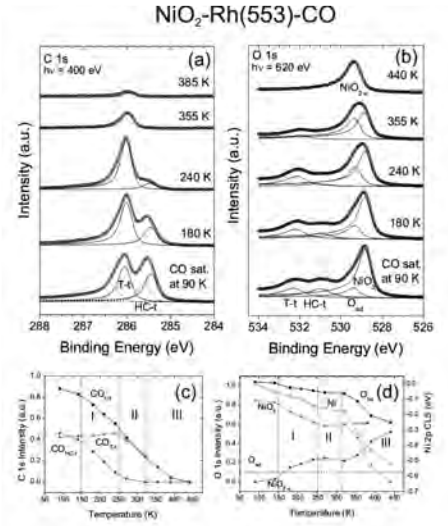

Fig.1: C 1s (a) and O 1s (b) core level spectra from the NiO_2 decorated Rh(553) surface exposed to CO saturation at 90 K and after heating to the indicated temperatures. Integrated C 1s (c) and O 1s (d) XPS intensities of the various spectral components as a function of temperature.

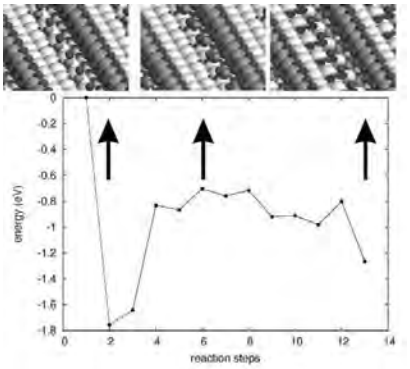

Fig.2: Energy diagram of the lowest energy reaction path of the initial step of the CO oxidation reaction on NiO_2 – Rh(553) (involving the reaction of CO with the low-step oxygen). The geometry models at the top from left to right correspond to the starting state of adsorbed CO in a HC site, the highest barrier transition state (TS 2), and the final desorbing CO_2 state, respectively, as indicated by the arrows (light grey: Pd; red: oxygen; dark yellow: Ni; blue: carbon).

In conclusion, we have shown that the 1-D Ni oxide-Rh hybrid system, formed by step decoration of a Rh(553) surface with pseudomorphic NiO_2 nanowires, exhibits a superior catalytic reactivity for the oxidation of CO as compared to the bare stepped Rh surface. The O atoms shared between Ni and Rh at the 1-D interface support more favourable transition state geometries with lower energy barriers than on the bare O covered Rh(553) surface. We have demonstrated with a simple model reaction that low-dimensional nanoscopic hybrid systems, i.e. electronically and elastically coupled oxide-metal nanostructures, can exhibit a higher catalytic reactivity than single phase systems.

Financial support was provided by the Austrian Science Funds (FWF) within projects Y218 and S90 "Nanoscience on Surfaces", and the ERC Advanced Grant SEPON. JNA acknowledges financial support by the Swedish Research Council. Support during experiments by MAX-Lab is gratefully acknowledged.

References:

[1] J. Schoiswohl et al., Surface Sci. 600 (2006) L274
[2] J. Schoiswohl et al., Phys. Rev. Lett. 97 (2006) 126102

Mn_3O_4(001) overlayers on Pd(100): structure and thermal reduction

[1]S. Surnev, [2]A.A. Zakharov, [1]F. Li, , [1]F. Allegretti, [3]P. Rahe, [3]A. Kühnle and [1]F.P. Netzer
[1]Institute of Physics, Surface and Interface Physics,
Karl-Franzens University Graz, A-8010 Graz, Austria
[2]MAX-lab, Lund University, S-22100 Lund, Sweden
[3]Institut für Physikalische Chemie
Johannes Gutenberg-Universität Mainz, D-55099 Mainz, Germany

Terminations of bulk Mn_3O_4 (hausmannite) crystal surfaces belong to the so-called polar surfaces, which are formally characterised by an uncompensated electrostatic potential giving rise to a non-zero dipole moment perpendicular to the surface [1]. The stabilisation mechanism of these surfaces is to a large extent unexplored, in particular when they are prepared in the form of ultrathin films with a thickness of only few atomic layers, the so-called oxide nanolayers. Here we investigate the structure nd thermal stability of Mn_3O_4(001) nanolayers (up to 20 ML thick) supported on a Pd(100) surface by a combination of LEEM, micro-LEED, PEEM and dynamic atomic force microscopy (AFM) measurements. Stoichiometric Mn_3O_4(001) structures have been prepared by heating MnO(001) films on Pd(100) in an oxygen pressure of $2x10^{-5}$ mbar at 450°C, as described previously [2].

LEEM images of the Mn_3O_4(001) films (Fig. 1a) display typically a fine-grained homogeneous surface, which does not show any contrast in PEEM. Micro-LEED images (Fig. 1b) exhibit a characteristic diffraction pattern, which could not be resolved in such a great detail in macroscopic LEED images, where only broad spots have been observed [2]. AFM Δf images (Fig. 1c) show that the surface consists of atomically flat terraces, displaying striped pattern, with the stripes separated by a distance of ~ 3nm and running along the two main substrate directions. Atomically-resolved images (inset of Fig. 1c) reveal that the distance (5.8 Å) along the stripes is consistent with the lattice parameter of the unreconstructed Mn_3O_4(001) surface. On the basis of the μ-LEED image real- and reciprocal-space models have been derived (Figs. 1d,e), which demonstrate that the extra diffraction spots can be realised as due to a uniaxial surface reconstruction with one of the unit cell vectors rotated by about 10° with respect to the unreconstructed lattice. This structure transformation generates a one-dimensional Moiré superstructure (Fig. 1f), which periodicity and topographic appearance are compatible with those of the experimentally observed stripe pattern in Fig. 1c, thus supporting the structure model.

LEEM and PEEM experiments (Fig. 2) have been performed during *in situ* annealing in UHV to identify thermal decomposition processes within the Mn_3O_4(001) film. After annealing to 500°C (Fig. 2a) small clusters nucleate on the initially homogeneous surface, which appear in bright contrast in both LEEM and PEEM (not shown) images, indicating that the clusters exhibit a lower work function that the pristine surface. The cluster density increases dramatically upon further annealing to 550°C (Fig. 2b), and eventually after 600°C (Fig. 2c) the surface becomes fully covered with this new phase. Micro-LEED images (Fig. 2d) of the latter display a completely different diffraction pattern, which is consistent with a MnO(100) surface.

Financial support was provided by the Austrian Science Funds (FWF) within project S90 "Nanoscience on Surfaces", the ERC Advanced Grant SEPON and the EU COST D41 programme. Support during experiments by MAX-Lab is gratefully acknowledged.

References:

[1] P.W. Tasker, J. Phys. C 12 (1979) 4977
[2] V. Bayer et al., Phys. Rev. B 76 (2007) 165248

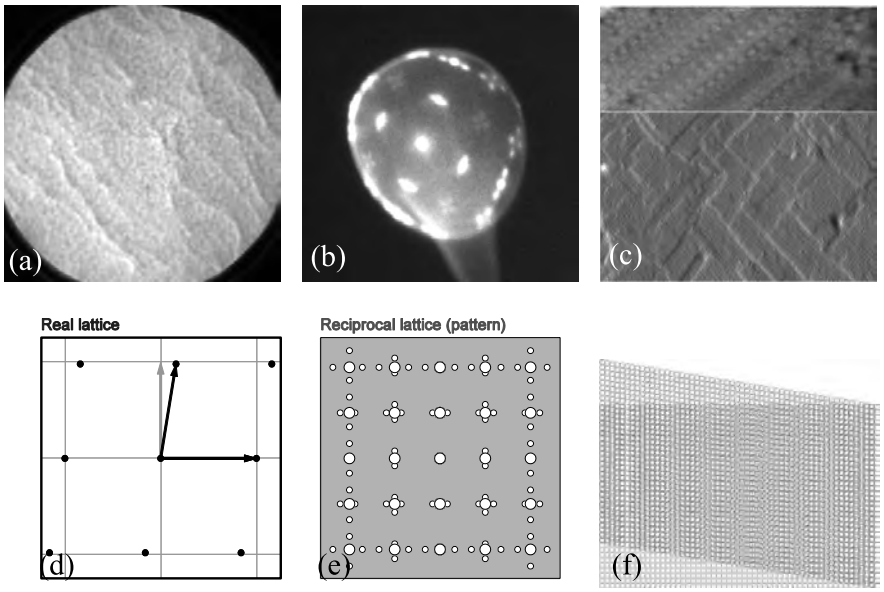

Fig.1: (a) Mirror LEEM image (filed of view 20 μm); (b) μ-LEED image (E=27.5 eV); and (c) AFM Δf image (250nmx250nm) of Mn_3O_4(001) nanolayers on Pd(100). The inset is an atomically resolved AFM Δf image (15nmx6nm); (d) and (e) represent real- and reciprocal lattice models of the unreconstructed (green lines) and reconstructed (dots) oxide surface unit cells; (f) schematic Moiré

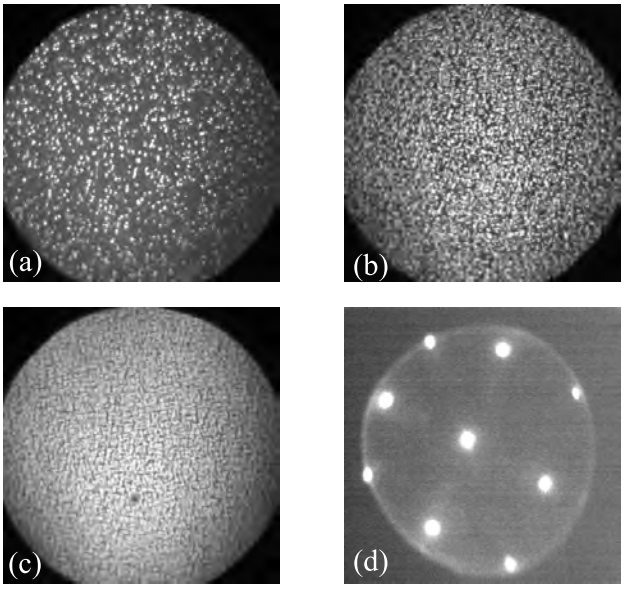

Fig.2: (a)-(c) LEEM images (filed of view 25 μm) obtained after annealing Mn_3O_4(001) films on Pd(100) in UHV to 500°C, 550°C and 600°C, respectively; (d) μ-LEED image (E=46 eV) of the surface annealed to 600°C .

Atomic layer deposited high-k oxides on InAs studied by XPS

R. Timm, M. Hjort, A. Fian, E. Lind, C. Thelander, L.-E. Wernersson, J. N. Andersen, and A. Mikkelsen

Department of Physics, Lund University

During the last years, metal-oxide-semiconductor (MOS) devices based on III-V semiconductors have been of increasing interest, with the possibility of even replacing Si/SiO_2 transistors [1]. Although most research has focused on GaAs or GaInAs [2], InAs is even more promising for high-speed electronic applications. However, for enabling device performance and in order to compete with Si technology, it is crucial to improve the quality of the semiconductor-oxide interface [3]. By using atomic layer deposition (ALD), it became possible to grow very thin films of high crystal quality. Nevertheless, the role of the native oxide on InAs, its reduction by the high-κ dielectric material, and the chemical composition of the resulting InAs-oxide interface still need to be further investigated [4].

For this study, about 2 nm thin films of HfO_2 and Al_2O_3, two of the most common high-κ dielectrics, were deposited on etched InAs substrates by ALD. The chemical composition of these passivation layers, of the oxide-semiconductor interface, and of the native oxide on reference InAs samples was investigated with core-level XPS. By thoroughly fitting the data from different samples, prepared under identical growth and etching conditions, and of different photon energies, bulk doublet peaks and different oxide components can be distinguished for In 3d [Fig. 1(a)], In 4d [Fig. 1(b)], and As 3d core-levels. From a comparison of the HfO_2- and Al_2O_3-containing samples with InAs reference samples, the ability of these thin high-κ dielectric films to reduce the native oxide and to passivate the underlying InAs substrate is confirmed [Fig. 2(a)]. It has to be noted that also the surface orientation of the underying InAs substrate is of significant influence for the formation of a passivation layer, as initial experiments comparing InAs(100), InAs(111)A, and InAs(111)B surfaces have shown.

Beside InAs bulk substrates, also InAs nanowires with and without ALD-deposited HfO_2 and Al_2O_3 films were studied, revealing a much stronger oxide component of the nanowires as compared with bulk InAs [Fig. 2(b)]. A sufficiently high nanowire density, leading to a reasonably strong XPS signal, is confirmed by Fig. 2(b). These spatially averaged XPS data of high energy resolution can additionally be compared with μ-XPS results obtained on single nanowires in the SPELEEM setup.

[1] R. M. Wallace, P. C. McIntyre, J. Kim, and Y. Nishi, MRS Bulletin **34,** 493 (2009).

[2] C. L. Hinkle, M. Milojevic, B. Brennan, A. M. Sonnet, F. S. Aguirre-Tostado, G. J. Hughes, E. M. Vogel, and R. M. Wallace, Appl. Phys. Lett. **94,** 162101 (2009).

[3] M. Houssa, E. Chagarov, and A. Kummel, MRS Bulletin **34,** 504 (2009).

[4] H. Hasegawa and M. Akazawa, Appl. Surf. Sci. **254,** 8005 (2008).

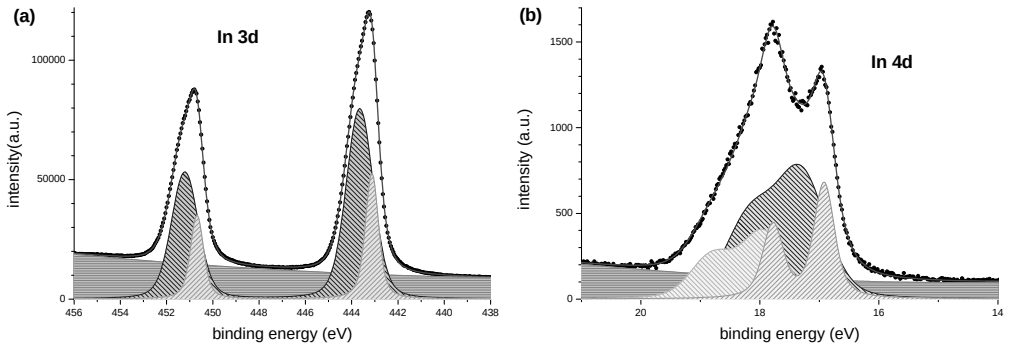

Figure 1: Fitted components of (a) In 3d and (b) In 4d core-level XPS spectra of an InAs substrate with native oxide. The kinetic energy of the photoemitted electrons is about 280 eV. Beside the doublets of the bulk In-As component, also doublets of (a) one and (b) two strong In-oxide components at higher binding energy are obtained.

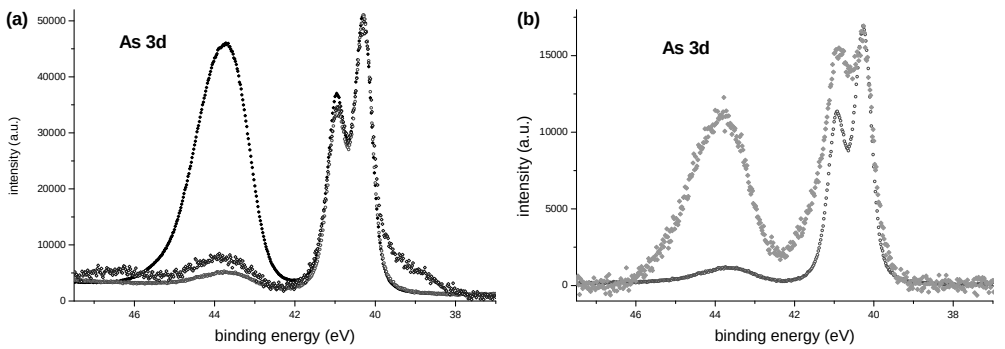

Figure 2: As 3d core-level XPS spectra of (a) InAs substrates with native oxide (black dots), with a HfO_2 layer (blue open diamonds), and with an Al_2O_3 layer (red open circles) and of (b) InAs with an Al_2O_3 layer for bulk substrate (red open circles) compared with InAs nanowires (green filled diamonds). The kinetic energy of the photoemitted electrons is about 280 eV. Beside the doublet of the As-In component at about 40 eV, a broad oxide component of significantly different size is obtained at higher binding energy around 44 eV. The shoulder at the low binding energy side of the As-In bulk peak for the sample with a HfO_2 layer is due to a Hf 5p ½ core-level.

Oxidation of $Pd_{0.57}Cu_{0.43}(100)$

L. E. Walle[a], I.-H. Svenum[a], T. H. Andersen[b], J. Gustafson[c], E. Lundgren[c], J. N. Andersen[c] and A. Borg[a]

[a] *Dept. of Physics, Norwegian University of Science and Technology (NTNU), NO-7491 Trondheim, Norway*
[b] *Sør-Trøndelag University College (HiST), Faculty of Technology, NO-7004 Trondheim, Norway*
[c] *Dept. of Synchrotron Radiation Research, Lund University, P. O. Box 118, SE-221 00 Lund, Sweden*

Palladium and palladium based alloys find important applications in catalytic membrane reactors due to their high hydrogen permeability and selectivity [1]. To prevent embrittlement occurring in pure Pd due to formation of hydride phases [2,3] Pd alloys are often chosen. A commonly used alloy for hydrogen extraction, separation and/or transport has been Pd/Ag. Alloying Pd with Ag in general increases the permeability and durability of the membrane. The hydrogen permeability at Pd/Ag alloys reaches a maximum at 23wt% Ag [4]. An alternative alloy element to Ag is Cu. Recently it has been found that Pd/Cu membranes consisting of 40wt% Cu have almost similar permeability to that of pure palladium [5]. Furthermore Pd/Cu membranes have high resistance to hydrogen sulfide and sulfurous constituents in gas mixtures [6]. Both in the case of Pd/Ag [7-9] and Pd/Cu [10] membranes, heat treatment in air has been reported to enhance the hydrogen permeation. However, a full understanding of the thermal treatment effects is still lacking.

In the present work, the surface composition and surface oxide formation on $Pd_{0.57}Cu_{0.43}(100)$ at low pressure conditions and the interaction of CO with this surface have been investigated using high resolution photoemission spectroscopy at beamline I311 as a step towards a better understanding of the Pd/Cu membrane system.

The $Pd_{0.57}Cu_{0.43}(100)$ crystal was cleaned by cycles of sputtering, oxygen treatment and annealing to temperatures in the range 600-800 K. By varying the annealing temperature and time it was possible to control the relative amount of Pd and Cu in the surface region, as shown in figure 1. For increased annealing temperatures, the low binding energy shoulder in the Pd 3d spectra, due to the Pd surface core level shift, became less pronounced, indicating a lower Pd contents at the surface. Also, the position of the bulk peak was shifted towards higher binding energy, indicating compositional changes in the outermost surface layers. In comparison, the Pd $3d_{5/2}$ bulk contribution has a binding energy of 335 eV for the pure Pd(100) surface [11].

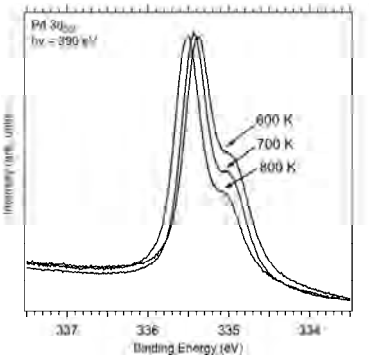

Figure 1: *Pd $3d_{5/2}$ spectra, normalised to the same peak intensity to ease the comparison, for preparations with different annealing temperatures for the $Pd_{0.57}Cu_{0.43}(100)$ surface.*

A surface oxide was formed by exposing the clean surface to ~1500 L O_2 ($p=5\cdot10^{-5}$ mbar) at 600 K, resulting in a new peak at 530.0 eV binding energy in the O 1s spectrum. Also, the component in the Pd 3d spectrum due to the surface core level shift, vanished. After oxidation LEED showed formation of a $(\sqrt{2}\times\sqrt{2})R45°$ structure, as shown in figure 2. Repeating the oxidation for surfaces with a different Pd/Cu surface composition gave exactly the same oxide. Previous experiments with oxides on Pd and PdAg surfaces [12] have shown the formation of a Pd surface oxide that can be reduced with CO, with a reduction rate that depends on temperature

and CO pressure. The rate has also been found to be much higher for the pure Pd-surface compared to the PdAg-alloy. In contrast, we found that the oxide on our PdCu alloy, both for Pd enriched and Cu enriched surfaces, showed very little reduction with CO. This, combined with the observed LEED pattern, indicate that a Cu-oxide is formed for all surface compositions investigated.

Figure 3 shows the C 1s spectra after adsorption of CO at different coverages and temperatures, for a surface prepared by annealing to 600 K. In each case we observed the same LEED pattern as for the oxide, a $(\sqrt{2}\times\sqrt{2})R45°$ structure (Fig. 2). This structure has previously been seen for CO adsorption on Cu(100), and on Cu/Pd alloy surfaces created by evaporating Pd on Cu(100) [13]. For low CO coverages and high adsorption temperatures, we see a clear component at ~286 eV in the C 1s spectra in figure 3. At lower adsorption temperatures and higher CO coverages, several new CO contributions emerge and the component at 286 eV turns into a low binding energy shoulder of the new structure at 286.3 eV. The peak at 286 eV can be attributed to CO bonded to Pd [11], while the larger structures at 286.3 eV, 287.2 eV and 293 eV are due to Cu-bonded CO (the latter two peaks are gigant shake-up satellites [14]). This assignment is also consistent with the lower relative intensity of the 286 eV peak seen for preparations with higher annealing temperatures and thus lower Pd content in the surface region (not shown).

This project has received support through the European Community - Research Infrastructure Action under the FP6 "Structuring the European Research Area" Program (through the Integrated Infrastructure Initiative "Integrating Activity on Synchrotron and Free Electron Laser Science"). The support of the MAX-lab staff is gratefully acknowledged.

References

[1] R. Hughes, Membr. Tech. **131**, 9 (2001).
[2] G. J. Grashoff, C. E. Pilkington and C. W. Corti, Plat. Met. Rev. **27**, 157 (1983).
[3] A. K. M. Kibria Fazle, T. Tanaka and Y. Sakamoto, Int. J. Hydrogen Energy **23**, 891 (1998).
[4] S. Uemiya, T. Matsuda and E. Kikuchi, J. Membr. Sci. **56**, 315 (1991).
[5] B. H. Howard et al., J. Membr. Sci. **241**, 207 (2004).
[6] H. T. Hoang et al., Materials Letters **58**, 525 (2004).
[7] A. L. Mejdell et al., J. Membr. Sci. **307**, 96 (2008).
[8] L. Yang et al., J. Membr. Sci. **252**, 145 (2005).
[9] L. Yang et al., AIChE Journal **52**, 2783 (2006).
[10] F. Roa and J. D. Way, Appl. Surf. Sci. **240**, 85 (2005).
[11] J. N. Andersen et al., Phys. Rev. Lett. **67**, 2822 (1991).
[12] K. Schulte et al., MAX-lab Annual report 2008, p. 154-155.
[13] Wadayama et. al, Surf. Sci. **601**, 2214 (2007).
[14] H. Tilborg, A. Nilsson and N. Mårtensson, J. Electron. Spectrosc. Relat. Phenom. **62**, 73 (1993).

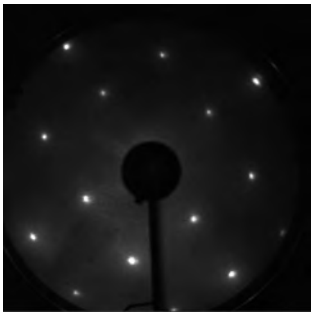

Figure 2: *LEED image of the $(\sqrt{2}\times\sqrt{2})R45°$ structure after oxidation and after CO adsorption, taken at 202 eV.*

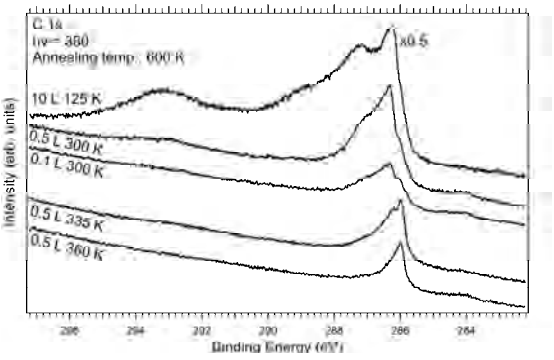

Figure 3: *C 1s spectra after adsorption of CO at different temperatures on the $Pd_{0.57}Cu_{0.43}(100)$ surface prepared by annealing to 600 K.*

Growth of ultrathin TiO_x films on Pt(110) studied by high resolution photoemission and X-ray absorption spectroscopy

L. E. Walle[1], I.-H. Svenum[1], A. Borg[1] and A. Sandell[2]

[1] *Dept. of Physics, Norwegian University of Science and Technology, NO-7491 Trondheim, Norway*
[2] *Dept. of Physics and Materials Science, Uppsala University, P. O. Box 530, SE-751 21 Uppsala, Sweden*

Nanostructured titania has recently gained considerable research interest because of the remarkable properties found for new and exotic phases like nanosheets, nanotubes, nanorods and nanoclusters [1,2]. Several of these new phases do not have a bulk counterpart and their properties are closely related to the surface structure and to interface effects. Titania nanosheets are thought to be the building blocks of titania nanotubes and nanorods calling for careful investigations of their physical and structural properties.

It was recently reported that a TiO_x double layer can be assembled on Pt(110) and Pt(111) surfaces with a geometric structure similar to that found for unsupported nanosheets [3,4]. Studying such ultrathin films on a single crystal metal support can hence serve both as a nanosheet model as well as a new material in its own right, which properties are determined by the combination of the oxide film properties and those of the support.

We have utilized synchrotron based photoemission (PES) and X-ray absorption spectroscopy (XAS) at beamline I311 to study the formation of an ultrathin TiO_x film on the Pt(110)-(1x2) surface complementing the detailed structural analysis performed by STM and LEED by Agnoli et al [5]. The film was deposited by evaporating titanium from a Ti wire filament in an oxygen atmosphere ($p = 1 \cdot 10^{-6}$ mbar), followed by a post annealing treatment in oxygen at 700 K.

Figure 1 shows Ti 2p XAS spectra for different TiO_x coverages. Included are also results for anatase TiO_2(001) and rutile TiO_2(110) single crystals. The Ti 2p XAS spectrum is sensitive to the local geometry of the Ti atoms and can be used to fingerprint different TiO_2 polymorphs [6]. A complete TiO_x bilayer is characterized by a 14x4 LEED pattern [5]. We were never able to observe the x4 periodicity. A maximum sharpness of the 14x pattern was observed after deposition 3, from which we concluded that this coverage is close to a full double layer.

Figure 1 shows that deposition 1-3 give rise to Ti 2p XAS spectra of very similar shape. The polymorph sensitive doublet structure at 460 eV suggests a structure different from both anatase and rutile. This is consistent with the proposed unique lepidocrocite structure model [5]. That this structure is adopted already at formation of islands is consistent with the previous STM study [5]. For coverages higher than a full bilayer, the peaks broaden and the LEED patterns become more diffuse and eventually disappear, due to the loss of order.

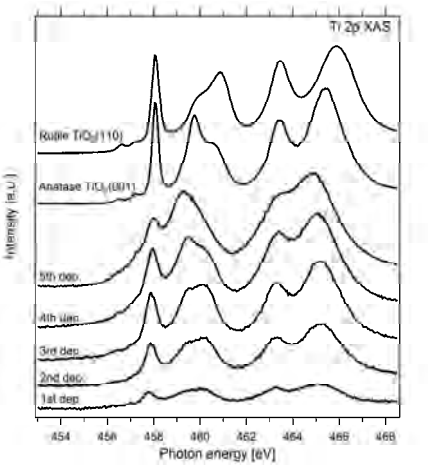

Figure 1. *Ti 2p X-ray absorption spectra for five increasing TiO_x coverages, as well as for anatase TiO_2(001) and rutile TiO_2(110) single crystals.*

The Ti $2p_{3/2}$ spectra for deposition 1 to 4 are shown in figure 2, indicating a rather complex behavior with increasing TiO_x coverage. The intensity maximum undergoes a positive binding energy shift of 0.28 eV between deposition 2 and 3, and a shift of 0.68 eV between deposition 3 and 4. Similar shifts are found for all TiO_x related PES structures in the O 1s and the valence band regions, suggesting a band bending effect. In the Ti $2p_{3/2}$ spectra, more than one state are present for all coverages. While the shift of the maximum is in accordance with a rigid band model, the low binding energy onset appears unchanged. We therefore expect to both have states that shift with coverage, in addition to at least one state that shifts very little. The low binding energy of this species suggests that it is associated with reduced Ti, that is, Ti of an oxidation state below +4. A

downshift in binding energy may also be the result of efficient final state screening from the Pt substrate. In either case, it is most likely that this component is related to direct Ti-Pt bonds.

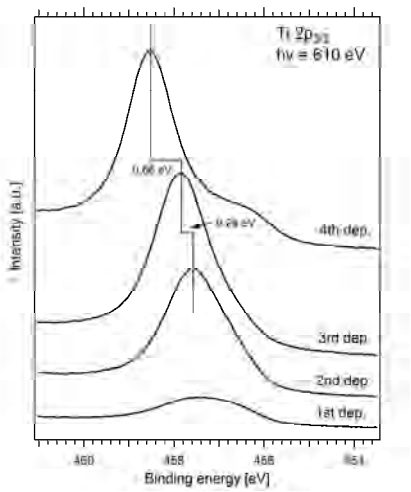

Figure 2. *Ti $2p_{3/2}$ spectra for deposition 1 to 4.*

In figure 3 valence band photoemission, after subtraction of the Pt contribution, and O 1s X-ray absorption spectra for different depositions, and for a clean anatase TiO_2(001) bulk sample, have been put on the same energy scale. In this way, the location of the valence and conduction band edges can be monitored [7,8]. Changes in the position of the leading peak in the O 1s XAS spectrum is expected to reflect changes in the location of the conduction band edge [7]. We see that the band alignment after the 4th deposition, which we believe has a coverage slightly higher than a full double layer, is very similar to that found for bulk anatase TiO_2(001). Also, the shift due to band bending when going from deposition 2 to 4, is clearly visible.

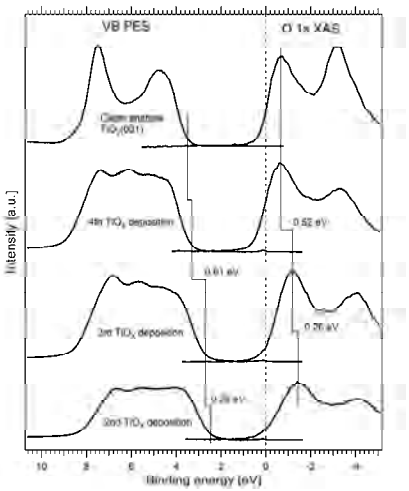

Figure 3. *Valence band photoemission and O 1s X-ray absorption spectra on the same energy scale compared to clean anatase TiO_2(001).*

In summary the results show that we have a positive binding energy shift for all TiO_x related PES structures for increased coverages, most likely due to a band bending effect. Also, when the coverage exceeds a full double layer, the LEED and XAS data indicate a structural change leading to loss of order.

References

[1] X. Chen and S. S. Mao, Chem. Rev. **107**, 2891 (2007).
[2] D. V. Bavykin, J. M. Friedrich, and F. C. Walsh, Adv. Mater. **18**, 2807 (2006).
[3] Y. Zhang, L. Giordano, G. Pacchioni, A. Vittadini, F. Sedona, P. Finetti, and G. Granozzi, Surf. Sci. **601**, 3488 (2007).
[4] T. Orzali, M. Casarin, G. Granozzi, M. Sambi, and A. Vittadini, Phys. Rev. Lett. **97**, 156101 (2006).
[5] S. Agnoli, T. Orzali, M. Sambi, A. Vittadini, M. Casarin, and G. Granozzi, J. Phys. Chem. C **112**, 20038 (2008).
[6] R. Ruus, A. Kikas, A. Saar, A. Ausmees, E. Nõmmiste, J. Aarik, A. Aidla, T. Uustare, and I. Martinson, Solid State Commun. **104**, 199 (1997).
[7] A. Sandell, P. G. Karlsson, J. H. Richter, J. Blomquist, P. Uvdal, and T. M. Grehk, Appl. Phys. Lett. **88**, 132905 (2006).
[8] A. Sandell, B. Sanyal, L. E. Walle, J. H. Richter, S. Plogmaker, P. G. Karlsson, A. Borg, and P. Uvdal, Phys. Rev. B **78**, 075113 (2008).

Studies of graphene growth on different SiC substrate orientation

C. Virojanadara, A. A. Zakharov[1], R. Yakimova
M. Syväjarvi, and L. I. Johansson
Department of Physics, Chemistry and Biology, Linköping University, S-58183, Linköping, Sweden
[1]Max Maxlab, Lund University, S-22100, Lund, Sweden

Graphene is one of the most advanced two-dimensional materials of today. It has superior transport properties and high potential for technological applications [1-4] However, for large scale integration of graphene based nanoelectronics a high quality graphene sheet on a suitable substrate is needed. Silicon carbide (SiC) is a good candidate for that since it is a robust wide band gap semiconductor and has a superior range of properties from inert to bio compatible and is excellent for high temperature and high power applications. For future applications involving patterning access to homogeneous large area graphene layers on SiC substrates is crucial. Very recently it was demonstrated [2-3] that large homogenous layers of graphene are possible to obtain by furnace growth at higher temperature and in an ambient gas.

Our graphene was grown on nominally on-axis 6H-SiC(0 0 0 1) substrates with a mis-orientation error within 0.03° and 0.25°[4]. The wafers were production grade *n*-type from SiCrystal with chemical and mechanical polishing on the Si face. The graphene growth was performed in an inductively heated furnace on both substrates at the same time, i.e. under as identical conditions as possible. The growth was carried out under highly isothermal conditions at a temperature of 2000 °C and at an ambient argon pressure of 1 atm [2]. The samples were then characterized [2,4] utilizing the end stations at beam line I311.

The LEEM image in Fig.1a) shows that a very large, homogeneous, and flat single layer of graphene was obtained on the 0.03°-SiC substrate. On the 0.25°-SiC substrate additional straight lines/steps are observed, as displayed in Fig. 1b). The graphene layer thickness was determined by measuring the electron reflectivity as a function of the electron kinetic energy. The reflectivity curve showed only one local minimum, dip, over essentially the whole surface area from both samples which, in line with earlier observations [2], reflects formation of monolayer (1 ML) graphene. It is worth mentioning that no mixture of 2 or 3 ML of graphene could be detected at, or close to, the step edges, which is opposite to recent findings by Emtsev et al. [3].

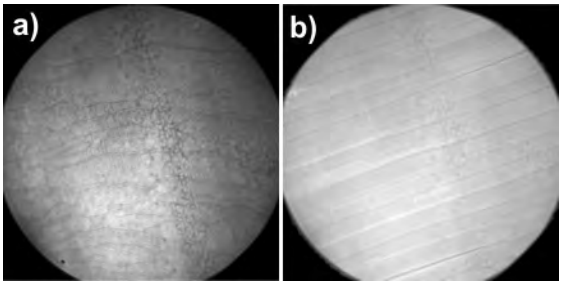

Fig. 1. LEEM images taken from monolayer graphene grown on a) 0.03°-SiC, the field of view (FOV) is 25 μm and the electron energy E_{vac} + 4.5 eV, b) 0.25°-SiC, the FOV is 25 μm and E_{vac} + 2.1 eV

Different domains of 1 ML graphene appear, however, in the LEEM images and are marked as areas A–C in Fig. 2a). The μ-LEED patterns from these areas, in Fig. 2b), show 3-fold rotation symmetry and that image A is rotated 120° relative to B and C. This symmetry and difference in μ-LEED patterns we suggest to originate from the underlying $6\sqrt{3}$ buffer layer and its interaction with the graphene layer.

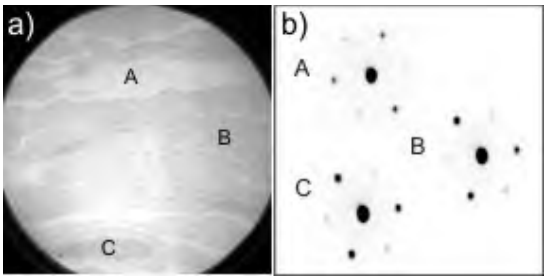

Fig. 2. a) 0.03°-SiC, the FOV is 25 μm and E_{vac} + 2.1 eV. b) Micro-LEED images collected at E = 16 eV from the three labeled areas in a) [4].

In summary, we have successfully prepared large sheets of monolayer graphene on two different 6H-SiC(0 0 0 1) substrates. We demonstrate an effect of the substrate orientation on the graphene morphology. Significant differences are observed on SiC substrates with different wafer mis-orientations from nominally on-axis. A larger and flatter monolayer graphene sheet is obtained on the substrates with a mis-orientation within 0.03°, and different fractions of domains are detected. On the substrate with a mis-orientation within 0.25° mainly one domain of monolayer graphene but narrower terraces and higher steps, i.e. more pronounced step bunching, are revealed. These findings are of fundamental interest but can also open up possibilities and opportunities for graphene–SiC based electronic devices.

References

[1]. A. K. Geim., Science 324, 1530 (2009) and ref there in.
[2]. C. Virojanadara, M. Syväjarvi, R. Yakimova, L. I. Johansson, A. A. Zakharov and T. Balasubramanian, Phys. Rev. B 78, 245403 (2008).
[3]. K. V. Emtsev, A. Bostwick, K. Horn, J. Jobst, G. L. Kellog, L. Ley, J. L. McChesney, T. Ohta, *et al* Nature Mater. 8 203 (2009).
[4]. C. Virojanadara, R. Yakimova, J. R. Osiecki, M. Syväjärvi, R. I. G. Uhrberg, and L. I. Johansson A. A. Zakharov, Surf. Sci. Lett. L87-L90 (2009)

Electronic Structure of PTCDA on Sn/Si(111)-2√3×2√3

H.M. Zhang, L.K.E. Ericsson, and L.S.O. Johansson

Department of Physics, Karlstad University, SE-651 88 Karlstad, Sweden

Interface interactions between organic molecules and semiconductor substrates are especially important since they affect the electronic structure and modify the growth mode of molecular films. The planar perylene derivative 3,4,9,10-tetracarboxylic dianhydride (PTCDA) has been widely used as a model compound for organic thin films since it has promising electronic and optical properties for organic electronic applications. In this context, a detailed understanding of the interface interactions between PTCDA molecules and semiconductor surfaces may therefore be used to optimize organic-inorganic devices.

A series of coverages (0.3-10 monolayer (ML)) of PTCDA were deposited on the Sn/Si(111)-2√3×2√3 surface at room temperature. As shown by O 1s core-level spectra (Fig. 1), at low coverage there are two major peaks located at binding energies of 530.3 and 532.6 eV. With increasing PTCDA coverage, the largest O 1s peak at 530.3 eV becomes sharp and shifts slightly towards a higher binding energy (located at 530.6 eV at 10 ML). The second largest peak roughly stays at a constant binding energy at different coverages. According to the previous studies [1,2], these two O 1s components should be O atoms in the carboxylic and anhydride groups. At 10 ML, the O 1s spectrum shows a line shape similar with the ones from PTCDA thick films on the H-terminated Si(111) and Ag/Si(111)-√3×√3 surfaces [1,2]. But also at low coverages (0.3-1.0 ML) the O 1s spectra are similar to the bulk one, which is very different from other cases. This is a clear evidence of a non-chemical interaction between PTCDA O atoms and the Sn/Si(111)-2√3×2√3 substrate.

Figure 2 shows high-resolution C 1s core-level spectra recorded from the same surfaces. At 10 ML the C 1s spectrum looks like a bulk one in a similar way as the O 1s spectrum. There is a strong peak at 284 eV, which originates from the perylene core of the PTCDA molecule. The second peak is located at 288.1 eV, which has previously been assigned to the carboxylic C. The other two small features at 286 eV and 289 eV in the 10 ML spectrum are mainly due to shake-up effects. Interestingly, the C 1s spectra at low coverages also look very different from the ones in the other systems. At 0.3 ML there is an extra peak located at a binding energy of 286.8 eV. The extra peak is well-defined and becomes saturated around 1 ML coverage. Judged from its line-shape and intensity, this peak seems to originate from the carboxylic C. This fits well with the fact that the carboxylic C 1s peak at 288.1 eV behaves in an opposite way as the extra peak, i.e. it grows with higher coverages. Thus PTCDA molecules strongly interact with the substrate through the carboxylic C, resulting a splitting of its C 1s peak. As clearly evidenced by the raw spectra, the O 1s and C 1s core-level spectra show a complicated, though basically physical, interaction between PTCDA molecules and the Sn/Si(111)-2√3×2√3 surface. Under such interaction strengths, one could expect that PTCDA molecules might grow into a layer-by-layer structure. Indeed, NEXAFS measurements from the normal and 70° incidence angle show clear spectral differences between the two geometries, which clearly points to a highly-ordered growth model.

References

[1] J.B. Gustafsson, E. Moons, S.M. Widstrand, L.S.O. Johansson, Surf. Sci. **572**, 23 (2004).
[2] J. B. Gustafsson, H. M. Zhang, E. Moons, and L. S. O. Johansson, Phys. Rev. B 75, 155413 (2007).

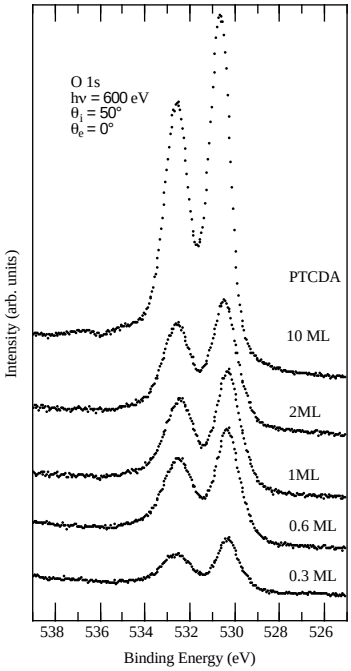

Fig. 1 O 1s core-level spectra for different PTCDA coverages on the Sn/Si(111)-2√3×2√3 surface.

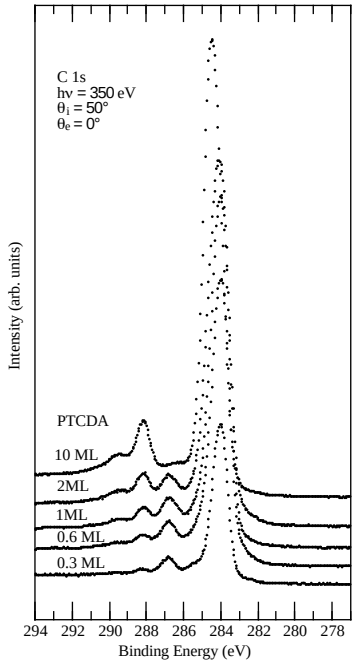

Fig. 2 C 1s core-level spectra for different PTCDA coverages on the Sn/Si(111)-2√3×2√3 surface.

Direct experimental determination of atom — molecule — solid binding energy shifts for Sb and Bi

S. Aksela, M. Patanen, S. Urpelainen, H. Aksela
Department of Physics, University of Oulu, P.O. Box 3000, FIN-90014 University of Oulu, Finland

Binding energy shifts Bi—Bi_2—Bi(solid) and Sb—Sb_2 — Sb_4 — Sb(solid) have been measured for the first time directly for Bi *4f* and Sb *4d* core levels applying synchrotron radiation exited photoelectron spectroscopy. Atomic, molecular, and solid state spectra are obtained by varying the temperature of evaporated metal vapors by means of a special multichamber oven and letting the vapor to condensate on a cool solid tip. Vapor and solid state spectra are created simultaneously in similar experimental conditions making direct and accurate shift determinations possible.

Binding energy (BE) shifts of atomic core levels between free atoms, molecules and their solid samples are very fundamental knowledge for different branches of electron spectroscopy and the theory of the electronic structures of the molecules, clusters, and solids. Besides their theoretical importance, the accurate atom—solid binding energies and their shifts are also very useful reference values in the experimental studies of clusters [1, 2]. The atom—solid BE shifts are, however, not very accurately known experimentally. The main reason is that for free atoms and molecules these values are measured using gaseous calibration lines and vacuum level as the reference energy level whereas the solid state values are measured with respect to the Fermi level. In order to bring the values to the common energy scale solid state values should be corrected by the appropriate work function of the sample. The work function is rather difficult to measure accurately, and it is very desirable to obtain shift values directly from one single experiment. In the course of our metal vapor studies we have developed a simple method in order to simultaneously observe both vapor and solid state spectra in identical experimental conditions. The idea is to locate a relatively cold needle like surface into the vapor beam and to simultaneously observe the spectra both from the vapor around the tip and from the condensed solid layer. The surface of the solid sample is covered by the negative work function potential and the vapor atoms are in this potential in the vicinity of the surface. Therefore the spectra have the same reference energy level and no work function correction is needed. In this study, we have measured the *4f* photolines of Bi and the *4d* photolines of Sb using this method. These samples are especially interesting because they are known to evaporate as molecular species which can be fragmented further pyrolytically with a special multichamber oven system (Fig. 1). This provides a very interesting possibility to experimentally determine the consecutive atom—molecule—solid shifts.

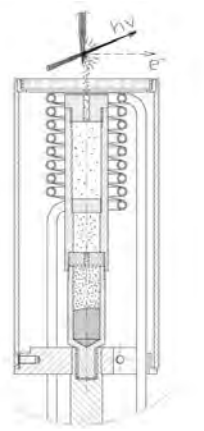

Fig. 1 Schematic picture of the vapour-solid measurement set up

Synchrotron radiation from undulator beamline I411 [3] at MAXII storage ring was used to ionize the vapor phase samples. Effusive vapor beam from the inductively heated oven and the synchrotron radiation light crossed at right angles and electrons were detected at the 54.7° angle with respect to the polarization vector of the horizontally polarized synchrotron radiation. A modified Scienta SES-100 electron energy analyzer [4] was used to record the emitted electrons. The electron spectrometer is equipped with a resistive anode position sensitive detection system making possible the gating of the detection of electrons during short inductive heating intervals. The energy of the ionizing radiation was 90 and 220 eV in the measurements of Sb and Bi, respectively.

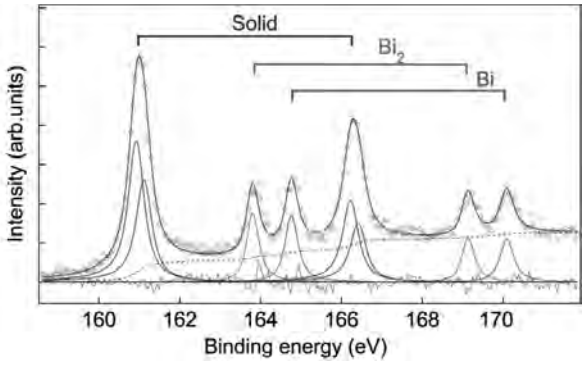

Fig. 2 Bi *4f* lines from atomic, molecular, and solid sample measured simultaneously with 220 eV photons.

Fig. 2 shows the *4f* spectrum taken at 220 eV photons simultaneously from vapor and solid Bi sample. Three doublets of spin—orbit split $4f_{7/2}$ and $4f_{5/2}$ components from Bi, Bi_2 and solid Bi are well resolved. Binding energies decrease when going from the atom to molecule and further to the solid as expected. For atom—diatom shift we obtain a value of 0.96 eV and for atom—solid(bulk) shift 3.65 eV.

Fig. 3 shows how the binding energy of the $4d^{-1}$ states evolves when going from the solid to atomic Sb. The *4d* PES of antimony vapour taken at increasing temperatures of upper part of the oven in Fig. 3 b) - e) emphasizes how the composition of the vapor can be varied smoothly. In the lowest temperatures the spectrum consists purely of Sb_4, but increasing temperature enhances the pyrolytic fragmentation, increasing signal from Sb_2, and finally almost atomic spectrum is observed. In the spectrum in Fig. 3 a) there might also be a small Sb_3 contribution (<10%), which has been reported in previous studies. One may notice a dramatic change in the fine structure of atomic spectrum compared with the molecular spectra. The atomic open shell structure is clearly observable splitting the *4d* lines into their fine structure components. This makes the determination of the atom to molecule shifts complicated. The atomic $4d^{-1}$ PES will be reported in detail elsewhere [5]. From the energies of the multiplets we obtained the average energy of the $4d^{-1}$ configuration (E_{av}) of atomic Sb to be 40.88 eV by weighting all the binding energies of the multiplets with their fitted intensity. This value is the combined binding energy of all the $4d_{5/2}$ and $4d_{3/2}$ multiplets, and allows us to determine the binding energy shifts more accurately if a corresponding average energy is also used for the spin-orbit split components of the molecular/solid state spectra. The BE shifts between E_{av} of atomic Sb and Sb_2, Sb_3, and Sb_4 are 1.30, 1.56, 1.87, and 3.97 eV, respectively.

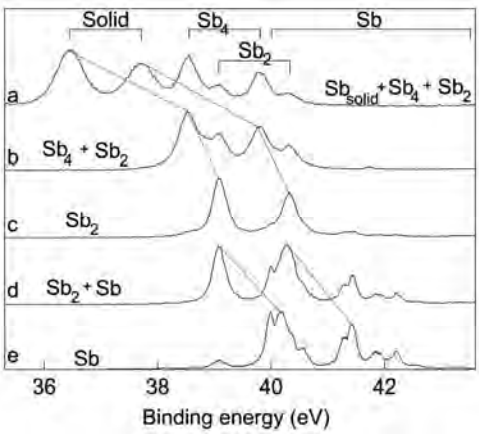

Fig. 3 Sb *4d* spectra taken at the increasing temperatures and different vapor compositions with 90 eV photons. a) Simultaneously measured vapor and solid spectrum. Vapor consist mainly of Sb_4 and minor fraction of Sb_2. b) Vapor spectrum consisting mainly of Sb_4 and Sb_2 components c) Almost pure Sb_2 vapor spectrum d) Vapor consists mainly of Sb and Sb_2 e) Almost pure atomic Sb spectrum. Dashed lines connect the positions of the main peaks.

[1] Tchaplyguine M *et al.* 2008 *J. Electron Spectrosc. Relat. Phenom.* **166-167** 38
[2] Björneholm O, Öhrwall G and Tchaplyguine M 2009 *Nucl. Instrum. Methods in Phys. A* **601** 161
[3] Bässler M et al. 2001 *Nucl. Instrum. Methods in Phys. A* **469** 382
[4] Huttula M, Heinäsmäki S, Aksela H, Kukk E, Aksela S 2007 *J. Electron Spectrosc. Relat. Phenom*. **156-158** 270
[5] Patanen M, Heinäsmäki S, Urpelainen S, Aksela S and Aksela H, $4d^{-1}$ *Photoelectron and subsequent $N_{4,5}OO$ Auger electron spectrum of atomic Sb*, manuscript

Photoelectron spectroscopy studies of free CdS clusters

T. Andersson[1], C. Zhang[1], S. Legendre [1, 2], M. Tchaplyguine[2],
G. Öhrwall[2], O. Björneholm[1], S. Svensson[1, 2], N. Mårtensson[1, 2]

[1]*Dept of Physics, Uppsala University, Box 530, Uppsala, Sweden*
[2]*MAX-lab, Lund University, Box 118, Lund, Sweden*

We have investigated the electronic structure of free CdS clusters by means of photoelectron spectroscopy. Using a gas aggregation source, which has been described in ref. 1, a beam of clusters was produced. In a modification of this source, first, a solid CdS sample was vaporized by magnetron-based sputtering in a way described in detail in ref. 2. Due to the semiconductor nature of the sample however, the DC-power sputtering has been replaced by an RF-fed process. The vapour atoms were then cooled using a liquid nitrogen-filled cryostat and condensed into clusters. The clusters in the beam coming out from the cryostat were ionized by synchrotron radiation crossing perpendicularly the cluster beam (in the same horizontal plane), and the emitted electrons were detected using the Scienta R4000 electron energy analyzer of the beamline, which in turn is placed perpendicularly to both the cluster beam and to the synchrotron radiation.

We probed the valence band and the shallowest core levels of both elements. In figure 1, the valence band and the Cd 4d level are shown, while the S 2p level is shown in figure 2.

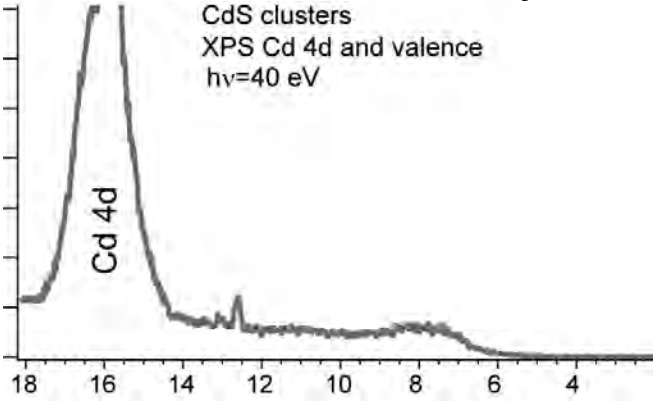

Figure 1. Photoelectron spectrum of the valence band and Cd 4d core level of free CdS clusters. The Cd 4d and Ar 3p features overlap. The intensity scale has been cut so that the top part of the Ar 3p feature is missing.

If one compares the spectrum in figure 1 with a photoelectron spectrum of pure Cd in the same energy region one can see that the 4d feature shows up at about the same position relative to the vacuum level, while the onset of the valence band in figure 1 is found at approximately 2 eV higher binding energy (the Cd work function is ~4.1 eV[3]). The shift of the onset is thus not due a shift of the whole spectrum. Also, it is probably not a size-determined shift as our source usually produces clusters of sizes causing shifts of the order of a few hundreds of meVs or less.

Compared to the photoelectron spectrum of solid CdS, if we align it so that the 4d features coincide, the valence band onset is found at quite similar energies[4]. The general

similarity between the present cluster spectrum and the solid state spectrum suggests that we are producing CdS binary clusters, with an electronic structure closely resembling the bulk semiconductor case.

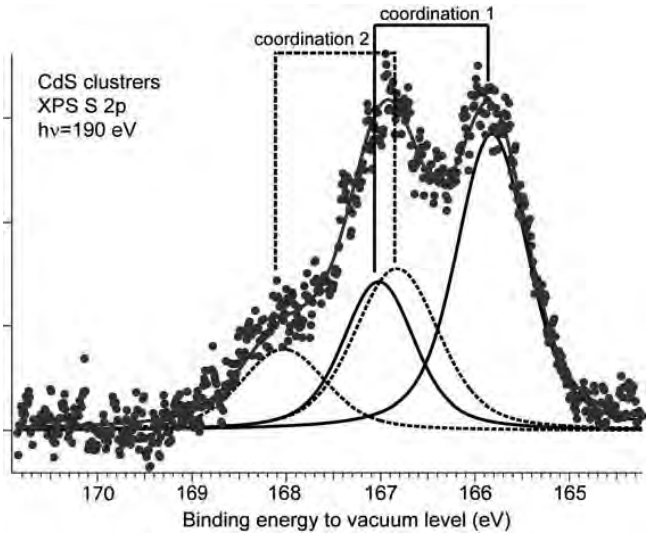

Figure 2. Photoelectron spectrum of S 2p core level of free CdS clusters. Straight background subtracted. Two doublets, denoted coordinations 1 and 2 are due to different chemical environments.

The solid state S 2p photoelectron spectrum is known to consist of features from the two spin-orbit split states, 1/2 and 3/2, each with separate bulk and surface peaks[5]. Under the assumption that the structure is similar in our cluster spectrum, the fitting presented in figure 2 is obtained. The bulk-surface shift is however much larger in our case, 1.1 eV compared to 0.4 eV for the macroscopic CdS[5]. It is thus not possible to directly explain our measured spectrum just from the analogy to the solid state spectrum.

References

1. M. Tchaplyguine, S. Peredkov, A. Rosso, J. Schulz, G. Öhrwall, M. Lundwall, T. Rander, A. Lindblad, H. Bergersen, W. Pokapanich, S. Svensson, S. L. Sorensen, N. Mårtensson, O. Björneholm, Eur. Phys. J. D **45**, 295-9 (2007)

2. M. Tchaplyguine, S. Peredkov, H. Svensson, J. Schulz, G. Öhrwall, M. Lundwall, T. Rander, A. Lindblad, H. Bergersen, S. Svensson, M. Gisselbrecht, S. L. Sorensen, L. Gridneva, N. Mårtensson, O. Björneholm, Rev. Sci. Instr. **77**, 033106 (2006)

3. http://www.hbcpnetbase.com/http://www.hbcpnetbase.com/ 25/3 2010

4. L. Ley, R. A. Pollak, F. R. McFeely, S. P. Kowalczyk, D. A. Shirley, Phys. Rev. B **9**, 600-21 (1974)

5. S. Wiklund, K. O. Magnusson, S. A. Flodström, Surf. Sci. **238**, 187-91 (1990)

Fragmentation dynamics of molecular clusters

M. Gisselbrecht[1], J. Laksman[1], E. Månsson[1], M Tchaplyguine[2], A. Sankari[1], O. Björneholm[3], S. Sorensen[1]

[1] *Dept. of Synchrotron Radiation Research, Institute of Physics, Lund University P.O. Box 118, S-221 00 Lund, Sweden*
[2] *MAXlab, Lund University, P.O. Box 118, S-221 00 Lund, Sweden*
[3] *Department of Physics, Uppsala University, P.O. Box 534, S-75121 Uppsala, Sweden*

While some clusters (like rare-gas clusters) are purely artificial creations, free molecular clusters exist in nature, especially in the atmosphere where, for example, water clusters are intermediates in cloud formation and contribute significantly to IR absorption [1]. By combining constituent molecules in a cluster, one can produce a material with novel functional and structural properties.

"Coulomb explosion" of multiply charged clusters enables studying the various channels of energy dissipation in matter and reveal new properties. Indeed, our results on atomic clusters demonstrate that nuclear motion acts actively to reach thermal equilibrium. Such mechanism in molecular clusters would activate vibrational modes resulting in new fragmentation pathways. Most molecular clusters are formed by stable molecules, which can have open or closed electronic shells. The intermolecular forces frequently encountered in the bonding of molecular clusters are: the dispersion interaction, the dipole-dipole interaction and hydrogen interaction [2-4]. We examined how the nature and the strength of these intermolecular forces affect the fragmentation using momentum-imaging technique to measure the mass and the kinetic energy of all fragments,

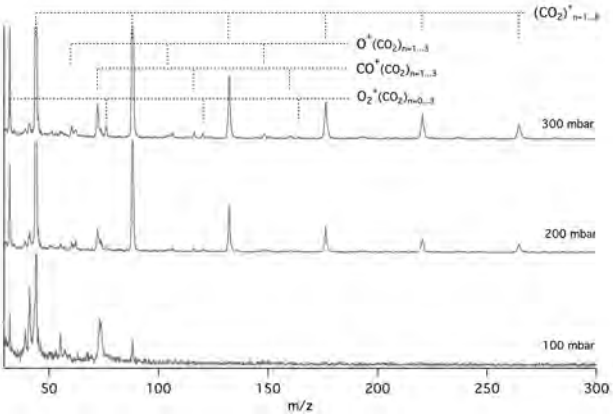

Figure 1: Mass spectra of $(CO_2)_n$ clusters as a function of the stagnation pressure of the supersonic expansion. The size of the cluster increases with the pressure accordingly.

We illustrate how $(CO_2)_n$ polar bound clusters fragment after photo-ionisation at 320 eV (above the C1s-edge). The clusters are produced after supersonic expansion CO_2 molecules through a nozzle. Increasing the stagnation pressure from 100 to 300 mbar increases the size of the clusters from a few molecules to a few tens of molecules. The smallest clusters produce fragments similar to what is expected for molecules, and the dimer signal is visible. For larger clusters the mass spectra show that several fragments of the molecular constituent are produced (O^+, CO^+ and O_2^+) in addition to the series of $(CO_2)_n$ cluster ions, and the series of cluster ions augmented by a single O_2 radical. Interestingly the intensity of molecular oxygen ion produced via photoionization increases with cluster size. This indicates that fragmentation of $(CO_2)_n$ clusters enhances the isomerization dissociation channel in clusters. Note that this channel has a very low probability for free molecules at this photon energy. The reason for this may lie in the excitation of the bending modes during the break-up.

References

[1] P. Chylek *et al.* Geophys. Res. Lett. **24**: 2015 (1997) and reference therein
[2] T. Rander ,Thesis, Fysik 5, Uppsala University 2007-2008
[3] A. Lindblad,Thesis from Uppsala University 2007-2008
[4] A. Rosso, Thesis, from Uppsala University 2007-2008

Anne Borg, Lars Johansson, Jens Birch, and Ulf Karlsson at the MAX-lab Annual User Meeting, November, 2009.
Photo: Martin Magnusson

Dan Cajander and Pierre Frediksson from the Ångström Workshop, Uppsala University, doing the final assembly of the new surface magnetism end- station for beamline I1011, December, 2009.
Photo: Annika Nyberg

Radiation damage and charge migration in atomic van der Waals clusters

M. Gisselbrecht[1], E. Månsson[1], J. Laksman[1], G. Örhwall[2], M Tchaplyguine[2], A. Sankari[1], S. Sorensen[1]

[1] *Dept. of Synchrotron Radiation Research, Institute of Physics, Lund University P.O. Box 118, S-221 00 Lund, Sweden*
[2] *MAXlab, Lund University, P.O. Box 118, S-221 00 Lund, Sweden*

The need to understand soft X-ray induced radiation damage to nanoscale objects is both a challenge and a necessity in order to design advanced materials. A localized photoexcitation will dissipate in different ways depending upon the size and geometry of the object. This in turn has an influence on the collective motion of electrons or nuclei.

Atomic van der Waals clusters are the simplest prototype of matter for the investigation of radiation damage. They provide a benchmark to understand the underlying damage mechanisms induced by soft X-rays in the weak interaction regime. Indeed such systems are by essence weakly bound and allow knowing how the initial energy is relaxed statistically into the nano-object. The parameters that we used to classify the various regimes of interaction are the average cluster size <N> and the number of initial charges q of the mother cluster before fragmentation.

Our approach is to map the final states reached after Coulomb explosion in momentum space by measuring the kinetic energy of all possible fragments. An understanding of the fast dynamics as probed by electron spectroscopy is crucial in order to know the initial conditions (before break-up), namely the charge localization of ionic valence shells [1] and the ionization rate, which is often enhanced by electronic relaxation or inelastic scattering [2,3]. Hence, we have access to the long time scale dynamics that enable us to understand the photo-induced reactions.

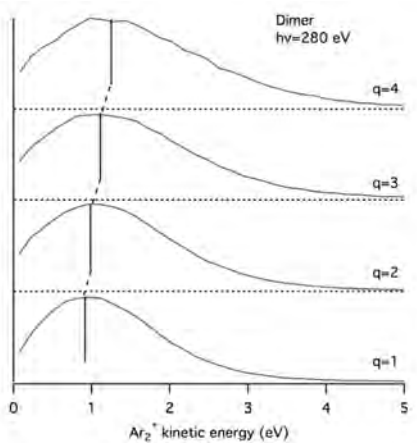

Figure 1 Kinetic energy distribution of dimer fragments as a function of the charge (q) of the mother cluster with <N>=50 atoms.

In figure 1, we present the kinetic energy distribution of dimer fragments arising from the fragmentation of multiply (singly) charged mother argon clusters with an average size of 50 atoms at 280 eV. The increase in the average kinetic energy as a function of the charge q of the mother ion is consistent with a Coulomb explosion picture: the higher the degree of ionization, the higher the kinetic energy of the fragments. In this Coulomb picture, the broadening of the peak is related to the distance between charges. Closer charges lead to higher kinetic energy. Consequently, the peak broadening reflects the disorder/order of the charge in the cluster at the time of the break-up. A depper look at the distances between charges using an onion-like shell structure for the clusters suggests that the charges are separated by one neutral atom, i.e. at the maximum of the kinetic energy distribution. Charge migration can then be seen as a simple charge exchange/transfer between two close neighbors.

It is worth noticing that at this photon energy, no quadruple mother ion charge is expected in the standard model of atomic van der Waals cluster photo-ionization. Apparently primary ionization and electronic energy dissipation lead to an order of magnitude enhancement of the quadruple ionization probability. This observation is in line with our previous work where we showed that the interplay between nuclear and electron motions in very small clusters increase auto-ionization mechanisms [4]. Further analysis is essential to rationalize the lower/higher kinetic energy of the fragments.

We developed a classical model relying on a statistical dissipation of the initial energy to understand the damage arising from Coulomb explosion and heat released by charge trapping [7]. In the model, the formation of large fragments is in principle the signature of the local temperature reached around the ionic core, in agreement to theoretical predictions of ionic cluster dynamics [8]. Quadrimer stabilization typically releases 300 meV more than dimers, and beyond that the other atoms

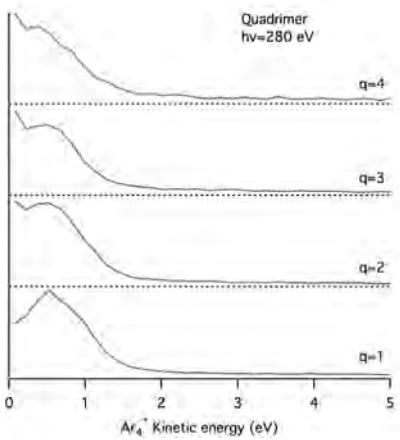

Figure 2: Kinetic energy distribution of the quadrimer as a function of the charge (q) of the mother cluster with <N>=50 atoms

do not contribute to the bonding of the ionic core (oligomer), since charge delocalization is essentially limited to trimer units. The gain in energy for a large ionic unit is small and the other atoms mainly act as a cooling bath near the transition to the liquid phase. A small excess of energy has a direct consequence: the evaporation of a neutral atoms and the formation of dimer ionic cores. Thus the formation of large units is in principle an indication of the local temperature reached around the oligomer, and is also an indirect measure of the Coulomb interaction.

In figure 2, we present the kinetic energy distribution of quadrimer fragments in the same parameters than previously. Higher is the charge lower is the kinetic energy of the fragment. This can only occur if the quadrimer originates from much larger fragments that did not acquire kinetic energy released during the fragmentation. Such relatively large fragment evaporates neutral atoms until it stabilizes as quadrimer.

The massive evaporation of neutral is simply related that the neutral atoms acts as a cooling bath. More there are charges on the clusters more heat is released, and thus larger fragments "melt". As we had previously found it is a signature that the collective nuclear motions slow down the overall fragmentation dynamic in large clusters [6]. Further analysis is in progress with different photon energy, cluster sizes, and cluster types.

References

[1] M. Lundwall *et al*, Surf. Sci. **594**, 12 (2005)
[2] G. Öhrwall *et al*, Phys. Rev. Lett. **93**, 173401 (2004)
[3] M. Lundwall *et al*, J. Phys. B. **39**, 3321, (2006)
[4] M. Gisselbrecht *et al*, J. Chem. Phys. **123**, 194301 (2005)
[5] P. Lablanquie *et al*, J. Chem. Phys **127,** 154323 (2007)
[6] M. Gisselbrecht *et al*, J. Chem. Phys. **128**, 044317 (2008)
[7] M. Gisselbrecht *et al*, submitted
[8]F. Calvo *et al*, J. Chem. Phys. **125**, 114307 (2006)

Ab initio and ion-ion coincidence study on the dissociation of d-ribose molecules

[1,2]D. T. Ha, [3,4]M. Huels, [5]M. Huttula, [1]E. Kukk
[1]Dept. of Physics and Astronomy, University of Turku, FI-20014 Turku, FINLAND
[2]Graduate School of Materials Research, Turku, FINLAND
[3]Royal Institute of Technology KTH, Atomic and Molecular Physics, Stockholm, SWEDEN
[4]Dept. of Nuclear Medicine and Radiology, Faculty of Medicine, University of Sherbrooke, Sherbroke, QC, CANADA
[5]Dept. of Physical Sciences, University of Oulu, FI-90014 Oulu, FINLAND

As a continuation of our recent series of studies on damage to DNA components by soft X-rays, namely DNA/RNA bases and some of their derivatives, we have recently investigated similar damage to DNA/RNA sugars. We used (PhotoElectron-PhotoIon-PhotoIon Coincidence) PEPIPICO methods to record the photodissociation of doubly charged d-ribose ($C_5H_{10}O_5$) molecules which are the result of initial core ionization, here C 1s, followed by normal Auger decay of the hole. Briefly, high resolution photoelectron spectra are recorded in coincident with time of flight mass spectra. The measurement instrument consists of a modified Scienta SES-100 hemispherical electron analyzer and a Wiley-Mclaren type ion time-of-flight spectrometer, the details of which can be found elsewhere [1]. The experiments were carried out at the undulator beamline I411 at the MAX-II storage ring.

To allow fragment identification we also performed PEPIPICO measurements deuterated d-ribose at C1 ($C_5H_9DO_5$), 2-deoxy-d-ribose ($C_5H_{10}O_4$) and a d-ribose where ^{12}C5 is replaced by isotope ^{13}C5 ($C_4{}^{13}CH_{10}O_5$).

Figure 1. Geometry optimized (6-311(dp) basis set) d-ribose is illustrated by using the MacMolPlt software [2].

Our main purpose is to study the dissociation channels of doubly ionized molecules following core-ionization by using synchrotron radiation. This is an essential step in attempting to understand radiation damage to DNA components in nature, by the very lethal low energy, or sof X-rays. The RNA / DNA sugars were irradiated at slightly above the C1s edge, viz. 330 eV, as well as in some cases near the O1s edge, viz. 578 eV . In addition, the GAMESS software [3] is used to perform *ab initio* calculations to model the dissociation processes. Properties such as appearance energies, equilibrium and intermediate states of the conformations of the molecules and their dissociated fragments are examined in order to outline the dissociating dynamics.

As the PEPIPICO map in figure 2 shows, induced by C1s ionization, the intensities of light mass ions pairs (e.g. 29,30) are much stronger than of the heavy ones (e.g. 43,73, not shown, off the map here), whereby the d-ribose in this process, following Auger decay, tends to Coulomb explode into smaller fragments rather than gently dissociate into heavier pairs. Nevertheless, heavier mass pairs can be seen weakly on the map and, it is believed that after formation, they fragment into several lighter fragments immediately. Exploring these dynamics is one of our key investigating points. While all the possible mass assignments are given in Fig. 2, it is clear that many of them are less likely, e.g. such as 43 amu $C_3H_7^+$ formation which would require too many concerted bond rearrangements and atom movements during a relatively fast dissociation process. However, calculations may aid in investigating these possibilities.

Moreover, we find that the formation of many of the intense low mass ion pairs requires significant bond rearrangements and atom movement, as seen in the 29 amu CHO^+ and 43 amu $C_2H_3O^+$, as well as formation of H_3O^+, CH_3^+, etc. Most saliently, this type of bond cleavage and

rearrangement is usually associated with densely ionizing heavy ion, or low energy electron damage, which may in part explain why soft X-rays have similar efficiency to kill cells than heavy particles. In addition, we find that while the mass spectra, recorded in coincidence with the main peak in the C1s photoelectron spectra (PES), do not contain a mass for the parent cation (150 amu), those mass spectra recorded in coincidence with a high KE shoulder in the PES do indeed show a non-negligible signal of a parent mass. Interestingly enough this high KE shoulder in the PES of d-ribose becomes a more resolved peak in the PES of 2-deoxy-d-ribose, which suggests that it is associated possibly with the C2 carbon. Thus the fact that a small intensity of parent cation mass at 150 amu is observed only for that structure in d-ribose, may suggest that core ionisation at the C2 in d-ribose (where there is an OH group) perhaps leads to a radiative decay, resulting in a singly charged molecular cation, that may or may not have its bonds intact – ring opening of course would not be detectable here. In any case, this would suggest a stabilizing influence of the OH group at the C2 in d-ribose upon core ionization of that atomic site.

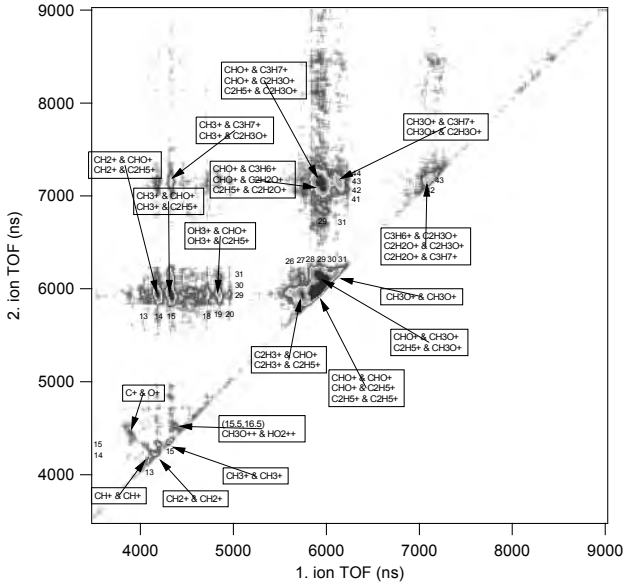

Figure 2. The PEPIPICO map of the d-ribose sample associated with C1s ionization and followed by normal Auger decay and fragmentation, recorded at a synchrotron photon energy of 330 eV.

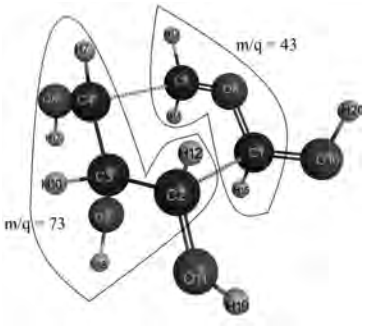

Figure 3. The transition state of doubly charged d-ribose illustrates the ion dissociating into two fragments and then possibly continuing the fragmentation process further in such a way that OH parts from both main fragments come off. As a result, the ion pair with m/q (43,73) is collected by the detector and can be seen on the PEPIPICO map in figure 2, whereas the two neutral OH fragments cannot be collected by the technique.

Above is a conformation of a saddle point of doubly charged d-ribose. The saddle point is found by the quasi-Newton algorithm with the help of the GAMESS software. This transition state depicts d-ribose after the initial C1s core ionization followed by normal Auger process and nuclear rearrangement. From this state d-ribose dissociates into two fragments (43/73) and then the fragments either begin to isomerize into their equilibrium states or continue to dissociate further into lighter fragments.

We would like to thank the Academy of Finland for the financial support and the staff of MAX-lab for their help. MAH would like to acknowledge support from the Natural Science Research Council of Canada, and the Canadian Space Agency.

[1] E. Kukk, R. Sankari, M. Huttula, A. Sankari, H. Aksela and S. Aksela, J. of Electron Spectrosc. Relat. Phenom. 155, 141, 2007.
[2] Bode, B. M. and Gordon, M. S. J. Mol. Graphics Mod., 16, 1998, 133-138. MacMolPlt (http://www.scl.ameslab.gov/~brett/MacMolPlt/)
[3] M. W. Schmidt, K. K. Baldridge, J. A. Boatz, S.T.Elbert, M. S. Gordon, J. J. Jensen, S. Koseki, N. Matsunaga, K. A. Nguyen, S. Su, T. L. Windus, M. Dupuis, J. A. Montgomery, J. Comput. Chem. 14, 1347-1363 (1993). GAMESS (http://www.msg.chem.iastate.edu/gamess/)

Solvent effects on the dye molecular layers on TiO_2

Maria Hahlin[a] , Tannia Marinado[b] , Erik M.J. Johansson[c] , Hans Siegbahn[a] , Håkan Rensmo[a]

[a]Department of Physics and Materials Science, Uppsala University, Box 530, 752 21 Uppsala, Sweden.
[b]Inorganic Chemistry, Centre of Molecular Devices, Chemical Science and Engineering, Royal Institute of Technology,100 44 Stockholm, Sweden,
[c]Department of Physical and Analytical chemistry, Uppsala University, Box 259, 751 05 Uppsala, Sweden.

Dye-sensitized solar cells (DSC) has received wide spread interest as a promising alternative to conventional solar cells with record efficiencies above 11%. [1–5] Much research efforts have been invested into the understanding of the complex interplay of the dye/electrolyte/semiconductor interface of the DSCs. In the present study an organic dye 3-(5-(4-(diphenyl amino) styryl) thiophen-2-yl)-2-cyanoacrylic acid (D5) is investigated using PES. The study concerns the structure of the dye when adsorbed onto TiO_2 using the three different solvents ethanol, acetonitrile, and dichlormethane. The D5 molecule is built up by three parts, an electron donor unit (diphenyl amino moiety), a linker unit (thiophene moiety), and an anchor unit (cyanoacetic acid moiety), see figure 1.

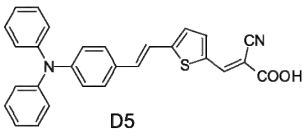

Figure 1: Molecular structure of D5

The photoelectron spectroscopy (PES) measurements are performed using synchrotron radiation at BL I411. The PES spectra are energy calibrated by setting the Ti2p substrate signal to 458.56 eV. Charging and radiation effects are monitored continuously and are negligible for all spectra reported in the present investigation.

The N1s core level spectra are shown in figure 2. In each spectrum two peaks are identified, one located at approximately a binding energy of 399.7 eV, attributed to the nitrogen atom in the diphenyl amino moiety, and another peak located at approximately a binding energy of 398.6 eV, attributed to the nitrogen atom in the cyanoacetic acid moiety. These two peaks are hereafter referred to as $N1s_D$ and N_{An} respectively.

In the N1s spectrum core level information about both the donor and the anchor unit is thus seen. In the figure it is noticed that the binding energy of the $N1s_{An}$ peak is located at very similar binding energies for all three samples. The binding energy of the $N1s_{An}$ core level differ only by at most 0.12 eV indicating that the energy levels of the anchor units line up towards the TiO_2 surface upon adsorption as a result of electronic interaction between the anchor group and the substrate. The binding energy of the $N1s_D$ energy level however is different depending on the solvent used. The $N1s_D$ core level is located at highest binding energy for the D5(MeCN), followed by D5(EtOH) and D5(DCM) samples. The total difference between $N1s_D$ of the D5(MeCN) and the D5(DCM) sample is as large as 0.42 eV.

Previous calculations on the D5 molecule indicate that the absorption of a photon involves an electron excitation from the HOMO, located dominantly around the diphenyl amino moiety, to the LUMO, located dominantly around the cyanoacetic

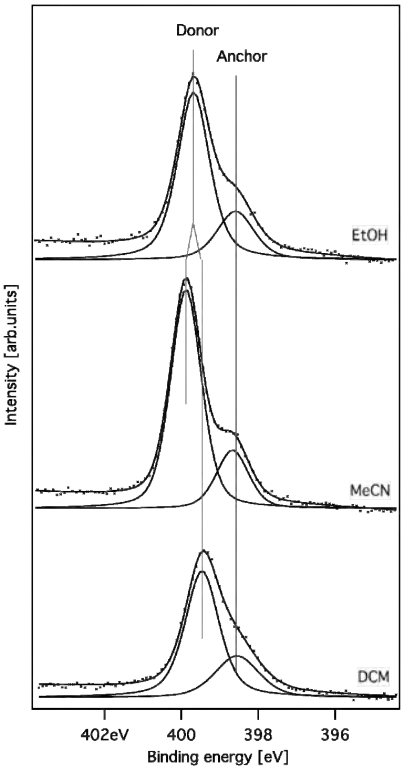

Figure 2. The N1s core level spectrum of D5 solved in EtOH, MeCN, and DCM.

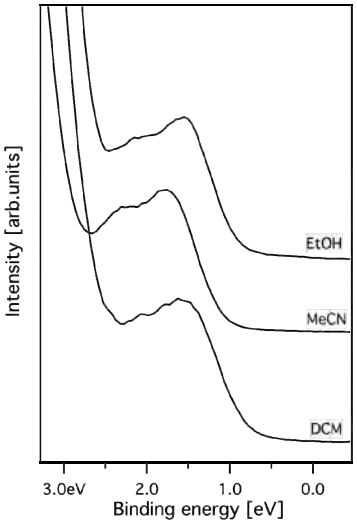

Figure 3: The highest occupied molecular orbitals (HOMO) of the D5(EtOH), D5(MeCN), and D5(DCM) samples located at the TiO_2 valenceband edge, measured with photonenergy 100 eV and energy calibrated versus the Ti3p energy level.

acid moiety. [6,7] Keeping this in mind, a shift of the $N1s_D$ energy level is thus expected to be accompanied with a shift of the HOMO level relative the TiO_2 substrate. The large shift of the donor $N1s_D$ level also implies that only a part of the molecular layer is affected by different solvents.

The outermost energy levels, occupied and unoccupied, are directly involved in the energy conversion process of a working DSC. The occupied levels, the HOMOs, can be probed using PES and is shown in figure 3. It is clear that the position of the HOMO level of D5 relative the TiO_2 is dependent on the solvent. The position of the HOMO peak is located at approximately 0.2 eV higher binding energies for the D5(MeCN) compared to the D5(EtOH) or D5(DCM) samples. Interestingly the D5(EtOH) and D5(DCM) has a similar HOMO position, which is not expected from the N1s core level measurements.

The energy matching between the D5 and the TiO_2 surface is vital for the function of the solar and changes in the matching may influence the spectral response for photocurrent generation. Such effects were indeed found and are shown in figure 4.

Acknowledgements

This work was supported by the Swedish Research Council (VR), the Göran Gustafsson Foundation, the Carl Trygger Foundation, the Knut and Alice Wallenberg foundation, and the Swedish Energy Agency. We thank the staff at MAX-lab for competent and friendly assistance and Dr. Leif Häggman for the supplying of theTiO_2 working electrodes.

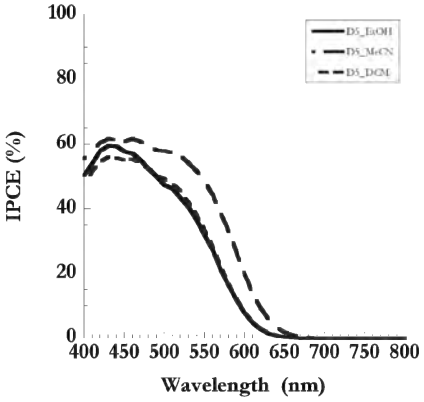

Figure 4: Spectra of monochromatic incident photon-to-current conversion efficiency (IPCE) for DSCs based on D5 sensitized in different solvents EtOH, MeCN, and in DCM. Electrolyte: 0.6MTBAI, 0.1MLiI, 0.5M4-TBP and 0.05M I_2 in acetonitrile.

References

[1] B. O'Regan and M. Grätzel, Nature, 1991, 353, 737.

[2] U. Bach, D. Lupo, P. Comte, J. E. Moser, F. Weissortel, J. Salbeck, H. Spreitzer andM. Gratzel, Nature, 1998, 395, 583.

[3] M.Nazeeruddin, A.Kay, I.Rodicio, R.Humphruy-Baker, E.Muller, P.Liska, N.Vlachopoulos and M. Grätzel, Journal of the American Chemical Society, 1993, 115, 6382–6390.

[4] M. Nazeeruddin, P. Pechy, T. Renouard, S. Zakeeruddin, R. Humphry-Baker, P. Comte, P. Liska, L. Cevey, E. Costa, V. Shklover, L. Spiccia, G. Deacon, C. Bignozzi andM. Gratzel, JOURNALOF THEAMERICANCHEMICALSOCIETY, 2001, 123, 1613–1624.

[5] M. Nazeeruddin, F. DeAngelis, S. Fantacci, A. Selloni, G. Viscardi, P. Liska, S. Ito, B. Takeruand M. Gratzel, Journal of the American Chemical Society, 2005, 127, 16835–16847.

[6] D. P. Hagberg, J.-H. Yum, H. Lee, F. DeAngelis, T. Marinado, K. M. Karlsson, R. Humphry-Baker, L. Sun, A. Hagfeldt, M. Graetzel and M. K. Nazeeruddin, Journal of the American Chemical Society, 2008, 130, 6259–6266.

[7] J. Wiberg, T. Marinado, D. P. Hagberg, L. Sun, A. Hagfeldt and B. Albinsson, Journal of Physical Chemistry C, 2009, 113, 3881–3886.

Carbon 1s photoelectron spectra of neutral CO_2 clusters: Theoretical models applied to experimental spectra.

J. Harnes,[a] M. Winkler,[a] M. Abu-samha,[b] A. Lindblad, [c] L. J. Sæthre,[a] and K. J. Børve[a]

[a] *Department of Chemistry, University of Bergen, Allégaten 41, NO-5007 Bergen, Norway*
[b] *Department of Physics and Astronomy, University of Aarhus, DK-8000 Aarhus C, Denmark*
[c] *Synchrotron SOLEIL, L'Orme des Merisiers, Saint-Aubin - 91192 Gif-sur-Yvette cedex, France*

While core-level photoelectron spectra of noble-gas clusters are often found to display two distinct domains of ionization energies corresponding to ionization of surface and bulk atoms, respectively, core-level spectra of molecular clusters usually contain too little structure to distinguish between surface and bulk molecules. However, information about the surface-bulk shift in core-ionization energy may be available from a theoretical analysis based on the evaluation of intermolecular interaction energies in structures obtained from molecular dynamics simulations of clusters.

In this study, theoretical spectra of CO_2 clusters of different sizes were constructed and compared to an experimental spectrum. CO_2 clusters have been made subject to both experimental and theoretical studies by other researchers earlier, see for instance refs. 3-5. Interestingly, while the carbon atoms in small CO_2 clusters prefer a polyicosahedral arrangement, in large CO_2 clusters the carbon atoms compose a face-centered-cubic (fcc) lattice.

Molecular dynamics simulations were performed on clusters containing 13, 19, 55 and 249 molecules. The simulations started out from structures prepared as spherical cuts from crystalline CO_2 with density and structure corresponding to the temperature of large carbon dioxide clusters.[1] Moreover, polarizable force fields[2] of high-quality were parametrized for both neutral and C1s-ionized CO_2 and used to calculate monomer-to-cluster shifts in C1s ionization energies.

The process of constructing a theoretical model spectrum of a cluster is shown in Fig. 1 for a 249-membered cluster. First, the ionization energy is computed for every molecule making up the cluster, in order to prepare the distribution of ionization energies (part a in Fig.1), subsequently to be convoluted with the experimental monomer lineshape (part b) to account for all molecular effects including intramolecular vibrations and lifetime broadening. Next, the effect of inelastic scattering (part c) [6] of photoelectrons that are generated in the interior of the cluster is accounted for. Finally, the model spectrum is convoluted with an extra Gaussian distribution which represents excitation of intermolecular vibrations, [7] the cluster-size distribution as well as a difference in experimental resolution between the cluster experiment and the experiment used

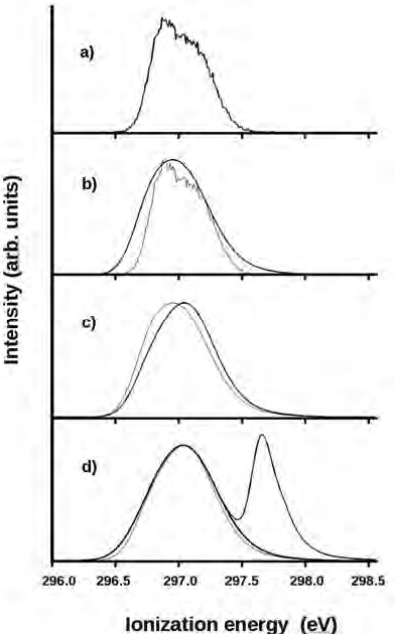

Figure 1. Steps a-d in the construction of a theoretical carbon 1s photoelectron model spectrum for carbon dioxide clusters with a mean cluster size of 249 molecules. See the text for further details.

to record the monomer spectrum used in step b. While the distribution of cluster sizes in a cluster beam has been found to be quite well described by a log-normal distribution, [7,8] convergence of the ionization energy with increasing cluster size makes the resulting distribution of ionization energies assume a more symmetric shape that is reasonably Gaussian. A monomer spectrum may be added to facilitate comparison to the experimental cluster spectrum, which always is recorded in the presence of free monomers. This results in the model spectrum at the bottom of Fig. 1.

Neutral free clusters of carbon dioxide were produced in a free-jet condensation source [10] by expanding carbon dioxide, CO_2, gas at a stagnation pressure of 0.84 bar and a nozzle temperature of 300K. C1s photoelectron spectra were acquired at beamline I411 at MAXLab, using a photon energy of 330 eV, see Fig. 2. A theoretical spectral model constructed as outlined above, is fit to the experimental spectrum by adjusting the intensity of the monomer and cluster peaks. In Fig. 2, a theoretical lineshape based on ionization energies calculated for an N= 55 cluster is used in combination with an attenuation length of 5Å. The good agreement between the model and the observed spectrum with respect to the energy position as well as the lineshape suggests that the mean cluster size in the experiment is around 50 molecules. Moreover, by using the distance from the center of mass in the cluster models to classify molecules into surface and bulk components, the calculations give a surface-bulk shift in ionization energy of about 0.12 eV for the 55-mer, increasing to 0.25 eV for the 249-mer. These values are significantly below the surface-bulk shifts that are seen for large noble gas clusters. [11]

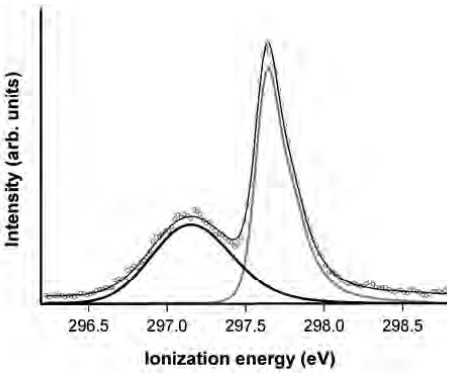

Figure 2. Experimental C1s photoelectron spectra (dotted) of condensed and free CO_2, recorded unde expansion conditions that favour the production of medium-sized clusters. Energy calibration is obtained by reference to the adiabatic energy for CO_2 of 297.651±0.010 eV. [9] The spectrum is fit by theoretical lineshape model (full line) with peak heights, Gaussian broadening terms and a linear background as free parameters.

Acknowledgments

We are pleased to thank the Research Council of Norway, NORDFORSK, the European Community through the FP6 programme, the Norwegian High Performance Computing Consortium NOTUR and the University of Bergen through the NanoUiB initiative. The authors would also like to acknowledge the help of the MAX-lab staff and in particular that of Dr. Maxim Tchaplyguine, as well as financial support from the Knut and Alice Wallenberg foundation, the Swedish Scientific Council (VR), The Swedish Foundation for strategic research (SSF), and the Göran Gustafsson's foundation.

[1] J. Farges, M. F. D. Feraudy, B. Raoult, G. Torchet, Surf. Sci. **106** (1981) 95.
[2] P. Ren, J. W. Ponder, J. Phys. Chem. **107** (2003) 5933; P. Ren, J. W. Ponder, J. Comp. Chem. **23** (2002) 1497.
[3] G. Torchet, M.-F. de Feraudy, A. Boutin, and A. H. Fuchs, J. Chem. Phys. **74** (1996) 3671.
[4] J.-B. Maillet, A. Boutin,. A. H. Fuchs, J. Chem. Phys. **111** (1999) 2095.
[5] A. Bonnamy, R. Georges, E. Hugo, and R. Signorell, Phys. Chem. Chem. Phys. **7** (2005) 963.
[6] F. G. Amar, J. Smaby, T. J. Preston, J. Chem. Phys. **122** (2005)244717.
[7] H. Bergersen et al., Phys. Chem. Chem. Phys. **8** (2006) 1891.
[8] C. Bobbert, S. Schüttke, C. Steinbach, U. Buck, Eur. Phys. J. D **19** (2002) 183.
[9] J. Nordgren, L. Selander, L. Pettersson, C. Nordling, K. Siegbahn, H. Ågren, J. Chem. Phys. **76** (1982) 3928.
[10] M. Tchaplyguine et al., Chem. Phys. **289** (2003) 3.
[11] M. Tchaplyguine et al., Phys. Rev. A **69** (2004) 031201.

Angular distribution of the shakedown satellites in the laser-excited potassium

M. Holappa, S. Heinäsmäki, T. Löytynoja, and H. Aksela

Department of Physical Sciences, P.O. Box 3000, 90014 University of Oulu, Finland

Potassium has recently been studied using the combination of laser and synchrotron radiation [1-3] but no β parameters have been reported. In this study we have combined laser and synchrotron radiation to study shakedown satellites and their β parameters in laser-excited potassium. Prior to excitation by synchrotron light, the K atoms were laser-polarized from the ground [Ar]4s ($^2S_{1/2}$) electronic configuration to the [Ar]4p ($^2P_{1/2}$) configuration using radiation from the Ti:Sa laser tuned at 769.9 nm. We then studied the conjugated shakedown satellites of the 3p photoelectron spectrum, corresponding to the $3p^5$4s and $3p^5$3d electronic configurations.

The photoelectron spectra were recorded using a Scienta SES-100 hemispherical electron energy analyzer at the I411 undulator beamline. The spectra were recorded with the angles of 0°, 30° and 54.7° with respect to the polarization direction of the synchrotron beam. The spectra were measured with the photon energy of 55 eV. Beta parameter of neon 2p photolines were used as a reference. Figures 1 and 2 show the $3p^5$4s and $3p^5$3d shakedown lines measured with the angles of 0° and 30°.

The shakedown lines correspond to ionization into p-type continuum waves only, when configuration interaction is neglible. Therefore, the angular asymmetry which depends on phase differences between the continua, should be small. We however observe intensity variation depending on the angle which points to unaccounted electronic correlation [4].

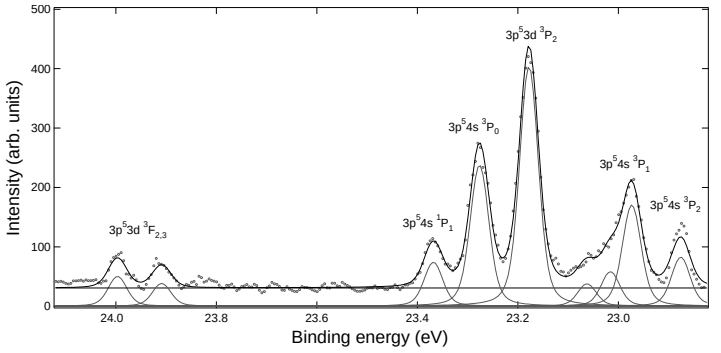

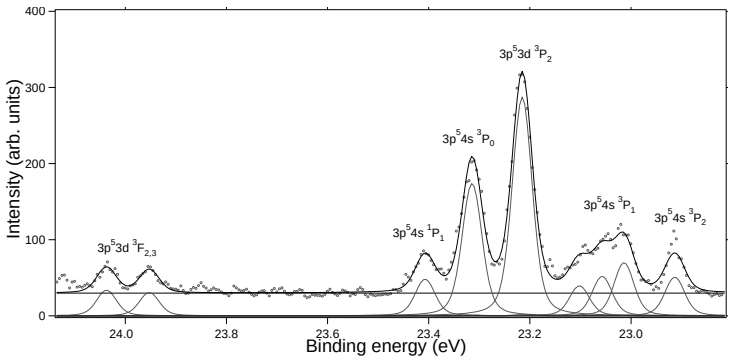

Figure 1 and 2. Experimental spectrum of potassium shakedown lines measured with the angles of 0° and 30°. Red circles are the data points and the sold black line represents the fitted spectrum.

References

[1] K. Jänkälä, R. Sankari, J. Schulz, M. Huttula, A. Caló, S. Heinäsmäki, S. Fritzsche, T. Rander, S. Svensson, S. Aksela, Phys. Rev. A, 73, 022720 (2006).

[2] J. Schulz, S. Heinäsmäki, R. Sankari, T. Rander, A. Lindblad, H. Bergersen, G. Öhrwall, S. Svensson, E. Kukk, S. Aksela, and H. Aksela, Phys. Rev. A, 74, 012705-1-6 (2006).

[3] M. Määttä, J. Schulz, S. Heinäsmäki, and H. Aksela, J. Electron Spectr. Rel. Phen. , 161,99-104 (2007).

[4] M. Holappa, S. Heinäsmäki, T. Löytynoja, and H. Aksela, in preparation

Carbon 1s photoelectron spectroscopy as a tool in molecular conformational studies

A. Holme[1], L. J. Sæthre[1], K. J. Børve[1], T. D. Thomas[2]

[1] *Department of Chemistry, University of Bergen, Allégaten 41, NO-5007 Bergen, Norway*
[2] *Department of Chemistry, Oregon State University, Corvallis, OR 97331-4003, USA*

Recently, it has become evident that inner-shell ionization energies may depend on the molecular conformation. In turn, this opens for the possibility that x-ray photoelectron spectroscopy (XPS) in combination with theoretical modelling may serve as a tool for investigating conformational effects. To date, this possibility has been explored for ethanol [1], butyronitrile, 1-fluoropropane, and propanal [2], proline [3], and 1-pentyne [4]. The conformational equilibria of these molecules are all fairly thoroughly studied by other experimental techniques, and the generally good agreement between conformational parameters obtained with XPS and those obtained by means of vibrational or rotational spectroscopy as well as gas electron diffraction, increases confidence in the new approach.

In the present contribution, we focus on 4-methyl-1-pentyne ($HC{\equiv}CCH_2CH(CH_3)_2$), which has been suggested [5] to possess two important conformers, denoted by their point-group symmetry as C_1 and Cs (see Figure 1).

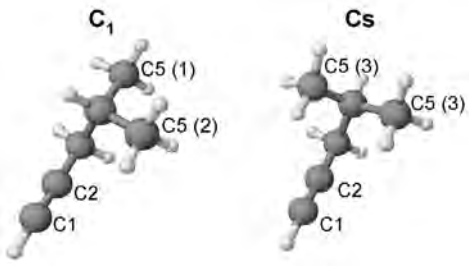

Figure 1: The two conformers of 4-methyl-1-pentyne.

Furthermore, *ab initio* calculations suggest that these two conformers have comparable stabilities [5]. However, there are no experimental data in the literature on the population of these conformers. In light of the encouraging performance of carbon 1s photoelectron spectroscopy as applied to the closely related compound 1-pentyne, we now use this approach to study the relative abundance of the conformers of 4-methyl-1-pentyne. As such, this is the first time XPS has been applied to predict the hitherto unknown composition of a molecular conformational equilibrium.

Gas phase measurements of the carbon 1s photoelectron spectrum of 4-methyl-1-pentyne were performed at room temperature at beamline I411 at MAX-lab in Lund, Sweden, with a photon energy of 330 eV and an instrumental broadening (fwhm) of 65 meV as determined from the carbon 1s photoelectron spectrum of carbon dioxide. The photoelectrons were analyzed in an SES200 electron spectrometer.

Theoretical lineshape models specific to each site of ionization in each conformer were prepared and fitted to the experimental spectrum. The result is shown in Figure 2.

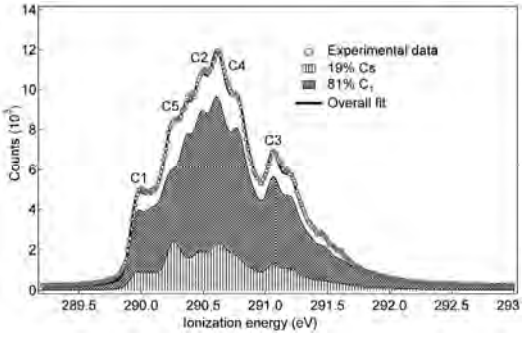

Figure 2: The experimental C1s photoelectron spectrum of 4-methyl-1-pentyne (circles) is shown together with theoretical fitting models (solid line) based on vibrational profiles derived for a fitting model that takes into account both C_1 and Cs conformers. The contributions from the two conformers are shown as cross-hatched areas. The final fit contains 81% C_1 and 19% Cs.

The contributions to the spectrum from carbons 1-4 are almost the same for the two conformers. They give rise to similar ionization energies and vibrational line shapes independent of conformations. However, this is not the case in the C5 contribution where there are differences in ionization energies (see Table 1) and line shapes between the terminal methyl carbons of the two conformers.

Table 1: Adiabatic C1s ionization energies (IE) of 4-methyl-1-pentyne.

Carbon	IE (eV)
C1	289.956
C2	290.474
C3	291.059
C4	290.602
C5 (1)	290.359
C5 (2)	290.175
C5 (3)	290.238

Hence, we need to include both conformers in order to obtain a theoretical spectrum that matches the experimental one. The fitted amount of each conformer is 19% Cs and 81% C_1.

The uncertainty obtained from the statistics of the fit is 1% while the uncertainty estimated from the choice of fit model is 0.5%. Hence, the total uncertainty is estimated to be ≈2%.

Table 2: The population of the Cs conformer of 4-methyl-1-pentyne, as computed at different levels of theory (298K) and as measured by XPS.

Level of theory[a]	% Cs population[b]
HF/6-31+G(d,p)	18 [5]
MP2/6-31+G(d,p)	33 [5]
MP2/6-311++G(2d,2p)	36 [5]
B3LYP/TZP[c]	24
G3	32
XPS	*19(±2)*

[a] Method/basis set

[b] % C1 population: 100% - % Cs population

[c] TZP: Dunning TZ + (d,p) from 6-311G**

Table 2 gives an overview of computed populations of the two conformers as obtained at different levels of theory. While MP2 and G3 predict considerably higher Cs population than obtained experimentally, Hartree-Fock and DFT (B3LYP) predict populations in close agreement with our experimental value of 19%.

Acknowledgments

We would like to thank Maxim Tchaplyguine at beamline I411 and the MAX-lab staff for their assistance during the beamtime, the Research Council of Norway (NFR), the Nordic Research Board (NORDFORSK) and the Norwegian High Performance Computing Consortium NOTUR.

[1] M. Abu-samha, K. J. Børve, L. J. Sæthre and T. D. Thomas, Phys. Rev. Lett. **95**, 103002 (2005)
[2] T. D. Thomas, L. J. Sæthre and K. J. Børve, Phys. Chem. Chem. Phys. **9**, 719 (2007)
[3] O. Plekan, V. Feyer, R. Richter, M. Coreno, M. de Simone, K. C. Prince and V. Carravetta,
Chem. Phys. Lett. **442**, 429 (2007)
[4] A. Holme, L. J. Sæthre, K. J. Børve and T. D. Thomas, J. Mol. Struct. **920**, 387 (2009)
[5] G. B. Churchill, R. L. Milot, R. K. Bohn, J. Mol. Struct. **837**, 86 (2007)

Fast decay of 4p and 4s core holes in Sb_4 clusters

M. Huttula, S.-M. Huttula, S. Urpelainen, L.Partanen, S. Aksela, and H. Aksela

Department of Physics, University of Oulu
P.O.Box 3000 90014 University of Oulu, Finland

Antimony (Sb) and its compounds are commonly used in various industries in the production of semiconductor devices, flame-retardant fabrics and paints etc. Due to the inherent property of antimony to produce Sb_4 clusters on evaporation, it has been a naturally interesting target to the electron spectroscopy. The electronic configuration of antimony atom in its ground state is $[Kr]4d^{10}5s^25p^3$ and the three valence electrons form the bonding of the cluster providing a closed valence shell structure. Electronic transitions from 4d-orbital has lately studied by Urpelainen *et al.* [1,2].

This report shows the 4s and 4p photoelectron spectra with remarkable different lifetime widths for the two energetically close-lying orbitals [3]. The spectral features are predicted using a closed valence shell approximation and atomic, relativistic multiconfiguration Dirac-Fock method. The closed valence is taken into account by filling the valence orbital after the determination of the one-electron wave functions. The atomic splitting of states due to the coupling is thus removed.

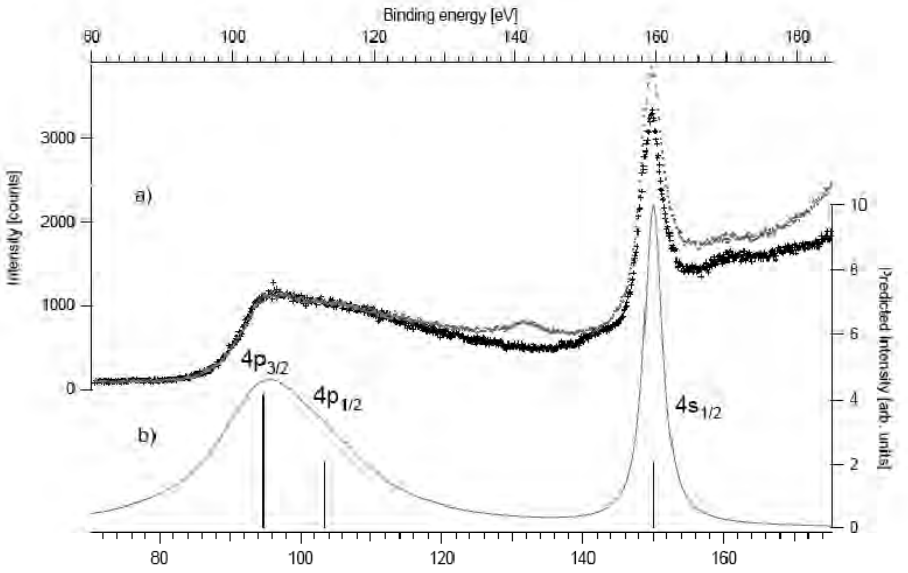

Figure 1. (a) The 4s and 4p photoelectron spectra of antimony measured using 210eV (dotted) and 220eV (crossed) photon energies. (b) The ab-initio simulated spectra. The vertical bars represent the calculated energy positions.

The experiments were carried out at the the high resolution soft X-ray undulator beamline I411 at MAX-laboratory [4]. The electron spectra were recorded using a modified Scienta SES-100 electron analyzer and at the magic angle of 54.7° with respect to the electric field vector of the linearly polarized undulator radiation. The antimony vapor was produced using an inductively heated oven described in [5] with a minor modifications in crucible design. The temperature was estimated to be around 500°. The experimental and calculated 4s and 4p photoelectron spectra are shown in Figure 1.

The 4p and the 4s photoelectron lines reflect very different widths, where the 4p features seem to be almost 10 times wider providing a smoothly descending structure for 50 eV wide region. In Sb_4, the mixing of the $4p^{-1}$ with $4d^{-2}nf$ configurations, taking place in isoelectronic Xe, is not possible as the $4d^{-2}$ threshold is located about 40 eV below the binding energy of $4p^{-1}$ states and the fast SCK decay follows both spin-orbit splitted core hole states. However, the molecular valence structure is seen to induce the mixing of the $4p_{1/2}$ and $4p_{3/2}^{-1}V^{-1}$ states thus redistributing the $4p_{1/2}$ intensity. Together with underlying satellite transitions of photolines the wide high binding energy tail of the spectrum may be explained. To fully understand the nature of the 4p and 4s photoelectron spectra, an electron-electron coincidence experiments is proposed to separate the main and satellite components of the photolines and the SCK and CK Auger decays. Molecular calculations would also be needed to predict the mixing of the $4p_{1/2}^{-1}$ and $4p_{3/2}^{-1}V^{-1}$ml states as here the valence is also involved.

[1] Urpelainen S, Calo A, Partanen L, Huttula M, Aksela S, Aksela H, Granroth S and Kukk E 2009 Phys. Rev. A **79** 023201
[2] Urpelainen S, Calo A, Partanen L, Huttula M, Kukk E, Aksela S and Aksela H 2009 Phys. Rev. A **80** 043201:1-6
[3] Huttula M., Huttula S.-M., Urpelainen S., Partanen L., Aksela S. and Aksela H. 2009 J. Phys. *B* **42** 235002:1-5
[4] Bässler M, Ausmees A, Jurvansuu M, Feifel R, Forsell J-O, de Tarso Fronseca P, Kivimäki A, Sundin S, Sorensen S L, Nyholm R and Björneholm O 2001 Nucl. Instrum. Methods Phys. Rev. A **469** 382-93
[5] Huttula M, Jänkälä K, Mäkinen A, Aksela H and Aksela S 2008 New J. Phys. **10** 013009

Charge correction study of calcite

L. Järvinen[1,2,3,4], J. A. Leiro[1], M. Heinonen[1] and O. Eklund[2]

[1]Laboratory of Materials Science, Department of Physics and Astronomy, University of Turku, FIN-20014 Turku, Finland.
[2]Department of Geology, University of Turku, FIN-20014 Turku, Finland.
[3]Graduate School of Materials Research, Turku, Finland.
[4]Finnish Graduate School in Geology.

Limestones are widely used as raw materials in various desulphurisation processes of flue gases from power plants utilising coal combustion [1]. Calcite is the main mineral constituting limestone, and fairly common around the earth in a multitude of mineralogical environments. In addition to flue gas desulphurisation, calcites can be used for example as crystals in X-ray spectrometers [2]. In our reactivity experiments [3] we have noticed, that the choice of raw material is an important part of the scrubbing process, since specimens with seemingly identical chemical composition have significant differences in their performance. Calcite is an insulator, with a band gap of 6 eV. Therefore, the neutralization of the sample surface is a crucial part of the measurements. In this study we have measured the Ca 2p spectra of Iceland spar calcite. We have taken advantage of an electron flood gun [4,5,6,7] and a conductive mask to reduce the effects of surface charging.

Single crystals of commercial Iceland spar calcite were cut to bars of suitable size that enable cleaving in UHV conditions. Before each measurement, the sample was cleaved in UHV to produce a clean surface, unless otherwise stated.
The measurements were carried out at the beamline I411 of MAX II. The beamline is equipped with a modified SX-700 monochromator and a hemispherical Scienta SES-200 electron energy analyzer. The pressure was typically around 10^{-9} mbar. A pass energy of 100 eV was used for all measurements, and the photon energy was either 500 or 700 eV.
The spectrometer was calibrated using gold and silver reference samples. Au $4f_{7/2}$ and Ag $3d_{5/2}$ photoemission lines were recorded with pass energies of 10, 20 and 50 eV, while the photon energy ranged from 450 to 750 eV. The energy distance between Au $4f_{7/2}$ and Ag $3d_{5/2}$ peaks were calculated to be 284.21 ± 0.16 eV for all combinations of pass and photon energies, which was taken as sufficiently accurate.
The value of 4.55 eV was obtained for the work function of the spectrometer with both gold and silver references for photon energies of 70, 100 and 150 eV. For higher photon energies of 550, 650 and 750 eV, the work function was measured to be 3.70, 3.25 and 3.20 eV, respectively.
A Perkin-Elmer Φ 04-015 electron flood gun was used to mitigate the effects of surface charging during the experiments. The main difficulty with the flood gun is to adjust it so that the positive charge left behind by the photoelectrons is uniformly balanced. This was done by regulating the voltage, the current and the point of electron impact until the minimum core level linewidth was reached for either Ca 2p or C 1s. Emission current from the filament was 1 mA, but based on current measurements done in situ for a Perkin-Elmer PHI 5400 spectrometer, the current has diminished to approximately 1 μm at the sample surface. In addition, a conductive mask made of stainless steel was later situated on top of the sample to improve surface neutralization. The mask was grounded. The conductive aluminium substrate was also grounded for all experiments.
Care must be taken in conventional or synchrotron based XPS studies of insulating materials, such as calcite, since various charging phenomena and attempts to neutralize them may alter the sample surface and/or the measured spectra. With a conventional ESCA, monochromatic X-ray source has been reported to cause unstable sample charging on the calcite surface that resulted in sample broadening [8]. In addition, electron irradiation causes decomposition [9].
Figure 1. shows two Ca 2p doublets (a) and one doublet (b) of Iceland spar calcite. Only the electron flood gun was used for charge correction. The doublet with the higher binding energy in figure 1 (a) is attributed to Ca in $CaCO_3$, while the other one could possibly represent CaO, since the energy of the X-ray beam has been reported to break $CaCO_3$ into CaO and CO_2 gas. However, chemical shifts between Ca 2p doublets of CaO have been reported to be 1.8 eV [10] and 1.3 eV[11], so the feature with 3.1 eV lower binding energy does not indicate the presence of CaO. Instead, a charging of the sample may be the cause of the second

feature. In figure 1. (b) only a single doublet can be seen. This was acquired from a fresh spot after moving the position of analysis. Figure 1. (b) supports the idea that the second doublet in figure 1. (a) is caused by charging effects.

Figure 2. depicts the Ca 2p spectra obtained with the cooperative use of a conductive mask and an electron flood gun. These two peaks have the smallest breadths, which indicates that the combination of an electron flood gun and a conductive mask works for charge correction better than the electron flood gun alone. The greater FWHM for the peak recorded with a photon energy of 500 eV (a) may indicate the presence of a surface component, since the doublet obtained with a more bulk-sensitive excitation energy of 700 eV is slightly narrower. The minor doublet is fitted into the spectrum with a slightly smaller binding energy.

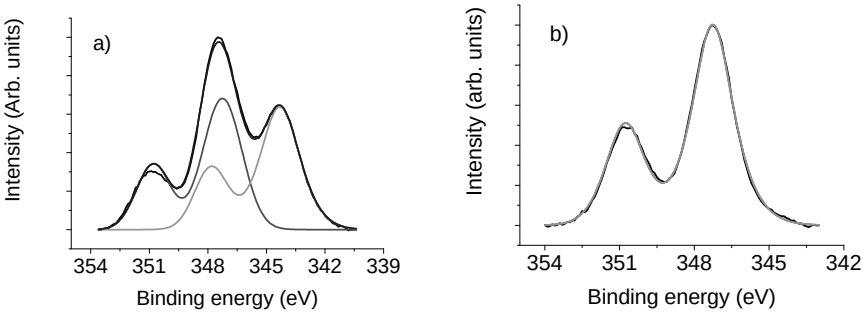

Figure 1. Ca 2p spectra of Iceland spar calcite, (a) two doublets and (b) one doublet.

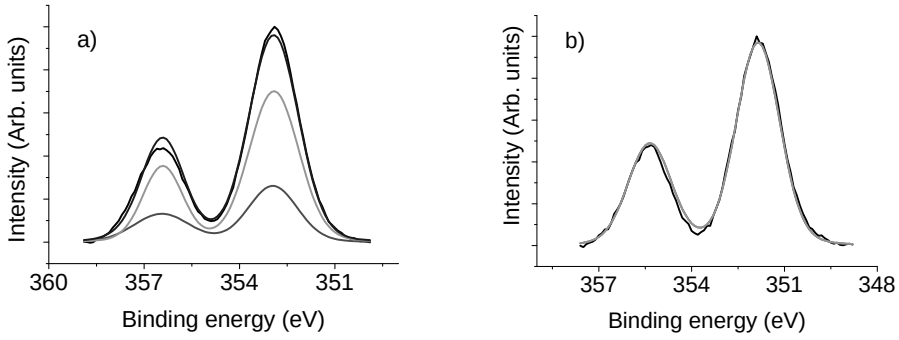

Figure 2. Ca 2p spectra of Iceland spar calcite obtained with an excitation energy of 500 eV (a) and 700 eV (b). A conductive mask was installed. The sample was cleaved in air.

References

[1] J. Cheng et. al, Progress in Energy and Combustion Science 29, 381 (2003).
[2] E. Suoninen, M. Pessa, Physica Scripta 7, 89 (1973).
[3] L. Järvinen, J. A. Leiro, F. Bjondahl, O. Eklund, Submitted for publication.
[4] F. J. Grunthaner, P. J. Grunthaner, Materials Science Reports 1 (2), 65 (1986).
[5] A. Cros, Journal of Electron Spectroscopy and Related Phenomena 59, 1 (1992) .
[6] D. R. Baer, M. H. Engelhard, D. J. Gaspar, A. S. Lea, C. F. Windisch Jr., SIA 33, 781 (2002).
[7] D. A. Huchital, R. T. McKeon, Appl. Phys. Lett. 20 (4), 158 (1972).
[8] S. L. Stipp, M. F. Hochella Jr., Geochimica et Cosmochmica Acta 55, 1723 (1991).
[9] A. B. Christie, I. Sutherland, J. M. Walls, Vacuum 31 (10-12), 513 (1981).
[10] C. S. Doyle, T. Kendelewicz, X. Carrier, G. E. Brown, JR., Surf. Rev. and Lett.6 (6), 1247 (1999).
[11] M. I. Sosulnikov, Y. A. Teterin, J. of Electron Spectrosc. and Relat. Phenom. 59, 111 (1992).

Study of Se clusters induced by direct vacuum evaporation

K. Kooser[1,2], E. Itälä[1], D. T. Ha[1], U. Joost[2], E. Nõmmiste[2] and E. Kukk[1]

[1]*Dept. of Physics and Astronomy, University of Turku, FI-20014 Turku, Finland*
[2]*Institute of Physics, Tartu University , Riia 142, 51014 Tartu, Estonia*

The chemistry of the chalcogene clusters like Se is an area of growing relevance because of their ability to form polyatomic complex chains and rings of a variety of sizes and shapes. These structural preferences influence the physical properties of their microclusters[1, 2]. Here we present the results of experimental study of the fragmentation of Se_n clusters (n<8) after Se *3d* photoionization and subsequent non-radiative decay, using the ion time-of-flight (TOF) spectroscopy and electron-ion-ion coincidence (PEPIPICO) technique.

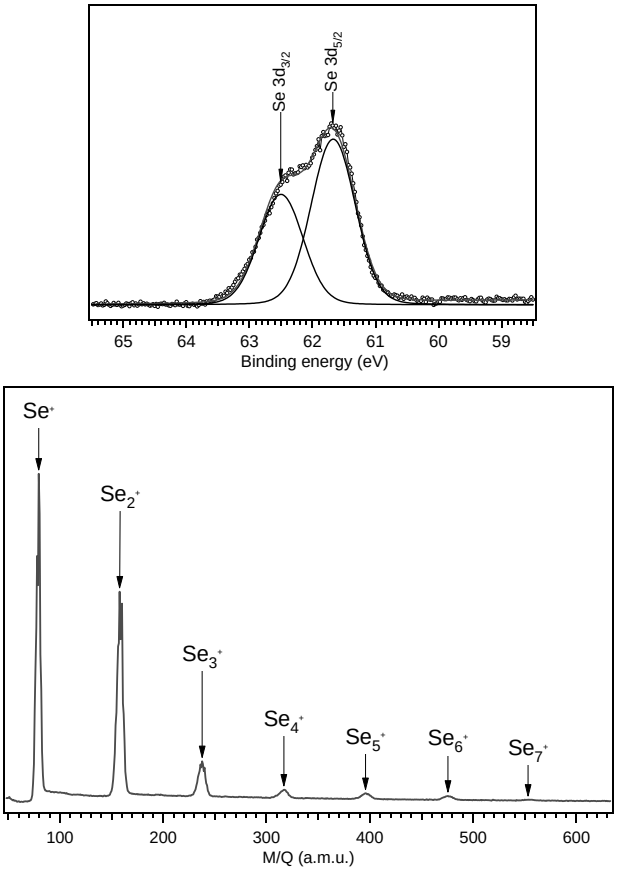

Figure 1. The Se 3d photoelctron spectrum of Se_n clusters (upper panel) measured with excitation energy 80 eV and TOF spectrum of Se clusters at excitation energy 55.8 eV (lower panel) .

The measurements were performed at beamline I411 in Max-Lab. In this work we used the experimental PEPIPICO setup which consists of a modified Scienta SES-100 electron analyser and a homemade Wiley-McLaren type ion TOF detector [3]. The Se sample was evaporated into the interaction area of the spectrometers from the boron nitride crucible (T≈235 ^{o}C) of effusion cell .

The base pressure of the system was below 6×10^{-7} mbar and the measurements were performed at room temperature.

In the upper panel of Figure 1 is depicted the Se *3d* photoelectron spectrum of Se_n clusters. From curve fitting results we determined the spin-orbit splitting 0.83 eV and the corresponding binding energy values for Se $3d_{3/2}$, $3d_{5/2}$ components, which are 62.5 eV and 61.67 eV, respectively. The FWHM of the spin-orbital splitting components was 0.82 eV. Energy calibration was done using the energies of Ar *3p* photolines for reference. The ion TOF spectrum (lower panel in Figure 1), recorded below the Se *3d* ionization level energy, shows seven ionized Se cluster peaks. The splitting of TOF peaks is caused by the five strong Se isotopes.

In Figure 2 is represented the PIPICO map of Se_n clusters in coincidence with Se *3d* photoelectrons. The detected fragmentation ion pairs are marked on the map and the patterns are indicated with arrows. The triply ionized final state corresponding to the fragment pair (Se^{2+}, Se^{+}) indicates either a second-step Auger decay or a direct double photoionization followed by the emission of an Auger electron. The slope of the shape of the fragment pair (Se^{+}, Se_2^{+}) (equal to -1.73) implies that this pattern is not created in direct two-body dissociation process, but is a combination with the three-body dissociation pathways of Se clusters containing more than 3 atoms.

The futher aim of this study is to continue a systematic investigation of dissociation of microclusters, for example, in the case of tellurium and bismuth, in order to collect more detailed fragmentation information for semimetallic Vb and Vb elements of periodic table.

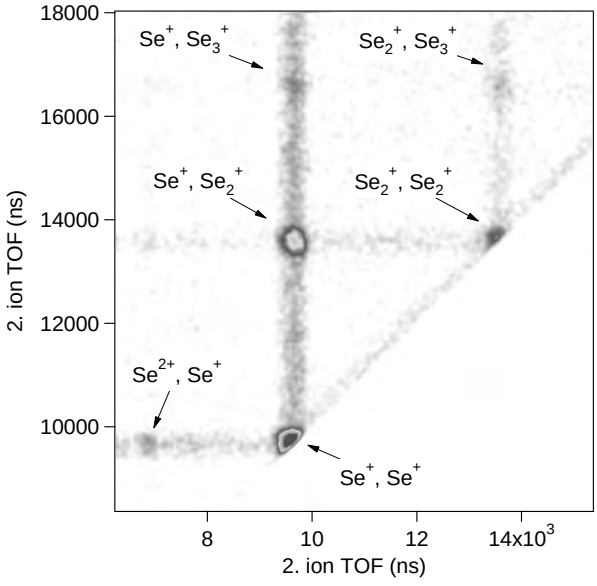

Figure 2. PIPICO map of selenium clusters recorded in coincidence with Se 3d photoionization.

This work was supported by Nordforsk Infrastructure Network "Advanced spectroscopy using MAX-laboratory in Lund" and the EU "Transnational Access to Research Infrastructures" programme. Financial support from the Academy of Finland is also acknowledged. The staff of MAX-lab is acknowledged for their help during the experiments. We thank the Electron Spectroscopy Group of Oulu University for the opportunity to share the experimental equipment.

[1] J. Berkowitz *et al.*, J. Chem. Phys. **48**, 4346 (1968).
[2] J. Becker *et al.*, Z. Phys. D **19**, 233 (1991).
[3] E. Kukk *et al.*, J. Electron Spectroscopy Relat. Phenomena **155**, 141 (2007).

Nuclear motion in Carbonyl Sulfide induced by resonant core excitation

J. Laksman, D. Céolin, M. Gisselbrecht and S. L. Sorensen
Department of Synchrotron Radiation Research, University of Lund, S-221 00 Lund, Sweden

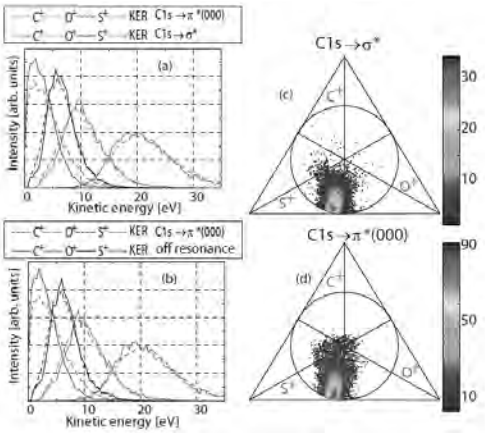

Figur 1. We compare KER distribution at C1s→ π∗ with (a) C1s→ σ∗ and (b) off resonance. The total KER displays no photon-energy dependence, but at C1s⁻¹1π¹∗ terminal fragments have more energy, while the central fragment gains less kinetic energy. In (c) and (d), by using Dalitz plots, we compare the fragment energy ratios. Decay from the C1s−1π1 ∗ state, imports a larger fraction of energy to the C⁺ fragment then from C1s⁻¹σ¹∗.

The imaging technique has since its introduction in the field of molecular spectroscopy had a significant impact on the research of molecular dynamics. Hsieh and Eland [1] developed techniques for data presentation and interpretation of three-body breakups. In the present investigation, we concentrate our study on OCS di- and trications produced after electron excitation to valence orbitals. The core-excited state decays rapidly via Auger transitions which populate ionized states that can dissociate. By analyzing the momentum of all fragments produced in dissociation we can filter out events connected with deformation from the initial linear geometry.

Fig. 1 (a) and (b) present individual fragment KER and the total KER at the C1s→ $\pi^*(000)$ excitation at 288.2 eV and C1s→ σ^* ionization at 311.5 eV. These are compared to the off C1s resonance case at 286 eV. Our measured total KER distributions exhibit no significant changes as a function of photon energy, and have the same mean-value and standard-deviation as Lavolleés results [2]. However, the terminal ions O^+ and S^+ are shifted to lower energies for C1s→ π^*, while C^+ has a rather significant shift to higher energies at this resonance. This behavior suggests that the bending motion is caused in the C1s$^{-1}\pi^{*1}$ excited state.

A consequence of the coincidence technique is that we measure not only the individual ion energy, but also their correlation with respect to each other. To present correlation between the three fragments KER, one can define the dimensionless parameter ε_i that is related to the energy as the normalized square of the linear momentum. p_i is the momentum vector of fragment $\varepsilon_i \in \{1, 2, 3\}$. It has been shown that due to the kinematic constraint $\sum_i \varepsilon_i \equiv 1$, all data must define a plane in space so after a suitable coordinate transformation the data can be presented in a 2D Dalitz plot. Conservation of linear momentum, $\sum_i p_i \equiv 0$, induces an additional constraint of the data to be defined within the unit-circle [3]. Fig. 1 (c) and (d) presents Dalitz plots for C1s→ π^* and C1s→ σ^* resonances. Off resonance is omitted since it is identical to C1s→ σ^* case. For both photonenergies the density has its maximum

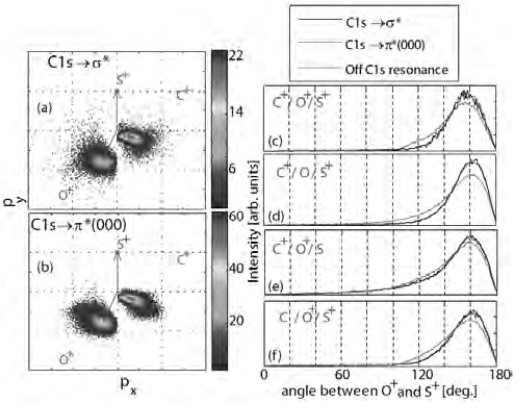

Figur 2. Newton diagrams for (a) C1s⁻¹σ¹∗ and (b) C1s⁻¹π¹∗. To compare angluar correlations a histogram is plotted in (c) for both photon energies as well as off resonance. At C1s$^{-1}\pi^1$ state smaller angles are reached. The same behavior is seen for all three-body breakups (d,e,f), thus suggesting that bending is induced in the core-excited state.

for small ε_{C+} values, which is expected considering that it is the center fragment. However, at the C1s→ π^* resonance, the density reaches higher ε_{C+} values, meaning that C^+ gains a larger fraction of the KER for that resonance, as was shown in the energy distribution plot.

An additional commonly used method to present data from three-body breakups is the Newton diagram that displays vector correlations. In Fig. 2 (a) and (b), Newton diagrams have been produced for $C^+/O^+/S^+$ at the $C1s^{-1}\pi^*$ and $C1s^{-1}\sigma^*$ states. Transformation of each triple coincidence event has been carried out into one plane so that p_{S+} is normalized and directed vertically. Considering what we saw in the Dalitz plots, we expect O^+ and S^+ to approach each other at the $C1s^{-1}\pi^*$ state, because the higher energy ratio for C^+ should be connected to a larger bending. To compare the Newton diagrams more easily we have, in Fig. 2 (c), plotted a histogram of the angle between O^+ and S^+. Clearly, as was anticipated, they reach smaller values at the $C1s^{-1}\pi^*$ state. The fact that correlations between angles gives the same information as the other data representations (KER, Dalitz and Newton) as an easily comparable and interpretable distribution, we continue our analysis by only studying angular correlations. To find more conclusive evidence that bending is induced by the core excitation rather than in one of the final states, we want to investigate also the other three body breakups. Fig. 2 (d-f) presents angular correlations for the pathways of the dication where the neutral has been estimated by conservation of momentum. Just as for $C^+/O^+/S^+$, off and above resonance distributions are identical while at the $C1s^{-1}\pi^{*1}$ state, smaller angles are always reached, which is an evidence that the bending motion takes place in that state.

Fig. 3 (a) presents total KER for the C^+/OS^+ channel. The peak lies between 4 and 5 eV, which considering the poor statistics, is in agreement with the predicted 4 eV [4]. Our fitting of the anisotropy parameter β, is displayed in Fig. 3 (b). The angle, θ, is taken as the two fragments meanvalue. The estimated positive value ($\beta \approx 0.39$) is far from totally anisotropic, but is still in qualitative agreement with a parallel transition, suggesting that the excitation induces the bending. Auger decay then populates electronic states in the dication and dissociation is prompt. The selection of this specific channel gives us important information not only on the final state dissociation but tells us that the nuclear motion in the core excited state and the photon absorption process cannot be regarded as separate for this particular case. Indeed, at the time of the excitation, photoabsorption triggers the nuclear motion. The bending mode can be excited and the corresponding transition dipole moment is in-plane and perpendicular to the initial $C_{\infty v}$ axis. By selecting the C^+/OS^+ fragment, we only monitor molecules undergoing a bending motion, with a transition dipole moment aligned with the polarization axis. The subsequent dissociation retains the memory of this alignment, which is reflected in the intensity distribution of the ejected fragments, parallel to the polarization vector. From the triple-coincidence channel, we have found that the bending motion that causes isomerization is induced in the $C1s^{-1}\pi^{*1}$ state.

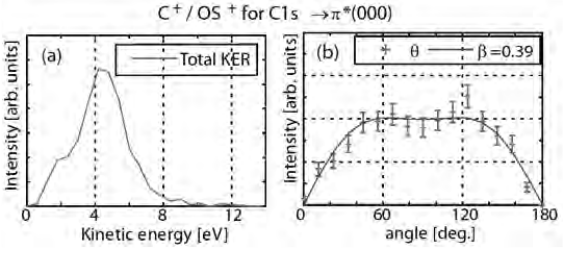

Figur 3. The pathway C^+/OS^+ was discovered, thus giving evidence for isomerization of the dication. (a) Displays KER distribution which is in agreement with the value predicted by Brites *et al.* in Ref. 4. (b) Gives a fitting of the β parameter. The positive anisotropy suggests that the bending motion cannot be separated from the core-excitation.

[1] S. Hsieh and J. H. D. Eland, J. Phys. B: At. Mol. Opt. Phys. 30, 4515 (1997)
[2] Private communication with M. Lavolleé
[3] C. Maul and K. H. Gericke, J. Phys. Chem. A 104, 2531 (2000)
[4] V. Brites, J. H. D. Eland and M. Hochlaf, Chem. Phys. 346, 23 (2008)

Materials and interfaces in organic electronics

L. Lindell, S. Braun and M. Fahlman

Department of Physics, Chemistry and Biology, Linköping University, SE-581 83 Linköping, Sweden

The growing field of organic electronics relies on the use of organic conjugated molecules and polymers as active components in multi-layer device applications such as light-emitting diodes (LEDs and by extension displays, lighting), solar cells, field-effect transistors (FETs and by extension integrated circuits), (bio)chemical sensors and storage devices. Since all organic-based devices are made by deposition of successive layers (metal, oxide, insulating or semiconducting layers), many key electronic processes (such as charge injection from metallic electrodes, charge recombination into light or light conversion into charges, etc.) occur at interfaces. Although a large body of knowledge has been accumulated on the characterization of such interfaces (especially morphological issues), a detailed and unified understanding of the electronic processes occurring at these interfaces is currently missing, though significant progress have recently been made on this topic [1-3]. It has now become clear that improvement of the device performances requires tuning the interfacial zones to either enhance or impede charge generation, recombination, or injection. Our research aims to generate the experimental data needed for further developing the theoretical description for energy level alignment of organic-organic and metal-organic heterojunctions in general [1-3] and multilayer stacks in particular [4,5] which will provide the underpinning for developing new materials and interface engineering concepts.

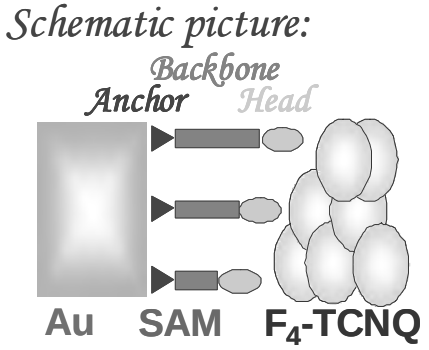

The so-called Integer Charge Transfer (ICT) model has been developed to describe the weakly-interacting interfaces typically present in organic electronic devices. A key feature of the model is the relation between the Fermi level of the substrate and the electron affinity (EA) / ionization potential (IP) of the molecules at the interface determine the size and direction of the interface dipole at the heterojunction. The EA and IP often will differ from the bulk film values due to differences in inter- and intramolecular order, screening, etc [2,3]. In order to probe the effect of heterojunction separation distance and polarizability on the EA/IP of the molecular overlayer, a series of well defined self assembled monolayers (SAM) deposited on gold substrates were used

(obtained form the group of Prof. K. Uvdal). Alkane thiols of differing lengths were chosen as spacers and F4-TCNQ as the molecular layer due to its excellent electron accepting properties, ensuring charge transfer from the gold substrate to F4-TCNQ and subsequent dipole formation for all SAM combinations. The intermolecular order of the SAM layer and the F4-TCNQ overlayer was determined using NEXAFS. The ionization potential of the F4-TCNQ molecules at the interface, referred to as the E_{ICT-} in the ICT model, where obtained for the various SAM samples and in combination with F4-TCNQ deposited on chemically cleaned gold provided an estimate for the distance dependent evolution of the substrate screening contribution to the E_{ICT-} value. In a separate set of experiments, SAMs of the same alkane length but with differing end groups: methyl, alkyl and carboxyl, were used to determine the effect of different polarizability at the interface with the F4-TCNQ overlayer.

References

1. C. Tengstedt, W. Osikowicz, W.R. Salaneck, I.D. Parker, C-H. Hsu and M. Fahlman, Appl. Phys. Lett. 88 (2006) 053502.
2. M. Fahlman, A. Crispin, X. Crispin, S.K.M. Henze, M.P. de Jong, W. Osikowicz, C. Tengstedt and W.R. Salaneck, J. Phys.: Condens. Matter 19 (2007) 183202.
3. S. Braun, W. R. Salaneck and M. Fahlman, Adv. Mater., 21 (2009) 1450.
4. S. Braun, M. P. de Jong, W. Osikowicz and W. R. Salaneck, Appl. Phys. Lett. 91 (2007) 202108.
5. S. Braun, X. Liu, W.R. Salaneck and M. Fahlman, Org. Electron. 11 (2010) 212.

Valence photoelectron spectroscopy of size varied alkali metal clusters

M.-H. Mikkelä, K. Jänkälä, S.-M. Huttula, S. Urpelainen, and M. Huttula

Department of Physical Sciences, University of Oulu, Box 3000, 90014 Oulu, Finland
[a] *email : mikko-heikki.mikkela@oulu.fi*

M. Tchaplyguine[1], Ch. Zhang[2], T. Andersson[2], and O. Björneholm[2]
[1]*MAX-lab, Lund University, Box 118, 22100 Lund, Sweden*
[2]*Department of Physics and Astronomy, Uppsala University, Box 530, 7121Uppsala, Sweden*

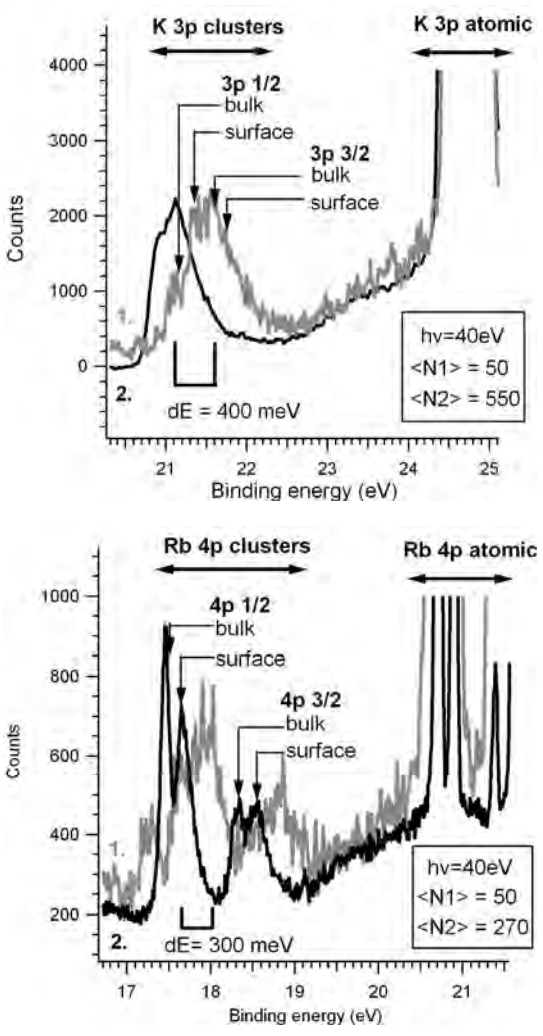

Figure 1. Experimental 3p and 4p core-level photoelectron spectra of varied size K clusters (above) and Rb clusters (below).

Clusters consist from finite number of atoms or molecules forming an intermediate phase of matter between individual atoms and solid state. Cluster's physical properties vary as function of cluster size. Large clusters pose physical properties similar with solid state where small clusters in quantum regime resemble molecules or atoms. Evolution and emergence of metallicity in clusters for metal and semiconductor type elements has been under a keen attention during the past decades [1]. Metallicity in clusters emerges upon semi-complete formation of valence-level bands. This is a cluster size depended process and typically insulator-to-metal transition of cluster occurs above specific critical cluster size. Thus variation of cluster size in-situ close to quantum regime can be used as viable method to probe evolution of conductivity in nanoscale particles.

Photoelectron spectroscopy (PES) is established tool to investigate electronic structure of clusters and solid. Core- and valence-level photoelectron spectroscopy of clusters provides insight to the chemical environment inside a cluster revealing information about the bonding mechanism of the cluster [2]. Relative binding energy values of core-level states can be also used to carry out approximative cluster size estimations using so called conduction sphere approximation [3].

In present project core- and valence-level photoemission of small and size varied Rb and K clusters were studied. All the experiments were carried out at soft X-ray undulator beamline I411 using R4000 hemispherical analyzer located at permanent end-station. Clusters were produced using Exchange

Cluster Source (EXMEC) which was recently designed especially for the production of small, neutral and size varied metal clusters. Detailed description of EXMEC is given in Ref [4]. Argon was used as a driver gas in the set-up and in parallel with metal clusters also argon clusters were produced. Presented results show that EXMEC is fully capable to produce adequate sample densities even for valence photoelectron spectroscopy measurements in the cluster size regime of 50-550 atoms. Rb and K samples were evaporated in resistively heated oven and vapor pressure in the range of 10^-3 mbar was achieved inside the crucible.

Experimental core-level photoemission spectra of Rb and K are presented in the figure 1. Conduction sphere approximation was applied to core-level photoelectron spectra to perform metal cluster size estimations. Valence-level photoemission spectra of Rb and K are shown in the figure 2. Apparent binding energy shift between spectral cluster components in core- and valence-level spectra is observed between different metal cluster formation conditions. In the case of valence photoelectron spectra also moderate change of line shape is detected for small clusters.

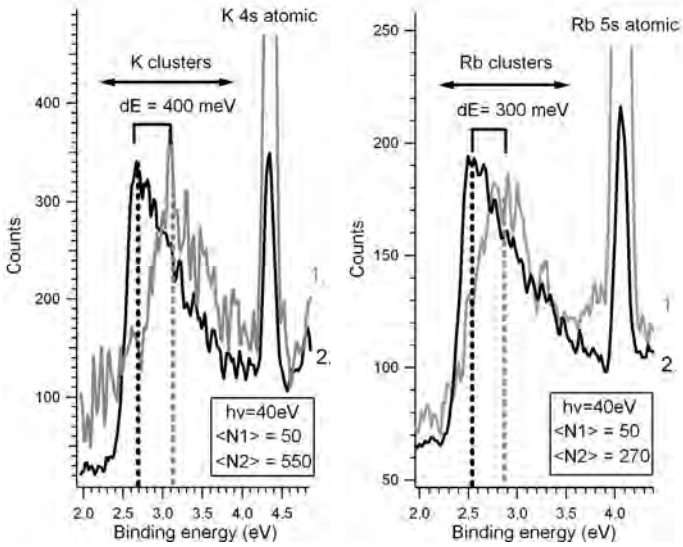

Figure 2. Experimental valence-level photoelectron spectra of varied size K clusters (left) and Rb clusters (right).

References:

[1] B.V. Issendorff, O. Cheshnovsky, Annu. Rev. Phys. Chem. 56, 549–580 (2005).

[2] V. Senz, T. Fischer, P. Oelßner, J. Tiggesbäumker, J. Stanzeld, C. Bostedt, H. Thomas, M. Schöffler, L. Foucar, M. Martins, J. Neville, M. Neeb, T. Möller, W. Wurth, E. Rühl, R. Dörner, H. Schmidt-Böcking, W. Eberhardt, G. Ganteför, R. Treusch, P. Radcliffe, K.-H. Meiwes-Broer, Phys. Rev. Lett. 102 , 138303 (2009).

[3] M. Seidl, J.P. Perdew, M. Brajczewska, C. Fiolhais, J. Chem. Phys. 108, 394 8182–8189 (1998).

[4] M. Huttula, M.-H. Mikkelä, M. Tchaplyguine, and O. Björneholm, J. Electron Spectrosc. Relat. Phenom. doi:10.1016/j.elspec.2010.02.012 accepted, (2010).

Photoelectron angular distribution and linear magnetic dichroism in the *4p* photoemission from Rb atoms

J. Niskanen[1,2], S. Urpelainen[1], K. Jänkälä[1], J. Schulz[1,3], S. Heinäsmäki[1], S. Fritzsche[1,4], N. M. Kabachnik[1,5], S. Aksela[1] and H. Aksela[1]

[1] *Department of Physics, P.O. Box 3000, 90014 University of Oulu, Finland*
[2] *Theoretical Chemistry, Royal Institute of Technology, Stockholm,Sweden*
[3] *Center for Free-Electron-Laser Science (CFEL) at DESY, D-22603 Hamburg, Germany*
[4] *GSI Helmholzzentrum f˙ur Schwerionenforschung, D-64291 Darmstadt, Germany*
[5] *Institute of Nuclear Physiscs, Moscow State University, Moscow RU-119991, Russia*

Introduction

In this work [1] the angular distribution of photoelectrons and linear magnetic dichroism in the angular distribution (LMDAD) for the 4*p* photoemission from Rb atoms in the ground state, oriented by laser pumping, were measured in the photon energy range from 50 to 100 eV. The experimental results were compared with the multiconfiguration Dirac-Fock (MCDF) calculations. In the study we showed that the zero-crossing of the LMDAD as a function of energy is connected with the Cooper minimum in the cross section. This fact can be used for an accurate determination of the position of the Cooper minimum.

The Experiment and Results

The experiments were carried out on the high-resolution soft-x-ray undulator beamline I411 on the 1.5 GeV MAX II electron storage ring. For the purposes of studying the angular anisotropy, the Rb photoelectron spectra were recorded using the permanent Scienta R4000 end-station mounted at the end of the beamline. To record the photoelectron spectra from the laser-pumped atoms a modified Scienta SES-100 electron analyzer with a resistive-anode position-sensitive detector [2, 3] mounted on the so-called 1 m section of the beamline was used.

The photoelectron spectra for determining the angular anisotropy parameters were recorded at a constant pass energy of 50 eV at photon energies of 50, 60, 72, and 100 eV. To determine the angular anisotropy parameter β the spectra were recorded at three different angles with respect to the electric-field vector of the incoming horizontally linearly polarized radiation. The chosen emission angles were 0°, 30°, and 54.7°. To account for possible instabilities in the photon-beam and electron-analyzer transmission effects at different kinetic energies, as well as at different emission angles due to the off-center rotation of the electron energy analyzer about the photon beams, the He 2*s* photoline was recorded for normalization purposes together with the Rb photolines. The He line also serves as an important calibration source as their β value is a well-known constant 2 at all photon energies.

The laser radiation was produced using a commercial Coherent 899 Ti:Sa laser pumped by a 10 W Coherent Verdi Nd Vanadate laser operating at 532 nm in multimode [4]. The output power at the desired excitation wavelength 780 nm corresponding to Rb $5s \longrightarrow 5p_{3/2}$ resonance was measured to be around 1.2 W directly after the laser; the laser was focused to a spot of approximately 2 mm in diameter. Both left-handed and right-handed circular polarization of the laser radiation were used and the polarization state was changed from the natural linear polarization produced by the laser to a circular polarization using a quarter wave plate after the laser optics.

The experimental spectrum and β parameter as well as LMDAD are shown in Figure 1. The zero-crossing of the LMDAD near 75eV is due to Cooper minimum of the d-wave amplitude. In

case of d and s continua like here, the β parameter also vanishes at the d-wave Cooper minimum. MCDF calculations were compared to the experiment and both LMDAD and the β parameter needed to be shifted +10 eV in photon energy to match the experiment. Interchannel coupling was suggested to be responsible for this shift.

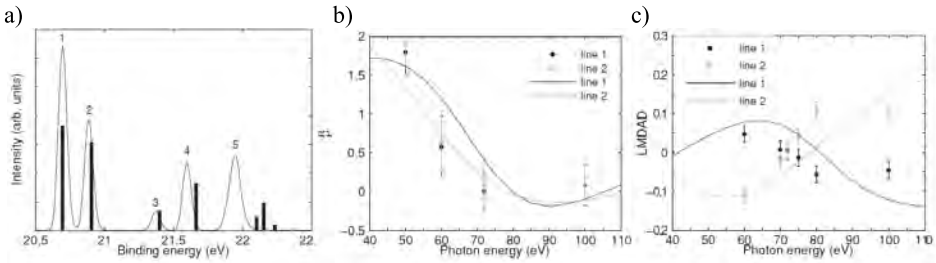

Figure 1. The 4p photoelectron spectrum of Rb atom with calculated states and cross sections (a). The angular distribution β parameter for lines 1 and 2 from calculation and from the experiment (b). The calculated and experimental LMDAD for lines 1 and 2 (c). A shift of +10 eV has been applied to the calculations.

Conclusions

We reported the first measurement of the angular distribution of photoelectrons from 4p photoionization of free Rb atoms and the linear magnetic dichroism in the angular distribution for the laser-oriented Rb ground state in the photon energy range of 50–100 eV. A high energy resolution of the experiment allowed us to perform the measurements for all fine-structure components of the first ionic multiplets. The experimental results were compared with the MCDF calculations. In general, the calculations reproduced well the experimental values of the angular anisotropy parameters of 4p photoelectrons and the relative LMDAD as well as their energy dependence in the considered energy range. In the energy dependence of LMDAD, we observed the zero-crossing connected with the Cooper minimum of the cross section. The zero-crossing of LMDAD can be used as a convenient and accurate method for measuring the position of the Cooper minimum.

References

[1] J. Niskanen, S. Urpelainen, K. Jänkälä, J. Schulz, S. Heinäsmäki, S. Fritzsche, N. M. Kabachnik, S. Aksela and H. Aksela Phys. Rev. A **81**, 013406 (2010).

[2] M. Huttula, M. Harkoma, E. Nõmmiste and S. Aksela, Nucl. Instrum. Methods Phys. Res. A **467**, 1514 (2001).

[3] M. Huttula, S. Heinäsmäki, H. Aksela, E. Kukk, and S. Aksela, J. Electron Spectrosc. Relat. Phenom. **156-158**, 270 (2007).

[4] J. Schulz, M. Tchaplyguine, T. Rander, H. Bergersen, A. Lindblad, G. Ö hrwall, S. Svensson, S. Heinäsmäki, R. Sankari, S. Osmekhin, S. Aksela, and H. Aksela, Phys. Rev. A **72**, 032718 (2005).

Observation of metal-to-semiconductor transition in small free tin clusters using photoelectron spectroscopy

S.Osmekhin [a], M.-H. Mikkelä, M. Huttula, and S. Aksela
Department of Physical Sciences, University of Oulu, Box 3000, 90014 Oulu, Finland
[a] *email : sergey.osmekhin@oulu.fi*

M. Tchaplyguine[1], T. Andersson[2], and O.Björneholm[2]
[1]*MAX-lab, Lund University, Box 118, 22100 Lund, Sweden*
[2]*Department of Physics and Astronomy, Uppsala University, Box 530, 7121Uppsala, Sweden*

.

Clusters as an intermediate phase of matter between a single atom and the solid state are a permanent subject of studies in fundamental and applied research. Among other issues the physical properties of clusters of group 14 elements (C, Si, Ge, Sn, and Pb) are of special interest because, on the macroscopic scale, substances made up of these elements with the same number of valence electrons switch from semiconductors to metals. In present study photoelectron spectroscopy using Exchange Metal Cluster Source (EXMEC) and synchrotron radiation is used to observe possible metal-to-semiconductor transition in small free tin clusters.

Tin is reported to be a substance with both semiconductor and metallic properties, depending on the adopted crystalline structure. The most direct method for obtaining information on the electronic structure and its transformation is photoelectron spectroscopy (PES). This has been shown lately for small lead clusters [1]. PES and synchrotron radiation are used to examine transformation of the valence electronic structure and 4d core levels for tin clusters over a wide size range, up to about 500 atoms per a cluster. The present studies demonstrate that the 4d core-level energy changes are a sensitive probe of the metal-to-semiconductor transition in the size range under investigation. A self-consistent picture arises from a comparison of the work functions derived from the 4*d* photoelectron spectra, the experimental ionization energies extracted from the 5*p* photoelectron valence spectra, and the expectations from the metallic sphere model for the clusters.

Measurements were carried out at the undulator beamline I411 using the permanent end-station equipped with a Scienta R4000 hemispherical electron energy analyzer. The EXMEC source was used to produce free Sn clusters in interactions between Ar clusters

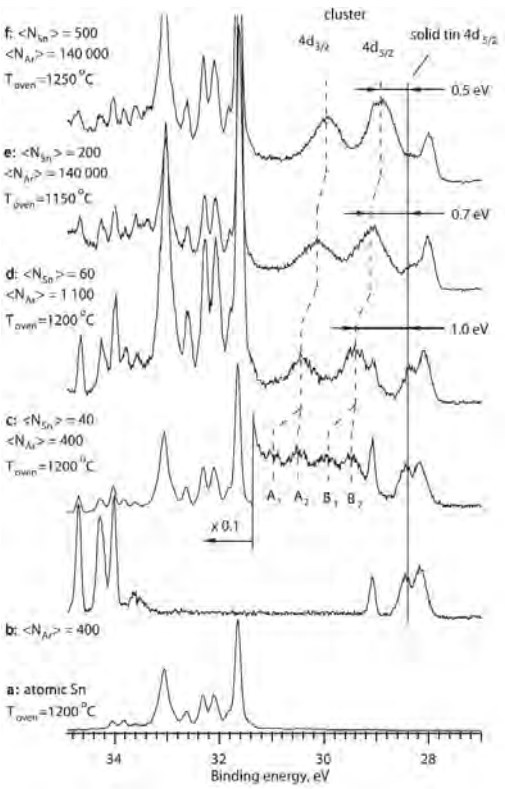

Figure 1 Spectra of tin and argon clusters using several EXMEC settings. Experimental settings are shown for each spectrum.

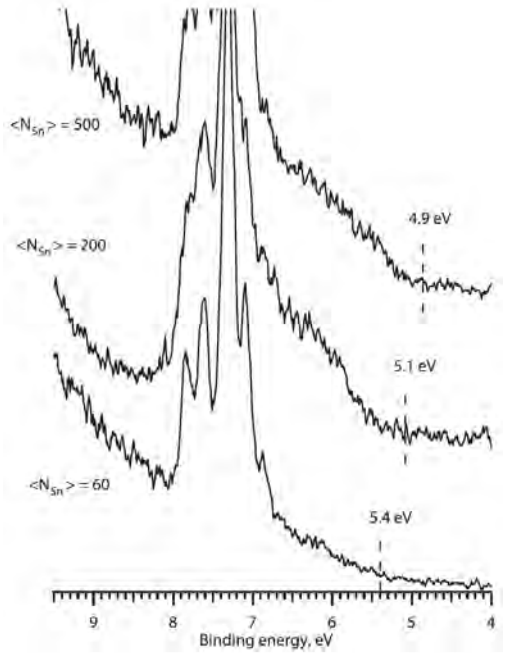

Figure 2 The 5p photoelectron spectra of atomic tin and tin clusters. In the lower spectrum the average size calculated from the difference in the core-level 4d energies is 60 atoms per tin cluster,and the ionization potential estimated from the same difference is 5.4 eV. In the middle spectrum the average size is 200 atoms per tin cluster and the ionization potential energy is 5.1 eV, and in the upper spectrum the average size is 500 atoms per tin cluster and the ionization potential energy is 4.9 eV.

and free Sn vapor. A detailed description of EXMEC set-up is given in Ref [2]. Induction heating specially designed for low vapor pressure metals was utilized to evaporate Sn in EXMEC source. The temperature of the molybdenum crucible in the oven was in the range of 1150–1250◦C producing Sn vapor pressure of 10^−3 mbar inside of the crucible.

Experimental spectra of atomic and varied size of free clusters of Sn are presented in figure 1 and 2. Sn cluster sizes were determined in the process of spectral analysis using the metallic droplet model [3] for the clusters. Radical spectral changes of Sn 4d spectra in figure 1 are observed when the estimated Sn cluster size is in the range of 40 atoms per cluster. In Ref [4] we have discussed about several possible explanations for the spectral pattern of the 4*d* core-level response for the smallest observed clusters. The assumption of presence of two different phases (metallic and nonmetallic) in the Sn cluster beam is believed to be correct explanation. Metal-to-semiconductor transition is reported to occur on size selected anion tin clusters at this size regime [5]. Within this assumption the phase-transition energy as seen by PES is determined to be ≈0.5 eV.

References:

[1] V. Senz, T. Fischer, P. Oelßner, J. Tiggesbäumker, J. Stanzeld, C. Bostedt, H. Thomas, M. Schöffler, L. Foucar, M. Martins, J. Neville, M. Neeb, T. Möller, W. Wurth, E. Rühl, R. Dörner, H. Schmidt-Böcking, W. Eberhardt, G. Ganteför, R. Treusch, P. Radcliffe, and K.-H. Meiwes-Broer, Phys. Rev. Lett. 102, 138303 (2009).

[2] M. Huttula, M.-H. Mikkelä, M. Tchaplyguine, and O. Björneholm, J. Electron Spectrosc. Relat. Phenom. doi:10.1016/j.elspec.2010.02.012 accepted (2010)

[3] M. Seidl, J.P. Perdew, M. Brajczewska, and C. Fiolhais, J. Chem. Phys. 108, 394 8182–8189 (1998).

[4] S. Osmekhin, M. Tchaplyguine, M.-H. Mikkelä, M. Huttula, T. Andersson, O. Björneholm, and S. Aksela, Phys. Rev. A 81, 023203, (2009)

[5] L-F Cui, L-M Wang, and L-S Wang, J. Chem. Phys. 126, 064505 (2007)

Effects of concentration on the molecular surface structure of simple inorganic aqueous electrolytes

Niklas Ottosson[a,*], Wandared Pokapanich[a], Svante Svensson[a], Gunnar Öhrwall[b] and Olle Björneholm[a,*]

[a]*Department of Physics and Materials Science, Uppsala University, SE-751 21 Uppsala, Sweden*

[b]*MAX-lab, Lund University, Box 118, SE-221 00 Lund, Sweden*

Our understanding of the aqueous solution/vapor interface has undergone dramatic changes over the last decades. Surface sensitive experiments[1-4] and molecular simulations[5,6] have shown that the surface structure of aqueous solutions is strongly dependent on the identity of the constituent ions to a much larger extent than what previously have been assumed. Contrary to the textbook description, based on classical electrostatic continuum models,[7] it must now be considered well established that certain large and polarizable anions can be surface enriched and locally display very different density profiles than that of their counter ions. While the main characteristics of this fascinating phenomenology is becoming accepted by the scientific community, the multi-dimensional parameter space governing the exact surface propensity of a given ionic species for the solution/vapor interface is large and the possible mutual dependencies are far from disentangled. As an example, while the iodide anion has been found to be surface enriched under normal conditions, Krisch *et al.* have recently demonstrated how even moderate concentrations of organic surfactants dramatically can suppress its surface activity,[8] illustrating how multi-component systems may behave very differently from what could be expected from their components in isolation.

Using photoelectron spectroscopy (PES), in conjunction with the liquid-jet setup we operate at I411, we here investigate how the ion composition in the interface region evolves with concentration in two simple aqueous alkali-halide solutions, LiBr and LiI. We pursue the following line of reasoning; if a system exhibits a structured interface with distinctly different anion and cation profiles in the low concentration regime, these differences should eventually be reduced at higher concentration, due to the increasing Coulomb energy penalty for maintaining such a spatial charge separation. Changes in the relative anion/cation surface composition at gradually higher concentrations thus carry indirect information about the system in the dilute limit. The considerable surface sensitivity achieved in PES is ideal to monitor the solution surface region and the photoemission lines pertaining to each ionic species are easily separated.

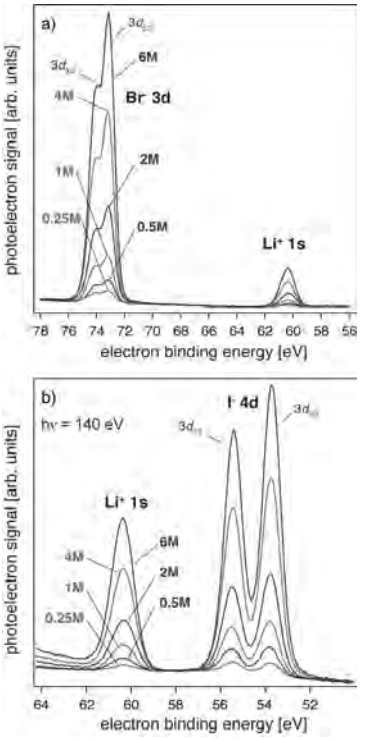

Figure 1 shows photoelectron spectra of LiI and LiBr aqueous solutions at concentrations ranging from 0.25M to 6M. Trace a), taken from LiBr solutions, displays $Li^+_{aq}1s$ and Br^-_{aq} $3d_{5/2,3/2}$ features at 60.1 and 73.2/74.3 eV BE, respectively. The lithium cations in the LiI solutions (trace b) are again monitored through the $Li^+_{aq}1s$ line but this time contrasted against the $I^-_{aq}4d_{3/2,5/2}$ feature at 53.8/55.5 eV

BE, a unique signature of the iodide anions. These values are consistent with previous reports[9] and no concentration dependence on the BEs is observed. All spectra were recorded at 140 eV photon energy, resulting in kinetic energies around the minimum of the photoelectron mean free path leading to an appreciable surface sensitivity.[10] The different anion and cation PE intensities at a given concentration primarily arise from differences in atomic ionization cross sections. The main concentration dependent effect is that the absolute PE signal intensities of the respective anion and cation features in figure 1 increase monotonously, while non-stoichiometric variations in the surface structure with concentration will be manifested in varying anion/cation signal intensity ratios. A small, relative decrease in the $I^-_{aq}4d/Li^+_{aq}1s$ PE signal ratio with increasing concentration can be discerned in figure 1b), while the evolution of $Br^-_{aq}3d/Li^+_{aq}1s$ ratio is less clear.

To quantitatively evaluate how the surface composition of simple LiBr and LiI solutions varies with total concentration, the respective photoemission features in figure 1 were fitted and the relative anion/cation PE signal intensity ratios obtained from integration of the fits at each concentration are shown in figure 2. The Y-axis values are arbitrarily chosen to be 1 for the observed ratio at the lowest studied concentration (0.25M). Apparently, the surface structure of the two salt solutions evolves very differently as function of concentration; while no significant change is observed in the Br^-/Li^+ ratio (filled squares), the I^-/Li^+ ratio (open circles) decreases with approximately 17% when going from 0.25M to 6M. We thus experimentally observe a gradual weakening of the I^-/Li^+ separation in the interface region at higher concentrations, while the corresponding situation for lithium bromide is less clear. The effect is apparently much less pronounced for the smaller halides, and already for LiBr and NaBr we could not observe a concentration dependence of the surface ionic structure using PES. These observations are compatible with recent MD simulations employing polarizable force fields, predicting that the charge-separation in the low concentration regime is much weaker for bromide salts than for iodide salts (and even weaker for chloride salts). While the saturation of available surface sites surely plays a role in reducing the surface activity of large polarizable anions it should be noted that the present observation cannot be accounted for by invoking a simple Langmuir isotherm model, which predicts a proportional reduction of the anion and cation surface activity as they are assumed to be non-interacting. Ion-ion interactions rather become increasingly important for determining the molecular surface structure of simple aqueous electrolytes.

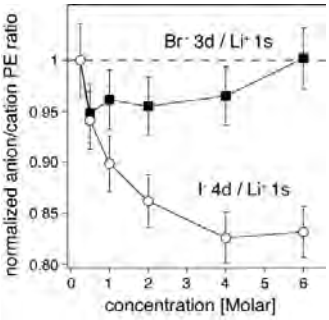

References

(1) Petersen, P. B.; Saykally, R. J.; Mucha, M.; Jungwirth, P. *J Phys Chem B* **2005**, *109*, 10915.
(2) Ghosal, S.; Hemminger, J. C.; Bluhm, H.; Mun, B. S.; Hebenstreit, E. L. D.; Ketteler, G.; Ogletree, D. F.; Requejo, F. G.; Salmeron, M. *Science* **2005**, *307*, 563.
(3) Ottosson, N.; Vacha, R.; Aziz, E. F.; Pokapanich, W.; Eberhardt, W.; Svensson, S.; Ohrwall, G.; Jungwirth, P.; Bjorneholm, O.; Winter, B. *J Chem Phys* **2009**, *131*.
(4) Winter, B.; Weber, R.; Hertel, I. V.; Faubel, M.; Vrbka, L.; Jungwirth, P. *Chem Phys Lett* **2005**, *410*, 222.
(5) Jungwirth, P.; Tobias, D. J. *J Phys Chem B* **2000**, *104*, 7702.
(6) Dang, L. X.; Chang, T. M. *J Phys Chem B* **2002**, *106*, 235.
(7) Onsager, L.; Samaras, N. N. T. *J. Chem. Phys.* **1934**, *2*, 528.
(8) Krisch, M. J.; D'Auria, R.; Brown, M. A.; Tobias, D. J.; Hemminger, J. C.; Ammann, M.; Starr, D. E.; Bluhm, H. *J Phys Chem C* **2007**, *111*, 13497.
(9) Winter, B.; Weber, R.; Hertel, I. V.; Faubel, M.; Jungwirth, P.; Brown, E. C.; Bradforth, S. E. *J Am Chem Soc* **2005**, *127*, 7203.
(10) Hüfner, S. *Photoelectron Spectroscopy*; Springer-Verlag Berlin Heidelberg, 1995.

Free atom *4f* photoelectron spectra of Au, Pb, and Bi

M. Patanen, S. Aksela, S. Urpelainen, T. Kantia, S. Heinäsmäki, H. Aksela
Department of Physical Sciences, P.O. Box 3000, 90014 University of Oulu, Finland

High resolution *4f* photoelectron spectra (PES) have been measured from Au, Pb, and Bi vapors using synchrotron radiation [1]. New accurate binding energy values are found to deviate more than 0.3 eV for Au from the previous results demonstrating the need for new precise values e.g. for chemical shift and cluster studies. For Bi both atomic and diatomic lines have been observed simultaneously, molecular lines at 0.96 eV lower binding energies. Fine structure splitting created by the coupling of the *4f* core hole to the open *6p* shell has been found to manifest itself in this high resolution experiment as slightly different line widths for *4f* spin components. The fine structure has been investigated also theoretically by calculating the *4f* photoionization energies, intensities, and lifetimes using the multiconfigurational Dirac-Fock (MCDF) approach.

Measurements were carried out using synchrotron radiation from undulator beamline I411 [2] at MAXII storage ring. Solid samples were evaporated with an inductively heated oven which has turned out to be very convenient in generating high temperatures for low volatile samples. It is much faster than resistive heating in reaching the operating temperatures, but due to the generated magnetic fields the heating needs usually to be pulsed: when the heating is applied the electron signal from detector is vetoed. This causes some unavoidable decrease in data collection efficiency, typically 10-30%. Our present setups have been described in some more detail in references [3-5].

Bi is known to evaporate in almost one to one ratio as atomic Bi and diatomic Bi_2 molecules. Therefore in Bi measurements a special molybdenum crucible consisting of two parts with different temperatures was used to effectively control the ratio between Bi and Bi_2. A modified Scienta SES-100 electron energy analyzer [4] was used to record the emitted electrons at the "magic" 54.7° angle corresponding to the angle-independent measurements. The electron spectrometer is equipped with resistive anode positive sensitive detection system making possible gating of the detection of electrons during short inductive heating intervals in order to avoid disturbances of the high frequency induction field. The energy of the ionizing radiation was 170, 200, and 220 eV in the measurements of Au, Pb, and Bi, respectively. The vapor PES were calibrated by recording very well known Kr *3d* PES simultaneously with the vapor lines. The estimated oven temperatures were 1420, 720, and 675 °C for Au, Pb, and Bi, respectively.

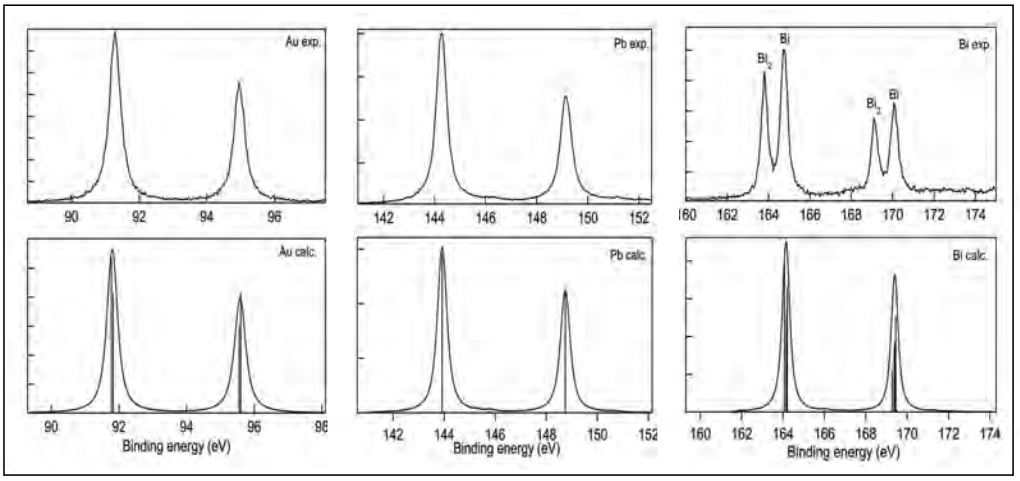

Fig. 1. Experimental and calculated 4f photoelectron spectra of Au, Pb, and Bi. Vertical lines in calculated spectra show the states with different total angular momentum.

4f core hole's lifetime is so short that the lifetime broadening prevents the fine structure in the *4f* PES to be distinguished experimentally. In order to clarify the fine structure inside the peaks, *ab initio* MCDF method based calculations were performed using GRASP92 and GRASP2K packages. In the case of Au, single configuration was needed for an appropriate description of the state. MC calculations for ionized states were needed to achieve better absolute energies for the states for Pb and Bi, where excitations from the *5p* and *5d* orbitals to the *6p* orbital were also implemented to the active space. Photoionization probabilities were approximated using a frozen-core scheme and for Au and Pb, and the lifetimes of the *4f* ionized states were approximated by computing transition rates to all possible Auger final states.

4f photoelectron lines for Au, Pb, Bi, and Bi_2 have been observed and revised or completely new binding energy values have been determined. Coupling between *4f* hole and open *6p* shell was found to cause different inherent widths for the *4f* doublets in the case of Au and Bi, but in the case of Pb, the outermost closed $6p_{1/2}$ shell does not significantly couple to open *4f* shell. The closed π-type orbital in molecular Bi_2 creates narrower lines in Bi_2 than in atomic Bi. Vibrational broadening in the dimer is thus smaller effect than the multiplet structure created by an open shell electron configuration.

Table 1. Experimental and theoretical 4f binding energies (eV) and inherent linewidths (meV) (consisting of lifetime broadening and multiplet splitting of the states) of Au, Pb, and Bi. [a] This work [b] Ref.[6] [c] Ref.[7]

	Experiment		Theoretical		Experiment		Theoretical	
	$E_b(4f_{5/2})$	$E_b(4f_{7/2})$	$E_b(4f_{5/2})$	$E_b(4f_{7/2})$	$\Gamma(4f_{5/2})$	$\Gamma(4f_{7/2})$	$\Gamma(4f_{5/2})$	$\Gamma(4f_{7/2})$
Au	94.95±0.03[a]	91.28±0.03[a]	95.58	91.80	280±10[a]	300±10[a]	350	320
	95.25±0.20[b]	91.60±0.20[b]						
Pb	149.17±0.03[a]	144.30±0.03[a]	148.74	143.92	290±10[a]	280±10[a]	230	220
		≈144[c]						
Bi	170.09±0.03[a]	164.76±0.03[a]	169.40	164.15	280±10[a]	260±10[a]	240	250
		164.9[c]						
Bi_2	169.13±0.03[a]	163.80±0.03[a]			240±10[a]	230±10[a]		

[1] M. Patanen, S. Aksela, S. Urpelainen, T. Kantia, S. Heinäsmäki, H. Aksela, *Free atom 4f photoelectron spectra of Au, Pb, and Bi*, *J. Electron Spectrosc. Relat. Phenom.* in press, doi: http://dx.doi.org/10.1016/j.elspec.2010.01.008
[2] M. Bässler et al., *Nucl. Instrum. Methods in Phys. A* **469** (2001) 382
[3] M. Huttula, K. Jänkälä, A. Mäkinen, H. Aksela and S. Aksela, *New J. Phys.* **10** (2008) 013009
[4] M. Huttula, S. Heinäsmäki, H. Aksela, E. Kukk, S. Aksela, *J. Electron Spectrosc. Relat. Phenom*. **156-158** (2007) 270
[5] M. Huttula, L. Partanen, A. Mäkinen, T. Kantia, H. Aksela and S. Aksela, *Phys. Rev. A* **79** (2009) 023412
[6] S. Aksela, M. Harkoma, M. Pohjola, and H. Aksela, *J. Phys. B: At. Mol. Phys.* **17** (1984) 2227
[7] Y. S. Khodeyev, H. Siegbahn, K. Hamrin, and K. Siegbahn, *Chem. Phys. Lett.* **19** (1973) 16

On the way to spintronics of free clusters

M. Tchaplyguine[2], T. Andersson[1], Ch. Zhang[1], O. Björneholm[1], S. Svensson[1, 2], N.Mårtensson[1, 2]

[1]*Dept of Physics, Uppsala University, Box 530, Uppsala, Sweden*
[2]*MAX-lab, Lund University, Box 118, Lund, Sweden*

Inherent properties of supported nanoscale semiconductors are to a great extent obscured by massive substrates imposing their geometric and energy structure on the deposited/grown particles. At the same time these are among the most promising objects in the electronics of the future, when separate electron spins are planned to be used as information-bit carriers (see, for example[1]). A way to overcome the difficulties induced by the substrate is to study free nanoparticles in a beam. Magnetron-sputtering-based gas-aggregation cluster sources have proven to be efficient cluster-production devices, capable to create particle densities high enough to be studied by synchrotron-based photoelectron spectroscopy – a unique method not only directly mapping valence density of states, but also giving site- and element-specific information when core-electron spectroscopy is applied.

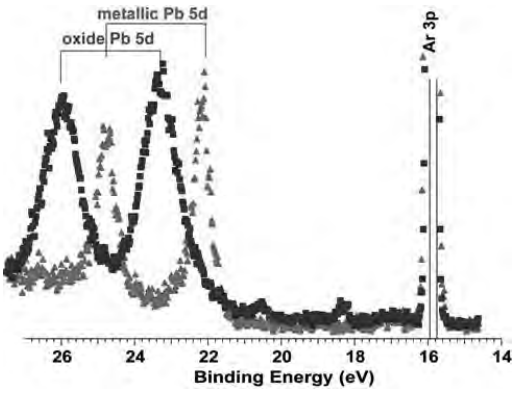

Fig.1. Typical spectra for metallic-Pb and oxide-Pb clusters.

Following a study of lead clusters created by a magnetron-based source a successful attempt has been made to produce lead oxide clusters by reactive sputtering in the atmosphere of mixed Ar and O_2 gases, and to study them by means of photoelectron spectroscopy. Furthermore Zn clusters have been generated and their first photoelectron spectra have been recorded, the spectra necessary in the ongoing project aimed at production and investigation of zinc oxide clusters.

Core-level photoelectron spectroscopy allows easily distinguishing between pure and oxidized metal samples: metal-element responses in oxides usually have noticeably higher binding energy positions than in metallic samples. Comparing the 5d Pb spectra for clusters created in Ar atmosphere, and those arising when oxygen is admixed, gives firm grounds for stating that in the latter case there are practically no non-oxidized Pb atoms in the clusters observed. Their response – a characteristic for the solid lead and its compounds spin-orbit-split doublet state -is more than 1 eV higher in binding energy than in the pure Pb case (figure 1). And indeed, reactive sputtering is a well-established technique in the field of thin-film deposition when high-purity oxides are the goal. In the present case the change in binding energy is too large to be explained by the possible variations of the cluster size or their different charge states[2] – due to different condensation conditions in the gas-aggregation source. Typically the source produces clusters in the range of several thousand atoms per cluster when the size-determined change of the energy is small relative to the difference in figure 1. The successful study of lead oxide clusters has, among other accomplishments, confirmed the principal possibility to use the setup for the outlined goal for entering the field of the functional oxide clusters.

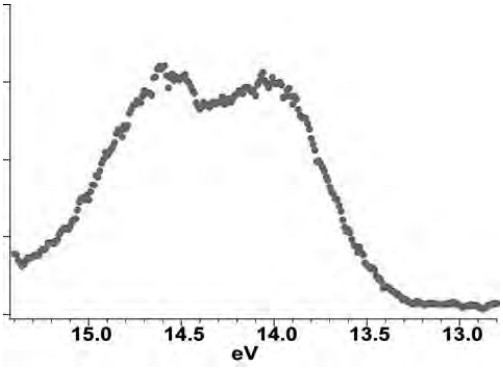

Fig.2. A typical Zn 3d spectrum with the spin-orbit-subcomponent resolution

Zinc has somewhat lower sputtering rates than lead, which anyway have proven to be sufficient to create a dense beam of clusters using our gas-aggregation source. Figure 2 shows an example of zinc 3d level spectrum with the spin-orbit subcomponent resolution. The next stage of the experimental quest will be to create ZnO clusters, and in the more distant future to dope them (in a setup incorporating two magnetrons) with magnetic manganese, what in prototype spintronics devices serves as a source of electrons with the oriented spins.

[1] Zhong LinWang. Annu. Rev. Phys. Chem. 2004. 55:159–96
[2] S.Peredkov, A.Rosso, G.Öhrwall, et al. Phys.Rev.B 75 (2007) 235407.

Fragmentation pathways of Auger final states following the 4d core ionization in Sb_4 clusters

S. Urpelainen, A. Caló, L. Partanen, M. Huttula, S. Aksela and H. Aksela
Department of Physics, P.O. Box 3000, 90014 University of Oulu, Finland

S. Granroth and E. Kukk
Department of Physics and Astronomy, University of Turku, 20014 Turku, Finland

A detailed experimental study of the fragmentation pathways of Sb_4 clusters after the $4d$ photoionization and subsequent Auger decay was performed by the photoelectron–photoion coincidence (PEPICO) and photoelectron–photoion–photoion (PEPIPICO) coincidence techniques. The experiments were performed at the I411 beamline at the MAX-II storage ring using the monochromatic photon energy of 90 eV. The electron–ion coincidence apparatus consisted of a SES100 electron analyzer and a Wiley-McLaren type ion time-of-flight (TOF) spectrometer[1].

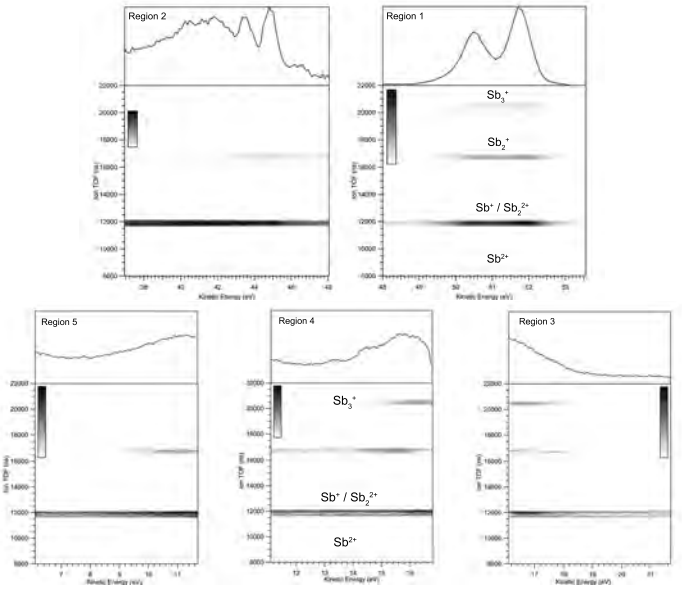

Figure 1: PEPICO map of $4d$ main photolines (region 1), the satellite lines (region 2), and of the Auger electrons (regions 3–5).

The molecular structure of the neutral ground state Sb_4 cluster has been predicted to be tetrahedrical T_d symmetry with the valence electronic configuration of $(4a_1)^2(5t_2)^6(5a_1)^2(6t_2)^6(2e)^4$. The three outermost orbitals, of which $5a_1$ and $6t_2$ are non-bonding and $2e$ is an Sb-Sb bonding orbital, are mainly linear combinations of the atomic Sb $5p$ orbitals. The inner valence $4a_1$ and $5t_2$ molecular orbitals are constructed from the Sb $5s$ atomic orbitals and they are the most bonding orbitals. Below the valence orbitals there are Sb $4d$-like molecular orbitals that retain most of their atomic character. The lowest unoccupied molecular orbitals (LUMOs) are the $7t_2$ and $3e$, which are mainly of Sb $5p$ character.

Table 1: The fragmentation pathways and processes following $4d$ photoionization and its shake-up satellites. Following abbreviations are used for dissociation processes: TD = two-body dissociation, DCS = deferred charge separation, SD = secondary dissociation.

Transition		Fragmentation pathways	Process
$4d$ main lines $\rightarrow$	$(4a_1,\, 5t_2)^{-1}(5a_1,\, 6t_2,\, 2e)^{-1}$	$Sb_4^{2+} \rightarrow Sb_3^{2+} + Sb$ $Sb_3^{2+} \rightarrow Sb^{+} + Sb_2^{+}$	DCS
$4d$ main lines $\rightarrow$	$(5a_1,\, 6t_2,\, 2e)^{-2}$	$Sb_4^{2+} \rightarrow Sb_3^{+} + Sb^{+}$	TD
$4d$ main lines $\rightarrow$	$(5a_1,\, 6t_2,\, 2e)^{-2}$	$Sb_4^{2+} \rightarrow Sb_2^{+} + Sb_2^{+}$	TD
$4d$ satellites $\rightarrow$	$(5a_1,\, 6t_2,\, 2e)^{-2}$	$Sb_4^{2+} \rightarrow Sb_3^{+} + Sb^{+}$ $Sb_3^{+} \rightarrow Sb_2^{+} + Sb$	SD

The photoelectron spectrum at the Sb_4 $4d$ core shell ionization region is dominated by two peaks at the center binding energies of 38.51 and 39.77 eV (referred as region 1 in Figure 1). The main peaks clearly resemble the closed shell atomic structure, corresponding to the atomic Sb $4d^{-1}_{3/2,5/2}$-like states with the spin-orbit splitting of 1.26 eV[2]. Furthermore, at the high-binding-energy side of the $4d$ core ionization lines is the $4d$ satellite structure (referred as region 2 in Figure 1) identified as the $4d$ shake-up structure where the $4d$ core ionization is accompanied by a valence electron excitation from two outermost molecular orbitals to LUMOs. The $4d$ Auger structure consists of two transition groups. The group located at the kinetic energies below 12 eV (coverred by regions 4 and 5 in Figure 1) was identified as the $4d \rightarrow (4a_1,\, 5t_2)^{-1}(5a_1,\, 6t_2,\, 2e)^{-1}$ transitions and the high-kinetic energy group located below 19 eV (coverred by regions 3 and 4 in Figure 1) was identified as the $4d \rightarrow (5a_1,\, 6t_2,\, 2e)^{-2}$ transitions[2].

With the aid of the PEPICO and PEPIPICO data, fragmentation pathways were determined. The fragmentation probabilities were not studied in this work. The PEPICO data in Figure 1 shows no events between photoelectrons and the Sb_4^{2+} ions, so it is found that the Sb_4 cluster fragments always after the core ionization and the following Auger decay. The fragmentation pathways corresponding different $4d$ core-valence-valence Auger transitions are given in Table 1. A more detailed discussion of the results can be found elsewhere[2]. The ion pair $Sb^+ + Sb^+$ appears after every Auger transition so it is not tabulated. Furthermore, the ion pair $Sb^+ + Sb^+$ is overlapping in measured data with the ion pair $Sb_2^{2+} + Sb^+$ so further analysis on fragmentation pathways cannot be made. The coincidence events between the ion pair $Sb^{2+} + Sb^+$ in the satellite region 2 and Auger region 3 was recorded. This suggests that the $4d^{-1}(5a_1,\, 6t_2,\, 2e)^{-1}$ direct double photoionization and subsequent Auger decay to the Sb^{3+} $(4a_1,\, 5t_2)^{-1}(5a_1,\, 6t_2,\, 2e)^{-2}$ states is possible.

[1]E. Kukk, R. Sankari, M. Huttula, A. Sankari, H. Aksela, and S. Aksela, J. Electron Spectrosc. Relat. Phenom. **155**, 141 (2007).

[2]S. Urpelainen, A. Caló, L. Partanen, M. Huttula, S. Aksela, H. Aksela, S. Granroth, and E. Kukk, Phys. Rev. A **79**, 023201 (2009).

Valence photoionization and the following fragmentation pathways in Sb_4 clusters

S. Urpelainen[1], A. Caló[1], L. Partanen[1], M. Huttula[1], J. Niskanen[1,2], E. Kukk[3], S. Aksela[1], and H. Aksela[1]

[1]*Department of Physics, University of Oulu, P.O. Box 3000, FI-90014 Oulu, Finland*

[2]*Theoretical Chemistry, Royal Institute of Technology, Roslagstullsbacken 15, SE-10691 Stockholm, Sweden*

[3]*Department of Physics and Astronomy, University of Turku, FI-20014 Turku, Finland*

The valence photoelectron spectrum of Sb_4 clusters and the following fragmentation patterns were studied using synchrotron radiation from the undulator beamline I411 of the MAX-II storage ring. The fragmentation of the Sb_4 cluster was studied using electron-ion coincidence technique (PEPICO). The valence photoelectron spectrum was recorded using a modified Scienta SES-100 electron energy analyzer mounted on the 1-m section of the beamline. The PEPICO events were recorded using a PEPICO apparatus consisting of the SES-100 and a Wiley-McLaren-type ion time-of-flight (TOF) spectrometer built in Turku. The Sb_4 vapor was generated using an inductively heated oven and a resistively heated oven for photoelectron spectroscopy and PEPICO events, respectively. The photoelectron spectroscopy and PEPICO experiments were performed at the photon energies of 60 eV and 60.5 eV, respectively. The photoelectron spectra were recorded at a constant spectrometer pass energy of 20 eV, monochromator exit slit of 100 μm and analyzer entrance slit of 0.8 mm (curved) corresponding to photon bandwidth of 40 meV and an analyzer broadening of approximately 80 meV. For PEPICO events the pass energy of the analyzer was set to 100 eV, corresponding to a 11 eV wide energy window for detected electrons. The analyzer entrance slit was chosen to be 1.6 mm. The monochromator exit slit was closed to a minimum in order to maintain good purity of the coincidence signal. The recorded photoelectron spectrum and 2D PEPICO map are presented in Fig. 1 and Fig. 2, respectively. The figures are taken from Ref. [1].

In Fig. 1 relatively strong features are seen in the 10.5 eV to 16 eV binding energy region that could be assigned earlier only tentatively due to too weak intensity as *5s*-like molecular orbitals and shake-up lines [2]. This difference in intensity is easily explained by the fact that the recent experiments were performed on the rising edge of the 4*d* giant resonance of Sb_4 resulting in significant enhancement of valence photoionization cross-section. With the help of the stronger intensity and more distinct features in the photoelectron spectrum, fragmentation pathways after ionization from different orbitals (Fig. 2) and qualitative information about the bonding properties of the molecular orbitals an improved assignment of the lines in this energy region was made. It was concluded that, instead of assigning the several broad features in this region as

Jahn-Teller split components of the $5t_2$ ionization as suggested in Ref. [3] for P_4 clusters, the lines are more likely to originate from correlated $5t_2^{-1}$ states and shake-up satellites accompanying the $(5a_1 6t_2 2e)^{-1}$ ionization. More details about the assignment can be found in Ref. [1].

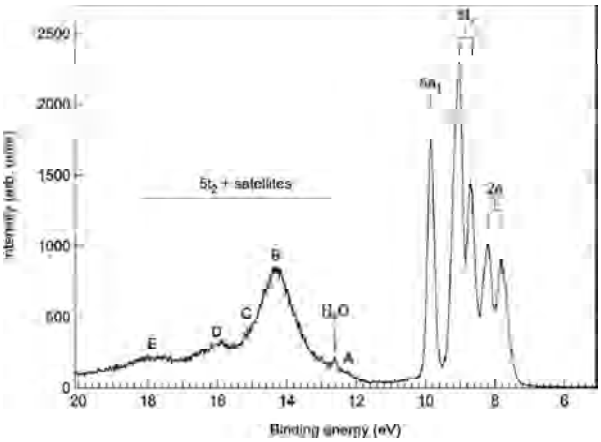

Fig. 1 Valence photoelectron spectrum with line assignment. Molecular orbitals are assigned according to the T_d point group.

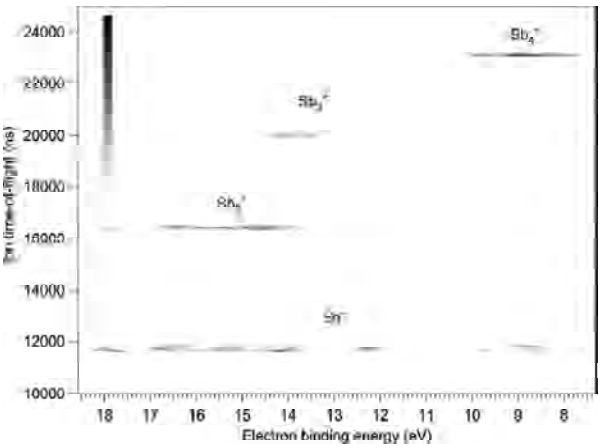

Fig. 2 2D PEPICO map of the valence photoionization in the TOF region of the observed antimony ions.

[1] S. Urpelainen, A. Caló, L. Partanen, M. Huttula, J. Niskanen, E. Kukk, S. Aksela, and H. Aksela, Phys. Rev. A **80**, 043201 (2009).

[2] S. Elbel, J. Kudnig, M. Grodzicki, and H. J. Lempka, Chem. Phys. Lett**. 109**, 312 (1984)

[3] C. R. Brundle, N. A Kuebler, M. B. Robin, and H. Basch, Inorg. Chem. **11**, 20 (1972)

Experimental observation of anomalous angular distribution in 2p photoionization of Ar atoms: Just how sensitive is the angular distribution to external fields?

S. Urpelainen[1,2], M. Huttula[1], S. Heinäsmäki[1], S. Aksela[1], and H. Aksela[1]

[1]*Department of Physics, University of Oulu, P.O. Box 3000, FI-90014 Oulu, Finland*

[2]*MAX-lab, Lund University, P.O. Box 118, SE-22100 Lund, Sweden*

The variation of the differential cross section of photoionization as a function of the angle between the polarization vector of the ionizing radiation and the electron momentum is given in terms of the angular distribution parameter, which encodes the interferences of various partial scattering amplitudes. The measurements of angular distribution parameters are used in modeling of the electron emission dynamics, and they are also used for calibration purposes such as determining the degree of linear polarization of the incoming radiation (see, e.g., [1, 2] and references therein). It is therefore extremely important to know all possible factors affecting the angular distribution measurements so that the experimental results could be interpreted correctly. The widespread use of synchrotron radiation sources has made the differential cross section measurements a common tool and the amount of data accumulated on angular parameters is at present very large. Within the present theoretical framework the angular distribution of emitted electrons in the dipole plane should be symmetrical with respect to reflection through the plane perpendicular to the dipole plane. Recent experiments have however shown deviation from this behavior [3-5].

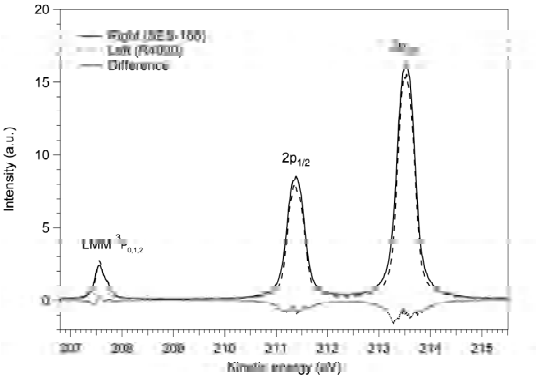

Fig. 1 Ar 2p PES recorded simultaneously with the two electron analyzers together with the Auger line group used for normalization.

In this work the angular distribution of the 2*p* photoelectrons of noble gas argon in the dipole plane was studied with two consecutive hemispherical electron energy analyzers placed on opposite sides of the plane perpendicular to the dipole plane. The experiments were performed at the undulator beamline I411 of the MAX-II storage ring with a Scienta SES-100 electron analyzer mounted at the 1-m section of the beamline. The PES were recorded simultaneously with both the SES-100 and the permanent Scienta R4000 end-station at the photon energy of 461.2 eV together with the isotropic $L_2M_{2,3}M_{2,3}$ $^3P_{0,1,2}$ Auger line group used for normalization purposes. The normalized electron spectra recorded at analyzer detection angle of 45^o are presented in Fig. 1 showing a clear difference in the observed cross-section between the left- and right-side. The deviation from the symmetrical case was measured through the asymmetry parameter (A_{LR}) defined in Ref. [1]. The asymmetry parameter as a function of the electron

detection angle with respect to the electric field vector of the linearly polarized radiation is presented in Fig. 2.

To rule out possible experimental sources of error that could cause the effect the transmission of both analyzers in the kinetic energy region of the experiments was determined to be constant, the pressure dependency of the effect was studied with no observable dependency on target pressure and stray magnetic fields were eliminated with careful μ-metal shielding of the analyzers and near-by vacuum gauges. Also a tilt in the polarization vector of the incoming light was considered, but determined not to be able to cause the observed effect. In addition a component of un-polarized or circularly polarized light in the incoming radiation would not be able to cause a non-symmetric angular distribution in the dipole plane.

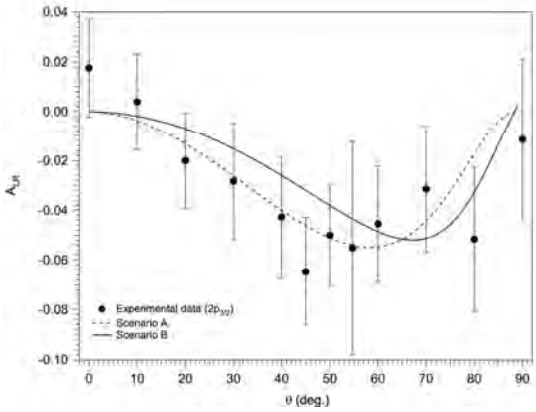

Fig. 2 The asymmetry parameter as a function of the electron detection angle together with two simulations taking into account a small external electric field in the target region.

A possible explanation for the observed behavior is a small external field affecting the momentum of the emitted electrons in the target region. For example a tiny electric potential in the order of few hundreds of mV would be able to cause large enough deviation to the electron emission direction with respect to the electric field vector of the incoming light that would result in an asymmetry parameter in the observed order of magnitude. In order to test this hypothesis two simulations were made for the effect of a small electric field on the angular distribution of the Ar 2*p* photoelectrons at the photon energy of 461.2 eV. As the analyzers were rotated around the photon beam to measure the angular distribution, the assumed electric field would rotate as well. Two types of scenarios were assumed for the simulations: one where the electric field is identical in both analyzers (dashed curve in Fig. 2) and one where both analyzers have separate electric fields pointing in different directions (solid line in Fig. 2). The strength and direction of the electric potential in the first case were 600 mV and θ+180^o and in the second case 300 mV and θ-306^o for the SES-100 and 200 mV and θ-153^o for the R4000. The simulation not only agrees with the magnitude of the effect but is able to reproduce the angular dependency of the asymmetry quite well. This indicates that great care should be taken when determining the angular anisotropy parameters as even extremely small external fields could cause significant deformation of the angular emission pattern.

[1] Schmidt V., Electron Spectroscopy of Atoms Using Synchrotron Radiation (Cambridge University Press, Cambridge(1997))
[2] D. Cubric, D. R. Cooper, M. C. A. Lopes, P. Bolognesi, and G. C. King, Meas. Sci. Technol. **10**, 554 (1999).
[3] S. Ricz, T. Rics´oka, ´A. K¨ov´er, M. Huttula, D. Varga, S. Urpelainen, H. Aksela S. Aksela, New J. Phys. **9**, 274 (2007).
[4] D. Ber´enyi, Nucl. Instrum. Methods Phys. Res. B **267**,184 (2009).
[5] T. Rics´oka, S. Ricz, ´A. K¨ov´er, K. Holste, A. Borovik Jr., D. Varga, S. Schippers A. M¨uller, J. Phys.: Conf. Ser. **194**, 012003 (2009).

Photoelectron spectroscopy of alkali-halide-salt clusters

C. Zhang[1], T. Andersson[1], M. Tchaplyguine[2], O. Björneholm[1], S. Svensson[1], M. -H. Mikkelä[3], and M.Huttula[3]

[1] *Department of Physics, Uppsala University, P.O. Box 516, SE-751 20 Uppsala, Sweden*
[2] *MAX-lab, Lund University, P.O. Box 118, SE-221 00 Lund, Sweden*
[3] *Department of Physical Sciences, Oulu University, Oulu, Finland*

Clusters of alkali halide salts are of a considerable environmental interest for they are present as aerosols in the atmosphere over the surface of the ocean. The study of alkali halide clusters at laboratory conditions can provide detailed information for the understanding of the Earth climate formation. In the last decades an extensive theoretical and experimental work has been done analysing binding energies in separate alkali halide molecules and macroscopic crystals, several models and calculation methods have been developed that have had some qualitative success in accounting for the changes of electron binding energies in different environments. This year, we have started a photoelectron spectroscopy study of alkali halide clusters which only contain a small amount of monomers. One of the goals of the project is to test the adequacy of the ionic- bonding model for the quantitative description of the experimentally observed binding energies

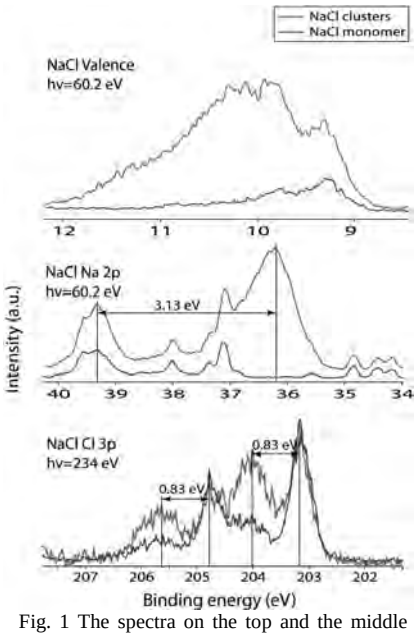

Fig. 1 The spectra on the top and the middle are the valence level and Na 2p of NaCl clusters taken at the photon energy 60.2 eV. The spectrum at the bottom is of Cl 3p at the photon energy 234 eV. The upper spectra in all three figures correspond to NaCl clusters.

The experiments were performed at the undulator beamline I411 at the MAX-II storage ring. The alkali halide clusters were created in a beam by a newly operational dedicated cluster source [1]. In such a source a beam of Ar clusters produced using a gas-aggregation source is let through the dense salt vapour created inside a high-temperature crucible. Core- and valence-photoelectron spectra were recorded in the experiment: for 2p levels of Na and Cl, and for 3p level of Cl.

In this investigation we have obtained results showing the evolution of the energy structure of alkali halides from one separate molecule to ~1 nm salt clusters, the evolution manifesting itself in the binding energy shifts. Inspection of figure 1, shows simultaneous presence of peaks due to monomers (free molecules) and clusters. The binding energy of the sodium 2p level showed an apparent decrease for the clusters as compared to the monomers of about 3.1 eV. On the other hand, the binding energy of the chlorine 2p level increased by about 0.8 eV.

Reference

1 M.Huttula, M.-H. Mikkelä, M. Tchaplyguine, O. Björneholm. *J. Electr. Spectr. Rel Phen.* doi:10.1016/j.elspec.2010.02.012

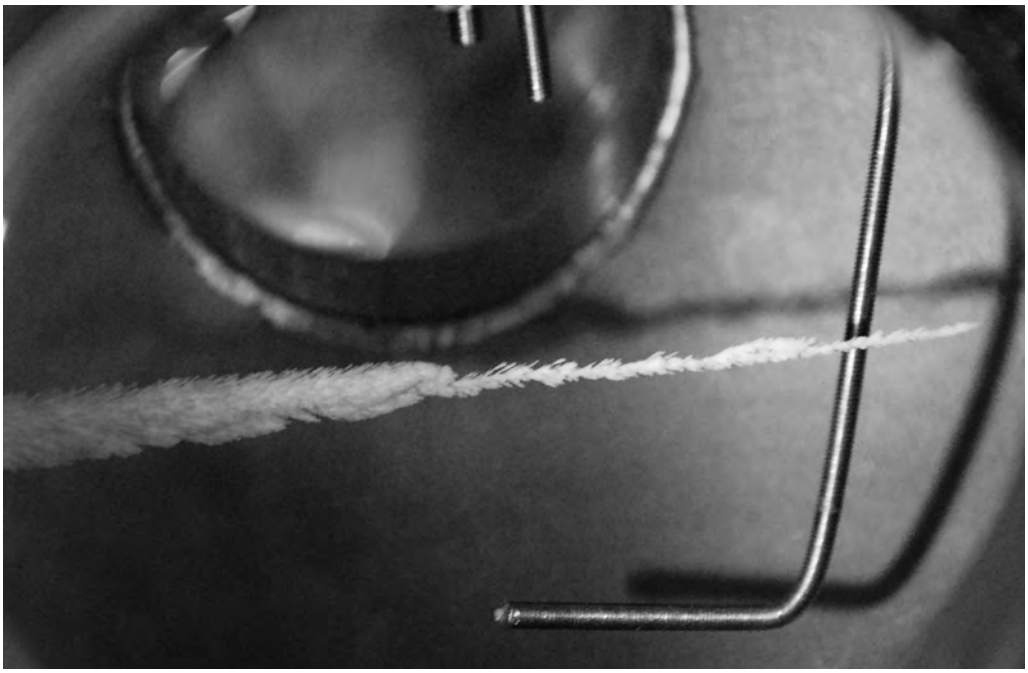

Ice crystal growth at beamline I411, January 2010.
Photo: Annika Nyberg

Roger Uhrberg and Jacek Osiecki, Linköping University, December 2009.
Photo: Annika Nyberg

Modification of electronic properties of FePc with alkali metal doping. Part I (PES).

V.Yu. Aristov [1,2], O.V. Molodtsova[1], D.V. Vyalikh[3], A.B. Preobrajenski[4], and M. Knupfer[1]

[1]*IFW Dresden, D-01069 Dresden, Germany*

[2]*Institute of Solid State Physics, Russian Academy of Sciences, Chernogolovka, Moscow Distr., 142432, Russia*

[3]*Institute of Solid State Physics, TU Dresden, D-01069 Dresden, Germany*

[4] *MAX-lab, 22100 Lund, Sweden*

The evolution of electronic structure of the organic semiconductor iron-phthalocyanine (FePc) with potassium doping has been studied by means of photoemission spectroscopy and near-edge x-ray absorption fine structure The data disclosed filling of the lowest unoccupied molecular orbital upon doping and associated changes of the core level absorption spectra. None of the films prepared in our studies showed a finite electronic density of states at the Fermi level.

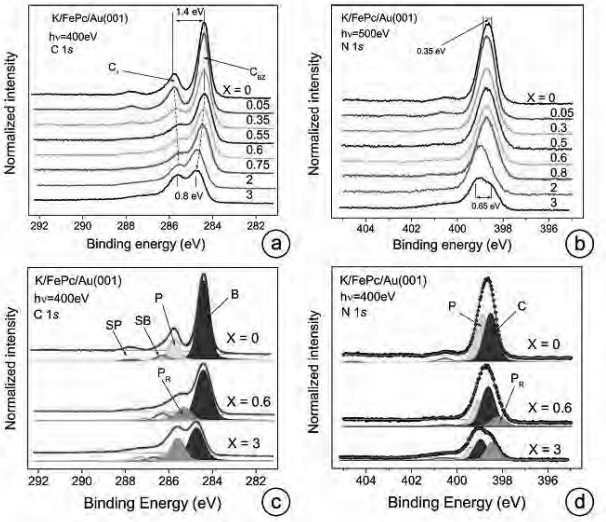

Fig. 1: C 1s core level (a) and N 1s core level (b) measured using photoemission spectroscopy of FePc thin film at RT as a function of X, which characterize the amount of potassium atoms per FePc molecule. Decomposition of the C 1s (c) and N 1s (d) spectra of pristine (X=0) and dopped (X=0.6 and X=3) FePc. See details in the text.

Figs. 1(a-b) show the C 1s and N 1s core levels recorded from a FePc film as a function of potassium doping. X indicates the amount of potassium atoms per FePc molecule. The top spectra (for X=0) represent the photoelectron emission from core levels of pristine FePc just after of organic film formation. The decomposition of the C 1s spectrum of pristine FePc is presented in Fig. 1(c) (X=0). The C 1s core level is comprised of two main components: B which corresponds to the aromatic carbon of the benzene rings of Metal-Pc (C2, C3, and C4 on the Fig. 2) and P shifted by 1.4 eV toward higher binding energy and attributed to the carbon C1 on the Fig. 2 linked to nitrogen atoms N_1 and N_2 (pyrrole carbon). The energy shift between C 1s (B) and C 1s (P) is due to a transfer of valence charge from pyrrole carbon to the more electronegative nitrogen in the -N-C=N- bonds. The shoulder SB and the feature SP are the satellites of the B and P components respectively.

The N 1s core-level spectrum of pristine FePc is shown in the Fig. 1(b). The spectrum consists of the strong peak centered at 398.62 eV and weaker peaks at 400.4 eV and 402.5 eV. We have managed to decomposed the peak of 398.62 eV by two components: C centered at 398.38 eV and P centered at 398.86 eV [Fig. 1(d), X=0].The energy difference between the peaks corresponds to 0.36 eV. Component C at lower BE can be assigned to the 4 nitrogen atoms connected to the central Fe atom (N1 in Fig. 2), while the P component can be assigned as originating from the 4 nitrogen atoms linked to the pyrolle carbons. Probably unlike to the case of CuPc, where both nitrogen sites N1 and N2 are characterized by the same or a very similar binding

energy (BE) and the main N 1s peak was fitted by only one component , the central Fe atom differently interacts with these N1 nitrogen atoms which is associated with a stronger charge transfer. The latter provokes the N1 chemical shift to lower BE by 0.36 eV. A similar shift of about 0.3 eV for FePc [1] was found from DFT calculations.

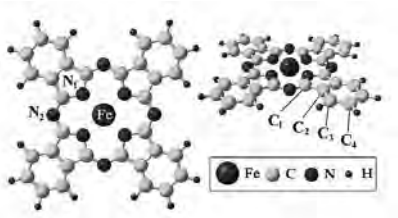

Fig. 2: Schematic demonstration of the molecular structure of the FePc molecule, where the central iron atom is surrounded by four nitrogen atoms.

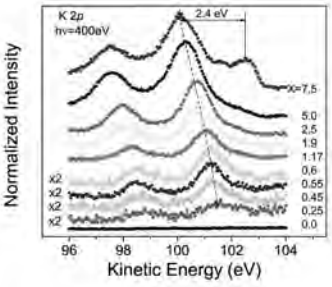

Fig. 3: K 2p core level measured using photoemission spectroscopy as a function of K

With potassium doping the K 2p spin-orbit doublet is observed at binding energies of 289.2 eV and 292 eV and increases in intensity with increasing potassium content (Fig. 3). The energy position of the doublet indicates that the outer s electrons of potassium are transferred to the FePc molecules upon intercalation. The shape of the K 2p doublet basically does not change with doping till a concentration of about 4 potassium atoms per FePc molecule which is an indication of the existence mostly of only one inequivalent potassium site in this doping range. At a higher potassium concentration (X=7.5) considered in the present investigation the spectrum shows one more feature shifted by about 2.4 eV to lower BE relative to K 2p3/2 component of main doublet. From such K 2p core level behavior we can conclude that at doping range $0<X\leq4$ most probably potassium ions occupy one type of equivalent positions in FePc molecule. As we will see below the first type of sites, corresponding to higher BE, is located near the asa-bridging nitrogens N2 of the FePc molecules and is fully saturated at potassium concentration $X\simeq4$, while another site type, corresponding to lower BE is located probable near the benzene carbons and is occupied by K ions at concentration $X\geq4$. In general starting from the first deposition up to $X\simeq7$ the total K 2p core-level shift of about 1 eV to higher BE was observed. With potassium doping the K 2p spin-orbit doublet is observed at binding energies of 289.2 eV and 292 eV and increases in intensity with increasing potassium content (Fig. 3). The energy position of the doublet indicates that the outer s electrons of potassium are transferred to the FePc molecules upon intercalation. The shape of the K 2p doublet basically does not change with doping till a concentration of about 4 potassium atoms per FePc molecule which is an indication of the existence mostly of only one inequivalent potassium site in this doping range. At a higher potassium concentration (X=7.5) considered in the present investigation the spectrum shows one more feature shifted by about 2.4 eV to lower BE relative to K 2p3/2 component of main doublet. From such K 2p core level behavior we can conclude that at doping range $0<X\leq4$ most probably potassium ions occupy one type of equivalent positions in FePc molecule. As we will see below the first type of sites, corresponding to higher BE, is located near the asa-bridging nitrogens N2 of the FePc molecules [see Fig. 2] and is fully saturated at potassium concentration $X\simeq4$, while another site type, corresponding to lower BE is located probable near the benzene carbons and is occupied by K ions at concentration $X\geq4$. In general starting from the first deposition up to $X\simeq7$ the total K 2p core-level shift of about 1 eV to higher BE was observed.

This work was supported by the EC Transnational Access to Research Infrastructure via MaxLab, by the DFG under grant no. 436RUS17/52/06, and by the SMWK. V.Yu.A. thanks the RFBR (Grant Num. 08-02-01170). We are grateful to MaxLab staff and personally Franz Hennies and Annette Pietzsch for help during the experiment.

[1] J. Ahlund, K. Nilson, J. Schiessling, L. Kjeldgaard, S. Berner, N. Martensson, C. Puglia, B. Brena, M. Nyberg, Y. Luo (2006) J. Chem. Phys. **125**, 034709.

Soft X-ray induced oxidation on acrylic acid grafted luminescent water dispersible silicon quantum dots

Yimin Chao[1], Qi Wang[1], Annette Pietzsch[2], Franz Hennies[2], and Hongjun Ni[3]

[1] School of Chemistry, University of East Anglia, Norwich NR4 7TJ, UK
[2] MAX-lab, Lund University, 221 00 Lund, Sweden
[3] School of Mechanical Engineering, Nantong University, China 226019

Basic material of semiconductor electronics, Silicon is largely available, comparatively cheap, ecologically friendly and technologically well developed. Since Canham found the visible light emitted from silicon nanostructure [1], the vast interests have been raised from the wide scientific communities. Due to quantum confinement effect silicon quantum dots emit red light, and no any toxicity has been found [2], it is one of the best candidates for the bio-imaging. The barrier for such application in bio-labelling is its water solubility. Several groups have attempted to make it water soluble in various routes [3, 4]. A simplified synthesis method of water dispersible luminescent silicon quantum dots (Si-QDs) has been developed in our lab. Acrylic acid grafted method has been adopted, but the raw silicon quantum dot core was obtained by etching a silicon chip to synthesize water dispersible luminescent Si-QDs [5]. Here we report a synchrotron study on the electronic structures of such water dispersible Si-QDs. Particularly, a photon induce oxidation has been observed based on the evolution of core level Si*2p* over the course of exposure procedure.

The preparation method of acrylic acid grafted water dispersible luminescent silicon quantum dots has been published elsewhere [6]; A few drops of suspension were casted onto gold film. The film was immediately introduced into a load-lock attached to ultra high vacuum (UHV) chamber in which the typical pressures were kept below 5×10^{-10} mbar. The film was then studied by soft X-ray photoemission spectroscopy (XPS) and X-ray absorption spectroscopy (XAS). The XPS and XAS experiments were carried out with a Scienta R4000 analyzer in beamline I511 of Maxlab at Lund, Sweden. In all photoemission spectra, binding energies are referred to the Fermi edge measured on a gold foil in direct electrical contact, which was found at binding energy of 4.62 eV.

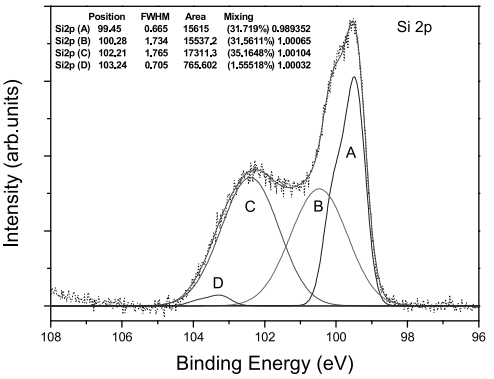

Figure 1 Si2p spectrum obtained at 20° to normal emission: dotted line was experimental data which was fitted by four mixed doublets and one Shirley background: the four components at 99.45, 100.28, 102.21 and 103.24 respectively

The surface chemical bonding were examined by employing high resolution XPS. Figure 1 shows a high resolution XPS spectrum at core level Si2p region of Si-QDs surface after the graft polymerization in 1 % v/v acrylic acid monomer solution. The spectrum was obtained at 20° to normal emission with photon energy 150 eV, and normalised to photon flux. The Si2p spectrum was fitted with four mixed doublets and one Shirley background. The four components were at 99.45, 100.28, 102.21and 103.24 eV respectively. The first component at 99.45 eV is assigned as Si – Si within silicon core of the Si-QDs. The second component at 100.28 is from Si in silicones. The third at 102.21 eV is from Si-C and the forth at 103.24 eV from SiO_2 at surface of Si-QDs, respectively. The existence of Si-C component implies surface silicon atoms of the nanoparticles changed from H- to PA- termination [4]. The broadened peak at 103.24 eV was observed, confirming the sample surface has been oxidized after several weeks kept at normal condition.

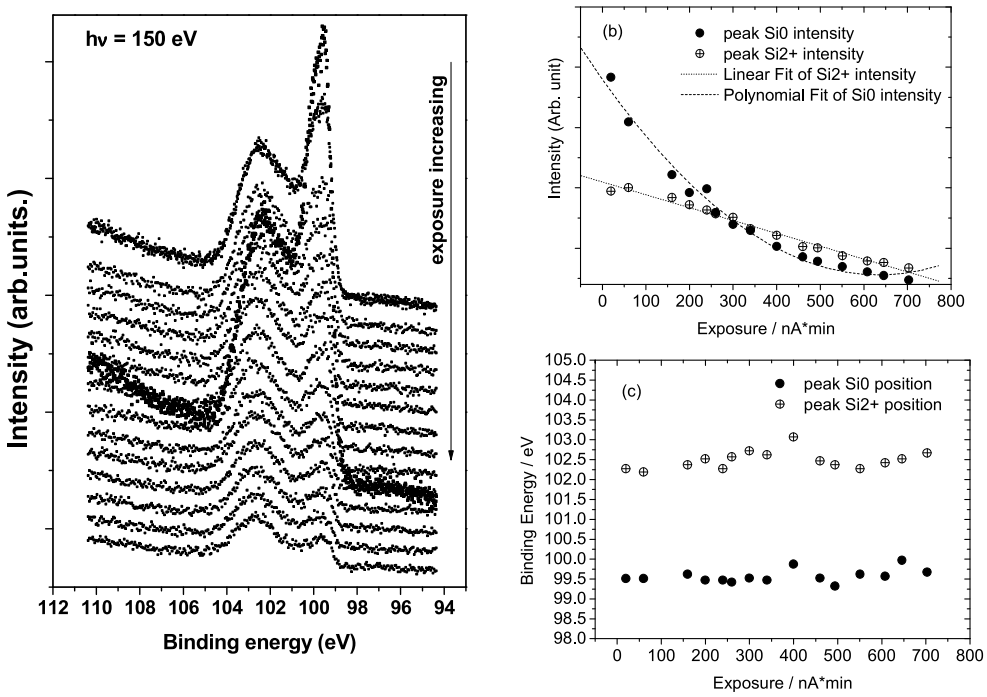

Figure 2 (a) the evolution of core level Si2p during the course of soft X-ray irradiation; (b) the intensity changing of two components before final steady state reached: the intensity of Si related peak decreasing faster than the intensity of oxide related peak during the course of exposure; (c) no significant changes of peak positions during the irradiation course

The intensities of the Si2p peaks were observed decreasing with the increasing exposure of irradiation, which is normal fingerprint of charging phenomena. Figure 2 shows the evolution of Si2p during the course of irradiation. Intensities of both peaks declined with exposure increased, however, the Si0 peak decreased more quickly, which had its intensity lower than the other peak after exposure of 259 nA*min, defined as X = flux * time. It is found that the intensity of Si^0 peak follows a polynomial regression *I = 18988.72341-51.09974*X + 0.04027*X^2 (with R = 0.98555 P<0.0001 perfectly fitted)*, and that of Si^{2+} follows linear regression: *I = 10486.69464 -10.6528* X (with R= -0.99101 P<0.0001 perfectly fitted).* This is the typical soft X-ray induced oxidation of silicon quantum dots [7].

In summary, the co-exist of core levels Si2p and C1s confirmed that acrylic acid grafted water soluble silicon nanoparticles have been successfully synthesized. Four components were needed to fit core level Si2p. This also indicated the existence of dangling bonds which could be oxidised under the irradiation. Soft X-ray induced oxidation was observed by monitoring the intensity changing of two components in core level Si2p.

1 L. T. Canham, Applied Physics Letters **57**, 1046 (1990).
2 N. H. Alsharif, C. E. M. Berger, S. S. Varanasi, et al., Small **5**, 221 (2009).
3 Z. F. Li and E. Ruckenstein, Nano Letters **4**, 1463 (2004).
4 S. Sato and M. T. Swihart, Chemistry of Materials **18**, 4083 (2006).
5 L. H. Lie, M. Duerdin, E. M. Tuite, et al., J. Electroanal. Chem. **538**, 183 (2002).
6 Q. Wang, A. Pietzsch, F. Hennies, et al., Journal of Nanoparticle Research, in press (2010).
7 Y. Chao, S. Krishnamurthy, M. Montalti, et al., Journal of Applied Physics **98**, 044316 (2005).

Charge state of cations and phase composition of cupric oxide subjected to shock-wave loading: X-ray absorption study

V. R. Galakhov[1,2]*, and A. S. Semenova[3], and B. A. Gizhevskii[1]

[1] *Institute of Metal Physics, Russian Academy of Sciences — Ural Division, 620990 Yekaterinburg, Russia*

[2] *Ural State Mining University, Yekaterinburg, Russia*

[3] *Institute of Solid State Chemistry, Russian Academy of Sciences — Ural Division, 620990 Yekaterinburg, Russia*

High-intensity external effects, such as bombardments by high-energy ions, plastic deformation, shock-wave loading can lead to change of cation charge state and phase transformation of materials [1,2]. The most interest among these external effects has a loading with shock-waves that can lead to appearance of nanostructure. Under the action of external agents, oxides can experience partial reduction or oxidation accompanied by a change in the valence of the cation. Copper monoxide CuO can serve as an example of such a system. An analysis of the phase composition by means of standard X-ray diffraction methods is very complicated since nanoparticles appeared after shock-wave loading lead to broadening diffraction peaks. That is why new methods of characterization of these objects are necessary.

In this work we have used methods of X-ray absorption spectroscopy (XAS) for characterization of phase transformation in CuO samples subjected to shock-wave loading.

Polycrystalline samples of CuO were prepared from CuO powder of 99.8 % purity by annealing in air at 900 °C for 10 h. The shock-wave loading of CuO spherical billet was performed by detonation of hexogen-based explosive layer, having a thickness of 8 mm, placed on the sphere of diameter 49 mm with an initial density constitution of $\sim$ 70 % of the theoretical value. The spherical billet (prior to its explosive compression) was prepared by static compression of CuO powder followed by fritting. Samples for the investigations were cut from different spherical layers of a loaded sphere characterized by the related radius r/r^*, where r is the radius of the layer under investigation and r^* is the radius of the CuO sphere after loading.

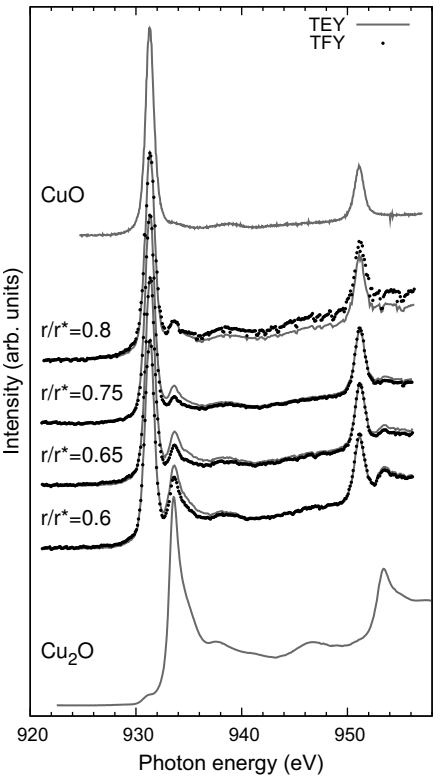

Fig. 1: Cu 2p X-ray absorption spectra for CuO subjected to shock-wave loading along the radius of the CuO sphere. The spectra are measured both in the total electron yield (TEY) and total fluorescence yield (TFY) modes.

X-ray absorption experiments in the total electron yield (TEY) and total fluorescence (TFY) modes were performed at the bulk branch line of beamline I511 at MAX II. The spectra were measured in different points of the sample (r/r^*), along the radius of the CuO sphere.

*e-mail: galakhov@ifmlrs.uran.ru

Cu 2p X-ray absorption spectra for CuO subjected to shock-wave loading along the radius of the CuO sphere are shown in Fig. 1. For comparison, the XAS spectra of single crystals of CuO and Cu_2O are presented.

In the Cu 2p-edge absorption spectra of CuO subjected to shock-wave loading, the two strong and narrow peaks at 931.3 and 951.1 eV are due to the Cu^{2+} ions. Both the peaks show shoulders on the high-energy side at 933.6 and 953.4 eV which formed by the Cu^{1+} ions. These spectral features correspond to the Cu 2p absorption peaks of CuO and Cu_2O (see Fig. 1). Thus, Cu 2p absorption spectra of CuO subjected to shock-wave loading can be presented as a linear superposition of the Cu 2p spectra of CuO and Cu_2O.

The intensity of peaks formed by Cu^{1+} ions increases from the edge of the CuO-sphere to its center. It means that going deep inside to the sphere center, concentration of the Cu_2O phase increases. Yearly, this effect was found in our works [1, 2] using O $K\alpha$ X-ray emission and Cu 2p photoelectron spectra. Note, the Cu^{1+}-peaks in the spectra obtained in the TEY mode are more intense than those obtained in the TFY mode. It is due to some degradation of CuO nanocrystallites at the surface of the specimen under investigations, i. e., CuO→Cu_2O transition.

We have demonstrated the effectiveness of the methods of X-ray absorption and X-ray emission spectroscopy in the study of phase transformations in CuO as a result of explosive shock-wave loading.

The authors thank Dr. A. Pietzsch for technical supports at MAX-II and E. A. Kozlov for explosive experiments. This work was supported by the Russian Foundation for Basic Research (Grant No 07-02-00540).

[1] D. A. Zatsepin, V. R. Galakhov, B. A. Gizhevskii, E. Z. Kurmaev, V. V. Fedorenko, A. A. Samokhvalov, S. V. Naumov, and R. Berger, Phys. Rev. B **59**, 211 (1999).

[2] B. A. Gizhevskii, V. R. Galakhov, D. A. Zatsepin, L. V. Elokhina, E. A. Kozlov, T. A. Belykh, S. V. Naumov, V. L. Arbuzov, K. V. Shal'nov, and M. Neumann, Phys. Solid State **44**, 1380 (2002).

X-ray spectra, nature of doping holes, and nonstoichiometry of $Li_xNa_yCoO_2$

V. R. Galakhov[1,2]*, A. S. Semenova[3], and D. G. Kellerman[3]

[1] *Institute of Metal Physics, Russian Academy of Sciences — Ural Division, 620990 Yekaterinburg, Russia*

[2] *Ural State Mining University, Yekaterinburg, Russia*

[3] *Institute of Solid State Chemistry, Russian Academy of Sciences — Ural Division, 620990 Yekaterinburg, Russia*

Nonstoichiometric cobaltites Li_xCoO_2 and Na_xCoO_2 can be expected to contain both Co^{3+} and Co^{4+} ions. It was shown that Co ions remain unaffected by Li or Na de-intercalation, i. e. doped holes are localized in O 2*p* states [1–3]. We expect that this effect occur in nonstoichiometric cobaltite $Li_xNa_yCoO_2$.

Polycrystalline samples of $Li_xNa_yCoO_2$ were prepared by standard solid state chemistry method from a mixture of Li_xCoO_2 and $Na_{0.7}CoO_2$. According to the X-ray diffraction analysis the synthesized compound has the same structure as that reported in [4] with $a = 2.827(6)$ Å, $b = 2.827(6)$ Å, $c = 20.323(1)$ Å which corresponds to the following compound: $Li_{0.42}Na_{0.36}CoO_{1.96}$. X-ray absorption and X-ray emission spectral experiments were performed at the bulk branch line of beamline I511 at MAX II. O 1*s* and Co 2*p* X-ray absorption spectra were measured in the total electron yield (TEY) and total fluorescence yield (TFY) modes.

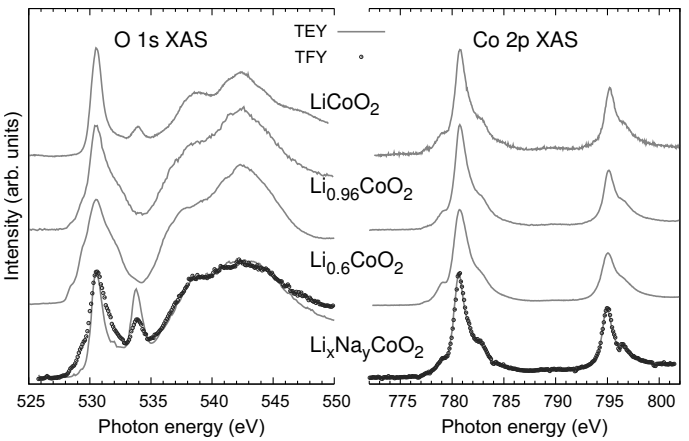

Fig. 1: O 1*s* and Co 2*p* X-ray absorption spectra of $Li_xNa_yCoO_2$ ($x \simeq 0.42$, $y \simeq 0.36$) and Li_xCoO_2 ($x = 1, 0.96, 0.6$). The spectra of $Li_xNa_yCoO_2$ are measured both in the total electron yield (TEY) and total fluorescence (TFY) modes. The spectra of Li_xCoO_2 are measured in the TEY mode.

In order to determine the valence states of cobalt and oxygen ions, we examine the O 1*s* and Co 2*p* X-ray absorption spectra presented in Fig. 1. The electric dipole-allowed $1s \rightarrow 2p$ transition of O 1*s* X-ray absorption spectra provides direct information of the oxygen charge state and Co–O bonding interaction, since the 2*p* orbitals of oxygen ligand are involved in bonding configuration with Co metal ions. The extra features in the O 1*s* spectra of nonstoichiometric cobaltites Li_xCoO_2

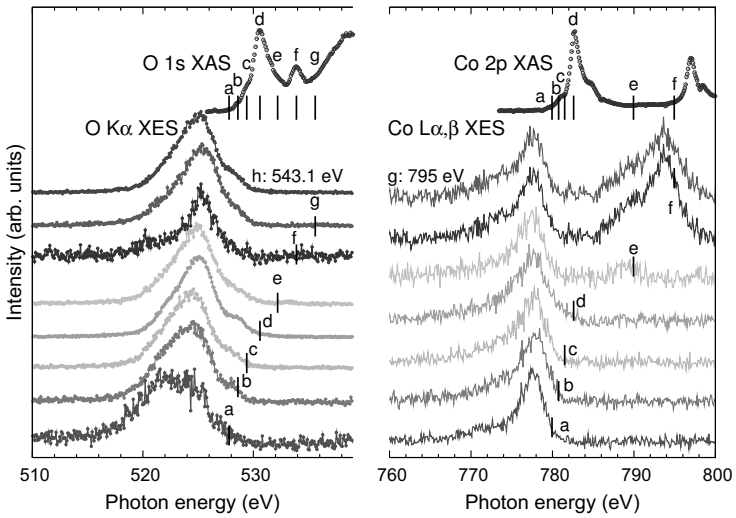

Fig. 2: O $K\alpha$ and Co $L\alpha, \beta$ X-ray emission spectra of $Li_xNa_yCoO_2$ measured at different excitation energies.

below the threshold indicate additional unoccupied O 2p state. Therefore, the doped holes induced by Li de-intercalation are of the O 2p nature.

The spectrum of $Li_xNa_yCoO_2$ measured in the TEY mode (surface sensitivity) has no extra features. This spectrum is similar to that of $LiCoO_2$. This means that at the surface (about some nanometers), the alkaline content of $Li_xNa_yCoO_2$ is stoichiometric. The O 1s spectrum of $Li_xNa_yCoO_2$ measured in the TFY mode (bulk sensitivity) shows extra features as for nonstoichiometric lithium cobaltites. This clearly points to the O 2p nature doped holes in $Li_xNa_yCoO_2$. Thus, there is a difference of Li/Na content of $Li_xNa_yCoO_2$ in the bulk and at the surface.

As one can see in Fig. 1, the Co $2p_{3/2,1/2}$ X-ray absorption spectrum of $Li_xNa_yCoO_2$ measured in the both TEY and TFY modes is not differ from the spectra measured for $LiCoO_2$ and nonstoichiometric cobaltites Li_xCoO_2. This means that cobalt ions for $Li_xNa_yCoO_2$ on the surface as well as in the bulk of $Li_xNa_yCoO_2$ are in Co^{3+} state (the electronic configuration $3d^6$ is conserved).

Fig. 2 shows O $K\alpha$ and Co $L\alpha, \beta$ resonant X-ray emission spectra for $Li_xNa_yCoO_2$ measured at different excitation energies. The excitation energies shown by the solid lines were chosen based on the corresponding X-ray absorption spectra. One can see that the O $K\alpha$ spectra do not change with the photon energies scale, thus they should be described as bandlike states. Due to the itinerant character of valent O 2p states, the O $K\alpha$ spectrum can be considered as a projection of the 2p-derived density. Note, the spectrum labeled "f" reveals the O 2p state of a carbonate phase. Therefore, it differs from the spectra excited at other energies.

The Co $L\alpha, \beta$ spectra so not changed with the excitations. No energy-loss feature, which is normally associated with various electron excitations and correlations, was displayed by the spectra.

The authors thank Dr. A. Pietzsch for technical supports at MAX-II. This work was supported by the Russian Foundation for Basic Research (Grant Nos 07-02-00540 and 10-03-00203).

[1] L. A. Montoro, M. Abbate, and J. M. Rosolen, Electrochem. Solid-State Letter **3**, 410 (2000).

[2] V. R. Galakhov, N. A. Ovechkina, A. S. Shkvarin, S. N. Shamin, E. Z. Kurmaev, K. Kuepper, A. F. Takács, M. Raekers, S. Robin, M. Neumann, G.-N. Gavrilă, A. S. Semenova, D. G. Kellerman, T. Käämbre, and J. Nordgren, Phys. Rev. B **7**4, 045120(6) (2006).

[3] V. R. Galakhov, M. Neumann, and D. G. Kellerman, Appl. Phys. A **94**, 497 (2009).

[4] R. J. Balsys, R. L. Davis, and J. M. Rosolen, Solid State Ionics **69**, 69 (1994).

Local electronic structure of functional groups in glycine as anion, zwitterion and cation in aqueous solution

Johan Gråsjö[1], Egil Andersson[2], Johan Forsberg[2], Laurent Duda[2], Ev Henke[2], Wandared Pokapanich[2], Olle Björneholm[2], Joakim Andersson[2], Annette Pietzsch[3], Franz Hennies[3], and Jan-Erik Rubensson[2,*]

[1]*Department of Pharmacy, Uppsala University, Box 580, SE-751 23 Uppsala, Sweden*
[2]*Department of Physics and Materials Science, Uppsala University, Box 530, SE-751 21 Uppsala, Sweden*
[3]*MAX-lab, Box 118, SE-221 00 Lund, Sweden*

Amino acids dissolve in water preferentially as cations at low, neutral zwitterions at intermediate, and anions at high pH. The variations in local environment will alter shape and reactivity of the molecules, which in turn can have dramatic effects on their biological function. The complexity of interaction of the molecules with each other and their aqueous environment hampers a closer look on the changes in the electronic structure of the single molecules.

Here we present soft X-ray emission (SXE) and absorption (SXA) spectra of glycine (NH_2–CH_2–COOH) in aqueous solution, by various pH taking zwitterionic, cationic and anionic forms. The experiments were carried out at beamline I511-3. Oxygen K emission spectra reflect the local electronic structure at the $–COO^-$ group of the zwitterion, and the –COOH group of the cation. Using selective excitation the oxygen spectra of glycine can be separated from the oxygen spectra of the surrounding water molecules. We demonstrate that protonation mediated by the aqueous environment has a strong influence on the local electronic structure, and that the overall shape of the spectra is specific to the functional group.

In Fig. 1 we show SXE spectra of glycine resonantly excited at the oxygen K edge. For excitations above 534 eV the emission spectra simulate the SXE spectra of liquid water. The resonance at around 532-533 eV in the absorption spectra cannot be related to water molecules, and we can therefore unambiguously assign it to absorption in the glycine molecule. Both at pH 6 and pH 1 the resonantly excited SXE spectra are dominated by a sharp peak at 526.5 eV. At pH 6, where glycine is terminated by the $–COO^-$ group, there is a second sharp peak on the low energy flank at 525.5 eV. There is also a broader structure with a maximum at 522.3 eV. At pH 1, where glycine is terminated by –COOH, the spectrum shows a very broad structure at lower energies with faint structure only.

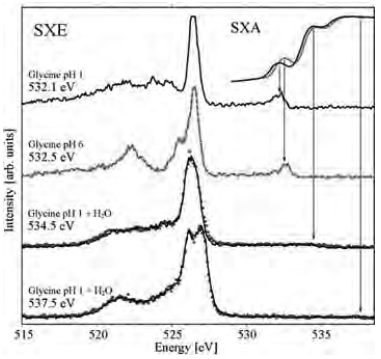

Figure 1. Oxygen K emission spectra of glycine in water solution at pH 1 (solid black line) and pH 6 (dashed red line). Above 534 eV, the absorption in water dominates the SXA spectrum, and the SXE spectra excited at higher energies are identical to the spectra of pure water (blue dots) within our experimental accuracy. Spectra excited at the resonance around 532-533 eV can be associated with excitations localized at the oxygen atom at the -CdO group of glycine. The absorption spectrum in the inset is not corrected for self-absorption.

The resonance at around 532 eV in the SXA spectrum of gas-phase glycine has been assigned to transitions to $\pi^*_{C=O}$ orbitals. Following this assignment we expect that the oxygen atom of the –C=O group, located at the–COOH termination (pH 1) is excited, and that the spectrum in the first approximation exhibits the local electronic structure of that group.

A comparison to the valence electronic structure of gas-phase glycine analyzed by photoelectron spectroscopy (PES) [1, 2] supports this assumption.. The observed sharp peak in the spectrum recorded for pH 1, corresponding to an intact –COOH group is found at 526.5 eV. The energy shift between the observed peak position and the transition energy

expected for gas-phase SXE may be a shift due to the polarization of the surrounding medium, but it may also be related to the screening associated with the excited electron.

In addition we find that the spectrum shows large similarities with the resonantly excited spectra of liquid acetic acid [3], demonstrating that the local electronic structure at the carboxyl oxygen site of a –COOH group in these two molecules is similar, and suggesting the use of the resonantly excited SXE spectrum as a –COOH group fingerprint.

Oxygen K emission spectra of cationic, zwitterionic and anionic glycine in aqueous solution have been measured. Our analysis shows that the molecular electronic structure is significantly changing upon protonation/deprotonation of the amino and carboxylic groups. Thereby, the modified functional groups exhibit a characteristic local electronic structure, similar to that of these groups in other chemical environments. The SXE spectra do not demonstrate any large modified by the liquid surrounding. Resonantly excited SXE provides a good probe for the occurrence of these functional groups in a complex liquid environment, using their spectral signature as a fingerprint.

References:

1. Cannington, P. H. and Ham, N. S. *J. Electron Spectrosc. Relat. Phenom.* **1983**, *32*, 139

2. Plekan, O.; Feyer, V.; Richter, R.; Coreno, M.; de Simone, M.; Prince, K. C. and Carravetta V. *J. Phys. Chem. A*, **2007**, *111*, 10998

3. Tokushima, T.; Horikawa, Y.; Harada, Y.; Takahashi, O.; Hiraya, A. and Shin, S. *Phys. Chem. Chem. Phys*., **2009**, *11*, 1679

Energy level line-up and interface chemistry in novel hybrid solar cells

S J O Hardman[1], D M Graham[1], W R Flavell[1] and F Hennies[2]

[1] *The Photon Science Institute, the University of Manchester, Alan Turing Building, Oxford Road, Manchester M13 9PL, UK*

[2] *Dept. of Synchrotron Radiation Research, Institute of Physics, Lund University, PO Box 118, S-221 00 Lund, Sweden*

There is an urgent requirement both to improve the efficiency of solar cells and to produce a step change in the cost of solar technology. Promising candidates for 'next-generation' cell technology include colloidal semiconductor quantum dots (QDs) that harvest the incident light, creating an electron-hole pair (exciton), and n-type and p-type conductors that separate the charge. These QDs have the advantages of a cheap, wet chemical synthesis[1], and a band gap that may be tuned to match the solar spectrum. A number of the QDs of interest, including PbS and InP been shown to exhibit multiple exciton generation (MEG) - the creation of several excitons from a single incident photon with an energy of several times the band gap[2,3,4] Successful exploitation of this effect would lead to a step change in solar cell efficiency. Crucial to the exploitation of MEG is control over the surface chemistry of the QD, as carriers may be trapped there. It is also essential that the energy levels of the dot are appropriately aligned with those of the materials around it in order to achieve efficient charge separation. Using beamline I511/1 at MAX II, we have used the tunability of the SR radiation to carry out depth-profiling XPS of both PbS and core-shell ZnS-InP QDs, and have measured energy-level line-up using valence band photoemission and workfunction measurements, combined with optical measurements of the bandgap.

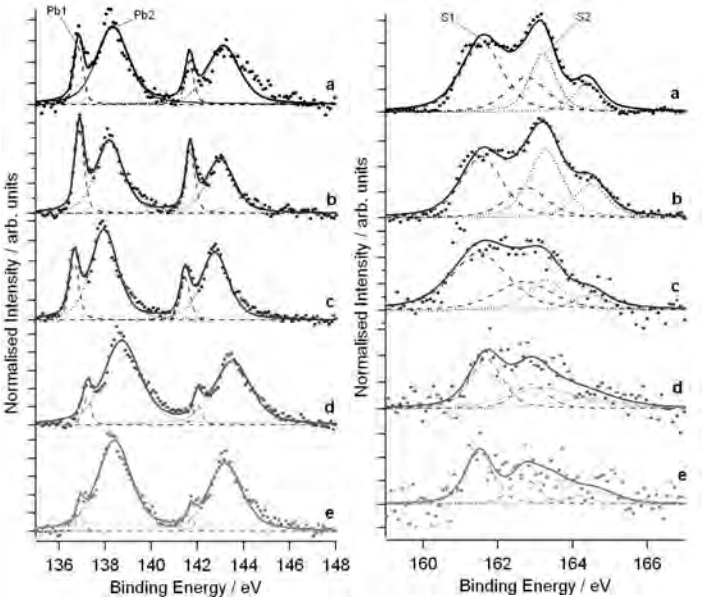

Figure 1. X-ray photoemission spectra of lead 4f (left) and sulphur 2p (right) core levels for a 4.9 nm diameter PbS nanoparticle sample at electron kinetic energies of approximately 75 (a), 200 (b), 400 (c), 600 (d) and 800 (e) eV. This corresponds to an increase in estimated inelastic mean free path of 0.53 – 1.82 nm from (a) to (e). Species present are neutral lead (Pb1, long dashes), lead as found in PbS (Pb2, dots), neutral sulphur (S2, dots) and sulphur as found in PbS (S1, long dashes).

In the case of PbS QDs (figure 1), in addition to PbS, we find neutral Pb and S species present at the surfaces of the dots. These may be caused by photodegradation under the SR beam. In these freshly-prepared systems, we find that the oxidised surface species (for example sulphate) which we have previously observed[1] are absent. We found that the nanoparticles were strongly n-type, with a LUMO (lowest unoccupied molecular orbital) energy 4.0 eV below the vacuum level. This should in principle allow successful charge injection into a number of metal oxides of interest, including ZnO, SnO_2 and TiO_2. This indicates that it is energetically possible to extract charge from the QD, a critical parameter in prototype cell design.

We have also used I511/1 to probe the surface composition and chemistry of so-called 'core-shell' QDs, consisting of an InP core and ZnS shell. InP has the advantage in this application that it is a relatively benign material. Here we again used variation of the electron mean free pathlength with photon energy to probe the QD surfaces[5], as shown in Figure 2.

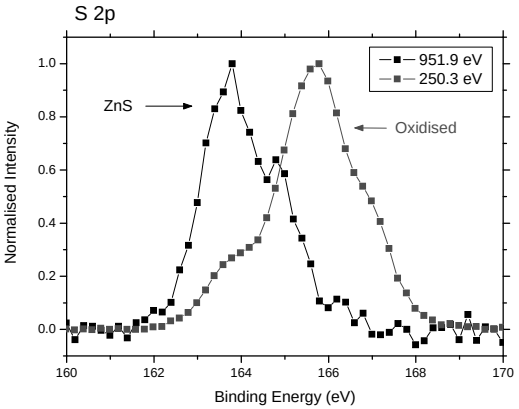

Figure 2: Sulphur 2p spectra of 'core-shell' ZnS-InP nanoparticles deposited on a gold substrate. At low photon energy (and short inelastic mean free pathlength, estimated to be 0.7 nm), the signal due to oxidised forms of sulphur (sulphates and sulphites) is considerably enhanced (red spectrum). The more bulk-sensitive spectrum (black, estimated inelastic mean free pathlength 1.8 nm) is characteristic of ZnS.

We found signficant oxidation (as shown by the presence of a large sulphate S 2p signal) at the surface of the ZnS shell. Measurement of the In 3d and Zn 3p signals as a function of photon energy allowed extraction of the average ZnS shell thickness (1.5 nm, in agreement with inferences from TEM). Importantly, the P 2p signal also revealed the presence of PO_4^{3-} as an oxidation product, with a photon energy variation that suggests it lies at the interface between the core and the shell. This suggests that the ZnS shell is not conformal around the InP core, allowing oxidation to occur. This is important information in device optimisation, that is not easy to extract by other means.

[1] J Akhtar, M A Malik, P O'Brien, K G U Wijayantha, R Dharmadasa *et al., J Mater Chem*, in press (DOI: 10.1039/b924436k.
[2] R J Ellingson *et al.*, Nano Letters, **5,** 865, (2005)
[3] R D Schaller *et al.*, Nature Physics, **1**, 189 (2005).
[4] S K Stubbs, S J O Hardman, D M Graham, B F Spencer, W R Flavell *et al., Phys Rev B* **81**, 081303(R), (2010).
[5] H Borchert, S Haubold, M Haase, H Weller, C McGinley, M Riedler and T Möller, Nano Lett., **2**, 151 (2004).

Soft X-ray photoabsorption of BeO

A. Kikas[1], T. Käämbre[1], I. Kuusik[1], K. Kooser[1,2], V. Ivanov[3] and V. Pustovarov[3]

[1]Institute of Physics, University of Tartu, Riia 142, 51014 Tartu, Estonia
[2]Department of Physics and Astronomy, University of Turku, FIN-20014 Turku, Finland
[3]Ural State Technical University-UPI, Mira street 19, Ekaterinburg, Russia, 620002

Insulating oxides have physical properties that make them useful in a wide range of applications. BeO has attracted attention due to its high thermal stability (melting temperature T=2550°C), wide transparency range extending from VUV to IR region (120–7000 nm), high heat conductivity, low electrical conductivity, mechanical hardness and radiation resistance. BeO crystallizes in the hexagonal wurtzite crystal structure; with the lattice point symmetry as low as C_{3V}. A consequence of the low symmetry is expected to be strong anisotropy of the optical constants.

Experimentally, anisotropy of the unoccupied states can be probed by X-ray absorption using polarised light. When the electric field (**E**) of the linearly polarised incident light is perpendicular to the **c** axis of the crystal (**E**⊥**c**), the transition is from Be 1s or O1*s* level to states of p_{xy}-symmetry. If the electric field of the absorbed light or the momentum transfer is parallel to the **c** axis (**E**∥**c**), spectra corresponding to p_z-symmetry projected final states can be acquired. Thus, measuring spectra at different geometries allows probing different final states.

Due to the large absorption coefficient, direct measurements of photoabsorption in soft X-ray region are not practical and indirect methods like partial and total electron yield are used. However, in case of good insulators like BeO the situation is further complicated due to charging effects, therefore the photon-in-photon out techniques like partial or total fluorescence yield (PFY and TFY) are more favourable. To the best of our knowledge, the Be 1s absorption of crystalline BeO has been studied experimentally using partial fluorescence yields [1] and also by nonresonant X-ray Raman Scattering [2]. In this report we present Be 1s and O 1s photoabsorption spectra, measured in the total fluorescence yield mode, and in two complementary geometries.

The measurements were performed at beamline I511-3 of MAX-lab. The fluorescence yield was detected using the (V-stack) microchannel plate detector, positioned in the plane of the incoming radiation, at an angle of 45 deg relative to the incident beam. The fluorescence yield spectra were

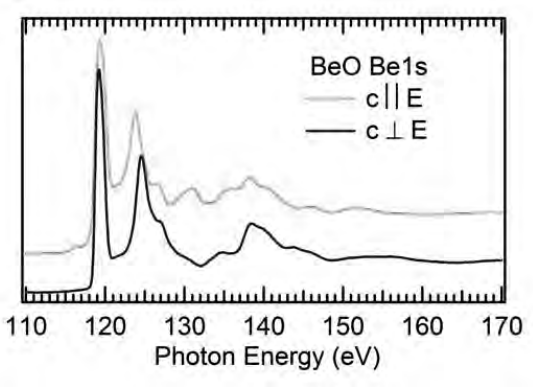

Fig. 1. Be 1s photoabsorption measured as total fluorescence yield.

measured in two geometries: a) the crystal symmetry axis parallel to the electric vector of the incoming radiation (**E**∥**c**) and b) the symmetry axis of crystal perpendicular to the electric vector (**E**⊥**c**). In the latter case the angle between surface normal and the incoming radiation was 35 deg due

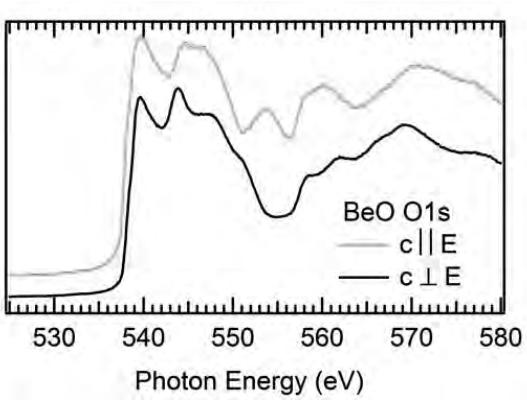

Fig. 2. The BeO O 1s TFY spectra in the two mutually perpendicular geometries.

to geometry of chamber. The SX700 monochromator exit slit was set to 50μm, which translates to 0.12 eV resolution at the O 1s and to better than 40 meV resolution at the Be 1s edge. The base pressure of the system was 9×10^{-10} mbar. Measurements were done at room temperature.

Fig. 1 shows the Be 1s photoabsorption spectra. These spectra reproduce well the earlier spectra of partial fluorescence yield [1] and are in good agreement of the measured nonresonant x-ray scattering spectra [2] and recently calculated soft X-ray absorption spectra [3]. These spectra reflect the transitions from Be 1s level to the conduction band states, which are almost completely composed of the Be 2p atomic orbitals with an insignificant admixture of the O 2p atomic orbitals [4]. Note that comparison of the presented spectra shows, that the distance between first two peaks is larger in the **E**⊥**c** spectrum than in the **E**∥**c** spectrum. This is similar to the luminescence excitation spectra, where minima are observed at the energies, corresponding to the maxima in photoabsorption spectra [5].

Fig. 2 shows the O 1s photoabsorption spectrum. In general, these spectra correspond to the transition of electron from O 1s state to the conduction band states of O 2p origin. Similar to the case of Be 1s, even here a shift of the second peak at different geometries is observed. To our knowledge the BeO O 1s photoabsorption has not been reported in the literature, therefore we cannot compare our results to earlier experimental data. It has previously been shown that it is possible to calculate the true photoabsorption spectrum from the fluorescence yield spectra, measured at different angles [6]. Using this approach for the O 1s spectra of MgO [7] led to considerable increase in the contrast of spectra. However, this procedure assumes that there is no angular dependence in the photoabsorption coefficients themselves, which is not true for BeO due to its low symmetry. We assume that the presented spectra suffer a loss of contrast due to self-absorption effects, but the elements of spectral structure are still visible. A detailed analysis of the values of photoabsorption cross sections is needed to correct the spectrum.

References:

1. T. Käämbre, A. Kikas, K. Kooser, V. Kisand, M. Kirm , A. Saar, E. Nõmmiste, V. Ivanov, V. Pustovarov, and I. Martinson, J. Electron Spectrosc. Related Phenom. **156-158**, 299 (2007).
2. J. A. Soininen, K. Hämäläinen, W. A. Caliebe, and Eric L. Shirley., J. Phys. Condens. Matter **13**, 8039 (2001).
3. S.-P. Gao, C.J Pickard, M.C. Payne, J. Zhu, and J Yuan, Phys. Rev. B **77**, 115122 (2008).
4. Yu.N. Makurin, A. A. Sofronov, V. S. Kijko, Yu. V. Emel'yanova, and A. L. Ivanovskii; Journal of Structural Chemistry **43**, 515, 2002.
5. V. Ivanov, M. Kirm, V. Pustovarov, and A. Kruzhalov, Rad. Measurements, 42, 2007, 742-745
6. S. Eisebitt, T. Boske, J.-E. Rubensson, and W. Eberhardt, Phys. Rev. B 47(1993) 14103.
7. A. Kikas, T. Käämbre, V. Kisand, A. Saar, K. Kooser, E. Nõmmiste, and I. Martinson J. Electron Spectrosc. Related Phenom. 144–147 (2005) 845–848.

X-Ray emission in doped sol-gel TiO_2 films

Ivar Kuusik[1], Tanel Käämbre[1], Arvo Kikas[1], Urmas Joost[1], Kuno Kooser[1,2] and Vambola Kisand[1]

[1]*Institute of Physics, University of Tartu, Riia 142, 51014 Tartu, Estonia*
[2]*Department of Physics and Astronomy, University of Turku, FIN-20014 Turku, Finland*

The light induced phenomena in solid titania films have been found useful in a rather broad range of applications, not least in solar cells, but also for example as a coating for self-cleaning windows, while the origin of the functionality still related to the generation of electron-hole pairs under light. The approximately 3 eV band gap is however not best fitted for use with sunlight. Our motivation to study the titania films with controlled levels of introduced impurities (a few per cent of substitute 3d elements) is to seek possibilities to shrink the band gap via charge transfer to the normally d^0 Ti^{4+} ions and cause changes in electronic structure. Due to the selection rules, RIXS is perfectly suitable to probe added d states.

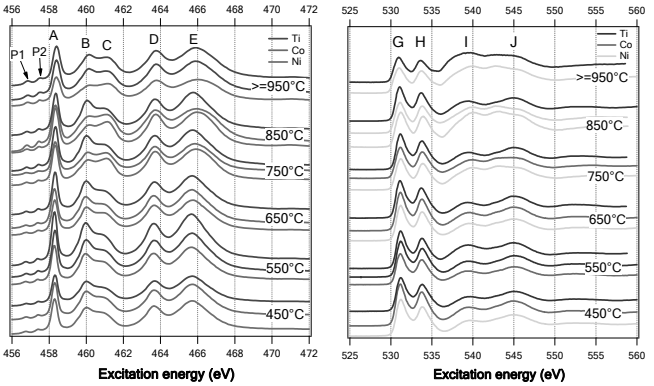

Figure 1. TEY absorption spectra of sol-gel TiO_2 thin films. Blue curves indicate samples with no additional doping, green curves are films with Ni(O) in them and red curves are with Co doping. Numbers next to the spectra indicate the post deposition annealing temperature in centigrade.

Near edge x-ray absorption fine structure (NEXAFS) and resonant X-Ray inelastic scattering spectra (RIXS) have been measured in thin (Ni and Co doped, and undoped) TiO_2 films, which were prepared using the sol-gel method. The precursor for titanium was titanium butoxide and NiCl-hexahydrate was used for nickel [1]. Cobalt was introduced by adding CoCl-hexahydrate to the solution. The films were deposited using the spin-coating method.

The measurements were performed at beamline I511-3 in Max Lab. The incidence angle for RIXS measurements was 77° from the surface normal. The Gammadata Scienta XES350 soft x-ray spectrometer was oriented along the polarisation of the incoming x-rays. The NEXAFS spectra were measured in total electron yield (TEY) mode. The incidence angle for NEXAFS measurements was 35° from the surface normal. The resolution of the beamline monochromator (a modified SX700 by Zeiss) was set to 0.12 eV during the NEXAFS measurements. Resonant x-ray emission spectra were measured with the excitation at the Ti 2p core resonances. During the RIXS measurements both the resolution of the spectrometer on the end station and the monochromator resolution were set to 0.4 eV. The base pressure of the system was 9×10^{-10} mBar. The measurements were performed at room temperature. The emission spectra have been smoothed slightly with a simple binomial algorithm to reduce their "roughness" because of their somewhat poor statistics.

In the most simplistic picture the Ti 2p NEXAFS spectra in TiO_2 can be described using atomic transitions in Ti^{4+} ion in a crystal field. In this picture the Ti ion undergoes a transition $2p^6\ 3d^0 \rightarrow 2p^5 3d^1$. The 2p core hole can be either a $2p_{1/2}$ or $2p_{3/2}$ whose energies are separated by the 5.4eV spin-orbit splitting.

The NEXAFS spectra for TiO_2 thin films undoped and doped with cobalt and nickel are shown in Figure 1. The absorption spectra reflect the TiO_2 conduction band, which is composed of Ti 3d, 4p, 4s and unoccupied O 2p orbitals. The spectra also show spin-orbit splitting (peaks A, B vs. D, E) and crystal field splitting (A vs B and D vs. E). The pre-peak P has triplet character, arises from jj coupling considerations [2] and is also crystal-field split (P1, P2).

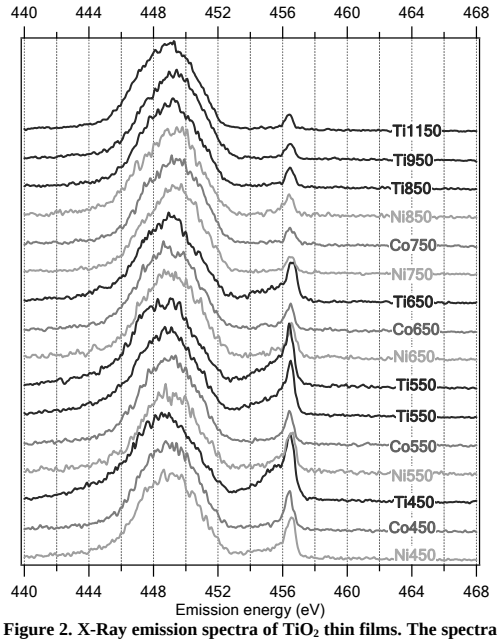

Figure 2. X-Ray emission spectra of TiO_2 thin films. The spectra are excited at the P1 peak on Figure 1. Text next to each spectrum indicates the dopant used in the sample (Ni for nickel, Co for cobalt, Ti means undoped) and post deposition annealing temperature in centigrade.

The spectra indicate a phase transition from anatase to rutile in-between 650-750°C for both Co and Ni doped films, while the spectrum of the undoped film shows no change. Namely, in anatase the peak B is stronger than the peak C and vice-versa in rutile [3], because the D_{2h} crystal symmetry of rutile is somewhat different from the symmetry of anatase. This difference appears in the e_g part because this state is more hybridized with the neighbouring oxygen atoms.

Figure 2 is a comparison of emission spectra for nickel doped and undoped TiO_2 thin films annealed at different temperatures with the excitation energy tuned to the first prepeak (P1 on Figure 1). The energy loss feature near the elastic peak at about 456 eV emission energy is decreasing in intensity as the samples are annealed to higher temperatures. The spectra in Figure 2 show energy loss sidebands up to annealing temperatures about 650°C. Cobalt doped films show no energy loss shoulder, nickel doped samples show a very weak tail and undoped films show the strongest and widest energy loss shoulder. One possibility here would be to see the availability of sub-bandgap excitations in RIXS primarily for the undoped sol-gel film as an indication that the impurities might act as stabilising agents for sol-gel deposited titania. However, such small energy loss shoulder is absent at $L_3\ t_{2g}$ excitation (at peak A on Figure 1; RIXS not shown here), and we would therefore avoid promptly proposing the presence of Ti^{3+} impurities to cause the sub-bandgap energy loss features at P1-excitation, but rather check alternative schemes considering carefully the symmetry arguments.

References

1. V. Kisand *et al.*, Appl. Surf. Sci. (2010), doi:10.1016/j.apsusc.2010.02.043
2. A. Augustsson *et al.*, Journal of Chemical Physics **119** (2003) 3983.
3. R. Ruus *et al.*, Solid State Communications **104** (1997) 199-203.

Modification of electronic properties of FePc with alkali metal doping. Part II. (DFT calculations).

O.V. Molodtsova[1], V.V. Maslyuk[2], D.V. Vyalikh[1], I. Mertig[2], T. Bredow[3], A.B. Preobrajenski[4], M. Knupfer[5], and V.Yu. Aristov [5,6]

[1]*Institute of Solid State Physics, TU Dresden, D-01069 Dresden, Germany*

[2]*Martin-Luther-Universität at Halle-Wittenberg, Fachbereich Physik, Germany*

[3]*Institute for Physical and Theoretical Chemistry, Bonn University, D-53115 Bonn, Germany*

[4]*MAX-lab, 22100 Lund, Sweden*

[5]*IFW Dresden, D-01069 Dresden, Germany*

[6]*Institute of Solid State Physics, Russian Academy of Sciences, Chernogolovka, Moscow Distr., 142432, Russia*

The evolution of electronic structure of the organic semiconductor iron-phthalocyanine (FePc) with potassium doping which was studied in part1 by means of photoemission spectroscopy using synchrotron radiation facilities at the beamline I511/1 at MaxLab is now proved by density functional theory (DFT) calculations. The DFT study and detailed analysis of the core-level spectra permit us to suggest possible lattice sites for the potassium ions.

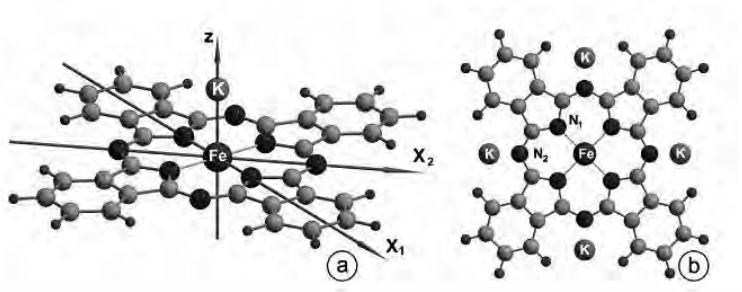

Fig. 1: (a) - schematic presentation of FePc molecule, potassium atom above of iron atom and two high symmetry axes X1 and X2 along which the K atom was moved being 2.0 °A above the molecular plane. (b) - schematic diagram of the possible positions of the K atoms or ions intercalated in FePc molecule for the doping concentration of 4 ions for one FePc molecule.

We present here a single molecule density functional theory (DFT) study, which allows us to determine the most favourable sites, which potassium ions occupy close to FePc molecules. The calculations were performed using the linear combination of atomic orbital (LCAO) formalism based on density functional theory and realized in the CRYSTAL code. We use the three parametric Becke+Lee-Yang-Parr (B3LYP) exchange-correlation functional which correct self-interaction error inherent in local density and generalised gradient approximations. The electron subsystem was described by the all electron basis sets in Gaussian form, namely, we use 6-311+G** basis set for C, N and H atoms and TZVP basis for Fe and K. The structure of the FePc molecule was optimized. We found that the FePc molecule has a planar structure and a total magnetic moment of 2 μB in the ground state. The next excited magnetic configuration is a quintet (μtotal=4 μB) with planar atomic structure. The excited magnetic state is only 0.62 eV higher in energy then the ground state.

Taking into account our previous conclusion, that potassium strongly reacts with the asa nitrogen atoms and pyrrole carbon, we move K across the FePc molecule along two high symmetry axes X1 and X2 as is shown in the Fig.1(a). For detailed investigations, we assume that the potassium atom can be neutral and ionized (K1+) and the FePc molecule can be in two magnetic states. The results of our calculations are shown in the Figure 2. The curve with square symbols in two Figures 2(a,b) corresponds to binding energy calculations between a FePc molecule in the excited magnetic state and neutral K. The circles show the binding energy data between a FePc molecule in the ground state and neutral potassium. Here, we have to note that we present the energetically preferable configuration where the magnetic moment of the molecule and the neutral K atom are antiparallel for both magnetic states of FePc. Thus, the curves with squares correspond to the the FePc+K system with a total magnetic moment of 3 μB and the circles are related to the system with the total magnetic moment of 1 μB. The triangles describe the interaction between ionized K+ and FePc molecule in the ground state (total magnetic moment is 2 μB).

For the X1 direction [Fig. 1(a)] the interaction energy between K atom or ion and the FePc molecule is positive for any distance up to 7.5 °A, which means a repulsion between potassium and molecule. The displacement of the K atom along X2 axis shows that the potassium atom and ion can create a stable bond with FePc molecule in both magnetic states. In this case, the potassium is situated close to the asa-bridging nitrogen N2. The energetically preferable configuration corresponds to the system with the smallest total magnetic moment μ(FePc+K0)=1μB. We also found the charge transfer from originally neutral K atom in amount of 1e− to FePc molecule. Now, taking into account that the binding energy between FePc molecule and ionized K1+ atom is quite large [see Fig.2(b)] we can assume that only ionized K atoms can migrate into the FePc slab. The further relaxation of the FePc molecule with the K atom or ion shows that the potassium is still situating close to N2 atom but out of the molecular plane. Therefore, for the comparison of the theoretical and experimental spectra one needs to analyze the interaction of the potassium with two or more FePc molecules. Finally, our theoretical data confirm conclusions above, that K atoms (ions) intercalated into FePc film occupy one type of equivalent positions in FePc molecule along X2 axis, namely - close to of asa-bridging nitrogens N2 as schematically shown in Fig.1(b).

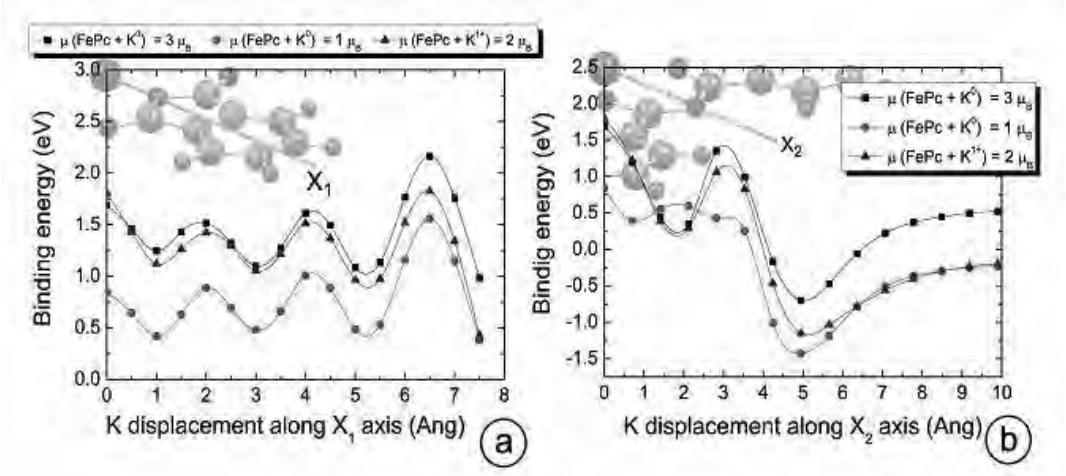

Fig. 2: The binding energy between FePc molecule in different magnetic states and potassium atom and ion as a function of K displacement along X1 (a) and X2 (b) axes. The details of the figure see in the text.

This work was supported by the EC Transnational Access to Research Infrastructure via MaxLab, by the DFG under grant no. 436RUS17/52/06, and by the SMWK. V.Yu.A. thanks the RFBR (Grant Num. 08-02-01170). We are grateful to MaxLab staff and personally Franz Hennies and Annette Pietzsch for help during the experiment.

Band Gap Opening in Graphane and Graphene Oxide

Prabir Pal[1,2], Pål Palmgren[1], Ronny Knut[1], Tobias Blom[3], and Olof Karis[1]
Rahul Nair[4], Andre K. Geim[4] and Kostya S. Novoselov[4]

1 Molecular and Condensed Matter Physics, Department of Physics and Astronomy, Uppsala University
2 MAX-lab, Lund University
3 Electron Microscopy and Nanoengineering, Department of Engineering Sciences, Uppsala University
4 Condensed Matter Physics, Department of Physics and Astronomy, University of Manchester, UK

Graphene, a single atomic layer of carbon atoms, has been extensively studied because of its intriguing electronic properties and, as a consequence, the promising performance in electronic devices [1]. Graphene is a zero-overlap semimetal, where the valence and conduction band meet at two equivalent points in the Brillouin zone, known as the Dirac points. Although such linear spectra is a source of a number of very interesting phenomena, for a number of applications (such as transistors, for instance) it is necessary to create a band gap in the material. This can be achieved by chemical reactions of atomic oxygen or hydrogen with the atomic layer of carbon, leading to two-dimensional layers of graphene oxide (GO) or hydrogenated graphene, known as graphane (GH). In contrast to graphene, GH and GO exhibits insulating or semiconducting behavior, as a band gap opens at the Fermi level due to bonding of foreign atoms to graphene scaffold, thus explaining the interest in future electronic devices of the GH and GO sheets. In this project, we compare the electronic properties of few layer graphene (FLG) with those of GH and GO, using near-edge x-ray absorption fine-structure (NEXAFS) spectroscopy and photoelectron spectroscopy and find evidence of a mixture of sp^2 and sp^3 hybridized carbon atoms in the GH and GO films as well as a shift of the conduction band edge to higher energy and a shift to lower binding energy of the valence band edge.

NEXAFS spectra were recorded in the partial electron yield mode with a MCP electron detector at the undulator beamline I511-1 at Max-Lab, Lund, Sweden. The photon energy resolution was set at 50 meV for the C K-edge absorption spectra. The PES measurements were performed using a Scienta R4000 analyzer, collected in an angle integrated mode in normal emission. The binding energy was calibrated using the Fermi-edge of a gold reference sample. The samples were heated to 300°C to desorb physisorbed contaminants. After heating, the FLG sample showed no oxygen contamination as evidenced by XPS.

In a simple picture, the structure of GO is assumed to be composed of a carbon network to which a variety of functional groups is attached, such as e.g. epoxy (C-O-C), hydroxyl (C-OH) or carboxyl (COOH), in a random fashion, while GH can be considered as a two-dimensional hydrocarbon with hydrogen atoms linked to carbon atoms on either side of the sheet. Attachment of different functional groups to the graphene lattice locally changes the hybridization from sp^2 to sp^3. Figure 1 presents absorption spectra from the samples in the same geometry, meaning that the E-vector of the light perpendicular to the surface, mainly probing states of π-character. The transition from sp^2 to sp^3 bonding is clearly seen in the spectra with the evolution of states C and D at around

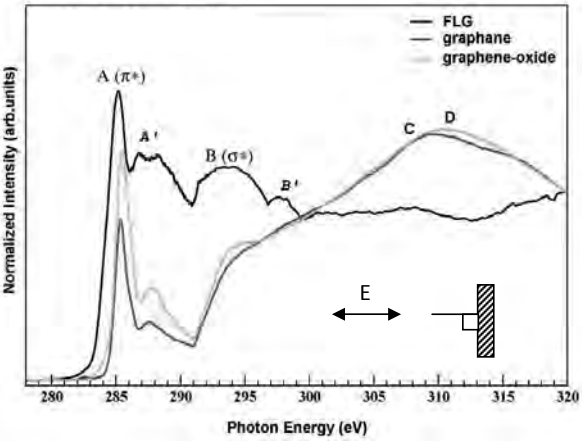

Figure 1: comparing x-ray absorption spectra obtained in from the few layer graphene, graphane and graphene oxide films.

310 eV which are interpreted as σ-type states having a short bond length. The excitation energy of the σ* resonance can be related to the σ bond length. The position of the σ* resonance peak of diamond, having a bond length of 1.54 Å, is about 291 eV and that of the graphite with a bond length of 1.42 Å is about 297 eV, while ethyne, with a triple bond length of 1.20 Å, has a σ* peak at about 310 eV [2]. Hence, the shorter the carbon-carbon bond, the higher energy for the excitation energy of the σ* resonance. Further noticeable is the increase of σ contribution in the spectra accompanied by a decrease of π* intensity which can be related to a more disoriented film, but more interesting is the shift of the leading edge to higher photon energy corresponding to an upward shift of the conduction band edge.

Figure 2 presents the valence band (VB) spectra measured with 110 eV photons. The FLG spectrum shows a set of states, denoted with roman numerals I-VII, which are similar to what is found in a graphite spectrum [3], while oxygen 2*p* derived states are clearly seen in the spectrum taken from the GO film with strong emission at about 7 eV binding energy. The Fermi level region is expanded in panel b), showing the expected metallic signature in the FLG case whereas both the GH and GO films lack emission from the Fermi level, typical behavior in insulating or semiconducting samples.

From C1s core level spectra (not shown), we find that the amount of hydrogenated carbon atoms is 61 % in GH and carbon atoms bonded to oxygen atoms is 42% in the GO films, leading to the pronounced change in hybridization, going from sp^2 for FLG to sp^3 for GH and GO. Furthermore, we have shown some important differences in electronic structure between the GH and GO with the FLG samples in the near Fermi-level, as an energy gap in the GH and GO films is opening up due to the chemical reaction with hydrogen and oxygen respectively.

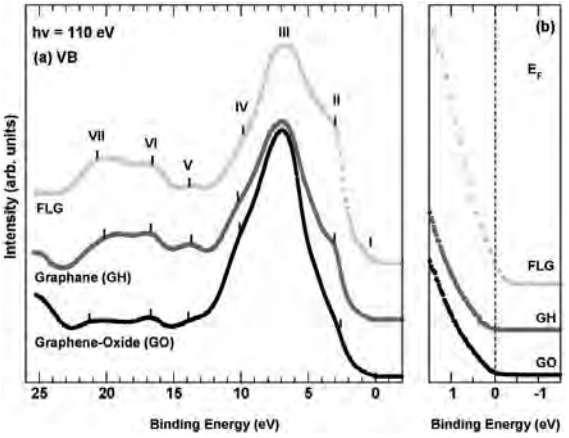

Figure 2: a) valence band spectra from the three films covering the entire VB *range, and b) close up of the Fermi level region to emphasize the band gap in the GH and GO films*

References:

1 A. K. Geim, K. S. Novoselov, Nature Materials 6, 183 (2007)
2 J. Stöhr, NEXAFS Spectroscopy, Springer Series in Surface Science Vol. 25, Springer-Verlag, New York (1992)
3 A. Bianconi, S. B. M. Hagstr¨om and R. Z. Bachrach, Phys. Rev. B 16, 5543 (1977)

Lowering the Barrier for Graphene Formation by Alloying Transition Metal Carbides

P. Palmgren[1], E. Lewin[2], R. Knut[1], P. Pal[1,3], A. Sandell[1], U. Jansson[2] and O. Karis[1]

1. Molecular and Condensed Matter Physics, Uppsala University
2. Materials Chemstry, Uppsala University
3. MAX-Lab, Lund University

Graphene production is today limited to micro mechanical cleavage of graphite or by epitaxial growth on transition metals and on metal carbides. These methods have different feasibility in up-scaling and mass fabrication; the epitaxial growth is the most promising route towards large areas of highly ordered graphene, and lift off of the graphene from the substrate has been demonstrated [1]. Graphene growth on SiC has been shown to result in wafer sized single layers, but very high temperatures (>1500 K) and minute process control are required [2,3]. On similar systems, such as e.g. single crystal TiC(111), has graphene been shown to grow epitaxially by chemical decomposition of hydrocarbons such as ethyne and ethene at high temperatures of about 1500 K [4], hence they represent potential candidates for the production of high quality graphene. However, the thermodynamic barrier for out-diffusion of carbon to the surface can be lowered if weakly carbide forming elements such as e.g. Ni are alloyed in the TiC [5]. In this project we investigate graphene formation on thin films of ternary alloys of (Ti,Ni)C grown on alumina.

Thin films of (Ti,Ni)C carbides were synthesized through non-reactive unbalanced magnetron sputtering from elemental targets of Ti and C and a segmented Ni/C target. The material was grown on single crystal Al_2O_3 (000l) substrates. A homogeneous coating with the composition $(Ti_{0.86}Ni_{0.14})C_{0.80}$ was achieved and no oxygen could be observed within the films except for a thin oxidized surface layer. Coating thickness was controlled by deposition time, chosen so to produce thickest possible coating with retained crystalline quality and found to be 14 nm thick determined by X-ray reflectivity measurements. X-ray diffraction measurements reveal that the sample is a solid solution of Ni in the TiC-lattice, where it substitutes the larger Ti atoms, the lattice parameter is 4.33 Å with a very slight tetragonal distortion and that the growth is epitaxial, the relationship to the substrate is Al_2O_3 (0001)[110] // TiC(111) [$10\bar{1}$]. Heating the samples in vacuum is done by passing a current through the thin films.

X-ray photoelectron spectroscopy experiments were performed at the undulator beam line I511-1 at MAX-Lab in Lund, Sweden. It delivers photons with an energy range of about 50-1000eV, monochromatized by a modified Zeiss SX700. The beam line is further described in Ref. [6]. The end station comprises a Scienta R4000 hemispherical electron analyzer which is rotatable around the axis of the synchrotron light, LEED optics and sample cleaning by inert gas sputtering. Spectra are taken in normal emission and grazing (~8°) incidence of the photon beam. Energy calibration is done by measuring the Fermi level on a Ta foil in electric contact with the sample. Energy resolution is estimated to be about 90 meV at 347 eV.

In Figure 1, we show the evolution of both core level and valence band spectra with temperature. In panel a), C1s spectra are presented in which the peaks at 281.7 eV originates from the bulk TiNiC while the peak at 285 eV is related to single layer graphene on the surface. A new feature develops with increasing temperature, seen as a more and more pronounced shoulder at about 284.5 eV. When comparing similar systems such as graphene growth on 6H-SiC0001, this spectral feature is identified as originating in several carbon layers (i.e. graphite) as it is located between the carbide signal and the single layer graphene signal [7]. The Ni*2p* and

Ti*2p* signal strength decreases with temperature, indicating growth of larger patches of graphene and/or thicker layers, the latter is partly supported by an orientation spread in the LEED patterns which may be due to domain formation (not shown here).

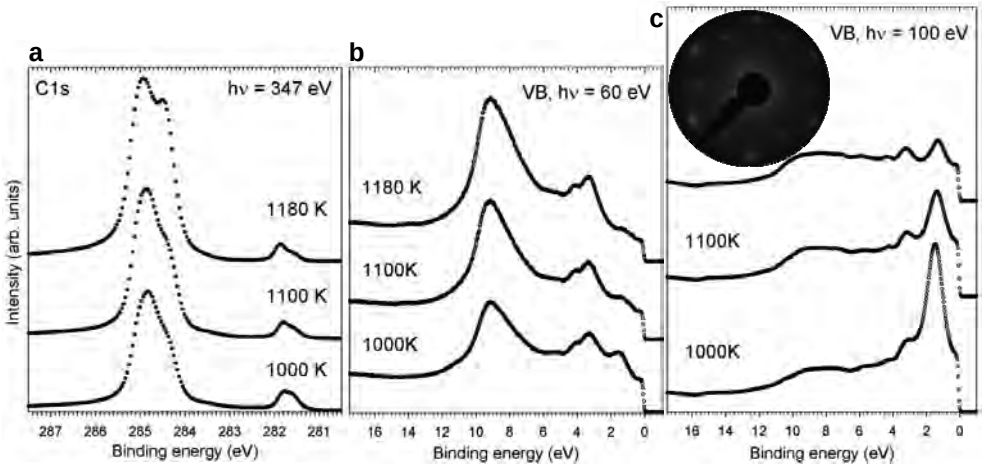

Figure 1: panel a) shows the C1s core level while panels b) and c) show valence band spectra at different photon energies as indicated. The insert in panel shows a LEED pattern (E_p=67.5eV) typical for this temperature range.

The electronic properties of the grown graphene are presented in panels b) and c). The increasing intensity of carbon related emission at 9 eV is clearly seen in b) at the same time as the TiC related emission at 1.8 eV (panel c) is strongly diminished. The film is metallic. The insert LEED pattern shows the dual 1x1 patterns from bulk TiNiC (inner hexagon) and the graphene layer. Graphene has a 30° rotational relationship with the substrate crystallographic directions and there is a slight tendency to form streaks, indicative of domain formation. This pattern emerges already at annealing temperatures as low as 975 K, well below those required for graphene growth on SiC by thermal decomposition. Reference samples of $TiC_{0.75}$ made in a similar fashion with the same magnetron sputtering system showed a $\sqrt{3}\times\sqrt{3}R30°$ reconstruction upon annealing to 1075 K which was replaced by a disordered 1×1 phase at 1360 K but no graphene formation was observed up to 1400 K, the maximum temperature used, indicating that the cause for driving carbon to the surface is the Ni incorporation.

We have shown that it is possible to lower the diffusion barrier, facilitating the formation of graphene on a transition metal carbide (TiC) by alloying with a weakly carbide forming element (Ni). Optimizing the growth parameters such as e.g. annealing time, concentration of and sort of alloying element could well lead to large areas of highly ordered graphene.

1 K.S. Kim, Y. Zhao, H. Jang, S.Y. Lee, J.M. Kim, K.S. Kim, J.-H. Ahn, P. Kim, J.-Y. Choi, B.H. Hong, Nature **457**, 706 (2009)
2 C. Virojanadara, M. Syväjarvi, R. Yakimova, L. I. Johansson, A. A. Zakharov, T. Balasubramanian, Phys. Rev. B **78**, 245403 (2008)
3 C. Virojanadara , R. Yakimova, J.R. Osiecki, M. Syväjärvi, R.I.G. Uhrberg, L.I. Johansson, A.A. Zakharov, Surf. Sci. **603**, L87 (2009)
4 H. Itoh, T. Ichinose, C. Oshima, T. Ichinokawa, Surf. Sci. Lett. **254** L437 (1991)
5 O. Wilhelmsson, M. Råsander, M. Carlsson, E. Lewin, B. Sanyal, U. Wiklund, O. Eriksson, U. Jansson, Advanced Functional Materials **17**, 1611 (2007)
6 R. Denecke, P. Väterlein, M. Bässler, N. Wassdahl, S. Butorin, A. Nilsson, J.-E. Rubensson, J. Nordgren, N. Mårtensson, R. Nyholm, J. Electron Spectrosc. Relat. Phenom. **101-103** (1999) 971
7 Th. Seyller, A. Bostwick, K.V. Emtsev, K. Horn, L. Ley, J.L. McChesney, T. Ohta, J.D. Riley, E. Rotenberg, F. Speck1, Phys. Stat. Sol. B **245** (2008) 1436

Core-level studies of metal-free phthalocyanine on Au (111)

M.N. Shariati [a], I.Bidermane [a,b], S.Ahmadi [c], E. Göthelid [a], P. Palmgren [a], M.N. Piancastelli [a] and C. Puglia [a]

[a] *Department of Physics and Astronomy, Uppsala University, Box 516, SE-751 20 Uppsala, Sweden*

[b] *Institut des Nanosciences de Paris, Université Pierre at Marie Curie, UMR CNRS 7588, Campus Boucicaut, Piéce 11.2.8, 140 Rue de Lourmel, 75015 Paris*

[c] *Materials Physics, Royal Institute of Technology, Electrum 229, SE 164 40 Kista, Sweden*

Self-assembling of organic molecules on the surface is a promising approach for the molecular film-base devices. Moreover, investigation of the electronic structure of the ordered organic adlayers on inorganic surfaces is one of the requirements to achieve this aim. Phthalocyanine molecules have many potential applications in solar cells[1,2], optical and electronic devices[3,4]. Adsorption of monolayer and multilayer of metal-free phthalocyanine molecules on the Au (111) surface was investigated by X-ray Photolectron Spectroscopy (XPS) and X-ray Absorption Spectroscopy (XAS) techniques to get information about the occupied and unoccupied electronic states, as well as the geometrical orientation of the molecules on the surface. The Au (111)-($\sqrt{3}\times22$) surface was prepared by cycles of Argon sputtering and annealing to 720 K. H_2Pc was purchased from Aldrich (98% dye content). The molecules were deposited, *in situ*, onto the sample as mentioned in one of our previous article[5].

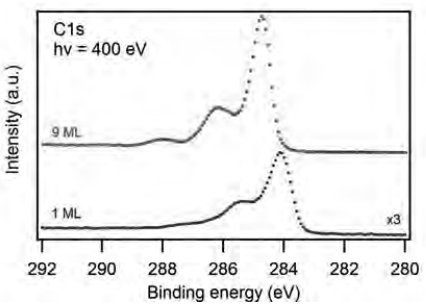

Figure1 : C1s XP spectra of monolayer and multilayer coverage

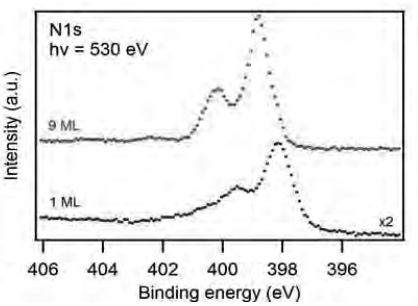

Figure 2 : N1s XP spectra of monolayer and multilayer coverage

Core-level XPS spectra of carbon and nitrogen were studied at monolayer and multilayer coverages. The C1s XP spectrum obtained at 1 ML coverage (Fig.1) exhibited a two-component line-shape. The peaks at the binding energies of 284.1 eV and 285.3 eV correspond to benzene-type carbon atoms and pyrrole-type carbon atoms together with the shake-up transition associated with the benzene-type carbons, respectively. The multilayer spectrum consists of three main features. The peak observed at 284.7 eV is due to the contribution of the carbon atoms of benzene-type and the peak at 286.1 eV is due to carbon atoms of pyrrole-type together with the shake-up structures associated with the benzene carbon atoms. The third peak at the binding energy of 288 eV is associated with the shake-up transition of the pyrrole carbons. The multilayer results are in good agreement with the previous finding[6].

The N1s core-level spectrum of the monolayer shown in Fig. 2 consists of a main peak at binding energy of 398.2 eV and a feature at 399.5 eV. The multilayer spectrum has two main peaks at binding energies of 398.8 eV, 400.1 eV, respectively and a broad low intensity feature at around 402.4 eV. These spectral features, in agreement with earlier investigations, are associated to the three non-equivalent nitrogen atoms in the molecule and the related shake-up structure[7].
Comparison of the monolayer and the multilayer spectra of the C1s and N1s show a shift in the peak positions. It can be addressed due to different core-hole screening for the different molecular coverages.

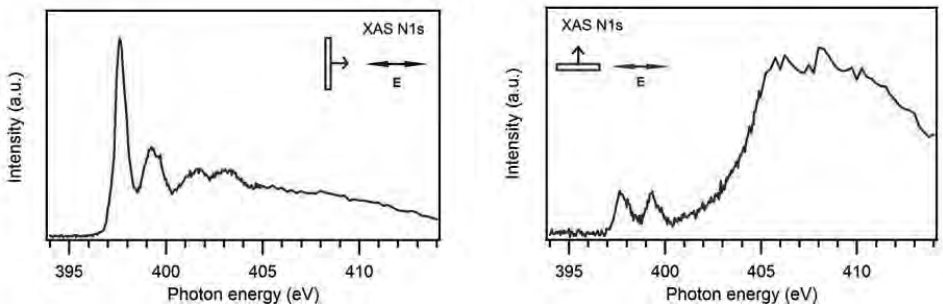

Figure 3 : N1s XAS spectra of multilayer coverage at two different geometries of the sample with respect to the E vector of the incoming light

N1s XAS spectra of multilayer coverage (Fig.3) were measured with the polarization E vector of the incoming light aligned perpendicular to the surface (E⊥, left spectrum) and parallel to the surface (E∥, right spectrum). At E⊥, a high intensity π^* feature is observed at 397.6 eV, followed by a lower intensity second π^* at 399.2 eV and two low intensities σ^* features at 401.6 eV and 403.1 eV. For the E∥ geometry, a high intensity σ^* feature is observed at about 406.2 eV as well as two π^* low intensity features at 397.6 eV and 399.2 eV. The relative intensity of the features for the two experimental geometries reveals that the molecules for the multilayer coverage are aligned with the molecular plane parallel to the surface, in contrast with what was reported for other systems where the molecules for multilayer coverage were oriented perpendicular to the surface[6,8].

References

[1] J. C. Conboy, E. J. Olson, and P.F. Barbara, et al. J. Phys. Chem. B **102**, 4516 (1998)
[2] M. Thelakkat, C. Schmitz, and H.-W. Schmidt, Adv. Mater. (Weinheim, Ger.) **14**, 577 (2002)
[3] S. Riad, Thin Solid Films **370**, 253 (2000)
[4] G. Gu, G. Parthasarathy, and S.R. Forrest, Appl. Phys. Lett. **74**, 305 (1999)
[5] K. Nilson, J. Åhlund, B. Brena, and C. Puglia, et al. J. Chem. Phys. **127**, 114702 (2007)
[6] Y. Alfredsson, B. Brena, and K. Nilsson, et al. J. Chem. Phys. **122**, 214723 (2005)
[7] Y. Niwa, H. Kobayashi, and T. Tsuchiya, J. Chem.Phys. **60**, 799 (1974)
[8] J.Åhlund, K. Nilson, and C. Puglia, et al. J. Chem. Phys. **125**, 34709 (2006)

Dry oxidation of SO_2 to SO_4 on $(\sqrt{2} \times \sqrt{2})R45°$-$Fe_3O_4(100)$

D. Stoltz[1], A. Önsten, J. Weissenrieder, U.O. Karlsson, M. Göthelid

Materialfysik, MAP, KTH-Electrum, SE-16440 Kista, Sweden

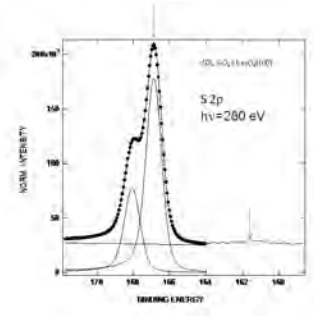

Figure 1: Normal emission S 2p spectrum of $(\sqrt{2} \times \sqrt{2})R45°$-$Fe_3O_4(100)$covered with 50 L SO_2.

Sulphur dioxide (SO_2) is an air pollutant known to have an accelerating effect on corrosion. [1] Corrosion which we talk about is deterioration of material properties caused by oxidation and it normally happens upon exposure of materials to water/oxygen in the air. Iron is known for its reaction (weakening and rust formation) due to oxidation. One way of corrosion protection of iron or steels is by the formation of protective iron oxide films (Fe_2O_3 and magnetite – Fe_3O_4). Magnetite is an inverse spinel material with a unit cell (a=8.3963 Å) containing 32 O^{2-} anions and 24 Fe^{2+} and Fe^{3+} cations. Study of exposure of magnetite surfaces to sulphur dioxide and/or water helps reveal the mechanisms of corrosion.

SO_2 is known to adsorb molecularly at most surfaces at low temperatures. At room temperature (RT) it decomposes at most surfaces leaving SO_3 on the surface. It is not known if full oxidation of SO_2 into SO_4 could happen without the presence of water. This is important because the formation of the sulfate ion leads to binding of the adsorbate to the surface and formation of a thin sulfate layer. This would also change the concept of SO_2 as accelerator of oxidation.

Fig. 1 shows a S 2p core-level spectrum from a $Fe_3O_4(100)$ surface exposed to 50 L of SO_2. It can be decomposed into one spin-orbit split doublet (spin-orbit splitting 1.2 eV, branching ratio 0.5-0.6, full-width at half-maximum (FWHM) ∼1 eV) with the binding energies 168.0 and 166.8 eV, similar to 168.3 and 167.1 eV for SO_4 from our previous study where both water and sulphur dioxide created S, SO_3 and SO_4 at the surface [2]. The lowest binding energy doublet (resolved only as a little bump in our spectrum) can be attributed to atomic sulphur according to position of its maximum (see arrow, 161.5 eV, similar to 161.3 [2]). Binding energy shifts of the doublet with respect to atomic S is thus 5.38 eV, which agrees very well with 5.6 eV shifts between S and SO_4 on a ZnO surface [3] and 5.8 eV on the water and sulphur dioxide covered $Fe_3O_4(100)$ [2] surface. This indicates that the surface is covered with SO_4.

In Fig. 2 we present O 1s core-level spectrum before (a) and after SO_2-treatment (b). Larger peak is the same as the one of the clean surface (Fig. 2), their binding energies are 529.9 on the pure magnetite and 530.0 eV after the sulphur dioxide surface treatment. After SO_2 deposition we notice another component, shown in Fig. 2b). The extra peak which we see is a bit broader than the others (1.5 eV, compared with 1 eV for the other peaks) and we assign it to SO_4. There is a possibility that more peaks are there, but we do not resolve any additional species.

After deposition of sulphur dioxide on the $Fe_3O_4(100)$, we still have a $(\sqrt{2} \times \sqrt{2})R45°$ LEED pattern (not shown). It is known that this reconstruction of the polar surface is characterized by enhanced stability [4]. Thus even a strongly oxidizing species used in our experiment (SO_2) becomes trapped by the periodicity of the $(\sqrt{2} \times \sqrt{2})R45°$-reconstruction. They bind to the substrate and the periodic potential of the $(\sqrt{2} \times \sqrt{2})R45°$ reconstruction stabilizes the overstructure.

Furthermore, as our results show, the presence of water at the surface of magnetite (100) is not necessary for further significant oxidation of SO_2 and/or SO_3 to SO_4. We clearly show presence of SO_4-groups at the surface of magnetite after exposure to SO_2 in vacuum. On some other surfaces dry oxidation of SO_2 to SO_4 has been reported. On polycrystalline ZnO films SO_2 was found to have enough mobility at the surface to react with O-centers and form SO_3 and SO_4 [3]. On the (001)-surface of Ru, which is in the same group of the periodic table as Fe, SO_2 had to be chemisorbed on the surface in order to enable the approach of the O atoms in order to form SO_4 [5]. The arrangement of the adsorbates along the $(\sqrt{2} \times \sqrt{2})R45°$-reconstruction at the $Fe_3O_4(001)$ surface, suggests that it is the mobility of SO_2 that is important. There is enough of the mobility at 200 K as well. The Fe-ions at the surface act as catalysts for oxidation of SO_2. The iron oxide surface already contains Fe^{2+} and/or Fe^{3+} ions, which facilitates the formation of sulfate ions and ferrous sulfate. Formation of sulfate is favorable for the corrosion protection, as it actually involves reduction and not oxidation of already highly oxidized substrate [2].

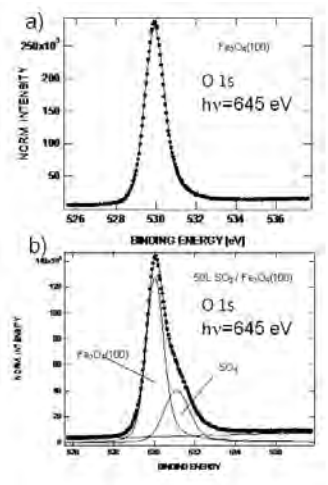

Figure 2: Normal emission spectra of O 1s core level, before and after exposure to SO_2.

Finally, there were two studies of SO_2 adsorption on metal and oxide surfaces in the past using STM. In the study of SO_2/Cu(110) [6] SO_3 moieties were found on the surface. In the case of TiO_2(110) [7], the reconstruction was found to play a role as a template for the adsorbate arrangement, similar as in our study. In this paper we show for the first time chemical identification of the adsorbed SO_2 in form of SO_4.

We show dry oxidation of SO_2 to SO_4 on a $(\sqrt{2} \times \sqrt{2})R45°$-reconstructed $Fe_3O_4(100)$ surface. At room temperature, we identify SO_4 groups on the surface. We conclude that oxidation of SO_2 to SO_4 on the surface of magnetite does not require presence of water, but does require surface mobility of SO_2.

We would like to thank A. Pietzsch (MAX-lab). VR is kindly acknowledged for financial support.

[1] C. Leygraf, *Corrosion Mechanisms in Theory and Practice*, (Marcel Dekker, Inc., 2002). Chapter 15, "Atmospheric Corrosion".

[2] D. Stoltz, A. Önsten, U. O. Karlsson, M. Göthelid, *Appl. Phys. Lett.* **91**, 093107 (2007).

[3] J. A. Rodriguez, T. Jirsak, S. Chaturvedi, M. Kuhn, *Surf. Sci.* **442**, 400 (1999).

[4] K. Jordan, S. Murphy, I. V. Shvets, *Surf. Sci.* **600**, 5150 (2006).

[5] T. Jirsak, J. A. Rodriguez, S. Chaturvedi, J. Hrbek, *Surf. Sci.* **418**, 8 (1998).

[6] A. R. Alemozafar, X.-C. Guo, R. J. Madix, *Surf. Sci.* **524**, L84 (2003).

[7] N. Hartmann, J. Biener, R. J. Madix, *Surf. Sci.* **505**, 81 (2002).

Concentration dependent Mn 3d spectra in (Ga,Mn)As.

I. Ulfat [1,2], J. Sadowski [2,3], L. Ilver [1], J. Kanski [1]

[1] *Department of Applied Physics, Chalmers University of Technology, SE-41296 Göteborg, Sweden*

[2] *MAX-lab, Lund University, SE-22100 Lund, Sweden*

[3] *Institue of Physics, Polish Academy of Sciences, al Lotników 32/46, 02-668 Warszawa, Poland*

It is generally accepted that the ferromagnetic state in dilute magnetic semiconductors is due to exchange interaction between magnetic ion spins and itinerant holes. This is the basis for important functionalities that result from the ability to control the magetic state via the density of free carriers. In the widely used RKKY model the holes are assumed to be located in the valence band, hence fully delocalized. However, there are experimental observations showing that the ferromagnetic state can occur in fully compensated systems [1]. Other recent studies of hole-concentration dependent transport and magnetic properties [2] also indicate that the holes mediating the magnetic coupling are rather located in a narrow impurity band. It is clear that further detailed studies of the electronic states of dilute magnetic semiconductors are needed to provide a basis for better understanding of the underlying physics. In the present report we show results from photoemission studies of the Mn 3d states in (Ga,Mn)As with Mn concentrations in the range 0.1 - 5 %, focusing on the low concentrations. This is an extension of the work reported last year, where we showed the result for 1% Mn.

The data discussed here were recorded at BL I511-1. The samples were prepared in the Kryovak MBE system at BL41, and were brought to BL511 in a portable UHV chamber. All data were recorded at room temperature on as-grown samples.

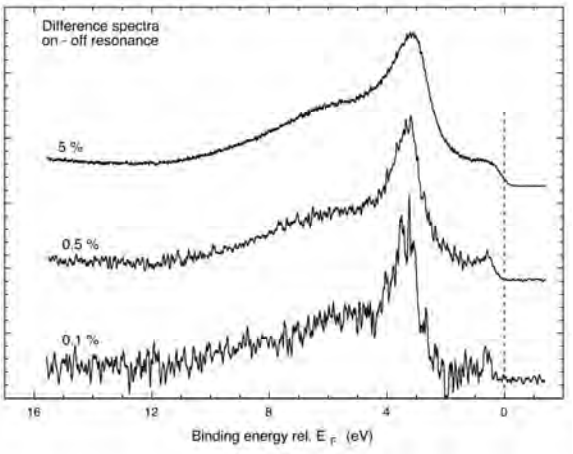

Figure 1. Normalized difference spectra obtained from spectra recorded with photon energies differing by 1 eV, one on the peak in the Mn2p XAS and one just below the peak.

Figure 1 shows three difference curves obtained by subtracting spectra recorded just below the Mn $2p_{3/2}$ absorption resonance from spectra recorded on the resonance peak. Three curves are shown, obtained for samples with 0.1%, 0.5%, and 5% Mn. In order to extract reliable difference spectra in situations with very low Mn concentrations, it is crucial that the original data are correctly normalized and energetically aligned. This was achieved by recording the Ga3d spectra along with each valence band spectrum on- and off-resonance, and adjust the data such that the Ga emission was optimally eliminated in the difference spectra.

Complementary magnetic studies of the same samples showed that only those with Mn concentration above 1.5 % exhibited ferromagnetism.

According to first principles calculations [3] the substitution of a Ga atom in GaAs with a Mn impurity introduces a pair of levels with t_2 symmetry, one localized primarily on the Mn atom (”crystal field resonance”, CFR) and the other localized primarily on the neighboring As sites (”dangling bond hybrids”, DBH). Comparing the theoretical results with our data it is clear that the large peak around 3 eV binding energy corresponds to the CFR states, while the structure near the Fermi energy is due to DBH states. This electronic structure results only from the local crystal field splitting and hybridization between the t_2 symmetry states, and should be best reflected by the data from the most dilute samples.

The most significant result from the present experiments is that the structures associated with the CFR and the DBH states are clearly broaened with increasing Mn concentration. The broadening results in a gradual filling of the minimum between the two structures, and relative reduction of the amplitude of the CFR peak. We can exclude that the filling of the minimum is be caused by increased inelastic scattering, since the intensity of the low-energy end of the spectrum is practically the same in all spectra. Therefore, we conclude that our data reveal additinal concentration-dependent hybridization between the Mn-induced states, reflecting increasing delocalization. It is noted that the broadening occurs in the range of concentrations where ferromagnetism starts to appear, around 1% Mn. The data therefore provide support for the importance of impurity band states.

References

1. M. A. Scarpulla, B. L. Cardozo, R. Farshchi, W. M. Hlaing Oo, M. D. McCluskey, K. M. Yu, and O. D. Dubon, Phys. Rev. Lett. **95**, 207204 (2005).
2. M. A. Mayer, P. R. Stone, N. Miller, H. M. Smith III, O. D. Dubon, E. E. Haller, K. M. Yu, W. Walukiewicz, X. Liu, and J. K. Furdyna, Phys. Rev. B **81**, 1 (2010)
3. P. Mahadevan and A. Zunger, Phys. Rev. B **69**, 115211 (2004)

X-ray spectroscopic study of amorphous Al-Zr alloy films

J. R. Vegelius,[1] I. L. Soroka,[2] P. Korelis,[1] B. Hjörvarsson,[1] and S. M. Butorin[1]
[1]*Department of Physics and Materials Science, Uppsala University, Box 530, S-751 21 Uppsala, Sweden*
[2]*Department of Materials Chemistry, Uppsala University, Box 538, SE-751 21 Uppsala, Sweden*

Industrial applications of amorphous Al_xZr_{100-x} materials are potentially vast. High pressure resistance and smooth surfaces without grain boundaries are properties that are of great intereset from a technological point of view. For example in nuclear reactors normally corrosion damage occurs due to hydrogen and oxygen penetration through grain boundaries[1]. Such problems could be prevented by using the considered materials. In addition Al and Zr have low absorption cross-section for thermal neutrons[2] suggesting long life times.

Another possible application is the production of tunnel barriers consisting of amorphous alloy oxides used for memory storage[3, 4]. An amorphous state of the metal films, used as oxide substrate, is advantageous for the formation of a smooth and likely defect-free oxide tunnel barrier layer, thus leading to an improved performance of a magnetic tunnel junction, as opposed to most sputter-deposited thin films of pure metals which are polycrystalline.

Al_xZr_{100-x} alloy films forms an amorphous state for certain values of x[5]. Such a film has been investigated here by means of a combination of X-ray diffraction and X-ray spectroscopic measurements in order to achieve information about the atomic and electronic structure of such materials under annealing processes.

$Al_{70}Zr_{30}$ alloy films were grown on thermally oxidized Si (001)/SiO_2 substrate by dc magnetron co-sputtering from Zr (99.9% purity) and Al (99.999% purity) targets. The base pressure in the chamber was less than 310^{-10} Torr. Sputtering was carried out in an Ar atmosphere (purity: 99.999%) at 2.5 mTorr pressure and at room temperature. The details of sample preparation can be found elsewhere [6]. The film of pure Al made at similar conditions is used as a reference point.

Subsequently, the sample was divided into several pieces, two of them were annealed at 400°C and at 700°C for one hour and after cooling down in the furnace the properties of as-deposited and annealed at different temperatures samples was studied.

Al L X-ray absorption spectroscopy (XAS) measurements were performed on Al metal using the total fluorescence yield (TFY) mode, amorphous $Al_{70}Zr_{30}$, amorphous as-deposited $Al_{70}Zr_{30}$ annealed to 400°C and amorphous $Al_{70}Zr_{30}$ annealed to 700°C by gradually changing the excitation energy while measuring the Total Fluorescence Yield (TFY) from the sample. The spectra were normalized to the incoming photon flux (I_0) measured by the current from a gold mesh. The monochromator resolution was 75 meV at 80 eV for Al L XAS. The same procedure was applied for Al K XAS with resolution less than 1.5 eV at 1500 eV. Non-resonant Al L valence XES was performed on all samples using the spectrometer. The monochromator resolution for emission measurements was 75 meV at 80 eV, the spectrometer resolution was 150 meV at 68 eV and the excitation energy was set to 100 eV at the first harmonic for maximum intensity. The emission energy dispersion was set by the elastic peak with 5 eV intervals covering the two-dimensional detector surface.

In figure 1 L-edge XAS of Al for Al(FCC), $Al_{70}Zr_{30}$ annealed to 400°C, as-deposited $Al_{70}Zr_{30}$ and $Al_{70}Zr_{30}$ annealed to 700°C is shown (from top to bottom). The Al L XAS spectra shown can be divided into two main regions. The region between 72 and 76 eV contains signal from crystalline Al, i.e., Al(0) and the region between 77 and 83 eV is constituted by oxidised aluminum, i.e., mainly γ-Al_2O_3 by comparison with the litterature[7–9] and thus, Al(+III). In both cases unoccupied states of Al are probed. Transitions involved are mainly $2p$ to $3d$ and $4s$, due to the dipole selection rule.

The double peak in the Al(FCC) spectrum around 73 eV reflects the spin-orbit splitting of the $2p$ core level[10, 11]. In the amorphous $Al_{70}Zr_{30}$ (RT) no double peak is present but instead a broad structure covering the whole energy interval considered (72-76 eV) suggesting several new states states in the amorphous structure. Due to the random atomic structure in amorphous Al systems local environments of individual Al atoms are different, giving rise to different electronic structures. The absorption spectrum of such a system, hence, reflects the sum of all electronic structures originating from all Al atoms probed by the measurement. When $Al_{70}Zr_{30}$ is annealed to 400°C it crystallizes (according to XRD) and the crystalline part of the absorption spectrum (second from above) shows a trace of the double-peak structure probably originating from crystallized Al. Between 74 and 76 eV the annealed sample has a significant broadening compared to Al(FCC) more resembling amorphous $Al_{70}Zr_{30}$ at room temperature. Hence, the spectrum might be a combination of an amorphous and a crystalline phase. This indicates that annealed $Al_{70}Zr_{30}$ is constituted by two phases of Al(FCC) and amorphous Al_xZr_{100-x} respectively. An estimation of the ratio of Al atoms contained in the amorphous and crystalline parts respectively was made by calculations using the L XAS spectra. The result was about one fourth of Al atoms were contained in crystalline regions, i.e., Al(BCC) while three quarters

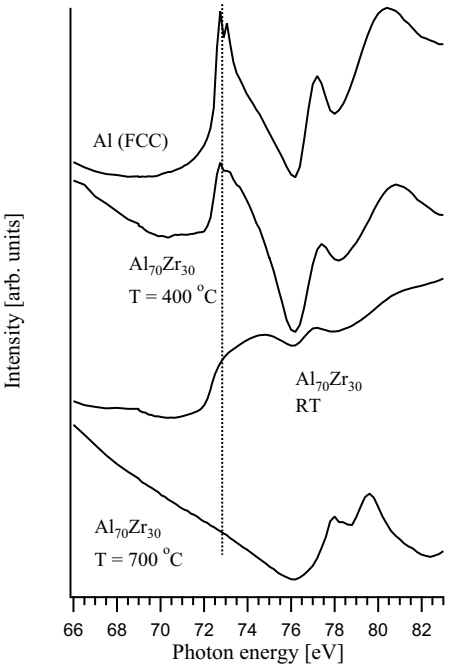

Figure 1: Al L-edge XAS data from four samples. From the top: Al(FCC) - 100% Al with a thin oxide layer on top, as-deposited $Al_{70}Zr_{30}$ annealed to 400°, amorphous $Al_{70}Zr_{30}$, as-deposited $Al_{70}Zr_{30}$ at room temperature (RT) and $Al_{70}Zr_{30}$ annealed to 700°. The data is offset for clarity. No background was subtracted and the normalization is arbitrary. The data is offset for clarity.

were contained in amorphous regions, i.e., Al_xZr_{100-x}.

X-ray diffraction and spectroscopy measurements on as-deposited and annealed $Al_{70}Zr_{30}$ thin films were performed. XRD measurements show local recrystallization (crystallites) below 400°C and a shift in the cell parameter, as compared to pure Al(BCC), due to Zr impurities in the Al crystallites. With XRD only crystalline phases are visible. In X-ray spectroscopies (XAS and XES) both amorphous and crystalline phases were monitored. In Al L and K XAS, amorphous phases were broader than corresponding crystalline phases. In Al L XAS the oxide layer was visible and well separated from the metallic bulk. The metallic region of the spectra were used to estimate the amount of Al atoms in crystalline and amorphous phases respectively in an annelaed (and partly recrystallized) sample.

Now looking at the region above 76 eV oxidation of the samples can be monitored. The as-deposited $Al_{70}Zr_{30}$ (T=20°C) show limited structures in the region of consideration suggesting a limited oxidation has taken place. The sample was fresh (less than a week) so limited oxidation was expected. The 400°C annealed sample show significant and expected oxidation due to the annealing process. However, the bulk signal still remains. The 700°C annealed sample, however, is fully oxidized leaving no bulk signal but pure, oxidized Al. The oxide is amorphous according to XRD The differences in background can also be understood in terms of oxidation. Below the bulk Al L edge the intensity of the fully oxidized sample increases rapidly with decreasing energy. This could be explained by the O L edge (41.6 eV binding energy) and the rapid intensity increase reflects heavy oxidation. Considering Al(FCC) and the annealed $Al_{70}Zr_{30}$ (400°C) the increase in intensity with decreasing energy is moderate but significant, while in the $Al_{70}Zr_{30}$ (20°C) the increase is the smallest. All in agreement with the interpretation from the oxidized Al part of the spectra above 76 eV. Thus, both the bulk and the oxide layer on top was monitored by L XAS.

[1] M. Itakura, H. Kaburaki and C. Arakawa, Phys. Rev. E 71, 055102 (2005).
[2] A.-J. Dianoux, G. Lander, Institut Laue-Langevin, "Neutron Data Booklet", 2nd edition, (2003)
[3] J. Joshua Yang, Y. Yang, K. Wu and Y. A. Changa, J. Appl. Phys. 98, 074508 (2005).
[4] H. Raanaei, H. Nguyen, G. Andersson, H. Lidbaum, P. Korelis, K. Leifer and B. Hjörvarsson, J. Appl. Phys. (2009) accepted for publication.
[5] M. Hansen, K. Anderko, New York: McGraw-Hill 1958.
[6] I. L. Soroka, J. Vegelius, P. T. Korelis, A. Fallberg, S. M. Butorin and B. Hjvarsson, submitted to J. Nucl. Mater
[7] W. L. O'Brien, J. Jia, Q-Y. Dong and T. A. Callcott, Phys. Rev. B **47**, 15482, (1993)
[8] Y. F. Hu, R. K. Xu, J.J. Dynes, R. I. R. Blyth, G. Yu, L. M. Kozak, P. M. Huang, Geochim. Cosmochim. Acta **72**, 1959, (2008)
[9] S. Sigurdson, V. Sundaramurthym, A. K. Dalai, J. Adjaye, J. Mol. Catal. A-Chem. **291**, 30, (2008)
[10] H. Piao. and N. S. McIntyre, Surf. Interface Anal. **31**, 874, (2001)
[11] P. H. Citrin, G. K. Wertheim and M. Schlüter, Phys. Rev. B **20**, 3067, (1979)

High-resolution PES measurements of 2D silicon layer on Ag(111)

P. Vogt[1,5], B. Aufray[1], P. De Padova[2], M. E. Dávila[3], A. Pietzsch[4], F. Hennies[4] and G. Le Lay[1†]

[1]CINaM-CNRS, Campus de Luminy, Marseille, France

[2]ISM-CNR, via Fosso de Cavaliere 100, Rome, Italy

[3]Instituto de Ciencia de Materiales de Madrid, CSIC, Cantoblanco 28049, Madrid, Spain

[4]MAX-Lab, Lund, Sweden

[5]Technische Universität Berlin, Institut für Festkörperphysik, Berlin, Germany

Corresponding author: lelay@cinam.univ-mrs.fr

Although silicene [1], the counterpart of graphene for silicon, is predicted theoretically [2] its synthesis has yet not been reported. However, if existing, it would reveal a wealth of new physics and potential applications which make it a technologically important material. Our previous results on the silicon deposition on Ag(110) demonstrate that the first stages of silicon growth performed at room temperature (RT) reveal the formation of silicon nano-ribbons (NRs) [3], in a massively parallel arrangement along the [-110] direction. At slightly higher temperatures these 1D silicon NR's self-assemble by lateral compaction to form a grating with a pitch of just ~ 2 nm covering the entire substrate surface [4] and giving rise to a 5x2/5x4 superstructure. More recently, the atomic geometry of these Si NR's was derived by high resolution STM images revealing a honeycomb arrangement, i.e., a graphene-like structure also supported by theoretical calculations [5,6]. On the Ag(111) face, the deposition of Si gives rise to a 4x4 plus $(2\sqrt{3}x2\sqrt{3})R30°$-like LEED pattern and STM investigations indicate as well the formation of a well-ordered 2D silicon layer which might be explained by the formation of silicene.

The objective of our beamtime was to determine the structural and electronic properties of the 2D Si-overlayer formed on the Ag(111) surface. In order to achieve this goal we performed high-resolution SXPS core-level and valence-band spectroscopy at Si/Ag(111) interfaces. The measurements were performed at the I511 beamline with an energy resolution better than 50 meV. The spectra were taken in normal emission at a base pressure of 5 10^{-10} mbar. The Ag(111) sample surface was cleaned by Ar^+-sputtering and annealing at 530°C. Si was evaporated from a home-build Si source while the Ag sample was kept at different temperatures in the range between 250°C and 330°C.

In particular, we investigated the growth behavior of the Si layer and could determine the linear growth regime and the exact 1ML coverage. The surface Si/Ag ratio, as determined by the ratio between the Si 2p and Ag 4d area, is plotted in

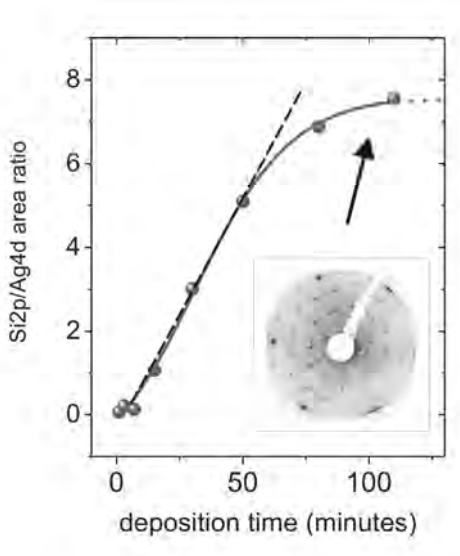

Fig. 1 Si 2p/Ag 3d ratio at hν=126 eV as a function of the Si deposition on the Ag(111) surface. The insert shows the typical LEED pattern indicating the formation of the 2D Si-overlayer

Fig. 1 vs. the Si deposition. During the deposition the sample temperature was kept constant at approximately 300°C. It can clearly be seen that the Si/Ag ratio changes first linearly before reaches a plateau for higher coverages. The formation of the Si overlayer can by monitored by the changes of the surface symmetry as determined by LEED (insert Fig.1).
Measurements of the Si 2p core-level emission line give first hints for the formation of a 2D-Silicon structure at the surface. The core level spectrum in Fig. 2 shows clearly two main components, S_1 and S_2, representing two different bonding sites for the silicon atoms within the overlayer. The single components appear very narrow indicating a good ordering within the Si-layer. The Si layer is stable up to temperatures of about 330°C. Whereas at higher temperatures in-diffusion of the Si into the Ag-bulk crystal or a surface dewetting occurs."

Following the preparation of the 1ML Si-layer iodine and potassium were deposited onto the layer in order to electronically dope the layer. Upon this deposition, the lineshape of the Si 2p core level changes indicating reaction and bond formation of K or I with the top Si atoms. For the deposition of iodine the deposition rate turned out to be critical as for higher rates we could observe an etching of the Si-layer by the iodine. However, these results allow to determine the interaction between the iodine and the silicon and will be helpful for future experiments.

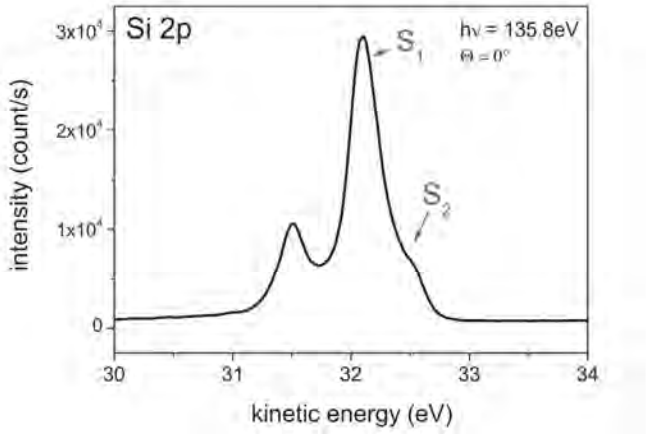

Fig. 2 Si 2p core level spectrum of the Si overlayer on Ag(111) measured in normal emission at a photon energy of 135.8eV

References

[1] Guzman-Verri, G. G. and Lew Yan Voon, L. C., Phys. Rev. B **76,** (2007) 75131
[2] S. B. Fagan, et al., Phys. Rev. B, **61**, (2000) 9994; S. Lebègue and O. Eriksson, Phys. Rev. B, **79** (2009) 115409, S. Cahangirov et al, Phys. Rev. Lett. **102,** (2009) 236804
[3] C. Léandri, et al., Surface Sci. **574**, (2005) L9
[4] H. Sahaf et al., Appl. Phys. Lett. **90**, (2007) 263110.
[5] B. Aufray et al., Appl. Phys. Lett., in press
[6] A. Kara et al., J. of Phys. – Cond. Mat. **22**, (2010) 045004

Triphenylamine-based Dye on Rutile TiO_2(110) I: Adsorption Geometry and Molecular Interaction

Shun Yu[1], Sareh Ahmadi[1], Marcelo Zuleta[2], Haining Tian[3], Karina Schulte[4], Annette Pietzsch[4], Franz Hennies[4], Jonas Weissenrieder[1], Xichuan Yang[3], and Mats Göthelid[1]

[1] Materials Physics, MAP, ICT, Royal Institute of Technology (KTH), Electrum 229, SE-16440 Kista , Sweden
[2] Physical & Analytical Chemistry Department, Uppsala University, Box 259, SE-75105 Uppsala, Sweden
[3] State Key Laboratory of Fine Chemicals, Dalian University of Technology, Box 46, 158 Zhongshan Rd., Dalian 116012, China
[4] Max-lab, Lund University, Box 118, S-221 00 Lund, Sweden

"The great discovery" of different sensitizers makes themselves the impetus to the boom of the development of the dye sensitized solar cell (DSSC). In aim of high efficiency, low cost and environmental friendliness, great endeavors never stop to fabricate new metal−free organic sensitizers. So far, a triphenylamine−hydrophilic cyanoacrylic acid (TPAC) dye has reached the record efficiency of 9.8 % for organic sensitizer[1], which is close to the record efficiency of 11.1% of DSSC from the ruthenium (Ru) complexes[2]. The fast development of new sensitizers, necessitates a better understanding of the complexity and significance of the adsorption process on TiO_2. For DSSC, the interface plays a role that separates photogenerated excitons and conducts electrons into the circuit. Meanwhile, the dye adsorption mode influences the electron lifetime and the open circuit potential[3], and indeed it also affects the molecular electronic structure during the sensitization process[4,5,6,7].

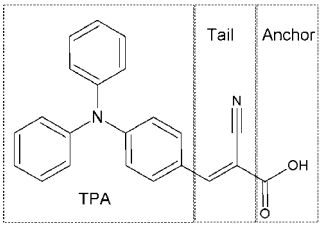

Figure 1. Triphenylamine- hydrophilic cyanoacrylic Dye (TPAC)

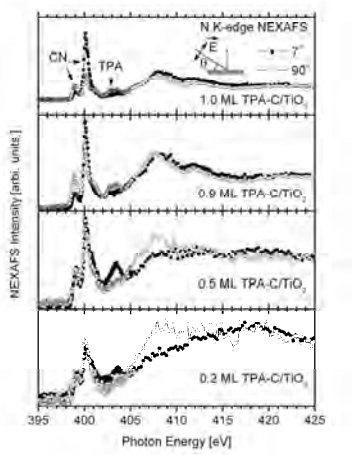

Figure 2. NEXAFS of TPAC at different coverages on TiO_2

By using synchrotron radiation based soft X-ray spectroscopy at I511 beamline, MAX-lab, we investigated adsorption behavior of TPAC dye on rutile TiO_2(110) surface[8]. The molecules were thermally evaporated onto the substrate from a glass crucible in ultrahigh vacuum (UHV) to control the coverage *in-situ*. Figure 2 shows the results of near edge X-ray absorption fine structure (NEXAFS) spectroscopy. The first two strong peaks at photon energies 399.0 eV and 400.0 eV is ascribed to the transition from N1s to out-of-plane and in-plane π^* orbital at cyano group (−CN), respectively. The peak observed at around 402.5~404.0 eV are due to the transition of N1s→π^* orbital at TPA part. The comparison of the relative intensity at different coverage under orthogonal polarization photon shows clearly that TPAC molecule experience a standing up process from a tilted geometry.

From O1s spectra (Figure 3), we can conclude that first layer TPAC binds to the surface through carboxylic anchor group accompanied with a deprotonization process (−COOH → −COO$^-$). Two oxygen atoms bind to surface Ti ions with almost equal charge distribution, which is not affected by the molecular configuration change. Meanwhile, TPAC tends to form a dense adsorbed layer which prevents the further chemisorption of the upper layer molecules, shown as two separated O1s peak.

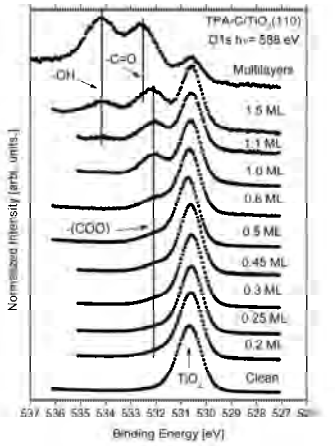

Figure 3. O1s core level spectra at different coverage

The molecular configuration is closely related with its electronic structure. N1s, C1s and highest occupied molecular orbital (HOMO) spectra are shown in Figure 4. N1s shows to two peak assigned to TPA (N1) and –CN (N2). C1s displays the dominant peak at 285.3 eV related with (C-C, and CH_x). The shoulder at higher binding energy is ascribed to the carbon atom linked with nitrogen. HOMO and HOMO' are assigned to the orbital from first layer and upper layer, respectively. Referred to the peak position as zero at the coverage of 1 ML, the peak positions at other coverage were plotted. As the coverage increases below one monolayer, all the molecular peaks shift to higher binding energy side in a similar extent. This process is accompanied with the densely packing process. Thus we can interpret that molecular interaction is the reason behind. Meanwhile, the surface dipole built up during the adsorption and final effects from the measurement could also contribute to the phenomenon. But both of them also relate to the molecular configuration change due to the interaction.

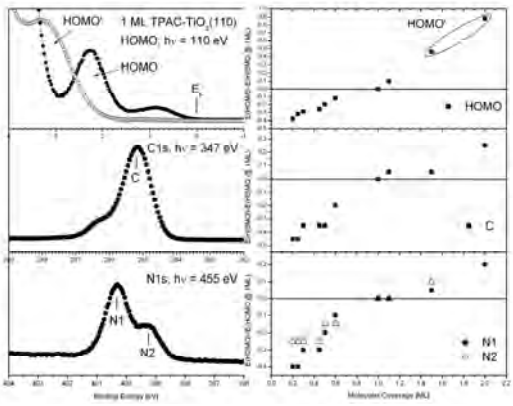

Figure 4. Left: HOMO (top), C1s (middle) and N1s (bottom); Right: corresponding peak position at different coverages.

By monitoring the adsorption process of TPAC organic dye on TiO_2, we observed the series change of both molecular configuration and electronic structure. We assign the molecular interaction as the impetus of those observations.

1 Guangliang Zhang, Hari Bala, Yueming Cheng, Dong Shi, Xueju Lv, Qingjiang Yu, and Peng Wang, Chemical Communications (Cambridge, England) 2198-200 (2009).
2 Yasuo Chiba, Ashraful Islam, Yuki Watanabe, Ryoichi Komiya, Naoki Koide, and Liyuan Han, Japanese Journal Of Applied Physics 45, L638-L640 (2006).
3 Tannia Marinado, Kazuteru Nonomura, Jarl Nissfolk, Martin K Karlsson, Daniel P Hagberg, Licheng Sun, Shogo Mori, and Anders Hagfeldt, Langmuir : The ACS Journal Of Surfaces And Colloids 26, 2592-8 (2010).
4 P. Palmgren, K. Nilson, S. Yu, F. Hennies, T. Angot, J.-M. Layet, G. LeLay, and M. Gothelid, Journal Of Physical Chemistry C 112, 5972-5977 (2008).
5 Shun Yu, Sareh Ahmadi, Pål Palmgren, Franz Hennies, Marcelo Zuleta, and Mats Göthelid, The Journal Of Physical Chemistry C 113, 13765-13771 (2009).
6 P Palmgren, S Yu, F Hennies, K Nilson, B Akermark, and M Göthelid, The Journal Of Chemical Physics 129, 074707 (2008).
7 Louise C Mayor, J Ben Taylor, Graziano Magnano, Anna Rienzo, Christopher J Satterley, James N O'Shea, and Joachim Schnadt, The Journal Of Chemical Physics 129, 114701 (2008).
8 Shun Yu, Sareh Ahmadi, Marcelo Zuleta, Haining Tian, Karina Schulte, Annette Pietzsch, Franz Hennies, Jonas Weissenrieder, Xichuan Yang, and Mats Göthelid, manuscript to be submitted.

Triphenylamine-based Dye on Rutile TiO_2(110) II: Polarization Related Intramolecular Charge Transfer of Donor-Acceptor System

Shun Yu[1], Sareh Ahmadi[1], Marcelo Zuleta[2], Haining Tian[3], Karina Schulte[4], Annette Pietzsch[4], Franz Hennies[4], Jonas Weissenrieder[1], Xichuan Yang[3], and Mats Göthelid[1]

[1] Materials Physics, MAP, ICT, Royal Institute of Technology (KTH), Electrum 229, SE-16440 Kista , Sweden
[2] Physical & Analytical Chemistry Department, Uppsala University, Box 259, SE-75105 Uppsala, Sweden
[3] State Key Laboratory of Fine Chemicals, Dalian University of Technology, Box 46, 158 Zhongshan Rd., Dalian 116012, China
[4] Max-lab, Lund University, Box 118, S-221 00 Lund, Sweden

Highest/Lowest Occupied/Unoccupied Molecular Orbitals (HOMO/LUMO) of the dye molecule are usually designed to be separated spatially in order to facilitate the charge separation during photo-excitation. The HOMO/LUMO parts can be referred as Donor/Acceptor, respectively. For the dye-sensitized solar cell application, it is critical to know that how fast the excitons can be separated and electrons can be injected into TiO_2 substrate. Resonant photoemission spectroscopy (RPES) has been successfully employed to investigate organic/inorganic interface system. In this work, we used RPES at beamline I511 to monitor the charge transfer process at donor and acceptor parts of triphenylamine−hydrophilic cyanoacrylic organic dye adsorbed on the TiO2 and reveal the "push-pull" effects.

PES and NEXAFS on N K–edge are aligned to the ionization potential (IP) of cyano nitrogen (−CN) with zero energy at Fermi level, based on the method introduced by Schnadt et al[1](**Figure 1**). TiO_2 substrate is an n-type semiconductor with the conduction band minimum about 0.1 eV above the Fermi level. Thus, the excitation state of cyano nitrogen with $\pi^*_\perp$ orbital occupied falls below the CB minimum (CBM) and charge transfer from dye to substrate is energetically forbidden in this case. However, excitations to the $\pi^*_{//}$ orbital are mainly above the CBM, thus RPES across the N K–edge is possible to deliver the charge transfer information.

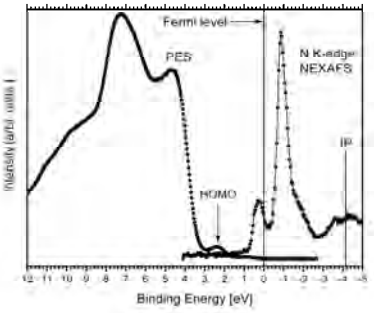

Figure 1. Alignment of PES and NEXAFS spectra

Figure 2 displays the RPES measurement cross the N K–edge threshold by two orthogonally polarized impinging photon beams (normal polarization (NP) and parallel polarization (PP)). The chosen photon energies are shown as red spots in the N K–edge NEXAFS spectra. The corresponding RPES are plotted in the kinetic energy scale (binding energy 0−25 eV) and stacked from bottom to top following the photon energy. Provided that the Fano−type behavior is not obvious[2,3,4], a subtraction of the photoelectron contribution has been processed in advance to enhance the resonant figures, which is measured several electron volts below the absorption threshold. The relative intensity change of the NEXAFS resonance has been discussed above due to the specific molecular orientation. The contributions can be related to the different decay modes.

The main decay channel for the first resonant transition should be resonant decays (participator and/or spectator decay) with a typical Auger Raman characteristic[4]: the peak at around 380.0 eV shifts to higher kinetic energy as the increased photon energy. The second transition from N1s to

the $\pi^*_{//}$ of the cyano group, leaves the excited electron above the CBM of TiO_2 (line 6-12). Roughly three strong enhancements can be resolved: a typical participator decay at around 391.0 eV and two broad features coupled with vibration mode[5,6,7] at 375.0−388.0 eV. Normal Auger decay and spectator decay contributes to the lower and higher kinetic energy part separately with a spectator shift[4], which can be supported by the calculation result from D5 dye on TiO_2[8]. The coexistence of resonant decay and normal Auger decay means that delocalization and localization of the excited electron can compete in the timescale about 6 fs for N1s core hole. The TPA nitrogen core level can be resonantly excited into empty states by the photon energy from 403.0 to 404.0 eV. As discussed above, strong enhancement is only found under PP rather than NP due to larger cross section induced by the optimal molecular geometry. However, no specific enhancement can be observed within our energy window under both polarizations. Considering that the TPA nitrogen p character contributions spread over the binding energy region below 20 eV[8], we can expect that a fast delocalization occurs within the core−hole decay time.

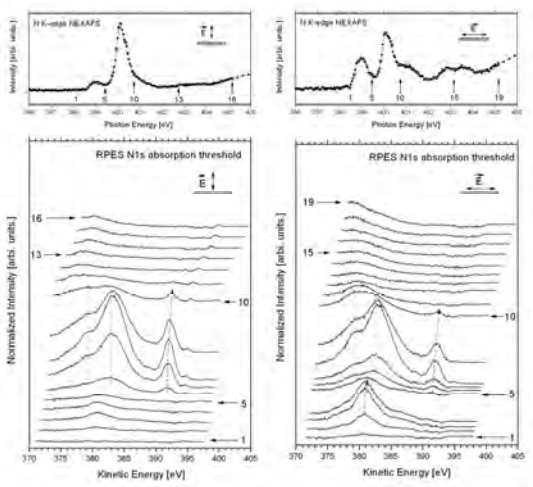

Figure 2. RPES under two orthogonal polarized photon

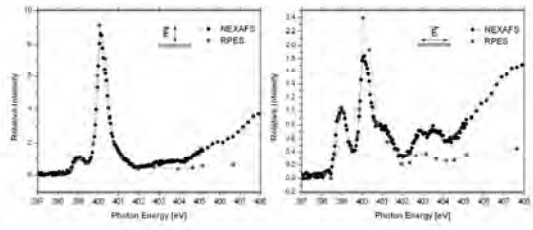

Figure 3. Comparison of integrated RPES and NEXAFS after normalizing to the first resonant peak

By comparing the normalized integrated RPES and normalized NEXAFS under different polarization, as for Ru−complex and its components analyses[2,9,10], we found that charge excitation and delocalization process is much easier and faster under PP than under NP for TPAC. Thus, we can depict a picture that an excited electron at TPA donor part is very easily delocalized, while at the Acceptor cyanoacrylic part delocalization and localization are two competing process. This image matches the "push−pull" effects for this D−A molecular system: electron is easily "pushed" out from the donor part and "pulled" into the acceptor in time scale.

[1] J. Schnadt, J. O'Shea, L. Patthey, J. Krempaský, N. Mårtensson, and P. Brühwiler, Physical Review B **67**, 1-7 (2003).
[2] J. Schnadt, J. N. O'Shea, L. Patthey, L. Kjeldgaard, J. A hlund, K. Nilson, J. Schiessling, J. Krempaský, M. Shi, O. Karis, C. Glover, H. Siegbahn, N. Ma rtensson, and P. a. Bru hwiler, The Journal Of Chemical Physics **119**, 12462 (2003).
[3] M. Weinelt, a. Nilsson, M. Magnuson, T. Wiell, N. Wassdahl, O. Karis, a. Föhlisch, N. Mårtensson, J. Stöhr, and M. Samant, Physical Review Letters **78**, 967-970 (1997).
[4] P. A. Brühwiler, O. Karis, and Nils Mårtensson, Reviews Of Modern Physics **74**, 703-740 (2002).
[5] J.J. Gallet, F. Bournel, S. Kubsky, G. Dufour, F. Rochet, and F. Sirotti, Journal Of Electron Spectroscopy And Related Phenomena **122**, 285–295 (2002).
[6] H Peisert, I Biswas, L Zhang, B-E Schuster, M B Casu, A Haug, D Batchelor, M Knupfer, and T Chassé, The Journal Of Chemical Physics **130**, 194705 (2009).
[7] R. Friedlein, S. L. Sorensen, A. Baev, F. Gel'mukhanov, J. Birgerson, A. Crispin, M. P. de Jong, W. Osikowicz, C. Murphy, H. Ågren, and W. R. Salaneck, Physical Review B **69**, 1-9 (2004).
[8] E.M.J. Johansson, T. Edvinsson, M. Odelius, D.P. Hagberg, L. Sun, A. Hagfeldt, H. Siegbahn, and H. Rensmo, Journal Of Physical Chemistry C **111**, 8580-8586 (2007).
[9] J Ben Taylor, Louise C Mayor, Janine C Swarbrick, James N O'Shea, Cristina Isvoranu, and Joachim Schnadt, The Journal Of Chemical Physics **127**, 134707 (2007).
[10] Louise C Mayor, J Ben Taylor, Graziano Magnano, Anna Rienzo, Christopher J Satterley, James N O'Shea, and Joachim Schnadt, The Journal Of Chemical Physics **129**, 114701 (2008).

Monitoring N719-dye Configurations on Anatase TiO_2 (100) by means of photoemission spectroscopy

Marcelo Zuleta[a,b], Shun Yu[b], Sareh Ahmadi[b], Gerrit Boschloo[a], Anders Hagfeldt[a] and Mats Göthelid[b]

a) Institution for Physical & Analytical Chemistry, Uppsala University (UU), The Ångström laboratory, Box 259, SE-751 05 Uppsala, Sweden,
b) Materials Physics, ICT, the Royal Institute of Technology (KTH), Electrum 229, SE-164 40 Stockholm, Sweden

The research of adsorption behavior of photosensitive dye molecules on TiO_2 is of both scientific and technological importance. However, due to poor thermal stability at high temperature for most of dyes, traditional thermal evaporation method can not be used in order to do ultrahigh vacuum based research. Instead, either low pressure electrospay system[1] or surface passivation[2,3] technique is required. The former can evaporate dye directly into the vacuum by Coulum repulsion and differential pumping system; the latter can however protect the sample by passivation organic layer from the ambient contamination when transport sample from vacuum to solution.

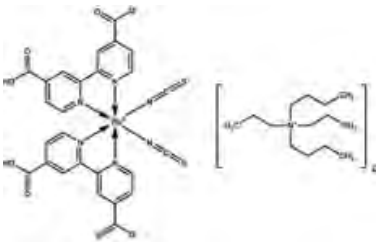

Figure 1. Molecular structure of N719

In the present work[4], we report experimental results concerning Cis-bis (isothiocyanate)-bis-(2,2'-bipyridyl-4,4'dicarboxylate)ruthenium(II)bis(tetrabutylammonium) dye (known as N719), adsorbed on a single crystal of anatase TiO_2 (100). The cleaning pretreatment, by sputtering and annealing, of TiO_2 (100) yields a reproducible (1xn) surface reconstruction. Previous to dye deposition, TiO_2 was covered with one monolayer 4-tert-butylpyridine (4-TBP) in ultra-high vacuum (UHV), in order to protect the surface against air-contamination. N719 was subsequently deposited by dipping the crystal into the dye solution. 4-TBP was removed partly in the solution and totally by heating the sample around 285-300 ^{o}C in UHV.

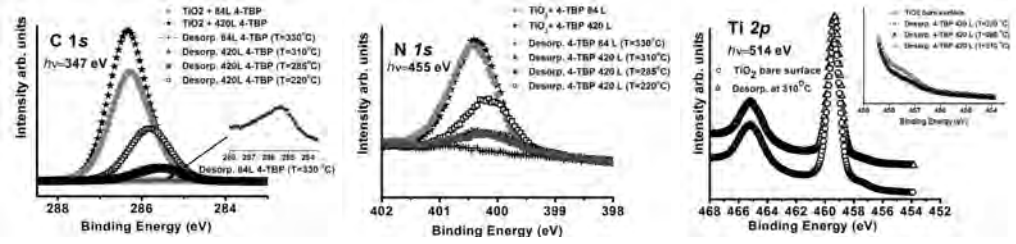

Figure 2. Core level spectra of 4TBP on TiO_2 at different annealing temperature: C1s (left, insert is enlarged peak after annealing at 330^{oC}), N1s (middle) and Ti2p (right, insert is enlarged part of Ti^{3+} region).

Figure 2 show the core level spectra of 4TBP adsorbed on TiO_2 and annealled to different temperature. sequently. As deposited, the intensity at the dose of 84 L and 420 L did not render big difference in the intensity, which are normalized to the background at the lower binding energy side. After the desorption at elevated temperature, the intensity decreased correspondently. Meanwhile, the peak shifted to lower binding energy side. Similar shift has been

found for 4TBP adsorbed on rutile TiO_2(110), which is related to the adsorption at oxygen vacancies on the surface[5]. A charge transfer from substrate to 4TBP has been suggested at the defect sites.

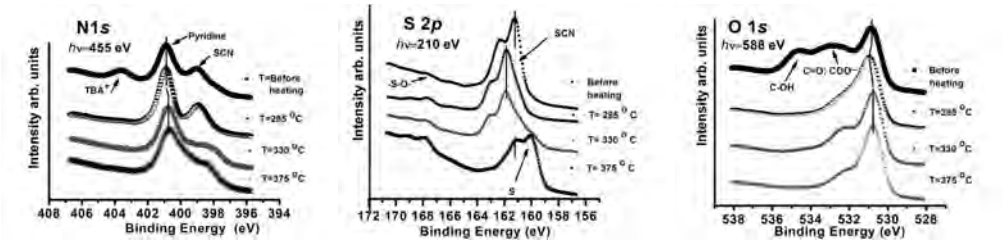

Figure 3. Core level spectra of N719 /4TBP on TiO_2 at different annealing temperature: N1s (left), S2p (middle) and O1s (Right).

Figure 3 shows the core level spectra from the coadsorption system of N719 and 4TBP on TiO_2. TBA^+ part of N719 can desorb at 225°C[6], which is can be verified by the spectrum of N1s after annealing at 285°C. Sight oxidation of (SCN) has been observed as deposited. After annealing, the oxidation become severer. Annealing at 285°C shifts the main S2p peak to higher bindng energy meaning the configuration change. Meanwhile, a shoulder at lower binding energy region developd as the increased temperature, which finally become dominant at the 375°C. From the line profile of N1s and S2p change at different annealing temperature, the decomposition can also be suggested. The line profile change for O1s is rather simpler. As deposite, two O1s peak at the higher binding energy side indicates parts of the carboxylic group do not attach to the surface, suggesting the possible existance of physisorbed dyes. Subsequent heating either desorbe /decompose the physisorbed dye or promote the unattached anchor group to chemisorb on the surface. Futhermore, the shift of Ti2p after different annealing process also support that after 285°C, the dye molecule started to change the configuration severely (even decomposiation), which render different charge transfer between the molecule and substrate.

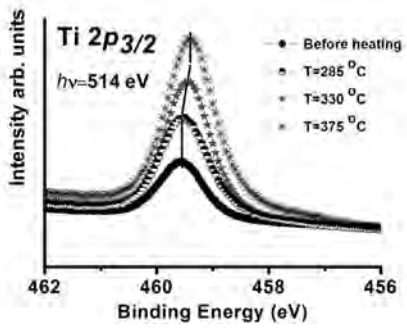

Figure 4. Ti2p of N719/4TBP/TiO_2 system

In conclusion, we have successfully deposited N719 adsorbed on TiO_2 by using 4TBP passivation method and investigated the response of N719 to the annealing temperature.

[1] Louise C Mayor, Taylor, J Ben, Graziano Magnano, Anna Rienzo, Christopher J Satterley, James N O'Shea, *J. Chem. Phys* **2008**, 129, 114701-114710
[2] Ikeda M., Koide N., Han L., Pang C. L., Sasahara A, Onishi H., *J. Photochem. Photobio. A*, **2009,** *202*, 185-190.
[3] Sasahara A., Pang C. L., Onishi H., J. Phys. Chem. B, 2006, 110, 4751-4755.
[4] Marcelo Zuleta, Shun Yu, Sareh Ahmadi, Gerrit Boschloo, Mats Göthelid and Anders Hagfeldt, manuscript submitted to Langmuir
[5] Shun Yu, Sareh Ahmadi, Chenghua Sun, Pål Palmgren, Franz Hennies, Marcelo Zuleta,and Mats Göthelid, J. Phys. Chem. C 2010, 114, 2315–2320
[6] Amirnasr M., Nazeeruddin Md.K., Grätzel M., Thermochimica Acta, 2000, 348, 105-114

A sub-picosecond hard X-ray streak camera using single-photon counting

H. Enquist[1], H. Navirian[2], R. Nüske[2], A. Jurgilaitis[2], M. Herzog[3], M. Bargheer[3], P. Sondhauss[1], J. Larsson[1]

[1]*Atomic Physics Division, Lund University, Sweden*
[2]*MAX-lab, Lund University, Sweden*
[3]*Institut für Physik und Astronomie, Universität Potsdam, Germany*

We have developed and characterized a hard X-ray accumulating streak camera that achieves sub picosecond time resolution by using single photon counting. A high repetition rate of 2 kHz was achieved by use of a readout camera with built in image processing capabilities. The effects of sweep jitter were removed by using a UV timing reference. The use of single photon counting allows the camera to reach high quantum efficiency by not limiting the divergence for the photoelectrons.

Presently the fastest kind of X-ray detector is the streak camera. It has been extensively used in time resolved measurements and a time resolution down to 233 fs [1] has been demonstrated using UV, and 350 fs using 1.5 keV X-rays [2]. This time resolution is however not yet reached for hard X-rays. Due to the dispersion of the photoelectrons and imperfect electron optics the fastest streak cameras rely on limiting the divergence of the photoelectrons to compensate. This implies a severe reduction in quantum efficiency.

We have developed a streak camera that uses single-photon counting to reduce the effects of dispersion and imperfect imaging. Images are analyzed in real time, and a UV timing reference is used to track and compensate the sweep jitter. The use of a readout camera with built-in image processing capabilities reduces the bandwidth required to transfer data to the host computer. Thus a frame rate of 2 kHz could be reached.

UV-UV correlation

To test the system a second UV pulse was generated by splitting off part of the power in the reference beam. This second beam was then used as a simulated X-ray signal at a fixed delay of 8 ps. Figure 1 shows the measured time delay in accumulating mode (dashed line) and photon counting mode (solid line). In single photon counting mode the time resolution is improved from 2.5 ps to 280 fs FWHM.

Ultrafast melting of InSb

When a sufficient fraction of the valence electrons InSb are excited to the conduction band the material melts and disorders on a sub picosecond timescale. The disordering can be detected as a fast drop of x-ray diffraction efficiency, with a fall time of less than one picosecond.

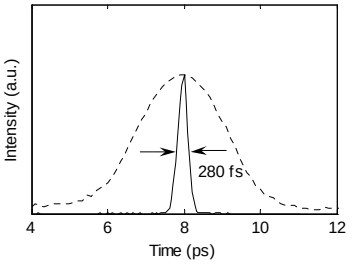

Figure 1. Measured arrival time of a UV-pulse with a fixed delay of 8 ps. FWHM is 280 fs. The dashed line shows the result in accumulating mode.

An asymmetrically cut InSb sample was illuminated with laser pulses with a fluence of 38 mJ/cm^2. The incidence angle between laser and sample surface was 15 degrees. The disordering was probed by X-rays with a photon energy of 3.15 keV at an incidence angle of 0.9 degrees, and a bandwidth of 2%. The intensity of the (111)-reflection was recorded. Figure 2 shows the drop in X-ray diffraction as recorded by the streak camera in single photon counting mode. Data was

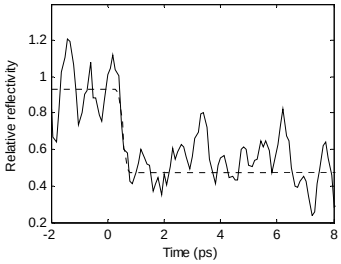

Figure 2: Time-resolved drop in X-ray reflectivity induced by non-thermal melting of InSb. The dashed curve shows the fitted error-function.

accumulated for 30 seconds. To extract the time resolution the curve is fitted with an error function, yielding an upper bound of 640 fs for the 90% - 10% fall time. The fall time of the (111)-reflection has been measured to 425 fs [3] and a quadratic deconvolution gives a time resolution for the streak camera of 480 fs.

Phonons in $SrTiO_3$/$SrRuO_3$ superlattices

When a superlattice of $SrTiO_3$ and $SrRuO_3$ is excited by a short laser pulse large-amplitude coherent acoustic superlattice phonons can be generated. For a superlattice consisting of 10 bilayers of 17.9 nm of $SrTiO_3$, and 6.3 nm of $SrRuO_3$, the (0 0 116) reflection shows a strong oscillating reduction of the reflectivity, with a period of 3 ps [4].

The sample was excited at a fluence of 30(?) mJ/cm^2, and the phonons were probed by x-rays with a photon energy of 5.8 keV. The resulting oscillations were compared to measurements done using a laser plasma x-ray source [4]. The amplitude of the oscillation is preserved, indicating a time resolution better than one picosecond.

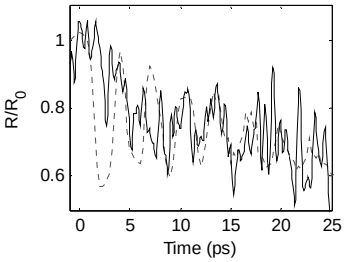

Figure 3: Oscillations in the x-ray reflectivity of the $SrTiO_3$ / $SrRuO_3$ superlattice as recorded by the streak camera (solid line), and from ref. [4] (dashed line).

[1] J. Feng et al., *Appl. Phys. Lett.*, vol. 91, no. 13, p. 134102, 2007.
[2] P. Gallant et al., *Rev. Sci. Instr.*, vol. 71, no. 10, pp. 3627–3633, 2000.
[3] A. Lindenberg et al., *Science*, vol. 308, no. 5720, pp. 392–5, 2005.
[4] C. von Korff Schmising et al., Appl. Phys. B, vol. 88, no. 1, pp. 1-4, 2007.

Acoustically driven ferroelastic domain switching observed by time-resolved x-ray diffraction

H. Navirian[1], H. Enquist[2], R. Nüske[1], A. Jurgilaitis[1], C. v. Korff Schmising[1], P. Sondhauss[2], and J. Larsson[1]

[1] *Atomic Physics Division, Lund University, Sweden*

[2] *MAX-lab, Lund University, Sweden*

In the present work we show ferroelastic domain switching in potassium dihydrogen phosphate (KDP) just below the critical temperature (T_C). A pulsed electric field was applied along the crystallographic *c* axis. The acoustic strain waves were generated via the converse piezoelectric effect. In the centre of the probed surface two waves interfered constructively inducing ferroelastic domain switching, in the absence of an external electric field, at a delay of 3 μs, corresponding to acoustic propagation at a velocity found to be 1500 m/s.

Time resolved experiments were carried out at beamline D611 at MAX-lab. The KDP sample had dimensions of 10 x 10 x 1 mm^3, and was mounted on a cryogenically cooled sample holder. Square voltage pulses were applied with a duration of 1 μs at a repetition rate of 500 Hz. The KDP 220 Bragg reflection in the paraelectric $I\bar{4}2d$ basis, corresponding to the 400 reflection in the ferroelectric *Fdd2* basis was studied. An electric field was applied parallel to the *c* axis by means of gold electrodes which were evaporated directly onto the crystal. The x-ray energy was scanned and the diffracted signal was recorded as a function of time for each energy step.

At room temperature the KDP has no permanent dipole moment and it is paraelectric, at T_C the crystal undergoes a phase transition. The structural change in KDP is explained by the double well potential of the hydrogen bond between the oxygen atoms that link the PO_4 groups. Above the T_C, the hydrogen atoms move freely between two potential minima. Below it, the thermal energy of the of the hydrogen atoms is not sufficient to overcome the potential barrier and hence they remain on one side or another. The structural changes in turn affect the unit cell, which undergoes shear deformation. The result of this that the unit cell has a permanent dipole moment along the *c* axis, making the KDP ferroelectric below T_C.

Figure 1 shows the X-ray energy scans above and below the T_C. The single paraelectric peak splits into four peaks. These are denoted as A+, A-, B+, B- domains according to the definition used by Bornarel[1]. Every domain fulfils the Bragg condition at a different x-ray energy for a certain angle of incidence. When a homogeneous electric field is applied to the KDP crystal an isotropic strain is created $\eta_i = d_{ij} E_j$, where d_{ij} is the piezoelectric modulus and E_i is the electric field.

At the beginning the uniform stress is created, which then relaxes to strain[2]. After 1 μs the stress vanishes. The strain due to the propagating waves can be estimated as shifts of the different domain peaks. In the Fig.2 time resolved energy scan is shown, here the two domain types are visible B+ and B-. The B^+ domains

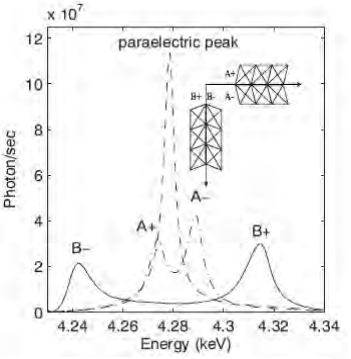

Fig. 1. X-ray energy scans. A paraelectric peak recorded above the T_C, B^+, B^-, A^+, A^- below the T_C.

have diffraction peaks at higher energy and the diffracted signal is stronger indicating that there is a larger volume fraction of B^+ domains in the probing volume. When the electric pulse is applied, the peak shifts. The shift reproduces the shape of 1 μs electrical pulse and after about 3 μs the large peak shift is observed, this is due to constructive interference of the Rayleigh waves propagating from the corners. When these waves are reflected at the respective opposite surfaces their phase changes from the expansion to compression, and as they travel back to the probe area a shift in the opposite direction is seen. This is repeated several times with a period of 13 μs determined by the propagation time in the crystal.

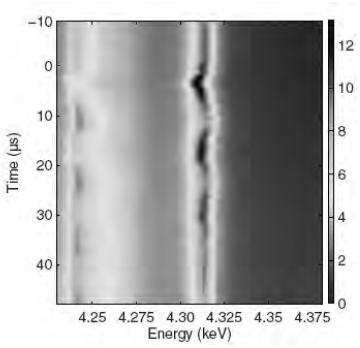

Fig. 2. Diffracted intensity as a function of time and x-ray energy.

The linear strain can be estimated from the changes in peak positions. If the relevant elastic constants are known the linear stress can be calculated by Hook's law $\sigma = C\eta$, where C is elastic constant. The linear shear strain at the applied field of 6 kV/cm can be calculated, and it corresponds to a linear tensile strain of 4.4 x 10^{-4}. This result agrees well with experimental data, where the initial strain from the shift in the energy was found to be 5 x 10^{-4}. By knowing the dimensions of the crystal the wave propagating speed in KDP was calculated to be 1500 m/s, which is in agreement with the room temperature measurements by Bakos et al[3].

Domain switching mechanism in KDP can be understood from the Gibbs free energy:

$$U_G = \frac{1}{2} Na\eta^2 - \varepsilon^s N - \beta\eta(N^+ - N^-) - (N^+ - N^-)\mu E - TS ,$$

where N^+ and N^- denote the number of dipoles in the unit cells belonging to the domains with polarity parallel or antiparallel to the *c* axis, *a* is a number proportional to the normal elastic constant, *N* is the total number of dipoles. The first term stands for the elastic energy, which is the same for both domain types. The second term represents the interaction of dipoles with each other, where ε^s is a constant parameter. The third term describes a correction to the elastic energy which has opposite signs for the two domain types and β is a constant. The fourth term accounts for the reorientation of domains of dipole moment μ in an external electric field. *T* is the temperature and *S* is the entropy which is a function of *N*, *N*+, and *N*−.

The domain ratio follows from the minimization of the free energy. When an external field is applied the domain switching occurs in order to minimize the U_G. In this experiment the field is turned off after 1 μs by grounding both electrodes, and the electrodes will rapidly redistribute the surface charges to compensate for the polarization induced by the piezoelectric effect as the strain waves propagate. This means that there is no macroscopic external field present and the only way to minimize the free energy is via the ferroelastic term which is independent of the field.

As a conclusion we show that generated and observed high amplitude strain waves below T_C drives the domain polarization switching in the absence of an electric field and that the mechanism responsible for domain switching is ferroelastic rather than ferroelectric.

1 J. Bornarel, Ferroelectrics 71, 255, 1987.
2 J. F. Nye, *Physical Properties of Crystals*, Clarendon Press, Oxford, 1957.
3 J. S. Bakos Zs. Sörlei, Cs. Kuti, and S. Szikora, Appl. Phys. A:Mater. Sci. Process. 19, 59, 1979.

Published in PHYSICAL REVIEW B 81, 024113 (2010)

Time-resolved x-ray scattering from laser-molten indium antimonide

R. Nüske[1], C. von Korff Schmising[1], A. Jurgilaitis[1], H. Enquist[2], H. Navirian[1], P. Sondhauss[2], and J. Larsson[1]

[1]Atomic Physics Division, Department of Physics, Lund University, Sweden

[2] MAX-lab, Lund University, Sweden

We demonstrate a concept to study transient liquids with picosecond time-resolved x-ray scattering in a high-repetition-rate configuration. Femtosecond laser excitation of crystalline indium antimonide (InSb) induces ultrafast melting, which leads to a loss of the long-range order. The remaining local correlations of the liquid result in broad x-ray diffraction rings, which are measured as a function of delay time. After two nanoseconds the liquid structure factor shows close agreement with that of equilibrated liquid InSb. The measured decay of the liquid scattering intensity corresponds to the re-solidification rate of 1 m/s in InSb.

To study the diffuse scattering of the liquid phase of InSb a single-photon-counting detection system was designed and set up as shown in Fig. 1.

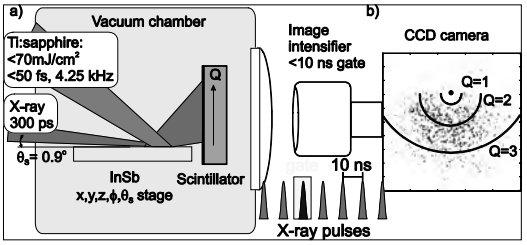

Figure 1:
a) Concept of the time-resolved liquid x-ray scattering setup. The diffusely scattered x-rays are detected by a scintillator. An image intensifier gates single x-ray bunches to achieve a time resolution limited by the x-ray bunch length.
b) A typical 2D image of the scattering pattern for a time delay of 2 ns; the lines indicate equivalent scattering vectors, Q.

This detection technique eliminates the necessity for x-ray choppers to select a single x-ray pulse for time resolved x-ray scattering experiments.[1] A hybrid- or single bunch filling pattern in the storage ring is not required. It offers a unique alternative to the gateable area pixel array detector PILATUS (gate time 150 ns), which was recently tested in time-resolved x-ray experiments.[2]

The Q-resolution in our experiment is limited to 0.4 $Å^{-1}$ at Q = 3 $Å^{-1}$ due to the size of the x-ray spot and the grazing incidence geometry.

Azimutal integration of the scattering pattern, corrected for the atomic form factors, yields a value directly proportional to the structure factor S(Q). This is shown in Fig. 2 for different time delays: 2 ns prior, 2.5 ns after, and 52 ns after the laser excitation.

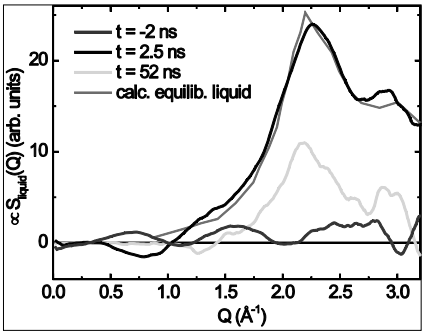

Figure 2:
Liquid structure factor S(Q) at various time delays: -2 ns, +2.5 ns, and 52 ns in respect to the laser pulse. Good agreement is seen with an ab initio calculation of equilibrated liquid InSb (solid line).[3]

The main feature at Q=2.2 A^{-1} has been attributed to the In-Sb bonds, whereas the second feature at Q=3.0A^{-1} has been interpreted as a covalent Sb-Sb bond in liquid InSb.

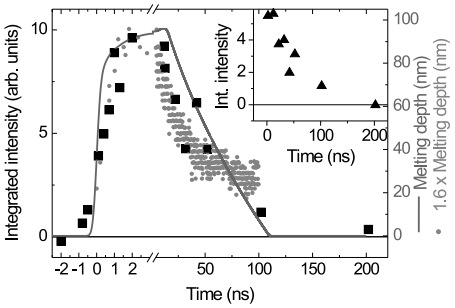

Figure 3:
Integrated structure factor S(Q) as a function of time. The melting depth (solid line) as calculated using a 1D heat flow equation matches the experimental data.

As can be seen in the inset in figure 3, the two features (squares and triangles) have the same temporal dependence showing that these coordination distances are inherent to the liquid. This corroborates the rapid thermalization of laser-molten InSb, i.e., within approximately 2 ns. The temporal evolution of the scattering intensity is well explained by a simple 1D heat flow model.

In conclusion, we have demonstrated that time-resolved diffuse x-ray scattering experiments can be carried out at a synchrotron radiation facility with a uniform bunch fill pattern. Excellent agreement with previously determined liquid structure factors has been shown.

The authors would like to thank the Swedish Research Council (VR), the Knut and Alice Wallenberg Foundation, the Crafoord Foundation, the Carl Trygger Foundation, and the European Commission via the Marie Curie Programme for their financial support.

[1] M. Cammarata, L. Eybert, F. Ewald, W. Reichenbach, M. Wulff, P. Aninrud, F. Schlotte, A. Plech, Q. Kong, M. Lorenc, B. Lindenau, J. Räbiger, S. Polachowski, Rev. Sci. Instrum., **80**, 015101 (2009).
[2] T. Ejdrup, H. T. Lemke, K. Haldrup, T. N. Nielsen, D. A. Arms, D. A. Walko, A. Miceli, E. C. Landahl, E. M. Dufresne, and M. M. Nielsen, J. Synchrotron Rad. **16**, 387 (2009).
[3] .Q. Zhang, Y.H. Wei, and C.F. Zhu, Chem. Phys. Lett., **408**, 4-6 (2005).

Investigations of the dynamic of particles formation in a flame system using a new SAXS detector.

Frederik Ossler[1], Linda Vallenhag[1], Sophie E. Canton[2], Jörgen Larsson[3], Peter Sondhauss[2].

[1]Division of Combustion Physics, Department of Physics, Lund University, LUND, Sweden; [2]MAXlab, Lund University, LUND, Sweden; [3]Division of Atomic Physics, Department of Physics, Lund University, LUND, Sweden.

The project concerns studies on dynamics of particles, liquids and phase transitions during combustion and other physically and chemically reactive systems. These investigations require special detectors to resolve mechanisms on the nanometer and subnanometer scales with sufficient temporal resolution and sufficient dynamic range. Experiments were previously performed using a multichannel Wide-Angle X-Ray Scattering (WAXS) detector and another channel in the forward scattering region to measure the Small-Angle X-Ray Scattering (SAXS) [1]. In order to study the size and structural changes for particle ranging up to so called primary particles up to 20 nm in diameter a multichannel detector has been constructed to complement the WAXS detector. The two were operated synchronously for the first time at beamline D611 measuring the scattering from a flame system.

The SAXS detector measured simultaneously at 20 different scattering angles between 0.5° and 10°. The WAXS and SAXS detectors were operated with synchronized sampling at a rate

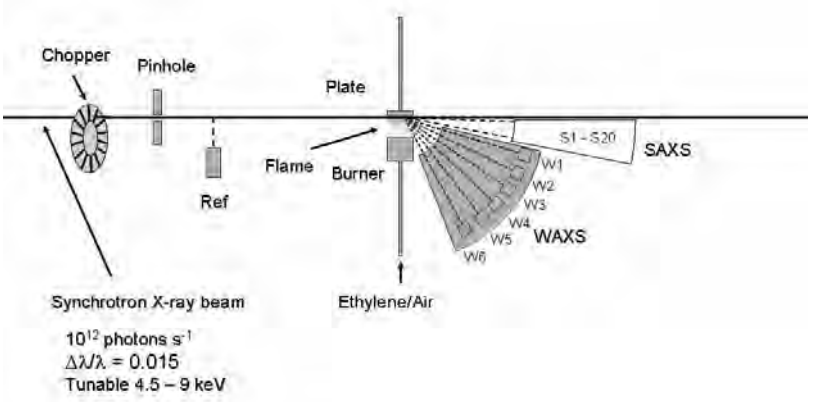

Fig1: The experimental set-up for the flame measurements.

faster than 100 k sample s^{-1}. The measurements were performed continuously for time spans of the order of one hour. The data was averaged typically during one s before being stored on the computer for data analysis. The detection system has a high dynamic range enabling studies on the formation of deposits and transformation of nanoparticles during phase transitions. In the experiments the transitions from gas phase to condensed phase of molecules and particles were investigated close to the surface of a metal plate inserted in the flame. Data is still being evaluated and will be presented for the public during 2010.

References

1. F. Ossler, S.E. Canton, J. Larsson, “X-ray scattering studies of the generation of carbon nanoparticles in flames and their transition from gas phase to condensed phase”, Carbon, 47, 3498 (2009).

Bioactive Nanocrystalline Hydroxyapatite Modified Implants

Martin Andersson, Paul Handa and Fredrik Currie

Dept. Chemical and Biological Engineering, Chalmers University of Technology
S-412 96 Göteborg, Sweden

The use of foreign materials, i.e. implants, for replacement of injured or lost body parts is rapidly expanding throughout the world and many new products are continuously being clinically introduced. Osseointegration (bone integration) meant a breakthrough in implant treatments and titanium, which is the most frequently used implant material, has been used successfully during the last 40 years. However, approximately ten percent of all controlled and placed oral implants will be lost within a period of ten years. The greatest failure rates, using titanium implants, are with patients having small volumes of bone due to severe bone resorption. Hence, improved novel materials that can improve the clinical results are needed. Bioactive materials, which include hydroxyapatite (HA), and some glass and glass-ceramics, are characterized by their ability to initiate a biological response, leading to a chemical and biological bonding to the living tissue. In our ongoing research, focus is on bioactive HA. The idea is to design the surface of the implant so that it resembles that of living tissue, and hence speed up the healing process.

A novel method for the preparation of nanosized HA has been developed based on surfactant self-assembly. The formed HA particles (2×20 nm) are the smallest HA ever produced and they are very similar to those found in hard tissue, i.e., bone. After particle formation, the particles are dispersed in a solution containing surfactants oil and water. This solution is then used to coat the implant resulting in a very thin layer of HA particles, approximately 3-15 nm thick. After coating, a heating step is applied burning off remaining solvents and surfactants at 500 °C for 5 min. *In vivo* data have demonstrated favorable results in terms of that these particles enhances the integration of the implants to a great extent resulting both in higher torque of implant removal as well as increased amount, of to the implant, attached bone.[1,2]

The aim of the proposed project was to study the formation process, *in situ*, of the formed HA particles in the liquid crystalline phase. Such a liquid crystal has a long-range order (~4 nm). In short, a calcium salt is dissolved in water and mixed with phosphoric acid at the desired ratio. This salt solution (15 g) is then mixed with surfactant (70 g L64 from BASF) and P-xylene (15 g) forming a liquid crystalline phase having the reversed hexagonal structure (H2).[3] The H2 can be illustrated as water channels, having a diameter of ~4 nm surrounded by a monolayer of surfactant, which are packed in a hexagonal arrangement. This liquid crystal is then put in a saturated ammonia atmosphere (vapor pressure a room temperature), which results in that the pH of the mixture is increased and the hydroxyapatite is formed within the liquid crystal. The formation takes about three days to complete. This formation process is of high interest to follow and we are interested in the growth of the particles, the change in crystallinity of the particles and also if the ordered liquid crystalline phase is kept during the synthesis. The reaction is performed at room. How the liquid crystalline phase is influenced by the particles during synthesis was examined using small angle X-ray (SAXS) diffraction at the I711 beamline, Maxlab.

Liquid crystals were prepared and analysed after 0, 7, 18, 30, 48 and 72 hours of ammonia treatment, in order to examine the influence of the hydroxyapatite crystal growth. In Figure 1, SAXS diffractograms obtained for the liquid crystals are shown.

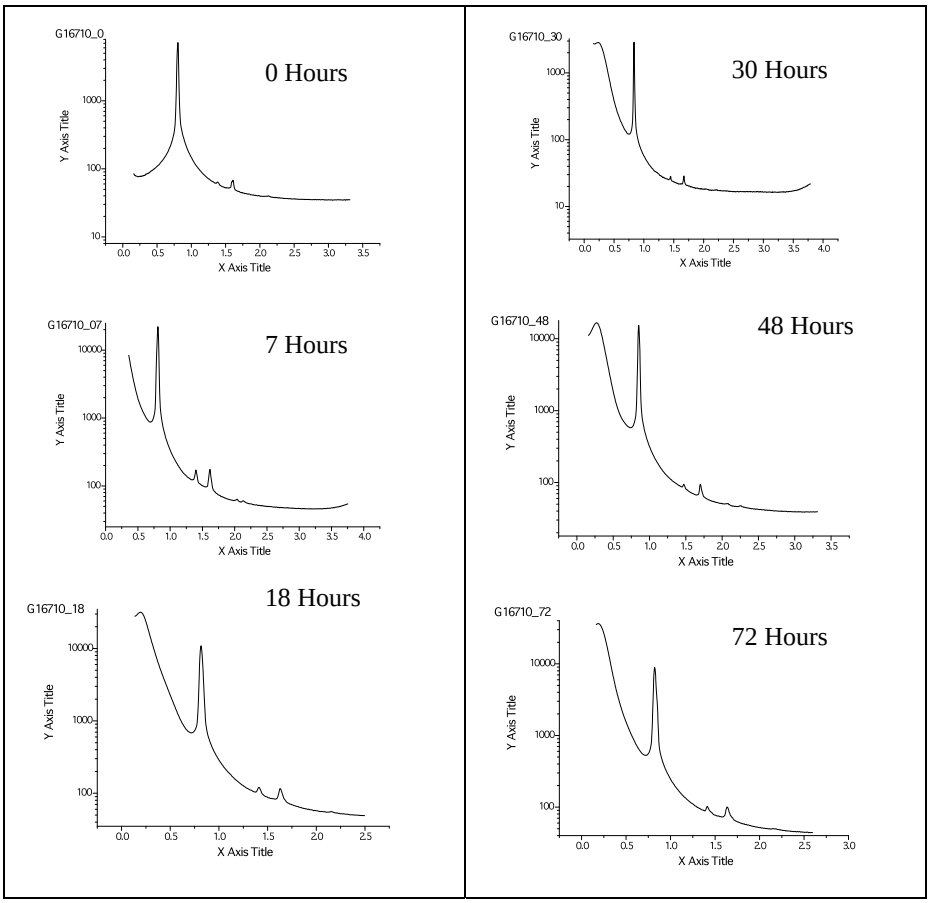

Figure 1. SAXS diffractograms obtained after 0, 7, 18, 30, 48 and 72 hours of crystallization. Intensity is plotted as a function of 2θ.

The observed Bragg peaks are consistent with the presence of a reversed liquid crystalline phase, $H2^3$. Since the peaks are observed independently of the time it can be concluded that the liquid crystal stays intact during the crystallisation and that the formed HA particles most probably are formed within the water confinements of the liquid crystal. It seems likely that the size of the formed HA particles are a direct effect of the size of the liquid crystal domains.

References

(1) Meirelles, L. Arvidsson, A.; Andersson, M.; Kjellin, P.; Albrektsson, T.; Wennerberg, A. *J. Biomed. Mater. Res. Part A* **2007**.

(2) Meirelles, L.; Albrektsson, T.; Kjellin, P.; Arvidsson, P.; Franke-Stenport, V.; Andersson,M.; Currie, F.; Wennerberg, A. *J. Biomed. Mater. Res. Part A* **2007**.

(3) Alexandridis, P.; Olsson, U.; Lindman, B. *Macromolecules* **1995**, *28*, 7700.

BioXTAS: A microfluidics approach to High-throughput SAXS studies of proteins in solution

Arleth, L.[a], Toft, K. N.[b], Nielsen, S. S.[c], Snakenborg, D.[c], Jeppesen, M. G.[b], Jacobsen, J. K.[d], Vestergaard, B.[b], Kutter, J. P.[c]

[a] *Biophysics, University of Copenhagen, Faulty of Life Sciences, Denmark, Thorvaldsensvej 40, DK-1871 Frederiksberg C, Denmark*
[b] *Biostructural Research, University of Copenhagen, Faculty of Pharmaceutical Sciences, Denmark*
[c] *Dept. Micro and Nanotechnology, Danish Technical University, Denmark*
[d] *Novo Nordisk A/S, Denmark*

Many of the most interesting biological systems are only available in very small quantities. This significantly limits which samples can be investigated in small-angle scattering experiments where typical required sample volumes of around 50-100 microliters are common. In the BioXTAS project we have tried to solve this problem by developing a microfluidics based chip that functions both as sample holder and sample mixer and incorporate this into a synchtrotron small-angle X-ray scattering (SAXS) instrument [1,2]. In a very recent experiment performed at beamline I711 at MAX-lab, we have shown that it is possible to mix, position and perform a SAXS measurement on as little as 5 microliter of sample, without sacrificing the SAXS data quality. Furthermore, the BioXTAS chip allows for very fast cleaning of sample cell between measurements, sample mixing and positioning. With our present set-up, this limits the dead-time lost between measurements to 60 seconds. The combination of extremely small sample volumes and minimal sample changing deadtime opens up for true high-troughput solution SAXS measurements.

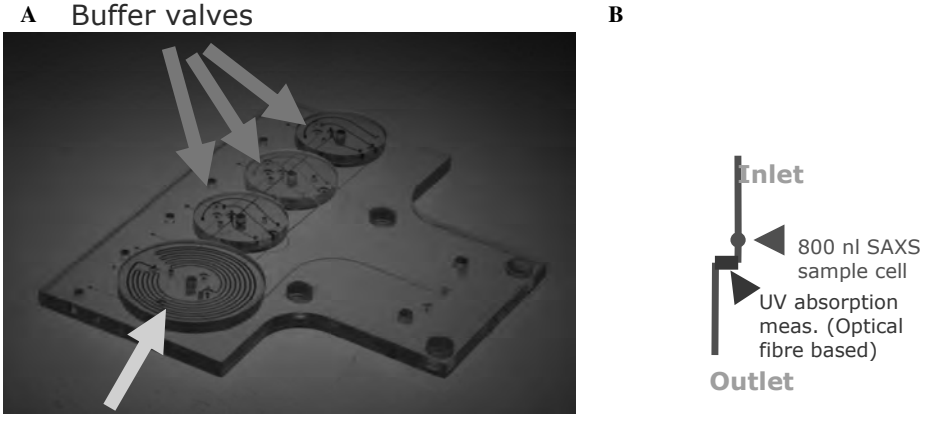

Figure 1. A) Next generation BioXTAS chip: Mixing with multiple rotary valves for better flow control. Buffers and the pressure on the protein stock are supplied via external syringe pumps. B) Mixing device directly coupled to PS-based flow-through SAXS sample cell.

The microfluidics device: A polystyrene based microfluidics device has been developed with the aim of minimizing both the sample consumption and the dead time lost for sample mixing and positioning between measurements.

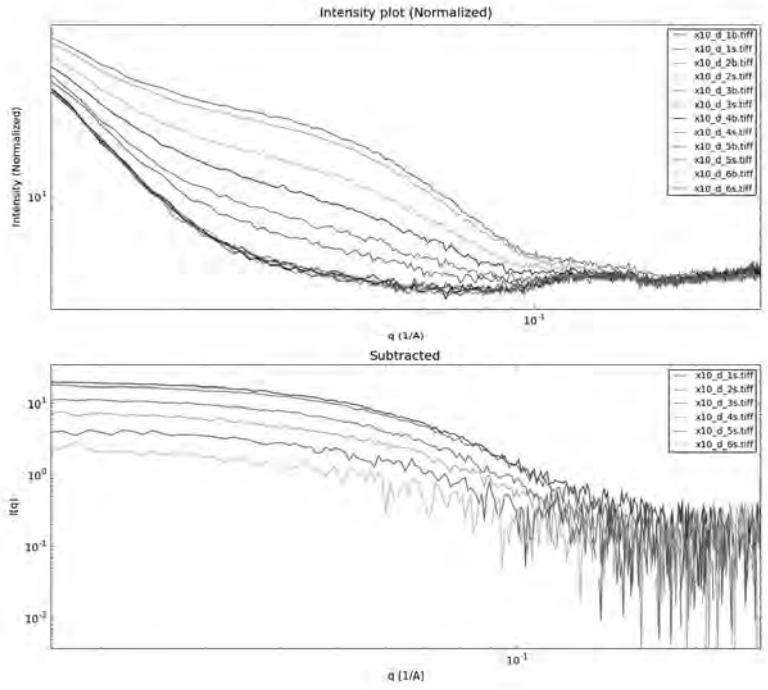

Figure 2. Upper plot) Data recorded at the BioXtas 2nd Generation Setup @ Beamline I711, MAXLab, September 2009. Dilution of BSA, sample vol. 5 µL. Sample concentrations from 1 mg/ml to 6 mg/ml. Lower plot) Background subtracted scattering intensities, *I(q)*.

Ultra-fast SAXS data collection with a minimal sample consumption: Using the BioXTAS microfluidics device in combination with a control unit coordinating both the sample mixing and SAXS data collection, it is possible to run e.g. a dilution series including background subtraction and cleaning in between measurements in a fully automated fashion. In the dilution series plotted in fig. 2, only 5 µl of each sample concentration was mixed and positioned in the beam. The applied measurement time lasted 120 secs, the subsequent (automatic) rinsing of the sample cell lasted 30secs and the sample mixing and positioning lasted another 30 secs. I.e. the total time for mixing, measuring and washing in between a sample and its buffer background is reduced to 6 minutes. -Of this time, only two minutes can be regarded as deadtime lost to sample changing. The full dilution series with six concentrations was therefore performed in less than 40 minutes and with a total consumption of the 6 mg/ml BSA stock solution of only 15 µL.

References

[1] Katrine Nørgaard Toft, Bente Vestergaard, Søren Skou Nielsen, Detlef Snakenborg, Mads G. Jeppesen, Jes K. Jacobsen, Lise Arleth and Jörg P. Kutter, Analytical Chemistry, 2008, 80, 3648-3654.

[2] Søren Skou Nielsen, Katrine Nørgaard Toft, Detlef Snakenborg, Mads Gravers Jeppesen, Jes K. Jacobsen, Bente Vestergaard, Jörg P. Kutter and Lise Arleth, J J. Appl. Cryst., 2009, 42, 959-964.

Following a drug delivery system when adding a drug

JOAKIM BALOGH[1,2] KARIN SCHILLÉN[2] MARIA GRAÇA MIGUEL[1] AND JAN SKOV PEDERSEN[3]

[1] Departamento de Quimica da Universidade de Coimbra, Rua Larga, 3004-535 Coimbra, Portugal

[2] Division of Physical Chemistry, Center for Chemistry and Chemical Engineering, Lund University, P.O. Box 124, SE-22100 Lund, Sweden

[3] Department of Chemistry and iNANO interdisciplinary Nanoscience Center, University of Aarhus, DK-8000, Aarhus C, Denmark

This work deals with microemulsions as a model drug delivery system and what effect addition of a drug to these systems has. Microemulsions are typically structured on length scales of the order of 5-20 nm, and can have several different morphologies. The structures consist in general of water and oil separated by a surfactant film[1-3]. The microemulsions have in general a region where small globular droplets are stable. This region is surrounded by upper and lower boundaries known as emulsification failure boundaries. Studies of these systems are readily performed at the temperature of the lower emulsification boundary, T_{EFB}, where the microemulsion droplets often are spherical. This present work describes the effects of a drug, lidocaine, on a model drug delivery system as observed by, SAXS. The experiments were performed at the newly developed SAXS setup at the I711 beamline in MAX-Lab, Lund, Sweden. The beamline is described by Cerenius et al[4] and the SAXS setup by Knaapilla et al[5]. The model drug delivery system is the well known nonionic ternary microemulsion system composed of $C_{12}E_5$, decane, and water studied previously amongst others by Olsson and co-workers[6-12]. We have therefore access to SANS, NMR and dynamic and static light scattering data for the microemulsion without drug. It is known from the above referenced literature that the system consists of spherical oil droplets covered with surfactant with a radius of 80 Å at T_{EFB} and that the droplets grow with temperature and to a small degree also with concentration. The growth leads to aggregates with a larger volume but in order to maintain the total area-to-total volume ratio of the droplets (i.e. the surfactant-to-oil ratio), the droplet needs to change its shape when growing. In this case the growth is one-dimensional and often pictured as a prolate aggregate. The ratio of the large axis divided with the small axis, known as the axial ratio, describes the shape of the prolate and thus also the growth of the aggregate. Recently, a dynamic and static light scattering investigation of the $C_{12}E_5$/decane/ water system with a drug (lidocaine) added has been published[13] as well as a partial phase diagram[14] and some initial SAXS results[15] on the same system. The resulting axial ratios, obtained from SAXS and DLS measurements, versus temperature are prestented in Figure 1 for a 1% substitution of the oil with lidocaine.

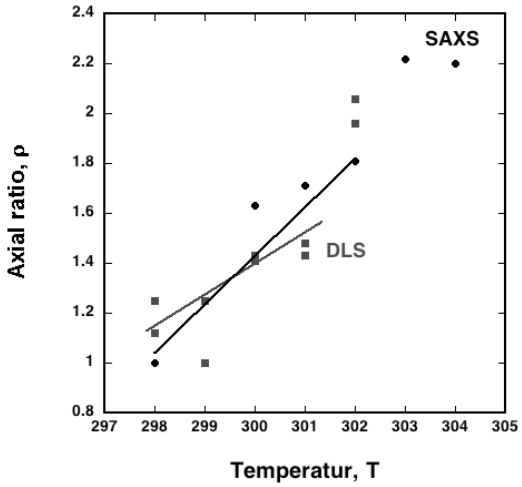

Figure 1. The axial ratio, ρ, for the system with 1% of the oil volume substituted by lidocaine versus temperature, T, calculated from DLS (squares) and from SAXS (circles). The lines are just guides for the eye. The system changes with temperature and the results from the different methods are in good agreement.

The results show that the aggregates change their shape (and by that their size) with temperature. Furthermore, there is a jump in the axial ratio at 301K and 302K, respectively. This temperature is close to the temperature where the aggregates become bicontinuous, as seen by NMR self diffusion experiments. At this condition, the models used to extract the axial ratios no longer are valid. This investigation will be presented in an upcoming article.[16]

(1) Evans, D. F.; Wennerström, H. *The Colloidal domain: where physics, chemistry, biology and technology meet*, 2nd ed.; John Wiley & Sons, Inc: New York, NY, 1999.
(2) Anderson, D.; Wennerström, H.; Olsson, U. *J Phys Chem* **1989**, *93*, 4243.
(3) Chen, S. J.; Evans, D. F.; Ninham, B. W.; Mitchell, D. J.; Blum, F. D.; Pickup, S. *J Phys Chem* **1986**, *90*, 842.
(4) Cerenius, Y.; Stahl, K.; Svensson, L. A.; Ursby, T.; Oskarsson, A.; Albertsson, J.; Liljas, A. *J Synchrotron Radiat* **2000**, *7*, 203.
(5) Knaapila, M.; Svensson, C.; Barauskas, J.; Zackrisson, M.; Nielsen, S. S.; Toft, K. N.; Vestergaard, B.; Arleth, L.; Olsson, U.; Pedersen, J. S.; Cerenius, Y. *J Synchrotron Radiat* **2009**, *16*, 498.
(6) Leaver, M. S.; Olsson, U.; Wennerström, H.; Strey, R. *J Phys II* **1994**, *4*, 515.
(7) Leaver, M.; Furo, I.; Olsson, U. *Langmuir* **1995**, *11*, 1524.
(8) Olsson, U.; Schurtenberger, P. *Langmuir* **1993**, *9*, 3389.
(9) Olsson, U.; Schurtenberger, P. *Prog Colloid Polym Sci* **1997**, *104*, 157.
(10) Balogh, J.; Olsson, U.; Pedersen, J. S. *J Disper Sci Technol* **2006**, *27*, 497.
(11) Balogh, J.; Olsson, U. *J Disper Sci Technol* **2007**, *28*, 223.
(12) Balogh, J.; Olsson, U.; Pedersen, J. S. *J Phys Chem B* **2007**, *111*, 682.
(13) Balogh, J.; Schillén, K.; Miguel, M. "Investigating a nonionic oil-in-water microemulsion containing a hydrophobic drug (Lidocaine)"; II Iberic Meeting of Colloids and Interfaces (RICI2), 2007, Coimbra, Portugal.
(14) Balogh, J.; Schillén, K.; Miguel, M. D. *The AAPS Journal* **2007**, *9*, W4179.
(15) Balogh, J.; Pedersen, J. S. *Colloids for Nano- and Biotechnology* **2008**, *135*, 101.
(16) Balogh, J.; Schillén, K.; Miguel, M.; Pedersen, J. S Manuscript in preparation.

SAXS study of the phase behavior of aqueous soy phosphatidyl choline/ glycerol dioleate mixtures

Justas Barauskas[1], Marija Jankunec[1], Markus Johnsson[2], Fredrik Tiberg[2,3]

[1] *Institute of Biochemistry, Mokslininkų 12, LT-08662 Vilnius, Lithuania*

[2] *Camurus AB, Sölvegatan 41, Ideon Science Park Gamma 1, SE-22370 Lund, Sweden*

[3] *Physical Chemistry 1, Center for Chemistry and Chemical Engineering, Lund University, P. O. Box 124, SE-22100 Lund, Sweden*

Depending on various molecular and ambient conditions lipids can form a variety of different liquid crystalline (LC) phases, where the lamellar phase is simplest and the most common in lipid systems.[1] In contrast, nanostructural architecture of reversed non-lamellar phases (like hexagonal and cubic) is much more complex possessing fascinating two- and three-dimensional periodicity. Due to their unique key property to exist in excess water, non-lamellar reversed LC have recently gained an increasing interest in medical uses, e.g. in the delivery of active substances.[2] In this respect, nanoporous lipid LCs have very large interfacial inner area and serve as a matrix for the incorporation (loading), protection and controlled release of drug molecules.[3]

This work concerns lipid mixture composed of soy phosphatidylcholine (SPC) and glycerol dioleate (GDO) which possess interesting and very useful bioadhesive properties which can be utilized for topical applications to e.g. the skin, eye or the oral mucosa. The nanostructural changes of the bulk SPC/GDO system have been investigated in excess water (90 wt%) conditions as a function of lipid composition.

Figure 1 shows the obtained SAXS curves for the SPC/GDO system in excess water as a function of weight ratio of SPC to GDO. At relatively high SPC content (SPC/GDO ratio range 70/30 – 57.5/42.5) the results clearly show the formation of birefringent reversed hexagonal phase (H_2) which is characterized by three very strong reflections at relative positions in ratios of 1: √3: √4. With increasing GDO content (between SPC/GDO ratio of 55/45 and 45/55) an extremely stiff and isotropic phase is observed. It shows clear 9 Bragg peaks with relative positions in ratios of √3: √8: √11: √12: √16: √19: √24: √27: √32 resembling reversed micellar cubic liquid crystalline structure of *Fd*3*m* crystallographic space group (Q^{227}). Very broad reflections of the liquid crystals formed in this SPC/GDO weight ratio region indicate quite disordered nanostructure consisting of rather small microdomains. Very surprisingly, at even more increased GDO content (between SPC/GDO ratio of 42.5/57.5 and 37.5/62.5) most likely another stiff and isotropic phase or phase mixture is observed which is characterized by at least 25 narrow reflections. Although some reflections coincide with the *Fd*3*m* phase we were *yet unable* to completely characterize nanostructure of the mixtures formed in this SPC/GDO content region. In our opinion, the observed diffraction patterns may correspond to either (i) mixtures of *Fd*3*m* phase and yet unrecognized phase or (ii) pure yet unrecognized phase, cubic or with completely different lattice, i.e. tetragonal, orthorhombic or other. In either case, quite narrow reflections indicate highly ordered nanostructure.

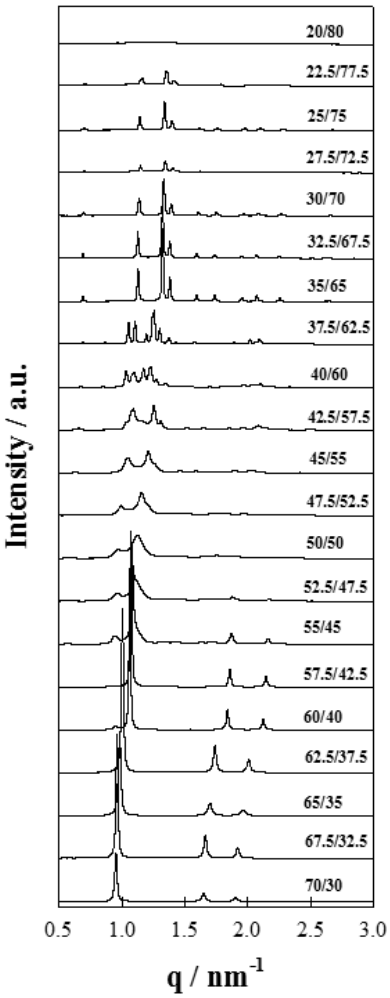

Figure 1. Characteristic SAXS patterns of the bulk SPC/GDO mixtures in excess water as a function of lipid composition at 25ºC measured between SPC/GDO weight ratios of 70/30 to 20/70.

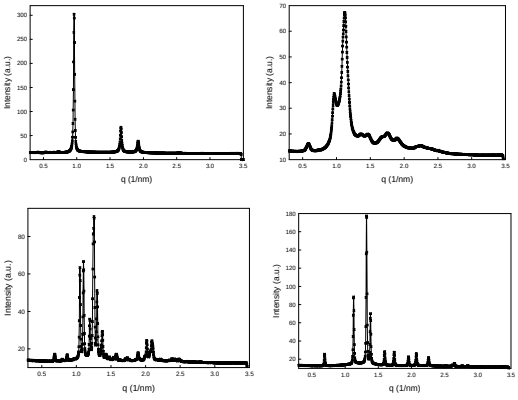

Figure 2. Characteristic diffractions patterns of the aqueous SPC/GDO mixtures in excess water from five structurally different regions at 25ºC. SPC/GDO ratios are (top left) 67.5/32.5, (top right) 50/50, (bottom left) 37.5/62.5, (bottom right) 35/65.

At the SPC/GDO ratio of 35/65 unrecognized phase or their phase mixture suddenly transforms into nice face-centered reversed micellar cubic phase of *Fd*3*m* crystallographic space group (Q^{227}) characterized by at least 15 Bragg peaks with relative positions in ratios √3: √8: √11: √12: √16: √19: √24: √27: √32: √35: √40: √43: √44: √48: √51, which can be indexed as the (111), (220), (311), (222), (400), (331), (422), (511/333), (440), (531), (620), (533), (622), (444), and (711/551) reflections. Starting from SPC/GDO ratio of 25/75 the pure *Fd*3*m* phase starts to transform into reversed micellar phase (L_2). At the SPC/GDO ratios lower than 20/80 only pure L_2 phase is detected. In summary, with increasing GDO content aqueous SPC/GDO mixtures undergo phase transition sequence: (i) H_2 phase, (ii) disordered isotropic phase resembling *Fd*3*m* structure, (iii) unrecognized phase or phase mixture, (iv) ordered *Fd*3*m* phase, and (v) L_2 phase. Characteristic diffraction patterns from observed five distinct SPC/GDO content regions are presented in Figure 2.

[1] V. Luzzati, F. Husson, *J. Cell Biol.* **1962**, *12*, 207-219.
[2] C. J. Drummond, C. Fong, *Curr. Opin. Colloid Interface Sci.* **2000**, *4*, 449-456.
[3] J. Barauskas, T. Nylander. In *Delivery and controlled release of bioactives in foods and nutraceuticals.* N. Garti, Ed. Woodhead Publishing Ltd: Cambridge, pp. 107-131, **2008**.

Nanostructure characterization using DSC coupled to SAXS

Kalnin Daniel, *Tomás Plivelic and *Yngve Cerenius

YKI Institute for Surface Chemistry, Drottning Kristinas Väg 45, 11486 Stockholm, Sweden
*MAX-Lab, 22100 Lund, Box 118, Sweden

The structural properties of oils and fats are of interest for different sectors of the technological and scientific community.
Molecules bearing one or several hydrocarbon chains display partial or total insolubility in water and self aggregation properties that are frequently used in pharmaceutical, chemical, food and cosmetic applications to generate lipid nanoparticles, emulsions, liposomes, cubosomes or hexosomes as well as mesophases, microemulsions or micellar solutions.
The self aggregation properties and the type of structures formed by these lipid molecules whatever their origins: biologic or synthetic, depend on the nature of the polar head groups (water affinity and eventual ionization) as well on the number, length, and unsaturation of the chains. A complex polymorphism generated by the fact that lipid molecules display multiple possibilities of self-association frequently complexifies the study of lipid structures. Moreover, this polymorphism is modulated for the lyotropic substances by their water affinities which are variable as a function of head groups, pH and ionic strength of aqueous solutions, etc and presence of added substances. Technical challenges arise from these features since novel materials based on structured lipid matrices are desired as well in food technology for structured products as in pharmaceutical technology for controlled release properties or in material science for tuning hardness of materials. The structural characterization of their organizations at the molecular and supramolecular scales and the determination of their associated thermal properties are simultaneously possible by the coupling of Differential Scanning Calorimetry (DSC) and SAXS (**Figure 1**).

Here we present the structural properties of formulated lipid materials relevant for their use and processing possible at 711 Beam line at MAX-Lab.

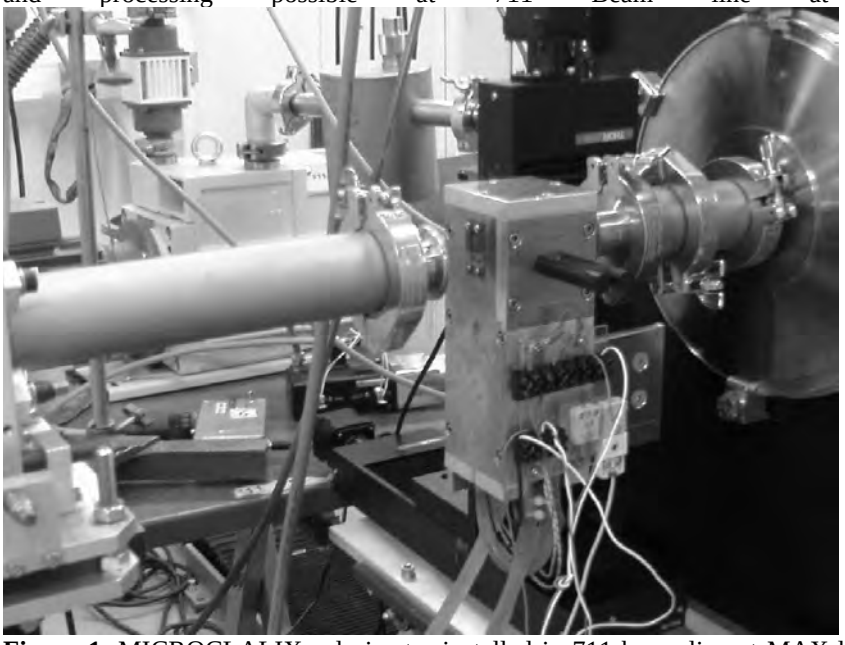

Figure 1: MICROCLALIX calorimeter installed in 711 beam line at MAX-lab for the first time

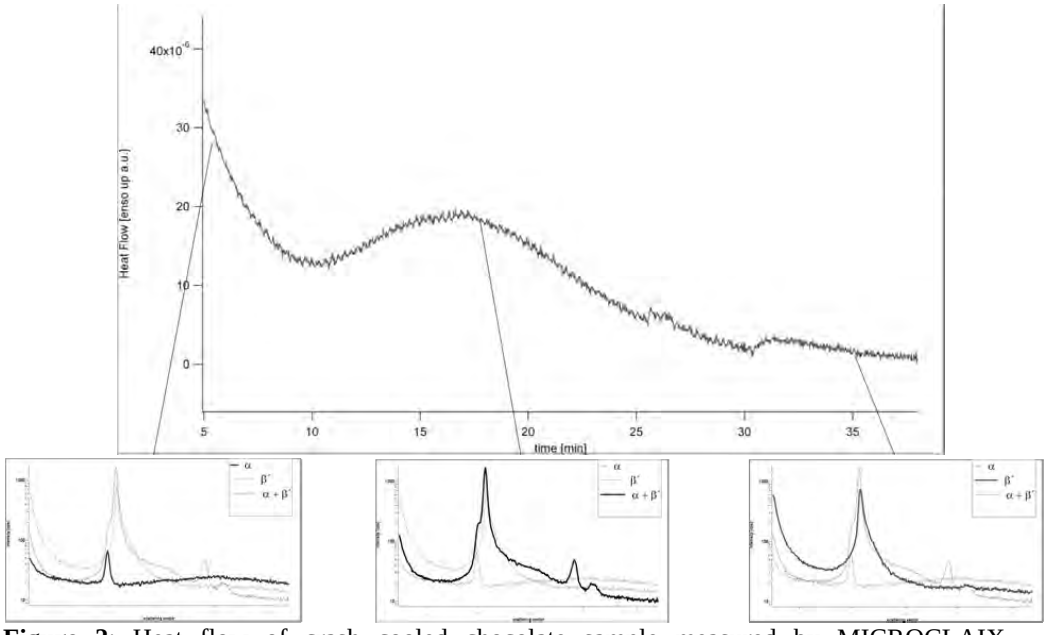

Figure 2: Heat flow of crash cooled chocolate sample measured by MICROCLAIX calorimeter on 711 Beam line. Sample was cooled from 60 °C to 15°C by introducing the 20µl containing sample directly in the precooled calorimeter. Corresponding SAXS pattern

were recorded as a function of time. Those SAXS patters show the structural changes occurring during the early state of untempered crystallization of chocolate.

The results in Figure 2 represent DSC and SAXS pattern recorded for the first time at beam line 711 at MAX-lab. We were able to correlate the phase transition of CB as a function of time and heat flow. First, a 2L α form crystallize during the rapid cooling. The exothermic reaction having an onset at 10 minutes in the DSC curve is indicative of recrystallization. Even if only an exothermic peak can be monitored there is an endothermic melting peak which is overlaid by an exothermic crystallization peak.
The SAXS curves represent CB in crystal forms 2L α, 2L α + 2L β´ and only 2Lβ´, respectively. Even after 35 min there are still liquid and solid phases. From this study we can start to identify structural changes. Further, these results can be compared to more complex chocolate structures. Even if structure determination and DSC cold have been carried out on two separate experiments, exact correlation of DSC and SAXS pattern is s only possible from simultaneous coupled time resolved experiment.

Acknowledgements:
The authors thank Dörthe Haase for the installation of the calorimeter and Christer Svensson for the programming efforts necessary. Thanks also go to UMR 8612 and especially to Gerard KELLER and Michel OLLIVON who unfortunately passed away too soon to see his calorimeter functioning on another synchrotron

Figure 2
References

[1] Kalnin D. J E; Characterization of Lipid Nanostructures using DSC coupled to SAXS and WAXS, JEEP 2009 00017, (2009) http://www.jeep-proceedings.org or http://dx.doi.org/10.1051/jeep/200900017
[2] Ollivon M., Keller G., Bourgaux C., Kalnin D., Villeneuve P., Lesieur P., DSC and High Resolution X-Ray Diffraction Coupling, *J. Therm. Anal. Calor.*, 2006, 83, 219-224.

Keywords: lipid polymorphism, nanostructures, DSC, SAXS

Structural Studies of Cu-Zn-Fe-O Materials

J. Darul[1], W. Nowicki[1], Y. Cerenius[2], D. Haase[2]

[1] *Faculty of Chemistry, Adam Mickiewicz University, Grunwaldzka 6, PL-60780 Poznań, Poland*
[2] *MAXLAB, Lund University, P.O. Box 118, S-221 00 Lund, Sweden*

As a kind of typical magnetic materials, ferrite has been widely used in many areas, such as ferrofluids, message recording, pigments, biology, medicine, magnetic sensors, aviation, and so on. When Mn^{3+} or Cu^{2+} ions are octahedrally coordinated in solids, electronic degeneracy can be lifted by structural distortion when the structural energy cost can be compensated with the electronic energy gain. This is called the Jahn-Teller (JT) effect, which is observed in a wide range of materials [1-2]. Since of Cu^{2+} is a Jahn-Teller ion, copper ferrite ($CuFe_2O_4$) gives the anomalous favorable properties and also exhibits phase transition from tetragonal to cubic, depending on the temperature [3].

Powder samples with nominal composition $Cu_{1-x}Zn_xFe_2O_4$ ($0.0 \leq x \leq 0.05$) were prepared by the combustion method. The stoichiometric quantities of starting materials, viz., $Cu(NO_3)_2 \cdot 6H_2O$, $Fe(NO_3)_3 \cdot 9H_2O$, $Zn(NO_3)_2 \cdot 4H_2O$ and $C_6H_8O_7 \cdot H_2O$ (Merck), were dissolved in distilled water. The mixed citrate-nitrate solution was heated at 120°C, with continuous stirring. After the evaporation of excess of water, a highly viscous gel was obtained. Ultimately, the powder was sintered at different temperatures (300, 600, 900°C) for 5h and slow-cooled to room temperature. Results presented in this paper deal with the temperature phase transition occurring in the $Cu_{0.95}Zn_{0.05}Fe_2O_4$ spinel. The structural change with increasing temperature has been compared with that of undoped copper ferrite. *In situ* powder X-ray diffraction data were collected at the beamline I711 at MAX II synchrotron at MAX-lab, Lund with a MAR165 CCD detector [4].The polycrystalline samples placed in quartz capillaries of diameter 0.3 mm were heated and cooled at the temperature range from RT to 500°C. The selected X-ray wavelengths were 1.26749 or 1.26700 Å and the X-ray exposure time was 120s. Powder X-ray diffraction raw data were converted to powder diffraction profiles using the program FIT2D [5].

Figure 1 illustrates that the synchrotron powder diffraction patterns of both synthesized materials recorded at room temperature could be indexed as that of single-phase tetragonal spinel (space group $F4_1/ddm$) with unit-cell ratio c/a=1.055 for $CuFe_2O_4$ and 1.040 for $Cu_{0.95}Zn_{0.05}Fe_2O_4$, respectively. However, it was found that the tetragonal structure is stable at room temperature, the substitution of Cu by Zn leads to a decrease of the *c/a* ratio - the resulting decrease in Cu^{2+} ions in the octahedral sites gives rise to a less distorted crystalline structure.

X-ray powder diffraction scans reveal that the structural phase transition is manifested by the disappearance of the reflections characteristic for tetragonally distorted lattice and appearance of a new peaks of the cubic spinel in the investigated temperature range. Substitution with very small quantities of Zn^{2+} ions clearly restrains this effect, decreasing the temperature of structural transformation for $Cu_{0.95}Zn_{0.05}Fe_2O_4$. This tetragonal $\rightarrow$ cubic transition becomes easier if the octahedral Cu^{2+} ions are replaced by zinc ions. On the basis of the results presented, we can expect that even small substitution of zinc can drastically involve essential changes in the crystal structure of copper ferrite, therefore further studies are in progress.

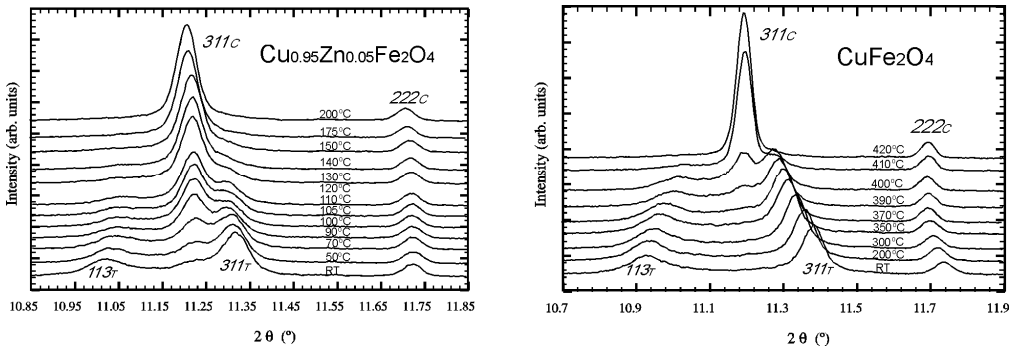

Figure1. Thermal evolution of the synchrotron X-ray diffraction spinel peaks *311* and *222*, in the temperature region of phase transition $F4_1/ddm \rightarrow Fd\bar{3}m$ for $Cu_{1-x}Zn_xFe_2O_4$ series, with x=0.00; 0.05. The non-standard face centered space group was selected instead of $I4_1/amd$ to better show the spinel structure deformation.

References

[1] L.R. Falvello, *J. Chem. Soc., Dalton Trans*. 4463, 1997.
[2] E. Dagotto, *Science* **309**, 257, 2005.
[3] Villette, C., Tailhades, Ph., Rousset, A, *J. Solid State Chem*. **117**, 64, 1995.
[4] Y. Cerenius, K. Ståhl, L.A. Svensson, T. Ursby, Å. Oskarsson, J. Albertsson and A. Liljas, *J. Synchrotron Rad.*, **7**, 203, 2000.
[5] J. Rodriguez-Carvajal, *Physica B*, **192**, 55, 1993.

Associative phase behaviour and disintegration of copolymer aggregates on adding poly(acrylic acid) to aqueous solutions of a PEO-PPO-PEO triblock copolymer

Salomé dos Santos[†], Bob Luigjes[†‡], Lennart Piculell[†*]

[†] Division of Physical Chemistry, Center for Chemistry and Chemical Engineering, Lund University, P.O. Box 124, SE-22100 Lund, Sweden

[‡]Current address: Van't Hoff Laboratory for Physical and Colloid Chemistry, Debye Institute for Nanomaterials Science, Utrecht University, P.O. Box 80.051, 3508 TB, Utrecht, The Netherlands

The influence of adding poly(acrylic acids) of two different chain lengths (PAA_{25} and PAA_{6000}) on the phase behaviour of the amphiphilic triblock copolymer Pluronic® P104 (P104 = $(EO)_{27}(PO)_{61}(EO)_{27}$, where EO = ethylene oxide, PO = propylene oxide) in H_2O was investigated. The resulting phase equilibria and structures were investigated by visual inspection, using crossed polarizers, and small angle x-ray scattering (SAXS). At low and intermediate P104 concentrations an associative phase separation was found, where a concentrated phase separated out from a dilute one on adding PAA. The corresponding phase separation region appeared in the phase diagram as a closed, droplet-shaped miscibility gap that was significantly larger for the longer PAA. Neither of the coexisting phases contained any long-range ordered structures. At higher concentrations of P104 (above ca. 25wt%) no miscibility gap appeared but, remarkably, the various ordered liquid crystalline phases observed in binary P104/H_2O mixtures were eventually destroyed upon the replacement of H_2O by PAA. A similar effect was found when propionic acid (PrA), corresponding to the repeating unit of the PAA chain, was added to aqueous P104. A decrease in the PAA length, in the series PAA_{6000} - PAA_{25} - PrA, increased the efficiency to destroy the structured phases. NMR self-diffusion measurements showed that the self-assembled P104 aggregates dissolved on replacing water with PrA. The same mechanism was found to be responsible for the effect of added PAA, that is, PAA (or PrA) acts as less selective "solvent" for the PEO and PPO blocks compared to water.

Ordered soft materials formed by polymerization reactions in surfactant systems.

Salomé dos Santos[a], Lennart Piculell[a], Ola Karlsson[a], and Maria da Graça Miguel[b]

a Physical Chemistry Division, Lund University, Lund, Sweden

b Chemistry Department, Coimbra University, Coimbra, Portugal

The implementation of polymerization reactions in organized media constitutes a modern approach for "freezing" or "templating" surfactant systems[1]. Although widely tried, most approaches so far have been based on trial and error and the resulting structures were often different from the original surfactant template. Classically, the reason for this failure is the development of a repulsive depletion interaction between the formed polymers and the surfactant aggregates. Not much attention has been given to the fact that, as it happens for silica and its templates in hard mesoporous materials, the interaction between the different components in the system should be attractive in order to preserve the structure during polymerization.

Our approach to polymerization in surfactant systems is based on a meticulous understanding of polymer-surfactant phase equilibria. An attractive interaction is a key element and, therefore, the polymer is not excluded from the mesophase but rather it aids in its formation. Furthermore, we have a particular point of departure.

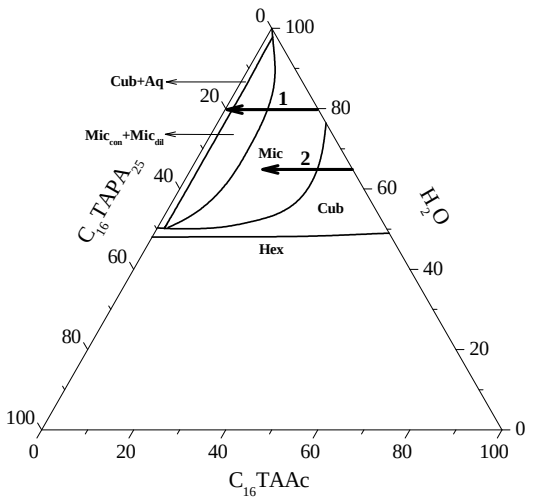

Figure 1 Phase diagram used for the predictions. The thick arrows with numbers represent the pathways of different outcomes from polymerization reactions as explained in the text.

Recently, equilibrium phase diagrams were established, in our laboratory, for associating polymer-surfactant systems involving aqueous mixtures of cationic surfactants (C_{16}TAAc and C_{12}TAAc) with the respective "complex salts" $C_{16}TAPA_{30}$[2], $C_{16}TAPA_{6000}$[2] and $C_{12}TAPA_{30}$, $C_{12}TAPA_{6000}$. In the "complex salts", the counterions to the surfactant ions were polyacrylate polyions of two different degrees of polymerization (30 and 6000). These ternary phase diagrams illustrate what happens, at equilibrium, when monomeric counterions to the surfactant are gradually replaced by polymeric counterions, as demonstrated by the arrows in the phase

diagram in Figure 1. Consequently, the phase diagrams predict the outcome of polymerization reactions.

To investigate these predictions, we performed free radical polymerizations of the acrylate, counterion of $C_{16}TA^+$ and $C_{12}TA^+$, under various conditions. The resulting structures were investigated by crossed polarizers and small angle x-ray scattering (SAXS) and were indeed in agreement with the predictions given by the different phase diagrams[2]. As predicted, if a dilute isotropic phase is polymerized a concentrated liquid crystalline phase separates out (pathway number 1), with the final structure depending on the initiator to monomer ratio; and a partial polymerization of the surfactant counterions in a cubic phase results in a change of the system to a viscous disordered micellar solution (pathway number 2). These two results are presented in Figure 2.

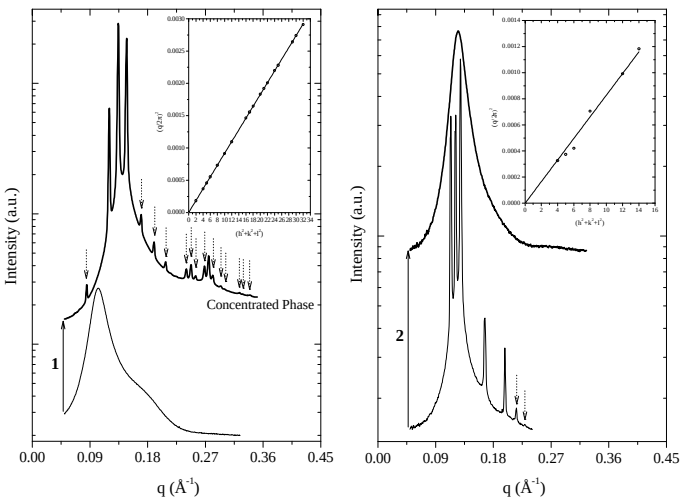

Figure 2 SAXS patterns from the start and end points in the different pathways in Figure 1. The thin and the thick line profile show the structure before and after polymerization, respectively.

Acknowledgments

We thank Fundação para a Ciência e a Tecnologia (FCT) in Portugal (SS, SFRH/BD/30929/2006) and the Swedish Research Council for funding.

[1] Arne Thomas, Frederic Goettmann, and Markus Antonietti *Chem. Mater.* **2008**, *20*, 738.
[2] Anna Svensson, Jens Norrman, and Lennart Piculell *J. Phys. Chem B* **2006**, *110*, 10332.

LiF-MgB_2 system for Reversible Hydrogen Storage

R. Gosalawit[1,*], J. M. Bellosta von Colbe[1], M. Dornheim[1], T. R. Jensen[2], Y. Cerenius[3], Christian M. Bonatto[1], Maik Peschke[1], R. Bormann[1]

[1]*Institute of Materials Research, Materials Technology, GKSS-Forschungszentrum Geesthacht GmbH, D-21502 Geesthacht, Germany, Email: rapee.gosalawit@gkss.de.*

[2]*Interdisciplinary Nanoscience Center (iNANO) and Department of Chemistry, University of Aarhus, Langelandsgade 140, DK-800 Aarhus C, Denmark.*

[3]*MaXLAB, Lund University, S-22100 Lund, Sweden.*

Introduction

The complex hydride $LiBH_4$ is a potential candidate to fulfill future hydrogen storage goals due to its high gravimetric and volumetric hydrogen density of 18.5 wt.% and 121 kg/m^3, respectively [1]. $LiBH_4$ can be decomposed into two steps:

$$LiBH_4 \leftrightarrow LiH + B + \frac{3}{2}H_2 \quad (1)$$

$$LiH \rightarrow Li + \frac{1}{2}H_2 \quad (2)$$

By Eq. (1), 13.5 wt.% of hydrogen is desorbed to LiH and B only at temperatures above 400 °C, while the further desorption (Eq. (2)) is not technically promising because of the requirement of very high temperature [2]. Based on these limitations, several research groups put a lot of efforts to improve the thermodynamic and kinetic properties of $LiBH_4$. Recently, an alternative strategy to adjust thermodynamic properties and destabilize complex hydrides was investigated via substituting hydrogen by fluorine [3, 4]. In this study, LiF–MgB_2 with fluorine substitution, prepared by hydrogenation of LiF and MgB_2, is proposed to alter the stability of the complex hydride. By means of synchrotron radiation powder X-ray diffraction (SR-PXD), the formation of $LiBH_{4-x}F_x$ complex hydridofluorides and absorption-desorption reaction mechanisms were observed.

Results and discussion

The hydrogenation of milled LiF and MgB_2 was carried out under 100 bar H_2 in the temperature range of 25-390 °C. From Fig. 1, the reflections corresponding to MgF_2 arise at about 316 °C and their intensity increases with temperature whereas the reflection intensities of LiF and MgB_2 decrease. This indicates the proceeding of reaction during hydrogenation. $LiBH_4$ might be

generated at the same time as MgF_2 but the reflections do not appear because of its molten state. However, $LiBH_4$ shows the reflections referring to hexagonal and orthorhombic phases at about 270-277 °C and 110-120 °C, respectively, during the cooling state. In addition, a significant peak shift of LiF reflections at around 380 °C is observed. This might be due to thermal expansion and contraction of LiF during heating and cooling, respectively. However, this also hints the formation of $LiH_{1-x}F_x$ as in the previous observations of the NaF–Al system reported elsewhere [5].

For dehydrogenation (P = 5 bar H_2, T = 25-390 °C), the sample fully absorbed sample from Sievert's type apparatus was investigated. Fig. 2 shows the reflections of both orthorhombic and hexagonal $LiBH_4$ phases at the temperatures corresponding to those from the hydrogenation step (Fig. 1). Moreover, it should be noted that some parallel reflections to those of $LiBH_4$ phases in the same temperature region are observed (Fig. 2). Based on the similarities of $F^-$and H^-, this might suggest the substitution of hydrogen anions (H^-) by fluorine anions (F^-) in the $LiBH_4$ phase during hydrogenation. This implies the formation of a single phase $LiBH_{4-y}F_y$ as well as the reversibility of LiF-MgB_2 hydrogen storage system.

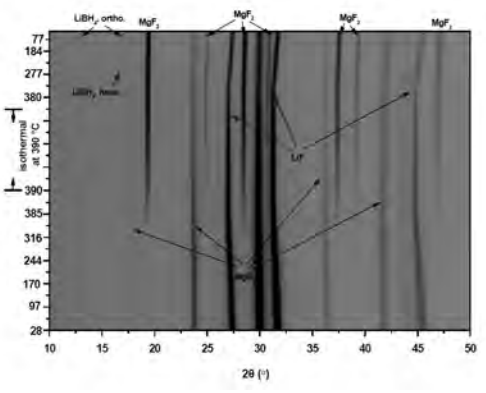

Fig. 1

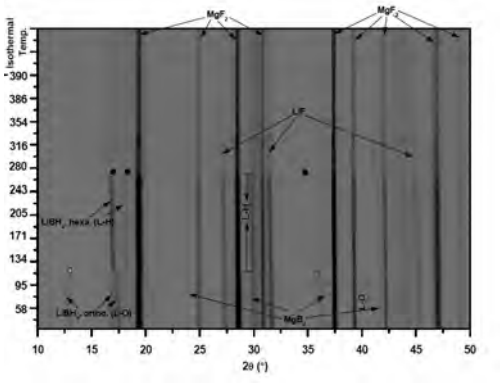

Fig. 2

References

[1] L. Schlapbach, A. Züttel, Nature 414 (2001) 353.

[2] M. Au, A. R. Jurgensen, W. A. Spencer, D. L. Anton, F. E. Pinkerton, S.-J. Hwang, C. Kim, R. C. Bowman Jr. II, J. Phys. Chem. C 112 (2008) 18661.

[3] H. W. Brinks, A. Fossdal, B. C. Hauback, J. Phys. Chem. C 112 (2008) 5658.

[4] J.-P. Soulié, J.-P. Laval, A. Bouamrane, Solid State Sci. 5 (2003) 273.

[5] N. Eigen, U. Bösenberg, J. Bellosta von Colbe, T. R. Jensen, Y. Cerenius, M. Dornheim, T. Klassen, R. Bormann, J. Alloys Compd. 477 (2009) 76–80.

THE AQUEOUS PHASE BEHAVIOR OF POLYION-SURFACTANT ION COMPLEX SALTS MIXED WITH NONIONIC SURFACTANTS

John Janiak, Salomé Santos, Lennart Piculell and Karin Schillén
Division of Physical Chemistry , Lund University, P.O. Box 124, SE-221 00 Lund, Sweden

The aim of this project is to understand the phase and association behavior of complex salts in aqueous solution. They consist of cationic surfactant ions of C_xTA^+ and polyacrylates (PA^-) as polymeric counterions. They are denoted C_xTAPA_y, where x is the number of carbons in the surfactant chain and y is the number of monomer units (or degree of polymerization) in the polyacrylate [1]. The solubility of the C_xTAPA_y complex salts in water varies and it increases when the complex salt is composed of a surfactant with short alkyl chain and a longer polyion [2]. In order to make the complex salts soluble, forming a composite self-assembled macromolecular aggregate, nonionic surfactants of the type C_iE_j (where E stands for poly(ethylene oxide), PEO) are added.

The project is divided into two parts: a) initial phase studies of ternary mixtures of $C_{16}TAPA_y$, nonionic C_iE_j surfactants and water, b) investigation (main part) of the dilute solution properties of these new composite self-assembled structures at different temperatures are investigated by using dynamic and static light scattering, small-angle X-ray scattering, cryo-transmission electron microscopy and isothermal titration calorimetry. Both the PEO-length of the surfactant ($C_{12}E_5$, $C_{12}E_8$) and the length of the polyion in the complex salt are varied, keeping the alkyl chain length of the surfactant ion constant (i.e. x = 16). The degree of polymerization of the polyacrylate is either y = 25 or 6000.

The beamline I711 at MAX-lab [3,4] has been used to characterize the differents structures found in the phase diagrams and for preliminary measurements in the dilute regime of the $C_{16}TAPA_{25}/C_{12}E_8/H_2O$ system. Examples are found in figure 1 and 2 respectively.

[1] Svensson, A.; Piculell, L.; Cabane, B.; Ilekti, P. *J. Phys. Chem. B* **2002**, *106*, 1013.
[2] Svensson, A.; Norrman, J.; Piculell, L. *J. Phys. Chem. B* **2006**, *110,* 10332.
[3] Knaapila, M et al., J. Synchrotron Rad. **2009**, 16, 498
[4] Cerenius Y et al., J. Synchrotron Rad. **2000**, 7, 203

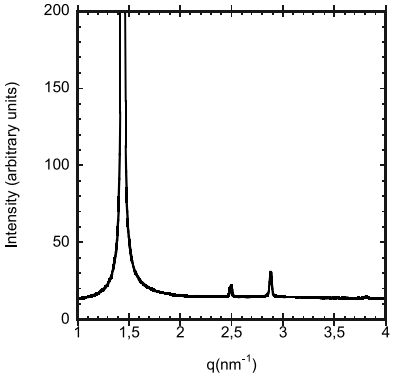

Figure 1. SAXS measurement indicating a hexagonal structure in a two phase region of the $C_{16}TAPA_{25}/C_{12}E_5/H_2O$ system.

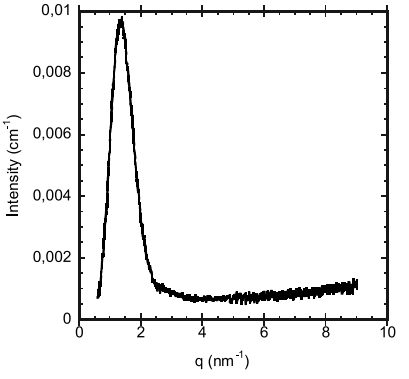

Figure 2. Measurement in the dilute regime of the $C_{16}TAPA_{25}/C_{12}E_8/H_2O$ system. The $C_{12}E_8/CTA_+$ molarratio is 7.3.

High pressure X-ray scattering experiments of polyfluorenes at I711

M. Knaapila[1], D. Haase[2], S. Carlson[2], Y. Cerenius[2], and S. Guha[3]

[1] *Institute for Energy Technology, NO-2027 Kjeller, Norway*

[2] *MAX-lab, Lund University, SE-22100 Lund, Sweden*

[3] *Department of Physics & Astronomy, University of Missouri-Columbia, MO 65211 USA*

We have worked on the wide-angle X-ray scattering experiments of poly[9,9-bis(2-ethylhexyl)fluorene] (or PF2/6) under hydrostatic pressure. High molecular weight polymer (>10 kg/mol) has a helical main chain and a hexagonal unit cell. Low molecular weight polymer (<10 kg/mol) has a helical main chain but a frozen-in nematic structure[1]. Both polymers show a morphological transition in the main chain structure at ~40 kbar. See an example in Fig. 1. These transitions are concomitant with the previously reported transition seen by Raman scattering[2].

Further data analysis is in progress. The X-ray scattering experiments of this work have been performed at I711/MAX-lab.

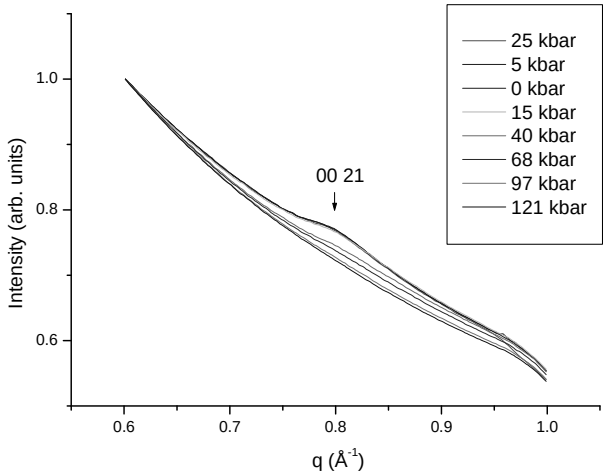

Figure. 1. A preview of 00 21 reflection of PF2/6 under hydrostatic pressure.

[1] M. Knaapila, R. Stepanyan, B. P. Lyons, M. Torkkeli, and A. P. Monkman, *Adv. Funct. Mater.* 16 599 (2006).
[2] C. M. Martin, S. Guha, M. Chandrasekhar, H. R. Chandrasekhar, R. Güntner, S. de Freitas, and U. Scherf, *Phys. Rev. B.* 68 115203, (2003).

Wheat gluten and industrial oil crop protein sheets: protein polymerization and structure morphology.

R. Kuktaite[1], T. S. Plivelic[2], Y. Cerenius[2], M. S. Hedenqvist[3], M. Gällstedt[4], S. Marttila[5], R. Ignell[5] and E. Johansson[1]

[1]*Dept. of Agriculture- Farming systems, Technology and Product Quality, The Swedish University of Agricultural Sciences, P.O. Box 104, SE-230 53 Alnarp, Sweden*
[2]*MAXlab, Lund University, P.O. Box 118, SE-221 00 Lund, Sweden*
[3]*Dept. Fibre and Polymer Technology, Royal Institute of Technology (KTH), SE-10044 Stockholm, Sweden*
[4]*Innventia, Box 5604, SE-11486 Stockholm, Sweden*
[5]*Dept. of Plant Protection Biology, The Swedish University of Agricultural Sciences, P.O. Box 102, SE-230 53 Alnarp, Sweden*

Plant proteins, such as wheat gluten (WG), in blend with glycerol showed a number of advantages to be used as biomaterials[1]. WG proteins easily polymerize in the presence of medium/high temperature and high mechanical energy input, and form unique bio-polymers, which are an attractive alternative to synthetic oxygen-barrier polymers in packaging applications. Wheat gluten/glycerol bio-plastic films produced by extrusion and thermomoulding reveal that temperature and mechanical energy input[2], components of the blend[3, 4], as well as molecular interactions and polymerisation behaviour of the WG proteins[5] stand-out among the factors affecting end-use quality of the biomaterials. Also other proteins (by-products) from industrial vegetable oil production could be of interest in the production of biomaterials due to the protein bulk quantities and low price.

In this report we show structural characterisation of various qualities of WG packaging sheets differing in chemical composition, extrusion temperatures and aging time. We have found the specific WG protein assemblies elucidated on a range of nano-length scales. Furthermore, the WG-based biomaterials seems to present a well defined supramolecular structure dependent on the blend components, higher extrusion temperature (around 120° C), greater protein interactions etc. The WG film morphologies could be well fitted with a tetragonal unit cell lattice, as well as with a bi-dimensional hexagonal close packed (HCP) structure, both arrangements have not previously been found in the plant protein based systems.

In Figure 1 we compare SAXS profiles for the WG protein based films analysed at the beamline I711 at MAX-lab Synchrotron. The wavelength was 1.1 Å and the sample to detector distance was 1403 mm.

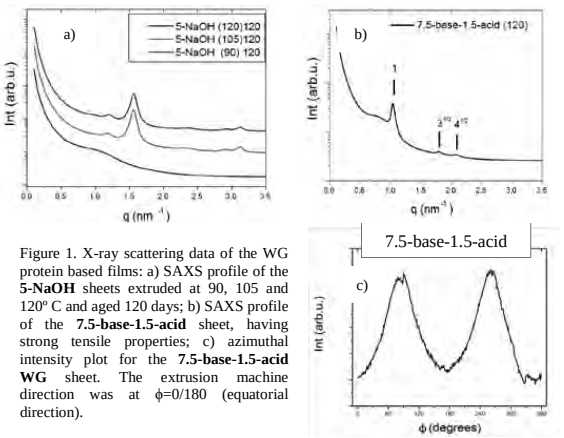

Figure 1. X-ray scattering data of the WG protein based films: a) SAXS profile of the **5-NaOH** sheets extruded at 90, 105 and 120º C and aged 120 days; b) SAXS profile of the **7.5-base-1.5-acid** sheet, having strong tensile properties; c) azimuthal intensity plot for the **7.5-base-1.5-acid WG** sheet. The extrusion machine direction was at ϕ=0/180 (equatorial direction).

All 2D-SAXS images for the **5-NaOH** samples, extruded at 90, 105 and 120° C, were found being isotropic, while the intensity plots were greatly influenced by the sample preparation procedure (i.e. extrusion processing method, temperature).

The WG sheet extruded at 90° C showed a poorly developed peak with a correlation distance of around 55 Å (Fig. 1a). In contrast, the sheets extruded at 105 and 120° C showed series of high intensity and well defined peaks indicating the presence of better organised structures. For the **5-NaOH** sheet extruded at 120° C, extended X-ray scattering measurement to higher q values (until q= 9 nm^{-1}) enabled fitting of all peaks positions with a tetragonal unit cell lattice[6,7]. In addition, SAXS pattern of the **7.5 base-1.5-acid** WG film extruded at 120° C, showed three well defined Bragg peaks with a positional ratio of $1:\sqrt{3}:\sqrt{4}$ (Fig. 1b). These results indicate a bi-dimensional hexagonal close packed (HCP) arrangement of the scattering objects. The obtained interdomain distance a was 70 Å. 2D-SAXS image of the WG film with specific composition (i.e. **7.5 base-1.5-acid)**, was anisotropic indicating a partially oriented structure morphology (see the azimuthal intensity plot for the first Bragg peak in Fig. 1c)[6, 7]. This structure complexity corresponds well with the changes in mechanical properties of the **7.5 base-1.5-acid** film (i.e. the strength increased up to more than four times (5.8±0.4 MPa) compared to control without additives (1.3±0.1) and the modulus increased from 10±2 (control) to 75±4 MPa (**7.5-base-1.5-acid**))[4].

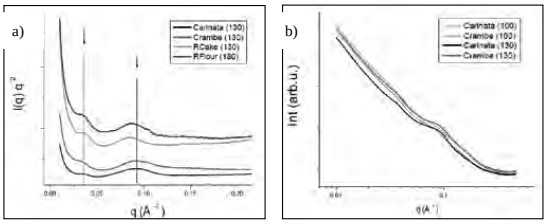

Figure 2. SAXS scattering data of the WG+oil crop sheets: a) WG+*Carinata*, WG+*Crambe*, WG+rapeseed cake and WG+rapeseed flour compression moulded at 130° C; b) WG+Carinata and WG+Crambe sheets compression moulded at 100 and

X-ray scattering experiments (SAXS and WAXS) on various qualities of the WG and the oil crops, i.e. *Crambe abyssinica*, *Brassica carinata*, rape seed cake and flour, protein sheets differing in chemical composition and extrusion temperatures were performed and preliminary results are shown in Fig. 2. The results indicate diverse structural morphology in various oil crops (Fig. 2a) and the compression moulding temperature affect on the morphology of the WG+*Carinata* and WG+*Crambe* sheets (Fig. 2b). Further investigations (SAXS and microscopy) have to be performed in order to understand the origin of these differences and how the higher compression moulding temperatures (> 130 ° C) and different chemical additives (i.e. protein cross-linkers) affect the protein polymerisation.

With this study we conclude that the observed a partially organized WG polymer arrangement in so called "natural" plant protein systems was due to the sheet composition and processing conditions. The WG protein based film morphologies seem to be related to the outstanding qualities of the biomaterial[4]. Further studies are needed in order to find a key structural model for being able to control the protein polymerization behaviour and tailor biomaterials for specific end-uses.

[1] M. Gällstedt, A. Mattozzi, E. Johansson, and M. S. Hedenqvist, *Biomacromolecules*, **5**, 2020 (2004).
[2] A. Redl, M. H. Morel, J. Bonicel, B. Vergnes, and S. Guilbert, *Cereal Chem.*, **76 (3)**, 361 (1999).
[3] I. Olabarrieta, M. Gällstedt, I. Ispizua, J.-R. Sarasua, and M. S. Hedenqvist, *J. Agric. Food Chem.*, **54**, 1283 (2006).
[4] H. Ullsten, M. Gällstedt, G. M. Spencer, E. Johansson, S. Marttila, R. Ignell, and M. S. Hedenqvist. Submitted to Adv. Materials, (2010).
[5] N. H. Ullsten, S.-W. Cho, G. Spencer, M. Gällstedt, E. Johansson, and M. S. Hedenqvist, *Biomacromolecules*, **10**, 479 (2009).
[6] R. Kuktaite, T. S. Plivelic, Y. Cerenius, M. S. Hedenqvist, M. Gällstedt, S. Marttila, R. Ignell, I. Popineau, O. Tranquet, P. Shewry, and E. Johansson. Submitted to J. Materials Chem., (2010 a).
[7] R. Kuktaite, T. S. Plivelic, Y. Cerenius, M. S. Hedenqvist, S. Marttila, R. Ignell, M. Gällstedt, and E. Johansson. Manuscript for the 239th ACS Chemistry for a Sustainable World meeting, San Francisco, USA, March 21-25, (2010

Structural basis for substrate recognition and specificity in aklavinone-11-hydroxylase from rhodomycin biosynthesis

Ylva Lindqvist[1], Hanna Koskiniemi[1], Anna Jansson[1], Tatyana Sandalova[1], Robert Schnell[1], Zhengliang Liu[2$], Pekka Mäntsälä[2], Jarmo Niemi[2] and Gunter Schneider[1*]

1. Department of Medical Biochemistry and Biophysics, Karolinska Institutet, S-171 77 Stockholm, Sweden
2. Department of Biochemistry and Food Chemistry, University of Turku, FIN-20014 Turku, Finland

In the biosynthesis of several anthracyclines, aromatic polyketides produced by many *Streptomyces* species, the aglycone core is modified by a specific FAD and NAD(P)H dependent aklavinone-11-hydroxylase. Here we report the crystal structure of a ternary complex of this enzyme from *Streptomyces purpurascens*, RdmE, with FAD and the substrate aklavinone. The enzyme is built up of three domains, a FAD binding domain, a domain involved in substrate binding and a C-terminal thioredoxin-like domain of unknown function. RdmE exhibits structural similarity to aromatic hydroxylases from the *p*-hydroxybenzoate hydroxylase (pHBH) family, but unlike most other related enzymes, RdmE is a monomer. The substrate is bound in a hydrophobic pocket in the interior of the enzyme, and access to this pocket is provided through a different route than for the isoalloxazine ring of FAD - the backside of the ligand binding cleft. The architecture of the substrate binding pocket and the observed enzyme-aklavinone interactions provide a structural explanation for the specificity of the enzyme for non-glycosylated substrates with C9-*R* stereochemistry. The isoalloxazine ring of the flavin cofactor is bound in the "out" conformation, but can be modeled in the "in" conformation without invoking large conformational changes of the enzyme. This model places the flavin ring in a position suitable for catalysis, almost perpendicular to the tetracyclic ring system of the substrate, and with a distance of the C4a carbon atom of the isoalloxazine ring to the C-11 carbon atom of the substrate of 4.8 Å. The structure suggests that a Tyr224-Arg373 pair might be involved in proton abstraction at the C-6 hydroxyl group, thereby increasing the nucleophilicity of the aromatic ring system and facilitating electrophilic attack by the perhydroxy-flavin intermediate. Replacement of Tyr224 by phenylalanine results in inactive enzyme, whereas mutants at position Arg373 retain catalytic activity close to wild-type level. These data establish an essential role of residue Tyr224 in catalysis, possibly as a catalytic base facilitating deprotonation of the substrate.

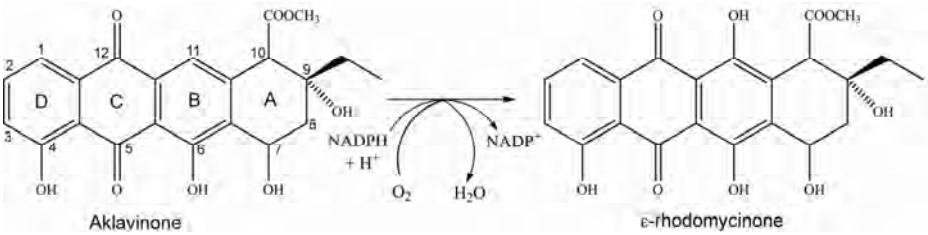

Figure 1: Overall reaction catalyzed by aklavinone-11-hydroxylases. Numbering of the carbon atoms and labeling of the tetracyclic ring system of aklavinone is also shown.

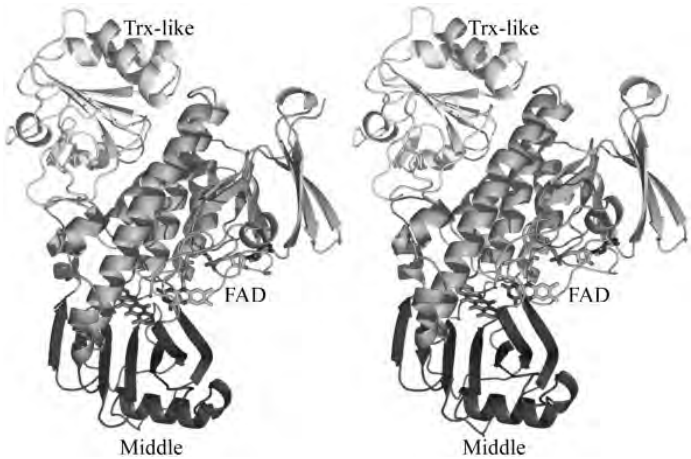

Figure 2: Overall structure of RdmE. The FAD domain is shown in green, the middle domain in red and the C-terminal domain in yellow. The bound ligands in the ternary complex, FAD (yellow) and aklavinone (blue) are shown as stick models.

Reference

Lindqvist Y, Koskiniemi H, Jansson A, Sandalova T, Schnell R, Liu Z, Mäntsälä P, Niemi J, Schneider G (2009) **Structural basis for substrate recognition and specificity in aklavinone-11-hydroxylase from rhodomycin biosynthesis.** *J Mol Biol.* **693**, 966-977**.**

Confinement of MgH_2 nanoclusters within nanoporous aerogel scaffold materials.

Thomas K. Nielsen,[1] Kandavel Manickam,[2] Michael Hirscher,[2] Flemming Besenbacher,[1] Torben R. Jensen.[1*]
[1] *Interdisciplinary Nanoscience Center (iNANO) and Department of Chemistry, Aarhus University, DK-8000 C, Aarhus, Denmark.*
[2] *Max-Planck-Institut für Metallforschung, Heisenbergstrasse 3, D-70569 Stuttgart, Germany*

Hydrogen has been suggested as a future carrier of renewable energy but a compact, efficient, robust, safe and inexpensive hydrogen storage system remains to be developed.[1,2] In the past magnesium and Mg-based alloys have been explored intensively due to the high theoretical gravimetric H_2 density in magnesium hydride, MgH_2, ρ_m = 7.6 wt% and the high volumetric H_2 density, ρ_v = 110 g/L. Magnesium is also a cheap and abundant metal, making it suitable for large scale hydrogen storage applications. Unfortunately, the use of magnesium hydride is hampered by relatively slow kinetics for hydrogen release and uptake, and also the thermodynamics, ΔH_f = -75 kJ/mol H_2 is rather unfavorable, *i.e*. MgH_2 must be heated to *ca*. 300 °C in order to release hydrogen, at $p(H_2)$ = 1 bar.[1] Nanoscience may provide novel ideas and solutions to these issues, since the nano-size of Mg induces several advantages: (*i*) reduction of diffusion distances enhances the rate at which hydrogen is distributed and decreases the influence of the oxide and/or hydride surface layer, (*ii*) an increased surface-area to bulk-volume ratio favors hydrogen bond dissociation and (*iii*) an increased ratio of hydrogen atoms in the grain boundary also enhances the hydrogen diffusion rates.[3] These properties all help to improve the hydrogenation / dehydrogenation kinetics of magnesium. Unfortunately, nanoparticles of, *e.g*., metal hydrides tend to agglomerate and grow into larger particles upon hydrogen release and uptake cycles.[3] Consequently, there is an urgent need for development of novel nanoconfinement systems which can prohibit agglomeration and grain growth and which are stable over many hydrogen release and uptake cycles. In this study, nanoparticles of magnesium hydride were embedded in nanoporous carbon aerogel scaffold materials in order to explore the kinetic properties of hydrogen uptake and release. The procedure makes use of monoliths (~ 0.4 cm^3) of two distinct types of nanoporous resorcinol-formaldehyde carbon aerogels loaded with dibutylmagnesium, $MgBu_2$. *In situ* synchrotron radiation powder X-ray diffraction showed that $MgBu_2$ transformed directly to MgH_2 at T ~137 °C and $p(H_2)$ = 50 bar, see Figure 1 left. Two distinct aerogel samples, denoted X1 and X2, with pore volumes of 1.27 and 0.65 mL/g and average pore sizes of 22 and 7 nm, respectively, were selected. In these samples the uptake of magnesium hydride was found to be proportional to the pore volume and aerogel X1 and X2 incorporated 18.2 and 10.0 wt% of MgH_2, respectively. For the two samples the volumetric

MgH_2 uptake was similar, ~12 vol%. The hydrogen storage properties of nano-confined MgH_2 by thermal desorption spectroscopy see Figure 1 right, which clearly demonstrated that the dehydrogenation kinetics of the confined hydride depends on the pore size distribution of the scaffold material, *i.e*. smaller pores mediated faster desorption rates possibly due to a size reduction of the confined magnesium hydride.[4]

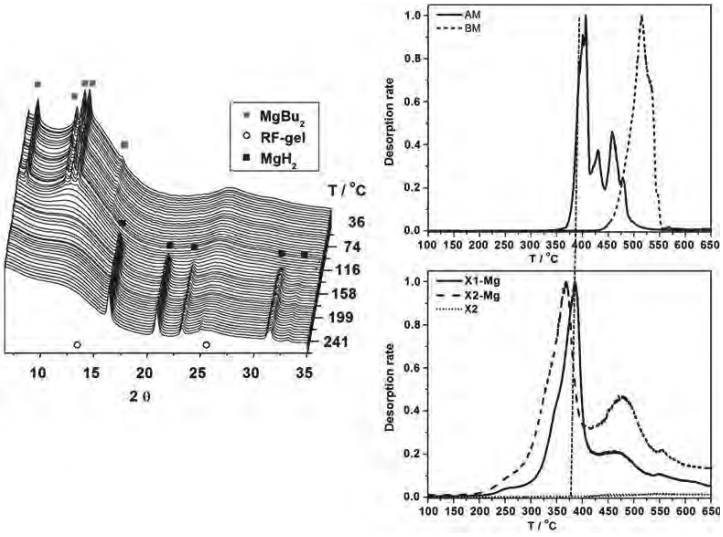

Figure 1. Left: Selected part of *in situ* SR-PXD data showing the synthesis of MgH_2 from dibutylmagnesium ($MgBu_2$) within sample X1-Mg. The sample was heated from RT to 350 °C (heating rate 7.5 °C/min) under a hydrogen pressure of $p(H_2)$ = 50 bar (λ = 0.9077 Å). Measured at MAX-lab, beamline I711.
Right: Normalized thermal desorption spectroscopy profiles measured from RT to 700 °C (heating rate 3.6 °C /min) by recording the mass spectrometer intensity of H_2^+ ions (m/e = 2). Upper graph shows hydrogen desorption from magnesium hydride prepared from dibutylmagnesium (AM) compared to bulk magnesium hydride (BM). The lower graph compares the two aerogel-magnesiumhydride samples X1-Mg and X2-Mg and the 'empty' aerogel X2. Aeorgel X1 and X2 have average pore sizes of D_{max} = 22 and 7 nm, respectively.

References.

1. Schlapbach, L.; Züttel, A. *Nature* **2001**, *414*, 353-358.
2. Ritter, J. A.; Ebner, A. D.; Wang, J.; Zidan, R. *Materials Today* **2003**, *6*, 18-23.
3. Bérube, V.; Radtke, G.; Desselhaus, M.; Chen, G. *Int. J. Energy. Res*. **2007**, *31*, 637-663.
4. Nielsen, T. K.; Manickam, K.; Hirscher, M.; Besenbacher, F.; Jensen, T. R. *ACS Nano*. **2009**, 3, 3521-3528.

Lipid phase behaviour in confinement

P. Nilsson and E. Sparr

Division of Physical Chemistry, Lund University
P.O. Box 124, S-221 00 Lund, Sweden

In a responding lipid membrane, the lipid phase behaviour can change in response to changes in its surrounding. This is different from the more common "static" model membrane that can be described by a simple permeability constant. A small change, e.g. in the osmotic pressure of the surrounding solution, can lead to a phase transition in the responding membrane, which dramatically affects the transport properties of the membrane.[1,2] As part of a larger effort to study responding lipid membranes, we want to characterize the lipid phase structure at different osmotic pressures, both with the lipid inside the pores of an inert polymer scaffold membrane, and in bulk samples. The lipid distribution in the membrane is verified using confocal scanning microscopy, and the permeability of the membrane is measured through transport of various solutes. Also, the position of the lipid phase transitions inside the pores and in bulk is investigated using differential scanning calorimetry.

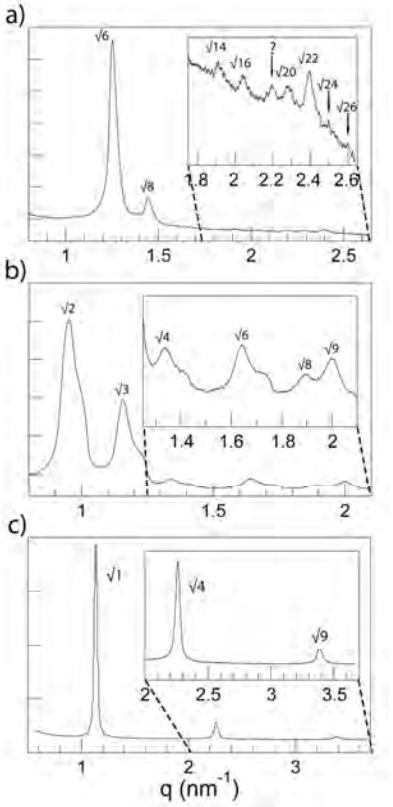

Figure 1. SAXS spectra for lipid inside porous membrane; a) MO in PEG solution, cubic *Ia3d* structure, b) MO in pure water, cubic *Pn3m* structure, c) DOPC in PEG solution, lamellar structure. Insets show magnifications of part of the q-range.

Hydrated monoolein (MO) forms different structures in bulk, such as lamellar or *Ia3d* or *Pn3m* bicontinuous cubic, depending on the osmotic pressure of the surrounding solution,[3] which in turn can be controlled by the concentration of polyethyleneglycol (PEG) 2000. We have also used 1,2-Dioleoyl-sn-Glycero-3-phosphocholine (DOPC), which forms a lamellar structure at all osmotic pressures used. While the phase behaviour in bulk is well known,[4,5] it is not necessarily valid for lipid inside the pores, due to the large membrane surface available for interactions and the potential for capillary condensation effects. The goal is therefore to explore the lipid phase behaviour inside the membrane pores, and compare it to bulk phase behaviour. The main difficulty is that the pore volume ratio of the membrane is low, which leads to very low amounts of lipid in the sample (around 10%, or 30 μg), and thereby an equally low signal to detect. Synchrotron SAXS at MAX-Lab (I711) should be sensitive enough to allow identification of the characteristic Bragg peaks of the different structures.

In Figure 1a we see the diffraction pattern for MO inside a porous membrane hydrated with PEG solution (making the lipid slightly dehydrated as compared to pure water). The eight

peaks indicated are consistent with a bicontinuous cubic *Ia3d* structure, with a unit cell length of 123 Å, slightly larger than the 121 Å measured for the bulk sample (data not shown). The same structure with a unit cell length of 120 Å has earlier been reported for lipid-filled tortuous pore PVF membranes,[2] while bulk MO samples have been reported at 130 Å.[3]
In Figure 1b, we also see MO inside a porous membrane, this time in pure water (fully hydrated). The six characteristic peaks visible are consistent with a bicontinuous cubic *Pn3m* structure with a unit cell length of 93 Å. Literature data has previously reported a *Pn3m* structure of 100 Å cell length,[3] while our bulk measurement for the technical grade MO showed 92 Å (data not shown).
Finally, in Figure 1c, we find three equidistant peaks consistent with a lamellar structure with repeat spacing 55 Å, for DOPC in PEG solution. The same result was obtained for the bulk sample (data not shown), as well as found in the literature.[5]
This clearly shows that the same lipid structures are formed inside the pores of the scaffold membrane, as in the bulk phase, with only small differences in the repeat spacings.

References

[1] Costa-Balogh, F. O.; Berg, C.; Sousa, J. J. S.; Sparr, E. *Langmuir* **2005**, *21*, 10307.
[2] Åberg, C.; Pairin, C.; Costa-Balogh, F. O.; Sparr, E. *Biochimica et Biophysica Acta, Biomembranes* **2008**, *1778*, 549.
[3] Chung, H.; Caffrey, M. *Nature* **1994**, *368*, 224.
[4] Qiu, H.; Caffrey, M. *Biomaterials* **1999**, *21*, 223.
[5] Parsegian, V. A.; Fuller, N.; Rand, R. P. *Proceedings of the National Academy of Sciences of the United States of America* **1979**, *76*, 2750.

Formation of $2NaBH_4+MgH_2$ by Hydrogenation of $2NaH+MgB_2$

Claudio Pistidda[1], Gagik Barkhordarian[1], Christian Bonatto Minella[1], Sebastiano Garroni[2], Torben Jensen[3], Ulrike Bösenberg[1], Yngve Cerenius[4], Rüdiger Bormann[1], Martin Dornheim[1]

[1] Institute of Materials Research, Materials Technology, GKSS Research Centre Geesthacht GmbH, Max-Planck-Straße 1, D-21502 Geesthacht, Germany. Email:Claudio.pistidda@gkss.de

[2] Departament de Física, Universitat Autònoma de Barcelona, 08193 Bellaterra, Spain

[3] Interdisciplinary Nanoscience Centre (*i*NANO) and Department of Chemistry, University of Aarhus, Langelandsgabe 140, DK-8000. Denmark

[4] MAX-lab, Lund University, S-22100 Lund, Sweden

The recent discovery of the unique kinetic property of MgB_2 [1-5] in facilitating the hydrogenation of light metal complex borohydrides at moderate pressure and temperature conditions has raised new prospects for the development of innovative high capacity - low enthalpy hydrogen storage materials. These new composite materials consist of a binary light metal hydride (like LiH, NaH and CaH_2) and MgB_2 and can be hydrogenated according to the following general reaction:

(1) $\quad 2/xMH_x + MgB_2 + 4H_2 \rightarrow 2/xM(BH_4)_x + MgH_2$

where M stands for an alkaline or an alkaline earth metal (x = 1,2). The required temperature and pressure conditions for reaction (1) are generally much more moderate than the respective reaction using elemental boron [1-3]. Although the use of composites also changes the thermodynamic properties, these finding suggest that MgB_2 is kinetically superior to pure boron for hydrogen absorption reaction. However, the underlying reaction mechanisms are not yet fully understood. Among the hydrogen storage materials listed above, recently, $2NaH-MgB_2$ composites received soaring attention [6-8].The system has a theoretical gravimetric hydrogen capacity of 7.8 wt.%, with an overall reaction enthalpy of 62 $kJmol^{-1}H_2$ resulting in an equilibrium pressure of 1 bar at 350°C [6]. However, although this system had been recently investigated in several works, little is known about the hydrogenation process. With the aim of clarifying the reaction mechanisms involved in the formation of complex borohydrides, we investigated the hydrogenation reaction of $2NaH+MgB_2$ by in-situ Synchrotron Radiation Powder X-ray diffraction (SR-PXD).

Figure 1 shows the measurement carried out at 50 bar of pressure, in scanning temperature from RT to 400°C and than cooled to 240°C both with a heating/cooling rate of 5°C/min. The phases in the starting material were NaH and MgB_2. Upon heating, due to thermal expansion all peaks shifted continuously towards lower 2Θ angles. At roughly

280°C, the formation of an unknown phase with major reflection at 14.36, 16.59, 19.54, 23.54 and 27.79 2Θ angle (wavelength = 1.072 Å) was observed. This phase is found to be stable up to 325°C, and then the diffraction peaks disappeared. Moreover at roughly 330°C, the formation of the $NaMgH_3$ starts. This was accompanied by a significant decrease of the NaH diffracted intensity. Formation of $NaMgH_3$ continues up to a temperature of 350 °C. $NaMgH_3$ formation and the disappearance of NaH are followed by the appearance of an amorphous background at 19.50 2Θ angle. It starts to form at 350°C and remains almost constant until the temperature reaches 400°C. At 380°C, reflections of crystalline $NaBH_4$ appear and continuously grow until the final temperature 400°C is reached.

The cooling period is characterized by two main events, which take place at 370 and 320°C, respectively. At roughly 370°C, the intensity of $NaBH_4$ and NaH peaks quickly rise and later at about 320°C, the peaks related to the unknown phase observed during the heating period reappear. Simultaneously with these two events, which are described above, the amorphous background disappears completely. This work shows that *in situ* SR-PXD at variable temperatures and gas pressures is a powerful tool for studying gas/solid reactions. These investigations prove the complicity of the hydrogen absorption reaction in the *Reactive Hydride Composites*.

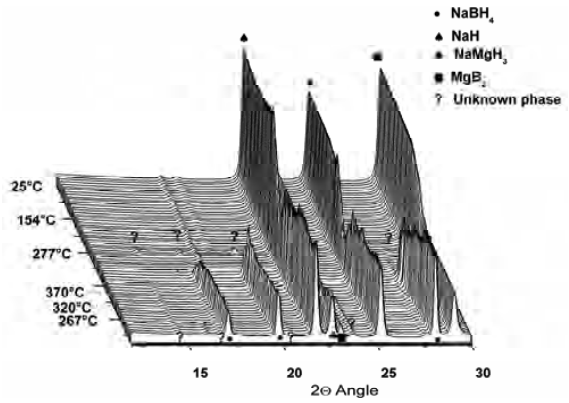

Figure1 *Series of SR-PXD patterns of the 2NaH+MgB_2 system heated under 50 bar hydrogen pressure from RT to 400°C and cooled to 240°C (5°C/min, wavelength = 1,072 Å). Symbols: ● $NaBH_4$, ♠ cubic NaH, ♣ $NaMgH_3$, ■ MgB_2,* ***?*** *Unknown phase.*

References

[1] G. Barkhordarian, T. Klassen, R. Bormann, Internetional patent pending ed., WO 2006/063627 A1.
[2] M. Dornheim, N. Eigen, G. Barkhordarian, T. Klassen, R. Bormann, *Advanced Engineering Materials* **2006**, *8*, 377.
[3] G. Barkhordarian, T. Klassen, M. Dornheim, R. Bormann, *Journal of Alloys and Compounds* **2007**, *440*, L18.
[4] J. J. Vajo, S. L. Skeith, F. Mertens, *Journal of Physical Chemistry B* **2005**, *109*, 3719.
[5] J. J. Vajo, F. O. Mertens, S. L. Skeith, M. P. Balogh, International patent pending ed., WO 2005/097671.
[6] S. Garroni, C. Pistidda, M. Brunelli, G. B. M. Vaughan, S. Surinach, M. D. Baro, *Scripta Materialia* **2009**, *60*, 1129.
[7] J. F. Mao, X. B. Yu, Z. P. Guo, H. K. Liu, Z. Wu, J. Ni, *Journal of Alloys and Compounds* **2009**, *479*, 619.
[8] T. Czujko, R. A. Varin, Z. Wronski, Z. Zaranski, T. Durejko, *Journal of Alloys and Compounds* **2007**, *427*, 291.

Investigation of anion substitution in $NaBH_4$

D. B. Ravnsbæk[1], L. H. Rude[1], Y. Cerenius[2], and T. R. Jensen[1]

[1] *iNANO and Department of Chemistry, University of Aarhus, Denmark*

[2] *MAX-lab, Lund University, S-22100 Lund, Sweden*

A major obstacle in the utilization of renewable energy sources is the lack of a safe, cheap and efficient energy storage material. Hydrogen has been suggested as a future energy carrier, however, safe, efficient and economic storage of hydrogen allowing it to be the successor of gasoline is still remaining.[1,2]

Complex metal hydrides such as borohydrides, based on BH_4^-, are currently of great interest as potential hydrogen storage materials, since they have high gravimetric hydrogen density and show a variety of decomposition temperatures. However, many of the known borohydrides are too stable for practical aplications. i.e. hydrogen is released at too high temperatures e.g. T_{des} = 400 °C for $NaBH_4$.[3] A ruote to tayloring the thermodymic properties of the borohydrides is by anion substitution in which the BH_4^- anion in the borohydride structure is substituted by halide anions, i.e. Cl^-, Br^-, or I^-. The differences in ionic radii between the BH_4^- anion (r_{ion} = 2.03 Å) and the halide anions (r_{ion} = 1.81 - 2.20 Å) may cause a lowering af the stability, hence release of hydrogen at lower temperatures. Partial anion substitution has recently been demonstrated by preparation of $Li(BH_4)_{1-x}Cl_x$.[4,5] In this study formation of $Na(BH_4)_{1-x}Cl_x$ by solid state diffussion is investigated by *in situ* time-resolved synchrotron radiation powder X-ray diffraction (SR-PXD).

Samples were prepared from $NaBH_4$ and NaCl mixed in molar ratios of 1:1 and ball milled for 120 min under argon atmosphere. *In-situ* time-resolved SR-PXD was measured at the MAX II Synchrotron in Lund, Sweden, at Beamline I711 using a MAR165 CCD detector system.[6] Samples were mounted in sapphire single-crystal tubes (1.09 mm o.d., 0.79 mm i.d., Al_2O_3), which were attached on a specially designed sample cell for studies of gas/solid reactions at elevated temperature and pressure.[7] The temperature was controlled with a thermocouple placed in the sapphire tube next to the sample. During the measurements p(Ar) = 1 bar was applied. All sample handling was perform in an argon-filled glove box (p(O_2, H_2O) < 0.3 ppm). The selected wavelength was 1.09994 Å and the X-ray exposure time was 30 s per powder diffraction pattern. The FIT2D program was used to transform raw data to powder patterns.[8]

Rietveld Refinement of the SR-PXD data measured at *RT* revieled that no substitution takes place during ball milling. However, upon heating (see figure 1, left) at ~200-300 ºC the peak position of $NaBH_4$ moves to higher 2θ-position, i.e. the unit cell is getting smaller during heating which is in contrast to positive thermal expansion which is normally observed for most compounds. This indicates that a solid solution of the composition $Na(BH_4)_{1-x}Cl_x$ is forming since the anionic radii of Cl^- is ~0.22 Å smaller than that for BH_4^-. This also results in a significant peak broadening. Furthermore, the plot of integrated normalized intensities (see figure 1, right) of selected peak from $Na(BH_4)_{1-x}Cl_x$ and NaCl, respectively shows that the amount of NaCl decreases, simultaneously with an increase in the intensity from the $Na(BH_4)_{1-x}Cl_x$ peaks, which further underlines that an anionic substitution is taking place.

Rietveld refinement was further utilized to study the change in cell parameters in more detail as well as determining the degree of dissolution, i.e. the composition of the solid solution $Na(BH_4)_{1-}$

$_xCl_x$. A structural model was used in the Rietveld refinement where Cl^- substitute for BH_4^-, i.e. Cl was constrained to the same set of *x,y,z* coordinates as B and the sum of their occupancy constrained to one in the structure of $NaBH_4$. The refinements show that the composition of the solid solution at *RT* after heating is $Na(BH_4)_{0.72}Cl_{0.28}$. The degree of substitution seems to be slightly higher at 300 ºC than after cooling to *RT* (31 and 28 mol%, respectively). This suggests that some NaCl diffuses out of $NaBH_4$ upon cooling, however, the difference in occupancy might be an effect of thermal vibration, since these are strongly correlated. The same effect is observed for the dissolution of LiCl in $LiBH_4$.[5]

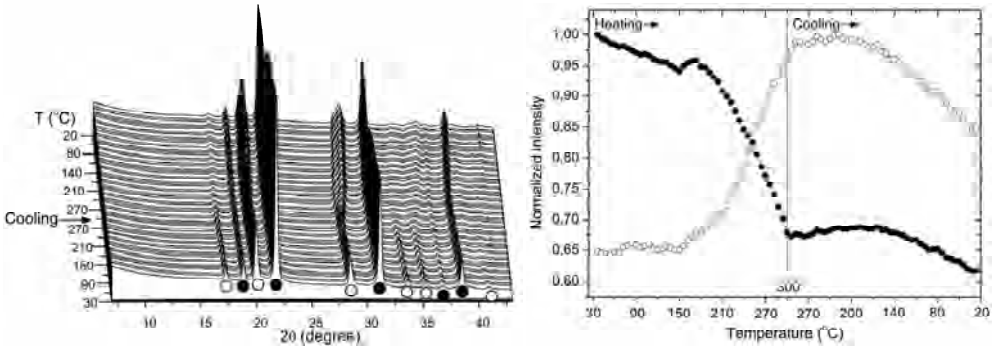

Figure 1 Left: *In situ* SR-PXD measured for a sample containing $NaBH_4$-NaCl (1:1) prepared by ball milling heated from *RT* to 300 ºC and cooled to *RT* ($\Delta T/\Delta t$ = 10 °C/min, λ = 1.09994 Å). **Right**: Integrated normalized intensity for the individual compounds. Symbols: ○ $NaBH_4$, ● NaCl, Red line: Temperature reaches 300 ºC and cooling to *RT* begins.

The refinement also showed that the cell parameter of $Na(BH_4)_{1-x}Cl_x$ still is decreasing at 300 ºC as opposed to reaching a plateau, which indicates that a higher degree of substitution could have been obtained by heating the sample for a longer period of time. This will be explored further in the near future as will the stability of the obtained solid solutions.[9]

Acknowledgement
We thank the research program DanScatt and the Center for Materials Crystallography (CMC) funded by The Danish National Research Foundation and the Danish Strategical Research Council's Center for Energy Materials (CEM).

[1] L. Schlapbach, A. Züttel, *Nature* **414**, 353, (2001).
[2] W. Grochala, P. P. Edwards, *Chem. Rev.* **104**, 1283, (2004).
[3] A. Züttel, S. Rentsch, P. Fischer, P. Wenger, P. Sudan, Ph. Mauron, Ch. Emmenegger, *J. Alloys Compd.* **356–357**, 515, (2003).
[4] L. Mosegaard, B. Møller, J. E. Jørgensen, Y. Filinchuk, Y. Cerenius, J. C. Hanson, E. Dimasi, F. Besenbacher, T. R. Jensen, *J. Phys. Chem. C* **112**, 1299, (2008).
[5] L. M. Arnbjerg, D. B. Ravnsbæk, Y. Filinchuk, R. T. Vang, Y. Cerenius, F. Besenbacher, J.-E. Jørgensen, H. J. Jakobsen , T. R. Jensen, *Chem. Mater.* **21**, 5772, (2009).
[6] Y. Cerenius, K. Ståhl, L.A. Svensson, T. Ursby, Å. Oskarsson, J. Albertsson, A. Lijas, *J. Synchrotron Radiat.* **7**, 203, (2000).
[7] D. Ravnsbæk, L. Mosegaard, J. E. Jørgensen, T. R. Jensen, *"In situ* synchrotron radiation powder x-ray diffraction for studies in materials science", *Proceedings of the 29th Risø International Symposium on Materials Science:Energy Materials – Advances in Characterization, Modelling and Application*, 349, (2008).
[8] A. P. Hammersley, S. O. Svensson, M. Hanfland, A. N. Fitch, D. Häusermann, *High Pressure Res.* **14**, 235, (1996).
[9] D. B. Ravnsbæk, L. H. Rude, Y. Cerenius, T. R. Jensen, To be submitted, (2010).

In-Situ Observation of the Eutectic Melting of $LiBH_4$-$Mg(BH_4)_2$ system

Bo Richter[1], Young-Su Lee[2], Young Whan Cho[2], Yngve Cerenius[3], Torben R. Jensen[1]

[1]*iNANO and Department of Chemistry, University of Aarhus, Denmark,*

[2]*Materials Science and Technology Research Division, Korea Institute of Science and Technology, Seoul 136-791, Republic of Korea,*

[3]*MAX-Lab, Lund University, S-22100 Lund, Sweden*

Borohydrides are considered as promising candidates for solid state hydrogen storage, e.g. $LiBH_4$ and $Mg(BH_4)_2$ hold as much as 18.5 and 14.9 wt % H_2, respectively. To utilize this capacity in an effective and rational manner, mixed cation metal hydrides are examined widely due to unfavorable properties of the individual constituents. In this study, the properties of the combined system $LiBH_4$ - $Mg(BH_4)_2$ are investigated.

Recently, we established that a physical mixture of $LiBH_4$ and $Ca(BH_4)_2$ exhibits eutectic melting at approximately 200 °C, multiple step decomposition patterns and at certain ratios releases hydrogen at lower temperatures than the individual borohydrides [1]. Furthermore, this was also proven to be the first such system to be reversible. The present composite of $Mg(BH_4)_2$ and $LiBH_4$ has been investigated by DSC, indicating that it undergoes eutectic melting, which is confirmed by *in situ* synchrotron radiation powder X-ray diffraction (SR-PXD). Also, the existence of complexes of the $LiMg(BH_4)_3$ composition type has previously been reported in the literature, e.g. by Soloveichik and co-workers [2] as well as by Orimo et al [3]. However, we cannot yet confirm the presence hereof from our measurements.

In situ time-resolved SR-PXD data were collected at the synchrotron MAX II, Lund, Sweden, MAX-Lab beamline I711 with a MAR165 CCD detector system [4]. The sample cell was specially developed for studies of gas/solid reactions and allows high pressure and temperature to be applied. The samples were mounted in a sapphire single-crystal tube (1.09 mm o.d., 0.79 mm i.d., Al_2O_3) in an argon-filled glove box ($p(O_2, H_2O) < 0.3$ ppm). The temperature was controlled with a thermocouple placed in the sapphire tube next to the sample. A gas supply system was attached to the sample cell, which allowed the change of gas and pressure via a vacuum pump during X-ray data acquisition [5]. The system was flushed with Ar and evacuated three times before the valve to the sample was opened prior to the X-ray experiment. The X-ray exposure time was 30-60 s per powder diffraction pattern.

We conducted experiments under ambient pressures (Ar) and in hydrogen gas ($p(H_2) = 2$ bar), observing some anomalous behavior with respect to decomposition patterns. Frequently, under hydrogen pressures the formation of MgB_2 is observed, but for the 1:1 mixture (figure 1) we see no such behavior under H_2 pressure. With excess $Mg(BH_4)_2$ (figure 2) early formation of MgH_2 and Mg (in comparison to observations for pure $Mg(BH_4)_2$) is seen. These preliminary results strongly indicate the sensitivity with which the decomposition patterns of these composite mixtures depend.

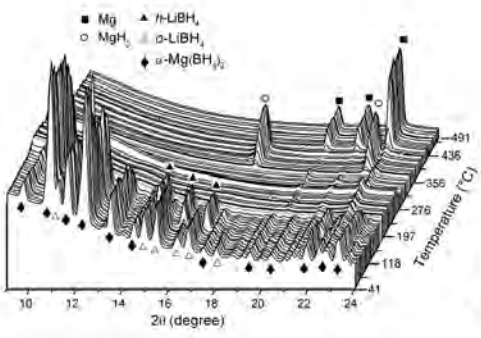

Figure 1. *In-situ* SR-PXD patterns of $Mg(BH_4)_2$ + $LiBH_4$ (1:1) as a function of temperature upon heating at 5 °C/min, $p(H_2) \approx 2$ bar. *o*-$LiBH_4$ phase transformation appears at 110 °C. The eutectic melt forms from approximately 160 °C (green line).

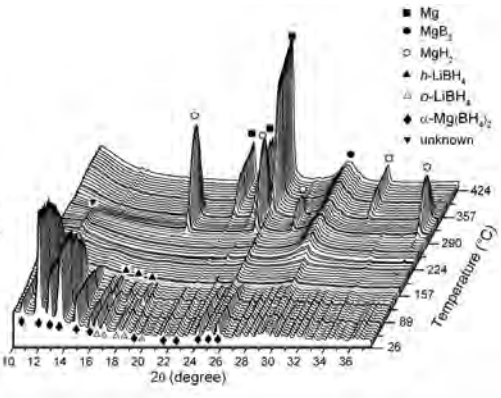

Figure 2. *In-situ* SR-PXD patterns of $Mg(BH_4)_2$ + $LiBH_4$ (2:1) as a function of temperature upon heating at 5 °C/min under ambient pressure (Ar). *o*-$LiBH_4$ phase transformation appears at 110 °C. The eutectic melt forms from approximately 160 °C (green line). β-$Mg(BH_4)_2$ is formed after the eutectic point due to excess $Mg(BH_4)_2$ present.

In combination with DSC measurements the SR-PXD data reveals a eutectic melting around 170 °C at a composition very close to 1:1. The diffraction from both constituents disappears swiftly, leaving no trace of neither until the relevant decomposition products appear at higher temperatures (figures 1 and 2). More detailed investigations are underway [6].

Acknowledgements

We thank the Danish Natural Science Research Council (DanScatt program) and the European Comission (contract NMP-2008-261/FLYHY) for financial support.

References

[1] Lee, J. Y.; Ravnsbæk, D.; Lee, Y.-S.; Kim, Y.; Cerenius, Y.; Shim, J.-H.; Jensen, T. R.; Hur, N. H.; Cho, Y.W. *J. Phys. Chem. C*, **2009**, *113*, 15080. **[2]** G. L. Soloveichik, M. Andrus, Y. Gao, J.-C. Zhao, S. Kniajanski, *Int. J. Hydrogen Energy*, **2009**, *34*, 2144. **[3]** Z.-Z. Fang, X.-D. Kang, P. Wang, H.-W. Li, S.-I. Orimo, *J. Alloys Comp.* 2010, 491, L1-L4. **[4]** Y. Cerenius, K. Ståhl, L. A. Svensson, T. Ursby, Å. Oskarsson, J. Albertsson, A. Lijas, *J. Synchrotron Radiat.* 2000, 7, 203-208. **[5]** L. Mosegaard, B. Møller, J. E. Jørgensen, U. Bösenberg, M. Dornheim, J. C. Hanson, Y. Cerenius, G. Walker, H. J. Jakobsen, F. Besenbacher, T. R. Jensen, *J. Alloys Comp.* 2007, 446-447, 301-305 **[6]** B. Richter, Y.-S. Lee, Y. Cerenius, T. R. Jensen, Y. W. Cho, 2010, to be submitted.

Tailoring the properties of lithium tetrahydridoboranate by anion substitution.

Line H. Rude,[1] Lene M. Arnbjerg,[1] Yngve Cerenius,[2] and Torben R. Jensen[1]

[1] *iNANO and Department of Chemistry, University of Aarhus, Denmark*
[2] *MAX-lab, Lund University, S-22100 Lund, Sweden*

Borohydrides are considered interesting materials for hydrogen storage in mobile applications due to their theoretical high hydrogen content, [1,2] *e.g.* 18.5 weight percent (wt.%) for lithium tetrahydridoboranate, $LiBH_4$. Unfortunately, the borohydrides are either too stable or unstable for practical hydrogen storage systems. $LiBH_4$ release hydrogen at a temperature of 410 °C ($p(H_2)$ = 1 bar) but the system can be modified by adding suitable compounds,[3] e.g. SiO_2, TiF_3 or $TiCl_3$, or by substitution of ions aiming to destabilize the structure.[4]

The aim for this investigation is to alter the properties of $LiBH_4$ by substitution of the anion BH_4^- with Br^- in $LiBH_4$ which is feasible due to the similar size in radii.[5]
The substitution is explored by *in situ* synchrotron radiation powder X-ray diffraction (SR-PXD) and by differential scanning calorimetry (DSC) on a sample of $LiBH_4$ + LiBr (1:1) synthesized by a mechano-chemical method, e.g. ballmilling for 2 hours effectively.

In situ time-resolved SR-PXD data was measured at the MAXII synchrotron beamline I711 at MAX-lab, Lund, Sweeden (λ = 1.07200 Å) with a MAR165 CCD detector system.[6] The samples were mounted in sapphire single crystal tubes (1.09 mm o.d., 0.79 mm i.d., Al_2O_3) in an argon filled glovebox ($p(O_2, H_2O) < 0.5$ ppm). The sample holder was constructed so that hydrogen pressures from vacuum up to 200 bar and temperatures from RT to 800 °C can be used during the experiment.[7] The system was flushed with argon and evacuated three times before the valve to the sample was opened prior to the X-ray experiment. The X-ray exposure time was 30-60 s per powder diffraction pattern. This *in situ* SR-PXD experiment was conducted with a constant hydrogen pressure of $p(H_2)$ = 1 bar and with a steadily increasing temperature (rate of 5 °C/min) from RT-427 °C.

Differential scanning calorimetry (DSC) and thermogravimetric analysis (TGA) was measured simultaneously with a Netzsch STA449C Jupiter instrument at heating rate of v = 2.0 °C/min from RT to 420 °C in a flow of He (50 mL/min). The samples were mounted in Al_2O_3 crucibles.

The *in situ* SR-PXD-data of a sample of $LiBH_4$ + LiBr ballmilled in the ratio 1 : 1 and preheated to 245 °C for 3 days is shown in Figure 1 in the temperature range RT – 420 °C. There is no indication of substitution at RT. At 300 °C the substitution of LiBr initializes and the intensity of LiBr decreases. At 360 °C a reaction of LiBr with the *h*-$LiBH_4$ phase is observed with the formation of a new hexagonal structure, denoted $Li(BH_4)_{1-x}Br_x$. The new phase must consist of an approx. equal amount of Br^- and BH_4^- anions since the LiBr diffraction disappears with the formation of the $Li(BH_4)_{1-x}Br_x$ phase.

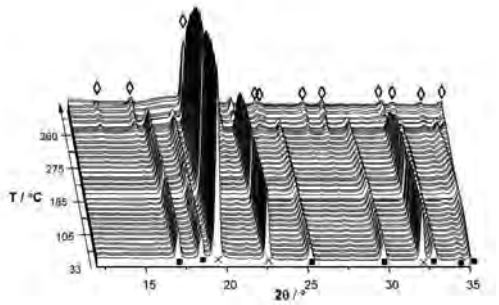

Figure 1 *In situ* SR-PXD on $LiBH_4$ + LiBr (1:1) preheated to 245 °C for 3 days, sample **S4**. The sample was heated from *RT* to 427 °C with a heating rate of 5 °C/min (λ = 1.07200 Å). Symbols: the crosses (X) represents the LiBr; the filled squares (■) represents *h*-$LiBH_4$; the empty diamonds (◊) represents the new phase, $Li(BH_4)_{1-x}Br_x$. At $T \approx 185$ °C the beam was cut for a minute. At $T \approx 420$ °C no crystalline materials was left in the sample due to melting.

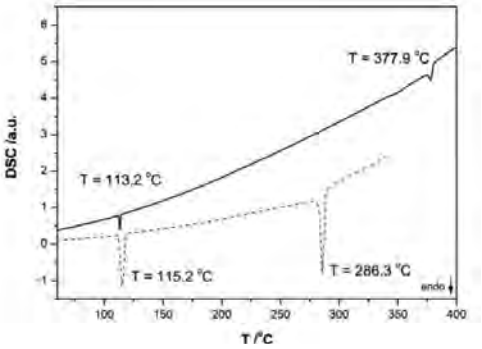

Figure 2 Differential scanning calorimetry shown in the temperature range from 60 to 400 °C. The reference sample of $LiBH_4$ is represented with a broken line and the sample of $LiBH_4$ + LiBr (1 : 1), **S3**, is represented by the solid line.

Further experiments with TGA and DSC reveals a stabilization of the hexagonal phase of $LiBH_4$ by approximately 90 °C altering the melting point of $LiBH_4$ at $T = 286$ °C (pure $LiBH_4$) to $T = 378$ °C ($Li(BH_4)_{1-x}Br_x$), see Figure 2. However, the stabilization of the hexagonal phase has no apparent impact on the hydrogen release temperature determined by sieverts measurements to be unchanged (not shown here).

The next step will be the investigation of the reversibility of the material upon hydrogen release and uptake.

Aknowledgements

The European Commission (contract NMP-2008-261/FLYHY) and the Danish Natural Science Research Council (DanScatt program) is thanked for financial support.

References

(1) Eberle, U.; Felderhoff, M.; Schüth, F. *Angew. Chem. Int. Ed.* **2009**, *48*, 6608-6630.
(2) Schlapbach, L.; Zuttel, A. *Nature* **2001**, *414*, 353–8.
(3) Mosegaard, L.; Moller, B.; Jorgensen, J.; Filinchuk, Y.; Cerenius, Y.; Hanson, J. C.; Dimasi, E.; Besenbacher, F.; Jensen, T. R. *J. Phys. Chem. C* **2008**, *112*, 1299-1303.
(4) Arnbjerg, L. M.; Ravnsbæk, D. B.; Filinchuk, Y.; Vang, R. T.; Cerenius, Y.; Besenbacher, F.; Jørgensen, J.; Jakobsen, H. J.; Jensen, T. R. *Chem. Mater.* **2009**, *21*, 5772-5782.
(5) Filinchuk, Y.; Hagemann, H. *Eur. J. Inorg. Chem.* **2008**, *2008*, 3127-3133.
(6) Cerenius, Y.; Stahl, K.; Svensson, L. A.; Ursby, T.; Oskarsson, A.; Albertsson, J.; Liljas, A. *J. Synchrotron Radiat.* **2000**, *7*, 203–208.
(7) Mosegaard, L.; Møller, B.; Jørgensen, J.; Bösenberg, U.; Dornheim, M.; Hanson, J. C.; Cerenius, Y.; Walker, G.; Jakobsen, H. J.; Besenbacher, F.; Jensen, T. R. *J. Alloys Compd.* **2007**, *446-447*, 301-305.

Hydrogen absorption for LiF/MgB_2 composites investigated by in situ powder X-ray diffraction

Ivan Saldan[1], Rapee Gosalawit[1], Claudio Pistidda[1], Ulrike Bösenberg[1], Jose Bellosta von Colbe[1], Torben R. Jensen[2], Yngve Cerenius[3], Martin Dornheim[1]

[1] *Institute of Materials Research, GKSS Forschungszentrum Geesthacht, 21502 Geesthacht, Germany*

[2] *Interdisciplinary Nanoscience Center (iNANO) and Department of Chemistry, University of Århus, DK-8000 C Århus, Denmark*

[3] *MAX-lab, Lund University, S-22100 Lund, Sweden*

Because of its high gravimetric hydrogen density lithium borohydride is considered as potential reversible hydrogen storage material. This complex light metal hydride can desorb theoretically up to ~ 13.8 wt.% H_2 by the following reaction:

$$LiBH_4 \rightarrow LiH + B + 3/2\ H_2 \qquad (1)$$

The experimental value of enthalpy for this reaction is ~ 69 kJ/mol H_2, therefore the temperature for hydrogen release at 1 bar H_2 pressure is close to ~ 400 ºC [1]. The mixtures $LiBH_4$ with light metals hydrides called as "reactive hydride composites" (RHCs) show lowered reaction enthalpies with about the same gravimetric hydrogen density. For example, reaction:

$$2\ LiH + MgB_2 + 4\ H_2 \leftrightarrow 2\ LiBH_4 + MgH_2 \qquad (2)$$

has a total reaction enthalpy of approximately 46 kJ/mol H_2 [2]. However, for most practical applications a reaction enthalpy about 30 kJ/mol H_2 or even less is desired.

In recent work [3] the decomposition reaction of $LiBH_4$ with F anion doping was investigated by first-principles calculations. According to these results H→F substitution can be possible under $LiBH_4$ formation as $Li_8B_8H_{32-x}F_x$ ($x \leq 4$) and under its decomposition as $Li_8H_{8-x}F_x$:

$$Li_8B_8H_{32-x}F_x \rightarrow Li_8H_{8-x}F_x + 8\ B + 12\ H_2\ (x \leq 4). \qquad (3)$$

Theoretically, partially H-atom substitution inside $[BH_4]^-$ anion results in a favourable thermodynamics (34.9 kJ/mol H_2 at x=3 or 27 kJ/mol H_2 at x=4 for (3) reaction). Experimentally evidencing these theoretical predictions may pave a new way to pursue improved hydrogen storage properties of $LiBH_4$ as reversible hydrogen storage materials for fuel-cells.

Now there is open question how to synthesise that $LiBH_4$ with F anion doping so called "borohydridofluoride". Recent experimental results for LiF/MgB_2 composite with molar ration 2:1 have shown a significant destabilisation for both hydrogen absorption and desorption, and synchrotron radiation power X-ray diffraction (SR-PXD) detected peak shift for LiF at around 380 ºC [4]. It means that the formation of $Li_8H_{8-x}F_x$ can be possible for this composite, but exact mechanism of that and *x*-value are not confirmed thoroughly.

In our present work hydrogen absorption at 390 ºC and 60 bar H_2 have been done for LiF/MgB_2 composites with molar ration 1:1 and 4:1, respectively. Phase composition for these composites was studied by *in-situ* SR-PXD at Beamline I711 at MAX-lab for 5 h. in isothermal regime (Fig. 1). The measurements were performed in a specially designed sample

cell [2] by *in situ* SR-PXD at beamline I711, MAX-lab. The selected wavelength was 1.072 Å. The composites were produced from LiF and MgB_2 powders with high purity by milling in Spex- 8000 M Mixer Mill for 5 h. Details of the sample preparation are described elsewhere [4]. All sample handling and preparation were performed under continuously purified argon atmosphere in a glove box.

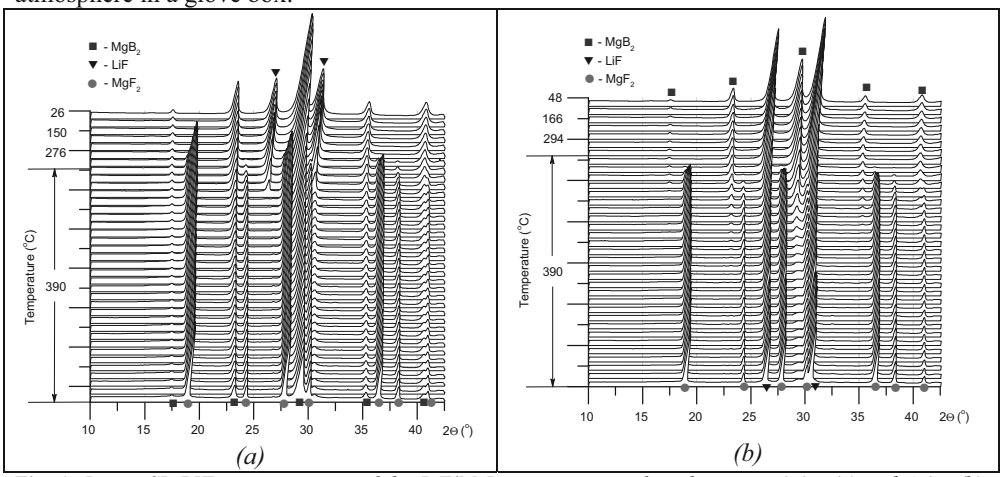

Fig. 1. *In-situ SR-PXD measurements of the LiF/MgB_2 composites with molar ratio: 1:1 - (a) and 4:1 - (b), respectively.*

The main difference between these two samples is different molar ratio between LiF and MgB_2. Experimental results showed us appearance of MgF_2 at ~ 375 ºC for composite with molar ratio 1:1 and ~ 390 ºC with molar ratio 4:1, respectively (see Fig.1). This difference between temperatures should be responsible for kinetic properties under hydrogen absorption. What is more, both samples showed the peak shift for LiF in a temperature region 380-390ºC. These *in-situ* SR-PXD results suggested that hydrogenation processes could be as following:

$$1\ LiF + 1\ MgB_2 + 2\ H_2 \leftrightarrow LiBH_4 + 1/2\ MgF_2 + 1/2\ MgB_2 \quad (4)$$

$$4\ LiF + 1\ MgB_2 + 4\ H_2 \leftrightarrow 2\ LiBH_4 + MgF_2 + 2\ LiF \quad (5)$$

$$I\ LiF + LiBH_4 \leftrightarrow I\ LiF_{1-x}H_x + LiBH_{4-ix}F_{ix}\ (i\leq 8;\ x\leq 1/2) \quad (6)$$

The last (6) reaction – high temperature disproportionation between parent compound LiF and product $LiBH_4$ is very possible, because reactions (4) and (5) were not complete, but it has not confirmed yet. Only $LiF_{1-x}H_x$ can be detected by *in situ* SR-PXD at 390 ºC, because of melting point above 270 ºC for $LiBH_4$ and obviously something less for $LiBH_{4-ix}F_{ix}$. Therefore another *in situ* experimental method would be a good idea to see specific signals for amorphous $LiBH_{4-ix}F_{ix}$ and $LiBH_4$ at high temperature.

[1] A. Züttel, P. Wenger, S. Rentsch, P. Sudan, Ph. Mauron, Ch.Emmenegger, *J. Power Sources* 118, (2003) 1.
[2] U. Bösenberg, S. Doppiu, L. Mosegaard, G. Barkhordarian, N. Eigen, A. Borgschulte, T. R. Jensen, Y. Cerenius, O. Gutfleisch, T. Klassen, M. Dornheim, R. Borman, *Acta Materialia* 55 (2007) 3951-3958
[3] L. Ying, P. Wang, Zh. Fang, H. Cheng, *Chemical Physics Letters* 450, (2008) 318-321
[4] R. Gosalawit, J.M. Bellosta von Colbe, M. Dornheim, T.R. Jensen, Y. Cerenius, K. Suarez, Ch.M. Bonatto, R. Borman, *J. Physical Chemistry, Submitted.*

SAXS studies of charged nanodiscs

J.B. Simonsen,[a] N. Skar-Gislinge,[a] B. Pallisgaard,[b] S.R Midtgaard,[a] Lean Pedersen,[b] K. Mortensen,[a] and L. Arleth[a]

[a] *Department of Basic Sciences and Environment, Faculty of Life Sciences, University of Copenhagen, Thorvaldsensvej 40, DK-1871 Frederiksberg C, Denmark*
[b] *Nano-Science Center, University of Copenhagen, Universitetsparken 5, 2100 Copenhagen, Denmark*

Nanodiscs are nanometer-sized self-assembled discoidal particles (diameter of ~10 nm and a height of ~5 nm), which consist of two identical engineered amphipathic helical membrane scaffolding proteins (MSP1D1) that wrap around the circumference of a phospholipid bilayer in a belt-like manner, see Figure 1A.[1,2] This membrane-like structure facilitates the reconstitution of membrane proteins into the nanodiscs, which enables us to study the native structure and function of membrane proteins.[3] It has been suggested that membrane proteins reconstituted in nanodiscs can be crystallized and their structure thereby mapped with high resolution by using X-ray crystallography.[4] To reach this elusive goal of forming such a crystalline matrix, however, several small steps to obtain controlled aggregations must be undertaken and described. Our approach towards a crystalline 3D nanodisc matrix is based on oppositely charged nanodiscs. It is our hope that well-defined nanodisc columns, as illustrated in Figure 1A, are formed by mixing oppositely charged nanodiscs, and that these 1D crystals self-assemble into a even higher hierarchy of order, a 3D crystal.

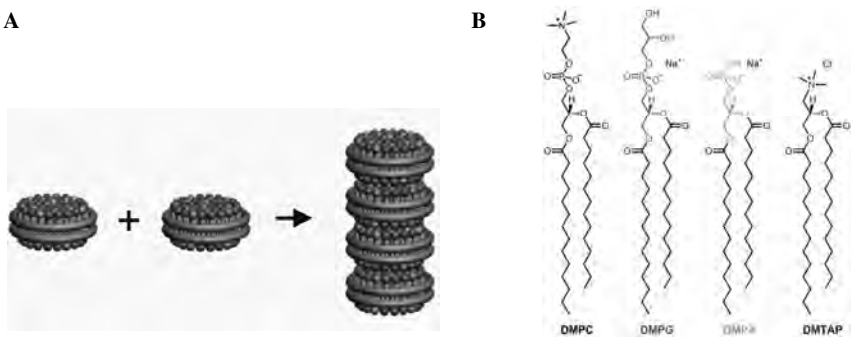

Figure 1. A) Schematic illustration of the proposed columnar aggregation of oppositely charged nanodiscs. B) The molecular structure of the lipids used throughout this study.

Small-angle X-ray scattering: SAXS measurements were conducted to provide information about the structure of the charged lipid-MSP aggregates.

We observe just as in the case of the size exclusion chromatograms (not shown), a high similarity between both the recorded SAXS data (Figure 2A) and the corresponding indirect Fourier transformation (IFT) profiles (Figure 2B) of the charged aggregates and the neutral nanodisc. The IFT of the SAXS data, also known as the pair distance distribution function, *p(r),* provide information about the frequency of the intradistances within the particle multiplied by the distance squared and convoluted by the scattering contrast.

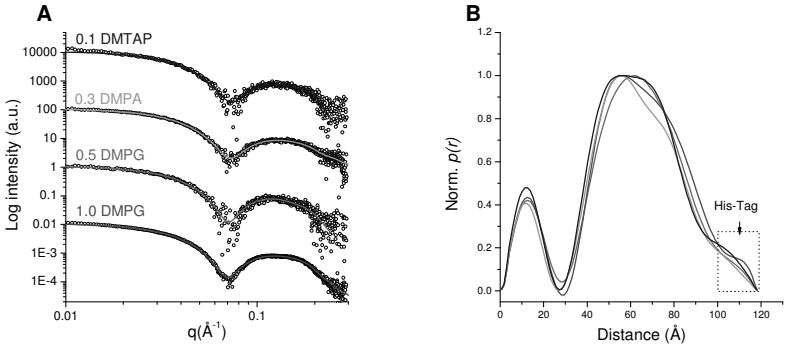

Figure 2. A) Scattering profiles from nanodiscs with different lipid compositions after averaging and subtraction of pure solvent scattering data (dots) and the corresponding *p(r)* fit. B) The normalized pair distance distribution functions *p(r)* calculated from the SAXS data presented in (A).

Hence, information about e.g. the maximum distance within the particle can be read of from the indirect Fourier transformation. The small tail present in the high *q*-range in Figure 3B has been ascribed to the flanking 22 amino acid long His-Tev-tag sequence attached to the C-terminal of the MSP1D1.

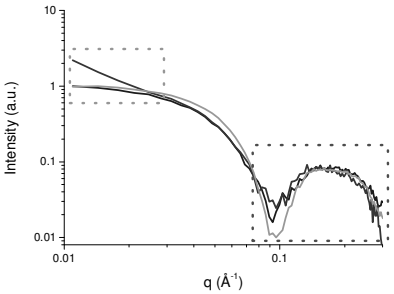

Figure 3. Scattering profiles from the 1:1 mixture of oppositely charged nanodiscs (purple) and from each of the charged nanodisc components.

A significant increase of the forward scattering at low q-values when a 1:1 mixture of χ_{DMPA} = 0.3 and χ_{DMTAP} = 0.1 nanodiscs were mixed is observed, marked by the green box in Figure 3. At higher q-values, corresponding to the resolution of the size of the nanodisc, the SAXS profile is similar to the SAXS profile of single charged nanodiscs showing that the aggregates are formed by nanodiscs (red box). Future studies in our lab will hopefully unravel whether or not the nanodiscs form a superstructure of columnar nanodisc aggregates.

Conclusions: In the present work, our objective has been to prepare and characterize both positively and negatively charged nanodiscs. We have found by means of SAXS that it is possible load the nanodiscs with up to 100 % DMPG, at least 30 % DMPA or ~10% DMTAP without disrupting the discoidal shape. Finally, SAXS showed that nanodisc aggregates are formed when oppositely charged nanodiscs are mixed. Future studies will hopefully tell whether or not the nanodiscs form a superstructure of columnar nanodisc aggregates.

[1] T.H. Bayburt, Y.V Grinkova, S.G. Sligar. Nano Letters **2002**, 2 (8), 853-856.
[2] N. Skar-Gislinge, J.B. Simonsen, K. Mortensen, S.G. Sligar, B.L. Møller, T. Bjørnholm, L. Arleth, Elliptical Structure of Phospholipid Bilayer Nanodisks Encapsulated by Scaffold Proteins: Casting the Roles of the Lipids and the Protein (**manuscript in preparation**).
[3] T.K. Ritchie, Y.V. Grinkova, T.H. Bayburt, I.G. Denisov, J.K. Zolnerciks, W.M Atkins, S.G. Sligar, Methods in Enzymology **2009**, 464, 211-231.
[4] Service, R. F. Science **2004**, 304, 674.

Hydrated phases of strontium ranelate.

K. Ståhl, C.G. Hartmann, C.B. Prag, S.R. Sørensen, A.C. Raffalt and J.E.T. Andersen.
Department of Chemistry, Technical University of Denmark, DK-2800 Lyngby, Denmark

Preclinical and clinical investigations have revealed that Sr^{2+} reduces bone re-sorption while at the same time it provides a stimulation of new bone formation [1]. This has lead to a growing interest in Sr^{2+} salts with different organic anions for osteoporosis therapy. Several organic strontium salts has recently been synthesized and structurally characterized by single-crystal methods [2,3,4,5]. Strontium ranelate (5-[bis(carboxymethyl) amino]-3-carboxy-methyl-4-cyano-2-thiophenecarboxylate), SR, is one promising pharmaceutical compound for treating osteoporosis marketed as Protelos® by Servier® [6]. The crystal structure of the as crystallized SR was solved from single-crystal data as the nona-hydrate. However, the nona-hydrate quickly dehydrates at ambient conditions to form a hepta-hydrate, also solved from single-crystal data. In order to clarify the thermal behaviour of SR, an in situ powder diffraction study was performed at beamline I711.

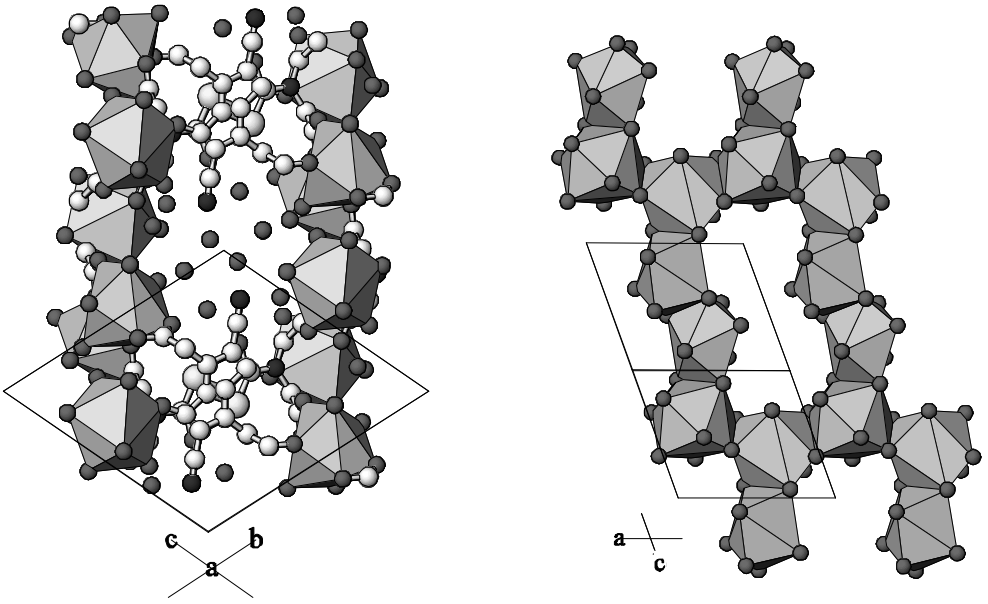

Figure 1. The crystal structure or strontium ranelate (SR) nona-hydrate. The strontium-oxygen coordination is shown as polyhedral. Left: Full structure along the a-axis. Right: One strontium layer viewed perpendicular to the bc-plane.

The crystal structure can be described as a metal-organic framework were Sr-O polyhedra join in sheets, which are further joined by the ranelate molecules. Water molecules are found as part of the strontium coordination as well as independent in the channels along the a-axis (c.f. Fig. 1).

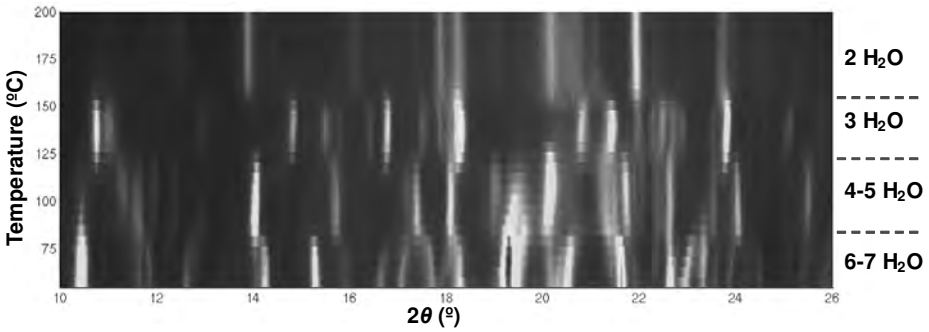

Figure 2. Part of the powder patterns collected in situ between 50 and 200 °C showing the existence of at least three phases above the hepta-hydrate.

In situ powder diffraction (Fig. 2) revealed three more phases above the first (room temperature) dehydration step, which could be correlated to a thermogravimetric analysis. The first phase, SR pentahydrate, has been indexed, but not yet solved (Table 1).

Table 1. Unit cell parameters for strontium ranelate hydrates.

	SR nonahydrate	SR heptahydrate	SR pentahydrate
a (Å)	8.3585(5)	8.3047(9)	8.2372(4)
b (Å)	12.6474(8)	11.528(1)	11.3904(5)
c (Å)	12.3865(8)	12.431(1)	11.3978(9)
α (°)	109.880(1)	112.939(2)	117.613(3)
β (°)	105.321(1)	101.971(2)	92.097(3)
γ (°)	97.148(1)	90.220(2)	94.297(3)

References

[1] Marie *et al.* (2001) Calcif. Tissue Int. **69**, 121–129.
[2] Christgau *et al.* (2005) Acta Cryst. C**61**, m259–m262.
[3] Stahl *et al.* (2006) Acta Cryst. C**62**, m144–m149.
[4] Stahl *et al.* (2006) Acta Cryst. E**62**, m1677–m1679.
[5] Christgau *et al.* (2006) J. Coord. Chem. **59**, 2023–2030.
[6] Damien, (2006). *Patent No. 11/140,822.* USA.

X-RAY POWDER DIFFRACTION STUDIES OF MINERALS IN CLAYS

Daniel Svensson[1,2], Eskil Hansen[3], Staffan Hansen[2]

[1]*Swedish Nuclear Fuel and Waste Management Co (SKB), Äspö Hard Rock Laboratory, P.O. Box 929, SE-572 29, Oskarshamn, Sweden*
[2]*Polymer & Materials Chemistry, Department of Chemistry, Lund University, P.O. Box 124, SE-221 00, Lund, Sweden*
[3]*Numerical Analysis, Centre for Mathematical Sciences, Lund University, P.O. Box 118, SE-221 00, Lund, Sweden*

Introduction

The KBS-3 concept for a Swedish repository for high-level radioactive waste includes three barriers: copper canister, swelling clay (smectite-rich) and suitable rock. It is vital that the clay retains its properties over a long period of time. Available clay materials are evaluated under repository-like conditions in the Alternative Buffer Materials experiment (ABM), which was started at the Äspö Hard Rock Laboratory in 2006 [1]. The first of the three ABM parcels, containing 11 different clay materials each, was retrieved in May, 2009. A deep repository is not expected to freeze during glacial periods, while levels closer to the surface can be affected by freeze-thaw cycles [1]. This will be of importance for back-filled shafts and sealed bore holes, if swelling clay is used as a filling material. Also clay barriers used in repositories for less radioactive waste, situated closer to the ground level, might be affected by permafrost. The aim of our project is to study fundamental processes of importance in this context [2-4], for example variations in the salt content of the ground water is one factor that will have great influence [1].

Experimental and results

(i) X-ray powder diffractograms were collected on the ABM-clays before and after exposure to conditions similar to those in a deep repository for one year. Phase analysis of the ABM samples using the increased 2θ-range, achieved by displacing the MAR-detector at beamline 711, yielded information on the mineralogical stability and spatial distribution of the swelling clay minerals and the minor phases present in the clay.

(ii) The freezing and thawing of smectite in different aqueous salt solutions was further studied after our initial study with pure water [4]. Homoionic montmorillonites (Na^+, Ca^{2+}) were tested in salt solutions of varying concentration and the results evaluated.

(iii) The hunt for the elusive four-layer hydrate, observed before when freezing Ca-montmorillonite (MX-80) [4], was extended to other divalent interlayer cations and smectite minerals. The results demonstrated a complex behaviour and the formation of the four-layer hydrate depended on the temperature, the specific cation and specific clay mineral. Things were further complicated by the sensitivity of the four-layer hydrate towards the beam.

(iv) In order to extend the data recorded on montmorillonite in aqueous solutions using the standard XRD equipment [4], SAXS measurements were undertaken at beamline I711. Interplanar spacings above approximately 40 Å could not be observed with the standard setup, while diffraction peaks in the range 40-100 Å were clearly observable in the SAXS experiments, see Fig. 1.

(v) The diffusion of liquid into capillaries with smectite powder, cf. Ref. 3, was further studied using powder x-ray diffraction resolved both in time and space. In order to facilitate the evaluation of the extensive data collected, a Matlab code was constructed (E. Hansen, unpublished). The code will be utilized to characterize the diffusion properties of different liquids in smectite powders by non-linear least squares fitting methods, cf. Fig. 2.

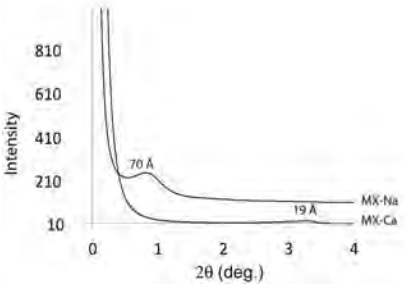

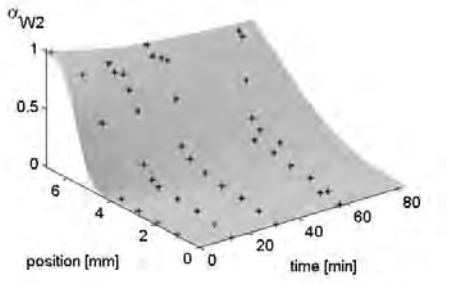

Fig. 1 (left). SAXS from homoionic MX-montmorillonite, 30 wt% solid in pure water.

Fig. 2 (right). The relative amount (α) of Ca-montmorillonite two-layer hydrate (W2) as a function of position and time in a glass capillary.

References

[1] SKB, 2007. RD&D Programme 2007. Programme for Research, Development and Demonstration of Methods for the Management and Disposal of Nuclear Waste. SKB Technical Report, TR-07-12, SKB, Stockholm.

[2] Svensson, P.D.: Experiments with Smectite Resolved in Time and Space by Synchrotron X-Ray Diffraction. Licentiate thesis, Lund 2009.

[3] Svensson, P.D. & Hansen, S.: Intercalation of Smectite with Liquid Ethylene Glycol – Resolved in Time and Space by Synchrotron X-Ray Diffraction. Applied Clay Science. *In press*.

[4] Svensson, P.D. & Hansen, S.: Freezing and Thawing of Montmorillonite – A Time Resolved Synchrotron X-ray Diffraction Study. *Submitted*.

Conference abstract for: Dynamics, Steady State and Arrest, 9th Annual Surface and Colloid Symposium, 18-20 November 2009, Lund, Sweden

Effect of Hydration on Structural Properties of Mucous Gel

Y Znamenskaya, J Engblom, J Sotres, T Arnebrant and V Kocherbitov

Faculty of Health and Society, Malmö University, SE-20506 Malmö, Sweden

Mucus barrier and its transport properties are essential for proper functioning of the digestive, respiratory and reproductive systems of vertebrates, including humans. From an engineering point of view, mucus is an outstanding water-based lubricant. The principal components of mucus are the glycoprotein mucin and water. Mucin forms the macromolecular matrix of mucus and dominates its rheological properties. Due to the large molecular weight of mucin, its polydispersity and high degree of glycosylation, it has been difficult to characterize its structure. There are several opinions about mucin structure presented in literature ranging from bottle brush to dumbbell type structures. The phase behaviour of mucin is a function of temperature and hydration level. It is known from literature that mucin can form liquid crystalline phase. It is still not exactly known what phases mucin forms at different temperatures and hydration levels, especially at low water contents in the water/mucin system.

We present results from atomic force microscopy (AFM), polarised light microscopy and small-angle X-ray scattering (SAXS). Samples were prepared from porcine gastric mucin (PGM) from Sigma and from a recently slaughtered pig. To characterise the molecular structure of PGM, it was studied both in air and in liquid by AFM operated in the tapping mode. Visual evaluation of the samples showed that with increasing mucin concentration the samples became more viscous and gel-like. A slight birefringence was observed in most samples, which increased as the sample got more concentrated. Strongly increased birefringence was observed close to the fluid – air interface which indicates that the presence of interfaces induces structuring mucin.

Aqueous mixtures with 1; 10; 19.5; 29.6; 50 and 100 wt% PGM were studied using SAXS (MaxLab, Lund university) at 25, 37, 70 ºC and at 25 ºC after heating. With the current setup we have covered the range of repeat distances 20-600 Å. At 19.5-50 wt% of mucin we see structural features corresponding to a rather small lattice parameter (about 100Å). There is a phase transition occurring in all these samples when heated from 37 to 70 ºC. These features are not seen in the dilute 1% and 10% mucin solutions and in the dry mucin.

Tomás Plivelic and Dörthe Haase, postdoc and research engineer at beamline I711, posing in their new T-shirts, November, 2009.
Photo: Annika Nyberg

In situ WAXS studies of nanoparticle formation and growth in sub- and supercritical fluids

Kirsten Ørnsbjerg Jensen, Christoffer Tyrsted, Nina Lock, Mogens Christensen, Jacob Becker-Christensen, Bo Brummerstedt Iversen

Department of Chemisty and iNano, Aarhus University, Langelandesgade 140, DK-8000 Århus C, Denmark

General project

In recent years, the specific properties of sub- and supercritical fluids have been exploited for synthesizing functional nanostructured materials, especially in the field of inorganic and hybrid materials. It is well known that control of the physicochemical properties of nanomaterials (size, morphology, structure and composition) can be achieved by choosing specific operating parameters, and many important results have been obtained in materials science in the last few years using sub- and supercritical fluids [1]. However, due to the use of high pressure and high temperature, the reactor of nanomaterials synthesis is often considered as a "black box". There is therefore a crucial need of *in situ* experiments to better understand and model the nucleation and growth of nanostructures in sub- and supercritical fluids. To meet this requirement we have developed an experimental setup allowing us to study the formation and growth of nanoparticles under these conditions, using X-ray scattering [2]. Our setup consists of a reactor, penetratable to X-rays of about 12 keV, where hydrothermal reactions at both high pressures (up to 250 bar) and high temperatures (up to 550 degrees) can be conducted. Furthermore, very fast heating rates can be achieved; >350°C in 10 seconds.

During two beamtimes at i711, MAXII, MAX-lab in 2009, we have used wide angle scattering (WAXS) to study the formation and growth of crystalline nanoparticles. We have studied several systems of nanoparticles with different applications, and a few examples will be given below.

Nanoparticles for Li-ion batteries

Recently, materials for Li-ion battery cathodes and anodes have attracted very much attention*[3]*. The properties of the materials are highly dependent on particle size and morphology, and understanding the mechanisms that control these particle characteristics durin g synthesis is therefore crucial. By means of WAXS, we have done extensive studies of the phase transformation from cobalt oxide hydroxide to lithium cobalt oxide under hydrothermal conditions. This

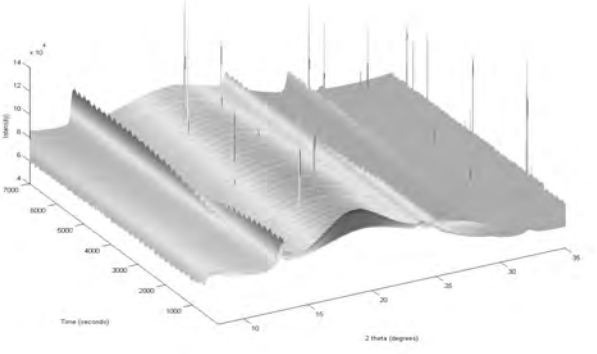

Figure 1: Timeresolved WAXS data, showing the phase transformation from cobalt oxide hydroxide to lithum cobalt oxide.

has provided a new understanding of the parameters controlling the mechanism of the phase transition, and thereby made us able to control the reaction rate, the particle size and the particle morphology.

Nanoparticles for catalysis

Zirconium dioxide or zirconia is a favoured ceramic material due to its toughness and by doping it with rare earth or transition metals it has found use in a wide range of technologies such as catalysis, solid-state fuel cell technology, and gas sensor applications.[4] In this context we studied the entire composition range of the CeO_2-ZrO_2 solid solution in order to examine how the final crystal structure and particle morphologies depended on the doping concentrations of CeO_2. We followed the nucleation and growth of the crystalline nanoparticles through time resolved WAXS during the supercritical synthesis in water. As seen in figure 2 (left) it is possible to stabilize the cubic/tetragonal crystal phase in the zirconia system by doping with ceria whereas the pure zirconia exhibits the monoclinic crystal phase. The right side of figure 2 shows the time resolved growth curves of the crystalline nanoparticles. It turned out that there is a clear size dependence on the crystallites when changing the doping concentration which also were confirmed by ex-situ studies. It was furthermore possible to describe the growth curves using theoretical kinetic modelling as seen by the grey lines displayed on top of the experimental datapoints thereby giving fundamental understanding of the growth process of the nanoparticles. [5]

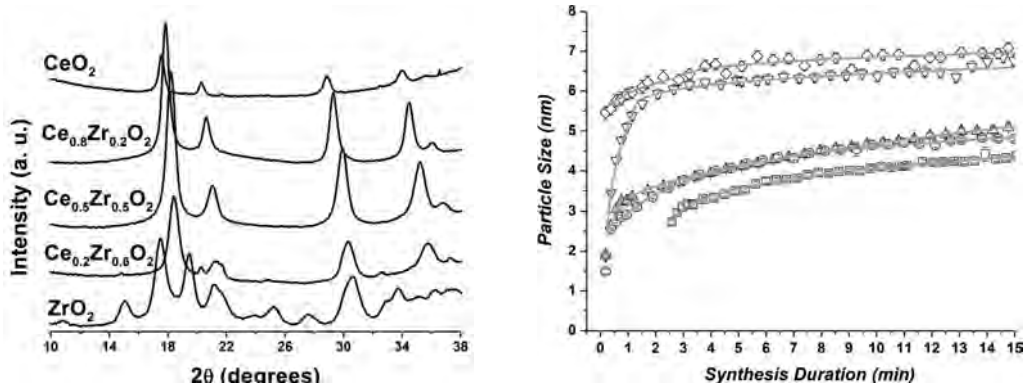

Figure 2: (Left) Diffractograms of the five different doping variants displaying the different crystal structures of the nanoparticles. (Right) Time-dependent growth in the *a,b* unit cell axis direction of $Ce_xZr_{1-x}O_2$ powders; x = 0.0 (□), x = 0.2 (○), x = 0.5 (Δ), x = 0.8 ( ) and x = 1.0 (◊).

[1] F. Cansell and C. Aymonier, Design of functional nanostructured materials using supercritical fluids, J. Supercrit. Fluids, 2009, 47, 508-516.
[2] Bremholm, M; Jensen, H; Iversen, SB, Iversen, BB: J. Supercriti. Fluids, 2008, 44, 385-390
[3] M. Armand, J. M. Tarascon, *Nature* **2008**, *451*, 652.
[4] Cabañas, A.; Darr, J. A.; Lester, E; Poliakoff, M. J. Mater. Chem. 2001, 11, 561–568.
[5] C. Tyrsted, J. Becker-Christensen, P. Hald, M. Bremholm, J. S. Pedersen, J. Chevallier, Y. Cerenius, S. Iversen, B. B. Iversen, Chem. Mater., 2010, 22 (5), pp 1814–1820, DOI**:** 10.1021/cm903316s

The local structure of Fe(III) in doped TiO_2 photocatalysts studied with X-Ray absorption spectroscopy

Éva Bajnóczi[1], Nándor Balázs[1], Károly Mogyorósi[1], Dávid F. Srankó[1], Zoltán Ambrus[1], Sophie E. Canton[2], Katarina Norén[2], Ernő Kuzmann[3], Attila Vértes[3], Zoltán Homonnay[3], Albert Oszkó[4], István Pálinkó[5], Pál Sipos[1*]

[1] *University of Szeged, Department of Inorganic and Analytical Chemistry, Szeged, Hungary*

[2] *Chemical Physics Department, Chemical Centre, Lund University, Lund, Sweden*

[3] *MTA-ELTE Research Group on the Application of Nuclear Techniques in Structural Chemistry, Loránd Eötvös University, Budapest, Hungary*

[4] *University of Szeged, Department of Physical Chemistryand Materials Science, Szeged, Hungary*

[5] *University of Szeged, Department of Organic Chemistry, Szeged, Hungary*

* *corresponding author, email: sipos@chem.u-szeged.hu*

Since the discovery of photocatalytic water splitting with sunlight[1], the study of titania (TiO_2) based semiconductor photocatalysts is one of the most active areas of materials science, both on fundamental and on applied levels[2-4]. A common way of photosensitizing TiO_2 photocatalyst is doping with metals (*e.g.,* transition metals like Fe(III), V(V), Cr(III), Cu(II), Mn(II), Co(II), *etc.*) or nonmetals (*e.g.,* I in various oxidation states, P(V), N(III), S(VI), *etc.*). Photocatalytic activity of transition metal doped TiO_2 catalysts usually passes through a maximum with increasing dopant concentration, but excessive amount of dopant usually causes a decrease in the photocatalytic activity. In other cases, metal doping was reported to cause detrimental effects on the photocatalytic activity even at the smallest dopant levels. The dopant atoms can be present in various forms: in some cases in separated "islands", either in crystalline or in amorphous forms or dispersed in the atomic level and substitute Ti(IV), either on the surface layer or in the bulk of the semiconductor. The actual form is likely to be related to the photoactivity and associated with the variations of the local structure of the dopant.

Recently, a kind of flame-hydrolytic technique has been established in our laboratories for the preparation TiO_2 photocatalysts with tailor made crystallinity, anatase-to-rutil ratio and surface properties.[5] It is based on the introduction of the vapor of an appropriately chosen volatile Ti(IV) compound into H_2/O_2 flame. The synthesis has been optimized in terms of mechanical settings and we managed to prepare *undoped* TiO_2 catalysts that are almost twice as active in photocatalytic degradation phenol and methanol, as Degussa P-25, which is usually considered to be the most efficient commercial photocatalyst.[5] Fe-doped TiO_2 samples were also prepared by flame-hydrolytic technique[5] (F-series hereafter). We found that doping with iron has a detrimental effect on the photoactivity of flame-synthesized samples. Oxidative hydrolysis of $TiCl_3$[6] was also utilized for preparing undoped or Fe-doped nanocrystalline TiO_2 (S-series hereafter). Doping enhanced the photoactivity of the samples within the S-series and it was found to pass through a maximum with increasing Fe-content.

First, the bulk properties of the products were characterized by standard analytical techniques which are conventionally used in photocatalysis (*i.e.*, powder X-ray diffraction, various microscopic techniques, UV-Vis diffuse reflectance spectroscopy, N_2 adsorption isotherms). From these measurements no difference was found in the bulk properties of the members of the F- and S-series: their anatase-to-rutile ratio, particle size, band-gap energy, specific surface area and particle morphologies were practically identical. From this we assumed, that the difference in the photoactivity stems from the differences in the chemical state of the doping metal. Therefore we embarked on measurements (including XAFS) to

elucidate the local structure of iron in these samples, X-Ray Absorption Spectra were taken at the beamline I811,MAX II, MaxLab, Lund. The measurements were taken in fluorescence mode, on the iron K-edge.

The pre-edge spectra of the samples in both series show a small octahedral distortion around the iron. The XANES spectra show a significant variation with the increasing iron content in the S series. The main peak at *ca.* 7130 eV gradually sharpens and a shoulder appears at *ca.* 7140 eV, and another shoulder disappear at *ca.* 7200 eV with the increasing iron content. The shoulder at 7140 eV belongs to a forbidden transition in symmetrical geometries, so we can say that the distortion increases with the increasing iron-content. Within the L series, no such variation is seen, therefore there is no change in the distortion.

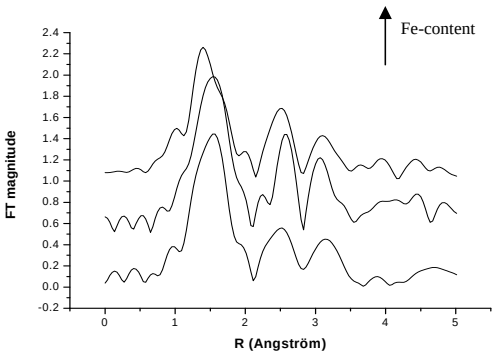

Figure1. Pseudo-radial distribution function of the S series

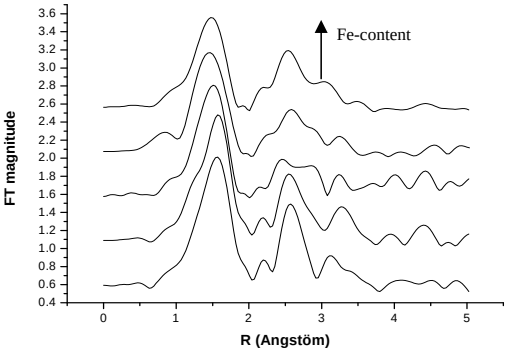

Figure 2. Pseudo-radial distribution functions of the L series

The evaluation of the EXAFS data was made by the EXAFSPAK programme. During the analysis spline Victoreen constants were used and the Fourier-transformation was taken between 2.5-14 $Å^{-1}$ without phase correction. Figures 1 and 2 show the pseudo-radial distribution functions for the two series. The second and the third coordination shells are qualitatively different in the two series. Moreover, in the S series the second coordination shell systematically changes with the Fe-content. This can explain why the photocatalytic activity go through a maximum with the increasing iron-content. After modelling the structures we can say that the local structure of the L series is much more regular, than the structure of the S one. In the S series there is a remarkable difference between the structure of the highly concentrated samples and the low concentrated ones. Mössbauer and X-ray photoelectron spectroscopic measurements further confirm the differences existing between the microenvironment of iron within the L- and S-series, corroborating the results from the XAFS measurements.

Based on these results, a clear relationship exists between the local structure of the Fe(III) and the photocatalytic activity of TiO_2 photocatlysts. These results make it possible to optimize the preparative ways of photocatalysts that are able to efficiently utilize the visible region of the solar light for heterogeneous photocatalysis.

[1] A. Fujishima, K. Honda, *Nature*, **238,** 37-38 (1972)
[2] A. Fujishima, T. N. Rao, D. Tryk, *J. Photochem. Photobiol. C: Photochem. Rew.*, **1,** 1-21 (2000)
[3] B. Oregan, M. Grëtzel, *Nature*, **353,** 737-739 (1991)
[4] W. Wang, B. Gu, L. Liang, W. A. Hamilton, D. J. Weselowski, *J. Phys. Chem., B.*, **108,** 14789-14792 (2004)
[5] Z. Ambrus, N. Balázs, T. Alapi, G. Wittman, P. Sipos, A. Dombi, K. Mogyorósi, *Appl. Catal. B: Environmental*, **81,** 27-36 (2008)
[6] a.) N. Balázs, D. Srankó, K. Mogyorósi, T. Alapi, A. Pallagi, A. Dombi, A. Oszkó, P. Sipos, *Appl. Catal. B: Environmental*, **84**, 356-362 (2008); b.) N. Balázs, D. F. Srankó, A. Dombi, P. Sipos, K. Mogyorósi, *Appl. Catal. B: Environmental*, in press, DOI: 10.1016/j.apcatb.2010.03.006; c.) K. Mogyorósi, N. Balázs, D.F. Srankó, E. Tombácz, I. Dékány, A. Oszkó, P. Sipos, A. Dombi, *Appl. Catal. B: Environmental*, in press, DOI: 10.1016/j.apcatb.2010.03.007

Determination of bromine species in peat soil by means of XANES spectroscopy

Magnus Bergknut[1], Katarina Norén[2] and Ulf Skyllberg[3]

[1]*Chemistry Dept., Umeå University, 90183 Umeå, Sweden*
[2]*MAX-lab, Lund University, P-O Box 118, 22100 Lund, Sweden*
[3]*Dept. of Forest Ecology and Management, Swedish University of Agricultural Sciences, 90183 Umeå, Sweden*

Background

The last decade it has been recognized that halogens (Cl, Br) are naturally incorporated into natural organic matter (NOM) in soils, sediments and surface waters. Some of the halogens may be released into the environments, and subsequently incorporated into NOM, as organic pollutants (chlorinated and brominated hydrocarbons), but the by far most quantitatively, important source of halogens are Cl^- and Br^- ions spread as sea salt spray or released as weathering products from minerals. Experiments with ^{36}Cl tracer in soil suggests that 25% of wet deposited Cl^- might be incorporated into NOM. Even if some low molecular mass (LMM) chlorinated compounds may form, such as the volatile chloroform and methyl bromide, most of the organically bound Cl and Br has been lumped together as organically bound halide. The mechanisms (abiotic and biotic) of halide incorporation into NOM are far from understood. The limited knowledge about the chemical forms of bromine incorporated into NOM severely hampers the possibility to judge the significance of Br-NOM when it comes to bioavailability, toxicity as well as its role for possible complexation of metals.

Materials and methods

Three peat soil samples from different geographic regions in Scandinavia and Br concentration of ~100 ppm: 1) Ifjord, northern Norway, 2) Falköping, Sweden and 3) Järnavik in Blekinge, Sweden, were prepared for XANES measurements. The samples were freeze-dried, grounded and pressed to pellets prior to measurements. XANES spectra were collected for Br reference compounds $NaBrO_3$ (s), KBr (s), Pentabromophenol (PentaBr-Phenol), 1-Bromoadamantane (Br-Adamantane) and 11-Bromo-1-undecanol (Br-Undecanol). The Br K-edge XANES spectra were collected at the I811 beamline at MAX-lab using Si(111) double crystal monochromator in quick scan mode. The experiments were performed in fluorescence mode using PIPS detector. Each XANES spectrum represents the average of 25-40 quick scans. For background subtraction and linear combination fitting procedure the Athena software was used.

Results and discussion

The results from XANES measurements are presented in figure 1. Evaluation of the XANES spectra of the reference compounds shows that difference between inorganically and organically bound Br can be observed from the position of the adsorption edge and variations in spectral features. The position of the Br adsorption edge shifts from 13477 eV in $NaBrO_3$ (s) and KBr (s) reference compounds to 13474 eV in the three reference compounds containing organically bound Br. There is also a significant difference in spectral features between $NaBrO_3$ (s) and KBr (s), where the white line in $NaBrO_3$ (s) spectrum is stronger than in KBr (s) spectrum. The three reference compounds with organically bound Br do not exhibit as strong difference in spectral features, as can be seen between $NaBrO_3$ (s) and KBr (s). However, a slight difference in the position of the second peak can be seen in XANES spectrum between Br atoms connected to aromatic carbon (Pentabromophenol) and Br connected to aliphatic carbon (1-Bromoadamantane and 11-Bromo-1-undecanol). In order to determine speciation of Br in three peat soil samples from different geographic regions in Scandinavia: 1) Ifjord, northern Norway, 2) Falköping, Sweden and 3) Järnavik in Blekinge, Sweden, a linear combination fitting (LCF) procedure was applied, using spectra of reference compounds. The results show that Br is predominately organically bound in all three soil samples. The LCF analysis also indicates that distinction can be made between aliphatic and aromatic Br species, and that the aromatic Br species predominates in the soil samples studied.

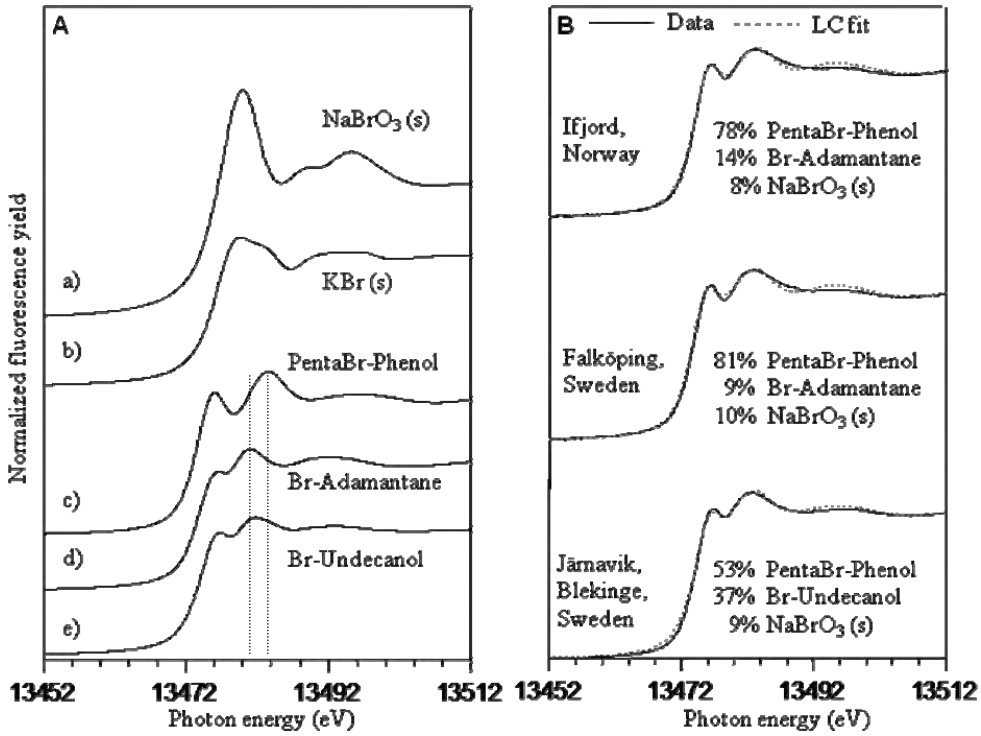

Figure 1. Br K-edge XANES data for A) reference compounds and B) pit soil samples with results from linear combination fitting. PentaBr-Phenol (Pentabromophenol), Br-Adamantane (1-Bromoadamantane) and Br-Undecanol (11-Bromo-1-undecanol).

References

Leri, A.C. 2006. Quantitative determination of absolute organohalogen concentrations in environmental samples by X-ray absorption spectroscopy. *Anal. Chem*. 78, 5711-5718.

Bergknut, M. et al. 2008. Molecular characterization of brominated persistant pollutants using X-ray absorption fin structure (EXAFS) spectroscopy. *Anal. Bioanal. Chem*. 390, 921-928.

X-Ray Absorption Study of the $BaAl_2O_4:Eu^{2+},R^{3+}$ Persistent Luminescence Materials

Hermi F. Brito[1], Maria C.F.C. Felinto[2], Jorma Hölsä[3,4], Taneli Laamanen[3,5], Mika Lastusaari[3,4], Marja Malkamäki[3,5], Lucas C.V. Rodrigues[1,3], Roberval Stefani[1]

[1] Universidade de São Paulo, Instituto de Química, Departamento de Química Fundamental, Av. Prof. Lineu Prestes, 748, CEP 05508-900, São Paulo-SP, Brazil
[2] Instituto de Pesquisas Energéticas e Nucleares, Centro de Química e Meio Ambiente, Av. Prof. Lineu Prestes, 2242, São Paulo-SP, Brazil
[3] University of Turku, Department of Chemistry, FI-20014 Turku, Finland
[4] Turku University Centre for Materials and Surfaces (MatSurf), Turku, Finland
[5] Graduate School of Materials Research (GSMR), Turku, Finland

Persistent luminescence materials emit light usually for several hours after the removal of the irradiation source. This phenomenon can be exploited *e.g.* in medical diagnostics, radiation detection, temperature sensing and in luminous paints in applications like self-lit signalization. At present, the Eu^{2+} doped alkaline earth aluminates $MAl_2O_4:Eu^{2+}$ (M: Ca, Sr, Ba) are among the most important persistent phosphors, especially because their persistent luminescence can be greatly enhanced by co-doping with selected R^{3+} (R: rare earth) ions as Dy^{3+} and Nd^{3+}. These phosphors remain visible to a naked eye for more than 10 h in the dark after the exposure to irradiation [1]. The $BaAl_2O_4:Eu^{2+},R^{3+}$ materials have also a special property that europium can be reduced without the use of a reducing atmosphere [2,3] thus facilitating the preparation. In these materials, the Eu^{2+} ion is the luminescent center whereas the role of the co-doping R^{3+} ions as well as that of other lattice defects is still not certain. The existence of the different $R^{2+}/R^{3+}/R^{IV}$ ions needs to be studied to clarify the mechanism of persistent luminescence as they may act as electron or hole traps or create lattice defects due to charge compensation [4].

In this work, the valences of selected rare earth dopants (Eu^{2+}; Ce^{3+}, Nd^{3+}, Dy^{3+}, and Yb^{3+}) in $BaAl_2O_4:Eu^{2+},R^{3+}$ persistent luminescence materials prepared both by combustion and solid state syntheses without the use of a reducing atmosphere were studied by room temperature XANES measurements using the beamline I811 at MAX-lab (Lund, Sweden). The measurements were carried out in the fluorescence mode using a 7 element Gresham Si(Li) detector.

Provided that the preparation, usually with a reducing atmosphere, has been successful, the aluminate based persistent luminescence materials can be assumed to be virtually free from Eu^{3+} due to the low dopant concentration and lack of a sufficiently large trivalent host cation. If any of these conditions are not fulfilled, there might be Eu^{3+} present. XANES spectroscopy was applied to the $BaAl_2O_4:Eu^{2+},Dy^{3+}$ phosphors, since in most cases probing Eu^{3+} in these matrices is not successful with the conventional luminescence techniques. The XANES results indicated the co-existence of both the di- and trivalent europium for the materials made with both preparation methods (Fig.). However, the trivalent form is by far the more dominant one. This may be due to several factors. First, during the preparation, the reduction of Eu^{3+} is not complete. Second, according to the proposed mechanism for persistent luminescence [*e.g.* 4], the creation of Eu^{3+} or a Eu^{2+}-h^+ (hole) pair is compulsory as a result of the escape of an electron from Eu^{2+} to the conduction band during the charging stage of persistent luminescence. Finally, the oxidation of Eu^{2+} by the X-rays should be considered. The first choice can be ruled out, since the sharp lines

attributed to the intraconfigurational $4f^7$ transitions of Eu^{3+} have not been observed either in the synchrotron radiation or UV excited emission spectra [5]. Moreover, the materials work very well as green persistent luminescence phosphors contradicting the dominance of Eu^{3+} over Eu^{2+}. The presence of Eu^{3+} is thus due to either the oxidation by X-rays or to the persistent luminescence mechanism. The former should be irreversible whereas the latter is reversible and thus they should be easily identified. Further work is in progress to clarify this matter.

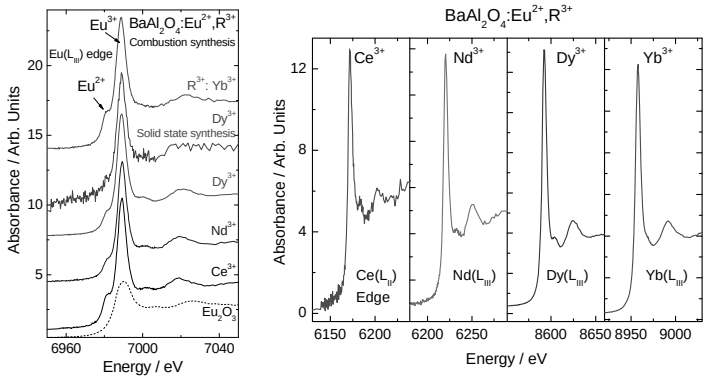

Figure. XANES spectra of the L_{III} edges of Eu, Ce (L_{II}), Nd, Dy and Yb in $BaAl_2O_4:Eu^{2+},R^{3+}$.

The co-dopants were observed to be in the trivalent form (Fig.). This is in agreement with the $Sr_2MgSi_2O_7:Eu^{2+},R^{3+}$ [6] and $CaAl_2O_4:Eu^{2+},R^{3+}$ [7] series, though the possibility of a trace amount of Ce^{IV} could not be ruled out for $Sr_2MgSi_2O_7:Eu^{2+},Ce^{3+}$.

Unfortunately, during our latest (May 2009) beamtime at the I811 we experienced difficulties with the monochromator and the cryostat. Nevertheless, measurements were also made for $SrAl_2O_4:Eu^{2+},R^{3+}$ and $HfO_2:Eu^{3+}$ materials. The data treatment and analysis is currently in progress. The results will be published promptly in appropriate international journals when additional measurements have been carried out.

Acknowledgments: The help of Dr. Katarina Norén and Dr. Stefan Carlson (MAX-lab) during the measurements is gratefully acknowledged. This work was supported by the European Community Research Infrastructure Action under the FP6 "Structuring the European Research Area" Programme (through the Integrated Infrastructure Initiative "Integrating Activity on Synchrotron and Free Electron Laser Science").

References:

1. Aitasalo, T., Hölsä, J., Jungner, H., Lastusaari, M., and Niittykoski, J., *J. Phys. Chem. B* **110** (2006) 4589.
2. Hölsä, J., Laamanen, T., Lastusaari, M., Malkamäki, M., and Novák, P., *J. Lumin.* **129** (2009) 1606.
3. Jia, W.Y., Yuan, H.B., Lu, L.Z., Liu, H.M., and Yen, W.M., *J. Cryst. Growth* **200** (1999) 179.
4. Hölsä, J., *ECS Interface* **18** 4(2009) 42.
5. Stefani, R., Rodrigues, L.C.V., Carvalho, C.A.A., Felinto, M.C.F.C, Brito, H.F., Lastusaari, M., and Hölsä, J., *Opt. Mater.* **31** (2009) 1815.
6. Carlson, S., Hölsä, J., Laamanen, T., Lastusaari, M., Malkamäki, M., Niittykoski, J., and Valtonen, R., *Opt. Mater.* **31** (2009) 1877.
7. Hölsä, J., Laamanen, T., Lastusaari, M., Malkamäki, M., Welter, E., and Zajac, D.A., *Spectrochim. Acta B* (2010), in press.

Reciprocal-space mapping at Beamline I811

C. Gundlach, K. Norén, S. Carlson.

MAX-Lab, Lund University, P.O. Box 118, SE-22100, Lund, Sweden

Beamline I811 has installed a new hybrid-pixel area detector on the surface-science dedicated diffractometer, and here we present preliminary results showing the capability for reciprocal-space mapping x-ray diffraction experiments.

The diffractometer and detector system

The x-ray diffraction station is based on a multipurpose diffractometer (Newport N6050-G+K), operated in a vertical 3D + 2S configuration [1]. That is, there are two rotation axes for sample orientation, and three rotation axes for the detector position. The sample surface normal is oriented in the horizontal or vertical plane by the use of a hexapod system (Physik Instrumente GmbH). The primary x-ray beam is transmitted through a ~2 m long beam collimation system and monitored by an ion chamber detector, and finally conditioned by an automatic filter unit (Fig. 1). A motorized slit system before the detector is used to remove unwanted background.

The detector system consists of a hybrid-pixel area detector (Pilatus 100K, Dectris Ltd.) mounted 1200 mm from the sample. The total detector area of 33.5 x 88.5 mm^2 is composed of 195 x 487 pixels. Each detector pixel is 172 x 172 μm^2, corresponding to an angular opening of 0.0082° x 0.0082° (0.8° x 2° for the total area). Each pixel also constitutes a photon counting detector with an energy resolution of 500 eV. The dynamical range is 20 bit and the maximum count rate is 10^6 photons/s. Very fast exposure series of up to a 300 Hz frame rate is possible (minimum readout time is 2.7 ms). In normal operation, the electronic shutter in the detector is used for exposure control. For radiation sensitive samples, a mechanical fast shutter system is available. The detector is controlled by special server software (CamServer, Dectris Ltd.), which communicates with a user interface written as scripts in MATLAB [2]. These scripts communicate in turn with SPEC that controls the diffractometer movements and all other beamline motors. To achieve a seamless implementation with SPEC, all MATLAB detector scripts are currently being migrated to the Python scripting language.

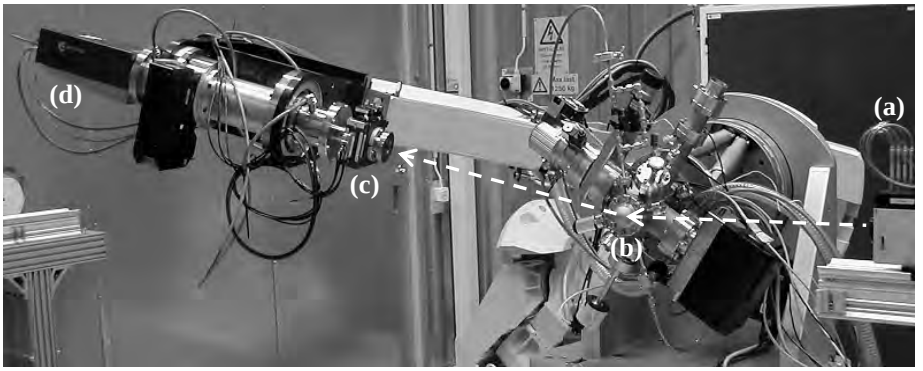

Figure 1. The diffractometer in operation. (a) Filter unit for the primary beam. (b) Sample in a Be-domed reactor chamber. (c) Slit system for the diffracted or reflected beam. (d) The Pilatus detector.

Reciprocal-space mapping

Scanning the reciprocal (*h*, *k*, *l*) space has traditionally been done along specific [*h*, *k*, *l*] directions, *e.g.* keeping *h* and *k* constant and scanning along *l* with a point detector. Combining a fast area detector like the Pilatus 100K with the diffractometer, it is possible to image 2D area slices in the reciprocal space. These 2D slices can be combined into a complete 3D reciprocal-space map, or the reciprocal space can be mapped around a given Bragg reflection by rotating the sample.

A set of MATLAB scripts, based on scripts provided by the MS beamline at the SLS [2], transforms each detector pixel coordinate into a reciprocal-space coordinate by using the angular information from the diffractometer. Due to the high dynamic range (20 bit) of the detector, it is possible to study weak diffuse scattering around intense diffraction peaks or crystal truncation rods. This method has been demonstrated at SLS in a study of GaAs nanowires [3]. The dynamical range can be extended by the use of calibrated beam attenuation filters before the sample.

At beamline I811, we have investigated a palladium crystal surface and mapped the reciprocal space around different crystal truncation rods and Bragg peaks. These measurements were made as part of the initial diffractometer/detector tests for surface catalysis experiments. In Figure 2, two slices from the 3D reciprocal space mapping around the Pd [110] Bragg peak with constant *h* value of 1.00 and 1.01 are shown. They are indicative of the level of detail that can be obtained in reciprocal-space mapping experiments. Once the 3D data set has been measured, slices or lines along any direction through the 3D map can be made, giving a complete description on Bragg peaks and the surrounding weak diffuse scattering.

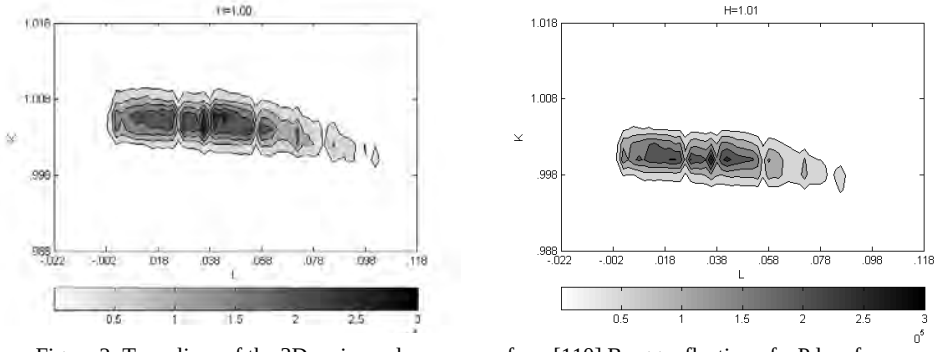

Figure 2: Two slices of the 3D reciprocal space map for a [110] Bragg reflection of a Pd surface.

Beamline I811 was funded by grants from the Swedish Research Council and Knut och Alice Wallenbergs Stiftelse. We are grateful to many people in the MAX-lab workshop, whose expertise made the installation of the detector system possible. The palladium sample was kindly provided by the group of E. Lundgren, Lund University.

[1] E. Vlieg, *J. Appl. Crystallogr.* **31**, 198-203 (1998).
[2] P.R. Willmott, R. Herger, C.M. Schleputz, S.A. Pauli, and D. Martoccia, Matlab function reference manual for the PILATUS pixel detector, Materials Science beamline, Swiss Light Source (2008).
[3] S. O. Mariager et al., *Physica status solidi A* **206**, 1771-1774 (2009).

Trace metal speciation in aquatic systems and soils

Jon Petter Gustafsson[1], Carin Sjöstedt[1], Ingmar Persson[2], and Dan Berggren Kleja[3]

[1]*Department of Land and Water Resources Engineering, KTH, Teknikringen 76, 100 44 Stockholm, Sweden*
[2]*Department of Chemistry, SLU, Box 7001, 750 07 Uppsala, Sweden*
[3]*Department of Soil and Environment, SLU, Box 7014, 750 07 Uppsala, Sweden*

Iron speciation in natural waters

The geochemical cycling of iron is important for the speciation of trace metals such as copper and lead, due to its large reactivity. Iron in the form of colloidal iron(III) (hydr)oxides may bind trace metals as surface complexes. Moreover, iron(III) competes strongly for coordination sites of natural organic matter (NOM) in waters.

In previous research we showed that iron(III) forms mononuclear complexes with NOM in pure fulvic acid solutions at pH 2 and pH 4 (van Schaik et al., 2008), although it undergoes reduction to iron(II) with time. In solid-phase NOM however, EXAFS spectra often show the presence of Fe···Fe distances, which have been interpreted as organically complexed di- and trimeric iron(III) species (c.f. van Schaik et al., 2008).

In the present project iron speciation of mildly acidic lake water samples is being studied at beamline I811. During the 2009 beamtime we analysed soils, aquatic colloids and particles. EXAFS spectra on these samples were recorded using a Si[111] double crystal monochromator at the iron K-edge. The experiments were performed in fluorescence mode using a Lytle detector with a manganese filter at ambient temperature.

So far results have been obtained for Lake Trehörningen (Tyresta National Park, county of Stockholm, Sweden) and for organic soils from the surrounding area. The results show that the samples are dominated by iron(III) (octahedral Fe(III)-O coordination in the first shell at ≈ 2.0 Å) (Sjöstedt et al., in prep.). Aquatic colloids and most soils are dominated by iron(III)-organic complexes; the EXAFS spectra usually had Fe···C single scattering and Fe-O-C three-leg scattering at 2.95 and 3.1 Å respectively, similar as was found for pure systems with fulvic acid (van Schaik et al., 2008). No clear evidence for Fe···Fe distances were found, suggesting a predominance of mononuclear iron(III)-organic complexes in these colloids. However, some soil samples and aquatic particles also contained ferrihydrite, as evidenced by Fe···Fe distances typical for this kind of mineral.

Future studies include (i) iron speciation in aquatic colloids and particles from other lakes, (ii) a more detailed study on the iron speciation in biofilms, which are believed to be important for the biogeochemical cycling of iron in lakes. PhD students Carin Sjöstedt and Satomi Shibutani are carrying out most of this work.

Vanadium chemistry in slags and in soils

Vanadium is elevated in steel slags that are used for road construction and soil improvement. The aim of our work is to determine the oxidation state of bound vanadium in soils and slags and, if possible, determine the structure of formed surface complexes.

For the vanadium oxidation states III, IV and V there are characteristic differences in the pre-edge region of XANES spectra. This allows for discrimination of oxidation states and symmetry, also in mixtures.

During our beamtime 2009 we performed initial tests on the use of vanadium K-edge XANES spectroscopy. XANES spectra were obtained in fluorescence mode for a number of

standards at MAX-Lab, Sweden, using Si[111] monochromator crystals (see image below). The XANES spectra were acquired from 5360 to 5660 eV in fluorescence mode with a 0.5 or 1 eV step size over most of the spectrum but with a smaller 0.2 eV step size in the pre-edge and main absorption edge region from 5450 to 5510 eV. The spectra were energy-calibrated (with vanadium foil), normalized, background-corrected, and merged using standard methods. The Athena software was used to deconvolute the pre-edge peak into a series of Gaussian peaks that allowed calculation of peak areas and intensities.

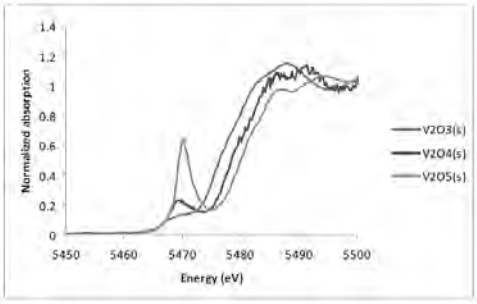

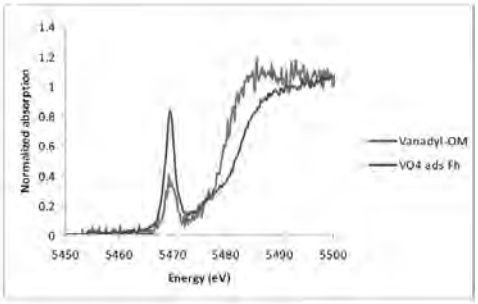

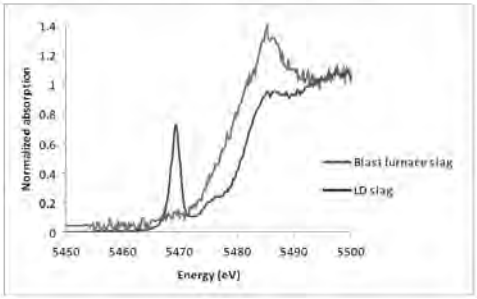

	Ox. state	Peak height	Height/area ratio
V_2O_3(s)	III	0.087	0.18
V_2O_4(s)	IV	0.20	0.21
Vanadyl-OM	IV	0.32	0.38
V_2O_5(s)	V	0.60	0.30
VO_4 ads Fh	V	0.75	0.42
Blast furnace slag		0.049	0.20
LD slag		0.69	0.43

The results show, as expected, that vanadium(V) have the largest pre-edge peak intensities, but with different peak shapes depending on whether V(V) is octahedral (as in V_2O_5(s), with a peak area/height ratio of 0.3), or tetrahedral (as in vanadate-sorbed ferrihydrite, having a peak area/height ratio of 0.42). Vanadium(IV) has intermediate peak intensities, but again with symmetry-dependent shapes, and vanadium(III) has the smallest peaks (c.f. Chaurand et al., 2007). As part of this preliminary investigation, we studied the V speciation in two types of metallurgical slag, LD slag and blast furnace slag, which are two common sources of local vanadium contamination in soils. The blast furnace slag, which is produced in a reduced environment, appears to be dominated by vanadium(III), probably with some contribution from even lower V oxidation states. On the other hand, LD slag, which is produced at a later stage of the steel-making process after addition of vanadate salts, contains vanadium that to about 90 % consists of tetrahedral vanadium(V).

EXAFS spectra are not possible to acquire with the present setup (because of significant glitches beyond 5660 eV). Future studies with soils and reference sorbents will therefore in part be performed at other synchrotron facilities.

References

Chaurand, P., Rose, J., Briois, V. et al.. New methodological approach for the vanadium K-edge X-ray absorption near-edge structure interpretation : Application to the speciation of vanadium in oxide phases from steel slag. J. Phys. Chem. 111, 5101, 2007.

J.W.J. van Schaik, I. Persson, D.B. Kleja, and J.P. Gustafsson, EXAFS study on the reactions between iron and fulvic acid in acid aqueous solutions, Environ. Sci. Technol., 42, 2367, 2008.

XANES on Al_2O_3-, SiO_2- and TiO_2-supported Fe-V-oxide catalysts

Robert Häggblad, Mariano Massa and Arne Andersson

Dept. of Chemical Engineering, Lund University, Chemical Center, P.O. Box 124, SE-221 00 Lund

Industrial production of formaldehyde by means of methanol oxidation is carried out over a $MoO_3/Fe_2(MoO_4)_3$ catalyst in the so-called oxide process. In many aspects the catalyst is superb, showing very high selectivity (>93%) at high conversion. However, in operation the molybdenum is volatile, limiting the lifetime of the catalyst [1]. Consequently, alternative more stable catalysts are of interest provided they give comparable selectivity to formaldehyde. Vanadium based catalysts are selective [2,3], but since vanadia is toxic low volatility is necessary not only to improve the lifetime of the catalyst but also to limit the spread of vanadia in the plant and into the nature. In the present study we have prepared dispersed Fe-V-oxide catalysts supported on low surface area α-Al_2O_3, SiO_2 and TiO_2 (anatase and rutile) and compared the catalyst with bulk phase $FeVO_4$ regarding catalytic and structural aspects as well as the resistance towards volatilization of vanadium [4].

For each support, three catalysts were prepared with loads of active metals (Fe:V = 1:1) corresponding to 0.5, 1, 5 theoretical monolayers [5], respectively, using incipient wetness impregnation. The impregnated supports were dried and calcined in air for 6 hours at 580°C. The short notations used in this study, e.g. 5FeVTi, stand for the number of theoretical oxide layers and the type of cations (FeV) and support (Ti = TiO_2, Al = Al_2O_3, Si = SiO_2). To obtain structural information about valence and coordination state of vanadium and iron, XANES measurements were performed at beamline I811 on the catalysts as prepared (denoted fresh) as well as after 16 hours use in methanol oxidation at 300°C with a feed consisting of 10% methanol and 10% O_2 in inert gas (denoted used). Besides the XANES characterizations, complementary XRD and XPS measurements were performed, providing information about the formation of crystalline phases (XRD) and the dispersion and valences of V and Fe (XPS) in the near-surface region (XPS). In Ref. [4] the complete characterization of the catalysts and the catalytic performances are presented.

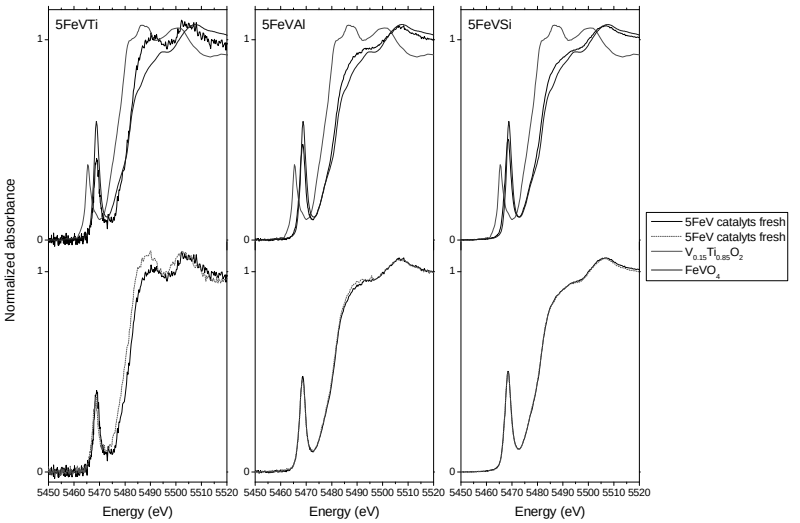

Fig. 1. V K-edge XANES spectra of the fresh and used 5FeV-samples (bottom) and the fresh FeV-samples together with the references $V_{0.15}Ti_{0.85}O_2$ and $FeVO_4$.

In Fig. 1 the V *K*-edge spectra of the fresh FeV catalysts are compared with the corresponding used catalysts (bottom), triclinic $FeVO_4$ (V tetrahedral) and rutile type $V_{0.15}(IV)Ti_{0.85}O_2$ (V octahedral). The main edge positions for the fresh 5FeVTi, 5FeVAl and 5FeVSi are 5481.7, 5481.3 and 5481.3 eV, respectively, and for the $V_{0.15}(IV)Ti_{0.85}O_2$, V_2O_5 (not shown) and $FeVO_4$ reference compounds they are 5476.8, 5480.0 and 5481.5 eV, respectively, revealing that vanadium is pentavalent in all fresh catalysts. After use in methanol oxidation the edge position for 5FeVTi has shifted 1.7 eV towards lower energy, showing some reduction of vanadium. However, the reduction observed by XANES is not seen in XPS. In contrast to XANES, XPS is more surface-sensitive, and therefore the results suggest that the reduced vanadium is from the bulk. Possibly, during the reaction some V^{4+} is formed, dissolving in the TiO_2 rutile phase to form $V_x(IV)Ti_{1-x}O_2$. Reduction of the vanadium is observed for neither 5FeVAl nor 5FeVSi after use in methanol oxidation.

Considering both the pre-edge intensity and the post-edge feature, the V *K*-edge spectrum for 5FeVTi clearly resembles that for $V_{0.15}(IV)Ti_{0.85}O_2$ suggesting a high degree of octahedrally coordinated vanadium to be present on 5FeVTi. However, an even better resemblance is obtained combining 70% of the $V_x(IV)Ti_{1-x}O_2$ spectrum and 30% of the $FeVO_4$ spectrum revealing the presence of also tetrahedrally coordinated vanadium on the surface. For both 5FeVAl and 5FeVSi the obvious resemblance of spectral feature to $FeVO_4$ reveals that most vanadium is tetrahedrally coordinated. In the former sample, the V reacts with Fe and the support forming a $(Fe_xAl_{1-x})VO_4$ surface structure [3,4] whereas in the latter sample the combination of poor dispersion [4] and the resemblance to $FeVO_4$ reveals that $FeVO_4$ crystallites is formed rather than dispersed Fe-V-oxide on the SiO_2 surface.

In Fig. 2 are displayed the Fe *K*-edge spectra for the fresh 5FeVTi, 5FeVAl and 5FeVSi catalysts and the references $FeVO_4$ and α-Fe_2O_3.

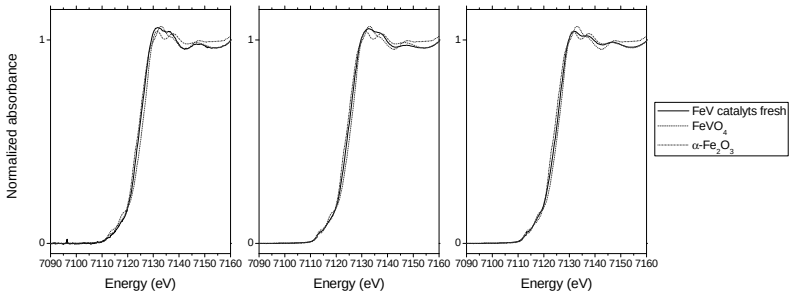

Fig. 2. Fe K-edge XANES spectra of the fresh 5FeV-samples and the references $FeVO_4$ and α-Fe_2O_3.

According to the XPS quantifications, the dispersion of Fe is poor on all the supports [4]. Instead, Fe-oxide particles are formed, which is confirmed by the strong resemblance of the Fe *K*-edge spectra for the 5FeV catalysts to that of α-Fe_2O_3 and $FeVO_4$. On 5FeVSi also the V dispersion is poor, explaining the fact that this sample is most like $FeVO_4$. No reduction of the Fe was observed after 16 h use in methanol oxidation for any sample.

[1] A. Andersson, M. Hernelind, O. Augustsson, Catal. Today 112 (2006) 40.
[2] L.E. Briand, J-M. Jehng, L. Cornaglia, A.M. Hirt, I.E. Wachs, Catal. Today 78 (2003) 257.
[3] R. Häggblad, J.B. Wagner, S. Hansen, A. Andersson, J. Catal. 258 (2008) 345.
[4] R. Häggblad, M. Massa, A, Andersson, J. Catal. 266 (2009) 218.
[5] P.-O. Larsson, A. Andersson, L.R. Wallenberg, B. Svensson, J. Catal. 163 (1996) 279.

EXAFS Study of the Structural Mechanism for Negative Thermal Expansion in MOF-5

N. Lock[1], M. K. Thomsen[1], M. Christensen[1], K. Norén[2], C. J. Kepert[3], B. B. Iversen[1]

[1]*Dept. of Chemistry and iNANO, Aarhus University, 8000 Aarhus C, Denmark*
[2]*MAX-lab, Lund University, SE-221 00 Lund , Sweden*
[3]*School of Chemistry, The University of Sydney, NSW-2006, Australia*

The majority of solids expand with heating, a property known as positive thermal expansion (PTE). Excitement has arisen with the discovery of a small number of oxide- and cyanide-based materials that display negative thermal expansion (NTE) due to transverse vibrations within their lattices. Notable examples in these classes include ZrW_2O_8 ($\alpha_\ell = d\ell/\ell dT = -9.1\times10^{-6}$ K^{-1})[1] and $Cd(CN)_2$ ($\alpha_\ell = -34\times10^{-6}$ K^{-1})[2]. The combination of NTE and PTE materials has potential applications in the generation of zero thermal expansion materials, which are sought after for a multitude of engineering purposes including fibre optic systems, electronics componentry, dental fillings, and oven-to-table cookware.
In the past years NTE has been discovered in a small number of metal-organic framework materials (MOFs). These materials are unique in being molecular in nature and having multiple-atom linkages rather than single- (M-O-M') or double-atom (M-CN-M') linkages within the structure. Whilst the NTE mechanism in the relatively simple metal cyanide frameworks is now well understood to involve the transverse vibration of the M-CN-M' linkages[3], the first experimental studies on the NTE mechanisms for the structurally more complicated MOFs have just recently been reported.[4,5]

We have performed EXAFS measurements at the MAX II synchrotron in Lund, Sweden, at the beamline I811 to complement powder and single crystal diffraction experiments in the investigation of nature of the isotropic NTE mechanism of the archetype cubic metal-organic framework $Zn_4O(BDC)_3$ (BDC=1,4-benzenedicarboxylate). This compound is also known as MOF-5 and as IRMOF-1 (Figure 1) and has previously mainly been investigated due to its gas sorption proporties. Multitemperature synchrotron powder X-ray diffraction data for MOF-5 reveal almost linear unit cell contraction in the temperature range 80-500 K with $\alpha_\ell = -12\times10^{-6}$ K^{-1}.[6]

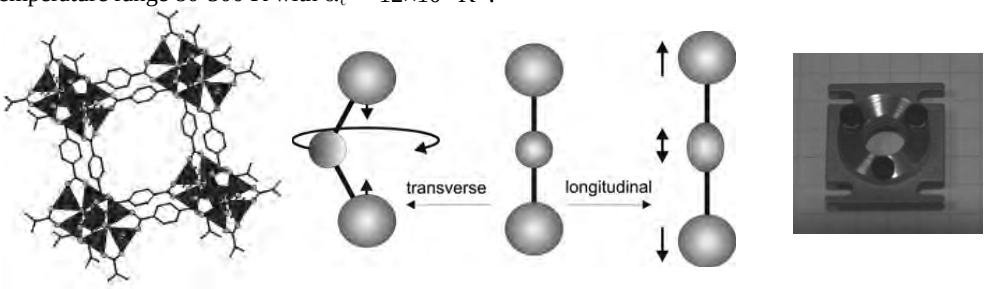

Figure 1. *(Left)* The structure of cubic MOF-5. Tetranuclear zinc clusters are linked by 1,4-benzenedicarboxylate. *(Middle)* A transverse vibration results in a decrease of the distance between next-nearest neighbour atoms, even though the distance between nearest neighbour atoms increases. *(Right)* Sample holder developed for data collection on moisture sensitive MOF-5 in the liquid nitrogen cooled cryostat at I811.

Phase pure single crystals of MOF-5 were prepared from $Zn(NO_3)_2{\cdot}4H_2O$ and 1,4-benzenedicarboxylic acid in diethylformamide (DEF) at 100°C. Subsequent replacement of DEF with 1) dimethyl-formamide and 2) chloroform allowed evacuation of solvent molecules from the crystal pores. After evacuating the crystals under dynamic vacuum for 24 hours, the sample was ground into a powder under inert atmosphere. A sample holder using Kapton windows was made at Aarhus University to enable data collection on moisture sensitive MOF-5 (Figure 1). Its cross-section has a 7.0 mm

diameter and may contain powder with a thickness of 1.5 mm. The sample was packed in an argon filled glove box and was attached to the center stick of the cryostat. EXAFS data were collected in the Zn *K*-edge in transmission mode on MOF-5 in 50 K intervals from 100-300 K using a liquid nitrogen cooled cryostat. An average of three scans were collected at each temperature setting. The Athena software was used to merge data, which were subsequently refined using the WinXAS program. Data in *k*-space and *R*-space for the two inner coordination shells of MOF-5 at 100 K are shown in Figure 2.

Our single crystal diffraction data indicate an apparent near-linear shortening of the Zn-O2 bond with temperature in the full data covered data range from 100-500 K. Furthermore, the diffraction data suggest a small decrease of the O1-Zn-O2 angle with increasing temperature. The apparent bond decrease appears unphysical, as the mean bond lengths are expected to increase with temperature due to the anharmonic nature of the chemical bond potential. However, the temperature dependent bond lengths decrease is a result of positional averaging inherent to Bragg scattering. The apparent nearest-neighbour bond distance decrease suggests preferential population of vibrational modes out-of-plane of the aromatic ring and of the oxygen atoms (in the carboxylate groups) which form bonds to the metal atoms. As the framework is highly porous, it is very likely to accomodate such vibrations. The EXAFS data is considered an evidence that the nearest-neighbour bond distance does not decrease linearly with temperature as suggested by diffraction data. Furthermore, the overall conclusion of the analysis of diffraction and EXAFS data point to the NTE effect being dynamic rather than static in its character.

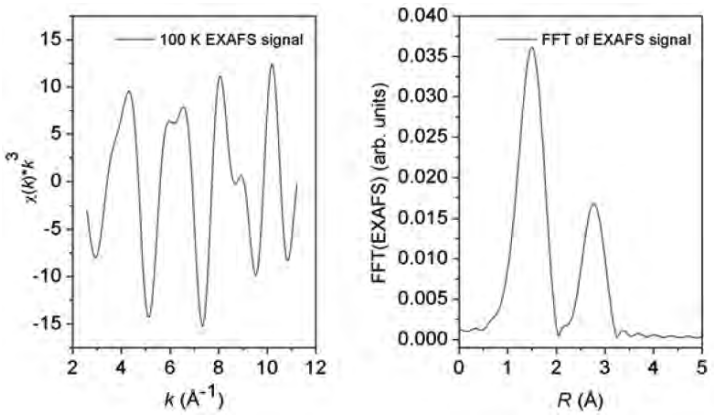

Figure 2. *(Left)* k^3-weighted EXAFS data of the first two coordination shells (100 K) and *(Right)* the corresponding Fourier transform.

Acknowledgements
We thank the Danish Natural Science Council (Danscatt program) for financial support.

References
[1] Evans, J. S. O. *Dalton Trans.* **1999**, 3317-3326. [2] Phillips, A. E.; Goodwin, A. L.; Halder, G. J.; Southon, P. D.; Kepert, C. J. *Angew. Chem. Int. Ed.* **2008,** *47*, 1396-1399. [3] Chapman, K. W.; Chupas, P. J.; Kepert, C. J. *J. Am. Chem. Soc.* **2005,** *127*, 15630-15636. [4] Wu, Y.; Kobayashi, A.; Halder, G. J.; Peterson, V. K.; Chapman, K. W.; Lock, N.; Southon, P. D.; Kepert, C. J. *Angew. Chem. Int. Ed.* **2008,** *47*, 8929-8932. [5] Peterson, V. K.; Kearley, G. J.; Wu, Y.: Ramirez-Cuesta, A. J.; Kemner, E.; Kepert, C. J.; *Angew. Chem. Int. Ed.* **2010,** *49*, 585-588. [6] Lock *et al. submitted*

XRPD and EXAFS studies of low temperature carburized stainless steel

J. Oddershede[1], T.L. Christiansen[2], K. Ståhl[3], and M.A.J. Somers[2]

[1] *Materials Research Division, Risø DTU, Frederiksborgvej 399, DK-4000 Roskilde*

[2] *Department of Mechanical Engineering, DTU, Kemitorvet, DK-2800 Lyngby*

[3] *Department of Chemistry, DTU, Kemitorvet, DK-2800 Lyngby*

Low temperature carburizing (<520°C) of stainless steel brings about a transformation of the surface into so-called carbon expanite, which is – ostensibly – a *solid solution* of large amounts of interstitial carbon in austenite (γ-Fe). This greatly improves the wear properties without compromising the corrosion resistance. Carbon expanite does not represent a thermodynamically stable state and will decompose into carbides if time and/or temperature allow diffusion of the carbon atoms. Recently, the *nitrogen expanite* interstitial system was investigated with EXAFS [1,2] and it was shown for the first time that nitrogen expanite indeed is a solid solution of nitrogen and that a strong affinity between nitrogen and chromium occurs, *i.e.* short range order of nitrogen. Hitherto, the chemical interaction and short range order between carbon and substitutional atoms in the *carbon expanite* system have not been investigated. The present instigation addresses this system.

The starting material for all the investigated samples was annealed 25 μm AISI 316 stainless steel foil. Low temperature carburizing in a vertical ceramic tube furnace in a C_2H_2-H_2 gas mixture at 420°C for 16.25 hours [3] resulted in an almost full transformation into carbon expanite, albeit a 2-3 micron core of the foil remained without carbon as evidenced by optical microscopy, *i.e.* composition and hence stress gradients were present. To obtain a controlled carbon redistribution and decomposition into carbides, carbon expanite samples were isochronally heated (20 K/min) in a Netzsch 449 thermal analyzer in an Ar-H_2 atmosphere and immediately cooled (20 K/min) upon reaching either 700°C (exp_700°C) or 1100°C (exp_1100°C). No weight loss was observed during isochronal annealing, *i.e.* retraction of carbon by formation of CH_4 did not occur. AISI 316 was also carburized in the thermal analyzer at 950°C in a CH_4-H_2 atmosphere for 100 min resulting in direct carbide formation (carb_950°C). The carbon uptake was measured to exceed the carbon concentration which is associated with chromium carbides exclusively.

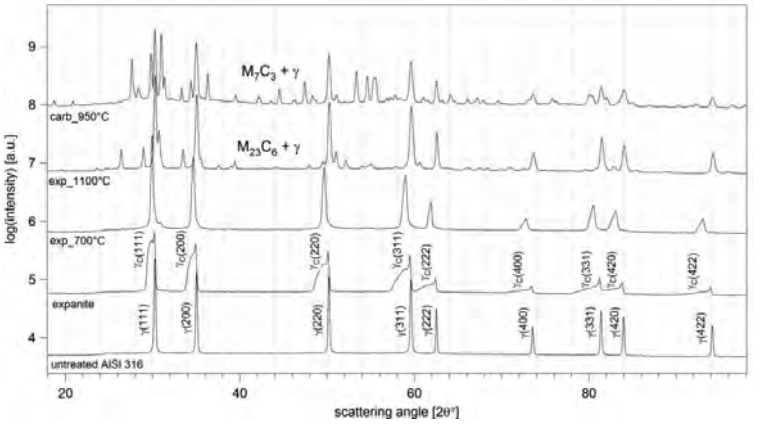

Figure 1. XRPD measured on the foils using the Huber G670 diffractometer at MAX-lab I711with λ=1.07198(1) Å.

The broad, shifted and asymmetric diffraction peaks of the expanite (Figure 1), as compared to the sharp peaks of the fully austenitic AISI 316 reference foil, confirms the presence of a lattice expansion gradient as a consequence of incorporating carbon in solid solution close to the surface, while the core of the sample contains no carbon. The exp_700°C diffractogram clearly show that carbon has been redistributed to form carbon expanite with a uniform composition. A slight indication of carbide formation may be observed on the right shoulder of the 111 peak. For exp_1100°C the combination of high resolution XRPD and Rietveld refinements could be used to show that the sample consists exclusively of $M_{23}C_6$ (M= Cr,Fe) and carbon free austenite. Likewise, carb_950°C was found to consist of M_7C_3 and carbon free austenite.

Cr, Fe and Ni K-edge EXAFS data collected in transmission mode at MAX-lab I811 were used to obtain the pseudo radial distribution functions (pRDFs) describing the average local environments of each atom type in the investigated samples. (AISI 316 contains ~19 at.% Cr and ~11 at.% Ni.) Figure 2 shows how the local environment of Cr varies significantly in the synthesized samples. The samples containing carbide where Cr resides preferentially can be compared with the carbon expanite sample. The Fe and Ni pRDFs (not shown) are very similar to the Cr pRDF of AISI 316 for all the investigated samples. This in particular means that (except for Fe in carb_950°C and perhaps exp_1100°C) only the Cr pRDFs show a significant number of M-C nearest neighbour distances (r=1.8-2.0 Å). From this it can be concluded that 1) the C atoms are in *solid solution* in carbon expanite and 2) they have a stronger affinity for Cr than for Fe and Ni, *i.e.* short range ordering (analogous to nitrogen expanite). Furthermore the results state that for the carbides formed in carb_950°C and exp_1100°C M=Cr and Fe, but not Ni. Finally the Cr pRDF of carb_950°C does not show any distances around the typical austenite interatomic distance of 4.5 Å, so practically all Cr atoms in this sample must be bound as Cr_7C_3, which is consistent with thermodynamic calculations and other characterisation techniques.

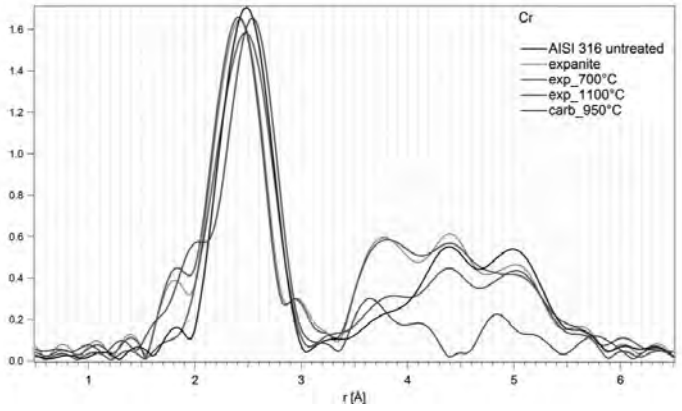

Figure 2. pRDFs showing the average environment of the Cr atoms in the foils.

[1] J. Oddershede, T.L. Christiansen, K. Ståhl, M.A.J. Somers, Journal of Materials Science 43(15) (2008) 5358-5367.
[2] J. Oddershede, T.L. Christiansen, K. Ståhl, M.A.J. Somers, Scripta Materialia, 62 (2010) 290-293.
[3] T. Christiansen, M.A.J. Somers; International patent application WO2006136166-A1 (2005).

Speciation of sulfur compounds in natural matrices using sulfur K edge XANES

Ingmar Persson

Department of Chemistry, Swedish University of Agricultural Sciences,
P.O.Box 7015, SE-750 07 Uppsala, Sweden.

I. Sulfur XANES as an analytical tool

Sulfur K edge XANES (X-ray Absorption Near Edge Structure) spectroscopy is an excellent tool to determine the speciation of sulfur compounds in complex matrices. A method to quantitatively determine the kinds of sulfur species in natural samples using internally calibrated reference spectra of model compounds has been developed. Due to significant self-absorption of formed fluorescence radiation in the sample itself the fluorescence signal displays a non-linear correlation with the sulfur content in a wide concentration range. Self-absorption is also a problem at low total absorption of the sample when the sulfur compounds are present as particles. Particles of elemental sulfur need to be smaller than 2 μm to be give a signal linear to the concentration [Morgan et al, J. Phys.: Conf. Ser. 190, 012144, 2009]. The post-edge intensity patterns of the sulfur K edge XANES spectra varies with kind of sulfur compound, with reducing sulfur compounds often having a higher post-edge intensity than the oxidized forms. Within a narrow concentration range of dilute solutions it is possible to use sulfur K edge XANES

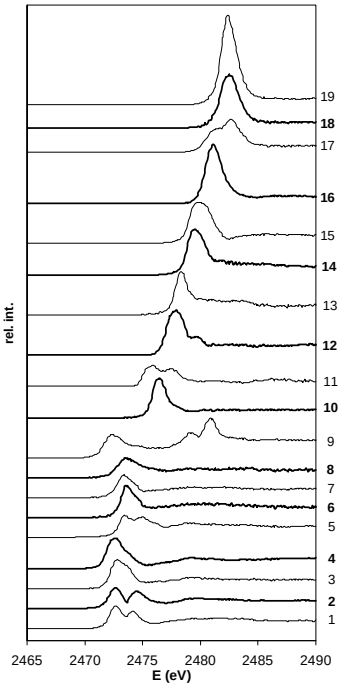

Figure 1. The individual sulfur K edge spectra of the compounds investigated. 1-L-cystine, 2-diphenyldisulfide, 3-dibenzyldisulfide, 4-elemetal sulfur, 5-diphenylsulfide, 6-L-menthionine, 7-tiosalicylic acid, 8-L-cysteine, 9-thiosulfate ion, 10-diphenylsulfoxide, 11-dimethylsulfoxide, 12-dimethylsulfite, 13-sulfite ion, 14-tetramethylenesulfon, 15- L-methionine sulfon, 16-methylsulfonate ion, 17-chondroitin sulfate ester, 18-sodium sulfate, decahydrate, 19-sulfate ion.

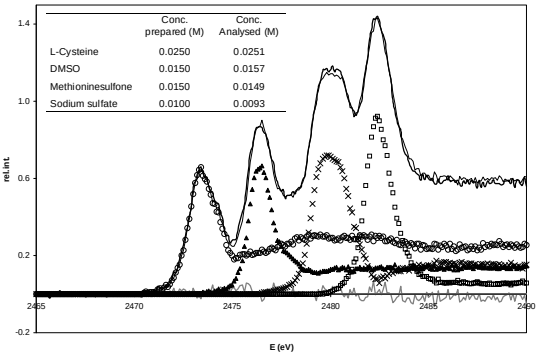

Figure 2. Sulfur Kedge spectrum of a solution containing L-cysteine, dimethylsulfoxide, L-methionine sulfone and sodium sulfate (thick line) and fitting with the individual normalized spectra of L-cysteine (○) , DMSO (▲), L-methionine sulfone (×), sodium sulfate ( ), sum of fit (thin line) and residuals (grey line). The prepared and calculated concentrations of the different species are given in the inset table.

reference data for quantitative analysis of the contribution from different species present in an unknown sample. The results show that it is of utmost importance to use an internal calibration system when performing quantitative XANES analysis. Quantitative measurements can only be performed on samples with the sulfur compounds homogenously separated in the sample at low concentrations, less than 0.3-0.5 %. Samples containing particles are very difficult to determine quantitatively due to high self-absorption in the individual particles giving a non-linear response. Sulfur K edge spectra of 19 compounds are plotted in Figure 1. A mixture of sulfur containing compounds in an aqueous solution with known concentrations is fitted by the internally calibrated spectra in Figure 1. The results are submitted for publication.

II. Sulfur speciation in preserved waterlogged archaeological wood from the Vasa

The accumulation of sulfur compounds in *Vasa* wood may be regarded as a result of both microbial activity *in situ* and diffusion of sulfate and hydrogen sulfide into the wood. A number of samples from the *Vasa* were analyzed by sulfur K-edge XANES. On the whole, the spectra were similar in appearance to previous reports: reduced organic sulfur compounds with a peak maximum at 2473 eV (thiols) and oxidized compounds at 2482 eV (sulfate). In between, from 2474 to 2483 eV, a series of different intermediates were found, generally to a minor extent. By fitting the XANES spectra of samples with spectra of calibrated standard compounds in accordance with the method presented in part I (see above) the relative concentration of the different species in the sample were estimated. In sulfur rich samples (from surface region) a satisfactory fitting of the XANES spectra is only provided by the use of both solid and dilute sulfur species. Since solid phases cannot be calibrated and thus not are included in the quantitative model (part 1), the relative concentration of the different sulfur species were not obtained. The peak position of the reduced sulfur species (2473-2474 eV) in different samples correlates with the sulfur concentration and to the iron–sulfur ratio. At a relatively higher sulfur level (1-15 mg/g) the peak position is found at lower energies, whereas it is displaced to higher energies in samples with low sulfur content (<0.1 mg/g). One explanation may be an influence from self-absorption in the sample during measurement, which is more pronounced at higher concentrations of the element studied. All samples with relatively high sulfur content showed a similar shape of the peak at 2473 eV irrespective of concentration and the extent of oxidized sulfur species in the samples (Figure 11B). No correlation between the small variations in the reduced peak and the pronounced variability in oxidized signals were found. This indicates a well-defined and non-varying composition of the sulfur species giving the spectral pattern at 2472-73 eV. Sulfur rich Vasa samples were subjected to extraction experiments by different solvents. The results show that both reduced and more oxidized sulfur compounds are highly insoluble in water but also in less polar solvents (e.g. acetone, dichloromethane). As expected, sulfate was readily dissolved. The uniform shape and intensity in the region 2472 to 2477 eV before and after extraction shows that the corresponding sulfur species are incorporated into non-soluble macromolecules. Parallels to soil chemistry and speciation of sulfur in humus can be drawn. The similarities between K-edge sulfur XANES spectra of the *Vasa* wood and humus containing sulfur are apparent, indicating the importance of (poly)sulfides bound to aromatic parts in the wood (i.e. lignin). The results are prepared for publication.

III. Sulfur mineralization in arable soils

The results from this study show that the newly developed XANES data treatment method, see above, with inclusion of post-edge structure and calibration between model samples, as well as the use of diluted solutions instead of solid samples for the model compounds and thus avoiding the problem with self-adsorption, has greatly improved the possibility to achieve reliable quantitative results for contributing sulfur compounds in soil samples and soil extracts. However, the separation between some compounds requires a high signal-to-noise ratio, which is not always so easy to achieve in natural samples with a low sulfur content, so grouping the contributing model compounds into for example reduced, intermediately oxidized and highly oxidized sulfur is probably more meaningful than quantifying on a more detailed compound level.

The XANES spectroscopy of soil samples and acetylacetone extracts revealed differences in soil chemistry between soils and between treatments, but also between treatment effects on different soils. It can be concluded that further studies are needed in order to deduct what is the norm and what are the outliers when it comes to the effect on sulfur chemistry by farmyard manure application. It is possible that farmyard manure application generally shifts the sulfur chemistry to the more reduced end of the spectrum, but that the effect is masked in soils with a high S turnover rate. A conclusion of this in turn is that the sulfur turnover rate is generally determined by other factors than the chemical composition of the organic sulfur, such as microbial activity, other nutrient deficiencies, physical properties of the soil etc.. The results are submitted for publication.

Structural characterization metal complexes in applied and fundamental systems

Ingmar Persson

Department of Chemistry, Swedish University of Agricultural Sciences,
P.O.Box 7015, SE-750 07 Uppsala, Sweden.

I. Iron speciation in preserved waterlogged archaeological wood from the Vasa

The elemental distribution of iron and sulfur in the *Vasa* shows that sulfur compounds are concentrated to the surface regions of the wood whereas the iron compounds have penetrated throughout the timbers. The reported observations of degraded of wood polymers (cellulose and hemicellulose), as well as the conservation agent polyethylene glycol (PEG) show close connection to a high iron content and accumulation of low molecular organic acids, particularly below the surface region. The hypothesis put forward is that processes of oxidative degradation have been initiated by iron compounds in Fenton type of reactions. The spectroscopic studies of the *Vasa* earlier reported have emphasized on the sulfur speciation. Iron does not possess the same prosperity as sulfur concerning speciation and possible oxidation states, albeit iron has certain properties as a potential catalyst in the formation of radicals. From a general point of view the nature and properties of the two common iron oxidation states (II and III) are highly diverse. Iron(II) ions forms weaker complexes and more soluble salts compared to iron(III), which forms relative strong complexes or hydrolyses to form un-soluble hydroxides and oxides. The difference is also reflected in the Fe-O bond distance where Iron(III) has generally a shorter bond distance (~2.0 Å) whereas compared to iron(II) (~2.1 Å) irrespective of the type of oxygen donor ligand. Hence, the average iron-oxygen bond distance in a certain sample may be regarded as reflecting the relative concentration of the two oxidation states of iron *in situ*. A number of EXAFS experiments were performed on subsamples from the Vasa hull. The shapes of the EXAFS waves generally showed a decrease of the amplitude as a function of *k* indicating contribution from lighter elements in the second sphere. The data treatment points out oxygen as the dominating coordination ligand atom. The calculated average distance between iron and oxygen among the wood samples varied from 1.99 to 2.06 Å. The Fe-O bond length showed a positive correlation with the depth indicating a less oxidative condition in the interior of the wood compared to the surface where a pure iron(III) condition was observed. Iron sulfur compounds (e.g. FeS, FeS_2) known to be present to a minor extent in the *Vasa* wood did not contribute significantly in the samples investigated. The analysis of multi-scattering contributions from elements beyond the first coordination sphere indicates a significant but diffuse influence in most of the samples. It was not possible in most cases to determine the type of atom in the second scattering shell. However, carbon bound to oxygen of different functional groups, e.g. carboxylic, phenolic or ether oxygen, is probably the major contributor in the second scattering sphere in the form of a donor ligand. An experiment was carried out in which iron was extracted by water from the wood and analyzed by EXAFS (Figure 9). The results showed hydrated iron(II) (Fe-O distance: 2.11 Å) in the aqueous phase supported by the absence of multi-scattering patterns except the FeO_6 core scattering paths and by a pre-edge maximum peak position at 7111.7 eV. Apparently iron(II) ions are mobile and can diffuse in the wood matrix under wet conditions as opposed to the iron(III) ions, which are immobilized in complexes or as hydroxide compounds. Thus, below the surface the iron is present in the wood as a mixture of its two valence states. It can be concluded that the large amount of iron compounds in the *Vasa* wood is a result of diffusion of iron(II). At the salvage of the ship almost all of the over 5000 original bolts in the hull were corroded leaving the former holes empty.

II. Structure of hydrated, solvated and hydrolyzed metal ions in solution

A tetramer with the composition $[Cr_4(\mu_2\text{-}OH)_2(\mu\text{-}OH)_4(OH)_n(H_2O)_{12-n}]^{(6-n)+}$ is the predominating hydrolysis species at pH = 3.7 after two years of aging [P1]. Data from dialysis, ultrafiltration and centrifugation studies indicates that n reaches the value of three at pH=3.7. The transition between different species took place in a narrow pH range, less than one pH unit, as determined by retention and UV-vis spectrophotometry, supports that several hydroxide ions bound are in the terminal positions giving a relative low charge of the complex. The tetramer has one double and four single hydroxo bridges with Cr···Cr distances of 2.98(1) and 3.59(1) Å. The configuration around the chromium(III) ions is octahedral with a mean Cr-O bond distance of 1.97(1) Å, left Figure below.

The hydrolyzed chromium(III) complex at pH = 15 is most probably a polymeric chain with double hydroxo bridges $[Cr(\mu_2\text{-}OH)_2(OH)_2]_n^{n-}$ with mean Cr-O and Cr···Cr distances of 2.00(1) and 2.98(1) Å, respectively [P1]. The lengthening of the Cr-O bond distance in this complex in comparison to the hydrated chromium(III) ion, 1.96 Å, supports a large number of hydroxide ions bound. A gel or an amorphous solid with structure similar to α-CrOOH precipitates from alkaline chromium(III) solution with pH < 15 over a period of weeks.

The coordination chemistry of the gallium(III) and indium(III) ions is quite different in the two oxygen donor solvents N,N'-dimethylpropyleneurea (DMPU) and dimethylsulfoxide (Me_2SO) [P2]. This is mainly due to the space-demanding properties of the former, and the significantly more soft electron-pair acceptor abilities of indium(III). The DMPU solvated gallium(III) and indium(III) ions are five- and six-coordinate in solution, respectively, with mean Ga-O and In-O bond distances of 1.924(5) and 2.146(3) Å, respectively. Indium(III) forms three medium strong complexes with bromide in DMPU, and the structural studies show that also gallium(III) form the third bromide complex in DMPU, $GaBr_3(DMPU)_2$. The DMPU solvated $GaBr_3$ and $InBr_3$ complexes are trigonal bipyramidal with the bromides in a trigonal plane, and with DMPU oxygens in the apical positions. Solid Me_2SO solvated gallium(III) bromide consists of hexakis(dimethylsulfoxide)gallium(III) and bromide ions, while the corresponding indium compound consists of *fac*-octahedral tris(dimethylsulfoxide)trisbromoindium(III) complexes. The complex formation of the indium(III)-bromide system in DMPU is of the same magnitude as in other aprotic oxygen donor solvents as expected as the DMPU solvated indium(III) ion is octahedral as the other oxygen donor solvent solvates, Table 1. On the other hand, gallium(III) form significantly stronger complexes with bromide in DMPU than in water in line with previous observations where the metal ion solvate is five-coordinate.

Publications

P1. N. Torapava, A. Radkevich, D. Davydov, A. Titov, and I. Persson, Composition and Structure of Polynuclear Chromium(III) Hydroxo Complexes.
Inorg. Chem. **48** (2009) 10383–10388.

P2. Ö. Topel, I. Persson, D. Lundberg and A.-S. Ullström, On the structure of the *N,N'*-dimethylpropyleneurea and dimethylsulfoxide solvated gallium(III) and indium(III) ions and bromide complexes in solution and solid state, and the complex formation of the gallium(III) and indium(III) bromide systems in *N,N'*-dimethylpropyleneurea
Inorg. Chim. Acta 363 (2010) 988–994.

Importance of free, low and high molecular mass amino acids and thiols for the complexation of Pb(II) in humic streams and soils

U. Skyllberg[1*], Torbjörn Karlsson[2], Fredrik Nordblad[3], Pieter Glatzel[4] et al.
[1]Dept. of Forest Ecology and Management, Swedish University of Agricultural Sciences, 90183 Umeå, Sweden
[2]Chemistry Dept., Umeå University, 90183 Umeå
[3] Dept. of Chemical Engineering and Geosciences, Luleå University of Technology, 97187 Luleå, Sweden
[4]ID26, BP 220, 6 Rue Jules Horowitz, 38043 Grenoble Cedex, France
* = Corresponding author

Metals form chemical bonds with low and high molecular mass organic molecules in the environment. The binding to small organic molecules like e.g. amino acids, keto acids and thiols not only make metals mobile, but also could make them bioavailable. Thus, knowledge about how different metals associate to functionalities of low and high molecular mass natural organic matter (NOM) fractions is a need if the mobility and bioavailability of metals in the environment is to be understood. In particular, the coordination chemistry of Pb in NOM is almost unknown.

Materials and methods

In this project two boreal, humic streams were sampled during high flows in spring and autumn. High molecular mass (HMM) NOM was extracted and separated into < 1kDa, 1-10kDa, and 10kDa - 0.22 μm size fractions by use of ultrafiltration (Millipor pellicon II Tangential Flow Filtration system). HMM NOM size fractions were characterized for the composition of C and N by XPS, for S by S K-edge XANES and for Fe by Fe K-edge EXAFS. The aromaticity was determined by specific UV absorption and the carboxyl group site densities of each fraction were determined by acid-base titration. Freeze-dried size fractions were added Pb at different concentrations (200 – 20 000 ppm) and pH-values (3-9) and subjected to Pb L_{III}-edge EXAFS analysis. Both conventional total fluorescence yield XAS (at I811, MAX-lab and ID26, ESRF, Grenoble) and partial fluorescence yield XES (L_{III} α_1-line, at ID26, ESRF) measurements were conducted. Low molecular mass (LMM) amino acids and thiols were determined in stream water samples using HPLC separation and UV detection.

Results

Characterisation of O, N and S functional groups of NOM size fractions

Sulfur K-edge XANES data were collected at I811, MAX-lab, revealing differences among the three size fractions. The 10kDa - 0.22 μm size fraction contained 45% reduced organic S (the sum of organic thiol, sulfide and disulfide), the intermediate fraction contained about 15% and the smallest fraction contained less than 5 % of reduced organic S. One explanation of these differences may be that a more abundant cross-linking of organic di- and polysulfides increases by size of organic molecules. Another factor could be that the smaller fractions are more prone to oxidation. If so, the effect may be partly an artefact caused by oxidation during ultrafiltration. However, the large difference between the two largest fractions is difficult to explain by differences in sensitivity for oxidation. The carboxyl group concentration of NOM increased from 6 $mmol_c\ g^{-1}$ in the 10kDa - 0.22 μm size fraction, to 12 $mmol_c\ g^{-1}$ in the 1-10kDa and 19 $mmol_c\ g^{-1}$ in the < 1kDa fraction. The aromatic content decreased with size of the NOM fractions. Both these results were expected given previous studies on humic substances. XPS determinations revealed no major differences in the composition of O and N groups with size.

Pb model compounds: XAS and XES

An interpretation of Pb EXAFS data for NOM requires proper model compounds with a combination of O, N and S functional groups. Actetate, malonate, salicylate, oxalate, glycine,

cysteine, as well as complexes and solid phases with water, hydroxyl, oxide, sulfide and chlorine were selected as model compounds. Our XES measurements on Pb lead compounds resulted in the first publication on the subject (1). One reason for using XES is that the presence of > 100 ppm of bromine in most NOM samples makes an EXAFS analysis beyond $k = 10$ Å^{-1} impossible, due to the interfering Br K-edge at 13474 eV. High energy resolution fluorescence detection (HERFD) XANES experiments, collecting the Pb L_{III} α_1-line, were conducted at ID26 at ESRF. Because the intensity of the α_1-line is low, a relatively high concentration of Pb was required in order to obtain a reasonable signal to noise ratio. Also conventional TFY XANES and EXAFs data were collected for the model compounds at I811, MAX-lab.

Pb associated to size fractions of NOM
Both TFY EXAFS and PFY EXAFS (Pb L_{III} α_1-line) were collected on Pb–NOM samples. Preliminary data interpretation suggests no major differences in the bonding of Pb to functional groups in the 1-10kDa and 10kDa - 0.22 μm NOM size fractions. The first coordination shell was best fitted by two O/N distances, quite similar to the Pb-glycine model compound. There were no signs of involvement of S ligands. A change in the concentration of Pb and pH reveal some changes in the coordination chemistry, but interestingly enough there were no signs of Pb association to iron hydroxides. This finding is corroborated by Fe EXAFS, showing no signs of hydrolysed Fe(III), e.g. $Fe(OH)_3$ or FeOOH(s), in the NOM samples despite significant concentrations of Fe and pH 7. This is in line with recent experiments by Karlsson et al., 2008, suggesting that the strong organic complexation of Fe(III) inhibits hydrolysis even at high pH. In contrast, organic soil samples included in this study as a reference showed that Pb was associated to Fe oxyhydroxides at pH 7. This may indicate that dissolved NOM are stronger complexation agents for Fe(III), and Pb(II), than particulate soil NOM. The smallest size fraction (< 1 kDa) was collected on an anion exchange resin, before addition of Pb. A first coordination shell analyses revealed no differences as compared to the larger size fractions. The data quality was not good enough to obtain information beyond the first shell of coordination in this fraction.

Publications
(1) Swarbrick, J.C., Skyllberg, U., Karlsson, T., and Glatzel, P. 2009. High-energy resolution X-ray absorption spectroscopy of environmentally relevant lead compounds. ***Inorg. Chem.*** 48, 10748-10756.

(2) Skyllberg, U., Karlsson, T., Nordblad, F., Persson, P., Ingri, J., Hruska, J., and Glatzel, P. Speciation of lead(II) and iron associated to dissolved and colloidal organic matter fractions in two boreal forest streams. *Ms in prep.*

Application of XAFS/XANES spectroscopy for the determination of the local structure of iron(III) in a novel Ba(II)Fe(III)-layered double hydroxide

D. F. Srankó[1], A. Pallagi[1,2], É. G. Bajnóczi[1], S. Canton[3], K. Norén[3], E. Kuzmann[4], Z. Homonnay[4], A. Vértes[4], I. Pálinko[2], P. Sipos[1]

[1]*Department of Inorganic and Analytical Chemistry, University of Szeged, Szeged, Hungary*

[2] *Department of Organic Chemistry, University of Szeged, Szeged, Hungary*

[3]*MAXLAB, Lund University, Lund, Sweden*

MTA-ELTE Research Group on the Application of Nuclear Techniques in Structural Chemistry, Eötvös Loránd University, Budapest, Hungary

Layered double hydroxides (LDHs) can generally be described by the following formula: $[M(II)_{1-x}M(III)_x(OH)_2]^{x+}[X^{m-}_{x/m}.nH_2O]^{x-}$ (1> x > 0). The positively charged layers are often comprised of metal hydroxides of divalent (*e.g.*, Mg^{2+}, Ca^{2+}, Zn^{2+}, *etc.*) and trivalent metal cations (*e.g.*, Al^{3+}, Mn^{3+}, Fe^{3+}, *etc.*), but the prerequisite is the similar size of the ionic radii. The positive charge of the layers is compensated by various anions, such as NO_3^-, OH^-, Cl^-, CO_3^{2-}, *etc.*, intercalated between the layers The fundamental crystal structure is mostly of brucit ($Mg(OH)_2$, wherein the magnesium cations are octahedrally surrounded by hydroxyl groups), and the divalent metal ions are partially and isomporphously substituted for the trivalent ones. Minerals with this structure do exist in Nature (*e.g.*, hydrotalcite, pyroaurite, sjogrenite, hydrocalumite, *etc.*), for applications, however, they are usually synthesized.

In a recent paper[1], we have described the structure of Fe(III) in ($[NaOH]_T$ = 20 M) aqueous solutions from EXAFS/XANES and Mössbauer measurements. We have concluded that even under these extremely alkaline conditions Fe(III) solution species are tetrahedrally coordinated, while octahedral Fe(III)-coordination prevails in the solid ferric-hydroxo complex salts precipitating from these strongly alkaline solutions. From the XRD patterns and thermogravimetric behavior of the solids precipitating from $Fe(OH)_3/Ba(OH)_2/NaOH$[2,3] mixtures these crystals belong to the family of LDHs. This observation is of importance on two counts. First, the preparation technique used by us (*i.e.*, coprecipitation of $Ba^{2+}/Fe^{3+}/OH^-$ LDHs from hot and extremely concentrated NaOH solutions) is a novel way of LDH preparation, which has not been described by others in the literature (for the latest reviews of LDH preparation, see ref 4.) We believe that this opens a completely new preparative pathway for producing unique Fe(III)-containing LDHs with a range of alkaline earth metal ions. Secondly, LDH-s are generally known to comprise of bivalent and trivalent metal ions of similar ionic radii – which is clearly not the case for our $Ba^{2+}/Fe^{3+}/OH^-$ systems ($r(Ba^{2+})$ = 13.5 Å; $r(Fe^{3+})$ = 6.5 Å).

Solid Ba/Fe LDH samples were prepared by co-precipitation. Aqueous solution containing the divalent metal ion (in form of $Ba(ClO_4)_2$) and the iron ($Fe(ClO_4)_3$ dissolved in $HClO_4$ was added dropwise to the hot, vigorously stirred and N_2-blanketed NaOH solution. The relative decrease of the $[OH^-]$ during the synthesis was less than 10%, therefore the pH of the solution can be considered constant in the course of the preparative process. The resulting mixture was rapidly filtered until air dry in a practically CO_2-free atmosphere with the aid of a caustic resistant vacuum filter unit equipped with an appropriate membrane. The solid material was washed with a

small amount of pure and hot NaOH with equivalent concentration, which was previously used. The moisture sensitive crystals were kept at room temperature in a desiccator over P_2O_5.

The samples obtained were studied with powder XRD, TG/DTG, FT-IR and Mössbauer spectroscopies and SEM/EDAX. To determine the local structure of Fe in these samples, Fe-K-edge (7112 eV) X-ray absorption spectra (XAS) were measured at beamline I811 in the MAXlab facility. Data were measured in the fluorescence mode for the crystalline samples. The pre-edge region of the XAS spectra is characteristic to octahedral structures of the iron (Figure 1).

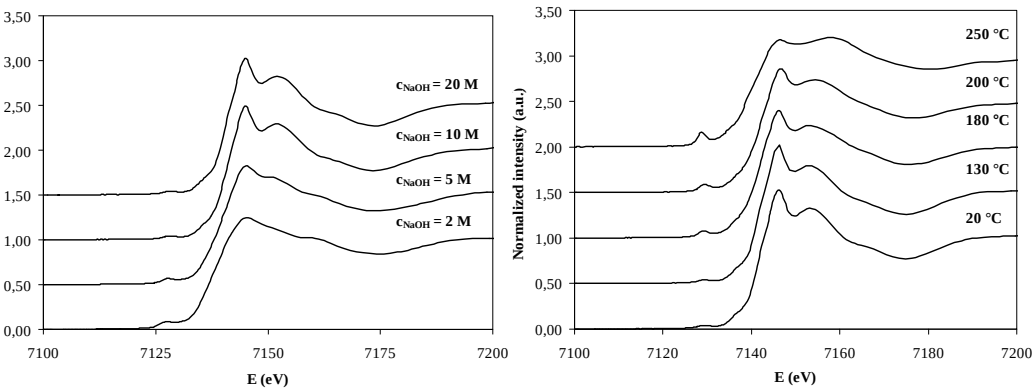

(a) (b)

Figure 1 The XANES region of Fe-K-edge XAFS spectra of various Ba/Fe LDHs made up at (a) different alkaline concentrations and (b) treated at various temperatures.

Fe(III) is found to be in distorted octahedral environment in our Ba/Fe LDHs and the extent of distortion appeared to increase with the decreasing base concentration (Figure 1a). High base concentrations favor LDH formation – this conclusion has been corroborated by powder X-ray diffraction measurements. Moreover, LDHs are known to undergo structural changes upon aging or heat treatments due to the dehydration of the interlayer space. Such changes are often reversible and the original structure can be reconstructed *via* rehydration (this is the so called "memory effect"). These processes are usually monitored via powder X-ray diffraction, IR/Raman spectroscopic and thermogravimetric measurements, *i.e.*, techniques which do not provide direct information about the local structure of the metal ions in the LDH layers. Our XANES measurements (Figure 1b) attest that the LDH structure is retained up to 200 ^{o}C; over this temperature, the LDH structure collapses.

[1] P. Sipos, D. Zeller, E. Kuzmann, A. Vértes, Z. Homonnay, M. Walczak, S. E. Canton, *Dalton Trans.* (2008) 5603.

[2] D. Srankó, A. Pallagi, , I. Pálinkó, E. Kuzmann, S. E. Canton, M. Walczak, P. Sipos, *Insights into Coordination, Bioinorganic and Applied Inorganic Chemistry* (Eds. M. Melník, P. Segľa, M. Tatarko) Press of Slovak University of Technology, Bratislava © 2009, 380-385.

[3] D. Srankó, A. Pallagi, E. Kuzmann, S. E. Canton, M. Walczak, A. Sápi, Á. Kukovecz, Z. Kónya, P. Sipos, I. Pálinkó, *Appl. Clay Sci.*, **48** (2010) 214.

[4] J. He, M. Wei, B. Li, Y. Kang, D. G. Evans, X. Duan, , *Struct. Bond.* **119** (2006) 89.

ABSORPTION X-RAY SPECTROSCOPY OF ALTERNATIVE BUFFER MATERIALS

Daniel Svensson[1,2], Staffan Hansen[2]

[1]*Swedish Nuclear Fuel and Waste Management Co (SKB), Äspö Hard Rock Laboratory, P.O. Box 929, SE-572 29, Oskarshamn, Sweden*
[2]*Polymer & Materials Chemistry, Department of Chemistry, Lund University, P.O. Box 124, SE-221 00, Lund, Sweden*

Introduction

Smectite rich clay is planned to be used as buffer material in high level radioactive waste repositories. The properties of smectite are known to be partly depending on the iron redox chemistry (Stucki et al., 2002). In the field experiment Alternative Buffer Material (ABM), started at Äspö Hard Rock Laboratory during 2006 (Svensson et al., 2007) eleven compacted clays of various qualities are in contact with metallic iron at a temperature of up to 130 °C. The first package (totally three) was excavated in May 2009 and samples from this package have been analyzed at Maxlab I811 during 2009-2010 (Svensson and Hansen, 2010). Iron is present in the smectites, in accessory minerals and also in the heater in the experiment. XANES data will not easily separate the iron in the different phases however it provides an average oxidation state of all included phases. Quantification of the Fe(II)/Fe(III) ratio can be performed using linear-combinations of reference spectra.

Experimental

In the static experiments, the excavated clay was sampled radially (Fig. 1) from the iron heater and studied using FeK XANES in order to: (i) give spatially resolved information about the Fe redox chemistry in the deposition hole, and (ii) indicate differences in behaviour of the clays. In dynamic experiments, the samples that were found to be rich in Fe(II) were later exposed to ambient atmospheric oxygen. The oxidation of Fe(II) to Fe(III) was followed in-situ with time. The purpose of the dynamic experiments was to establish the oxidation sensitivity of the samples, in order to obtain input data for the design of the sample handling procedure.

Results

The static experiments indicate a high relative increase of Fe(II) towards the heater in two of the five investigated clays (Fig. 2). The others show a small or intermediate increase in Fe(II). Other observations are that several of the clays at some distances from the heater are lower in Fe(II) than the corresponding unexposed reference clay. This indicates oxidation of Fe(II) phases present in the clay from the start (e.g. pyrite or siderite). A third observation was that the outermost part of the sample, i.e. towards the rock, in some cases had a small relative increase in Fe(II). This is probably explained by Fe(II) ions coming from the ground water or from corroding steel in the pellet cages present at some positions in the experiment.

Dynamic experiments were performed with material that had been in direct contact with the heater and with material situated somewhat further into the clay. The material in closest contact with the heater showed no significant decrease of the relative Fe(II) content with time during exposure to the ambient atmosphere, while the material present further into the clay showed a significant gradual decrease within minutes. This indicated differences in the Fe(II)-phases present and that some of them were not stable in contact with oxygen. Hence, the procedure of the sampling and the measurement was of great importance, due to the risk of unwanted oxidation. Handling of large compacted blocks in air for a short period of time seemed to have no or a very small impact on the oxidation state of iron. Depending on the type of clay, different processes were indicated and some important parameters were: total iron content, relative Fe(II) content in the starting material, the corrosivity of the clay on the heater and the mass transfer rate of Fe(II) inside the clay.

Figure 1. Example of a clay ring exhibiting signs of reduction. The inner part of Calcigel block #5 showing a radial change in colour (the dark part to the right was in direct contact with the iron heater). The cracking of the clay is due to dehydration in the dry glove-box.

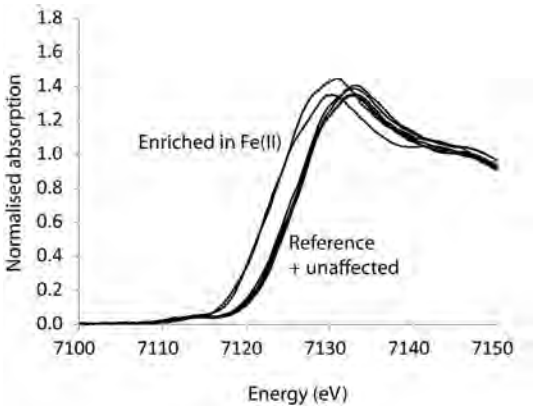

Figure 2. XANES spectra of samples taken at various radial positions of the clay in Fig. 1, together with the unused Calcigel reference clay.

References

- Stucki, J. W., Lee, K., Zhang, L., Larson, R. A. (2002): Effects of iron oxidation state on the surface and structural properties of smectites. Pure and Applied Chemistry 74, 2081-2094.
- Svensson, D., Eng, A., Sellin, P. : Alternative buffer material experiment. Abstract: 3rd International meeting, Clays in natural & engineered barriers for radioactive waste confinement, Lille, September 17-18, 2007.
- Svensson, D., Hansen, S.: Studying Iron Redox Chemistry in the Alternative Buffer Material Experiment Using XANES. Abstract: 4th International meeting, Clays in natural & engineered barriers for radioactive waste confinement, Nantes, March 29-April 1, 2010.
- Svensson, P.D., Hansen, S.: Studying Iron Redox Chemistry in the Alternative Buffer Material Experiment Using X-ray Absorption Near Edge Structure Spectroscopy. *Manuscript*.

How to remove ADP-ribosylations: Structure, ligand complexes and mechanism of the dimanganese mono-ADP-ribosylhydrolase DraG

Catrine L. Berthold, He Wang, Stefan Nordlund and Martin Högbom

Stockholm Center for Biomembrane Research, Department of Biochemistry and Biophysics, Arrhenius Laboratories for Natural Sciences, Stockholm University, SE-10691 Stockholm, Sweden.

ADP-ribosylation is a ubiquitous regulatory posttranslational modification involved in numerous key processes such as DNA repair, transcription, cell differentiation, apoptosis and the pathogenic mechanism of certain bacterial toxins. The ADP-ribosylation regulatory cycle has attracted significant interest because of its role in regulating several key metabolic processes and since it is the pathogenetic mechanism of a number of toxins. The structure and function of ADP-ribose transferases have been studied extensively but very little is known about the structure and mechanism of the hydrolases removing ADP-ribosylations, thus providing the reversibility of the regulation. In particular, no substrate, product or reaction intermediate complex structures were available, for any enzyme removing ADP-ribosylations, to serve as foundations for mechanistic suggestions and inhibitor design. Moreover, there was no structure of a mono-ADP-ribosylhydrolase, removing the protein bound ADP-ribose. Experiments performed at MAX II have now revealed the details of this process (1).

In the phototrophic bacterium Rhodospirillum rubrum, ADP-ribosylation plays a key role in regulation of nitrogen fixation where it is used to control the activity of dinitrogenase reductase (DR). Dinitrogenase reductase ADP-ribosyltransferase (DraT) catalyses the inactivation of DR by attachment of a single ADP-ribose molecule to an arginine residue (Arg-101) on one of the subunits of the homodimeric DR. DraT activity increases in response to environmental stimuli such as darkness and excess of a fixed nitrogen source. The reverse reaction is catalyzed by the monomeric 32 kDa dinitrogenase reductase-activating glycohydrolase (DraG), a peripheral membrane protein, which removes ADP-ribose upon exposure of the bacteria to light or depletion of the nitrogen source, regenerating the arginine guanidino group and an active DR dimer. DraG has long served as a model enzyme for the de-ADP-ribosylation process in numerous biochemical and functional studies, but structural data has been lacking. DraG differs from other ADP-ribsoyl hydrolases in that maximum catalytic activity is observed with Mn^{2+} followed by Fe^{2+}, while Mg^{2+}, that is used by homologous enzymes, function poorly in DraG.

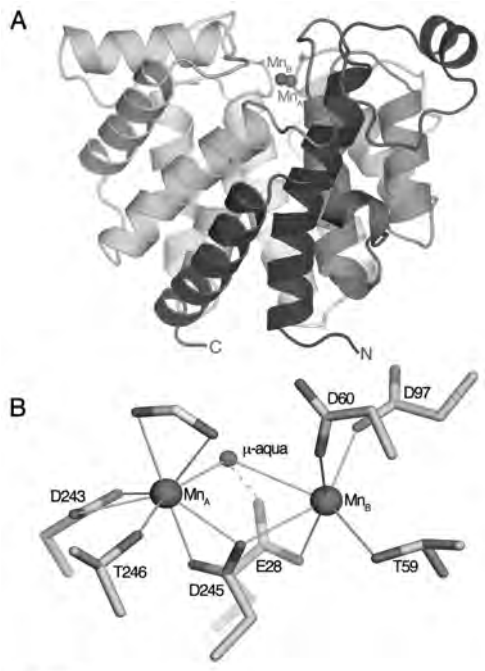

Figure 1

The experiments revealed the crystal structure of DraG, a mono-ADP-ribosylhydrolase, in the apo and ADP-ribose bound forms (Fig. 1A and 2C). The manganese coordination in DraG is characterized by long metal-ligand distances and high coordination numbers, suggesting a rationale for the enzyme's preference for manganese over magnesium, though not requiring a redox active metal for the reaction (Fig. 1B). A fortuitous crystal packing, that positions a lysine residue from a neighboring molecule in the active site (Fig. 2A), also enabled determination of the structure of a trapped reaction intermediate analogue. In large excess of ADP-ribose, the enzyme has performed the reverse reaction, and ADP-ribosylated a surface lysine on a neighboring DraG molecule, forming a ring-opened covalent ADP-ribosyllysine complex (Fig. 2B).

The structural data shows that the substrate ribose coordinates directly to the metal cofactor and that opening of the ribose ring leads to a shift in metal coordination where the hydroxyl derived from the previously ring-bound oxygen moves to a metal coordinating position, thus shifting the substrate and positioning the scissile bond at a location suitable for cleavage (Fig. 2D). Together with mutagenesis studies, the structural data allows the proposal of a detailed catalytic mechanism for the de-ADP-ribosylation reaction. In particular we suggest that the reaction proceeds through a ring-opened form of the ribose, a feature that has not been presented previously, and that a solvent-derived molecule bridged between the two manganese ions acts as a potent nucleophile in the reaction.

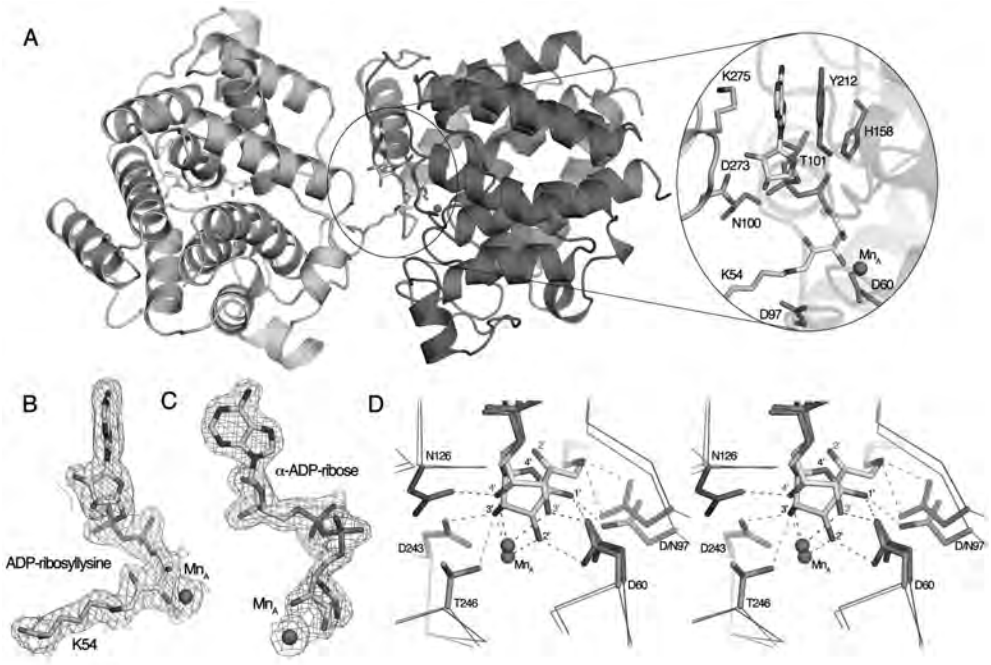

Figure 2

1. Berthold CL, Wang H, Nordlund S, & Högbom M (2009) Mechanism of ADP-ribosylation removal revealed by the structure and ligand complexes of the dimanganese mono-ADP-ribosylhydrolase DraG.
Proc Natl Acad Sci U S A 106(34):14247-14252.

Structure determination of tryptophan hydroxylase

J. Boesen[1], L.T. Haahr[1], O. Kristensen[2] and H.E.M. Christensen[1]

[1]*Metalloprotein Chemistry and Engineering, Department of Chemistry, Technical University of Denmark, Denmark*
[2]*Department of Medicinal Chemistry, Faculty of Pharmaceutical Sciences, University of Copenhagen, Denmark*

Tryptophan hydroxylase (TPH) catalyzes the first and rate-limiting step in the biosynthesis of serotonin. Serotonin is important in physiological functions, such as food intake and sleep rhythm, and imbalance in brain serotonin levels is implicated in a range of neuropsychiatric disorders such as depression and obsessive-compulsive disorder [1].

TPH is a mononuclear non-heme iron enzyme which catalyses the reaction between L-tryptophan, O_2 and tetrahydrobiopterin to produce 5-hydroxytryptophan and 4a-hydroxy-tetrahydrobiopterin. TPH consists of three domains; a regulatory, a catalytic and an oligomerisation domain [1]. To date the production of soluble and active enzyme has been very laborious and only two crystal structures of the catalytic domain of TPH have been solved [2,3]. Therefore, the aim is to produce crystals of TPH with and without bound substrates in order to identify structural changes in the active site upon substrate binding.

Two variants of the catalytic domain of TPH1 from *homo sapiens* (*h*cTPH1) and *gallus gallus* (*gg*cTPH1), were recombinantly expressed in *E. coli* and purified to high purity using a simple two step procedure [4]. The variants were crystallized using sitting drop vapor diffusion without bound substrates. In figure 1 a single crystal of *h*cTPH1 is shown. Data sets were collected to resolutions of 4 Å for *h*cTPH1 and 3.5 Å for *gg*cTPH1. The structure of *h*cTPH1 was solved and belong to the space group P222, with unit cell parameters a = 84.08, b = 123.60 and c = 148.35 Å, but further optimization is needed to obtain crystals that give data sets of higher resolution.

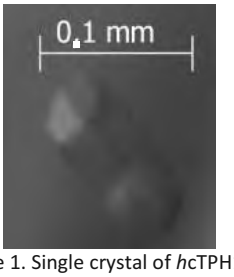

Figure 1. Single crystal of *h*cTPH1.

References:

1) P.F. Fitzpatrick, *Biochemistry*, **42**, 14083-14091 (2003)

2) L. Wang, H. Erlandsen, J. Haavik, P. M. Knappskog and R. C. Stevens, *Biochemistry*, **41**, 12569-12574 (2002)

3) M. S. Windahl, C.R. Petersen, H.E.M. Christensen and P. Harris, *Biochemistry*, **47**, 12087-12094 (2008)

4) M.S. Nielsen, C.R. Petersen, A. Munch, T.V. Vendelboe, J. Boesen, P. Harris and H.E.M. Christensen, *Prot. Expr. Purif.* **57**, 116-126 (2008)

Crystal structure of parasite cysteine protease inhibitor – chagasin in complexes with cathepsin B

G. Bujacz[1], I. Redzynia[1], A. Bujacz[1], M. Abrahamson[2], A. Ljunggren[2], M. Jaskolski[3], J.S. Mort[4], J. Krupa[4]

[1] *Faculty of Biotechnology and Food Sciences, Technical University of Lodz, Stefanowskiego 4/10, 90-924 Łódź, Poland*

[2] *Department of Laboratory Medicine, Division of Clinical Chemistry and Pharmacology, Lund University, University Hospital, SE-221 85 Lund, Sweden*

[3] *Department of Crystallography, Faculty of Chemistry, A. Mickiewicz University, Grunwaldzka 6, 60-780 Poznan, Poland*

[4] *Joint Diseases Laboratory Shriners Hospital for Children, 1529 Cedar Avenue, Montreal, Quebec H3G 1A6, Canada*

Chagas disease is found mainly in Latin America and its causative agent is the *Trypanosoma cruzi* parasite. People infected with the pathogen will develop an irreversible and often fatal medical condition. The disease is second in mortality only to malaria among tropical sicknesses caused by parasites.

An appropriate balance between cysteine proteases and their specific inhibitors is of key importance for many physiological processes of the pathogen. Protein inhibitors of proteolytic enzymes play a central role in this system, regulating proteolysis and preventing the pathological effect of excessive endogenous or exogenous proteases. Chagasin is a cysteine protease inhibitor identified in *Trypanosoma cruzi*. The parasite also expresses a papain-like cysteine protease called cruzipain[1]. Chagasin belongs to a new, recently defined structural family of cysteine protease inhibitors. Although in size and function it resembles some well-characterized cysteine protease inhibitors, such as cystatins, it has a unique amino acid sequence and a completely different structure.

Chagasin is associated with cruzipain and takes part in regulation of its activity and is essential both for the life cycle of the parasite and for its interaction with host cells. Chagasin is secreted outside of the parasite at the site of infection and interacts with host proteases. The balance between cysteine proteases and specific inhibitors is crucial for the proper functioning of both unicellular and multicellular organisms. Inactivation of the proteolytic enzymes is one of the postulated mechanisms of host infection by the parasite.

The aim of the project was to determine the structure of chagasin in *apo* form, as well as in complexes with proteolytic enzymes from plants and humans. Detailed knowledge of the structure and inhibition mode of chagasin can provide information about the role of this inhibitor in the life cycle of the parasite and its role in the host infection by the parasite. At the site of infection, chagasin is secreted outside of the parasite and interacts with host cysteine proteases - cathepsins.

Cathepsin B is a papain-like cysteine protease showing both endo- and exopeptidase activity, the latter due to a unique occluding loop restricting access to the active site cleft. To clarify the mode by which natural protein inhibitors manage to overcome this obstacle, we have determined a high-quality crystallographic structure of cathepsin B in complex with the *T. cruzi* inhibitor chagasin. X-ray diffraction data were collected for crystal forms I and II. The measurements were performed using synchrotron radiation generated at the MAX-lab (Lund, Sweden) beamlines I-911-2 and I-911-5. Crystals of form I are monoclinic, space group $C2$, and diffract X-rays to 1.80 Å resolution. Crystals of form II are tetragonal, space group $P4_22_12$, and diffract X-rays to 2.67 Å resolution. A partial solution of the structure of the chagasin-cathepsin B complex in crystal form I was obtained by molecular replacement using MolRep[2]. The structure of human liver cathepsin B (PDB code 1HUC)[3] provided the

initial search model. The complete model of the complex was obtained by superposition of the chagasin-cathepsin L model (PDB code 2NQD)[4] on the oriented cathepsin B portion as the target. The chagasin molecule derived from the cathepsin L complex fitted the electron density map very well. The structure of the tetragonal crystal (form II) was solved by molecular replacement using MolRep and the form I model of the chagasin-cathepsin B complex. In both cases, structure refinement was carried out in Refmac5[5] from the CCP4 package[6], using the maximum-likelihood targets.

The inhibitory epitope of chagasin is composed of three loops, L4, L2 and L6, which interact with the catalytic cleft of the enzyme, with only the central loop (L2) inserted directly into the catalytic center. The two lateral loops are used for docking on target surfaces and exhibit different modes of interaction. The overall shape of the chagasin-cathepsin B complex resembles a rider on a horse, where the "rider" is formed by the cylindrical Chagasin molecule and the "horse" by the globular cathepsin B (Fig. 1). Chagasin is a more potent inhibitor of cathepsin B than cystatins. Inhibition of this enzyme involves a conformational change of the so-called occluding loop. Proper understanding of these changes is only possible with reliable atomic models of cathepsin B inhibitor complexes.

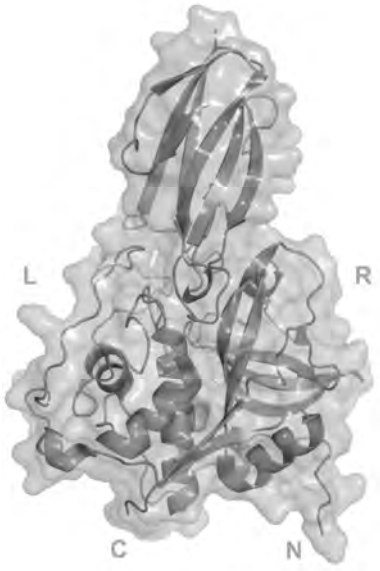

The chagasin-cathpesin B complex structure provides a detailed view of how the parasite protein inhibits host enzymes that may be of paramount importance as the first line of host defence. The high level of structural and functional similarity between cathepsins L and B and cruzipain also offers interesting clues as to how the cysteine protease activity of the parasite could be targeted. This information will guide the development of drugs for possible prevention and treatment of Chagas disease.

It was important to solve the structures of complexes of chagasin with these enzymes to aid the determination of the molecular mechanisms in Chagas disease. Designing the drugs on the basis of the crystallographic structure of proteins involved in pathological processes is very common. The structure of chagasin will help parasitologists explain its role in the life cycle of the parasite and drug designers to disrupt the molecular mechanism of Chagas disease.

Figure 1. Overall structure of chagasin-cathepsin B complex. A ribbon diagram of the monoclinic structure (crystal form I). The inhibitor molecule is colored orange and the enzyme limegreen. The semitransparent surfaces of both proteins have analogous colors. The view corresponds to the standard orientation used for papain-like cysteine proteases, along the cleft between the left (L) and right (R) domains of cathepsin B. The structural illustration was prepared in PyMol.

[1] A. C. Monteiro, M. Abrahamson, A.P. Lima, M.A. Vanier-Santos, J. Scharfstein *J.Cell Sci.* **114,** 3933-3942 (2001)
[2] Vagin, A. A., and Teplyakov, A. *J. Appl. Crystallog.* **30**, 1022-1025 (1997)
[3] Musil, D., Zucic, D., Engh, R. A., Mayr, I., Huber, R., Popovic, T., Turk, V., Towatari, T., Katunuma, N., and Bode, W. *EMBO J.* **10**, 2321-2330 (1991)
[4] Ljunggren, A., Redzynia, I., Alvarez-Fernandez, M., Abrahamson, M., Mort, J. S., Krupa, J. C., Jaskolski, M., and Bujacz, G. *J. Mol. Biol.* **371**, 137-153 (2007)
[5] Murshudov, G. N., Vagin, A., and Dodson, E. *Acta Crystallogr. Sec. D* **53**, 240-255 (1997)
[6] Potterton, E., Briggs, P., Turkenburg, M., and Dodson, E. *Acta Crystallogr. Sec. D* **59,** 1131-1137 (2003)

Structural Analysis of Mycobacterial Branched-Chain Aminotransferase - Implications for Inhibitor Design

Alina Castell, Christian Mille, and Torsten Unge
Department of Cell and Molecular Biology, Uppsala University
BMC, SE-751 24 Uppsala, Sweden.

The branched-chain aminotransferase (BCAT) of *Mycobacterium tuberculosis* has been characterized as essential for the survival of the bacteria. The enzyme is pyridoxal-5'-phosphate dependent and belongs to the aminotransferase IIIa subfamily, to which also the human BCATs belong. Three diffracton data sets was collected earlier at I911-3 and two new data sets were now collected at I911-2. The data sets were of the *Ms*-BCAT apoenzyme (*Ms*-BCAT-apo), the holo enzyme co-crystallized wih the inhibitor Obe (*Ms*-BCAT-holo), and the holo enzyme without the inhibitor. The crystal structures include the apo form at 2.2 Å resolution, as well as a 1.9 Å structure of the holo form co-crystallized with the inhibitor O-benzylhydroxylamine (Obe). In the absence of the inhibitor crystals diffracted to 2.4 Å. Completeness of data varied from 98 to 87%. R_{work} and R_{free} of the refined structures were around 0.20 and 0.24 respectively. The structures showed unique mode of PLP binding and the structure of the inhibitor in an intermediate position. The manusctript for this work will be published in Acta Cryst (Castell, Mille et al. 2010).

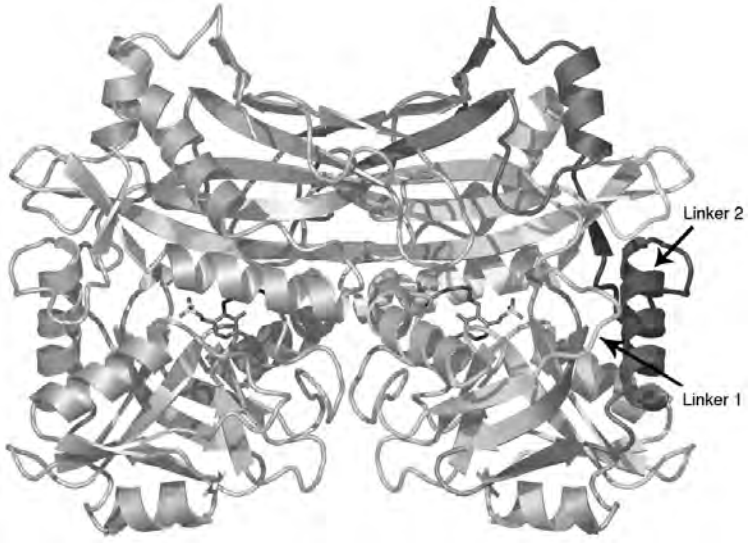

Figure. Ribbon diagram of the *M. smegmatis* BCAT homodimer. One subunit is colored grey and the other is colored red to blue from the N- to the C-terminus. Each subunit is built up by two domains, with the active site at the interface, in which the co-factor PLP is covalently linked to Lys204 through a Schiff base. Two linkers associate the domains. Linker 1 is inserted in the substrate pocket whereas the C-terminal linker (linker 2) folds back onto the N-terminal domain.

Castell, A., C. Mille, et al. (2010). "Structural Analysis of Mycobacterial Branched-Chain Aminotransferase - Implications for Inhibitor Design." Acta Cryst.

Structural Studies of the Surface Adhesin SspB from *Streptococcus gordonii.*

Nina Forsgren and Karina Persson

Dept. of Odontology, Umeå University, SE-901 87 Umeå, Sweden

Surface proteins on microorganisms that build up the oral biofilm (dental plaque) are key factors in the formation of the biofilm. Antigen I/II (AgI/II) proteins are surface adhesins found on virtually all oral streptococci that share a conserved multidomain architecture. The adhesins bind surface components on other bacteria and on host cells and are crucial for the development of the biofilm. The AgI/II proteins comprise 1310-1653 residues divided into six distinct regions: a signal peptide, an alanine-rich domain, a variable domain, a proline-rich segment and a C-terminal domain followed by a cell-wall anchoring region.

Here we report two crystal structures representing two of the domains of the AgI/II protein SspB expressed by the commensal bacteria *Streptococcus gordonii* (**Figure 1**). The first crystal structure is of the SspB variable domain. It was solved using selenomethionine SAD, collected at beamline I911-3, and refined to 2.3 Å resolution.[1] The domain comprises a β-supersandwich and a putative binding cleft stabilized by a calcium ion. The domain was previously suggested to be carbohydrate binding. However, we tested that hypothesis by screening the SspB variable domain for binding to over 400 glycoconjucates and found that the domain does not interact with any of the carbohydrates, therefore the function of the protein remains to be elucidated.

The second structure is of a truncated form of the SspB C-terminal domain.[2,3] The domain was crystallized in two forms, SspB-$C_{1083\text{-}1413}$ and SspB-$C_{1061\text{-}1413}$. Data of the latter form was collected at beamline I911-3 and refined to 2.1 Å resolution. The structure contains two structurally related domains, C2 and C3, each containing one calcium ion and one intramolecular isopeptide bond, formed between a lysine and an aparagine (**Figure 2**). Intramolecular isopeptide bonds are suggested to be a common feature in proteins from gram-positive organisms to retain stability in harsh environments. The SspB C-terminal domain was previously shown to contain a recognition motif for the periodontal pathogen *Porphyromonas gingivalis*. By the crystal structure it was revealed how the attachment motif protrudes from the core of the protein as a handle available for recognition.

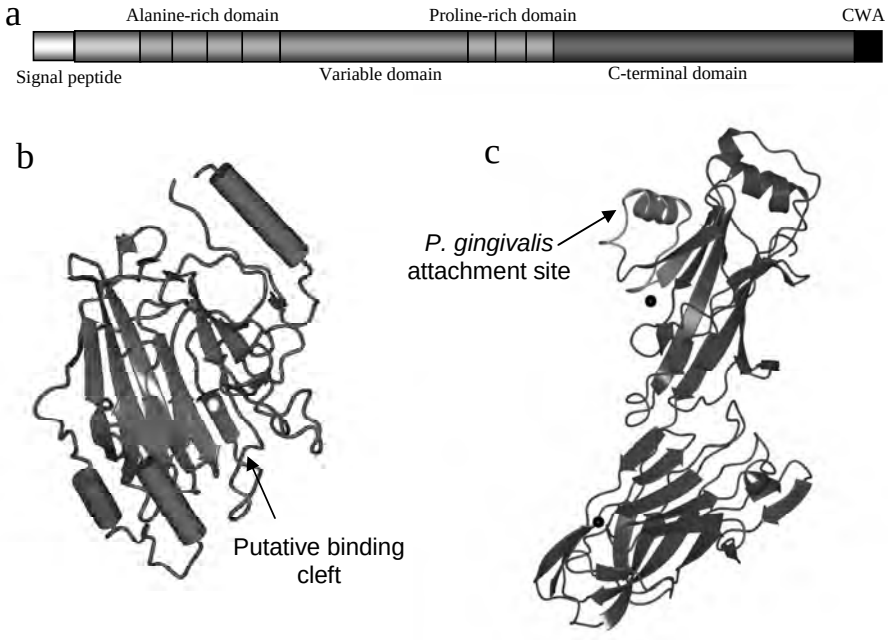

Figure 1. The structure of the AgI/II protein SspB. a) Domain architecture of AgI/II proteins. b) Overall structure of the variable domain. c) The truncated C-terminal domain. The *P. gingivalis* attachment motif is indicated.

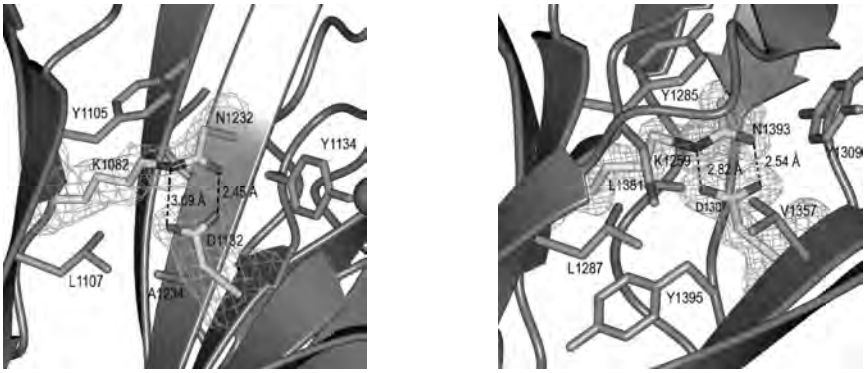

Figure 2. The isopeptide bonds in the SspB C-terminal domain. Covalent isopeptide bonds are formed between a lysine and an asparagine. The bond is stabilized by an aspartic acid and surrounded by hydrophobic residues. The left figure represents the C2 domain and the right the C3 domain.

1. Forsgren, N., Lamont, R. J. & Persson, K. (2009). Crystal structure of the variable domain of the Streptococcus gordonii surface protein SspB. *Protein Sci*. 18(9):1896-905
2. Forsgren, N., Lamont, R. J. & Persson, K. (2009). A crystallizable form of the Streptococcus gordonii surface antigen SspB C-domain obtained by limited proteolysis. *Acta Crystallogr Sect F Struct Biol Cryst Commun* **65**, 712-4
3. Forsgren N, Lamont RJ, Persson K. (2010). Two Intramolecular Isopeptide Bonds are Identified in the Crystal Structure of the Streptococcus gordonii SspB C-terminal Domain. *J Mol Biol*. 397, 740-751

Structural Investigations of Proton Coupled Peptide Transporters

H. Hald, H. A. Ernst and O. Mirza

Biostructural Research, Department of Medicinal Chemistry, Faculty of Pharmaceutical Sciences, University of Copenhagen, Universitetsparken 2, DK-2100 Copenhagen, Denmark

Proton coupled peptide transporters mediates the uptake of di- and tri-peptides from the small intestine in mammals (1). Due to their broad substrate specificity and ability to translocate peptidomimetics and prodrugs, these transporters have become a prime target of investigation in drug research. Peptide transporters function as solute carriers. They act as symporters, coupling the transport of a single proton down an inwardly directed electrochemical proton gradient with that of an oligopeptide (hereby the name Proton Oligopeptide Transporters (POTs) (2)). Detailed knowledge about the three-dimensional architecture of the substrate-binding pocket would substantially aid the drug-design process. However, no crystal structure of any of the peptide transporters is yet available. The aim of this project is to determine the crystal structure of a bacterial homologue of the human PEPT1.

We have successfully obtained small crystals of the YjdL peptide transporter from *E. coli*. In 2009, we have tested 10 of these crystals for diffraction at the MAX-lab I-311 beamline, where we saw diffraction to approximately 40 Å.

References

1. Daniel, H., Spanier, B, Kottra, G. and Weitz, D. (2006) Physiology 21: 93-102.
2. Rubio-Aliaga, I. and Daniel, H. (2008) Xenobiotica 38; 1022-1042.

Bengt Nelander, Ingmar Persson, Carsten Gundlach, Stefan Carlson, and Yngve Cerenius during lunch at the MAX-lab Annual User Meeting, November 2009.
Photo: Bengt-Erik Wingren

300 users participated at Scandic Star, Lund, during the MAX-lab Annual User Meeting in November 2-4 2009.
Photo: Annika Nyberg

Yeast Leukotriene A_4 hydrolase undergoes induced fit upon inhibitor binding.

Charlotte Helgstrand[1,2], Mahmudul Hasan[1], Hüseyin Uysal[1,3], Jesper Z Haeggström[4] & Marjolein MGM Thunnissen[1*]

1 Center of Molecular Protein Science, Lund University, Getingevägen 60 22100 Lund Sweden
2 Present address: Department of Medicinal Chemistry, The Faculty of Pharmaceutical Sciences, University of Copenhagen, Universitetsparken 2, DK-2100 Copenhagen
3 Present address: Medical Inflammation Research, Dept. of Medical Biochemistry and Biophysics Karolinska Institute SE 171-77 Stockholm, Sweden
4 Physiological Chemistry II, Dept. of Medical Biochemistry and Biophysics Karolinska Institute SE 171-77 Stockholm, Sweden

For a number of years we have worked on the structure determination of the yeast LTA4 hydrolase (scLTA$_4$H) in order to investigate the evolutionary relationship of the two catalytic mechanisms in this class of enzymes. Whereas the human enzyme has two different catalytic activities within the same active site (epoxide hydrolase and aminopeptidase), the yeast enzyme lacks the epoxide hydrolase activity. On a sequence level this is difficult to explain since the important catalytic residues are conserved (Tholander et al., 2008). Despite the fact that we easily obtained crystals (Andersson et al., 2003) we were not able to solve the structure due to internal twinning of the crystals, a problem we were not able to overcome.
Eventually it was decided to change the purification protocol for the protein and recrystallise it. This approach was successful and a dataset was collected at MAX-Lab and using the human enzyme as a starting model the structure could be solved.

Figure 1 Figure of the conformational change of the different domains in scLTA$_4$H compared to the humLTA$_4$H. The proteins are drawn as ribbons with yellow scLTA$_4$H, green scLTA$_4$H in complex with bestatin, pink humLTA$_4$H in complex with bestatin..

The structure of scLTA$_4$H shows a large domain movement of the C-terminal domain that creates an open active side. In the human equivalent enzyme the LTA$_4$ binding side is a narrow hydrophobic channel which protects the labile substrate when bound to the enzyme. This channel has become more shallow and is exposed to the solvent. The large conformation change of the C-terminal domain opened the possibility that scLTA$_4$H undergoes an induced fit upon substrate or inhibitor binding. In order to explore this possibility the structure of the complex between scLTA$_4$H and the aminopeptidase inhibitor Bestatin was solved. In order to avoid possible crystal induced bias, crystals of the complex were obtained by co-crystallisation rather then a soaking procedure. Data were collected at station I911-3. The structure could be solved using the native scLTA$_4$H as a model and

after refinement unambiguous density could be seen for the whole model. Fo-Fc difference density maps showed clearly the presence of the Bestatin molecule in the active site. The most obvious effect of the binding of Bestatin is a closing of the wide open cavity present in the native scLTA$_4$H. When the overall structures of the native and complexed enzyme are compared, it can be seen that the C-terminal domain rotates 13.4° and the overall arrangement is more alike the human enzyme. The large cavity seen in the native scLTA$_4$H has become smaller and the distance from one wall of the cavity to the other has decreased an average 3 to 4Å with a maximum difference of 6 Å in width near the position where the phenyl-ring of the Bestatin is located.

The main triggers for the domain movement are a change in conformation of the side chain of Y312 and a change in backbone conformation of the PYGAMEN fingerprint region upon inhibitor binding (Tholander et al, 2008). This leads to a change in the hydrogen bonding network which pulls the C-terminal domain into a different position. These structures show that the introduction of the epoxide hydrolase activity in LTA$_4$ hydrolases has most probably been a subtle process where small alterations made an impact. Since all the required catalytic residues for the epoxide hydrolase activity are present in scLTA$_4$H the main adaptation seems to be to place these residues at the right relative positions and providing a hydrophobic environment in which the labile lipid LTA$_4$ is protected such that unwanted premature cleavage of the epoxide bond does not occur and the hydroxyl group is introduced at the right position. In the yeast enzyme the pocket is both too limited and too accessible to provide this exact environment.

Many members of the M1 family display a certain degree of induced fit, however for humLTA$_4$H is has never been observed. It is attractive to speculate whether a preformed pocket functioning according to a lock and key mechanism is more suited to supply the protective and precise environment that the catalysis of LTA$_4$ into LTB$_4$ requires. Further studies are however required to fully understand the adaption of this intriguing class of proteins into bifunctional enzymes.

References:

Andersson B, Kull F, Haeggström JZ & Thunnissen MMGM. (2003) Crystallization and X-ray diffraction data analysis of Leukotriene A$_4$ hydrolase from *Saccharomyces cerevisiae. Acta Crystall. D* **59**, 1093-1095

Tholander F, Kull P, Ohlson E, Thunnissen MMGM. & Haeggström JZ. (2005) Leukotriene A$_4$ hydrolase: Insights to the molecular evolution by homology modeling and mutational analysis of enzyme from *Saccharomyces cerevisiae. JBiol. Chem.* 280, 33477-33486

Tholander F, Muroya A, Roques BP, Fournié-Zaluski MC, Thunnissen MM, Haeggström JZ. (2008) Structure-based dissection of the active site chemistry of leukotriene A4 hydrolase: implications for M1 aminopeptidases and inhibitor design. *Chem. Biol*. 15,920-929.

Structure of the complex between falcipain-2 and the intrinsic inhibitor of cysteine proteases (ICP) of the malaria parasite Plasmodium

Hilgenfeld R., Hansen G.

Institute of Biochemistry, Center for Structural and Cell Biology in Medicine, University of Lübeck

Falcipain-2 (FP-2) is an essential cysteine protease of the malaria parasite *Plasmodium falciparum*. During the merozoite stage of the parasite's life cycle, the enzyme facilitates escape from the erythrocyte and subsequent reinvasion. In the trophozoite stage, it is critical for the degradation of hemoglobin. We have previously determined the crystal structure (Hogg et al., 2006) of this attractive drug target (*e.g.,* Li et al., 2009). Because of FP-2's high proteolytic activity, the parasite controls the enzyme by a relatively large protease inhibitor designated inhibitor of cysteine proteases (ICP). We have crystallized the complex between FP-2 and ICP and aim at determining its structure by X-ray crystallography. In collaboration with V. Heussler and coworkers (Bernard Nocht Institute, Hamburg), we have characterized ICP from the malaria parasites *Plasmodium berghei* (PbICP) and *falciparum* (PfICP) (Rennenberg et al., 2010). According to sequence analysis, PbICP and PfICP consist of a chagasin-like C-terminal part (ICP-C) and a non-homologous N-terminal part. The C-terminal part alone acts as a very potent inhibitor of falcipain-2 and other cysteine proteases.

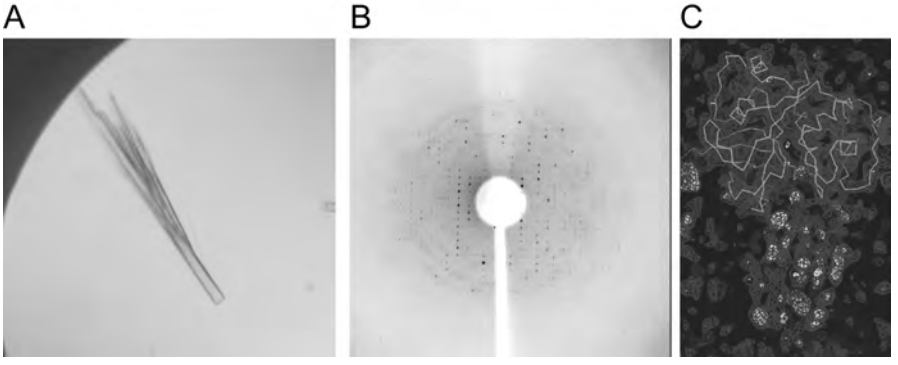

Using the facilities at MAX-lab, we were able to efficiently evaluate the diffraction properties of several crystal forms of the FP-2:ICP-C complex. Although crystals could be obtained from a diverse set of conditions, even after extensive optimization, diffraction was initially limited to less than 7 Å. Recently, we were able to identify a crystal form of inactivated FP-2 in complex with PbICP-C with improved diffraction properties (Fig. 1A, B). A complete dataset to 3.7 Å resolution was collected at MAX-Lab. Preliminary data analysis indicated that the crystals belong to space group $P4_3$ with unit-cell dimensions $a = b = 71.3$ Å, $c = 121.3$ Å. Using the structure of wild-type FP-2, a molecular-replacement solution was obtained for the protease in the complex. The resulting electron density clearly showed the position of PbICP-C in the asymmetric unit but a tracing of the main chain is difficult due to the limited resolution (Fig.1C). We now aim to obtain a higher-resolution dataset that will enable us to solve the structure of the whole complex.

Hogg, T., Nagarajan, K., Herzberg, S., Chen, L., Shen, X., Jiang, H., Wecke, M., Blohmke, C.J., Hilgenfeld, R. & Schmidt, C.L. (2006). *J. Biol. Chem.* **281**, 25425-25437

Li, H., Huang, J., Chen, L., Liu, X., Chen, T., Zhu, J., Lu, W., Shen, X., Li, J., Hilgenfeld, R. & Jiang H. (2009). *J. Med. Chem.* **52**, 4936-4940.

Rennenberg, A., Lehmann, C., Heitmann, A., Witt, T., Hansen, G., Nagarajan, K., Deschermeier, C., Turk, V., Hilgenfeld, R. & Heussler, V. T. (2010). *PLoS Pathog*. [In press].

Current status: diffraction data to 3.7 Å available, further optimization ongoing.

Acknowledgements
This work is supported by the Deutsche Forschungsgemeinschaft (DFG), the "Transnational Access to Research Infrastructures" program of the European Commission, and the Schleswig-Holstein Innovation Fund. R.H. thanks the DFG Cluster of Excellence "Inflammation at Interfaces" and the Fonds der Chemischen Industrie for continuous support.

Structure determination of the N-terminal domain of Rel from Streptococcus equisimilis in complex with small molecule inhibitors

Hilgenfeld R., Hansen G., Saleem Batcha R.

Institute of Biochemistry, Center for Structural and Cell Biology in Medicine, University of Lübeck

The stringent response is a molecular mechanism of bacteria that allows the adaptation of metabolism and gene expression upon changes of environmental conditions such as nutrient depletion. The enzyme Rel (also called stringent factor) is responsible for the synthesis of the effector molecule (p)ppGpp that in turn affects the gene expression profile of the bacterium. We have previously determined the crystal structure of the N-terminal domain of Rel from *Streptococcus equisimilis* (Rel_{Seq} NTD), including the catalytic sites responsible for (p)ppGpp-synthesis and –hydrolysis (Hogg et al., 2004). Now we have crystallized Rel_{Seq} NTD in the presence of small molecule inhibitors and aim to determine the structures of the resulting complexes by X-ray crystallography. Using the facilities at MAX-lab, we were able to collect a high-quality dataset to 2.8 Å on a Rel_{Seq} NTD crystal incubated in a solution containing Inh1 (Inhibitor1) and a dataset to 3.1 Å on a crystal grown in presence of a non-hydrolyzable nucleotide analogue. Both crystals belong to space group C2, with unit-cell parameters a = 173 Å, b = 45 Å, c = 128 Å, β = 110° (Rel_{Seq} NTD & Inh1) and a = 175 Å, b = 46 Å, c = 130 Å, β = 110° (Rel_{Seq} NTD & non-hydrolyzable GTP analogue).

The X-ray crystal structure was determined by molecular replacement as implemented in the program PHASER from the protein crystallography suite CCP4. Two Rel_{Seq} NTD monomers were found in the asymmetric unit. Following a rigid body-domain refinement with the program REFMAC5 to account for the packing of the synthetase and hydrolase domains in the monoclinic unit cell, a restrained and TLS refinement was performed. At this stage, R_{work} and R_{free} of ~30% clearly indicate the need of further rebuilding and subsequent refinement of the structures. Yet, simple- and double-difference Fourier maps indicate a bound GTP molecule from the crystallization solution present in the synthetase active site of one monomer.

The calculated $2F_o$-F_c map showed clear electron density for a bound Inh1 molecule (A) in the second monomer. To improve the electron density especially at the synthetase active sites, protein backbone conformations have to be remodeled. However, refinement of the structure to determine the exact binding mode of Inh1 and the GTP molecule is not finished at this stage.

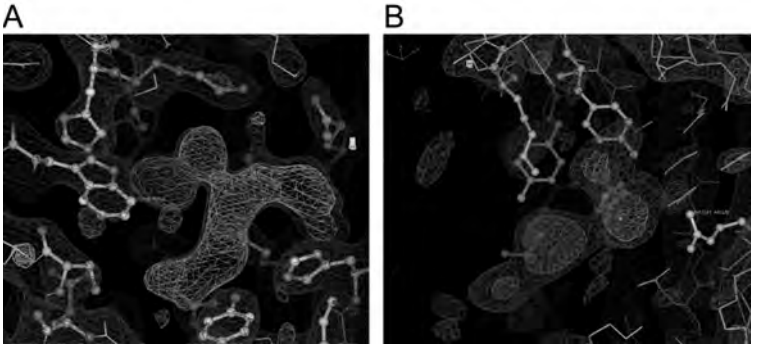

Furthermore, a dataset to a resolution of 3.1 Å was collected on a crystal grown in the presence of non-hydrolysable ATP and GTP analogues. After molecular replacement, electron density for non-hydrolysable GTP analogues was observed in both synthetase active sites (B).

Current status: crystallographic refinement is ongoing.

Hogg, T., Mechold, U., Malke, H., Cashel, M. & Hilgenfeld, R. (2004). Conformational antagonism between opposing active sites in a bifunctional RelA/SpoT homolog modulates (p)ppGpp metabolism during the stringent response. *Cell* **117,** 57-68.

Acknowledgements
This work is supported by the German-Israeli Foundation, the “Transnational Access to Research Infrastructures” program of the European Commission and the Schleswig-Holstein Innovation Fund. R.H. thanks the DFG Cluster of Excellence “Inflammation at Interfaces” and the Fonds der Chemischen Industrie for continuous support.

Structural characterization of the HtrA homologue from Legionella pneumophila

Hilgenfeld R., Hansen G., Wrase R.

Institute of Biochemistry, Center for Structural and Cell Biology in Medicine, University of Lübeck

HtrA is a periplasmatic stress response protein that contributes to virulence of many bacterial pathogens (Spiess et al., 1999, Pedersen et al., 2001). Chaperone and protease activities of HtrA, responsible for repair or degradation of misfolded proteins, are regulated by oligomerization. For DegP, a well-characterized HtrA homologue in *E. coli*, crystal structures of 6-mers and 24-mers are available (Krojer et al., 2002, 2008) and specific functions have been assigned to both assemblies. Recently, we have determined the X-ray structure of the HtrA homologue from *Legionella pneumophila* to a resolution of 2.8 Å. The protein comprising the protease domain and one PDZ-domain (HtrAΔPDZ2$_{Lp}$) was crystallized in space group H3 with unit-cell parameters of a = 110.8 Å, b = 110.8 Å, c = 68.2 Å and a solvent content of 43% (Fig. 1A). Interestingly, crystals with good diffraction properties could be obtained only in the presence of Cd^{2+} ions and subsequent structure determination showed that tightly bound Cd^{2+} ions mediate important crystal contacts (Fig. 1B).

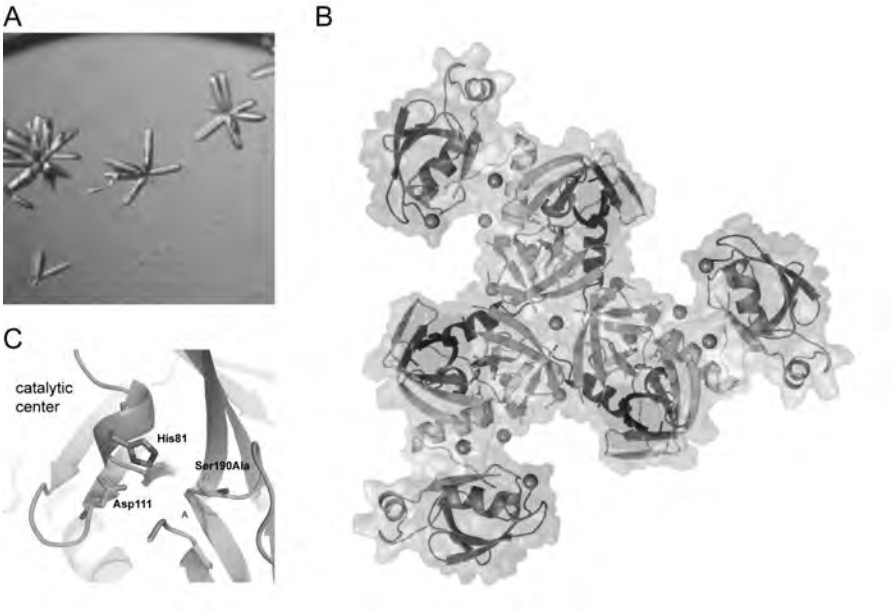

While the asymmetric unit contains one molecule, space group symmetry revealed a very stable trimeric assembly of HtrAΔPDZ2$_{Lp}$ in the crystal lattice (Fig. 1B). 3-mers are stabilized by extensive intermolecular contacts between protease domains of three molecules. Although the structure displays the catalytic triad of the serine protease domain in a catalytically competent conformation (Fig. 1C), HtrAΔPDZ2 is not proteolytically active in biochemical assays. A detailed analysis of the structure in comparison with available *E. coli* DegP structures led us to propose that the activity of HtrA$_{Lp}$ is regulated by the PDZ1-domain, which exhibits a unique orientation in respect to the protease domain.

Current status: manuscripts on structure and biochemical characterization are in preparation.

Krojer, T., Garrido-Franco, M., Huber, R., Ehrmann, M. & Clausen, T. (2002): Crystal structure of DegP (HtrA) reveals a new protease-chaperone machine. *Nature* **416**, 455-459.

Krojer, T., Sawa, J., Schafer, E., Saibil, H. R., Ehrmann, M. & Clausen, T. (2008): Structural basis for the regulated protease and chaperone function of DegP. *Nature* **453**, 885-890.

Pedersen, L. L., Radulic, M., Doric, M. & Abu Kwaik, Y. (2001): HtrA homologue of *Legionella pneumophila*: an indispensable element for intracellular infection of mammalian but not protozoan cells. *Infect. Immun.* **69**, 2569-2579.

Spiess, C., Beil, A. & Ehrmann, M. (1999): A temperature-dependent switch from chaperone to protease in a widely conserved heat shock protein. *Cell* **97**, 339-347.

Acknowledgement

Our research is supported by the Transnational Access to Research Infrastructures program of the European Commission (EC), the OptiCryst project of the EC (LSH-2005-037793; http://www.opticryst.org), as well as the Schleswig-Holstein Innovation Fund. R.H. thanks the DFG Cluster of Excellence “Inflammation at Interfaces” and the Fonds der Chemischen Industrie for continuous support.

Crystallographic studies on Kdo transfer in Aquifex aeolicus

Hilgenfeld R., Mesters J.R., Hansen G., Schmidt H.

Institute of Biochemistry, Center for Structural and Cell Biology in Medicine, University of Lübeck

The outer leaflet of the outer membrane (OM) of Gram-negative bacteria is composed almost exclusively of the glycolipid lipopolysaccharide (LPS), which consists of the OM-embedded lipid A, a Kdo-containing oligosaccharide core region, and an O-specific polysaccharide. The LPS of most Gram-negative bacteria includes at least one 3-deoxy-D-*manno*-octulosonate (Kdo) molecule, which links lipid A to the carbohydrate domain of LPS. The glycosyltransferase WaaA (Mamat et al., 2009), which is associated with the inner membrane, utilizes CMP-Kdo as a donor substrate for the attachment of Kdo to a lipid-A precursor acceptor substrate. The incorporation of Kdo is essential for LPS synthesis and for the integrity of the OM.

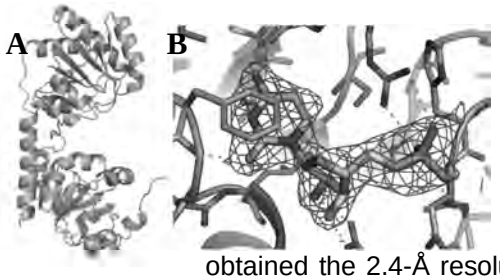

Fig. 1: A) overall structure of WaaA, B) 2Fo-Fc electron density (1σ) of the CMP-molecule

We determined the 2.0-Å resolution crystal structure of WaaA (Fig.1). Initial phases were obtained by "single isomorphous replacement anomalous scattering" (SIRAS) and subsequently improved employing density modification, phase combination and phase extension. Furthermore, we obtained the 2.4-Å resolution crystal structure of the CMP-bound form (Fig.1). WaaA belongs to glycosyltransferase superfamily B (GT-B), showing the typical two-domain architecture. The enzyme adopts an open conformation with the CMP and the acceptor-binding site located in the C- and N-terminal domain, respectively.

Current status: manuscript on structure is in preparation.

Mamat, U., Schmidt, H., Munoz, E., Lindner, B., Fukase, K., Hanuszkiewicz, A., Wu, J., Meredith, T.C., Woodard, R.W., Hilgenfeld, R., Mesters, J.R. & Holst, O. (2009). WaaA of the hyperthermophilic bacterium aquifex aeolicus is a monofunctional 3-deoxy-D-manno-oct-2-ulosonic acid transferase involved in lipopolysaccharide biosynthesis. *J. Biol. Chem.* **284**, 22248-22262.

Acknowledgement
This work was supported by the Deutsche Forschungsgemeinschaft (grant ME 2741/1 to J.R.M. and R.H.) and the “Transnational Access to Research Infrastructures” program of the European Commission. Optimization of $WaaA_{AAE}$ crystals was performed within the OptiCryst project of the EC (LSH-2005-037793; http://www.opticryst.org). RH acknowledges support by the DFG Cluster of Excellence “Inflammation at Interfaces” and by the Fonds der Chemischen Industrie.

The NS1 effector domain of the highly pathogenic influenza A/Vietnam/1203/ 2004 (H5N1) virus: X-ray structure and interaction with host proteins

Hilgenfeld R., Ponnusamy R., Xiao Y., Chen S.

Institute of Biochemistry, Center for Structural and Cell Biology in Medicine, University of Lübeck

Influenza A viruses are important pathogens causing seasonal epidemics and highly mortal pandemics. Segment 8 of the viral genome encodes the nonstructural protein NS1, a protein that is associated with various regulatory activities including protein-protein and protein-RNA interactions, therefore increasing the pathogenicity and virulence of virus during infection. NS1 has two domains to accomplish its multiple functions: The N-terminal RNA-binding domain (RBD) and the C-terminal effector domain. We determined the X-ray structure of the NS1 effector domain of a highly virulent H5N1 strain (A/Vietnam/1203/2004). Different dimeric forms of the H5N1 NS1 effector domain can be observed in our crystal structure. Therefore, we mutated Trp187, which participates in the monomer-monomer interface of the helix-helix dimer, to Ala and found that the mutant predominantly exists as a monomer in solution, indicating that the helix-helix dimer likely is the relevant form of the NS1 effector domain in solution. The monomeric W187A mutant of H5N1 NS1 effector domain has also been crystallized and determination of the crystal structure of this mutant is underway. During the time period covered by this report, diffraction data for the W187A mutant were collected to ~2.6 Å. To better elucidate the mode of action of NS1, determination of crystal structures of H5N1 NS1 in complexes with putative interaction partners will be necessary. Therefore, diffraction data collection of these crystals is proposed to be carried out in the future.

Current status: The W187A mutant of H5N1 NS1 effector domain has been successfully crystallized and diffraction data of this mutant were collected recently. Structure determination and refinement of this mutant is underway. Meanwhile, we have been able to clone and express gene constructs for the NS1-interacting host protein domains iSH2 of p85beta and CPSF30 F2F3. Complex formation was demonstrated for the H5N1 NS1 effector domains with p85beta iSH2 as well as CPSF30 F2F3. Both of these two complexes have successfully been crystallized, and diffraction of the H5N1 NS1-CPSF30 complex and the H5N1 NS1-p85beta iSH2 complex was determined to ~3.6 Å and 8.0 Å. After further optimization of crystal growth, high-resolution diffraction data collection from these complex crystals is proposed to be performed in the future.

Acknowledgement
This work is supported by the International Consortium on Antivirals (ICAV), the "Transnational Access to Research Infrastructures" program of the European Commission, and the Schleswig-Holstein Innovation Fund. R.H. thanks the DFG Cluster of Excellence "Inflammation at Interfaces" and the Fonds der Chemischen Industrie for continuous support.

Structural studies on complexes of SARS coronavirus main protease with peptide aldehyde inhibitors

Hilgenfeld R., Zhu L.

Institute of Biochemistry, Center for Structural and Cell Biology in Medicine, University of Lübeck

In contrast to chloromethyl ketones, aldehydes bind reversibly to the active-site sulfhydryl of cysteine proteases. In collaboration with J. Rademann of the Leibniz Institute for Molecular Pharmacology in Berlin, we have developed a novel procedure that makes use of this property in the search for non-peptidic competitive inhibitors of these proteases. This procedure is called "Dynamic Ligation Screening" (DLS). We used the SARS coronavirus main proteinase (SARS-CoV M^{pro}) as an example to test the DLS concept. First, a peptidic aldehyde inhibitor was reacted with the protease. This led to the formation of a covalent adduct between the catalytic Cys145 and the inhibitor. Then, we screened a small library (234 compounds) of non-peptidic amines and other nucleophiles for compounds that would react with the protease-bound aldehyde and replace the active-site cysteine. The resulting imine was assumed to occupy subsites P5 to P2'. Subsequently, the compound discovered had its amine replaced by an aldehyde warhead. It was reacted with the native protease and formed a covalent adduct. The same library of nucleophiles was then screened for another non-peptidic compound that would replace Cys145 from the aldehyde. The ligation product discovered inhibited the enzyme with a Ki of 2.9 μM. Remarkably, this non-peptidic, competitive inhibitor was ligated from two halves each of which had no inhibitory activity on its own. These reactions will only work in the presence of the target enzyme. Thus, the reversibility of the covalent adduct formation between aldehydes and cysteine proteases can be used to discover non-peptidic inhibitors that block the target by non-covalent interaction. We have determined three crystal structures of SARS-CoV M^{pro} in complex with peptide aldehydes, explaining the mechanism of aldehyde inhibitor binding to SARS-CoV M^{pro}. The crystals belonged to space group C2. Co-crystallization experiments with the ligation imine product are underway and performing the reaction in the crystals is also being tested.

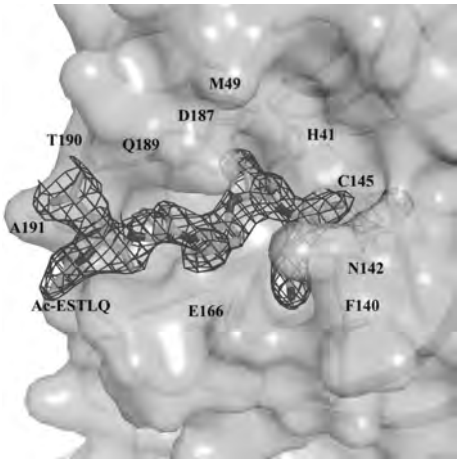

Current status: further co-crystallization experiments ongoing.

Schmidt, M.F., Isidro-Llobet, A., Lisurek, M., El-Dahshan, A., Tan, J., Hilgenfeld, R. & Rademann, J. (2008). *Angew. Chem. Int. Ed. Engl.* **47**, 3275-3278.
Al-Gharabli, S.I., Shah, S.T., Weik, S., Schmidt, M.F., Mesters, J.R., Kuhn, D., Klebe, G., Hilgenfeld, R. & Rademann, J. (2006). *Chembiochem* **7**, 1048-1055.

Acknowledgements
This work was supported by the "Sino-European Project on SARS Diagnostics and Antivirals" (SEPSDA) and the "Transnational Access to Research Infrastructures" program of the European Commission, the Deutsche Forschungsgemeinschaft (DFG), the Sino-German Center for the Promotion of Research, Beijing, and the Schleswig-Holstein Innovation Fund. R.H. thanks the DFG Cluster of Excellence "Inflammation at Interfaces" and the Fonds der Chemischen Industrie for continuous support.

FeoB - the ferrous iron transporter of Legionella pneumophila

Hilgenfeld R., Schmidt C.L., Hansen G., Petermann N.

Institute of Biochemistry, Center for Structural and Cell Biology in Medicine, University of Lübeck

Prokaryotic pathogens have developed specialized mechanisms for efficient uptake of ferrous iron (Fe^{2+}) from the host. In *Legionella pneumophila*, the causative agent of Legionnaires' disease, the transmembrane GTPase FeoB, plays a key role in Fe^{2+}-acquisition and virulence. Using synchrotron radiation at MAX-Lab, we determined the crystal structure of the N-terminal, cytosolic domains of FeoB from *Legionella pneumophila* ($NFeoB_{Lp}$) to a resolution of 2.5 Å. Crystals belonged to space group $P2_12_12_1$ with unit-cell dimensions of *a* = 53.06 Å, *b* = 130.70 Å, *c* = 157.62 Å, and a solvent content of 51%. Atomic coordinates have been deposited in the Protein Data Bank under accession code 3IBY. The structure revealed a monomeric protein comprising two separate domains with GTPase and guanine-nucleotide dissociation inhibitor (GDI) functions (Fig.1A, B). The GDI domain displays a novel fold, whereas the overall structure of the GTPase domain resembles that of known G domains but is in the rarely observed nucleotide-free state. The presence of an intramolecular GDI domain is a unique feature distinguishing FeoB from typical small GTPases (Fig.1A, B).

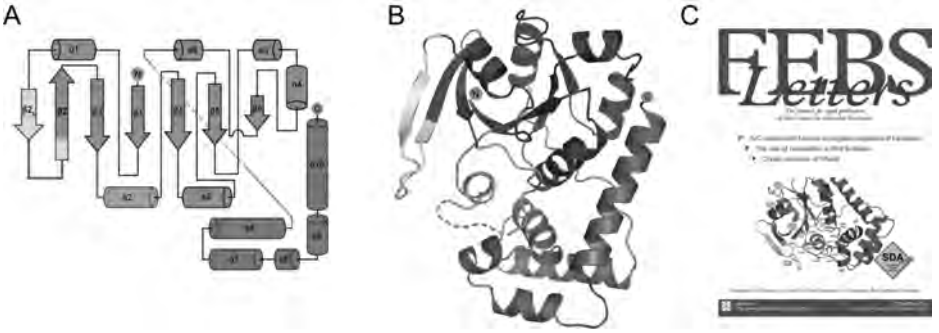

It has been suggested, that the GTPase domain of FeoB regulates Fe^{2+} transport via the transmembrane domain. The structure of $NFeoB_{Lp}$ reveals that conformational changes in switch regions could be relayed to the GDI and transmembrane domains, facilitating the coordinated uptake of iron. Our results provide the structural basis for the discussion of functional data on prokaryotic ferrous iron uptake and shed light on an important virulence mechanism of *Legionella pneumophila.* The journal FEBS Letters featured the structure of $NFeoB_{Lp}$ as cover illustration (Fig. 1C), reflecting the high relevance of this work.

Current status: published

Petermann, N., Hansen, G., Schmidt, C. L. & Hilgenfeld, R. (2010): Structure of the GTPase and GDI domains of FeoB, the ferrous iron transporter of *Legionella pneumophila*. *FEBS Lett.* **584**, 733-738.

Acknowledgement
This work was supported by the “Transnational Access to Research Infrastructures” program of the European Commission and the Schleswig-Holstein Innovation Fund. R.H. thanks the Fonds der Chemischen Industrie for continuous support.

Status report from the macromolecular crystallisation facility at MAX-lab

Maria Håkansson[1] & Derek T. Logan[1,2]
[1]*SARomics Biostructures AB, Box 724, 222 07 Lund, Sweden*
[2]*Dept. of Biochemistry and Structural Biology, Lund University, Box 124, 221 00 Lund, Sweden*

The production of "diffraction quality" crystals is absolutely essential for studies of macromolecular structure and function using X-ray crystallography. Almost all initial crystallisation conditions for new proteins are nowadays found using “sparse matrix” screening, using kits of carefully chosen conditions that will maximise the chances of crystallising the new protein. Increasingly these screens are performed using low-volume liquid dispensing robotics. A efficient facility for low-volume screening of crystallisation conditions has been in operation at MAX-lab since late 2005. The proximity of the facility to beamline I911 means that potential new crystals can be tested quickly and easily. At present the facility, open to all academic users, is run by staff from the company SARomics Biostructures AB. The equipment park consists of a Tecan Freedom EVO 150 robot for general liquid handling, a Mosquito nanolitre pipettor from TTP Labtech that is used to set up crystallisation drops down to approximately 100 nl in size, and a CrystalPro imaging system from Tritek Corporation for photographic documentation and database storage of the experiments. We also have a Stratagene Mx3500p qPCR machine for differential scanning fluorimetry (DSF). DSF can be used to identify the most stabilising conditions for a proteins, e.g. the optimal storage buffer or a ligand or additive. It has been shown that identification of optimal stabilising conditions generally increases the chances of finding a hit in crystallisation screens.

Use of the instruments at the facility is scheduled on Google Calendars. Each instrument has its own calendar and users have access (read only) to see when the instruments are available.

Use of the facility is continually increasing. During 2009 the facility was used by 22 scientists from 10 different research groups: 9 at Lund University (among others Molecular Biophysics, Biochemistry, Biotechnology, Cell and Organism Biology and Glycobiology) and one external: in September 2009 the facility was used for an ambitious collaboration between the Universities of Lund and Göttingen. Tobias Beck, Ph.D. student in the group of Prof. George Sheldrick, used the facility to test the influence on crystallisation of five new compounds he had synthesised, in the family of “magic triangle” phasing aids (see http://shelx.uni-ac.gwdg.de/~tbeck/research.html). The five compounds were tested on seven new proteins from research groups in Lund and Göttingen, leading to the creation of 56 crystallisation plates in one week, with a total of 10 752 drops. These experiments are still being analysed, but appear to have led to new crystal forms for some of the proteins.

In addition to the above, SARomics Biostructures has carried out 4 academic projects (in collaboration with the Depts. of Immunotechnology, Biotechnology, Biophysical Chemistry, Organic Chemistry and Infectious Medicine (BMC) at LU, resulting in two new crystal structures. The integration of the crystallisation facility with the macromolecular crystallography beamlines at MAX-lab is a great advantage for rapid characterisation of the crystals and eventual data collection. Due to the time required for data collection, structure solution and publication for the average project, the impact on the scientific literature is modest at present, but a couple of publications appeared during the past year (Nordlund et al., 2009; Pozzo et al., 2010).

References

A. Nordlund, L. Leinartaité, K. Saraboji, C. Aisenbrey, G. Gröbner, J. Danielsson, D.T. Logan, and M. Oliveberg. Functional features cause misfolding of the ALS-provoking enzyme SOD1: non-native metal coordination obstructs active-site packing. *Proc. Natl. Acad. Sci. U.S.A* (2009) **106**, 9667-9672.

T. Pozzo, J. Linares Pasten, E. Nordberg Karlsson & D. T. Logan. Structural and functional analysis of β-glucosidase 3B from *Thermotoga neapolitana*: a thermostable three-domain representative of glycoside hydrolase 3. *J. Mol. Biol.* (2010) **397**, 724-739.

Structural Analysis of *Mycobacteria Smegmatis* Methionyl tRNA Synthetase

Henrik Ingvarsson and Torsten Unge
Department of Cell and Molecular Biology, Uppsala University
BMC, SE-751 24 Uppsala, Sweden.

Methionyl-tRNA synthetase (MetRS) is one out of 20 aminoacyl-tRNA synthetases (aaRS) catalyzing the aminoacylation of tRNA with their corresponding amino acids. We have determined two crystal complexes of *Ms* MetRS. The first structure is a complex with the ligands Met and Ado (*Ms* MetRS M/A) determined to 2.3 Å resolution, and the second is with Met (*Ms* MetRS M) and determined to 2.8 Å resolution. These structures gives detailed information on new intermediate structures, flexibility and domain communication within the MetRS molecule and also indication of an allosteric inhibitor binding site. X-ray Diffraction data were collected at beamline I911-2 at MAX-lab Lund. The wavelength was 1.038 Å. The Rmerge values for the two data sets were 9.3 and 8.6 respectively and the Rpim values 5.1 and 3.3. A manuscript on this work has been sent to EMBO Journal.

Figure. An overall view of the structure of *Ms* MetRS M/A. The structure is contains into four domains: the Catalytic domain, the CP domain, the KMSKS domain and the anticodon domain. The two ligands Met and Ado bound to the active site are represented in gray.

Structural and mechanistic basis for a new mode of glycosyltransferase inhibition

R. Jørgensen[1], T. Pesnot[2], M. M. Palcic[1] & G. K. Wagner[2]

[1]*Carlsberg Laboratory, Copenhagen, Denmark*

[2]*School of Pharmacy, University of East Anglia, Norwich, United Kingdom.*

In all domains of life, the biosynthesis of complex glycoconjugates requires the concerted action of a multitude of glycosyltransferases (GTs)-enzymes that catalyze the transfer of a mono- or oligosaccharide from a glycosyl donor (for example, a sugar-nucleotide) to a suitable acceptor (for example, a glycan, peptide or lipid)[1-4]. GTs play a key role in many fundamental biological processes underpinning human health and disease, such as cell signaling, cellular adhesion, carcinogenesis and cell wall biosynthesis in human pathogens[5-8]. The development of small-molecule GT inhibitors is therefore of considerable scientific interest in chemical glycobiology and drug discovery[9].

We have developed several new, base-modified UDP-Gal derivatives with an aromatic or heteroaromatic substituent in position 5 of the uracil base as chemical tools for the investigation of glycosyltransferases and other UDP-Gal dependent glycoprocessing enzymes (Figure 1). The most potent of these new derivatives act toward five different GTs, as a inhibitors of glycosyl transfer, with K_i values in the low micromolar to nanomolar range.

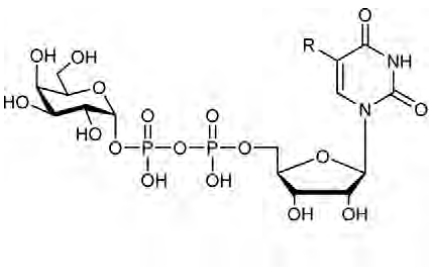

Figure 1. UDP-Gal derivative where different substituents (R) are placed at position 5 of the uracil base.

To understand the molecular basis for the enzymological behavior of these inhibitors we chose a mutant of the ABO(H) blood group A and B glycosyltransferases which catalyze the final step in the synthesis of the A and B antigens. This mutant is a cis-AB mutant capable of transferring both Gal and GalNAc to the H-antigen with equal efficiency. We have solved high-resolution crystal structures of several of these inhibitors bound to the cis-AB mutant, which crystallizes particularly well, and for direct comparison, structures of the enzyme in its unliganded apo form and in complex with UDP. Several of the data sets for these structures were collected at beamline I911 at MAX II of which many of the crystals diffracted to near-atomic resolution (1.2 – 1.4 Å resolution).

Surprisingly the inhibitors block the closure of a flexible loop in the active site of a human blood group GT by preventing the stacking of two amino acid residues where one is placed in the flexible loop and one in the C-terminus. This is a new mode of inhibition for GTs that, given the strong mechanistic similarities between many GTs[1-4,10], will probably also be applicable to other enzymes in this class.

[1] Weadge, J.T. & Palcic, M.M. Wiley Encyclopedia of Chemical Biology. DOI 10.1002/9780470048672.wecb213 1–13 (2008).
[2] Lairson, L.L., Henrissat, B., Davies, G.J. & Withers, S.G. Annu. Rev. Biochem. 77, 521–555 (2008).
[3] Schuman, B., Alfaro, J.A. & Evans, S.V. Top. Curr. Chem. 272, 217–257 (2008).
[4] Breton, C., Snajdrova, L., Jeanneau, C., Koca, J. & Imberty, A. Glycobiology 16, 29R–37R (2006).
[5] Marth, J.D. & Grewal, P.K. Nat. Rev. Immunol. 8, 874–887 (2008).
[6] Rexach, J.E., Clark, P.M. & Hsieh-Wilson, L.C. Nat. Chem. Biol. 4, 97–106 (2008).
[7] Dube, D.H. & Bertozzi, C.R. Nat. Rev. Drug Discov. 4, 477–488 (2005).
[8] Berg, S., Kaur, D., Jackson, M. & Brennan, P.J. Glycobiology 17, 35R–56R (2007).
[9] Qian, X. & Palcic, M.M. in Carbohydrates in Chemistry & Biology (eds. Ernst, B., Hart, G. & SinaÃ, P.) 293–328 (Wiley-VCH, Weinheim, Germany, 2000).
[10] Qasba, P.K., Ramakrishnan, B. & Boeggeman, E. Trends Biochem. Sci. 30, 53–62 (2005).

Atomic resolution structures of carbohydrate binding protein Galectin-3C

Saraboji Kadhirvel[1], Maria Håkansson[5], Carl Diehl[2], Ulf Nilsson[3], Hakon Leffler[4], Mikael Akke[2] & Derek T. Logan

Departments of [1]Biochemistry and Structural Biology, [2]Biophysical Chemistry, [3]Organic Chemistry, [4]Laboratory Medicine (Section MIG), Lund University, SE-221 00, Lund, Sweden.
[5]SARomics Biostructures AB, Lund, Sweden

Galectins, a family of carbohydrate binding proteins, have been strongly implicated in inflammation and cancer and may be useful targets for development of new anti-inflammatory and anti-cancer therapies. Understanding the molecular basis of carbohydrate–protein interactions is a prerequisite for rational design of synthetic ligands with therapeutic or biotechnological applications. Here, we report the atomic resolution crystal structures of the carbohydrate recognition domain of galectin-3 (Gal-3) in the complex with lactose (0.86 Å), glycerol (0.9 Å) and a ligand-free state (1.08 Å). The resolution of 0.86Å is to our knowledge the highest from a protein crystal achieved so far at Max-lab.

Crystals of the lactose Gal-3 complex were obtained using hanging-drop vapour-diffusion with equal volumes of protein solution (17mg/ml galectin-3c, 10 mM PBS pH 7.5, 100 mM NaCl, 10 mM β-mercaptoethanol and 0.02 % NaN_3) and reservoir solution (30 % w/v PEG 4000, 0.1 M Tris-HCl pH 7.5, 0.1 M $MgCl_2$, 0.4 M NaSCN, 8 mM β-mercaptoethanol). Prior to crystallization, the protein was mixed with 100 mM lactose (L2) and incubated for 2h. The drops were streak-seeded immediately after set-up using apo Gal-3 crystals, which were grown under the same conditions but without L2. Crystals appeared overnight and grew within a few days.

Fig 1: Close-up view of a binding site residue His 158; H- atoms are clearly visible in the F_o- F_c map contoured at 2σ (black) and the $2F_o$-F_c map contoured at 4σ (grey).

A crystal of dimensions 0.1 × 0.1 × 0.1 mm^3 was flash-cooled to 100 K using 15% glycerol as cryoprotectant supplemented in the mother liquor. The same composition without L2 was used to cryoprotect the glycerol-Gal3 complex crystals whereas 15% PEG400 was used for apo-Gal3. For the room temperature data collection, the crystal was mounted using the MiTeGen MicroRT kit. The X-ray diffraction data for all the crystals were collected on a marResearch CCD detector at wavelength of 0.9078Å on I911-5 beam line at MAX-lab synchrotron in Lund, Sweden. All diffraction images were indexed and scaled using XDS[1].

The structure of the lactose-Gal-3 complex was solved by molecular replacement where the L3-Gal-3 complex was taken as the initial model. The apo and glycerol-Gal-3 structures were solved with standard rigid body refinement using Refmac5[2] as implemented in CCP4 suite with our L2-Gal-3 complex as a starting model. At the initial stage all the crystallographic refinement was carried out to a resolution of 1.4 Å using Refmac; subsequently, the resolution was extended to the full resolution range and refinement carried out using SHELXL-97[3]. The model correction, manual building of disordered residues and addition of water molecules were done using Coot[4]. In the final stages of refinement, most of the hydrogen atoms were visible in difference electron-density maps and added at the calculated positions using the SHELXL riding model (Fig1). Alternating steps of

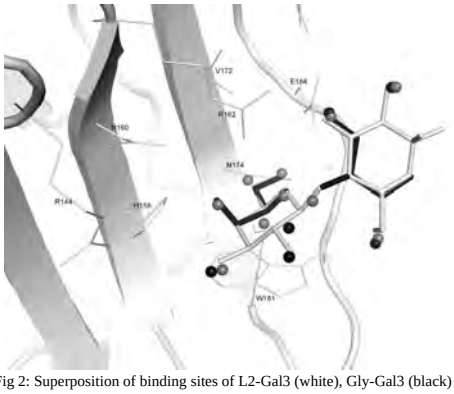

Fig 2: Superposition of binding sites of L2-Gal3 (white), Gly-Gal3 (black) and apo-Gal3 (grey) molecules. The water molecules are shown as spheres.

anisotropic refinement and minor structure adjustment were performed until the R-values converged. All the data collection and refinement statistics are shown in Table 1.

The crystal structures of apo, glycerol-bound and lactose-bound states were all determined at atomic resolution and are highly isomorphous . The conformation of lactose and the ligands in the binding site are identical to the previously reported L2 and LacNAc bound forms[5,6]. The 0.86Å resolution structure of lactose-bound Gal-3 clearly shows the presence of α and β anomers of lactose with equal occupancy. With respect to the earlier lactose bound structure[5], in the present atomic resolution structure 6 additional water molecules were identified, stabilizing L2.

As a result of quick soak of apo Gal-3 crystals with the cryoprotectant glycerol, the carbohydrate-binding site of Gal-3 at 0.90Å resolution includes electron density that can be fitted with a glycerol molecule in the conformation identical to the atoms of the galactose moiety in the lactose bound form. Further an additional glycerol molecule with 50% occupancy was found in the same orientation of identical to the atoms of glucose moiety. In addition to glycerol, the electron density also reveals six bound waters.

Table 1: Crystallographic data-collection and refinement statistics

Data statistics	**L2-Gal3**	**Glycerol-Gal3**	**apo-Gal3 (cryo)**	**apo-Gal3 (RT)**
Resolution (Å)	30.0-0.86 (0.88-0.86)	30.0-0.90 (0.92-0.90)	30.0-1.08 (1.11-1.08)	30.0-1.25 (1.28-1.25)
Space group	P 2_1 2_1 2_1	P 2_1 2_1 2_1	P 2_1 2_1 2_1	P 2_1 2_1 2_1
Unit-cell parameters (a,b,c) (Å)	37.75, 58.30, 63.08	35.83, 58.20, 62.54	35.71, 58.25, 62.85	36.53, 58.22, 63.68
No. of measured / unique reflections	680438/111079	549501/93342	319133/56940	294647/37798
Completeness (%)	98.9 (95.4)	95.8(87.3)	99.9 (99.9)	98.6 (97.7)
R_{merge} (%)[a]	5.0 (85.3)	3.8(79.2)	7.0 (68.2)	5.3 (85.2)
I/σI	19.3 (1.8)	20.4(2.1)	11.6 (2.4)	18.7 (2.5)
Refinement statistics				
Resolution limits	10.0-0.86	10.0-0.90	10.0-1.08	10.0-1.25
R factor (%)[b]	12.30	13.07	14.70	11.43
R_{free} (%)[c]	14.26	15.03	18.18	16.26
R factor (all data) (%)	12.32	13.08	14.76	11.55
r.m.s. deviation from ideal values				
Bond length (Å)	0.017	0.015	0.013	0.015
Angle distance (Å)	0.042	0.031	0.032	0.033
Average B-factor, [protein/solvent/ligand ($Å^2$)]	11.5/25.8/18.0	12.7/24.8/15.1	15.3/31.9/na	16.6 /42.8/na
Ramachandran plot statistics				
Ramachandran favored	98.5% (134/136)	98.5% (134/136)	97.1% (132/136)	97.8% (133/136)

In the apo form of Gal-3 the electron density at the binding site reveals ten bound water molecules, which aligns well with the 10 oxygen positions of L2. In order to verify the cause of glycerol occurrence in the glycerol bound form, the structure of apo-Gal-3 was solved at room temperature and this data confirms the position of observed water molecules found in the cryo data. These observations clearly demonstrate that in any of liganded state, Gal-3 readily coordinates water or hydroxyl oxygens at identical positions in its binding site (Fig 2). Furthermore, from the crystal structures of apo- and glycerol bound Gal-3, it can be seen that the amino-acid side chains within the binding site and the loop regions on the either side of the binding groove are indistinguishable from the lactose-bound form, i.e., the site is fully pre-organised to accommodate lactose like framework of oxygens.

References

1. Kabsch, W. *J Appl Cryst* **26**, 795-00 (1993).
2. Murshudov, G.N., Vagin, A.A. & Dodson, E.J. *Acta Crystallogr D Biol Crystallogr* **53**, 240-55 (1997).
3. Sheldrick, G.M. *Acta Crystallogr A* **64**, 112-22 (2008).
4. Emsley, P. & Cowtan, K. *Acta Crystallogr D Biol Crystallogr* **60**, 2126-32 (2004).
5. Collins, P.M., Hidari, K.I. & Blanchard, H. *Acta Crystallogr D Biol Crystallogr* **63**, 415-9 (2007).
6. Seetharaman, J. et al. *J Biol Chem* **273**, 13047-52 (1998).

Structure of an engineered *Cellulomonas fimi* endo-β-1,4-mannanase

Jurate Kamarauskaite[1], Omid Hekmat[2], Anna Rosengren[2], Katarina Kolenova[2], Henrik Stålbrand[2] and Leila Lo Leggio[1] (leila@kemi.ku.dk)

1-Biophysical Chemistry Group, Department of Chemistry, University of Copenhagen, Universitetsparken 5, DK-2100 Copenhagen, Denmark and 2-Department of Biochemistry, Center for Chemistry and Chemical Engineering, Lund University, Box 124, SE-221 00, Lund, Sweden

Endo-β-1,4-mannanases (EC 3.2.1.78) are glycoside hydrolases (GH) belonging to sequence-based GH families 5, 26, and 113 (http://www.cazy.org/)[1]. These enzymes catalyze the hydrolysis of β-1,4-mannosidic bonds in mannans and heteromannans of plant cell walls. GHs involved in plant cell wall degradation are of great interest in industrial processing of food products and biomass conversion. GH families 5 and 26 belong to Clan GH-A, whose members share the $(\beta/\alpha)_8$ barrel fold and a retaining double-displacement reaction mechanism.

The structure of a 50KDa fragment of a modular GH26 endo-β-1,4-mannanase from the soil bacterium *Cellulomonas fimi* (CfMan26A) has previously been determined by X-ray crystallography[2] to 2.25 Å resolution. CfMan26A consists of five modules in total, whereas the structurally elucidated recombinant fragment (WT-CfMan26A-50K) consists of the N-terminal GH26 catalytic domain and an immunoglobulin-like module (Fig 1). The fragment has also been extensively characterized in terms of biochemical activity[2,3], including hydrolytic action pattern, and a structure in complex with mannotriose occupying subsites -4, -3 and -2 has been obtained[2].

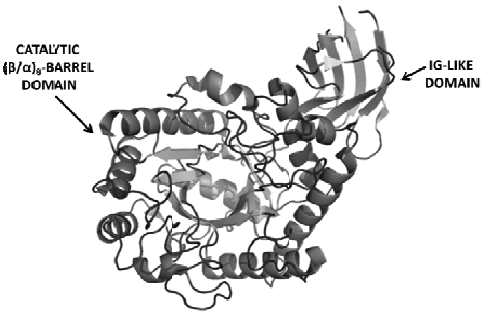

Figure 1- Overall structure of WT-CfMan26A-50K[2] (pdb code: 2BVY)

To date, rational re-design of glycosidase active-site clefts has been mainly limited to the removal of essential functionalities rather than their introduction. The rationale behind the engineering of the glycone-binding distal subsites of WT-CfMan26A-50K presented here came from the comparison of the structure and the hydrolytic action pattern of WT-CfMan26A-50K to those of another well characterized and homologous GH26 endo-β-mannanase: the non-modular endo-β-1,4-mannanase (CjMan26A) from *Cellvibrio japonicus*[4]. Although the catalytic machinery and most of residues involved in substrate binding are conserved, differences are observed between the two enzymes at the -2 and -3 subsites with non-conserved amino acids as candidates responsible for the differences in the hydrolytic patterns of these two enzymes.

A striking difference is that Arg361 of CjMan26A hydrogen bonds to the C2 and C3 hydroxyls of the mannosyl in the -2 subsite but these interactions are lacking in WT-CfMan26A-

50K since the equivalent residue is Ala323 (Fig 2). Conversely, Phe325 of WT-CfMan26A-50K provides a hydrophobic stacking platform for the mannose unit at the -3 subsite but this interaction is missing in CjMan26A since the equivalent residue is Ala363 (Fig 2). The structural data alone thus may indicate that the relative affinities at the -2 and -3 subsites are inverted in the two enzymes, which indeed show differences in their patterns of hydrolysis of oligosaccharides.

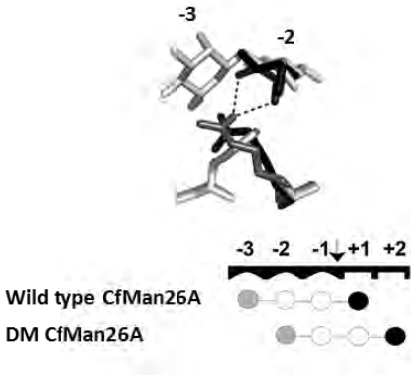

Figure 2- Close up of the substrate binding subsites -3 and -2. In light gray, WT-CfMan26A-50K in complex with mannotriose[2] with Phe325 as aromatic platform for the -3 subsite (pdb code: 2BVT). In black, structure of ligand complex of a variant of CjMan26A (pdb code: 1ODZ), the Arg side chain hydrogen bonds with the -2 sugar ring (bonds not shown). In dark gray, structure of the engineered DM-CfMan26A-50K presented here with an A323R/F325A double substitution. The engineered Arg is in not in an identical position as in CjMan26A, but is still potentially able to form hydrogen bonds with the -2 subsite carbohydrate. This gives a structural rationale for one effect of the mutation, a change of preferred products from hydrolysis of mannotetraose as shown. WT-CfMan26A-50K preferentially hydrolyzes to mannotriose and mannose, while DM-CfMan26A-50K to mannobiose, because the -3 subsite is now impaired while the -2 subsite is strengthened.

The two nonconserved amino acid residues at two distal glycone-binding subsites of the *C. fimi* enzyme were replaced, Ala323Arg at subsite -2 and Phe325Ala at subsite -3, in order to achieve inverted mannosyl affinities in the respective subsites, mimicking CjMan26A. The crystal structure of this engineered mannanase (DM-CfMan26A-50K) was determined by X-ray crystallography to 2.35 Å using data collected at beamline 911-2 ($R_{(r.i.m)}$ = 11.2 %, completeness = 99.8%). The final R-work after refinement was 15.9 %, with an R-free of 19.9 %. As shows in Fig 2 the introduced Arg323 is in a position suitable for hydrogen bonding to C2 and C3 hydroxyls of mannosyl at subsite -2 although non-identical. The non-identical orientation of the Arg side chain is dictated by the different structural contexts in the two enzymes.

Furthermore, detailed steady-state kinetic and initial hydrolysis product analyses showed that the double mutant has an altered hydrolytic action pattern that stems from the promotion of substrate binding at subsite -2 and the demotion of it at subsite -3 (Fig 2). We have thus impaired a functionality, but also created one at a different substrate binding subsite.

References

1. Couthino P M and Henrissat B. In: Gilbert H J, Davies G, Henrissat B and Svensson B, editor. Recent Advances in Carbohydrate Bioengineering. The Royal Society of Chemistry, Cambridge; 1999. p 3-12.
2. Le Nours J, Anderson L, Stoll D, Stålbrand H and Lo Leggio L (2005) Biochemistry 44, 12700-12708.
3. Anderson L, Hägglund P, Stoll D, Lo Leggio L, Drakenberg T and Stålbrand H (2008) Biocatal. Biotransform. 26, 86-95.
4. Jahn M, Stoll D, Warren RA, Szabó L, Singh P, Gilbert HJ, Ducros VM, Davies GJ and Withers SG (2003) Chem. Commun. 12, 1327-1329.

Structural fundament for structure-based design of ligands for ionotropic glutamate receptors

C. Krintel, K. Frydenvang, A. Ceravalls de Rabassa, O. de Barrios, M. Gajhede and J.S. Kastrup

Biostructural Research, Department of Medicinal Chemistry, Faculty of Pharmaceutical Sciences, University of Copenhagen, Universitetsparken 2, DK-2100 Copenhagen, Denmark

Ionotropic glutamate receptors (iGluRs) are responsible for the major part of the fast excitatory synaptic transmission in the mammalian brain. The iGluRs are divided into 2-amino-3-(3-hydroxy-5-methyl-4-isoxazolyl)propionic acid (AMPA), kainic acid and N-methyl-D-aspartic acid (NMDA) receptors based on selective agonist-binding properties and sequence similarity of the receptor subunits. The three classes of iGluRs each consist of a number of subunits: GluA1-4 for AMPA receptors, GluK1-5 for kainate receptors and GluN1, GluN2A-D and GluN3A-B for NMDA receptors. The iGluRs share a similar tetrameric structure where the subunits assemble as a set of two dimers. Each subunit contains a bi-lobed ligand-binding core attached to the transmembrane regions forming the ion channel pore.

Since the first crystal structure of the genetically engineered form of the GluA2 ligand-binding domain (LBD) was reported (1), several structures of this protein and other subunits have been determined. The majority of the structures are co-crystals of the ligand-binding domains with agonists, antagonists and positive allosteric modulators. Even though a representative structure has been reported for all classes of iGluRs, structures of several iGluR subunits are still lacking. The crystal structure of the rat full-length homotetrameric GluA2 receptor was recently determined to 3.6 Å resolution in complex with the competitive antagonist ZK 200775 (2). A comparison of the full-length GluA2 structure with the GluA2-LBD structure in complex with the antagonist UBP282 shows that the soluble protein is a good model system of the full length-receptor for studying binding of agonists, antagonists and allosteric modulators binding at the LBD dimer interface as the dimeric unit is very similar.

In 2009, we have successfully worked on this project at MAX-Lab (I911). The studies have mainly been focused on the LBDs of GluA2, GluK1 and Delta2, but also briefly on PSD93 and PSD95 that are intracellular interaction partners of iGluRs. We have succeeded to collect five full data sets on iGluR complexes (3 modulators, 1 agonist and 1 antagonist), and the structures have been solved using molecular replacement.

The iGluR project work is heavily dependent on the use of synchrotron radiation.

References

1. N.Armstrong, and E. Gouaux, Neuron 28, 165, 2000.

2. A.I. Sobolevsky, M.P. Rosconi, E. Gouaux, Nature 462, 745, 2009.

Bengt Sommarin at a test set-up for the MAX IV ring temporarily located inside the MAX II ring, March, 2009.
Photo: Annika Nyberg

Structural comparison of bovine and camel chymosin

Jesper Langholm Jensen[a,b], Anne Mølgaard[a], Jens-Christian Navarro Poulsen[a], Johannes M van den Brink[b], Marianne Kirsten Harboe[b], Karsten Bruun Qvist[b], and Sine Larsen[a]

[a]*Centre for Crystallographic Studies, Department of Chemistry, University of Copenhagen, Universitetsparken 5, DK-2100 Copenhagen, Denmark and* [b]*Chr. Hansen A/S, Bøge Allé 10-12, DK-2970 Hørsholm, Denmark.*

Chymosin is an aspartic protease that clots milk, thus initiating cheese formation. Cows are the major source for milk, but contrary to what would be expected, bovine chymosin is not the best milk-clotting enzyme known chymosin from camels is better!. This surprising observation and the lack of an explanation initiated this project in an attempt to come up with suggestions that could explain this difference. The camel chymosin obtained from expression in *Aspergillus niger* was examined. Fermentation produced camel chymosin displays some heterogeneity with respect to glycosylation, activity and N-terminal truncation. It was possible to separate the different variants of camel chymosin by hydrophobic interaction chromatography, the variants differed slightly in activity, the doubly glycosylated protein being the least active.
The structure of the double glycosylated camel chymosin was determined based on data measured at the Cassiopeia beamline (I911) to 1.85 Å resolution, it was not possible to localize the first ten amino acids in the electron density. As no experimental data have been deposited for the previously determined structures of bovine chymosin, diffraction data were also measured for this enzyme to a higher resolution (1.8 Å) than those previously reported. The overall structures of bovine and camel chymosin are similar to the other gastric proteases. But where the N-terminus of bovine chymosin forms a β-sheet on the “back”, the camel N-terminus folds into the binding cleft, most likely due to charge and steric differences, reversibly inactivating the camel chymosin. Most of the amino acids differing between bovine and camel chymosin point into the solvent. However, Val6 of bovine is partially buried in a hydrophobic pocket, whereas Glu6 of camel is charged and larger, resulting in an unstable conformation.

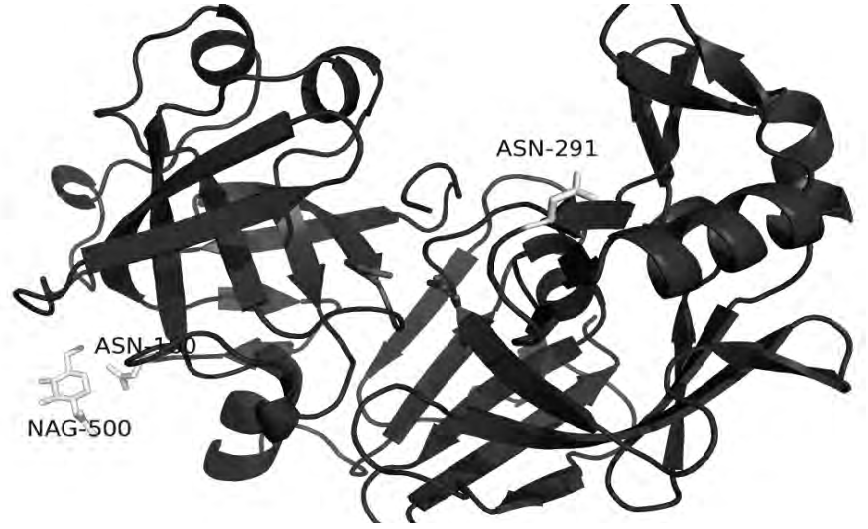

Figure 1 Location of glycosylation sites at Camel chymosin peak 2. Active site residues D34 and D216 are shown in red. The glycosylation sites and the N-acetylglucosamine (NAG) residue at Asn100 are shown in yellow.

Glycosylation at Asn100 is located far from the binding site (Figure 1), explaining why single glycosylated variants show no decrease in activity. The other glycosylation, at Asn291 and present only on double glycosylated variants, is located close to the binding cleft suggesting it is responsible for an observed decrease in activity.
The natural substrate for chymosin is micelles of milk proteins with chymosin acting on kappa-casein. It could therefore be expected that secondary interactions (outside specificity pockets, usually electrostatic) can play a role in substrate binding and release. Bovine and camel chymosin display some significant differences in their surface charges as shown in figure 2. Area 1: close to the binding cleft with many charge differences from bovine to camel. Area 2: positive patch with only one charge difference. Area 3: negative patch. The net charge is -4 for bovine and -1 for camel, a significant difference.

Figure 2 Electrostatic properties of the surfaces of bovine and camel chymosin. The numbered areas correspond to the sequences shown below.

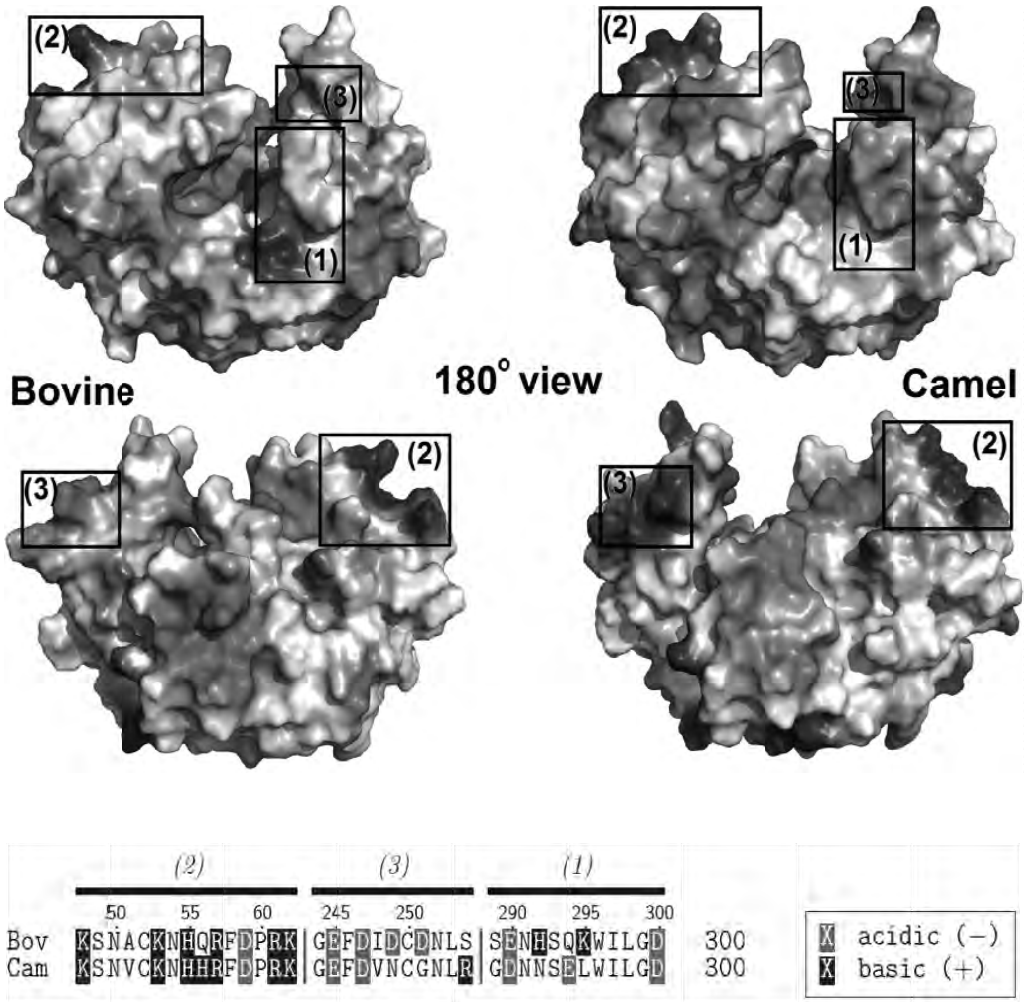

Crystal structure of amyloidogenic protein stabilized against aggregation

K. Michalska[1], R. Kolodziejczyk[1], M. Wahlbom[2], A. Grubb[2] and M. Jaskolski[1,3]

[1]*Department of Crystallography, Faculty of Chemistry, A. Mickiewicz University, Poznan, Poland*

[2]*Department of Clinical Chemistry, Lund University, Sweden*

[3]*Center for Biocrystallographic Research, Institute of Bioorganic Chemistry, Polish Academy of Sciences, Poznan, Poland*

Human cystatin C (HCC) is a potent physiological inhibitor of papain-like cysteine proteases, essential for the protection of our tissues against endogenous proteases and pathogen invasion. Its presence is especially important in the cerebrospinal fluid. In pathophysiological processes, the nature of which is not well understood, HCC is co-deposited in the amyloid plaques of Alzheimer's disease and Down's syndrome. The amyloidogenic properties of HCC are greatly increased in an L68Q variant naturally occurring in an Icelandic subpopulation, which results in fatal cerebral amyloid angiopathy in early adulthood. In all crystal structures of cystatin C studied to date, the protein has been found to form 3D domain-swapped dimers, created through a conformational change of a β-hairpin loop L1 from the papain-binding epitope. Recently, we have created monomer-stabilized human cystatin C (HCC-stab1), with an engineered disulfide bond (L47C)-(G69C) between the structural elements that get separated upon domain swapping (β2-β3). The mutant has drastically reduced dimerization and fibril-formation properties but its inhibition of papain is unaltered.

The crystal structure of HCC-stab1 has been solved using X-ray diffraction data collected at the MAX-lab synchrotron. It confirms the success of the protein engineering experiment to abolish 3D domain swapping and, in consequence, oligomerization and amyloid fibril formation. It illustrates for the first time the fold of monomeric cystatin C and allows to verify earlier predictions based on the domain-swapped forms and on the structure of chicken cystatin. Importantly, the structure defines the so-far unknown conformation of loop L1, which is essential for the inhibition of papain-like cysteine proteases.

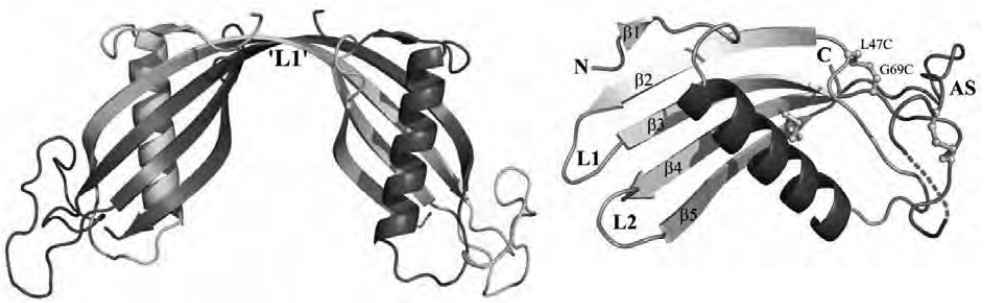

Figure 1. Left: the structure of 3D domain-swapped dimeric HCC (PDB code 1G96). 'L1' labels the hinge region that changes conformation on dimerization and participates in the creation of the 'open interface' of the 3D domain-swapped oligomer. Right: the crystal structure of monomeric HCC (this work) with secondary structure elements labeled. The engineered C47-C96 disulfide bond links strands β2-β3, thus preventing their separation and the possibility of domain swapping. The enzyme-binding epitope is formed by the N-terminus and loops L1 and L2. AS is a poorly structured loop system at the opposite end of the molecule.

The Polish Government has decided to build a Synchrotron in Kraków, Poland. Adriana Wawrzyniak and her colleague Piotr Goryl from Jagiellonian University in Kraków, are visiting scientists at MAX-lab and participating in the MAX IV project. November, 2009.

Photo: Annika Nyberg

Testing of a new SAXS detector for the study of dynamic processes of particles and liquids related to combustion.

Frederik Ossler[1], Linda Vallenhag[1], Sophie E. Canton[2], Dörthe Haase[2], Thomas Ursby[2], Yngve Cerenius[2]

[1]Division of Combustion Physics, Department of Physics, Lund University, LUND, Sweden; [2]MAXlab, Lund University, LUND, Sweden

The project concerns studies on dynamics of particles, liquids and phase transitions during combustion and other physically and chemically reactive systems. These investigations require special detectors to resolve these mechanisms on the nanometer and subnanometer scales with sufficient temporal resolution and sufficient dynamic range. For some years a set of combined Wide-Angle X-Ray Scattering (WAXS) and Small-Angle X-ray Scattering (SAXS) detectors have been constructed at the Division of Combustion Physics and used at MAX-lab [1-3]. The instrumentation is constantly being developed and is intended to be transportable to different synchrotron stations, where various types of experiments can be performed and adapted to the specific end station to be used. Today at MAX-lab beamlines D611 on one hand and I711 together with I911 on the other offer great possibilities for detector and experimental set-up developments and assessments because of their complementary performances that enable applications of WAXS and SAXS, respectively.

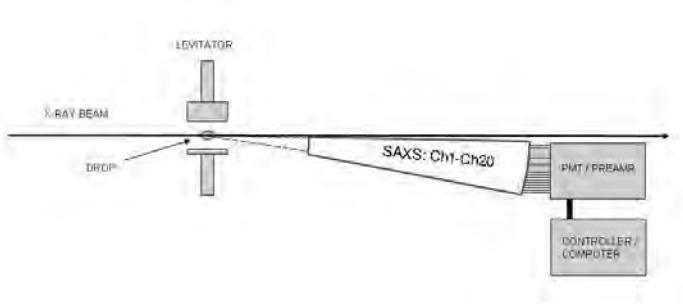

Fig1: The experimental set-up for the SAXS measurements liquid drops using the new multichannel detector, which contains 20 separate channels covering scattering-angle range up to 10°.

Recently a new SAXS detector was tested and compared with the performance of an area CCD detector (MAR-CCD) at beamline I911-5. Measurements were performed on capillaries and drops. The SAXS contains 20 channels that work synchronously with a sampling rate shorter than 10 μs. Measurements on droplet dynamics were performed with time integrations between 20 ms and 1s depending on the experiment. Data is still being evaluated and will be presented for the public during 2010.

1. F. Ossler and J. Larsson, “Exploring the formation of carbon-based molecules, clusters and particles by in situ detection of scattered X-ray radiation”, Chem. Phys. Letters **387**, 367 (2004).
2. F. Ossler and J. Larsson, “Measurements of the structure of nanoparticles in flames by in-situ detection of scattered X-ray detection”, J. Appl. Phys. 98, 114317 (2005).
3. F. Ossler, S.E. Canton, J. Larsson, “X-ray scattering studies of the generation of carbon nanoparticles in flames and their transition from gas phase to condensed phase”, Carbon, 47, 3498 (2009).

Solving structures of extra cellular carbohydrate degrading enzymes.

Mats Sandgren, Nils Egil Mikkelsen, Saeid Karkehabadi, Henrik Hansson and Jerry Sthålberg

Department of Molecular Biology, Swedish University of Agricultural Sciences , Biomedical Center, Box 590, SE-751 24 Uppsala, Sweden.

We study extra cellular carbohydrate degrading enzymes and our group has been able to solve 4 new structures during 2009 using the recourses at MAXLab. In addition, we have been able to crystallize and solve the structure of a mutant of *H. jecorina* Cel6A and also 2 other glycoside hydrolases in complex with ligands. The resolution of the solved structures is in the range of 2.5-1.3Å. Below you will find a brief description of one project that has been released to public.

The filamentous fungus *Hypocrea jecorina* (formally called *Trichoderma reesei*) secretes profuse quantities of different cellulases and hemicellulases.[1] These enzymes act in an orchestrated fashion on plant biomass and degrade this into monomeric or oligomeric sugars that can be used by the fungus as nutrition and energy source.

Among all those glycoside hydrolases produced by the fungus a β-xylosidase (Bxl1) can be found that belongs to glycoside hydrolase family 3 (GH3), Bxl1 is an exo glycoside hydrolase that mainly hydrolases unbranched xylans, glucuronoxylans, and β-1,4-xylooligosaccharides, with different degree of polymerization, into the main reaction product D-xylose. Bxl1 also exhibits some α-L-arabinofuranosidase activity.[2]

Xylan is one of the major structural polysaccharides in plant cell walls.[3] Xylan is, after cellulose, the second most abundant polysaccharide in nature, accounting for approximately one third of all renewable organic carbon on earth.[4] Because of its abundance in nature, there has been an increasing industrial interest in utilizing xylans and the enzymes hydrolyzing these carbohydrates, in a wide range of industrial applications such as; supplement in animal feed, bleaching of cellulose pulp, in the production of bread, drinks, food, textile, ethanol and xylitol.[5]

Here we present the three dimensional structure of the first GH family 3 β-xylosidase, Bxl1 from *H. jecorina*. The structure of Bxl1 has been determined to 1.8Å resolution by X-ray crystallography. The overall structure of Bxl1, to a large extent, resembles the structures of the only two members of GH3 with known three-dimensional structure (barley β-D-glucan exohydrolase, Pdb code 1ex1[6], and *Vibrio cholera* β-hexosaminidase; Pdb code 1tr9, unpublished data), i.e a N-terminal $(\alpha/\beta)_8$ TIM barrel domain followed by a $(\alpha/\beta)_6$ sandwich interconnected by a helix linker.

Results from small-angle X-ray scattering (SAXS) and circular dichroism spectroscopy (CD) experiments[7] have shown that Bxl1 has an additional distinct third domain compared to the two other enzyme members of GH3 enzyme with known structure. The crystal structure of Bxl1 clearly shows the presence of an extra domain located at the C-terminus.

Figure 1. Overall structure of Bxl1 colored by domain: domain 1, green; domain 2, yellow; domain 3, pink. Glucose moieties bound to the enzyme is shown as ball and stick in gold

1. Foreman, P. K., Brown, D., Dankmeyer, L., Dean, R., Diener, S., Dunn-Coleman, N. S., Goedegebuur, F., Houfek, T. D., England, G. J., Kelley, A. S., Meerman, H. J., Mitchell, T., Mitchinson, C., Olivares, H. A., Teunissen, P. J., Yao, J. & Ward, M. (2003). Transcriptional regulation of biomass-degrading enzymes in the filamentous fungus *Trichoderma reesei*. *J Biol Chem* **278**, 31988-31997.
2. Herrmann, M. C., Vrsanska, M., Jurickova, M., Hirsch, J., Biely, P. & Kubicek, C. P. (1997). The beta-D-xylosidase of Trichoderma reesei is a multifunctional beta-D-xylan xylohydrolase. *Biochem J* **321 (Pt 2)**, 375-81.
3. Kulkarni, N., Shendye, A. & Rao, M. (1999). Molecular and biotechnological aspects of xylanases. *FEMS Microbiol Rev* **23**, 411-56.
4. Prade, R. A. (1996). Xylanases: from biology to biotechnology. *Biotechnol Genet Eng Rev* **13**, 101-31.
5. Polizeli, M. L., Rizzatti, A. C., Monti, R., Terenzi, H. F., Jorge, J. A. & Amorim, D. S. (2005). Xylanases from fungi: properties and industrial applications. *Appl Microbiol Biotechnol* **67**, 577-91.
6. Varghese, J. N., Hrmova, M. & Fincher, G. B. (1999). Three-dimensional structure of a barley beta-D-glucan exohydrolase, a family 3 glycosyl hydrolase. *Structure* **7**, 179-90.
7. Rojas, A. L., Fischer, H., Eneiskaya, E. V., Kulminskaya, A. A., Shabalin, K. A., Neustroev, K. N., Craievich, A. F., Golubev, A. M. & Polikarpov, I. (2005). Structural insights into the beta-xylosidase from Trichoderma reesei obtained by synchrotron small-angle X-ray scattering and circular dichroism spectroscopy. *Biochemistry* **44**, 15578-84.

Acetylcholine binding protein as a model system for nicotinic acetylcholine receptors

L.A.H. Thomsen, C. Helgstrand, C. Krintel, T. Balle, M. Gajhede and J.S. Kastrup

Biostructural Research, Department of Medicinal Chemistry, Faculty of Pharmaceutical Sciences, University of Copenhagen, Universitetsparken 2, DK-2100 Copenhagen, Denmark

Nicotinic acetylcholine receptors (nAChRs) form ligand-gated ion channels and are directly linked to an ion channel. nAChRs are activated by the binding of the neurotransmitter acetylcholine. nAChRs are present in many tissues and are some of the best studied ionotropic receptors. The neuronal receptors are found in the central nervous system and the peripheral nervous system, whereas the neuromuscular receptors are found in the neuromuscular junctions of somatic muscles. The nAChR family comprises 17 different subunits in humans and the assembly of combinations of subunits results in a large number of different receptors.

Therapeutic intervention in receptor signaling has proven beneficial in several neurological and psychiatric disorders. In addition to being targeted by marketed smoking cessation aids, the acetylcholine receptors constitute promising targets for the treatment of a wide range of neurodegenerative and psychiatric disorders, such as Alzheimer's disease, Parkinson's disease, schizophrenia and depression. Therefore, much effort has been and needs to be directed toward understanding the structure, function and basis for subtype selective drug targeting of these receptors.

3D-structural information are available from a low resolution cryo-electron microscopy image of a torpedo electric ray nAChR (1), a high resolution X-ray structure of the mouse alpha1 nAChR monomer (2), two different species of distantly related bacterial ion channels (3,4) as well as from the acetylcholine binding proteins from the water snails *Lymnaea stagnalis* (5), *Bulinus truncatus* (6) and *Aplysia californica* (7). Although not ion channels, the snail proteins have the dimension and shape of the N-terminal domain of the nAChRs and furthermore, they have been shown to reproduce the relative binding affinities of a number of nAChR ligands. Despite more than 25 AChBP-ligand co-crystal structures deposited in the Protein Data Bank, there is a need for structures addressing *e.g.* the differences between a good binder and a good agonist, subtype selectivity and binding sites for allosteric modulators.

During the last year we have established a pipeline for expression, purification and crystallization of the AChBPs from *Lymnaea stagnalis* (LS) and *Applysia californica*, and we have established screening assays to guide the selection of ligands for co-crystallization. In winter 2009, we collected the first data set to 2.47 Å resolution at

MAX-lab (I911-3) of a complex of LS-AChBP with an agonist from NeuroSearch A/S. The structure has been solved by molecular replacement and contains 4 pentamers (ca. 4000 amino acid residues) within the asymmetric unit of the crystal (figure 1). We consider LS-AChBP to be the best surrogate of nAChRs for studying binding of agonists and partial agonists, due to a high sequence identity and good correlation between binding affinities when compared to nAChRs.

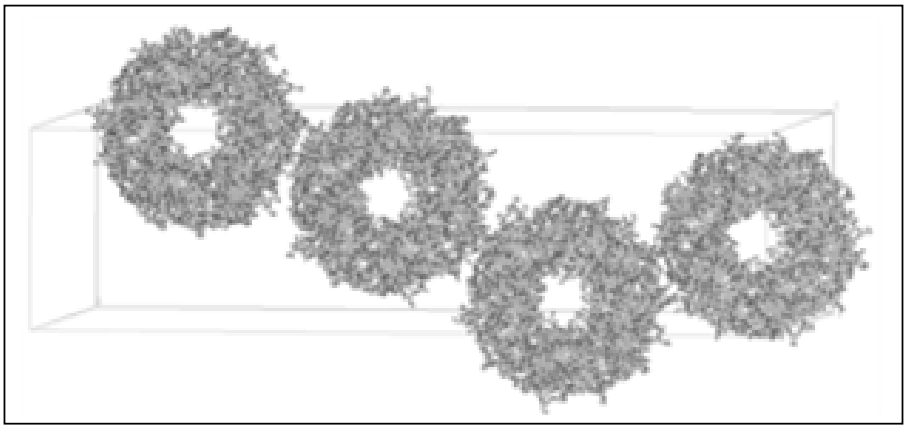

Figure 1. Structure of a complex of LS-AChBP with an agonist from NeuroSearch A/S determined at 2.47 Å resolution.

References

1. N. Unwin, *Refined structure of the nicotinic acetylcholine receptor at 4A resolution*, J. Mol. Biol. 346, 967, 2005.

2. C.D. Dellisanti, Y. Yao, J.C. Stroud, Z.Z. Wang, and L Chen, *Crystal structure of the extracellular domain of nAChR alpha1 bound to alpha-bungarotoxin at 1.94 A resolution*, Nat. Neurosci. 10, 953, 2007.

3. N. Bocquet, H. Nury, M. Baaden, C. Le Poupon, J.P. Changeux, M. Delarue, and P.J. Corringer, *X-ray structure of a pentameric ligand-gated ion channel in an apparently open conformation*, Nature 457, 111, 2009.

4. R.J. Hilf and R. Dutzler, *Structure of a potentially open state of a proton-activated pentameric ligand-gated ion channel*, Nature 457, 115, 2009.

5. K. Brejc, W.J. van Dijk, R.V. Klaassen, M. Schuurmans, J. van Der Oost, A.B. Smit, and T.K. Sixma, *Crystal structure of an ACh-binding protein reveals the ligand-binding domain of nicotinic receptors*, Nature, 411, 269, 2001.

6. P.H. Celie, R.V. Klaassen, S.E. van Rossum-Fikkert, R. van Elk, P. van Nierop, A.B. Smit, and T.K. Sixma, *Crystal structure of acetylcholine-binding protein from Bulinus truncatus reveals the conserved structural scaffold and sites of variation in nicotinic acetylcholine receptors*, J. Biol. Chem. 280, 26457, 2005.

7. Hansen SB, Sulzenbacher G, Huxford T, Marchot P, Taylor P, Bourne Y., *Structures of Aplysia AChBP complexes with nicotinic agonists and antagonists reveal distinctive binding interfaces and conformations*, EMBO J. 24, 3635, 2005.

The structure of odorant binding protein 4 from *Anopheles gambiae*.

Katerina E. Tsitsanou[1], Christina E. Drakou[1] and Spyros E. Zographos[1*]

[1] *Institute of Organic and Pharmaceutical Chemistry, The National Hellenic Research Foundation, 48, Vas. Constantinou Ave. Athens 11635, Greece.*
*e-mail: sez@eie.gr

Malaria is one of the world's most common diseases caused by the parasite *Plasmodium falciparum*, which is transmitted to humans by female anopheline mosquitoes, particularly *Anopheles gambiae*, during blood feeding. Odorant-binding proteins (OBPs), present in the olfactory sensilla of mosquito antenna, bind the hydrophobic odorant molecules entering the sensillum lymph cavity from the outside air space and transport them to the odorant receptors. These proteins may serve as molecular targets for the development of environmentally-friendly mosquito attractants and repellents hence preventing them from identifying their human hosts, obtaining blood meals from them, and transmitting the malaria parasite in the process.

A. gambiae's odorant-binding protein 4 (AgamOBP4) is the second OBP after AgamOBP1 [1] that has been crystallised to date. Herein, we have determined the structure of AgamOBP4 in various pH conditions. Single crystal diffraction data were collected on the MaxLab-ID911-2 station. AgamOBP4 is a novel mosquito odorant-binding structure and has been solved by molecular replacement methods using Drosophila's odorant binding protein LUSH (PDB: 3B7A, [2]) structure as molecular replacement model. The structure refinement and the comparative structural analysis of AgamOBP4 are in progress.

Table 1. Data collection and refinement statistics

Experiment	**AgamOBP4 (pH 4.6)**	**AgamOBP4 (pH 6.5)**	**AgamOBP4 (pH 8.5)**
Space group	$P3_121$	$I121$	$P22_12_1$
Unit cell dimensions (Å, °)	a= b= 51.80, c= 87.15, 90.0 90.0 120.0	a= 59.98, b= 56.82, c= 67.39, 90.0 100.8 90.0	a=33.96, b=55.59, c=56.26, 90.0 90.0 90.0
Resolution range (Å)	25.9-2.1 (2.21-2.10)	28.4-2.1 (2.21-2.10)	29.05-2.10 (2.21-2.10)
No. of observations	79775	83994	33322
No. of unique reflections	8343	12984	6603
$<I/\sigma(I)>$	22.1 (6.8)	12.6 (3.8)	19.4 (10.4)
Completeness (%)	99.9 (99.9)	99.3 (98.2)	99.8 (100.0)
R_{merge}	0.065 (0.316)	0.094 (0.437)	0.057 (0.124)
Redundancy	9.6 (8.3)	6.5 (6.1)	5.0 (5.2)
Molecules/asymmetric unit	1	2	1

Values in parenthesis correspond to the highest resolution shell.

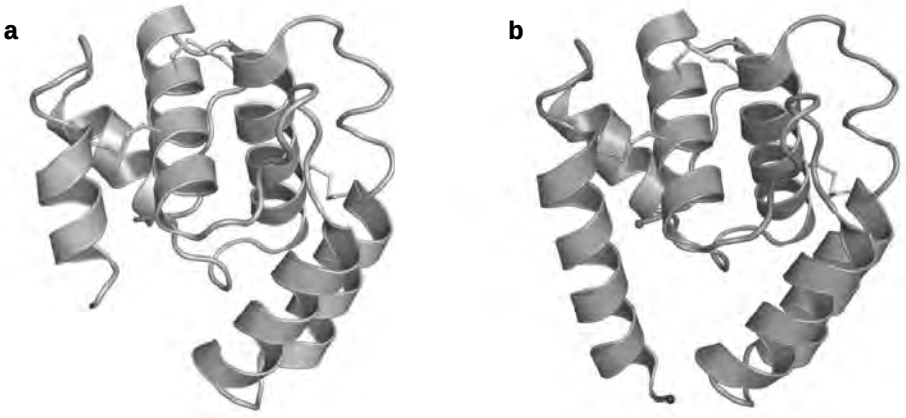

Figure 1. Ribbon representation of AgamOBP4 structure at **a)** acidic pH (4.6) and **b)** neutral or alkaline pH (6.5 or 8.0). N-terminal half shows an apparently disordered conformation at acidic pH.

[1] Wogulis M., Morgan T., Ishida Y., Leal W. S. and Wilson D. K. The crystal structure of an odorant binding protein from Anopheles gambiae: Evidence for a common ligand release mechanism. Biochem Biophys Res Commun 339, 157-164, 2006.
[2] Thode, A.B., Kruse, S.W., Nix, J.C. and Jones, D.N. The role of multiple hydrogen-bonding groups in specific alcohol binding sites in proteins: insights from structural studies of LUSH. J.Mol.Biol. 376, 1360-1376, 2008.

Commissioning of a Humidity Control Device (HC1) at station I911-5

Wimal Ubhayasekera[1], Thomas Ursby[1] and Marjolein MGM Thunnissen[2]

1: Beamline I911/Cassiopeia, MAX-lab, Lund University, Olle Römersväg 1, S-221 00 Lund Sweden
2: CMPS, Lund University, Getingevägen 60, S-221 00 Lund Sweden.

In order to obtain good quality diffraction data, it is necessary to obtain well-ordered crystals of biological macromolecules that diffract to high resolution with low mosaicity. This is one of the major bottlenecks in structure determination by X-ray diffraction. A typical protein crystal consists of 30 to 70% solvent and experiments have shown that post-crystallisation treatments that are correlated with defined and reversible unit cell modifications which influence the solvent content most, can be a tool for "recrystallisation" and optimisation (e.g. annealing experiments, reordering of the crystal, dehydration) (For reviews see Heras and Martin, 2005; Newman, 2006). However, although these experiments have shown that improvements in diffraction quality are obtainable, these treatments are not widely used mainly because of the difficulty of setting up reliable and repeatable experiments. A free mounting system (FMS) was developed to use more effectively the method of dehydration and although it was quite successful in a home laboratory set-up (Kiefersauer et al., 1996, 2000), the FMS requires very careful handling and is difficult to mount and operate within a synchrotron environment with a high turn-over of users.

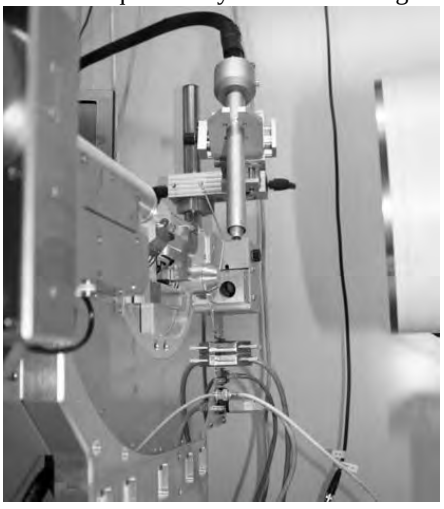

Figure 1 The HC1 mounted at I911-5

At the EMBL-Grenoble/ESRF a novel device for hydration control of macromolecular crystals has been developed, the HC1 (Sanchez-Weatherby, 2009), which has been developed to address an ease of use especially in a synchrotron environment. This HC1 has been thoroughly tested at several ESRF beamlines and is available for users. Since hydration experiments are carried out at room temperature, the effect of radiation damage will be more pronounced. This is especially a problem at the more intensive beam lines at the ESRF. At I911-5 the flux is relatively low and this would be an ideal environment for hydration type of experiments. In collaboration with the EMBL-Grenoble, ESRF and the Diamond synchrotron we have installed a HC1 at I911-5 (Figure 1) and we are currently testing the device on several test-systems. We foresee that the first real test-cases will follow shortly and at the end of the spring we will give our user community the opportunity to use this device.

Heras B. & Martin, J. L. (2005). *Acta Cryst.* D61, 1173–1180.
Kiefersauer R., Stetefeld J., Gomis-Rüth F. X., Romao M. J., Lottspeich F. & Huber R. (1996). *J. Appl. Cryst.* 29, 311–317.
Kiefersauer R., Than M. E., Dobbek H., Gremer L., Melero M., Strobl S., Dias J. M., Soulimane T. & Huber R. (2000). *J. Appl. Cryst.* 33, 1223–1230.
Newman J. (2006). *Acta Cryst.* D62, 27–31.
Sanchez-Weatherby J, Bowler M.W., Het J., Gobbo A., Felisaz F., Lavault B., Moya R., Kadlec J., Ravelli R.B.G. and Cipriani F. (2009) *Acta Cryst*. D66, 1237-1246.

X-ray Structure Studies of complexes of an inhibitor with activity against the drug resistant forms F227C and F227L of HIV-1 Reverse Transcriptase

Torsten Unge

Department of Cell and Molecular Biology, Structural Biology, BMC, Uppsala University, Box 596, SE-751 24 Uppsala, Sweden

A new generation of HIV-1 reverse transcriptase (RT) non nucleoside inhibitors (nnRTI) with potency against the drug resistance mutations F227C and F227L and I84V has been developed. X-ray data were collected at the beam lines 911.1-5 of a number of different co-crystallize complexes. Two structures of the most efficient inhibitor 109512 in comples with the two resistant forms of RT were determined to 2.2 and 2.7 Å resolution. The quality of the data as measured with Rmerge and Rpim were for the F227L mutant 0.06 and 0.03 respectively and for the F227C mutant 0.10 and 0.04. Figure 1 below shows a detail of the inhibitor interacting with the mutated residues V82T and I84V. Crystals produced under those the conditions are sensitive to dehydratization under the cryo conditions during X-ray data collection. 25% glycerol was used as cyo-protectant and flash freezing had to be done immediately before mounting in the xray-beam. Freezing immediately before the start of the data collection improved the resolution of the data with about 0.3 Å. The structure calculations were done with molecular replacement and simulated annealing with the program CNS [1]. Model building and was done in O [2]. Publication of this work is in progress.

1 Brunger AT (2007) Version 1.2 of the Crystallography and NMR system. *Nature protocols* **2**, 2728-2733.

2 Jones TA, Zou JY, Cowan SW & Kjeldgaard M (1991) Improved methods for building protein models in electron density maps and the location of errors in these models. *Acta Crystallogr A* **47 (Pt 2)**, 110-119.

Substrate binding in *Phanerochaete chrysosporium* laminarinase Lam16A and synthesis of cyclic β-glucan using glycosynthase mutant E115S

Jonas Vasur[1], Rie Kawai[1,2], K. Hanna M. Jonsson[3], Göran Widmalm[3], Åke Engström[4], Martin Frank[5], Evalena Andersson[1], Henrik Hansson[1], Zarah Forsberg[1], Kiyohiko Igarashi[2], Masahiro Samejima[2], Mats Sandgren[1] and Jerry Ståhlberg[1]

[1]Department of Molecular Biology, Swedish University of Agricultural Sciences, PO Box 590, SE-751 24 Uppsala, Sweden; [2]Dept. Biomaterials Sciences, Graduate School of Agricultural and Life Sciences, The University of Tokyo, Tokyo, Japan; [3]Dept. Organic Chemistry, Stockholm University, Stockholm, Sweden; [4]Dept. Medical Biochemistry and Microbiology, Uppsala University, Uppsala, Sweden; [5]Molecular Structure Analysis, German Cancer Research Center, Heidelberg, Germany.

Laminarinase Lam16A from the wood-degrading basidiomycete fungus *Phanerochaete chrysosporium* is a 36 kDa endo-β-1,3(4)-glucanase enzyme that consists of a single GH family 16 catalytic module of 298 amino acids [1]. Lam16A can hydrolyze both β-1,3 and β-1,4 glucosidic bonds, displays broad substrate specificity and cleaves linear β-1,3-glucan, branched β-1,3/1,6-glucan (e.g. laminarin) and β-1,3-1,4-glucan (e.g. lichenan), and is of potential interest for processing of β-glucans in cereals and fungal biomass to added-value products. Our studies aim at elucidating substrate-binding and hydrolysis mechanisms and structural determinants for transglycosylation vs. hydrolytic activity.

Figure 1. Apo-structure of Lam16A wt

We have previously solved the apo-structure of Lam16A wildtype by native sulphur-SAD (Fig. 1; PDB code 2CL2) [2], and have after that obtained more than 10 structures in complex with various oligosaccharides (Fig. 2) using Lam16A wt (PDB codes 2W39, 2W52) [3] and catalytic mutants E115G, E115S, and E120A [4]. Most of the diffraction data was collected at MAX-lab. The structures show how the enzyme binds linear β-1,3-glucan (curdlan), branched β-1,3/1,6-glucan (laminarin) and β-1,3-1,4-glucan (lichenan), how it can hydrolyse both β-1,3 and β-1,4-linkages, and how β-1,6-branches can be accomodated in the substrate-binding cleft [3,4].

Surprisingly, the structure of the Lam16A nucleophile variant E115S in complex with β-1,3-glucan laminariheptaose (L7) revealed that the bound oligosaccharide "bent back upon itself", forming a loop with seven glucosyl residues with the ends meeting at the catalytic center of the enzyme (Fig. 3).

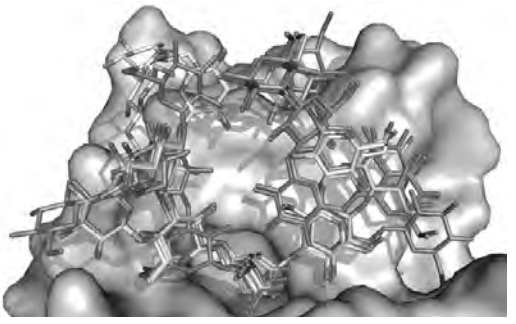

Figure 2. Overlay of Lam16A structures with ligands

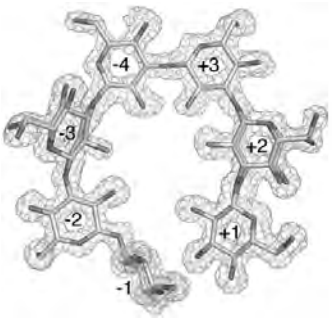

Figure 3. L7 ligand bound in Lam16A E115S with electron density at 0.42 eÅ^{-3}

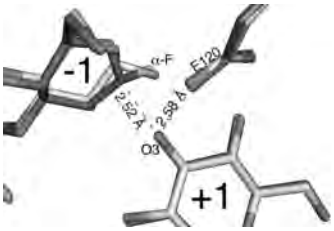

Figure 4. Overlay at catalytic centre, of L7 and αL7F in Lam16A E115S.

Inspired by these results, we synthesized α-laminariheptaosyl fluoride (αL7F) to test whether the ends of the ligand may be joined via a glycosynthase reaction. Figure 4 shows an overlay of the Lam16A E115S complex structures with L7 and the L7 α-fluoride (αL7F) bound at the active site (PDB codes 2WLQ, 2WNE). A cyclic heptaglucan was indeed formed upon reaction of αL7F with the Lam16A E115S variant, as confirmed by matrix-assissted laser desorption/ionization (MALDI) MS and by NMR spectroscopy [5]. To our knowledge this was the first report of a glycosynthase that joins the reducing and nonreducing ends of a single oligosaccharide and the first reported synthesis of cyclic β-glucan.

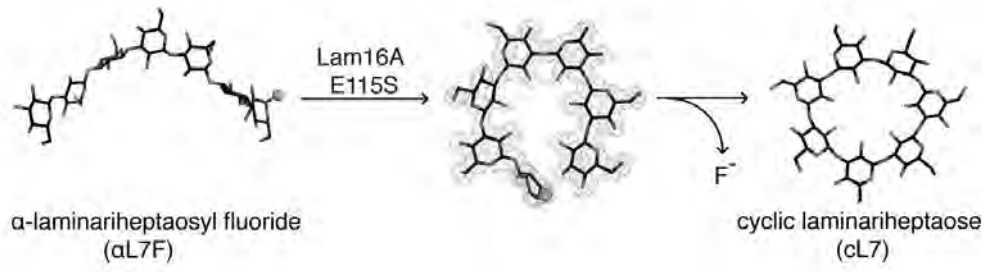

[1] Kawai R, Igarashi K, Yoshida M, Kitaoka M, Samejima M. (2006) Hydrolysis of β-1,3/1,6-glucan by glycoside hydrolase family 16 endo-1,3(4)-β-glucanase from the basidiomycete *Phanerochaete chrysosporium.* Appl Microbiol Biotechnol **71**, 898–906.

[2] Vasur J, Kawai R, Larsson AM, Igarashi K, Sandgren M, Samejima M, Ståhlberg J. (2006) X-ray crystallographic native sulfur SAD structure determination of laminarinase Lam16A from *Phanerochaete chrysosporium*. Acta Crystallogr D **62**, 1422-1429.

[3] Vasur, J., Kawai, R., Andersson, E., Igarashi, K., Sandgren, M., Samejima, M. and Ståhlberg, J. (2009) X-ray crystal structures of *Phanerochaete chrysosporium* Laminarinase16A in complex with products from lichenan and laminarin hydrolysis. FEBS Journal **276**, 4282-4293.

[4] Vasur, J. (2009) Probing promiscuity: Structural studies of *Phanerochaete chrysosporium* Laminarinase 16A. Acta Universitatis Agriculturae Sueciae, Doctoral Thesis No. 2009:98. Department of Molecular Biology, Swedish University of Agricultural Sciences, Uppsala, Sweden, ISBN 978-91-576-7445-6.

[5] Vasur, J., Kawai, R., Jonsson, K.H.M., Widmalm, G., Engström, Å., Frank, M., Andersson, E., Hansson, H., Forsberg, H., Igarashi, K., Samejima, M., Sandgren, M. and Ståhlberg, J. (2010) Synthesis of Cyclic β-Glucan Using Laminarinase 16A Glycosynthase Mutant from the Basidiomycete *Phanerochaete chrysosporium*. J. Am. Chem. Soc. **132**, 1724-1730.

Structural Studies of Barley Limit Dextrinase

M.B. Vester-Christensen[1,2], M.A. Hachem[1], B. Svensson[1] & A. Henriksen[2]

[1]*Enzyme and Protein Chemistry, Department of Systems Biology, Technical University of Denmark, Kgs. Lyngby, Denmark*

[2]*Carlsberg Laboratory, Copenhagen, Denmark.*

Barley limit dextrinase (HvLD) catalyses hydrolysis of the α-1,6-glycosidic linkages of amylopectin derived limit dextrins in germinating barley[1]. Barley seed starch is composed of approximately 70% amylopectin (Figure 1), which has an α-1,4-glucosidally linked core decorated with α-1,6-glucosidally linked branches[2].

HvLD catalyses hydrolysis *via* a general acid catalysis that requires a catalytic nucleophile and a catalytic acid/base proton donor. Hydrolysis results in the retention of the anomeric conformation through a double displacement mechanism characteristic of the glycoside hydrolase 13 family, to which HvLD belong.

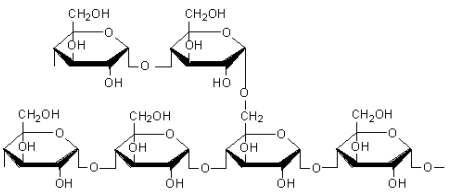

Figure 1. Pattern of α-1,4 and α-1,6-glucosidic linkages in the amylopectin component of starch.

Debranching of limit dextrins is needed for an efficient mobilization of stored energy *in-vivo,* and the end result is a degradation of the amylopectin component of starch to maltose and glucose. Starch debranching enzymes are also involved in starch biosynthesis. Absence of debranching activity can give rise to changed starch grain morphology and even abolished starch grain synthesis.

Besides the role in germination and starch synthesis, HvLD is critical for the malting and mashing steps in beer production. Here, limit dextrins are hydrolysed to fermentable sugars for ethanol production. In malt, LD is present in a free, active form and in an inactive form, bound to its endogenous proteinaceous inhibitor, HvLDI.

To understand the molecular basis for the substrate specificity of HvLD and its activation, HvLD has been recombinantly expressed in *Pichia pastoris*[3] for crystallisation. Crystals have been obtained and diffraction data have been collected to 2.5 Å at the I911-5 beam line at MAX-lab II.

[1] M. Kristensen, F. Lok, V. Planchot, I. Svendsen, R. Leah, & B. Svensson, Biochim. Biophys. Acta 1431, 538-546 (1999),
[2]T. Vasanthan, & R. Hoover (2009) Barley Starch: Production, properties, modification and uses. in *Starch: Chemistry and technology* (BeMiller, J., and Whistler, R. eds.), 3 Ed., Elsevier, Burlington, MA, USA. pp 601-628 (2009),
[3]M.B. Vester-Christensen, M.A. Hachem, H. Næsted & B. Svensson, Prot. Expres. Purif. 69, 112-119 (2010).

Alexei Preobrajenski preparing a sample holder for his next beamline, January, 2010.
Photo: Annika Nyberg

NEXAFS study of surface composition in blend films of APFO3:PCBM

Ana Sofia Anselmo, Krister Svensson, Ellen Moons

Department of Physics and Electrical Engineering, Universitetsgatan 1, Karlstad University, 65188 Karlstad, Sweden

Solution-processing and bulk-heterojunction (BHJ) architectures in organic photovoltaic (OPV) devices are some of the most promising technological solutions to the challenge of low-cost renewable energy[1]. While the conversion efficiency of polymer-based OPV devices has now reached 7.4%,[2] it is still lower than that of inorganic solar cells in first and second generation photovoltaics. Many factors contribute to the limiting performance of OPVs, among them the difficulty to control the morphology in the active layer. This morphology is mainly due to the low entropy of mixing of polymer blends which leads to phase-separated domains when the solvent is extracted during film preparation. Characterizing and controlling the morphology is a very important factor to improve the understanding of the device performance.

Recently, spontaneous vertical phase separation has been demonstrated for several polymer blend systems through a variety of characterization techniques.[3-8] For 1:1 blends of poly(3-hexylthiophene) (P3HT) with the fullerene derivative [6,6]-phenyl-C61-butyric acid methyl ester (PCBM), variable-angle spectroscopic ellipsometry[4] studies, as well as NEXAFS measurements[5], have shown compositional differences between front- and backside surfaces of the film. By neutron reflectivity,[6] a compositional depth profile has been determined for this blend. The observed self-stratification, with polymer-enrichment of the free surface and PCBM-enrichment of the interface region, can be explained by surface-directed spinodal decomposition, triggered by surface energy minimization in a system where the polymer has a lower surface energy than the fullerene. Our previous dynamic secondary ion mass spectrometry (dSIMS) studies[3] of blends of the low-bandgap polymer poly[(9,9-dioctylfluorenyl-2,7-diyl)-co-5,5-(4',7'-di-2-thienyl-2',1',3'-benzothiadiazole] (APFO3) with PCBM resulted in depth profiles that show that composition gradients spontaneously form in a APFO3:PCBM 1:4 (w/w) film during spincoating when a high vapour pressure solvent is used. The composition of the corresponding 1:1 blend film was homogeneous, while the 1:4 blend exhibited a multilayer structure with a polymer-enriched surface.

A near-edge x-ray absorption fine structure (NEXAFS) spectroscopy study of APFO3 blended with PCBM films in 1:1 and 1:4 w/w ratios was carried out at the D1011 beamline at MAX-lab. Spectra for the pure components were also measured and differences in the π^*- and σ^*- resonance peaks in those spectra served as labels for the analysis of the composition of the blend films. In the blend spectra, the relative intensities of the resonance peaks gave an estimate of the blend composition. Spectra obtained in partial (PEY) and in total (TEY) electron yield modes, which probe the surface and sub-surface regions of the films respectively, were also compared. The main findings are shown in figure 1.

The results confirm the existence of compositional gradients in the vertical direction in the 1:4 blend. The surface compositions of the 1:1 and 1:4 blends are only slightly different, as evidenced by their PEY spectra (see figures 1a and 1b). The PEY spectra of the 1:4 blend was fitted with a linear combination of the spectra of the pure components, taking into account the densities of the components (figure 1d). The fitting parameters were 1 and 0.98, for the polymer and the PCBM respectively. This provides evidence that the surface composition of

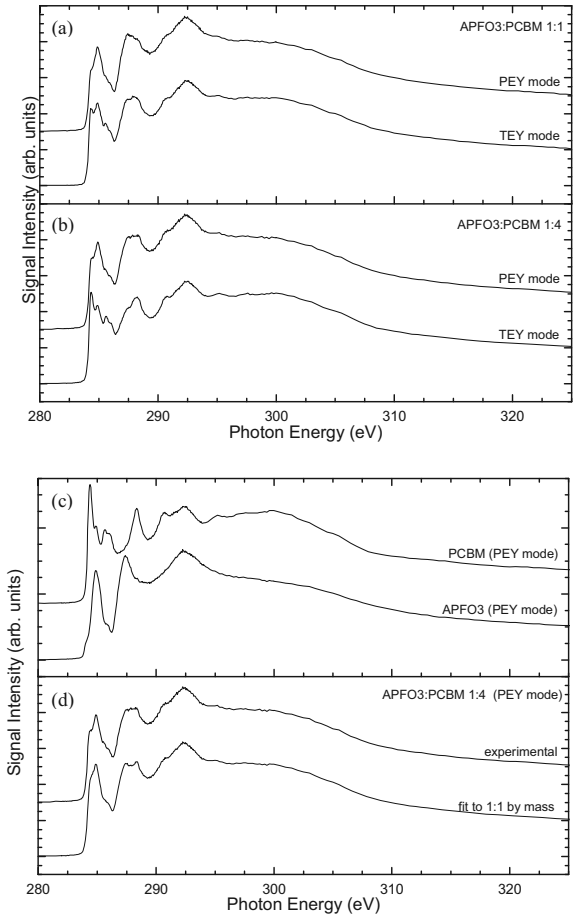

Figure 1. *NEXAFS spectra of thin films of APFO3, PCBM, and APFO3:PCBM blends in 1:1 and 1:4 w/w ratios collected in PEY and TEY modes: (a) and (b) spectra for the 1:1 and 1:4 w/w APFO3:PCBM blends collected in PEY and TEY modes; (c) spectra of the pure components collected in PEY mode; (d) spectra of the 1:1 w/w blend film collected in PEY mode and a fitted curve, with 1:0.98 w/w fitting parameters.*

the 1:4 blend is close to that of the 1:1 blend. The sub-surface compositions, seen in the TEY spectra in figures 1a and 1b, on the other hand, are clearly distinct. In both cases, the sub-surface composition contains a higher PCBM fraction than the surface. These results are in good agreement with results from our dSIMS studies on this system.[3] The detailed account of the experiment and results is in preparation and should be published within the next months.

References

(1) Dennler, G. et al *Advanced Materials* **2009**, *21*, 1323 – 1338;
(2) Liang, Y. et al Advanced Materials **2010**, *22*, 1-4.
(3) Björström, C.M. et al *J. Phys.: Condens. Matter* **2005,** *17,* L529 – L534;
(4) Campoy-Quiles, M. et al *Nature Materials* **2008**, *7*,158 – 164;
(5) Germack, D.S. et al *Applied Physics Letters* **2009,** *94,* 233303-1 – 233303-3;
(6) Kiel, J.W. et al. Soft Matter **2010**, *6*, 641 – 646;
(7) Arias, A.C. et al *Applied Physics Letters* **2002,** *80,* 1695 – 1697;
(8) Yan, Y. et al *Adv. Funct. Mater.* **2008,** *18,* 1783 – 1789.

Synthesis of graphene on β-SiC(001)

V.Yu. Aristov [1,2], G. Urbanik [1], K. Kummer[3], D. V. Vyalikh[3], O. V. Molodtsova[3], A. B. Preobrajenski[4], A. Zakharov[4], C. Hess[1], T Hänke[1], B. Büchner[1], I. Vobornik[5], J. Fujii[5], G. Panaccione[5], Yu. A. Ossipyan[2], and M. Knupfer[1]

[1] *Leibniz Institute for Solid State and Materials Research, D-01069 Dresden, Germany*

[2] *ISSP, Russian Academy of Sciences, Chernogolovka, Moscow Distr., 142432, Russia*

[3] *ISSP, Dresden University of Technology, D-01062 Dresden, Germany*

[4] *MAX-lab, Lund University, Box 118, 22100 Lund, Sweden*

[5] *TASC National Laboratory, INFM-CNR, SS 14, km 163.5, I-34012 Trieste, Italy*

The substrate considered in this paper, cubic 3C-SiC (*β*-SiC) is readily grown in large size (> 300 mm in diameter) commercially available Si wafers. Apparently, due to its cubic lattice, *β*-SiC does not appear suitable for graphene growth. Contrary to common belief, we succeeded in growing high quality graphene on cubic *β*-SiC and found that the interaction with the substrate is almost negligible, rendering this system a perfect candidate for future graphene-based electronics.

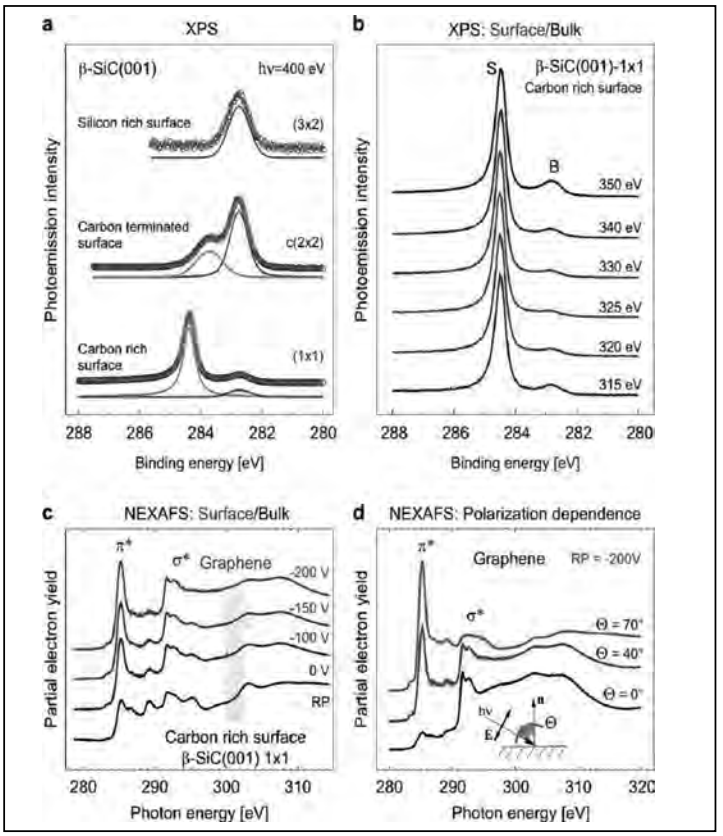

Fig. 1. Core-level photoemission and near-edge X-ray absorption fine structure spectroscopy. a) C 1*s* photoemission taken from the *β*-SiC(001) at different stages of the surface preparation procedure using hν = 400 eV photon energy. b) C 1*s* photoemission of the C-rich *β*-SiC(001) 1*x*1 surface as a function of photon energy. As hν is tuned away from the most surface sensitive regime at 325 eV component B rises which proves its bulk origin. The binding energy of the surface component S equals that found for graphene or graphite. c) C 1*s* NEXAFS spectra recorded with increasing retard potential in order to separate bulk and surface features. At the most surface sensitive regime (RP = - 200 eV) the

spectral shape equals those found for graphene/graphite. d) With changing incidence angle Θ of the linearly polarized light a strong anisotropy is found. The behavior of the resonances suggests that the π* orbitals are collectively oriented parallel to the surface normal and the σ* orbitals perpendicular, as expected for graphene/graphite.

We exposed our cubic 3C-SiC (*β*-SiC) samples with Si-rich surface to a series of annealing cycles with increasing temperature from 1200 *K* up to 1550 *K*. We have got perfect graphene layer, which was investigated by different methods. The results PES, and NEXAFS measurements are presented in Fig. 1, while the results of STM investigation are presented in Fig. 2.

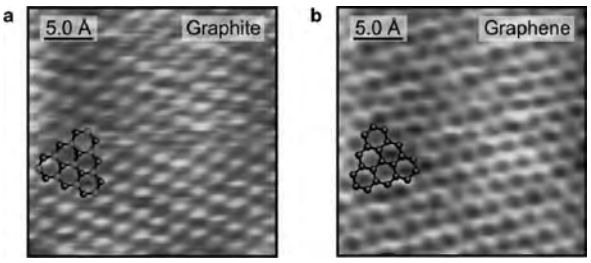

Fig. 2. Scanning tunneling microscopy. a) Graphite structure: The two non-equivalent atom sites are colored black and blue, respectively. b) Graphene structure: All carbon atom sites are equivalent. Hence the characteristic honeycomb pattern shows up.

The electronic band structure of the occupied electronic states was examined by ARPES. A typically observed energy-momentum map is shown in Fig. 3.

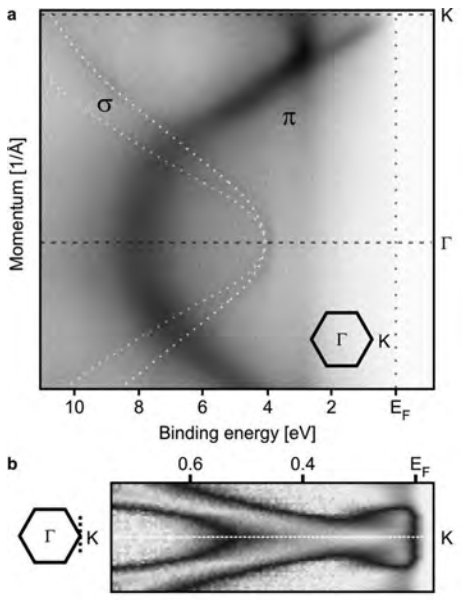

Fig. 3. Electronic states in graphene on the *β*-SiC(001) surface. a) Overview ARPES intensity map taken along the ΓK direction. b) ARPES intensity map taken at the K point along the black dotted line.

In summary, we demonstrated for the first time the feasibility of graphene synthesis on cubic *β*-SiC. Very simple procedure for obtaining graphene on the cheap, commercially available *β*-SiC/Si wafers of large diameters represents a huge step towards technological application of this material as the synthesis is compatible with industrial mass-production. The ability to grow large single-crystal-domains is a major target of graphene growth. As the next step of the investigation we plan to evaluate the size of the graphene grains grown so far on cubic *β* -SiC and find the approach of formation of relatively large domains, for example by annealing in argon atmosphere of about 1 bar.

Acknowledgments. This work was supported by the EC Transnational Access to Research Infrastructure via MaxLab, V.Yu.A. thanks the RFBR (Grant Num. 08-02-01170).

[1] V.Yu. Aristov, G. Urbanik, K. Kummer, D. V. Vyalikh, O.V. Molodtsova, A.B. Preobrajenski, A. Zakharov, C. Hess, T Hänke, B. Büchner, I. Vobornik, J. Fujii, G. Panaccione, Yu.A. Ossipyan and M. Knupfer, *Nano Lett.* **2010**, 10, 992-995.

Adsorption of long-chain alkanethiols on Au(111) - a look from the substrate

Frederick Chesneau[1], Jianli Zhao[1], Cai Shen[2], Manfred Buck[2], and Michael Zharnikov[1]

[1]*Angewandte Physikalische Chemie, Universität Heidelberg, 69120 Heidelberg, Germany*

[2]*EaStCHEM School of Chemistry, University of St Andrews, St. Andrews KY16 9ST, United Kingdom*

We have performed detailed measurements of the Au $4f_{7/2}$ HRXPS spectra for several differently prepared hexanethiolate (C6S) and dodecanethiolate (C12S) self-assembled monolayers (SAMs) on Au(111) to prove the reliability of different adsorption models (Figure 1). The SAMs were characterized by HRXPS and STM and exhibited, with one exception, well-defined identities of the chemical species, chemical homogeneity and distinct crystallographic structures with either a sole $(2\sqrt{3}\times3)$rect lattice (Figure 2) or a coexistence of $(2\sqrt{3}\times3)$rect and $(\sqrt{3}\times\sqrt{3})$R30° arrangements. The emphasis of the Au $4f_{7/2}$ HRXPS experiments was put on the detailed analysis of the respective spectra. In accordance with previous work,[1-3] these spectra exhibited a single asymmetric peak comprised of the merging bulk (**B**) and surface ($\mathbf{S_T}$) components of the Au $4f_{7/2}$ emission resulting from the adsorbate-induced shift of the latter component as compared to its position for clean Au surface ($\mathbf{S_C}$) (Figures 3 and 4). However, in contrast to our previous report[1] but similar to the recent results for methylthiolate (C1S) and butylthiolate (C4S) monolayers on Au(111)[2,3], the joint peak was not the only spectral feature, but an additional weak shoulder at its high binding energy (BE) side was observed (Figure 4). Following the interpretation of refs 2 and 3, the existence of the shoulder was associated with the adsorbate-induced splitting of the surface components ($\mathbf{S_C}$) into the peak ($\mathbf{S_T}$) merging with the bulk component and a stronger shifted peak (**T**) appearing as a shoulder. Such a splitting suggests that different gold atoms at the SAM/Au(111) interface are differently affected by the alkanethiolate (AT) adsorbates. One

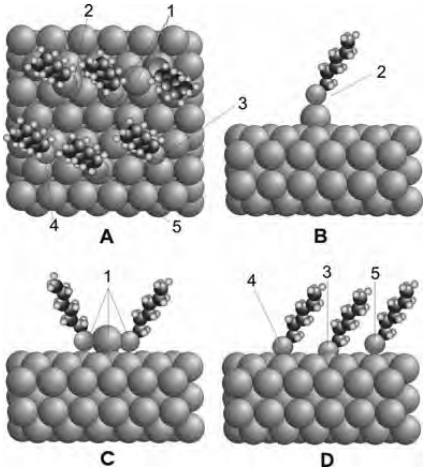

Figure 1. Schematic view of the proposed local binding geometries for the bonding of ATs to Au(111) substrate; A: top view, B-D: side views. (1) Au-adatom-dithiolate bonding configuration; (2) Au-adatom-monothiolate bonding configuration; (3-5) adsorption into hollow, bridge, and atop site on the unreconstructed (111) surface, respectively.

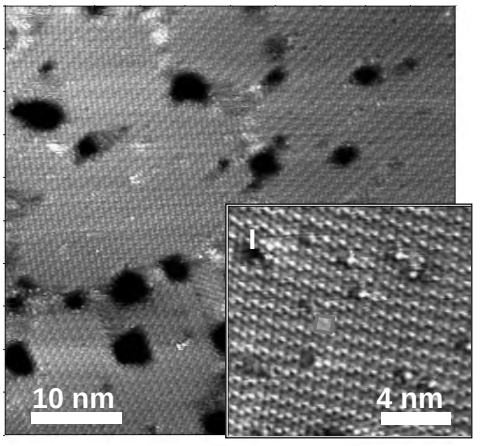

Figure 2. STM image of C6S/Au/mica; the SAMs were prepared at room temperature. A selected area of the image is magnified to show the crystallographic structure - $(2\sqrt{3}\times3)$rect lattice in the given case. The respective unit cell is shown by red.

possibility in this regard is that only a part of the Au atoms (**T**) at the SAM/Au interface is directly bonded to the thiolate moieties whereas the other atoms ($\mathbf{S_T}$) are weakly bonded or not directly bonded to adsorbates. Another possibility is that a part of the Au-atoms at the interface is distinctly different, as e.g Au-adatoms the existence of which is claimed by almost all recent models of the interface. Considering that the high BE shoulder is observed for both short-chain[2,3] and long-chain (this work) AT monolayers on Au(111), such a heterogeneous interface architecture seems to be characteristic of these systems, independent of the chain length.

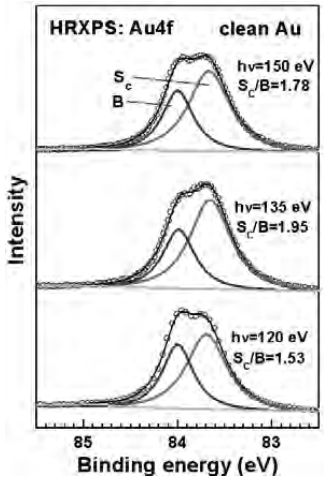

Figure 3. Au $4f_{7/2}$ HRXPS spectra of clean Au surface acquired at photon energies of 120, 135, and 150 eV (open circles). The spectra are decomposed into the bulk (**B**; blue lines) and surface ($\mathbf{S_C}$ with **C** for the clean surface; red lines) components; the resulting fitting curves are depicted by thin black solid lines. The $\mathbf{S_C/B}$ intensity ratios are

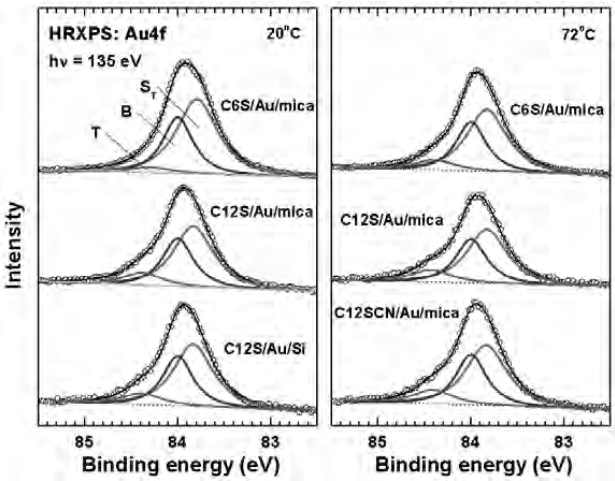

Figure 4. Au $4f_{7/2}$ HRXPS spectra of C6S/Au/mica, C12S/Au/mica, C12/Au/Si prepared at a temperature of 20°C (left panel) and Au $4f_{7/2}$ HRXPS spectra of C6S/Au/mica, C12S/Au/mica, and C12SCN/Au/mica prepared at a temperature of 72°C (right panel). The spectra are decomposed into the bulk (**B**; blue lines) and two surface ($\mathbf{S_T}$ and **T**) components; the resulting fitting curves are depicted by thin black solid lines. The $\mathbf{S_T}$ (with **T** for the thiolated surface) and **T** components are depicted by red and dark yellow lines, respectively.

The exact details of the interface structure can be, however, different for the short-chain and long-chain monolayers. Whereas the $\mathbf{S_T/T}$ intensity ratio, which can be considered as a fingerprint parameter of the different adsorption models, was found to be either 3 or 2.2 (relaxed fitting parameters) for C1S and C4S monolayers,[2,3] it is close to 5 for the hexanethiolate and dodecanethiolate SAMs of this study. In spite of the self-consistent fitting procedure over the entire data set in our case and very careful data processing in the case of C1S and C4S, it is not clear at the moment whether this difference is significant or just related to the different constraint and parameter settings. It looks, however, that all possible values of the $\mathbf{S_T/T}$ intensity ratio are far away from the values characteristic of the unreconstructed Au(111) surface. In this sense, the Au $4f_{7/2}$ HRXPS data provide a strong evidence for the existence of Au adatoms at the interface between AT monolayers and Au(111) substrate. To derive an exact adsorption model an input by theory regarding the core level shifts for different adsorption configurations is necessary. This work has been supported by DFG (ZH 63/10-1).

[1]K. Heister, M. Zharnikov, M. Grunze, and L. S. O. Johansson, J. Phys. Chem. B **105**, 4058 (2001).
[2]A. Chaudhuri, T. J. Lerotholi, D. C. Jackson, D. P. Woodruff, and V. Dhanak, Phys. Rev. Lett. **102**, 126101 (2009).
[3]A. Chaudhuri, T. J. Lerotholi, D. C. Jackson, D. P. Woodruff , and V. R. Dhanak, Surf. Sci. 604, 227 (2010).

NEXAFS studies on pristine and photo-polymerized P3HT:PCBM blends

Andrzej Dzwilewski[*], Ana Sofia Anselmo[#], Ellen Moons[#]

[*]*Department of Applied Physics, Eindhoven University of Technology, P.O. Box 513, 5600 MB Eindhoven, The Netherlands*

[#]*Department of Physics and Electrical Engineering, Universitetsgatan 1, Karlstad University, 65188 Karlstad, Sweden*

Photo-dimerization of [6,6]-phenyl-C61-butyric acid methyl ester, *PCBM*, has proven to be a powerful tool for patterning of organic electronic devices, specifically organic field effect transistors (OFETs) prepared from blends of poly(3-hexylthiophene) *P3HT* and *PCBM*.[1] Moreover, as we have shown in a recent paper,[2] Photo-induced and Resist free Imprint pattering (PRI) based of photo-dimerization of *PCBM* allowed the single solution step production of organic complementary (CMOS) circuits. The PRI technique consists of two major processing steps: 1) local photo-irradiation of the *P3HT*/*PCBM* blend by visible laser light and 2) subsequent development of the film in an organic solvent mixture that is selective for PCBM. As a result of the local exposure to laser light in the PRI treatment two electronically and morphologically different materials can be obtained in one solution processing step, i.e. the exposed and developed (ED) material, and the unexposed and developed (UD) material. The *PCBM* component in the irradiated area of the blend becomes effectively insoluble in a mixture of solvents, while the non-irradiated area of the blend loses its *PCBM* component during development. Therefore, we expect that the composition of the ED material is left unchanged, while the composition of the UD material should be the pure polymer film. This hypothesis is confirmed by electrical transport measurements that show p-type conductivity in the ED region, and partially by the use of Raman spectroscopy. However, the use of Raman spectroscopy for the described system is problematic, because the Raman active modes in *P3HT* overlap with the most interesting modes for fullerene material (Ag(2) mode at 1469-1454 cm^{-1}).

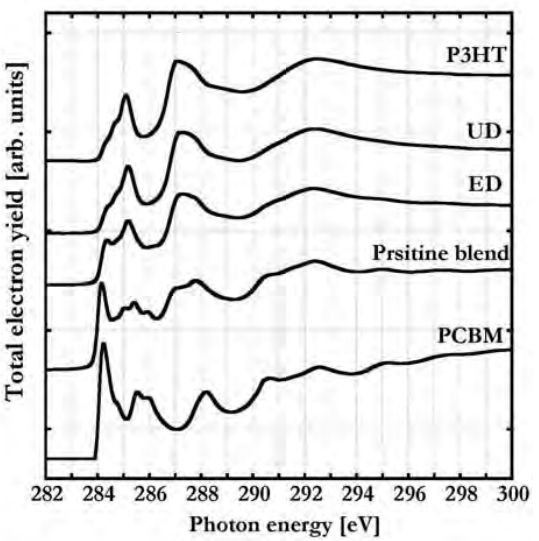

Fig 1. NEXAFS spectra of P3HT, PCBM and the P3HT:PCBM (1:3) blend films spincoated on HMDS-treated silicon, after the various treatments: pristine blend: no treatment; ED: exposed to laser light and developed in solvent mixture; UD: unexposed and developed in solvent mixture.

A systematic NEXAFS study of pure components, pristine, photo-treated and developed blends of P3HT:PCBM (1:3) on 1,1,1,3,3,3-hexamethyldisilazane *HMDS* treated substrates was carried out at the D1011 beamline at MAX-lab. The manuscript describing the whole study is in preparation and is expected to be submitted during spring 2010.

NEXAFS proved to be a very powerful tool for studying this system, as the main peaks in spectra for *P3HT* and *PCBM* do not overlap and pure *PCBM*, pure *P3HT*, and the blend can be clearly distinguished. The method gave spectroscopic proof that the composition of the remaining material after washing the pristine blend (UD material) is pure *P3HT* polymer, and the photo-irradiated blend (ED material) retains its two component character. (see Figure 1)

Based on the relative intensities of *P3HT* and *PCBM* peaks we were able to estimate the actual blend composition both on the surface using partial electron yield (PEY) and deeper in the subsurface region of the film using total electron yield (TEY). The samples of pristine and photo-irradiated blends show clear differences between their surface and subsurface compositions suggesting the existence of the vertical composition gradients. These differences in PEY and TEY correlate well with the existence of a polymer-enriched surface of the blend film. Such gradients have been observed in thin films of *P3HT/PCBM* blends by others using variable-angle spectroscopic ellipsometry[3] and neutron reflectivity[4] and also in other polymer/*PCBM* blends by dynamic secondary ion mass spectrometry (d-SIMS).[5] All these results show a polymer-enrichment of the surface of the blend film, which is the low surface energy component in the blend, and are due to surface-directed spinodal decomposition.

References

(1) Dzwilewski, A.; Wagberg, T.; Edman, L. *Journal of the American Chemical Society* **2009**, *131*, 4006-4011.
(2) Dzwilewski, A.; Matyba, P.; Edman, L. *Journal of Physical Chemistry B* ***2010***, *114*, 135-140.
(3) Campoy-Quiles, M., et al., *Nature Materials* **2008**, *7*,158-164
(4) Kiel, J.W. et al., *Soft Matter* **2010**, *6*, 641-646.
(5) Björström, C.M. et al, *J. Phys.: Condens. Matter* **2005,** *17,* L529–L534.

X-ray photoemission spectroscopy and magnetization study at the solubility limit of Co doped ZnO

R. Knut,[1] M. Wikberg,[2] K. Lashgari,[1,3] V. A. Coleman,[1] P. Svedlindh,[2] G. Westin,[3] and O. Karis[1]

[1]*Department of Physics, University of Uppsala, Sweden*
[2]*Department of Engineering Sciences, Uppsala University, Sweden*
[3]*Department of Materials Chemistry, University of Uppsala, Sweden*

INTRODUCTION

A number of questions regarding the magnetic properties of dilute magnetic semiconductor (DMS) systems have been raised, and many attempts to understand the influence of both extrinsic and defect induced *n*-doping in transition metal doped ZnO have been made[1]. Today, there is a general agreement that the properties of these materials are strongly dependent on the magnetic and chemical configuration of the dopant atoms.There have been many reports of ferromagnetism (even at room temperature) for many different DMS systems but the extracted magnetic moments are in most cases very small compared to the expected magnetic moment of the dopant atom. The question which is always raised is whether the material is phase pure or not. All characterization methods have limitations and even though several complementary techniques may be employed, it can be difficult to eliminate all doubts concerning the purity of a sample. This shows the importance of this question and the necessity of studying samples on the borderline of phase/non-phase pure to enable phase pure samples to be identified with high certainty. In this study we focus on the electronic structure and magnetic properties of Co doped ZnO at the solubility limit.

EXPERIMENT

The samples used in this study were ZnO doped with 15 at.% Co fabricated through solution based alkoxide chemistry. Details of the synthesis of the alkoxide precursors is described elsewhere[2]. The samples were post annealed for 15 min in Ar atmosphere at 250, 400, 500, 600 and 800°C after which they were characterized using grazing incidence (GI) x-ray diffraction (XRD). Prior to spectroscopic measurements, all samples were heated to 250°C in vacuum to desorb physisorbed surface adsorbates. Magnetic measurements were performed in SQUID magnetometer.

RESULTS

From magnetization (M) versus magnetic field (H) measurements (not shown), all samples exhibit a linear low field dependence with no remanent magnetization or coercivity. From the low field slope of the M versus H curves, effective magnetic moments (μ_{eff}) have been extracted (given in Table I) with values deviating

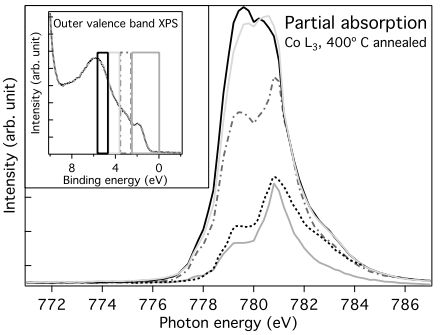

FIG. 1. Partial absorption of the Co L_3 edge. The inset shows the VB XPS and the boxes indicate which BE ranges have been integrated. The inner part shows an absorption similar to what is expected for Co 2+. The outer VB states have a different shape with a sharp peak at 781 eV photon energy. The dashed black line is a reference spectrum of Co_3O_4 obtained from Bazin et al.[4].

significantly from the value ($3\mu_B$) expected for tetrahedrally coordinated Co 2+. Comparing μ_{eff} with magnetic moments extracted from the saturation magnetization (μ_{HF}) a large discrepancy is found, which together with the very small μ_{HF} values, indicates that small antiferromagnetic (AFM) clusters with uncompensated spins are the source of the magnetic behavior for the 150, 250, 600 and 800°C samples[1]. The 400°C sample reaches saturation at significantly lower field and can therefore not be analyzed in the same manner.

By integrating over a specific binding energy (BE) range from a resonant photoemission spectrum (not shown) we are able to construct a partial absorption spectrum. In Fig. 1 we show a partial Co L_3 absorption spectrum for the 400°C sample. The inset shows the valence band (VB), and the colored boxes show which BE ranges have been integrated. The absorption obtained at binding energies corresponding to the inner parts of the VB looks similar to what can be expected for substituted Co 2+.The absorption obtained for the outer VB has a very different shape. Comparing it to the reference spectra of Co_3O_4 (dashed black line in Fig. 1) we can assign these to a spinel phase. The XPS data have been fitted using two different model spectra measured at the high kinetic energy (HIKE) beamline KMC-1 at the Helmholtz center in Berlin[3]. The first

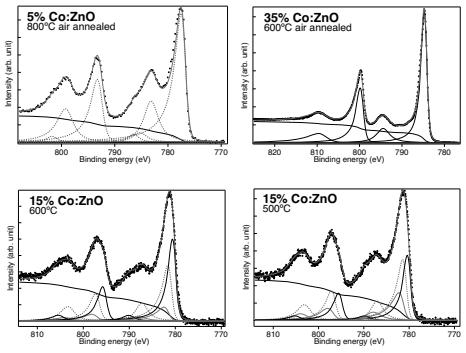

FIG. 2. Core level XPS of Co $2p_{3/2,1/2}$. The top left graph is a low concentration Co doped ZnO sample and represents the model spectrum of substituted Co 2+. Top right graph is a spectrum of a high concentration Co doped ZnO sample which is used as a model spectrum for pure Co 3+. The bottom two graphs are fitted using substituted Co 2+ (dashed red), Co 3+ (solid black) and an unknown Co 2+ component (solid orange).

TABLE I. High field magnetic moments (μ_{HF}) and effective magnetic moments (μ_{eff}) obtained from M versus H curves.

Annealing temp.	$\mu_{HF}(\mu_B/\text{Co})$	$\mu_{eff}(\mu_B/\text{Co})$	n_c	$m(\mu_B/\text{Co})$
150°C	0.24	1.66	48	3.16
250°C	0.12	0.97	65	1.95
400°C	0.031	1.40	-	-
600°C	0.14	0.98	49	1.87
800°C	0.18	1.27	50	2.44

model spectrum is 5 at.% Co doped ZnO which has a Co 2p spectrum described as substituted Co^{2+} shown in the top left graph of Fig. 2. Also data of 35 at.% Co doped ZnO annealed in air at 600°C, top right graph of Fig. 2, which shows a pure Co 3+ character of cobalt is used as a model. The pure Co 3+ character can be deduced from the lack of satellite structure 5 eV BE above the Co $2p_{3/2}$ main line. The BE difference between the main lines of Co 2+ and Co 3+ is 1 eV and a good fitting is possible due to the relatively large difference of 0.8 eV in spin-orbit splitting and the large difference in BE and intensity of the satellite structures.The splitting into main and satellite lines are due to different final states after the photoemission of a Co 2p core level electron. The spectra of the 15% Co doped samples could be fitted well by using a model consisting of a Co 3+ spectrum (solid black) and two different types of Co 2+ spectra (dashed red and solid orange) differing only by the BE. The solid orange component which has about 1 eV higher BE is of an uncertain origin but since a good fit is possible by using a BE shifted Co 2+ component it can be determined to be in a 2+ ionic state. Some possibilities could be Co 2+ with different amounts of Co neighbors as in the center and on the surface of a Co cluster, or Co 2+ in octahedral coordination as in CoO.

As it is now evident that there is a significant amount of impurity phases in the samples it is now possible to analyze the magnetic results in a more quantitative way. Using a model described by Néel [5] for antiferromagnetic nanoparticles we are able to calculate the cluster size to be about 50 atoms, see table I. The cluster size is almost constant throughout the annealing series which would suggest that the clusters are produced already during the synthesis of the samples and are only effected chemically during heat treatment. For the 150°C sample we obtain a magnetic moment of 3.16 μ_B which is very close to the expected 3 μ_B for Co 2+. For intermediate temperatures we obtain a magnetic moment of about 2 μ_B which is expected since the Co 3+ usually obtains a low spin state (0 μ_B) and does not contribute to the total magnetic moment. Since the clusters are small it is enough that only the outermost Co layer reacts with the Zn and forms $ZnCo_2O_4$ in order to explain the large amount of Co 3+ observed. This can also explain why the spinel (i.e. AB_2O_4) was not observed in XRD for low annealing temperatures since such a thin layer will have difficulty to relax into a spinel structure unless there is enough thermal energy. Another possibility is that the spinel structure is small enough to be below the detection limit for XRD.

The 400°C sample has a different magnetic behavior than the other samples, a possible explanation is that the Co 3+ containing compound actually obtains a weak ferromagnetic component under certain conditions[6].

CONCLUSIONS

We have shown that 15 at.% Co doped ZnO annealed at temperatures between 400 and 600°C contains a significant amount of Co 3+. The samples did not show any secondary phases in the initial XRD measurements and a repeated statistically improved XRD measurement had to be conducted in order to confirm a weak spinel peak. Most of the samples show a magnetic behavior which can be explained by antiferromagnetic clusters with uncompensated spins. The cluster size is in the order of 50 atoms and the average magnetic moment is reduced when low spin Co 3+ are formed in the sample.

[1] D. Iuşan R. Knut, B. Sanyal, O. Karis, O. Eriksson, V. A. Coleman, G. Westin, J. M. Wikberg, and P. Svedlindh, Phys. Rev. B **78**, 085319 (2008)
[2] G. Westin et al., Thin Solid Films **515**, 7751 (2007)
[3] M. Gorgoi et al., Nuclear Instruments and Methods in Physics Research Section A: Accelerators, Spectrometers, Detectors and Associated Equipment **601**, 48 (2009)
[4] D. Bazin et al.,, J. Catal. **189**, 456 (2000)
[5] L. Néel, C.R. Hebd. Seances Acad. Sci. **252**, 4075 (1961)
[6] H. J. Kim et al.,, Phys. Status Solidi B **241**, 1553 (2004)

XMCD study of MnAs films grown on GaAs(100)

R. Knut,[1] M. Wikberg,[2] P. Palmgren,[1] P. Pal,[1,3] M. Ottosson,[4] J. Sadowski,[3] P. Svedlindh,[2] and O. Karis[1]

[1]*Department of Physics, University of Uppsala, Sweden*
[2]*Department of Engineering Sciences, Uppsala University, Sweden*
[3]*MAX-lab, Lund University, Sweden*
[4]*Department of Materials Chemistry, Uppsala University, Sweden*

INTRODUCTION

The search for suitable materials for spintronic application has spurred a large interest in materials that like MnAs can be deposited on ordinary semiconductors such as Si and GaAs. Bulk MnAs exhibits a ferromagnetic (FM) transition temperature (T_c) of 313 K where it is accompanied by a structural phase transition going from the FM α-phase to the orthorhombic β-phase [1]. When MnAs is deposited on a GaAs substrate as a thin film, it undergoes a strain induced increase in T_c and moreover develops a two phase region where the α- and β-phases coexist between approximently 283 and 340 K. Investigations of the magnetic anisotropy have determined that for MnAs the easy axis of magnetization lies along the a-axis of the hexagonal α-phase ($a_{\rm hex}$) and the hard axis along the c-axis ($c_{\rm hex}$). Since both $c_{\rm hex}$ and $a_{\rm hex}$ lie in the film plane of MnAs:GaAs(001) films the magneto crystalline anisotropy can be measured by simply rotating the film 90°. We present an investigation of 100 nm thick MnAs films grown on GaAs(100) substrates. X-ray magnetic circular dichroism (XMCD) reveals a behavior of the spin magnetic moment which deviates from magnetization measurements by SQUID. Moreover, the orbital moment does not strictly follow the spin magnetic moment in the temperature range where both α and β-phases co-exists.

EXPERIMENT

X-ray magnetic circular dichroism (XMCD) measurements were performed at beamline D1011 at the synchrotron facility MAX-lab. Before measuring, the As cap was removed by heating the sample to 320°C for 30 min in vacuum. All measurements were performed by magnetizing the sample with an in plane magnetic field in the easy magnetization direction after which the absorption spectrum was measured in remanence using total electron yield. The measurements were performed using 75±5% circularly polarized light and with the sample 13° from grazing incidence. The same procedure was repeated after magnetizing the sample in the opposite magnetic direction. Saturation effects which are prominent at low angels are compensated for according to Nakajima *et al.*[2]. The spectra are normalized at low photon energies after which a step function is subtracted. We have used a correction factor for the spin magnetic moment of 1.47, due to the relatively small spin-orbit splitting leading to a mixing of Mn $2p_{1/2}$ and $2p_{3/2}$ levels[3].

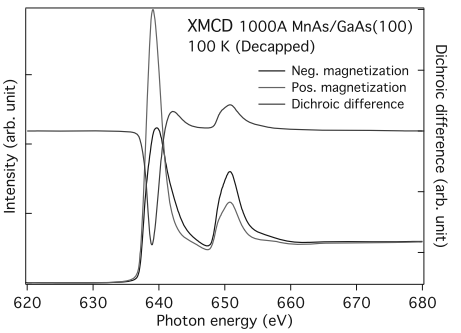

FIG. 1. XMCD spectra at 100 K. The red and black spectra are measured over the Mn $L_{2,3}$ edges for two opposite directions of magnetization. The blue spectrum is the difference between the black and red spectra.

RESULTS

Electronic structure calculations show a hybridization between As-$4p$ and Mn-$3d$ states resulting in an itinerant character of the d orbitals. This is also supported by the spectroscopic measurements which show an absorption similar to metallic Mn. Using the spin sum rule for Mn has been controversial since there is a mixing between the L_2 and L_3 edges and therefore a constant of 1.47[3] is commonly used in order to compensate for this effect. We find that using a reasonable d-hole count (between 3.6 and 4.9) results in too large spin magnetic moments compared to SQUID measurements. Therefore we have chosen to present our XMCD magnetization data in Fig. 2 as magnetic moment per hole. As shown in Fig. 2 the orbital moment (middle graph) has magnetic behavior which is clearly different compared to the spin magnetic moment (top graph). The M_l/M_s ratio (bottom graph) which is expected to be constant for a second order magnetic transition shows an increase in the temperature range where both α- and β-phases co-exist. This is an indication of structural changes in the α-phase as it goes into the co-existance region. The α-phase is compressed in the plane due to a small lattice mismatch to the substrate. This strain becomes smaller with the inclusion of β-phase since it has a smaller $a_{\rm hex}$ lattice constant. While the α-phase can relax out of plane, the inclusion of β-phase is likely to induce strain in this direction and a large (1-3 nm) topological hight difference

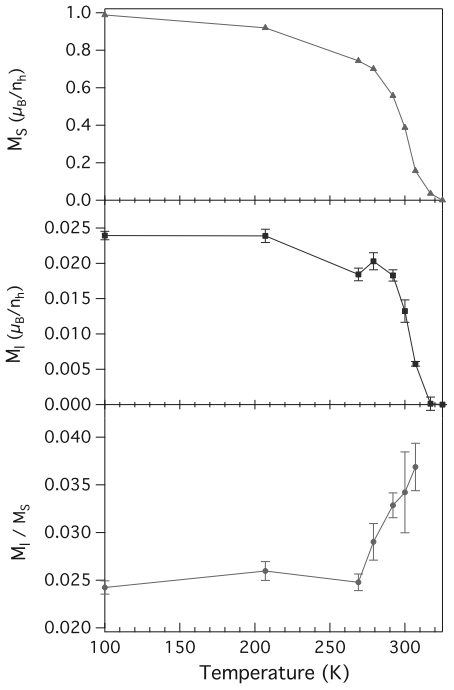

FIG. 2. Magnetic moments and ratios obtained from XMCD sum rules. Spin magnetic moment (top). Orbital magnetic moment (middle). Ratio between orbial and spin magnetic moment (bottom).

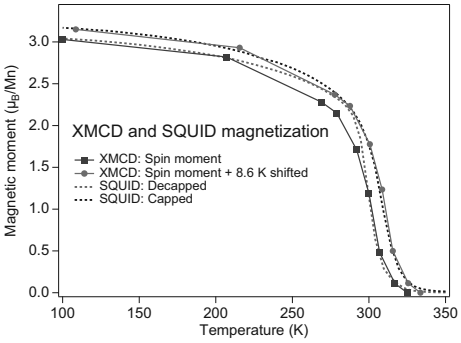

FIG. 3. Magnetization vs. temperature obtained with both SQUID and XMCD. The full lines (XMCD) are normalized to fit with magnetization obtained from SQUID. The green line is the XMCD spin moment but normalized and shifted to fit with the SQUID magnetization of the capped sample.

between the phases has been observed in AFM. The large increase of almost a factor 2 in the M_l/M_s ratio can not be reproduced by electronic structure calculations in which a simple stretching of $a_{\rm hex}$ or $c_{\rm hex}$ is performed within reasonable values. Also, the measured orbital moment is considerably larger than what is found by calculations. This could indicate that the α- phase does not have a perfect hexagonal structure which would results in a lower symmetry and increased orbital moment. SQUID measurements of the magnetic anisotropy energy (MAE) normalized to the estimated amount of α-phase also show an increase around 300 K compared to low temperatures. This is in accordance to Bruno[4] which showed that the MAE is proportional to the difference in orbital magnetic moment between the easy and hard magnetization directions. The magnetic moment from XMCD is found to have the same T_C as obtained for the decapped sample in SQUID but a relatively large discrepancy is observed between 250-300K, shown in Fig. 3. A temperature shift (green) shows that the shape of the XMCD magnetization is very similar to the capped sample. This suggests that the heat treatment during the decapping process, which according to XRD relaxes the crystal structure of the sample, only effects the Tc. However, after the sample is removed from the vacuum chamber to be measured in SQUID the magnetization between 250-300K increases compared to the XMCD measurement, see Fig. 3. This effect on magnetization due to the oxidation of MnAs indicates that the surface is important for the bulk magnetic behavior of the sample, possibly as a nucleation area for the α- and/or β-domains.

CONCLUSIONS

We have shown that the orbital magnetic moment does not strictly follow spin magnetic moment which is expected in a first order structural transition. The M_l/M_s ratio increases in the temperature range where both the α- and β- phase co-exists. Also an increase in the magnetic anisotropy energy has been observed at these temperatures which fits well to the theory where the orbital magnetic moment and MAE are strongly connected. Comparing XMCD and SQUID magnetization results there are indications that surface oxidation has an effect on the bulk magnetic behavior of the sample. Further XMCD and magnetization studies have also been conducted on thinner MnAs films and with different substrates. These results will be presented elsewhere.

[1] I. Däweritz, Rep. Prog. Phys. **69**, 2581 (2006).
[2] R. Nakajima *et. al.*, Phys. Rev. B. **59**, 6422 (1999).
[3] K. W. Edmonds *et. al.*, Phys. Rev. B. **71**, 064418 (1989).
[4] P. Bruno, Phys. Rev. B. **39**, 6422 (1989).

Element specific characterization of (Ga,Fe)N: magnetism and structure

I.A. Kowalik[1], A. Persson[2], A. Bonanni[3], T. Dietl[1], D. Arvanitis[2]
[1] *Institute of Physics, Polish Academy of Sciences, Al Lotnikow 32/46, PL-02-668 Warszawa, Poland*
[2] *Department of Physics and Astronomy, Uppsala University, Box 516, SE-7120 Uppsala, Sweden*
[3] *Institut für Halbleiter-und-Festkörperphysik, Johannes Kepler University, Altenbergerstr. 69, A-4040 Linz, Austria*

Despite the progress in the field of Diluted Magnetic Semiconductors (DMS), the understanding and control of these systems has emerged as an extremely challenging and controversial field in today's materials science and condensed matter physics [1]. In particular, the understanding of the magnetic properties at the atomic level for magnetically doped nitrides and oxides is still an open issue. It has been possible to demonstrate that high temperature ferromagnetism of semiconductors can result from nanoscale, crystallographic or chemical, phase separations into regions containing a large concentration of the magnetic constituent. The limited solubility of transition metals in semiconductors leads eventually to chemical phase separation (spinodal decomposition) of the alloy into nanoscale regions containing a high concentration of the magnetic constituent embedded coherently in a non-magnetic host [2,3]. This effect has been demonstrated in particular for the here investigated (Ga,Fe)N, where for concentrations of Fe above the solubility limit wurtzite Fe_xN crystalline phases are detected in the GaN matrix [4,5].

The interest in (Ga,Fe)N epitaxial thin layers is especially related to their magnetic properties: the Curie temperature lies above room temperature (RT) even for a relatively low Fe content (few per cent) [4,5,6], and diluted GaN:Fe has been proven to be an ideal work-bench to study the magnitude of the exchange integrals governing the strength of the interactions responsible for the magnetic response in transition-metal (TM) doped semiconductors [7]. However, the nature of the ferromagnetic ordering of the Fe spins needs further investigations, in particular concerning the role of the electric doping.

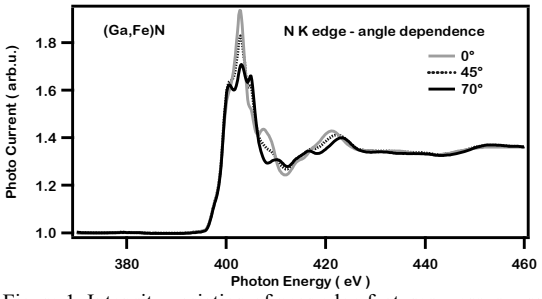

Figure 1. Intensity variation of near edge features, versus x-ray incidence angle in x-ray absorption at the N K-edge of a typical (Ga,Fe)N sample. The polar sample angle is varied, normal incidence corresponding to normal x-rays (0 degrees).

We measure high quality single crystal epilayers of (Ga,Fe)N, widely characterized, in terms of dopant, and impurity concentration and structural properties. The samples are grown on GaN buffer layers deposited on sapphire substrates by metallorganic vapor phase epitaxy (MOVPE) at the University of Linz, Austria [4]. The x-ray absorption measurements were performed in the total electron yield mode by measuring the photocurrent of the sample. After a few soft sputtering cycles we could not see, in particular, any oxidic contribution in the spectra and a magnetic response was also obtained. By using the wide soft x-ray energy range of the D1011 beam line, a characterization of the stoichiometry of the near surface region (a few nm, about 6 nm probed here) can be given. We can identify the N K-edge, Ga L-edges, Fe L-edges. The beam has a cross section of order 0.5 mm square at normal x-ray incidence; within the length range of a few mm the sample appears to be homogeneous. A comparison with the theoretical Henke

Tables [8] for the atomic continuum cross sections, known as being proportional to the ”edge Jump” x-ray absorption edge jump ratio, indicates an overall Fe atom content about 0.5% per Ga atom. N K-edge data taken using linear x-rays are shown in Fig. 1,. These data and the observed angular dependance, match the available literature. The 2p final states of the N atoms are probed and a shoulder at the low energy side of the edge is attributed to hybridization with the Fe electronic states. The angle dependence confirms that the film is indeed high quality and *c*-axis oriented. We observe that in the Fe L-edge spectra for the Fe precipitates the white lines are broader and more intense than in the case of a standard bcc Fe sample measured *in situ* under the same conditions. Such effects can be ascribed to inhomogeneous broadening for the Fe precipitates indicating Fe atoms in different chemical states. If we assume for each Fe precipitate a less perturbed “core” and a more perturbed surface region, one can expect that the 3*d* electron donation will lead to higher number of 3*d* holes which is then averaged over the whole particle, leading to a smaller measured overall effect. The increase in the white line intensity in comparison to bcc Fe evidences electron transfer away from the Fe ion cores in agreement with theoretical expectations.

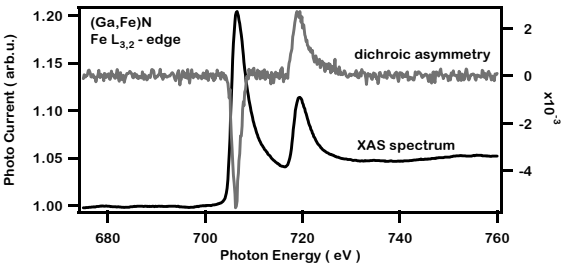

Figure 2. Absorption edge Fe $L_{3,2}$-edge obtained for (Ga,Fe)N (left scale) shown together with dichroic asymmetry (right scale, right).

Using circular x-rays, a clear XMCD signal has been recorded at the Fe L-edge under an applied field of 800 Gauss at RT, as shown in Fig. 2. This is a weak signal given the fact that the Fe x-ray absorption signal is already small to start with, due to the high Fe dilution. Data were taken at 45 degrees x-ray incidence and at normal x-ray incidence. At normal x-ray incidence an out of plane magnetization is probed. In magnetic remanence the samples exhibit a very weak, but non-zero, XMCD signal. Here we show the larger XMCD response under applied field (Fig. 2b). The comparison of the Fe-rich precipitate data at respectively normal and 45° x-ray incidence indicates a stronger XMCD effect at 45° degrees, suggesting that it is easier to magnetize the precipitates in the surface plane. The XAS results confirm that in the (Ga,Fe)N samples we have Fe atoms in different environments. From the observed XMCD we verify that some of the Fe phases are ferromagnetic and the magnetic response measured by conventional magnetometry comes from the Fe ion cores and not from *e.g.* lattice defects. The XMCD signal, even for a low Fe content, is measurable and of good quality (Fig. 2) allowing for a quantitative analysis with the magneto-optical “sum rules” for the determination of the spin and orbital moments per Fe atom.

This work is partially supported by the European Research Council through the FunDMS Advanced Grant within the “Ideas” 7th Framework Programme of the EC.

[1] T. Dietl, J. Appl. Phys. **103**, 07D111 (2008).
[2] T. Dietl, J. Phys. Cond. Mat. **19**, 165204 (2007).
[3] H. Katayama-Yoshida et al., Phys. Status Solidi (a) **204**, 15 (2007).
[4] A. Bonanni et al., Phys. Rev. B **75**, 125210 (2007).
[5] A. Navarro-Quezada, et al., arXiv:1001.5418v1, cond-mat.mtrl-sci 29 Jan 2010.
[6] E. Malguth at al., Phys. Rev. B **74**, 165201 (2006).
[7] W. Pacuski et al., Phys. Rev. Lett. **100**, 037204 (2008).
[8] Atomic Data and Nuclear Data Tables **54** (no.2), 181-342 (July 1993).

Covalently bonded porphyrin networks studied by x-ray absorption and photoemission

S.A. Krasnikov[1], C.M. Doyle[1], A.B. Preobrajenski[2], N.N. Sergeeva[3], N.A. Vinogradov[2], Y.N. Sergeeva[3], M.O. Senge[3] and A.A. Cafolla[1]

[1] *School of Physical Sciences, Dublin City University, Glasnevin, Dublin 9, Ireland;*
[2] *MAX-lab, Lund University, Box 118, S-22100 Lund, Sweden;*
[3] *School of Chemistry, Trinity College Dublin, Dublin 2, Ireland.*

Molecular self-assembly may be defined as the spontaneous association of molecules under equilibrium conditions into stable, structurally well defined aggregates joined by non-covalent bonds [1]. The basic idea is to synthesize molecular building blocks with predetermined intermolecular bonding properties. However, since molecular self-assembly is based on non-covalent interactions (e.g. hydrogen bonding, metal ligand bonding or van der Waals interactions), the stabilization energies are usually very low [1, 2]. As a consequence conventional self-assembled structures are often unstable even at moderate temperatures. A strategy to overcome this low stabilization energy relies on inducing covalent reactions between the molecular components, thus forming two-dimensional covalently bonded networks. The formation of covalent bonds between complementary molecular components is an appealing approach in the fabrication of nanoscale structures, such as nanomeshes and nanolines, because of their high selectivity, strength and directionality [1, 3]. These nanostructures are attractive for their intrinsic properties; for their potential applications such as novel sensing, energy conversion or catalytic devices; for their ability to 'trap' other molecules such as fullerenes, creating even more interesting complexes and for their use as templates to direct the growth of, for example, metal clusters with interesting catalytic or magnetic properties.

Here we apply x-ray absorption (XAS) and core-level photoemission spectroscopy (XPS) to study the formation of covalently bonded porphyrin networks on the Au(111) surface constructed from the free-base 5,10,15,20-tetra(4-bromophenyl)porphyrin (H_2TBrPP) building blocks via thermally controlled release of bromine from the porphyrin.

XAS and XPS measurements were performed at the D1011 beamline at MAX II storage ring in Lund, Sweden. The XPS spectra were measured with a Scienta SES-200 electron energy analyzer. The kinetic energy resolution was set to 75 meV for the Br 3d spectra. The photon energy resolution was set to 70 meV at the C K-edge (~280 eV) and to 100 meV at the N K-edge (~400 eV). The XAS spectra were recorded in the partial electron yield mode (U = -100 V) by a multichannel plate detector and normalized to the background curves recorded from the clean substrate. The H_2TBrPP was evaporated onto the clean Au(111) surface at a rate of about 0.1 ML (monolayer) per minute.

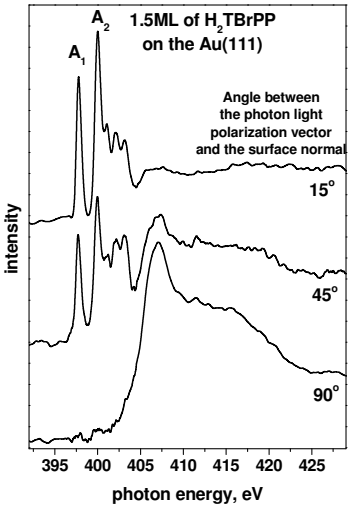

Fig. 1. Angular dependent N 1s XAS of 1.5 ML of H_2TBrPP on the Au(111).

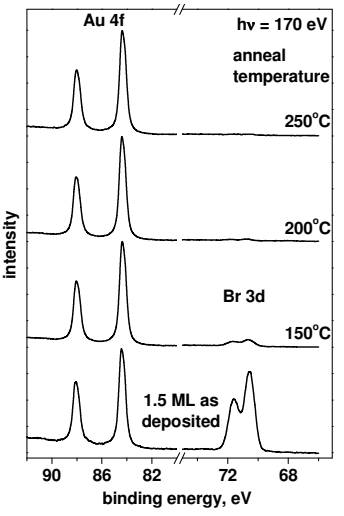

Fig. 2. Br 3d XPS of 1.5 ML of H_2TBrPP on the Au(111) after annealing at different temperatures.

When deposited onto the Au(111) surface at room temperature the H_2TBrPP self-assembles forming large well-ordered molecular domains with a close-packed square structure. In the H_2TBrPP overlayer each molecule has a flat orientation on the surface with the molecular plane lying parallel to the substrate. This is

confirmed by angular dependent N 1s XAS shown in Fig. 1. It is clearly seen that there is only broad σ resonance observed at normal incidence (90°), while π resonances become very intense at grazing incidence (15°). There are two strong low-energy absorption structures A_1 and A_2 that are related to the π MOs and arise due to the two different N sites in the centre of the free-base porphyrin macrocycle. The structure A_1 observed at a photon energy of 397.9 eV is produced by iminic (-C=N-) nitrogens, while the structure A_2 at 400.0 eV results from pyrrolic (-NH-) nitrogens [4].

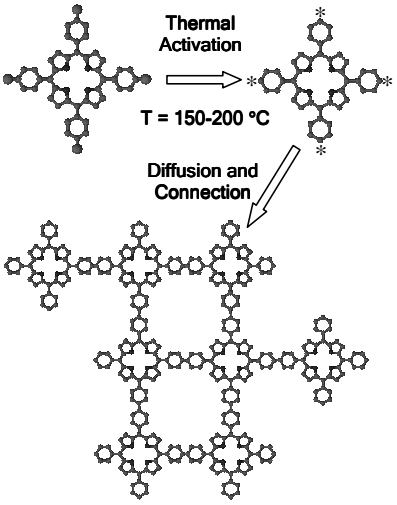

Fig. 3. Schematic representation of the activation and covalent bonding between the molecules.

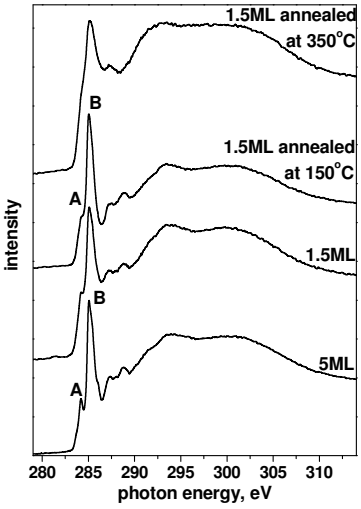

Fig. 4. C 1s XAS of of H_2TBrPP on the Au(111) after annealing at different temperatures.

Annealing of the H_2TBrPP layer on the Au(111) surface up to 200-250 °C leads to dramatic changes in the molecular overlayer structure. Fig. 2 shows changes in the Br 3d core-level XPS as a result of the substrate anneal. The Br 3d signal starts to decrease at a temperature of 150 °C and disappears completely after annealing the system at 250 °C for 30 min. The total amount of deposited H_2TBrPP is reduced from 1.5 ML to 0.8 ML as a result of annealing (the value is calculated by comparing N 1s and C 1s core level intensities measured before and after the anneal). Annealing to such temperature results in release of bromine from the phenyl rings of the porphyrin. This process is followed by a formation of covalent bonds between phenyl rings linking the porphyrin molecules to each other. Activation of the H_2TBrPP followed by a formation of H_2TPP molecular network is shown schematically in Fig. 3.

C 1s XAS measured from the molecular layer after annealing at different temperatures are shown in Fig. 4. The C 2pπ unoccupied MOs have a similar structure in all spectra. However, the initial sharp π resonances A and B become broader after annealing the molecular layer at 350 °C. This is a result of formation of a large covalently bonded porphyrin network, which can be considered as a π-conjugated macromolecule. π-conjugation causes a significant delocalization of π molecular orbitals, which, in turn, results in a broadening of the corresponding absorption structures.

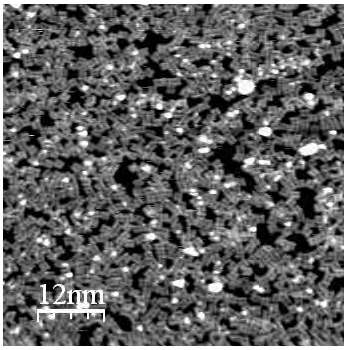

Fig. 5. STM image of the covalently bonded H_2TPP network.

STM image of the H_2TPP network is shown in Fig. 5. All porphyrins are covalently bonded to each other forming robust nanoporous macromolecule suitable for hosting other molecules or metal clusters.

This work was supported by Science Foundation Ireland and by the Swedish Research Council.

[1] J.V. Barth, *Ann. Rev. Phys. Chem.* **2007**, *58*, 375.
[2] J.A.W. Elemans, R. van Hameren, R.J.M. Nolte, A.E. Rowan, *Adv. Mater.* **2006**, *18*, 1251.
[3] L. Grill, M. Dyer, L. Lafferentz, M. Persson, M.V. Peters, S. Hecht, *Nat. Nanotech.* **2007**, *2*, 687.
[4] S.A. Krasnikov, N.N. Sergeeva, et al. *J. Phys. Condens. Matter* **2008**, *20*, 235207.

Ni porphyrins and N-confused porphyrin: electronic structure studied by x-ray absorption

S.A. Krasnikov[1], A.S. Vinogradov[2], N.N. Sergeeva[3], A.B. Preobrajenski[4], N.A. Vinogradov[4], Y.N. Sergeeva[3], M.O. Senge[3] and A.A. Cafolla[1]

[1] *School of Physical Sciences, Dublin City University, Glasnevin, Dublin 9, Ireland;*
[2] *V.A. Fock Institute of Physics, St. Petersburg State University, St. Petersburg, Russia;*
[3] *School of Chemistry, Trinity College Dublin, Dublin 2, Ireland;*
[4] *MAX-lab, Lund University, Box 118, S-22100 Lund, Sweden.*

Due to their unique properties transition metal porphyrins are widely used in many technological applications such as sensors, solar cells, nonlinear optics and nanomaterials [1]. During the last decade the coordination properties and conformational flexibility of porphyrins were heavily exploited in a search of prospective isomers able to deliver better functionality in specific technological applications [1]. One such important class of porphyrins is the nitrogen-confused porphyrins (NCPs), which are novel and prospective materials with improved properties for use as acid catalysts and anion/cation sensors [2]. These porphyrin isomers differ greatly from the parent porphyrins, particularly in their chemical structure and their physical and coordination properties. The multivalent nature of NCPs as a metal ligand provides a potential strategy for stabilising and studying higher or atypical oxidation states of metals, e.g. Ni(I), Ni(III), Cu(III), Ag(III), or unusual coordination geometries [2]. In addition, the outer nitrogen or carbon atoms of the inverted pyrrole ring can be directly connected resulting in oligomeric porphyrin arrays with interesting applications. Using NCPs in such molecular arrays provides new modes of linking single molecules and different coordination properties of the resulting oligomers [2]. In order to realize their full potential a detailed knowledge of the electronic structure and chemical bonding in porphyrins is required. Such information can be obtained with x-ray absorption spectroscopy (XAS).

Here we apply XAS to study the chemical bonding features in Ni porphyrins. The main goal is to understand in detail how the electronic structure changes in going from Ni porphyrin to Ni N-confused porphyrin by a direct comparison of the corresponding x-ray absorption spectra.

XAS measurements were performed at the D1011 beamline at MAX II storage ring in Lund, Sweden. Thick porphyrin layers (~20 nm) were prepared *in situ* by thermal evaporation of powder material onto a polished polycrystalline copper substrate. The XAS spectra were recorded in the total electron yield detection mode by measuring the sample drain current. The estimated photon-energy resolution at the Ni 2p (~850 eV) and N 1s (~400 eV) absorption thresholds was better than 200 meV and 100 meV, respectively.

The molecular formulas of the Ni porphine (NiP), Ni tetraphenylporphyrin (NiTPP), Ni nitrogen-confused tetraphenylporphyrin (NiNCTPP) and free-base porphine (H_2P) are shown in Fig. 1. The measured Ni 2p x-ray absorption spectra for the Ni compounds under study are shown in Fig. 2. The Ni $2p_{3/2}$ XAS of the NiP and NiTPP have a very similar shape: the main absorption line A at the photon energy of 853.9 eV is accompanied by high-energy lines A_2, C and D. The difference between them and the Ni $2p_{3/2}$ XAS of metallic Ni can be understood within the framework of quasi-molecular approach [3, 4] with inclusion of the covalent mixing between the Ni and ligand (N and C) atoms. The main line A in the Ni $2p_{3/2}$ XAS of Ni porphyrins is associated with transitions of Ni $2p_{3/2}$ electrons to the LUMO, which is the antibonding σ-MO of b_{1g} symmetry with predominantly Ni $3d_{x2-y2}$ character. In turn, the structures A_2, C, C* and D are associated with transitions to empty states with hybridized Ni 3d – ligand 2p character. The high-energy shift of the Ni $2p_{3/2}$ absorption in going from Ni metal to Ni porphyrins (1.2 eV) is a result of the decrease in the effective number of 3d electrons on the Ni atom due to the strong Ni 3d – ligand 2p π-type covalent bonding. This metal-to-ligand charge transfer (back-donation) in the Ni porphyrins occurs from the occupied Ni $3d_{xz,yz}$ π (e_g) orbitals to the unoccupied ligand $2p\pi^*$ (e_g) orbitals [3].

Three main differences are observed between the Ni $2p_{3/2}$ XAS (Fig. 2) of the NiNCTPP and NiP (and/or NiTPP): (i) the reliably measured high-energy shift of the main absorption line A by 0.5 eV in the NiNCTPP compared to NiP (NiTPP), (ii) an additional low-energy shoulder A_1 separated in energy by approximately 0.8 eV from the main line A in the XAS of the NiNCTPP and (iii) the presence of the high-energy doublet structure A_2-A_3 in the spectrum of the NiNCTPP compared to the

single absorption line A_2 in the NiP (NiTPP). The first two findings reflect a larger transfer of the 3d electron density from the Ni atom to the ligands and the stronger Ni 3d – ligand 2p covalent bonding in the case of the NiNCTPP compared to the other Ni porphyrins indicating a smaller effective number of 3d electrons on the central Ni atom (higher oxidation state) in this nitrogen-confused porphyrin. The third finding is due to a lowering of the symmetry of the porphyrin macrocycle (Ni atom and its nearest neighbours) from D_{4h} (NiP, NiTPP) to C_{2v} in the NiNCTPP [1, 2].

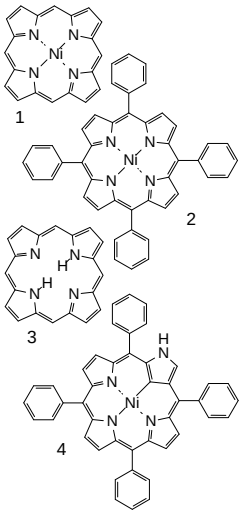

Fig. 1. NiP (1), NiTPP (2), H_2P (3) and NiNCTPP (4).

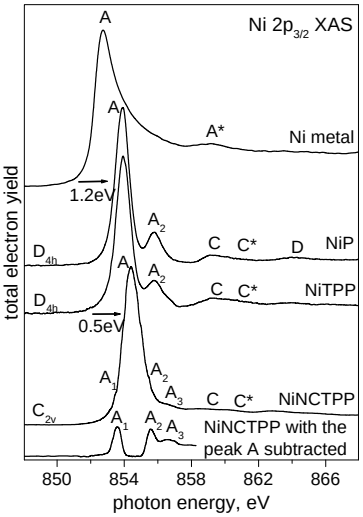

Fig. 2. Ni $2p_{3/2}$ XAS of the Ni metal and Ni porphyrins under study.

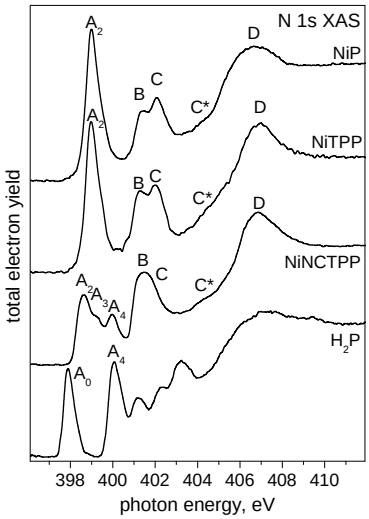

Fig. 3. N 1s XAS of the Ni porphyrins and free-base porphine H_2P.

Comparing the N 1s XAS (Fig. 3) of the Ni porphyrins an interesting shape is observed for the low-energy absorption structures related to the π MOs (structures A_2-A_4) in the spectrum of NiNCTPP. This is associated with (i) the non-equivalence of the confused N atom and the three N atoms bonded to the central Ni atom and (ii) the C_{2v} symmetry of the NiNCTPP macrocycle. In the N 1s XAS of the H_2P, shown in Fig. 3, there are two strong low-energy absorption structures A_0 and A_4 that are related to the π MOs and arise due to the two different N sites in the centre of free-base porphyrin macrocycle. The structure A_0 observed at a photon energy of 397.9 eV is produced by iminic (-C=N-) nitrogens, while the structure A_4 at 400.0 eV results from pyrrolic (-NH-) nitrogens [5]. Thus, in the N 1s spectrum of the NiNCTPP the absorption structure A_4 (400.0 eV) can be associated with the confused N atom, which is of pyrrolic type in this porphyrin (i.e. protonated). In turn, taking into account the C_{2v} symmetry of the NiNCTPP macrocycle and the relative intensities of the A_2-A_4 absorption structures, the structure A_2 is associated with electron transitions to MOs localized on two diagonally opposed N atoms bonded to the central Ni atom, while the structure A_3 is associated with the N atom bonded to the Ni atom and opposite to the inner C atom.

Thus, applying XAS to Ni porphyrins information about their electronic structure can be obtained. Furthermore, the experimentally observed energy shift of band A can be used as a qualitative, and possibly as a quantitative, characterization of back-donation strength (charge-transfer) and the oxidation state of a metal atom in similar Ni compounds.

This work was supported by Science Foundation Ireland, by the Russian Foundation for Basic Research (grant No. 09-02-01278) and by the Swedish Research Council.

[1] K.M. Kadish, K.M. Smith, R. Guilard (Eds.), The Porphyrin Handbook, Academic Press, 2000.
[2] P.J. Chmielewski and L. Latos-Grażyński, Coord. Chem. Rev. **249** (2005) 2510.
[3] S.A. Krasnikov, A.B. Preobrajenski, N.N. Sergeeva, et al. Chem. Phys. **332** (2007) 318.
[4] A.S. Vinogradov, S.I. Fedoseenko, S.A. Krasnikov, *et. al.*, Phys. Rev. B **71** (2005) 045127.
[5] S.A. Krasnikov, N.N. Sergeeva, et al. J. Phys. Condens. Matter **20** (2008) 235207.

Controlling hydrogenation of graphene on transition metals

M. L. Ng[1,2], R. Balog[3], L. Hornekær[3], A. B. Preobrajenski[1], N. Vinogradov[1,2], N. Mårtensson[1,2] and K. Schulte[1]

[1] *MAX-lab, Lund University, 22100 Lund, Sweden*
[2] *Department of Physics, Uppsala University, 75121 Uppsala, Sweden*
[3] *Department of Physics and Astronomy, Aarhus University, 8000 Aarhus C, Denmark*

Graphene or monolayer graphite (MG) offers tantalizing opportunities in the relentless race towards smaller and faster electronics due to its two-dimensional structure and excellent electron mobility [1,2]. A controllable band gap opening is, however, a prerequisite for such applications. It has been shown that electronic changes in graphene can be realized by means of controllable chemical functionalization [3]. In particular, hydrogenation of graphene is an elegant route towards tailoring electronic and magnetic properties of graphene. In our previous work [4], we have reported that graphene forms corrugated overlayer on Ir and Pt due to lattice mismatch. This results in bonding (pores) and non-bonding (wires) patches, whereas the size of the pores is governed by the strength of the MG-TM interfacial interaction.

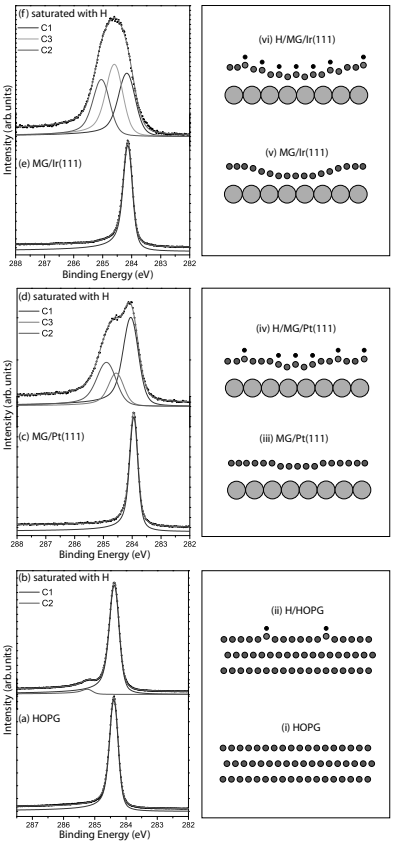

Fig. 1: C 1s XPS of MG/TM before and after hydrogenation and the respective schematics.

In this work, we compare the hydrogenation processes for graphene grown on various transition metals (TMs), namely Pt(111), Ir(111) and Ni(111) to correlate between the strength of MG-TM interaction with the hydrogen uptake. As the reference experiment, we hydrogenate the highly oriented pyrolytic graphite (HOPG) under the same conditions to demonstrate the general impact of the metal substrates on the hydrogenation process.

The TM(111) single crystals were cleaned by several cycles of Ar^+ sputtering and annealing in oxygen. The respective MG/TM overlayers were prepared *in-situ* by thermal cracking of propylene molecules on the hot TM crystal surfaces, i.e. 650°C on Pt, 780°C on Ir and 670°C on Ni for 30 min. Next, atomic hydrogen is dosed to the respective substrates at room temperature to saturation. All samples were characterized comprehensively both before and after hydrogenation to saturation with XPS, NEXAFS and LEED at Beamline D1011.

From the NEXAFS at C K-edge (not shown) [5], it is apparent that a new peak appears between the π and σ resonances after hydrogenation, which originates from the C-H bond. This confirms the chemisorption of H on the MG/TM surfaces. C 1s angle dependent NEXAFS spectra of these samples (not shown) verify that the C-H bonds are standing up on the MG plane.

By comparing the C 1s PE spectra for these samples before and after hydrogenation (Fig. 1, a – f), we identify

the amount of C=C bonds (component C1) with sp^2 hybridization of the MG overlayer that is converted to sp^3 C-H bonds (component C2 and C3) after hydrogenation. Component C2 originated from the hydrogenated carbon in the wire area while C3 from the pore area. These components are illustrated in the schematics shown in Fig. 1. The estimation of the hydrogen uptake is done by summing the area under component C2 and C3 and compared to the total area. The core level of MG on Ni is not shown because it is a special case, i.e. MG on Ni is a strongly bonded, commensurate overlayer [6].

Graphene's ability to adsorb atomic hydrogen is strongly dependent on the character of the underlying substrate. Without a reactive substrate, the saturated H coverage is relatively low. By adsorption of graphene on a reactive metal substrate, the H uptake value can be increased significantly. At the present hydrogen dosing conditions, the highest values are observed for MG/Ir(111), less for MG/Pt(111), even less for MG/Ni and the least for the adsorption on bulk graphite. On the lattice-mismatched MG/Pt and MG/Ir interfaces graphene is slightly corrugated on the nanometer scale inducing site selectivity for H adsorption. The more bonding graphene patches (pores) are able to achieve 50% H coverage by forming graphane-like structures. This process becomes possible due to the strengthening the C $2p_z$ – TM 5d bonds, which can involve the unpaired electrons released upon breaking the C=C bonds in the course of H adsorption. The total area of more strongly bonding graphene sites (pores) is higher for MG on Ir than on Pt, thus resulting in the higher H coverage. The non-bonding graphene patches (wires) are much more passive, and hydrogenation of these sites is expected to be similar to that of HOPG. For the already strongly bound and lattice matched interfaces (MG/Ni) no further bond strengthening is possible, and moreover the hollow site sub-lattice is excluded from hydrogenation entirely. A graphane-like structure can therefore not be found and the dangling bonds have to be accommodated on the same sub-lattice (top sites). This produces a strong reduction in the H uptake value, where each formed C-H bond means the blocking of at least two C atoms from further hydrogen adsorption. A detailed discussion of the observed phenomena is presented elsewhere [5].

This work was funded by the Swedish Foundation for Strategic Research, the Swedish Research Council and the Russian Foundation for Basic Research (Grant N06-02-16998).

[1] K. S. Novoselov, A. K. Geim, S. V. Morosov, D. Jiang, M. I. Katsnelson, I. V. Grigorieva, S. V. Dubonos, A. A. Firsov, Nature 438, 197 (2005).
[2] S. V. Morosov, K. S. Novoselov, M. I. Katsnelson, F. Schedin, D. C. Elias, J. A. Jaszczak, A. K. Geim, Phys. Rev. Lett. 100, 016602 (2008).
[3] D. W. Boukhalov, M. I. Katsnelson, J. Phys.: Condens. Matter 21, 344205 (2009).
[4] A. B. Preobrajenski, M. L. Ng, A. S. Vinogradov, N. Mårtensson, Phys. Rev. B 78, 073401 (2008).
[5] M. L. Ng, R. Balog, L. Hornekær, A. B. Preobrajenski, A. S. Vinogradov, N. Mårtensson, *submitted for publication.*
[6] J. Rusz, A. B. Preobrajenski, M. L. Ng, N. A. Vinogradov, N. Mårtensson, O. Wessely, B. Sanyal, O. Eriksson, Phys. Rev. B, 81, 073402 (2010).

Magnetic anisotropy and spin reorientation transitions in nanomagnet arrays

A. Persson[1], A. Estrada[2], M. Á. Niño[3], D. Arvanitis[1], R. Miranda[2,4], and J. J. de Miguel[2]

[1] *Department of Physics, Uppsala University, Box 530, S-75121, Uppsala, Sweden*

[2] *Departamento de Física de la Materia Condensada, Universidad Autónoma de Madrid, Cantoblanco, 28049 Madrid, Spain*

[3] *Sincrotrone Trieste, S.S. 14, km 163.5, 34012 Basovizza, Trieste, Italy*

[4] *Madrid Institute of Advanced Studies in Nanoscience (IMDEA-Nanociencia), Cantoblanco, 28049-Madrid, Spain*

The focus of our study is on the magnetic characteristics of nanomagnet arrays obtained by self-organization methods on solid surfaces. In the course of a long-standing collaboration between the group from Uppsala University led by Prof. Dimitri Arvanitis and our team from the Surface Science Group at the University Autónoma in Madrid we have been able to establish that, in nanometre-sized structures, the effects caused by the different contributions to the total magnetic anisotropy energy for several materials or combinations thereof differ considerably from those previously observed and well characterized in non-structured systems such as thin films or superlattices. In particular, the spin reorientation transition (SRT) between the out-of-plane and the in-plane directions in layered structures such as Pt/Co and Au/Co exhibits a markedly different behavior in our nanodot arrays,[1,2] with a much reduced range of Co thicknesses for which out-of-plane magnetization dominates.

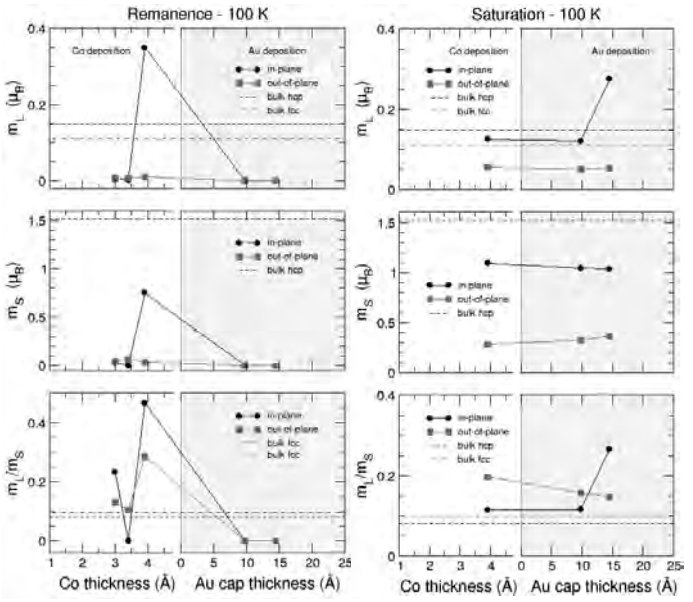

Figure 1: Values of the orbital (m_L) and spin (m_S) magnetic moments, and the m_L/m_S ratio measured on Co/Au and Au/Co/Au nanodot arrays at 100 K for different film thicknesses. The measurements were carried out for both in-plane and out-of-plane magnetized samples, in remanence after applying a magnetic field pulse (left panel) and in saturation (right panel) in the presence of a DC applied magnetic field.

During the experiments carried out at beamline D1011 in February, 2009 we studied by means of X-ray magnetic circular dichroism (XMCD) the magnetism of Co/Au nanodot arrays produced *in situ* by grazing incidence deposition[3,4] on self-organized nanodot arrays of ~40 nm diameter and similar height created by ion bombardment of a GaSb substrate.[5,6] The semiconductor substrate was first covered with a 15 Å buffer layer of Au deposited at normal incidence to prevent the oxidation of the magnetic material by its contact with the substrate's native oxide. Co was then deposited incrementally at an incidence angle of 74 degrees with respect to the surface normal, in order to take advantage of the substrate's topographic relief to create an array of magnetic deposits following the distribution dictated by the surface template. Finally, we also characterized the changes induced in the dots' magnetic behavior by the

deposition of a Au capping layer.

The data displayed in Figure 1 summarize some of our results and reveal several interesting facts. In the first place, one can see how uncapped Co deposits show no remanence even at 100 K for thicknesses below 3 Å. For this reason, many measurements had to be performed in saturation, in the presence of an applied magnetic field of 800 Oe; the setup of the experimental station at beamline D1011 proved crucial for the successful completion of these experiments. Such a low Curie temperature is a hint of the reduced dimensions of the nanomagnets; 2-dimensional Co films of about 2 ML thickness have been shown to have Curie temperatures around 300 K.[7] It is also interesting to remark that, in spite of the well-known perpendicular anisotropy characteristic of layered Co/Au systems,[8,9] our dots display predominantly in-plane magnetization, both in remanence and in saturation. We interpret these results as being due to the absence of well-defined interfaces and also to structural relaxations within the Co lattice. In fact, the data point corresponding to 3.9 Å Co/15 Å Au shows a very large orbital magnetic moment m_L of 0.35 μ_B, almost twice as large as that of bulk hcp Co, and correspondingly also of the orbital-to-spin moment ratio, m_L/m_S. Similar enhancements of the orbital magnetic moment have been reported for biatomic Co wires on a stepped Pt surface[10].

All magnetic signal in remanence is lost upon capping the above mentioned Co film with Au. From this point on, only measurements performed in the presence of the 800 Oe magnetic field did show dichroism. It is also noteworthy that the magnetic moments measured in saturation (i.e., in the presence of an applied magnetic field) are almost always larger than those determined in remanence (after magnetizing the sample with a magnetic field pulse). This points towards a certain dispersion in the distribution of magnetic easy axes. Furthermore, the tendency to show out-of-plane magnetization is somewhat larger in the dotted samples than in equivalent films deposited on the non-patterned, flat part of the substrate, as it was to be expected due to the stronger contribution of the shape anisotropy in this latter system. Nevertheless, in-plane anisotropy always dominates even after capping the Co deposits with Au, confirming the reduced effect of the Co/Au interfaces to promote the out-of-plane alignment of the magnetization.

The evolution of the dots' magnetic characteristics with increasing Au capping thickness is also interesting. Our measurements in magnetic saturation reveal a gradual increase of the out-of-plane spin moment, m_S, consistent with the expected effect of adding a second Au/Co interface. Nevertheless, our data suggest that the wetting of the Au capping may not be complete: the effect of Au deposition extends over a range of at least 10 Å thickness. Most significantly, the orbital magnetic moment m_L, which remains practically constant upon the deposition of the first, 5 Å thick Au cap and close to the expected value for bulk fcc Co, rapidly shoots up when the thickness of the Co film increases from 5 to 10 Å. This effect, visible only in the in-plane data, must probably be ascribed to structural relaxation taking place in the Co lattice. Our investigations thus highlight the strong influence that the crystal lattice distortions can have in the magnetic properties of nanometre-sized structures.

This research has been supported in part by the European Community - Research Infrastructure Action under the FP6 "Structuring the European Research Area" Programme (through the Integrated Infrastructure Initiative "Integrating Activity on Synchrotron and Free Electron Laser Science"), and also by a Grant from the STINT Foundation.

[1] L. Gridneva, A. Persson, M. Á. Niño, J. Camarero, J. J. de Miguel, R. Miranda, C. Hofer, C. Teichert, T. Bobek, A. Locatelli, S. Heun, S. Carlsson and D. Arvanitis, Phys. Rev. B **77**, 104425 (2008).
[2] A. Persson, L. Gridneva, M. Á. Niño, J. Camarero, J. J. de Miguel, R. Miranda, C. Hofer, C. Teichert, T. Bobek, A. Locatelli and D. Arvanitis, in preparation.
[3] C. Teichert, J. Barthel, H. P. Oepen, and J. Kirschner, Appl. Phys. Lett. **74**, 588 (1999).
[4] A. M. Mulders, A. Fraile Rodríguez, D. Arvanitis, C. Hofer, C. Teichert, M. Á. Niño, J. Camarero, J. J. de Miguel, R. Miranda , K. Lyutovich, E. Kasper , S. Heun and A. Locatelli, Phys. Rev. B **71**, 214422 (2005).
[5] S. Facsko, T. Dekorsy, C. Koerdt, C. Trappe, H. Kurz, A. Vogel and H. Hartnagel, Science **285**, 1661 (1999).
[6] T. Bobek, S. Facsko, H. Kurz, T. Dekorsy, M. Xu and C. Teichert, Phys. Rev. B **68**, 085324 (2003).
[7] C. M. Schneider, P. Bressler, P. Schuster, J. Kirschner, J. J. de Miguel and R. Miranda, Phys. Rev. Lett. **64**, 1059 (1990).
[8] Z. G. Li, P. F. Garcia and Y. Cheng, J. Appl. Phys. **73**, 2433 (1993).
[9] T. Suzuki, T. Kiya, N. Honda, and K. Oguchi, IEEE Trans. Magn. **36**, 2417 (2000).
[10] P. Gambardella, A. Dallmeyer, K. Maiti, M. C. Malagoli, W. Eberhardt, K. Kern and C. Carbone, Nature **416**, 301 (2002).

UHV study of the binding geometry of an organic perylene dye on single crystalline anatase TiO_2 (101)

S. Plogmaker[1], E. M. J. Johansson[1,2*], R. Schölin[1], L. E. Walle[3], A. Borg[3], A. Sandell[1], and H. Rensmo[1]

[1)] Department of physics and material science, Uppsala university, SE-75121 Uppsala Sweden
[2)] Department of physical and analytical chemistry, Uppsala university, SE-75121 Uppsala Sweden
[3)] Department of physics, Norwegian university of science and technology, NO7491, Trondheim, Norway

Since their discovery about 20 years ago,[1] dye sensitized solar cells are investigated intensively to make them more stable, efficient and in the end commercially available as well as competitive to standard silicon solar cells.

The main standard components are nanoporous TiO_2 as an electron acceptor, a dye-molecule as light absorbing material and a liquid hole-conductor to reduce the oxidized sensitizer. A promising improvement of this combination is the change of the standard liquid electrolyte to solid hole-conductors. The organic hole conductor, spiroMeOTAD, is one promising candidate making solid state dye-sensitized solar cell devices with good efficiency and stability possible. Reported are up to 5% [2] conversion efficiency which is about half of the record of liquid electrolyte cells. In the solid-state solar cells improved molar extinction coefficient is crucial and organic sensitizers like the perylene dyes, see Figure 1, are therefore a promising alternative to the commonly used ruthenium based molecules.

In dye-sensitized solar cells the binding geometry of the dye molecules to the TiO_2 is crucial for their performance. Preferably, the lowest unoccupied molecular orbital (LUMO) is located close to the TiO_2 surface to make electron injection efficient while the highest occupied molecular orbital (HOMO) should preferably be located in a distance to keep unwanted recombination processes from the TiO_2 to the dye-molecule negligible.

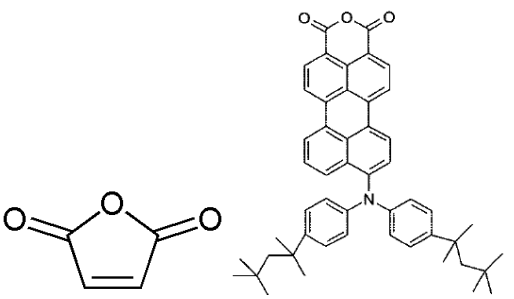

Figure 1: The deposited molecules maleic anhydride (left) and the perylene dye ID28 are shown.

In this study the perylene dye ID28 [3] is deposited by sublimation onto single crystalline anatase TiO_2 (101) surface in UHV conditions (base pressure 10^{-10} torr). Measurements of maleic anhydride on the same substrate were also performed in order to further model the anhydride anchoring group. The crystal was cleaned by a procedure of argon ion sputtering and oxygen atmosphere annealing [4]. LEED and PES measurements were used to determine the quality of the surface and the defects where found to be less than a few percent. The oxygen spectra (figure 2) are calibrated versus the Fermi level of a gold foil connected to the sample. In the spectra of the monolayers the substrate peak has been removed by comparison to a clean surface. Photon energy calibration of the XAS spectra is done using first and second order light.

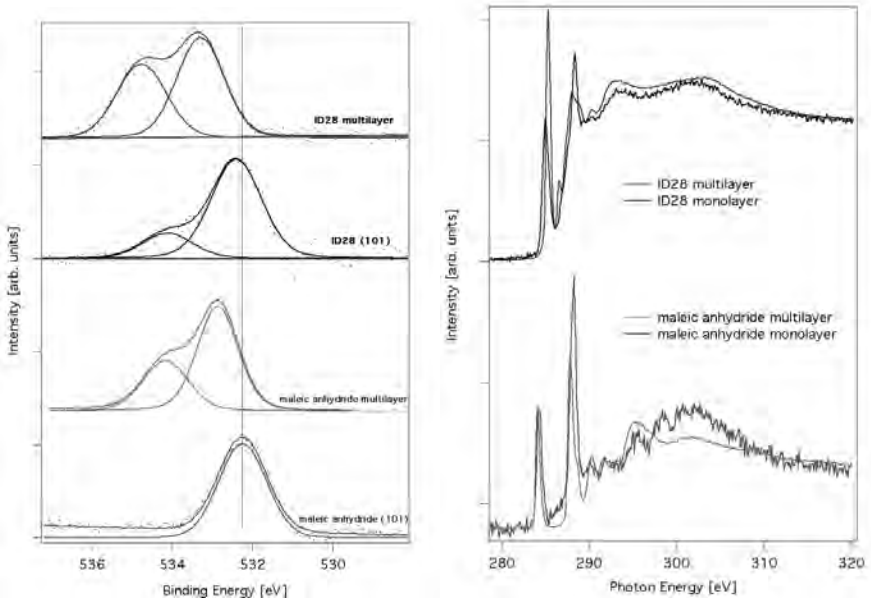

Figure 2:

In the case of maleic anhydride the change in the O1s spectra of the multilayer and monolayer show the oxygen atoms interact with the substrate. The removal of the high binding energy peak indicate that a ring opening occurs in order to bind the molecule to the TiO_2. Measurments on ID28 show similar behavior but the decrease of the oxygen peak at higher binding energy, which is assigned to the oxygen in the carbon ring, is not complete indicating a mixture of binding configurations. Comparing the intensities of the multi- and monolayer we calculate that about 64% of the molecules bind similar to maleic anhydride via a ring opening and 36% in another configuration.

When comparing the C1s NEXAFS spectra (normal emission) for multilayers and monolayers of maleic anhydride and ID28 we note the following: The signature from C-C double bond in maleic anhydride at 284 eV is missing while the perylene π^* region system in ID28 mainly appear at 285 eV. In ID28 a comparison between the σ and π resonances for the molecule indicate that the molecule is not flat at the surface. At higher energy a sharp feature appear at about 288.3 eV in the monolayer spectra for both molecules. This resonance has previously been interpreted to originate from the C-O bond and its appearance in both spectra support the conclusion that a large fraction of the ID28 molecules have a similar bonding configuration as observed for maleic anhydride.

Using the decrease in the intensity of the Ti2p signal as a measurement for the coverage the film thickness was found to be 2.3Å for the ID28 monolayer. This result also indicates that the molecule is not standing perpendicular to the surface..

1. O'Regan, B.; Grätzel, M. *Nature* **1991**, *353*, 737.
2. Snaith, H. J.; Moule, A. J.; Klein, C.; Meerholz, K.; Friend, R. H.; Grätzel, M. *Nano Lett.* **2007**, *7*, 3372.
3. Ute B. Cappel, Elizabeth A. Gibson, Anders Hagfeldt, and Gerrit Boschloo, *J. Phys. Chem. C,* 19 March 2009
4. A. Sandell,1,* B. Sanyal,1 L. E. Walle,2 J. H. Richter,1 S. Plogmaker,1 P. G. Karlsson,1 A. Borg,2 and P. Uvdal3, PHYSICAL REVIEW B **78**, 075113 2008

Investigations of sol-gel prepared cobalt doped titania by XPS and XAS

R. Pärna[1], U. Joost[1,2], V. Kisand[1], E. Nõmmiste[1], T. Käämbre[1], A. Kikas[1], M. Hirsimäki[3], I. Kink[1,2]

[1]Institute of Physics, University of Tartu, Riia 142, 51014 Tartu, Estonia
[2]Estonian Nanotechnology Competence Center, Riia 142, 51014 Tartu, Estonia
[3]Surface Science Laboratory, Tampere University of Technology, P.O. Box 692, FIN-33101, Tampere, Finland

During the last two decades, titanium dioxide (TiO_2) has received great attention due to many advanced applications of the material in photocatalysis, solar energy cells, gas sensors, antifogging and self-cleaning coatings etc. For practical applications sol-gel method is widely used for titania polycrystalline film preparation, since it has many advantages over other fabrication techniques [1].

In addition to pure titanium dioxide the interest has been steadily grown to study metal-ion doped titanium dioxide [2]. The key idea is to modify the electronic structure of the material to shrink the band gap. Narrower band gap offers more effective electron-hole pair generation that is especially important for applications using sunlight, for example in photocatalysis. One promising dopant is cobalt. When titania has been doped with cobalt advances in catalytic properties have been achieved [3].

In this study cobalt doped TiO_2 films were prepared by spin-coating sol-gel technique. Firstly cobalt doped TiO_2 gel was formed by mixture of cobalt nitrate hexahydrate, distilled water, butanol and titanium (IV) 1-butoxide. Then precursor material was deposited by spin-coating on Si (100) substrate. The obtained precursor film was aged couple of days and after that thermal treatment at 450 °C or higher temperatures was used to remove organic components and to obtain crystalline structure. Films were characterised by the X-ray Photoelectron Spectroscopy (XPS) and X-ray Absorption Spectroscopy (XAS), the measurements were performed at beamline D1011.

Photoelectron spectra of Ti 2p, O 1s, and Co 2p of cobalt doped TiO_2 samples after thermal treatments at different temperatures are shown on Figure 1. The spectrum of aged precursor film (marked as 25 °C) is also shown. The spectra of Ti 2p show Ti $2p_{3/2}$ and Ti $2p_{1/2}$ peaks located at 458.7 eV and 464.4 eV, the separation of Ti 2p spin orbit split components was 5.7 eV. This was in good agreement with literature data for annealed TiO_2 film [4].

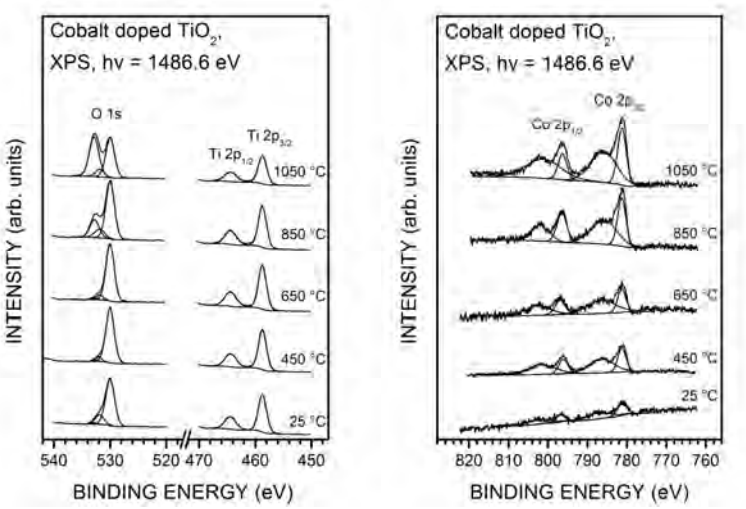

Fig. 1. Photoelectron spectra of Ti 2p, O 1s and Co 2p of cobalt doped TiO_2 samples after thermal treatment at different temperatures. XPS spectra of non-heated aged precursor film (marked as 25°C) are demonstrated as well.

Photoelectron spectra of O 1s showed that oxygen related to TiO_2 was located at 530 eV. All spectra contained shoulder at 531.8 eV. This originates from OH groups on the surface of titanium dioxide [5]. Another shoulder appeared at 532.8 eV when films were annealed over 650 °C. This was related to silicon dioxide, from the Si (100) substrate.

Photoelectron spectra of cobalt (on the right of figure 1) showed that for precursor film Co $2p_{3/2}$ and Co $2p_{1/2}$ photolines were located at 781.3 eV and 796.8 eV. Separation between these peaks was 15.5 eV and increased slightly when samples were annealed at higher temperatures. Also wide satellites were observed above Co $2p_{3/2}$ and Co $2p_{1/2}$ photolines. Such behavior is typical to cobalt oxides.

X-ray absorption spectra of Ti L_{23} edge, O K edge and Co L_{23} edge of cobalt doped TiO_2 samples prior to and after thermal treatment at different temperatures are shown in Figure 2. Ti L_{23} edge provides the basic information about crystal structure of titania [6]. When intensity of feature at 460.5 eV is higher than intensity of feature at 461.4 eV then anatase dominates, when vice versa then rutile dominates in the film. It was found that anatase phase dominates when samples were annealed below 650 °C and rutile phase was detected when annealing temperatures over 850 °C were used.

O K edge XAS spectra of films annealed between 450 °C and 850 °C were typical of TiO_2. Spectrum of aged precursor film was different due to the different composition compared to the annealed films. Spectra of film annealed at 1050 °C differed from typical TiO_2 spectrum. The reason was that silicon dioxide from substrate was detected when films were annealed at 1050 °C.

Cobalt L_{23} edge XA spectra differed from Co_2O_3 and were more similar to CoO [7]. This indicates that probably we have mainly Co^{2+} species in our films.

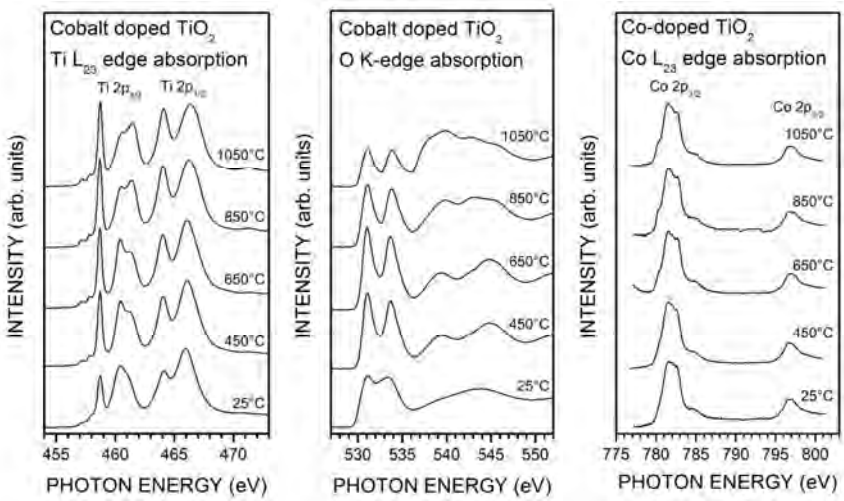

Fig. 2. X-ray absorption spectra of Ti L_{23} edge, O K edge and Co L_{23} edge of cobalt doped TiO_2 samples after thermal treatment at different temperatures. Spectra of non-heated aged precursor film (marked as 25°C) are demonstrated as well.

References

[1] O. Carp, C.L. Huisman, A. Reller, *Prog. Solid State Chem.* 32 (2004) 33.
[2] V. Kisand, U. Joost, V. Reedo, R. Pärna, T. Tätte, J. Shulga, A. Saar, L. Matisen, A. Kikas, I. Kink, *Appl. Surf. Sci.* (2010), doi:10.1016/j.apsusc.2010.02.043.
[3] S. H. Lim, C. Ferraris, M. Schreyer, K. Shih, J. O. Leckie, T. J. White, *J. Sol. State Chem.* 180 (2007) 2905.
[4] R. Sanjinés, H. Tang, H. Berger, F. Gazzo, G. Margaritondo, F. Lévi, *J. Appl. Phys.* 75 (1994) 2945.
[5] J. Yu, J. C. Yu, W. Hoa, Z. Jianga, *New J. Chem.*, 26 (2002) 607.
[6] R. Ruus, A. Kikas, A. Saar, A. Ausmees, E. Nõmmiste, J. Aarik, A. Aidla, T. Uustare, I. Martinson, *J. Elec. Spec. Rel. Phenom.* 104 (1997) 199.
[7] Frank de Groot, Ph.D Thesis, University of Nijmegen, Netherlands, 1991.

Large porphyrin oligomers on Au(111): XAS, XPS and *in-situ* electrospray deposition

A. Saywell[1], A. J. Britton[1], A. Rienzo[1], J K Sprafke[2], L J Esdaile[2], H L Anderson[2], P. H. Beton[1] and J. N. O'Shea[1]

[1] *School of Physics & Astronomy, University of Nottingham, Nottingham, UK*

[2] *Department of Chemistry, University of Oxford, Chemistry Research Laboratory, Oxford, UK*

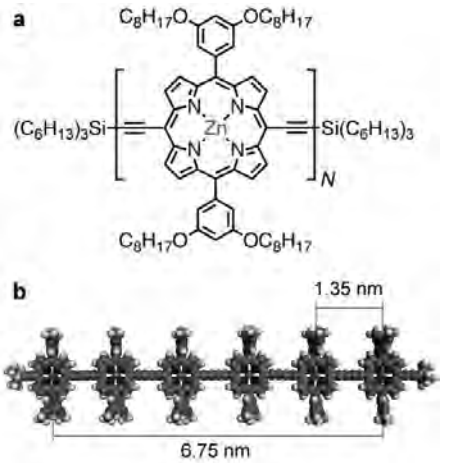

Figure 1. (a) Chemical structure of porphyrin oligomers and polymers: (a) shows the general formula for **P4** (N = 4), **P6** (N = 6), and **Pn** (N = 30-50), and (b) the geometry of the porphyrin hexamer **P6**. The separation between the centres of the porphyrin sub-units is indicated (as calculated from X-ray crystallographic data). The octyl chains and $Si(C_6H_{13})_3$) end groups have been truncated for clarity.

The self-assembly of very large, complex, three-dimensional molecules on surfaces is an exciting new avenue in surface science. With the advent of novel deposition techniques capable of extending high-resolution scanning tunnelling microscopy and synchrotron-based electron spectroscopy to such systems, rapid progress is being made. The molecules chosen for this study are π-conjugated porphyrin oligomers, and polymers, which have recently attracted great interest as molecular wires for applications including single molecule conduction[1,2] and light harvesting[3,4]. We have investigated the adsorption of two oligomers, a porphyrin tetramer (**P4**, $N = 4$), a hexamer (**P6**, $N = 6$), and a polymer **Pn** ($N \approx 30$-50) on the Au(111) surface. Specifically, at beamline D1011 at MAX-lab we have studied the P4 oligomer, while the general chemical structure of all the molecules studied is in figure 1. STM studies reveal new modes of molecular organization on the gold surface, which will be discussed in detail in a forthcoming paper. Here, we present only the additional insight afforded by the high-resolution photoemission and x-ray absorption.

An obvious obstacle to the formation of well defined monolayers of porphyrin oligomers, polymers, or any other large and fragile molecules is that they are non-voltaile, and therefore cannot be deposited by thermal evaporation. In order to overcome this hurdle and to facilitate the study of non-volatile molecules with high resolution synchrotron-based spectroscopy, we developed, a few years ago, a novel in-situ UHV deposition system, based on electrospray ionisation. Essentially, the system forms nanoscale droplets of a liquid solution at the tip of a high voltage capillary. These droplets undergo a succession of Coulomb fission events and solvent evaporation to leave a beam of desolvated molecular ions which are transported through 4 stages of differential pumping before arriving at the sample surface at pressures in the 10^{-8} mbar range [5-7].

In this experiment we successfully deposited the P4 oligomer onto a single crystal Au(111) surface under UHV conditions. The molecules were deposited using a commercial UHV-compatible electrospray deposition source (Molecularspray Ltd, UK) from a toluene/methanol (1:1) solution at an emitter voltage of 2kV and a flow rate of 500 nlmin^{-1}. The pressure during the deposition was ~4x10^{-8} torr.

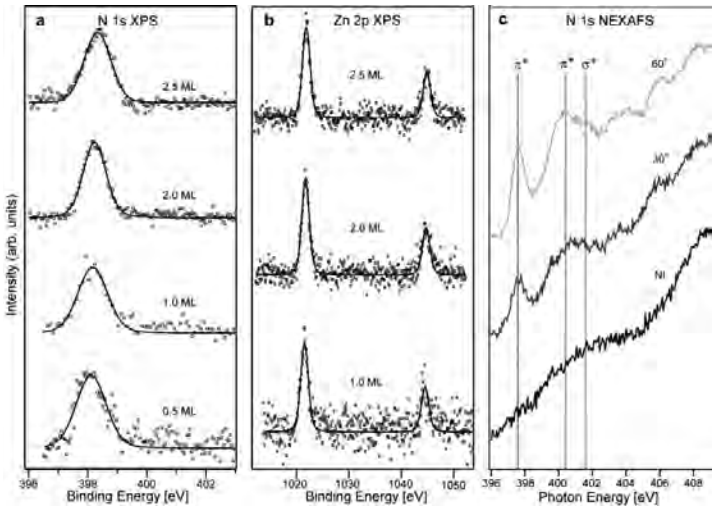

Figure 2. **a** Zn 2p core-level spectrum measured using hv=1250eV for a range of coverages. One chemical environment is observed in all cases. **b** N 1s core-level spectrum measured using hv=500eV. One chemical environment is observed in all cases. **c** N k-edge NEXAFS spectra. The growth of the 2p→π^* transition with increased grazing angle shows that the porphyrin sub-units are lying flat relative to the Au(111) plane.

N 1*s* NEXAFS acquired at coverages ranging from 0.5 – 2.5 monolayers show that the porphyrin cores of the molecule are parallel to the Au(111) surface. This is demonstrated in figure 2c where the growth of the 1s→π^*_1 peak with increasingly grazing angle of incidence, consistent with the nitrogen π^* bond being parallel to the surface. The XPS demonstrates that the Zn atoms within the porphyrin are not displaced when the molecule is deposited, exhibting only single Zn 2*p* and N 1*s* peaks for all coverages, at binding energies expected for the intact porphyrin.

References

[1] Sedghi, G. et al. Single molecule conductance of porphyrin wires with ultralow attenuation. *J. Am. Chem. Soc.* **130**, 8582-8583 (2008).

[2] Winters, M. U. et al. Probing the efficiency of electron transfer through porphyrin-based molecular wires. *J. Am. Chem. Soc.* **129**, 4291-4297 (2007).

[3] Chang, M. H., Hoffmann, M., Anderson, H. L. & Herz, L. M. Dynamics of excited-state conformational relaxation and electronic delocalization in conjugated porphyrin oligomers. *J. Am. Chem. Soc.* **130**, 10171-10178 (2008).

[4] Lin, V. S. Y., Dimagno, S. G. & Therien, M. J. Highly conjugated, acetylenyl bridged porphyrins - new models for light-harvesting antenna systems. *Science* **264**, 1105-1111 (1994).

[5] *Photoemission, resonant photoemission and X-ray absorption of Ru-535 adsorbed on rutile TiO_2(110) prepared by in situ electrospray deposition*, L. C. Mayor et al, J. Chem. Phys. 129, 114701 (2008)

[6] *Electrospray deposition of C_{60} on a hydrogen-bonded supramolecular network*, A. Saywell et al, J. Phys. Chem. C 112, 7706 (2008)

[7] *Electrospray deposition of fullerenes in ultra-high vacuum: in situ scanning tunneling microscopy and photoemission spectroscopy*, C. J Satterley et al. Nanotechnology 18, 455304 (2007)

Single molecule magnets on Au(111): XAS and *in-situ* electrospray deposition

A. Saywell[1], A. J. Britton[1], N. Taleb[2], M. Gimenex-Lopez[2], N. R. Champness[2], P. H. Beton[1] and J. N. O'Shea[1]
[1] *School of Physics & Astronomy, University of Nottingham, Nottingham, UK*
[1] *School of Chemistry, University of Nottingham, Nottingham, UK*

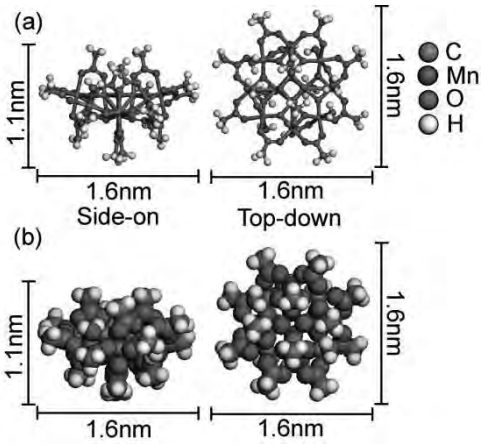

Figure 1. (a) Chemical structure of $Mn_{12}O_{12}(O_2CCH_3)_{16}(H_2O)_4$ ($Mn_{12}(acetate)_{16}$), (b) Structure of $Mn_{12}(acetate)_{16}$ shown as a space filling CPK model. The dimensions of the molecule are indicated.

The single molecule magents (SMMs) investigated here are based on the mixed valence dodecamanganese (III, IV) cluster which contains four Mn^{+4} ions within the core and eight Mn^{+3} ions around the periphery as shown in figure 1. The magnetic core is protected by an organic shell which may be altered by conventional wet chemistry techniques such as ligand exchange and direct synthesis from the appropriate carboxylate reagents. This type of SMM exhibits magnetic properties, such as hysteresis cycles, magnetic anisotropy originating from a purely molecular basis, quantum magnetic tunnelling effects and also has potential for molecular information storage devices.

An obstacle to the formation of well defined monolayers or network-isolated clusters however is that SMM shown in figure 1 and its derivatives are non-volatile and therefore cannot be sublimed onto a surface under UHV conditions. In order to overcome this hurdle and to facilitate the study of non-volatile molecules with high resolution synchrotron-based spectroscopy, we developed, a few years ago, a novel in-situ UHV deposition system, based on electrospray ionisation. Essentially, the system forms nanoscale droplets of a liquid solution at the tip of a high voltage capillary. These droplets undergo a succession of Coulomb fission events and solvent evaporation to leave a beam of desolvated molecular ions which are transported through 4 stages of differential pumping before arriving at the sample surface at pressures in the 10^{-8} mbar range [2-4].

In this experiment we successfully deposited two single molecule magnet molecules *in-situ* onto atomically clean Au(111) surfaces under UHV conditions at beamline D1011. The molecules were the one shown in figure 1, and a second derivate with a larger organic shell. The molecules were deposited using a commercial UHV-compatible electrospray deposition source (Molecularspray Ltd, UK) [5] from a methanol solution at an emitter voltage of 2kV and a flow rate of 500 $nlmin^{-1}$. The pressure during the deposition was ~$4x10^{-8}$ torr.

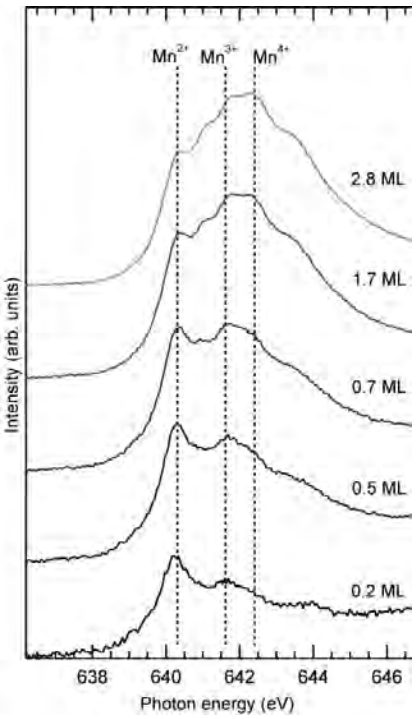

Figure 2. NEXAFS spectra measured at the Mn 2*p* adsorption edge (Mn L–edge) for a range of SMM coverages (0.2 ML – 2.8 ML)

Figure 2 shows the Mn 2*p* (L-edge) NEXAFS for a range of $Mn_{12}O_{12}(O_2CCH_3)_{16}(H_2O)_4$ (Mn_{12}(acetate)$_{16}$), coverages coverages between 0.2ML and 2.8ML from which the oxidation state of the manganese atoms in the core of the SMM may be identified. For multi-layer coverages the spectra are consistent with a mixture of Mn^{3+} and Mn^{4+} oxidation states similar to that previously observed [6] for the undamaged Mn_{12}(acetate)$_{16}$ molecule (4 Mn^{4+} and 8 Mn^{3+} atoms). However for sub-monolayer coverages (0.2ML, 0.5ML, and 0.7ML) the spectra observed are consistent with that of a sample consisting predominantly of the Mn^{2+} oxidation state. Thus for sub-monolayer coverages of the SMM Mn_{12}(acetate)$_{16}$ deposited by UHV-ESD the majority oxidation state for the Mn atoms is 2+. In common with previous studies we observe the growth over several hours of a peak corresponding to the Mn^{2+} oxidation state. This time dependent feature is attributed to beam damage and was observed for all coverages.

References

[1] *Magnteic-properties of a Mn cluster organic-compound* Novak, M. *et a*l.. J. Magn. Magn. Mater. **146**, 211-213(1995).

[2] *Photoemission, resonant photoemission and X-ray absorption of Ru-535 adsorbed on rutile TiO_2(110) prepared by in situ electrospray deposition*, L. C. Mayor et al, J. Chem. Phys. 129, 114701 (2008)

[3] *Electrospray deposition of C_{60} on a hydrogen-bonded supramolecular network*, A. Saywell et al, J. Phys. Chem. C 112, 7706 (2008)

[4] *Electrospray deposition of fullerenes in ultra-high vacuum: in situ scanning tunneling microscopy and photoemission spectroscopy*, C. J Satterley et al. Nanotechnology 18, 455304 (2007)

[5] http://www.molecularspray.co.uk

[6] Electronic structure of Mn-12 derivatives on the clean and functionalized Au surface. Voss, S. *et al*. Phys. Rev. B **75**, (2007).

Biotinylation of ZnO Nanoparticles and Thin Films: a NEXAFS and XPS Study

Linnéa Selegård, Cecilia Vahlberg, Maria Ahrén, and Kajsa Uvdal[1]

Division of Molecular Surface Physics and Nanoscience, Department of Physics, Chemistry and Biology (IFM), Linköping University, SE-581 83 Linköping, Sweden

The interest of ZnO nanoparticles for biosensing and bioimaging is due to the excellent and suitable optical properties of ZnO for these applications, such as a narrow excitonic band gap, broad emission spectrum and low photo-bleaching probability [1-2].

The aim of this project is to acquire ZnO particles as specific nanoprobes to be used for biorecognition and biosensing applications. Efforts have been made in order to achieve stable ZnO nanoparticles with appropriate luminescent properties together with high specificity. In order to address these issues we first coated the ZnO nanoparticles with a layer of 3-mercaptopropyl)trimethoxysilane (MPTS). In a second step an iodized biotin molecule was coupled to MPTS via the thiol group, see Figure 1. For comparison, surface modification studies using the same coupling strategy were also done on ZnO surfaces.

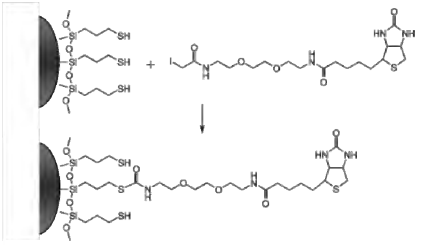

Figure 1. A schematic figure showing MPTS- and MPTS-Biotin functionalized ZnO nanoparticles

Characterization of the biofunctionalized ZnO nanoparticles and surfaces were done at beamline D1011, MaxLab, Lund using X-ray photoelectron spectroscopy and near - edge x-ray absorption fine structure (NEXAFS) spectroscopy.

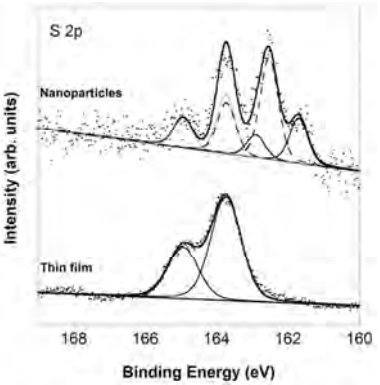

Figure 2. S (2p) core level XPS spectrum of MPT functionalized ZnO nanoparticles and ZnO films.

A high resolution core level S(2p) XPS spectrum of ZnO nanoparticles and ZnO films functionalized with MPTS is presented in Figure 2. Due to spin-orbit splitting, each sulphur species is fitted with a doublet peak with a binding energy separation of 1.2 eV and an area ratio of 2:1, corresponding to the $2p_{3/2}$ and $2p_{1/2}$ levels, respectively. The main double peak in the XPS S(2p)spectrum of functionalized ZnO nanoparticles, with the $S2p_{3/2}$ binding energy peak positioned at 162.5, is in good agreement with the binding energy positions earlier found for thiolate species[3] meaning that sulphur on the MPTS molecules can coordinate to the particle surface. This peak might also have contribution from sulphur chemically bound to Au (S-Au) since the particles are spin coated on a gold

substrate. Two other sulphur species were also present in the sample. There is a S(2p) binding energy peak presented as a double peak (due to spin- orbit splitting, see above) with the $2p_{3/2}$ peak positioned at 163.7 eV. This S(2p) bindig energy peak corresponds to unbound thiols (-SH) originating from MPTS. The S(2p) peak found at lower binding energies, with the $2p_{3/2}$ peak positioned at 161.5 eV corresponds to atomic sulphur.[4,5] In the case of MPTS functionalized ZnO film, only one chemical state of sulphur is found with the $2p_{3/2}$ binding energy peak positioned at 163.7 eV which we assign to unbound thiols (-SH). Hence, both the ZnO nanoparticles and the ZnO thin films showed presence of MPTS after functionalization, accordingly, both systems have -SH available, which mean that they are prepared for additional linking procedure/processes.

O K-edge NEXAFS spectra of (a), ZnO thin films functionalized with MPTS (b) ZnO films stepwise functinalized with MPTS and biotin as well as (c) a multilayer of biotin as a reference, for comparison, are presented in Figure 3.

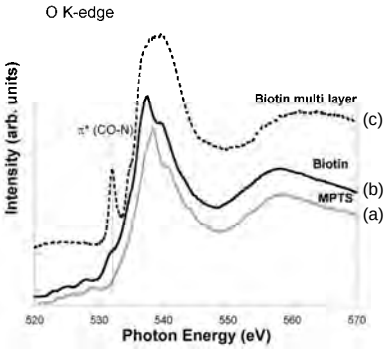

Figure 3. O K-edge NEXAFS spectrum of (a) MPTS functionalized ZnO thin film, (b) MPTS-biotin functionalized ZnO thin film, and (c) Biotin

The O K-edge NEXAFS spectrum of the biotin reference(c) showed a narrow peak positioned at 532 eV, which we assign as 1s to $\pi^*_{C=O}$ transitions in agreement values found in the literature for amide containing molecules [6-8]. This resonance was, as expected not detected for the ZnO films functionalized with MPTS before second step of biotinylation, see Figure 3 (a), but was present as a shoulder in the ZnO films functionalized with both MPTS and biotin indicating a successful biotin functionalization, see Figure 3 (b).

This project is supported by grants from the Swedish Research Council (VR), The Swedish Governmental Agency for Innovation Systems (VINNOVA) and Carl Tryggers Foundation. The authors are also grateful for all help from the Max-lab staff during the measurements.

References:

(1) Bahnemann, D.W.; Kormann, C.; Hoffman, M. R. *J. Phys. Chem.* **1987**, *91*, 3789.
(2) Jana, N. R.; Yu, H.; Ali, E. M.; Zheng, Y.; Ying, J. Y. *Chem. Commun.* **2007**, 1406.
(3) Pesika, N. S.; Hu, Z.; Stebe, K. J.; Searson, P. C. *J. Phys. Chem. B.* **2002**, *106*, 6985.
(4) Cavalleri, O.; Gonella, G.; Terreni, S.; Vignolo, M.; Pelori, P.; Floreano, L.; Morgante, A.; Canepa, M.; Rolandi, R. *J. Phys.: Condens. Matter*. **2004**, *16*. 2477.
(5) Allen, C. G.; Baker, D. J.; Albin, J. M.; Oertli, H. E.; Gillaspie, D. T.; Olson, D. C.; Furtak, T. E.; Collins, R. T. *Langmuir* **2008**, *24*, 13393.
(6) Gordon, M. L.; Cooper, G.; Morin, C.; Araki, T.; Turci, C. C.; Kaznatcheev, K.; Hitchcock, A. P. *J. Phys. Chem. A.* **2003**, *107*, 6144.
(7) Cooper, G.; Gordon, M.; Tulumello, D.; Turci, C.; Kaznatcheev, K.; Hitchcock, A. P. *Journal of Electron Spectroscopy and Related Phenomena* **2004**, *137-140*,795.
(8) Zubavichus, Y.; Shaporenko, A.; Grunze, M.; Zharnikov, M. *J, Phys. Chem. B.* **2007**, *111*, 9803.

Experimental evidence for mixed dissociative and molecular adsorption of water on a rutile TiO_2(110) surface without oxygen vacancies

L. E. Walle[1], A. Borg[1], P. Uvdal[2] and A. Sandell[3]

[1] *Dept. of Physics, Norwegian University of Science and Technology, NO-7491 Trondheim, Norway*
[2] *Chemical Physics, Dept. of Chemistry, Lund University, P.O. Box 124, SE-221 00 Lund, Sweden*
[3] *Dept. of Physics and Materials Science, Uppsala University, P. O. Box 530, SE-751 21 Uppsala, Sweden*

Rutile TiO_2(110) has for many years been regarded as the benchmark surface for fundamental studies of metal oxide surface chemistry [1]. Since water is an integral part of the environment, the H_2O/TiO_2(110) system has received more attention than any other comparable system [1,2]. While the dissociation of water on the oxygen deficient TiO_2(110) surface has been characterized in detail [3-6], there is as of yet no consensus reached between experimentalists and theorists regarding a very fundamental question: Does water dissociate upon adsorption on the defect-free TiO_2(110) surface?

Theoretical studies of water adsorption on the defect-free TiO_2(110) surface presented over the years are contradictory. Early studies predicted dissociative adsorption at all coverages [7], while more recent studies suggest a delicate balance between dissociated, partial dissociated and molecular configurations [8-10]. When it comes to experimental studies, the most common view is that at all coverages water adsorbs molecularly on the ideal TiO_2(110) surface and dissociation only take place at defect sites [1,11].

In this work, we study the interaction of water with the rutile TiO_2(110) surface using synchrotron radiation photoemission at beamline D1011. We demonstrate that O 1s spectra recorded at grazing emission angle at optimized photon energy in conjunction with valence spectra allow for the observation of OH on the surface even when substrate oxygen is present.

A TiO_2(110) surface free from oxygen vacancies was prepared following the recipe in ref. [12]. Sputtering and annealing in vacuum produce a reduced surface, denoted r-TiO_2(110). At room temperature, water dissociates on the O_{bridge} vacancies on the r-TiO_2(110) surface giving a hydrated surface. The capping H atoms can then be reacted off by subsequent exposure to O_2 resulting in a surface with perfect O_{br} rows [12]. In the last step, the capping H atoms are titrated away in a stepwise fashion by careful monitoring of the intensity of the OH 3σ peak.

Figure 1 shows valence photoemission results for such a preparation sequence, performed at RT. Spectra are shown for: the clean r-TiO2 surface, after a subsequent dose of 5 L H_2O, after a total dose of 5 L O_2 deposited in three steps and finally after another 5 L of H_2O. An OH 3σ peak at a binding energy of 11.0 eV is evident in the spectrum measured after 5 L H_2O on the r-TiO2(110) surface. A much lower OH 3σ intensity is found after O_2 dosing. Consistently, if the surface is subsequently exposed to water at RT there is negligible increase of the OH 3σ peak intensity. We find that between 75 and 90% of the capping H atoms can be reacted off by this procedure, leaving hydroxylated defects with a density of about 1.5%.

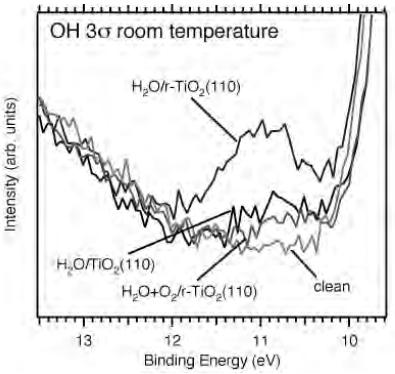

Figure 1. *OH 3σ spectra for the clean r-TiO_2 surface (measured at elevated temperature), after 5 L H_2O on the r-TiO_2 surface (H_2O/r-TiO_2(110)), after a subsequent dose of 5 L O_2 (H_2O+O_2/r-TiO_2(110)) and after adsorption of another 5 L of H_2O (H_2O/TiO_2(110)).*

In Fig. 2 O 1s spectra have been used to monitor desorption of OH and H_2O during annealing of a multilayer of water to different temperatures. Molecular water gives rise to the O 1s peak at 534.2 eV, while OH shows up as a shoulder at 532 eV. The spectra have been delineated into individual contributions from TiO_2, OH and H_2O. The presence of a mixed OH/H_2O monolayer is clearly demonstrated after annealing to 210 K, confirming previous theoretical work [8-10].

Based on the O 1s intensities at ML coverage (210 K) [11], the coverages of OH and

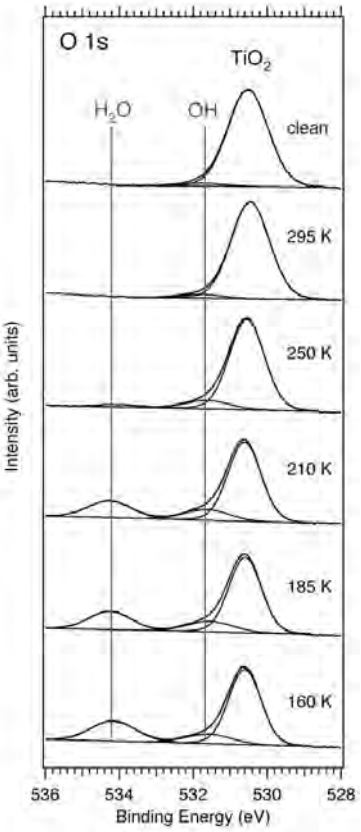

Figure 2. *O 1s spectra for water adsorption on a rutile TiO_2(110) surface free from oxygen vacancies, after progressive heating of a multilayer of water. Each spectrum has been delineated into individual contributions from the substrate, OH and H_2O.*

H_2O are estimated for the different temperatures in Fig. 3. No species originating from the mixed monolayer can be detected on the surface at RT. The absence of water is consistent with previous TPD studies [3,11].

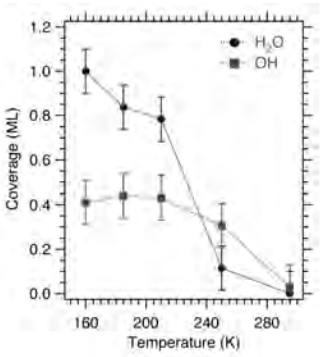

Figure 3. *Estimated OH and H_2O coverages, given in monolayers (ML) where one ML corresponds to the density of Ti(5) sites on the surface, derived from the spectra presented in Fig. 2.*

The OH coverage stays essentially at 0.43 ML up to 210 K. Assuming that all the OH is in a pseudo-dissociated state [5], 0.22 ML will be accommodated on terminal [Ti(5)] sites (OH_t). The H_2O coverage at the monolayer point is 0.78 ML. This means that the Ti rows comprise 0.22 ML OH_t and 0.78 ML H_2O. In the theoretical treatment the energies of a pure water phase and a mixed phase (with a OH:H_2O ratio of two) were found to be very similar at monolayer coverage [8,9]. Applying this model, we obtain 0.44 ML of the mixed phase and 0.56 ML of the water phase. This suggests rather similar energies with a slightly higher probability for the pure water phase to form.

In this work we have demonstrated that the formation of a monolayer of water on a rutile TiO_2(110) surface free from oxygen vacancies at low temperature under UHV conditions involves both molecular and dissociative adsorption. Lower coverages are characterized by an increased OH:H_2O ratio. At room temperature, water adsorption is only possible through dissociation at oxygen vacancies.

References

1. U. Diebold, Surf. Sci. Rep. **48**, 53 (2003).
2. C. L. Pang, R. Lindsay, and G. Thornton, Chem. Soc. Rev. **37**, 2328 (2008).
3. M. A. Henderson, Surf. Sci. **400**, 203 (1998).
4. C. Di Valentin, G. Pacchioni, and A. Selloni, Phys. Rev. Lett. **97**, 166803 (2006).
5. S. Wendt, J. Matthiesen, R. Schaub, E. K. Vestergaard, E. Laegsgaard, F. Besenbacher, and B. Hammer, Phys. Rev. Lett. **96**, 066107 (2006).
6. O. Bikondoa, C. L. Pang, R. Ithnin, C. A. Muryn, H. Onishi, and G. Thornton, Nature Mater. **5**, 189 (2006).
7. J. Goniakowski and M. J. Gillan, Surf. Sci. **350**, 145 (1996).
8. P. J. D. Lindan, N. M. Harrison, and M. J. Gillan, Phys. Rev. Lett. **80**, 762 (1998).
9. P. J. D. Lindan and C. Zhang, Phys. Rev. B **72**, 075439 (2005).
10. W. Zhang, J. Yang, Y. Luo, S. Monti, and V. Caravetta, J. Chem. Phys. **129**, 064703 (2008).
11. M. A. Henderson, Surf. Sci. **355**, 151 (1996).
12. S. Wendt, P. T. Sprunger, E. Lira, G. K. H. Madsen, Z. Li, J. Ø. Hansen, J. Matthiesen, A. Blekinge-Rasmussen, E. Laegsgaard, B. Hammer, and F. Besenbacher, Science **320**, 1755 (2008).

Energy level pinning in self-assembled alkanethiol monolayers

Tobias Weidner,[1] Yan Ge,[2] Heejoon Ahn,[2] James E. Whitten,[2] and Michael Zharnikov[1]

[1]*Angewandte Physikalische Chemie, Universität Heidelberg, 69120 Heidelberg, Germany*

[2]*Department of Chemistry and Center for Advanced Materials, The University of Massachusetts Lowell, Lowell, MA 01854*

We have studied potassium deposition on dodecanethiolate (C12) self-assembled monolayers (SAMs) on Au(111) by UPS, XPS, and HRXPS. A significant portion of potassium atoms penetrates to the SAM-Au interface. However, a large fraction is imbedded in the aliphatic matrix, resulting in its disordering and chemical inhomogeneity (Figure 1). These processes were analyzed within a simplified model assuming a homogeneous distribution of imbedded potassium in the aliphatic matrix.[1] While the real distribution may be different to some extent, the model provides estimates for the relative portions of the penetrating and imbedded potassium atoms. The deposition of potassium is accompanied by a progressive decrease in the work function of the K/C12/Au sample,[1,2] which is related to the formation of a surface dipole layer at the SAM/Au interface that, in turn, is mediated by potassium atoms in the vicinity of the interface. The second dominant effect is the upward shift of the binding energy (BE) position of the C1s peak characteristic of the aliphatic chain of the SAM constituents in the course of K deposition (Figure 2). This shift correlates exactly with the work function change.[1,2] In contrast, the BE position of the S2p doublet characteristic of the headgroup of the SAM constituents remained unchanged upon potassium deposition (Figure 3). The results have been rationalized by assuming that different energy level alignment frameworks are applicable to the description of photoemission from the aliphatic chain and headgroup atoms of the SAM constituents. While the standard Fermi level pining model is suitable for the headgroups, the electronic system of the alkyl matrix is pinned to the substrate and spectrometer in a complex way, involving both Fermi and vacuum level alignment (Figure 4).

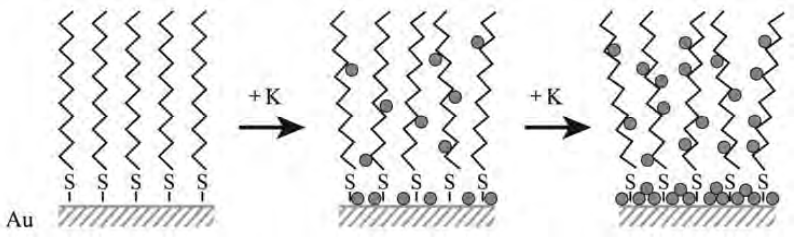

Figure 1. Cartoon illustrating the fate of deposited potassium. While about a half of the deposited atoms penetrate to the SAM/Au interface, the residual atoms remain "stuck" in the organic layer.

The different pinning of the electronic systems of the headgroup and matrix can be explained by the different proximity of the respective moieties to the metal substrate. While the thiolate headgroup is in electronic contact with the substrate, which ensures rapid charge compensation after photoelectron ejection, the carbon atoms in the methyl and methylene groups are decoupled or, in other words, electrically isolated from the substrate on the timescale of the photoemission process. Charge compensation in this case occurs on a longer time scale and results only in the lack of charge buildup on the surface.

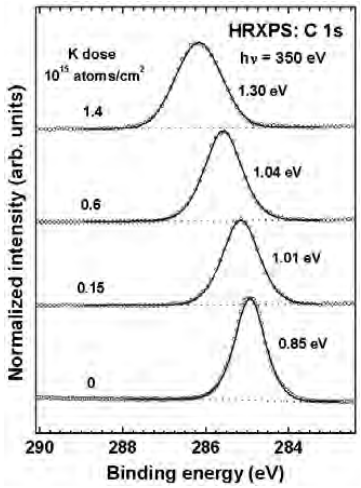

Figure 2. C 1s HRXPS spectra of K/C12/Au acquired in the course of potassium evaporation. The binding energy scale is referenced to the Fermi level of the spectrometer. The fwhm of the observed peak (a measure of non-heterogeneity) is listed next to it.

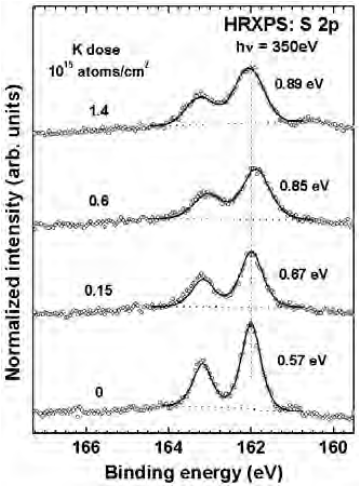

Figure 3. S 2p HRXPS spectra of K/C12/Au acquired in the course of potassium evaporation. The binding energy scale is referenced to the Fermi level of the spectrometer. The fwhm of the S $2p_{3/2,1/2}$ peaks (a measure of non-heterogeneity) are listed next to it.

The above findings and considerations suggest that photoemission from SAMs cannot always be described in the standard framework of the chemical shift, even though this description is sufficient in most of cases. There are, however, some special situations when the insulating character of the SAM comes into the foreground, so that electrostatic effects should be taken into account. Apart from the potassium deposition case discussed here, the most prominent examples include the embedded dipole layer in alkanethiolate SAMs[3] and the effect of the head group dipole in mixed films of unsubstituted and partially semifluorinated alkanethiolates[4]. Another "highlight" example of the electrostatic effects, which was for a long time not understood as such, is the BE position difference of the C1s emission in alkanethiolate SAMs on Au and Ag.[5] This difference correlates exactly with the work function difference between Au(111) and Ag(111) and can, therefore, be perfectly explained by electrostatic effects within. This work has been supported by DFG (ZH 63/10-1).

[1]Y. Ge, T. Weidner, H. Ahn, J. E. Whitten, and M. Zharnikov, J. Phys. Chem. C **113**, 4575 (2009).
[2]H. Ahn, M. Zharnikov, and J. E. Whitten, Chem. Phys. Lett. **428**, 283 (2006).
[3]O. M. Cabarcos, A. Shaporenko, T. Weidner, S. Uppili, L. S. Dake, M. Zharnikov, and D. L. Allara, J. Phys. Chem. C **112**, 10842-10854 (2008).
[4] N. Ballav, A. Terfort, and M. Zharnikov, J. Phys. Chem. C **113**, 3697 (2009).
[5] K. Heister, M. Zharnikov, M. Grunze, and L. S. O. Johansson, J. Phys. Chem. B **105**, 4058 (2001).

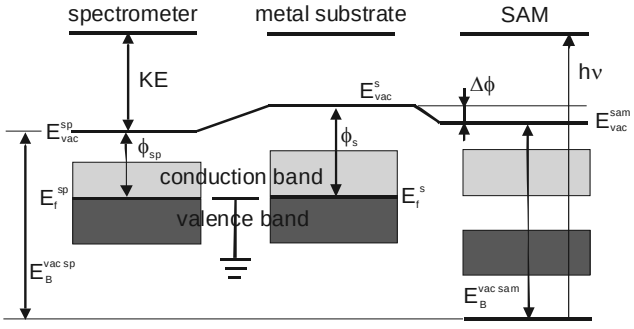

Figure 4. Energy level diagram for a SAM film on a conductive substrate. Vacuum levels (E_{vac}), Fermi levels (E_f), and work functions (ϕ) of the spectrometer (sp), substrate (s), and SAM (sam) are shown. $\Delta\phi$ is the work function difference between the bare and SAM-covered surfaces; hν is the photon energy and KE is kinetic energy of photoelectrons; $E_B^{vac\ sam}$ and $E_B^{vac\ sp}$ are the BEs of a SAM core level referenced to the vacuum level of the SAM and spectrometer, respectively.

X-ray absorption and magnetic circular dichroism of the graphene/Ni(111) interface

M. Weser,[1] Y. Rehder,[1] K. Horn,[1] A. B. Preobrajenski,[2] and Yu. S. Dedkov[1,*]

[1]*Fritz-Haber Institut der Max-Planck Gesellschaft, 14195 Berlin, Germany*
[2]*MAX-lab, Lund University, 22100 Lund, Sweden*

Among the allotropes of carbon, graphene, the two-dimensional hexagonally coordinated sp^2-bonded form has received enormous attention in recent years, because of its unique physical properties [1,2]. Graphene-based spin electronic, proposed recently, devices possess a tremendous potential for high-density non-volatile memories, reconfigurable electronic devices and, possibly, solid-state quantum computing elements. In particular, recent theoretical studies [3,4] suggested to use graphene as a building block in spin-filtering devices, where the perfect spin-filtering was calculated for sandwiches composed of Ni(111) electrodes separated by graphene layers. As the spin dependent transport depends on the interface quality, the graphene/Ni(111) system is of special interest providing an ideal interface from a structural point of view. However, prior to being able to implement graphene/ferromagnet systems in any kind of spintronic device, a study of the electronic, magnetic, and interfacial properties has to be performed.

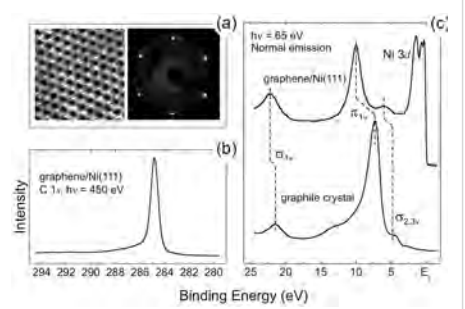

Fig. 1. (a) STM and LEED characterization of the graphene layer on Ni(111). (b) C 1*s* photoemission spectrum of the graphene/Ni(111) system. (c) Comparison of the normal emission valence band photoelectron spectra of the pure graphite crystal and graphene/Ni(111).

Experiments were performed at the D1011 beamline of MAX-Lab. A well-ordered graphene/Ni(111) system was prepared via procedure described in Ref. [5]. LEED pattern of the graphene/Ni(111) system revealed a well-ordered (1×1) pattern, without any additional reflexes, as expected from the small lattice mismatch [Fig. 1(a)]. STM measurements (performed in a separate experimental station under the same experimental conditions; M. Fonin, Uni Konstanz) indicate that a high quality epitaxial graphene layer was formed on the Ni(111) substrate [Fig. 1(a)]. XAS and XMCD spectra were collected at the Ni $L_{2,3}$ and C *K* absorption edges in partial and total electron yield modes (PEY and TEY) with an energy resolution of 100 meV. Magnetic dichroism spectra were obtained with circularly polarized light (the degree of polarization was P=0.75) at different angles, α, in the remanence magnetic state of the graphene/Ni(111) system. All spectra were recorded at room temperature.

Fig. 1 (b) and (c) show the XPS C 1*s* ($h\nu$ = 450 eV) and normal emission valence band spectra ($h\nu$ = 65 eV), respectively, of graphene/Ni(111). The normal emission valence band spectra of single-crystalline graphite and graphene/Ni(111) presented in Fig. 1 (c) were found to be in perfect agreement with previously published data. The shift to larger binding energy is different for σ and π valence band graphene-derived states. This behavior can be explained by the different strength of hybridization between these states and Ni 3*d* valence band states which is larger for the out-of-plane oriented π states.

In order to address the orbital anisotropy at the graphene/Ni interface, linearly polarized light was used and the sample orientation relative to the x-ray wave vector was varied (Fig. 2, upper panel). Spectral features observed in the regions 283-289 eV and 289-315 eV are ascribed to $1s\rightarrow\pi^*$ and $1s\rightarrow\sigma^*$ transitions, respectively. The shape of XAS lines in both absorption regions is influenced by considerable excitonic effects through poor core-hole screening. In the case of the graphene/Ni(111) system, the XAS C $1s\rightarrow\pi^*,\sigma^*$ spectrum shows considerable changes compared with the graphite spectrum, indicating a strong chemisorption. The present XAS results can be analyzed on the basis of recent calculations of spin-resolved electronic structure and C *K*-edge electron energy loss spectra (EELS) for the graphene/Ni(111) interface [6,7] and very good agreement between experimental XAS

* Corresponding author. E-mail: dedkov@fhi-berlin.mpg.de

and calculated EELS spectra was found: (i) they posses the same angle (scattering vector) dependence and (ii) the spectral features in the experimental spectra are well reproduced in the theoretical ones. For example, the peak in the XAS spectra at 285.5 eV of photon energy in the 1*s*→π^* spectral region can be assigned to the transition of the electron from the 1*s* core level on the interface state which originates from C p_z-Ni 3*d* hybridization and corresponds to carbon atom C-*top* and interface Ni atom antibonding state. The second peak at 287.1 eV of photon energy corresponds to the transition of the electron from 1*s* core level on the interface state above the Fermi level (around the *M*-point in the hexagonal Brillouin zone) which originates from C p_z-Ni p_x,p_y,3*d* hybridization and corresponds to a bonding between the two carbon atoms, C-*top* and C-*fcc*, which involves the nickel atom at the interface.

The existence of a considerable magnetic interaction between the Ni substrate and the graphene film is proven by the analysis of both Ni $L_{2,3}$ and C *K* XMCD spectra shown in Fig. 2 (lower panel). Our Ni $L_{2,3}$ XMCD spectrum of the graphene/Ni(111) system is in perfect agreement with previously published data (the bulk values of the spin and orbital magnetic moments μ_S=0.69μ_B and μ_L=0.07μ_B of Ni calculated from the XAS spectra are in very good agreement with previously published experimental values). Fig. 2 depicts the dichroic signal at the C *K* edge. This signal shows unambiguously that Ni induces a magnetic moment in the graphene layer. The C *K* XMCD spectrum shows that the major magnetic response stems from transitions of the 1*s* electron into the π^*-states, while transitions into the σ^*-states yield practically no magnetic signal, indicating that only the C 2p_z orbitals which hybridize with the Ni 3*d* band are spin-polarized. Due to the impossibility to extract the spin magnetic moment form the *K* edge XMCD spectra, comparison of the present results with previous works on the observation of induced magnetism in non-magnetic atoms shows, that the spin moment can be estimated in the range of 0.05-0.1μ_B per C atom. Observed magnetism in graphene layer induced by a ferromagnetic substrate is of crucial importance for the design of new carbon-based spintronic devices.

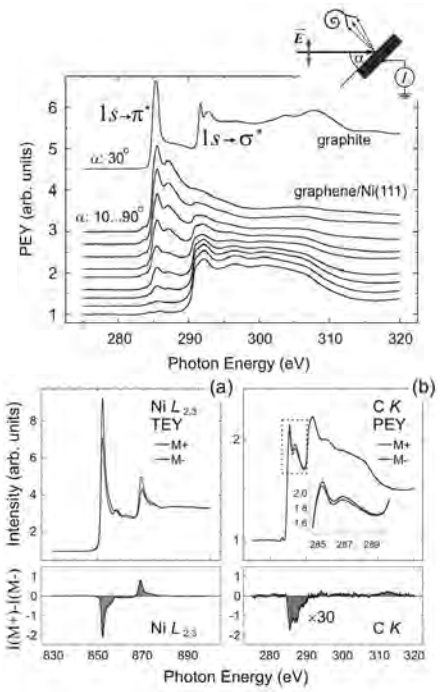

Fig.2. (Upper panel) A series of the angle-dependent XAS spectra of the graphene/Ni(111) system. For comparison the XAS spectrum of bulk graphite is shown in the upper part of the plot. (Lower panel) XMCD spectra of the graphene/Ni(111) system: absorption spectra measured for two opposite orientations of the magnetization are shown in the upper part for the Ni $L_{2,3}$- (a) and C *K*-edges (b). The corresponding differences are shown in the lower part of the respective figures.

[1] A. K. Geim and K. S. Novoselov, Nature Materials **6**, 183 (2007).
[2] A. H. C. Neto *et al*., Rev. Mod. Phys. **81**, 109 (2009).
[3] V. M. Karpan *et al*., Phys. Rev. Lett. **99**, 176602 (2007).
[4] O. V. Yazyev and A. Pasquarello, Phys. Rev. B **80**, 035408 (2009).
[5] Yu. S. Dedkov *et al*., Phys. Rev. Lett. **100**, 107602 (2008).
[6] G. Bertoni *et al*., Phys. Rev. B **71**, 075402 (2005).
[7] M. Weser *et al*., Appl. Phys. Lett. **96**, 012504 (2010).

Intercalation of Ni under h-BN and graphene films grown on Ir(111)

N.A. Vinogradov[1,2], M.L. Ng[1,2], A.S. Vinogradov[3], A.B. Preobrajenski[1] and N. Mårtensson[1,2]

[1] *MAX-Lab, Lund University, 22100 Lund, Sweden*

[2]*Department of Physics, Uppsala University, 75121 Uppsala, Sweden*

[3]*V.A. Fock Institute of Physics, St. Petersburg State University, 198504 St. Petersburg, Russia*

Intercalation of metal atoms under thin films grown on various substrates can modify the substrate-adsorbate interaction and therefore lead to a controllable tuning of the interfacial electronic structure [1]. In the present study we report on the temperature-driven intercalation of Ni atoms under graphene and h-BN film grown on the Ir(111) surface.

The process of Ni intercalation under graphene and h-BN film has been studied by means of high-resolution core-level photoelectron spectroscopy (HRCLS), near-edge x-ray absorption spectroscopy (NEXAFS) and low-energy electron diffraction (LEED). Graphene and h-BN films have been grown on the Ir(111) surface by chemical vapor deposition; the crystal treatment and preparation procedures can be found elsewhere [2,3]. Additionally, the impact of oxygen co-adsorption on intercalation process has been investigated for the sake of comparison with the earlier studied systems [4]. The broad range of experimental conditions has been used to clarify the role of annealing temperature, Ni coverage and partial O_2 pressure in the intercalation process. Ir(111) is known to be a suitable substrate for growing graphene and h-BN films of high quality and low defect density. The high quality of films has been verified by LEED and HRCLS.

Fig.1 *Core-level photoelectron (PE) spectra of a) C 1s, b) N 1s and c) B1s evolution upon Ni intercalation under graphene/Ir(111) and h-BN/Ir(111), respectively. Ni has been deposited in ultra-high vacuum conditions, P=3x10^{-10}mbar, annealing time t=30 min for every step.*

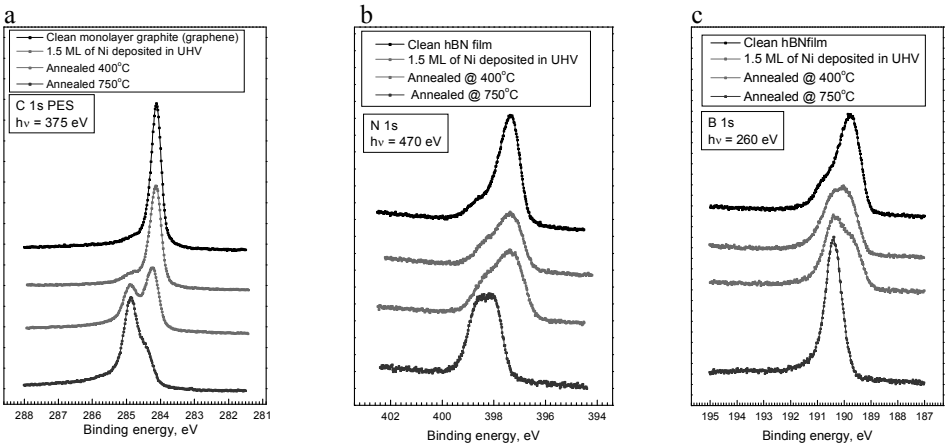

Both graphene and h-BN are known to form slightly corrugated films on the Ir(111) surface with the period of several nanometers. Due to the weak interaction with Ir, graphene and h-BN monolayer do not form real nanomesh with pronounced interacting and non-interacting sites. Therefore, the splitting of the core level PE signals into "pore" and "wire" components [2-4] is negligible in the case of graphene and visible only as a small shoulder for h-BN (Fig.1, a, b, c - top). As soon as Ni is deposited, the component corresponding to the chemisorbed areas of the film starts to grow in the C1s, N 1s and B 1s spectra, showing that the intercalation has begun (Fig.1, second top). The third top

curve (all graphs in Fig.1) shows the spectra after annealing the samples at 400 °C for 30 min. The splitting of the core levels is due to the duality of the adsorbate phase; a part of it is tightly bonded to the intercalated metal, while there is still a lot of film material weakly bonded to the substrate. The bottom line (Fig.1, all graphs) shows that at higher temperatures the sp^2-bonded monolayers become tightly bound to the substrate, indicating that the amount of intercalated Ni approaches a monolayer.

Fig. 2 *Ir 4f PE spectrum evolution upon Ni intercalation under graphene and h-BN film.*

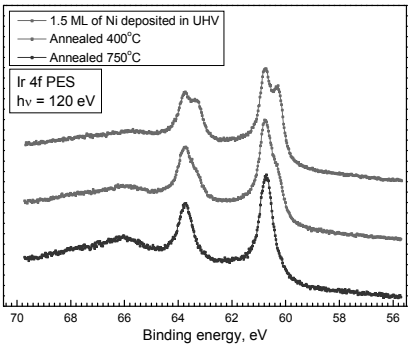

The Ir 4f PE spectrum from the pristine graphene/Ir and h-BN/Ir samples is clearly separated into the surface- and bulk-related components, as a consequence of weak substrate-to-adsorbate interaction. After Ni deposition, the shape of the spectrum does not change considerably, indicating that Ni lies mainly on top, without affecting the interaction between graphene (h-BN) and the substrate (Fig.2, top curve). Upon annealing to 400°C and further to 750°C the surface-related component of the spectrum is gradually vanishing (Fig. 2, middle and bottom curves, respectively). This is assigned to the Ni intercalation under the sp^2-bonded monolayers and its interaction with the Ir substrate. The temperature range for the intercalation is in agreement with the recent studies [5]. The intercalation of Ni under graphene on Ir(111) is reversible – upon annealing to 950°C for 30-60 min all the spectra return to their initial shape. Since Ir 4f spectrum also returns to its initial shape, this process can be explained by a reduction of Ni content at the interface in the course of either desorption or dissolving in the bulk. The reversibility of Ni intercalation could not be checked for h-BN/Ir(111) due to thermal decomposition of h-BN at temperatures above 850°C. The co-adsorption of oxygen did not make any drastic effect on the rate of Ni intercalation or on the amount of intercalated material. For both graphene and h-BN there was no complete vanishing of the "wire" spectral component observed upon the intercalation thus revealing saturation of intercalation process for intercalated material amount close to a monolayer.

References:

[1] A. Grueneis and D. Vyalikh, *Phys. Rev. B* **77**, 193401 (2008).

[2] A.B. Preobrajenski, M.A. Nesterov, M.L. Ng et al., *Chem. Phys. Lett*., **446** (2007) 119-123.

[3] A.B. Preobrajenski, M.L. Ng, A.S. Vinogradov and N. Mårtensson, *Phys. Rev. B* **78,** 073401 (2008).

[4] A.B. Preobrajenski, M.L. Ng, N.A. Vinogradov et al., *NanoLett*., Vol. 9, No. 7, **2009.**

[5] N.R. Gall, E.V. Rut'kov, A.Ya. Tontegode, *Carbon*, **38** (2000) 336-667.

Materials and interfaces in organic spintronics

Y. Zhan, E. Carlegrim, F. Li, and M. Fahlman

Department of Physics, Chemistry and Biology, Linköping University, SE-581 83 Linköping, Sweden

Organic spintronics is a newly established research field with a series of future potential applications, including spin-valves used in reading and writing modes of magnetic information and memory devices, magnetic field effects on organic conductivity and electroluminescence. In such devices, organic semiconductors (OSECs) are used as the spin transport layer, as they consist mainly of atoms with low atomic number *Z*, leading to a low spin–orbit coupling and thus to extremely long spin relaxation times. Though advances in device performances have been made in the past several years, the fundamental knowledge about spin injection at the OSECs/ferromagnet heterojunction in organic spintronic devices is still missing.

More recently, many research groups including us have shown the capability of studying the fundamental questions in organic spintronics using synchrotron radiation facility. In the present contribution we demonstrate that three naval approaches in organic spintronics using D1011 MAX II.

1, efficient spin injection through exchange coupling at organic semiconductor/ferromagnet heterojunctions.

Recently, we have reported the experimental observation of strong interaction and exchange coupling at OSECs/ferromagnet heterojunctions, and proposed a mechanism for spin injection in organic spintronic devices. We have investigated *in-situ*-prepared submonolayer coverage of Alq_3 on Fe and Co surfaces. Alq_3-Co and Alq_3-Fe interfaces are used in most of the reported OSVs. Strong interaction of both Fe and Co and π-conjugated orbitals of Alq_3 at this interface has been discovered by X-ray photoelectron spectroscopy (XPS) and ultraviolet photoelectron spectroscopy (UPS). In addition, near edge X-ray absorption fine structure (NEXAFS) measurements reveal that the contact between Fe and Alq_3 is Ohmic-like. Furthermore, the exchange coupling between Alq_3 molecules and Fe is here observed for the first time using X-ray

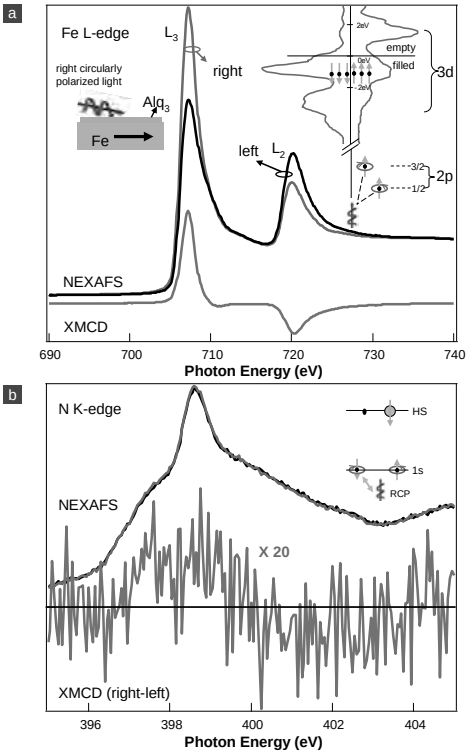

magnetic circular dichroism (XMCD) measurements. We demonstrate that the magnetically coupled Alq_3 interface layer acts as not only a spin acceptor but also as a spin injector.

2, the electronic and magnetic properties of ferromagnetic electrode LSMO

In order to investigate the electronic and magnetic properties of ferromagnetic electrode LSMO，we carried out XAS and XMCD measurements of Mn L-edge. After the solution so-called TL1 (5 H_2O, 1 NH_4OH, 1 H_2O_2), not only WF of LSMO increased from 4.3 eV to 4.7 eV but also the peak corresponding to Mn^{2+} became weakened obviously due to the removal of some contaminants and an increase of oxygen content at the surface. Moreover TL1 treatment did not lead to a disappearance of XMCD signals of Mn L-edge. In order to check the influence of the deposition of pentacene on the oxidized states of Mn at the surface of LSMO, XAS spectra of 5 nm pentacene on LSMO treated by TL1 were also collected using V_{su} = 0 V, 300 V and 500 V. A main peak at 642.1 eV with a shoulder around 640.2 eV appears in the top spectra. An obvious deference can not be found for the three probing depths. The reason may be an island growth of pentacene on LSMO which will be discussed in the following AFM images. The shape and peak position of the top spectra for after the deposition of pentacene do not show an obvious difference from the middle spectra for before the deposition of pentacene. This suggests an absence of covalent bonding and/or significant charge transfer at the interface.
The carbon K-edge NEXAFS spectra were collected with linearly polarized synchrotron radiation at several incident angles relative to substrate plane to characterize the molecular orientation of pentacene on LSMO. Based on an analysis, the molecular long axis of pentacene is found to stand on the LSMO substrate surface with a tilt angle of about 22 ± 2^{o} between the main molecular axis and the substrate surface normal. It is quite similar to the molecular orientation of thermally evaporated pentacene thin film on SAM and inert substrates.

3, Electronic structure of thin film cobalt tetracyanoethylene, Co(TCNE)x

V(TCNE)x, TCNE=tetracyanoethylene, x~2, is a semiconducting organic-based magnet and one of very few organic-based magnets with critical temperature above room temperature (RT). With the aim to understand the key design criteria for achieving RT organic-based magnets we have begun to study the electronic and chemical structure of members of the M(TCNE)x family with significantly lower critical temperatures than V(TCNE)x. Co(TCNE)x, x~2, (TC~44 K, derived from its powder form) were prepared by a method based on physical vapor deposition, resulting in oxygen-free thin films. The results propose Co(TCNE)x to contain local bonding disorder in contrast to V(TCNE)x thin films which can be grown virtually defect free. In addition, the Co L-edge does not show any pronounced fine structure, suggesting the crystal field to be very weak. By using resonant photoemission and x-ray absorption techniques the highest occupied molecular orbital (HOMO) of Co(TCNE)x was determined to mainly be TCNE--derived while the states originating from Co(3d) are localized at higher binding energies. This is in stark contrast to V(TCNE)x where V(3d) is mainly responsible for the HOMO. As the HOMO of Fe(TCNE)x (TC~121 K, derived from its powder form) is TCNE-derived these results show that Co(TCNE)x is more similar to Fe(TCNE)x than to V(TCNE)x in terms of electronic structure.

X-ray Absorption and Magnetic Circular Dichroism on a Prussian blue analogue: first results

I. A. Kowalik[1], H. Prima Garcia[2], J. P. Prieto[2], F. Romero[2], E. Jiménez[3,4], J. Camarero[3,4], M. Makarewicz[2], D. Arvanitis[5], R. Miranda[3,4] and E. Coronado[2]

[1] *Institute of Physics, Polish Academy of Sciences, Al Lotnikow 32/46, PL-02-668 Warszawa, Poland*
[2] *Instituto de Ciencia Molecular, Universidad de Valencia, Polígono de la Coma s/n, 46980 Paterna, Spain*
[3] *Dpto. de Física de la Materia Condensada and Instituto "Nicolás Cabrera", Universidad Autónoma de Madrid, 28049-Madrid, Spain*
[4] *IMDEA-Nanociencia, Campus UAM, 28049-Madrid, Spain*
[5] *Department of Physics and Astronomy, Uppsala University, Box 516, SE-7120 Uppsala, Sweden*

Molecular magnets has become a very active and increasingly exciting area of research lately. They constitute truly nanometric objects and massive numbers of totally identical entities can be easily produced by chemical synthesis techniques. These objects typically show magnetic hysteresis at low temperatures and magnetization reversal by quantum tunneling. They are attractive candidates for qubits, the quanta of information employed in quantum computing [1,2]. Another interesting characteristic of molecular magnets lies in the fact that the quantum coupling between pairs of molecules (needed to obtain the superposition of pure quantum states) can be controlled through the intermolecular interactions by adequately tuning the spatial arrangement of the molecules on a solid substrate.

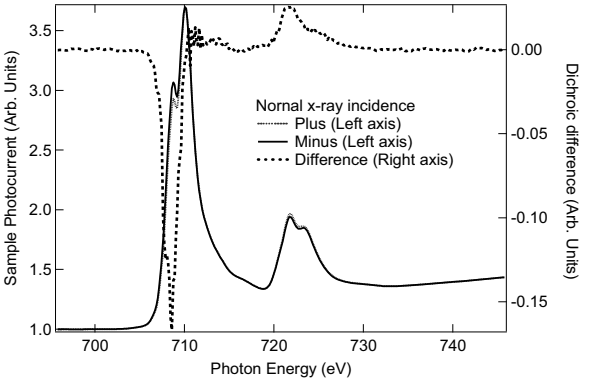

Figure 1. The sample photocurrent is measured for the Prussian blue analogue containing Fe and Cr to obtain the x-ray absorption spectra. Left: Normal x-ray incidence data at 300K under an applied magnetic field of 0.28T along the x-ray propagation direction. Right: The difference of the two spectra is shown in the same units. The degree of circular polarization is close to 0.8. The exit slit had a full width of 100 micron.

Among the different classes of molecular magnets being investigated nowadays, Prussian blue and its derivatives deserve special attention. The pure compound, containing iron and cyanide ions, shows long-range ferromagnetic ordering at 5.6 K [3]. However, Curie temperatures well above 300 K have been reported for several analogues containing also Cr ions [4-6]. The magnetic behavior of these compounds can be explained using a localized orbital approach [7]. They also show a high flexibility for tailoring their magnetic properties, since metal substitutions induce only small lattice constant changes. From the electronic point of view, Prussian blue analogues are characterized by electronic delocalization between the metal sites across the bridging cyanide anion. The

combination of charge transfer effects with the strong magnetic interactions mediated by the cyanide anion gives rise to interesting properties. For instance, reversible magnetization switching mediated by external agents such as irradiation with light [8,9], temperature [10] or pressure [11,12], among others, has been observed; electron transfer plays a key role in all these cases.

X-ray magnetic circular dichroism (XMCD) experiments were carried out at beamline I1011 to study the Prussian blue analogue containing Fe and Cr, $K_{0.4}Fe_4[Cr(CN)_6]_{2.8} \cdot 16H_2O$. XMCD results were presented already earlier in the literature for this type of Prussian blue analogue [12]. Here are presented first results taken at BL I1011 using the octupole end station. We focus on the Fe L-edge data which exhibit a lesser number of multiplet components and are easier for a first, qualitative discussion. In Figure 1 a dichroic pair is shown for normal x-ray incidence at room temperature. The Cr edge data exhibit more complex multiplet features, in agreement to earlier work [12]. The samples we measure are thin films grown by electrodeposition onto conducting substrates (Au-covered mylar). Their Curie temperatures lie around 200 K, as determined by Magneto-optic Kerr effect (MOKE) measurements. For this particular sample, MOKE *ex situ* measurements indicated the occurence of ferromagnetic order with a Curie temperature of 220K. Still, a clear XMCD response is observed around 300K under an applied magnetic field at the Fe L-edges. The Fe L-edge spectra shown in Figure 1 indicate a mixture of at least the "unisomerized" and the "metastable" state for this material refering to the detailed work of E. Coronado et al. [12] on this compound, where the metastable state contained isomerized Fe^{II}-CN fragments [12]. In this earlier work two main contributions are found for the Fe L_3 white line, one around 707 eV the other around 710 eV [12]. Here these two lines are clearly identified (Figure 1), however the component around 710 eV appears to be more intense, in contrast to the earlier literature results [12] even if one would consider a continuum step which would be showing a slow onset, taking intensity away only from around 709 eV.

The XMCD difference (dashed line, right scale, Figure 1) which is obtained from the dichroic pair by reverting the magnetic field, presents similarities with both the "unisomerized" and the "metastable" states. The XMCD difference of those states is reported to be rather close [12]. Here at the L_3 white line, the main contribution to the XMCD dichroic intensity appears to come from the first peak around 707 eV but being asymmetric with a broad cointribution towards the low energy side. In the work of E. Coronado et al. [12] the XMCD difference appears to be asymmetric with a broad contribution towards the high energies. Again like for the x-ray absorption spectra it presents strong similarities but also some differences to the data of E. Coronado et al. [12]. In conclusion, the present data highlight the need for further measurements and analysis in combination to theory as was performed earlier in the literature to disentangle the various contributions to the spectra. [12] Still, it indicates that XMCD experiments at BL I1011 on molecular magnets are feasible under applied magnetic field in combination with the octupole end station. The accuracy of the experimental setup to small dichroic signals appears to be sufficient to operate in the high temperature region, extending the available range of experimental parameters for these compounds.

[1] M. N. Leuenberger and D. Loss, Nature **410,** 789 (2001).
[2] S. Hill et al., Science **302,** 1015 (2003).
[3] A. N. Hoden et al., Phys. Rev. **102**, 1463 (1956).
[4] S. Ferlay et al., Nature **378**, 701 (1995).
[5] S. M. Holmes and G. S. Girolami, J. Am. Chem. Soc. **121**, 5593 (1999).
[6] Ø. Hatlevik et al., Adv. Mater. **11**, 914 (1999).
[7] M. Verdaguer, Polyhedron **20**, 1115 (2001).
[8] A. Goujon et al., Eur. Phys. J. B **14**, 115 (2000).
[9] H. Tokoro et al., J. Appl. Phys. **97**, 508 (2005).
[10] S. Ohkoshi, H. Tokoro and K. Hashimoto, Coord. Chem. Rev. **249**, 1830 (2005).
[11] V. Ksenofontov et al., Phys Rev. B **68**, 024415 (2003).
[12] E. Coronado et al., J. Am. Chem. Soc. **130**, 15519 (2008).

XMCD studies of the Mn^+ implanted silicon crystals

A. Wolska[1], K. Lawniczak-Jablonska[1], D. Arvanitis[2], A. Misiuk[3]

[1]*Institute of Physics PAS, al. Lotników 32/46, 02-668, Warsaw, Poland*
[2]*Physics Department, Uppsala University, Box 530, 75121 Uppsala, Sweden*
[3]*Institute of Electron Technology , Al. Lotnikow 46, 02-668 Warsaw, Poland*

Mn-doped III-V and II-VI compounds forming diluted magnetic semiconductors (DMS) have been extensively investigated in the pursuit of novel ferromagnetic materials, which can be used in spintronic devices. In contrast, relatively little is known about another interesting class of materials, namely the Si-based DMS. Among those, silicon implanted with Mn ions seems to be a promising combination. The implantation of Mn^+ ions into a silicon matrix is a good way of exceeding the solubility limit of Mn in Si. Moreover, it has been already shown that the Mn-implanted Si samples can be ferromagnetic with a Curie temperature (T_C) higher than 400 K [1]. On the other hand, the ferromagnetic properties were also reported for silicon samples implanted with non-magnetic ions, e.g. Si. Therefore, the question arises, what is the origin for the magnetic properties in this kind of materials at the atomic level. The direct way to check whether the magnetism is related with the Mn atom cores is to perform XMCD studies, which allow to detect the local magnetic moments for the specific element what is not possible in the SQUID measurements.

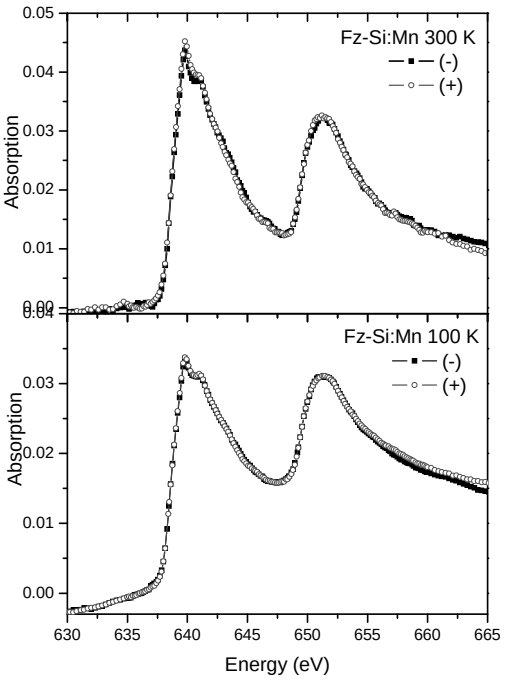

Fig. 1) XANES spectra of Mn $L_{3,2}$ edges measured at RT and LN temperature for opposite polarities of magnetic field.

In order to work out a procedure of producing samples with the desirable properties, two sets of the Si:Mn samples were prepared. The Mn^+ ions with the energy 160 keV and a dose of $1x10^{16}$ cm^{-2} were implanted into Si crystals grown by Floating zone (Fz-Si:Mn) and Czochralski (Cz-Si:Mn) methods. The obtained samples were subsequently annealed at temperatures from 275°C to 1000°C under pressures of 1 bar or 11 kbar. The SQUID measurements showed that samples after low temperature annealing (up to 450°C) exhibited ferromagnetic properties [2].

In this report, as an example, the Fz-Si:Mn and Cz-Si:Mn samples annealed at 275°C under atmospheric pressure are shown. Both samples were pointed out by SQUID as those where Curie temperature exceeded 300 K.

The XMCD measurements were carried out at room (RT ~300 K) and liquid nitrogen (LN ~100 K) temperatures under the magnetic field equal to 0.1 T. The total electron yield detection mode was

used. Two angles of incidence were chosen as follows: grazing (20° to the sample surface) and normal (90° to the surface). Both gave similar results, therefore, only spectra taken in normal incidence are shown in this report.

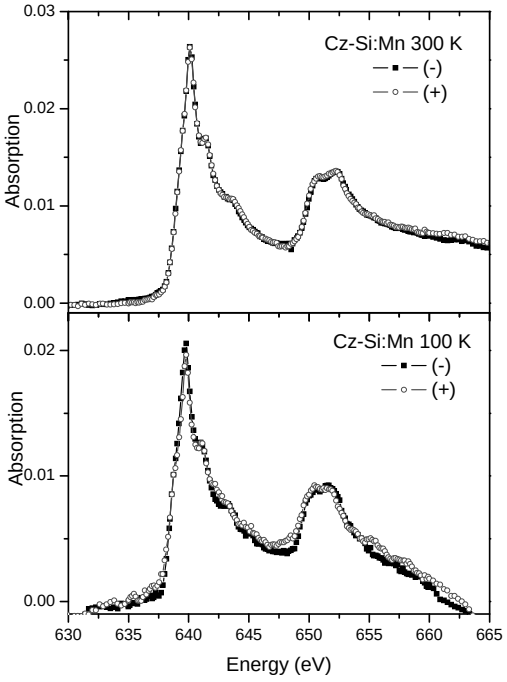

Fig. 2) XANES spectra of Mn $L_{3,2}$ edges measured at RT and LN temperature for opposite polarities of magnetic field.

Fig. 1 presents the spectra of the Fz-Si:Mn sample measured for opposite polarities of magnetic field. There is no difference observed that could be interpreted as a dichroic signal. The effect did not appear even after cooling the sample to 100 K. The same conclusion can be drawn also in case of the Cz-Si:Mn sample (Fig. 2).

The shapes of the absorption spectra differ between the samples what reflects differences in the local neighborhoods. Indeed, the local structure around the Mn atoms found out by EXAFS analysis at the K-edge of Mn, showed the differences between the samples prepared by both methods. In the case of Fz-Si:Mn sample, the Mn atoms gather together forming nanoinclusions consisting of a Mn_xSi_y compound [3]. In the case of Cz-Si:Mn annealed at low temperature, the EXAFS analysis showed only silicon neighbors. [4]

The dichroic signal was not found for any of the considered Si:Mn samples. Therefore, it can be concluded that the Mn atoms are not the main source of ferromagnetism in these samples. It is possible that ferromagnetism is induced mainly by the defects in the matrix caused by implantation. This conclusion is supported by a fact that the high temperature treatment leading to recrystallization seems to eliminate ferromagnetic properties in the investigated samples.

This work was partially supported by national grant of Ministry of Science and High Education N202-052-32/1189. The research leading to these results has received funding from the European Community's Seventh Framework Programme (FP7/2007-2013) under grant agreement n° 226716.

---

[1] M. Bolduc, C. Awo-Affouda, A. Stollenwerk, M.B. Huang, F. G. Ramos, G. Agnello, and V. P. LaBella, Phys. Rev. B **71**, 033302 (2005).
[2] A. Misiuk, J. Bak-Misiuk, B. Surma, W. Osinniy, M. Szot, T. Story, J. Jagielski, J. Alloys Comp. **423**, 201 (2006).
[3] A. Wolska, K. Lawniczak-Jablonska, M.T. Klepka, M.S. Walczak, A. Misiuk, Phys. Rev. B **75** , 113201 (2007).
[4] A. Wolska, K. Lawniczak-Jablonska, S. Kret, P.Dłużewski, A. Szczepańska, M.T. Klepka, M.S. Walczak, Y. Lefrais, M. J. Hÿtch,and A. Misiuk, J. Non-Cryst. Sol. **354,** 4189 (2008).

A spin- and angle-resolving photoelectron spectrometer

M. H. Berntsen[1] P. Palmgren[2], M. Leandersson[2], A. Hahlin[3], J. Åhlund[3], B. Wannberg[3,4], M. Månsson[5], and O. Tjernberg[1]

1*Materials Physics, KTH Royal Institute of Technology, S-16440 Kista, Sweden*
2*MAX-lab, P.O. Box 118, S-22100 Lund, Sweden*
3*VG Scienta AB, P.O. Box 12120, SE-75015 Uppsala, Sweden*
4*BW Particle Optics AB, P.O. Box 55, SE-82222 Alfta, Sweden*
5*Laboratory for Neutron Scattering, ETH Zurich and Paul Scherrer Institut, CH-5232 Villigen PSI, Switzerland and Laboratory for Synchrotron and Neutron Spectroscopy, EPFL, CH-1015 Lausanne, Switzerland*

In a standard angle resolved photoelectron spectroscopy (ARPES) experiment, the energy and emission angle of the photoemitted electron is determined. Depending on sample, geometry, and light polarization, the photoemitted electron may also carry spin information. Determining the electron spin is, however, a complicated task and there are at present no available techniques that permit parallel acquisition in angle and energy together with spin analysis. The common implementation of spin- and angle-resolved photoelectron spectroscopy (SARPES) therefore relies on selecting a particular energy and angle for spin analysis. Since the spin analysis is also a very inefficient process in itself, it becomes a very time-consuming process to map out the spin-resolved energy dispersion. In practice one would therefore first like to perform normal ARPES, in order to rapidly determine orientation and energy dispersion, and then perform spin resolved measurements at selected points in reciprocal space.

To make this possible, a new type of hemispherical electron energy analyzer that permits angle and spin resolved photoelectron spectroscopy has been developed and commissioned at the I3 beamline at MAX-III. The analyzer allows standard angle resolved spectra to be recorded with a two-dimensional detector in parallel with spin detection using a mini-Mott polarimeter. The analyzer is based on the VG Scienta R4000 analyzer (general analyzer layout is shown in Fig. 1). Its lens, slits, apertures, and hemispheres are identical to those of the standard R4000 analyzer. However, the standard 40 mm diameter detector has been replaced by a smaller one (25 mm diameter) in order to make room for the circular aperture for the spin-transfer lens (see Fig 1(c)). The mini-Mott polarimeter is of the Rice University type[1] with a 120° scattering geometry, four individual 25 mm diameter channeltrons, and a thorium target at 25 kV potential. This polarimeter has an expected Sherman function of S_{eff}=0.17[1], a value which is also verified by our experimental test results performed on the Au(111) surface state (presented on next page).

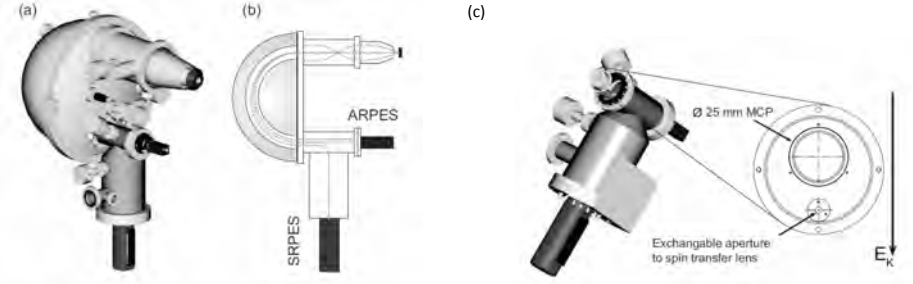

Figure 1. (a) A three-dimensional view of the hemispherical analyzer including the CCD camera for angle-resolved photoelectron spectroscopy (ARPES), the spin-transfer lens and the Mott detector used for spin-resolved photoelectron spectroscopy (SRPES). (b) Schematic overview of electron trajectories through the analyzer. (c) The transfer lens and the Mott detector shown together with a detailed view of the placement of the two-dimensional detector and the transfer lens entrance aperture.

In order to demonstrate the functionality of the system and verify the assumed Sherman function for the polarimeter, the surface state of Au(111) has been studied. As shown in previous photoemission experiments[2,3,4] the parabolic surface state of Au(111) is split into two branches. Theoretical studies[2,5] indicate that the splitting is an electron spin related phenomena and that the surface state is fully spin polarized. The observed splitting is a consequence of the broken inversion symmetry which occurs at the surface where the bulk crystal is terminated. The broken symmetry allows spin-orbit interaction to lift the degeneracy of the surface state producing a splitting of the free-electronlike parabolic dispersion into two branches with energies[5] $E(k) = \hbar^2k^2/2m \pm \alpha\hbar^2k^2/8\pi^2m^2 \pm \alpha k$, where $\hbar$ is the Planck constant, m is the effective electron mass, k is the electron in-plane momentum, and α is the so-called strength parameter. The fact that theory predicts 100% polarization makes the surface state a suitable candidate for initial calibration of the spin detector.

Figure 2(a) shows the raw data spectrum acquired with the MCP detector parallel to the Γ−*M* direction (*ky*-axis) at a polar angle θ =6.8° from normal emission. The two branches reach the Fermi level at k_F=−0.059 Å^{-1} (upper) and k_F=−0.091 Å^{-1} (lower) resulting in Δk_F=0.032 Å^{-1}, in agreement with previously obtained values[2,6]. In Fig. 2(b) we display the second-derivative of the intensity with respect to binding energy of the spectrum in Fig. 2(a). From this figure we see that the two dispersive branches of the free-electronlike surface state are clearly distinguishable. The spin-resolved measurement was performed using the Angular 15 mode with pass energy 20 eV and a spin-transfer lens aperture of 2 mm. The resulting energy-and angle resolution for the spin detector is 100 meV and 1.5°, respectively. Figure 3(a) shows the resulting intensities from the spin up and down channels after subtraction of integrated background and normalization. From these intensities, the polarization shown in Fig. 3(b) is determined using the expected Sherman function S_{eff}=0.17[1].We clearly see that the polarization approaches +(−)1 at lower(higher) binding energies, indicating a fully polarized state. Hence, the results presented here does not only confirm the assumed Sherman function S_{eff}=0.17 and the proper function of the instrument but also provide strong support for the predictions regarding the spin structure of the Au(111) surface state. The spin resolved spectra presented in Fig. 3(c) shows a splitting of approximately 100 meV, a value in agreement with previous measurements[2,6].

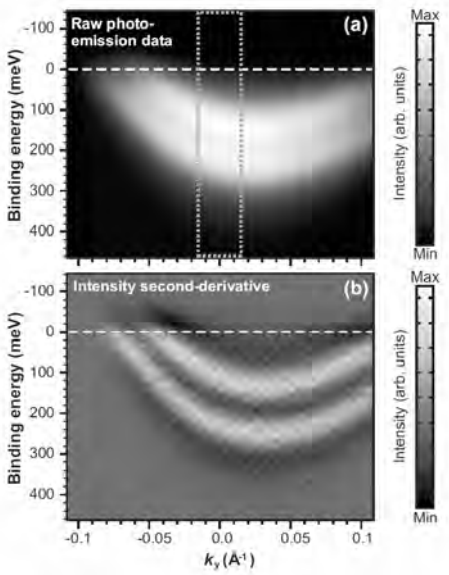

Figure 2. (a) Room-temperature photoemission spectrum (raw data) of Au(111) surface state measured at θ =6.8° from normal emission using linearly polarized light at $h\nu$ =10 eV. Dotted rectangle indicates *k*-interval corresponding to the 1.5° window for which the spin-resolved data is acquired. Intensities are given by the color bar to the right. (b) Second derivative of the intensity with respect to energy for the spectrum showed in (a). Two distinct branches of the free-electronlike parabola are clearly resolved.

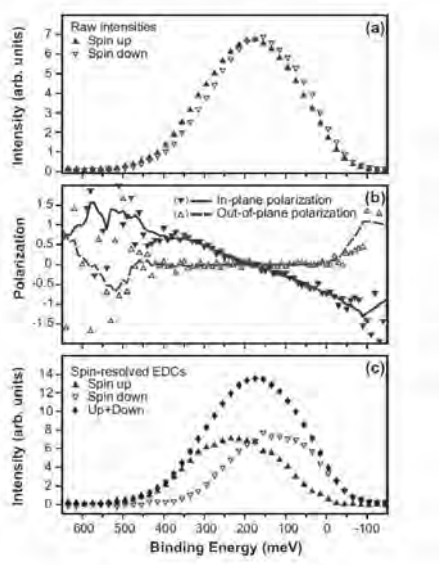

Figure 3. (a) Raw data from spin-up and spin-down channels of the mini-Mott detector. Filled triangles correspond to spin up, open triangles to spin down. (b) Measured polarization as a function of binding energy. Filled triangles correspond to the in-plane polarization calculated from the intensities in (a) assuming a Sherman function S_{eff}=0.17. Open triangles indicate the out-of plane polarization using the same S_{eff}. Solid and dotted lines are running averages. (c) Spin resolved spectra of Au(111) surface state measured at room temperature and 6.8° away from normal emission.

[1] G. Burnett, T. Monroe, and F. Dunning, Rev. Sci. Instrum. **65**, 1893 (1994).

[2] S. LaShell, B. McDougall, and E. Jensen, Phys. Rev. Lett. **77**, 3419 (1996).

[3] F. Reinert, G. Nicolay, S. Schmidt, D. Ehm, and S. Hufner, Phys. Rev. B **63**, 115415 (2001)

[4] G. Nicolay, F. Reinert, S. Hüfner, and P. Blaha, Phys. Rev. B **65**, 033407 (2001)

[5] L. Petersen and P. Hedegard, Surf. Sci. **459**, 49 (2000).

[6] M. Hoesch, M. Muntwiler, V. Petrov, M. Hengsberger, L. Patthey, M. Shi, M. Falub, T. Greber, and J. Osterwalder, Phys. Rev. B **69**, 241401 (2004).

High resolution study of the inner-shell 3p→3d resonance in calcium

D. Iablonskyi[1], S.-M. Huttula[1], S. Fritzsche[1], S. Urpelainen[1], S. Osmekhin[1], M. Huttula[1], H. Aksela[1] and S. Aksela[1]

[1]*Department of Physics, P.O. BOX 3000, 90014 University of Oulu, Finland*

In this report we present results of an experimental investigation of the resonant decay spectrum of calcium in the 3p→3d inner-shell region. The high photon and kinetic energy resolution made possible to resolve much more photoelectron lines than in previous measurement by Ueda *et al* [1].

Measurements were performed at the FINEST branchline of I3 beamline of MAX-III storage ring. The electron spectra were recorded using a modified Scienta SES-100 electron spectrometer [2]. The Ca vapour beam was generated by application of induction heating oven at the temperature of about 600 °C.

The cross section of the decay was scanned over the Ca $3p^6 4s^2 \rightarrow 3p^5 4s^2 3d$ range between 31 and 32 eV using 50 eV pass energy with 1 meV steps (see Fig. 1). As you can see from Fig. 1, the cross section was measured for two different central binding energy with detection energy range of 5 eV, it means that detector can collect electrons that were ejected atoms by decay with different final states. In addition, spectra were measured at two angles which correspond to horizontal and vertical polarizations of light allowing angular resolved experiment. The calibration of the electron analyzer was carried out with the helium gas using standard methods.

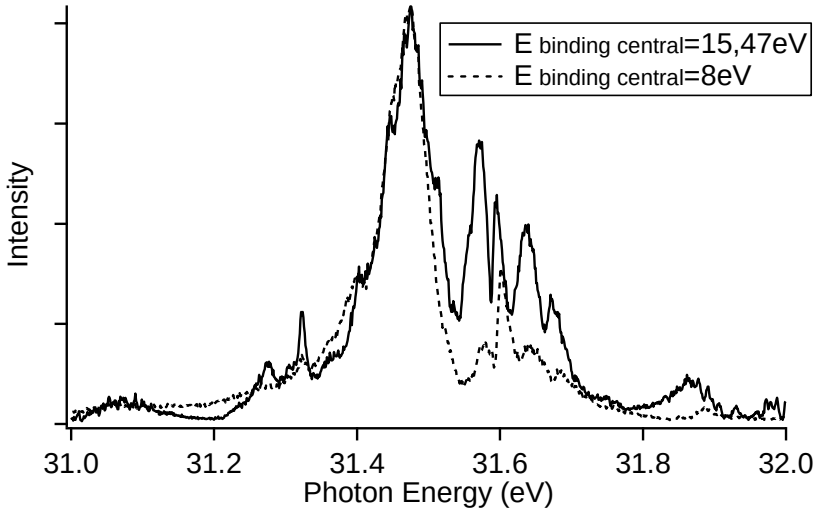

Figure 1: Experimental cross section of the 3p→3d resonance region for the 4s,3d,4p satelites (solid line) and 5s, 4d, 5p 4f, 6s, 5d, 6p, 5f, 5g (dashed line) using the vertical polarization of light.

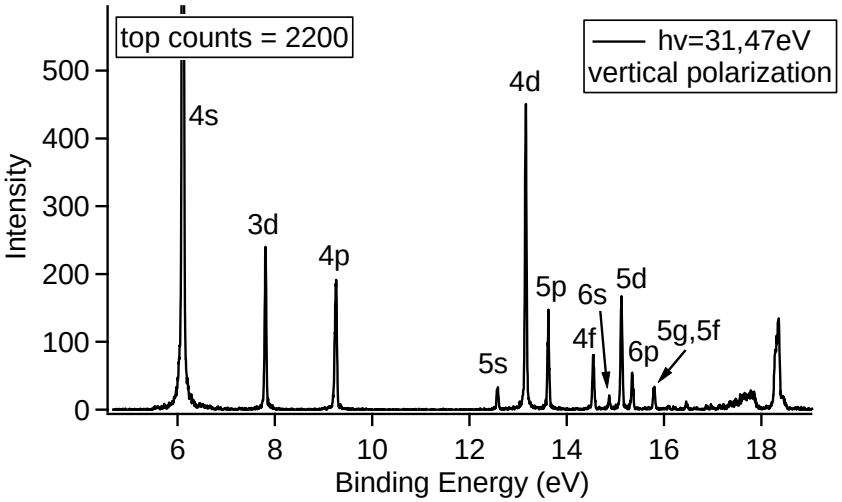

Figure 2: Spectrum of electrons ejected from Ca by decay after exitation with photon energy 31.473 eV that correspond to the $3p^6 4s^2\ ^1S_0 \rightarrow 3p^5 4s^2 3d\ ^1P_1$ resonance. Spectrum obtained for vertical polarization of light.

Fig. 2 shows photoelectron spectrum taken at the biggest peak on the Fig. 1 that correspond to the $3p^6 4s^2\ ^1S_0 \rightarrow 3p^5 4s^2 3d\ ^1P_1$ resonance excitation at 31.473 eV photon energy. The electron resolution and pass energy were 5 meV and 10 eV, respectively. From this spectrum we can easy see that final Ca^+ states are very widely distributed including levels with higher principal numbers. The changes in branching ratios have been monitored by measuring the decay spectrum at several photon energies over the resonant range. In general, any resonance from Fig. 1 leads to resonant enhancement of large groups of photoelectron lines (like in Fig. 2), the distribution of which characterizes the intermediate state. And in some particular cases resonance appear only in few specific satellite lines that giving clues to the identity of the intermediate state. The further data handling and interpretation is a work in process.

[1] Ueda K. et al, *J. Phys. B: At. Mol. Opt. Phys.* 30 (1997) 2093
[2] Huttula M. et al, *Electron Spectrosc. Relat. Phenom* 156-158 (2007) 270

Measurements of VUV transitions of iron group elements for astrophysical applications using I3 at MaxIII

Hampus Nilsson, Henrik Hartman, Sven Huldt, Richard Blackwell-Whitehead, Thomas Lennartsson
Lund Observatory, Department of Astronomy and Theretical Physics, Lund University, Box 43, SE-221 00 Lund, Sweden

Stacey Sörensen
Synchrotron Radiation Physics, Department of Physics, Lund University, Box 118, SE-221 00 Lund, Sweden

Abstract Iron lines are of great importance in analyses of stars and nebulae, not only for abundance studies, but also for diagnostics of the plasma conditions and derivation of physical properties such as temperature, electron density and radiation field.

We develop a project where the goal is to measure transition rates for specific FeII transitions at vacuum UV wavelengths, 100-130 nm. These transitions are important for many astrophysical applications, e.g. in objects where line fluorescence is prominent as well as stars observed in the ultraviolet FUSE and HST/STIS region. In this wavelength region many other iron-group element ions have important transitions, which also will be measured in later projects. This work is performed as absorption measurements using an iron hollow-cathode discharge, illuminated by synchrotron radiation at the MAX-lab facility.

We describe the experimental setup at the I3 beam line at Max III, and the early performance.

Introduction In spectroscopic studies of astrophysical objects iron is an important tracer, and its relatively high cosmic abundance and complex atomic structure result in many spectral lines. Iron is often used as a probe of metal abundance in distant objects, such as quasars and Active Galactic Nuclei (AGNs). Many stars and nebulae have representative temperatures around 10 000 K, and for this temperature the favored ionization stage is singly-ionized iron, Fe^+, whose spectrum is denoted FeII. The lines of FeII are thus of great importance in analyses of stars and nebulae.

Fluorescence lines can be used to probe active plasma regions. Since these lines are optically thin, they offer more possibilities for plasma diagnostics than most other lines, which in general are low-excitation lines and therefore optically thick. To model the radiative pumping process, a number of atomic parameters need to be known, among them the transition rates (*A*-values) or oscillator strengths (*f*-values).

The present project aims at measuring the intrinsic line strengths for these transitions by letting the synchrotron light pass through a plasma hosting the ions. When proved successful this technique will enable us to measure a wealth of lines important for several astrophysical applications.

Experimental setup The synchrotron light from MAX-III is used as a background source to study the absorption from gas-phase iron atoms. The plasma responsible for the absorption is produced in a hollow-cathode (HC) discharge, which is run with neon as carrier gas. The electronic transitions in iron produce narrow absorption lines in the continuous light from the synchrotron. Comparisons of different absorption lines from a common lower level give the relative internal strengths for the lines, and the values are put on an absolute scale by using known reference lines. A similar technique has been used by Wiese et al. [1] to measure a few ground-state FeII lines. The 6.6m high spectral resolution (R>100,000) normal incidence monochromator (NIM) on the I3 beamline is used to produce monochromatic light, and with its performance in terms of resolution and photon intensity ideal for the purpose. The energy of the monochromator is scanned over the transition to obtain the absorption line. Since the intrinsic width of the absorption line, determined by the thermal motion of the atoms in the plasma, is of the same order magnitude we need the full resolution to obtain reliable and accurate results.

The HC producing the plasma is also a source of strong line emission in the same spectral region, which is far stronger than the synchrotron light studied. This emission light is removed by chopping the synchrotron light with a frequency of up to 1000 Hz. The signal from the photomultiplier tube (PMT) and the chopping frequency are fed into a Lock-In amplifier to extract the absorption signal in the synchrotron light.

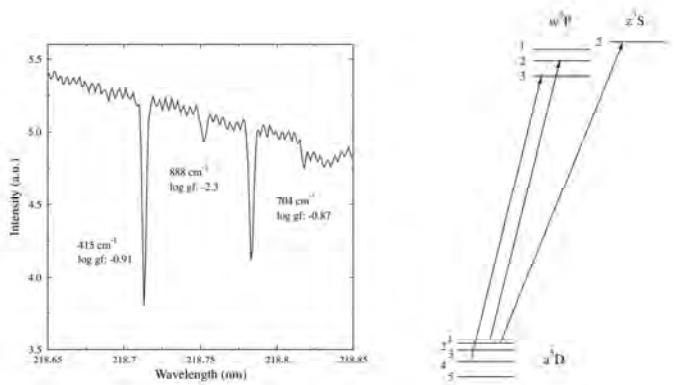

Figure 1: (left) Absorption lines from neutral iron (Fe I). The excitation energy and oscillator strength (log gf) is indicated. (right) Partial energy level diagram showing the observed transitions.

Early results The HC discharge produces primarily neutral atoms and singly-ionized ions. To test the setup and the technique, we have sampled FeI lines around 210 nm, which includes the strong resonance lines but also weaker lines and lines from higher excitation energies.
In Figure 1 a sample region holding the Fe I lines is shown, along with a partial energy level diagram where the observed transitions are marked. Initial measurements were able to sample absorption features from both Fe I and Fe II, and from the former from a number of different excitation energies and intrinsic strengths, as is displayed in Figure 1.
Planned improvements are a setup to monitor possible variations in the photon flux, and the reproducibility and stability of the ion production and excitation conditions in the plasma.

Acknowledgment: We are very grateful to the MAX-lab staff for providing excellent support and superior experiment environment.

References

[1] Wiese, L.M., Bonvallet, G.A., and Lawler, J.E. 2002 ApJ **569**, 1032-1036
[2] '*VUV oscillator strengths for iron lines of astrophysical importance*', Hartman, H.; Nilsson, H.; Huldt, S.; Johansson, S.; Sörensen, S.; Johnson, M. S.; von Hessberg, P., (2008) Journal of Physics: Conference Series, **130**, 012010

Valence photoionization of LiCl monomer and dimer

J. Niskanen[1,2], S. Urpelainen[1,3], S. Aksela[1], H. Aksela[1], O. Vahtras[2], V. Carravetta[4], H. Ågren[2]

[1] *Department of Physics, P.O. Box 3000, 90014 University of Oulu, Finland*
[2] *Theoretical Chemistry, Royal Institute of Technology, Stockholm,Sweden*
[3] *MAX-lab, Lund University PO Box 118, 22657 Lund, Sweden*
[4] *CNR - Institute of Chemical Physical Processes, via Moruzzi 1, 56124 Pisa, Italy*

Introduction

Alkali halide vapor beams produced by in-vacuum heating are known to consist not only of single molecule monomers but also of a considarable amount of dimer and other polymers [1]. As the ratio of amounts of different molecular species produced in evaporation depends strongly on the temperature of the heated sample [2], simple alkali halide molecules are an ideal subject for studying the effects of molecular cluster formation on molecular electronic properties. Noble gases have served as a bench-mark in spectroscopy of atoms. Beside their value as a fundamental research topic they can be used for calibration purposes because of the extensive high-precision experiments performed [3,4] on them. To calibrate the cross section of the studied sample as a function of photon energy, the knowledge of noble gas ionization cross sections can be utilized.

In this work [5] we have studied the behavior of valence photoionization cross sections of LiCl monomer and dimer. By introducing Kr to the interaction region for calibration, the relative partial photoionization cross sections for molecular valence orbitals could be measured as a function of photon energy between 15 and 35 eV. A theoretical method based on projection of the excited states on a set of square-integrable basis functions [6,7] was used to compute the ionization partial cross sections energy in independent particle independent channel approximation.

The Experiment and Results

The experiments were carried out on the FINEST gas phase branch line on the I3 beamline of the 700 MeV MAX-III electron storage ring. The instrumentation and characteristics of the beamline have been described in detail elsewhere [8-11].

For recording the electron spectra a Scienta SES-100 hemispherical electron energy analyzer equipped with a position sensitive resistive anode detector and mounted on an multipurpose experimental chamber [12,13] was employed. The experiments were performed with the electron analyzer at the magic 54.7° electron emission angle with respect to the electric field vector of the vertically linearly polarized radiation from the EPU corresponding to angle independent measurements.

The valence orbitals of LiCl monomer are of σ and π symmetry leading to singly ionized states $^2\Sigma$ and doubly degenerate $^2\Pi$. As seen from Figure 1 (a), a noteable energy shift (approximately 6.5 eV) between calculated and experimetal cross section is seen for both $^2\Sigma$ and $^2\Pi$ states. Otherwise the trends of cross section observed in the experiment are well reproduced by the calculations. If an energy shift of 6.5 eV is applied, the calculated cross section is within the error limits in most of the data points.

The valence shell of rhombic LiCl dimer consists of six orbitals a_g, b_{2g}, b_{3u}, b_{2u}, b_{1u} and b_{3g} giving rise to ionized states of $^2B_{3g}$, $^2B_{1u}$, $^2B_{2u}$, $^2B_{3u}$, $^2B_{2g}$ and ^2A_g symmetries of the molecular point group D_{2h}. All six final states cannot be distinguished in the valence photoelectron spectrum of pure LiCl dimer [2]. In this work we focused only on the valence partial cross

section because it could be extracted more reliably from the data than its individual components. Figure 1 (b) shows the measured and calculated valence ionization cross section for LiCl dimer. The errorbars are quite large because the error of monomer $^2\Pi$ line is directly affecting the calibration of LiCl dimer cross section. As is immediately seen, the shape resonance is shifted in calculation as it was also in case of monomer.

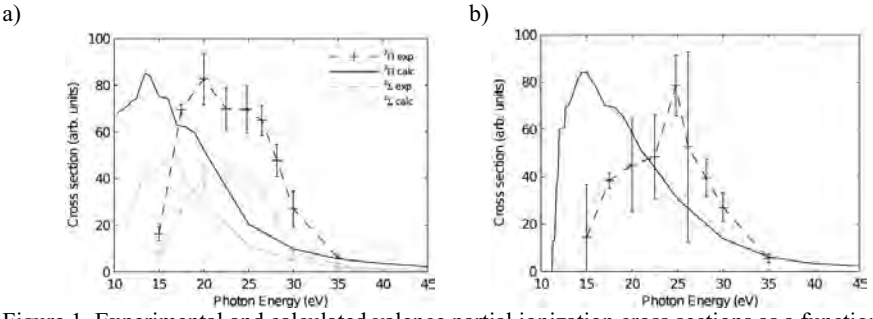

Figure 1. Experimental and calculated valence partial ionization cross sections as a function of photon energy. Cross section for LiCl monomer is shown on the left hand side (a) and for dimer on the right hand side (b).

Conclusions

We presented the first measurement of the partial valence photoionization cross sections as a function of photon energy between 15 and 35 eV for LiCl monomer and dimer. The use of Kr as calibration enabled us to record the behaviour of partial photoionization cross section of the valence shell doublet states. The trend of the cross section for monomer lines was reproduced well by the calculations, but a shift of 6.5 eV was seen between the calculated and experimental maxima of the ionization cross sections. The maximum for $^2\Pi$ state was seen to have a shoulder towards higher kinetic whereas the $^2\Sigma$ state does not have this feature. The valence total ionization cross sections of LiCl dimer was recorded as a function of photon energy and calculated using the same methods. A shift of 6.5 eV was also observed in the maximum of the cross section.

References

[1] R. C. Miller and P. Kusch, J. Chem. Phys **25**, 860 (1955).
[2] J. Berkowitz, C. H. Batson, and G. L. Goodman, J. Chem. Phys. **71** (6), 2624 (1979).
[3] U. Becker and D. A. Shirley, VUV and Soft X-Ray Photoionization, Plenum, New York (1996) and references therein.
[4] J. A. R. Samson and W. C. Stolte, J. Electron Spectrosc. Relat. Phenom. **123**, 265 (2002).
[5] J. Niskanen, S. Urpelainen, S. Aksela, H. Aksela, O. Vahtras, V. Carravetta and H. Ågren, Phys. Rev. A (in press) (2010).
[6] I. Cacelli, V. Carravetta, A. Rizzo, and R. Moccia, Phys. Rep. **205**, 283 (1991) and references therein.
[7] V. Carravetta, H. Ågren, O. Vahtras, and H. J. Aa. Jensen, J. Chem. Phys **113,** 7790 (2000).
[8] Instrumentation for spectroscopy and experimental studies of some atoms, molecules and clusters, Phd Thesis Samuli Urpelainen, University of Oulu (2009).
[9] T. Balasubramanian *et al.*, Proceedings of the 10th International Conference on Synchrotron Radiation Instrumentation, submitted (2009).
[10] M. Patanen, S. Urpelainen, M. Huttula, R. Sankari, V. Kisand, E. Nõmmiste, E. Kukk, H. Aksela, and S. Aksela, Phys. Rev. A **80**, 013414, (2009).
[11]S. Urpelainen *et al.*, Proceedings of the 10th International Conference on Synhchrotron Radiation Instrumentation, submitted (2009).
[12] M. Huttula, M. Harkoma, E. Nõmmiste and S. Aksela, Nucl. Instrum. Methods Phys. Res. A **467**, 1514 (2001).
[13] M. Huttula, S. Heinäasmäki, H. Aksela, E. Kukk, and S. Aksela, J. Electron Spectrosc. Relat. Phenom. **156-158**, 270 (2007).

Fragmentation of toxic organotin compounds

S. Osmekhin[1], J. Niskanen[1], S. Urpelainen[1], E. Kukk[2], M. Huttula[1] and H. Aksela[1]

[1]*Department of Physics, University of Oulu, PO Box 3000, FIN-90014, Finland*
[2]*Department of Physics and Astronomy, University of Turku, FIN-20014, Finland*

Organotin compounds (OTC) have been in a wide commercial and industrial use during the last 50 years. The biocide function of the OTC is the main property for applications. Environmentally harmful effect of the OTC was discovered in the end of the 1970s, but nevertheless they are in a worldwide usage [1]. In an organotin compound, one or more organic substituent like phenyl and butyl is attached to tin atom with a covalent bond. Organotins like triphenyltin chloride which are trisubstituted R_3SnX (R = for example phenyl, X = halogen) have usually higher toxicity than mono- or disubstituted organotin compounds. The anion X has minor influence on the toxicity of trisubstituted organotins, if the X itself is not toxic. Tributyltin chloride (TBTCl), dibutyltin dichloride (DBTCl) and triphenyltin chloride (TPTCl) are the most common compounds which are used in antifouling paints, agrochemicals and other applications. Pollution of the environment by OTC is high priority problem nowadays. As an cumulative process high concentration of OTC is found in the aqueous-systems which has sever effects on fish, mussels, molluscs and other living substances.

In present work we study how radiation by photons influences the dissociation of TBTCl, DBTCl and TPTCl molecules to smaller, less toxic fragments. The measurements were carried out at the undulator beamline I3 branch FINEST at the 700 MeV MAX-III synchrotron storage. Synchrotron radiation is monochromatized by three different gratings to cover the photon energy region of 5-50 eV. A LiF filter was used in the energy range below 11 eV in order to remove the higher order energies from the grating. Ionization cross sections of the studied samples are very low in the photon energies above 35 eV, and present results are taken in the photon energy region of 5-35 eV. The experimental setup consist of a vacuum chamber equipped with a home-made Wiley-Mclaren type ion time-of-flight (TOF) detector with a 400 mm long drift tube with 77 mm Hamamatsu MCP detector. Calibration of the m/q range of the TOF spectrometer was done with Xe noble gas.

The liquid sample TBT chloride (96%, Aldrich) was kept in a vacuum reservoir at room temperature and delivered to interaction region in vapour phase by gas line [2]. For the vapour production of the DBT dichloride (96%, Aldrich) and TPT (95%, Aldrich) chloride a resistively heated oven was used. The temperature of the crucible in the oven was 25^{o}C and 85^{o}C for DBTCl and TPTCl, respectively. The pressure of the residuals in the experimental chamber was in the range of 10^{-7} mbar during the measurements. As an example of the results, the very strongly photon energy dependent fragmentation scheme of TPTCl is shown in Figure 1 at the photon energy region of 5-35eV. The further evaluation of the data and comparison between the different compounds is in progress[3].

[1] M. Hoch, Applied Geochemistry 16 (2001) 719-743
[2] S. Osmekhin et al, Inter. J. Mass. Spectrom. 273 (2008) 48-52
[3] S. Osmekhin et al, manuscript

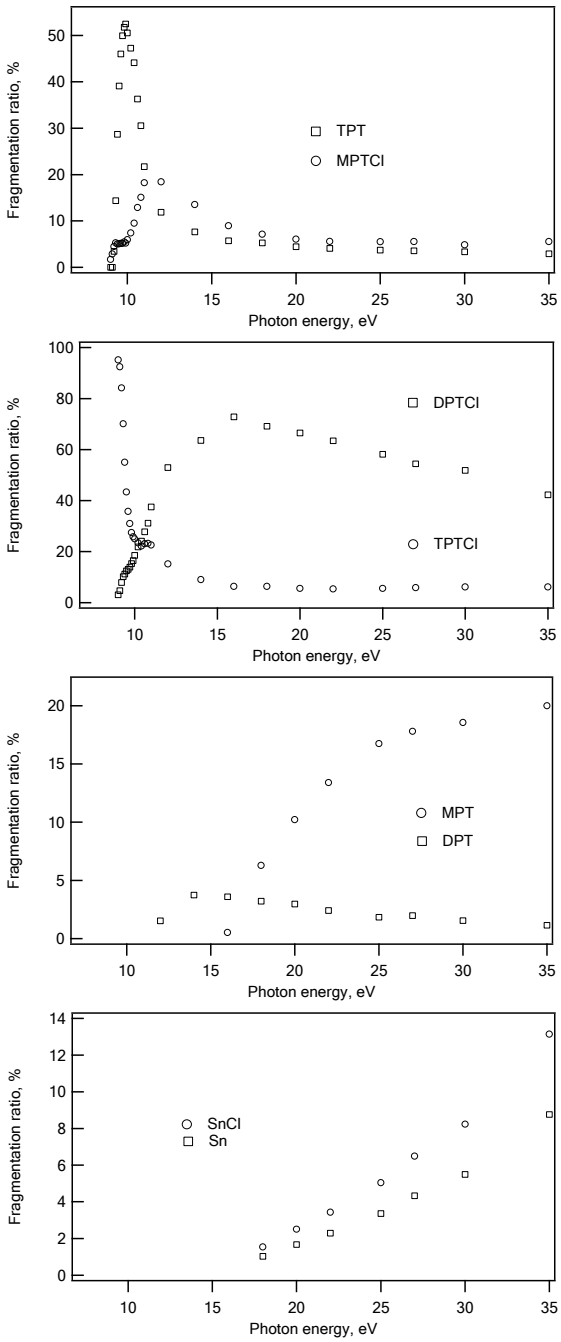

Figure 1. Fragmentation patterns of TPTCl at the photon energy region of 5-35eV.

K 3pσ/π→K4sσ resonant Auger decay in KF

M. Patanen[1], S. Urpelainen[2], M. Huttula[1], R. Sankari[2], V. Kisand[3], E. Nõmmiste[3], E. Kukk[4], H. Aksela[1], S. Aksela[1]
[1]*Department of Physical Sciences, P.O. Box 3000, FIN-90014 University of Oulu, Finland*
[2]*Max-lab, Lund University, Box 118, SE-22100 Lund, Sweden*
[3]*Institute of Physics, University of Tartu, Riia 142, 51014 Tartu, Estonia*
[4]*Department of Physics, University of Turku, Turku FIN-20014, Finland*

Tunable and monochromatized high-intensity synchrotron radiation facilities have offered enormous possibilities to study specific excited states of molecules, and even to select, not only the electronic, but also the vibronic state. Resonant Auger (RA) spectroscopy is an excellent tool for studying nuclear dynamics and electronic decay of excited molecular states. In this study we have used RA spectroscopy to study the K 3pσ/π→K4sσ excitation in KF.

The K 3pσ/π→K4sσ excitation decays via participator resonant Auger transition. The resonance states were mapped in the photon energy range of 18.2-19.4 eV recording total ion yield spectrum, and the RA spectra were measured at the highest resonances [1]. Spectra were measured at the FINEST branch on the I3 beamline on MAX III. The emitted Auger electrons were recorded using the Scienta SES-100 electron analyzer [2] and a resistively heated oven [3] was used to evaporate KF from the solid crystalline form. The temperature inside the stainless steel crucible used during the measurements was around 900 K.

The experimental spectrum is interpreted using non-relativistic *ab initio* molecular calculations corrected with perturbation theory treatment to account for spin-orbit interaction. Molecular calculations for the electronic states of KF were performed using the quantum chemistry software package GAMESS. Valence quadruple zeta basis sets with polarization functions were used for F and K atoms. Configuration interaction (CI) method with ORMAS (Occupation Restricted Multiple Active Space determinant CI) determinants was used to calculate the non-relativistic potential energy curves (PEC) for ground state, excited states, and final state of KF molecule.

It was found that the selected resonance states (a-d in Fig.1 C) are vibronic states within the same electronic state, and therefore only one PEC was needed for RAS simulation, and no interference between the excited electronic states is present. The simulations were made taking the life-time vibrational interference (LVI) [4] into account, but as the vibrational energy levels within an electronic state are separated by approximately 50 meV in energy, also the LVI effects were found to be small. In the simulations the direct ionization channel was not taken into account, although it is open and may lead to some discrepancies between the simulations and the experimental spectra show in Fig.1. The binding energies in the simulated spectrum differ by 0.9 eV from the experimental values. This is because of the restricted CI space used in the energy calculations, and the small errors in the forms of the PECs, because the simulation is quite sensitive to the form of the PECs and their relative places with respect to the internuclear distance axis. In the simulations it was supposed that the decay of the excited state leads to only one final state, which seems to be a reasonable approximation. The structure of the RA spectra reflects the different nodal structures of the wavefunctions at different vibrational levels in the excited electronic state.

It can be concluded that the time scales of the nuclear relaxation and the electronic decay are of the same order of magnitude, so the electronic decay has high probability to take place before the vibrational wavepacket reaches its second turning point. This study demonstrates the potential of the FINEST branchline when high resolution is needed, e.g. in studies of the vibrational fine structure in molecular spectra.

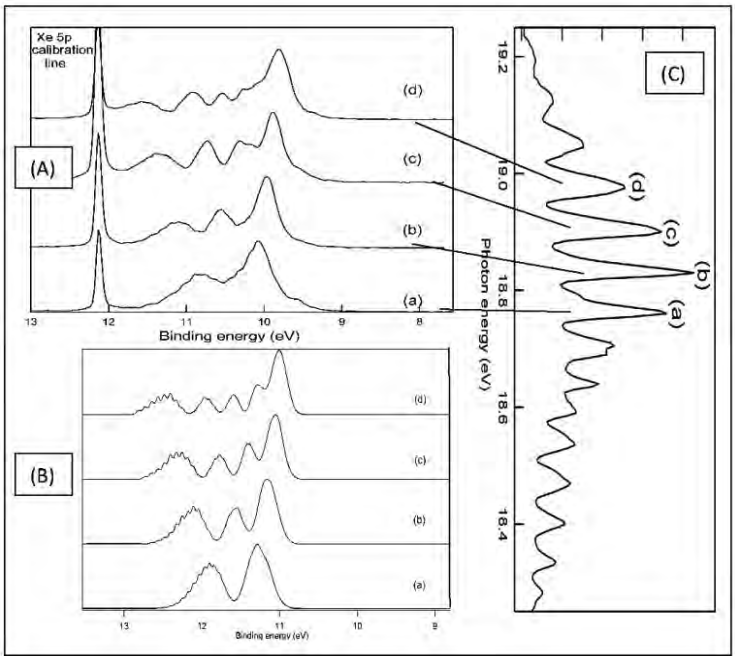

Fig. 1 (A) RA spectra taken at photon energies of (a) 18.756eV, (b) 18.824eV (c) 18.892eV, (d) 18.973eV. Xe 5p photoline was used for calibration. (B) Simulated photoelectron spectra calculated at experimental absorption maxima. (C) Total ion yield spectrum of the KF molecule. Labels (a), (b), (c), and (d) refer to the photon energies where the autoionization spectra were measured.

[1] M.Patanen, S.Urpelainen, M.Huttula, R.Sankari, V.Kisand, E.Nõmmiste, E.Kukk, H.Aksela, S.Aksela *Phys. Rev. A* **80**, 013414 (2009)
[2] M. Huttula, M. Harkoma, E. Nõmmiste, and S. Aksela, *Nucl. Instrum. Methods Phys. Res. A* **467**, 1514-8 (2001)
[3] M. Huttula, S. Heinäsmäki, H. Aksela, E. Kukk, and S.Aksela, *J. Electron Spectrosc. Relat. Phenom*. **156–8**, 270–3 (2007)
[4] A. Cesar, and H. Ågren, *Phys. Rev. A* **45**, 2833-41 (1992)

Polarization study at I3 FINEST branch

R. Sankari[1], T. Balasubramanian[1], B.N. Jensen[1],
E. Wallén[1], S. Urpelainen[1,2], R. Nyholm[1]

[1]MAX-lab, Lund University P.O. Box 118, S-221 00 Lund, Sweden

[2]Department of Physical Sciences, University of Oulu, Finland

The beamline is based on an elliptically polarizing undulator (EPU) and operates in the VUV region, 5-50 eV. The first harmonic of the undulator radiation is used to cover that energy range. Two of the four sub girders of the undulator move in a coupled way and this provides phase difference of 90 or -90 degree between the horizontal and vertical electric fields of the undulator radiation. It is known that the beamline optics can modify the polarization properties of the radiation - these modification are strong at low photon energies and at high grazing incidence angles i.e. at typical conditions of any normal incidence monochromator beamline. Therefore the polarization affecting properties (reflectivity to both s and p-polarized light and their phase differences upon reflection) were studied both by simulations and with a quick test with improvised equipment.

The I3 beamline was modeled using the RAY ray tracing software [2] developed at BESSY. The Stokes parameters of the artificial source can be defined and one can follow the development of the Stokes parameters when the beam passes each optical element of the beamline. In these simulations, the grating was replaced by a spherical mirror of the same radius – the polarization properties are in practice the same to the grating [1]. The incidence angle to the grating in the non dispersive plane is as low as 0.75° which means that there will be a phase shift of about 180° in the grating (mirror) i.e. the right hand circularly polarized light (RCP) would be left hand circularly polarized light (LCP) at the experiment.

The pre-optics of the beamline are all polished Si blocks whereas the three installed gratings are coated with MgF2/Al (2400 l/mm), SiC (4300 l/mm), or Pt (4300 l/mm) coated. The post-focusing optics at the branch which is dedicated to solid state spin and angle resolved photoemission are also Si coated whereas the toroidal refocusing mirror for the gas phase (FINEST) branch is coated with gold to ensure high reflectivity also at about 50 eV. For the simulations, only an energy of 20 eV was chosen and the Pt grating was used - same setting was used for the experiment.

The results of the simulations, which are presented in Table 1, show that the degree of circular polarization, P_C, at 20 eV is only about 30 % (estimated as |S3|/S0) even if the undulator produces completely circularly polarized light. The last gold coated mirror, which has a grazing incidence angle of 20^o, modifies very strongly the polarization - at the main branch, where the refocusing mirrors are mounted on lower grazing angle, the degree of circular polarization should be more than 90 %.

For quick test, a He-lamp polarizer [3] was borrowed from the Electron spectroscopy research group in Oulu [4]. The polarizer is based on triple reflection, like

Table 1: Evolution of the Stokes parameters in I3. Subscript GP refers to gas phase branch and SS to solid state branch.

Element	S1/S0	S2/S0	S3/S0
Source	0.000	0.000	1.000
M1 (spherical)	0.045	0.539	0.841
M2 (planar)	0.035	0.413	0.910
M3 (plane elliptical)	0.025	0.277	0.961
SG (spherical)	0.025	-0.277	-0.961
M4 (planar)	0.032	-0.378	-0.925
$M5_{GP}$ (toroidal)	0.571	-0.763	-0.303
$M5_{SS}$ (Plane elliptical)	0.014	-0.133	-0.991
$M6_{SS}$ (Plane elliptical)	0.029	-0.343	-0.939

the typical polarization analyzers [5]. For complete analysis of the polarization, two of this kind of reflectors must be used - the first one as the polarizer and the second one as the analyzer. The degree of linear (P_l) and circular polarization (P_c)can, however, be extracted from the measurement even if only one element is used: P_l directly from experiment and P_c from equation $P_l^2+P_c^2 = 1$, which holds if the degree of polarization for the incident radiation is 100%. The horizontal and vertical linear polarizations were studied first as those measurements could be used to estimate the performance of the polarizer. The results show sinusoidal oscillation of transmitted intensity as a function of polarizer angle. The period of this oscillation is about 180° as expected and the difference between the maxima corresponding to horizontal and vertical polarization is about 90°. The background level is, however, far from constant and that hinders the detailed analysis of circular case. The changes in the background are not very surprising as the reflecting surfaces were visibly detoriated, also the polarizer geometry is not ideal for this experiment.

The undulator was nevertheless tuned to circular mode (both left and right hand circular polarization) and transmitted intensity was measured. The fitting procedure gives P_c ∼70% for both left and right hand circular light - that is higher than expected from simulations but the uncertainties with this quick experiment are large. This pre-study encouraged to continue with improving the design of the polarizer - further experiments are planned for the future.

References

[1] L. Nahon and C. Alcaraz, Applied Optics **43**, 1024 (2004).

[2] F. Schäfers, in Modern Developments in X-Ray and Neutron Optics, eds. A. Erko, M. Idir, Th. Krist, A.G. Michette, Springer Berlin/Heidelberg, (2008) and in Technischer Bericht, BESSY TB **202**, 1-37 (1996).

[3] http://www.specs.de

[4] http://physics.oulu.fi/elsp.php

[5] A. Gaupp and M. Mast, Rev. Sci. Instrum. **60**, 2213 (1988).

Valence and inner-valence photoionization and autoionization of Sb_4 clusters at 4*d*→n*l* resonances

S. Urpelainen[1,2], J. Niskanen[1], A. Kettunen[1], D. Iablonskyi[1], S. Osmekhin[1], M. Huttula[1], and H. Aksela[1]

[1]*Department of Physics, University of Oulu, P.O. Box 3000, FI-90014 Oulu, Finland*

[2]*MAX-lab, Lund University, P.O. Box 118, SE-22100 Lund, Sweden*

Antimony (Sb) together with its various compounds is a commonly used material in various industrial processes, especially in the production of semiconductor devices. For cluster studies Sb is an ideal target as it evaporates readily as tiny clusters at low temperatures [1], predominantly as Sb4 clusters. To be able to understand the electronic structure and dynamics of largers clusters, the properties of their building blocks from elemental atoms to clusters made of a few to some tens of atoms need to be well known. This is especially true, when studying the evolution of band formation as a function of cluster size, as an addition of only a few atoms to the cluster can drastically change its behavior.

This study is a continuation to our earlier work on the photoionization of Sb_4 clusters [1,2], where the fragmentation of the clusters following 4*d* core ionization and outer- and inner-valence ionization was studied using the photoelectron-ion and photoelectron-ion-ion coincidence techniques. In the earlier work the wide bands appearing in the valence photoelectron spectra at binding energies between 10.5 eV and 20 eV were assigned as a combination of correlated $5t_2^{-1}$ states and shake-up satellites accompanying the $(5a_1 6t_2 2e)^{-1}$ ionization based on molecular calculations, bonding properties of the orbitals and the fragmentation products observed in coincidence with the photoelectrons. In this work the absorption spectrum of Sb4 clusters just below the 4d ionization threshold using the constant ionic state (CIS) method is presented together with electron spectra recorded at the photon energies corresponding to 4*d*→5*p* type resonances.

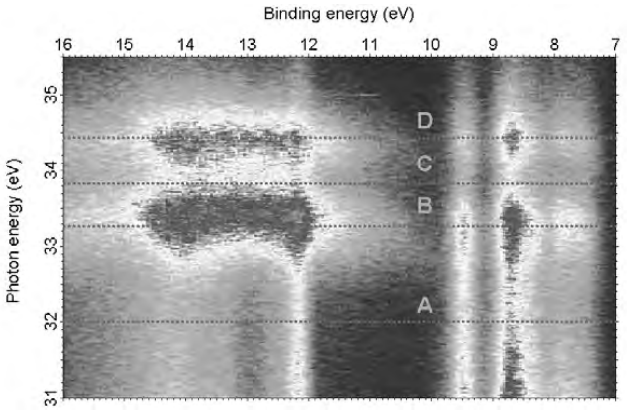

Fig. 1 2D CIS map of the valence and inner-valence photoelectron lines at the 4d 5p type resonances. Label A-D correspond to spectra recorded at photon energies of 32 eV, 33.27 eV, 33.83eV, and 34.43 eV, respectively.

The experiments were performed at the FINEST beamline branch of the I3 beamline of the MAX-III storage ring. For recording the CIS and electron spectra a modified Scienta SES-100 hemispherical electron

analyzer was used. The Sb vapor was produced using an inductively heated oven. The CIS was recorded using electron analyzer pass energy of 100 eV and entrance slit of 0.8 mm (curved). The monochromator slits were open as the inherent energy broadening of the resonant transitions is close to 1 eV, where as open monochromator slits were approximated to correspond to a photon energy bandwidth in the order of a few tens of meVs. The recorded CIS spectrum is presented in Fig. 1. The photoelectron spectra of valence and inner-valence region were recorded off-resonance (A, 32 eV), at resonances (B, and D, 33.27 eV and 34.43 eV, respectively) and between the resonances (C, 33.83 eV) and are presented in Fig. 2. These spectra were recorded with analyzer pass energy of 20 eV, entrance slit of 0.8 mm (curved) and monochromator slits open. From Fig. 2 it can be seen that the spectrum recorded away from the resonances (A), is similar to the one recorded at I411 at the photon energy of 60 eV, except for the weaker intensity due to the fact that in this work the photon energy is below the giant resonance. The other features measured at the resonant photon energies, however, show a strong enhancement of intensity especially in the $5t_2$ and satellite region.

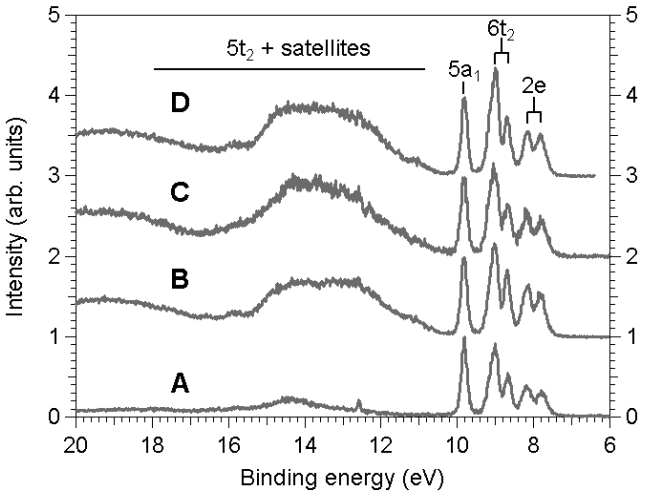

Fig. 2 Transmission corrected photoelectron spectra of the valence and inner-valence region at the photon energies 32 eV, 33.27 eV, 33.83 eV, and 34.43 eV (labels A-D, respectively). The spectra are normalized to tha $5a_1$ line.

As the resonant excitation lifts an electron from the 4*d* orbital to a higher lying LUMO or a Rydberg orbital a spectator Auger decay process becomes available leading to same ionic states as direct photoionization accompanied by a shake-up transition to the LUMO or Rydberg orbitals. The strong enhancement of lines in this region following the excitation strongly supports the earlier conclusion that the broad bands consist mostly of shake-up and correlated $5t_2^{-1}$ photolines.

[1] S. Urpelainen, A. Caló, L. Partanen, M. Huttula, S. Aksela, H. Aksela, S. Granroth, and E. Kukk, Phys. Rev. A **79**, 023201 (2009).

[2] S. Urpelainen, A. Caló, L. Partanen, M. Huttula, J. Niskanen, E. Kukk, S. Aksela, and H. Aksela, Phys. Rev. A **80**, 043201 (2009).

Atomic and electronic structures of the molten 1x1 phase on the Si(111):Sn surface

P.E.J. Eriksson[1], J. R. Osiecki[1], Kazuyuki Sakamoto[2], and R.I.G. Uhrberg[1]
[1]*Department of Physics, Chemistry and Biology, Linköping University, S-581 83 Linköping, Sweden*
[2]*Graduate School of Advanced Integration Science, Chiba University, Chiba 263-8522, Japan*

The Si(111) surface with about one monolayer of Sn shows a reversible transition from a $2\sqrt{3}$x$2\sqrt{3}$ phase below 463 K to a 1x1 phase corresponding to a molten Sn layer, above that temperature. It is found that the surface band structure just below the transition temperature is quite similar to that at 100 K. The surface band structure undergoes a dramatic change at the transition. A strong surface state, showing a 1x1 periodicity, can be detected above the transition temperature. This state resembles parts of two surface states that has begun a transformation and lost much of their $2\sqrt{3}$x$2\sqrt{3}$ periodicities already before the transition temperature is reached. Calculated surface band structures obtained from 1x1 models with 1 ML of Sn are compared with ARPES and STM results. It is found that the strong surface state present above the transition temperature shows a dispersion similar to that of a calculated surface band originating from the Sn-Si interface with the Sn atoms in T_1 sites [1].

All theoretical results were obtained by density functional theory calculations in the generalized gradient approximation using the full-potential (linearized) augmented plane-wave+local orbitals method within the WIEN2k code [2]. The atomic slabs used for the structure relaxation of the $2\sqrt{3}$x$2\sqrt{3}$ models, which had an inversion center in the middle and Sn on both surfaces, were constructed of 12 Si layers. To avoid artificial splitting of the surface bands, the surface band structure calculations were performed on a H-terminated slab with six Si layers. For the 1x1 model cases, a H-terminated slab with 12 Si layers was used.

ARPES data at elevated temperatures were obtained using the VG ARUPS 10 analyzer mounted on a goniometer and the total energy- and angular resolutions were 50 meV and ±2°, respectively. The Si(111) sample (*n*-doped, Sb, 3 Ωcm) was cleaned by direct resistive heating, reaching a temperature of 1530 K, at which the sample was held for a few seconds before it was allowed to cool down slowly. Sn was deposited from an evaporation source at a rate of approximately1/3 ML/min. A sharp $2\sqrt{3}$x$2\sqrt{3}$ LEED pattern was observed at RT after annealing at 900 K for two minutes. For the measurements at elevated temperatures, a custom built heating device was used. The device alternated, with a kHz frequency, between 1) passing the heating current through the sample while blocking the signal from the electron analyzer to the data taking computer; and 2) grounding the sample while acquiring data. To prevent accumulation of heat in the sample holder it was cooled with liquid nitrogen. The quality of the $2\sqrt{3}$x$2\sqrt{3}$ surface prepared for the photoemission study was determined by inspection of the LEED pattern. To ensure that measurements were performed exclusively on the $2\sqrt{3}$x$2\sqrt{3}$ phase, the sample was prepared in such a way that neither the $\sqrt{3}$ phase was observed at temperatures above 463 K, nor were any reconstructions with larger unit cells visible in LEED at RT.

[1] P.E.J. Eriksson, J. R. Osiecki, K. Sakamoto, and R.I.G. Uhrberg, submitted to Phys. Rev. B
[2] P. Blaha, K. Schwarz, G. K. H. Madsen, D. Kvasnicka and J. Luitz, *WIEN2k*, An Augmented Plane Wave + Local Orbitals Program for Calculating Crystal Properties (Karlheinz Schwarz, Tech. Universität Wien, Austria), 2001. ISBN 3-9501031-1-2

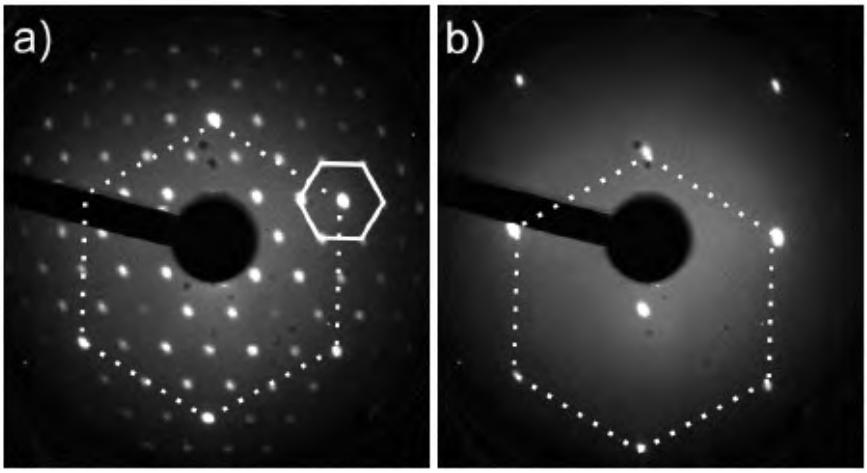

FIG. 1: Si(111):Sn LEED patterns obtained with a 95 eV electron beam energy. The 1x1 and 2√3x2√3 unit cells are shown by dotted and solid lines, respectively. a) 2√3x2√3 surface at a temperature slightly below 463 K. b) 1x1 surface at a temperature slightly above 463 K

FIG. 2: Maps showing the dispersions of features in angle resolved photoemission spectra. a) Surface state band structure at a temperature slightly below the phase transition. Surface state dispersions from the 2√3x2√3 surface at 100 K are drawn with dotted curves. b) Surface band structure at a temperature slightly above the phase transition. Solid and dotted curves show calculated surface band dispersions from a 1x1 surface with 1 ML Sn at T_1 and H_3 sites, respectively. The shaded region indicates the projection of the bulk bands. The strong experimental surface band of the molten phase is reproduced by the calculated bands when Sn atoms are in on-top sites (T_1). This indicates that the molten phase shows partly a solid-like character slightly above the transition temperature.

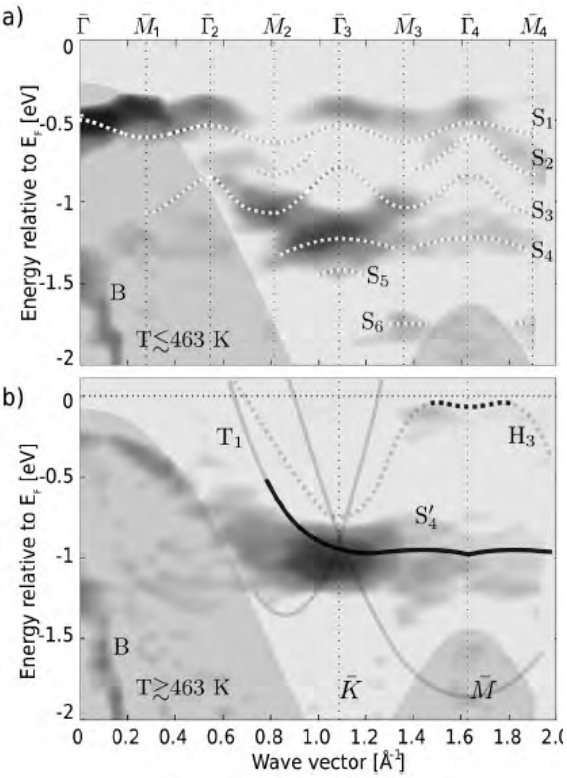

Atomic and electronic structures of the ordered 2√3x2√3 phase on the Si(111):Sn surface

P.E.J. Eriksson[1], J. R. Osiecki[1], Kazuyuki Sakamoto[2], and R.I.G. Uhrberg[1]
[1]*Department of Physics, Chemistry and Biology, Linköping University, S-581 83 Linköping, Sweden*
[2]*Graduate School of Advanced Integration Science, Chiba University, Chiba 263-8522, Japan*

The Si(111) surface with an average coverage of slightly more than one monolayer of Sn, exhibits a 2√3x2√3 reconstruction below 463 K. In the literature, atomic structure models with 13 or 14 Sn atoms in the unit cell have been proposed based on scanning tunneling microscopy (STM) results, even though only four Sn atoms could be resolved in the unit cell. High resolution angle resolved photoelectron spectroscopy (ARPES) and STM are used in this study [1] to test theoretically derived results from an atomic structure model comprised of 14 Sn atoms, ten in an under layer and four in a top layer [2]. Low temperature ARPES reveals six occupied surface states. The calculated surface band structure only reproduces some of these surface states. However, simulated STM images show that certain properties of the four atoms that are visible in STM are reproduced by the model. The electronic structure of the Sn atoms in the under layer of the model does not correspond to any features seen in the ARPES results. New STM images are presented which indicate the presence of a different under layer consisting of eight Sn atoms, that is not compatible with the model. These results indicate that a revised model is called for.

All photoemission measurements were performed at the MAX-lab synchrotron radiation facility in Lund, Sweden. Linearly polarized light from the MAX-III storage ring was used for the ARPES measurements at beam line I4. For the low temperature ARPES study a fixed Specs Phoibos 100 analyzer was used, resulting in total energy- and angular resolutions of about 50 meV and ±0.1°, respectively.

All theoretical results were obtained by density functional theory calculations in the generalized gradient approximation using the full-potential (linearized) augmented plane-wave+local orbitals method within the WIEN2k code [3]. The atomic slabs used for the structure relaxation of the 2√3x2√3 models, which had an inversion center in the middle and Sn on both surfaces, were constructed of 12 Si layers. A vacuum of 15 Å separated the slabs in the [111] direction. Usually 5 **k**-points in the irreducible Brillouin zone and an energy cut-off of 72 eV were used. To avoid artificial splitting of the surface bands, the surface band structure calculations were performed on a H-terminated slab with six Si layers using an energy cut-off of 99 eV.

The agreement of the calculated surface band based on the model in Ref. 2 is just partial. The strong band, S_4, is not reproduced by the theory. This and the STM results call for a new model of the 2√3x2√3 surface. Based on STM data we conclude that the 2√3x2√3 reconstruction is composed of 12 Sn atoms. A detailed account of the study is presented in Ref. 1.

[1] P.E.J. Eriksson, J. R. Osiecki, K. Sakamoto, and R.I.G. Uhrberg, submitted to Phys. Rev. B
[2] Törnevik, *et al*., Phys. Rev. B 44, 13144 (1991)
[3] P. Blaha, K. Schwarz, G. K. H. Madsen, D. Kvasnicka and J. Luitz, *WIEN2k*, An Augmented Plane Wave + Local Orbitals Program for Calculating Crystal Properties (Karlheinz Schwarz, Tech. Universität Wien, Austria), 2001. ISBN 3-9501031-1-2

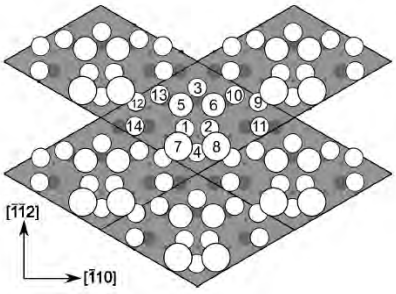

FIG. 1: Atomic configuration after relaxation of the 2√3x2√3 model based on Ref. 2. Open circles, gray circles and dots indicate the positions of Sn atoms, first layer Si atoms and second layer Si atoms, respectively.

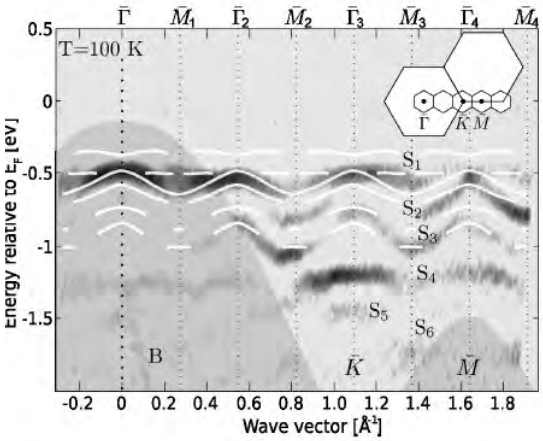

FIG. 2 Band structure of the 2√3 Si(111):Sn surface. The map indicates features in ARPES data ($h\nu$ =27 eV) obtained at 100 K. Six surface states and one bulk feature are labeled S_1-S_6 and B, respectively. Calculated bands that show surface character are indicated by white curves. The shaded regions indicate the projection of the bulk bands. Vertical dotted lines indicate symmetry points in the 2√3x2√3 SBZs.

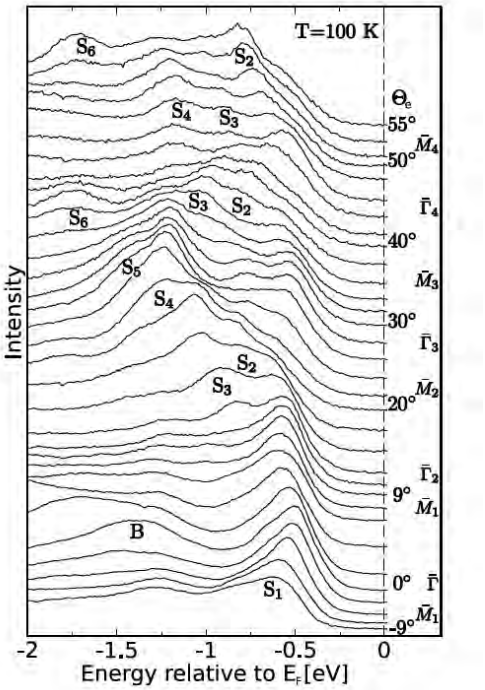

FIG. 3: Subset of the ARPES spectra ($h\nu$=27 eV, obtained at 100 K) used for creating the map in Fig. 2. Six surface states, S_1-S_6, and a bulk feature, B, are labeled. The emission angles, Θ*e*, and the high symmetry points of the 2√3x2√3 SBZs are indicated.

Surface core-level shifts on clean Ge(001) studied with photoelectron spectroscopy and DFT calculations

P.E.J. Eriksson and R.I.G. Uhrberg
Department of Physics, Chemistry and Biology, Linköping University, S-581 83 Linköping, Sweden

The atomic structure of Ge(001)c(4x2) is very similar to that of Si(001)c(4x2), see Fig. 1. Also the PES data on the Ge 3d core-level show similarities to Si 2p data. However, the Ge 3d core-level spectra show significantly less features than Si 2p spectra. This appears to be an intrinsic property of Ge 3d, since pushing the experimental resolution of state of the art equipment only results in sharper spectra to some limited degree. As a consequence of the lack of distinct features it is difficult to decompose the Ge 3d core-level spectra from Ge(001)c(4x2) based on experimental data alone.

Ge 3d spectra were acquired at BL I4 at MAX-III using a Specs Phoibos 100 electron analyzer. The experimental energy resolution was about 70 meV and the acceptance angle was about ± 2°. The clean Ge(001) sample (n-type Sb, 0.01-0.1 Ωcm) was prepared by several cycles of Ar^+ sputtering (500 eV) and heating to about 960 K. The quality of the surface reconstruction was assessed by inspection of the low-energy electron diffraction pattern. The sample temperature was 100 K during the measurements.

All calculated results were obtained by density functional theory calculations in the generalized gradient approximation using the full-potential (linearized) augmented plane-wave+local orbitals method within the WIEN2k code [1]. The repeated slabs consisted of eleven (001)-layers.

The dotted curves in Fig. 2 show a Ge 3d core level spectrum recorded using a photon energy of 85 eV (~50 eV electron kinetic energy) and 60° emission angle, resulting in enhanced surface sensitivity. Despite this, the only apparent feature is a peak on the low binding energy side. Similar to Si 2p this feature has in earlier studies been attributed to the dimer up-atom. The bulging shape on the right side of the main peak suggests that there are components hidden on the low binding energy side. Compared to published spectra, the up-atom component in Fig. 2 is much better resolved. That, in combination with the calculated surface core-level shifts (SCLS) facilitates a more detailed decomposition of the Ge 3d spectrum. The calculated Ge 3d SCLS are all negative, of which some are very close to zero. This indicates a qualitative agreement between the general appearance of the spectrum and the calculations. The fitting result using the theoretically derived shifts of Σ_u and Σ_d, i.e. the shifts corresponding to atoms 1u and 1d, is shown in Fig. 2 a). Four shifted components, Σ_u, Σ_d, Σ' and L' in addition to the bulk component, B, were necessary. An improved fit was obtained when the constraints were relaxed, see Fig. 2 b). The three last lines of table I give the atomic contribution to the various components based on the calculated surface core-level shifts. It is possible to identify contributions to the Ge 3d spectrum from atoms as deep as the fourth layer, which goes far beyond the any published results.

[1] P. Blaha, K. Schwarz, G. K. H. Madsen, D. Kvasnicka and J. Luitz, *WIEN2k*, An Augmented Plane Wave + Local Orbitals Program for Calculating Crystal Properties (Karlheinz Schwarz, Tech. Universität Wien, Austria), 2001. ISBN 3-9501031-1-2.
[2] P.E.J. Eriksson and R.I.G. Uhrberg, Phys. Rev. B 81, 125443 (2010).

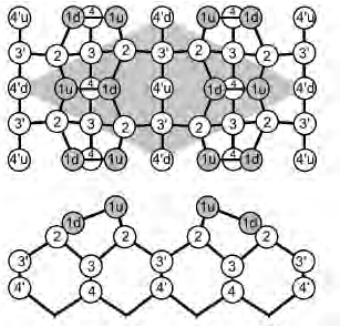

FIG. 1: Top and side views of the c(4x2) reconstruction.

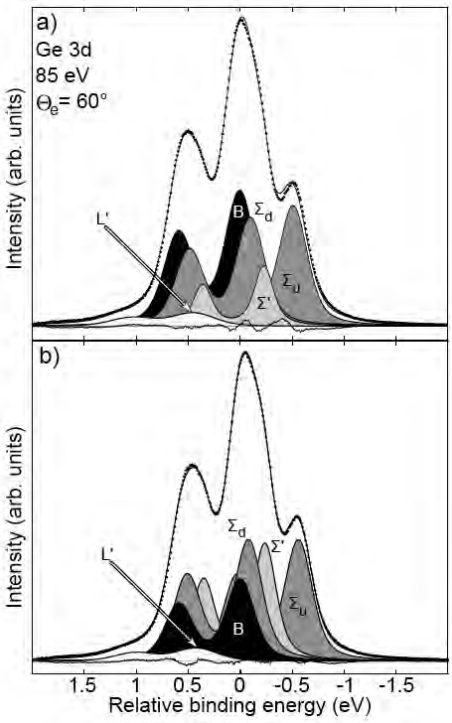

FIG. 2: Ge 3d core-level spectrum (dots) obtained at 100 K. A bulk (black) and four shifted surface components (gray) constructed of spin-orbit split Voigt functions are used to generate the fit (solid curve). In a), the up and down atom components Σ_u and Σ_d were positioned relative to the bulk component using the calculated values. In b), these constraints were relaxed resulting in a better fit. Fitting parameters are given in Table I.

TABLE I: Fitting parameters of the Ge 3d components in Fig. 2. The parameters are binding energy relative to the bulk (E), Gaussian width (GW) and percentage (%) of the total intensity. The Lorentzian width was 0.15 eV and the spin-orbit split was 0.59 eV. The branching ratios were in the range 0.649-0.707. The last three rows summarize the identification of the atomic origins of the various components. The number that appears as a subscript on the atom label is the calculated core-level shift.

		L'	B	Σ_d	Σ'	Σ_u
Fig. 2 a)	E (eV)	0.45	0	−0.10	−0.23	−0.51
	GW (eV)	0.41	0.26	0.24	0.12	0.24
	%	4.4	30.7	25.2	10.2	27.8
Fig. 2 b)	E (eV)	0.42	0	−0.08	−0.24	−0.56
	GW (eV)	0.39	0.23	0.22	0.17	0.22
	%	4.1	18.7	27.2	22.9	27.1
			$\text{Bulk}_{0.00}$	$1d_{-0.10}$	$2_{-0.23}$	$1u_{-0.51}$
			$3'_{-0.00}$	$4'd_{-0.06}$	$3_{-0.21}$	
			$4'u_{-0.01}$	$(4_{-0.15})$		

Self-organization of trimesic-acid on Cu(100): molecular orientation in the nanogrid as investigated by ARUPS

M. Hirsimäki [1], R. Pärna[2], H. Ali-Löytty[1], P.Jussila[1], E. Nõmmiste[2], and M. Valden[1]

[1]*Surface Science Laboratory, Tampere University of Technology (TUT), P.O. Box 692, FIN-33101 Tampere, Finland (www.tut.fi/surfsci)*
[2]*Institute of Physics, University of Tartu, Riia 142, 51014 Tartu, Estonia*

Self-organization of organic molecules into metallosupramolecular nanotemplates on metals and metal oxides is a promising avenue for bottom-up fabrication of functional surfaces. In particular, molecular species with functional groups for both intermolecular hydrogen bonding and covalent surface bonding readily facilitate self-assembly of highly organized and robust nanostructures.[1] Potential applications range from enhanced surface corrosion resistance to covalent and specific immobilization of proteins in specific conformations and orientations for biosensor and implant technologies.

In the present study, the adsorption of trimesic acid (TMA) has been investigated on metallic (Fig. 1, on the right). While Cu is not widely used in bioapplications, its propensity to adopt a nanopatterned surface structure upon adsorption of molecules such as oxygen and nitrogen is highly useful for future studies in this field.[2]

The Cu(100) surface was cleaned by cycles of Ar-ion bombardment at 500 K followed by annealing to 650 K. TMA was adsorbed on the surface at 300 K with physical vapor deposition in ultra high vacuum. Adlayers were investigated by Angle Resolved Ultraviolet Photoelectron Spectroscopy (ARUPS) at beamline I4 at MAX III. Scanning tunneling microscopy (STM) experiments were performed at TUT.

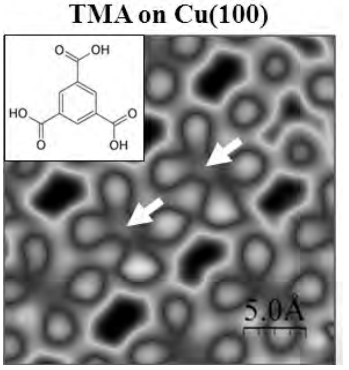

Figure 1: STM image of the cloverleaf-like arrangement of TMA on metallic Cu(100), where Cu adatoms (marked by white arrows) are coordinated by four carboxylate ligands each. The molecular structure of TMA is shown in the inset.

[1] L. Prins, D. Reinhoudt, P. Timmermann, *Noncovalent synthesis using hydrogen bonding*, Angewandte Chemie International Edition 40 (2001) 2382-2426.

[2] K. Lahtonen, *Oxygen adsorption-induced nanostructures on copper and silver-copper alloy surfaces investigated by scanning tunneling microscopy and electron spectroscopy*, Ph.D. Thesis, Department of Physics, Tampere University of Technology, Tampere, Finland, 2008.

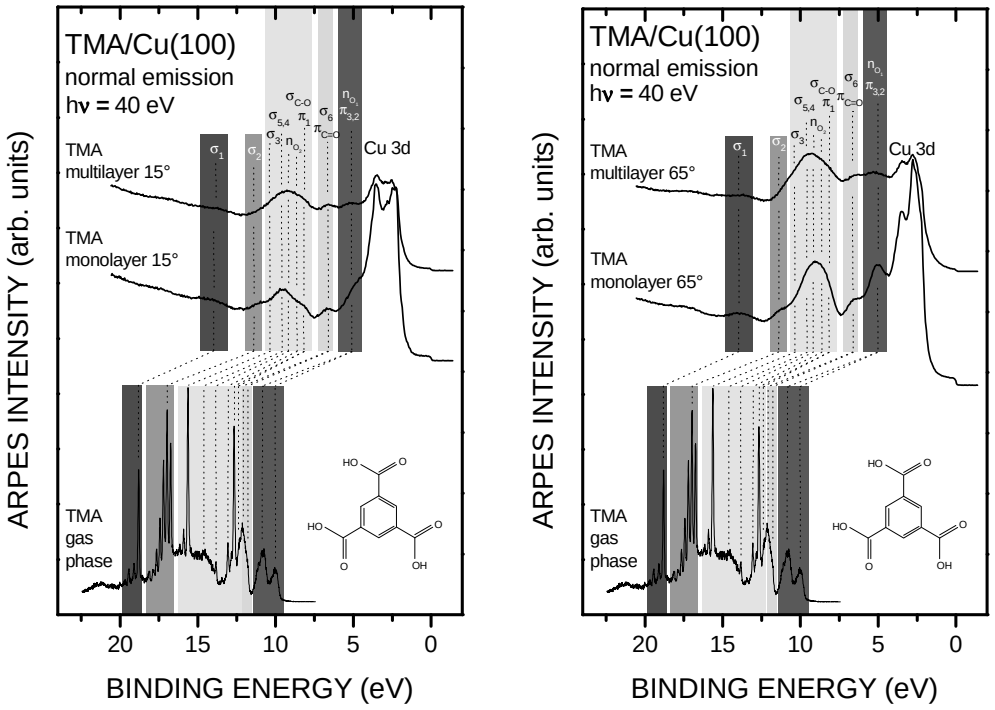

Figure 2. Selected ARUPS data from TMA/Cu(100) and UPS spectra from gas-phase TMA. Molecular orbitals showing π and σ orbitals as well as oxygen lone pairs (n_{O2}) were identified from the gas-phase data.

For applications it is essential to know the orientation of molecules in the nanotemplate. ARUPS measurements and polarization dependent selection rules in based on the symmetry of the molecule yield such information. Figure 2 shows selected spectra from TMA/Cu(100) measured at normal incidence by using plane polarized light. Photon energy was 40 eV. The angle of incidence was increased from 15° to 65° to increase the degree of p-polarization in the incident light. Gas-phase UPS spectra were measured at I411 using photon energy of 40 eV. The binding energy axis was calibrated to Ar signal. Gas-phase data facilitated the identification of transitions from molecular orbitals shown in the Figure 2.

The presence of $\sigma_{2,3,4,5}$ and $\pi_{1,2}$ signals from the aromatic ring indicates that the benzene-like molecular backbone has not become dissociated. As the degree of p-polarization is increased, the relative intensity of σ transitions from the aromatic ring ($\sigma_{2,3,4,5}$) increases. However, the observed polarization dependence is rather weak and the π signals are not completely extinguished. This indicates that the adsorption geometry of TMA is not completely planar as one might expect from the STM results. Instead, the molecular plane appears to be at an angle with respect to the surface plane. This finding is supported by our tentative analysis of XAS data measured at D1011, suggesting that the angle of aromatic ring relative to the surface plane is approximately 40°. A more pronounced polarization dependence of σ orbitals of the aromatic ring is seen from TMA multilayer. This signifies a shift towards more planar adsorption geometry.

Atomic arrangement and Si 2*p* spectral line shape of Yb/Si(100(2×6)

M. Kuzmin,[1] M.P.J. Punkkinen,[1] P. Laukkanen,[1,2] R.E. Perälä,[1] J.J.K. Lång,[1] V. Tuominen,[1] M. Ahola-Tuomi,[1] T. Balasubramanian,[3] and I. J. Väyrynen[1]

[1] *Department of Physics, University of Turku, FIN-20014 Turku, Finland*

[2] *Optoelectronics Research Centre, Tampere University of Technology, FIN-33101 Tampere, Finland*

[3] *MAX-lab, Lund University, SE-221 00 Lund, Sweden*

A typical structural unit on clean and metal-adsorbed Si(100) surfaces is known to be buckled silicon dimers. In core-level photoelectron spectroscopy, such dimers usually give rise to two Si 2*p* surface core-level shifts (SCLS's) of which energy splitting can exceed 0.5 eV, leading to specific line shapes and additional broadening of Si 2*p* spectra [1,2]. Recently, based on density functional theory (DFT) calculations, we proposed a plausible structural model of Yb/Si(100)(2×6) reconstruction in which the silicon dimers are unbuckled (Fig. 1) [3]. Although the model is well consistent with scanning tunneling microscopy images [4], it calls for a further support by core-level spectroscopy. One can tentatively expect that the Si substrate with the symmetrical dimers in Fig. 1 leads to a relatively narrow Si 2*p* line shape.

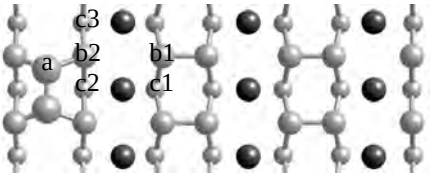

Fig. 1. A top view of the atomic model of Yb/Si(100)(2×6). The black balls denote Yb atoms. The first-layer Si atoms are shown larger gray balls and the third-layer Si atoms are shown by smaller balls.

In this study, we have measured Si 2*p* SCLS's for the Yb/Si(100)(2×6), and compared those with the calculated data. The measurements were made on beamline I4 at the MAX III storage ring using a SPECS Phoibos 100 electron analyzer. The spectra were taken at 100 K with an acceptance angle of ±8°. The overall energy resolution was 75 meV at the photon energy $h\nu$ = 135 eV. The clean substrates [P-doped (*n*-type), 1−2 Ω·cm] and Yb/Si(100)(2×6) reconstruction were prepared by a standard method [4]. A LEED pattern from the Yb/Si(100)(2×6) at 100 K is depicted in Fig. 2. It exhibits the characteristic half-order streaks, which are consistent with earlier observation [4] and due to the "out-of-the-phase" shift of the topmost-layer Si dimer rows in Fig. 1.

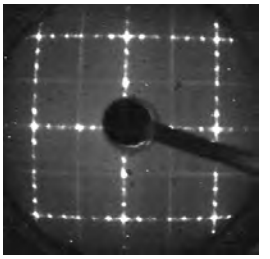

Fig. 2. A LEED pattern of Yb/Si(100)(2×6) at 100 K. The electron energy is 45 eV.

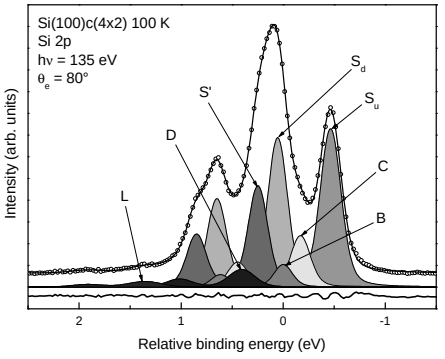

Fig. 3. Si 2*p* spectrum of the clean Si(100)*c*(4×2) at 100 K (open dots). The photon energy is 135 eV and the emission angle is 80°. The solid lines show the resulting fitting curve and residual. The shadowed doublets show the identified SCLS components (*B*, S_u, *C*, S_d, *S'*, *D*, and *L*).

Fig. 3 shows a Si 2*p* spectrum from the clean Si(100)*c*(4×2) surface at 100 K, measured at $h\nu$ = 135 eV and the emission angle θ_e = 80° (open dots). The spectrum is fitted by using seven spin-orbit-split Voigt functions (*B*, S_u, *C*, S_d, *S'*, *D*, and *L*) (shadowed doublets). The solid lines represent the resulting fitting curve and residual. The Lorentzian full width at half maximum (LW) is found to be 67 meV. It is fixed for all the components and then also applied in the fit of spectra from the Yb/Si(100)(2×6). The spin-orbit-splitting (SOS) is 610 meV, and the branching ratio (BR) is allowed to vary around 0.5 within 10% due to the diffraction effects. The Gaussian width (GW) of *B*, $S_u(S_d)$, *C*, *S'*, *D*, and *L* is 175, 203, 188, 192, 202, and 346 meV, respectively.

The SCLS's of S_u, C, S_d, S', D, and L are -0.48, -0.18, 0.06, 0.24, 0.39, and 1.35 eV relative to B. These fitting results agree well with those of earlier studies [5,6].

In Fig. 4 Si 2*p* spectra of Yb/Si(100)-(2×6) at 100 K are shown along with fitting results. The reasonable fit is obtained with six spin-orbit-split components (*B*, *S*1, *S*2, *S*3, *S*4, and S^*). The SCLS's of *S*1, *S*2, *S*3, *S*4, and S^* are -0.305, -0.145, 0.128, 0.335, and 0.59 eV. The GW of *B* is 179 meV, and those of the other components are 209−277 meV. The SOS and BR parameters are the same as for the clean Si. The minor component S^* is required to reproduce adequately the lower-binding-energy tail of the spectra. Since the intensity of S^* is much lower than those of *S*1−*S*4, we assume that the origin of S^* is different from the Si atoms in the Yb/Si(100)(2×6). Thus we conclude that the Yb/Si(100)(2×6) reconstruction causes the four SCLS's (*S*1−*S*4) in the range of -0.305 to 0.335 eV.

To interpret the above finding, Si 2*p* SCLS's were calculated for the structure of Fig. 1. These data are obtained using the initial state model which is found to be reasonable for the related Yb/Si(100)(2×3)/(2×4) surface [7]. In Fig. 5 the calculated and measured SCLS's are compared. The intensity of vertical bars is proportional to the number of respective Si atoms for the calculated shifts and the intensity of measured peaks in experiment. The comparison indicates that the calculated and experimental data are located in very similar energy ranges (-0.25/+0.28 and -0.305/+0.335 eV, respectively). Furthermore, the relative intensities of measured and calculated shifts are also consistent. We suggest that the Si atoms b1 (Fig. 1) contribute to *S*1, the atoms b2 to *S*2, the atoms a and c1 to *S*3, and the atoms c2 and c3 to *S*4. Thus, the number ratio of b1:b2:(a+c1):(c2+c3) is 8:4:10:4. Neglecting the attenuation and diffraction effects, this agrees well with the intensity ratios of *S*1:*S*2:*S*3:*S*4, which are 2.4:1:3.1:1.6 and 4:1:3.9:2.2 at θ_e = 0° and 60°, respectively.

In conclusion, the present experimental and theoretical Si 2*p* core-level study supports well the structure model of Yb/Si(100)(2×6) in Fig. 1 and explains the pronounced narrowness of the Si 2*p* line shape from this reconstruction.

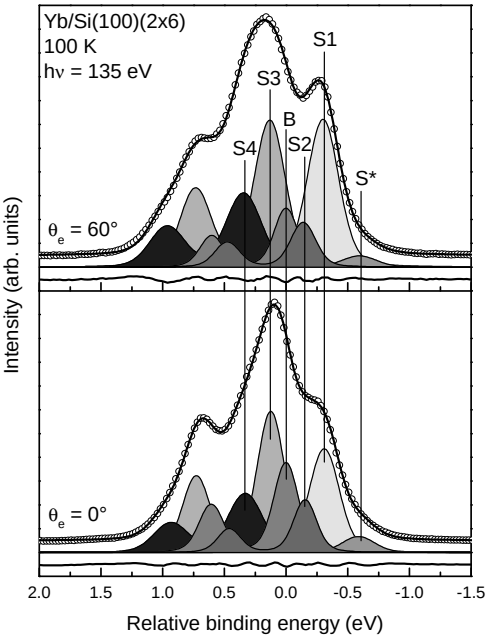

Fig. 4. Si 2*p* spectra of Yb/Si(100)(2×6) at 100 K. (open dots). The photon energy is 135 eV and the emission angles are 0° and 60°. The *B*, *S*1, *S*2, *S*3, *S*4, and *S** components are shown by shadowed doublets.

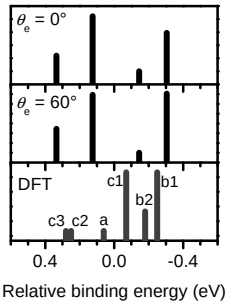

Fig. 5. Comparison of calculated and measured SCLS's for Yb/Si(100)(2×6).

[1] E. Landemark, C.J. Karlsson, Y.–C. Chao, and R.I.G. Uhrberg, Phys. Rev. Lett. **69**, 1588 (1992).
[2] E. Pehlke and M. Scheffler, Phys. Rev. Lett. 71, 2338 (1993).
[3] M.P.J. Punkkinen, M. Kuzmin, P. Laukkanen, R.E. Perälä, M. Ahola-Tuomi, J. Lång, M. Ropo, M. Pessa, I.J. Väyrynen, K. Kokko, B. Johansson, and L. Vitos, Phys. Rev. B **80**, 255307 (2009).
[4] M. Kuzmin, R.E. Perälä, P. Laukkanen, R.-L. Vaara, M.A. Mittsev, and I.J. Väyrynen, Appl. Surf. Sci. **214**, 196 (2003).
[5] R.I.G. Uhrberg, J. Phys.: Condens. Matter **13,** 11181 (2001).
[6] H. Koh, J.W. Kim, W.H. Choi, and H.W. Yeom, Phys. Rev. B **67**, 073306 (2003).
[7] M. Kuzmin, M.P.J. Punkkinen, P. Laukkanen, R E. Perälä, M. Ahola-Tuomi, T. Balasubramanian, and I. J. Väyrynen, Phys. Rev. B **78**, 045318 (2008).

Reinvestigation of the Sn line shape of Sn/Ge(111)3x3

J.R. Osiecki, I. Razado-Colambo and R.I.G. Uhrberg
Department of Physics, Chemistry and Biology,
Linköping University, S-581 83 Linköping, Sweden

Many studies have been devoted to the √3×√3 to 3×3 phase transition on the Sn/Ge(111) surface. The puzzling line shape of the Sn 4d core-level is an issue that is still discussed in the literature. In the past, any influence on the Sn 4d line shape from surface defects/irregularities has been essentially neglected. We have prepared the √3×√3/3×3 surfaces using different methods described in the literature and investigated the surfaces using LEED, STM and PES. Our STM studies show that a typical Sn/Ge(111) surface not only shows √3×√3/3×3 areas but there are also islands, disorder and 2×2/5×5/7×7 patches that will influence the Sn 4d line shape. The common use of LEED to verify the quality of the surfaces is not sufficient since we found that most surfaces showed high quality LEED patterns even though the island structure and disorder could differ significantly [1]. We have obtained new Sn 4d and valence band spectra from the optimized preparation method of the 3×3 surface. We here address the issue whether the Sn 4d spectrum of a high quality Sn/Ge(111)3×3 surface should show a clear shoulder [2] or just a very weak one [3]. This is of significant importance for the decomposition of the Sn 4d spectrum and for the discussion of the 3×3 structure.

From the detailed STM study in Ref. 1, we conclude that the Sn/Ge(111)√3x√3 surface with the lowest defect density is obtained when 0.33-0.36 ML of Sn is deposited onto a sample at approximately 250 °C. This optimized sample preparation results, after cool down, in a sharp 3x3 LEED pattern with low background and maximum surface state intensity in the valence band spectra.

The figure shows examples of sample preparations resulting in LEED patterns of different quality and the corresponding Sn 4d core-level spectra. The topmost row shows low background LEED patterns with sharp spots. The corresponding Sn 4d spectra show just a very small shoulder indicated by the arrow to the left of the main spin-orbit split component. The left column shows how the shoulder develops with annealing. The development of 5×5 and 7×7 spots leads to an increased shoulder intensity. We conclude that the imperfections related to 5×5 and 7×7 are one reason for the appearance of a shoulder. The right column shows the coverage dependence. For a coverage lower than 1/3 monolayer there is a contribution from a 2x2 phase that also gives rise to a shoulder. When there are clear 2x2 spots in the LEED pattern the intensity of the shoulder is significant. However, in both cases, i.e., for increasing annealing and decreasing coverage the shoulder appears well before any defect related diffraction spots appear. We conclude that the correct Sn 4d spectrum from the 3x3 phase of Sn/Ge(111) should just show a very small shoulder or possibly no shoulder at all. This is also supported by the valence band spectra as those show the strongest surface state (SS) intensity when the shoulder is negligible.

[1] I.C. Razado-Colambo, J.R. Osiecki, and R.I.G. Uhrberg, submitted to Surf. Sci.
[2] A. Tejeda, *et al.* Phys. Rev. Lett. 100, 026103 (2008)
[3] R. I. G. Uhrberg, H.M. Zhang, and T. Balasubramanian Phys. Rev. Lett. 85, 1036 (2000)

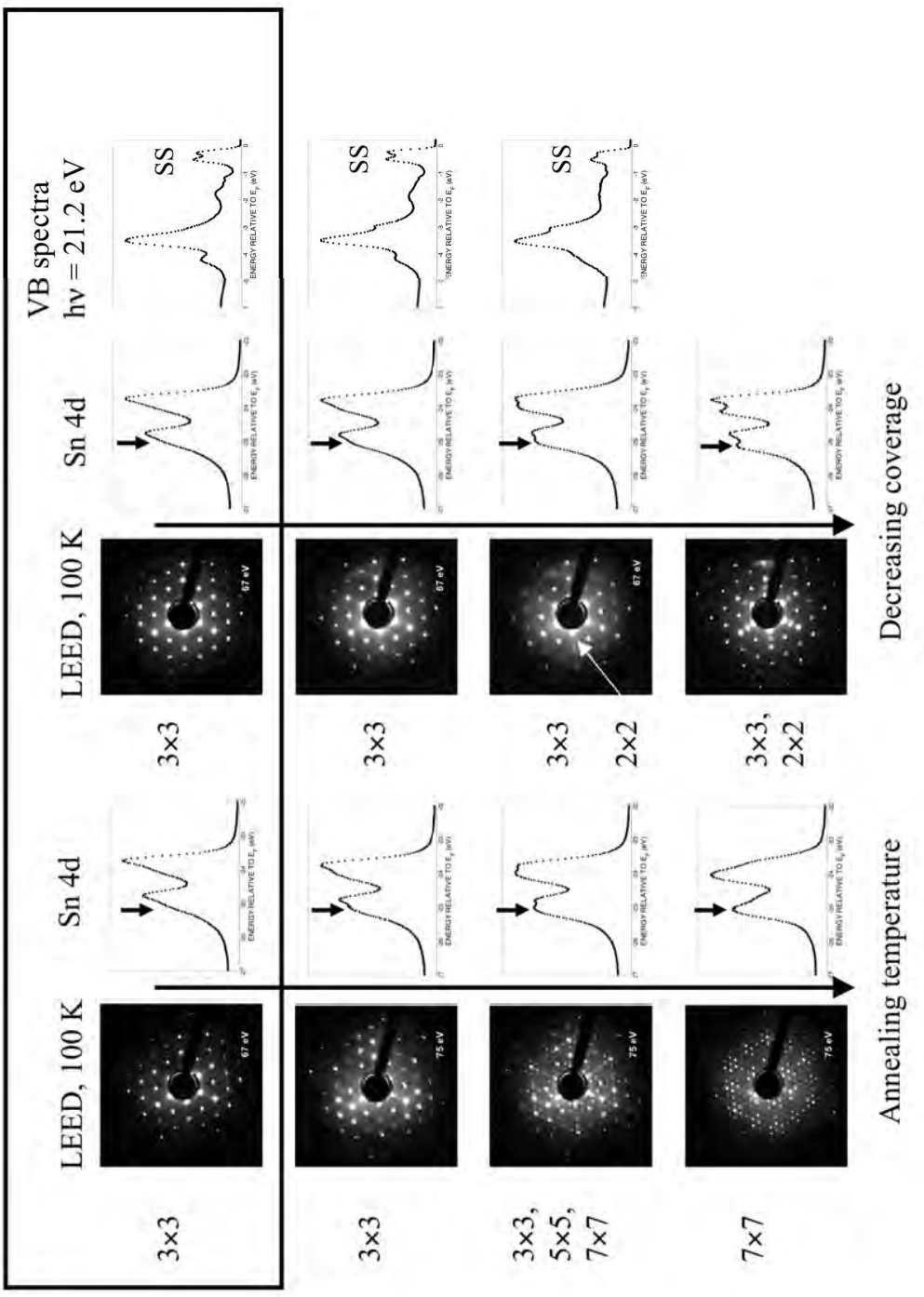
LEED, 100 K
Sn 4d
VB spectra
hν = 21.2 eV
3×3
3×3
SS
3×3
3×3
SS
3×3,
5×5,
7×7
3×3
2×2
SS
7×7
3×3,
2×2
Annealing temperature
Decreasing coverage

Yb-induced reconstructions on the Ge(100) surface

R. E. Perälä, M. Kuzmin, V. Tuominen, J. Lång, M. Ahola-Tuomi, P. Laukkanen, M. P. J. Punkkinen, I. J. Väyrynen

Department of Physics and Astronomy, University of Turku, FIN-20014 UNIVERSITY OF TURKU, Finland

In this report we present an overview of preliminary results for the Yb/Ge(100)-2×1 surface, including the phase diagram of this system and Ge 3d core level line shape as a function of metal coverage.

The Ge(100) substrates (n-type, Sb-doped) were cleaned using several cycles of sputtering at 670 K and subsequent annealing at 900 K. Yb was deposited from a W-coil evaporator keeping the substrate at room temperature. Ordered Yb-induced reconstructions were produced by subsequent annealing the sample at ~ 670 K for 5 min.

The phase diagram of Yb/Ge(100) is shown in Fig. 1. The phase transition from the disordered Yb layer to the ordered reconstructions occurs at ~ 650 K. A series of reconstructions (*c*(4×8), 2×4, 2×3, 5×1, and 3×1) is found with an increase of Yb coverage culminating in 3D Yb-germanide phase at ≥ 1.5 ML (1 ML = 6.24×10^{14} atoms/cm^2). All the reconstructions are double domain, e.g., '3×1' means 3×1 + 1×3.

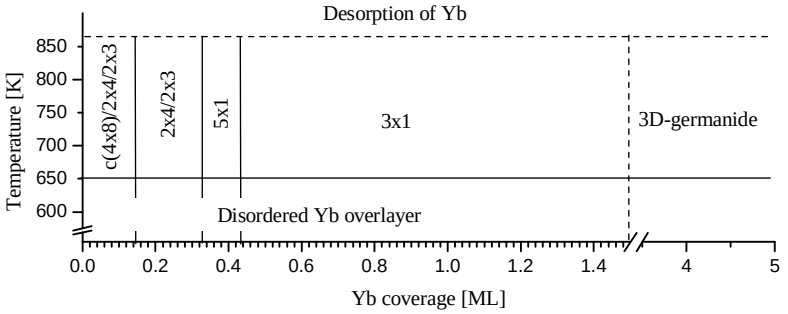

Fig. 1. Phase diagram of Yb/Ge(100).

The 3d core level spectrum of clean Ge(100) surface measured at 100 K is represented in Fig. 2 and the fitting parameters are given in Table I. The spectrum was measured by using SPECS Phoibos 100 analyzer, and the overall energy resolution was below 70 meV. Comparing to the well-defined 2p spectrum of Si(100) [1,2], the Ge 3d spectrum in Fig. 2 shows up a pronounced shoulder at the lower binding energy side as well as asymmetrical line shape of the main peak, implying at least two surface core level shift (SCLS) components. The spectrum was fitted using spin-orbit split Voigt functions. Besides the bulk component B, four surface components L, S_d, S', and S_u with SCLS's of +0.37 eV, -0.14 eV, -0.255 eV, and -0.565 eV, respectively, were found. The components S_u and S_d are due to dimer-up and dimer-down atoms, respectively, and both of them are shifted to the lower binding energy (BE) side from B. The origin of S' can be assigned to other surface atoms, most likely to the second and third layer atoms. The broad component L was added to fit the higher BE side tail of the spectrum adequately, and it is assigned to loss features. In general, these results agree with those of earlier studies [3-5], however, the further analysis is required to clarify the presence and SCLS of S'.

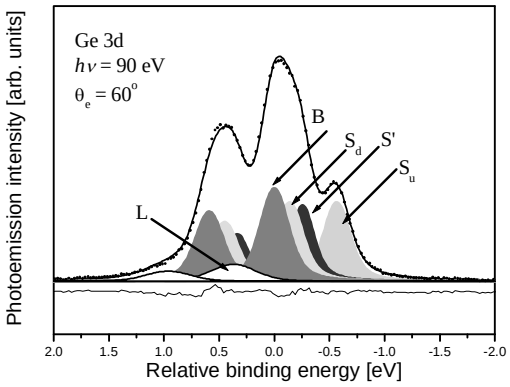

Fig. 2. Ge 3d spectrum of clean Ge(100) surface taken at 100 K. The raw data is shown by dots and the fit by a solid curve. The residual intensity is plotted below the spectrum.

Table I. Fitting parameters of the Ge 3d components in Fig. 2. Surface core level shifts (SCLS) relative to the bulk component B and Gaussian widths (GW) are shown. Other parameters used in the fit are: spin-orbit split 0.59 eV, Lorentzian width 0.15 eV, and branching ratios between 0.6 and 0.75. The intensity was constrained to be the same for S_d and S_u.

	L	**B**	**S_d**	**S'**	**S_u**
SCLS [eV]	+0.37	0	-0.14	-0.255	-0.565
GW [eV]	0.40	0.22	0.20	0.16	0.20

The changes in Ge 3d spectral line shape induced by the Yb deposition and the formation of Yb/Ge(100) reconstructions and Yb germanide (at 5 ML) are summarized in Fig. 3. The detailed analysis of these data will be performed later.

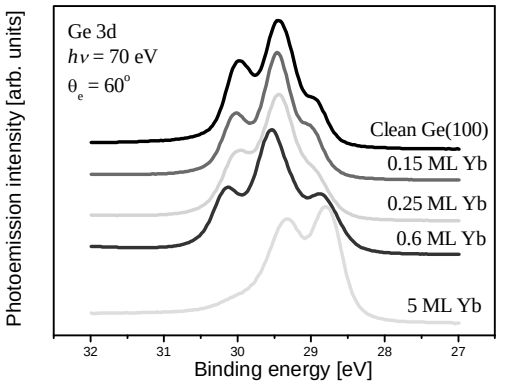

Fig. 3. Ge 3d spectra of Yb/Ge(100) as a function of Yb coverage taken at room temperature.

[1] E. Landemark, C. J. Karlsson, Y.-C. Chao, R. I. G. Uhrberg, Phys. Rev. Lett. 69, 1588 (1992).
[2] R. I. G. Uhrberg, J. Phys.: Condens. Matter 13, 11181 (2001).
[3] E. Landemark, C. J. Karlsson, L. S. O. Johansson, R. I. G. Uhrberg, Phys. Rev. B 49, 16523 (1994).
[4] A. Goldoni, S. Modesti, V. R. Dhanak, M. Sancrotti, A. Santoni, Phys. Rev. B 54, 11340 (1996).
[5] L. Ferrari, M. Pedio, N. Barrett, R. Gunnella, M. Capozi, C. Ottaviani, P. Perfetti, Surf. Sci. 482-485, 1287 (2001).

Effect of hydrogen on graphene growth on SiC(0001)

C. Virojanadara, R. Yakimova, A. A. Zakharov[1] and L. I. Johansson

Department of Physics, Chemistry and Biology, Linköping University, S-58183, Linköping, Sweden
[1]Max Maxlab, Lund University, S-22100, Lund, Sweden

The production of homogeneous large area epitaxial graphene sheets on SiC and investigations of their electronic properties have attracted intense recent interest [1-5]. Nowadays, truly atomic single-layer graphene samples are available by mechanical exfoliation[6] or by epitaxial growth on different substrates. The former method is known to be delicate and time consuming. The latter, especially growth on silicon carbide substrate, is considered a champion route to achieve graphene wafers for electronic applications. Growth of homogeneous, large area and high quality monolayer graphene on SiC(0 0 0 1) was recently proven possible [3-5]. Bi-layer graphene of similar quality on SiC(0 0 0 1) has, however, not yet been reported.

It is well known [1, 2, 7] that the first carbon layer grown on the SiC(0 0 0 1) substrate forms strong covalent bonds with the SiC substrate and does not exhibit graphitic electronic properties. This layer acts as a buffer layer and allows the next carbon layer, i.e. first graphene layer, to behave electronically like an isolated graphene sheet. Reported DFT calculations [1] show that the buffer layer exhibits a large band gap and a Fermi level pinned by a state having a small dispersion and related to the dangling bonds in-between the bulk SiC and this buffer layer. The existence of this buffer layer is regarded as a major obstacle for the development of future electronic devices from graphene on SiC(0 0 0 1). It is therefore of interest if exposures to atomic hydrogen could have a positive effect on the interface buffer layer of a monolayer graphene sample.

We therefore investigated the effects of atomic hydrogen exposes to graphene samples. The graphene samples were prepared in a prototype of an inductively heated furnace based on the SB generation Epigress heating systems on production grade n-type 6H-SiC(0001) substrates from SiCrystal. The crucible was specially designed so that the axial and radial temperature gradients were minimized in order to prevent mass transfer from and to the sample. The base pressure in the reactor was $5x10^{-6}$ mbar. The graphene growth was carried out under highly isothermal conditions at a temperature of 2000^{o}C and at an ambient argon pressure of 1 atm [3].

The ARPES results obtained from this sample showed interesting results as displayed in Fig. 1. Before hydrogenation the monolayer graphene sample showed a single π-band and a linear dispersion across the K point, as illustrated in Fig. 1a). After hydrogenation two π-bands are clearly seen around the K point, Fig. 1b), which represents bi-layer graphene. Of particular interest is that this samples was left in air for about two months and the intense and well defined π-bands were recorded already from the as introduced sample. The new phase created by atomic hydrogen exposure was found to be stable and inert from room temperature up to a temperature of about 800°C, and even after storage in the open atmospheric for about two months [8, 9].

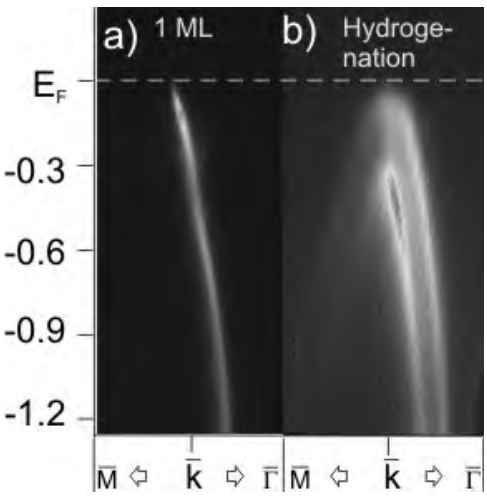

Fig. 1. The π band around the K point recorded from a) monolayer graphene, b) after hydrogenation [9].

References

[1]. C. Berger, X. Wu, P.N. First, E.H. Conrad, X. Li, M. Sprinkle, J. Hass, F. Varchon, L. Magaud, M.L. Sadowski, M. Potemski, G. Martinez and W.A. de Heer, *Adv. Solid State Phys.* **47** (2008), p. 145 (and references therein)

[2]. A. Bostwick, K.V. Emtsev, K. Horn, E. Huwald, L. Ley, J.L. McChesney, T. Ohta, J. Riley, E. Rotenberg, F. Speck and Th. Seyller, *Adv. Solid State Phys.* **47** (2008), p. 159 (and references therein).

[3]. C. Virojanadara, M. Syväjarvi, R. Yakimova, L. I. Johansson, A. A. Zakharov and T. Balasubramanian, Phys. Rev. B 78, 245403 (2008).

[4]. K. V. Emtsev, A. Bostwick, K. Horn, J. Jobst, G. L. Kellog, L. Ley, J. L. McChesney, T. Ohta, *et al* Nature Mater. 8 203 (2009).

[5]. C. Virojanadara, R. Yakimova, J. R. Osiecki, M. Syväjärvi, R. I. G. Uhrberg, and L. I. Johansson A. A. Zakharov, Surf. Sci. Lett. L87-L90 (2009)

[6]. A.K. Geim, *Science* **324** (2009), p. 1530 (and references therein).

[7]. P. Mårtensson, F. Owman and L.I. Johansson, *Phys. Status Solidi (b)* **202** (1997), p. 501

[8]. C. Virojanadara, A.A. Zakharov, R. Yakimova and L.I. Johansson, Surf. Sci. Lett. 604, L4, 2010

[9]. C. Virojanadara, R. Yakimova, A. A. Zakharov and L. I. Johansson, to be published.

Quantum-well states of Ag films on Sn/Si(111)√3×√3

H.M. Zhang and L.S.O. Johansson

Department of Physics, Karlstad University, SE-651 88 Karlstad, Sweden

Ultrathin layer systems, which may show discrete quantum-well states (QWS) due to spatial confinement of electrons, have attracted a lot of attention in the fields of the surface and solid-state physics. Over the past decades, a large number of studies have been devoted to metal thin films on metal substrates. However, the observation of quantum-well states has been restricted to a few systems. In semiconductor layer systems, on the other hand, these effects are well known and some of them have been used in electronic devices. Recently several studies have reported thin metal films (Ag or Pb) grown on clean Ge or Si surfaces at reduced sample temperature [1,2]. These films show an energy quantization effect in their valence band states. Inspired by these findings, we have investigated the electronic structure of Ag films on the Sn/Si(111)√3×√3 surface by angle-resolve valence band and core-level photoelectron spectroscopy.

A series of coverages (8-32 monolayers(ML)) of Ag were deposited on the Sn/Si(111)√3×√3 surface at low temperature (120 K). As shown in Fig. 1, there is a dramatic change in the low-energy electron diffraction (LEED) pattern after 8 ML deposition of Ag. The initial √3×√3 LEED spots were replaced by large, elongated 1x1 spots, which originated from the Ag(111)1x1 surface. One thus can calculate the surface unit cell of the Ag(111) film by comparing with the Sn/Si(111)√3×√3 cell. The estimated value for the epitaxial Ag(111)1x1 surface is about 2.96 Å, which is ~2.4% larger than the surface unit length (2.89 Å) of the Ag(111) crystal. Obviously, the grown ultrathin Ag film was slightly expanded compared to the bulk Ag(111) crystal due to a lattice mismatch between Si and Ag.

Figure 2 shows a gray-scale valence band image recorded with a photon energy of 40 eV from a thin Ag film at 100 K. The new analyzer (Phoibos 100) was used with wide angle mode (angular resolution 0.4°), which covers an angular range of ±13°. The pass energy was set 10 eV, together with 0.2 mm entrance and 0.5 mm exit slits in the detector, which give an energy resolution of 17.5 meV. For the current system with a thickness in the nanometer range, the valence electrons in Ag with energies within the fundamental gap of Si will be fully confined. The resulting quantum-well states disperse with in–plane momentum $k_{//}$ to form subbands. As illustrated in Fig. 2, the valence band of the Ag film clearly shows dispersions of its quantum-well states. There is a strong emission just located at the $\overline{\Gamma}$ point near the Fermi-level. A parabolic-like metallic band (n=1) starts from ±7° at the Fermi-level, and steeply disperses downwards. Interestingly, this band seems to break down at -0.5 eV. The second and third bands (n=2,3) have similar behaviors as the first one. They also break down at -0.7 and -0.9 eV. These breaks in the subbands form wiggles and kinks that resemble the concave curves observed in the Ag/Ge(111) system [1]. They originate from the top valence band of the substrate states. This is a clear indication of an interaction between the Ag film and the underlying Si substrate. In fact, there are more subbands (fringes) dispersing steeply around ±14°, from -0.3 towards -1.3 eV, which shows an interesting quantization of subbands away from the classical sp bands.

References

[1] S.-J. Tang, L. Basile, T. Miller, and T.-C. Chiang, *Phys. Rev. Lett.* **93**, 216804 (2004).
[2] Yan-Feng Zhang *et al.*, *Phys. Rev. Lett.* **95**, 096802 (2005).

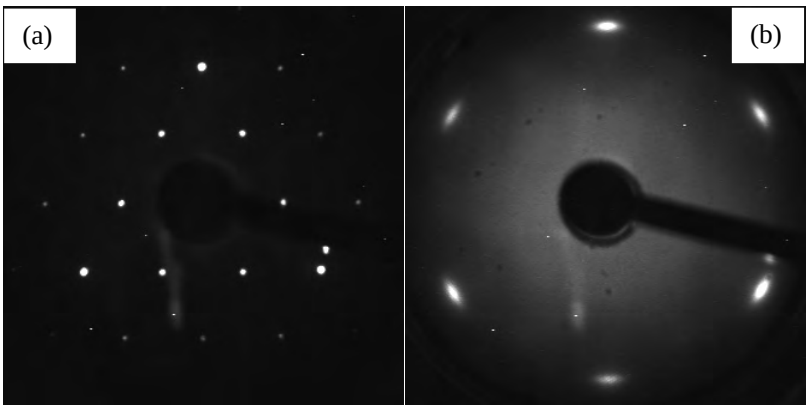

Fig. 1 LEED patterns recorded at 78 eV at room temperature. (a) the Sn/Si(111)√3×√3 surface. (b) 8 ML Ag deposited on Sn/Si(111)√3×√3, which shows a Ag(111)1×1 pattern.

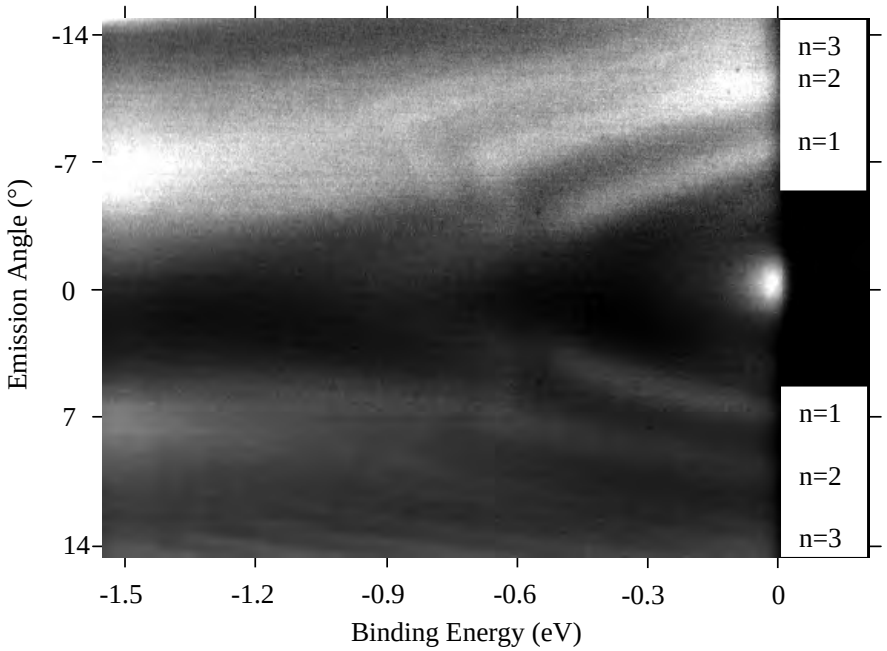

Fig. 2 Dispersions of quantum-well states from a thin Ag film on the Sn/Si(111)√3×√3 substrate along the $\overline{\Gamma K}$ direction. The wide angle range was obtained by adding three partially overlapping frames, each covering ±13°. The individual frames were stitched together using the software provided by SPECS.

Lars Malmgren and Robert Andersson next to the old modulator, August 2009.
Photo: Annika Nyberg

Dionis Kumbaro next to the new modulator, August 2009.
Photo: Annika Nyberg

Energetic Electrons

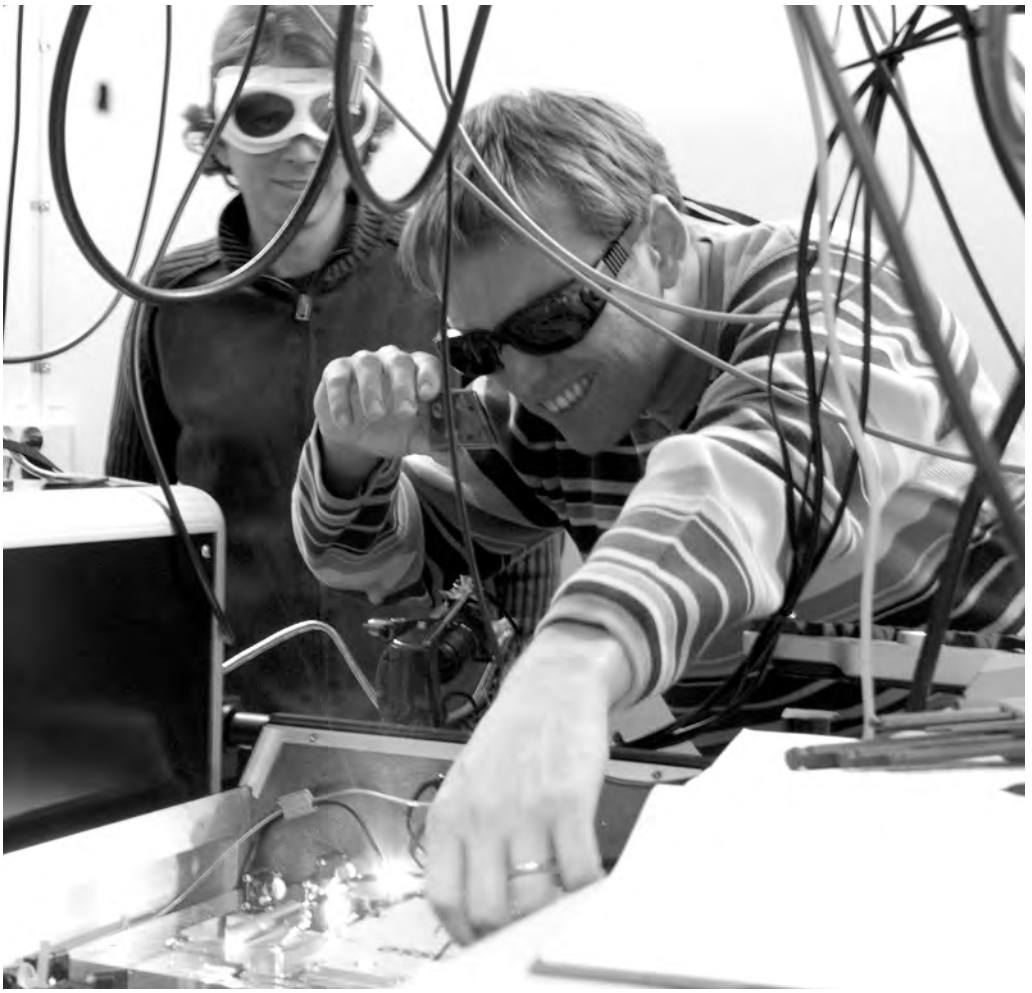

Filip Lindau assisted by Christian Erny aligning the Ti:sapphire laser oscillator in the laser hutch. The oscillator is part of the testFEL laser system, seeding amplifiers that generate UV laser pulses both for the RF photocathode gun and the FEL seed laser, May 2009.
Photo: Nino Čutić

Energetic Electrons

During 2009 the available beam time for the nuclear physics program at MAX-lab was the same as in 2008, 18 weeks. A detailed account of the program during these weeks may be found on the homepage of MAX-lab[1].

The tagged photon facility consists of an injector, two linear accelerators equipped with SLED cavities, operating at 10 Hz providing an electron pulse width of about 150 ns. This pulsed beam is injected into the pulse stretcher ring MAX I, and slowly extracted over 100 ms resulting in an almost continuous electron beam in the nuclear physics area. For an average current in the ring of typically 20 mA, the stretched beam current, measured in a Faraday cup, is about 20 nA. The electron beam impinges on a thin Al-foil and bremsstrahlung is produced. The residual (final) electron is momentum analyzed in one of two magnetic spectrometers[2]. The non-interacting part of the electron beam is dumped in a shielded Faraday cup. The extracted beam contains an initial, short burst of electrons which are not contained in the ring. An abort kicker is used to dump these electrons before they reach the experimental cave.

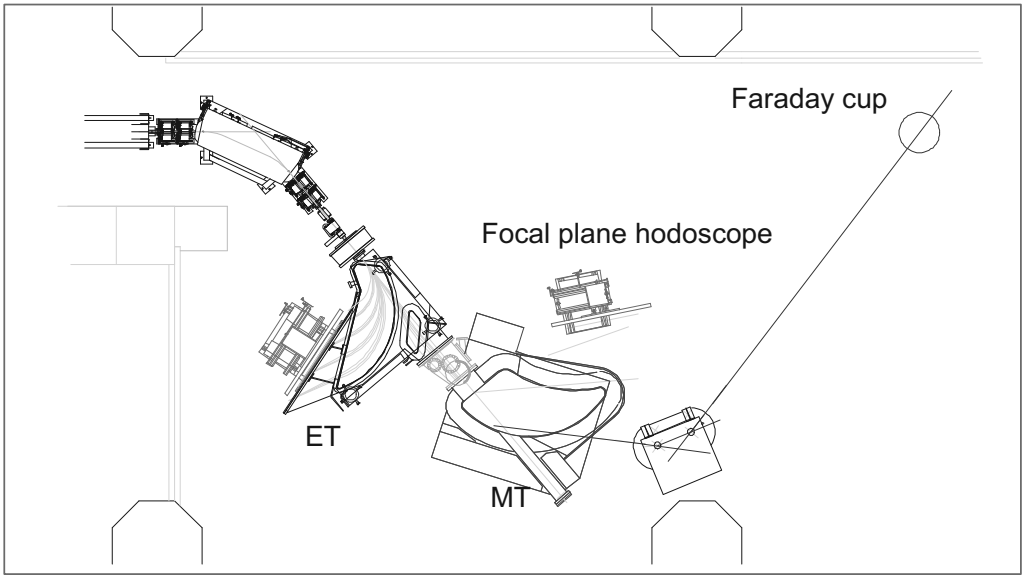

The two magnetic spectrometers are the main tagger (MT) which covers photon energies corresponding to 10 – 70 per cent of the incoming electron energy, and the end point tagger (ET) which allows the use of tagged photons as close as 10 MeV from the endpoint of the bremsstrahlung spectrum. Full energy coverage implies that the focal plane hodoscope has to be shifted along the focal plane. This applies to both tagging magnets. The focal plane hodoscope was provided, along with the tagging spectrometers, by the Saskatchewan Accelerator Laboratory in Saskatoon. The SAL hodoscope consists of 63 overlapping scintillators (3 mm thick, 50 mm high and 25 mm wide) providing 62 coincidence channels. The same hodoscope is used at both tagging magnets.

[1] http://www.maxlab.lu.se/kfoto/ExperimentalProgram/runperiods/periods.html
[2] http://www.maxlab.lu.se/kfoto/UserInfo/index.html

A new focal plane hodoscope with 160 scintillators has been designed and has been funded by the Knut and Alice Wallenberg Foundation. The construction is well underway and the hodoscope is expected to be commissioned in the summer of 2010.

The bremsstrahlung beam produced enters into the experimental cave (from the top left in the figure) through a collimator (with diameter 4, 12 or 19 mm). The energy of a photon interacting in a nuclear target is obtained from a time coincidence between a reaction product, measured in the detection system, and an overlap channel in the focal plane hodoscope. The photon energy is obtained from the energy difference between the incoming and residual electrons. During 2009 three electron beam energies were used, 144 MeV, 165 MeV and 195 MeV. The count rate in the focal plane hodoscope is typically 1 – 1.5 MHz per MeV.

The normal mode of operation of the MAX I as a stretcher ring is the following. The beam is available Tuesday morning until Monday morning the following week. There are normally two interruptions per day to allow filling the two storage rings MAX II and MAX III. In a normal week some 120 hours of stretched beam is delivered to the nuclear physics area. Students operate the accelerator during evening, night and weekend shifts. This system has worked well over the 18 weeks in 2009.

The Association of Nuclear Physics Users at MAX-lab met on November 3 at the MAX-lab Annual User Meeting. Status reports from the ongoing experiments were presented and the research activities at the tagged photon facility were discussed. The PAC did not meet this time.

The possibilities for a laser backscattering facility at MAX-IV were discussed at a workshop at the User Meeting. For the electron energy of the MAX IV ring, a 500 MeV polarized photon beam would be obtained, of large interest for hadronic and nuclear research, extending the research program to the delta resonance region and polarization variables. Similar existing facilities (although at different energies) were presented by four invited speakers and the opportunities at MAX IV were discussed.

A summary of the activities in the beam time periods during 2009

A summary of the activities in the beam time periods during 2009

Period	Electron energy Photon energy range	Projects
20; 2009-01-26 – 02-09	142.9 MeV; 12.7 – 60.5 MeV	Tests of total photon absorption in ^{6,7}Li
- " -	142.9 MeV; 43.2 – 84.2 MeV	^{12}C(γ,p)
21; 2009-03-09 – 04-06	142.9 MeV ; 12.7 – 60.5 MeV	Total photon absorption in ^{4}He
- " -	142.9 MeV ; 12.7 – 60.5 MeV 142.9 MeV ; 43.1 – 84.2 MeV	PWO-crystal measurements
- " -	191.9 MeV ; 172 – 181 MeV	(γ,π^+) setup and tests
22; 2009-05-25 – 06-22	192.4 MeV ; 172.6 – 181.7 MeV	(γ,π^+)CH_2, CD_2, C, Ta
23; 2009-09-07 – 10-05	164.8 MeV; 12.7 – 60.5 MeV 164.8 MeV; 59.0 – 99.0 MeV	Total photon absorption in ^{6,7}Li
- " -	164.8 MeV; 13.7 – 68.8 MeV	Total photon absorption in ^{4}He
24; 2009-11-02 – 11-29	164.7 MeV ; 81.6 – 115.8 MeV	Compton scattering on ^{2}H

During 2009 the following students carried out their Project work for the BSc or the MSc at MAX-lab: David Jacobsson and Johan Sjögren.

Reports from Nuclear Physics at MAX-lab

Total Photo-absorption Cross Section of ^{6,7}Li Below π-threshold

S. Al Jebali,[1] J. R. M. Annand,[1] M. Boselli,[2] J. Brudvik,[3] K. Fissum,[4] P. Grabmayr,[5] K. Hansen,[3] L. Isaksson,[3] K. Livingston,[1] M. Lundin,[3] I. J. D. MacGregor,[1] D. G. Middleton,[5] B. Nilsson,[3] and B. Schröder[4]

1. Department of Physics and Astronomy, University of Glasgow, Glasgow G12 8QQ, Scotland, UK
2. Dipartimento di Fisica, Università degli Studi di Trento, and Istituto Nazionale di Fisica Nucleare, Gruppo Collegato di Trento, I-38100 Povo (Trento), Italy
3. MAX-lab, Lund University, SE-221 00 Lund, Sweden
4. Department of Physics, Lund University, SE-221 00 Lund, Sweden
5. Kepler Centre for Astro and Particle Physics, Physikalisches Institut, Universität Tübingen, D-72076 Tübingen, Germany

The study of few body systems via electromagnetic probes is of particular interest to the field of nuclear physics. The electromagnetic interaction of the photon (both real and virtual) with the nucleus is well known and due to progress in theoretical techniques the final state of reactions involving these systems can now be described exactly. This allows the different components of the theoretical descriptions of such reactions, like the choice of nucleon-nucleon (NN) potential used, to be tested without having to resort to using approximations, as is necessary for heavier nuclei.

The Li nucleus is of particular interest as calculations which employ the Lorentz Integral Transform method [1] exist for both the ^{6}Li and ^{7}Li isotopes [2, 3] with which experimental measurements can be compared. Results of these calculations for the total photo-absorption cross section of ^{6}Li and ^{7}Li can be seen in figure 1; the ^{7}Li calculations are compared to data from a previous measurement [4]. As can be seen in figure 1a the use of different NN-potentials yields different results for the calculated cross section. With a measurement of high enough precision these different potentials can be compared to see which gives the best description of the data.

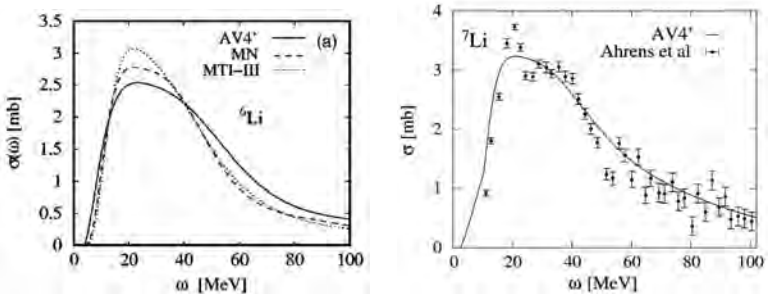

(a) ^{6}Li (b) ^{7}Li

Figure 1: Theoretical calculations for the total photo-absorption cross section for ^{6}Li [2] and ^{7}Li [3]. The data in figure 1b are from a previous measurement [4].

The aim of this experiment is to measure the total photo-absorption cross section of the ^{6}Li and ^{7}Li isotopes. The cross section will be measured using the flux attenuation method. The basic equation

$$N(E_\gamma) = N_0(E_\gamma) \exp\{-n\sigma_{tot}(E_\gamma)\} \quad (1)$$

gives the flux of photons $N(E_\gamma)$ at a photon energy E_γ that pass through a piece of matter of number of nuclei n and total photo-absorption cross section $\sigma_{tot}(E_\gamma)$ for an incident photon flux of $N_0(E_\gamma)$. The cross section is determined by taking the ratio of $N(E_\gamma)/N_0(E_\gamma)$ where $N(E_\gamma)$ and $N_0(E_\gamma)$ are determined by measuring the photon flux with and without the material in the incident photon beam. The total cross section σ_{tot} consists of two parts

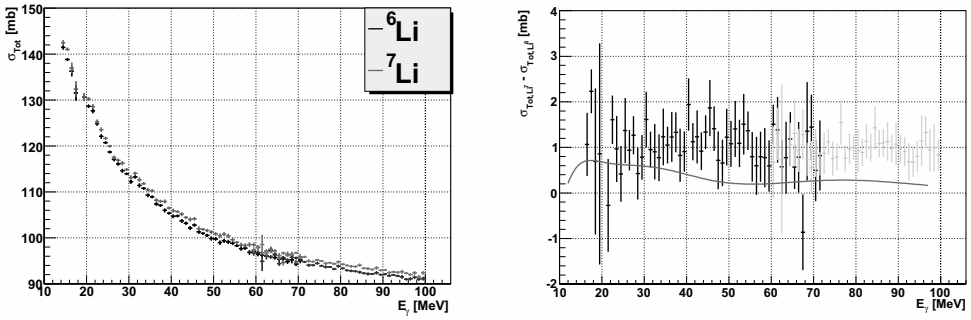

(a) σ_{Tot} (b) $\sigma_{^7Li} - \sigma_{^6Li}$

Figure 2: The measured total cross section for the two Li targets, figure 2a, and the difference between the two Li total cross sections, 2b. The different coloured points represent data taken at different incident photon energy ranges. The red line in figure 2b is a theoretical calculation [5].

$$\sigma_{tot} = \sigma_n + \sigma_a \tag{2}$$

where σ_n and σ_a are the total nuclear and atomic cross sections respectively. The atomic cross section is about two orders of magnitude greater than the nuclear cross section and will be subtracted from the measured total cross section leaving the total nuclear cross section. The atomic cross section is well known and will be determined using a Monte Carlo simulation of the experimental set-up.

Two beam periods were used for this measurement in 2010, a short one in January used as a final test of the full experimental set-up and a three week period in September for the full measurement. The experimental set-up consisted of a frame with four targets, an empty one (to determine $N_0(E_\gamma)$), the two Li targets and a ^{12}C target for normalisation and monitoring purposes. A BaF_2 detector was used for detection of photons that traversed the target material with a veto detector placed in front of this to remove charged particles produced in the target. Two incident photon energy ranges were used for the measurement.

The measured total cross sections for the two Li targets are shown in figure 2, the data taken for the two different photon energy ranges, these are shown by the different coloured points for each target. A correction for background events in the experimental hall has been applied in determining the cross sections. As can be seen there is a difference between the cross section strength for the two targets with the ^{7}Li cross section being greater than the ^{6}Li one as would be expected.

Figure 2b shows the difference between the two measured cross sections of figure 2 ($\sigma_{^7\mathrm{Li}} - \sigma_{^6\mathrm{Li}}$). This difference roughly represents the difference in nuclear cross sections for the two targets as the atomic cross section should be very similar for both targets. As can be seen the difference in measured total cross section is roughly 1 mb for the whole photon energy range covered and statistical errors on the data points are smaller than the measured difference. The data are compared to the calculated difference in nuclear cross sections [5] shown by the red line. The theoretical difference is smaller than the experimental one for the whole incident photon range covered. The discrepancy between measurement and theory could be due to slightly different things being compared in the figure and this may improve after a full analysis of the measured data.

References

[1] V.D. Efros, W. Leidemann and G. Orlandini, Phys. Lett. B**338** (1994) 130; Phys. Rev. Lett. **78** (1997) 4015.

[2] S. Bacca et al., Phys. Rev. C **69**, (2001) 057001.

[3] S. Bacca et al., Phys Lett B **603**, (2004) 159.

[4] J. Ahrens et al., Nucl. Phys. A **251**, (1975) 479.

[5] S. Bacca, *private communication.*

Helium Photodisintegration using the Mk III Active Target at MAX-lab

S. Al Jebali[1], J.R.M. Annand[1], M. Boselli[4], J. Brudvik[3], K. Fissum[3], P. Grabmayr[2], K. Hansen[1], L. Isaksson[3], K. Livingston[1], M. Lundin[3], I.J.D. MacGregor[3], D.G. Middleton[2], B. Schröder[3] and J. Sjögren[3]

1. University of Glasgow, Glasgow, Scotland, UK
2. Universität Tübingen, Tübingen, Germany
3. MAX-lab, Lund University, Lund, Sweden
4. Università degli Studi di Trento, Italy

MAX-lab has an active programme to measure photodisintegration reactions on few-body nuclei from breakup threshold to pion production threshold. The obtained data will be used to test the latest ab initio methods to construct nuclear wave functions, based either on the best phenomenological nucleon-nucleon interaction potentials or alternatively on potentials derived using Chiral Perturbation Theory. Photonuclear observables are sensitive to the wave function and recent ab initio theoretical predictions [1, 2] are in urgent need of experimental verification. The present series of experiments extends previous measurements at MAX-lab [3] and seeks to measure total and partial cross sections for ^{3,4}He photodisintegration using a gas-scintillator Active Target (AT). The AT was placed in the tagged-photon beam for the first time on 23rd October 2008 and after modification to improve high-pressure gas seals, internal gas flow and scintillation light collection, took two weeks of beam time in March 2009, followed by a further 1 week in October 2009. In both runs the AT operated at a pressure 20 bar and could run comfortably at the maximum available tagged-photon beam intensity. However with open trigger conditions the band width of the data acquisition system (DAQ) effectively limited the luminosity of the experiment. In addition to the AT, 2 10-inch NaI(Tl) counters were placed to detect coincident, Compton-scattered photons from ^{4}He, and an array of 12 liquid scintillators (Nordball) detected neutrons from breakup reactions in ^{4}He.

The experimental setup was very similar in March and October 2009 and can be viewed at the *Electronic Logbooks for Nuclear Physics at MAX-lab* (http://np1.maxlab.lu.se:7713/). In October one Nordball liquid scintillator at 30 deg. scattering angle was replaced by a prototype Lund detector[4], and the NaI detector at 90 deg. was positioned 450 mm (as opposed to 500 mm previously) from the target centre. Using an electron beam energy of 164.8 MeV, the focal-plane detector (FPD) of the main tagging spectrometer was positioned to select a photon energy range of 11.5 - 67.4 MeV. The details of calculated photon energy as a function of FPD channel are also given in the Electronic Log.

The experiment was performed with three different trigger conditions: AT OR + M1, + M2, + M3, where M1, M2, M3 relate to the hit multiplicity from the 16 photomultipliers (PMT) attached to the main cells of the AT. Hit multiplicity is just a majority logic decision, i.e. the minimum number of simultaneous PMT hits from the target. M1 is the most open trigger decision which in principle should have the smallest threshold effects on detection efficiency. However this open trigger premits (in addition to the AT scintillations) the recording of spurious signals which arise from direct electron interactions in the PMT's and also Cerenkov light produced in optical components.

Most of the running in March 2009 was performed at M3, with a small amount of M2. In October we started with some M3, for comparison with the March data, and then spent roughly equal times on M1 and M2. The multiplicity has a strong effect on the trigger rate. At standard stretched-beam currents of a few tens of nA, incident on a 50 μm Al radiator (the thinnest available on the radiator wheel), M3 gives a comfortable trigger rate of around 250 Hz (90% DAQ live time). In contrast M2 and M1 caused the DAQ to saturate at around 1200 Hz. Thus it was necessary to reduce the beam intensity, by performing a de-optimisation of the timing of the accelerator trigger system. With such an accelerator setting, M2 ran at around 650 Hz (60% live time), although M1 still saturated at around 1200 Hz (20% live time). As will be described below this de-optimisation procedure may have caused some instability in the time structure of the stretched-beam.

In total we accumulated around 14 Gbyte of data in March 2009 and 35 Gbyte in October 2009. The second run lost around 2 days due to the failure of a supply powering quadrupole elements of the MAX-I ring, so that an initial plan to take data at a different tagged-photon energy range was abandoned.

A preliminary analysis of a sample of the October data, taken with an M3 trigger, produced an excitation curve which is displayed in Fig.1. M3 preferentially selects good scintillation events in the target, which produce a balanced pulse-height response from the PMT's. The yield was extracted from active-target, tagger time coincidence spectra after random-background subtraction, but variations in counting efficiency of the focal-plane detectors still have to be accounted for fully. There is some spurious signal below breakup

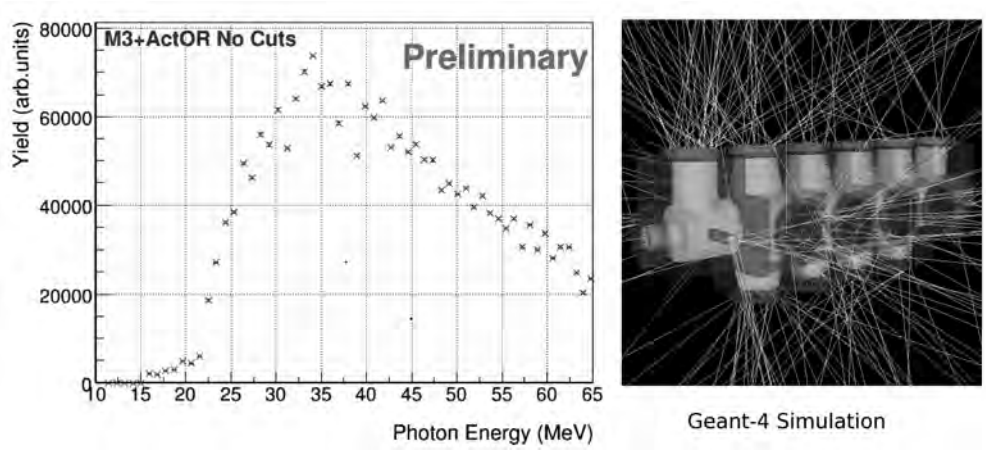

Figure 1: Left: uncorrected active-target excitation function for an M3 trigger. Right: display of simulated scintillation photons propagating through the AT.

threshold at 20 - 21 MeV photon energy, presumably from entrance or exit windows, which should be removed by a more careful analysis involving the end-cap AT cells. The trigger threshold affects the detection efficiency immediately above breakup threshold, distorting the excitation curve in this region, and this was the main motivation for concentrating on the more open triggers in October.

However the analysis of M1 and M2 data is proving to be rather more complicated than M3, mainly due to an instability in the time structure of the stretched beam. This may have been caused by the accelerator de-optimisation procedure mentioned above, as M3 runs with optimised intensity beam have a more stable time structure. The instability complicates the background subtraction procedure since the variations in background shape from run to run (and also within individual runs) must be identified and fitted.

In parallel with the data analysis we have developed a Monte Carlo model of the AT, based on the cern toolkit Geant-4. This model is vital to understand the effect of trigger thresholds on detection efficiency, as close to the photodisintegration energy threshold the breakup-particle energies are small. Initially the model has been used to calculate scintillation-light transport through the active target (Fig.1), in order to identify possible position dependence of the signal. This will complement measurements, made with internal alpha-particle sources, of the detector response. Now the model is being extended to calculate the energy deposition of various ion species in the He gas, where photodisintegration events are being generated using realistic models of the reaction processes.

The primary analysis objective, to obtain the inclusive $\gamma + {}^4\mathrm{He}$ cross section, is making good progress. It will be followed by analyses of partial reaction channels, producing coincident photons or neutrons in the final state which are not stopped in the robust walls of the AT. This will provide a feasibility study of possible experiments on He Compton scattering and also a measurement of ${}^4\mathrm{He}\,(\gamma, \mathrm{n})$. The AT signal gives the time reference to determine neutron momentum by time-of-flight and in this case the random-coincidence background is largely unaffected by the stretched-beam time structure.

References

[1] D. Gazit et al., Phys. Rev. Lett. 96: 112301, 2006.

[2] V.D. Efros et al., J. Phys. G34: R459, 2007.

[3] B. Nilsson et al., Phys. Rev. C75: 014007, 2007.

[4] J. Sjögren, *Construction and Testing of a Neutron Detector Prototype*, Masters Thesis, Lund University 2009, http://www.maxlab.lu.se/kfoto/Publications/Master/sjogren.pdf

International Research Experience for Students (IRES)

C.M. Allen [a], J. Lemrise [a], M. Litwack [b],
W.J. Briscoe [c], N. Benmouna [b], K.G. Fissum [d] and G.V. O'Rielly [a]

[a)] *University of Massachusetts Dartmouth, North Dartmouth MA, 02740, USA*
[b)] *Montgomery College, Rockville, MD 20850*
[c)] *The George Washington University, Washington DC 22201, USA*
[d)] *Lund University & MAX-lab, Lund SE-221 00, Sweden*

Supported by the US National Science Foundation's Office of International Science and Engineering through an *International Research Experience for Students (IRES)* grant (Award 0853760), three undergraduate students from US institutions participated in the pion photoproduction experiment NP-014 being performed by the PIONS@MAXLAB Collaboration during the summer of 2009. Ms. Colleen Allen and Mr. Jason Lemrise, both from the University of Massachusetts Dartmouth, and Mr. Matty Litwack from Montgomery College were integral members of the collaboration and participated in the apparatus set-up, took experiment shifts monitoring the equipment and data quality, and were responsible for a research project involving system calibration or event analysis. The work performed by the students was crucial for the success of both their projects and the pion photoproduction measurements.

Mr. Litwack worked on the measurement of the photon tagging efficiency which determines the fraction of bremsstrahlung photons which make it to the measurement target. This quantity is essential to the calculation of the absolute cross sections for the pion photoproduction process. Daily measurements of the tagging efficiency were made during dedicated calibration runs. The resulting set of data were analyzed to determine the tagging efficiency for the individual tagger channels and to provide an estimate of its contribution to the overall systematic uncertainty.

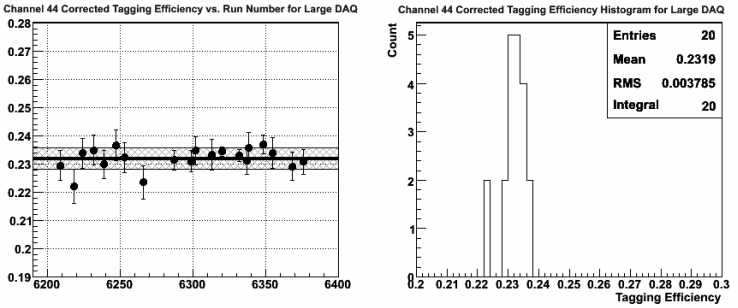

Corrected tagging efficiency for a single tagger channel (ch. 44) determined during experiment NP-014 in June 2009. The error bars are statistical only while the shaded band indicates the systematic variation.

Mr. Lemrise's project involved developing techniques for particle identification. Standard particle identification methods are based on ΔE vs. E histograms. These are 2-dimensional plots and cuts made on these to select a particular particle species are difficult to optimize. Worse, it is impossible to characterize the fraction of good events lost and wrong events misidentified by such cuts. Such corrections will be crucial for determining the pion yield amongst the much more numerous background proton and electron events. A *linearized particle identification (PID)* based on rotation and projection of the standard ΔE vs. E particle bands has been developed. The peaks for the different particle species in the 1-dimensional PID histogram can be fitted to determine the misidentification and loss fractions for the final particle selection cuts used.

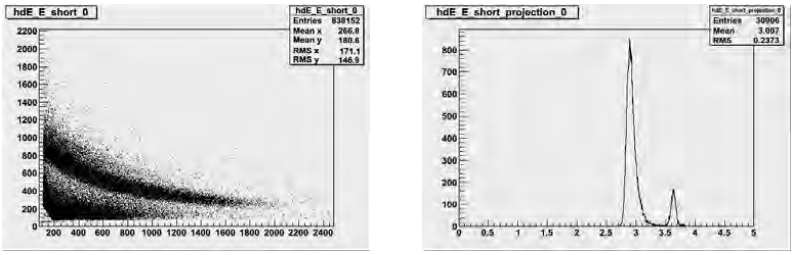

(left) Standard ΔE vs. E histogram showing proton and electron events. (right) Linearized particle ID after rotation and projection, proton events are clearly separated from electrons.

Ms. Allen worked on identifying pion events in the data. Due to the very low event rate for the (γ,π^+) reaction, standard methods using ΔE vs E *stopping power* are insufficient to separate pion events from the much larger electron and proton background. To reliably identify the pion events, analysis methods based on detecting the $\pi^+ \rightarrow \mu^+$ decay were used. The first of these methods identifies the 4.12 MeV muon based on the energy deposited in a short- versus long-gated QDC.

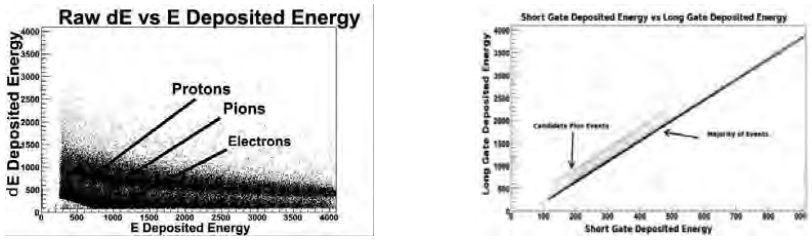

(left) ΔE vs. E histogram for all events in an xSAL counter. The pion events are swamped by the background electrons and protons. (right) Energy deposited in long- vs short-gated QDC. The candidate pion events are located above the *equal energy* band produced by the background events.

To determine the absolute detection efficiency, a second method investigates the time distribution of the candidate pion events - this must match the known 26 ns lifetime for the $\pi^+ \rightarrow \mu^+$ decay.

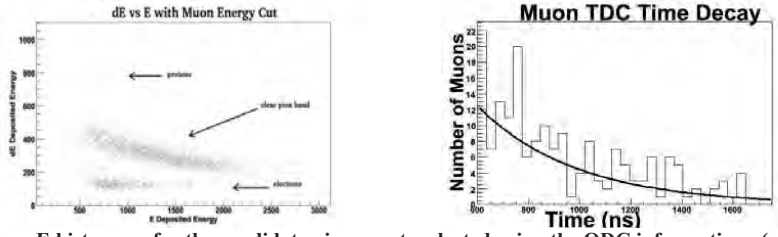

(left) ΔE vs. E histogram for the candidate pion events selected using the QDC information. (right) Time distribution for these events exhibits a decay time of (26.7 ± 2.2) ns, consistent with the π → μ lifetime.

The combination of using both energy and timing information from the π^+ decay in the E-counter enables the reliable identification of pion events with a well-understood detection efficiency.

All three students presented posters describing their research projects at the Spring meeting of the *American Physical Society* held in Washington, DC. Both Ms. Allen and Mr. Litwack continued their research project after the summer, writing and defending a "*kandidatarbete*" thesis for credit at Lund University.

The new focal plane hodoscope at the tagged photon facility

J.R.M. Annand[1], P. Lumsden[1], J Brudvik[2], E. El Afifi[2], K. Fissum[3], K. Hansen[2], L. Isaksson[2], M. Lundin[2], B. Nilsson[2], B. Schröder[2,3]

[1]*Department of Physics and Astronomy, University of Glasgow, Glasgow G128QQ, Scotland, UK*

[2]*MAX-lab, Lund University, 221 00 Lund, Sweden*

[3]*Department of Physics, Lund University, 221 00 Lund, Sweden*

Two new magnetic spectrometers and a focal plane hodoscope were moved from the Saskatchewan Accelerator Laboratory (SAL), Canada, to MAX-lab, in connection with the upgrade of the tagged photon facility. The SAL hodoscope consists of 63 overlapping plastic scintillators with a total length of 842 mm. The energy resolution depends on the incoming electron energy E_0 and the magnetic field of the tagging magnet. For the Main Tagger (MT) 0.5 MeV is a typical energy resolution. The central momentum of the MT, $P_0 = 198.6 \cdot E_0 / S$, where S is a number related to the exit path of the direct electron beam towards the beam dump. We use S = 345 or 475. The focal plane of the MT is linear from 0.8 P_0 to 1.4 P_0 and slightly curved over the range 0.6 P_0 to 0.8 P_0. The length of the focal plane is about 1240 mm. It is possible to use also the part of the focal plane that is above 1.4 P_0, however, the characteristics of this part has to determined for each setting using a NaI spectrometer in the direct tagged photon beam.

A new hodoscope is under construction funded by the Knut and Alice Wallenberg Foundation and by MAX-lab. The hodoscope consists of 160 scintillators, each 10.5 mm wide and 3 mm thick. The trajectories of the electrons form a 45^o angle with respect to the focal plane and will pass the scintillators at 90^o, see figure 1. The dimensions are chosen to obtain as high an energy resolution as possible with the smallest available PM tubes (Hamamatsu R1635). The total length of the new focal plane hodoscope is 1200 mm. The light guides from the scintillators to the PM tubes are designed to allow for two rows of PM tubes, every second PM tube is along one row. The distance between the rows is determined by the size of the mymetal shield (diameter 15 mm) around the tubes.

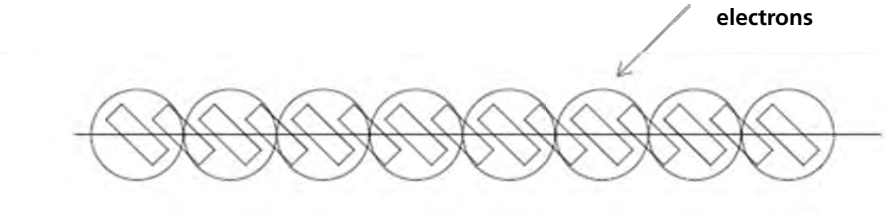

Figure 1

Each PM tube is mounted on a separate HV/discriminator card similar to the Glasgow design used at the tagging system at MAMI in Mainz. Each card has an analogue signal and two ECL signals, the three signals will be transported about 30 m to the counting rooms outside the shielded experimental area.

Examples of energy ranges and energy resolutions expected at the hodoscope are given in Table 1 for the MT with two values of S. The ET will provide tagged photon energies as close as 10 MeV from the endpoint of the bremsstrahlung spectrum.

Table 1

Electron energy (MeV)	Photon energy range (MeV)	Photon energy resolution (MeV)	Tagging system
140	12 - 75	0.39	MT (345)
165	68.4 – 123.6	0.35	MT (475)
190	78.8 – 142.3	0.40	MT (475)
190	15.0 – 102.5	0.55	MT (345)

A frame has been designed and constructed to house the scintillators, PM tubes, and HV/discriminator cards with signal cables and power supply cables. A model showing part of the frame is shown in figure 2.

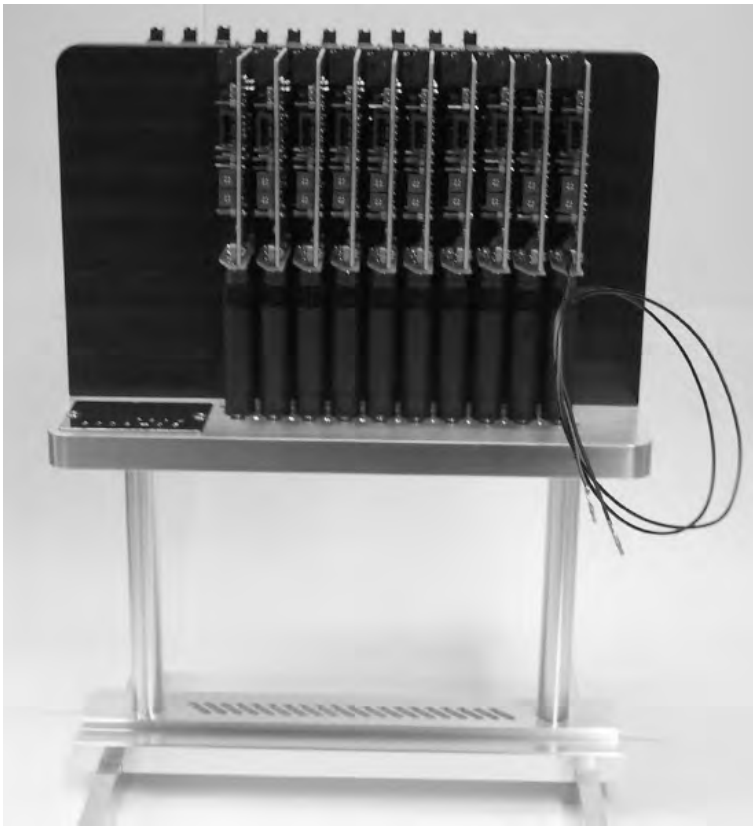

Figure 2

Measurement of Coherent Bremsstrahlung Beam Polarization

J. Brudvik [2], D. Burdeinyi [3], K. Fissum [1], V. Ganenko [3], K. Hansen [2], L. Isaksson [1], K. Livingston [4], M. Lundin [2], V. Morokhovskyi [3], B. Nilsson [2], B. Schröder,[1,2], G. Vashchenko [3]

[1] *Department of Physics, Lund University, SE-221 00 Lund, Sweden*

[2] *MAX-lab, Lund University SE-221 00 Lund, Sweden*

[3] *National Scientific Center "Kharkov Institute of Physics & Technology", 61108 Kharkov, Ukraine*

[4] *Department of Physics and Astronomy, University of Glasgow, Glasgow G12 8QQ, Scotland, UK*

In the course of test experiment on studies of the MAX-lab coherent bremsstrahlung (CB) beam features [1] the value of its polarization was measured. These measurements were carried out using reaction of deuteron photodisintegration d(γ,p)n, because the reaction has large asymmetry (analyzing power) in the energy range below E_γ~60 MeV and its value was measured with high enough accuracy in many experiments [2].

A 1 mm CD_2 plate was used as the deuteron target and a CH_2 target of the same thickness was applied for removing background contribution from carbon disintegration. The emitted protons were detected with CsI/SSD telescope placed [3] at an angle $\theta_p=90^0$ to the photon beam and identified with using standard dE-E technique. The reaction channel was selected with help of the missing energy method.

The diamond crystal 0.1 mm thick was orientated in such a way that only one point (0-22) gave contribution to the CB cross section and the coherent maximum was at energy E_γ~50 MeV. At this orientation the maximal polarization is produced. The focal plane (FP) hodoscope had 62 channels and provided measurements of uncollimated CB spectra in the energy range E_γ=21.86-78.8 MeV. The results are shown in Fig. 1. The spectrum well agrees with ANB code [4] calculation. Coherent effect for uncollimated CB spectrum is low, β_{max}~1.35. (β_{max} is the ratio value $\beta=(I_{coh}+I_{in})/I_{in}$ at the coherent peak energy, I_{coh} and I_{in} are intensities of the coherent and incoherent parts of the CB).

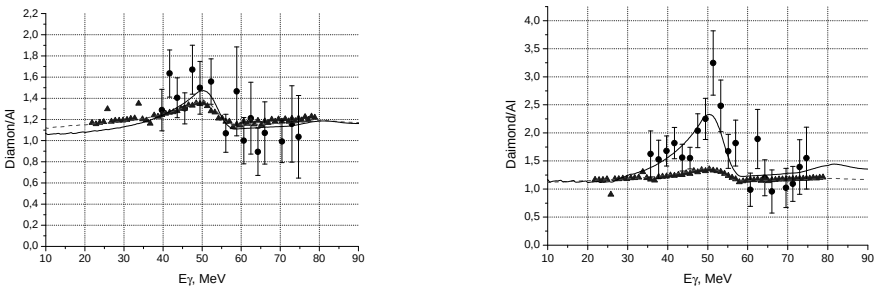

Fig. 1. Spectra of CB for (0-22) orientation measured with FP array without collimation (triangles) and obtained from deuteron photodisintegration (circles) at collimator 12 mm (θ_c~1.2θ_γ) (left) and 4 mm (θ_c~0.4θ_γ) (right). Curves are calculations with ANB code [4]: solid – with and dash - without collimation.

The spectrum of the CB which hit the nuclear target can be obtained from the ratio of the d(γ,p)n reaction yields measured at the beam polarization directed parallel N_{par} and perpendicular N_{per} to the reaction plane and for unpolarized bremsstrahlung from Al radiator N_{Al},

$$R_{D/Al}=(N_{par}+N_{per})/N_{Al} \sim (I_{coh}+I_{in})/I_{in} \quad (1)$$

The spectra measured for collimator 12 mm (θ_c~1.2θ_γ) and 4 mm (θ_c~0.4θ_γ) are presented in Fig. 1. ($\theta_\gamma=mc^2/E_0$, m is the electron mass). There is reasonable agreement with the calculations within the data accuracy. The results demonstrate increasing of the coherent effect value with increasing the beam collimation up to β_{max}~2.5 for collimation angle θ_c~0.4θ_γ

The beam polarization can be obtained from measured experimental asymmetry A_{exp} of the d(γ,p)n reaction in accordance with the relation,

$$P_\gamma=A_{exp}/\Sigma, \quad (2)$$

where $A_{exp}=(N_{par}-N_{per})/(N_{par}+N_{per})$ and Σ is asymmetry of the d(γ,p)n reaction cross sections. For conditions of our experiment (E_γ~50 MeV, $\theta_p=90^0$) $\Sigma\approx0.6$ [2]. The experimental results are shown in Fig. 2. The polarization reaches P_γ~0.25 for collimator 12mm (θ_c~1.2θ_γ) and P_γ~0.48 for collimator 4mm (θ_c~0.4θ_γ). The experimental data are in agreement with the calculations within the data accuracy.

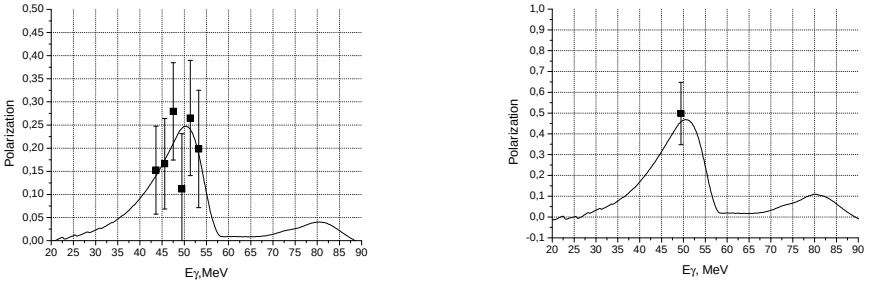

Fig. 2. Polarization of CB for (0-22) orientation for collimator 12 mm (θ_c~1.2θ_γ) (left) and 4 mm (θ_c~0.4θ_γ) (right). Curves are calculations with ANB code [4].

A collimation dependence of the polarization is presented in Fig. 3 for the CB peak energy $E_{\gamma,p}$~50 MeV. It is typical and for other peak energies. For the diamond 0.1 mm thick and E_0=192.66 MeV the polarization is P_γ~0.18 even without beam collimation and begins to increase for the angles θ_c~<0.9θ_γ. If assume that polarization should be no less P_γ~0.2 to be used in photonuclear experiments one can estimate the energy interval to be acceptable for photonuclear researches in MAX-lab at electron energy E_0~200MeV. The calculations were produced with ANB code [4] which well describes the experimental results. In principle the interval can be extend from Giant Dipole Resonance region up to E_γ~80-100 MeV at the collimation θ_c~0.4θ_γ, Fig. 4. For collimator hole 6 mm (θ_c~0.6θ_γ) the energy range is extended up to E_γ~80 MeV.

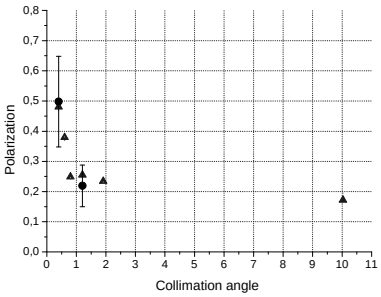

Fig. 3. Polarization as a function of the collimation angle for $E_{\gamma p}$~50 MeV. Triangles are calculation with ANB code [4], circles are our measurements.

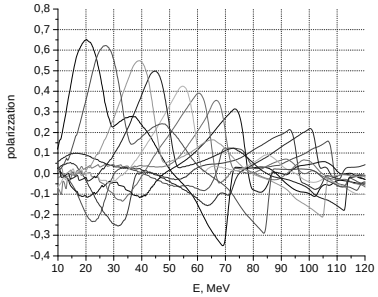

Fig. 4. Expected polarization as a function of CB peak position for collimation angle θ_c~0.4θ_γ.

References

1. J. Brudvik et al. MAX-lab Activity Report 2008, p.490.
2. D. Babusci et al. Nucl. Phys. A633 (1998) 683; V.P. Barannik et al. Sov. Journ. Nucl. Phys. V 38 (1983) 1108 ; W. Del Bianco et al. Phys. Rev. Lett. 47 (1981) 1118; K.-H. Krause et al. Nucl. Phys. A549 (1992) 387.
3. K. Hansen et al. MAX-lab Activity Report 2005-2006, p.460.
4. F.A. Natter, P. Grabmayr, T. Helh et all. Nucl. Instr. and Meth. B211 (2003) 465-486.

Measurement of Cross section Asymmetry of Deuteron and Carbon Disintegration with Polarized Photon Beam

J. Brudvik [2], D. Burdeinyi [3], K. Fissum [1], V. Ganenko [3], K. Hansen [2], L. Isaksson [1], K. Livingston [4], M. Lundin [2], V. Morokhovskyi [3], B. Nilsson [2], B. Schröder,[1,2], G. Vashchenko [3]

[1] *Department of Physics, Lund University, SE-221 00 Lund, Sweden*

[2] *MAX-lab, Lund University SE-221 00 Lund, Sweden*

[3] *National Scientific Center "Kharkov Institute of Physics & Technology", 61108 Kharkov, Ukraine*

[4] *Department of Physics and Astronomy, University of Glasgow, Glasgow G12 8QQ, Scotland, UK*

Recently a linear polarized tagged photon beam has been produced in MAX-lab [1] on the base of coherent bremsstrahlung (CB) process of electrons in 0.1 mm thick diamond crystal, and for the first time the beam has been applied in photonuclear researches. A reaction d(γ,p)n was chosen for testing of the polarized beam quality and procedure of photonuclear reactions cross section asymmetry measurement. For the d(γ,p)n process this physical observable has been well studied in many experiments. A 1 mm CD_2 plate was used as the deuteron target and a CH_2 target of the same thickness was applied for removing background contribution from carbon disintegration. These targets allow to study simultaneously the carbon photodisintegration $^{12}C(\gamma,p)$, as well.

The crystal was orientated in such a way that CB peak was at energy E_γ~50 MeV. Energy of the electron beam was E_0=192.66 MeV. Photon collimator with openings 12 and 4 mm was used that allowed to carry out the measurements with two different polarization of the beam.

The cross section asymmetry is defined as

$$\Sigma=(d\sigma_{||}-d\sigma_{\perp})/(d\sigma_{||}+d\sigma_{\perp}), \quad (1)$$

where $d\sigma_{||(\perp)}$ is the reaction cross section with photon polarization parallel (perpendicular) to the reaction plane. Protons were detected with CsI/SSD telescope [2] placed at an angle $\theta_p=90^0$ to the photon beam. The telescope consists of two single-sided silicon strip (ΔE) detectors and a CsI counter functioned as (E) detector. The protons were identified using standard ΔE-E technique, Fig. 1. Time coincidences between the SSD/CsI signals (corresponding to the proton band) and the focal plane (FP) array were applied to select the reaction events (sharp peak in Fig. 2).

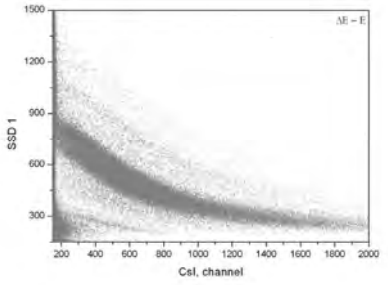

Fig. 1. ΔE-E plot. The proton band dominates.

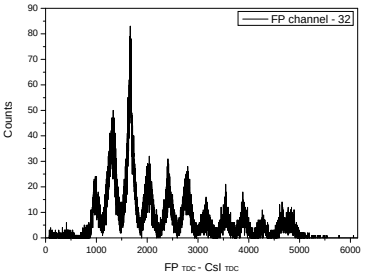

Fig. 2. Time coincidence spectrum between SSD/CsI telescope and FP array 32 channel (E_γ=51.4 MeV)

A missing energy method was additionally applied for the reaction channels selection. The missing energy is determined as $E_m=E_\gamma-E_p-E_r$, where E_γ is the photon energy, E_p and E_r are the kinetic energies of the proton (measured with CsI and corrected to energy losses on its way from the target to the detector) and recoil neutron or ^{11}B, calculated from the reaction kinematics. One clear peak is observed against a background at E_m≈16 MeV in the missing energy spectrum of the $^{12}C(\gamma,p)^{11}B$ reaction on the CH_2 target, Fig. 3 (left), and there are two peaks in the spectrum for the d(γ,p)n reactions, Fig. 3 (right). They correspond to the reactions d(γ,p)n (peak at E_m≈2.2 MeV) and $^{12}C(\gamma,p)^{11}B$. For finding true the reaction yields for the d(γ,p)n process subtraction of the proton yields from CD_2 and CH_2 targets was applied. For the $^{12}C(\gamma,p)^{11}B$ process the background contribution was evaluated using results of the background fitting.

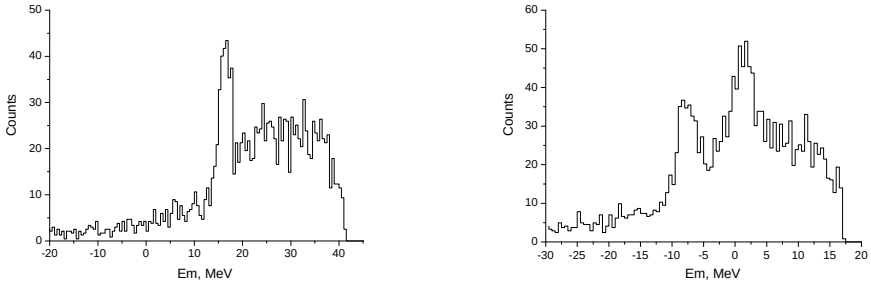

Fig. 3. Missing energy spectra, E_γ=51.4 MeV. Left - $^{12}C(\gamma,p)^{11}B$, CH_2 target; right - d(γ,p)n, CD_2 target

The cross section asymmetry of the reactions was obtained from true proton yields obtained at the photon beam polarized parallel N_{par} and perpendicular N_{per} to the reaction plane,

$$\Sigma = \frac{1}{P_\gamma}\frac{N_{par} - N_{per}}{N_{par} + N_{per}}. \qquad (2)$$

P_γ is the photon polarization. It was calculated with ANB code [3] with taking into account the experimental conditions. The experimental results are shown in Figs. 4. The measured asymmetry of the d(γ,p)n reaction (Σ~0.6) within experimental errors agrees with existing experimental data. Asymmetry of the $^{12}C(\gamma,p)^{11}B$ process is larger, Σ~0.8. Our results agree with data [5] and better agree with calculation on RPA theory than the quasi-deuteron model. The range E_γ>50MeV is more critical for these models testing because there is strong difference between model's predictions in this range.

A full analysis of this experiment is in progress.

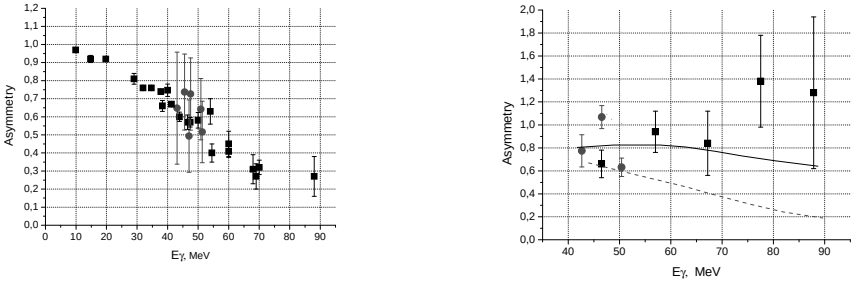

Fig. 4. Cross section asymmetry of d(γ,p)n (left) and $^{12}C(\gamma,p)^{11}B$ reactions (right). Circles are our data, squares are summarize data for the d(γ,p)n [4] for 90^0 c.m. on the left panel and data [5] for the $^{12}C(\gamma,p)^{11}B$ on the right panel. Solid line is the asymmetry predicted by the RPA theory, dash line – by the quasi-deuteron model from [5]

References

1. K. Fissum et al. MAX-lab Activity Report 2007, p.416.
2. K. Hansen et al. MAX-lab Activity Report 2005-2006, p.460.
3. F.A. Natter, P. Grabmayr, T. Helh et all. Monte Carlo Simulation and Analytical Calculation of Coherent Bremsstrahlung and its Polarization. Nucl. Instr. and Meth. B211 (2003) 465-486.
4. D. Babusci et al. Nucl. Phys. A633 (1998) 683; V.P. Barannik et al. Sov. Journ. Nucl. Phys. V 38 (1983) 1108 ; W. Del Bianco et al. Phys. Rev. Lett. 47 (1981) 1118; K.-H. Krause et al. Nucl. Phys. A549 (1992) 387.
5. T.Terasawa et al. NIM A248(1986) 429

Spectra and Polarization of Coherent Bremsstrahlung Beam at MAX-lab Facility for Typical Orientations

J. Brudvik [2], D. Burdeinyi [3], K. Fissum [1], V. Ganenko [3], K. Hansen [2], L. Isaksson [1], K. Livingston [4], M. Lundin [2], V. Morokhovskyi [3], B. Nilsson [2], B. Schröder, [1,2], G. Vashchenko [3]

[1] *Department of Physics, Lund University, SE-221 00 Lund, Sweden*

[2] *MAX-lab, Lund University SE-221 00 Lund, Sweden*

[3] *National Scientific Center "Kharkov Institute of Physics & Technology", 61108 Kharkov, Ukraine*

[4] *Department of Physics and Astronomy, University of Glasgow, Glasgow G12 8QQ, Scotland, UK*

Processing and analysis of experimental data obtained in the test beam run [1,2] on production of a coherent bremsstrachlung (CB) polarized photon beam at MAX-lab has been continued. A schematic picture of the beam line and experimental area were presented in [1]. The CB beam was produced at interaction of electron beam with energy E_0=192.66 MeV with a diamond crystal 0.1 mm thick which was fixed in a 3-axes goniometer. Methods of the crystal orientation were described in [2]. Photon spectra were measured at reduced electron beam intensity with a NaI detector (25x25x25 cm^3) and simultaneously by focal plane (FP) detectors of the main tagger in coincidence with the NaI. The FP array had 62 channels for scattered electron measurements and was placed along the tagging magnet focal plane to cover photon energy range E_γ=21.86-78.8 MeV.

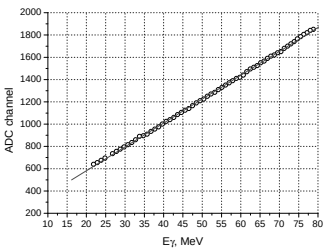

Fig.1. Energy deposited in the NaI detector as a function of photon energy.

The NaI energy calibration (dependence of the NaI signal from detected photon energy) was obtained from measurements ADC spectra of the NaI signals in coincidences with the FP detectors. Energy deposited in the NaI as a function of photon energy is shown in Fig. 1. The curve is a linear fit to the data in whole energy range of the tagger. There is a linear dependence in the range E_γ=32.8-78.8 MeV and deviation from the linearity at energy $E_\gamma \lesssim 32$ MeV (the 50-62-th channels of the FP array). It was assumed that the effect was due to position of the FP hodoscope 50-62 channels in the range where the linearity between the detectors position and scattered electron energy was broken [2]. So, the NaI energy calibration was established in the range E_γ=32.8-78.8 MeV and extended to photon energies less 32.8 MeV.

The CB spectra were measured for two types of the crystal orientations which were usually used for polarized CB beam generation. It is so-called "row" and "point" orientations when many points of the crystal reciprocal lattice or only one give contribution to the CB cross section. Typical spectra for the "row" orientations and expected polarization in that case are shown in Figs. 2 for two coherent peak positions, $E_{\gamma,p}$~30 and 48 MeV. The spectra are normalized to Al and to theory. Measurements were produced with collimator 19 mm that corresponds to collimation angle $\theta_c \sim 1.9\theta_\gamma$ ($\theta_\gamma = mc^2/E_0$, m is the electron mass). The spectra demonstrate typical coherent maxima with rather large coherent effect β_{max}~2-2.4. (β_{max} is the ratio value $\beta=(I_{coh}+I_{in})/I_{in}$ at the coherent peak energy, I_{coh} and I_{in} are intensities of the coherent and incoherent parts of the CB). Calculations produced with ANB code developed by P.Grabmayer [3] are in a good agreement with the experimental spectra. Expected polarization for this type orientations is low, P_γ~6-8% in the coherent maximum, resulted from destructive contributions of the reciprocal lattice points to the polarization.

Analogical results are shown in Figs. 3 for the "point" orientations. The measurements were produced for energies of the coherent peak, $E_{\gamma,p}$~50 and 60 MeV and collimator holes 12 and 19 mm, respectively. The experimental spectra well agree with the calculated ones, as well. In these orientations the coherent effect is less (β_{max}~1.5-1.6) but expected polarization is much more, P_γ~0.25 at the CB peak energy $E_{\gamma,p}$~50 MeV and P_γ~0.18 for $E_{\gamma,p}$~60 MeV. Strengthening of the collimation up to 12 mm ($\theta_c \sim 1.2\theta_\gamma$) slightly increases the polarization to P_γ~0.2.

The experimental data shows that the CB beam at present time provides even without collimation the polarization enough for photonuclear researches in the range up to 60 MeV.

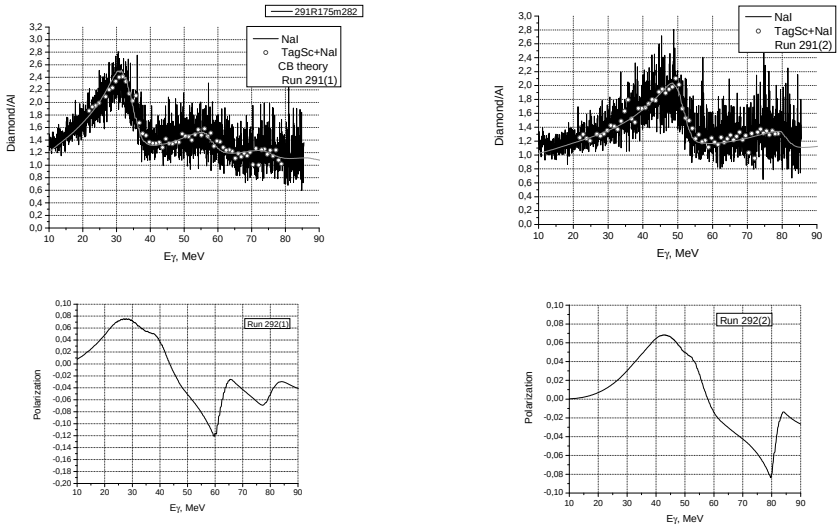

Fig. 2. Spectra of CB measured with NaI (lines) and with FP array in coincidence with the NaI (points) for "row" (022)+(004)+(040)+(02-6)+(06-2)+…orientation and expected polarization. Curves are calculations with ANB code [3] for these conditions.

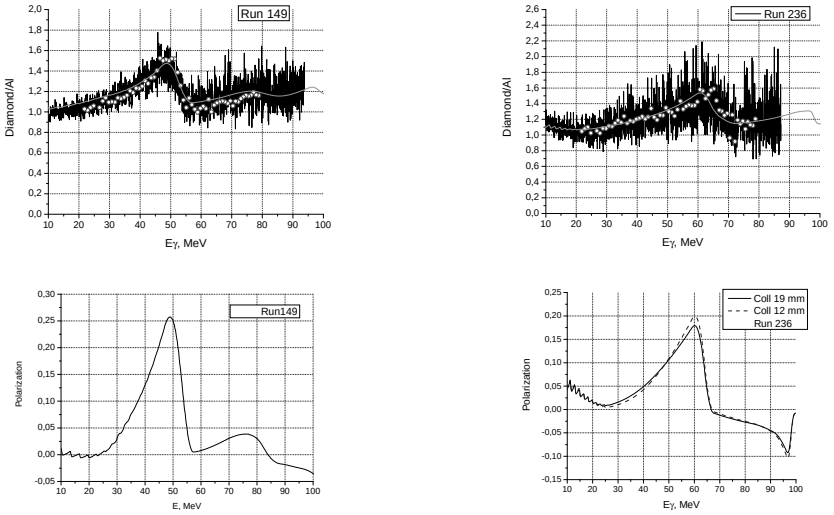

Fig. 3. Spectra of CB measured with NaI (lines) and with FP array in coincidence with the NaI (points) and expected polarization for "points" (0-2-2) (left, collimator 12mm (θ_c~1.2θ_γ)) and (0-2-2)+(004) (right, collimator 19mm (θ_c~1.9θ_γ)). Curves are calculations with ANB code [3].

References

1. J. Brudvik et al. MAX-lab Activity Report 2008, p.490.
2. J. Brudvik et al. Summary of the run period 04.14-04.28.2008.
3. F.A. Natter, P. Grabmayr, T. Helh et all. Monte Carlo Simulation and Analytical Calculation of Coherent Bremsstrahlung and its Polarization. Nucl. Instr. and Meth. B211 (2003) 465-486.

RESPONSE OF THE PANDA ELECTROMAGNETIC CALORIMETER TO PHOTONS IN THE ENERGY RANGE 10 – 120 MeV.

Jason Brudvik[1], Kevin Fissum[3], Kjell Fransson[2], Linda Gerén[4], Sophie Grape[2], Kurt Hansen[1], Lennart Isaksson[1], Tord Johansson[2], Magnus Lundin[1], Klas Marcks[4], Bent Schröder[3], Per-Erik Tegnér[4] and Erik Thomé[2]

[1]MAXLAB, Lund University, P.O. Box 118, S-221 00 Lund, Sweden
[2]Department of Nuclear and Particle Physics, Uppsala University, P.O. Box 535, S-751 21 Uppsala, Sweden
[3]Department of Nuclear Physics, Lund University, P.O. Box 118, S-221 00 Lund, Sweden
[4]Department of Physics, Stockholm University, S-106 91 Stockholm, Sweden

The upcoming FAIR (Facility for Antiproton and Ion Research) facility in Darmstadt will be the major European resource for Hadron Physics in the future. The availability of cooled antiproton beams at the high-energy storage ring HESR will offer completely new perspectives. The physics of systems with strange and charm quarks will be accessible which, in combination with high precision experiments, will open new frontiers in hadron physics. The energy region of HESR with momenta between 1.5 GeV/c and 15 GeV/c is exactly the transition region between the perturbative QCD at short scales and strong QCD.

The envisaged physics programme at PANDA relies heavily on the capability to measure photons with high energy, position and timing resolution over a wide dynamic range from a few MeV up to several GeV. The identification of a single photon as well as the coincident detection of the decay photons from multi-meson exit channels relies heavily on a high and homogenous efficiency. The invariant mass reconstruction requires also a precise determination of the opening angles between decay photons. This can only be achieved by a highly granular calorimeter. A compact scintillator material with a short Molière radius will provide a minimum occupancy of the detector modules. These requirements makes the PANDA electromagnetic calorimeter one of the most difficult and expensive part of the whole detector system. It is one of the most important detector components from physics point-of-view. The electromagnetic calorimeter of the target spectrometer consists of a barrel part with 11 360 crystals, a forward end cap with 3600 crystals and a backward end cap with 592 crystals. $PbWO_4$ (PWO) will be used as detector material. Very encouraging results have been obtained by operating such crystals at temperatures down to -25° C where the light yield increases by a factor of 2.5 as compared to room temperature. A new material composition for the PWO crystals has given an additional increase of the light output by a factor more than 2. This gives a substantially increased performance with respect to the PWO used at the CMS experiment at LHC. Avalanche Photo Diodes (APDs) will be used for the read-out of barrel part and Vacuum Photo Triods (VPTs) are anticipated for the forward end cap.

The nuclear physics groups at KTH, Lund University, Stockholm University and Uppsala University are members of the PANDA collaboration. They have jointly decided to focus on the electromagnetic calorimeter (EMC) with special emphasis of the front end cap as the Swedish hardware contribution to PANDA.

A good understanding of the EMC response for low-energy photons is very important in order to reach the desired resolution in PANDA. MAX-lab is a unique facility for the investigation of the PWO response to such low-energy photons, *i.e.* linearity and energy resolution. The response at higher energies will be measured at MAMI, Mainz and ELSA, Bonn. The

response of PWO crystals to photons in the lower energy region (10 – 120 MeV) has been measured at the tagged photon facility at MAX-lab in a series of experiments. In March 2009 a matrix comprising 25 crystals for the forward end cap of PANDA, equipped with photo-multiplier tubes, was exposed to a collimated photon beam. With two settings of the tagger we covered photon energies in the range 13 to 84 MeV. The measurements at the lower energy setting were done at three temperatures, -25 ^{o}C, -15 ^{o}C and -5 ^{o}C, using a climate chamber, cf. Fig. 1. For the high energy setting the temperature was -25 ^{o}C. Two different pulse-handling electronics were used. In the first preamplifiers, shaping amplifiers and peak-sensing ADCs were used. In the second, the anode signals were fed directly to flash-ADCs. For calibration purposes the photon beam could be aimed at the individual crystals by moving the matrix inside the chamber with a coordinate table.

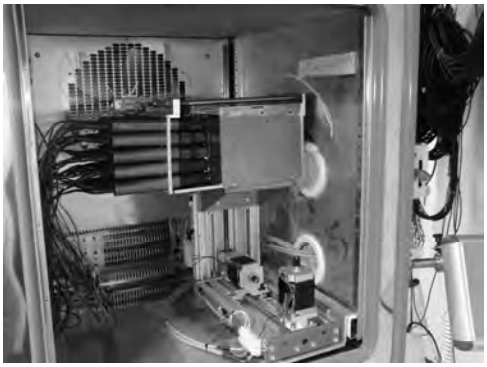

Figure 1. The climate chamber containing the PWO 5 x 5 matrix in place on the coordinate table at the tagged photon beam.

Fig. 2 shows preliminary results for the energy resolution at -25 ^{o}C, using the data from both pulse-handling electronics. The data for the two set-ups are analyzed completely independently. The contributions from the detectors surrounding the central one have been added in this plot using individual thresholds of approximately 1 MeV. There is a good agreement between the results for the two set-ups. The unexpectedly large resolution for photon energies around 25 MeV is due to the energy resolution of the tagged photon beam.

In 2010, the energy resolution of the tagged photon beam will be independently measured using a large sodium iodide detector (CATS). A new prototype matrix of 25 PWO crystals, using the envisaged mounting structure at PANDA, is built and will be tested in beam at MAX-Lab.

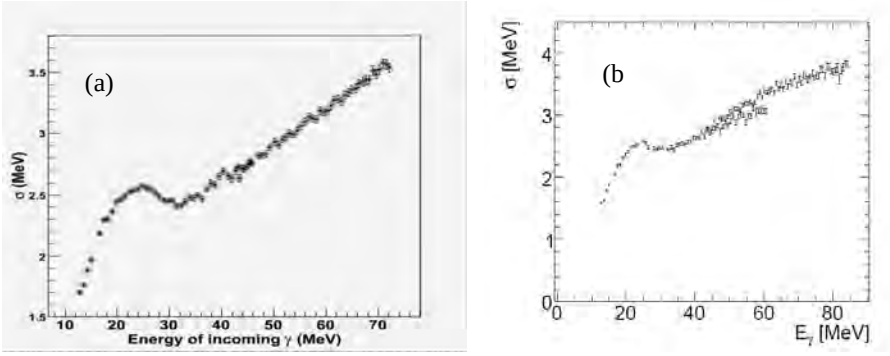

Figure 2 Example of results for the energy resolution σ (= FWHM/2.35) as a function of tagged photon energy at -25 ^{o}C using peak-sensing ADCs (a) and using flash ADCs (b).

Photo-fission Studies of Nuclei by Virtual Photon Tagging at MAX-lab

J. Brudvik[1], N. Grigoryan[2], K. Fissum[1], K. Hansen[1] (cospokesperson), L. Isaksson[1], M. Lundin[1], S. Knyazyan[2], A. Margaryan[2] (cospokesperson), G. Marikyan[2], B. Nilsson[1], L. Parlakyan[2], B. Schroder[1], L. Tang[3], H. Vardanyan[2], Z. Yasin[4], S. Zhamkochyan[2]

[1]MAX-lab, Lund University, Sweden
[2]Yerevan Physics Institute, 2 Alikhanian Bros. St., Yerevan-36, 375036, Armenia
[3]Department of Physics, Hampton University, Hampton VA, USA
[4]Department of Nuclear Engineering, PIEAS, P.O. Nilore, Islamabad, Pakistan

The excitation of nuclei by electromagnetic probes such as real photons (γ-quanta) or virtual photons (inelastic electron scattering) offers attractive features for the study of nuclear phenomena over a broad range of excitation energies. The use of photons in the study of fission of highly excited nuclei is advantageous, since photons are very effective, due to their volume absorption, in heating nucleus, transferring at the same time, relatively low angular momentum to the struck nucleus. In the intermediate and high energy ($E_\gamma \geq 40$ MeV) region the gamma-nucleus reaction has been currently explored in the framework of a two-step interaction models [1-3]. In this approach, firstly a rapid intranuclear cascade, INC, develops through binary intranuclear collisions. During the second stage of the reaction, the excited residual nucleus slowly reaches its final state through a competition between the fission and the particle–evaporation process. The two-step picture clearly assumes that fission is a relatively slow process which samples the target residues only after they have lost a large fraction of their excitation energy. Therefore, the fission of a heavy nuclear system provides an excellent tool for studying the both stages of a complex, high-energy nuclear reaction. Coulomb energy systematics give a clear indication for the binary fission process while fragment angular correlations and mass and energy distributions can be used to estimate average quantities such as linear momentum transfer and mean mass and excitation energy of the fissioning system.

In this respect, interesting possibilities are offered by the measurement of mass-energy-momentum distributions of fission fragments, FF, with monochromatic photons, to investigate the excitation energy dependence of mass distributions comparing the data taken at different photon energy E_γ [3]. In fact such an experimental data allows to study in clean way the thermal effects, in particular the excitation energy dependence of the fission barrier [2]. To date current studies have concentrated on total photofission cross-section measurements of the heavy actinides and only in a few experiments with $E_\gamma \geq 40$ MeV monochromatic photons the mass of FF was indirectly determined [4, 5]. Therefore, more data with mass-energy-momentum distributions of FF, measured directly and precisely by monochromatic photons, were highly desirable.

MAX-lab, where tagged-photon systems from 15 to 190 MeV are exists and development of a large acceptance, two angles, two energy and two velocity, FF detector [6, 7] are planned, is uniquely suited to carry out such a programme. In addition zero angle electron scattering or virtual photon tagging technique [8] is envisaged.

According to this concept, the active fissile target, i.e. the FF detector with a fissile target insight, will be placed instead of radiator (see Fig. 1) and the tagged photon system will be used as a magnetic spectrometer for zero degree scattering electrons. The spectrum and flux of virtual photons produced by relativistic electron scattering at zero degrees can be expressed approximately as t^v/ω, where $t^v \approx 0.02$, is the equivalent radiation length and ω is the virtual photon energy. According to this formula the intensity of virtual photons for 200 MeV and 100 nA electron beam will be about 6×10^7 phton/MeV/sec. In an experiment requiring a thin target, t (r.l.) < t^v, e.g. experiments requiring detection of heavy recoil products or fission fragments, this technique has a clear advantage over conventional photon tagging. First such kind of fission experiment, zero degree electro-fission of ^{238}U, has been performed at Yerevan electron

synchrotron [9]. The virtual photon tagging technique is currently exploited extensively in the hypernuclear spectroscopy experiments at JLab (see e.g. [10]), where thin targets are used to minimize the dE/dx effect.

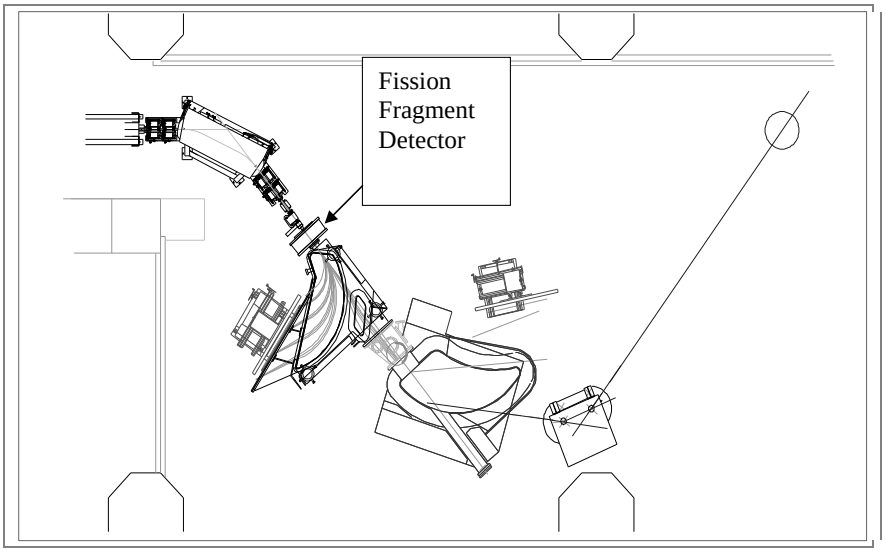

Figure 1: Floor plan of fission study experiments by virtual tagging technique.

The MAX-lab tagging photon system with a dedicated FF detector and small angle electron scattering technique results a powerful experimental setup for performing precise measurements of nearly complete photofission data in the energy range $40 < E_\gamma < 190$ MeV and for nuclei in a wide mass range $50 \leq A \leq 240$. Such an experiment is like a microscope through which we can have a close look at the nature of excited nuclear matter.

We propose these new photofission experiments start with U-238, Th-232 and Bi-209 targets and to take ~10^6 data in the every 10 MeV energy bin and for each of the target.

References

[1] V. S. Barashenkov et al., Nucl. Phys. **A231**, 462 (1974).
[2] A. S. Iljinov et al., Sov. J. Nucl. Phys. **32**, 166 (1980).
[3] T. E. Rodrigues et al., Phys. Rev. **C69**, 064611 (2004).
[4] D. I. Ivanov et al., Sov. J. Nucl. Phys. **55**, 506 (1992).
[5] Th. Frommhold et al., Z. Phys. **A350**, 249 (1994).
[6] K. Assamagan et. al., Nucl. Instr. and Meth. **A426**, 405 (1999).
[7] J.-O. Adler et al., MAX lab Activity Report, 502 (2008).
[8] C. E. Hyde-Wright, W. Bertozzi, J. M. Finn, Electron Scattering at 0°: A Photon Tagging Technique, 1985 Summer Workshop, CEBAF, Newport News, Virginia.
[9] E. A. Arakelyan et al., Sov. J. Nucl. Phys. **49**, 1022 (1989).
[10] O. Hashimoto, H. Tamura, Progress in Particle and Nuclear Physics, **57**, 564 (2005).

Detection of positively charged pions with a CsI/SSD telescope

J. Brudvik, K. Hansen, L. Isaksson, M. Lundin
MAX-lab, Lund

K. Fissum, B. Schröder
Department of Physics, Lund University, Lund

Pion photoproduction experiments are one of the few ways to explicitly test predictions made at low energies by QCD based effective theories. The research program within the Nuclear Physics group at MAX-lab focuses strongly on this area.

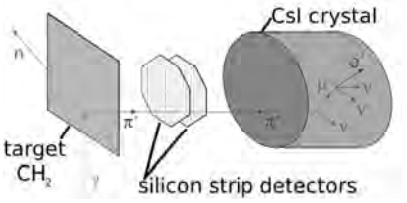

Figure 1: Diagram of a π^+ produced by a photon interacting with a proton in a CH_2 target, which is then detected by the CsI/SSD telescope.

One of the detector setups used in the detection of positively charged pions is a ΔE-ΔE-E telescope formed by two thin silicon strip detectors (SSD) and a CsI(Tl) crystal. The two SSDs are 0.5 mm thick, 64 mm wide, octagonal in shape and are comprised of 64, 1 mm wide strips. The strips are read out in groups of two, which, for a separation distance between the SSDs of 15 mm, gives an angular resolution of approximately 15°. The CsI(Tl) crystal is cylindrical in shape, 4 inches in length with a 5 inch diameter, read out by a 5 inch photomultiplier attached to the end. The setup was arranged with the first SSD placed at 90° to the photon beam, approximately 10 cm from a 1 mm thick CH_2 target lying in the photon beam path, and the CsI(Tl) crystal placed 15 mm behind the second SSD, as depicted in Figure 1. In this arrangement, the solid angle of the telescope is set by the second SSD, and is approximately 330 msr. The separation of particles of different mass is accomplished with the standard ΔE-E method, by examining the energy deposited in the SSDs compared to that deposited in the CsI(Tl). An example of this is shown in Figure 2-a, where clear separations between different particles are seen. This method however cannot be used to distinguish between positively and negatively charged pions. To separate pions with opposite charges from each other, the decay signature of the π^+ was searched for. A π^- entering the CsI(Tl) detector is quickly captured by a nucleus, while a π^+ is repelled by a nucleus and decays according to the following two step process:

$$\pi^+ \rightarrow \mu^+ + \nu \quad (\tau_{\pi^+} = 26.0\,ns,\ E_{\mu^+} = 4.12\,MeV)$$

$$\mu^+ \rightarrow e^+ + 2\nu \quad (\tau_{\mu^+} = 2.197\,\mu s,\ E_{e^+} = 5 - 50\,MeV)$$

The use of a 20 MHz Flash ADC attached to the CsI(Tl) detector makes it is possible to look for the presence of this process. An example of events recorded in the Flash ADC is shown in Figure 3. Choosing events such as these, with certain peak separations and heights, it is possible to better separate positively charged pions from other particles, as was done in constructing Figure 2-b.

An experimental beam-time dedicated to the photoproduction of positively charged pions took place over approximately 4 weeks during May and June of 2009. During this time, various types of targets were used in conjunction with the CsI/SSD telescope, with the emphasis being on CH_2, of which approximately 215 hours of data were recorded. The aim of this experiment was to study the photoproduction of pions from the hydrogen nucleus, therefore background measurements with a pure Carbon target were also performed, 60 hours of such data were recorded. Photons striking the target were produced via bremsstrahlung using electrons with energies of 194 MeV.

The time separation between the two Flash ADC pulses for selected events can be seen in Figure 4, which has a distribution of that which is expected for the second pulse to have come from μ^+ decay. Figure 5 shows the focal plane tagger channel hit versus

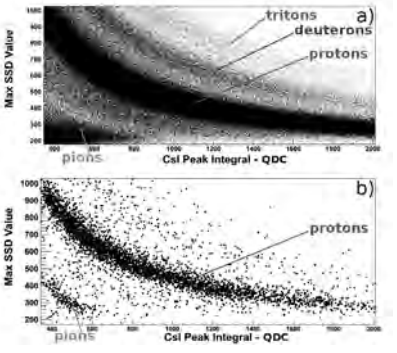

Figure 2: Energy deposits (in arbitrary units) in the first SSD versus in the CsI(Tl) crystal, a) without any event selection, and b) with cuts on the pulses seen in the CsI(Tl) using the Flash ADC. Pions are clearly separated from protons and from the background in b).

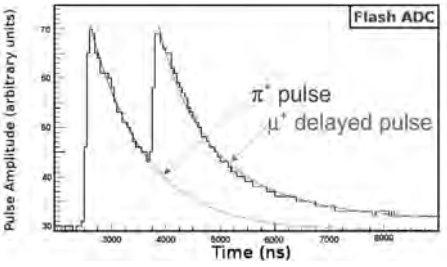

Figure 3: Readout of the CsI(Tl) detector as a function of time for one event using the Flash ADC.

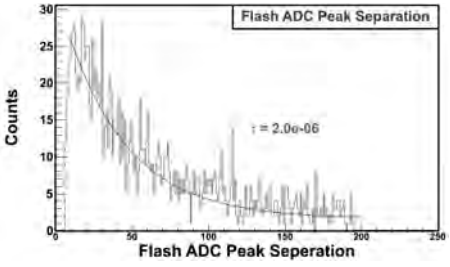

Figure 4: Time separation between the two pulses in the Flash ADC for approximately 1,400 selected events, both tagged an untagged. The fit to the distribution gives strong support to these events being the result of a π^+ decay, which decays into a μ^+, which in turn has a lifetime of 2.197 μs.

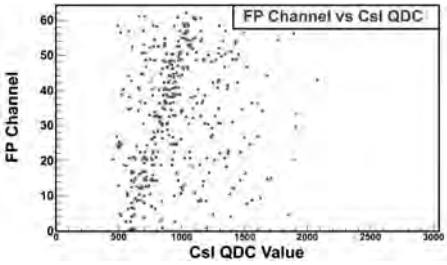

Figure 5: Correlation between CsI energy deposit and focal plane channel.

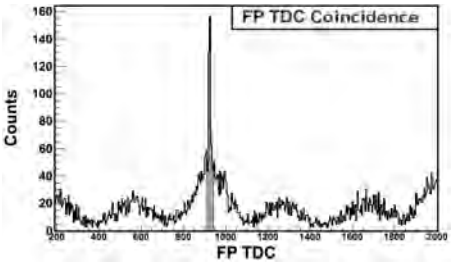

Figure 6: Timing coincidences between events in the focal plane and pion events striking the detectors. The broad background comes from random coincidences, while the large yellow colored spike comes from true event coincidences.

energy deposit in the CsI detector. Figure 6 shows the time coincidences between the focal plane and experimental detectors, with events in the coincidence spike being used to produce 5. Figures 4, 5, and 6 together are strong evidence that tagged pions have been detected.

This marks the first time tagged pions have been produced at MAX-lab. Having tagged pions means that individual photons can be associated with the pions they produced through interactions with the target. A full analysis of the data is still in progress, however preliminary results appear promising with approximately 1000 tagged pions being detected by the CsI/SSD telescope.

The amount of data existing world wide for the process $\gamma + p \rightarrow \pi^+ n$ is lacking at energies close to pion production threshold. Eventually, differential cross sections will be calculated for this process at various angels and energies, in order to fill-in the gaps in the world data set. These measurements will then be compared with various competing theoretical predictions.

Elastic Compton Scattering from Deuterium at 40-110 MeV

The Compton@MAX-lab Collaboration

The COMPTON@MAX-lab collaboration has been analyzing the $\gamma\,(d,d)\,\gamma$ data collected in 2007 and 2008 in parallel to our continued experimental efforts in 2009. The small absolute cross section of this reaction (on the order of 10 nb/sr) necessitates careful and detailed analysis in order to extract the cross sections with minimum error bars. Given our unique beam and setup - 10^6 electrons/s/channel, 50% overlap in the focal plane - we have had to tackle issues not considered by other nuclear physics collaborations at MAX-lab.

Figure 1: The liquid-deuterium target cell. The photon beam passes along the symmetry axis of the cylinder.

The details of the experimental setup can be found in previous MAX-lab activity reports as well as in another report in this issue by M. A. Kovash. The analysis can be broken down into three parts:

1) Photon Spectrometers: The three large (20"x20") NaI detectors, as depicted in Figure 2 are used to collect the scattered photons. The good energy resolution of these detectors, better than 2% at 100MeV, al lows for the separation of inelastic scattering events which has not always been the case in earlier measurements of this reaction. The analysis has revealed the need to carefully correct for gain drifts in the PMTs and pedestal drifts in the ADCs, otherwise the energy resolution we require would be lost.

2) Focal Plane Hodoscope: The SAL focal plane allows for precise measurement of the recoil electron counts and timing information. The timing information is used to identify the prompt photons, as well as correcting for rate dependent effects in the focal plane electronics. The largest effects are due to accidental electrons stopping the TDC before the true event occurs (stolen trues) and accidental coincidences in the overlap modules when no electron is present (ghosts). The size of these effects increase with beam intensity and can be quite difficult to deduce from scattering data. These corrections are just now being understood and a dedicated run period is scheduled for early 2010 to investigate the effects in a controlled setting.

3) Monte Carlo Simulations: A working GEANT4 code has been implemented for the photon spectrometers and is used to correct for the finite geometry effects of the experimental setup. The simulation also allows for corrections as a result of cosmic ray and charged particle cuts. A second simulation is in development as we continue to work on the corrections due to the rate dependent effects in the focal plane electronics. The details of this simulation are dependent on the specific setup and, as a result, will not be in a final state until after the aforementioned 2010 run period.

Currently, most of the data has been analyzed. Final results will not be shared until the rate dependent tagger corrections have been applied. However, at this time, the uncertainties on the yields are understood (these are believed to be the major sources of errors in the analysis). The

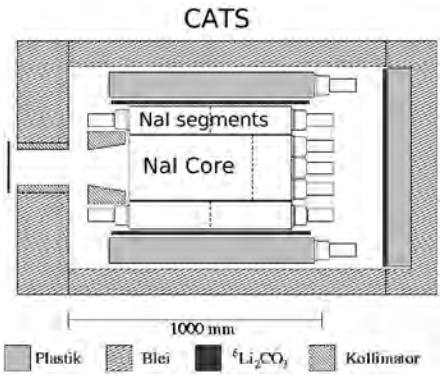

Figure 2: The CATS detector, one of the three large NaI photon detectors used. The other two, BUNI and DIANA, have similar designs.

Figure 3: The focal plane hodoscope shown in position next to the main tagger.

statistical errors vary from 3-8% (summed over all the focal plane channels) with an average of 6%. The systematics run from 2-4% and average about 3%. In general, the larger errors are associated from the lower photon energy runs. The errors that will be introduced as a result of the simulations can not yet be stated definitively. However, current estimates put these uncertainties at the 2-4% level. More will be known once the controlled test run takes place in 2010.

For perspective, the error bars on the current twenty-nine data points for $\gamma\,(d,d)\,\gamma$ are typically larger than 7% (stat) on large energy bins (7-20 MeV wide). This collaboration has twenty-four data points, at a wider energy region, with comparable statistical uncertainty and energy bins that are 7-8 MeV wide. The resulting improvement in the world data set is expected to greatly improve our knowledge of the neutron polarizabilities and its underlying structure.

Elastic Compton Scattering on Deuterium
Compton@MAX-lab Collaboration

The Compton collaboration collected 4 weeks of additional scattering data on targets of carbon, kapton, and liquid deuterium during November, 2009. The goals of this run were three-fold: to add to the statistical precision of the collaboration's previous data set at this same energy; to test for consistency with previous data sets after having completed improvements to the tagging system; and to add new scattering data at a previously unmeasured angle.

Compton scattering data were collected with the BUNI, CATS, and DIANA NaI spectrometers operating independently in singles trigger mode. In order to maximize the number of scattered Compton events which were collected, DIANA was positioned on beam-right at a (lab) scattering angle of 150°, CATS on beam-left at 90°, and BUNI on beam-right at 60°. This run then provided new cross section data at 90°, and a remeasurement of the 60° cross section using a different detector. No significant changes were made to either the setup or the electronics for these detectors since the previous runs, and all three detectors were found to perform normally.

Following calibration of each detector with low-intensity in-beam runs, scattering data were collected from both natural carbon and thick (multi-layered) kapton targets. The carbon data were accumulated over a period of 17 hours and will provide a cross-check of the overall cross section normalization required to analyze the deuterium results. Six hours of kapton data were also collected, and these will be used to make a small background subtraction of the deuterium spectra.

The liquid deuterium cell was operated with essentially no change from the way it was used in November, 2008. The target performed well throughout its 3 weeks of use.

An electron beam energy of 164.7 MeV was used, along with the main tagger operated with a setting of 477 giving tagged gamma ray energies spanning the range from 81.6 to 115.8 MeV. The beam collimator diameter was 19 mm. Throughout most of the run we used an aluminum converter with a thickness of 150 μm. Tagger hits were recorded in both single-hit and multi-hit TDCs for every event.

Analysis of our previous Compton data has revealed difficulties thought to be associated with operating the tagger electronics at a very high instantaneous counting rate. We therefore took several steps to lower this rate as well as to reduce the dead time in the tagger

electronics. First, the pulse widths from the individual tagger hodoscope discriminators were reduced to 25 nsec. Most tagger channels had previously used pulse widths set near to 50 nsec. Also, a time delay was added to the tagger TDC start signal so that the true coincidence events appeared with a relatively short time delay in the TDC spectra. This significantly reduced the correction needed for accidental stolen-stops in the single-hit TDCs. We also made a deliberate attempt to increase the average duty factor of the electron beam. This involved operating a software version of a beam duty-factor meter while making adjustments to the beam tuning. We found that the greatest improvement to the duty factor resulted from increasing the frequency of the extraction kicker to over 100 MHz. Finally, we limited the average beam current such that the instantaneous rate in the individual tagger counters did not exceed 3 MHz.

A total of approximately 260 hours of scattering data were collected from the deuterium target – a fairly typical number for three 'metric weeks' of running which also included daily measurements of the tagging efficiency and calibrations of the quad segments of BUNI using a radioactive source. Replays of the missing-energy spectra were generated daily using an off-line analysis code. It was found that all three detectors produced easily discernible elastic peaks from deuterium. The figure below shows one such missing-energy spectrum as recorded in CATS during a total of just 59 hours of data-taking. The elastic deuterium peak, appearing between the cursors, is readily apparent in this histogram.

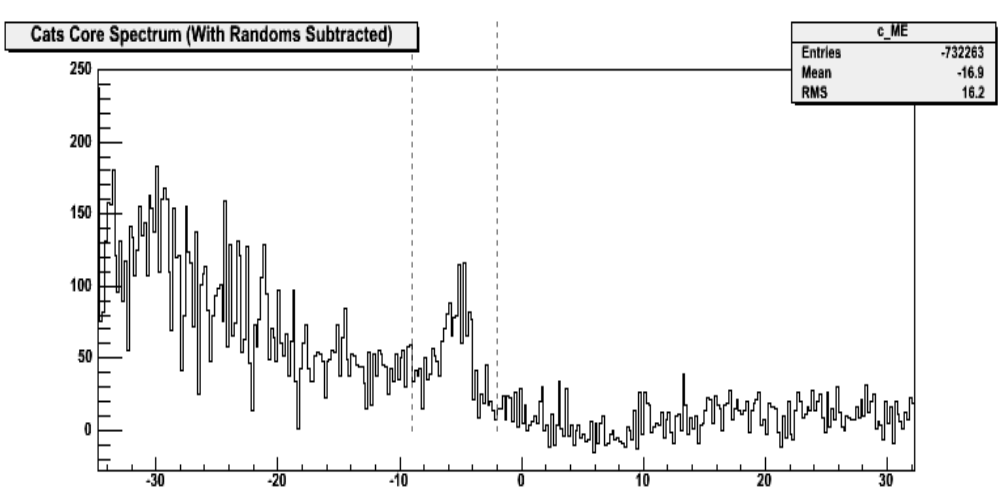

Positive Pion Photoproduction from the Proton Experiment NP-014

G.V. O'Rielly
University of Massachusetts Dartmouth, North Dartmouth MA 02740, USA
for the
PIONS@MAX-lab Collaboration

The development of modern descriptions of the strong interaction based on QCD can now provide detailed predictions for pion photoproduction from the nucleon in the nuclear regime. Comparison of these predictions with the results from accurate measurements serves as a stringent test of these QCD-based models, and will confirm our understanding of the underlying dynamics in the nuclear system. In addition, measurements of the angular distributions for the $\gamma p \rightarrow n\pi^+$ reaction channel are needed to extract the p-wave contribution for comparison with the predictions from Chiral Perturbation Theory calculations. These measurements are also essential for the partial-wave analyses performed by the MAID and SAID groups. Despite this interest, there are few modern data sets for the $\gamma p \rightarrow n\pi^+$ reaction at energies below the Δ-resonance, with extensive angular distributions only at threshold and above 200 MeV, and no tagged photon data in the energy range between 155 and 185 MeV.

To address this need for new, high-quality data on the charged pion channels at energies below 200 MeV, the PIONS@MAXLAB collaboration is performing measurements of the $\gamma p \rightarrow n\pi^+$ reaction using the MAX-lab tagged photon facility. To detect the out-going pion, several different detector systems are being used. This summary reports on results from the xSAL detectors, which are a set of four monolithic plastic scintillator counters configured as ΔE-E telescopes. The stopping counters have dimensions chosen to stop the highest energy pions produced by the MAX-lab tagged photon beam. Complementing the measurements with the xSAL telescopes are measurements with different detector systems and pion identification methods; RANGE and CsI. The use of independent detectors will provide important cross-checks throughout the analysis and for the final cross section results.

A dedicated four-week production run with the three independent detector systems operational took place during the summer of 2009. The set-up of the xSAL trigger and tagger electronics was done in March/April 2009 ensuring this system was fully configured and maximizing the production run time. The four xSAL telescopes were installed at laboratory angles of 43°, 137° and two at 90°, these angles have been identified as having the maximum sensitivity to differences between the existing MAID and SAID partial-wave analysis solutions [1]. Data were collected from CD_2, CH_2, C and Ta targets. The analysis of the $\gamma d \rightarrow np$ reaction (from the CD_2 target) will provide a crucial energy calibration for the tagged photon beam. Data for the $\gamma p \rightarrow n\pi^+$ reaction will come from the CH_2 target, with the C target used for background subtraction. The data obtained from the Ta target will be used to investigate the A-dependence of the (γ,π^+) reaction and to compare with modern theories [2, 3].

Due to the very low event rate for the (γ,π^+) reaction, standard particle identification techniques based on ΔE vs. E *stopping power* are insufficient to separate pions from the much larger electron and proton background. To reliably identify pion events, analysis methods based on detecting the $\pi^+ \rightarrow \mu^+$ decay in the xSAL E-counter were used. This technique identifies the 4.12 MeV muon

based on the energy deposited in a short- versus long-gated QDC. Using this method, pion events are clearly identified in the data.

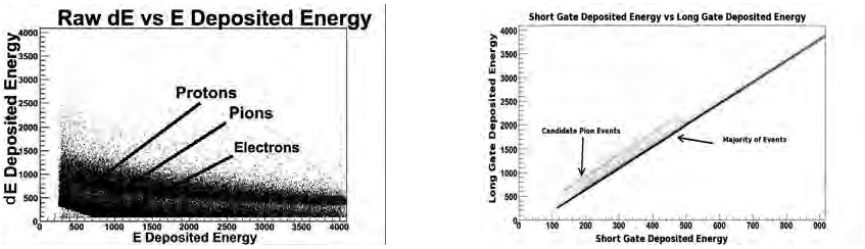

(left) ΔE vs. E *stopping power* for all events in an xSAL counter. The pion events are swamped by background electrons and protons. (right) Energy deposited in long- vs. short-gated QDC. The candidate pion events are located above the *equal energy* band produced by the background events.

Due to variations in the signal pulse shapes, the efficiency for the π^+ detection using this method is difficult to calculate precisely. To determine the efficiency accurately, a second method investigates the time distribution of the candidate pion events – this must match the known 26 ns lifetime for the $\pi^+ \rightarrow \mu^+$ decay. The results of this analysis are shown below.

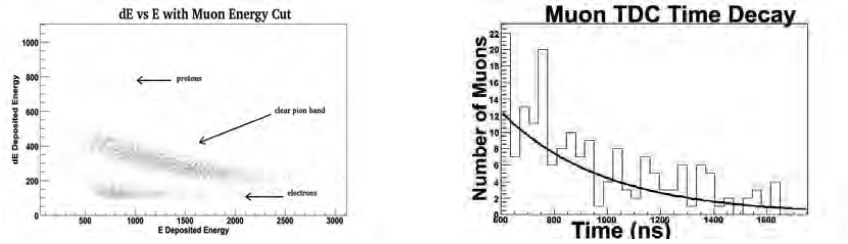

(left) ΔE vs. E *stopping power* for candidate pion events selected using information from the energy deposited in the long- vs. short-gated QDC. The pion events are now clearly seen well separated from background events. (right) The time distribution of these candidate pion events exhibits a decay time of (26.7 ± 2.2) ns, consistent with the $\pi \rightarrow \mu$ lifetime.

The combination of using both energy and timing information from the π^+ decay in the xSAL E-counter, with the appropriate calibration of the data acquisition electronics, enables the reliable identification of pion events with a well-understood detection efficiency. This is essential for determining accurate differential cross sections for the $\gamma p \rightarrow n\pi^+$ reaction.

The pion yields from each xSAL telescope have been determined. Additional work is required to subtract the background due to accidental coincidences with electron events in the tagger focal plane and to apply corrections for the misidentification and loss fractions due to analysis cuts, and for the π^+-detection efficiency. Monte-Carlo simulations, using the *GEANT-4* package, of the experiment and detector systems are currently underway to determine the acceptance for each xSAL telescope. This will be combined with the tagging efficiency measurements to determine final differential cross sections.

[1] K. Magno, M.S. thesis, University of Massachusetts Dartmouth (2007)
[2] A. S. Iljinov, I. A. Pshenichnov, N. Bianchi *et al*., Nucl. Phys. A616, 575, (1997)
[3] I. A. Pshenichnov, B. L. Berman, W. J. Briscoe *et al*., Eur. J. Phys. A. 24, 69, (2005)

Threshold π^+ production in tagged photonuclear reactions with heavy nuclei

S. V. Shende, B. Jakobsson, P. Golubev, V. Avdeichikov and the MAX-Tagg collaboration

Pion photoproduction cross sections on heavy nuclei close to threshold provides information of in-medium pion-nucleon interaction and pion propagation through nuclear matter, much less excited than in corresponding nucleus-nucleus or proton-nucleus reactions. Experiments at higher energies have been performed at several international facilities but in the near-threshold region data is scarce. The first non-tagged pion photoproduction results of this kind, obtained at MAX-lab with light target nuclei, ^{2}H, ^{12}C and ^{27}Al were presented in Ref. [1]. Comparing these data to standard cascade models [2] indicates that a deep , -20 MeV, optical potential is needed [1]. In order to follow this up we decided to introduce a heavy, mono-isotopic target nucleus, ^{181}Ta, for the next run. This run has now been carried out and it coincided with the first successful operation of the tagger device. Consequently, we could store energy-tagged data from $\gamma + {}^{181}$Ta, $\gamma + {}^{12}$C, and $\gamma + CH_2$ reactions at 172 – 182 MeV.

Three types of detector systems [1,3], in all 7 telescopes, were used to register pions. Here we present the data analysis of the two RANGE telescopes [1], α and β, each with five NE102 plastic scintillators with different thicknesses (5, 10, 20, 50, 5 mm respectively), read out by Philips XP2002 photomultipliers. The data was taken in two angular positions: 30 – 90 deg and 60 – 120 deg and in all cases we could register protons (22 – 108 MeV) with little or no bias.

Fig 1 (left) shows an example of a raw $QDC_{\Delta E}$ - QDC_E correlation and 1 (right) the same data after a bit-pattern definition of the stop detector has been made. The proton structure (p) is quite easy to identify and the effect of pattern recognition provides a useful guide for defining the area of stopped protons. However pions (π^+ and π^-) are not visible as a structure separated from the background. In order to identify π+ we use instead the method of pulse shape analysis, described in Ref. [1], to look for the extra energy coming from the μ+ particle of the 99.9 %, $\pi^+ \rightarrow \mu^+ \nu$ decay with 26 ns decay time. Apart from the usual losses of π^+ due to decay in flight, reactions in detector and other material and escaping muons there is now also a random background not associated with tagger signals. The method to obtain this non-tagged background is easier to establish for protons where statistics is higher and the only correction apart from this one comes from reactions in material.

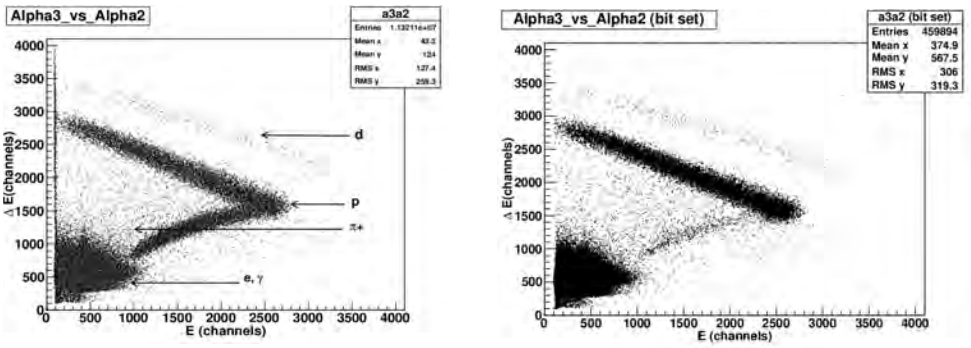

Fig 1. E vs ΔE (left - raw data and right – pattern condition introduced)) for two α–detectors.

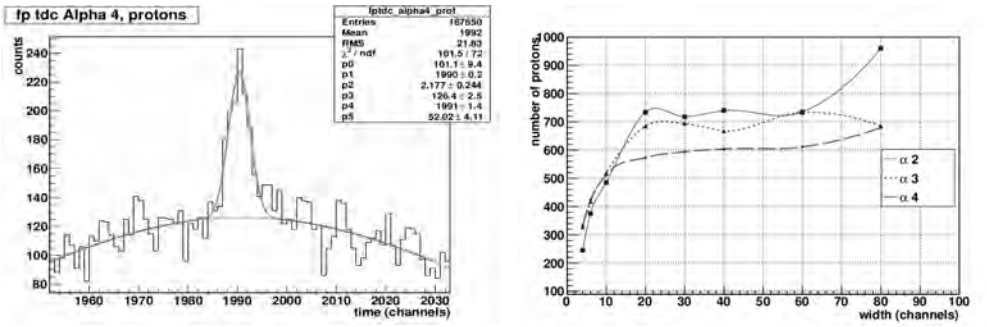

Fig 2. (left) Focal Plane TDC spectrum for stopped protons in α4. Signal and background is fitted by two Gaussian functions (solid cures). (right) Proton yield as a function of the width of the integration window.

Fig. 2 (left) shows a typical focal plane TDC spectrum (detector α4) for stopped protons. A coincidence signal is visible on top of the background which can be described by two Gaussians, one representing background particles in coincidence with tagger signals and the other the general (random) component. To extract the actual number of protons coming from the reactions, the sum of the two background distributions is subtracted from the total number of counts in each bin. The true coincidences fall in a finite time interval determined by the dynamical width (flight time interval in stop detector) and electronics resolution. Instead of defining this interval we

plot the number of excess protons as a function of the interval (width in Fig. 2 – right). The idea is that when the proper time interval is obtained the excess number should remain constant if the background is well fitted. Fig 2 (right) shows examples where this is true (α3) and false (α4) but in all examples a plateau level can be well defined.

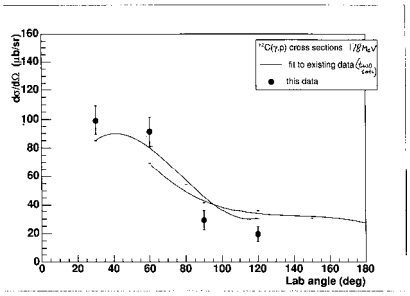

Fig. 3. Proton differential cross section, dσ/dΩ, compared to existing data.

The proton cross sections, calculated with this background subtraction and a simple correction for reactions in material based on known mean-free-paths, are compared with the existing data for the $\gamma + {}^{12}C$ reaction in fig.3. The agreement indicates that the tagger efficiency and the background subtraction are under control. The pion identification, which is in progress will benefit from the possibility to determine absolute cross sections both directly and by normalizing to protons.

References:

[1] P. Golubev et al., Nuclear Physics A, 806, 216-229 (2008).
[2] B.Jakobsson et al., MAX-lab/NP proposal 3
http://www.maxlab.lu.se/kfoto/ExperimentalProgram/PAC/2008/props.html

Towards a large acceptance neutron-spectrometer array
MAX-lab, Lund University

J. Sjögren*, J. Annand, S. Al Jebali, J. Brudvik, K. Fissum, K. Hansen, L. Isaksson, M. Lundin, B. Nilsson, B. Schröder, H. Svensson

April 18, 2010

During 2009, work began on a new neutron-spectrometer array specifically designed for the Photonuclear group. Funding for this project has been provided by Fysiografen in Lund and the Crafoord Foundation. The goal is a highly configurable, liquid-scintillator based multi-cell neutron spectrometer which will eventually be of use for both unpolarized and polarization-transfer experiments. Protoype work has commenced (see Ref. [1, 2] for details).

In the spring of 2009, the design and construction of a prototype detector cell commenced (see Fig. 1). Components impossible to produce onsite were ordered from local companies and from specialist companies abroad. Sufficient NE-213 liquid scintillator to complete several detector cells was supplied by Glasgow U. The detector prototype was completely assembled by the end of August 2009.

Once assembled, source testing of the performance of the detector began. Unfortunately, the existing neutron fission-fragment source (^{252}Cf) had completed its useful lifetime. Fortunately, the Sep09 runperiod included an experiment on the photodisintegration of ^{4}He, a process which has several reaction channels that produce neutrons. In fact, the setup of this experiment already included the existing Nordball neutron detector cells. Thus, the prototype was used to replace one of the least efficient Nordball detectors. Data were collected with beam prior to thorough source testing of the detector cell. A subset of the data acquired are presented and briefly explained in Fig. 2.

The design of the next version of the detector cell has commenced based upon our experience with this first prototype.

References

[1] Luis El-Sheikh. Design and Simulation of Neutron Detectors. Master's thesis, Lund University, 2009.

[2] J. Sjögren. Construction and initial testing of a neutron detector prototype. Master's thesis, Lund University, 2009.

*Corresponding author

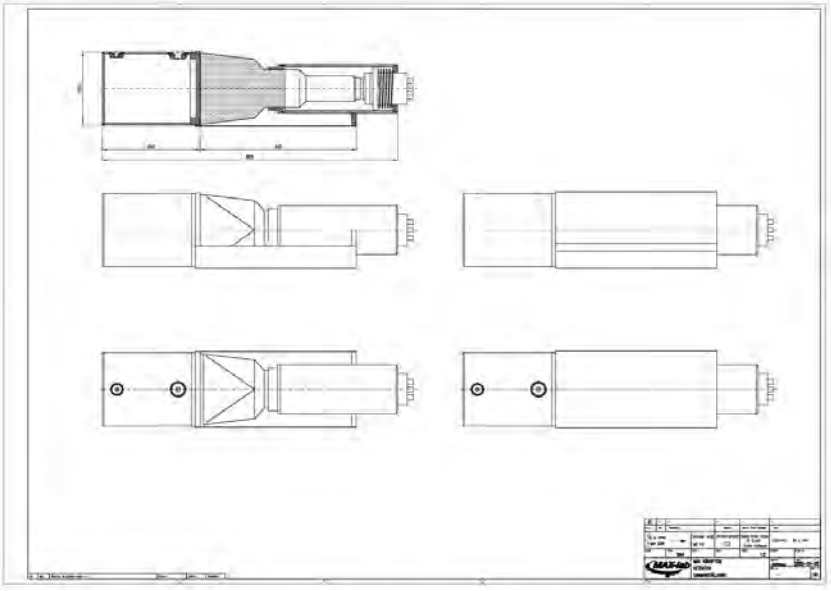

Figure 1: Drawing of the prototype

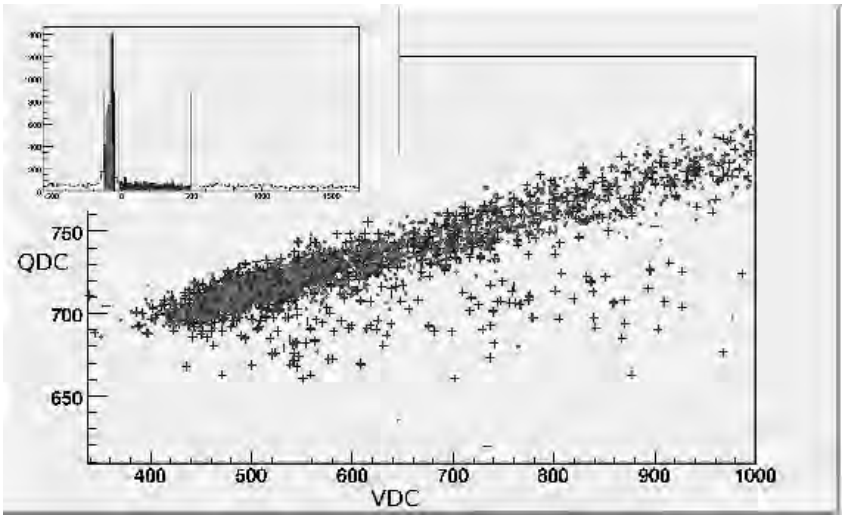

Figure 2: Data acquired during the Sep09 run. The small window shows the time distribution (TDC plot), where red indicates the very prominent gamma flash and blue indicates the timing region where neutrons are expected. A random photon background is present in all parts of the time distribution. In the larger (QDC/VDC) window, red dots correspond to data from the gamma flash and blue crosses to data in the region where neutrons can be expected. Separation clearly exists, but more neutron data are needed.

Publications based upon work done at MAX-lab

M. Abu-samha, K.J. Børve, M. Winkler, J. Harnes, L.J. Sæthre, A. Lindblad, H. Bergersen, G. Öhrwall, O. Björneholm, and S. Svensson,
The structure of small water clusters: Imprints on the core-level photoelectron spectrum,
J. Phys. B: At. Mol. Opt. Phys., 42, 055201, 2009.

J. Adell, M. Adell, I. Ulfat, L. Ilver, J. Sadowski, and J. Kanski,
Formation of MnBi layders on (Ga,Mn)As,
Phys. Rev. B 80, 075204, 2009.

B. Agnarsson, B. Qi, K. Szamota-Leandersson, S. Olafsson, and M. Göthelid,
Investigation on the role of indium in the removal of metallic gallium from soft and hard sputtered GaN(0001) surfaces,
Thin Solid Films, 517, 6023, 2009.

D. Agren, R. Schnell, and G. Schneider,
The C-terminal of CysM from Mycobacterium tuberculosis protects the aminoacrylate intermediate and is involved in sulfur donor selectivity,
Febs Lett., 583, 330, 2009.

A. Agui, T. Uozumi, M. Mizumaki, and T. Käämbre,
Intermetallic charge transfer in $FeTiO_3$ probed by resonant inelastic soft X-ray scattering,
Phys. Rev. B 80, 229905, 2009.

M. Ahrén, L. Olsson, A. Klasson, F. Söderlind, M. Engström, P.-O. Käll, and K. Uvdal,
Synthesis and characterization of PEGylated Gd_2O_3 nanoparticles for MRI contrast enhancement,
Langmuir, in press.

T. Aitasalo, J. Hassinen, J. Hölsä, T. Laamanen, M. Lastusaari, M. Malkamäki, J. Niittykoski, and P. Novák,
Synchrotron Radiation Investigations of the $Sr_2MgSi_2O_7:Eu^{2+},R^{3+}$ Persistent Luminescence Materials,
J. Rare Earths, 27, 529, 2009.

S. Aksela, M. Patanen, S. Urpelainen, and H. Aksela,
Direct experimental determination of atom-molecule-solid binding energy shifts for Sb and Bi,
Submitted to Phys. Rev. Lett.

F. Allegretti, M. Leitner, G. Parteder, B. Xu, A. Fleming, M.G. Ramsey, S. Surnev, and F.P. Netzer,
The (100) -> (111) Transition in Epitaxial Manganese Oxide Nanolayers,
In: Physics and Engineering of New Materials, Eds.: D.T. Cat, A. Pucci, K. Wandelt, Springer-Verlag, p.163, 2009.

V.Yu. Aristov, O.V. Molodtsova, V.V. Maslyuk, D.V. Vyalikh, T. Bredow, I. Mertig, A.B. Preobrajenski, and M. Knupfer,
Electronic properties of potassium-doped FePc,
Submitted to Org. Electr.

V.Yu. Aristov, G. Urbanik, K. Kummer, D.V. Vyalikh, O.V. Molodtsova, A.B. Preobrajenski, C. Hess, B. Büchner, I. Vobornik, J. Fujii, G. Panaccione, Yu.A. Ossipyan, and M. Knupfer,
Graphene synthesis on a SiC/Si wafer opening perspectives for mass production,
Nano Lett., 10, 992, 2010.

L.M. Arnbjerg, D.B. Ravnsbæk, Y. Filinchuk, R.T. Vang, Y. Cerenius, F. Besenbacher, J.-E. Jørgensen, H.J. Jacobsen, and T.R. Jensen,
Structure and dynamics for $LiBH_4$ – LiCl solid solutions,
Chem. Mater., 21, 5772, 2009.

A. Bakali, R. Knaust, and P. Nordlund,
Crystal structure of the kinase domain of the human EphB1,
In manuscript.

T. Balasubramanian, B.N. Jensen, S. Urpelainen, B. Sommarin, U. Johansson, M. Huttula, R. Sankari, E. Nõmmiste, S. Aksela, H. Aksela, and R. Nyholm,
The Normal Incidence Monochromator Beamline I3 on MAX III,
AIP Conference Proceedings, in press.

A. Baldacci, P. Stoppa, S. Giorgianni, and R. Wugt Larsen,
High-Resolution Fourier Transform Infrared Spectrum of $CH_2D^{79}Br$: The Ground, $v_5 = 1$, and $v_9 = 1$ State Constants,
Mol. Phys. 108, doi: 10.1080/00268970903567270, 2010.

G. Barkhordarian, T.R. Jensen, S. Doppiu, U. Bösenberg, A. Borgschulte, R. Gremaud, Y. Cerenius, M. Dornheim, T. Klassen, and R. Bormann,
Formation of $Ca(BH_4)_2$ by Hydriding CaH_2-MgB_2 Composites,
J. Phys. Chem. C 112, 2743, 2008.

M. Bergknut, P. Persson, and U. Skyllberg,
Molecular characterization of brominated persistent pollutants using extended X-ray absorption fine structure (EXAFS) spectroscopy,
Anal. Bioanal. Chem., 390, 921, 2008.

M.H. Berntsen, P. Palmgren, M. Leandersson, A. Hahlin, J. Åhlund, B. Wannberg, M. Månsson, and O. Tjernberg,
A spin- and angle-resolving photoelectron spectrometer,
Rev. Sci. Instr., 81, 035104, 2010.

C.L. Berthold, H. Wang, S. Nordlund, and M. Högbom,
Mechanism of ADP-ribosylation removal revealed by the structure and ligand complexes of the dimanganese mono-ADP-ribosylhydrolase DraG,
Proc. Natl. Acad. Sci. USA (PNAS), 106, 14247, 2009.

P. Bhatt, E. Carlegrim, A. Kanciurzewska, M.P. de Jong, and M. Fahlman,
Electronic structure of thin film iron-tetracyanoethylene $Fe(TCNE)_x$
Appl. Phys. A 95, 131, 2009.

P. Bhatt, A. Kanciurzewska, E. Carlegrim, M. Kapilashrami, L. Belova, K. Venkat Rao, and M. Fahlman,
Ferromagnetism above room temperature in nickel-tetracyanoethylene thin films,
J. Mater. Chem., 19, 6610, 2009.

S. Biedron, L. Giannissi, M. Ferrrario, and S. Werin,
Workshop on high-harmonic seeding for present and future short wavelength Free-Electron Lasers,
Synchr. Rad. News, Vol. 22, No. 4, 2009.

O. Björneholm, G. Öhrwall, and M. Tchaplyguine,
Free clusters studied by core level spectroscopies,
Nucl. Instrum. and Methods in Phys. Res. A 601, 161, 2009.

C. Bonneau, J. Sun, R. Sanchez-Smith, B. Guo, D. Zhang, and X.D. Zou,
An Open-Framework Germanate Built from the Hexagonal Packing of Rigid Cylinders,
Inorg. Chem., 48, 9962, 2009.

Ø. Borck, I.-H. Svenum, and A. Borg,
Adsorption of methanol on NiAl(110) and Ni_3Al(111): A DFT study,
Surf. Sci., 603, 2378, 2009.

J.M. Bourhis, C. Vignaud, N. Pietrancosta, F. Gueritte, D. Guenard, F. Lederer, and Y. Lindqvist,
Structure of human glycolate oxidase in complex with the inhibitor 4-carboxy-5-[(4-chlorophenyl)sulfanyl]-1,2,3-thiadiazole,
Acta Cryst. F 65, 1246, 2009.

M. Bremholm, J. Becker-Christensen, and B. Brummerstedt Iversen,
High-Pressure, High-Temperature Formation of Phase-Pure Monoclinic Zirconia Nanocrystals Studied by Time-Resolved in situ Synchrotron X-Ray Diffraction,
Adv. Mater., 21, 3572, 2009.

B. Brena, P. Palmgren, K. Nilsson, Shun Yu, F. Hennies, B. Agnarsson, A. Önsten, M. Månsson, and M. Göthelid,
InSb-TiOPc interfaces: band alignment, ordering and structure dependent HOMO splitting,
Surf. Sci., 603, 3160, 2009.

W.J. Briscoe, J. Brudvik, K.G. Fissum, K. Hansen, L. Isaksson, M. Lundin, B. Nilsson, and B. Schroder,
Nuclear physics program at MAX-lab,
Chinese Phys. C 33, 1159, 2009.

A.J. Britton, A. Rienzo, K. Schulte, and J.N. O'Shea,
Charge transfer between a Au(111) surface and adsorbed C60 molecules revealed by core-hole decay channels in resonant photoemission,
Submitted to J. Chem. Phys.

M.M. Brzhezinskaya, V.E. Muradyan, N.A. Vinogradov, A.B. Preobrajenski, W. Gudat, and A.S. Vinogradov,
Electronic structure of fluorinated multiwalled carbon nanotubes studied using X-ray absorption and photoelectron spectroscopy,
Phys. Rev. B 79, 155439, 2009.

S. Bucak, C. Cenker, I. Nasir, U. Olsson, and M. Zackrisson,
Peptide Nanotube Nematic Phase,
Langmuir 25, 4262, 2009.

H.D. Burrows, M.J. Tapia, S.M. Fonseca, A.J.M. Valente, V.M.M. Lobo, L.L.G. Justino, S. Qiu, S. Pradhan, U. Scherf, N. Chattopadhyay, M. Knaapila, and V.M. Garamus,
Aqueous Solution Behavior of Anionic Fluorene-co-thiophene-Based Conjugated Polyelectrolytes,
ACS Appl. Mater. Interfaces, 1, 864, 2009.

U. Bösenberg, J.W. Kim, D. Gosslar, N. Eigen, T.R. Jensen, J.M. Bellosta von Colbe, Y. Zhou, M. Dahms, D.H. Kim, R. Günther, Y.W. Cho, K.H. Oh, T. Klassen, R. Bormann, and M. Dornheim,
Role of Additives in $LiBH_4$-MgH_2 Reactive Hydride Composites for Sorption Kinetics,
Acta Mater., in press.

E. Carlegrim, Y. Zhan, F. Li, X. Liu, and M. Fahlman,
Characterization of the Ni/V(TCNE)x interface for hybrid spintronics applications,
Organic Electronics, in press.

S. Carlson, J. Hölsä, T. Laamanen, M. Lastusaari, M. Malkamäki, J. Niittykoski, and R. Valtonen,
X-Ray Absorption Study of Rare Earth Ions in $Sr_2MgSi_2O_7$:Eu^{2+},R^{3+} Persistent Luminescence Materials,
Opt. Mater., 31, 1877, 2009.

T.X. Carroll, T.D. Thomas, L.J. Sæthre, and K.J. Børve,
Additivity of substituent effects. Core-ionization energies and proton affinities of the fluoromethylbenzenes.
J. Phys. Chem. A 113, 3481, 2009.

R. Černý, D.B. Ravnsbæk, G. Severa, Y. Filinchuk, V. d'Anna, H. Hagemann, D. Haase, C.M. Jensen, and T.R. Jensen,
Structure and reactivity of $KSc(BH_4)_4$ – A novel scandium-based borohydride,
To be submitted.

R. Černý, G. Severa, D. Ravnsbæk, Y. Filinchuk, V. d'Anna, H. Hagemann, D. Haase, C.M. Jensen, and T.R. Jensen,
$NaSc(BH_4)_4$: A novel scandium-based borohydride,
J. Phys. Chem. C 114, 1357, 2010.

Y. Chao, Q. Wang, A. Pietzsch, F. Hennies, and H. Ni,
Soft X-ray induced oxidation on acrylic acid grafted luminescent water dispersible silicon quantum dots,
Submitted to J. Appl. Phys.

Q. Cheng, T. Sandalova, Y. Lindqvist, and E.S. Arnér,
Crystal structure and catalysis of the selenoprotein thioredoxin reductase 1,
J. Biol. Chem., 284, 3998, 2009.

F. Chesneau, B. Schüpbach, K. Szelągowska-Kunstman, N. Ballav, P. Cyganik, A. Terfort, and M. Zharnikov,
Self-assembled monolayers of perfluoroterphenyl-substituted alkanethiols: characteristics and odd-even effects,
submitted to J. Am. Chem. Soc.

F. Chesneau, J. Zhao, C. Shen, M. Buck, and M. Zharnikov,
Adsorption of long-chain alkanethiols on Au(111) – a look from the substrate by high resolution X-ray photoelectron spectroscopy,
Submitted to J. Phys. Chem. C.

A.N. Christensen, L.M. Arnbjerg, E. DiMasi, Y. Cerenius, B.C. Hauback, and T.R. Jensen,
Thermally induced phase transitions of barium oxalates and the structure of α-BaC_2O_4,
Submitted.

A.N. Christensen, M. Olesen, Y. Cerenius, and T.R. Jensen,
Formation and analysis of five phases in the $CaSO_4 \bullet H_2O$ system: $CaSO_4 \bullet H_2O$, α-$CaSO_4 \bullet 0.5H_2O$, β-$CaSO_4 \bullet 0.5H_2O$, soluble $CaSO_4$, and insoluble $CaSO_4$,
Chem. Mater., 20, 2124, 2008.

S. Christoffersen, A. Kadziola, E. Johansson, M. Rasmussen, M. Willemoës, and K.F. Jensen,
Structural and Kinetic Studies of the Allosteric Transition in Sulfolobus solfataricus Uracil Phosphoribosyltransferase: Permanent Activation by Engineering of the C-Terminus,
J. Mol. Biol., 393, 464, 2009.

Yu.S. Dedkov, M. Holder, G. Mayer, M. Fonin, and A.B. Preobrajenski,
Spin-resolved photoemission of a ferromagnetic Mn_5Ge_3(0001) epilayer on Ge(111),
J. Appl. Phys., 105, 073909, 2009.

M. Dornheim and T. Klassen,
Fuels-Hydrogen Storage: High Temperature Hydrides,
Encyclopedia of Electrochemical Power Sources, Elsevier, Amsterdam, 3, 459, 2009.

S. dos Santos, B. Luigjes, and L. Piculell,
Associative phase behaviour and disintegration of copolymer aggregates on adding poly(acrylic acid) to aqueous solutions of a PEO-PPO-PEO triblock copolymer,
Submitted.

K. Dossi, V.G. Tsirkone, J.M. Hayes, J. Matousek, P. Pouckova, J. Soucek, M. Zadinova, S.E. Zographos, and D.D. Leonidas,
Mapping the ribonucleolytic active site of bovine seminal ribonuclease. The binding of pyrimidinyl phosphonucleotide inhibitors,
Eur. J. Medicinal Chem., 44, 4496, 2009.

A. Dowiercial, A. Jarmula, W. Rypniewski, M. Sokolowska, T. Fraczyk, J. Ciesla, and W. Rode,
Crystal structures of substrate- and sulfate-bound mouse thymidylate synthase,
Pteridines, 20, 163, 2009.

K. Döring, N. Ballav, M. Zharnikov, and H. Lang,
Synthesis, electrochemical behavior and self-assembly of metallocene-functionalized thiolfluorenes,
Submitted to Chem. Eur. J.

R.K. Egdal, A.D. Bond, and C.J. McKenzie,
Air oxidation of divanadium(IV) complexes,
Dalton Trans., 19, 3833, 2009.

N. Eigen, U. Bösenberg, J. Bellosta von Colbe, T.R. Jensen, Y. Cerenius, M. Dornheim, T. Klassen, and R. Bormann,
Reversible hydrogen storage in NaF–Al composites,
J. Alloys and Compounds, 477, 76, 2009.

J.M. Eklöf, T.-C. Tan, C. Divne, and H. Brumer,
The crystal structure of the outer membrane lipoprotein YbhC from Escherichia coli sheds new light on the phylogeny of carbohydrate esterase family 8,
Proteins, 76, 1029, 2009.

F. Ekström, A. Hörnberg, E. Artursson, L.-G. Hammarström, G. Schneider, and Y.-P. Pang,
Structure of HI6 Sarin-acetylcholinesterase determined by X-Ray crystallography and molecular dynamic simulation: reactivator mechanism and design,
PLoS One, 4, e5957, 2009.

L.K.E. Ericsson, A.A, Zakharov, and K.O. Magnusson,
ZnO nanocrystals on SiO_2/Si surfaces thermally cleaned in ultrahigh vacuum and characterized using Spectroscopic PhotoEmission and Low Energy Electron Microscopy,
J. Vac. Sci. Technol. A, in press.

P.E.J. Eriksson, J.R. Osiecki, K. Sakamoto, and R.I.G. Uhrberg,
Atomic and electronic structures of the ordered $2\sqrt{3}x2\sqrt{3}$ and the molten 1x1 phase on the Si(111):Sn surface,
Submitted to Phys. Rev. B.

P.E.J. Eriksson, K. Sakamoto, and R.I.G. Uhrberg,
Electronic structure of the thallium induced 2x1 reconstruction on Si(001),
Submitted to Phys. Rev. B.

P.E.J. Eriksson and R.I.G. Uhrberg,
Surface core-level shifts on clean Si(001) and Ge(001) studied with photoelectron spectroscopy and DFT calculations,
Phys. Rev. B, in press.

G.C. Faria, T.S. Plivelic, R.F. Cossiello, A.A. Souza, T.D.Z. Atvars, I.L. Torriani, and E.R. de Azevedo,
A Multitechnique Study of Structure and Dynamics of Polyfluorene Cast Films and the Influence on their Photoluminescence,
J. Phys. Chem. B,113, 11403, 2009.

N. Forsgren, R.J. Lamont, and K. Persson,
Two Intramolecular Isopeptide Bonds are Identified in the Crystal Structure of the Streptococcus gordonii SspB C-terminal Domain,
J. Mol. Biol., 397, 740, 2010.

N. Forsgren, R.J. Lamont, and K. Persson,
Crystal structure of the variable domain of the Streptococcus gordonii surface protein SspB,
Protein Sci., 18,1896, 2009.

N. Forsgren, R.J. Lamont, and K. Persson,
A crystallizable form of the Streptococcus gordonii surface antigen SspB C-domain obtained by limited proteolysis,
Acta Cryst. F 65, 712, 2009.

I. Fritzon, B. Svensson, S. al-Karadaghi, B. Walse, U. Wellmar, U.J. Nilsson, D. da Graça Thrige, and S. Jönsson,
Inhibition of Human DHODH by 4-hydroxy coumarins, fenamic acids and N-(alkylcarbonyl) anthranilic acids identified by structure-guided fragment selection,
ChemMedChem, in press.

S. Fritzsche, K. Jänkälä, M. Huttula, S. Urpelainen, and H. Aksela,
Photoelectron satellite structure in the 3d and 4d inner-shell ionization of rubidium and cesium: Role of atomic relaxation,
Phys. Rev. A 78, 032514, 2008.

K. Frydenvang, L.L. Lash, P. Naur, P.A. Postila, D.S. Pickering, C.M. Smith, M. Gajhede, M. Sasaki, R. Sakai, O.T. Pentikaïnen, G.T. Swanson, and J.S. Kastrup,
Full domain closure of the ligand-binding core of the ionotropic glutamate receptor iGluR5 induced by the high affinity agonist dysiherbaine and the functional antagonist 8,9-dideoxyneodysiherbaine,
J. Biol. Chem., 28, 14219, 2009.

V.R. Galakhov, M. Neumann, and D.G. Kellerman,
Electronic structure of defective lithium cobaltites Li_xCoO_2,
Appl. Phys. A 94, 497, 2009.

V. Ganenko, K. Fissum, K. Hansen, L. Isaksson, K. Livingston, M. Lundin, L. Morokhovskii, B. Nilsson, D. Pugachov, B. Schroder, and G. Vashchenko,
Production of Linearly Polarized Photon Beam at MAX-lab,
Problems of Atomic Sci. and Technol., 3, 95, 2009.

Y. Ge, T. Weidner H. Ahn, J.E. Whitten, and M. Zharnikov,
Energy level pinning in self-assembled alkanethiol monolayers,
J. Phys. Chem. C 113, 4575, 2009.

M.J. Gladys, A.A. El-Zein, A. Mikkelsen, J.N. Andersen, and G. Held,
Coverage-dependant changes from partially dissociated to molecular water adsorption on O-precovered Ru{0001} surfaces,
To be submitted to J. Am. Chem. Soc.

A. González-Pérez, S. Bulut, U. Olsson, and B. Lindman,
Temperature Induced DNA Compaction in a Nonionic Lamellar Phase,
Progress in Colloid and Polymer Science, Colloids for Nano- and Biotechnology, 135, 174, 2008.

R. Gosalawit, M. Dornheim, J.M. Bellosta von Colbe, T.R. Jensen, Y. Cerenius, C.M. Bonatto, M. Peschke, and R. Bormann,
LiF-MgB_2 system for Reversible Hydrogen Storage,
Submitted.

A. Gratien, E. Nilsson, L. Bache-Andreassen, J.-F. Doussin, M.S. Johnson, C.J. Nielsen, Y. Stenstrøm, and B. Picquet-Varrault,
UV and IR absorption cross-sections and relative photolysis rates of HCHO, HCDO and DCDO,
Submitted to J. Phys. Chem. A.

L. Gridneva, A. Persson, M.A. Niño, J. Camarero, J.J. de Miguel, R. Miranda, C. Hofer, C. Teichert, T. Bobek, A. Locatelli, S. Heun, S. Carlsson, and D. Arvanitis,
Experimental investigation of the spin reorientation of Co/Au based magnetic nano-dot arrays,
Phys. Rev. B 77, 104425, 2008.

J. Gråsjö, E. Andersson, J. Forsberg, E.F. Aziz, B. Brena, C. Johansson, J. Nordgren, L. Duda, J. Andersson, F. Hennies, J.-E. Rubensson, and P. Hansson,
Electronic structure of water molecules confined in a micelle lattice,
J. Phys. Chem B 113, 8201, 2009.

J. Gråsjö, E. Andersson, J. Forsberg, L. Duda, E. Henke, W. Pokapanich, O. Björneholm, J. Andersson, A. Pietzsch, F. Hennies, and J.-E. Rubensson,
Local electronic structure of functional groups in glycine as anion, zwitterion and cation in aqueous solution,
J. Phys. Chem. B 113, 16002, 2009.

M. Gurnett, L.J. Holleboom, H.M. Zhang, and L.S.O. Johansson,
Photoemission study of the Li/Ge(111)-3x1 reconstruction,
Surf. Sci., 603, 727, 2009.

A. Gutacker, S. Adamczyk, A. Helfer, L.E. Garner, R.C. Evans, S.M. Fonseca, M. Knaapila, G.C. Bazan, H.D. Burrows, and U. Scherf,
All-Conjugated Block Copolymers,
J. Mater. Chem., 20, 1423, 2010.

A. Gutacker, N. Koenen, U. Scherf, S. Adamczyk, J. Pina, S.M. Fonseca, A.J.M. Valente, R.C. Evans, J. Seixas de Melo, H.D. Burrows, and M. Knaapila,
Cationic Fluorene-Thiophene Diblock Copolymers: Aggregation Behaviour in Methanol/Water and its Relation to Thin Film Structures,
Polymer, DOI: 10.1016/j.polymer.2010.03.010

H. Hald, P.K. Ahring, D.B. Timmermann, T. Liljefors, M. Gajhede, and J.S. Kastrup,
Distinct structural features of cyclothiazide are responsible for effects on peak current amplitude and desensitization kinetics at iGluR2,
J. Mol. Biol., 391, 906, 2009.

A. Hansson, E. Wallén, M. Berglund, R. Kersevan, and M. Hahn,
Experiences from nonevaporable getter coated vacuum chambers at the MAX II synchrotron light source,
J. Vac. Sci. and Technol. A 28, 220, 2010.

S. Hansson and D.T. Logan,
New insights into the role of the P-loop lysine: nucleotide binding, regulation and GTP hydrolysis in elongation factor G.
Submitted.

S.J.O. Hardman, D.M. Graham, S.K. Stubbs, B.F. Spencer, W.R. Flavell, A.G. Thomas, K.L. Syres, D.J. Binks, F. Sirotti, M. El Kazzi, M. Silly, F. Hennies, J. Akhtar, P. O'Brien, G. Miller, and V. Dhanak,
An X-ray photoemission study of PbS nanoparticles that show efficient carrier multiplication,
In manuscript.

P.V. Harris, D. Welner, K.C. McFarland, E. Re, J.-C.N. Poulsen, K. Brown, R. Salbo, H. Ding, E. Vlasenko, S. Merino, F. Xu, J. Cherry, S. Larsen, and L. Lo Leggio,
Stimulation of lignocellulosic biomass hydrolysis by proteins of glycoside hydrolase family 61: Structure and function of a large, enigmatic family,
Biochemistry, in press.

S. Heinäsmäki, K. Jänkälä, and J. Niskanen,
Angular distribution of resonant Auger electrons from atoms with multiple overlapping resonances,
J. Phys. B, 42, 085002, 2009.

F. Hennies, Z. Bao, O. Travnikova, and M.N. Piancastelli,
Structure and Bonding of Ethylene Oxide on Si (100),
J. Phys. Chem. C 113, 16077, 2009.

J. Hirvonen Grytzelius, H.M. Zhang, and L.S.O. Johansson,
Surface Electronic Structure of Mn/Si(111)-$\sqrt{3}x\sqrt{3}$,
Phys. Rev. B 78, 155406, 2008.

B.N. Holland, N. Peltekis, T. Farrelly, R.G. Wilks, G. Gavrila, D.R.T. Zahn, C. McGuinness, and I.T. McGovern,
NEXAFS studies of copper phthaloyanine on Ge(001)-2x1 and Ge(111)-c(2x8) surfaces,
Phys. Stat. Solidi. B 246, 1546, 2009.

M. Huttula, S.-M. Huttula, S. Urpelainen, L. Partanen, S. Aksela, and H. Aksela,
Fast decay of 4p and 4s core holes in Sb_4 clusters,
J. Phys. B 42, 235002, 2009.

M. Huttula, M.-H. Mikkelä, M. Tchaplyguine, and O. Björneholm,
Size-varied photoelectron spectroscopy of metal clusters using the exchange metal cluster source,
Submitted to J. Electron Spectrosc. and Relat. Phenom.

M. Huttula, L. Partanen, A. Mäkinen, T. Kantia, H. Aksela, and S. Aksela,
KLL Auger decay in free aluminum atoms,
Phys. Rev. A 79, 023412, 2009.

R. Häggblad, M. Massa, and A. Andersson,
Stability and Performance of Supported Fe-V-oxide Catalysts in Methanol Oxidation,
J. Catal., 266, 218, 2009.

P. Hägglund, K.G. Kirkensgaard, A. Henriksen, and B. Svensson,
Molecular recognition in NADPH dependent plant thioredoxin systems – catalytic mechanisms, structural snapshots and target identifications,
Adv. Bot. Res., 52, 461, 2009.

R. Høiberg-Nielsen, P. Westh, L. Kobberøe Skov, and L. Arleth,
Interrelationship of steric stabilization and self-crowding of a glycosylated protein,
Biophys. J., 97, 1445, 2009.

J. Hölsä, H.F. Brito, L.C.V. Rodrigues, M. Lastusaari, T. Laamanen, and M. Malkamäki,
Synchrotron Radiation Induced Persistent Luminescence of $Sr_2MgSi_2O_7:Eu^{2+},R^{3+}$,
Submitted.

J. Hölsä, T. Laamanen, M. Lastusaari, M. Malkamäki, and P. Novák,
Persistent Luminescence – Quo Vadis?,
J. Lumin., 129, 1606, 2009.

A. Hörnberg, E. Artursson, R. Wärme, Y.-P. Pang, and F. Ekström,
Crystal structures of oxime-bound fenamiphos-acetylcholinesterases: reactivation involving flipping of the His447 ring to form a reactive Glu334-His447-oxime triad,
Biochem. Pharmacol., 79, 507, 2009.

H. Ingvarsson, T.A. Jones, and T. Unge,
Crystallization of Mycobacterium smegmatis methionyl-tRNA synthetase in the presence of methionine and adenosine,
Acta Cryst. F 65, 618, 2009.

C. Isvoranu, J. Åhlund, B. Wang, E. Ataman, N. Mårtensson, C. Puglia, J.N. Andersen, M.-L. Bocquet, and J. Schnadt,
Electron spectroscopy study of the initial stages of iron phthalocyanine growth on highly oriented pyrolitic graphite,
J. Chem. Phys., 131, 214709, 2009.

E. Itälä, E. Kukk, D.T. Ha, S. Granroth, A. Caló, L. Partanen, H. Aksela, and S. Aksela,
Fragmentation patterns of doubly charged acrylonitrile molecule following carbon core ionization,
J. Chem. Phys., 131, 114314, 2009.

A.M. Jansson, E. Jakobsson, P. Johansson, V. Lantez, B. Coutard, X. de Lamballerie, T. Unge, and T.A. Jones,
Structure of the methyltransferase domain from the Modoc virus, a flavivirus with no known vector,
Acta Cryst. D 65, 796, 2009.

G.V. Jensen, M. Bremholm, N. Lock, G.R. Deen, T.R. Jensen, B.B. Iversen, M. Niederberger, J.S. Pedersen, and H. Birkedal,
Anisotropic crystal growth kinetics of anatase TiO_2 nanoparticles synthesized in a non-aqueous medium,
Submitted.

T.R. Jensen, A. Goncalves, R.G. Hazell, and H.J. Jakobsen,
New amine templated zinc phosphates $Zn_2(HPO_4)_3(C_6N_2H_{14})$ with very low framework density; Synthesis, crystal structure, solid state MAS NMR and thermal transformation,
Micropor. Mesopor. Mater., 109, 383, 2008.

P. Jiříček, M. Cukr, I. Bartoš, and J. Sadowski,
Photoemission from α and β phases of the GaAs(001)-c(4x4) surface,
Surf. Sci., 603, 3088, 2009.

P. Jussila, H. Ali-Löytty, K. Lahtonen, M. Hirsimäki, and M. Valden,
Inhibition of initial surface oxidation by strongly bound hydroxyl species and Cr segregation: H_2O and O_2 adsorption on Fe-17Cr,
Surf. Sci., 603, 3005, 2009.

K. Jänkälä, S. Urpelainen, M. Huttula, S. Fritzsche, S. Heinäsmäki, S. Aksela, and H. Aksela,
Inner-shell 2p photoionization and Auger decay of atomic silicon,
Phys. Rev. A 77, 062504, 2008.

J.-E. Jørgensen, T.R. Jensen, and J.C. Hanson,
An in situ X-ray Diffraction Study of the Hydrothermal Synthesis of nanocrystalline ZnSe,
J. Solid State Chem., 181, 1925, 2008.

R. Jørgensen, T. Pesnot, G.K. Wagner, and M. Palcic,
Novel UDP-Gal derivative interferes with active site closure and inhibits transfer in human blood group glycosyltransferases,
Glycoconjugate J., 26, 836, 2009.

M. Karlsson, J.-O. Adler, L.E.M. Andersson, V. Avdeichikov, B.L. Berman, M.J. Boland, W.J. Briscoe, J. Brudvik, J.R. Calarco, G. Feldman, K.G. Fissum, K. Hansen, D.L. Hornidge, L. Isaksson, N.R. Kolb, A.A. Kotov, P. Lilja, M. Lundin, B. Nilsson, D. Nilsson, G.V. O'Rielly, G.E. Petrov, B. Schroder, I.I. Strakovsky, and L.A. Vaishnene,
Measurement of the differential cross section for the two-body photodisintegration of ^{3}He at theta_LAB = 90deg using tagged photons in the energy range 14 -- 31 MeV,
Phys. Rev. C 80, 044001, 2009.

T. Karlsson, P. Persson, U. Skyllberg, C.-M. Mörth, and R. Giesler,
Characterization of iron(III) in organic soils using extended X-ray absorption fine structure spectroscopy,
Environ. Sci. Technol., 42, 5449, 2008.

K.G. Kirkensgaard, P. Hägglund, B. Svensson, and A. Henriksen,
Structure of Hordeum vulgare NADPH-dependent thioredoxin reductase 2. Unwinding the reaction mechanism,
Acta Cryst. D 65, 932, 2009.

A. Kivimäki, G. Vall-llosera, M. Coreno, M.A. Huels, M. Stankiewicz, and E. Rachlew,
Line shape narrowing in the ultraviolet yield at the N 1s → π resonance of the N_2 molecule,*
J. Phys. B: At. Mol. Opt. Phys., 42, 075102, 2009.

A. Kivimäki, G. Vall-llosera, M. Coreno, M.A. Huels, M. Stankiewicz, and E. Rachlew,
Fluorescence emission at core-to-Rydberg excitations in the N_2 molecule,
J. Phys. B: At. Mol. Opt. Phys., 42, 185103, 2009.

M. Knaapila, R.C. Evans, A. Gutacker, V. Garamus, M. Torkkeli, S. Adamczyk, M. Forster, U. Scherf, and H.D. Burrows,
Solvent Dependent Assembly of a Polyfluorene-Polythiophene "Rod-Rod" Block Copolyelectrolyte: Influence on Photophysical Properties,
Langmuir, DOI: 10.1021/la903520w.

M. Knaapila, C. Svensson, J. Barauskas, M. Zackrisson, S.S. Nielsen, K.N. Toft, B. Vestergaard, L. Arleth, U. Olsson, J.S. Pedersen, and Y. Cerenius,
A new small-angle X-ray scattering set-up on the crystallography beamline I711 at MAX-lab,
J. Synchrotron Rad., 16, 498, 2009.

J. Knudsen, L.R. Merte, L.C. Grabow, F.M. Eichhorn, S. Porsgaard, H. Zeuthen, R.T. Vang, E. Lægsgaard, M. Mavrikakis, and F. Besenbacher,
Reduction of FeO/Pt(111) thin films by exposure to atomic hydrogen,
Surf. Sci., 604, 11, 2010.

R. Kolodziejczyk, K. Michalska, A. Hernandez-Santoyo, M. Wahlbom, A. Grubb, and M. Jaskolski,
Crystal structure of human cystatin C stabilized against amyloid formation,
FEBS J., 277, 1726, 2010.

H. Koskiniemi, T. Grocholski, G. Schneider, and J. Niemi,
Expression, purification and crystallization of the cofactor-independent monooxygenase SnoaB from the nogalamycin biosynthetic pathway,
Acta Cryst. F 65, 256, 2009.

I.A. Kowalik, G. Öhrwall, B.N. Jensen, R. Sankari, E. Wallén, U. Johansson, O. Karis, and D. Arvanitis,
Description of the new I1011 beamline for magnetic measurements using synchrotron radiation at MAX-lab,
J. Phys.: Conf. Series, 211, 012030, 2010.

B.J. Kowalski, M.A. Pietrzyk, W. Knoff, A. Łusakowski, J. Sadowski, J. Adell, and T. Story,
Angle-resolved photoemission study and pseudopotential calculations of GeTe and $Ge_{1-x}Mn_xTe$ band structure,
Phys. Procedia, 3, 1357, 2010.

R. Kuktaite, T.S. Plivelic, Y. Cerenius, M.S. Hedenqvist, M. Gällstedt, S. Marttila, R. Ignell, I. Popineau, O. Tranquet, P. Shewry, and E. Johansson,
Wheat gluten bio-plastics: From polymeric aggregates towards unusual hexagonal structures,
Submitted to J. Mater. Chem.

R. Kuktaite, T.S. Plivelic, H. Türe, M.S. Hedenqvist, M. Gällstedt, S. Marttila, I. Popineau, O. Tranquet, P. Shewry, and E. Johansson,
Unique protein structure in urea containing wheat gluten bio-plastics: a study by SAXS, WAXS, LM and CLSM,
To be submitted to J. Mater. Chem.

J. Laksman, D. Céolin, M. Gisselbrecht, S.E. Canton, and S.L. Sorensen,
Dynamics of proton migration and dissociation in core-excited ethyne probed by multiple ion momentum imaging,
J. Chem. Phys., 131, 244305, 2009.

P. Laukkanen, M.P.J. Punkkinen, M. Ahola-Tuomi, J. Lång, K. Schulte, A. Pietzsch, M. Kuzmin, J. Sadowski, J. Adell, R.E. Perälä, M. Ropo, K. Kokko, L. Vitos, B. Johansson, M. Pessa, and I.J. Väyrynen,
Core-level shifts of the c(8x2)-reconstructed InAs(100) and InSb(100) surfaces,
J. Electron Spectrosc. and Relat. Phenom., 177, 52, 2010.

P. Laukkanen, M.P.J. Punkkinen, N. Räsänen, M. Ahola-Tuomi, J. Sadowski, J. Adell, M. Kuzmin, J. Lång, R.E. Perälä, M. Ropo, K. Kokko, L. Vitos, B. Johansson, M. Pessa, and I.J. Väyrynen,
Bismuth-stabilized c(2x6) reconstruction on InSb(100) substrate: Violation of the electron counting model,
Phys. Rev. B 81, 035310, 2010.

M. Laursen, M. Bublitz, K. Moncoq, C. Olesen, J.V. Moeller, H.S. Young, P. Nissen, and J.P. Morth,
Cyclopiazonic acid is complexed to a divalent metal ion when bound to the sarcoplasmic reticulum Ca^{2+}-ATPase,
J. Biol. Chem., 284, 13513, 2008.

K. Lawniczak-Jablonska, A. Wolska, J. Bak-Misiuk, E. Dynowska, P. Romanowski, J.Z. Domagała, R. Minikayev, D. Wasik, M.T. Klepka, J. Sadowski, A. Barcz, P. Dluzewski, S. Kret, A. Twardowski, M. Kamińska, A. Persson, D. Arvanitis, E. Holub-Krappe, and A. Kwiatkowski,
Structural and magnetic properties of MBE grown MnSb layers on GaAs substrates,
J. Appl. Phys., 106, 083524, 2009.

J. Le Nours, L. De Maria, D. Welner, C.T. Jørgensen, L.L.H. Christensen, T.V. Borchert, S. Larsen, and L. Lo Leggio,
Investigating the binding of β-1,4-galactan to Bacillus licheniformis β-1,4-galactanase by crystallography and computational modeling,
Proteins, 75 , 977, 2009.

J.Y. Lee, D. Ravnsbæk, Y. Cerenius, Y. Kim, Y.-S. Lee, J.-H. Shim, T.R. Jensen, and Y.W. Cho,
Dehydrogenation pathway and reversibility of the $LiBH_4$–$Ca(BH_4)_2$ composite system,
J. Phys. Chem. C 113, 15080, 2009.

V. Lee, D.J. Peake, B. Sobott, B. Schröder, Ch. Brönnimann, B. Henrich, K. Hansen, G.J. O'Keefe, G.N. Taylor, M.J. Boland, M.N. Thompson, and R.P. Rassool,
Imaging High Energy Photons with PILATUS II at the Tagged Photon Beam at MAX-lab,
Nucl. Instr. and Meth. in Phys. Res. A 603, 379, 2009.

S.C. Leemann, Å. Andersson, M. Eriksson, L.-J. Lindgren, E. Wallén, J. Bengtsson, and A. Streun,
Beam dynamics for the MAX IV 3 GeV storage ring,
Phys. Rev. ST-AB, 12, 120701, 2009.

K. Leppänen, S. Andersson, M. Torkkeli, M. Knaapila, N. Kotelnikova, and R. Serimaa,
Structure of cellulose and microcrystalline cellulose from various wood species, cotton and flax studied by X-ray scattering,
Cellulose, 16, 999, 2009.

J. Lewis, J. Sjostrom, U. Skyllberg, and L. Hagglund,
Distribution, chemical speciation and mobility of Pb and Sb originating from small arms ammunition in a coarse grained unsaturated surface sand,
J Environ. Qual., in press.

F. Li, G. Parteder, F. Allegretti, C. Franchini, R. Podloucky, S. Surnev, and F.P. Netzer,
Two-dimensional manganese oxide nanolayers on Pd(100): the surface phase diagram,
J. Phys. Condens. Matter, 21, 134008, 2009.

F. Li, Y. Zhou, F. Zhang, X.J. Liu, Y.Q. Zhan, and M. Fahlman,
Tuning work function of noble metals as promising cathodes in organic electronic devices,
Chem. Mater., 21, 2798, 2009.

A. Lindblad, H. Bergersen, W. Pokapanich, M. Tchaplyguine, G. Öhrwall, and O. Björneholm,
Charge delocalization dynamics of ammonia in different hydrogen bonding environments: Free clusters and in liquid water solution,
Phys. Chem. Chem. Phys., 11, 1758, 2009.

A. Lindblad, M. Winkler, M. Tchaplyguine, G. Öhrwall, S. Svensson, and O. Björneholm,
The geometric structure of pure SF_6 and mixed Ar/SF_6 clusters investigated by core-level photoelectron spectroscopy,
Surf. Sci., 603, 433, 2009.

Y. Lindqvist, H. Koskiniemi, A. Jansson, T. Sandalova, R. Schnell, Z. Liu, P. Mäntsälä, J. Niemi, and G. Schneider,
Structural basis for substrate recognition and specificity in aklavinone-11-hydroxylase from rhodomycin biosynthesis,
J. Mol. Biol., 393, 966, 2009.

X. Liu, Y. Zhan, S. Braun, F. Li, and M. Fahlman,
Interfacial electronic properties of pentacene tuned by a molecular monolayer of C60,
Phys. Rev. B 80, 115401, 2009.

T. Marinado, D.P Hagberg, M. Hedlund, T. Edvinsson, E.M.J. Johansson, G. Boschloo, H. Rensmo, T. Brinck, L.C. Sun, and A. Hagfeldt,
Rhodanine dyes for dye-sensitized solar cells: Spectroscopy, energy levels and photovoltaic performance,
Phys. Chem. Chem. Phys., 11, 133, 2009.

V.V. Maslyuk, V.Yu. Aristov, O.V. Molodtsova, D.V. Vyalikh, V.M. Zhilin, Yu.A. Ossipyan, T. Bredow, I. Mertig, and M. Knupfer,
The electronic structure of cobalt phthalocyanine,
Appl. Phys. A 94, 485, 2009.

L.C. Mayor, A. Saywell, G. Magnano, C.J. Satterley, J. Schnadt, and J.N. O'Shea,
Adsorption of a Ru(II) dye complex on the Au(111) surface: Photoemission and scanning tunneling microscopy,
J. Chem. Phys., 130, 164704, 2009.

L. Mosegaard, B. Møller, J.-E. Jørgensen, Y. Filinchuk, Y. Cerenius, J.C. Hanson, E. Dimasi, F. Besenbacher, and T.R. Jensen,
Additives in $LiBH_4$: in-situ synchrotron radiation powder X-ray diffraction study,
J. Phys. Chem. C 112, 1299, 2008.

M. Myllykoski, K. Kuczera, and P. Kursula,
Complex formation between calmodulin and a peptide from the intracellular loop of the gap junction protein connexin43: Molecular conformation and energetics of binding,
Biophys. Chem., 144, 130, 2009.

N. Mårtensson, A.B. Preobrajenski, and F. Hennies,
Bonding and dynamics of surface systems probed by soft X-rays,
Eur. Phys. J. Special Topics. 169, 133, 2009.

M. Nayeri, M. Zackrisson, and J. Bergenholtz,
Scattering Functions of Core–Shell-Struct ured Hard Spheres with Schulz-Distributed Radii,
J. Phys. Chem. B 113, 8296, 2009.

F. Neiers, C. Madhurantakam, S. Fälker, C. Manzano, A. Dessen, S. Normark, B. Henriques-Normark, and A. Achour,
Two Crystal Structures of Pneumococcal Pilus Sortase C Provide Novel Insights into Catalysis and Substrate Specificity,
J. Mol. Biol., 393, 704, 2009.

F.P. Netzer, F. Allegretti, and S. Surnev,
Low-dimensional oxide nanostructures on metals: Hybrid systems with novel properties,
J. Vac. Sci. Technol. B, 28, 1, 2010.

W.R. Newson, M.S. Hedenqvist, M. Gällstedt, R. Kuktaite, T.S. Plivelic, and E. Johansson,
Bio-plastic sheets composed of proteins from oil crops Crambe abyssinica and Brassica carinata mechanical properties, structural morphology and potential use for packaging,
In manuscript.

M.L. Ng, A.B. Preobrajenski, A.A. Zakharov, A.S. Vinogradov, S.A. Krasnikov, A.A. Cafolla, and N. Mårtensson,
Effect of substrate nanopatterning on the growth and structure of pentacene films,
Phys. Rev. B 81, 115449, 2010.

M.S. Nielsen, C.R. Petersen, H.E.M. Christensen, and P. Harris,
The crystal structure of tryptophan hydroxylase with bound amino acid substrate,
Biochem., 47, 12087, 2008.

M.S. Nielsen, C.R. Petersen, A. Munch, T.V. Vendelboe, J. Boesen, P. Harris, and H.E.M. Christensen,
A simple two step procedure for purification of the catalytic domain of chicken tryptophan hydroxylase 1 in a form suitable for crystallization,
Protein Expression and Purification, 57, 116, 2008.

S.S. Nielsen, K.N. Toft, D. Snakenborg, M.G. Jeppesen, J.K. Jacobsen, B. Vestergaard, J.P. Kuttern, and L. Arleth,
BioXTAS RAW, a software program for high-throughput automated small-angle X-ray scattering data reduction and preliminary analysis,
J. Appl. Cryst., 42, 959, 2009.

T.K. Nielsen, F. Besenbacher, and T.R. Jensen,
The properties of MgH_2/Mg modified by Nb_2O5 and NbF_5 – An in situ SR PXD study,
To be submitted.

T.K. Nielsen, U. Bösenberg, R. Gosalawit, M. Dornheim, Y. Cerenius, F. Besenbacher, and T.R. Jensen,
Nanoconfined reversible chemical reaction,
To be submitted

T.K. Nielsen, K. Manickam, M. Hirscher, F. Besenbacher, and T.R. Jensen,
Confinement of MgH_2 nanoclusters within nanoporous aerogel scaffold materials,
ACS nano, 3, 3521, 2009.

J. Niskanen, M. Huttula, S. Heinäsmäki, J. Schulz, S. Urpelainen, K. Jänkälä, A. Moise, M. Alagia, and L. Avaldi, K.C. Prince, R. Richter, S. Aksela, and H. Aksela,
Core level absorption of laser-excited Rb and Cs atoms,
J. Phys. B, 42, 175001, 2009.

J. Niskanen, S. Urpelainen, S. Aksela, H. Aksela, O. Vahtras, V. Carravetta, and H. Ågren,
Valence photoionization of LiCl monomer and dimer,
Phys. Rev. A, in press.

J. Niskanen, S. Urpelainen, K. Jänkälä, J. Schulz, S. Heinäsmäki, S. Fritzsche, N.M. Kabachnik, S. Aksela, and H. Aksela,
Photoelectron angular distribution and linear magnetic dichroism in the 4p photoemission from Rb atoms,
Phys. Rev. A 81, 013406, 2010.

A. Nordlund, L. Leinartaité, K. Saraboji, C. Aisenbrey, G. Gröbner, J. Danielsson, D.T. Logan, and M. Oliveberg,
Functional features cause misfolding of the ALS-provoking enzyme SOD1,
Proc. Natl. Acad. Sci. (PNAS), 106, 9667, 2009.

K. Nørgaard Toft, B. Vestergaard, S.S. Nielsen, D. Snakenborg, M.G. Jeppesen, J.K. Jacobsen, L. Arleth, and J.P. Kutter,
High-Throughput Small Angle X-ray Scattering from Proteins in Solution Using a Microfluidic Front-End,
Anal. Chem., 80, 3648, 2008.

J. Oddershede, T.L. Christiansen, K. Ståhl, and M.A.J. Somers,
Extended X-ray absorption fine structure investigation of nitrogen expanded austenite,
Scripta Materialia, 62, 290, 2010.

F.G.J. Odille, S. Jónsson, S. Stjernqvist, T. Rydén, and K. Wärnmark,
A General Association Model for the Formation of Supramolecular Copolymers,
Submitted.

A. Olsson, J. Nordgren, K. Okada, and A. Kotani, L.-C. Duda, T. Schmitt, M. Magnuson, and J. Forsberg,
Reply to comment by Hüfner on NiO,
Phys. Rev. Lett., in press.

S. Olsson, J.P. Gustafsson, D. Berggren Kleja, D. Bendz, and I. Persson,
Metal leaching from MSWI bottom ash as affected by salt or dissolved organic matter,
Waste Management, 29, 506, 2009.

J.N. O'Shea, A. Saywell, G. Magnano, L.M.A. Perdigao, C.J. Satterley, P.H. Beton, and V.R. Dhanak,
Adsorption of PTCDI on Au(111): Photoemission and scanning tunneling microscopy,
Surf. Sci., 603, 3094, 2009.

S. Osmekhin, M. Tchaplyguine, M.-H. Mikkelä, M. Huttula, T. Andersson, O. Björneholm, and S. Aksela,
Size-dependent transformation of energy structure in free tin clusters studied by photoelectron spectroscopy,
Phys. Rev. A 81, 023203, 2010.

F. Ossler, S.E. Canton, and J. Larsson,
X-ray scattering studies of the generation of carbon nanoparticles in flames and their transition from gas phase to condensed phase,
Carbon, 47, 3498, 2009.

Y.-P. Pang, F. Ekström, G.-A. Polsinelli, Y. Gao, S. Rana, D.-H. Hua, B. Andersson, P.-O. Andersson, L. Peng, S.-K. Singh, R.-K. Mishra, K.-Y. Zhu, A.-M. Fallon, D.-W. Ragsdale, and S. Brimijoin,
Selective and irreversible inhibitors of mosquito acetylcholinesterases for controlling malaria and other mosquito-borne diseases,
PLoS One, 4, e6851, 2009.

L. Partanen, J. Schulz, M. Holappa, H. Aksela, and S. Aksela,
Electron-correlation-induced interchange of lifetime broadenings of 5s-1 multiplet states in atomic Cs,
Phys. Rev. A 80, 042518, 2009.

L. Pasquini, E. Callini, E. Piscopiello, A. Montone, T.R. Jensen, M. Vittori Antisari, and E. Bonetti,
Hydrogen Sorption in Magnesium Nanoparticles: Size- and Surface-Related Phenomena, in Hydrogen Storage Materials,
In: Mater. Res. Soc. Symp. Proc., eds. E. Akiba, W. Tumas, P. Chen, M. Fichtner, S. Zhang,
Vol. 1216E, 1216-W05-04, Warrendale, PA, 2010.

W. Paszkowicz, P. Piszora, Y. Cerenius, S. Carlson, R. Minikayev, and E. Werner-Malento,
Silver behenate under high pressure: A powder diffraction study,
Rad. Phys. Chem., 78 Suppl. 1, S105, 2009.

M. Patanen, S. Aksela, S. Urpelainen, T. Kantia, S. Heinäsmäki, and H. Aksela,
Free atom 4f photoelectron spectra of Au, Pb and Bi,
J. Electron Spectrosc. and Relat. Phenom., in press.

M. Patanen, J. Niskanen, M. Huttula, K. Jänkälä, S. Urpelainen, H. Aksela, and S. Aksela,
Strong molecular field effects in Auger decay of potassium 2p core hole state in molecular KCl, KBr and KI,
J. Phys. B: At. Mol. Opt. Phys., 41, 215103, 2008.

M. Patanen, S. Urpelainen, M. Huttula, R. Sankari, V. Kisand, E. Nömmiste, E. Kukk, H. Aksela, and S. Aksela,
High-resolution study of K 3p photoabsorption and resonant Auger decay in KF,
Phys. Rev. A 80, 013414, 2009.

N. Peltekis, B. Holland, S. Krishnamurthy, C. Stephens, G. Cabailh, I.T. McGovern, L. Kjeldgaard, J.E. Downes, H.J. Trodahl, S. Wang, K.E. Smith, and C. McGuinness,
Synchrotron radiation induced beam damage studies in the phtalocyanine family of organic molecular semiconductors,
Submitted to Surf. Sci.

L.M.A. Perdigão, A.J. Britton, N. Taleb, M. Gimenex-Lopez, N.R. Champness, J.N. O'Shea, and P.H. Beton,
Self-assembled chains of single molecule magnets on a gold surface,
Submitted to Nature Nanotechnology.

A. Persson, L. Gridneva, M.A. Niño, J. Camarero, J.J. de Miguel, R. Miranda, C. Hofer, C. Teichert, T. Bobek, A. Locatelli, and D. Arvanitis,
On the spin reorientation of ordered magnetic nano-dot arrays: Pt/Co/Pt versus Au/Co/Au,
In manuscript.

T. Pesnot, R. Jørgensen, M.M. Palcic, and G.K. Wagner,
Structural and mechanistic basis for a new mode of glycosyltransferase inhibition,
Nature Chem. Biol., published online 4 April, 2010.

N. Petermann, G. Hansen, C.L. Schmidt, and R. Hilgenfeld,
Structure of the GTPase and GDI domains of FeoB, the ferrous iron transporter of Legionella pneumophila,
FEBS Lett. 584, 733, 2010.

R.M. Petoral Jr., F. Söderlind, A. Klasson, A. Suska, M.A. Fortin, P.-O. Käll, M. Engström, and K. Uvdal,
Synthesis and Characterization of Tb^{3+}-Doped Gd_2O_3 Nanocrystals: A Bifunctional Material with Combined Fluorescent Labeling and MRI Contrast Agent Properties,
J. Phys. Chem. C 113, 6913, 2009.

P. Piszora,
Balancing of manganese oxidation state in lithium-manganese oxides by chemical reaction conditions and initial stoichiometry,
Submitted.

P. Piszora, W. Nowicki, J. Darul, B. Bojanowski, S. Carlson, and Y. Cerenius,
Synchrotron X-ray diffraction studies of $LiMn_2O_4$ and $Li_4Mn_5O_{12}$ structures at high pressure,
Rad. Phys. Chem., 78 Suppl. 1, S89, 2009.

W. Pokapanich, H. Bergersen, R.R.T. Marinho, A. Lindblad, I. Bradeanu, S. Legendre, T. Rander, A. Rosso, M. Tchaplyguine, S. Svensson, O. Björneholm, and G. Öhrwall,
Auger electron spectroscopy as a probe of the solution of aqueous ions,
J. Am. Chem. Soc., 131, 7264, 2009.

M. Polanski, T.K. Nielsen, Y. Cerenius, J. Bystrzycki, and T.R. Jensen,
Synthesis and decomposition mechanisms of Mg_2FeH_6 studied by in-situ synchrotron X-ray diffraction and high pressure DSC,
Int. J. Hydrogen Energy, in press.

T. Pozzo, J. Linares Paste, E. Nordberg Karlsson, and D. Logan,
Structural and functional analyses of b-glucosidase from Thermatoga neapolitana: A thermostable three-domain representative of glycoside hydrolase 3,
J. Mol. Biol., 397, 724, 2010.

A.B. Preobrajenski, M.L. Ng, N.A. Vinogradov, A.S. Vinogradov, E. Lundgren, A. Mikkelsen, and N. Mårtensson,
Impact of oxygen coadsorption on intercalation of cobalt under the h-BN nanomesh,
Nano Lett., 9, 2780, 2009.

M.P.J. Punkkinen, P. Laukkanen, M. Ahola-Tuomi, J. Pakarinen, M. Kuzmin, A. Tukiainen, R.E. Perälä, J. Lång, M. Ropo, K. Kokko, L. Vitos, B. Johansson, M. Pessa, and I.J. Väyrynen,
Core-level shifts of InP(100)(2x4) surface: Theory and experiment,
Surf. Sci., 603, 2664, 2009.

B. Qi, S. Olafsson, B. Agnarsson, and M. Göthelid,
High resolution X-ray photoemission spectroscopy study of AlN nano-columns grown by nitridation of Al nano-squares on Si(111) substrates with ammonia,
Thin Solid Films, in press.

M. Quick, A.L. Winther, L. Shi, P. Nissen, H. Weinstein, and J.A. Javitch,
Binding of an octylglucoside detergent molecule in the second substrate (S2) site of LeuT establishes an inhibitor-bound conformation,
Proc. Natl. Acad. Sci. USA (PNAS), 106, 5563, 2009.

T. Rander, A. Lindblad, M. Lundwall, M. Tchaplyguine, G. Öhrwall, S. Svensson, and O. Björneholm,
A dose dependence study of O_2 adsorbed on large Ar clusters,
J. Chem. Phys., 130, 224305, 2009.

D. Ravnsbæk, Y. Filinchuk, Y. Cerenius, H.J. Jakobsen, F. Besenbacher, J. Skibsted, and T.R. Jensen,
A Series of Mixed-Metal Borohydrides,
Ang. Chem. Int. Ed., 48, 6659, 2009.

D.B. Ravnsbæk, Y. Filinchuk, R. Černý, M.B. Ley, D. Haase, H.J. Jakobsen, J. Skibsted, and T.R. Jensen,
Thermal polymorphism and decomposition of $Y(BH_4)_3$,
Inorg. Chem., doi: 10.1021/ic902279k, 2010.

D.B. Ravnsbæk and T.R. Jensen,
Tuning hydrogen storage properties and reactivity; Investigation of the system $LiBH_4$ – $NaAlH_4$,
J. Phys. Chem. Sol., in press.

D.B. Ravnsbæk, L.H. Rude, and T.R. Jensen,
Anion substitution in $NaBH_4$,
To be submitted.

I.C. Razado-Colambo, J. He, H.M. Zhang, G.V. Hansson, and R.I.G. Uhrberg,
Electronic Structure of Ge(111) c(2x8): STM, angle-resolved photoemission and theory,
Phys. Rev. B 79, 205410, 2009.

I.C. Razado-Colambo, J.R. Osiecki, and R.I.G. Uhrberg,
STM studies of the Sn/Ge(111)√3x√3 and 3x3 surfaces,
Submitted to Surf. Sci.

I.C. Razado-Colambo, H.M. Zhang, G.V. Hansson, and R.I.G. Uhrberg,
The electronic structure of H/Ge(111) 1x1 studied by angle-resolved photoelectron spectroscopy,
Phys. Rev. B 80, 193403, 2009.

A. Resta, J. Blomquist, J. Gustafson, H. Karhu, A. Mikkelsen, E. Lundgren, P. Uvdal and J.N. Andersen,
Acetate formation during the ethanol oxidation on Rh(1 1 1),
Surf. Sci., in press.

J.H. Richter, P.G. Karlsson, J. Blomquist, P. Uvdal, G. Westin, O. Karis, and A. Sandell,
Sol-gel prepared cobalt modified anatase titanium dioxide studied by synchrotron radiation electron spectroscopies,
In manuscript.

C. Riedl, C. Coletti, T. Iwasaki, A.A. Zakharov, and U. Starke,
Quasi-free standing epitaxial graphene layers on SiC by hydrogen intercalation,
Phys. Rev. Lett., 103, 246804, 2009.

C. Riedl, C. Coletti, T. Iwasaki, A.A. Zakharov, and U. Starke,
Hydrogen intercalation below epitaxial graphene on SiC(0001),
Mat. Sci. Forum, 645-648, 623, 2010.

A. Rienzo, L.C. Mayor, G. Magnano, C.J. Satterley, J.N. O'Shea, E. Ataman, J. Schnadt, and K. Schulte,
X-ray absorption and photoemission spectroscopy of Zinc-protoporphyrin adsorbed on rutile TiO_2(110) prepared by in situ electrospray deposition,
J. Chem. Phys., 132, 084703, 2010.

L.C.V. Rodrigues, R. Stefani, H.F. Brito, M.C.F.C. Felinto, J. Hölsä, M. Lastusaari, T. Laamanen, and M. Malkamäki,
Thermoluminescence and synchrotron radiation studies on the persistent luminescence of $BaAl_2O_4:Eu^{2+},Dy^{3+}$,
J. Mater. Sci., in press.

J.-E. Rubensson, F. Hennies, L.O. Werme, and O. Karnland,
Soft X-ray Spectroscopic Characterization of Montmorillonite,
In: Scientific Basis for Nuclear Waste Management XXXII, MRS Proc., Vol. 1124, Eds.: R.B. Rebak, N.C. Hyatt, and D.A. Pickett, 2008.

L.H. Rude, Y. Filinchuk, Y. Cerenius, and T.R. Jensen,
Investigation of structures and stability in the $LiBH_4$-LiBr,
To be submitted.

L.H. Rude, Y. Filinchuk, M.H. Sørby, B.C. Hauback, H.J. Jakobsen, and T.R. Jensen,
Tuning the stability of $Ca(BH_4)_2$ by substitution of CaI_2,
To be submitted.

J. Rusz, A.B. Preobrajenski, M.L. Ng, N.A. Vinogradov, N. Mårtensson, O. Wessely, B. Sanyal, and O. Eriksson,
Dynamical effects in X-ray absorption spectra of graphene and monolayered h-BN on Ni(111),
Phys. Rev. B 81, 073402, 2010.

V. Sablinskas, M. Pucetaite, J. Ceponkus, and L. Kimtys,
Structure of propanoic acid dimers as studied by means of MIR and FIR spectroscopy,
J. Mol. Struct., in press, doi: 10.1016/j.molstruc.2010.02.067.

L.J. Sæthre, K.J. Børve, and T.D. Thomas,
Chemical shifts of carbon 1s ionization energies,
J. Electron Spectrosc. and Relat. Phenom., in press.

M. Sahlberg, P. Beran, T. Kollin Nielsen, Y. Cerenius, K. Kadas, M.P.J. Punkkinen, L. Vitos, O. Eriksson, T.R Jensen, and Y. Andersson,
A new material for hydrogen storage, $ScAl_{0.8}Mg_{0.2}$,
J. Sol. Stat. Chem., 182, 3113, 2009.

K. Sakamoto, T. Oda, A. Kimura, K. Miyamoto, M. Tsujikawa, A. Imai, N. Ueno, H. Namatame, M. Taniguchi, P.E.J. Eriksson, and R.I.G. Uhrberg,
Abrupt Rotation of the Rashba Spin to the Direction Perpendicular to the Surface,
Phys. Rev. Lett., 102, 096805, 2009.

K. Sakamoto, M. Setvin, K. Mawatari, P.E.J. Eriksson, K. Miki, and R.I.G. Uhrberg,
Electronic structure of the Si(110)-(16x2) surface: High-resolution ARPES and STM investigation,
Phys. Rev. B 79, 045304, 2009.

E. Salomon, T. Angot, C. Thomas, J.M. Layet, P. Palmgren, C.I. Nlebedim, M. Göthelid, H. Sahaf, and G. Le Lay,
Etching of silicon nanowires on Ag(110) by atomic hydrogen,
Surf. Sci., 603, 3350, 2009.

A. Sandell, B. Sanyal, L.E. Walle, P. Uvdal, and A. Borg,
Probing the conduction band edge of transition metal oxides by X-ray absorption spectroscopy,
Submitted to J. Electron Spectrosc. and Relat. Phenom.

F. Sander, T. Peterle, N. Ballav, F. von Wrochem, M. Zharnikov, and M. Mayor,
Loops vs. stems: benzylic sulfide oligomeres forming carpet type monolayers,
J. Phys. Chem. C, in press.

A. Saywell, J. Sprafke, L. Esdaile, H.L. Anderson, A.J. Britton, A. Rienzo, J.N. O'Shea, and P.H. Beton,
Surface mediated unfolding of electrospray-deposited porphyrin oligomers and polymers,
Submitted to Nature.

A. Schaefer, V. Zielasek, Th. Schmidt, A. Sandell, M. Schowalter, O. Seifarth, L.E. Walle, Ch. Schulz, J. Wollschläger, T. Schroeder, A. Rosenauer, J. Falta, and M. Bäumer,
Growth of praseodymium oxide on Si(111) under oxygen deficient conditions,
Phys. Rev. B 80, 045414, 2009.

K. Schulte, L. Wang, K. Muthukumar, A. Larsson, M.A. Phillips, M. Kanai, T.J.S. Dennis, and P.J. Moriarty,
4f and 5d resonance photoemission in Ce endohedral fullerenes,
To be submitted to Phys. Rev. B.

L. Selegård, V. Khranovskyy, F. Söderlind, C. Vahlberg, M. Ahrén, P.-O. Käll, R Yakimova, and K. Uvdal,
Biotinylation of ZnO nanoparticles and thin films, a two step surface modification study,
Submitted to J. Phys. Chem.

A. Shavorskiy, T. Eralp, E. Ataman, C. Isvoranu, J. Schnadt, J.N. Andersen, and G. Held,
Dissociation of water on oxygen-covered Rh{111},
J. Chem. Phys., 131, 214707, 2009.

L. Shi, K.E. Christensen, K. Jansson, Z. He, and X.D. Zou,
SU-46: Synthesis and characterization of a new three-dimensional open-framework aluminogermanate,
To be submitted to Inorg. Chem.

J.B. Siggaard, E. Johansson, T. Vognsen, S.S. Helt, P. Harris, S. Larsen, and M. Willemoës,
Concerted bifunctionality of the dCTP deaminase-dUTPase from Methanocaldococcus jannaschii. A structural and pre-steady state kinetic analysis,
Arch. Biochem. Biophys., 490, 42, 2009.

C. Silien, M. Buck, G. Goretzki, D. Lahaye, N.R. Champness, T. Weidner, and M. Zharnikov,
Self-assembly of a pyridine-terminated thiol monolayer on Au(111),
Langmuir, 25, 959, 2009.

L. Šiller, Y. Chao, S. Krishnamurthy, and K. Svensson,
Vacuum ultraviolet photoinduced reactions in solid CO_2 and solid CO_2 with coadsorbed water at 20K: a photoemisson spectroscopy study,
Submitted to Phys. Rev. B.

L. Šiller, S. Krishnamurthy, L. Kjeldgaard, B.R. Horrocks, Y. Chao, A. Houlton, A.K. Chakraborty, and M.R.C. Hunt,
X-ray absorption, X-ray emission and X-ray optical luminescence from passivated Si nanocrystals at the Si $L_{2,3}$ edge: direct evidence for the exciton,
Submitted to Phys. Rev. B.

M. Sjöström, E. Wallén, M. Eriksson, and L.-J. Lindgren,
The MAX III storage ring,
Nucl. Instr. and Meth. in Phys. Res. A, 601, 229, 2009.

U. Skyllberg and A. Drott,
Competition between Disordered Iron Sulfide and Natural Organic Matter Associated Thiols for Mercury (II) – an EXAFS study,
Environ. Sci. Technol., 44, 1254, 2010.

C. Solano Arribas, S. Jonsson, A. Pillai, O.F. Wendt, and K. Wärnmark,
Chiral Cu(I) and Ag(I) Complexes of a 2-Pyridone-Fused 2,2'-Bipyridine Analogue: Formation of Rods Containing Hetero- and Homochiral Metal Centers in the Solid State,
Submitted.

E. Sparr, C. Åberg, P. Nilsson, and H. Wennerström,
Diffusional transport in responding lipid membranes,
Soft Matter, 5, 3225, 2009.

D. Srankó, A. Pallagi, E. Kuzmann, S.E. Canton, M. Walczak, A. Sápi, Á. Kukovecz, Z. Kónya, P. Sipos, and I. Pálinkó,
Synthesis and Characteristic Properties of Novel Ba(II)/Fe(III) Layered Double Hydroxides,
Appl. Clay Sci., 48, 214, 2010.

D. Srankó, A. Pallagi, I. Pálinkó, E. Kuzmann, S.E. Canton, M. Walczak, and P. Sipos,
Synthesis and Structural Features of a Novel Ba(II)-Fe(III)-Layered Double Hydroxide,
In: Insights into Coordination, Bioinorganic and Applied Inorganic Chemistry, pp. 380-385, eds.: M. Melník, P. Segľa, and M. Tatarko, Press of Slovak University of Technology, Bratislava, 2009.

U. Starke,
Non-basal plane SiC surfaces: Anisotropic structures and low-dimensional electron systems,
Phys. Stat. Sol. (b), 246, 1569, 2009.

U. Starke and C. Riedl,
Epitaxial graphene on SiC(0001) and SiC($000\bar{1}$): from surface reconstructions to carbon electronics,
J. Phys.: Cond. Matt., 21, 134016, 2009.

A. Stroppa, F. Mittendorfer, J.N. Andersen, G. Parteder, F. Allegretti, S. Surnev, and F.P. Netzer
Adsorption and Dissociation of CO on Bare and Ni-Decorated Stepped Rh(553) Surfaces,
J.Phys. Chem. C 113, 942, 2009.

K. Ståhl, J.E.T. Andersen, I. Shim, and S. Christgau,
Structures of strontium diformate and strontium fumarate. A synchrotron powder diffraction study,
Acta Cryst. B 65, 481, 2009.

P.D. Svensson and S. Hansen,
Intercalation of Smectite with Liquid Ethylene Glycol – Resolved in Time and Space by Synchrotron X-Ray Diffraction,
Appl. Clay Sci., in press.

P.D. Svensson and S. Hansen,
Freezing and Thawing of Montmorillonite – A Time Resolved Synchrotron X-ray Diffraction Study,
Submitted.

I.-H. Svenum, Ø. Borck, K. Schulte, L.E. Walle, and A. Borg,
Adsorption of methanol on Ni_3Al(111) and NiAl(110): A high resolution PES study,
Surf. Sci., 603, 2370, 2009.

A. Talavera, R. Friemann, S. Gómez-Puerta, C. Martinez-Fleites, G. Garrido, A. Rabasa, A. López-Requena, A. Pupo, R.F. Johansen, O. Sánchez, U. Krengel, and E. Moreno,
Nimotuzumab, an Antitumor Antibody that Targets the Epidermal Growth Factor Receptor, Blocks Ligand Binding while Permitting the Active Receptor Conformation,
Cancer Res., 69, 5851, 2009.

J. Tan, C. Vonrhein, O.S. Smart, G. Bricogne, M. Bollati, Y. Kusov, G. Hansen, J.R. Mesters, C.L. Schmidt, and R. Hilgenfeld,
The SARS-unique domain (SUD) of SARS coronavirus contains two macrodomains that bind G-quadruplexes,
PLoS Pathog., 5, e1000428, 2009.

M. Tchaplyguine, S. Legendre, A. Rosso, I. Bradeanu, G. Öhrwall, S.E. Canton, T. Andersson, N. Mårtensson, S. Svensson, and O. Björneholm,
Purely minority-component surface observed for self-assembled free NaK nano-alloy clusters,
Phys. Rev. B 80, 033405, 2009.

C. Teichert, J.J. de Miguel, and T. Bobek,
Ion Beam Sputtered Nanostructured Semiconductor Surfaces as Templates for Nanomagnet Arrays,
J. Phys.: Condens. Matter, 21, 224025, 2009.

M. Tengelin-Nilsson, L. Ilver, and J. Kanski,
Valence electron structure in CuPc,
Submitted to J. Chem. Phys.

M. Tengelin-Nilsson, L. Ilver, J. Kanski, and P. Klason,
Bonding character of Cu in CuPc,
Submitted to Phys. Rev. B.

S. Thorin, N. Čutić, F. Lindau, S. Werin, and F. Curbis,
Photocathode operation of a thermionic RF gun,
Nucl. Instr. and Meth. in Phys. Res. A, 606, 291, 2009.

Ö. Topel, I. Persson, D. Lundberg, and A.-S. Ullström,
On the structure of the N,N'-dimethylpropyleneurea and dimethylsulfoxide solvated gallium(III) and indium(III) ions and bromide complexes in solution and solid state, and the complex formation of the gallium(III) and indium(III) bromide systems in N,N'-dimethylpropyleneurea,
Inorg. Chim. Acta, 363, 988, 2010.

N. Torapava, A. Radkevich, D. Davydov, A. Titov, and I. Persson,
Composition and Structure of Polynuclear Chromium(III) Hydroxo Complexes,
Inorg. Chem., 48, 10383, 2009.

V.G. Tsirkone, K. Dossi, C. Drakou, S.E. Zographos, M. Kontou, and D.D. Leonidas,
Inhibitor design for ribonuclease A: the binding of two 5'-phosphate uridine analogues,
Acta Cryst. F 65, 671, 2009.

I. Ulfat, J. Adell, J. Sadowski, L. Ilver, and J. Kanski,
As3d core level studies of (GaMn)As annealed under As capping,
Surf. Sci., 604, 125, 2010.

J. Unga, F. Tajarobi, O. Norder, G. Frenning, and A. Larsson,
Relating solubility data of parabens in liquid PEG 400 to the behaviour of PEG 4000-parabens solid dispersions,
Eur. J. Pharmaceutics and Biopharmaceutics, 73, 260, 2009.

S. Urpelainen, A. Caló, L. Partanen, M. Huttula, S. Aksela, H. Aksela, S. Granroth, and E. Kukk,
Sb_4 clusters: 4d core ionization, subsequent Auger decay, and fragmentation pathways of the Auger final states,
Phys. Rev. A 79, 023201, 2009.

S. Urpelainen, A. Caló, L. Partanen, M. Huttula, J. Niskanen, E. Kukk, S. Aksela, and H. Aksela,
Valence photoionization and the following fragmentation pathways in Sb_4 clusters,
Phys. Rev. A, 80, 043201, 2009.

S. Urpelainen, S. Heinäsmäki, M.-H. Mikkelä, M. Huttula, S. Osmekhin, H. Aksela, and S. Aksela,
5d photoionization and Auger decay in atomic Pb,
Phys. Rev. A 80, 012502, 2009.

S. Urpelainen, M. Huttula, T. Balasubramanian, R. Sankari, P. Kovala, E. Kukk, E. Nõmmiste, S. Aksela, R. Nyholm, and H. Aksela,
FINEST: A high performance branch-line for VUV photon energy range gas phase studies at MAX-lab,
AIP Conference Proceedings, in press.

C. Vahlberg, R. Petoral Jr., and K. Uvdal,
XPS and NEXAFS study of Noradrenaline-terminated propanethiol adsorbed on gold,
In manuscript.

K. Walldén, A. Rinaldo-Matthis, B. Ruzzenente, C. Rampazzo, V. Bianchi, and P. Nordlund,
Structure of Human Cytosolic Deoxyribonucleotidase: Insights into Recognition of Substrates and Nucleoside Analogs,
In manuscript

K. Walldén, B. Ruzzenente, V. Bianchi, and P. Nordlund,
Structures of the human mitochondrial deoxyribonucleotidase in complex with nucleoside analogue monophosphates: Implications for the structure-aided design of novel nucleoside analogues,
In manuscript.

L.E. Walle, A. Borg, P. Uvdal, and A. Sandell,
Experimental evidence for mixed dissociative and molecular adsorption of water on a rutile TiO_2(110) surface without oxygen vacancies,
Phys. Rev. B 80, 235436, 2009.

Q. Wang, A. Pietzsch, F. Hennies, H. Ni, and Y. Chao,
Synthesis of Water dispersible Photoluminescent Silicon Nanoparticles and Their Use in Biological Fluorescent Imaging,
J. Nanopart. Res., in press.

J. Vasur, R. Kawai, E. Andersson, K. Igarashi, M. Sandgren, M. Samejima, and J. Ståhlberg,
X-ray crystal structures of Phanerochaete chrysosporium Laminarinase16A in complex with products from lichenan and laminarin hydrolysi,
FEBS Journal, 276, 4282, 2009.

J. Vasur, R. Kawai, K.H.M. Jonsson, G. Widmalm, Å. Engström, M. Frank, E. Andersson, H. Hansson, H. Forsberg, K. Igarashi, M. Samejima, M. Sandgren, and J. Ståhlberg,
Synthesis of Cyclic β-Glucan Using Laminarinase 16A Glycosynthase Mutant from the Basidiomycete Phanerochaete chrysosporium.
J. Am. Chem. Soc., 132, 1724, 2010.

S. Watcharinyanon, C. Puglia, E. Göthelid, J.-E. Bäckvall, E. Moons, and L.S.O. Johansson,
Molecular orientation of thiol-derivatized tetraphenylporphyrin on gold studied by XPS and NEXAFS,
Surf. Sci., 603, 1026, 2009.

T. Weidner, N. Ballav, U. Siemeling, D. Troegel, T. Walter, R. Tacke, D.G. Castner, and M. Zharnikov,
Tripodal binding units for self-assembled monolayers on gold: A comparison of thiol and thioether headgroups,
J. Phys. Chem. C 113, 19609, 2009.

S. Werin, S. Thorin, M. Eriksson, and J. Larsson,
Short Pulse Facility for MAX-lab,
Nucl. Instr. and Meth. in Phys. Res. A 601, 98, 2009.

M. Weser, Y. Rehder, K. Horn, M. Sicot, M. Fonin, A.B. Preobrajenski, E.N. Voloshina, and Yu. S. Dedkov,
Induced magnetism of carbon atoms at the graphene/Ni(111) interface,
Appl. Phys. Lett., 96, 012504, 2010.

R. Westerström, C.J. Weststrate, J. Gustafson, A. Mikkelsen, J. Schnadt, J.N. Andersen, E. Lundgren, N. Seriani, F. Mittendorfer, G. Kresse, and A. Stierle,
Lack of surface oxide layers and facile bulk oxide formation on Pd(110),
Phys. Rev. B 80, 125431, 2009.

C.J. Weststrate, A.C. Gluhoi, I.M.N. Groot, E.D.L. Rienks, J.W. Bakker, B.E. Nieuwenhuys, E. Lundgren, and J.N. Andersen,
CO Adsorption on Au(310) and Au(321): 6-fold Coordinated Gold Atoms,
Surf. Sci., 603, 2152, 2009.

C. Virojanadara, M. Hetzel, L.I. Johansson, W.J. Choyke, and U. Starke,
Atomic and electronic structure of the (2×1) and c(2×2) 4H-SiC$(1\bar{1}02)$ surfaces,
Mat. Sci. Forum, 600-603, 291, 2009.

C. Virojanadara, R. Yakimova, J.R. Osiecki, M. Syväjärvi, R.I.G. Uhrberg, and L.I. Johansson, and A.A. Zakharov,
Substrate orientation: A way toward higher quality monolayer graphene growth on 6H-SiC(0001),
Surf. Sci., 603, L87, 2009.

D. Vlachos, S.D. Foulias, and M. Kamaratos,
Barium adsorption on the chemisorbed O(2×1)/Ni(110) surface: A combined Auger electron spectroscopy and synchrotron radiation study,
J. Phys.: Condens. Matt., 21, 445004, 2009.

D. Vlachos, S.D. Foulias, and M. Kamaratos,
Development and characterization of an ultrathin barium oxide film on a surface oxidized Ni(110) substrate,
Synthesis and Reactivity in Inorganic, Metal-Organic, and Nano-Metal Chemistry, 38, 400, 2008.

S. Yu, S. Ahmadi, P. Palmgren, F. Hennies, M. Zuleta, and M. Göthelid,
Modification of charge transfer and energy level alignment at Organic/TiO_2 Interfaces,
J.Phys.Chem. C 113, 13765, 2009.

S. Yu, S. Ahmadi, C. Sun, P. Palmgren, F. Hennies, M. Zuleta, and M. Göthelid,
4-tert-butyl pyridine bond site and band bending on TiO_2(110),
J. Phys. Chem. C 114, 2315, 2010.

M.G. Zahl, V. Myrseth, T.H. Andersen, A. Borg, L.J. Sæthre, and K.J. Børve,
Molecular Photoelectron Spectra as a Tool in Adsorption Studies,
Submitted to J. Phys. Chem.

Y. Zhan, E. Holmström, R. Lizárraga, O. Eriksson, X. Liu, F. Li, E. Carlegrim, S. Stafström, and M. Fahlman,
Efficient Spin Injection Through Exchange Coupling at Organic Semiconductor/Ferromagnet Heterojunctions,
Adv. Mater., doi: 10.1002/adma.200903556.

Y.Q. Zhan, X.J. Liu, F.H. Li, I. Bergenti, P. Graziosi, V. Dediu, and M. Fahlman,
The role of aluminum oxide buffer layer in organic spin-valves performance,
Appl. Phys. Lett., 94, 053301, 2009.

M. Zharnikov,
High-resolution X-ray photoelectron spectroscopy in studies of self-assembled organic monolayers,
J. Electron Spectrosc. and Relat. Phenom., in press.

M. Zuleta, S. Yu, S. Ahmadi, G. Boschloo, M. Göthelid, and A. Hagfeldt,
Monitoring N719-dye configurations on (1xn) reconstructed anatase (100) by means of STM: reversible configurational changes upon illumination,
Submitted to Langmuir.

A. Önsten, D. Stoltz, P. Palmgren, S. Yu, M. Göthelid, and U.O. Karlsson,
Water adsorption on ZnO(0001): Transition from triangular reconstructions to hydroxyl termination,
Submitted to J. Phys. Chem. C.

Theses

Ph.D. Theses

J. Adell,
Synchrotron light based spectroscopy of MBE-grown (GaMn)As structures,
Department of Applied Physics, Chalmers University of Technology, Göteborg, Sweden,
ISBN 978-91-7385-313-2, 2009.

G. Barkhordarian,
Novel Mg-Based Hydride Composites for Hydrogen Storage,
Techn. Universität Hamburg-Harburg, Germany, 2007.

R. Bruce,
Beam loss mechanisms in relativistic heavy-ion colliders,
Department of Accelerator Physics, MAX-lab, Lund University, Lund, Sweden,
ISBN 978-91-628-7852-8, 2009.

U. Bösenberg,
$LiBH_4$-MgH_2 Composites for Hydrogen Storage,
Techn. Universität Hamburg-Harburg, Germany, 2009.

H. Enquist,
Studies of phonons and phase transitions by time-resolved X-ray diffraction,
Department of Physics, Lund University, Lund, Sweden, ISBN 978-91-628-7868-9, 2009.

N. Forsgren,
Structural Studies of the Surface Adhesin SspB from Streptococcus gordonii,
Department of Odontology, Umeå University, Umeå, Sweden, ISBN 978-91-7264-955-2, 2010.

S. Gavrilyuk,
Molecular electronic, vibrational and rotational motion in optical and X-ray fields,
Department of Theoretical Chemistry, Royal Institute of Technology (KTH), Stockholm, Sweden,
ISBN 978-91-7415-483-2, 2009.

H. Hald,
The ionotropic glutamate receptors. Structural and functional studies using the methods of protein crystallography and patch clamp electrophysiology,
Department of Medicinal Chemistry, Faculty of Pharmaceutical Sciences,
University of Copenhagen, Copenhagen, Denmark, ISBN 87-92199-65-8, 2009.

M.D. Hansson,
Structural and physicochemical studies on metal and porphyrin binding by the Bacillus subtilis ferrochelatase,
Department of Biochemistry, Lund University, Lund, Sweden, ISBN 978-91-7422-222-7, 2009.

E. Hilner,
Characterization of surfaces relevant to nanotechnology,
Department of Physics, Lund University, Lund, Sweden, 2009.

R. Høiberg-Nielsen,
Small Angle X-Ray Scattering of Proteins in Solution, Self-assembly and Protein-Protein Interactionsy,
Biophysics Group, Department of Basic Sciences and Environment,
University of Copenhagen, Faculty of Life Sciences, Copenhagen, Denmark, 2009.

P. Jussila,
Advances in nanoscale functionalization of stainless steel surfaces,
Institute of Physics, Tampere University of Technology, Tampere, Finland, ISBN 978-952-15-2267-3, 2009.

H. Koskiniemi,
Enzymatic activation of oxygen in the biosynthesis of polyketide antibiotics,
Department of Medical Biochemistry and Biophysics, Karolinska Institutet, Stockholm, Sweden,
ISBN 978-91-7409-615-6, 2009.

J.-C. Liu,
Dynamics of multiphoton processes in nonlinear optics and X-ray spectroscopy,
Department of Theoretical Chemistry, Royal Institute of Technology (KTH), Stockholm, Sweden,
ISBN 978-91-7415-480-1, 2009.

A. Ljunggren,
Structural and Functional Studies of Chagasin, a Parasite Protease Inhibitor,
Department of Laboratory Medicine, Lund University, Lund, Sweden, 2009.

H.A. Navirian,
Structural studies of materials using time-resolved X-ray diffraction,
Department of Physics, Lund University, Lund, Sweden, ISBN 978-91-628-7888-7, 2009.

G. Parteder,
Growth of surface supported low dimensional nanostructures: oxide and metal-on-oxide systems,
Department of Experimental Physics, Karl-Franzens University, Graz, Austria, 2009.

A. Persson,
X-ray Absorption Spectroscopy on Nanomagnet Arrays and Thin Films: Magnetism and Structure,
Department of Physics, Uppsala University, Uppsala, Sweden, ISBN 978-91-554-7712-7, 2010.

M. Pietrzyk,
The contribution of the 3d and 4f shells to the electronic structure of selected IV-VI semiconductors doped with Mn, Gd, and Eu,
Institute of Physics, Polish Academy of Sciences, Warsaw, Poland, 2010.

A. Ramachandran,
Surface studies of palladium based membranes and model systems,
Department of Physics, Norwegian University of Science and Technology (NTNU), Trondheim, Norway,
ISBN 978-82-471-1504-6, 2009.

I. Razado-Colambo,
Scanning Tunneling Microscopy and Photoelectron Spectroscopy Studies of Si(111) and Ge(111) Surfaces: Clean and Modified by H or Sn Atoms,
Department of Physics, Chemistry and Biology, Linköping University, Linköping, Sweden,
ISBN 978-91-7393-705-4, 2009.

I. Redzynia,
Crystal structure of chagasin – cysteine protease inhibitor from Trypanosoma cruzi and its complexes with proteases,
Department of Biotechnology and Food Sciences, Technical University of Lodz, Lodz, Poland, 2009.

M. Sjöström,
Accelerator physics studies of the MAX-lab storage rings,
Department of Accelerator Physics, MAX-lab, Lund University, Lund, Sweden,
ISBN 978-91-628-7793-4, 2009.

I.-H. Svenum,
Interactions of Functional Groups with Surfaces,
Department of Physics, Norwegian University of Science and Technology (NTNU), Trondheim, Norway,
ISBN 978-82-471-1641-8, 2009.

S. Urpelainen,
Instrumentation for spectroscopy and experimental studies of some atoms, molecules and clusters,
Department of Physical Sciences, University of Oulu, Oulu, Finland, ISBN 978-951-42-9266-9, 2009.

L.E. Walle,
Surface science studies of TiO_2 single crystal systems,
Department of Physics, Norwegian University of Science and Technology (NTNU), Trondheim, Norway,
ISBN 978-82-471-1887-0, 2009.

H. Wang,
Metabolic regulation of nitrogen fixation in Rhodospirillum rubrum,
Department of Biochemistry and Biophysics, Stockholm University, Stockholm, Sweden,
ISBN 978-91-7155-920-3, 2009.

J. Vasur,
Probing promiscuity: Structural studies of Phanerochaete chrysosporium Laminarinase 16A,
Department of Molecular Biology, Swedish University of Agricultural Sciences, Uppsala, Sweden,
ISBN 978-91-576-7445-6, 2009.

M.B. Vester-Christensen,
Production, Purification and Structural Characterisation of Recombinant Barley Limit Dextrinase and Charaterisation of its interaction with the Endogenous Limit Dextrinase Inhibitor,
Department of Systems Biology, Technical University of Denmark, Kgs. Lyngby, Denmark, 2009.

D. Ågren,
Structural enzymology of dormancy related proteins from Mycobacterium tuberculosis,
Department of Medical Biochemistry and Biophysics, Karolinska Institutet, Stockholm, Sweden,
ISBN 978-91-7409-298-1, 2009.

Magnus Sjöström is congratulated on his doctoral thesis by Mikael Eriksson, June 2009.
Photo: Bengt-Erik Wingren

Licentiate Theses

B. Agnarsson,
Surface studies on a–sapphire for potential use in GaN epitaxial growth,
Department of Materials Physics, Royal Institute of Technology (KTH), Stockholm, Sweden,
ISBN 978-91-7415-286-9, 2009.

E. Ataman,
X-ray Photoelectron Spectroscopy Studies of Amino Group-Containing Compounds on Gold and Titanium Dioxide,
Divison of Synchrotron Radiation Research, Lund University, Lund, Sweden, 2010.

C. Isvoranu,
Metal-Organic Complexes and Related Compounds Studied by Electron Spectroscopy,
Divison of Synchrotron Radiation Research, Lund University, Lund, Sweden, 2009.

M.L. Ng,
Layered materials on transition metal surfaces studied by spectroscopic and microscopic techniques,
Department of Physics, Uppsala University, Uppsala, Sweden, 2009.

N. Ottosson,
Structure, excited-state dynamics and surface composition of simple aqueous systems,
Department of Physics and Materials Science, Uppsala University, Uppsala, Sweden, 2009.

P.D. Svensson,
Experiments with Smectite Resolved in Time and Space by Synchrotron X-Ray Diffraction,
Polymer & Materials Chemistry, Lund University, Lund, Sweden, 2009.

M.Sc., Bachelor and Diploma Theses

R.W. Andersen,
Crystallographic studies of Sulfolobus solfataricus phosphoribosyl-pyrophosphate (PRPP) synthase,
Department of Chemistry, Faculty of Science, University of Copenhagen, Copenhagen, Denmark, 2010.

L. Blomster,
Fluoresenssispektrografiasta,
Department of Physics, University of Oulu, Oulu, Finland, 2009.

A.M. Chaudry,
Investigation of pH dependence of Aspergillus aculeatus β-1.4-galactanase on galactan,
Department of Chemistry, Faculty of Science, University of Copenhagen, Copenhagen, Denmark, 2010.

M. Hetzel,
Atomic and Electronic Properties of 4H-SiC ($1\bar{1}02$) and 4H-SiC ($\bar{1}10\bar{2}$),
Institut für allgemeine Physik, Technische Universität Wien, Austria.

D. Jacobsson,
Calibration of plastic-scintillator detectors at MAX-lab in preparation for (γ,π^+) experiments,
Department of Physics, Lund University, Lund, Sweden, 2009.

J. Langholm Jensen,
Structural Comparison of Bovine and Camel Chymosin in relation to their Milk Clotting Properties,
Department of Chemistry, Faculty of Science, University of Copenhagen, Copenhagen, Denmark, 2010.

A. Kettunen,
Software development for an electron-ion coincidence spectrometer,
Department of Physics, University of Oulu, Oulu, Finland, 2009.

J. Lång,
Tin layers on GaAs(100) and InAs(100) semiconductor surfaces: Theoretical and experimental study,
Department of Physics and Astronomy, University of Turku, Turku, Finland, 2009.

M.-H. Mikkelä,
Metal Clusters,
Department of Physics, University of Oulu, Oulu, Finland, 2009.

C. Mårup Osmundsen,
Syntheses of zeolitic Lewis acids using post-treatment,
Department of Chemistry. Technical University of Denmark, Lyngby, Denmark. 2010.

B. Pallisgaard,
Charged nanodiscs – Preparation of charged nanodiscs and investigation of their shape and stacking by SAXS,
Biophysics Group, Department of Basic Sciences and Environment,
Faculty of Life Sciences, University of Copenhagen, Copenhagen, Denmark, 2009.

J. Sjögren,
Construction and initial testing of a neutron detector prototype,
Department of Physics, Lund University, Lund, Sweden, 2009.

N. Skar-Gislinge,
Small Angle X-Ray Scattering of phospholipid Nanodiscs,
Biophysics Group, Department of Basic Sciences and Environment,
Faculty of Life Sciences, University of Copenhagen, Copenhagen, Denmark, 2009.

S. Strazdaite,
Conformational Studies of 1-butene Secondary Ozonide by Means of FTIR Spectroscopy,
Department of General Physic and Spectroscopy, Vilnius University, Vilnius, Lithuania, 2009.

P. Turunen,
Auger-spektrien mittaaminen höyryistä ja kiinteistä aineista,
Department of Physics, University of Oulu, Oulu, Finland, 2009.

T. Reinholdt Vognsen,
Structural investigations of dCTP deaminase:dUTPase from Mycobacterium typerculosis,
Department of Chemistry, Technical University of Denmark, Kgs. Lyngby, Denmark, 2008.

C. Wilkens,
A novel insect antifreeze protein and some type III fish anti-freeze proteins – structure and function,
Department of Chemistry, Faculty of Science, University of Copenhagen, Copenhagen, Denmark, 2009.

Erasmus projects

O. de Barrios,
Structure determination of a double mutant of the ionotropic glutamate receptor iGluR2 in order to characterize the binding of positive allosteric modulators diazoxide and cyclothiazide,
Department of Medicinal Chemistry, Faculty of Pharmaceutical Sciences,
University of Copenhagen, Copenhagen, Denmark, 2009.

A. Ceravalls de Rabassa,
Structure determination of the iGluR2 and iGluR5 crystallized under the presence of L-aspartate and kanate respectively,
Department of Medicinal Chemistry, Faculty of Pharmaceutical Sciences, University of Copenhagen, Copenhagen, Denmark, 2009.

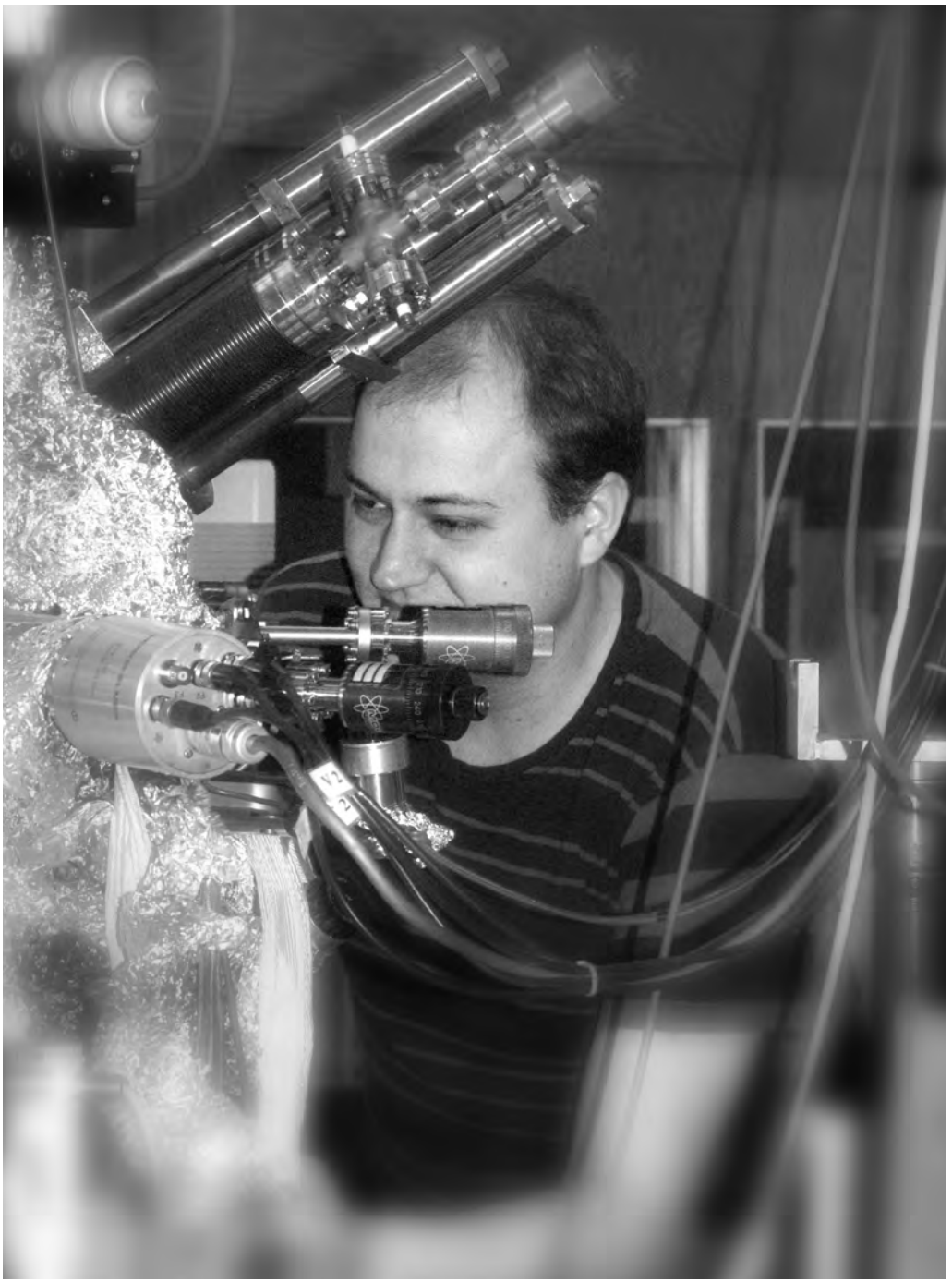

Lars Erik Walle defended his Ph.D. thesis at the Norwegian University of Science and Technology in Trondheim, Norway, 2009.
Photo: Annika Nyberg

Conference Contributions

S. Ahmadi, S. Yu, F. Hennies, M. Zuleta, and M. Göthelid,
Adsorption mode dependent charge transfer on MgPc-TiO_2(110): effects of annealing and surface structure,
European Materials Research Society (EMRS), Strasbourg, France, June 8-9, 2009.

F. Allegretti,
Step-induced stabilization of strained Mn_xO_y overlayers on vicinal Pd(100) surfaces,
6th International Workshop on Oxide Surfaces (IWOX-6), Schladming, Austria, January 18-23, 2009.

V.Yu. Aristov, O.V. Molodtsova, D.V. Vyalikh, M. Knupfer, P. De Padova, and G. Le Lay,
Origin of the metal-insulator transition in the prototypical In/Si(111) quasi-one-dimensional system,
12th International Conference on the Formation of Semiconductor Interfaces, From Semiconductors to Nanoscience and Applications with Biology (ICFSI-12), Weimar, Germany, July 5-10, 2009.

V.Yu. Aristov, A.M. Ionov, O.V. Molodtsova, and M. Knupfer,
UHV cryomanipulators for electron spectroscopy at 5K - 400 K,
10th International Conference on Synchrotron Radiation Instrumentation (SRI-09),
Melbourne, Australia, September 27 - October 2, 2009.

V.Yu. Aristov, V.V. Maslyuk, O.V. Molodtsova, I. Mertig, T. Bredow, and M. Knupfer,
Electronic properties of pristine magnetic transition metal phthalocyanine thin films,
11th International Conference on Electronic Spectroscopy and Structure (ICESS-11)
Nara, Japan, October 6-10, 2009.

V.Yu. Aristov, O.V. Molodtsova, V.V. Maslyuk, D.V. Vyalikh, A.B. Preobrajenski, I. Mertig, T. Bredow, and M. Knupfer,
Electronic structure of potassium doped magnetic transition metal phthalocyanine thin films,
International Workshop on Electronic Spectroscopy for Gas-phase Molecules and Solid Surfaces (IWES 2009),
Sendai, Japan, October 12-15, 2009.

V.Yu. Aristov, V.V. Maslyuk, O.V. Molodtsova, I. Mertig, T. Bredow, and M. Knupfer,
Electronic properties of pristine magnetic transition metal phthalocyanine thin films: experiment and DFT calculations,
First Joint BER II and BESSY II Users Meeting, Berlin, Germany, November 12-13, 2009.

L. Arleth,
BioXTAS: Combining microfluidics and SAXS to study biomolecules in solution with minimal sample consumption,
NIB2009, Neutrons in Biology International Meeting, Lund, Sweden, June 22-24, 2009.

L. Arleth,
BioXTAS: A microfluidics approach to high-throughput SAXS studies of proteins in solution,
International Conference on Small-Angle Scattering (SAS2009),
Oxford, United Kingdom, September 13-18, 2009.

M. Asad Ayoubi, U. Olsson, A.R. Khokhlov, and L. Piculell,
Structures of Block Copolymers Containing Amphiphilic Repeating Units,
9th Annual Surface and Colloid Symposium, Lund, Sweden, November 18-20, 2009.

E. Ataman, C. Isvoranu, J. Knudsen, J. Andersen, J. Schnadt, K. Schulte, J. Carrasco, and A. Michaelides,
L-cysteine on a rutile TiO_2(110) surface,
Workshop – Hands-on Tutorial on Ab Initio Molecular Simulations: Toward a First-Principles Understanding of Materials Properties and Functions, Berlin, Germany, June 22 - July 1, 2009.

E. Ataman, C. Isvoranu, J. Knudsen, J. Andersen, J. Schnadt, K. Schulte, J. Carrasco, and A. Michaelides,
L-cysteine as a molecular spacer between Au clusters on rutile TiO_2(110),
26th European Conference on Surface Science (ECOSS-26), Parma, Italy, August 30 - September 4, 2009.

T. Balasubramanian, B.N. Jensen, S. Urpelainen, B. Sommarin, U. Johansson, M. Huttula, R. Sankari, E. Nõmmiste, S. Aksela, H. Aksela, and R. Nyholm,
The Normal Incidence Monochromator Beamline I3 on MAX III,
10th International Conference on Synchrotron Radiation Instrumentation (SRI-09), Melbourne, Australia, September 27 - October 2, 2009.

V. Balevičius, V. Šablinskas, V. Pogorelov, and I. Doroshenko,
H-bond clustering of methanol in Ar matrix: 2D FTIR correlation spectroscopy,
National Lithuanian Conference in Physics, (LNFK-2009), Vilnius, Lithuania, June 8-10, 2009.

N. Ballav, B. Schüpbach, O. Dethloff, P. Feulner, A. Terfort, and M. Zharnikov,
A new approach to probe molecular orientation in aromatic self-assembled monolayers,
73rd DPG Spring Meeting, Symposium Organic Photovoltaics: From Single Molecules to Devices (SYOP), Dresden, Germany, March 22-27, 2009.

N. Ballav, A. Terfort, and M. Zharnikov,
Irradiation-promoted exchange reaction as a tool for Chemical Lithography,
73rd DPG Spring Meeting, Symposium Organic Photovoltaics: From Single Molecules to Devices (SYOP), Dresden, Germany, March 22-27, 2009.

J. Balogh,
Nonionic microemulsions: Constructing phase diagrams and some scaling properties,
3rd Iberian Conference on Colloids and Interfaces, (RICIIII), Grenada, July 13-15, 2009.

J.M. Bellosta v. Colbe, R. Gosalawit, M. Dornheim, and R. Bormann,
Fluorite Substitution in Complex Hydrides as Hydrogen Storage Materials,
Gordon Research Conference on Hydrogen Metal Systems, Lucca, Italy, July 12-17, 2009.

C.L. Berthold, H. Wang, S. Nordlund, and M. Högbom,
Removal of ADP-ribosylations; Structure, mechanism and ligand complexes of the mono-ADP- ribosylhydrolase DRAG from R. rubrum,
13th Annual Conference of the Swedish Structural Biology Nework, Tällberg, Sweden, June 12-15, 2009.

C. Bonatto Minella, G. Barkhordarian, U. Bösenberg, M. Dornheim, T.R. Jensen, Y. Cerenius, and R. Bormann,
Hydrogen Sorption Properties of Modified Calcium Borohydride,
3rd Symposium Hydrogen and Energy, Braunwald, Switzerland, January 25-30, 2009.

C. Bonatto Minella, G. Barkhordarian, U. Bösenberg, R. Gosalawit, C. Pistidda, C. Rongeat, O. Gutfleisch, M. Dornheim, R. Bormann, T.R. Jensen, Y. Cerenius, M. Sorby, and B.C. Hauback,
Effect of Transition Metal Fluorides on $Ca(BH_4)_2$ Sorption Properties,
MRS Fall Meeting, Boston, Massachusetts, USA, November 30 - December 4, 2009.

Ø. Borck, I.-H. Svenum, L.E. Walle, T.H. Andersen, and A. Borg,
Adsorption of methylamine on NiAl(110) and Ni_3Al(111) surfaces,
Fysikermøtet 2009, Røros, Norway, August 12-14, 2009.

W.J. Briscoe,
Near Threshold Photoproduction at MAX-lab,
Workshop on the Physics of Excited Nucleon (NSTAR2009), Beijing, P.R. China, April 19-22, 2009.

W.J. Briscoe,
The MAX-lab tagged photon facility,
Workshop on the Physics of Excited Nucleon (NSTAR2009), Beijing, P.R. China, April 19-22, 2009.

W.J. Briscoe,
The Experimental Nuclear Physics Program at MAX-lab,
XII International Seminar on Electromagnetic Interactions of Nuclei (EMIN-2009),
Moscow, Russia, September 17-20, 2009.

J. Brudvik, D. Burdeinyi, K. Fissum, V. Ganenko, K. Hansen, L. Isaksson, K. Livingston, M. Lundin, V. Morokhovskyi, B. Nilsson, B. Schröder, and G. Vashchenko,
Radiation Spectra of 200 MeV Electrons in Diamond and Silicon Crystals at Axial and Planar Orientations,
7th Conference on High Energy and Nuclear Physics and Accelerators, Kharkov, Ukraine, February 23-27, 2009.

J. Brudvik, D. Burdeinyi, K. Fissum, V. Ganenko, K. Hansen, L. Isaksson, K. Livingston, M. Lundin, V. Morokhovskyi, B. Nilsson, B. Schröder, and G. Vashchenko,
The Coherent Bremsstrahlung Beam at MAX-lab,
7th Conference on High Energy and Nuclear Physics and Accelerators, Kharkov, Ukraine, February 23-27, 2009.

J. Brudvik,
The Near-Threshold Pion Photoproduction Program at MAX-lab,
European Nuclear Physics Conference, Bochum, Germany, March 16-20, 2009.

J. Brudvik,
The Tagged Photon Facility at MAX-lab,
XII International Seminar on Electromagnetic Interactions of Nuclei (EMIN-2009),
Moscow, Russia, September 17-20, 2009.

J. Brudvik,
The Near-Threshold Pion Photoproduction Program at MAX-lab,
Swedish Nuclear Physics Meeting XXIX, Örebro, Sweden, November 17-18, 2009.

G. Bujacz, I. Redzynia, A. Bujacz, M. Jaskolski, A. Ljunggren, and M. Abrahamson,
Complexes of cysteine proteases with chagasin,
25th European Crystallographic Meeting, Istanbul, Turkey, August 16-21, 2009.

U. Bösenberg, U. Vainio, P.K. Pranzas, J.W. Kim, Y.W. Cho, D.H. Kim, K.H. Oh, J.M. Bellosta von Colbe, M. Dornheim, and R. Bormann,
Function and mechanism of additives in Reactive Hydride Composites,
Gordon Research Conference on Hydrogen Metal Systems, Lucca, Italy, July 12-17, 2009.

J.I. Capone and G. Feldman,
Elastic Compton Scattering from Carbon,
Meeting of the American Physical Society, Denver, Colorado, USA, April 9, 2009.

J.I. Capone and G. Feldman,
Elastic Compton Scattering from Carbon,
American Physical Society's Division of Nuclear Physics and the Japanese Physical Society,
Hawaii, October 16, 2009.

Y. Chao, Q. Wang, A. Pietzsch, F. Hennies, and H. Ni,
Soft X-ray induced oxidation on acrylic acid grafted luminescent water dispersible silicon quantum dots,
UK IOP Condensed Matter and Materials Physics Conference (CMMP09),
Warwick, United Kingdom, December 15-17, 2009.

Ye. Chernolevskaya, V. Pogorelov, I. Doroshenko, and O. Ievglevskyi,
Spectroscopy of higher alcohols,
10th International Young Scientists Conference Optics and High Technology Material Science,
Kyiv, Ukraine, October 22-26, 2009.

C.E. Christensen, V.E. Pye, P. von Wettstein-Knowles, B.B. Kragelund, and A. Henriksen,
Interactions in peroxisomal β-oxidation, a structural point of view,
4th European Symposium on Plant Lipids, Göttingen, Germany, March 15-18, 2009.

C.E. Christensen, V.E. Pye, B.B. Kragelund, P. von Wettstein-Knowles, and A. Henriksen,
Structure and redox-regulation of peroxisomal 3-ketoacyl-CoA thiolase,
CoLuAa XVIII, Bagsvaerd, Denmark, November 4-5, 2009.

N. Čutić, F. Lindau, S. Thorin, S. Werin, and C. Erny,
An Electro-optical System for MAX-lab Test-FEL Facility,
31st International Free Electron Laser Conference, Proceedings,
Liverpool, United Kingdom, August 23-28, 2009.

M. Dornheim,
Reaction Mechanism and Kinetics of MgH_2+(Li, Na, Ca) Borohydride Reactive Hydride Composites,
Gordon Research Conference on Hydrogen Metal Systems, Lucca, Italy, July 12-17, 2009.

M. Dornheim,
Thermodynamic and Kinetic Properties of Reactive Hydride Composites,
International Conference on Processing and Manufacturing of Advanced Materials, (THERMEC 2009), Berlin, Germany, August 14, 2009.

M. Dornheim,
Reaction mechanism and kinetics of MgH_2/borohydrides based Reactive Hydride Composites,
11th International Conference on Advanced Materials (ICAM-2009),
Rio de Janeiro, Brasil, September 20-25, 2009.

I. Doroshenko, V. Pogorelov, Ye. Chernolevska, V. Balevicius, and V. Sablinskas,
The kinetics of cluster formation during the phase transition gas-liquid in alcohols,
IV Russian-Ukrainian-Polish Conference on Molecular Interactions,
Jastarnia, Poland, October 4-10, 2009.

S. dos Santos, L. Piculell, O. Karlsson, and M. da Graça Miguel,
Ordered mesoporous soft materials synthesised from surfactant templates,
9th National Meeting of Physical Chemistry, Aveiro, Portugal, June 15-16, 2009.

S. dos Santos, L. Piculell, O. Karlsson, and M. da Graça Miguel,
Structured soft materials formed by polymerization reactions in surfactant systems,
Association in Soluiton II – Structure, Function & Performance, Tomar, Portugal, July 26-30, 2009.

S. dos Santos, L. Piculell, O. Karlsson, and M. da Graça Miguel,
Ordered soft materials formed by polymerization reactions in surfactant systems,
23rd Conference of the European Colloid and Interface Society (ECIS 2009),
Antalya, Turkey, September 7-9, 2009.

S. dos Santos, B. Luigjes, and L. Piculell,
The associative interaction between PEO-PPO-PEO triblock copolymer P104 and polyacrylic acid results in dissolution of the surfactant ordered phases,
23rd Conference of the European Colloid and Interface Society (ECIS 2009),
Antalya, Turkey, September 7-9, 2009.

A. Dowierciał, A. Jarmuła, W. Rypniewski, M. Sokołowska, T. Frączyk, J. Cieśla, and W. Rode,
Crystal structure of mouse thymidylate synthase,
14th International Symposium on Pteridines and Folates, Jeju, Korea, June 7-12, 2009.

C. Doyle, S.A. Krasnikov, A.B. Preobrajenski, N.A. Vinogradov, A.A. Zakharov, N.N. Sergeeva, Y.N. Sergeeva, H.L. Lee, M.O. Senge, and A.A. Cafolla,
The formation of covalently bonded porphyrin networks on metal surfaces,
26th European Conference on Surface Science (ECOSS-26), Parma, Italy, August 30 - September 4, 2009.

F. Ekström and Y.-P. Pang,
Structure of HI-6•sarin-acetylcholinesterase determined by X-ray crystallography and molecular dynamics simulation: reactivator mechanism and design,
10th International Meeting on Cholinesterases, Sibenik, Croatia, September 20-25, 2009.

M. Fahlman et al.,
Materials and interfaces for organic spintronics,
2nd Topical Meeting on Spins in Organic Semiconductors, Salt Lake City, Utah, USA, February 4-7, 2009.

W.R. Flavell,
Unravelling the mysteries of solar nanocells using synchrotron radiation and laser techniques,
UK IOP Condensed Matter and Materials Physics Conference (CMMP09),
Warwick, United Kingdom, December 15-17, 2009.

V.R. Galakhov,
X-ray spectroscopy of 3d oxides in the nanocrystalline state,
3rd All-Russian Conference on Nanomaterials, (NANO-2009), Yekaterinburg, Russia, April 20-24, 2009.

M. Gisselbrecht, M. Tchaplyguine, F. Burmeister, S. Svensson, O. Björneholm, and S.L. Sörensen,
Soft X-ray radiation damage in argon clusters,
26th International Conference on Photonic, Electronic and Atomic Collisions (ICPEAC),
Kalamazoo, Michigan, USA, July 22-28, 2009.

L. Gragnaniello,
Surface structure of CoO_x thin films on Pd(100)
26th European Conference on Surface Science (ECOSS-26), Parma, Italy, August 30 - September 4, 2009.

M. Göthelid, S. Yu, S. Ahmadi, P. Palmgren, and M. Zuleta,
Charge transfer, band alignment and surface modifications on dye sensitized TiO_2 surfaces,
European Materials Research Society (EMRS), Strasbourg, France, June 8-9, 2009.

M. Göthelid, S. Yu, S. Ahmadi, P. Palmgren, and M. Zuleta,
Charge transfer, band alignment and surface modifications on dye sensitized TiO_2 surfaces,
12th International Conference on the Formation of Semiconductor Interfaces, From Semiconductors to Nanoscience and Applications with Biology (ICFSI-12), Weimar, Germany, July 5-10, 2009.

M. Hagelstein, T. Baumbach, S. Casalbuoni, A.W. Grau, B. Kostka, R. Rossmanith, D. Saez de Jauregui, B. Diviacco, J. Chavanne, P. Elleaume, A. Bernhard, D. Wollmann, E. Wallén, and E. Mashkina,
Design, Development and Testing of Diagnostic Systems for Superconducting Undulators,
23rd Particle Accelerator Conference (PAC09), Vancouver, Canada, May 4-8, 2009.

S.J.O. Hardman, D.M. Graham, B.F. Spencer, W.R. Flavell, D.J. Binks, F. Sirotti, M. El Kazzi, M. Silly, F. Hennies, J. Akhtar, M.A. Malik, and P. O'Brien,
An XPS investigation into the electronic structure of nanoparticulate lead sulphide and the implications for novel hybrid photovoltaic cell design,
26th European Conference on Surface Science (ECOSS-26), Parma, Italy, August 30 - September 4, 2009.

J. Harnes, M. Winkler, M. Abu-Samha, K.J. Børve, and L.J. Sæthre, and A. Lindblad,
Large polarization-induced cluster-to-monomer shifts in C1s XPS ionization energy of neutral of CS_2 Clusters,
NANOMAT Conference 2009 and Satellite Meetings, Lillehammer, Norway, June 15-19, 2009.

C.G. Hartmann, J.E.T. Andersen, and K. Ståhl,
Locating strontium Ions in bone tissue using EXAFS,
39th Danish Crystallographer Meeting, Lyngby, Denmark, June 2-3, 2009.

S. Heinäsmäki, J. Schulz, R. Sankari, and H. Aksela,
Large linear magnetic dichroism in laser-excited K atoms,
41st European Group for Atomic Systems Conference (EGAS), Gdansk, Poland, July 8-11, 2009.

G. Held,
The interaction of Water with (Pt-Group) Metal Surfaces,
CCPCC-2, Oxford, United Kingdom, July 20-22, 2009.

M. Hirsimäki, L. Kanninen, K. Lahtonen, P. Jussila, R. Pärna, N. Jokinen, O. Tarvainen, M. Kuzmin, E. Nõmmiste, and M. Valden,
Synchrotron light based investigations of benzene-1,3,5-tricarboxylic acid on Cu(100): the role of surface nanopatterning in self-organization,
26th European Conference on Surface Science (ECOSS-26), Parma, Italy, August 30 - September 4, 2009.

J. Hirvonen Grytzelius, H.M. Zhang, and L.S.O. Johansson,
Electronic structure of Mn/Ge(111)-√3×√3 thin films studied by photoelectron spectroscopy,
10th International Conference on Atomically Controlled Surfaces, Interfaces and Nanostructures (ACSIN-10), Granada, Spain, September 22-25, 2009.

J. Hirvonen Grytzelius, H.M. Zhang, and L.S.O. Johansson,
Core-level spectroscopy studies of Mn/Si(111)-√3×√3,
14th International Conference on Solid Films and Surface (ICSCF), Dublin, Ireland, June 29 - July 4, 2008.

J.P. Hofmann et al.,
The Surface Selective Chlorination of RuO_2(110),
GDCh-JCF Frühjahrssymposium, Essen, Germany, March 11-14, 2009.

J.P. Hofmann et al.,
The Surface Selective Chlorination of RuO_2(110),
73rd DPG Spring Meeting, Dresden, Germany, March 22-27, 2009.

J.P. Hofmann et al.,
Model Catalysis on Chlorinated Ruthenium Dioxide (110),
Bunsentagung der Deutschen Bunsen-Gesellschaft für Physikalische Chemie, Köln, Germany, May 21-23, 2009.

A. Holme, K.J. Børve, L.J. Sæthre, and T.D. Thomas,
Carbon 1s photoelectron spectroscopy as a tool in molecular conformational studies,
5th Norwegian Synchrotron User Meeting, Lillehammer, Norway, June 19-20, 2009.

A. Holme, K.J. Børve, L.J. Sæthre, and T.D. Thomas,
Accurate Calculation of Chemical Shifts in Carbon 1s Ionization Energies,
Computational Chemistry Autumn Meeting, Bergen, Norway, October 12-13, 2009.

M. Håkansson, D.T. Logan, C. Diehl, C. Öberg, H. Leffler, and U. Nilsson,
Galectin-3C in Complex with Inhibitors: Two High Resolution Structures,
13th Annual conference of the Swedish Structural Biology Nework, Tällberg, Sweden, June 12-15, 2009.

R. Häggblad, M. Massa, and A. Andersson,
Bulk Phase or Supported Vanadium-(iron)-oxide Catalyst for the Selective Oxidation of Methanol to Formaldehyde?
6th World Congress on Oxidation Catalysis, Lille, France, July 5-10, 2009.

J. Hölsä, T. Laamanen, M. Lastusaari, M. Malkamäki, and P. Novák,
Synchrotron Radiation Studies of Rare Earth Persistent Luminescence Materials,
7th International Conference on f-Elements, Köln, Germany, August 23-27, 2009.

J. Hölsä, T. Laamanen, M. Lastusaari, and M. Malkamäki,
Valence and Environment of Rare Earth Ions in Persistent Luminescence Materials,
36th Colloquium Spectroscopicum Internationale (CSI XXXVI),
Budapest, Hungary, August 30 - September 3, 2009.

J. Hölsä, T. Laamanen, M. Lastusaari, M. Malkamäki, and P. Novák,
Defect Structure in Rare Earth Persistent Luminescence Materials,
216th ECS Meeting, Phys. Chem. Lumin. Mater., W.M. Yen Mem. Symp. (Lumin. Display Mater.),
Vienna, Austria, October 4-9, 2009.

L. Isaksson,
The MAX-lab tagged photon facility,
European Nuclear Physics Conference, Bochum, Germany, March 16-20, 2009.

L. Isaksson,
The MAX-lab tagged photon facility,
First Nordic Meeting in Physics, Copenhagen, Denmark, June 16-18, 2009.

L. Isaksson,
Compton Scattering at MAX-lab,
XII International Seminar on Electromagnetic Interactions of Nuclei (EMIN-2009),
Moscow, Russia, September 17-20, 2009.

C. Isvoranu, B. Wang, E. Ataman, J. Knudsen, K. Schulte, J.N. Andersen, M.-L. Bocquet, and J. Schnadt,
Gas adsorption properties probed by spectroscopic techniques and DFT,
26th European Conference on Surface Science (ECOSS-26), Parma, Italy, August 30 - September 4, 2009.

C. Isvoranu, E. Ataman, K. Schulte, J.N. Andersen, and J. Schnadt,
Atomic-Scale Study of Gas Adsorption Properties of Iron Phthalocyanine Molecules,
The Annual International Conference of the Romanian Society of Biochemistry and Molecular Biology,
Cluj-Napoca, Romania, September 30 - October 3, 2009.

J. Janiak, L. Piculell, and K. Schillén,
The Aqueous Phase Behavior of Polyion-Surfactant Ion Complex Salts Mixed with Nonionic Surfactants,
Sixth Nordic Workshop on Scattering from Soft Matter, Aarhus, Denmark, January 28-29, 2009.

J. Janiak, L. Piculell, and K. Schillén,
The Aqueous Phase Behavior of Polyion-Surfactant Ion Complex Salts and Nonionic Surfactants,
European Student Colloid Conference, Almería, Spain, July 15-18, 2009.

M.H. Jensen, U. Christensen, H. Otten, T. Borchert, L.H. Christensen, S. Larsen, and L. Lo Leggio,
Structure and Function of Microbial and Plant Rhamnogalacturonan Lyases,
ESRF User meeting, Grenoble, France, February 2-5, 2009.

M.H. Jensen, U. Christensen, H. Otten, T. Borchert, L.H. Christensen, S. Larsen, and L. Lo Leggio,
Structural and Kinetic Studies elucidate the Mechanism of Rhamnogalacturonan Lyase from Aspergillus aculeatus,
CoLuAa XVIII, Bagsvaerd, Denmark, November 4-5, 2009.

P. Jiříček, M. Cukr, I. Bartoš, and J. Sadowski,
GaAs(100)-c(4x4) surface studied by photoelectron diffraction,
26th European Conference on Surface Science (ECOSS-26), Parma, Italy, August 30 - September 4, 2009.

R. Johansson, J. Sprenger, B. Walse, M. Sahlin, B.M. Sjöberg, and D.T. Logan,
High-resolution structure of the class Ib RNR salvage protein Nrdl,
Enzymes in Deoxyribonucleotide Synthesis, Hemavan, Sweden, March 29 - April 1, 2009.

R. Johansson, J. Sprenger, B. Walse, M. Sahlin, B.M. Sjöberg, and D.T. Logan,
High-resolution structure of the class Ib RNR salvage protein Nrdl,
13th Annual Conference of the Swedish Structural Biology Nework, Tällberg, Sweden, June 12-15, 2009.

L. Kanninen, K. Lahtonen, N. Jokinen, P. Jussila, O. Tarvainen, M. Kuzmin, M. Hirsimäki, and M. Valden,
Chemical and Structural Characterization of Trimesic Acid on Cu(100) and O/Cu(100) studied by XPS and STM,
26th European Conference on Surface Science (ECOSS-26), Parma, Italy, August 30 - September 4, 2009.

K.G. Kirkensgaard, P. Hägglund, C. Finnie, B. Svensson, and A. Henriksen,
Reaction mechanism of barley thioredoxin reductase,
39th Danish Crystallographer Meeting, Lyngby, Denmark, June 2-3, 2009.

J. Knudsen, L.R. Merte, L.C. Grabow, F.M. Eichhorn. S. Porsgaard, H. Zeuthen, R.T. Vang, E. Laegsgaard, M. Mavrikakis, and F. Besenbacher,
The surface chemistry of a reduced FeO(111) film,
26th European Conference on Surface Science (ECOSS-26), Parma, Italy, August 30 - September 4, 2009.

I.A. Kowalik, G. Öhrwall, B.N. Jensen, R. Sankari, E. Wallén, U. Johansson, O. Karis, and D. Arvanitis,
Commissioning of beamline I1011 at MAX-lab – First results,
10th International Conference on Synchrotron Radiation Instrumentation (SRI-09),
Melbourne, Australia, September 27 - October 2, 2009.

B.J. Kowalski, M.A. Pietrzyk, W. Knoff, A. Łusakowski, J. Sadowski, J. Adell, and T. Story,
Angle-resolved photoemission study and pseudopotential calculations of GeTe and $Ge_{1-x}Mn_xTe$ band structure,
14th International Conference on Narrow Gap Semiconductors and Systems, Sendai, Japan, July 13-17, 2009.

J. Langholm Jensen, A. Mølgaard, J.-C.N. Poulsen, J.M. van den Brink, M. Harboe, K.B. Qvist, and S. Larsen,
Structural comparison of Bovine and Camel chymosin in relation to their milk-clotting properties,
CoLuAa XVIII, Bagsvaerd, Denmark, November 4-5, 2009.

S. Larsen, M. McDonough, M. Thymark, M.H. Jensen, H. Otten, L. Lo Leggio, T. Borchert, L.H. Christensen, H. Frisner, and C. Sonksen,
Substrate Recognition and Catalysis of Family 1 and 4 Polysaccharide Lyases,
American Crystallographic Association Annual Meeting, Toronto, Canada, July 25-20, 2009.

S. Larsen, M. McDonough, M. Thymark, M.H. Jensen, H. Otten, L. Lo Leggio, T. Borchert, L.H. Christensen, H. Frisner, and C. Sonksen,
Substrate recognition and catalysis of polysaccharide lyases,
25th European Crystallographic Meeting, Istanbul, Turkey, August 16-21, 2009.

G. Le Lay, V.Yu. Aristov, O.V. Molodtsova, D.V. Vyalikh, M. Knupfer, P. De Padova, F. Ronci, S. Colonna, and A. Cricenti,
High resolution synchrotron radiation study of the one and two dimensional phases of the prototypical In/Si(111) and Sn/Si,Ge(111) systems by photoelectron spectroscopy down to 10K,
10th International Conference on Synchrotron Radiation Instrumentation (SRI-09),
Melbourne, Australia, September 27 - October 2, 2009.

K. Lewis,
Elastic Compton Scattering from Carbon,
Meeting of the American Physical Society, Denver, Colorado, USA, April 9, 2009.

F. Li,
One-dimensional MnPd alloy and Mn-oxide nanowires on stepped Pd(100) surfaces,
26th European Conference on Surface Science (ECOSS-26), Parma, Italy, August 30 - September 4, 2009.

F. Li et al.,
Work function modification of ferromagnetic electrode $La_{0.7}Sr_{0.3}MnO_3$ for organic spintronic applications using molecular scale engineering,
2nd Topical Meeting on Spins in Organic Semiconductors, Salt Lake City, Utah, USA, February 4-7, 2009.

D.T. Logan,
Structural studies on B12 bond cleavage in class II ribonucleotide reductases,
Gordon Conference on Vitamin B12 and Corphins, Oxford, United Kingdom, August 2-7, 2009.

D.T. Logan,
MAX IV and the ESS,
1st Symposium Läkemedel i Lund, Lund, Sweden, October 21, 2009.

M.N. Løvgreen,
Studies of WT and variants of the bifunctional dCTP deaminase-dUTPase from M tuberculosis,
CoLuAa XVIII, Bagsvaerd, Denmark, November 4-5, 2009.

D.G. Middleton,
Total Photo-absorption Cross Section of $^{6,7}Li$ Below π-threshold,
Nuclear Physics User Meeting, Lund, Sweden, November 3, 2009.

O.V. Molodtsova, M. Knupfer, and V.Yu. Aristov,
Molecular orientation and ordering in CoPc and FePc thin films grown on Au(001)-5x20 in UHV conditions,
27th BESSY Users Meeting, Berlin, Germany, December 4-5, 2008.

O.V. Molodtsova, M. Knupfer, A.N. Chaika, D.V. Vyalikh, A.B. Preobrajenski, and V.Yu. Aristov,
Electronic properties of potassium doped CoPc and FePc,
73rd DPG Spring Meeting, Symposium Organic Photovoltaics: From Single Molecules to Devices (SYOP),
Dresden, Germany, March 22-27, 2009.

O.V. Molodtsova, M. Knupfer, V.V. Maslyuk, Yu.A. Ossipyan, A.N. Chaika, T. Bredow, I. Mertig, and V.Yu. Aristov,
Electronic properties of pristine FePc and CoPc thin films: experiment and calculations,
73rd DPG Spring Meeting, Symposium Organic Photovoltaics: From Single Molecules to Devices (SYOP),
Dresden, Germany, March 22-27, 2009.

O.V. Molodtsova, M. Knupfer, Yu.A. Ossipyan, B.P. Doyle, S. Nannarone, and V.Yu. Aristov,
Magnetic transition metals on a molecular semiconductor: chemistry and electronic properties,
11th International Conference on Electronic Spectroscopy and Structure (ICESS-11)
Nara, Japan, October 6-10, 2009.

O.V. Molodtsova, M. Knupfer, Yu.A. Ossipyan, and V.Yu. Aristov,
Magnetic transition metal phthalocyanine thin films on Au(001): molecular arrangement,
International Workshop on Electronic Spectroscopy for Gas-phase Molecules and Solid Surfaces (IWES 2009),
Sendai, Japan, October 12-15, 2009.

O.V. Molodtsova, M. Knupfer, and V.Yu. Aristov,
Magnetic transition metal-organic semiconductor interface Fe/CuPc: chemistry and electronic properties,
First Joint BER II and BESSY II Users Meeting, Berlin, Germany, November 12-13, 2009.

M.Á. Niño, E. Jiménez, J. Camarero, N. Mikuszeit, J.J. de Miguel, C. Hofer, C. Teichert, L. Gridneva, A. Persson, D. Arvanitis, T. Bobek, H. Kurz, and R. Miranda,
Towards Large-Scale Arrays of Magnetic Nanostructures by Self-Organization Processes,
International Conference on Magnetism (ICM 09), Karlsruhe, Germany, July 26-31, 2009.

J. Niskanen, S. Urpelainen, S. Heinäsmäki, H. Ågren, and H. Aksela,
Valence photoionization of molecular LiCl,
13th International Conference in Quantum Chemistry (13th ICQC), Helsinki, Finland, June 22-27, 2009.

J. Niskanen, M. Vapa, S. Urpelainen, and H. Aksela,
Following dissociation pathways of molecules and small clusters in excited electronic state after valence photoionization,
11th International Conference on Electronic Spectroscopy and Structure (ICESS-11),
Nara, Japan, October 6-10, 2009.

G.V. O'Rielly,
The Near-Threshold Pion Photoproduction Program at MAX-lab,
2009 APS April Meeting, Denver, Colorado, USA, May 4, 2009.

J.N. O'Shea, L.C. Mayor, A.J. Britton, A. Saywell, A. Rienzo, J.B. Taylor, G. Magnano, C.J. Satterley, E. Ataman, J. Schnadt, and K. Schulte,
Soft X-ray electron spectroscopy of big molecules: electrospray deposition at the synchrotron,
UK IOP Condensed Matter and Materials Physics Conference (CMMP09),
Warwick, United Kingdom, December 15-17, 2009.

J.R. Osiecki, I. Razado-Colambo, and R.I.G. Uhrberg,
Reinvestigation of the Sn 4d Line Shape of Sn/Ge(111)3x3,
26th European Conference on Surface Science (ECOSS-26), Parma, Italy, August 30 - September 4, 2009.

F. Ossler, S.E. Canton, and J. Larsson,
In Situ X-Ray Scattering Studies of the Formation Dynamics of Carbon Nanoparticles in an Ethylene Flame,
Italian Section of The Combustion Institute, Combustion Colloquia dedicated to Prof. Antonio D'Alessio,
Naples, Italy, April 26-28, 2009.

F. Ossler, S.E. Canton, and J. Larsson,
In situ Measurements of the dynamics of nanoparticle formation with subnanometer structural resolution based on X-ray scattering diagnostics using a new detector prototype,
The Annual Conference on Carbon, Biarritz, France, June 14-19, 2009.

F. Ossler, L. Jonsson, S.E. Canton, J. Larsson, and P. Sondhauss,
X-ray scattering measurements for studies of particle formation dynamics in reactive systems,
Gordon Research Conferences on X-ray Science (GRC), Waterville, Maine, USA, August 2-7, 2009.

F. Ossler, L. Jonsson, S.E. Canton, J. Larsson, and P. Sondhauss,
X-ray scattering measurements for studies of particle formation dynamics in reactive systems,
Gordon Research Conferences, Laser Diagnostics in Combustion,
Waterville Valley, New Hampshire, USA, August 16-21, 2009.

H. Otten, D. Welner, R. Salbo, P. Harris, K. McFarland, J.-C.N. Poulsen, S. Larsen, and L. Lo Leggio,
Biologically Relevant Metal Ions in the Structures of GH61 Proteins,
8th Carbohydrate Bioengineering Meeting, Ischia, Italy, May 10-13, 2009.

H. Otten, S. Gauer, G.-W. Kohring, and L. Lo Leggio,
Quarternary Structure Evaluation of Dehydrogenases,
First Symposium on Structural Systems Biology, Hamburg, Germany, September 24-25, 2009.

N.A. Ovechkina, V.R. Galakhov, B.A. Gizhevskii, K. Taubitz, M. Raekers, A.R. Cioroiani, M. Neumann, A.S. Semenova, D.G. Kellerman, R. Ovsyannikov, and S.L. Molodtsov,
Valence states of Co ions in nanostructured $LiCoO_2$, obtained by high pressure torsion method,
3rd All-Russian Conference on Nanomaterials, (NANO-2009), Yekaterinburg, Russia, April 20-24, 2009.

H. Over et al.,
Mikroskopische Einsichten in die katalysierte Gasphasen HCl Oxidierung auf RuO_2 (ein neuartiger Deacon Prozess),
42nd Jahrestreffen Deutscher Katalytiker, Weimar, Germany, March 11-13, 2009.

M. Patanen, S. Urpelainen, M. Huttula, E. Nõmmiste, E. Kukk, H. Aksela, and S. Aksela,
High resolution photoabsorption spectrum of KF in the energy range of 18.2-19.4 eV,
13th International Conference in Quantum Chemistry (13th ICQC), Helsinki, Finland, June 22-27, 2009.

A. Persson, L. Gridneva, M.Á. Niño, J. Camarero, J.J. de Miguel, R. Miranda, C. Hofer, C. Teichert, T. Bobek, A. Locatelli, and D. Arvanitis,
Experimental Investigation of the Spin Reorientation in Self-Organized Magnetic Nano-dot Arrays,
European Workshop on Self-Organized Nanomagnets, Aussois, France, March 30 - April 3, 2009.

A. Persson, L. Gridneva, M.Á. Niño, J. Camarero, C. Hofer, T. Bobek, A. Locatelli, J.J. de Miguel, C. Teichert, R. Miranda, and D. Arvanitis,
On the Spin Reorientation of Co/Au and Co/Pt Magnetic Nanodot Arrays,
20th International Colloquium on Magnetic Films and Surfaces (ICMFS'09), Berlin, Germany, July 20-24, 2009.

C. Pistidda, G. Barkhordarian, C. Bonatto Minella, S. Garroni, T.R. Jensen, M. Dornheim, W. Lohstroh, M. Fichtner, and R. Bormann,
Reaction Mechanisms of Formation of $2NaBH_4$+MgH_2 during Hydrogenation of 2NaH+MgB_2,
Gordon Research Conference on Hydrogen Metal Systems, Lucca, Italy, July 12-17, 2009.

V. Pogorelov, I. Doroshenko, O. Karpenko, V. Sablinskas, and V. Balevicius,
The kinetics of cluster formation during the phase transition gas-liquid in alcohols,
3rd International Symposium on Methods and Applications on Computational Chemistry,
Odessa, Ukraine, July 1-3, 2009.

V. Pogorelov, I. Doroshenko, V. Sablinskas, and V. Balevicius,
The kinetics of cluster formation during the phase transition gas-liquid in alcohols,
41st European Group for Atomic Systems Conference (EGAS), Gdansk, Poland, July 8-11, 2009.

V. Pogorelov, I. Doroshenko, O. Karpenko, and O. Ievglevskyi,
Cluster structure of monohydric alcohols: matrix isolation and quantum-chemical calculations,
XIX International School-Seminar Spectroscopy of Molecules and Crystals,
Beregove, Ukraine, September 20-27, 2009.

V. Pogorelov, I. Doroshenko, V. Sablinskas, and V. Balevicius,
The kinetics of cluster formation during the phase transition gas-liquid in alcohols,
XIX International School-Seminar Spectroscopy of Molecules and Crystals,
Beregove, Ukraine, September 20-27, 2009.

V.E. Pye, S. Arent, C.E. Christiansen, and A. Henriksen,
Structural insights into the catabolism of fatty acids in plants,
25th European Crystallographic Meeting, Istanbul, Turkey, August 16-21, 2009.

K.K. Rasmussen, M. Pedersen, L. Arleth, and L. Lo Leggio,
Structural Biology of Transcription Factor CI from TP901-1 by Crystallography and Small-Angle Scattering,
CoLuAa XVIII, Bagsvaerd, Denmark, November 4-5, 2009.

C. Riedl, M. Franke, J. Bernhardt, C. Virojanadara, A.A. Zakharov, K. Heinz, and U. Starke,
Epitaxial Graphene Layers on SiC(0001): Growth, Atomic and Electronic Structure,
14th International Conference on Solid Films and Surface (ICSCF), Dublin, Ireland, June 29 - July 4, 2008.

C. Riedl, C. Coletti, D.S. Lee, L. Vitali, B. Krauß, R. Ohmann, I. Brihuega, A.A. Zakharov, K. von Klitzing, K. Kern, J.H. Smet, and U. Starke,
Structural and Electronic Properties of Epitaxial Graphene on SiC(0001),
7th European Conference on Silicon Carbide and Related Materials, (ECSCRM),
Barcelona, Spain, September 7-11, 2008.

C. Riedl, C. Coletti, T. Iwasaki, A.A. Zakharov, and U. Starke,
Hydrogen Intercalation below Epitaxial Graphene on SiC(0001),
7th International Conference on Silicon Carbide and Related Materials, (ICSCRM), Nürnberg, Germany,
October 11-16, 2009.

L.C.V. Rodrigues, R. Stefani, H.F. Brito, M.C.F.C. Felinto, J. Hölsä., M. Lastusaari, and T. Laamanen,
Thermoluminescence and synchrotron radiation studies on the persistent luminescence $BaAl_2O_4:Eu^{2+}Dy^{3+}$,
11th International Conference on Advanced Materials (ICAM-2009),
Rio de Janeiro, Brasil, September 20-25, 2009.

V. Sablinskas, S. Strazdaite, and J. Ceponkus,
Conformational analysis of 1-alkene secondary ozonides by means of matrix isolation FTIR spectroscopy,
64th International Symposium on Molecular Spectroscopy, Columbus, Ohio, USA, June 22-26, 2009.

V. Šablinskas, V. Balevičius, V. Pogorelov, and I. Doroshenko,
H-bond clustering of methanol in Ar matrix: 2D FTIR correlation spectroscopy,
XIX International School-Seminar Spectroscopy of molecules and crystals,
Beregove, Ukraine, September 20-27, 2009.

K. Sakamoto, T. Oda, A. Kimura, K. Miyamoto, M. Tsujikawa, A. Imai, N. Ueno, H. Namatame, M. Taniguchi, P.E.J. Eriksson, and R.I.G. Uhrberg,
Abrupt upstanding of the Rashba spin,
International Workshop on Strong Correlations and Angle-Resolved Photoemission Spectroscopy,
(CORPES09), Zürich, Schweiz, July 19-24, 2009.

K. Sakamoto, T. Oda, A. Kimura, K. Miyamoto, M. Tsujikawa, A. Imai, N. Ueno, H. Namatame, M. Taniguchi, P.E.J. Eriksson, and R.I.G. Uhrberg,
Abrupt rotation of the Rashba spin,
26th European Conference on Surface Science (ECOSS-26), Parma, Italy, August 30 - September 4, 2009.

K. Sakamoto, T. Oda, A. Kimura, K. Miyamoto, M. Tsujikawa, A. Imai, N. Ueno, H. Namatame, M. Taniguchi, P.E.J. Eriksson, and R.I.G. Uhrberg,
Abrupt Rotation of the Rashba Spin to the Direction Perpendicular to the Surface,
11th International Conference on Electronic Spectroscopy and Structure (ICESS-11)
Nara, Japan, October 6-10, 2009.

K. Sakamoto,
Abrupt change in the direction of the Rashba spin,
IUPAC 5th International Symposium on Novel Materials and Synthesis, (NMS-V), Shanghai, October 18-22, 2009.

A. Saywell, L.M.A. Perdigao, G. Magnano, C.J. Satterley, N. Taleb, M. Gimmenez-Lopez, N.R. Champness, J.N. O'Shea, and P.H. Beton,
Ultra-high vacuum electrospray deposition of single molecule magnets,
UK IOP Condensed Matter and Materials Physics Conference (CMMP09),
Warwick, United Kingdom, December 15-17, 2009.

A. Shavorskiy, T. Eralp, K. Schulte, J.N. Andersen, and G. Held,
Surface chemistry of glycine at the water – Pt{111} interface,
26th European Conference on Surface Science (ECOSS-26), Parma, Italy, August 30 - September 4, 2009.

A. Shavorskiy, T. Eralp, K. Schulte, J.N. Andersen, and G. Held,
Surface chemistry of glycine at the water – Pt{111} interface,
Fourth Annual Conference on The Physics, Chemistry and Biology of Water,
Mount Snow, Vermont, USA, October 22-25, 2009.

E. Seif and B.M. Hallberg,
RNA-protein mutually induced fit: Structure of E. coli isopentenyl-tRNA transferase in complex with tRNA(Phe),
Gordon Conference in RNA Editing, Galveston, TX, USA, January 11-16, 2009.

P. Sipos, D. Zeller, E. Kuzmann, A. Vértes, Z. Homonnay, M. Walczak, and S.E. Canton,
Mössbauer and EXAFS Study of Fe(III) Ions in Strongly Alkaline Aqueous Solutions ,
International Conference on the Applications of the Mössbauer Effect, Book of abstracts,
(ICAME 2009), Vienna, Austria, July 19-24, 2009.

C. Sjöstedt, J.P. Gustafsson, M. Hassellöv, and I. Persson,
Iron phases in softwater lakes,
6th International Symposium on Ecosystem Behavior (BIOGEOMON), Helsinki, Finland, June 29 - July 3, 2009.

D.F. Srankó, N. Balázs, É.G. Bajnóczi, K. Mogyorósi, and P. Sipos,
Optimization of a Flame-synthetic Method for the Preparation of Pristine and Fe-doped TiO_2 Photocatalysts,
14th International Chemistry Conference, Cluj-Napoca, Romania, November 13-15, 2008.

D. Srankó, A. Pallagi, I. Pálinkó, E. Kuzmann, S.E. Canton, M. Walczak, and P. Sipos,
Synthesis and Structural Features of a Novel Ba(II)-Fe(III)-Layered Double Hydroxide,
22nd International Conference on Coordination and Bioinorganic Chemistry,
Smolenice, Slovakia, June 7-12, 2009.

D.F. Srankó, M. Sipiczki, A. Pallagi, É. Bajnóczi, I. Pálinkó, and P. Sipos,
Preparation Pathways for the Synthesis of Layered Double Hydroxides Containing Alkaline Earth Metal Ions and Iron(III),
32nd Symposium of Young Hungarian Chemists, Szeged, Hungary, October 26-28, 2009.

U. Starke, C. Virojanadara, M. Hetzel, L.I. Johansson, and W.J. Choyke,
Electronic and atomic structure of the 4H-SiC(1102) surface: One-dimensional surface states, adatom chains and dimer reconstruction patterns,
14th International Conference on Solid Films and Surface (ICSCF), Dublin, Ireland, June 29 - July 4, 2008.

U. Starke, C. Riedl, J. Bernhardt, M. Franke, K. Heinz, A.A. Zakharov, L. Vitali, R. Ohmann, I. Brihuega, K. Kern, D.S. Lee, B. Krauß, K.v. Klitzing, J. Smet, C. Coletti, I. Gierz, and C.R. Ast,
Structural and Electronic Properties of Epitaxial Graphene on SiC(0001),
55th AVS international symposium, Boston, New York, USA, October 19-24, 2008.

U. Starke,
Growth, characterization, molecular doping and bandstructure engineering of epitaxial graphene on SiC(0001),
3rd International Workshop on Physics and Technology of Thin Films, (IWTV3),
Espoo, Finland, August 26-28, 2009.

U. Starke,
Epitaxial graphene on SiC: Structure and electronic properties,
22nd International Microprocesses and Nanotechnology Conference (MNC2009),
Sapporo, Japan, November 16-19, 2009.

H.I. Starnberg,
Photoemission study of calcium adsorption on surfaces of layered transition metal dichalcogenides,
11th International Conference on Electronic Spectroscopy and Structure (ICESS-11)
Nara, Japan, October 6-10, 2009.

H.I. Starnberg, M. Kalläne, K. Rossnagel, M. Marczynski-Bühlow, S.E. Stoltz, and L. Kipp,
New bonding mechanism in misfit layer compounds,
11th International Conference on Electronic Spectroscopy and Structure (ICESS-11)
Nara, Japan, October 6-10, 2009.

K. Ståhl, C.G. Hartmann, C.B. Prag, S.R. Sørensen, A.C. Raffalt, S. Christgau, and E.T.A. Andersen,
Dehydration properties of strontium ranelate,
39th Danish Crystallographer Meeting, Lyngby, Denmark, June 2-3, 2009.

K. Ståhl, C.G. Hartmann, C.B. Prag, S.R. Sørensen, A.C. Raffalt, S. Christgau, and E.T.A. Andersen,
The crystal structures of polymorphs of strontium ranelate,
25th European Crystallographic Meeting, Istanbul, Turkey, August 16-21, 2009.

J. Ståhlberg,
Molecular wood choppers: Structure/function studies of fungal cellobiohydrolases,
UMB, Ås, Norway, March 7, 2008.

J. Ståhlberg,
A twist on beta-glucans: Structure studies of substrate binding by Laminarinase Lam16A from the white-rot fungus Phanerochaete chrysosporium,
β-Xylosidases, Xylanases and other Plant Polysaccharide Degrading Enzymes,
Ghent, Belgium, December 1-2, 2008.

J. Ståhlberg,
Enzymatic saccharification of plant biomass,
Processing Biomass Course, Bioenergy Graduate School, Uppsala, Sweden, September 28 - October 2, 2009.

J. Ståhlberg,
Enzymes for Biofuel,
University of Tokyo/SLU Bioenergy Workshop, Uppsala, Sweden, September 29, 2009.

S. Surnev,
Low dimensional Mn-oxide structures on stepped Pd(100) surfaces,
COST D41 Workshop, London, United Kingdom, April 2-4, 2009.

S. Surnev,
One-dimensional NiO_2-Rh(553) hybrid structures: site specific enhanced reactivity for CO oxidation,
8th NFN Workshop Nanoscience on Surfaces, Schloss Seggau, Leibnitz, Austria, May 11-13, 2009.

S. Surnev,
Surface structure of nickel oxide layers on a Rh(111) surface,
26th European Conference on Surface Science (ECOSS-26), Parma, Italy, August 30 - September 4, 2009.

K.L. Syres, A.G. Thomas, W.R. Flavell, B. Spencer, and A. Preobrajenski,
Comparison of adsrption of pyrocatechol on anatase TiO_2 (101) and rutile TiO_2 (110) using photoemision and NEXAFS spectroscopy,
17th Interdisciplinary Surface Science Conference (ISSC-17), Reading, United Kingdom, March 30 - April 2, 2009.

C. Teichert, C. Hofer, Z. Seyidov, M.Á. Niño, N. Mikuszeit, E. Jiménez, J. Camarero, J.J. de Miguel, R. Miranda, T. Bobek, and H. Kurz,
Nanomagnet Arrays Fabricated on Ion Bombardment Induced Semiconductor Nanostructures,
European Workshop on Self-Organized Nanomagnets, Aussois, France, March 30 - April 3, 2009.

S. Thorin, N. Čutić, F. Lindau, S. Werin, and F. Curbis,
Characterization of the Beam from Thermionic RF-Gun Adapted for Photo Cathode Operation,
31st International Free Electron Laser Conference, Liverpool, United Kingdom, August 23-28, 2009.

M.M.G.M. Thunnissen, E. Nurmemmedov, and R. Yengo,
Probing the function of the individual zinc fingers of WT1 in DNA and RNA binding,
9th German Peptide Symposium, Göttingen, Germany, March 11-14, 2009.

R. Timm, M. Hjort, M.T. Borgström, A. Fian, E. Lundgren, L. Samuelson, and A. Mikkelsen,
Structural and electronic properties of InP nanowires across p-n-junctions, studied with scanning tunneling microscopy and X-ray photoemission,
3rd International Conference on One-dimensional Nanomaterials, (ICON2009),
Atlanta, Georgia, USA, December 7-9, 2009.

S. Torpenholt, J.-C.N. Poulsen, K.S. Johansen, and L. Lo Leggio,
Crystal structure of Paenibacillus ehimensis β-1,4-chitosanase,
8th Carbohydrate Bioengineering Meeting, Ischia, Italy, May 10-13, 2009.

Ch. Täschner, R. Klingeler, S. Klod, O.V. Molodtsova, L. Dunsch, M. Knupfer, N. Sato, and B. Büchner,
Hydrothermal synthesis of crystalline $LiMnPO_4$ nanopowder,
4th Lithium Batteries Discussion (LiBD-4), Arcachon, France, September 20-25, 2009.

I. Ulfat, J. Adell, J. Kanski, M. Leandersson, L. Ilver, and J. Kanski,
In-situ Characterization of (GaMn)As based structures at MAX-lab: Summary of Results & Future Plans,
National Conference on Physics and the World of Today, Karachi, Pakistan, December 16-17, 2009.

S. Urpelainen, M. Huttula, T. Balasubramanian, R. Sankari, P. Kovala, E. Kukk, E. Nõmmiste, S. Aksela, R. Nyholm, and H. Aksela,
FINEST: a high performance branch-line for VUV photon energy range gas phase studies at MAX-lab,
10th International Conference on Synchrotron Radiation Instrumentation (SRI-09),
Melbourne, Australia, September 27 - October 2, 2009.

T. Ursby, K. Larsson, M. Thunnissen, C. Svensson, J. Unge, D.T. Logan, M. Håkansson, Y. Cerenius, D. Haase, T. Plivelic, S. Carlson, and K. Norén,
Structural biology facilities at MAX-lab,
13th Annual conference of the Swedish Structural Biology Nework, Tällberg, Sweden, June 12-15, 2009.

L.E. Walle, J. Blomquist, A. Borg, and A. Sandell,
Lithium insertion in anatase TiO_2 films on Si(111) Studied by Synchrotron based Photoelectron Spectroscopy,
5th Norwegian Synchrotron User Meeting, Lillehammer, Norway, June 19-20, 2009.

Q. Wang, A. Pietzsch, F. Hennies, H. Ni, and Y. Chao,
Synthesis of Water dispersible Photoluminescent Silicon Nanoparticles and Their Use in Biological Fluorescent Imaging,
UK IOP Condensed Matter and Materials Physics Conference (CMMP09),
Warwick, United Kingdom, December 15-17, 2009.

D. Welner, H.A Ernst, A.N Olsen, K. Skriver, and L. Lo Leggio,
Structural characterization of ANAC019, a member of the NAC family of plant specific transcription factors,
CoLuAa XVIII, Bagsvaerd, Denmark, November 4-5, 2009.

S. Werin, N. Čutić, F. Lindau, S. Thorin, J. Bahrdt, K. Holldack, and C. Erny,
The Test FEL Facility at MAX-lab,
31st International Free Electron Laser Conference, Liverpool, United Kingdom, August 23-28, 2009.

M. Weser, Y. Rehder, A. Preobrajenski, Yu.S. Dedkov, and K. Horn,
XMCD studies of graphene on Ni(111) and Fe/Ni(111),
26th European Conference on Surface Science (ECOSS-26), Parma, Italy, August 30 - September 4, 2009.

M. Winkler, H. Bergersen, M. Abu-Samha, J. Harnes, A. Lindblad, L.J. Sæthre, and K.J. Børve,
Neutral Binary Clusters of CF_4/CH_4 Studied by X-ray Photoelectron Spectroscopy,
NANOMAT Conference 2009 and Satellite Meetings, Lillehammer, Norway, June 15-19, 2009.

M. Winkler, J. Harnes, A. Lindblad, M. Abu-Samha, L.J. Sæthre, and K.J. Børve,
A New Approach to Study Inelastic Scattering of Electrons in Free Nanoparticles,
11th International Conference on Electronic Spectroscopy and Structure (ICESS-11)
Nara, Japan, October 6-10, 2009.

C. Virojanadara, M. Syväjarvi, R. Yakimova, L.I. Johansson, A.A. Zakharov, and T. Balasubramanian,
High quality graphene growth on 6H-SiC(0001),
Materials Research Society, San Francisco, California, USA, April 14-16, 2009.

C. Virojanadara, M. Syväjarvi, R. Yakimova, L.I. Johansson, A.A. Zakharov, and T. Balasubramanian,
High quality graphene growth on 6H-SiC(0001),
International Conference on Materials for Advanced Technologies, Singapore, June 28 - July 3, 2009.

C. Virojanadara, M. Syväjarvi, R. Yakimova, L.I. Johansson, A.A. Zakharov, and T. Balasubramanian,
High quality graphene growth on 6H-SiC(0001),
10th International Conference on Atomically Controlled Surfaces, Interfaces and Nanostructures (ACSIN-10),
Granada, Spain, September 22-25, 2009.

D. Vlachos, S.D. Foulias, and M. Kamaratos,
Ultrathin barium oxide layers on nickel surface,
4th International Conference on Materials for Advanced Technologies (ICMAT 2007),
Singapore, July 1-6, 2007.

D. Vlachos, S.D. Foulias, and M. Kamaratos,
Barium adsorption on an oxygen chemisorbed O(2x1)/Ni(110) surface,
23rd Hellenic Conference on Solid State Physics & Materials Science, Athens, Greece, September 23-26, 2007.

S. Yu, S. Ahmadi, P. Palmgren, F. Hennies, M. Zuleta, and M. Göthelid,
Modification of charge transfer and energy level alignment on TiOPc-sensitized TiO_2(110) surface,
European Materials Research Society (EMRS), Strasbourg, France, June 8-9, 2009.

H. Zhang, J. Gustafsson, and L. Johansson,
Photoemission and NEXAFS Studies of PTCDA on Sn/Si(111)$\sqrt{3}\times\sqrt{3}$,
26th European Conference on Surface Science (ECOSS-26), Parma, Italy, August 30 - September 4, 2009.

Y. Zhan et al.,
Amplified spin polarization through exchange coupling at organic semiconductor/ferromagnet heterojunction,
2nd Topical Meeting on Spins in Organic Semiconductors, Salt Lake City, Utah, USA, February 4-7, 2009.

M. Zharnikov,
Charge transfer dynamics in self-assembled monomolecular films,
WE-Heraeus-Seminar Molecular and Organic Electronics: Briging the gaps,
Bad Honnef, Germany, January 26-29, 2009.

M. Zharnikov,
Self-assembled monomolecular films and their application for lithography,
Molecular Modification of Inorganic Surfaces for Nanomedicine, Pavia, Italy, February 8, 2009.

M. Zharnikov, O.M. Cabarcos, T. Weidner, S. Uppili, L.S. Dake, and D.L. Allara,
Embedded dipoles in monomolecular films: physical and electronic structure effects,
73rd DPG Spring Meeting, Symposium Organic Photovoltaics: From Single Molecules to Devices (SYOP),
Dresden, Germany, March 22-27, 2009.

M. Zharnikov,
Electron Beam Chemical Lithography with aliphatic monomolecular templates,
26th European Conference on Surface Science (ECOSS-26), Parma, Italy, August 30 - September 4, 2009.

M. Zharnikov,
Chemical Lithography and Nanofabrication with self-assembled molecular templates,
10th International Conference on Atomically Controlled Surfaces, Interfaces and Nanostructures (ACSIN-10), Granada, Spain, September 22-25, 2009.

Y. Znamenskaya, J. Engblom, and V. Kocherbitov,
Effect of Hydration on Structural Properties of Mucuous Gel,
Biofilms 5th Annual Workshop, Malmö, Sweden, October, 6-7, 2009.

Y. Znamenskaya, J. Engblom, J. Sotres, T. Arnebrant, and V. Kocherbitov,
Hydration on Structural Properties of Mucuous Gel, Dynamics, Steady State and Arrest,
9th Annual Surface and Colloid Symposium, Lund, Sweden, November 18-20, 2009.

M. Zuleta, S. Yu, S. Ahmadi, G. Boschloo, M. Göthelid, and A. Hagfeldt,
Comparative study of the adsorption of N719 on TiO_2(100) and TiO_2(101) by means of scanning tunneling microscopy,
European Materials Research Society (EMRS), Strasbourg, France, June 8-9, 2009.

S. Zweidinger et al.,
Heterogeneously Catalysed Process for HCl Oxidation over Stabilised RuO_2(110),
DPG Conference, Dresden, Germany, March 22-27, 2009.

S. Zweidinger et al.,
Heterogeneously Catalysed Process for HCl Oxidation over Stabilised Ruthenium Dioxide (110),
Bunsentagung der Deutschen Bunsen-Gesellschaft für Physikalische Chemie, Köln, Germany,
May 21-23, 2009.

MAX-lab

MAX-lab, Box 118, SE - 221 00 Lund
Visiting address: Ole Römers väg 1, Lund
Phone: +46 (0) 46 222 98 72, Fax: +46 (0) 46 222 47 10
E-mail: maxlab@maxlab.lu.se or
firstname.lastname@maxlab.lu.se
www.maxlab.lu.se